

申 报	系列：教师系列 教学科研并重 型
	专业：材料科学 与工程
	职称：教授

## 业绩成果材料

（申报人的业绩成果材料包括论文、科研项目、获奖以及其他成果等）

单 位（二级单位） 材料与化学工程学院

姓 名 胡超凡

材料核对人：

单位盖章：

核对时间：

华南农业大学制

## 目 录

### 一、教学研究业绩

1. 校级教改项目：新农科背景下的《无机及分析化学》教学改革与实践项目的立项通知及有关佐证材料 ..... 1
2. C 类教改论文：碳点与硼氮氧化物复合材料的制备及表征——化学、材料相关专业研究性综合实验设计，化学通报，2025, 88 (10), 1117 (附检索证明) ..... 5

### 二、科研项目

#### 1. 主持:

1.1 碳点/氧化物复合长余辉材料多发射中心形成机制及性能调控研究（国家自然科学基金面上项目，52472160）有关佐证材料 ..... 17

1.2 缺陷对碳点/氧化硼复合材料长余辉发光性能的调控机理研究（广东省自然科学基金面上项目，2025A1515010658）有关佐证材料 ..... 22

1.3 杂原子掺杂对氧化硼基质-碳点余辉能量传递的调控机理研究（广东省自然科学基金面上项目，2023A1515012003）有关佐证材料 ..... 25

1.4 具有聚集诱导发光特性的碳点的合成、表面改性和生物成像应用（广东省自然科学基金面上项目，2020A1515010443）有关佐证材料 ..... 28

#### 2. 主参:

2.1 缺陷对碳点长余辉发光的调控和作用机制（国家自然科学基金面上项目，12174119，排名第二）有关佐证材料 31

2.2 光波频率对烟草吸收特性与有效成分释放特性的研究



(横向课题, xh20250718, 排名第二) 有关佐证材料.... 33

### 三、论文、著作等

1. 检索证明 ..... 37

2. 以通讯作者发表本专业论文情况

2.1. Hydrophobic carbon dots with blue dispersed emission and red aggregation-induced emission, *Nature Communications*, 2019, 10, 1789. .... 46

2.2. Construction of Carbon Dots with Color-Tunable Aggregation-Induced Emission by Nitrogen-Induced Intramolecular Charge Transfer, *Advanced Materials*, 2021, 33. 2104872. .... 57

2.3. A universal strategy for activating multi-color room temperature afterglow of carbon dots in boric acid matrix. *Angewandte Chemie International Edition*, 2019, 58, 7278-7283. .... 68

2.4. High-Efficiency Solid-State Luminescence from Hydrophilic Carbon Dots with Aggregation-Induced Emission Characteristics. *Advanced Functional Materials*, 2023, 2207296. .... 74

2.5. Calcination temperature tuning of RTP and TADF with wide range of emission color from carbon dots confined in Al<sub>2</sub>O<sub>3</sub>, *Chemical Engineering Journal*, 2023, 474, 145597..... 85

2.6. Carbon dots as protective agent alleviating abiotic stresses on rice (*Oryza sativa* L.) through promoting nutrition assimilation and defense system. *ACS Applied Materials & Interfaces*, 2020, 12, 33575-33585. .... 96

2.7. Time-Dependent Room-Temperature Afterglow of

Carbon Dots Constructed by Trap-Induced Multiemission Centers. <i>Nano Letters</i> , 2025, 25, 6993-7002.....	107
2.8. Multiemissive Room-Temperature Phosphorescent Carbon Dots@ZnAl <sub>2</sub> O <sub>4</sub> Composites by Inorganic Defect Triplet-State Energy Transfer. <i>ACS Applied Materials &amp; Interfaces</i> , 2021, 13, 34705-34713. ....	117
2.9. Multicolor Afterglow from Carbon Dots: Preparation and Mechanism, <i>Small Methods</i> , 2024, 8.....	126
2.10. Energy Transfer Mediated Enhancement of Room-Temperature Phosphorescence of Carbon Dots Embedded in Matrixes, <i>Advanced Optical Materials</i> , 2021, 2100704. ....	151
2.11. Cascade Resonance Energy Transfer for the Construction of Nanoparticles with Multicolor Long Afterglow in Aqueous Solutions for Information Encryption and Bioimaging, <i>Advanced Optical Materials</i> , 2022, 2102666.....	160
2.12. Self-quenching-resistant red emissive carbon dots with high stability for warm white light-emitting diodes with a high color rendering index, <i>Advanced Optical Materials</i> . 2020, 2000251. ....	169
2.13. pH-responsive carbon dots with red emission for real-time and visual detection of amines. <i>Journal of Materials Chemistry C</i> , 2020, 8, 11563-11571.....	179
2.14. Efficient Preparation of Hydrophilic Boron Nitride Nanosheets for Human Heat Dissipation Applications, <i>ACS Applied Nano Materials</i> , 2024, 7, 11487-11497. ....	188
2.15. 前驱体结构调控策略制备碳点基多色室温磷光材料, <i>高等学校化学学报</i> , 2025, 46(6), 20240412.....	199

2.16. Room Temperature Long Afterglow from Boron Oxide: A Boric Acid Calcined Product, <i>Materials Letters</i> , 2020, 276, 128226. ....	208
2.17. Morphology-controlled synthesis of molybdenum oxide with tunable plasmon absorption for photothermal therapy of cancer. <i>ChemNanoMat</i> , 2020, 6, 1407-1416. ....	212
2.18. Carbon Dots as Light Converter for Plant Photosynthesis: Augmenting Light Coverage and Quantum Yield Effect, <i>Journal of Hazardous Materials</i> , 2021, 410, 124534. ....	222
2.19. Effects and mechanisms of proanthocyanidins-derived carbon dots on alleviating salt stress in rice by multi-omics analysis, <i>Food Chemistry: X</i> , 2024, 101422. ....	233
2.20. Bingfu Lei, Dual-mode photochromic luminescence of carbon dots induced by photoinduced electron transfer, <i>SCIENCE CHINA Materials</i> , 2025, 10, 3591-3599. ....	243
2.21. Enhancement of fluorescence emission for tricolor quantum dots assembled in polysiloxane toward solar spectrum-simulated white light-emitting devices. <i>Small</i> , 2019, 16, 1905266. ....	252
2.22. Anchoring Carbon Nanodots onto Nanosilica for Phosphorescence Enhancement and Delayed Fluorescence Nascence in Solid and Liquid States, <i>Small</i> , 2020, 2005228. ....	260
2.23. A review on the effects of carbon dots in the plant system. <i>Materials Chemistry Frontiers</i> , 2020, 4, 437-448. ....	270
2.24. Red, green and blue aggregation-induced emissive carbon dots. <i>Chinese Chemical Letters</i> , 2021. 32, 3927-3930. ....	282

2.25. Synthesis of dual-emissive carbon dots with a unique solvatochromism phenomenon, <i>Journal of Colloid and Interface Science</i> . 2019, 555, 607-614.....	286
2.26. Magnesium-nitrogen co-doped carbon dots enhance plant growth through multifunctional regulation in photosynthesis, <i>Chemical Engineering Journal</i> , 2021, 422, 130114. ....	294
2.27. Multifunctional carbon dots reinforced gelatin-based coating film for strawberry preservation, <i>Food Hydrocolloids</i> , 2024, 147, 109327. ....	304
2.28. Synthesis of silicon quantum dots with highly efficient full-band UV absorption and their applications in antiyellowing and resistance of photodegradation, <i>ACS Applied Materials &amp; Interface</i> , 2019, 11, 6634-6643. ....	317

## 四、科研成果

### 1. 科技奖励证书

1.1 新型碳材料微纳结构调控和性能研究，2021 年广东省自然科学二等奖 .....	327
---	-----

### 2. 知识产权

2.1. 专利授权证书：一种溶剂敏感的多模荧光碳量子点墨水及其制备方法和应用，授权，2019.01.30，中国，CN201910092285.9 .....	328
--	-----

2.2. 专利授权证书：一种红色固态荧光碳点及其制备方法和应用，授权，2019.01.30，中国，CN201910091560.5	329
---	-----

2.3. 专利授权证书：一种溶剂热法制备荧光氧化钨量子点的方法及其制备而成的荧光氧化钨量子点和应用，授权，	
---	--

2019.06.14, 中国, ZL201710501762.3 ..... 330

**五、其他业绩**

**1. 指导学生学科竞赛**

1.1. 2023 年广东省大学生材料创新大赛三等奖“氧化物缺陷对碳点室温长余辉发光的影响机制研究”..... 331

1.2. 2024 年广东省大学生材料创新大赛三等奖“缺陷诱导的时间依赖型变色长余辉材料”..... 332

1.3. 2025 年广东省大学生材料创新大赛三等奖“具有紫外、红光双模余辉发射的碳点/铝酸镁复合材料”..... 333

1.4. 2025 年广东省大学生材料创新大赛三等奖 “新型碳点基双介质光致变色材料的合成和多功能应用研究”..... 334





# 关于公示2025年度校级本科教学质量与教学改革工程项目拟立项名单的通知

来源单位及审核人：      编辑：      审核发布：本科生院（招生办公室）      发布时间：2025-09-25

各学院、部处、各单位：

根据《关于开展2025年度校级本科教学质量与教学改革工程项目申报工作的通知》精神,经项目负责人申报、所在单位推荐和学校组织专家评审或本科生院审核等程序，拟立项“基于OBE理念的‘数字赋能、思政融合、产教协同’的《制药设备与工艺设计》课程育人模式研究与实践”等127个项目为2025年度校级本科教学改革项目；拟立项“农林院校‘智能建造’人才特色班”等52个项目为2025年度校级本科质量工程项目。现予以公示，具体名单见附件。

公示期自2025年9月25日至9月29日。如有异议，请在公示期内以书面方式提交至行政楼329房（附必要的证据材料，并署真实姓名），未署真实姓名或逾期者不予受理。

- 附件：1.  2025年度校级本科教学改革拟立项名单.xlsx
2.  2025年度校级本科质量工程拟立项名单.xls

62	60	教学改革项目	人工智能赋能基因工程智慧教学模式改革	自筹	生命科学学院	陈亮
63	61	教学改革项目	AI赋能“新农科”背景下植物生理学课程改革的探索与应用	自筹	生命科学学院	刘宇婷
64	62	教学改革项目	学科交叉融合助推卓越农林人才培养 ——以传感器与检测技术课程为例	自筹	工程学院	黄培奎
65	63	教学改革项目	基于AI赋能的《机械制造基础》课程“三位一体”贯通式教学改革与实践	自筹	工程学院	曹亚超
66	64	教学改革项目	“AI+教学”模式下控制理论课程思政教学体系构建与实践	自筹	工程学院	邢航
67	65	教学改革项目	基于OBE理念的混合AI智慧教学模式在机械制造工艺学和夹具设计课程中的应用与实践探索	自筹	工程学院	黄光文
68	66	教学改革项目	科研反哺教学在《食品包装学》课程中的探索与实践	自筹	食品学院	葛文娇
69	67	教学改革项目	虚拟仿真实验技术在“食品微生物检验实验”教学中的应用探索	自筹	食品学院	邹苑
70	68	教学改革项目	城市更新导向的智能数字化城市设计课程教学体系改革研究	自筹	水利与土木工程学院	屈寒飞
71	69	教学改革项目	基础工程学生可以带手机的课程考核改革实践探索	自筹	水利与土木工程学院	黄金林
72	70	教学改革项目	以智能建造为目标的土木工程专业升级转型及实践研究	自筹	水利与土木工程学院	杨雨冰
73	71	教学改革项目	AI/CG赋能的《造型设计基础》课程教学改革研究	自筹	材料与能源学院	鲁群霞
74	72	教学改革项目	“AI赋能-产教融合-思政贯通”导向的《胶合材料学（双语）》新工科教学改革与实践	自筹	材料与能源学院	樊奇
75	73	教学改革项目	基于构建科学素养的无机及分析化学习题课线上线下混合式教学探索	自筹	材料与能源学院	彭一鸣
76	74	教学改革项目	新农科背景下的《无机及分析化学》教学改革与实践	自筹	材料与能源学院	胡超凡
77	75	教学改革项目	《Z世代大学生心理健康教育课程创新研究—短视频与亚文化影响的教育应对》	自筹	数学与信息学院、软件学院	余丹华
78	76	教学改革项目	AI背景下“线上线下”教学模式在计量经济学理论和实践教学中的应用研究	自筹	数学与信息学院	彭泓毅
79	77	教学改革项目	课程思政视域下的《数字电路与逻辑设计》课程建设的探索与实践	自筹	数学与信息学院	崔金荣
80	78	教学改革项目	AI赋能信息系统开发实践课教学创新研究	自筹	数学与信息学院	邓成剑
81	79	教学改革项目	可视化微积分助力智慧课程建设	自筹	数学与信息学院	马立华
82	80	教学改革项目	AI赋能《数据结构》教学重构：基于DeepSeek的实践	自筹	数学与信息学院	杨秋妹
83	81	教学改革项目	AI背景下统计学专业课程的教学方式变革研究	自筹	数学与信息学院	杨志程
84	82	教学改革项目	《大学生创新创业基础》课程教学方式方法改革研究	自筹	电子工程学院（人工智能学院）	刘永明

# 华南农业大学教育教学研究和改革项目

## 申 报 书

项目类别 实践性教改自筹项目

项目名称 新农科背景下的《无机及分析化学》教学改革与实践

项目负责人 胡超凡

职 称 副教授

手机号码 15521501455

所在单位 材料与能源学院（公章）

申报日期 2025 年 6 月 18 日

华南农业大学 本科生院 制

二 〇 二 五 年 五 月

## 申请者的承诺与成果使用授权

本人自愿申报华南农业大学教育教学改革项目，承诺对所填写的《申报书》所涉及各项内容的真实性负责，保证没有知识产权争议。课题申请如获准立项，在研究工作中，接受华南农业大学教务处及本人所在单位的管理，并对以下约定信守承诺：

1. 遵守相关法律法规。遵守我国著作权法和专利法等相关法律法规；遵守我国政府签署加入的相关国际知识产权规定。

2. 遵循学术研究的基本规范，恪守学术道德，维护学术尊严。研究过程真实，不得以任何方式抄袭、剽窃或侵吞他人学术成果，杜绝伪注、伪造、篡改文献和数据等学术不端行为；成果真实，不重复发表研究成果；维护社会公共利益，不以项目名义牟取不当利益。

3. 遵守华南农业大学教育教学改革项目有关管理规定以及华南农业大学财务规章制度。

4. 凡因项目内容、成果或研究过程引起的法律、学术、产权或经费使用问题引起的纠纷，责任由相应的项目研究人员承担。

5. 项目获批后务必按项目计划要求及时开展研究工作，确保研究工作如期完成。

6. 同意华南农业大学或其授权（委托）单位有权基于公益需要公布、使用、宣传《项目申请·评审书》内容及相关成果。

项目负责人（签章）：

2025 年 6 月 18 日

此页须手写签字后扫描成 PDF 电子版。



			产生的必不可少的差旅费用
5	咨询费	1000	用于咨询相关领域专家产生的专家咨询费
6	其他支出	0	无

六、单位意见

所在单位意见:

同意申报.



单位负责人 孙理超

2025 年 6 月 18 日

检索证明

根据委托人提供的论文材料，委托人华南农业大学材料与化学工程学院 胡超凡(学科类型:自然科学) 1 篇论文收录情况如下表。

序号	论文名称	发表刊物及发表的年月卷期/页码等	作者排名	论文等级	作者文中单位	收录情况	影响因子	中科院大类分区
1	碳点与硼氮氧化物复合材料的制备及表征——化学、材料相关专业研究性综合实验设计	化学通报(中英文) 出版年: 2025 出版日期: 2025-10-13 卷期: 88 10 页码: - 文献号: 文献类型: 期刊论文	第一作者、通讯作者	C类	华南农业大学材料与能源学院	北大核心	无	无

说明: 论文等级和中科院大类分区按《华南农业大学学位论文评价方案(试行)》划分。

报告免责声明: 如未盖章, 报告无效





ISSN 0441-3776  
CN 11-1804/O6  
<http://www.hxtb.org>

# 化学通报 (中英文)

## CHEMISTRY

# 10

第88卷  
2025

中国科学院化学研究所  
中国化学会

主 办





2025 年 10 月 第 88 卷 第 10 期



CHINESE  
CHEMICAL  
SOCIETY

## 目 次

### 进展评述

- 多肽基纳米递药体系靶向肿瘤治疗的研究进展 ..... 蔺兰兰 李鸿岩 张 红 甘 蓉 (1025)
- 聚集诱导发光有机小分子材料手印显现的研究进展 ..... 徐敏娜 李建军 李海燕 侯碧海 (1041)
- 盐湖提锂锰系离子筛结构调控与放大成型研究进展 ..... 刘孝燕 扎西措 常立坤 王东东 (1054)
- 碳点在重金属离子检测领域的研究进展 ..... 张小玉 赵冬梅 何 蒙 宋 阳 左宇飞 张明辉 (1065)
- 自由基脱羧 Giese 反应在天然产物全合成中的应用研究进展 .....
- ..... 周子谕 王思昀 胡依琳 洪明哲 章昱然 赵一凡 郇 勇 葛盼瑜 程 凯 (1075)

### 知识介绍

- 氢元素的新单质:金属氢假说的验证及技术的发展 ..... 李 猛 王美琼 袁振东 (1091)

### 研究论文

- 可注射性二甲双胍水凝胶微球修复骨缺损的研究 ..... 刘正伟 王岩松 翟 妍 董 浩 王永祥 (1098)
- 新型氧杂环丁烷衍生物的合成及体外抗肿瘤活性研究 .....
- ..... 刘 斌 徐小娜 仝红娟 朱周静 王艳娇 曹召勇 (1109)

### 化学教学

- 碳点与硼氮氧化物复合材料的制备及表征——化学、材料相关专业研究性综合实验设计 .....
- ..... 胡超凡 张晓琴 庄健乐 张学杰 刘应亮 (1117)
- 新旧两版有机化合物命名原则对比分析 ..... 孙志琴 刘 杰 武爱萍 徐变珍 (1126)

本期责任编辑 郇 慧 田艳文



## 化学教学

碳点与硼氮氧化物复合材料的制备及表征  
——化学、材料相关专业研究性综合实验设计

胡超凡\* 张晓琴 庄健乐 张学杰 刘应亮

(华南农业大学材料与能源学院 广州 510642)

**摘 要** 为推进化学、材料专业实验教学与学科前沿研究的深度融合,本文设计了一项以碳点(CDs)与硼氮氧化物(BNO)复合材料(CDs@BNO)的制备及表征为主题的研究性综合实验。实验围绕纳米复合材料制备技术,采用水热法和固相煅烧法制备碳点,并通过微波法制备 CDs@BNO 复合材料,系统开展材料形貌、结构及发光性质表征。教学设计强调科研思维训练与创新能力培养,通过实验方案优化、参数调控及发光机理探究等环节,使学生掌握荧光光谱、透射电镜、X 射线衍射、X 射线光电子能谱等现代分析技术。实践表明,该综合实验通过将前沿科研成果转化为教学项目,能够有效提升学生的材料设计能力、仪器操作水平及数据分析技能,同时通过固态发光猝灭问题的探索式研究,培养了学生解决复杂科学问题的创新思维,为新型功能材料相关课程的教学改革提供了有益借鉴。

**关键词** 碳点 硼氮氧化物 白光 LED 固态发光 研究性综合实验

Preparation and Characterization of Carbon Dots and Boron Nitrogen  
Oxide Composite Materials —— Research-Oriented Comprehensive  
Experiment Design for Chemistry and Materials-Related MajorsHu Chaofan\*, Zhang Xiaoqin, Zhuang Jianle, Zhang Xuejie, Liu Yingliang  
(College of Materials and Energy, South China Agricultural University, Guangzhou, 510642)

**Abstract** To promote the in-depth integration of experimental teaching in chemistry and materials with cutting-edge disciplinary research, this study designed a comprehensive investigative experiment centered on the preparation and characterization of carbon dots (CDs) and boron nitrogen oxide (BNO) composite material (CDs@BNO). The experiment focused on nanocomposite preparation techniques, employing hydrothermal or solid-phase calcination method for CDs and microwave-assisted synthesis for CDs@BNO composites, followed by systematic characterization of material morphology, structure, and luminescent properties. The instructional design emphasized training in scientific research thinking and cultivation of innovation capabilities. Through experimental scheme optimization, parameter adjustment, and exploration of luminescence mechanisms, students were guided to master modern analytical techniques including fluorescence spectroscopy, transmission electron microscopy, X-ray diffraction and X-ray photoelectron spectroscopy. Practical implementation demonstrated that this comprehensive experiment, by transforming frontier research achievements into pedagogical projects, effectively enhanced students' material design capabilities, instrumentation operation proficiency, and data analysis skills. Furthermore, exploratory investigations into solid-state luminescence quenching mechanisms fostered students' innovative thinking in solving complex scientific problems, providing valuable insights for educational reform in courses related to novel functional materials.

**Keywords** Carbon dots, Boron nitrogen oxide, WLED, Solid-state luminescent, Research comprehensive experiment

\* 联系人,胡超凡 男,博士,副教授,主要从事碳基发光材料研究,E-mail: thucf@scau.edu.cn

国家自然科学基金面上项目(52472160)和广东省自然科学基金面上项目(2025A1515010658)资助

2025-06-11 收稿,2025-07-24 接受



随着化学教育改革的深入推进,研究性综合实验设计已成为培养学生创新思维、科研素养和实践能力的重要途径<sup>[1-3]</sup>。近年来,有机-无机复合材料因其独特的物理化学性质及广泛的应用前景,成为化学、材料科学领域的研究热点<sup>[4,5]</sup>。碳点(Carbon dots, CDs)作为新兴的碳基纳米材料,具有合成简便、生物相容性好、光学性能可调等优势,在光电器件、生物成像、传感等领域展现出巨大潜力<sup>[6-8]</sup>。硼氮氧化物(Boron nitride oxide, BNO)因其高稳定性、优异的热导率和化学惰性,常被用作复合材料的载体或功能组分。两者的复合可结合碳点的功能特性与BNO的结构优势,实现性能协同增强,在光电功能器件中具有重要的应用潜力<sup>[9-11]</sup>。然而,现有研究多聚焦于单一材料的合成或单一性能的探索,缺乏对复合材料设计原理、制备工艺与结构-性能关联的系统性研究。在化学实验教学中,涉及纳米复合材料制备与表征的综合实验设计仍较为匮乏,学生难以通过实验深入理解材料复合的界面调控机制及多尺度表征方法。此外,传统实验内容与前沿科研的脱节问题显著,导致学生难以掌握材料设计的创新思维和跨学科技术整合能力。

基于此,本研究以“碳点与BNO复合材料的制备及表征”为核心,设计了一个贯穿材料合成、结构分析、性能测试的全链条研究性综合实验。实验内容探索绿色合成路径,采用水热法和固相煅烧法制备碳点,通过微波法合成复合材料;整合透射电镜(TEM)、X射线衍射(XRD)、X射线光电子能谱(XPS)等分析手段,解析复合材料的形貌、化学键合及晶体结构;通过荧光光谱和紫外可见吸收光谱,分析材料的发光性质和荧光增强机

理;通过热稳定性、光稳定性和色坐标测试等实验,探究复合材料在白光发光二极管(White light emitting diode, WLED)器件中的潜在应用。

本实验设计旨在通过跨学科(材料化学、纳米技术、分析化学)知识融合,培养学生从原料选择到工艺优化再到性能评价的系统科研思维,同时强化其对先进表征技术的实操能力。此外,实验设计中引入可持续材料和绿色合成理念,呼应“双碳”背景下的化学教育社会责任。通过这一教学实践,期望为化学相关专业提供兼具前沿性与实用性的综合实验案例,推动科研反哺教学的新型教育模式发展。

## 1 实验原理

如图1所示,本实验选择三种不同颜色的CDs,通过简单的微波加热策略复合到BNO基质中合成杂化复合材料CDs@BNO。微波反应时,硼酸和尿素发生脱水反应,形成BNO结构基质。碳点嵌入到BNO基质中,获得具有固态发光性质的CDs@BNO。进一步分析了选取CDs所需满足的条件,由于复合到基质时需要经过微波加热,因此CDs需具有良好的水溶性和热稳定性,经过加热后依旧能保持良好的发光。此外,单纯的BNO基质发射出紫外和蓝光波段的光,因此CDs的吸收带应重叠于BNO的发射波段,以满足CDs与BNO之间的能量传递,进而提高CDs的光致发光量子产率(Photoluminescence quantum yield, PLQYs)。因此,选取的这三种不同颜色CDs均在紫外和蓝光波段具有较强吸收。基于此合成策略,有望获得具有蓝色、绿色和橙色荧光的碳点基固态发光复合材料。

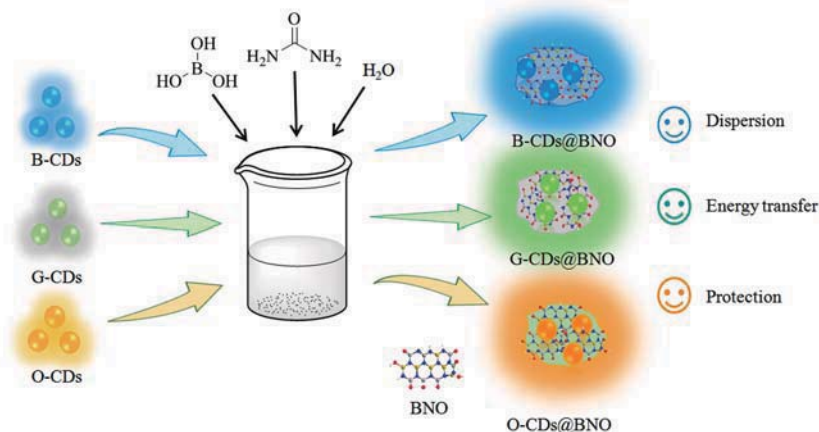


图1 三色荧光发射CDs@BNO材料的制备过程示意图

Fig. 1 Schematic diagram of the preparation process of three-color fluorescent CDs@BNO material



2 实验安排与流程

表 1 实验安排表

Tab. 1 The experimental arrangement

阶段	教学内容	教学目标
实验准备阶段	组建实验小组,查阅国内外相关文献	培养团队精神,提升文献检索能力
	实验原理的课堂讲解与实验室现场参观	强化理论知识,建立感性认识
	实验室安全培训	培养实验室安全意识
	实验方案设计、讨论及可行性分析	确立自主实验意识,培养科学精神
实验操作阶段	执行实验方案,观察实验现象,记录实验数据	培养良好的实验习惯,提升创新能力和科学精神
	分析实验结果,表征和测试材料性能	培养知识的综合应用能力,提升分析与解决问题的能力
	实验产品展示、评价及工艺改进	培养科学研究成果的表达能力
素质提高阶段	分析实验数据,总结实验规律	培养实验总结和归纳分析能力
	撰写实验报告,撰写研究性科技论文	培养论文写作能力及综合表达能力

3 实验部分

3.1 仪器与试剂

仪器:紫外-可见光吸收光谱仪、荧光光谱仪、瞬态荧光光谱仪、X 射线粉末衍射仪、透射电子显微镜、高分辨透射电子显微镜、X 射线光电子能谱、烘箱、玛瑙研钵、磁力搅拌器等。

试剂:L-半胱氨酸、柠檬酸、柠檬酸三钠、尿素、茚三酮、邻苯二胺、硼酸、N,N-二甲基甲酰胺等,均为市售分析纯级试剂。

3.2 实验步骤

3.2.1 荧光碳点的合成

蓝色荧光碳点(B-CDs)的合成<sup>[12]</sup>:将 0.83g 柠檬酸和 1g L-半胱氨酸加入 5mL 水中,在 70℃ 加热 12h,形成一层棕色浆料。将浆液转移到 20mL 聚四氟乙烯反应器中,200℃ 下反应 3h,得到酸性黑色物质。用 20mL 1mol/L 氢氧化钠中和酸性物质,离心(6000r/min,10min)后取上清液,再经过滤(0.22μm 滤膜)去除上清液中大颗粒碳材料,将滤液转移至透析袋(截留分子量 3500Da,下同)在去离子水中透析 48h 时,每 12h 换一次水,最后冷冻干燥得到固态 B-CDs。

绿色荧光碳点(G-CDs)的合成<sup>[13]</sup>:0.2g 柠檬酸铵和 0.2g 尿素放入玛瑙研研磨充分混合后,转移到坩埚,在 200℃ 加热 1h,反应后用 40mL 去离子水溶解,离心(10000r/min,10min)去除大颗粒,过滤(0.22μm 滤膜),将滤液转移至透析袋在去离子水中透析 48h,每 12h 换一次水,最后冷冻干燥得到固体 G-CDs。

橙色荧光碳点(O-CDs)的合成<sup>[14]</sup>:在 20mL 水中加入 0.16g 茚三酮和 0.324g 邻苯二胺,搅拌溶解。随后,将混合物转移到 50mL 聚四氟乙烯

反应器中,180℃ 下反应 12h。反应结束后,冷却至室温,离心(18000r/min,10min),过滤(0.22μm 滤膜),将滤液转移至透析袋在去离子水中透析 48h,每 12h 换一次水,最后冷冻干燥得到固体得到固态 O-CDs。

3.2.2 碳点与硼氮氧化物复合材料的合成

在配制好的 15mL B-CDs 溶液(0.03mg/mL)中加入 0.3g 尿素和 0.6g 硼酸,超声至混合均匀,将混合物倒入 250mL 烧杯,放入微波炉中高火加热 5min,最终得到固体产物 B-CDs@BNO。采用类似方法合成 G-CDs@BNO 和 O-CDs@BNO。

3.2.3 WLED 的构建

工作电压为 10V、最大功率为 10W 的 UVLED 芯片由广宏光电科技(深圳)有限公司研制。这些芯片是 LED 灯的激发光源。三种颜色的产品用玛瑙砂浆研磨成粉末。采用分层覆盖的方法,将 B-CDs@BNO 均匀分散在 AB 胶中(体积比 1:1),然后覆盖在 UV LED 芯片上。待固化后,将 UV LED 芯片依次覆盖绿色层(G-CDs@BNO)和橙色层(O-CDs@BNO),最终制备了 WLED。

3.3 结果与讨论

3.3.1 CDs@BNO 的结构和形貌表征与分析

通过 TEM 和高分辨率透射电子显微镜(HRTEM)对 CDs 和 CDs@BNO 复合材料的尺寸和形貌进行表征。在图 2(a)中,TEM 图像显示,B-CDs 粒径大小分布在 3.0~6.0 nm 范围内,HRTEM 图像中显示,该 B-CDs 的晶格间距为 0.21nm,与石墨烯(100)平面相对应,这表明 B-CDs 含有类石墨结构<sup>[15]</sup>。如图 2(c)所示,可以清晰地看到 B-CDs 成功复合到 BNO 基质中。G-CDs 和 O-CDs 的粒径大小分别分布在 1.0~3.0 和 2.4~5.1 nm 范围,晶格间距均为 0.21nm,表



明有机小分子的原材料在高温碳化和脱水形成石墨化结构(图 2(d) 和 2(g))。从图 2(f) 和 2(i)

可以清晰观察到 G-CDs 和 O-CDs 嵌入到 BNO 基质中。

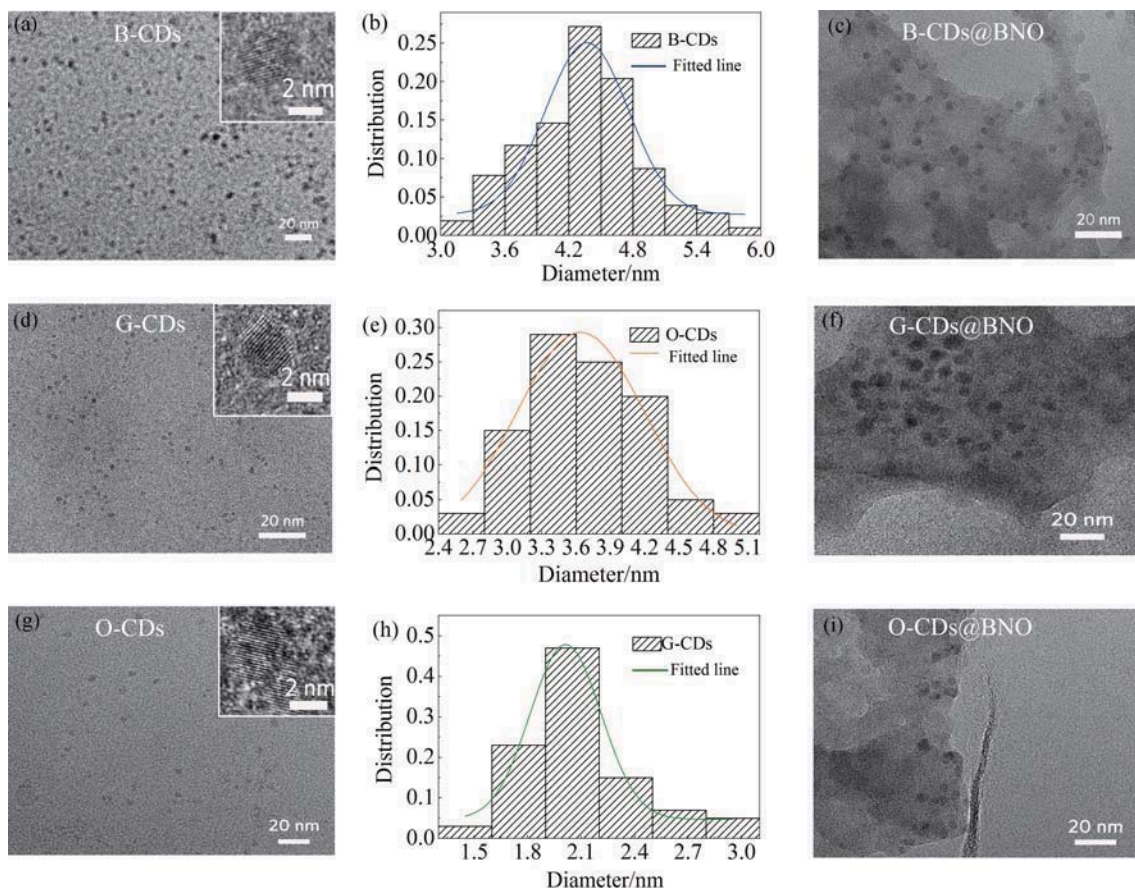


图 2 (a) B-CDs 的 TEM 图像(插图: B-CDs 的 HRTEM 图像); (b) B-CDs 的粒径分布图; (c) B-CDs@BNO 的 TEM 图像; (d) G-CDs 的 TEM 图像(插图: G-CDs 的 HRTEM 图像); (e) G-CDs 的粒径分布图; (f) G-CDs@BNO 的 TEM 图像; (g) O-CDs 的 TEM 图像(插图: O-CDs HRTEM 图像); (h) O-CDs 的粒径分布图; (i) O-CDs@BNO 的 TEM 图

Fig. 2 (a) TEM images of B-CDs (Insert: the related size distribution and HRTEM images of B-CDs); (b) TEM images of B-CDs@BNO; (c) TEM images of G-CDs (Insert: the related size distribution and HRTEM images of G-CDs); (d) TEM images of G-CDs@BNO; (e) TEM images of O-CDs (Insert: the related size distribution and HRTEM images of O-CDs); (f) TEM images of O-CDs@BNO

通过 XRD 对 CDs@BNO 的晶体结构进行表征分析。由图 3(a) 可知, 在  $25^\circ$  附近有明显的无定型峰, 这归因于石墨化结构的非晶态<sup>[15]</sup>。除无定型峰外, CDs@BNO 的其他峰也可以归因于尿素(JCPDS No. 000-31-1979), 证明未反应的尿素覆盖在产物表面。B-CDs@BNO、G-CDs@BNO、O-CDs@BNO 产物的硬度依次降低, 这与 XRD 图显示的产品表面尿素含量相对应, 即表面尿素越多, 产品越硬。由图 3(b) 可知, B-CDs@BNO、G-CDs@BNO、O-CDs@BNO 的 XPS 谱图中均包含  $B_{1s}$ 、 $C_{1s}$ 、 $N_{1s}$ 、 $O_{1s}$  四种元素。从图 3(c~e) 可见, N-B-O 和  $B_2O_3$  的  $B_{1s}$  的高分辨率 XPS 谱图显示出约为 192.6 eV 和 193.2 eV 的两个峰, 在

192.6 eV 处的信号表明硼原子被氮原子和氧原子包围, 即样品中存在 BNO 基质<sup>[9]</sup>。上述结果表明, CDs 均匀地分散在硼碳键连接的 BNO 基质中。

### 3.3.2 CDs@BNO 光学性能及荧光增强机理分析

通过荧光光谱对产物的发光性质进行了测试和分析。如图 4(a) 所示, B-CDs@BNO、G-CDs@BNO 和 O-CDs@BNO 粉末在 365 nm 紫外线激发时相比相应的 CDs 水溶液呈现出更亮的蓝色、绿色和橙色荧光, 说明 CDs 组装到 BNO 基质后实现了荧光增强。为了进一步证实荧光强度的增强, 在相同的最佳激发下, 对 CDs@BNO 和分散相



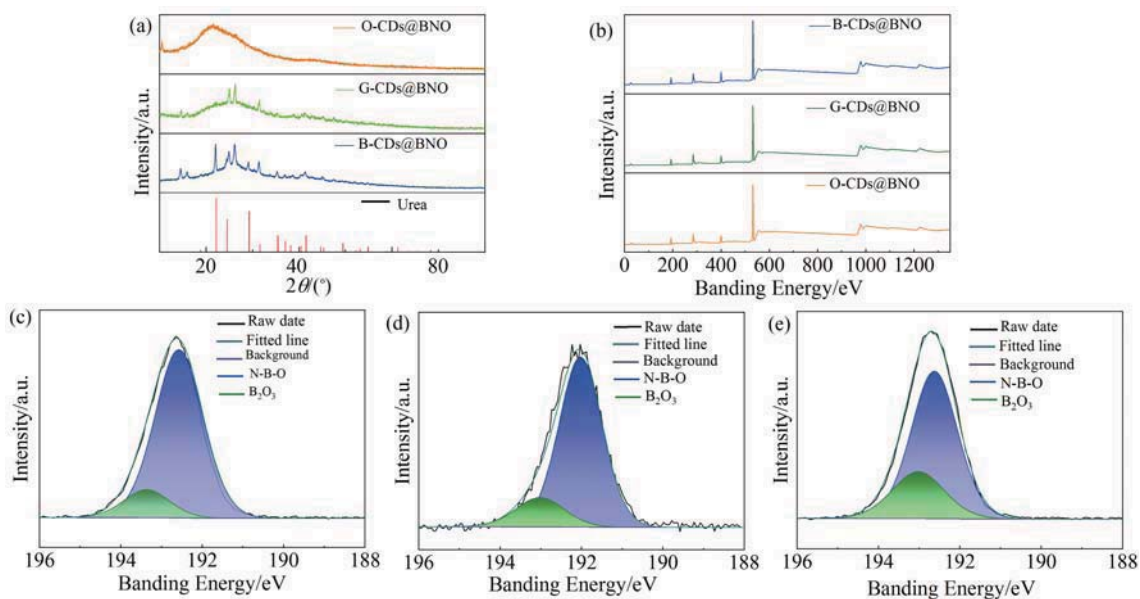


图 3 (a) B-CDs@BNO、G-CDs@BNO、O-CDs@BNO 的 XRD 图谱; (b) B-CDs@BNO、G-CDs@BNO、O-CDs@BNO 的 XPS 图谱; (c-e) B-CDs@BNO、G-CDs@BNO、O-CDs@BNO 的 XPS B1s 能谱

Fig. 3 (a) X-ray diffraction (XRD) pattern of B-, G-, O-CDs@BNO. (b) XPS spectra of B-, G-, O-CDs@BNO. (c-e) High-resolution XPS spectra of B 1s of B-, G-, O-CDs@BNO

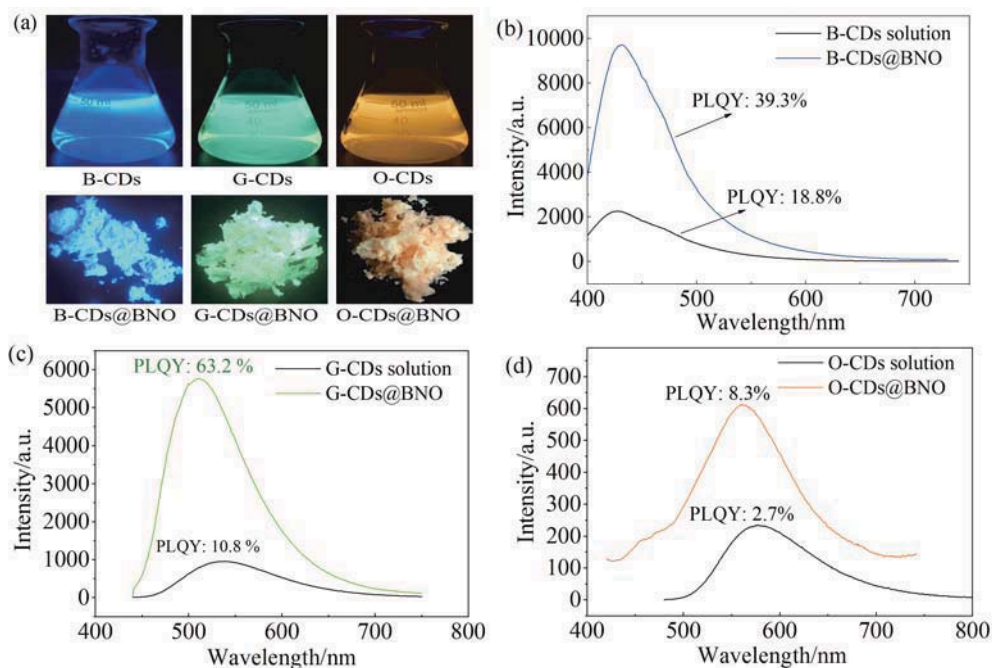


图 4 (a) UV 光照下产物的图像; (b~d) B-CDs@BNO、G-CDs@BNO 和 O-CDs@BNO 粉末与相应 CDs 溶液的荧光光谱对比

Fig. 4 (a) The photographs under UV illumination, and (b~d) the fluorescence spectra of B-CDs@BNO, G-CDs@BNO, and O-CDs@BNO powders compared with the corresponding CDs solutions, respectively

同浓度 CDs 的水分散液进行光致发光 (Photoluminescence, PL) 强度测试, 结果发现 CDs @ BNO 的荧光强度远高于水分散液。B-CDs@BNO、G-CDs@BNO 和 O-CDs@BNO 的 PLQYs 分别为 39.2%、63.2% 和 8.3%, 在水溶液中相应 PLQYs 分别为 18.8%、10.8% 和 2.7%, 即 CDs 掺

杂到 BNO 基质后, B-CDs@BNO、G-CDs@BNO 和 O-CDs@BNO 的 PLQYs 分别增加了约 2.1 倍、5.9 倍和 3.1 倍(图 4(b~d))。此外, 由图 4(c, d) 可知, 复合材料的波长相比碳点发生了轻微的蓝移, 其原因主要是碳点的荧光发射主要源自于其表面结构, 当碳点被包埋 BNO 基质中, 基质与碳点

存在氢键和共价键作用,使得碳点表面的化学结构发生变化,进一步导致其带隙增大,发射波长发生轻微的蓝移。

BNO 增强 CDs 的 PLQYs 的机理图如图 5 所示,CDs 的激发光谱曲线与 BNO 的发射光谱曲线有很大的重叠(图 5(a~c)),主要集中在紫外和蓝光波段,说明 CDs 可以有效吸收 BNO 发射的光,通过基质与碳点之间的能量传递提升材料的 PLQYs(图 5(d~f))。为了满足激发带位于紫外

和蓝光区域,对于长波长发射的 O-CDs,其激发波长和发射波长之间的 Stokes 位移较大。本文选取的 B-CDs、G-CDs 和 O-CDs 的 Stokes 位移分别为 45、85 和 120 nm,逐渐增大。因此,选择这三种 CDs 有以下三个原因:(1) 它们的吸收带能够匹配 BNO 的发射波长;(2) 它们必须能够分散在水中,因为复合基质的是通过微波反应合成的;(3) 它们应具有良好的稳定性,经历高温微波反应后能够保持其发光特性。

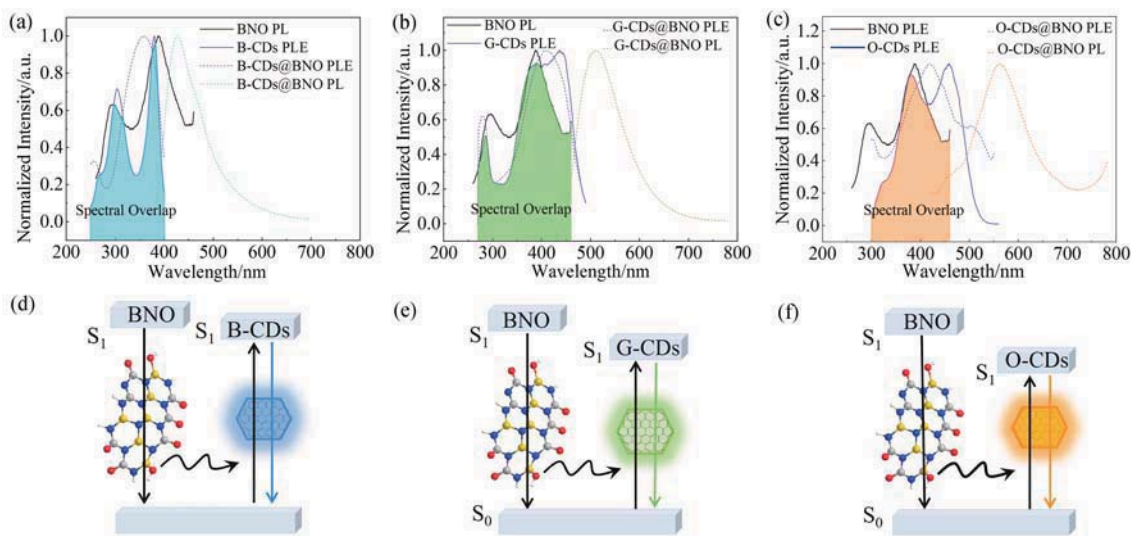


图 5 (a~c) BNO 的 PL 谱, B-CDs、G-CDs、O-CDs 的 PLE 谱以及 B-CDs@BNO、G-CDs@BNO、O-CDs@BNO 的 PLE 和 PL 谱;  
(d~e) 分别为 BNO 和 B-CDs、G-CDs、O-CDs 的能级图

Fig. 5 (a~c) The PL spectrum of BNO, the PLE spectrum of B-, G-, O-CDs and the PLE and PL spectrum of B-, G-, O-CDs@BNO; (d~e) The energy levels diagram of BNO and B-, G-, O-CDs, respectively

### 3.3.3 CDs@BNO 的稳定性研究

为了确定 CDs@BNO 是否适合用于构建 WLED, 本实验分别评估该材料的热稳定性和光稳定性。将 CDs@BNO 在不同温度下放置 30min, 自然冷却至室温后测试光致发光(PL)强度, 结果表明, B-CDs@BNO 在 190℃ 加热处理 30min 后, 仍能保持室温下 PL 强度的 90.2% (图 6(a))。G-CDs@BNO 的 PL 强度随温度升高而增大, 超过 170℃ 时才减小, 这是由于 G-CDs@BNO 比 B-CDs@BNO 松软, 加热后更加稳固, 因此 PL 强度比室温下高。在 190℃ 处理 30min 后, G-CDs@BNO 的 PL 强度可以达到室温 PL 强度的 120% (图 6(c)), 而 O-CDs@BNO 的 PL 强度为室温的 118% (图 6(e))。综上所述, 复合材料表现出优异的热稳定性。对于 LED 来说, 工作芯片一般不超过 110℃, 否则 LED 的 PL 衰减会非常快。因此, 三色 CDs@BNO 符合正常工作的 LED 器件的热稳定性要求。此外, 本实验对发光

材料的光稳定性进行了评价。如图 6(b, d, f) 所示, 样品在紫外线照射下连续照射 180min, CDs@BNO 的 PL 强度与初始强度相比变化不大, 表明它们具有良好的光稳定性。

### 3.3.4 CDs@BNO 在 WLED 器件中的应用

基于前述的表征和测试可知, 三种 CDs@BNO 复合材料具有覆盖整个可见区域的宽带发射, 并且表现出优异的热稳定性和光稳定性等特点, 适合于构建 WLED。本实验采用分层封装 WLED 技术, 根据 B-CDs@BNO 的最佳激发光谱, 选择 365nm 紫外芯片作为激发光源。如图 7(a~c) 所示, 由 B-CDs@BNO、G-CDs@BNO 和 O-CDs@BNO 构建的 LED 的 EL 光谱的色坐标(CIE)分别位于 (0.18, 0.15)、(0.29, 0.49) 和 (0.38, 0.45)。三种颜色发射 CDs@BNO 的色坐标连线构成的区域非常靠近白光区(图 7(d)), 因此通过调整三种颜色发射的 CDs@BNO 质量比, 可以获得 WLED。在图 7(e) 和 7(f) 中, 基于三色

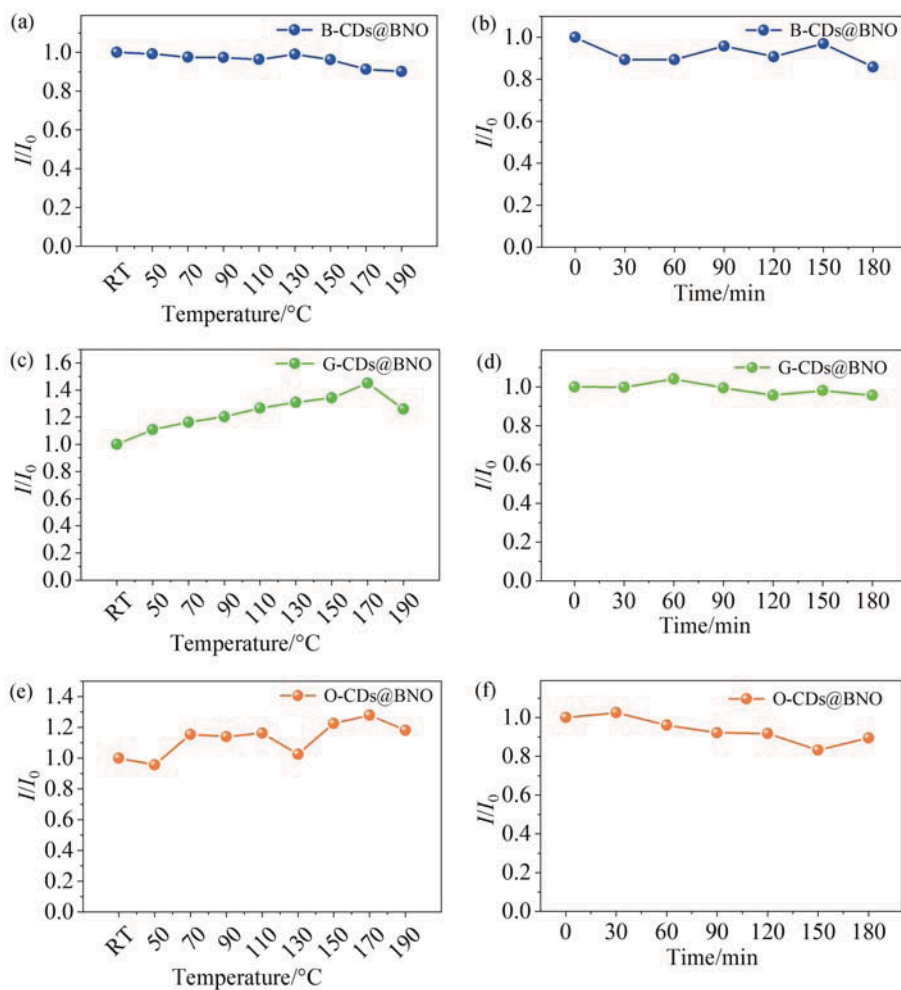


图 6 (a, c, e) B-CDs@BNO、G-CDs@BNO 和 O-CDs@BNO 荧光粉在不同温度下处理 30min 的相对 PL 强度;  
(b, d, f) B-CDs@BNO、G-CDs@BNO 和 O-CDs@BNO 荧光粉在连续紫外灯照射下不同时间的相对 PL 强度  
Fig. 6 (a, c, e) The integrated PL intensity of B-, G-, O-CDs@BNO phosphors at different temperatures for 30 min, respectively; (b, d, f) The integrated PL intensity of B-, G-, O-CDs@BNO phosphors at different time under continuous radiation with a UV lamp, respectively

CDs@BNO 构建的 WLED 的 CIE 为 (0.32, 0.36), 显色指数 (CRI) 为 80.1, 色温 (CCT) 为 6321K。以上结果表明, CDs@BNO 荧光粉在构建高显色指数 WLED 中具有应用潜力。然而, 碳点作为一种新型的发光材料, 在发光器件应用中仍然存在诸多不足之处, 主要体现在: (1) 大规模制备方法和高效分离手段的匮乏; (2) 发光量子效率与传统发光材料存在差距; (3) 光稳定性和热稳定性与商业应用荧光粉还存在差距。

### 3.3.5 实验小结

综上所述, 本实验采用简单微波加热的方法可将 CDs 复合到 BNO 基质中, 合成了多色固态荧光材料。与相应的三色 CDs 相比, B-CDs@BNO、G-CDs@BNO 和 O-CDs@BNO 的 PLQY 性能分别提高了 2.1、5.9、3.1 倍。对 CDs 复合到 BNO 基

质中实现荧光增强的机理进行了分析, 发现 CDs 能够有效地分散在 BNO 基质中, 基质的阻隔效应可以避免 CDs 聚集引起的猝灭, BNO 基质的刚性结构有效地防止了 CDs 在旋转或振动过程中产生的能量损失, BNO 与 CDs 之间发生能量传递作用可以实现 CDs 的荧光增强。CDs@BNO 具有良好的热稳定性和光稳定性, 基于三种复合材料构建的 WLED 器件表现出较高的显示指数和较低的色温, 在 WLED 构建中具有潜在的应用价值。

在实验教学过程中, 通过分析各小组实现情况, 发现学生在上述材料合成和表征过程中容易在以下几个方面出现问题: (1) 在透析纯化的过程中没有按照操作规程按时换水, 导致未反应原料的残留; (2) 碳点前驱体在反应前未充分混匀导致产物发光性质发生变化; (3) 透射电镜制样



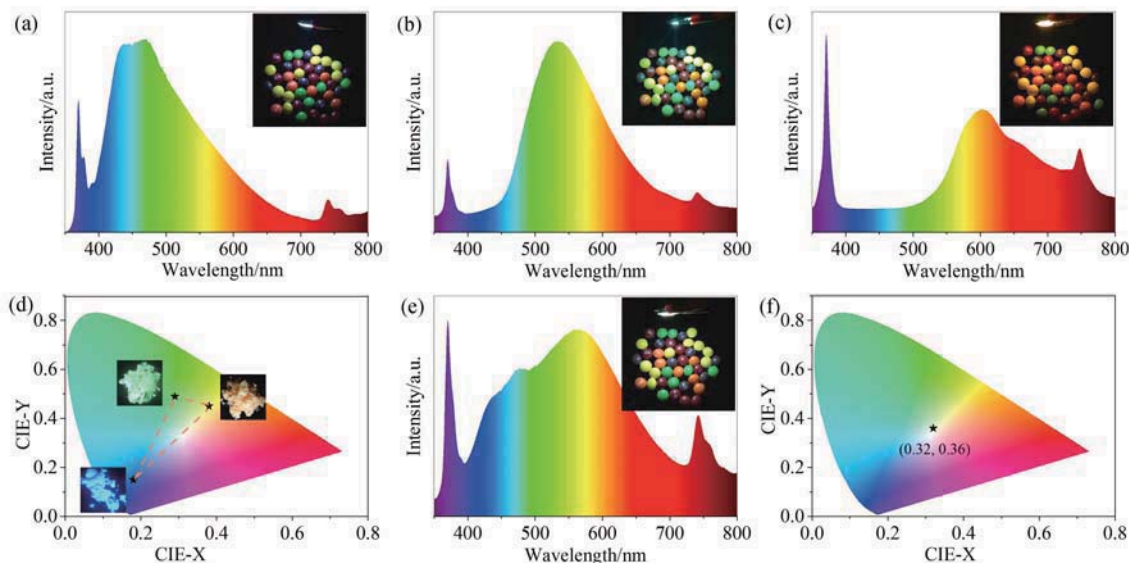


图 7 (a~c) 基于不同 CDs@BNO 复合材料分别和 LED 芯片构建单发射型 LED 的 EL 光谱及其 LED 的工作照片;  
(d) B-CDs@BNO、G-CDs@BNO、O-CDs@BNO 粉末的色坐标 CIE; (e) 基于 B-CDs@BNO、G-CDs@BNO、O-CDs@BNO 粉末和  
紫外芯片共同构建 WLED 的 EL 谱图及工作照片; (f) WLED 的色坐标 CIE

Fig. 7 (a~c) The photoluminescence spectrum of single emissive LED coating B-CDs@BNO, G-CDs@BNO, O-CDs@BNO powders, respectively, and their photographs inset of figures; (d) CIE 1931 chromaticity coordinates diagram of B-CDs@BNO, G-CDs@BNO, O-CDs@BNO powders; (e) The photoluminescence spectrum of white LED coating B-CDs@BNO, G-CDs@BNO, O-CDs@BNO powders and the photograph inset of figure; (f) CIE 1931 chromaticity coordinates diagram of white LED

时,样品浓度控制不对,导致电镜观察时无法找到样品或者拍摄效果不佳。

### 3.4 实验拓展

#### 3.4.1 实验研究内容的拓展

(1)在现有 CDs 与 BNO 复合体系基础上,可引入新型纳米发光材料或功能基质,进一步探究发光材料与基质之间的相互作用的普遍规律;(2)对现有的合成方法进行创新和优化,探究通过一步合成法精简合成步骤,通过优化碳点前驱体类型及反应条件,分析其对复合材料发光性能的作用规律,提升复合材料的量子效率;通过基质结构的优化,提升碳点在发光器件应用中的长效稳定性;(3)除固态发光性能外,实验过程中还观察到该体系的长余辉特性,通过进一步的性能测试和研究,拓展该类材料防伪、信息加密等领域的应用。

#### 3.4.2 以科研创新为导向的项目延伸

鼓励学生参与成果转化实践,将 CDs@BNO 的荧光增强方法申请专利,并在此基础上与企业开展横向课题研究,联合企业试制高显色指数 WLED 照明产品;组织学生参加“广东省大学生材料创新大赛”、“挑战杯”等赛事,以实验成果为基础设计创新方案,提升科研转化意识。

通过上述拓展设计,实验教学可突破传统模式,形成“基础-创新-应用”的进阶培养路径。学生不仅能掌握跨学科技术整合能力,还能在真实科研场景中锤炼解决问题的创新思维,为化学及相关专业的教学改革提供更具前瞻性的实践案例。

## 4 结语

通过持续的教学改革实践发现,研究性综合实验教学模式在创新型人才培养方面成效显著。本文构建的跨学科实验体系深度融合材料科学与工程、材料化学、应用化学等专业的核心理论,形成了涵盖材料制备、结构表征、性能测试及数据分析的完整科研训练闭环。教学实践表明,该模式通过“基础强化-实践深化-素养提升”三阶段渐进式培养体系,有效实现了三个维度的突破:从知识建构维度,项目驱动的学习方式促使学生主动构建专业知识网络,通过文献研读、方案论证等环节深化对材料化学基础理论的理解;在实践能力层面,学生经历从原料筛选、工艺优化到设备操作的完整流程,显著提升了实验设计与技术实施能力;科研素养方面,通过团队协作、数据分析及成果展示等环节的系统训练,培养了学生的批判性思维和学术表达能力。值得关注的是,本体系特别设



置的创新拓展模块,要求学生在完成基础实验后进行应用延伸研究。这种“验证-探究-创新”的进阶式培养路径,不仅强化了学生的知识迁移能力,更培育了其解决复杂工程问题的综合素质。

### 参 考 文 献

- [ 1 ] 郑明涛,卢其明,雷炳富等,化学通报,2018,81(6): 562~570.
- [ 2 ] 雷炳富,陈炜彬,张学杰等,化学通报,2021,84(10): 1114~1119.
- [ 3 ] 周子宁 张声森,陈敏等,化学通报,2020,83(9): 844~849.
- [ 4 ] Lebeau B, Innocenzi P. Chem. Soc. Rev., 2011, 40(2): 886~906.
- [ 5 ] Parola S, Julián-López B, Carlos L, et al. Adv. Funct. Mater., 2016, 26(36): 6506~6544.
- [ 6 ] Ran Z, Liu J, Zhuang J, et al. Small Methods, 2024, 8(1): 2301013.
- [ 7 ] Dorđević L, Arcudi F, Cacioppo M, et al. Nat. Nanotechnol., 2022, 17(2): 112~130.
- [ 8 ] Panwar N, Soehartono A, Chan K, et al. Chem. Rev., 2019, 119(16): 9559~9656.
- [ 9 ] Park M, Yoon H, Lee J, et al. Adv. Mater., 2018, 30(38): 1802951.
- [ 10 ] Park M, Kim H S, Yoon H, et al. Adv. Mater., 2020, 32(31): 2000936.
- [ 11 ] Jiang W, Liu L, Wu Y, et al. Nanoscale Adv., 2021, 3(15): 4536~4540.
- [ 12 ] Kalytchuk S, Poláková K, Wang Y, et al. ACS Nano, 2017, 11(2): 1432~1442.
- [ 13 ] Khan W, Wang D, Wang Y. Inorg. Chem., 2018, 57(24): 15229~15239.
- [ 14 ] Xu X, Hu G, Mo L, et al. Nanoscale, 2021, 13(14): 6846~6855.
- [ 15 ] Wan Z, Li Y, Zhou Y, et al. Adv. Funct. Mater., 2023, 33(11): 2207296.

# 国家自然科学基金资助项目批准通知

## ( 预算制项目 )

胡超凡 先生/女士：

根据《国家自然科学基金条例》、相关项目管理办法规定和专家评审意见，国家自然科学基金委员会（以下简称自然科学基金委）决定资助您申请的项目。项目批准号：52472160，项目名称：碳点/氧化物复合长余辉材料多发射中心形成机制及性能调控研究，直接费用：48.00万元，项目起止年月：2025年01月至2028年12月，有关项目的评审意见及修改意见附后。

请您尽快登录科学基金网络信息系统（<https://grants.nsfc.gov.cn>），**认真阅读《国家自然科学基金资助项目计划书填报说明》并按要求填写《国家自然科学基金资助项目计划书》（以下简称计划书）**。对于有修改意见的项目，请您按修改意见及时调整计划书相关内容；如您对修改意见有异议，须在电子版计划书报送截止日期前向相关科学处提出。

请您将电子版计划书通过科学基金网络信息系统（<https://grants.nsfc.gov.cn>）提交，由依托单位审核后提交至自然科学基金委。自然科学基金委审核未通过者，将退回的电子版计划书修改后再行提交；审核通过者，打印纸质版计划书（一式两份，双面打印）并在项目负责人承诺栏签字，由依托单位科研、财务管理等部门审核、签章并在承诺栏加盖依托单位公章，且将申请书纸质签字盖章页订在其中一份计划书之后，一并报送至自然科学基金委项目材料接收工作组。纸质版计划书应当保证与审核通过的电子版计划书内容一致。**自然科学基金委将对申请书纸质签字盖章页进行审核，对存在问题的，允许依托单位进行一次修改或补齐。**

向自然科学基金委提交电子版计划书、报送纸质版计划书并补交申请书纸质签字盖章页截止时间节点如下：

1. **2024年9月9日16点**：提交电子版计划书的截止时间；
2. **2024年9月16日16点**：提交修改后电子版计划书的截止时间；
3. **2024年9月23日**：报送纸质版计划书（一式两份，其中一份包含申请书纸质签字盖章页）的截止时间。
4. **2024年10月8日**：报送修改后的申请书纸质签字盖章页的截止时间。

请按照以上规定及时提交电子版计划书，并报送纸质版计划书和申请书纸质签字盖章页，逾期不报计划书或申请书纸质签字盖章页且未说明理由的，视为自动放弃接受资助；未按要求修改或逾期提交申请书纸质签字盖章页者，将视情况给予暂缓拨付经费等处理。

附件：项目评审意见及修改意见表

国家自然科学基金委员会

2024年8月23日



项目批准号	52472160
申请代码	E0207
归口管理部门	
依托单位代码	51064208A0499-0932



524721601006279

# 国家自然科学基金 资助项目计划书 (预算制项目)

资助类别: 面上项目

亚类说明:

附注说明:

项目名称: 碳点/氧化物复合长余辉材料多发射中心形成机制及性能调控研究

直接费用: 48万元

执行年限: 2025.01-2028.12

负责人: 胡超凡

BRID: 03609.00.23017

通讯地址: 广东省广州市天河区五山路483号

邮政编码: 510642

电话: 15521501455

电子邮件: hcf0000@126.com

依托单位: 华南农业大学

联系人: 唐家林

电话: 020-85280070

填表日期: 2024年08月25日

国家自然科学基金委员会制





简表

项目负责人信息	姓 名	胡超凡	性 别	男	出生年月	1984年08月	民 族	汉族
	学 位	博士			职称	副教授		
	是否在站博士后	否			电子邮件	hcf0000@126.com		
	电 话	15521501455			个人网页			
	工 作 单 位	华南农业大学						
	所 在 院 系 所	材料与能源学院						
依托单位信息	名 称	华南农业大学					代码	51064208A0499
	联 系 人	唐家林			电子邮件	kyc.jhk@scau.edu.cn		
	电 话	020-85280070			网站地址	http://kjc.scau.edu.cn/		
合作单位信息	单 位 名 称							
项目基本信息	项 目 名 称	碳点/氧化物复合长余辉材料多发射中心形成机制及性能调控研究						
	资 助 类 别	面上项目				亚 类 说 明		
	附 注 说 明							
	申 请 代 码	E0207:无机非金属半导体与信息功能材料				A2207:光谱学与固体发光		
	基 地 类 别							
	执 行 年 限	2025.01-2028.12						
	直 接 费 用	48万元						



项目组主要成员

编号	姓名	出生年月	性别	职称	学位	单位名称	电话	证件号码	项目分工	每年工作 时间 (月)
1	胡超凡	1984.08	男	副教授	博士	华南农业大学	15521501455	43102719840809001X	项目负责人	10
2	肖勇	1980.02	男	教授	博士	华南农业大学	02085280319	430524198002032415	材料的物化性质表征	6
3	郭晓仙	1990.10	女	实验师	硕士	华南农业大学	020-85280199	450331199010010348	材料的微观结构分析	6
总人数				高级	中级	初级	博士后		博士生	硕士生
11				2	1	0	0		2	6

受理编号: c25140500002417

项目编号: 2025A1515010658

文件编号: 粤基金字(2025)10号

# 广东省基础与应用基础研究基金项目 任务书

项目名称: 缺陷对碳点/氧化硼复合材料长余辉发光性能的调控机理研究

项目类别: 广东省自然科学基金-面上项目

项目起止时间: 2025-01-01 至 2027-12-31

管理单位(甲方): 广东省基础与应用基础研究基金委员会

依托单位(乙方): 华南农业大学

通讯地址: 广东省广州市天河区五山路483号

邮政编码: 510642

单位电话: 020-85283435

项目负责人: 胡超凡

联系电话: 15521501455



(广东科技微信公众号)



(查看任务书信息)



(受理纸质材料二维码)

广东省基础与应用基础研究  
基金委员会  
二〇二〇年制

## 五、人员信息

## 项目负责人

姓名	证件号码	年龄	性别	职称	学历	在项目中承担的任务	所在单位	签名
胡超凡	43102719840809001X	41	男	副教授	博士研究生	项目负责人	华南农业大学	胡超凡

## 项目组主要成员

姓名	证件号码	年龄	性别	职称	学历	在项目中承担的任务	所在单位	签名
胡航	513622198312120045	42	女	讲师	博士研究生	材料形貌和组成分析	华南农业大学	胡航
冉准	422802199807076012	27	男	未取得	本科	长余辉发光机理分析	华南农业大学	冉准
贾宏洁	120224199912085343	26	女	未取得	本科	碳点/氧化硼材料合成和反应条件优化	华南农业大学	贾宏洁
钟紫婷	440923200003270762	25	女	未取得	本科	材料组成和结构表征测试	华南农业大学	钟紫婷

## 八、本任务书签约各方

管理单位（甲方）：

广东省基础与应用基础研究基金委员会（盖章）

法定代表人（或法人代理）：

（签章）

2025 年 03 月 21 日

依托单位（乙方）：华南农业大学

法定代表人（或法人代理）：薛红卫

联系人（项目主管）姓名：夏杰

Email: kjcgxk@scau.edu.cn

电话：020-85283435 / 13711343768

开户单位名称：华南农业大学

开户银行名称：广东广州工行五山支行

开户银行账号：3602002609000310520

2025 年 4 月 9 日

联系人（项目负责人）姓名：胡超凡

（签名）

Email: thucf@scau.edu.cn

电话：15521501455

2025 年 4 月 9 日



受理编号: c23140500000319

项目编号: 2023A1515012003

文件编号: 粤基金字(2023)2号

## 广东省基础与应用基础研究基金项目 任务书

项目名称: 杂原子掺杂对氧化硼基质-碳点余辉能量传递的调控机理研究

项目类别: 广东省自然科学基金-面上项目

项目起止时间: 2023-01-01 至 2025-12-31

管理单位(甲方): 广东省基础与应用基础研究基金委员会

依托单位(乙方): 华南农业大学

通讯地址: 广东省广州市天河区五山路483号

邮政编码: 510642

单位电话: 020-85283435

项目负责人: 胡超凡

联系电话: 15521501455



(广东科技微信公众号)



(查看任务书信息)



(受理纸质材料二维码)

广东省基础与应用基础研究  
基金委员会  
二〇二〇年制



## 五、人员信息

## 项目负责人

姓名	证件号码	年龄	性别	职称	学历	在项目中承担的任务	所在单位	签名
胡超凡	43102719840809001X	39	男	副教授	博士研究生	项目负责人	华南农业大学	胡超凡

## 项目组主要成员

姓名	证件号码	年龄	性别	职称	学历	在项目中承担的任务	所在单位	签名
刘维	411424198809230940	35	女	讲师	博士研究生	材料的发光性能表征	华南农业大学	刘维
刘金坤	440785199712276617	26	男	未取得	本科	材料的合成和反应条件优化	华南农业大学	刘金坤
陈春锦	440882199805100713	25	男	未取得	本科	材料组成和结构分析	华南农业大学	陈春锦
万芷君	441625199705215022	26	男	未取得	本科	材料的发光机理分析	华南农业大学	万芷君

## 八、本任务书签约各方

管理单位（甲方）：

广东省基础与应用基础研究基金委员会（盖章）

法定代表人（或法人代理）：

曾路（签章）

2023 年 02 月 14 日

依托单位（乙方）：

华南农业大学

（盖章）

法定代表人（或法人代理）：

刘雅红

（签章）

联系人（项目主管）姓名：

倪慧群

（签章）

Email: kjcgxk@scau.edu.cn

电话： 020-85283435 / 15920301530

开户单位名称：

华南农业大学

开户银行名称：

广东广州工行五山支行

开户银行帐号：

3602002609000310520

2023 年 3 月 1 日

联系人（项目负责人）姓名：

胡超凡

（签名）

Email: thucf@scau.edu.cn

电话： 15521501455

2023 年 2 月 22 日



受理编号: c20140500001185

项目编号: 2020A1515010443

文件编号: 粤基金字〔2020〕4号

# 广东省基础与应用基础研究基金项目 任务书

项目名称: 具有聚集诱导发光特性的碳点的合成、表面改性和生物成像应用

项目类别: 广东省自然科学基金-面上项目

项目起止时间: 2019-10-01 至 2022-09-30

管理单位(甲方): 广东省基础与应用基础研究基金委员会

依托单位(乙方): 华南农业大学

通讯地址: 广东省广州市天河区五山路483号

邮政编码: 510642

单位电话: 020-85283435

项目负责人: 胡超凡

联系电话: 15521501455



(广东科技微信公众号)

广东省基础与应用基础研究  
基金委员会  
二〇一九年制



(受理纸质材料二维码)

## 五、人员信息

项目负责人								
姓名	证件号码	年龄	性别	职称	学历	在项目中承担的任务	所在单位	签名
胡超凡	43102719840809001X	36	男	副教授	博士研究生	项目负责人	华南农业大学	胡超凡

项目组主要成员								
姓名	证件号码	年龄	性别	职称	学历	在项目中承担的任务	所在单位	签名
董汉武	440982198109121458	39	男	讲师	博士研究生	材料结构分析与理论计算	华南农业大学	董汉武
张晓琴	441881199508195925	25	女	未取得	本科	碳点的合成与条件优化	华南农业大学	张晓琴
周芷珊	440921199504030427	25	女	未取得	本科	碳点的结构和物化性能表征	华南农业大学	周芷珊
孙宇琼	340823199602295641	24	女	未取得	本科	碳点的荧光性能测试	华南农业大学	孙宇琼
庞小亮	421003199411013252	26	男	未取得	本科	碳点的可控聚集和表面改性	华南农业大学	庞小亮
李亚东	130132199206255030	28	男	未取得	硕士研究生	细胞培养与生物成像实验	华南农业大学	李亚东

## 八、本合同签约各方

管理单位（甲方）：广东省基础与应用基础研究基金委员会（盖章）

法定代表人（或法人代理）：（签章）

年 月 日

依托单位（乙方）：华南农业大学（盖章）

法定代表人（或法人代理）：刘雅红（签章）

联系人（项目主管）姓名：郑鹏（签章）

Email: kjcgxk@scau.edu.cn

电话：020-85283435 / 13560344902

开户单位名称：华南农业大学

开户银行名称：广东广州工行五山支行

开户银行帐号：3602002609000310520

联系人（项目负责人）姓名：胡超凡（签名）

Email: thucf@scau.edu.cn

电话：15521501455

2020年3月24日

胡超凡

2020年3月24日



项目批准号	12174119
申请代码	A2207
归口管理部门	
依托单位代码	51064208A0499-0932



121741191003371

# 国家自然科学基金 资助项目计划书 (预算制项目)

资助类别: 面上项目

亚类说明:

附注说明:

项目名称: 缺陷对碳点长余辉发光的调控和作用机制

直接费用: 61万元 执行年限: 2022.01-2025.12

负责人: 刘应亮

通讯地址: 广州市天河区五山路483号华南农业大学材料与能源学院

邮政编码: 510642 电 话: 020-85283313

电子邮件: tliuy1@scau.edu.cn

依托单位: 华南农业大学

联系人: 唐家林 电 话: 020-85280070

填表日期: 2021年10月18日

国家自然科学基金委员会制





## 项目组主要成员

编号	姓名	出生年月	性别	职称	学位	单位名称	电话	证件号码	项目分工	每年工作 时间 (月)
1	刘应亮	1960.12	男	教授	博士	华南农业大学	020-85283313	220104196012010337	项目负责人	6
2	胡超凡	1984.08	男	副教授	博士	华南农业大学	15521501455	43102719840809001X	物理机制	8
3	李亚东	1992.06	男	博士生	硕士	华南农业大学	13392601159	130132199206255030	材料制备	10
4	许晓凯	1995.01	女	博士生	硕士	华南农业大学	15192483075	370784199501051528	能量传递	10
5	张伟财	1995.02	男	博士生	硕士	华南农业大学	15818265973	441622199502102571	分析表征	10
6	周芷珊	1995.04	女	硕士生	学士	华南农业大学	17818521270	440921199504030427	材料制备	10
7	马昱	1995.01	男	硕士生	学士	华南农业大学	18813291809	411325199501140012	材料制备	10
8	徐智强	1997.04	男	硕士生	学士	华南农业大学	15700492375	513902199704302177	材料制备	10
9	陈聪聪	1998.09	女	硕士生	学士	华南农业大学	19918086755	430626199809218061	分析表征	10
10	邱健敏	1997.02	女	硕士生	学士	华南农业大学	18881206125	510121199702158848	能量传递	10
总人数		高级		中级		初级		博士后		硕士生
10		2						3		5



## 2025 年光波频率对烟草吸收特性与有效成分释放特性的 研究—华南农业大学合同

甲方: 湖南中烟工业有限责任公司  
乙方: 华南农业大学  
签约地点: 湖南省长沙市雨花区

合同编号: 202543000834077  
采购编号: /

### 一、鉴于条款

鉴于乙方为甲方科研项目(项目编号: KY2025KF0018、项目名称: 光波频率对烟草吸收特性与有效成分释放特性的研究)合作计划中的合作方。甲乙双方依据《中华人民共和国民法典》等法律法规的规定, 双方本着平等、自愿、诚实信用的原则, 经友好协商, 就(光波频率对烟草吸收特性与有效成分释放特性的研究--华南农业大学)事宜, 签订本合同, 以资双方共同遵守。

### 二、定义

为避免双方理解上的分歧, 双方对本合同所涉及的有关名词和术语, 特作如下确认:

2.1“技术开发”指用于本项目的开发, 签订技术开发合同时尚未掌握的产品、工艺、材料、源代码等技术方案。

2.2“技术开发成果”指签订本合同时, 甲乙双方尚未掌握的、经过本合同项目研究开发的创造性劳动所获得的技术方案和产品。技术开发成果形式包括但不限于各类数据、工艺流程、试验过程和结果、图表、设备图纸、源代码、专利申请权、专利权、著作权、技术资料、技术秘密、相关技术的后续研究权及其它技术资料等。

2.3 一方在本合同签订前已经掌握的技术, 在本项目中的实现或者应用, 不属于本合同所说的“技术开发成果”。

### 三、业务内容

#### 3.1 委托开发内容

探明不同光波频率对于烟草物质的吸收特性和有效成分释放特性的影响; 建立烟草物质的光吸收模型, 为加热卷烟烟支筛选出适宜的光波频率; 阐明光加热烟草释放烟气物质的技术原理, 开发光加热原型机; 论证稀土纳米光热转换材料在加热卷烟光加热技术中的应用可行性。

#### 3.2 阶段委托开发内容及要求

##### (1) 第一阶段

内容: 研究不同光波频率对于加热卷烟烟草薄片、卷烟材料、烟草中主要化学成分的吸收特性, 建立光吸收模型, 为加热卷烟烟支筛选出适宜的光波频率。

要求: 完成加热卷烟烟草薄片、卷烟材料、烟草主要化学成分(不少于3种)在不同光波频率下的光吸收测试, 建立相应的光吸收模型并筛选出适宜波段。

##### (2) 第二阶段

内容: 研究光波频率对烟草有效成分释放特性的影响。



要求：研究测试不同光波频率下烟草有效成分（不少于3种）的释放特性，探究光波频率对烟草有效成分释放特性的影响规律。

### (3)第三阶段

内容：开发光加热原型机，论证稀土纳米光热转换材料在加热卷烟光加热技术中的应用可行性。

要求：开发光加热原型机，实现加热烟草释放烟气物质；筛选2种以上稀土纳米光热转换材料，论证其应用于加热卷烟的可行性；发表论文不少于2篇（其中SCI/EI论文至少1篇，甲方为第一单位第一作者），申请国家发明专利不少于1件；提交项目结题资料。

### 3.3 甲乙双方参与该项目研究人员名单如下：

甲方项目参与人员：崔雨琪、丁莎、刘琦、梁秋菊、赵子昱。

乙方项目参与人员：庄健乐、胡超凡、陈凤琼、黄炜岚、马安娜、沈烨楷、陈梦婷、宋苗苗。

## 四、合同期限

4.1 委托开发期限为：自合同生效之日起，至2026-12-31。

4.2 如本合同所关联的科研项目（项目编号：KY2025KF0018）的项目结束日期发生了变更，则合同期限的结束日期以变更后的项目结束日期为准。

## 五、合同价款

5.1 本合同为总价合同，甲乙双方确定合同不含税总金额：人民币485436.89元（大写）肆拾捌万伍仟肆佰叁拾陆元捌角玖分；含税金额：500000元（大写）伍拾万元整，增值税税率3%。合同金额已包含了乙方业务开展以及为了实现最终目标所应发生的全部成本、费用和税金。具体明细见附件。

5.2 如国家增值税率调整，合同不含税金额保持不变，按照调整后的增值税税率相应调整合同含税金额。

## 六、合同履行期限、内容、方式、验收标准及支付

### （一）第一阶段

2025年09月30日前，乙方向甲方申请第一阶段履约验收，提请验收的履约内容为：第一阶段委托开发内容。履约验收标准为：第一阶段委托开发要求。乙方应当提交的履约结算资料为：第一阶段研究报告。甲方验收人员为：专家评审组，验收方式为：线上成果验收。

甲方收到乙方履约验收资料后，15个工作日内组织验收。验收通过后30个工作日内，甲方向乙方支付合同款项：人民币175000.00元（大写：壹拾柒万伍仟元整）。乙方应当在甲方付款前，出具本阶段付款金额等额的增值税专用发票。

### （二）第二阶段

2025年12月31日前，乙方向甲方申请第二阶段履约验收，提请验收的履约内容为：第二阶段委托开发内容。履约验收标准为：第二阶段委托开发要求。乙方应当提交的履约结算资料为：第二阶段研究报告。甲方验收人员为：专家评审组，验收方式为：线上成果验收。

甲方收到乙方履约验收资料后，15个工作日内组织验收。验收通过后30个工作日内，甲方向乙方支付合同款项：人民币175000.00元（大写：壹拾柒万伍仟元整）。乙方应当在甲方付款前，出具本阶段付款金额等额的增值税专用发票。

### （三）第三阶段

2026年12月31日前，乙方向甲方申请第三阶段履约验收，提请验收的履约内容为：第三阶段委托开发内容。履约验收标准为：第三阶段委托开发要求。乙方应当提交的履约结算资料为：



合同编号: 202543000834077

审结时间: 20250716



甲 方	乙 方
甲方 (盖章): 湖南中烟工业有限责任公司	乙方 (盖章): 华南农业大学
单位地址: 长沙市雨花区万家丽中路三段 188 号	单位地址: 广州市
法定代表人: 籍涛	法定代表人 (负责人): 薛红卫
委托代理人 (签字): 虞苏行	委托代理人 (签字): 庄健乐
电话: 0731-85903086	电话: 020-85280319
传真: 0731-85559531	传真:
开户银行: 中国工商银行长沙市井湾子支行	开户银行: 中国工商银行股份有限公司广州五山支行
账号: 1901009119020178686	账号: 3602002609000310520
税号: 91430000740640740W	税号: 124400004554165634
邮编: 410007	邮编:
日期: 2025 年 7 月 28 日	日期: 2025 年 7 月 21 日





## 附件四

## 知识产权承诺书

本人参与湖南中烟工业有限责任公司科研开发项目合作, 对相关知识产权事宜做以下承诺:

1. 本人为项目合作方专职人员或在校学生, 无其他单位兼职 (如有, 必须提交兼职单位出具的对该技术开发成果放弃权利主张的相关文件)。
2. 本人保证交付给湖南中烟工业有限责任公司的设备及技术开发成果不侵犯任何与项目无关的第三人合法权益。
3. 本人仅有该项目技术开发成果参与者 (或专利发明人) 的署名权, 其个人对于该项目技术开发成果 (或专利) 奖励、实施、许可、转让后收益分配及奖励, 按照所在单位相关规定执行。湖南中烟工业有限责任公司在其技术开发成果 (或专利) 奖励、实施、许可、转让后, 本人无权参与该公司收益分配及奖励。

承诺人:

刘伟东 胡文红 黄炜兴 马安娜  
宋苗苗 沈梓楷 陈阳阳 陈梦婷

2025年 7 月 21 日

## 检索证明

根据委托人提供的论文材料, 委托人华南农业大学 材料与化学工程学院 胡超凡(学科类型: 自然科学) 28 篇论文收录情况如下表。

序号	论文名称	发表刊物及发表的年月卷期/页码等	作者排名	论文等级	作者文中单位	收录情况	影响因子	中科院大类分区
1	Hydrophobic carbon dots with blue dispersed emission and red aggregation-induced emission	NATURE COMMUNICATIONS 出版年: 2019 出版日期: APR 17 卷期: 10 页码: - 文献号: 1789 文献类型: Article	共同通讯 作者(倒数 第一)	T2 类	华南农业大学 材料与能源学 院	SCI	IF2-year=12.121 IF5-year=13.611 (2019)	综合性期刊 1 区 Top 期刊: 是 (2019)
2	Construction of Carbon Dots with Color-Tunable Aggregation-Induced Emission by Nitrogen-Induced Intramolecular Charge Transfer	ADVANCED MATERIALS 出版年: 2021 出版日期: DEC 卷期: 33 49 页码: - 文献号: 2104872 文献类型: Article	共同通讯 作者(倒数 第一)	T2 类	华南农业大学 材料与能源学 院	SCI	IF2-year=32.086 IF5-year=37.095 (2021)	材料科学 1 区 Top 期刊: 是 OA 期刊: 否 (2021)
3	A Universal Strategy for Activating the Multicolor Room-Temperature Afterglow of Carbon Dots in a Boric Acid Matrix	ANGEWANDTE CHEMIE-INTERNATIONAL EDITION 出版年: 2019 出版日期: MAY 27 卷期: 58 22 页码: 7278-7283	共同通讯 作者(倒数 第一)	T2 类	华南农业大学 材料与能源学 院	SCI	IF2-year=12.959 IF5-year=12.659 (2019)	化学 1 区 Top 期刊: 是 OA 期刊: 否 (2019)

	文献类型: Article							
4	High-Efficiency Solid-State Luminescence from Hydrophilic Carbon Dots with Aggregation-Induced Emission Characteristics	ADVANCED FUNCTIONAL MATERIALS 出版年: 2023 出版日期: MAR 卷期: 33 11 页码: - 文献类型: Article	通讯作者	T2 类	华南农业大学 材料与能源学 院	SCI	IF2-year=18.5 IF5-year=19.6 (2023)	材料科学 1 区 Top 期刊: 是 OA 期刊: 否 (2023)
5	Calcination temperature tuning of RTP and TADF with wide range of emission color from carbon dots confined in Al <sub>2</sub> O <sub>3</sub> /SiO <sub>2</sub> /SiO <sub>2</sub> /SiO <sub>2</sub> /SiO <sub>2</sub>	CHEMICAL ENGINEERING JOURNAL 出版年: 2023 出版日期: OCT 15 卷期: 474 页码: - 文献号: 145597 文献类型: Article	通讯作者	T2 类	华南农业大学 材料与能源学 院	SCI	IF2-year=13.4 IF5-year=13.2 (2023)	工程技术 1 区 Top 期刊: 是 OA 期刊: 否 (2023)
6	Carbon Dots as a Protective Agent Alleviating Abiotic Stress on Rice (Oryza sativa L.) through Promoting Nutrition Assimilation and the Defense System	ACS APPLIED MATERIALS & INTERFACES 出版年: 2020 出版日期: JUL 29 卷期: 12 30 页码: 33575-33585 文献类型: Article	共同通讯作者 (倒数第 ·)	T2 类	华南农业大学 材料与能源学 院	SCI	IF2-year=9.229 IF5-year=9.57 (2020)	材料科学 1 区 Top 期刊: 是 OA 期刊: 否 (2020)

7	Time-Dependent Room-Temperature Afterglow of Carbon Dots Constructed by Trap-Induced Multiemission Centers	NANO LETTERS 出版年: 2025 出版日期: APR 18 卷期: 25 17 页码: 6993-7002 文献类型: Article	共同通讯作者(倒数第一)	华南农业大学 材料与能源学院	SCI	IF2-year=9.1 IF5-year=9.9 (2024)	材料科学 2 区 Top 期刊: 是 OA 期刊: 否 (2025)
8	Multiemissive Room-Temperature Phosphorescent Carbon Dots@ZnAl <sub>2</sub> O <sub>3</sub> Composites by Inorganic Defect Triplet-State Energy Transfer	ACS APPLIED MATERIALS & INTERFACES 出版年: 2021 出版日期: JUL 28 卷期: 13 29 页码: 34705-34713 文献类型: Article	通讯作者	华南农业大学 材料与能源学院	SCI	IF2-year=10.383 IF5-year=10.382 (2021)	材料科学 2 区 Top 期刊: 是 OA 期刊: 否 (2021)
9	Multicolor Afterglow from Carbon Dots: Preparation and Mechanism	SMALL-METHODS 出版年: 2024 出版日期: JAN 卷期: 8 1 页码: - 文献类型: Review	通讯作者	华南农业大学 材料与能源学院	SCI	IF2-year=9.1 IF5-year=10.5 (2024)	材料科学 2 区 Top 期刊: 否 OA 期刊: 否 (2025)
10	Energy Transfer Mediated Enhancement of Room-Temperature Phosphorescence of Carbon Dots Embedded in Matrices	ADVANCED OPTICAL MATERIALS 出版年: 2022 出版日期: JAN 卷期: 10 1 页码: -	共同通讯作者(倒数第一)	华南农业大学 材料与能源学院	SCI	IF2-year=9.0 IF5-year=9.5 (2022)	材料科学 2 区 Top 期刊: 否 OA 期刊: 否 (2022)



	文献号: 2100704 文献类型: Article							
11	Cascade Resonance Energy Transfer for the Construction of Nanoparticles with Multicolor Long Afterglow in Aqueous Solutions for Information Encryption and Bioimaging	ADVANCED OPTICAL MATERIALS 出版年: 2022 出版日期: MAY 卷期: 10 10 页码: - 文献号: 2102666 文献类型: Article	通讯作者	A类	华南农业大学 材料与能源学 院	SCI	IF2-year=9.0 IF5-year=9.5 (2022)	材料科学 2区 Top 期刊: 否 OA 期刊: 否 (2022)
12	Self-Quenching-Resistant Red Emissive Carbon Dots with High Stability for Warm White Light- Emitting Diodes with a High Color Rendering Index	ADVANCED OPTICAL MATERIALS 出版年: 2020 出版日期: AUG 卷期: 8 15 页码: - 文献号: 2000251 文献类型: Article	共同通讯 作者(倒数 第一)	A类	华南农业大学 材料与能源学 院	SCI	IF2-year=9.926 IF5-year=9.63 (2020)	材料科学 2区 Top 期刊: 是 OA 期刊: 否 (2020)
13	pH-Responsive carbon dots with red emission for real-time and visual detection of amines	JOURNAL OF MATERIALS CHEMISTRY C 出版年: 2020 出版日期: SEP 7 卷期: 8 33 页码: 11563- 11571 文献类型: Article	共同通讯 作者(倒数 第一)	A类	华南农业大学 材料与能源学 院	SCI	IF2-year=7.393 IF5-year=6.853 (2020)	材料科学 2区 Top 期刊: 否 OA 期刊: 否 (2020)

第 4 页/共 9 页

14	Efficient Preparation of Hydrophilic Boron Nitride Nanosheets for Human Heat Dissipation Applications	ACS APPLIED NANO MATERIALS 出版年: 2024 出版日期: MAY 7 卷期: 7 10 页码: 11487-11497 文献类型: Article	通讯作者	B 类	华南农业大学 材料与能源学院	SCI	IF2-year=5.5 IF5-year=5.6 (2024)	材料科学 3 区 Top 期刊: 否 OA 期刊: 否 (2025)
15	Preparation of Carbon Dot-based Multicolor Room-temperature Phosphorescent Materials via Precursor Structure Regulation Strategies	CHEMICAL JOURNAL OF CHINESE UNIVERSITIES-CHINESE 出版年: 2025 出版日期: JUN 10 卷期: 46 6 页码: - 文献号: 20240412 文献类型: Article	共同通讯作者(倒数第一)	B 类	华南农业大学 材料与能源学院	SCI	IF2-year=0.6 IF5-year=0.5 (2024)	化学 3 区 Top 期刊: 否 OA 期刊: 否 标注: 中英文期刊“同质等效”评价 (2025)
16	Room temperature long afterglow from boron oxide: A boric acid calcined product	MATERIALS LETTERS 出版年: 2020 出版日期: OCT 1 卷期: 276 页码: - 文献号: 128226 文献类型: Article	共同通讯作者(倒数第一)	B 类	华南农业大学 材料与能源学院	SCI	IF2-year=3.423 IF5-year=3.003 (2020)	材料科学 3 区 Top 期刊: 否 OA 期刊: 否 (2020)
17	Morphology-controlled Synthesis of Molybdenum Oxide with Tunable Plasmon Absorption for Photothermal	CIEMMOMAT 出版年: 2020	共同通讯作者(倒数第一)	B 类	华南农业大学 材料与能源学院	SCI	IF2-year=3.154 IF5-year=3.435 (2020)	材料科学 4 区 Top 期刊: 否 OA 期刊: 否

第 5 页/共 9 页

	Therapy of Cancer	出版日期: SEP 卷期: 6 9 页码: 1407-1416 文献类型: Article						(2020)
18	Carbon dots as light converter for plant photosynthesis: Augmenting light coverage and quantum yield effect	JOURNAL OF HAZARDOUS MATERIALS 出版年: 2021 出版日期: MAY 15 卷期: 410 页码: - 文献号: 124534 文献类型: Article	共同通讯作者	T2 类	华南农业大学 材料与能源学院	SCI	IF2-year=14.224 IF5-year=12.984 (2021)	环境科学与生态学 1 区 Top 期刊: 是 OA 期刊: 否 (2021)
19	Effects and mechanisms of proanthocyanidins-derived carbon dots on alleviating salt stress in rice by multi-omics analysis	FOOD CHEMISTRY-X 出版年: 2024 出版日期: JUN 30 卷期: 22 页码: - 文献号: 101422 文献类型: Article	共同通讯作者	T2 类	华南农业大学 材料与能源学院	SCI	IF2-year=8.2 IF5-year=8.2 (2024)	农林科学 1 区 Top 期刊: 是 OA 期刊: 是 (2025)
20	Dual-mode photochromic luminescence of carbon dots induced by photoinduced electron transfer	SCIENCE CHINA-MATERIALS 出版年: 2025 出版日期: OCT 卷期: 68 10 页码: 3591-3599 文献类型: Article	共同通讯作者	T2 类	华南农业大学 材料与能源学院	SCI	IF2-year=7.4 IF5-year=6.5 (2024)	材料科学 1 区 Top 期刊: 是 OA 期刊: 否 标注: 中国 SCI 期刊支持计划 (2025)

21	Enhancement of Fluorescence Emission for Tricolor Quantum Dots Assembled in Polysiloxane toward Solar Spectrum-Simulated White Light-Emitting Devices	SMALL 出版年: 2020 出版日期: JAN 卷期: 16 1 页码: - 文献号: 1905266 文献类型: Article	共同通讯作者	A类	华南农业大学 材料与能源学院	SCI	IF2-year=13.281 IF5-year=12.463 (2020)	材料科学 2区 Top 期刊: 是 OA 期刊: 否 (2020)
22	Anchoring Carbon Nanodots onto Nanosilica for Phosphorescence Enhancement and Delayed Fluorescence Nascence in Solid and Liquid States	SMALL 出版年: 2020 出版日期: DEC 卷期: 16 49 页码: - 文献号: 2005228 文献类型: Article	共同通讯作者	A类	华南农业大学 材料与能源学院	SCI	IF2-year=13.281 IF5-year=12.463 (2020)	材料科学 2区 Top 期刊: 是 OA 期刊: 否 (2020)
23	A review on the effects of carbon dots in plant systems	MATERIALS CHEMISTRY FRONTIERS 出版年: 2020 出版日期: FEB 1 卷期: 4 2 页码: 437-448 文献类型: Review	共同通讯作者	A类	华南农业大学 材料与能源学院	SCI	IF2-year=6.482 IF5-year=6.176 (2020)	材料科学 2区 Top 期刊: 否 OA 期刊: 否 (2020)
24	Red, green and blue aggregation-induced emissive carbon dots	CHINESE CHEMICAL LETTERS 出版年: 2021 出版日期: DEC 卷期: 32 12 页码: 3927-3930	共同通讯作者	A类	华南农业大学 材料与能源学院	SCI	IF2-year=8.455 IF5-year=5.935 (2021)	化学 2区 Top 期刊: 否 OA 期刊: 否 (2021)



	文献类型: Article								
25	Synthesis of dual-emissive carbon dots with a unique solvatochromism phenomenon	JOURNAL OF COLLOID AND INTERFACE SCIENCE 出版年: 2019 出版日期: NOV 1 卷期: 555 页码: 607-614 文献类型: Article	共同通讯作者	A类	华南农业大学 材料与能源学院	SCI	IF2-year=7.489 IF5-year=6.171 (2019)	化学 2区 Top 期刊: 否 (2019)	
26	Magnesium-nitrogen co-doped carbon dots enhance plant growth through multifunctional regulation in photosynthesis	CHEMICAL ENGINEERING JOURNAL 出版年: 2021 出版日期: OCT 15 卷期: 422 页码: - 文献号: 130114 文献类型: Article	共同通讯作者	T2类	华南农业大学 材料与能源学院	SCI	IF2-year=16.444 IF5-year=14.61 (2021)	工程技术 1区 Top 期刊: 是 OA 期刊: 否 (2021)	
27	Multifunctional carbon dots reinforced gelatin-based coating film for strawberry preservation	FOOD HYDROCOLLOIDS 出版年: 2024 出版日期: FEB 卷期: 147 页码: - 文献号: 109327 文献类型: Article	共同通讯作者	T2类	华南农业大学 材料与能源学院	SCI	IF2-year=12.4 IF5-year=13.3 (2024)	农林科学 1区 Top 期刊: 是 OA 期刊: 否 (2025)	

	Synthesis of Silicon Quantum Dots with Highly Efficient Full-Band UV Absorption and Their Applications in Antiyeellowing and Resistance of Photodegradation	ACS APPLIED MATERIALS & INTERFACES 出版年: 2019 出版日期: FEB 13 卷期: 11 6 页码: 6634-6643 文献类型: Article	共同通讯作者	T2类	华南农业大学 材料与能源学院	SCI	IF2-year=8.758 IF5-year=8.901 (2019)	材料科学 I 区 Top 期刊: 是 OA 期刊: 否 (2019)
--	---	--	--------	-----	-------------------	-----	--	---

说明: 论文等级和中科院大类分区按《华南农业大学学术论文评价方案(试行)》划分。

报告免责声明: 如未盖章, 报告无效



## ARTICLE

<https://doi.org/10.1038/s41467-019-09830-6>

OPEN

# Hydrophobic carbon dots with blue dispersed emission and red aggregation-induced emission

Haiyao Yang<sup>1,2</sup>, Yingliang Liu<sup>1</sup>, Zhouyi Guo<sup>2</sup>, Bingfu Lei<sup>1</sup>, Jianle Zhuang<sup>1</sup>, Xuejie Zhang<sup>1</sup>, Zhiming Liu<sup>2</sup> & Chaofan Hu<sup>1</sup>

Carbon dots (CDs) have been studied for years as one of the most promising fluorescent nanomaterials. However, CDs with red or solid-state fluorescence are rarely reported. Herein, through a one-pot solvothermal treatment, hydrophobic CDs (H-CDs) with blue dispersed emission and red aggregation-induced emission are obtained. When water is introduced, the hydrophobic interaction leads to aggregation of the H-CDs. The formation of H-CD clusters induces the turning off of the blue emission, as the carbonized cores suffer from  $\pi$ - $\pi$  stacking interactions, and the turning on of the red fluorescence, due to restriction of the surfaces' intramolecular rotation around disulfide bonds, which conforms to the aggregation-induced-emission phenomenon. This on-off fluorescence of the H-CDs is reversible when the H-CD powder is completely dissolved. Moreover, the H-CD solution dispersed in filter paper is nearly colorless. Finally, we develop a reversible two switch-mode luminescence ink for advanced anti-counterfeiting and dual-encryption.

<sup>1</sup>Guangdong Provincial Engineering Technology Research Center for Optical Agriculture, College of Materials and Energy, South China Agricultural University, 510642 Guangzhou, China. <sup>2</sup>MOE Key Laboratory of Laser Life Science & SATCM Third Grade Laboratory of Chinese Medicine and Photonics Technology, College of Biophotonics, South China Normal University, 510631 Guangzhou, China. Correspondence and requests for materials should be addressed to Y.L. (email: [tliuyl@scau.edu.cn](mailto:tliuyl@scau.edu.cn)) or to Z.L. (email: [liuzm@scnu.edu.cn](mailto:liuzm@scnu.edu.cn)) or to C.H. (email: [thucf@scau.edu.cn](mailto:thucf@scau.edu.cn))

Many types of carbon dots (CDs) have been reported because they are more eco-friendly and potentially a carbon-based fluorescent nanomaterial; however, in solution, most CDs show emission in the blue to green-light regions only<sup>1–3</sup>. Therefore, there is an urgency to attain long-wavelength and multicolor emission of CDs for further applications, particularly in biologically relevant and anticounterfeiting fields<sup>1,2,4–9</sup>. The most common method for inducing long-wavelength and multicolor emission is doping heteroatoms into the lattices of carbon. The addition of heteroatoms leads to defects with the framework of the CDs. Therefore, contraction of the CDs' band gaps further induces a redshift of the CDs' fluorescence. Recently, Liu and coworkers fabricated red emission B, N, S-codoped CDs using 2,5-Diaminobenzenesulfonic acid and 4-aminophenylboronic acid hydrochloride. Earlier, Ge et al.<sup>9</sup> designed a series of Suzuki reactions to synthesize polythiophene derivatives as precursors for red emission S-doped CDs.

However, previous studies on red emission CDs did not obtain CDs that exhibit red fluorescence in the solid state. Most reported CDs only fluoresce when dissolved in solution. The currently accepted mechanism of this phenomenon is similar to the H-aggregation of organic fluorescent molecules; CDs suffer from  $\pi$ – $\pi$  stacking in the solid state and the aggregation of large conjugated systems consumes the transition energy, therefore, resulting in the quenching of the CDs' fluorescence. While the extinction of the CDs' luminescent solid-state has hindered their application in LED and anticounterfeiting technology<sup>8,10–13</sup>. The current method to maintain CDs' solid-state-fluorescence (SSF) is to block the CD monomers from direct contact. Most reported studies on SSF CDs attempt to dope CDs into matrices or introduce polymer chains into CDs<sup>8,11</sup>. For instance, Chen et al.<sup>13</sup> prepared N-doped CD's (NCDs) with yellow-green SSF by hydrothermal treatment of poly (vinyl alcohol) (PVA) and ethylenediamine (EDA). The abundant surface PVA chains covered around the NCDs prevented the graphitizing cores from  $\pi$ – $\pi$  interactions; thus, resisting the aggregation-caused-quenching (ACQ) of the NCDs' fluorescence. However, these studies did not achieve red SSF of CDs. Moreover, the introduction of matrices or polymer chains restricted the concentration of the doped CDs; if too many CDs are introduced, their ACQ will still take place.

Unlike the ACQ<sup>14</sup> property of nanomaterials, B.Z Tang<sup>15–18</sup> and coworkers discovered a series of organic fluorescent materials and found that luminogen aggregation played a destructive role in the light-emitting process. In their studies, a series of symmetrical molecules were found to be nonluminescent in the dissolved state, but emissive in the aggregated state. The term “aggregation-induced emission” (AIE) was coined for this phenomenon, as the nonluminescent symmetrical molecules were induced to emit via aggregate formation. This theory has not been utilized in the SSF of carbon dots yet.

Incidentally, we find another approach for maintaining a CDs' SSF, in addition to introducing them into solid dispersed systems: crowning the CDs' graphitized cores with rotatable symmetric surfaces, through a series of amidation and rearrangement during a solvothermal carbonization process. When fully dispersed as a homogeneous solution, our CDs exhibit similar PL characteristics as the reported blue emission CDs. By adding water, the CDs continuously assemble due to their hydrophobicity, the blue fluorescence turns off while a red SSF turns on. Like AIE molecules in solution, the surficial groups of CDs can rotate around the intramolecular disulfide bonds and consume the absorbed energy, thus, not producing fluorescence. However, in the solid state, as a result of the intramolecular rotation being banned, the excitation energy can transfer dominantly into fluorescence. Therefore, we have designed a method to synthesize hydrophobic N, S-doped CDs (H-CDs) with a two-switch-mode luminescence

between a blue dissolved fluorescence and a red AIE. Moreover, the output of the H-CD powders is higher (after purification, the mass ratio of H-CD powders to raw materials is approximately 80%) than prior methods. Several characterizations are taken to determine the properties of H-CDs. When H-CD powder dissolves into certain organic solvents (ethanol or acetic acid), it displays the same blue fluorescence as the as-prepared H-CD solution. However, in DMF the H-CD displays both blue and red fluorescence, due to the existence of mono-dispersed and aggregated H-CDs. To confirm the fluorescence mechanism and the relationship between the H-CD dispersed state and fluorescence, we have designed a control experiment (replaced dithiosalicylic acid with benzoate to remove the disulfide bonds). Finally, we fill the as-prepared H-CD solution into a mark pen and conduct a series of anticounterfeit and encryption experiments to develop a reversible two-switch-mode luminescence ink.

## Results

**Preparation and characterization of the H-CDs.** The H-CD powder was easily prepared through a one-pot solvothermal process of melamine (MA) and a dithiosalicylic acid (D TSA)/acetic acid solution, followed by a simple purification (Fig. 1). It should be noted that acetic acid plays a vital role during the formation of H-CDs. In addition to being an environmentally friendly solvent with low cost, it is also a catalyst for H-CDs' carbonization and the constitution of H-CD surface (Supplementary Fig. 1a). To further investigate the effect of acetic acid, we applied a series of control experiments which replaced acetic acid with formic acid, propionic acid and saturated aqueous solution of oxalic acid. When propionic acid is added, the product (named as PA-CDs) shows a similar PL property as the H-CDs: blue emission in dispersion and yellow AIE in the powder state (Supplementary Fig. 1b, c). However, propionic acid is much more expensive and toxic than acetic acid, and the fluorescence of PA-CD powder is yellow unlike the red AIE of the H-CDs. Through continuous water addition, the transparent as-prepared H-CD solution gradually turns into a turbid liquid, and the blue emission fades away. Then, a red fluorescence emerges. H-CD powder displaying red SSF under 365 nm UV irradiation can be obtained with further purification and drying. Remarkably, under 2 nm UV, the red emission of the H-CD powder remains while the H-CD dispersion displays nearly no fluorescence.

The as-prepared H-CDs have been characterized with transmission electron microscopy (TEM), X-ray diffraction (XRD) and Raman spectroscopy to confirm the nature of the carbon nanoparticles. As shown in Fig. 2a, b, the TEM image of the H-CDs presents size distributions between 4 and 10 nm, with an average diameter of approximately 6.5 nm. High-resolution TEM (HR-TEM) shows a lattice spacing of 0.21 nm corresponding to the (100) facet of graphite and reveals that the H-CDs contain graphite-like structures<sup>19–21</sup>. The XRD pattern of the H-CDs (Fig. 2c) has an apparent peak at approximately 25°, which is attributed to an interlayer spacing of 0.34 nm, while the peak near 41° represents the 0.21 nm interlayer spacing<sup>5,8,13,22</sup>. The Raman spectrum in Fig. 2d displays two peaks at 1348 cm<sup>–1</sup> (D band) and 1584 cm<sup>–1</sup> (G band), referring to areas of disordered surfaces and *sp*<sup>2</sup> carbon networks in the H-CDs' frameworks, respectively. The calculated intensity ratio  $I_D/I_G$  is 5.61, indicating the amorphous surface of the H-CDs<sup>1,5,6,19</sup>.

Fourier transform infrared (FT-IR) spectra, X-ray photoelectron spectra (XPS) and nuclear magnetic resonance (NMR) spectroscopy were taken to further analyze the chemical structure of the H-CDs. The FT-IR spectrum (Fig. 2i) uncovers that the surface of the H-CDs contains methylene (2876 and 2973 cm<sup>–1</sup>), C≡N (2034 cm<sup>–1</sup>), S–H (2650 cm<sup>–1</sup>), amide carbonyl (1682 cm<sup>–1</sup>),



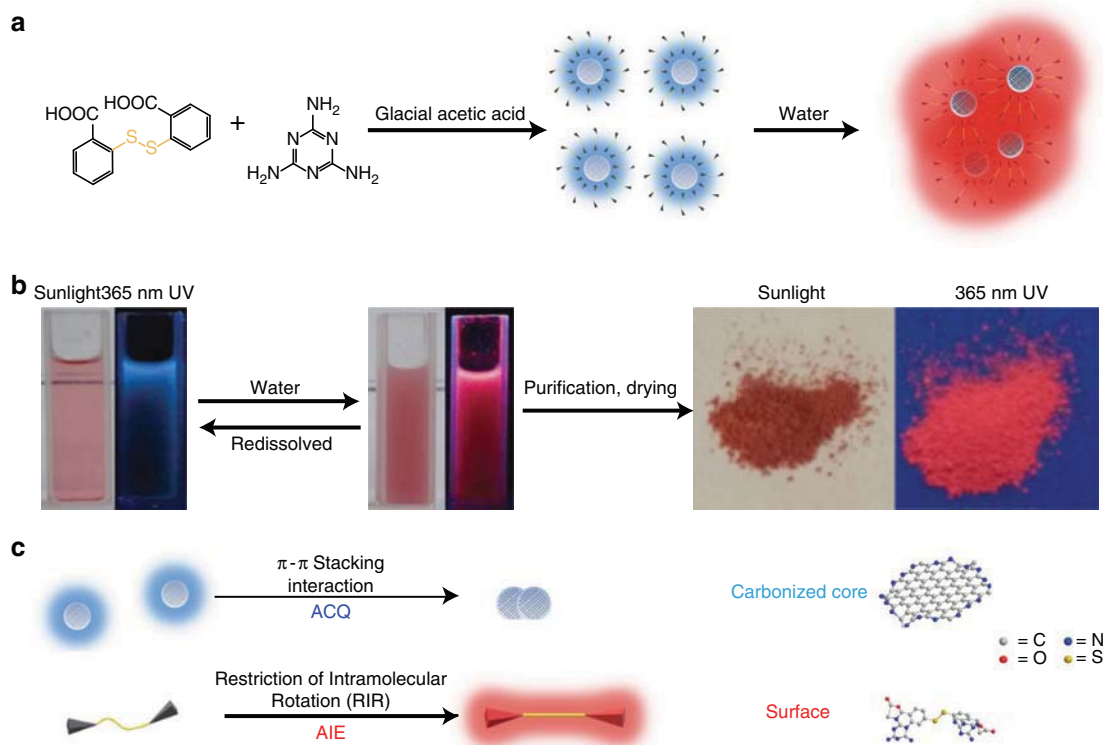


**Fig. 1** H-CDs' formation, structure, fluorescence and appearance in different state. **a** Formation of H-CD monomers and their aggregates (the disulfide bond in dithiosalicylic acid molecular is highlighted with yellow). **b** Photographs of the H-CDs' two-switch-mode luminescence principle. **c** Fluorescence principle and proposed structure of H-CD's core and surface (the colors of glowing edges represent the color of their fluorescence). H-CD, hydrophobic carbon dot

C=C ( $1469\text{ cm}^{-1}$ ), C-N ( $1407\text{ cm}^{-1}$ ), C-S ( $685\text{ cm}^{-1}$ ), S-S ( $491\text{ cm}^{-1}$ ), aromatic C-NH ( $1261\text{ cm}^{-1}$ ) and C-O ( $1124\text{ cm}^{-1}$ ) functional groups or chemical bonds. Additionally, the FT-IR spectra of MA and DTSA exhibit that these raw materials contain an hydroxyl or amino ( $3064$  and  $3411\text{ cm}^{-1}$ )<sup>1,4,8</sup>. Furthermore, after the amidation and carbonization, these hydrophilic groups almost disappear in the H-CDs, thus, contributing to the hydrophobic properties of the H-CDs<sup>23–34</sup>. The full XPS spectrum presented in Fig. 2e shows four peaks at  $284.81$ ,  $399.62$ ,  $532.22$ , and  $163.89\text{ eV}$ , suggesting that the H-CDs consisted of C, N, O, and S elements, and the atomic ratios were calculated to  $79.28\%$ ,  $6.47\%$ ,  $10.99\%$ , and  $3.26\%$ , respectively. In Fig. 2f, the high-resolution XPS spectrum of the C 1s band was separated into three peaks at  $284.81$ ,  $286.41$ , and  $288.95\text{ eV}$ , which are assigned to C-C/C=C, C-N and C=O/C=N, respectively. The N 1s band (Fig. 2g) exhibits two peaks at  $399.07$  and  $400.27\text{ eV}$ , respectively, which correspond to pyridinic C<sub>3</sub>-N and pyrrolic C<sub>2</sub>-N-H groups. The S 2p band in Fig. 2h contains three peaks at  $163.35\text{ eV}$  for S-C,  $163.81\text{ eV}$  for S-H and  $164.57\text{ eV}$  for S-S. These three high-resolution spectra collectively indicate the successful insertion of S and N atoms into the H-CDs. Furthermore, NMR spectra ( $^1\text{H}$  and  $^{13}\text{C}$ ) were employed to distinguish the  $sp^3$ -hybridized carbon atoms from the  $sp^2$ -hybridized carbon atoms (Fig. 2j, k). Deuterium-labeled DMSO- $d_6$  ( $\text{CD}_3\text{SOCD}_3$ ) was used as a solvent. In the  $^1\text{H}$  NMR spectra,  $sp^2$  carbons were detected. The peak at  $9.99\text{ ppm}$  in Fig. 2j is the chemical shift of the carboxyl protons. Furthermore, signals from the aromatic rings are detected at  $8.3\text{ ppm}$ , which can be attributed to graphitized cores' proton resonances. The emergence of the  $-\text{NH}_2$  protons at  $5.75\text{ ppm}$  implies the introduction of primary amines into the heterocyclic surface<sup>19,22,35</sup>. In the  $^{13}\text{C}$  NMR spectrum, signals in the range of  $30$ – $45\text{ ppm}$  are associated with the aliphatic ( $sp^3$ ) carbon atoms, and signals from  $100$  to  $185\text{ ppm}$  are indicative of  $sp^2$  carbon

atoms. Signals in the range of  $170$ – $185\text{ ppm}$  correspond to carboxyl/amide groups<sup>36–38</sup>. Based on the aforementioned characterizations, which support the reaction mechanism proposed in Supplementary Fig. 1a, a molecular model for the H-CDs can be constructed: a nanoscale graphite-like skeleton with defects caused by pyridinic nitrogen atoms and disulfide bonds, covered with C, N, O and S containing symmetrical heterocycle rotatable structures. Notably, there are few amino and hydroxyl functional groups on the surface of the H-CDs, which is quite different from the water-soluble CDs reported in prior works. This model explains the hydrophobicity and optical properties.

#### Optical properties and fluorescence mechanism of the H-CDs.

The UV-Vis absorption, PL excitation, and emission of the as-prepared H-CD solution and powder were examined to evaluate their optical properties. As shown in Fig. 3a, the UV-Vis absorption of the as-prepared H-CDs has two peaks at  $\lambda_{\text{max}1} \approx 280\text{ nm}$  and  $\lambda_{\text{max}2} \approx 360\text{ nm}$  due to the  $\pi$ - $\pi^*$  transitions of the C=C in the core of the H-CD. While the H-CD powder exhibits a different broad absorption, with a dominating band at  $\lambda_{\text{max}} \approx 560\text{ nm}$  (Fig. 3b), which is attributed to the  $n$ - $\pi^*$  transitions of the surface states containing C=N/C=O, C-O and C-S structures. Figure 3d represents the PL emission of the H-CD powder under different excitation wavelengths, showing a stable red emission at  $\lambda_{\text{max}} \approx 620\text{ nm}$ , with a different excitation wavelength that is more similar to traditional inorganic phosphors than reported CDs. However, the as-prepared H-CD solution (Fig. 3c) exhibits excitation-dependent PL features; similar to most CDs in prior works, the optimal excitation and emission are near  $360$  and  $467\text{ nm}$ <sup>1,6,10,11,20,39</sup>, respectively. The computational process of the H-CDs' molecular orbital energy level and fluorescence lifetime ( $4.56\text{ ns}$ ) is described in the "Methods" section. The quantum yield of the H-CDs can be calculated as  $5.96\%$ ,

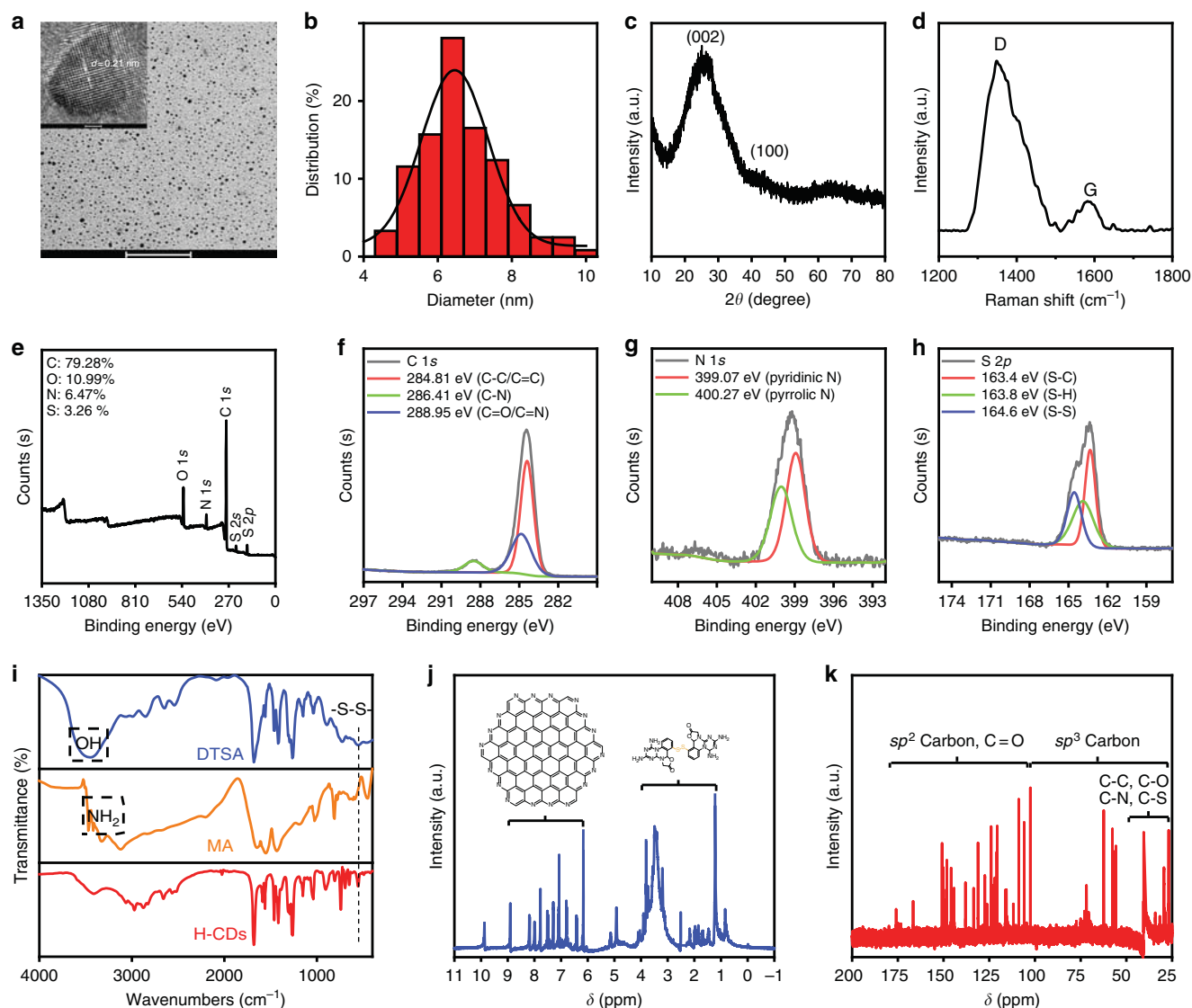


**Fig. 2** Basic characterizations of H-CDs. **a** TEM image of the H-CDs, inset: high-resolution TEM (HR-TEM) image of the H-CDs. **b** Particles size distribution measured by TEM. **c** X-ray diffraction (XRD) pattern of the H-CDs. **d** Raman spectrum of the H-CDs. **e** XPS spectrum and high-resolution **f** C 1s, **g** N 1s, and **h** S 2p spectra of the H-CDs. **i** FT-IR spectrum of DTSA, MA and the H-CDs (the position marked by dotted rectangles refer to hydroxyl and amino group, peaks belong to disulfide bond are marked by dotted line). **j**  $^1\text{H}$  NMR (insets: proposed structure of the H-CD core and surface, the braces mark out the regions they belong to separately) and **k**  $^{13}\text{C}$  NMR spectra (the braces mark out the regions related to carbon different with different molecular orbital) of the H-CDs in DMSO- $d_6$ . Scale bars: 100 nm (**a**) and 10 nm (**a**—inset). H-CD, hydrophobic carbon dot, TEM transmission electron microscopy

due to their photon absorption and emission (Supplementary Fig. 2b, c)<sup>4,7,11,21,40,41</sup>. Visually, bright field and fluorescence microscopy images (Supplementary Fig. 3) of excess H-CD powder in ethanol indicate that thick stacking H-CD powder produces red fluorescence, and the dissolved H-CD solution displays blue emission. At the thin periphery of the H-CD powder infiltrated with the solution, the red and blue emission hybridize together, giving rise to a pink hybrid fluorescence<sup>8,10,13</sup>.

More intuitively, the photographs in Fig. 4a show that the pure as-prepared H-CD solution and the solution with an addition of less than 50% water (volume ratio) are orange to red homogeneous and transparent liquids. When the volume ratio of the water is greater than 50%, the as-prepared H-CD solution starts to separate the red powder out and turns into a turbid liquid with a suspension. Under a 365 nm UV excitation (Fig. 4b), the aforementioned transparent liquids display blue fluorescence, while the turbid liquid with the suspension glows red. In addition,

correlated to the variation trend of the size distribution by adding more water, the intensity of the H-CD solution's blue emission decreases, while the red emission is heightened (Fig. 4c). The H-CDs in solvents with different polarities exhibit a similar fluorescence phenomenon (Fig. 4d) to the as-prepared H-CDs with varying ratios of water. The red emission increases when the polarity of the solvent decreases. The UV–Vis absorption spectra and absorbance trend of the H-CD solutions with varying ratios of water (Fig. 4e, f) reveal that with the injection of water, the absorbance at 360 nm continues decreasing, while a redshifted absorbance at 559 nm appears and continues increasing. This trend provides strong evidence for the presence of  $\pi$ – $\pi$  stacking in the H-CDs. Conjugated systems can form two distinct types of  $\pi$ – $\pi$  aggregates, a sandwich-type arrangement (H-aggregates) and a head-to-tail arrangement (J-aggregates)<sup>42</sup>. According to the molecular exciton coupling theory, the spectral redshift indicates that the H-CDs form J-aggregates, with a head-to-tail

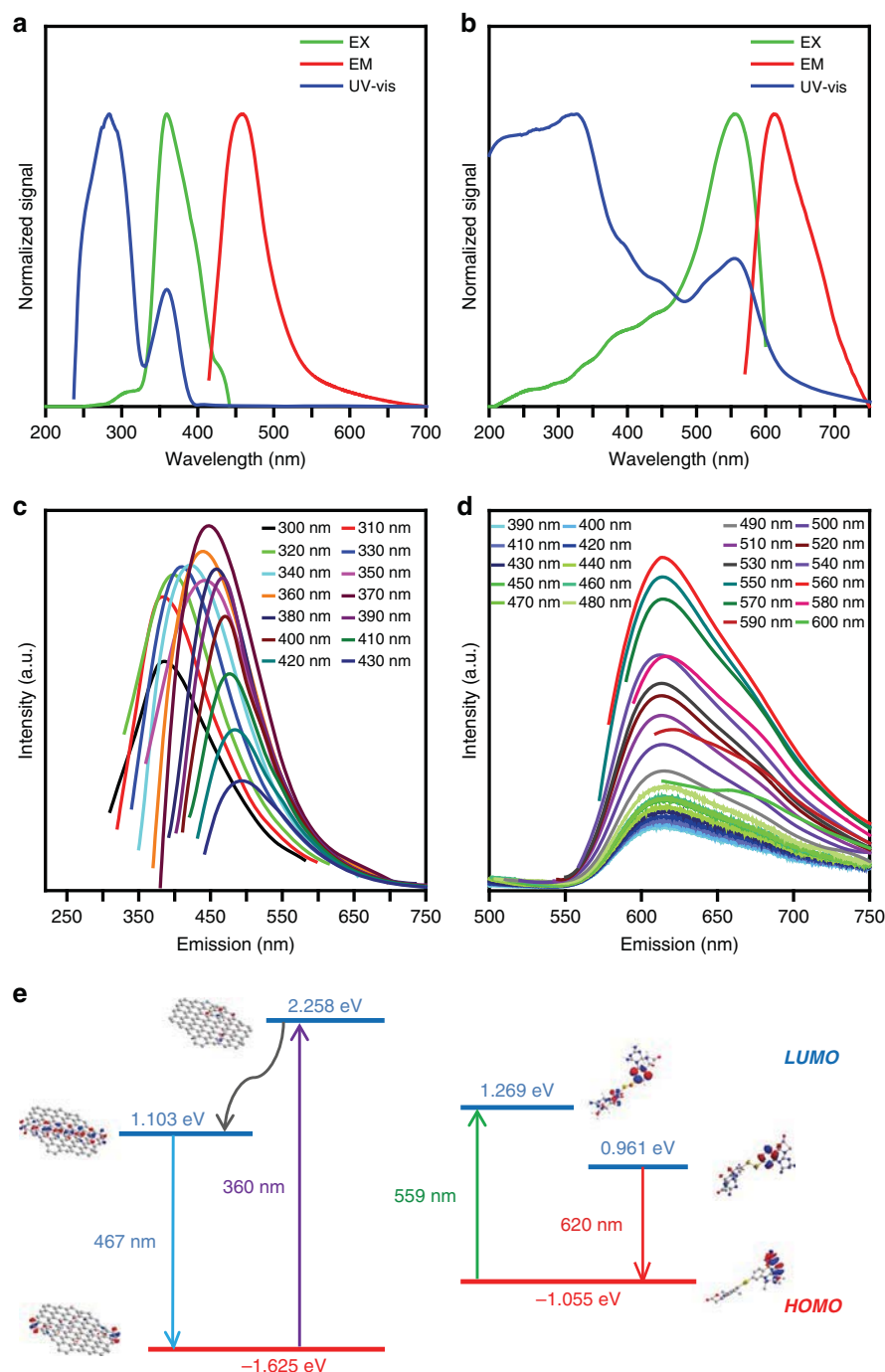


**Fig. 3** Absorption and emission properties of H-CDs and concerned orbital energy level. **a** UV-Vis absorption (blue line), PL excitation (EX) ( $\lambda_{\text{em}} = 467$  nm, orange line), and emission (EM) ( $\lambda_{\text{ex}} = 360$  nm, red line) spectra of as-prepared H-CD solution. **b** UV-Vis absorption (green line), PL excitation (EX) ( $\lambda_{\text{em}} = 620$  nm, orange line), and emission (EM) ( $\lambda_{\text{ex}} = 559$  nm, red line) spectra of the H-CD powder. **c, d** PL emission spectra with different excitation wavelengths of H-CD powder and as-prepared solution. **e** Energy level diagram of proposed H-CDs' graphitizing core, and the surface symmetrical heterocycle's molecular orbital. H-CD, hydrophobic carbon dot

arrangement<sup>43–46</sup>. Based on the red SSF of the H-CD powders, a fluorescent organic glass was fabricated and assembled into a WLED with a cyan LED-chip (Supplementary Fig. 4).

As mentioned above, when the H-CD powders dissolve into DMF, an orange transparent liquid is obtained (Fig. 5c, left inset). Under 365 nm UV excitation, the H-CD powder DMF solution exhibits a pinkish red fluorescence (Fig. 5c, right inset). The PL mapping spectrum (Fig. 5c) reveals that there are both blue and red emission centers in the H-CD powder DMF solution.

Relatively, the H-CD powder acetic acid solution (Fig. 5a) has only a blue emission center, and the H-CD powder (Fig. 5b) solely obtains a red emission center. TEM images (Fig. 5d–f) indicate that the H-CD aggregates, with an average diameter of approximately 56 nm, exist in the DMF solution around the H-CD monomers. The HR-TEM images (Fig. 5g–i) of the H-CD aggregates, and the FFT diffraction pattern (inset of Fig. 5i) of the carbon lattice reveals there are different carbon lattice planes in the H-CD aggregates, meaning that the H-CDs assemble with

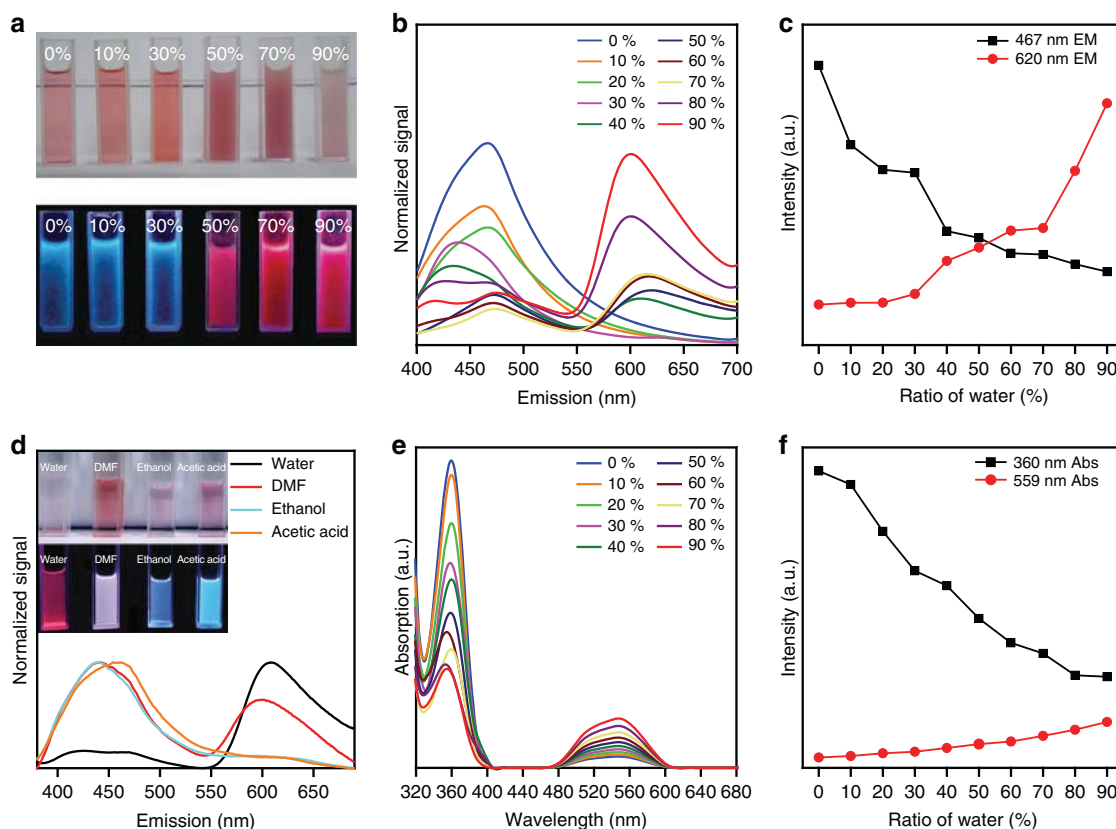


**Fig. 4** H-CDs' absorption and emission varied with different solvent. **a** Photographs of the as-prepared H-CD solution with varying volume ratios of water (from 0 to 90%) under sunlight (top) and 365 nm ultraviolet radiation (bottom). **b** PL emission spectra of the H-CD as-prepared solution with varying ratios of water. **c** Trend of the H-CD as-prepared solutions' fluorescence intensity at 467 and 620 nm, varying with the ratio of water. **d** PL emission spectra of the H-CD powder solutions in different solvents (insets: photographs of the H-CD powder solutions in solvents with different polarities (from high to low) under sunlight (top) and 365 nm ultraviolet radiation (bottom)). **e** UV-Vis absorption spectra of the H-CD as-prepared solution with different ratios of water. **f** Trend of the H-CD as-prepared solutions' absorbance at 360 and 559 nm, varying with the ratio of water. H-CD, hydrophobic carbon dot

random orientation<sup>47–49</sup>. Therefore, the H-CD aggregates generate red SSF and the monomers contribute to the blue emission, which reveals the relationship between the H-CDs' luminous mechanism and their dispersed state.

To further verify the structure and fluorescence mechanism of the H-CDs, we carried out two control experiments, the first displaced DTSA with benzoate to remove the effect of the disulfide bonds. The produced CDs are named B-CDs. As shown in Supplementary Fig. 5a, c, the as-prepared B-CDs solution displays similar blue emission to the H-CDs. However, the B-CDs in the solid state exhibit no fluorescence (Supplementary Fig. 5b, d). Moreover, the solid-state B-CDs can easily dissolve into water (Supplementary Fig. 5e). According to the FT-IR spectra of B-CDs and H-CDs, the chemical structure of the B-CDs is similar to the H-CDs, except for the disulfide bonds. Thus, the relationship between the symmetrical surface around the disulfide bonds and the H-CDs' hydrophobicity and red AIE can be affirmed.

The second control experiment used a postmodification method to synthesize dithiosalicylic acid-modified CDs, which are named P-CDs. First, MA is dissolved into acetic acid and undergoes a solvothermal pretreatment. The P-CD intermediate is water-soluble and displays blue fluorescence (Supplementary Fig. 6a). The TEM image of this intermediate in Supplementary Fig. 6d and its inset indicates that a carbonized dot structure with a 0.25 nm lattice spacing (111 lattice plane of carbon), which can further verify that the blue emission of the H-CDs comes from its carbonized core. P-CDs were then fabricated by mixing DTSA with the aforementioned intermediate and acetic acid, after a

post-solvothermal processing. As shown in Supplementary Fig. 6b, c, e, f, P-CDs exhibit same hydrophobicity and PL properties as the H-CDs, which confirms the root of the H-CDs' hydrophobicity and red AIE is the DTSA-modified surface.

Therefore, we can build a model comprised of the core formed by MA with an N, S, O-containing, rotatable symmetrical heterocyclic surface. Optical properties and calculated energy level transitions reveal the correspondence of blue emission to the core and red emission to the surface. Photoluminescence videos (Supplementary Movies 1, 2, 3) of the H-CDs in different dispersed-states suggest that H-CDs show blue emission in a dissolved state, and red emission in a solid state. The H-CD ethanol solution was added onto a copper grid and dried, then deionized water was sprayed onto the copper grid. The TEM image (Supplementary Fig. 7) of the copper grid revealed that the H-CD monomers were becoming closer than H-CD solution displayed in Fig. 2a. Thus, a convincing aggregate and luminous mechanism can be proposed: in solution, H-CDs' graphitized cores are dominant while the rotatable symmetrical heterocycles around the disulfide bond is recessive; therefore, the H-CD solution exhibits excitation-correlated blue fluorescence, similar to reported carbon dots. When the H-CD monomers contact water, the hydrophobicity of their surfaces cause them to approach each other. Then the conjugated system of the surfaces conducts  $\pi$ - $\pi$  stacking to overlay each other. Finally, the H-CDs take the shape of J-aggregates. Due to this aggregation, the graphitized cores will suffer a  $\pi$ - $\pi$  stacking interaction and further turn off the blue emission via ACQ. Furthermore, the



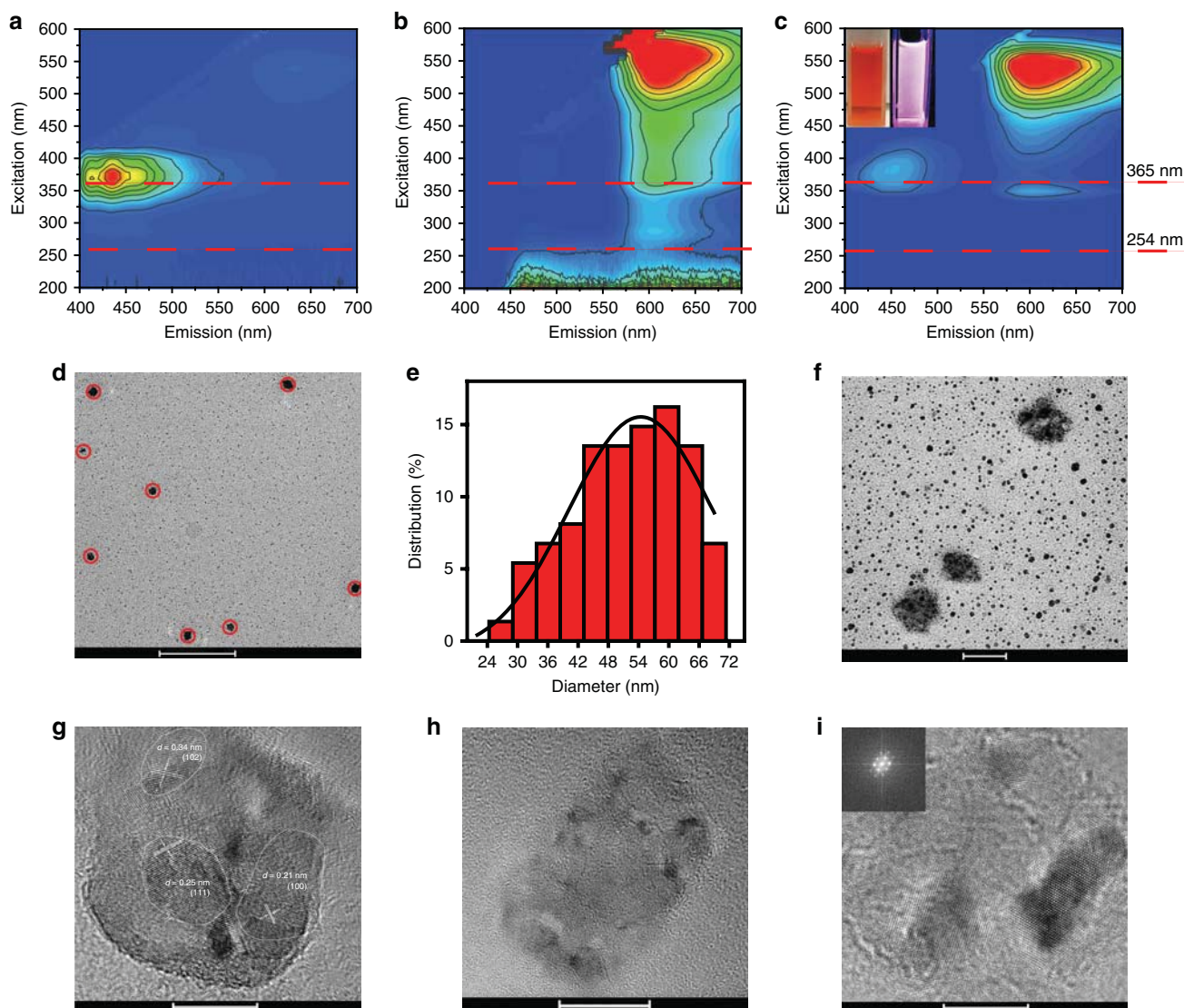


**Fig. 5** Different fluorescence and morphology of H-CDs in varying state. PL mapping spectra of **a** the H-CD powder acetic acid solution, **b** H-CD powder and **c** the H-CD powder DMF solution (insets: photos of the H-CD DMF solution under white light (left) and 365 nm (right) irradiation, dash line marks out emission under 365 or 254 nm UV). **d**, **f** TEM image and **e** particles size distribution of H-CD aggregates (marked by red circles) in the DMF solution. **g–i** High-resolution TEM (HR-TEM) image of the H-CD aggregates in the DMF solution, inset: FFT diffraction pattern of carbon lattice. Scale bars: 500 nm (**d**), 50 nm (**f**), 20 nm (**h**) and 10 nm (**g**, **i**). H-CD, hydrophobic carbon dot, TEM transmission emission microscopy

axisymmetric heterocycles shown in Supplementary Fig. 2 suffer from the restriction of intramolecular rotation (RIR) of symmetrical heterocycles about their disulfide bonds axes, like other reported symmetrical molecules with AIE<sup>17,18,50</sup>, resulting in red AIE<sup>15,16,51</sup>.

**H-CD-based two-switch-mode luminescence ink.** As shown in Fig. 6a, the as-prepared H-CD solution was painted on a filter paper. Under white light, it is almost colorless and shows a blue fluorescence under 365 nm UV excitation. At 254 nm the UV irradiation cannot produce any fluorescence, which conforms to the PL property of the H-CD monomers shown in Fig. 5. By adding water and air-drying, its fluorescence under 365 nm UV turns to pink. Furthermore, it appears as a red fluorescence, which suggests the H-CDs on the filter paper contains both H-CD monomers and H-CD aggregates, compared with the former data. With the addition of ethanol and air-drying, the liquid H-CD displays the same optical properties as the H-CD

monomers. Furthermore, the addition of water can turn on the red emission again. This phenomenon suggests that the as-prepared H-CD solution can be utilized as a reversible two-switch-mode ink. A schematic mechanism for the ink is shown in Fig. 6b. The square frames in Fig. 6b represent the filter paper, the wavy lines represent the paper's fibers. Blue dots represent the H-CD monomers dispersed in the filter paper due to the restriction of the paper's fibers. As mentioned above, H-CD monomers cannot be excited at 254 nm but can be excited at 365 nm. When water is introduced, some of the H-CD monomers aggregate and surface. Furthermore, the other monomers remain joint to the fibers. Therefore, under 365 nm irradiation, both the monomers in the filter paper and the aggregates on surface can be excited to glow blue and red emission, which display as a hybrid pink fluorescence. While under 254 nm irradiation, the monomers are not excited further, resulting in the red emission only. Once ethanol is applied, the aggregates will dissolve into the filter paper as monomers again; therefore, this process is reversible. A video has been taken to show this reversible process (Supplementary

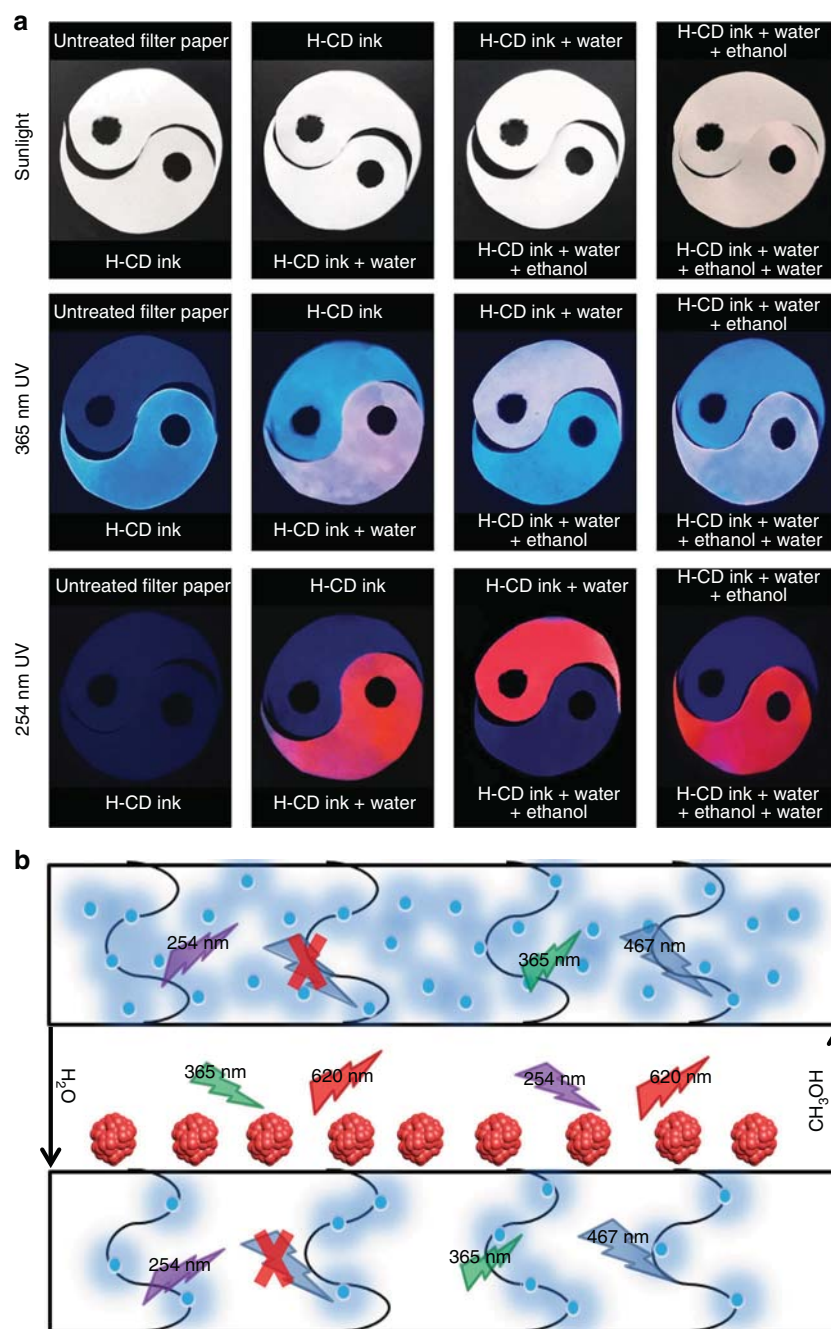


**Fig. 6** Presentation and principle of H-CDs' reversible dual-fluorescence. **a** Photographs of filter papers with different treatment under variable irradiation. **b** Schematic diagram of the H-CDs precipitated with water addition and redissolving into ethanol, with the resulting multimode fluorescence. (The square frames represent the filter paper, the wavy lines represent the paper's fibers, the blue dots represent the H-CD monomers, the flash symbols upward refer to admit light while the downwards ones present emission, the red crosses mean no emission). H-CD, hydrophobic carbon dot

Movie 4). In this video, we observed that the transfer of the different fluorescence is extremely fast. The excellent reversibility of the process makes the H-CDs promising candidates for practical anticounterfeiting and encryption applications.

Finally, the as-prepared H-CD solution was filled into an empty mark pen to form a convenient anticounterfeiting and encryption tool. Two school badges painted with a commercially available highlighter pen (CAHP) and an H-CD as-prepared solution-filled mark pen (HMP) (Fig. 7a) based on the filter papers were fabricated. The badges underwent the same treatments as Fig. 6a, c in order. Under white light, the badges are as white as empty filter papers. The CAHP-painted badge

exhibits cyan fluorescence under 365 nm UV and blue emission under 254 nm UV. Additionally, water addition does not make an obvious change. While under the different treatments and irradiation, the HMP-painted badge can display four different luminescence characteristics (with HMP, under 365 nm UV, blue emission; under 254 nm UV, no emission; with HMP and water, under 365 nm UV, pink emission; under 254 nm UV, red emission). Evidently, the H-CD as-prepared solution-filled mark pen manifests distinctly unique luminescent properties and stability through the injection of different solvents. The HMP dual-encryption utilization is presented in Fig. 7b. "SC", "US" and "NU" are painted by HMP; moreover, "C", "S" and

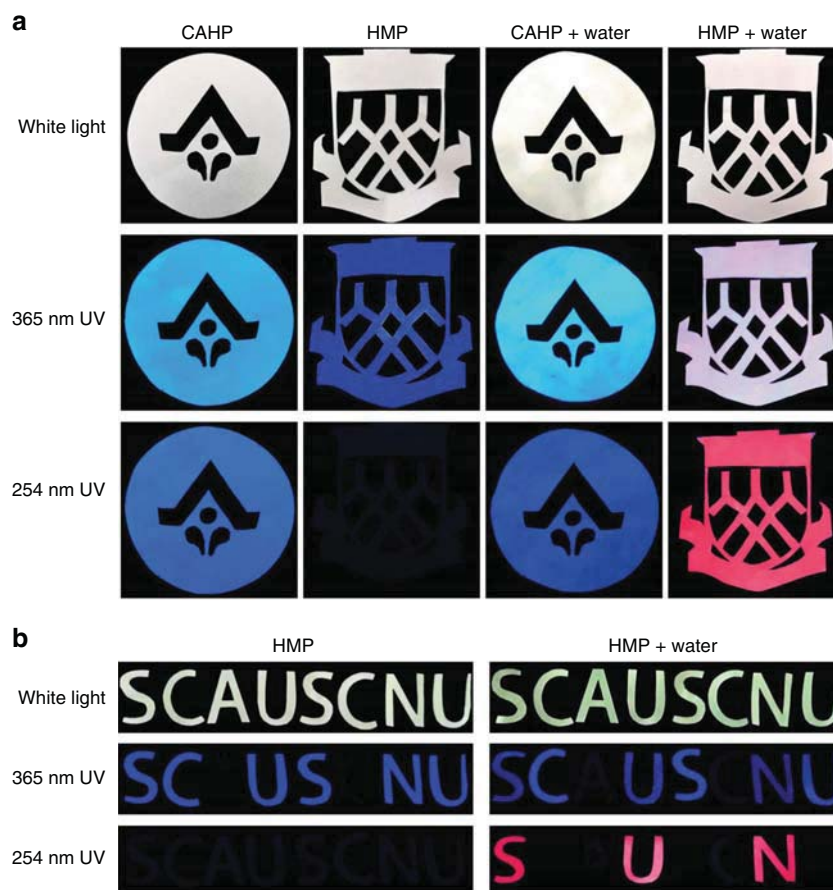


**Fig. 7** Application of H-CDs ink. **a** H-CD as-prepared solution-filled mark pen (HMP) utilized as an anticounterfeiting badge compared with commercially available highlighter pen (CAHP); **b** HMP utilized as a dual-encryption badge. H-CD, hydrophobic carbon dot

“U” are covered with wax after the ink is air-dried. With 365 nm UV excitation, with or without water, only a series of meaningless fake-codes are shown in blue fluorescence. With 254 nm UV irradiation and no water addition, only darkness is observed. Specifically, the true code “SUN” appears as red fluorescence with simultaneous water treatment and 254 nm UV excitation.

## Discussion

In summary, H-CDs with reversible two-switch-mode luminescence (blue dissolved fluorescence and red AIE) are attained from an eco-friendly, low-cost one-pot solvothermal treatment. TEM, XRD and Raman spectra were taken to confirm the nature of the H-CD carbon nanoparticles. Afterwards, the hydrophobic disulfide bond, containing a symmetrical heterocyclic surface of H-CDs was confirmed by XPS, FT-IR spectra and NMR. The hydrophobicity stems from the abundance of pyridinic and epoxy groups on their symmetrical heterocyclic surfaces. As dispersed monomers in organic solvents, such as AC and ethanol, the as-prepared CDs display a “traditional” ultraviolet absorption ( $\lambda_{\text{EX}} = 315 \text{ nm}$ ) and blue emission ( $\lambda_{\text{EM}} = 467 \text{ nm}$ ). The as-prepared CDs are extremely hydrophobic because of the epoxy and pyridyl groups on their surfaces. Thus, the as-prepared CDs will precipitate if water is injected. The precipitations show no blue emission, as the CDs aggregate into J-aggregates and the carbonized cores suffer from aggregation-caused-quenching (ACQ) due to the  $\pi$ - $\pi$  stacking interaction of their vast conjugated system. Furthermore, the dominated surficial energy transition turns into the production of fluorescence, as the

intramolecular rotation of the symmetrical heterocycles about the disulfide bonds is restricted, leading to red AIE ( $\lambda_{\text{EM}} = 621 \text{ nm}$ ,  $\lambda_{\text{EX}} = 559 \text{ nm}$ ). This mechanism is confirmed by the aforementioned characterization methods as well as experiments on monomers and aggregates of H-CDs in a DMF solution: pure H-CD monomers in AC or ethanol solutions solely exhibit blue emission; pure H-CD powder only show red AIE; in a DMF solution, when the monomers and aggregates of H-CD coexist, the blue dissolved fluorescence and red AIE take place. Two control experiments were conducted to further confirm this theory. The turning off of the H-CDs’ blue emission and turning on of the red AIE is reversible. As a result, an anticounterfeiting fluorescence ink for advanced anticounterfeiting and dual encryption has been fabricated based on the two-switch-mode luminescence of H-CDs.

## Methods

**Materials.** Melamine, dithiosalicylic acid, and benzoate were obtained from Shanghai Adamas Reagent Co., Ltd. Acetic acid was purchased from Guangdong Guanghua Sci-Tech Co., Ltd. All reagents were of analytical grade and used directly without further purification. Deionized water was produced through a Millipore water purification system (Milli-Q, Millipore) and used throughout the study.

**Instruments and measurements.** UV–Vis absorption spectra of the powder samples were performed using a Shimadzu UV-2550 ultraviolet-visible spectrophotometer. PL spectra were measured using a Hitachi FL7000 fluorescence spectrophotometer instrument apparatus. The XRD pattern was collected using a XD-2x/M4600. The HR-TEM images were recorded using a JEOL-2010 electron microscope. FT-IR spectra were taken on a Nicolet Avatar 360 FT-IR spectrophotometer. X-ray photoelectron spectroscopy (XPS) experiments were performed using a Kratos AXIS Ultra DLD X-ray photoelectron spectrometer with a monochromatic Al K $\alpha$  X-ray source. Raman spectra were obtained by a Renishaw via a



microspectrometer with an excitation wavelength of 785 nm laser. Particle size analysis is achieved from a Malvern Nano 2SE laser particle size analyzer. NMR measurements were taken by AVANCEIII500 (Bruker). The absolute quantum yield and lifetime are respectively measured by a Hamamatsu C11347 and a Quantaurus Tau C11367.

**Synthesis of the H-CDs.** 201.6 mg MA and 544 mg DTSA were dissolved into 40 mL acetic acid with ultrasonic treatment, then the solution was transferred into an 80 mL Teflon reactor and kept at 180 °C for 10 h in an air oven. After the solvothermal treatment, the as-prepared H-CD solution was added into 1 L boiled water to form H-CD powder and wash out the residual raw materials and solvent. Finally, purified H-CD powder was achieved through vacuum filtration. To confirm the reliability of this water-wash method, we applied column chromatography to purify the H-CD solution for comparison, and the H-CDs obtained from this approach are named CC-H-CDs. FT-IR and UV–Vis spectra of H-CDs and CC-H-CD powders in Supplementary Fig. 8 suggest the components are approximately identical. Therefore, the water-wash method is considered as reliable as column chromatography.

**Synthesis of the P-CDs.** 201.6 mg MA was dissolved into 40 mL acetic acid with ultrasonic treatment, then the solution was transferred into an 80 mL Teflon reactor and maintained at 180 °C for 5 h in an air oven. The as-prepared solution was purified by centrifuge and column chromatography and intermediate powders were collected from freeze-drying. Afterwards, 150 mg intermediate powder and 544 mg DTSA were dissolved into 40 mL acetic acid, transferred into an 80 mL Teflon reactor, and maintained at 180 °C for 5 h in an air oven. After the solvothermal treatment, the as-prepared H-CD solution was added into 1 L boiled water to form H-CD powders and wash out residual raw materials. Finally, the purified P-CDs powder was obtained through vacuum filtration.

**Synthesis of the B-CDs.** 201.6 mg MA and 434 mg were dissolved into 40 mL acetic acid with ultrasonic treatment, then transferred into an 80 mL Teflon reactor and maintained at 180 °C for 10 h in an air oven. After the solvothermal treatment, the as-prepared B-CDs solution was dialyzed in deionized water for a week to remove residual raw materials. Finally, the purified solid-state B-CDs were obtained through freeze-drying.

**Preparation of H-CD-powders-based fluorescence organic glass.** 150 mg H-CD powders, 53.7 mg dibenzoyl peroxide, 1 mL dibutyl phthalate and 15 mL methyl methacrylate were added into a 250 mL flask, the mixture was maintained at 90–92 °C for 15 min in water bath. Afterwards, the flask was cooled down to 40 °C rapidly, and the mixture was poured into a template and maintained at 100 °C for 2 h. After reverse molding, fluorescent organic glasses (Supplementary Fig. 4) based on H-CD powders were obtained.

**Computational process of H-CDs' molecular orbital energy level and fluorescence lifetime.** The energy level transitions (Fig. 3e) of the H-CDs' carbonized cores and symmetrical heterocyclic surfaces were calculated by the formula

$$E = h \frac{c}{\lambda} \quad (1)$$

according to their absorptive and emissive properties, which fit the molecular orbital energy level of the proposed structure simulated by the Gaussian 09 plug-in in ChemBioOffice 2014®. The fluorescence decay curve and double-exponential fitting results are shown in Supplementary Fig. 2a. The fitting function is shown in the formula below

$$y = y_0 + A_1 * \exp(-(x - x_0)/t_1) + A_2 * \exp(-(x - x_0)/t_2) \quad (2)$$

and the fluorescence lifetime is calculated as 4.56 ns by the formula below:

$$t = (A_1 t_1^2 + A_2 t_2^2) / (A_1 t_1 + A_2 t_2) = 4.56 \text{ ns.} \quad (3)$$

## Data availability

Data are available from the corresponding author upon reasonable request.

Received: 15 September 2018 Accepted: 25 March 2019

Published online: 17 April 2019

## References

- Wang, Z. et al. 53% efficient red emissive carbon quantum dots for high color rendering and stable warm white-light-emitting diodes. *Adv. Mater.* **29**, 1702910 (2017).
- Wang, B. et al. Self-assembled core-shell-corona multifunctional non-viral vector with AIE property for efficient hepatocyte-targeting gene delivery. *Polym. Chem.* **8**, 7486–7498 (2017).
- Jiang, K. et al. Red, green, and blue luminescence by carbon dots: full-color emission tuning and multicolor cellular imaging. *Angew. Chem. Int. Ed.* **54**, 5360–5363 (2015).
- Yuan, F. et al. Multicolor fluorescent graphene quantum dots colorimetrically responsive to all-pH and a wide temperature range. *Nanoscale* **7**, 11727–11733 (2015).
- Song, Y. et al. Drug-derived bright and color-tunable N-doped carbon dots for cell imaging and sensitive detection of Fe<sup>3+</sup> in living cells. *ACS Appl. Mater. Interfaces* **9**, 7399–7405 (2017).
- Miao, X. et al. Synthesis of carbon dots with multiple color emission by controlled graphitization and surface functionalization. *Adv. Mater.* **30**, 1704740 (2018).
- Hu, S., Trinchì, A., Atkin, P. & Cole, I. Tunable photoluminescence across the entire visible spectrum from carbon dots excited by white light. *Angew. Chem. Int. Ed.* **54**, 2970–2974 (2015).
- He, J. et al. Solid-state carbon dots with red fluorescence and efficient construction of dual-fluorescence morphologies. *Small* **13**, 1700075 (2017).
- Ge, J. et al. Red-emissive carbon dots for fluorescent, photoacoustic, and thermal theranostics in living mice. *Adv. Mater.* **27**, 4169–4177 (2015).
- Zhang, Y. et al. A self-quenching-resistant carbon nanodot powder with multicolored solid-state fluorescence for ultra-fast staining of various representative bacterial species within one minute. *Nanoscale* **8**, 19744–19753 (2016).
- Shao, J. et al. Full-color emission polymer carbon dots with quench-resistant solid-state fluorescence. *Adv. Sci.* **4**, 1700395 (2017).
- Lou, Q. et al. Water-triggered luminescent “nano-bombs” based on supra-(carbon nanodots). *Adv. Mater.* **27**, 1389–1394 (2015).
- Chen, Y. et al. A self-quenching-resistant carbon-dot powder with tunable solid-state fluorescence and construction of dual-fluorescence morphologies for white light-emission. *Adv. Mater.* **28**, 312–318 (2016).
- Spano, F. C. The spectral signatures of Frenkel polarons in H- and J-aggregates. *Acc. Chem. Res.* **43**, 429–439 (2010).
- Yeh, H. C., Wu, W. C. & Chen, C. T. The colourful fluorescence from readily-synthesised 3,4-diaryl-substituted maleimide fluorophores. *Chem. Commun.* **3**, 404–405 (2003).
- Wang, Y. et al. Aggregation-induced emission luminogen with deep-red emission for through-skull three-photon fluorescence imaging of mouse. *ACS Nano* **11**, 10452–10461 (2017).
- Tang, B. Z. et al. Efficient blue emission from siloles. *J. Alloy. Compd.* **11**, 2974–2978 (2001).
- Hong, Y. & Lam, J. W. & Tang, B. Z. Aggregation-induced emission: phenomenon, mechanism and applications. *Chem. Commun.* **29**, 4332–4353 (2009). <https://doi.org/10.1039/B904665H>.
- Zhu, S. et al. Highly photoluminescent carbon dots for multicolor patterning, sensors, and bioimaging. *Angew. Chem. Int. Ed.* **52**, 3953–3957 (2013).
- Wang, T. Y., Chen, C. Y., Wang, C. M., Tan, Y. Z. & Liao, W. S. Multicolor functional carbon dots via one-step refluxing synthesis. *ACS Sens.* **2**, 354–363 (2017).
- Lu, S. et al. Piezochromic carbon dots with two-photon fluorescence. *Angew. Chem. Int. Ed.* **56**, 6187–6191 (2017).
- Lai, L. F. et al. One-step synthesis of NH<sub>2</sub>-graphene from in situ graphene-oxide reduction and its improved electrochemical properties. *Carbon* **49**, 3250–3257 (2011).
- Tan, L. et al. Synthesis of highly bright oil-soluble carbon quantum dots by hot-injection method with N and B Co-Doping. *J. Nanosci. Nanotechnol.* **16**, 2652–2657 (2016).
- Tan, J., Zhang, J., Li, W., Zhang, L. Q. & Yue, D. M. Synthesis of amphiphilic carbon quantum dots with phosphorescence properties and their multifunctional applications. *J. Mater. Chem. C* **4**, 10146–10153 (2016).
- Panniello, A. et al. Luminescent oil-soluble carbon dots toward white light emission: a spectroscopic study. *J. Phys. Chem. C* **122**, 839–849 (2017).
- Nandi, S. et al. Membrane analysis with amphiphilic carbon dots. *Chem. Commun.* **50**, 10299–10302 (2014).
- Moon, B. J. et al. Facile and purification-free synthesis of nitrogenated amphiphilic graphitic carbon dots. *Chem. Mater.* **28**, 1481–1488 (2016).
- Lu, L. et al. Hydrophobic-carbon-dot-based dual-emission micelle for ratiometric fluorescence biosensing and imaging of Cu<sup>2+</sup> in liver cells. *Biosens. Bioelectron.* **92**, 101–108 (2017).
- Kozak, O. et al. Surfactant-derived amphiphilic carbon dots with tunable photoluminescence. *J. Phys. Chem. C* **117**, 24991–24996 (2013).
- Kong, D. et al. Amphiphilic carbon dots for sensitive detection, intracellular imaging of Al<sup>3+</sup>. *Anal. Chim. Acta* **953**, 63–70 (2017).
- Jones, S. S., Sahatiya, P. & Badhulika, S. One step, high yield synthesis of amphiphilic carbon quantum dots derived from chia seeds: a solvatochromic study. *New J. Chem.* **41**, 13130–13139 (2017).





32. Gu, J. J. et al. Green synthesis of amphiphilic carbon dots from organic solvents: application in fluorescent polymer composites and bio-imaging. *RSC Adv.* **8**, 12556–12561 (2018).
33. Fowley, C. et al. Highly luminescent biocompatible carbon quantum dots by encapsulation with an amphiphilic polymer. *Chem. Commun.* **48**, 9361–9363 (2012).
34. Chen, J. et al. Understanding the capsanthin tails in regulating the hydrophilic-lipophilic balance of carbon dots for a rapid crossing cell membrane. *Langmuir* **33**, 10259–10270 (2017).
35. Li, F. et al. Selenium-doped carbon quantum dots for free-radical scavenging. *Angew. Chem. Int. Ed.* **56**, 9910–9914 (2017).
36. Geng, S. et al. Synthesis of lipid-black phosphorus quantum dot bilayer vesicles for near-infrared-controlled drug release. *Chem. Commun.* **54**, 6060–6063 (2018).
37. Fan, X. et al. Deoxygenation of exfoliated graphite oxide under alkaline conditions: a green route to graphene preparation. *Adv. Mater.* **20**, 4490–4493 (2008).
38. Ding, D. et al. Ultrabright organic dots with aggregation-induced emission characteristics for real-time two-photon intravital vasculature imaging. *Adv. Mater.* **25**, 6083–6088 (2013).
39. Zheng, M. et al. One-pot to synthesize multifunctional carbon dots for near infrared fluorescence imaging and photothermal cancer therapy. *ACS Appl. Mater. Interfaces* **8**, 23533–23541 (2016).
40. Yeh, T. F. et al. Elucidating quantum confinement in graphene oxide dots based on excitation-wavelength-independent photoluminescence. *J. Phys. Chem. Lett.* **7**, 2087–2092 (2016).
41. Cai, S. et al. Visible-light-excited ultralong organic phosphorescence by manipulating intermolecular interactions. *Adv. Mater.* **29**, 1701244 (2017).
42. Deng, Y. H., Feng, X. J., Yang, D. J., Yi, C. H. & Qiu, X. Q.  $\pi$ - $\pi$  stacking of the aromatic groups in lignosulfonates. *Bioresources* **7**, 1145–1156 (2012).
43. Deng, Y. et al. Investigation of aggregation and assembly of alkali lignin using iodine as a probe. *Biomacromolecules* **12**, 1116–1125 (2011).
44. Li, X. et al. Self-assembled graphene quantum dots induced by cytochrome c: a novel biosensor for trypsin with remarkable fluorescence enhancement. *Nanoscale* **5**, 7776–7779 (2013).
45. Ma, Z. et al. Seeking brightness from nature: J-aggregation-induced emission in cellulolytic enzyme lignin nanoparticles. *ACS Sustain. Chem. Eng.* **6**, 3169–3175 (2018).
46. Su, M. et al. Nano-assemblies from J-aggregated dyes: a stimuli-responsive tool applicable to living systems. *J. Am. Chem. Soc.* **141**, 402–413 (2019).
47. Xie, Z., Du, Q., Wu, Y., Hao, X. & Liu, C. Full-band UV shielding and highly daylight luminescent silane-functionalized graphene quantum dot nanofluids and their arbitrary polymerized hybrid gel glasses. *J. Mater. Chem. C* **4**, 9879–9886 (2016).
48. Zhang, Z. et al. New transparent flexible nanopaper as ultraviolet filter based on red emissive Eu(III) nanofibrillated cellulose. *Opt. Mater.* **73**, 747–753 (2017).
49. Feng, X. et al. Use of carbon dots to enhance UV-blocking of transparent nanocellulose films. *Carbohydr. Polym.* **161**, 253–260 (2017).
50. Li, Y. et al. Aggregation induced red shift emission of phosphorus doped carbon dots. *RSC Adv.* **7**, 32225–32228 (2017).

51. Chen, C. et al. Highly luminescent Inks: aggregation-induced emission of copper-iodine hybrid clusters. *Angew. Chem. Int. Ed.* **57**, 7106–7110 (2018).

## Acknowledgements

The present work was supported by the National Natural Science Foundation of China (Grant Nos. 21571067, 51402207, 61675072, 11874021), the National Natural Science Foundation of China Joint Fund with Guangdong under Key Project (Grant No. U1501242) and the Teamwork Projects funded by the Guangdong Natural Science Foundation (Grant No. S2013030012842).

## Author contributions

H.Y., C.H., Y.L. and Z.L. conceived the experiments. H.Y. synthesized all materials, made all measurements and wrote the paper. B.L., J.Z. and X.Z. gave suggestions to optimize the system. All authors discussed the results and commented on the manuscript at all stages.

## Additional information

**Supplementary Information** accompanies this paper at <https://doi.org/10.1038/s41467-019-09830-6>.

**Competing interests:** The authors declare no competing interests.

**Reprints and permission** information is available online at <http://npg.nature.com/reprintsandpermissions/>

**Journal peer review information:** *Nature Communications* thanks Zaicheng Sun, and the other anonymous reviewer(s) for their contribution to the peer review of this work. Peer reviewer reports are available.

**Publisher's note:** Springer Nature remains neutral with regard to jurisdictional claims in published maps and institutional affiliations.



**Open Access** This article is licensed under a Creative Commons Attribution 4.0 International License, which permits use, sharing, adaptation, distribution and reproduction in any medium or format, as long as you give appropriate credit to the original author(s) and the source, provide a link to the Creative Commons license, and indicate if changes were made. The images or other third party material in this article are included in the article's Creative Commons license, unless indicated otherwise in a credit line to the material. If material is not included in the article's Creative Commons license and your intended use is not permitted by statutory regulation or exceeds the permitted use, you will need to obtain permission directly from the copyright holder. To view a copy of this license, visit <http://creativecommons.org/licenses/by/4.0/>.

© The Author(s) 2019

# Construction of Carbon Dots with Color-Tunable Aggregation-Induced Emission by Nitrogen-Induced Intramolecular Charge Transfer

Xiaokai Xu, Luoqi Mo, Yadong Li, Xiaoqin Pan, Guangqi Hu, Bingfu Lei, Xuejie Zhang, Mingtao Zheng, Jianle Zhuang,\* Yingliang Liu,\* and Chaofan Hu\*

As one of the most promising fluorescent nanomaterials, the fluorescence of carbon dots (CDs) in solution is extensively studied. Nevertheless, the synthesis of multicolor solid-state fluorescence (SSF) CDs is rarely reported. Herein, CDs with multicolor aggregation-induced emission are prepared using amine molecules, all of them exhibiting dual fluorescence emission at 480 nm (Em-1) and 580–620 nm (Em-2), which is related to the S–S bonds of dithiosalicylic acid and the conjugated structure attached to C=O/C=N bonds, respectively. As a strong electron-withdrawing group, the increase of C=N content makes dual-fluorescent groups on the surface of CDs produce push and pull electrons, which determines intramolecular charge transfer (ICT) between the double emission. With the increase in C=N content from 35.6% to 58.4%, the ICT efficiency increases from 8.71% to 45.94%, changing the fluorescence of CDs from green to red. The increase of ICT efficiency causes fluorescence quantum yield enhancement by nearly five times and redshift of the fluorescence peak. Finally, based on the multicolor luminescence properties induced by the aggregation of CDs, pattern encryption and white-LED devices are realized. Based on the fat solubility and strong ultraviolet absorption characteristics of CDs, fingerprint detection and leaf anti-UV hazards are applied.


## 1. Introduction

Fluorescent carbon dots (CDs) are a unique class of spherical nanometer-sized materials contributing to the most recent advances in the fields of biosensors, bioimaging, drug delivery, light-emitting devices, and photocatalysis.<sup>[1–4]</sup> Easy preparation and purification, adjustable optical and surface properties, and superior biocompatibility make it focused.<sup>[5–8]</sup> Unfortunately, the lack of a systematic method to regulate the emission bandgap of CDs and aggregation-caused quenching (ACQ) of solid-state fluorescence (SSF) CDs due to excessive resonance energy transfer (ET) or direct  $\pi$ – $\pi$  stacking<sup>[9–12]</sup> hindered the development and application of CDs. To solve the ACQ in SSF of CDs, most researchers embed CDs in solid substrates to realize the self-stable solid-state CDs-based composites,<sup>[13–18]</sup> and the other possible solution is to introduce a certain steric hindrance between the CD particles that can be kept at a proper interval

by introducing a long chain structure on the outer surface to reduce the interaction of CDs and achieve SSF.<sup>[19,20]</sup> Polymers and matrices increase the cost of preparation and affect some of the properties of the CDs. What is more important, it restricted the concentration of the doped CDs, and the high loading fraction still causes a serious decrease in the photoluminescence quantum yield of CDs.<sup>[21,22]</sup>

To date, aggregation-induced emission (AIE) CD-based materials have been reported and several rational strategies have been proposed to generate and enhance its fluorescence in the aggregation state.<sup>[23–25]</sup> However, the emission source of these CDs is still fuzzy and tunable emission multicolor seems to be difficult to establish. Preliminary studies have already demonstrated that the photoluminescence (PL) of CDs can be attributed to the “extrinsic” emission of C=O, C=N, and other functional groups.<sup>[3,9,26,27]</sup> Therefore, the doping of N with electron-donating ability can generate new energy state and absorption domain through the  $n$ – $\pi^*$  transition of C=N. The fluorescence emission of AIE CDs often occurs on the surface of CDs<sup>[23,28]</sup> and the dual fluorescence emission on the surface of CDs is attractive in the construction of intramolecular charge transfer

X. Xu, L. Mo, Y. Li, X. Pan, B. Lei, X. Zhang, M. Zheng, J. Zhuang, Y. Liu, C. Hu  
Key Laboratory for Biobased Materials and Energy of Ministry of Education/Guangdong Provincial Engineering Technology Research Center for Optical Agriculture  
College of Materials and Energy  
South China Agricultural University  
Guangzhou 510642, China  
E-mail: zhuangjl@scau.edu.cn; tliuyi@scau.edu.cn; thucf@scau.edu.cn  
X. Xu, L. Mo, Y. Li, X. Pan, B. Lei, X. Zhang, M. Zheng, J. Zhuang, Y. Liu, C. Hu  
Guangdong Laboratory for Lingnan Modern Agriculture  
Guangzhou 510642, China  
G. Hu  
College of Photoelectric Engineering  
Guangdong Polytechnic Normal University  
Guangzhou 510665, China

 The ORCID identification number(s) for the author(s) of this article can be found under <https://doi.org/10.1002/adma.202104872>.

DOI: 10.1002/adma.202104872

(ICT) donor–acceptor pairs. Although dual emission fluorescence centers have been observed, little attention has been paid to the interaction between them. The phenomenon of ICT is common in the fluorescence process of dye molecules, and there must be a mutual conjugate system composed of electron donors and electron acceptors, and electron transfer occurs under the action of light induction.<sup>[29,30]</sup> This theory has not been utilized in the pure CDs yet.

Based on the above situation, we construct tunable AIE multicolor CDs with dual fluorescence centers by nitrogen-triggered ICT. XPS measurement and multiple sets of control experiments verify that the dual emission fluorescence centers are attributed to S–S-based symmetrical fluorescent molecules and C=N-based conjugated structures, respectively. We believe that the increase in the ratio of Em-2 to Em-1 is attributable to ICT, and the increase of C=N content leads to an enhanced gradual push–pull electron effect, which indicates an increase in ICT efficiency. By taking advantage of these unique properties of CDs, pattern encryption and fingerprint detection are proposed. Besides, white LEDs are constructed by CD powders with a dual-emission fluorescence form in the organic medium. The preparation is simplified and the cost is reduced. Finally, based on the strong UV absorption properties of CD, we constructed CDs@PVA composite film to protect plant leaves from UV radiation, illustrating the immense potential of the AIE CDs in various fields.

## 2. Results and Discussion

The synthesis of CD involves the solvothermal treatment of reaction precursor at 180 °C for 10 h, followed by purifying via boiling water (Figure S1, Supporting Information). The starting material dithiosalicylic acid (DTSA) possesses a unique structure with an S–S bond-forming symmetrical molecular, which is a key portion for the synthesis of CDs with SSF. For tuning their emission color, small-molecule amines with different numbers of nitrogen atoms were added as reaction precursors to control the nitrogen content in CDs. Visually, multi-color luminescent solid matrix-free CDs ranging from green to red can be obtained, suggesting that the nitrogen atoms play a key role in producing long-wavelength emissions as shown in Figure S1, Supporting Information. The color of the CDs powder gradually deepens under daylight with the increase of nitrogen, which may be related to the degree of carbonization of the CDs. For convenience, these samples were labeled as CD<sub>1</sub>, CD<sub>2</sub>, CD<sub>3</sub>, CD<sub>4</sub>, and CD<sub>5</sub>, respectively.

As shown in Figure 1a–e; Table S1, Supporting Information, PL emission spectra of CD<sub>1</sub>–CD<sub>5</sub> show regular changes that have dual fluorescence centers (Em-1: 480 nm and near Em-2: 600 nm). With the increase of the nitrogen atoms in the amine precursor, the red fluorescence peak gradually increases compared with the green fluorescence peak, and finally, leaves a single red light emission peak in CD<sub>5</sub>. Exposed to continuously ultraviolet light for 10 h, no obvious photobleaching or quenching was observed in the fluorescence (monitored at 620 nm) of CD<sub>5</sub> (Figure S2, Supporting Information). Furthermore, the excitation spectra of the five CDs at different emission centers are shown in Figure S3a–e and Table S1, Supporting Information. The green and red emission of the CDs

originates from the excitation at 440 nm and 512–555 nm, respectively (Table S1, Supporting Information). Besides, Figure 1f shows strong UV–vis absorption of CDs powder in UV and visible-light region (200–600 nm), which is directly related to the photoluminescence emission. In the higher-energy region (447 nm), the absorption band from CD<sub>1</sub> to CD<sub>5</sub> is weaker, while the absorption band of the lower-energy region (≈550 nm) is the opposite and redshifts slightly. Furthermore, the absorption peaks at 447 and ≈550 nm match the fluorescence excitation spectra (Figure S3a–e, Supporting Information) well, indicating that these two absorption bands contribute to the double emission centers of CDs, but the absorption peaks around 320 nm do not. Furthermore, the as-prepared CDs solution (Figure S4a–e, Supporting Information) exhibits blue PL features, and the optimal excitation and emission are near 370 and 430 nm, respectively. The fluorescence of CDs in the solution state shows the luminescence of the carbon core of ordinary CDs, which is caused by the  $\pi$ – $\pi$  transition and the large conjugate structure of the CDs (Figure S4f, Supporting Information).<sup>[23,31]</sup> Besides, the optical properties of CD<sub>5</sub> solution in the presence of various metal ions were studied respectively in Figure S5, Supporting Information; the fluorescence intensity of CD<sub>5</sub> remained at an acceptable level (>80%) when confronted with metal ions, which reveals the luminescence of CD<sub>5</sub> is relatively stable in the environment with the interference of potentially existing metal ions. The CDs powder exhibits a different broad absorption (447 and 550 nm), which is attributed to the  $n$ – $\pi^*$  transitions of the surface states containing C=N/C=O, C–O, C–S, and S–S structures.<sup>[15,23]</sup> Therefore, the absorption spectra (Figure 1f) show the clear energy absorbance centers in terms of carbon core and surface states. A positive correlation was also observed between the emission (Em-2) wavelength and the Abs-2, Ex-2 of CD<sub>1</sub>–CD<sub>5</sub> (Figure 1g; Table S1, Supporting Information). With the redshift of Abs-2 (550–560 nm), both the excitation center and emission center of CDs tend to redshift. Em-1 shows a stable emission center (480 nm), and the correspondence is excitation center (≈440 nm) and absorption center (447 nm). Although small shifts are found between the different types of CDs, their absorbance, excitation, and emission are highly comparable and can be related to the same radiative process. The calculated photoluminescence lifetimes are also similar; time-resolved PL decay curves were measured for the different emissions of these samples by 430 nm laser (Figure 1h,i). The plots of fluorescence intensity decay reveal the kinetics of the deactivation of electrons from an excited state to the ground state via radiative and nonradiative pathways. The curves observed of a lifetime here can be fitted to two exponential functions:

$$I(t) = B_1 \exp(-t/\tau_1) + B_2 \exp(-t/\tau_2) \quad (1)$$

where  $B_1$  and  $B_2$  are the pre-exponential factors; and  $\tau_1$  and  $\tau_2$  are the fitted lifetimes, respectively (Table S2, Supporting Information). The  $A_1$  (%) and  $A_2$  (%), calculated from weighing  $B_1$  and  $B_2$ , represent the lifetime weighted fractional intensity of each component of the two-exponential fits. From CD<sub>1</sub> ( $\tau = 4.63$  ns) to CD<sub>5</sub> ( $\tau = 2.73$  ns) monitored at 480 nm, the fast component  $\tau_1$  weight increases from 86.8% to 97.4%, and the  $\tau_2$  weight decreases from 13.2% to 2.6%. On the other hand, from CD<sub>1</sub> ( $\tau = 3.10$  ns) to CD<sub>5</sub> ( $\tau = 4.15$  ns) monitored at



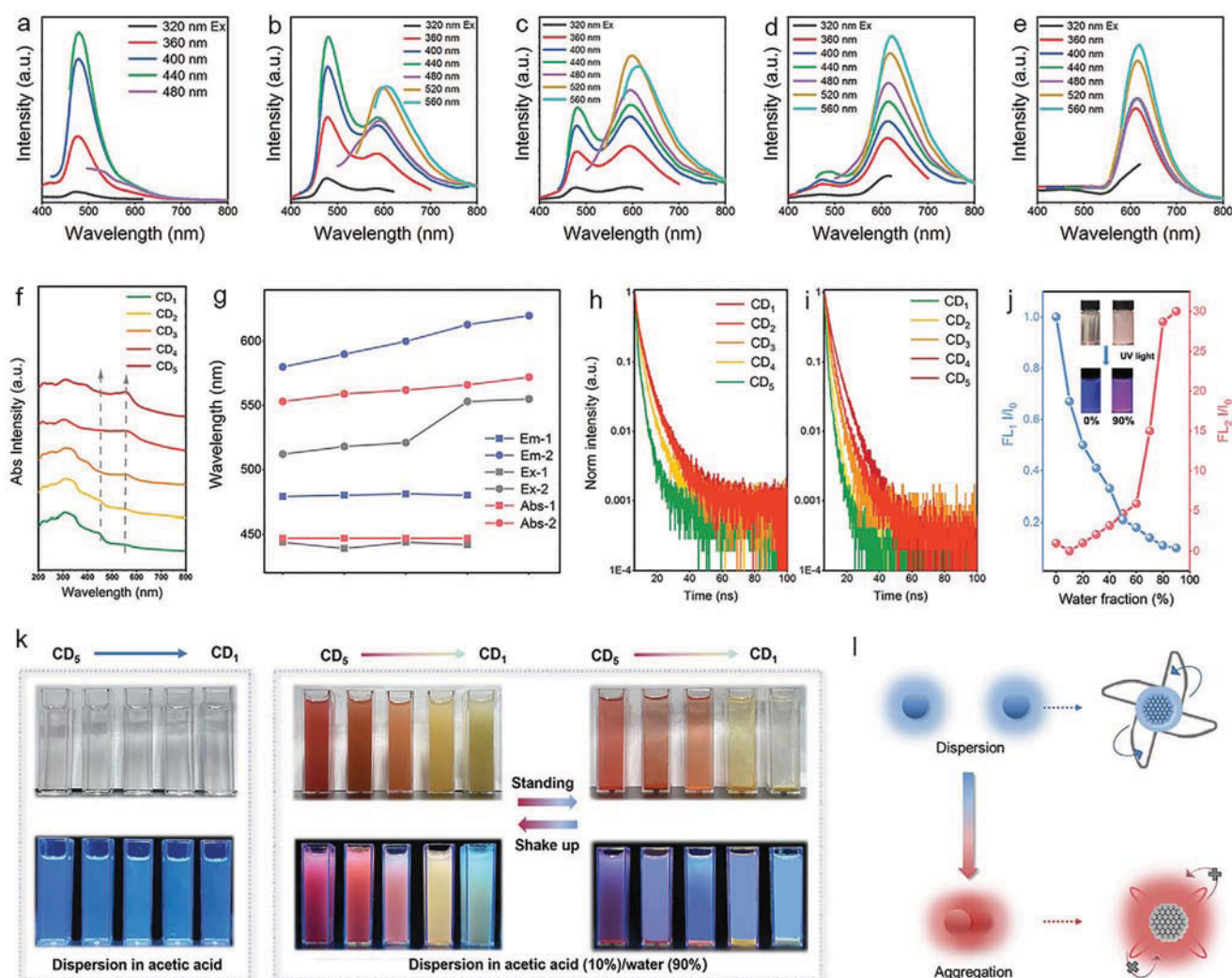


**Figure 1.** a–e) Photoluminescence (PL) emission spectra of CD<sub>1</sub>–CD<sub>5</sub> powder at the different excitation wavelengths; inset: photographs of CDs powder under UV light. f) UV–vis absorption spectra of CD<sub>1</sub>–CD<sub>5</sub> powder. g) Dependence of the wavelengths of the first and second absorption peaks (Abs-1 and Abs-2), first and second excitation peaks (Ex-1 and Ex-2), and emission peaks (Em-1 and Em-2) on the CD<sub>1</sub>–CD<sub>5</sub> (data presented in Table S1, Supporting Information). h,i) Lifetime decay curves of CD<sub>1</sub>–CD<sub>5</sub> emission at 480 nm and red luminescence center at room temperature. j) PL intensity ratio ( $I/I_0$ ) of CD<sub>5</sub> with varying volume ratios of water (from 0–90%) at 480 and 620 nm. k) Images of CDs dissolved in acetic acid and acetic acid/water (10%/90%) mixture solution under visible and UV light, respectively. l) Schematic of AIE effect at CDs.

580–620 nm, the fast component  $\tau_1$  weight decreases from 50.0% to 0%, and the  $\tau_2$  weight increases from 50.0% to 100%. It is not difficult to see that green and red emission centers from CD<sub>1</sub> to CD<sub>5</sub> are of a short lifetime and long lifetime, respectively, and red emission centers finally reach 100% in CD<sub>5</sub>. The quantum yields (QY) for the single fractions were 2.15% for CD<sub>1</sub>, 3.61% for CD<sub>2</sub>, 3.76% for CD<sub>3</sub>, 7.17% for CD<sub>4</sub>, and 11.7% for CD<sub>5</sub> (Table S3, Supporting Information). It is important to note that these lower values manifest that the fluorescence is related to their high photon absorption (Figure S6, Supporting Information). Interestingly, the fluorescence emission of CD<sub>5</sub> changes from blue to red when the water volume increases to 80%, and it appears as a turbid aqueous solution under daylight (Figure 1j). In detail, CD<sub>1</sub>–CD<sub>5</sub> is dissolved in acetic acid stably, but not in water. As the water volume increases, the red light from the aggregated state and the blue light from the

solution state compete with each other. In the water volume content of 90%, the CD system is cloudy, and the precipitation is complete within 30 min (Figure 1k). This phenomenon is consistent with the widely recognized and accepted AIE.<sup>[28]</sup> Highly viscous medium causes restriction of rotation (RIR) and the excited state relaxation occurs by enhanced fluorescence emission.<sup>[32–36]</sup> By this strategy, AIE-CD<sub>5</sub> was dispersed in solvents with different viscosities (acetic acid and PVA) and their fluorescence spectra were detected. It can be seen from Figure S7, Supporting Information, that the CD<sub>5</sub> in the PVA solution exhibits a phenomenon of increased fluorescence due to the restricted rotation of molecules at emission 620 nm wavelength. According to our proposed mechanism, the RIR process is responsible for the AIE effect. The QY of CD<sub>1</sub>–CD<sub>5</sub> in the dispersion system is 0.7%–2.6%, and calculated that  $\alpha_{AIE}$  is greater than 1 (Table S4, Supporting Information), which proves that



CD<sub>1</sub>–CD<sub>5</sub> has AIE activity. The time-resolved PL spectrum of CD<sub>1</sub>–CD<sub>5</sub> in acetic acid solution (Figure S8a, Supporting Information) has average lifetimes of 1.095–1.511 ns. Furthermore, the  $K_R$  (radiation decay rate) and  $K_{NR}$  (nonradiation decay rate) of CD<sub>1</sub>–CD<sub>5</sub> in solid and solution are calculated according to the following equations.

$$K_R = QY/\tau \quad (2)$$

$$QY = K_R / (K_R + K_{NR}) \quad (3)$$

The calculated  $K_R$  and  $K_{NR}$  values are shown in Table S5, Supporting Information, showing a lower non-radiative decay rate ( $K_{NR}$ ) in solid state, while  $K_R$  is not significant change. Therefore, CD<sub>1</sub>–CD<sub>5</sub> have the basic rules that comply with AIE activity.<sup>[37]</sup> With the increase of solvent polarity, the emission band of CD<sub>5</sub> has a significant redshift from hexane to H<sub>2</sub>O (Figure S9, Supporting Information), which is consistent with the characteristic of most fluorophores that show ICT-character. In addition, we tested the CD<sub>5</sub> lifetime decay curve of different volume ratios of water (from 30–70%) at 620 nm (Figure S8b and Table S6, Supporting Information). This indicates that CD<sub>5</sub> in the mixed solvent may exist in two different environments, and the values of  $A_1$  and  $A_2$  represent the fraction of molecules in each environment.<sup>[38]</sup> One pathway has a short decay time, while the other pathway has a relatively long decay time. As the volume fraction of water in the mixture becomes higher and higher, the decay time of molecules passing through the fast channel is more than three times longer than that in pure

solvents. Time-resolved measurement can separate short-life-time and long-life-time components, observed slow PL decay components with <50% water content, indicating that some aggregates have formed in the solution with less water content. As shown in Figure 1l, the restriction of molecular movement or vibration on the surface of the aggregated CDs can inhibit the non-radiative transition, which greatly enhances the surface state fluorescence of CDs and achieve SSF. However, the emission of carbon core is quenched due to excessive Forster resonance energy transfer.<sup>[9]</sup> The moving molecules on the surface of dispersed CDs will consume excessive non-radiative energy to quench the surface radiation, which makes the CDs luminescence present carbon core blue fluorescence.<sup>[23]</sup>

CDs were thoroughly analyzed by high-resolution transmission electron microscopy (HRTEM), atomic force microscopy (AFM), X-ray photoelectron spectroscopy (XPS), X-ray diffraction (XRD), and Fourier transform infrared (FT-IR) to analyze the redshifted fluorescence. TEM images presented in Figure 2a–e reveal that the samples were well-dispersed, with similar average particle sizes of ≈3–4 nm (inset image). The HRTEM images (Figure 2f–j) show that all the CDs exhibited identical well-resolved lattice fringes with a spacing of 0.21 nm, corresponding to the (100) plane lattice of graphene.<sup>[39]</sup> The AFM images (Figure 2k–o) also show that these CDs are monodispersed, with a similar thickness of ≈4–5 nm, which displays that the structure is subspherical. It can be seen from the result that there is no obvious difference in the particle size of these CDs, which indicates that the PL emission redshift of the samples from CD<sub>1</sub> to CD<sub>5</sub> could not be ascribed to quantum size effects.

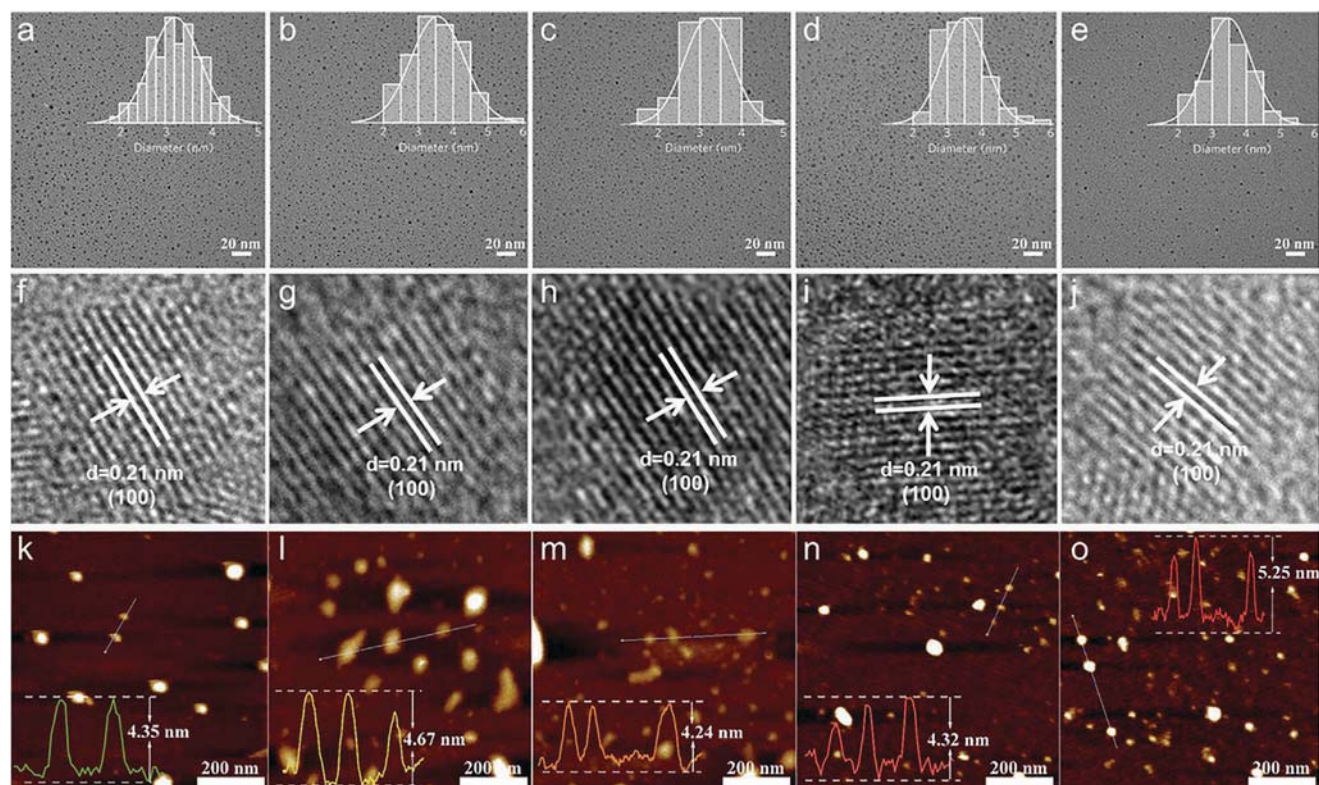


**Figure 2.** a–e) TEM images of CD<sub>1</sub>–CD<sub>5</sub>, inset: particles size distribution. f–j) High-resolution TEM (HR-TEM) images of single-particle CDs. k–o) Atomic force microscopy (AFM) image of CD<sub>1</sub>–CD<sub>5</sub>, inset: height profiles analysis of CDs.

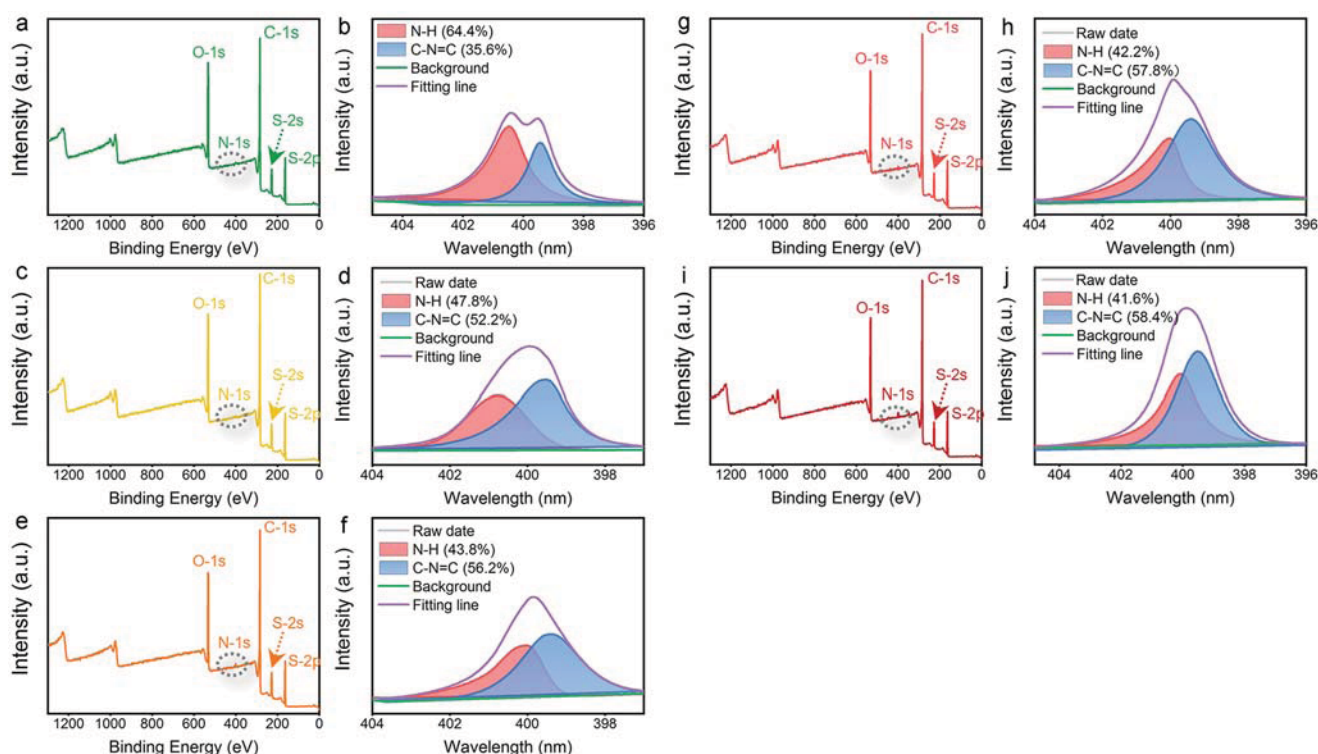


**Figure 3.** a,c,e,g,i) XPS spectra of the CD<sub>1</sub>–CD<sub>5</sub>, b,d,f,h,j) XPS high-resolution N 1s spectra of the CD<sub>1</sub>–CD<sub>5</sub>, respectively.

The X-ray diffraction (XRD) patterns of the five CDs (Figure S10, Supporting Information) exhibit an obvious broad peak centered at 21°, and two weak peaks at ≈26.4° and 41.5°. The broad peak corresponds to amorphous carbon derived from deformations caused by the heteroatomic dopants or sp<sup>3</sup> C defects in graphitic structures. The weak peak at 26.4° and 41.5° corresponds to the (002) and (100) facet with an interlayer spacing of 0.34 and 0.21 nm, respectively. The XRD data revealed that these CDs contain a more amorphous structure. In Figure S11, Supporting Information, FT-IR analysis confirms the presence of amide carbonyl (1680.5 cm<sup>-1</sup>), O–H (3470.0 cm<sup>-1</sup>), S–H (2656.5 cm<sup>-1</sup>), C=C (1555.7 cm<sup>-1</sup>), C–N (1258.8 cm<sup>-1</sup>), C–S (693.0 cm<sup>-1</sup>), and S–S (550.0 cm<sup>-1</sup>) functional groups or chemical bands in these CDs samples. The existence of structures connected to O– and N– containing functional groups is confirmed. Previous studies have shown that the S–S is a non-rigid structure and that the surface structure of the CDs can rotate around the S–S.<sup>[23,40]</sup> Surface groups of CDs suffering from the restriction of intramolecular rotation (RIR) show the AIE effect. Besides, XPS has been employed to characterize the surface groups of the CD powders. As shown in the full survey of the XPS spectra in Figure 3a,c,e,g,i, there are four kinds of elements (C, N, O, and S) that existed in the CD powders. The high-resolution Cls XPS envelope can be deconvoluted into three Gaussian peaks as shown in Figure S12a–e and Table S7, Supporting Information, which are attributed to sp<sup>2</sup> C (C–C/C=C), C–N/C–O/C–S, C=O, and COOH groups, respectively. The N 1s band (Figure 3b,d,f,h,j) could be split into C–N=C and N–H, whereas the O 1s spectra (Figure S13a–e, Supporting Information) reveals the existence of C–O and C=O groups, respectively. The relevant data in Table S8,

Supporting Information, show that the proportion of C=O in the O 1s spectrum increased from 23.2% (CD<sub>1</sub>) to 62.7% (CD<sub>5</sub>), which shows a trend consistent with Abs-2. The photoluminescence (PL) origin of CDs can be attributed to “extrinsic” emissions from oxygen, carbon, and sulfur functional groups. In this case, Abs-2 is most likely due to the CDs surface n–π\* transition caused by C=O.<sup>[27,41,42]</sup> Besides, the S 2p band in Figure S14a–e contains three peaks for S–C, S–H, and S–S. Similarly, the relevant data in Table S9, Supporting Information, show a trend consistent with Abs-1 that the proportion of S–S in the S 2p spectrum decreased from 53.2% (CD<sub>1</sub>) to 30.7% (CD<sub>5</sub>), which indicates that Abs-1 is most likely caused by symmetric molecules associated with S–S. More importantly, the three high-resolution spectra collectively indicate the successful insertion of S and N atoms into the CDs. Furthermore, Table S10, Supporting Information, shows that the proportion of nitrogen gradually increases from 1.02% to 1.87%. As revealed by the N 1s data in Table 1, the proportion of N–H decreases from 64.4% (CD<sub>1</sub>) to 41.6% (CD<sub>5</sub>); by contrast, the proportion of C=N increases from 35.6% (CD<sub>1</sub>) to 58.4% (CD<sub>5</sub>), which shows that N-based groups are important induced luminescence functional groups. Due to its electron doping effect, N causes a redshift of the CDs absorption spectra and reduces the energy level gap between electrons.<sup>[43,44]</sup> Moreover, it is found by calculation that

**Table 1.** Chemical bond content of high-resolution N 1s of CD<sub>1</sub>–CD<sub>5</sub>.

Sample	CD <sub>1</sub>	CD <sub>2</sub>	CD <sub>3</sub>	CD <sub>4</sub>	CD <sub>5</sub>
N–H	64.4%	47.8%	43.8%	42.2%	41.6%
C–N=C	35.6%	52.2%	56.2%	57.8%	58.4%



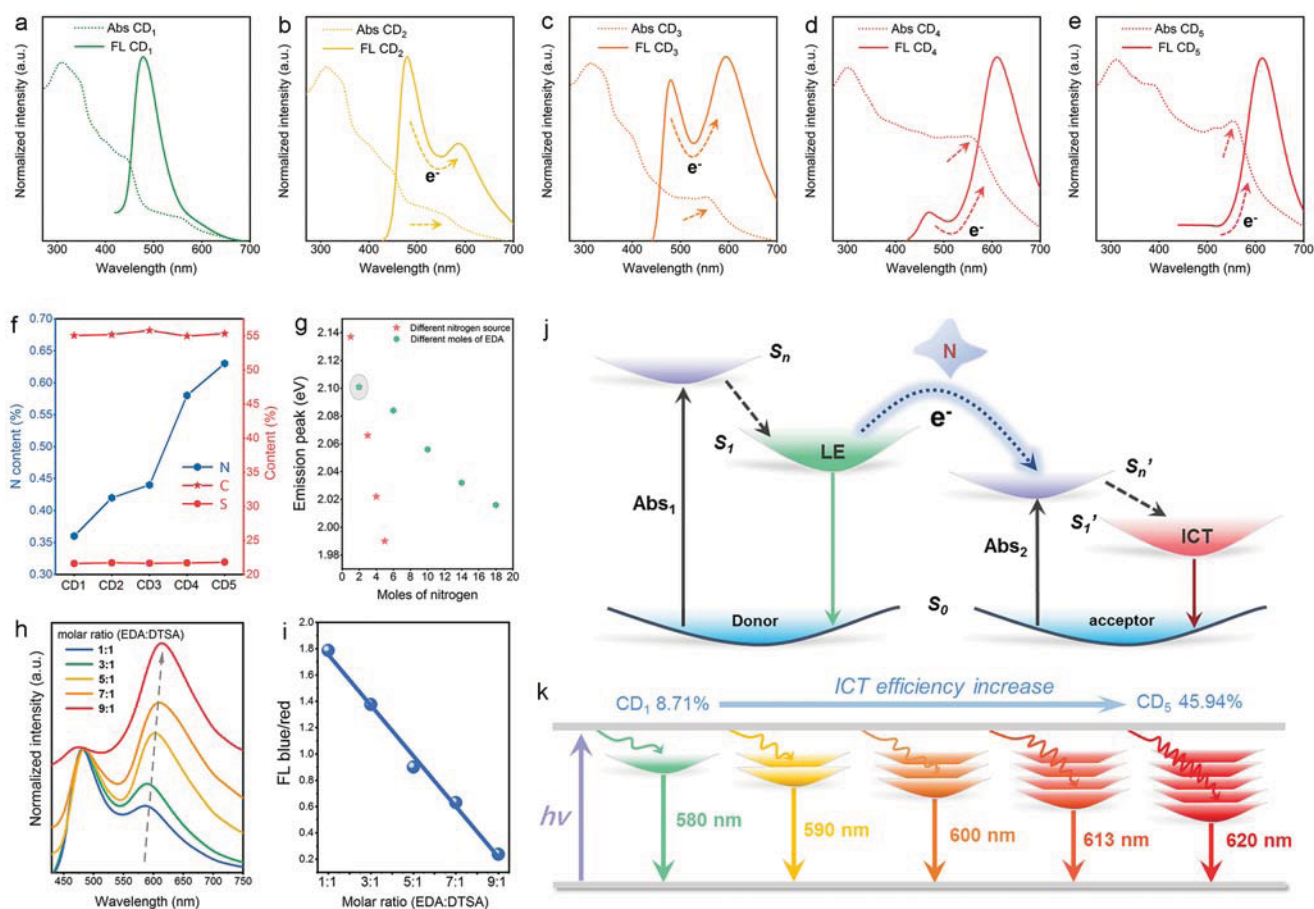


**Figure 4.** a–e) The absorption and emission spectra of CD<sub>1</sub>–CD<sub>5</sub>. f) Element content line diagram of CD<sub>1</sub>–CD<sub>5</sub>. g) The relationship between the spectrum emission peaks of the CDs and the number of nitrogen atoms contained in the precursor.  $E = 1240/\lambda$  ( $E$ , optical band gap energy;  $\lambda$ , wavelength). h) Normalized PL spectra (480 nm emission) of CD<sub>2</sub>, CD<sub>2-3</sub>, CD<sub>2-5</sub>, CD<sub>2-7</sub>, and CD<sub>2-9</sub> synthesized by different raw-material ratios at 400 nm wavelength excitation. i) Plot of PL intensity ratio for the FL<sub>blue/red</sub> emission center. j) Mechanism diagram of ICT between Em-1 and Em-2 induced by nitrogen. k) Illustration of the tunable PL emission from CD<sub>1</sub>–CD<sub>5</sub> containing different N-related surface groups and ICT efficiency.

the ratio of C=N to N–H increases gradually with the redshift of CDs. As a contrast, CD<sub>6</sub> was obtained when acetic acid and DTSA were used as reaction precursors (Figure S15, Supporting Information). CD<sub>6</sub> shows SSF and produces a wide fluorescence peak at 480 nm and a weak fluorescence peak near 580 nm, indicating that DTSA is an important factor in the formation of SSF and double fluorescence luminescence center. Besides, CD<sub>6</sub> shows an average fluorescence lifetime of 5.05 ns (Table S11, Supporting Information). Thus, the probable mechanism of inducing the increasing ratio of Em-2 to Em-1 is nitrogen induces ICT from Em-1 to Em-2. Abs-2 is produced from the conjugated structure attached to C=O bands on the surface of CDs, and the conjugated structure attached to C=N bands will promote Abs-2 absorption enhancement greatly. With the above discussion and according to the absorption redshift and the spectral transition between Em-1 and Em-2 (Figure 4a–e), it is believed that the extra-large ratio of Em-2 to Em-1 is ascribed to ICT, which displays that the electron transfer increases with the increase of introduced nitrogen. According to reports, the ICT process is related to the larger distorted structure of the molecule itself and the electron donating ability of the donor group or the electron-withdrawing ability of the acceptor group.<sup>[45–47]</sup> With the

increase of the electron acceptor intensity in the molecule, the components of the ICT state in the mixed excited state increase correspondingly, the dipole moment of the excited state also increases significantly, and the maximum peak of the absorption and FL of the compound also show redshift gradually.

At the same time, with the enhancement of the electron acceptor intensity, the transition moment corresponding to the transition from the excited state to the ground state in the compound increases significantly, showing a gradually increasing luminous efficiency (Table S3, Supporting Information). Furthermore, the ICT efficiency of these CD-based can be quantified according to the equation

$$\eta = 1 - (\tau_{DA} / \tau_D) \quad (4)$$

in which  $\tau_{DA}$  and  $\tau_D$  represent the PL lifetimes of the energy donor in the presence and absence of energy acceptor, respectively. Based on this, the ICT efficiencies from CD<sub>1</sub>–CD<sub>5</sub> are calculated as 8.71%, 10.49%, 18.22%, 29.50%, and 45.94%, respectively (Table S12, Supporting Information). Because of this property, the increase of C=N content is conducive to the electron transfer of Em-1 to Em-2. To confirm whether the

spectral changes of CDs comply with FRET, the CDs are dispersed in the PVA film, and the fluorescence spectra of the CDs are still consistent with the fluorescence emission spectra of the CDs powder (Figure S16, Supporting Information). Therefore, the generation of CD<sub>1</sub>–CD<sub>5</sub> multicolor fluorescence is attributed to ICT between single carbon sites rather than FRET because it does not follow the basic law of FRET that the fluorescence intensity varies with the interparticle distance. To investigate the influence of nitrogen content on the luminescence of CDs, element analysis (EA) of CD<sub>1</sub>–CD<sub>5</sub> is tested and displays the distribution of nitrogen content in CDs as showing an increasing trend, while other elements (C, S) are constant (Figure 4f). To verify the above conclusion, EDA is selected as the nitrogen source and reacted with DTSA at different molar ratios in acetic acid solvent to prepare CD<sub>2</sub>–CD<sub>2.9</sub> (Figure S17, Supporting Information). The fluorescence spectra of these CDs show obvious regularity features. The PL spectra of CDs (Figure S18a–d, Supporting Information) show that the intensity of red emission is enhanced with the increase of EDA content and CDs powder changes color from yellow to red under UV light, which is consistent with the rule of CD<sub>1</sub> to CD<sub>5</sub>. As the content of EDA increases, the red luminescence center of CDs gradually redshifts (Figure 4g,h). Figure 4i illustrates the corresponding plots which show a linear relation between fluorescence intensity ratio ( $F_{\text{blue}}/F_{\text{red}}$ ) against the moles' ratio for DTSA and EDA, and good linearity was obtained. From the relationship between the emission peaks of the CDs prepared by the two sets of experiments and the nitrogen content parameter, the nitrogen content is conducive to the reduction of the CDs energy level and the emission redshift (Figure 4k). In summary, an increase in C=N content is the cause for the redshift observed for the Abs-2 peaks and led to Ex-2 peaks with longer wavelengths. To provide a more rigorous confirmation of the molecular configuration, we characterized the N structure of AIE-CDs by Raman spectroscopy (Figure S19, Supporting Information) and detailed examination of the formation of functional groups by <sup>13</sup>C-NMR and <sup>1</sup>H-NMR spectrum (Figures S20 and S21, Supporting Information). Figure S18, Supporting Information reveals that the Raman spectra of each CD exhibits D-bands and G-bands related to disordered and graphitic structures. The content of C=N is increased from CD<sub>1</sub> to CD<sub>5</sub>. Furthermore, <sup>13</sup>C-NMR spectra were employed and signals from 168 ppm were C=N/C=O structure.<sup>[48,23]</sup> Figure S20, Supporting Information shows the increasing number of C=N/C=O structures from CD<sub>1</sub> to CD<sub>5</sub>. Multiple peaks in the range from 130–140 ppm appear in consistency with Ph–S groups, while the peaks at 131.5 and 132.6 ppm.<sup>[49]</sup> Besides, a <sup>1</sup>H NMR spectrum is employed to distinguish the hydrogen protons in different environments (Figure S21, Supporting Information). Deuterium-labeled methanol was used as a solvent. It reveals a larger number of alkyl chains on the CDs surface, evidenced by the main peak at 1.28 ppm and a peak at 0.88 ppm, corresponding to the protons of –CH<sub>2</sub>– and –CH<sub>3</sub> groups, respectively. For these samples, there are three strong peaks located at 2.07, 2.22, and 2.51 ppm ascribed to the carboxyl hydrogen, and the other four peaks located at 3.45, 3.85, 3.93, and 4.16 ppm associated with the Ar–NH<sub>2</sub> protons. Upon increasing the nitrogen content from CD<sub>1</sub> to CD<sub>5</sub>, two new peaks at 3.17 ppm and 6.35 ppm assigned to the carbonyl hydrogen and amide

hydrogen appear. These results are consistent with the results of XPS analysis that the increased content of C=O and nitrogen element cause redshift of CDs. Furthermore, signals from the aromatic rings are detected at 6.8–8.8 ppm, which can be attributed to graphitized cores' proton resonances. It is shown that the CD<sub>1</sub> to CD<sub>5</sub> includes two components: graphitized cores and surface state. On that basis, possible surface structures of CD<sub>1</sub>, CD<sub>3</sub>, and CD<sub>5</sub> have simulated the configuration and carried DFT calculation. The dipole moments at the excitation state are listed in Table S13, Supporting Information. It is clear that the dipole moment increases with increasing the number of –C=N–C, and it is reasonable that more –C=N–C groups may induce larger polarization in the CD surface system. In Table S14, Supporting Information for CD<sub>1</sub>, there are mainly two transitions from ground state to the excitation state: HOMO to LUMO (H → L) and HOMO to LUMO+1 (H → L+1). From the electron distribution of the frontier orbital of CD<sub>1</sub>, the electrons at the ground state are located at the S–S–Ph group, while the electrons are distributed around the molecules at excitation state. Therefore, the excitation state exhibits both local excitation (LE) and intermolecular charge transfer (ICT). However, the intensity of electron acceptor in CD<sub>5</sub> excited state is further enhanced, and the properties of intramolecular charge transfer ICT state in the lowest excited state are more obvious. The electron at the ground state is mainly located on the S–S–Ph group, while the electron transfers to the N-containing anthracene group at the excitation state. The ICT type of CD<sub>5</sub> excited state can be clearly determined from the transition characteristics of the orbital. For CDs with ICT state, with the enhancement of electron acceptors in the fluorescence molecule, the composition of ICT state in the lowest excited state increases correspondingly and the intensity of excited state increases, which showed an excited state dipole characteristic. Thus, it is sufficient to indicate that the electron donor and acceptor are composed of C=N–C groups and the electron donor is –S–S– groups. Table S15, Supporting Information, lists the excitation energy of the considered molecules. Combining the trend of dipole moment with that of excitation energy, one may find that molecules with larger dipole moments have lower excitation energies.

Based on the suggested mechanism, we conducted a series of comparative experiments that replace the amino group of the precursor with a hydroxyl group and hydrogen group, respectively. Different molar amounts of ethylene glycol reacted with DTSA and were named CD<sub>7</sub>–CD<sub>11</sub>, respectively. The fluorescence spectra (Figure S22, Supporting Information) showed that the emission of these CDs did not change significantly with the increase of the molar amount of ethylene glycol in the precursor, showing the same 480 and 580 nm double emission fluorescence peaks. With the previous exploration, it was found that the emission peak at 580 nm came from C=O on the surface of the CDs. Therefore, the intensity of the peak at 580 nm of CD<sub>7</sub>–CD<sub>11</sub> was significantly higher than that of CD<sub>6</sub>. The hydroxyl group in the ethylene glycol on the surface participated in the formation of CDs and formed C=O group on the surface of the CDs, showing emission at 580 nm. Similarly, the reaction products of n-hexane with different moles of DTSA were named CD<sub>12</sub>–CD<sub>16</sub>, respectively, and the fluorescence spectra showed that the emission of these CDs did not change significantly with the increase of the moles of n-hexane in



the precursor (Figure S23, Supporting Information). The CD spectra show that the same 480 and 580 nm double emission fluorescence peaks are like CD<sub>6</sub>, indicating that n-hexane did not play a role in this reaction. The results of the two groups of experiments confirmed that the introduction of amino nitrogen is the key to the formation of energy transfer, and DTSA is the source of the formation of double fluorescent morphology.

Besides, CD<sub>17</sub>–CD<sub>21</sub> are prepared with ethylenediamine in different amounts with acetic acid solvent, respectively, and the emission wavelength (Figure S24, Supporting Information) of these CDs is redshifted (435 to 554 nm) with the increase of N content in the precursor. Therefore, it is concluded that the increase of nitrogen can induce the decrease of the electronic gap. In short, besides the above basic characterization and usual features, we prove that the source of the red luminescence emission center of CDs is related to the C=O/C=N, and the emission center at 480 nm is derived from the S–S bonds of DTSA on the surface of the CDs. The luminescence mechanism is shown in Figure 4j. The SSF of the CDs is caused by the surface state luminescence after the CDs are aggregated, and the Em-1 comes from the Abs-1 from the  $n-\pi^*$  transition of the S–S bonds of DTSA and the Em-2 comes from the Abs-2 of the conjugated structure attached to C=O/C=N bonds. The increase in nitrogen content increases the content of electron-withdrawing functional groups (C=N) on the surface of the

CDs and induces the generation of ICT on the surface of the CDs. Interestingly, the AIE luminescence for CDs in the solution presents dual emission assigned to the local excitation (LE) and ICT states. When ICT transfer efficiency reaches 45.94% by introducing nitrogen, the CDs show a single emission of red luminescence. ICT not only induces a change in the ratio of dual emission, but also can make redshift of the absorption and reduce the emission level of the ICT state (Em-2) (Figure 4k).

Finally, the as-prepared CDs were made for various applications. First, utilizing the hydrophobic characteristics of the CDs and the different colors in different solvent environments, the CDs are dissolved in acetic acid to prepare ink and write on the filter paper. When water is introduced, the CDs aggregate to present a different luminous color at 365 nm excitation (Figure 5a). Then, the color returned to blue emission after the acetic acid was sprayed again, which realized the information encryption. In the second aspect, we use the liposolubility light-emitting properties of CDs with high quantum efficiency. As shown in Figure 5c; Figure S25a–d, Supporting Information, latent fingerprints (LFPs) are detected successfully on the glass sheet. The ridge patterns of all samples, such as arches, loops, and whorls, classified in level one, are recognized clearly because of the high contrast of fluorescent signals. The six parts of the fingerprint pattern prepared by CD<sub>5</sub> are enlarged and bifurcation, island, termination, eye, core, ridge divergence, and crossover feature

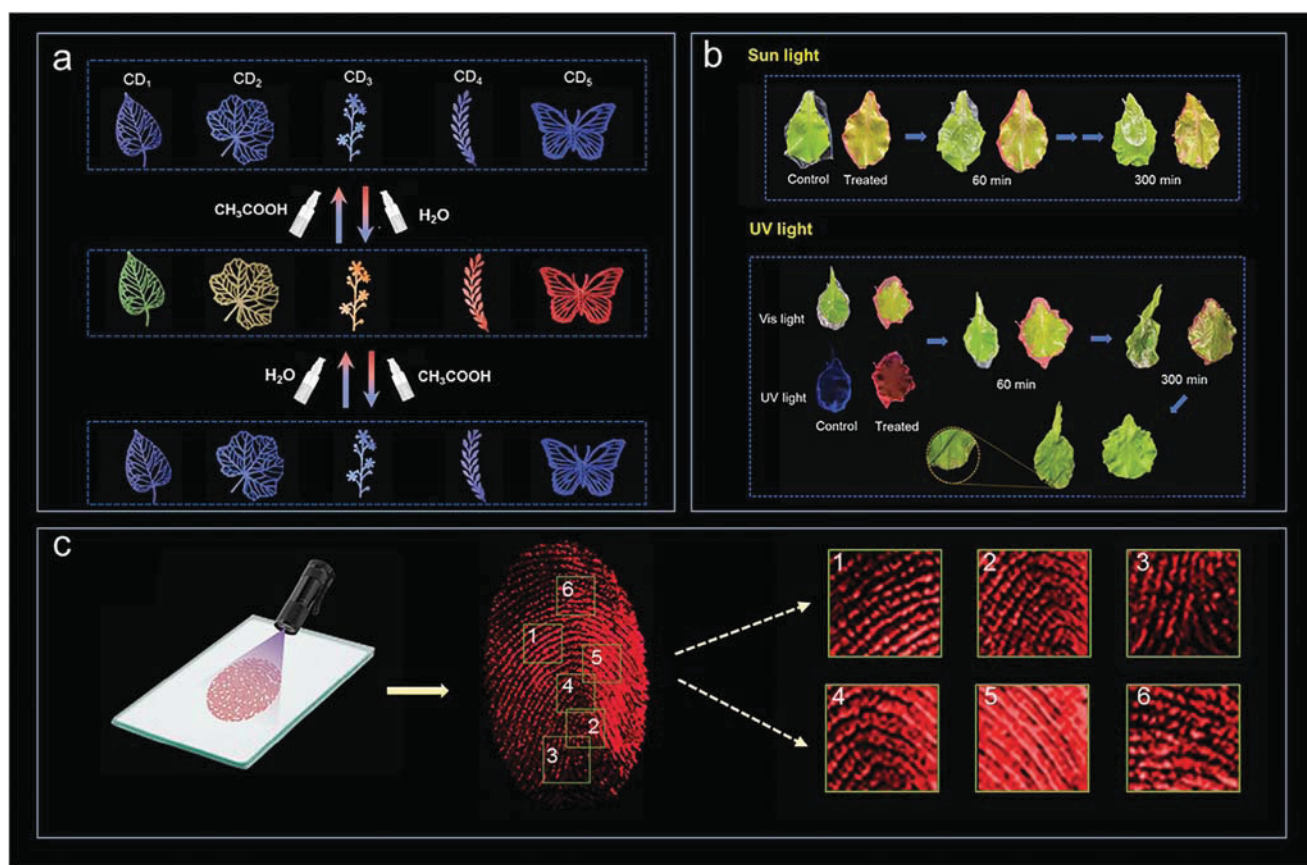


**Figure 5.** Application of CDs. a) Photographs of the varying pattern drawn on different CDs solution before and after spraying water. b) Photographs of a leaf wrapped with CD<sub>5</sub>@PVA film (treated) and PVA film (control) in sunlight and UV light at different times. c) Photographs of the CDs powder-stained latent fingerprints (LFPs) on glass substrates under UV light irradiation, respectively. Images for (c-1–6): magnified images showing six kinds of detail in CD<sub>5</sub> LFPs.

points are observed clearly, respectively. In the third aspect, using the dual emission fluorescence characteristics, the WLED may be achieved solely by those CDs phosphors with appropriate commercial UV chips. As shown in Figure S26a–d, Supporting Information, LEDs based on CD<sub>2</sub>, CD<sub>2-3</sub>, CD<sub>2-5</sub>, and CD<sub>2-7</sub> exhibit white and warm white color with the CIE coordinates of (0.2977, 0.3645), (0.3576, 0.3836), (0.3827, 0.3965), and (0.4933, 0.4433), respectively (Table S16, Supporting Information). Therein, the WLED can be achieved in CD<sub>2-5</sub>-based LEDs approaching the coordinate (0.3827, 0.3965) of warm-white light packaged into LEDs with high color rendering index of 88. Under 400 nm excitation, variable temperature spectroscopy image (Figure S27a–d, Supporting Information) shows that the fluorescence intensity of CDs remained stable as the temperature increased from 303 to 443 K. The results show that the PL intensities remain nearly unchanged, indicating the high thermal stability of CDs. Fourth, we mix CDs and poly(vinyl alcohol) (PVA) to prepare the CD@PVA composite film; as shown in Figure S16, Supporting Information, the CDs can be uniformly mixed with PVA. The composite film changed from yellow to red under sunlight, and blue-green to deep red under ultraviolet light. The transmittance at wavelengths above 400 nm remains above 80%, and the UV absorption gradually increases from CD<sub>1</sub> to CD<sub>5</sub> (Figure S28a,b, Supporting Information). In Figure S29a, Supporting Information, compared with the control group (PVA film), the treated group (CD<sub>5</sub>@PVA composite film) has excellent red-light emission under UV light. Plant leaves tend to lose water and grow spots when exposed to strong sunlight and UV light. The CD<sub>5</sub>@PVA composite film can absorb ultraviolet and some visible light to avoid this damage (Figure S29b, Supporting Information). As shown in Figure 5b, the treated group and the control group dissolved in water are coated on the surface of the plant leaf, and it can be attached to the leaf surface well. After 60 min of exposure to sunlight, the edge of the control film shrinks and rises, while the treated film is attached to the surface of the leaf. After 300 min, the control film was completely erected because of water loss and shrinkage, while the treated film was still attached to the surface of the leaf. Similarly, under UV light for 300 min, the treated film is tightly wrapped on the leaf surface, while the control leaf gathers together and grows spots due to loss of water and ultraviolet radiation. A proposed mechanism is shown in Figure S30, Supporting Information. When CDs are added to PVA, the CDs@PVA composite film can be made to absorb UV light and used as an additive to enhance the surface viscosity of the film. When the CDs@PVA composite film loses water, the CDs make the deformation of the PVA chain tend to extend to the periphery, and the CDs@PVA composite film has more surface attachment sites due to the rich groups of the CDs, which overlaps with the leaf surface combine. It's worth noting that the PVA film will automatically fall off to recycle by spraying water on the surface of the leaves, which can greatly reduce the cost.

### 3. Conclusion

By using molecular amines with different nitrogen numbers and DTSA as precursors, AIE-CDs with different emission colors were prepared. These AIE-CDs have dual emission centers for blue light (480 nm) and red light (near 600 nm). The CDs

prepared from the precursor with higher nitrogen content has stronger red light emission and redshift. Through data analysis, the ICT effect within the AIE-CDs was discovered for the first time, which will not only effectively promote the luminescence QY, but also achieve a unique photophysical phenomenon-dual fluorescence emission. Finally, we verify that Em-1 and Em-2 are the fluorescent luminescence centers produced by the structure of DTSA with S–S bonds and a conjugated structure attached to C=O/C=N bonds, respectively, and increasing the nitrogen content will induce the ICT from Em-1 to Em-2 through a series of comparative experiments. On this basis, white light LEDs with high color rendering index of 88 were prepared using AIE-CDs. It is also applied to pattern encryption, fingerprint identification, and leaf protection to meet different application requirements.

### 4. Experimental Section

**Materials:** Ethylamine, ethylenediamine, and PVA which were of analytical reagent grade, were purchased from Aladdin Shanghai, China. Diethylenetriamine was purchased from Tianjin Damao Chemical Reagent Factory. Triethylenetetramine was purchased from Chengdu Kelong Chemical Reagent Factory. Tetraethylenepentamine was purchased from Tianjin Fuchen Chemical Reagent Factory. Acetic acid, ethylene glycol, and n-hexane were purchased from Shanghai Titan Technology Co., LTD. with analytical reagent grade. Dithiosalicylic acid was purchased from Shanghai Yi'en Chemical Technology Co., LTD. And, the deionized water was supplied by a water purifier nano pure water system (Master-E, Hitech-science tool, Shanghai, China).

**Synthesis of CD<sub>1</sub>–CD<sub>5</sub>:** First, 490.16 mg dithiosalicylic acid (DTSA) was dissolved in 40 mL of acetic acid solution with stirring until dissolved completely. 9  $\mu$ L ethylamine was added to the mixed solution and stirred for 1 h. Subsequently, the mixed solution was transferred into the 100 mL Teflon reactor and kept at 180 °C for 10 h. After cooling down to room temperature naturally, the reaction solution was poured into 1 L boiling water, then it was filtered and dried to get pure CD<sub>1</sub>. The preparation method of CD<sub>2</sub>–CD<sub>5</sub> is similar, that is, 9  $\mu$ L ethylamine was replaced by 107  $\mu$ L of ethylenediamine and 173  $\mu$ L of diethylene Triamines, 238  $\mu$ L of triethylenetetramine, and 303  $\mu$ L of tetraethylenepentamine.

**Synthesis of CD<sub>6</sub>:** Similarly, 490.16 mg DTSA was dissolved in 40 mL of acetic acid solution with stirring until dissolved completely. The mixed solution was transferred into the 100 mL Teflon reactor and kept at 180 °C for 10 h. After cooling down to room temperature naturally, the reaction solution was poured into 1 L boiling water, then it was filtered and dried to get pure CD<sub>6</sub>.

**Synthesis of CD<sub>2</sub> and CD<sub>3</sub>, CD<sub>2</sub>–CD<sub>5</sub>, CD<sub>2</sub>–CD<sub>7</sub>, and CD<sub>2</sub>–CD<sub>9</sub>:** First, 490.16 mg DTSA was dissolved in 40 mL of acetic acid solution with stirring until dissolved completely. 321, 535, 749, and 963  $\mu$ L ethylenediamine was added to the mixed solution and stirred for 1 h, respectively. Then, the mixed solution was transferred into the 100 mL Teflon reactor and kept at 180 °C for 10 h. After cooling down to room temperature naturally, the reaction solution was poured into 1 L boiling water, then it was filtered and dried to get pure CD<sub>2</sub> and CD<sub>3</sub>, CD<sub>2</sub>–CD<sub>5</sub>, CD<sub>2</sub>–CD<sub>7</sub>, and CD<sub>2</sub>–CD<sub>9</sub>.

**Synthesis of CD<sub>7</sub>–CD<sub>11</sub>:** First, 490.16 mg DTSA was dissolved in 40 mL of acetic acid solution with stirring until dissolved completely. 89, 267, 445, 623, and 801  $\mu$ L ethylene glycol were added to the mixed solution and stirred for 1 h, respectively. Subsequently, the mixed solution was transferred into the 100 mL Teflon reactor and kept at 180 °C for 10 h. After cooling down to room temperature naturally, the reaction solution was poured into 1 L boiling water, then it was filtered and dried to get pure CD<sub>7</sub>–CD<sub>11</sub>.

**Synthesis of CD<sub>12</sub>–CD<sub>16</sub>:** First, 490.16 mg DTSA was dissolved in 40 mL of acetic acid solution with stirring until dissolved completely. 199, 597, 995, 1393, and 1792  $\mu$ L n-hexane were added to the mixed solution and stirred for 1 h, respectively. Subsequently, the mixed solution was

transferred into the 100 mL Teflon reactor and kept at 180 °C for 10 h. After cooling down to room temperature naturally, the reaction solution was poured into 1 L boiling water, then it was filtered and dried to get pure CD<sub>12</sub>–CD<sub>16</sub>.

**Synthesis of CD<sub>17</sub>–CD<sub>21</sub>:** 107, 321, 535, 749, and 963 µL ethylenediamine was added to 40 mL of acetic acid solution with stirring for 1 h, respectively. Subsequently, the mixed solution was transferred into the 100 mL Teflon reactor and kept at 180 °C for 10 h. After cooling down to room temperature naturally, the reaction solution was poured into 1 L boiling water, then it was filtered and dried to get pure CD<sub>17</sub>–CD<sub>21</sub>.

**Synthesis of CDs@PVA Composite Film:** PVA (0.25g) was dissolved in deionized water (5 mL) at 60 °C. Then, CDs were added into PVA solution, and the mixed material was obtained through stirring for 2 h at room temperature. The composite film was finally fabricated by molding at 60 °C for 4 h.

**Characterizations:** The FT-IR spectrum was recorded on a Nicolet Avatar 360 Fourier transformation infrared spectrophotometer. The fluorescence spectrum was measured on F-7000 fluorescence spectrometer (Hitachi, Japan). The UV–vis absorption spectrum was measured using a UV/Vis spectrometer UV-2550 (Shimadzu, Japan). Transmission electron microscopy (TEM) images were recorded using an FEI Tecnai 12 transmission electron microscope and the high-resolution TEM (HRTEM) images were recorded using a JEOL-2010 transmission electron microscope. The X-ray photoelectron spectroscopy (XPS) was carried out on a Thermo Scientific Escalab 250Xi.hA. NMR measurements were taken using an AVANCEIII500 (Bruker). The fluorescence decay curves were measured on an FLS980 fluorescence spectrophotometer. Photoluminescence quantum yield measurements were performed with a calibrated integrating sphere on an Edinburgh FLS980 spectrometer. The photoelectric properties of the fabricated LEDs were measured by an integrating sphere spectroradiometer system (ZPH1272, Zhongpu).

## Supporting Information

Supporting Information is available from the Wiley Online Library or from the author.

## Acknowledgements

This work was supported by the Guangzhou Science and Technology Project (No 202007020005, 202103000059), the National Natural Science Foundation of China (12174119, 52172142, 51602108), and the Guangdong Basic and Applied Basic Research Foundation (2020A1515011210, 2017A030313256).

## Conflict of Interest

The authors declare no conflict of interest.

## Data Availability Statement

The data that support the findings of this study are available from the corresponding author upon reasonable request.

## Keywords

aggregation-induced emission, carbon dots, intramolecular charge transfer, multicolor fluorescence, nitrogen doping

Received: June 25, 2021

Revised: September 13, 2021

Published online: October 13, 2021

- [1] Y. J. Chung, J. Kim, C. B. Park, *ACS Nano* **2020**, *14*, 6470.
- [2] L. Jiang, H. Ding, M. Xu, X. Hu, S. Li, M. Zhang, Q. Zhang, Q. Wang, S. Lu, Y. Tian, H. Bi, *Small* **2020**, *16*, 2000680.
- [3] J. Liu, Y. Geng, D. Li, H. Yao, Z. Huo, Y. Li, K. Zhang, S. Zhu, H. Wei, W. Xu, J. Jiang, B. Yang, *Adv. Mater.* **2020**, *32*, 1906641.
- [4] X. Y. Dong, X. Q. Niu, Z. Y. Zhang, J. S. Wei, H. M. Xiong, *ACS Appl. Mater. Interfaces* **2020**, *12*, 29549.
- [5] C. Xia, S. Zhu, T. Feng, M. Yang, B. Yang, *Adv. Sci.* **2019**, *6*, 1901316.
- [6] M. J. Molaei, *Anal. Methods* **2020**, *12*, 1266.
- [7] S. Bhattacharya, R. S. Phatake, S. Nabha Barnea, N. Zerby, J. J. Zhu, R. Shikler, N. G. Lemcoff, R. Jelinek, *ACS Nano* **2019**, *13*, 7396.
- [8] C. L. Shen, Q. Lou, C. F. Lv, J. H. Zhang, S. N. Qu, L. Dong, C. X. Shan, *Adv. Sci.* **2019**, *6*, 1802331.
- [9] Y. Chen, M. Zheng, Y. Xiao, H. Dong, H. Zhang, J. Zhuang, H. Hu, B. Lei, Y. Liu, *Adv. Mater.* **2016**, *28*, 312.
- [10] Y. Wang, S. Kalytchuk, Y. Zhang, H. Shi, S. V. Kershaw, A. L. Rogach, *J. Phys. Chem. Lett.* **2014**, *5*, 1412.
- [11] C. L. Chiang, M. F. Wu, D. C. Dai, Y. S. Wen, J. K. Wang, C. T. Chen, *Adv. Funct. Mater.* **2005**, *15*, 231.
- [12] M. Shimizu, Y. Takeda, M. Higashi, T. Hiyama, *Angew. Chem., Int. Ed.* **2009**, *48*, 3653.
- [13] X. Miao, D. Qu, D. Yang, B. Nie, Y. Zhao, H. Fan, Z. Sun, *Adv. Mater.* **2018**, *30*, 1704740.
- [14] B. Wang, J. Yu, L. Sui, S. Zhu, Z. Tang, B. Yang, S. Lu, *Adv. Sci.* **2020**, *8*, 2001453.
- [15] F. Yan, Y. Jiang, X. Sun, J. Wei, L. Chen, Y. Zhang, *Nano Res.* **2019**, *13*, 52.
- [16] S. Qu, D. Zhou, D. Li, W. Ji, P. Jing, D. Han, L. Liu, H. Zeng, D. Shen, *Adv. Mater.* **2016**, *28*, 3516.
- [17] Z. Wang, F. Yuan, X. Li, Y. Li, H. Zhong, L. Fan, S. Yang, *Adv. Mater.* **2017**, *29*, 1702910.
- [18] Y. Wu, H. Zhang, A. Pan, Q. Wang, Y. Zhang, G. Zhou, L. He, *Adv. Sci.* **2019**, *6*, 1801432.
- [19] B.-P. Jiang, Y.-X. Yu, X.-L. Guo, Z.-Y. Ding, B. Zhou, H. Liang, X.-C. Shen, *Carbon* **2018**, *128*, 12.
- [20] S. Tao, S. Lu, Y. Geng, S. Zhu, S. A. T. Redfern, Y. Song, T. Feng, W. Xu, B. Yang, *Angew. Chem., Int. Ed.* **2018**, *57*, 2393.
- [21] D. Zhou, D. Li, P. Jing, Y. Zhai, D. Shen, S. Qu, A. L. Rogach, *Chem. Mater.* **2017**, *29*, 1779.
- [22] S. Qu, D. Shen, X. Liu, P. Jing, L. Zhang, W. Ji, H. Zhao, X. Fan, H. Zhang, *Part. Part. Syst. Charact.* **2014**, *31*, 1175.
- [23] H. Yang, Y. Liu, Z. Guo, B. Lei, J. Zhuang, X. Zhang, Z. Liu, C. Hu, *Nat. Commun.* **2019**, *10*, 1789.
- [24] K. Jiang, X. Gao, X. Feng, Y. Wang, Z. Li, H. Lin, *Angew. Chem., Int. Ed.* **2019**, *59*, 9986.
- [25] Y. Zhang, P. Zhuo, H. Yin, Y. Fan, J. Zhang, X. Liu, Z. Chen, *ACS Appl. Mater. Interfaces* **2019**, *11*, 24395.
- [26] D. Li, P. Jing, L. Sun, Y. An, X. Shan, X. Lu, D. Zhou, D. Han, D. Shen, Y. Zhai, S. Qu, R. Zboril, A. L. Rogach, *Adv. Mater.* **2018**, *30*, 1705913.
- [27] M. Park, H. S. Kim, H. Yoon, J. Kim, S. Lee, S. Yoo, S. Jeon, *Adv. Mater.* **2020**, *32*, 2000936.
- [28] Y. N. Hong, J. W. Y. Lam, B. Z. Tang, *Chem. Soc. Rev.* **2011**, *40*, 5361.
- [29] H. Naito, K. Nishino, Y. Morisaki, K. Tanaka, Y. Chujo, *Angew. Chem., Int. Ed.* **2017**, *56*, 254.
- [30] W. Zhang, T. Huang, J. Li, P. Sun, Y. Wang, W. Shi, W. Han, W. Wang, Q. Fan, W. Huang, *ACS Appl. Mater. Interfaces* **2019**, *11*, 16311.
- [31] T. Tong, H. Hu, J. Zhou, S. Deng, X. Zhang, W. Tang, L. Fang, S. Xiao, J. Liang, *Small* **2020**, *16*, 1613.
- [32] J. Chen, C. C. W. Law, J. W. Y. Lam, Y. Dong, S. M. F. Lo, I. D. Williams, D. Zhu, B. Z. Tang, *Chem. Mater.* **2003**, *15*, 1535.
- [33] Y. N. Hong, J. W. Y. Lam, B. Z. Tang, *Chem. Soc. Rev.* **2011**, *40*, 5361.
- [34] H. S. Kumbhar, S. S. Deshpande, G. S. Shankarling, *ChemistrySelect* **2016**, *1*, 2058.

- [35] C. Yu, Z. Huang, W. Gu, Q. Wu, E. Hao, Y. Xiao, L. Jiao, W. R. Wong, *Mater. Chem. Front.* **2019**, 3, 1823.
- [36] L. F. Xu, L. Ni, F. Zeng, S. Z. Wu, *Analyst* **2020**, 145, 844.
- [37] J. Wang, X. Gu, P. Zhang, X. Huang, X. Zheng, M. Chen, H. Feng, R. T. K. Kwok, J. W. Y. Lam, B. Z. Tang, *J. Am. Chem. Soc.* **2017**, 139, 16974.
- [38] Y. Ren, J. W. Y. Lam, Y. Q. Dong, B. Z. Tang, K. S. Wong, *J. Phys. Chem. B* **2005**, 109, 1135.
- [39] X. Chen, W. Zhang, Q. Wang, J. Fan, *Carbon* **2014**, 79, 165.
- [40] Y. S. Liu, H. Y. Yang, Y. Wang, C. H. Ma, S. Luo, Z. W. Wu, Z. S. Zhang, W. Li, S. X. Liu, *Chem. Eng. J.* **2021**, 424, 130426.
- [41] H. Yoon, Y. H. Chang, S. H. Song, E. S. Lee, S. H. Jin, C. Park, J. Lee, B. H. Kim, H. J. Kang, Y. H. Kim, S. Jeon, *Mater. Adv.* **2016**, 28, 5255.
- [42] P. Yang, Z. Zhu, T. Zhang, W. Zhang, W. Chen, Y. Cao, M. Chen, X. Zhou, *Small* **2019**, 15, 1902823.
- [43] C. Liu, Y. Jin, R. Wang, T. Han, X. Liu, B. Wang, C. Huang, S. Zhu, J. Chen, *iScience* **2020**, 23, 101546.
- [44] S. Sarkar, M. Sudolska, M. Dubecky, C. J. Reckmeier, A. L. Rogach, R. Zboril, M. Otyepka, *J. Phys. Chem. C* **2016**, 120, 1303.
- [45] A. Neubauer, S. Murali, W. Rettig, *Int. J. Phytoenergy* **2005**, 7, 270176.
- [46] H. E. Gezawy, W. Rettig, *Chem. Phys.* **2006**, 327, 385.
- [47] X. Fan, W. Peng, Y. Li, X. Li, S. Wang, G. Zhang, F. Zhang, *Adv. Mater.* **2008**, 20, 4490.
- [48] J. Xie, B. Liao, H. Zhu, Y. Yuc, R. Tang, *RSC Adv.* **2021**, 11, 25639.



## Phosphorescence

International Edition: DOI: 10.1002/anie.201814629  
German Edition: DOI: 10.1002/ange.201814629

## A Universal Strategy for Activating the Multicolor Room-Temperature Afterglow of Carbon Dots in a Boric Acid Matrix

Wei Li, Wan Zhou, Zhishan Zhou, Haoran Zhang, Xuejie Zhang, Jianle Zhuang, Yingliang Liu,\* Bingfu Lei,\* and Chaofan Hu\*

**Abstract:** Carbon dots (CDs) have attracted attention in metal-free afterglow materials, but most CDs were heteroatom-containing and the afterglow emissions are still limited to the short-wavelength region. A universal approach to activate the room-temperature phosphorescence (RTP) of both heteroatom-free and heteroatom-containing CDs was developed by one-step heat treatment of CDs and boric acid (BA). The introduction of an electron-withdrawing boron atom in composites can greatly reduce the energy gap between the singlet and triplet state; the formed glassy state can effectively protect the excited triplet states of CDs from nonradiative deactivation. A universal host for embedding CDs to achieve long-lifetime and multi-color (blue, green, green-yellow and orange) RTP via a low cost, quick and facile process was developed. Based on their distinctive RTP performances, the applications of these CD-based RTP materials in information encryption and decryption are also proposed and demonstrated.

Afterglow materials with long lifetime are highly desirable in wide applications such as optoelectronic, bioscientific technologies, and security systems.<sup>[1–7]</sup> Currently, most efficient room-temperature phosphorescence (RTP) materials are metal-doped inorganics and organometallic compounds.<sup>[8]</sup> These materials commonly contain noble metals, thus causing high cost and cytotoxicity, poor flexibility, and low stability. Meanwhile, pure organic RTP materials, as another alternative, are less efficient because of their poor intersystem crossing (ISC) and rapid rate of nonradiative deactivation.<sup>[9]</sup> Therefore, it is of great urgency to develop a new type of metal-free RTP materials with low toxicity, facile preparation, and long lifetime.

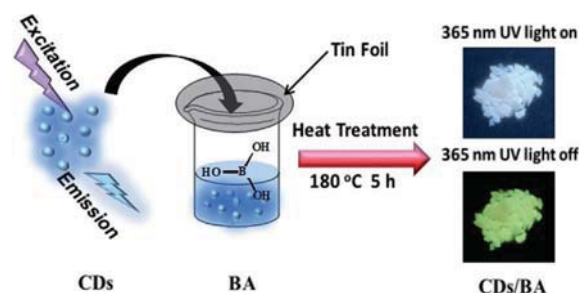
In recent years, carbon dots (CDs) as a new kind of zero-dimensional carbon nanomaterials have attracted increasing attention in constructing metal-free RTP materials owing to their low toxicity,<sup>[10,11]</sup> biocompatibility,<sup>[12]</sup> easy preparation, and unique optical properties.<sup>[13,14]</sup> But realizing the long-

lifetime RTP of CDs is difficult owing to deficient triplet excitons and nonradiative deactivations. So far, CDs with polymer-like structure benefit from crosslink-enhanced emission (CEE) effect can greatly suppress nonradiative transitions and generate RTP. But these polymer CDs generally exhibit relative short lifetimes (ca. 1.46 s).<sup>[15–17]</sup> On the other hand, by embedding CDs into various matrices, such as polyvinyl alcohol,<sup>[18]</sup> potash alum,<sup>[19]</sup> aluminum sulfate,<sup>[20]</sup> zeolites,<sup>[21]</sup> silica gel,<sup>[22]</sup> urea/biuret,<sup>[23]</sup> and polyurethane,<sup>[24]</sup> more superior RTP performances have been obtained in these CD-based materials. These matrices can effectively fix emissive species and prevent the CD triplet states from quenching. Further summary and analysis show that reported CDs all contained heteroatoms, such as N,<sup>[22]</sup> P,<sup>[16,17]</sup> F,<sup>[25]</sup> which can promote ISC and facilitate spin-orbit coupling. Despite these inspiring achievements, these host matrices only allow specific guest CDs to present RTP, and none of a host matrix is universal for other guest CDs as reported. Furthermore, the phosphorescence emission bands of these CD-based RTP materials mainly located in the short wavelength (blue- to green-light) region. These unfavorable limitations largely hinder the development and application of CD-based RTP materials.

Herein, we designed a universal method to activate RTP of CDs by one-pot heating treatment of CDs with boric acid (BA). To more directly reveal the feasibility of this method, we deliberately chose heteroatom-free CDs (a-CDs) as the emissive fluorophore. This kind of CDs only contains carbon, hydrogen, and oxygen atoms, so they exhibit few hybrid orbital and consequently occupy fewer energy level structures for electron transitions.<sup>[26]</sup> Thus, heteroatom-free CDs have a larger energy gap ( $\Delta E_{ST}$ ) between the lowest singlet state ( $S_1$ ) and triplet state ( $T_1$ ) and are more difficult to exhibit RTP. Surprisingly, as shown in Scheme 1, after the incorporation of a-CDs into BA matrix, the composite (a-CDs/BA) exhibits yellow-green RTP with a lifetime as high as 1.6 s.

[\*] W. Li, W. Zhou, Z. Zhou, Prof. H. Zhang, Prof. X. Zhang, Prof. J. Zhuang, Prof. Y. Liu, Prof. B. Lei, Prof. C. Hu  
Guangdong Provincial Engineering Technology Research Center for Optical Agriculture, College of Materials and Energy  
South China Agricultural University  
Guangzhou 510642 (P. R. China)  
E-mail: tliuyi@scau.edu.cn  
tleibf@scau.edu.cn  
thucf@scau.edu.cn

Supporting information and the ORCID identification number(s) for the author(s) of this article can be found under:  
<https://doi.org/10.1002/anie.201814629>.



**Scheme 1.** Illustration for the formation procedure of a-CDs/BA.

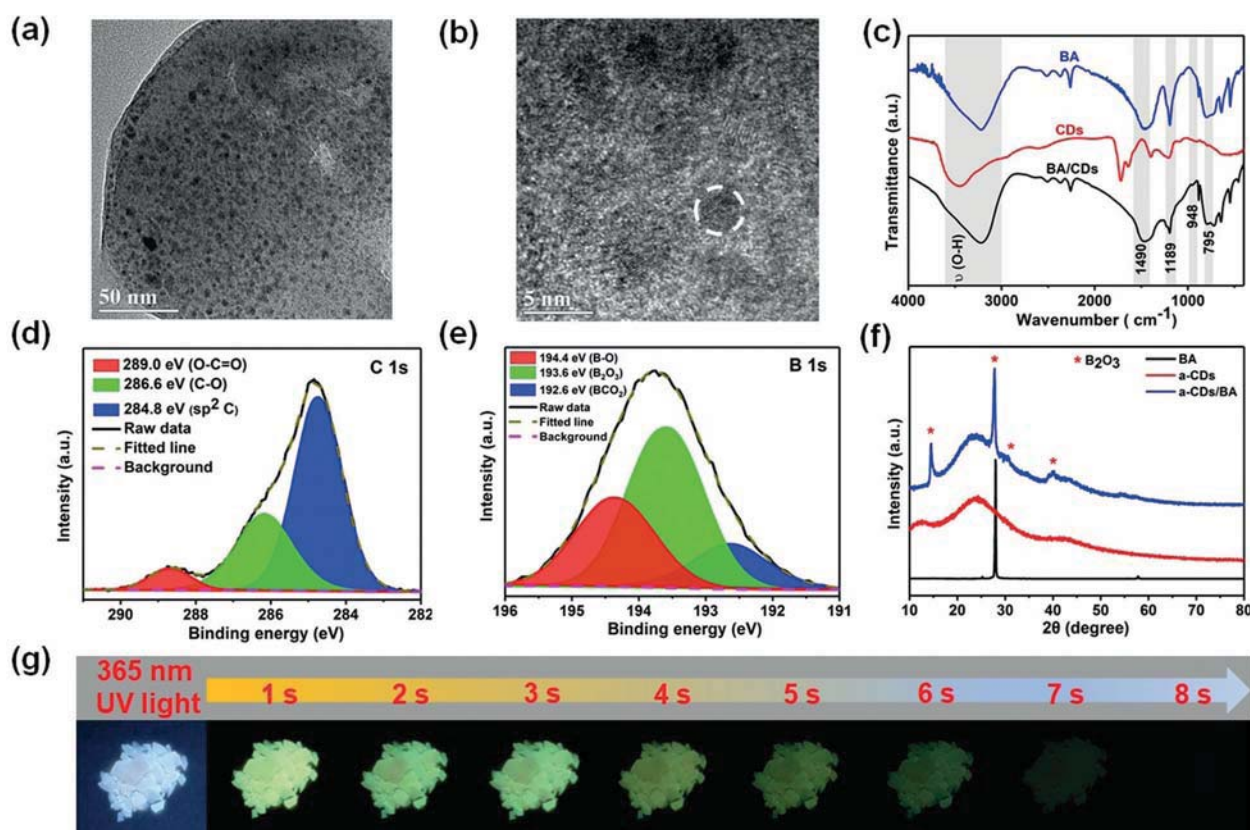


**Figure 1.** a) TEM image of a-CDs/BA. b) HRTEM image of a-CDs/BA; inset: HRTEM image of a-CDs with higher magnification. c) FTIR spectra of BA, a-CDs, and a-CDs/BA. d) and e) XPS high-resolution C 1s and B 1s spectra of a-CDs/BA. f) XRD patterns of BA, a-CDs, and a-CDs/BA. g) Digital photographs of a-CDs/BA before and after turning off 365 nm UV light.

Moreover, we successfully prepared multi-color (blue, green, green–yellow, and orange) RTP CDs-based materials by one-step treatment of different kinds of CDs with BA, demonstrating the universality of this effective strategy. The obtained RTP materials also shows great potentials in the fields of information encryption and decryption.

The a-CDs were prepared according to a previous work.<sup>[26]</sup> After further combination with BA, a-CDs are successfully dispersed in BA matrix as shown in Figure 1a, which was also supported by the high-resolution (HR) TEM image (Figure 1b; Supporting Information, Figure S1a,b). To understand the composition of a-CDs and BA, the Fourier transform infrared spectroscopy (FTIR) and X-ray photoelectron spectroscopy (XPS) spectra were obtained. As shown in Figure 1c, FTIR spectra of a-CDs/BA display characteristic absorption bands at 3226  $\text{cm}^{-1}$  and 1490  $\text{cm}^{-1}$ , which are attributed to –OH and B–O stretching vibrations, respectively.<sup>[27]</sup> The band peaked at 1189  $\text{cm}^{-1}$  is originated from an asymmetrically stretched oxygen atom connecting the trigonal boron atoms.<sup>[28]</sup> The new band at 948  $\text{cm}^{-1}$  is attributed to the characteristic boron–carbon bond.<sup>[28]</sup> These results are consistent with XPS analysis. The HR C 1s spectrum of a-CDs/BA exhibit three peaks at 284.8 eV, 286.6 eV and 289 eV for  $\text{sp}^2$  C, C–O, and O–C=O, respectively (Figure 1d). The HR B 1s spectra of a-CDs/BA can be fitted to three bands centered at 194.4 eV, 193.6 eV, and 192.6 eV, which belong to B–O,  $\text{B}_2\text{O}_3$ , and  $\text{BCO}_2$ , respectively (Figure 1e).<sup>[28]</sup> The signal

at 192.6 eV reveals that boron atoms are surrounded by carbon and oxygen atoms ( $\text{BCO}_2$ ), indicating the presence of oxidized boron atoms in this sample.<sup>[30]</sup> Furthermore, the X-ray diffraction (XRD) pattern of a-CDs/BA also present the characteristic peaks of boron oxide and amorphous glassy state in a-CDs/BA (Figure 1f). The above results indicate that a-CDs were uniformly dispersed in the matrix, and covalent coupling reactions occurred between a-CDs and BA, resulting in the introduction of electron-withdrawing boron atom and the formation of boron–carbon bond.

As shown in Scheme 1 and Figure 1g, a-CDs/BA presents greenish-blue FL under 365 nm UV lamp, while yellow–green afterglow appears after the lamp is switched off. To ascertain the origin of afterglow emission, photophysical properties of a-CDs/BA and a-CDs were fully investigated. Figure 2a display that the afterglow emission of a-CDs/BA mainly peaked at 530 nm and gradually red-shifted to 575 nm with the increased wavelength of excitation. The excitation-dependent behavior of afterglow can be attributed to the existence of multiple triplet-excited states in a-CDs/BA,<sup>[16]</sup> which is further confirmed by the fact that the afterglow lifetime decay curve of a-CDs/BA at 350 nm excitation can be fitted to a triexponential function (Figure 2b). According to the following Equation (1):

$$\tau_{\text{avg}} = \frac{\sum A_i \tau_i^2}{\sum A_i \tau_i} \quad (1)$$

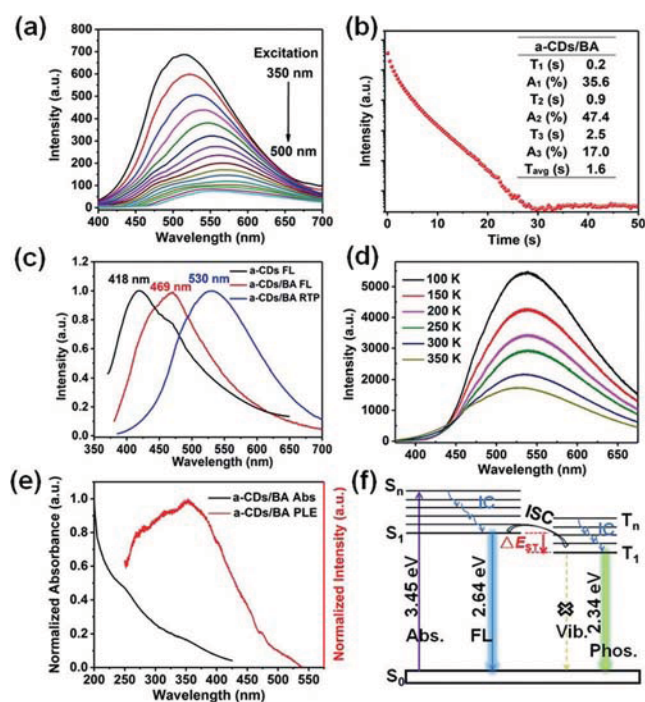


**Figure 2.** a) Phosphorescence spectra of a-CDs/BA excited at different wavelengths. b) Afterglow decay curve and lifetimes of a-CDs/BA monitored at 530 nm with 350 nm excitation. c) FL emission spectra of a-CDs and a-CDs/BA, and afterglow emission spectrum of a-CDs/BA, respectively, excited at 350 nm. d) Afterglow emission spectra of a-CDs/BA at different temperature under 350 nm excitation. e) UV/Vis absorbance spectrum and afterglow excitation spectrum of a-CDs/BA monitored at 530 nm. f) Energy-level diagram of a-CDs/BA (Abs.: absorption; IC: intersystem crossing; Vib.: vibration; Phos.: phosphorescence).

the average afterglow lifetime was calculated to be 1.6 s, which is far longer than the reported CDs-based afterglow materials.<sup>[18–25]</sup> As presented in Figure 2c, the FL and afterglow emission peaks of solid-state a-CDs/BA are, respectively located at 469 nm and 530 nm under the optimal excitation. The difference between FL and afterglow spectra of a-CDs/BA demonstrates the RTP nature of afterglow. The phosphorescence quantum yield (PQY) of a-CDs/BA was measured to be as high as 8.7%. With the temperature increased from 100 K to 350 K, the intensities of afterglow emission of a-CDs/BA declined (Figure 2d), which is corresponding well to the feature of phosphorescence due to the higher nonradiative deactivation at elevated temperatures.

Figure 2e indicates that a-CDs have two absorption bands peaked at 255 and 350 nm (black line), which can be attributed to the  $\pi \rightarrow \pi^*$  transition of C=C and  $n \rightarrow \pi^*$  transition of C=O, respectively. The overlap of afterglow excitation spectrum and absorption spectrum at 300–400 nm shows that RTP mainly originates from C=O bond of a-CDs. Moreover, the FL emission peak of a-CDs solution is located at 418 nm (Figure 2c), which is different from that of a-CDs/BA under the same excitation, indicating that different aggregation process induced mutation of energy levels (Supporting Information, Figure S2),<sup>[13]</sup> and which might be one reason of the activation of RTP from a-CDs.

To gain a further insight of the activation of RTP, the influence of heating temperature and ratio of a-CDs in a-CDs/BA were also explored. As we observed, the samples treated above 160 °C could present RTP. The XRD patterns show that when the temperature reaches over 160 °C, the characteristic peak of amorphous glassy state become more obvious (Supporting Information, Figure S3a). Accordingly, as shown in the Supporting Information, Figure S3b, phosphorescence emission of a-CDs/BA become stronger as the temperature of heat treatment rises from 160 °C to 250 °C. Noted that the intensities of phosphorescence emission distinctly dropped under 300 °C and 400 °C treatment, it is because that further carbonization of CDs at higher temperatures consumed the partial emissive species, and thereby greatly affecting the optical properties of a-CDs by reducing their surface molecules.<sup>[31]</sup>

In another experiment, a-CDs/BA samples with different ratios of a-CDs, denoted as a-CDs<sub>x</sub>/BA ( $x=0, 0.2, 0.5, 2$ ), were prepared. As displayed in XPS HR B 1s spectra (Supporting Information, Figure S4), with the addition of a-CDs in a-CDs<sub>x</sub>/BA, BCO<sub>2</sub> bands appear and gradually increases. The enhanced absorption at 950 cm<sup>-1</sup> in FTIR spectra of a-CDs<sub>0.2</sub>/BA, a-CDs<sub>0.5</sub>/BA and a-CDs<sub>2</sub>/BA further confirm the existence and increase of boron-carbon bond (Supporting Information, Figure S5). Meanwhile, the optical properties of a-CDs<sub>x</sub>/BA samples have also been systematically studied. a-CDs<sub>0</sub>/BA is barely fluorescent or phosphorescent compared to other a-CD-containing samples (Supporting Information, Figure S6), whose RTP properties are largely dependent on the concentration of a-CDs in a-CDs<sub>x</sub>/BA. Combined phosphorescence spectra with afterglow lifetimes of a-CDs<sub>x</sub>/BA, it is apparent that a-CDs<sub>2</sub>/BA present the optimal RTP behavior (Supporting Information, Figure S7a,b and Table S1). These findings validly demonstrate that the RTP performance of a-CDs<sub>x</sub>/BA mainly comes from a-CDs and depends on the new emerged covalent bond between a-CDs and BA. Furthermore, XRD patterns reveal that as the ratio of a-CDs increases (Supporting Information, Figure S7c), the characteristic peaks of amorphous phases become more obvious, further indicate that the amorphous glassy state is beneficial for the introduction and enhancement of RTP.

Based on the above analysis and discussion, a possible mechanism for the activation of RTP from heteroatom-free CDs could be tentatively proposed as followed. First, the C=O bond of a-CDs gives rise to RTP of a-CDs/BA. It should be noted that no RTP of a-CDs in other matrices (that is, PVA, silica) has been observed. Thus, second, the selected BA matrix is crucial for the activation of RTP. In the above experiment and analysis, it has been confirmed that a-CDs were embedded in the glassy state BA and new boron-carbon bond between a-CDs and BA matrix formed. We believed that these covalent bonds and glassy state are able to lock the triplet species (that is, C=O containing moieties) on the a-CDs and protect the excited triplet excitons from quenching, thereby promoting RTP emission. More importantly, what make the BA more specific is that boron atom has the vacant p orbit that can attract  $\pi$  transition to form the p  $n\pi^*$  conjugate system, which can effectively reduce the minimum



unoccupied orbital energy level of the system.<sup>[32,33]</sup> Therefore, the newly formed boron–carbon bond can also effectively reduce the  $\Delta E_{ST}$  and consequently facilitating the ISC between  $S_1$  and  $T_1$  (Figure 2 f). As a result, the  $\Delta E_{ST}$  was calculated to be 0.3 eV, which is a small value for effective intersystem crossing.<sup>[34]</sup>

To prove the universality of our strategy, we designed a series of CDs/BA composites by incorporating various guest CDs into the BA matrix, respectively. Among them, another two kinds of heteroatom-free CDs (b-CDs<sup>[35]</sup> and c-CDs<sup>[36]</sup>) were deliberately selected. As shown in Figure 3 a, both of the

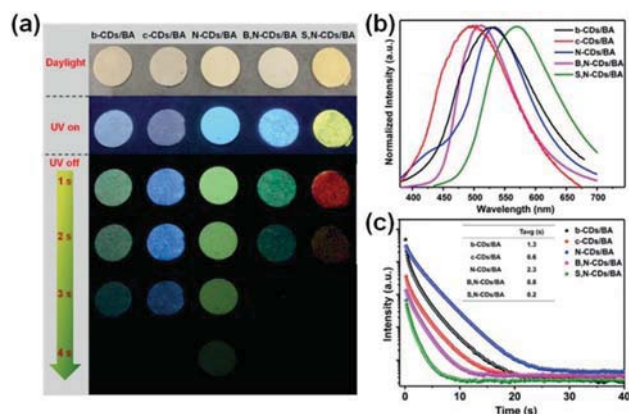


**Figure 3.** a) Digital photographs of b-CDs/BA, c-CDs/BA, N-CDs/BA, B,N-CDs/BA, and S,N-CDs/BA before and after turning off 365 nm UV light. b) Afterglow emission spectra of b-CDs/BA, c-CDs/BA, N-CDs/BA, B,N-CDs/BA, and S,N-CDs/BA, excited at 350 nm, respectively. c) Afterglow decay curves and lifetimes of b-CDs/BA, c-CDs/BA, N-CDs/BA, B,N-CDs/BA, and S,N-CDs/BA, excited at 350 nm and monitored at their optimal wavelengths.

b-CDs/BA and c-CDs/BA composites exhibit blue and bluish-green RTP, respectively, indicating the feasibility of this method to activate RTP of heteroatom-free CDs. According to the basic feature of phosphorescence, the energy level of  $T_1$  is always lower than that of  $S_1$ ,<sup>[18–25]</sup> so CDs with long-wavelength FL emission are favorable for acquiring longer-wavelength RTP. On the one hand, heteroatom doping is widely used to regulate the FL emission wavelength of CDs.<sup>[18–25]</sup> On the other hand, the doped heteroatom, especially N, P, and halogens are favoring the  $n \rightarrow \pi^*$  transition to facilitate the populate of triplet excitons for RTP.<sup>[18–25]</sup> Since the successful achievement of RTP from heteroatom-free CDs in BA matrix, we propose that it is possible to achieve multi-color RTP by incorporating long-wavelength-emitting heteroatom-containing CDs with BA in the same way. As shown in the Figure 3 a, nitrogen-doped CDs<sup>[37]</sup> (N-CDs), boron and nitrogen co-doped CDs<sup>[38]</sup> (B,N-CDs) and sulfur and nitrogen co-doped CDs<sup>[39]</sup> (S,N-CDs), respectively, were employed. As expected, all the corresponding N-CDs/BA, B,N-CDs/BA and S,N-CDs/BA composites exhibit RTP. More impressively, the different stokes shifts between FL and phosphorescence of these CDs endow them with different colors of RTP. Therefore, by adopting different types of guest CDs, multi-color RTP (blue to orange) of CDs/BA composites were obtained (Figure 3 a). As shown in the Supporting

Information, Figure S8, under the optimal excitation of 350 nm, their phosphorescence emission peaks range from 490 nm to 570 nm (Figure 3 b). Combined with FL emission spectra of these CDs/BA composites (Supporting Information, Figure S9), the  $\Delta E_{ST}$  were calculated and listed in the Supporting Information, Table S2, all of which are small values (that is, 0.2–0.48 eV) for effective ISC process and spin–orbit coupling. Based on the phosphorescence decay curves and fitting of triexponential function (Figure 3 c), the average RTP lifetimes of composites were calculated and listed in Figure 3 c. It is noted that N-CDs/BA has the longest phosphorescence lifetime up to 2.26 s with a high PQY of 17.5%, which is the highest record for CDs-based RTP materials to date. This is due to that N can help to promote ISC and facilitate spin–orbit coupling of CDs.<sup>[22]</sup> Moreover, their RTP performances are stable and their RTP intensities almost remains the same after 12 months. Furthermore, FTIR spectra of these CDs/BA materials confirm the existence of B–O bond and B–C bond (Supporting Information, Figure S10a), and XRD patterns also present that all samples display the characteristic peaks of boron oxide in amorphous glassy state (Supporting Information, Figure S10b). These results not only prove that BA is a universal matrix for the activation of RTP of CDs, but also provides a promising strategy for tuning the color of RTP of CD-based materials.

Thanks to the distinctive RTP performance of different CDs/BA composites, their potential application in anti-counterfeit technology and information encryption was demonstrated. As shown in Figure 4 a, we simply developed a graphic security scheme by using a-CDs/BA, N-CDs/BA, and B,N-CDs. Under the daylight, it is hard to distinguish

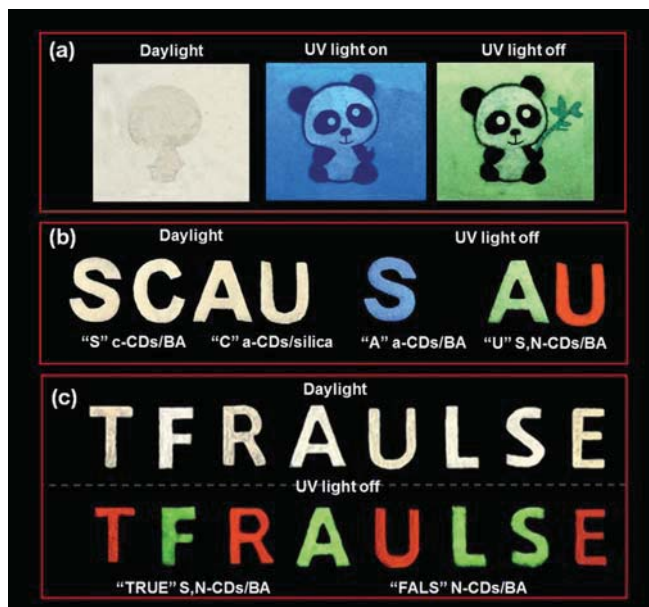


**Figure 4.** a) Digital photographs of graphic security made from a-CDs/BA (covered the panda body pattern), N-CDs/BA (covered the bamboo pattern), and B,N-CDs (covered the rest of square area). UV light: 365 nm. b) Digital photographs of information encryption made from c-CDs/BA, a-CDs/silica, a-CDs/BA, and S,N-CDs/BA. UV light: 365 nm. c) Digital photographs of information encryption made from S,N-CDs/BA and N-CDs/BA. UV light: 365 nm.



each part. Upon 365 nm irradiation, the pattern of panda body exhibits white FL, the FL from bamboo part and the rest of square area are indistinguishable. After turning off the excitation, the green RTP from bamboo pattern shows up and different from other parts. This indicates that these CDs/BA composites could be successfully applied in graphic protection. Likewise, as displayed in Figure 4b, because the multi-color RTP emitting from CDs/BA composites and no phosphorescence observed from a-CDs/silica, a colorful “SAU” was obtained after switch off the lighting source. Furthermore, the application of CDs/BA composites in information encryption has also been proved in Figure 4c. The capital letters “TFRAULSE” is a mixture of “TRUE” and “FALSE”. Once the excitation is turned off, the information of “TRUE” and “FALS” could be recognized from each other, so the information can be decrypted in this way.

In summary, a universal and effective approach to activate RTP of CDs in BA matrix has been developed. The newly formed boron carbon bond between CDs and BA effectively locked the triplet species (that is, C=O) on the a-CDs, and the introduction of boron atoms that contained lone pair electrons can exactly reduce the  $\Delta E_{ST}$  and facilitate the ISC between  $S_1$  and  $T_1$ , thereby increasing the quantity of triple excitons. At the same time, the emerging glassy state can help to rigidify the triplet excited states of CDs from nonradiative deactivation. All of these made BA to be a universal matrix to overcome the difficulties in acquiring heteroatom-free CDs-based RTP materials, and also provides a convenient method to obtain metal-free RTP materials with rarely observed multi-color RTP by changing the type of guest CDs. Furthermore, these CDs/BA composites are promising in anti-counterfeit technology and information encryption with a higher level of security owing to their distinctive RTP performance.

## Acknowledgements

The present work was supported by the National Natural Science Foundations of China (Grant Nos. 21571067, 21671070), the Project of GDUPS (2018) for Prof. Bingfu LEI, the Project for Construction of High-level University in Guangdong Province, the Key Foundation for Basic and Application Research in Higher Education of Guangdong, China (No. 2017KZDXM005), and the Guangzhou Science & Technology Project (No. 201707010033).

## Conflict of interest

The authors declare no conflict of interest.

**Keywords:** afterglow · carbon dots · information encryption · phosphorescence · universal hosts

**How to cite:** *Angew. Chem. Int. Ed.* **2019**, *58*, 7278–7283  
*Angew. Chem.* **2019**, *131*, 7356–7361

- [1] S. N. Baker, G. A. Baker, *Angew. Chem. Int. Ed.* **2010**, *49*, 6726; *Angew. Chem.* **2010**, *122*, 6876.
- [2] O. Bolton, K. Lee, H. J. Kim, K. Y. Lin, J. Kim, *Nat. Chem.* **2011**, *3*, 205.
- [3] M. S. Kwon, D. Lee, S. Seo, J. Jung, J. Kim, *Angew. Chem. Int. Ed.* **2014**, *53*, 11177; *Angew. Chem.* **2014**, *126*, 11359.
- [4] H. Wang, L. Meng, X. Shen, X. Wei, X. Zheng, X. Lv, Y. Yi, Y. Wang, P. Wang, *Adv. Mater.* **2015**, *27*, 4041.
- [5] L. Xiao, Z. Chen, B. Qu, J. Luo, S. Kong, Q. Gong, J. Kido, *Adv. Mater.* **2011**, *23*, 926.
- [6] A. C. Grimsdale, K. L. Chan, R. E. Martin, P. G. Jokisz, A. B. Holmes, *Chem. Rev.* **2009**, *109*, 897.
- [7] Y. You, *Curr. Opin. Chem. Biol.* **2013**, *17*, 699.
- [8] S. Cai, H. Shi, J. Li, L. Gu, Y. Ni, Z. Cheng, S. Wang, W. Xiong, L. Li, Z. An, *Adv. Mater.* **2017**, *29*, 1701244.
- [9] Y. Gong, C. Chen, Q. Peng, W. Z. Yuan, Y. Xie, S. Li, Y. Zhang, B. Tang, *Adv. Mater.* **2015**, *27*, 6195.
- [10] S. Y. Lim, W. Shen, Z. Gao, *Chem. Soc. Rev.* **2015**, *44*, 362.
- [11] H. Li, Y. Zhang, L. Wang, J. Tian, X. Sun, *Chem. Commun.* **2011**, *47*, 961.
- [12] X. Li, Y. Liu, X. Song, H. Wang, H. Gu, H. Zeng, *Angew. Chem. Int. Ed.* **2015**, *54*, 1759; *Angew. Chem.* **2015**, *127*, 1779.
- [13] Y. Chen, M. Zheng, Y. Xiao, H. Dong, H. Zhang, J. Zhuang, H. Hu, B. Lei, Y. Liu, *Adv. Mater.* **2016**, *28*, 312.
- [14] S. Qu, D. Zhou, D. Li, W. Ji, P. Jing, D. Han, L. Liu, H. Zeng, D. Shen, *Adv. Mater.* **2016**, *28*, 3516.
- [15] S. Tao, S. Lu, Y. Geng, S. Zhu, S. A. T. Redfern, Y. Song, T. Feng, W. Xu, B. Yang, *Angew. Chem. Int. Ed.* **2018**, *57*, 2393; *Angew. Chem.* **2018**, *130*, 2417.
- [16] K. Jiang, Y. Wang, C. Cai, H. Lin, *Adv. Mater.* **2018**, *30*, 1800783.
- [17] K. Jiang, Y. Wang, X. Gao, C. Cai, H. Lin, *Angew. Chem. Int. Ed.* **2018**, *57*, 6216; *Angew. Chem.* **2018**, *130*, 6324.
- [18] K. Jiang, L. Zhang, J. Lu, C. Xu, C. Cai, H. Lin, *Angew. Chem. Int. Ed.* **2016**, *55*, 7231–7235; *Angew. Chem.* **2016**, *128*, 7347–7351.
- [19] Y. Zhang, X. Dong, L. Wei, Y. Su, Z. Li, H. Geng, C. Yang, *J. Mater. Chem. C* **2015**, *3*, 2798.
- [20] J. Joseph, A. A. Anappara, *ChemistrySelect* **2017**, *2*, 2017.
- [21] Y. Mu, N. Wang, Z. Sun, J. Wang, J. Li, J. Yu, *Chem. Sci.* **2016**, *7*, 3564.
- [22] J. Tan, R. Zou, J. Zhang, W. Li, L. Zhang, D. Yue, *Nanoscale* **2016**, *8*, 4742.
- [23] J. Joseph, A. A. Anappara, *Phys. Chem. Chem. Phys.* **2017**, *19*, 15137.
- [24] Q. Li, M. Zhou, Q. Yang, Q. Wu, J. Shi, A. Gong, M. Yang, *Chem. Mater.* **2016**, *28*, 8221.
- [25] P. Long, Y. Feng, C. Cao, Y. Li, J. Han, S. Li, C. Peng, Z. Li, W. Feng, *Adv. Funct. Mater.* **2018**, *28*, 1800791.
- [26] Y. Dong, G. Li, N. Zhou, R. Wang, Y. Chi, G. Chen, *Anal. Chem.* **2012**, *84*, 8378.
- [27] X. Liu, S. Ye, Y. Qiao, G. Dong, Q. Zhang, J. Qiu, *Chem. Commun.* **2009**, 4073.
- [28] M. G. Rodríguez, O. V. Kharissova, U. Ortiz-Méndez, *Rev. Adv. Mater. Sci.* **2004**, *7*, 55.
- [29] Z. Ling, G. Wang, M. Zhang, X. Fan, C. Yu, J. Yang, N. Xiao, J. Qiu, *Nanoscale* **2015**, *7*, 5120.
- [30] Z. Sheng, H. Gao, W. Bao, F. Wang, X. Xia, *J. Mater. Chem. C* **2012**, *22*, 390.
- [31] S. Zhu, Q. Meng, L. Wang, J. Zhang, Y. Song, H. Jin, K. Zhang, H. Sun, H. Wang, B. Yang, *Angew. Chem. Int. Ed.* **2013**, *52*, 3953; *Angew. Chem.* **2013**, *125*, 4045.
- [32] A. Wakamiya, T. Taniguchi, S. Yamaguchi, *Angew. Chem. Int. Ed.* **2006**, *45*, 3170–3173; *Angew. Chem.* **2006**, *118*, 3242–3245.
- [33] J. Yang, X. Zhen, B. Wang, X. Gao, Z. Ren, J. Wang, Y. Xie, J. Li, Q. Peng, K. Pu, *Nat. Commun.* **2018**, *9*, 840.

- [34] Y. Deng, D. Zhao, X. Chen, F. Wang, H. Song, D. Shen, *Chem. Commun.* **2013**, 49, 5751.
- [35] S. Zhu, J. Zhang, Y. Song, G. Zhang, H. Zhang, B. Yang, *Acta. Chim. Sinica* **2012**, 70, 2311.
- [36] L. Tang, R. Ji, X. Cao, J. Lin, H. Jiang, X. Li, K. S. Teng, M. L. Chi, S. Zeng, J. Hao, *ACS Nano* **2012**, 6, 5102.
- [37] K. Jiang, S. Sun, L. Zhang, Y. Lu, A. Wu, C. Cai, H. Lin, *Angew. Chem. Int. Ed.* **2015**, 54, 5360; *Angew. Chem.* **2015**, 127, 5450.
- [38] C. Shen, J. Wang, Y. Cao, Y. Lu, *J. Mater. Chem. C* **2015**, 3, 6668.
- [39] W. Zhou, J. Zhuang, W. Li, C. Hu, B. Lei, Y. Liu, *J. Mater. Chem. C* **2017**, 5, 8014.

Manuscript received: January 22, 2019

Revised manuscript received: February 27, 2019

Accepted manuscript online: March 29, 2019

Version of record online: April 16, 2019

## RESEARCH ARTICLE

# High-Efficiency Solid-State Luminescence from Hydrophilic Carbon Dots with Aggregation-Induced Emission Characteristics

Zhijun Wan, Yuemiao Li, Yizi Zhou, Dongping Peng, Xuejie Zhang, Jianle Zhuang, Bingfu Lei, Yingliang Liu, and Chaofan Hu\*

Carbon dots (CDs) have excellent properties and have made great progress in synthesis and applications. However, it is still a challenge to realize convenient preparation and highly emissive solid-state luminescence without the assistance of matrix. In this study, high-efficiency hydrophilic yellow emissive CDs (Y-CDs) with aggregation-induced emission (AIE) characteristics are synthesized by a one-pot microwave method. Y-CDs show weak yellow emission with a photoluminescence quantum yield (PLQY) of 6.14% in aqueous solutions, but exhibit a significantly enhanced PLQY of 58.35% in the solid state. The AIE characteristic is confirmed by the phenomenon that the fluorescence emission intensity of Y-CDs continues to increase with the gradual increase of the poor solvent fraction. The AIE phenomenon of Y-CDs is derived from the suppression of surface piperazine groups motions and decrease of the non-radiative rate, as is verified by a series of experiments. Finally, based on the high PLQY and AIE property, Y-CDs are applied as a color-converting layer on blue-light-emitting chips to fabricate white-light-emitting diodes with color coordinates of (0.31, 0.35), while Y-CDs are also explored for their potential applications in anti-counterfeiting, encryption and bioimaging.

tion-caused-quenching (ACQ) like organic molecules on account of their excessive resonance energy transfer or direct  $\pi$ - $\pi$  stacking, hindering their high-concentration or solid-state applications.<sup>[5]</sup> At present, the most conventional method to realize the solid state emission of carbon dots is the dispersion of CDs into other matrix materials to form composite materials, such as transparent polymers,<sup>[6]</sup> silica xerogels,<sup>[7]</sup> starch,<sup>[8]</sup> and inorganic salts,<sup>[9]</sup> etc. However, these methods increase the preparation cost and have an impact on some of the properties of CDs. For example, the high load rate still leads to a serious decrease in the photoluminescent quantum yield (PLQY) of CDs, which is still not conducive to the commercialization of CDs-based WLEDs.


Delightfully, some novel luminescent material displays the opposite phenomenon of ACQ. They are non-emissive or weakly emissive in dispersed solutions,

but appear brightly luminescent upon aggregation. This unique phenomenon was first reported by Tang's group in 2001 and was defined as aggregation-induced emission (AIE).<sup>[10]</sup> Then, through systematic research, the restriction of the intramolecular motion (RIM) mechanism has now been recognized as the universal mechanism of AIE; that is, in the state of aggregation, the vibration and rotation of AIE intramolecular bonds are greatly restricted by interactions from the surrounding molecules or natural physical constraints, which restrains the non-radiative decay channels and leads to high luminescence.<sup>[11]</sup> Therefore, the AIE effect has become an extremely effective strategy to solve the ACQ dilemma, and to construct high PLQY solid state emitters for applications in optoelectronic devices,<sup>[12]</sup> distinguished chemosensors,<sup>[13]</sup> and biosensors.<sup>[14]</sup> Several types of AIE materials have been reported during the past decade, including organic molecules,<sup>[15]</sup> polymers,<sup>[16]</sup> and metal particles.<sup>[17]</sup> In 2019, our group first reported a kind of hydrophobic CDs with the AIE property.<sup>[18]</sup> These CDs displayed blue emission in a dispersed state and the intramolecular rotation of the symmetrical heterocyclic around the disulfide bonds was restricted in the solid state, leading to red emission. But it was a pity that the PLQY was only 5.96%. Subsequently, we constructed carbon dots with color-tunable aggregation-induced

## 1. Introduction

Carbon dots (CDs) are a popular class of luminescent nanomaterials because of their easy preparation and purification,<sup>[1]</sup> low cost,<sup>[2]</sup> excellent biocompatibility,<sup>[3]</sup> and adjustable optical and surface properties.<sup>[4]</sup> Although carbon dots have excellent properties, it is difficult to satisfy mass industrial production and application. The hydrothermal or solvothermal synthesis typically used to prepare CDs requires several hours and dangerous conditions including high temperatures and pressures, increasing both their construction costs and preparation time. On the other hand, most CDs tend to be subject to aggrega-

Z. Wan, Y. Li, Y. Zhou, D. Peng, X. Zhang, J. Zhuang, B. Lei, Y. Liu, C. Hu  
Key Laboratory for Biobased Materials and Energy of Ministry of Education/Guangdong Provincial Engineering Technology Research Center for Optical Agriculture, College of Materials and Energy  
South China Agricultural University  
Guangzhou 510642, P. R. China  
E-mail: thucf@scau.edu.cn

 The ORCID identification number(s) for the author(s) of this article can be found under <https://doi.org/10.1002/adfm.202207296>.

DOI: 10.1002/adfm.202207296

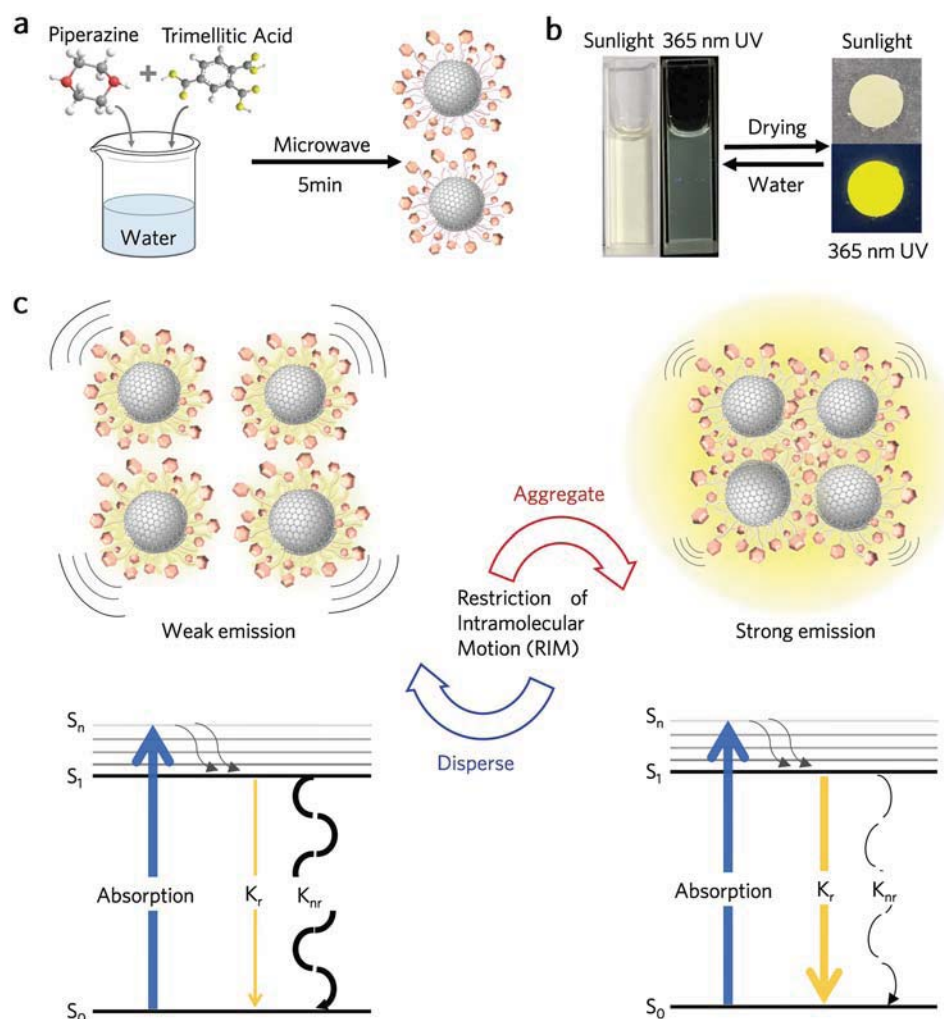


**Figure 1.** a) Synthesis of Y-CDs. b) Photographs of Y-CDs powder dissolved in aqueous solvent and under sunlight and ultraviolet (365 nm) irradiation. c) Schematic and energy level diagram of effect of AIE on CDs, respectively.

emission by nitrogen-induced intramolecular charge transfer,<sup>[19]</sup> in which the PLQY of CDs with red emission was effectively increased to 11.7%. They still have relatively low PLQY, which hinders their application in luminescent devices. And they are prepared through solvothermal synthesis, which requires a long time and dangerous conditions including the high temperature of 180 °C and high pressure. They are hydrophobic, which also makes their excellent AIE properties difficult to apply in a watery environment, as in bioimaging and biosensing. Moreover, only a few studies on hydrophilic carbon dots with AIE characteristics have been reported.<sup>[20]</sup> Hence, it is meaningful to synthesize hydrophilic CDs with AIE characteristics, high-efficiency solid-state luminescence and convenient preparation.

In this study, we reported a simple one-step microwave-assisted heating method to prepare hydrophilic CDs (Y-CDs) with high-efficiency solid-state luminescence (Figure 1a,b). Moreover, the Y-CDs showed weak yellow emission (PLQY = 6.14%) when dispersed well in aqueous solutions, but significantly enhanced (PLQY = 58.35%) in solid-state aggregates like most reported AIEgens. The literature concerning CDs with solid-state yellow emission is summarized in Table S1

(Supporting Information). Compared with the reported CDs, the solid-state Y-CDs revealed higher PLQY, which overcame the problem that the solid-state PLQYs of CDs with long wavelength emission were mostly <50%. By comparing  $K_r$  and  $K_{nr}$  of the aqueous solution and powder, this phenomenon was attributed to the suppression of surface groups motions and a significant decrease of the non-radiative rate in the aggregation state (Figure 1c). Therefore, the PL efficiency of Y-CDs powder is obviously increased. Meanwhile, it is found through the control experiment that the AIE behavior was indeed related to the piperazine group. Based on the unique luminescent properties of Y-CDs, we explored their applications in white-light-emitting diodes (WLEDs), anti-counterfeiting, encryption, and bioimaging.

## 2. Results and Discussion

The Y-CDs were prepared from trimellitic acid and piperazine using an energy-saving and time-saving microwave-assisted method. After purification treatment, the production yield of



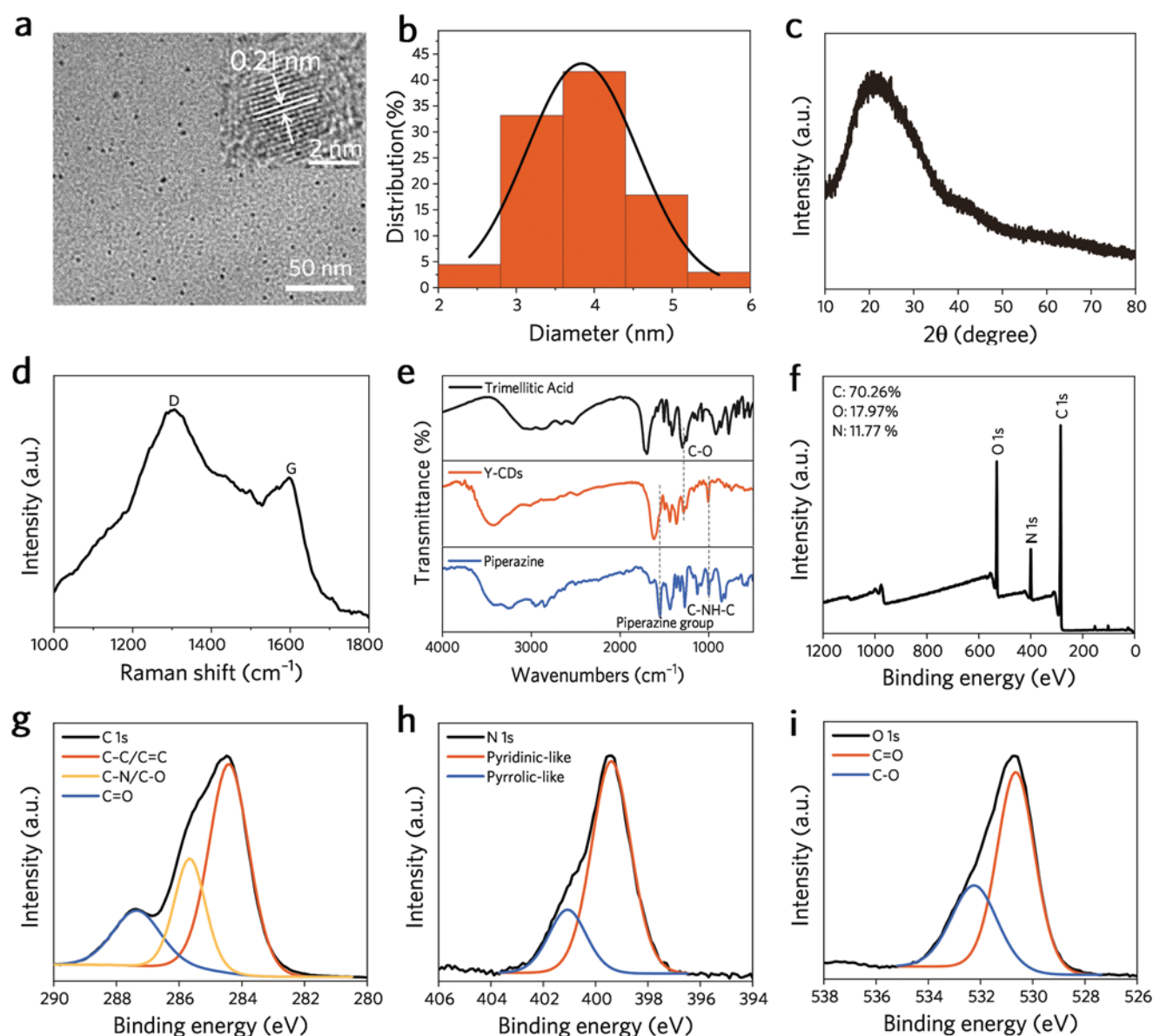


**Figure 2.** a) TEM image of the Y-CDs. Inset: HR-TEM image of Y-CDs. b) Particle size distribution measured by TEM. c) XRD pattern of the Y-CDs. d) Raman spectrum of the Y-CDs. e) FT-IR spectrum of the trimellitic acid, Y-CDs and piperazine. f) XPS spectra of Y-CDs. High resolution XPS spectra and the corresponding fitting curves of g) C 1s, h) N 1s and i) O 1s of Y-CDs.

the obtained product was at 22.41% and it was characterized by transmission electron microscopy (TEM), X-ray diffraction (XRD) and Raman spectroscopy to affirm the character of the carbon nanoparticles. The TEM image of the Y-CDs presents size distributions from 2 to 6 nm (Figure 2a,b), with an average diameter of  $\approx 3.8$  nm. High-resolution TEM (HR-TEM) shows a lattice spacing of 0.21 nm corresponding to the (100) facet of graphite, indicating that the Y-CDs contain graphite-like structures.<sup>[21]</sup> Meanwhile, the XRD pattern of the Y-CDs exhibits an obvious broad peak at  $\approx 21^\circ$  (Figure 2c), which is attributed to amorphous carbon derived from deformations caused by the heteroatomic dopants or  $sp^3$ C defects in graphitic structures,<sup>[19,22]</sup> while a weak peak at  $\approx 42^\circ$  corresponds to the (100) facet with an interlamellar spacing of 0.21 nm.<sup>[6]</sup> There are two

peaks of  $1328\text{ cm}^{-1}$  (D band) and  $1567\text{ cm}^{-1}$  (G band) displayed on the Raman spectrum, which refer to areas of structural defects and  $sp^2$  carbon networks in the Y-CDs' frameworks, respectively (Figure 2d). The calculated intensity ratio  $I_D/I_G$  is 1.46, indicating the disordered surface of the Y-CDs.<sup>[23]</sup>

The chemical composition, structure and surface functional groups of the Y-CDs were examined by Fourier transform infrared (FT-IR) and X-ray photoelectron spectroscopy (XPS). As depicted in the FT-IR spectrum (Figure 2e, orange line), a relatively broad absorption band at  $3426\text{ cm}^{-1}$  can be attributed to the stretching vibration of N–H and O–H on the Y-CDs surface.<sup>[24]</sup> The characteristic absorption peak located at  $1496\text{ cm}^{-1}$  originates from the stretching vibrations of C=C bonds. Meanwhile, the strong peaks at  $1006$  and  $1626\text{ cm}^{-1}$  reflect the

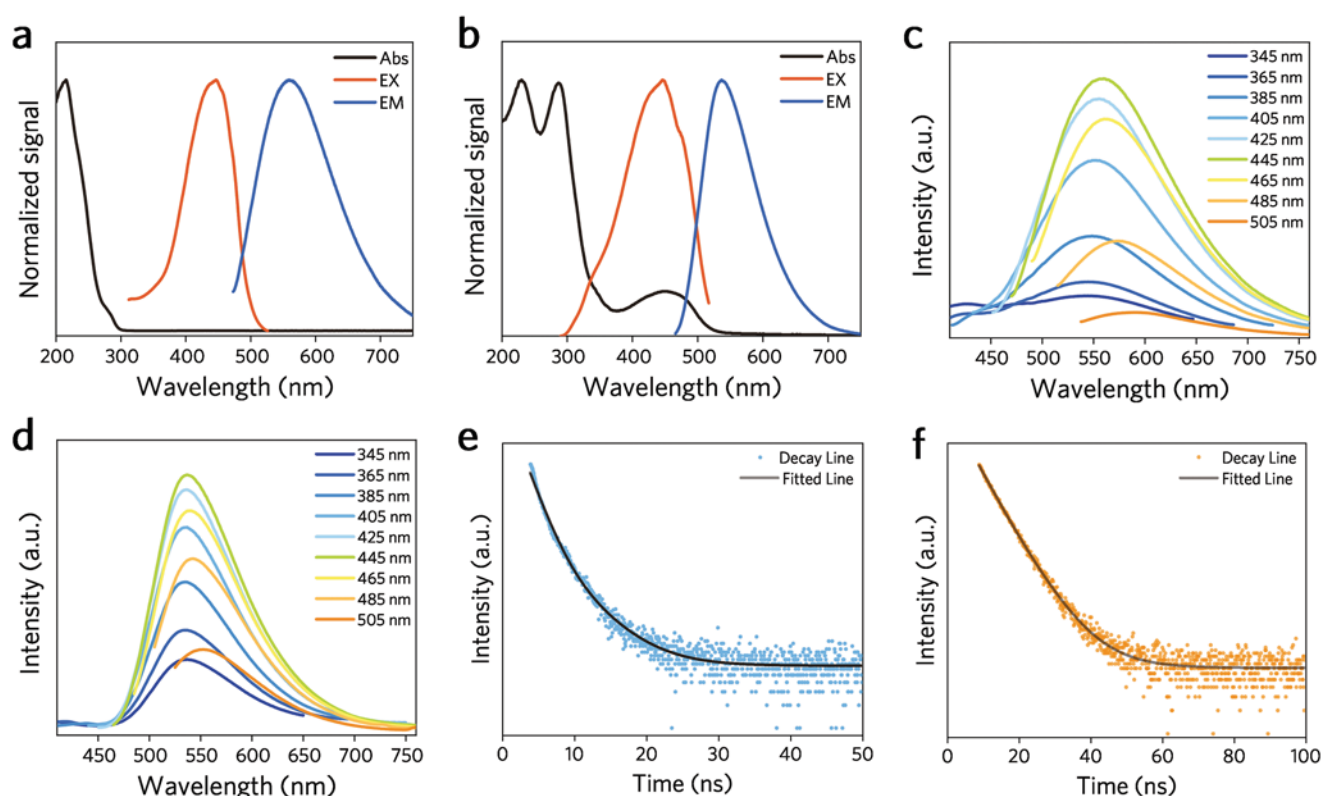


**Figure 3.** a) UV-vis absorption (black line), PL excitation (EX) ( $\lambda_{\text{em}} = 560$  nm, orange line), and emission (EM) ( $\lambda_{\text{ex}} = 448$  nm, blue line) spectra of as-prepared Y-CDs solution. b) UV-vis absorption (black line), PL excitation (EX) ( $\lambda_{\text{em}} = 537$  nm, orange line), and emission (EM) ( $\lambda_{\text{ex}} = 448$  nm, blue line) spectra of the Y-CDs powder. c,d) PL emission spectra with different excitation wavelengths of as-prepared Y-CDs solution and powder, respectively. e,f) Fluorescence decay curve of as-prepared Y-CDs solution and powder.

presence of C—NH—C bonds and amide carbonyls, respectively, indicating that the piperazine successfully conjugated with carboxyl group of phthalic acid and was incorporated into carbon chain. To further clarify the formation and chemical structure of the Y-CDs, FT-IR spectra of the precursors (piperazine and trimellitic acid) were also measured and compared with that of the Y-CDs. Specifically, in the FT-IR spectra from piperazine and trimellitic acid to Y-CDs, the obvious decreases of absorption at  $1554\text{ cm}^{-1}$  (characteristic absorption peak of piperazine group) and  $1290\text{ cm}^{-1}$  (C—O stretching vibration) mean the loss of piperazine and carboxyl groups in the Y-CDs.<sup>[23b,25]</sup> The full XPS spectrum presented in Figure 2f exhibits three peaks at 285.09, 399.89, and 531.10 eV, indicating that the Y-CDs consisted of C, N, and O elements, and the atomic ratios were calculated as 70.26%, 11.77%, and 17.97%, respectively. In the high-resolution spectrum, the C 1s spectra was separated into three peaks at 284.41, 285.66, and 287.35 eV (Figure 2g), which are allocated to C—C/C=C, C—N/C—O, and C=O, respectively.<sup>[26]</sup> The N 1s spectra can be divided into two peaks at 399.40 and 401.07 eV (Figure 2h) due to pyridine-like N and pyrrole-like N, confirming the newly formed polyaromatic structures containing C=N.<sup>[27]</sup> The O 1s spectra (Figure 2i) exhibited two oxygen states of C=O at 530.64 eV and C—O at 532.24 eV.<sup>[28]</sup> Based on the above characterizations, the Y-CDs are composed of carbonized graphitic cores with surface functional groups.

The UV-vis absorption, PL excitation, and emission of the Y-CDs solution and powder were examined to assess their

optical properties. Figure 3a shows that the UV-vis absorption of the Y-CDs has two peaks at 215 and 280 nm, which are often ascribed to the  $\pi$ — $\pi^*$  transitions of C=C in the core of the Y-CDs and C=N bonds, respectively.<sup>[29]</sup> Significantly, a new absorption band of Y-CDs powders appears from 400 and 500 nm in the low energy region, while overlapping the PL excitation spectrum (Figure 3b). This absorption characteristic indicates that the solid surface structure contributed to capturing energy and producing strong yellow light emission.<sup>[30]</sup> Figure 3c represents the PL emission of the Y-CDs solution under different excitation wavelengths. As the excitation wavelength increases from 345 to 505 nm, the emission peak position gradually red shifts, while the optimal excitation and emission are near 448 and 560 nm, respectively. This indicates that the Y-CDs solution exhibits typical excitation wavelength-dependent luminescence behavior, which is probably due to the emissions originating from surface defects.<sup>[31]</sup> Interestingly, the Y-CDs powder (Figure 3d) exhibits weak excitation-wavelength-dependent PL behavior when the excitation wavelength changes from 345 to 505 nm; that is, the emission peak mainly appears at 537 nm. In addition, the PL spectra of the precursors (piperazine and trimellitic acid) were also measured. As shown in Figure S1 (Supporting Information), the solution and powder of the precursors all showed very weak emission and their emission peaks were in the ultraviolet region, which is different from carbon dots.

To further assess their optical properties, the PL quantum yield and the time-resolved PL spectra of the Y-CDs were

measured in both solid state and aqueous solution. The quantum yield of CDs in solid state is universally low due to ACQ, which will seriously limit their application in several fields. Nevertheless, the absolute quantum yield of the Y-CDs was measured to be as high as 58.35% (Figure S2, Supporting Information), which is very beneficial for application in the lighting fields. Additionally, considering that the mass ratio of the precursors may influence the quantum yield of CDs, another two CDs with the mass ratios (w/w, trimellitic acid: piperazine) of 2:3 and 3:2 were also synthesized and named as Y-CDs1 and Y-CDs2, respectively. The results revealed that the absolute quantum yield of Y-CDs1 and Y-CDs2 was measured to be 53.44% and 49.91%, respectively, while their PL spectra were similar to those of Y-CDs (Figures S3–S5, Supporting Information). Next, the absolute quantum yield of Y-CDs measured is merely 6.14% (Figure S6, Supporting Information) in aqueous solution (3.5 mg mL<sup>-1</sup>) and far below that in the solid state. This is a typical phenomenon of aggregation-induced enhancement emission. The time-resolved PL spectrum (Figure 3e,f) showed that the average lifetime of Y-CDs in aqueous solution and solid state was 1.89 and 5.23 ns, respectively, when excited by 448 nm. Then the  $K_r$  (radiative rate constants) and  $K_{nr}$  (non-radiative rate constants) of the Y-CDs powder, Y-CDs aqueous solution, Y-CDs1 powder, and Y-CDs2 powder were calculated according to the following equations:

$$K_r = QY/\tau \quad (1)$$

$$K_{nr} = (1 - QY)/\tau \quad (2)$$

The calculated values of the Y-CDs in aqueous solution and solid state are shown in **Table 1**, and of Y-CDs1 and Y-CDs2 powder in Table S2 (Supporting Information). Table 1 shows a slightly higher  $K_r$  and a significantly lower  $K_{nr}$  in the solid state. This is well in accordance with the AIE mechanism of RIM.<sup>[11b]</sup> And Table S2 (Supporting Information) revealed that the QY of the Y-CDs was the highest and  $K_{nr}$  was the lowest, while the QY of Y-CDs2 was the lowest and  $K_{nr}$  was the lowest. Therefore, we speculated that the aggregation could result in the suppression of surface groups motions and the obvious decrease of the non-radiative rate, so as to significantly increase the PL efficiency of the Y-CDs.

In the following, the fluorescence properties in water-ethanol mixtures were studied at the same concentration of 2 mg mL<sup>-1</sup>, because Y-CDs can be soluble in water, but insoluble in ethanol (**Figure 4a**). Figure 4b gives us an intuitive impression that the fluorescence emission intensity of the Y-CDs continues to increase with the gradual increase of the ethanol fraction ( $f_e$ ), indicating their typical AIE characteristics.<sup>[11b]</sup> And when the value of  $f_e$  reached 80%, the homogeneous solution

transformed into a turbid solution with suspension and the emission peaks were blue-shifted (**Figure 4c**). Furthermore, **Figure S7** (Supporting Information) shows us that very similar absorption bands were observed with the increase of  $f_e$ , which excluded the existence of  $\pi$ – $\pi$  interaction in the aggregation state.<sup>[32]</sup> Moreover, an absorption tail was observed in the long wavelength segment when  $f_e$  increased beyond 90%, caused by light scattering or a Mie effect caused by precipitation of nanoparticles.<sup>[33]</sup> The aggregation was further verified by the TEM imaging (**Figure 4d–f**). The large aggregates were formed by the Y-CDs monomers in the water-ethanol mixed solution, and the carbon lattice indicates that there are different carbon lattice planes in the Y-CDs aggregates, which means that the Y-CDs assemble with random orientation. Therefore, the Y-CDs' enhanced emission in water-ethanol mixtures is derived from their aggregation in poor solvents. A highly viscous medium can also cause RIM and the excited state relaxation is caused by enhanced fluorescence emission.<sup>[34]</sup> Adopting this strategy, the PL emission of the Y-CDs was measured in water-glycerin mixtures of various proportions. **Figure 4g** shows that the fluorescence intensity continuously increases with the increase of the glycerin content. Therefore, the RIM process is responsible for the AIE effect.<sup>[35]</sup> In addition, the concentration experiment also supports the AIE characteristic of Y-CDs, since much enhanced absorption intensity and emission intensity can be observed at higher concentrations (**Figure 4h,i**).<sup>[36]</sup> And the PL intensity increased when the temperature was decreased from 27 to 0 °C (**Figure S8**, Supporting Information). Thus, the cooling could also retard the movement of piperazine groups on the surface of the Y-CDs, so as to reduce the non-radiative rate and increase the PL intensity of the Y-CDs.<sup>[37]</sup>

In addition, we designed two experiments to verify the relationship between the structure and fluorescence mechanism of the Y-CDs. In the first experiment, using citric acid and phthalic acid instead of trimellitic acid, carbon dots with yellow emission (C-CDs) and carbon dots with green yellow emission (P-CDs) were synthesized (**Figure S9**, Supporting Information), respectively. As shown in **Figure S10** (Supporting Information), the powders of C-CDs and P-CDs both exhibit weak excitation-wavelength-dependent PL behavior and their emission intensity was stronger than those of the solution. These phenomena were similar to those observed for Y-CDs powder. Besides, C-CDs and P-CDs can be soluble in water, but insoluble in tetrahydrofuran (THF). Hence, water was used as a good solvent and THF was used as a poor solvent. H<sub>2</sub>O/THF as the solvent system was chosen to explore the AIE properties of C-CDs and P-CDs. **Figure S11a,b** (Supporting Information) showed that with the gradual increase of the percentage of THF, enhancement of the fluorescent emission intensities was observed for the C-CDs and P-CDs, which were consistent with the AIE behaviors. An FT-IR spectrum was carried out to characterize the surface groups of the CDs, and **Figure S11c** (Supporting Information) shows that the C-CDs and P-CDs had alicyclic bonds and C–NH–C bonds like Y-CDs. This can confirm the relationship between piperazine and the AIE behavior. Meanwhile, comparing the optimal excitation and emission of C-CDs, P-CDs, and Y-CDs under the same test condition, it is found that the emission intensity of Y-CDs is the greatest (**Figure S11d**, Supporting Information).

**Table 1.** QY,  $\tau$ ,  $K_r$ , and  $K_{nr}$  of Y-CDs solution and powder excited by 448 nm.

	QY	$\tau$ [ns]	$K_r$ [ns <sup>-1</sup> ]	$K_{nr}$ [ns <sup>-1</sup> ]
Y-CDs solution	6.14%	1.812	0.0339	0.5180
Y-CDs powder	58.35%	5.188	0.1125	0.0803



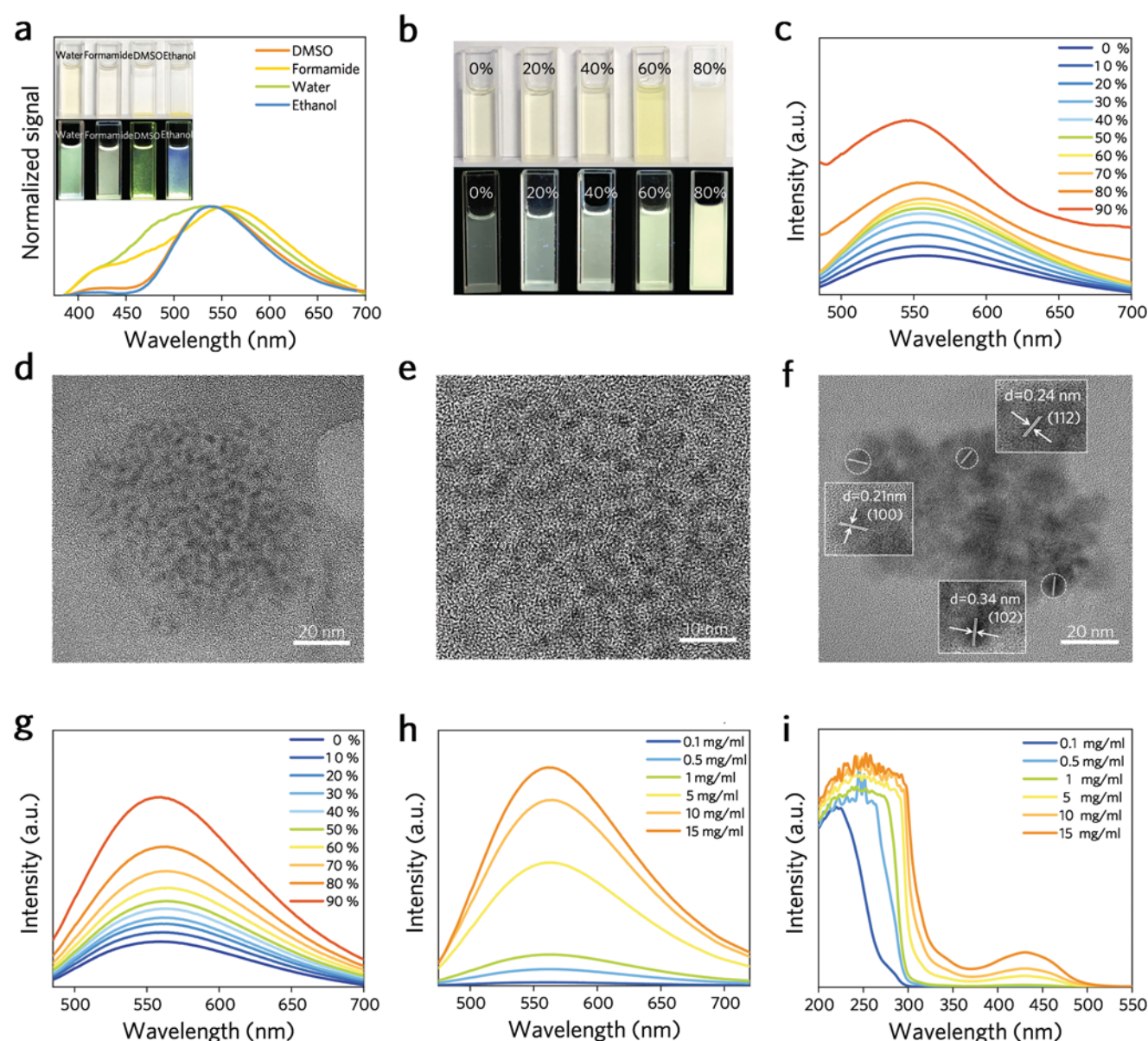


**Figure 4.** a) PL emission spectrum of the Y-CDs powder dissolved in different solvents under 365 nm excitation (insets: photographs of the Y-CDs powder dissolved in solvents with different polarities (from high to low) under sunlight (top) and 365 nm ultraviolet radiation (bottom)). b) Photographs of the as-prepared Y-CDs solution with varying volume ratios of ethanol (from 0 to 80%) under sunlight (top) and 365 nm ultraviolet radiation (bottom). c) PL emission spectra of the as-prepared Y-CDs solution with varying ratios of ethanol (Ex = 448 nm). d–f) High-resolution TEM (HR-TEM) image of the Y-CDs aggregates in the ethanol solution. g) PL emission spectra of the as-prepared Y-CDs solution with varying ratios of glycerol (Ex = 448 nm). h) PL emission spectra of the Y-CDs powder dissolved in aqueous solvents at various concentrations from 0.1 to 15 mg mL<sup>−1</sup> (Ex = 448 nm). i) UV–vis absorption spectra of the Y-CDs powder dissolved in aqueous solvents at various concentrations from 0.1 to 15 mg mL<sup>−1</sup>.

We designed a second experiment that replaced piperazine with diethylenetriamine to remove the effect of the alicyclic bonds, and the produced CDs were named G-CDs. The prepared G-CDs solution shows different blue emission from the Y-CDs, and the powder emission enhancement is not as strong as Y-CDs (Figure S12, Supporting Information). G-CDs can be soluble in water but insoluble in THF. The emission properties of G-CDs in mixed water/THF solvent were performed to discuss the relationship between aggregation and emission intensity. Figure S13 (Supporting Information) shows that the

fluorescence intensity of the G-CDs increased gradually and then decreased with the increasing percentage of THF in the solvent mixture. When the percentage of THF reached 60%, aggregation took place in the component solvent and the emission intensity started to be lower than that of 0%. However, the fluorescence emission intensity of Y-CDs continues to increase with the gradual increase of the poor solvent fraction. This indicates that the G-CDs do not have AIE characteristics. According to the FT-IR spectrum of the G-CDs and Y-CDs (Figure S14, Supporting Information), the chemical structure of the G-CDs



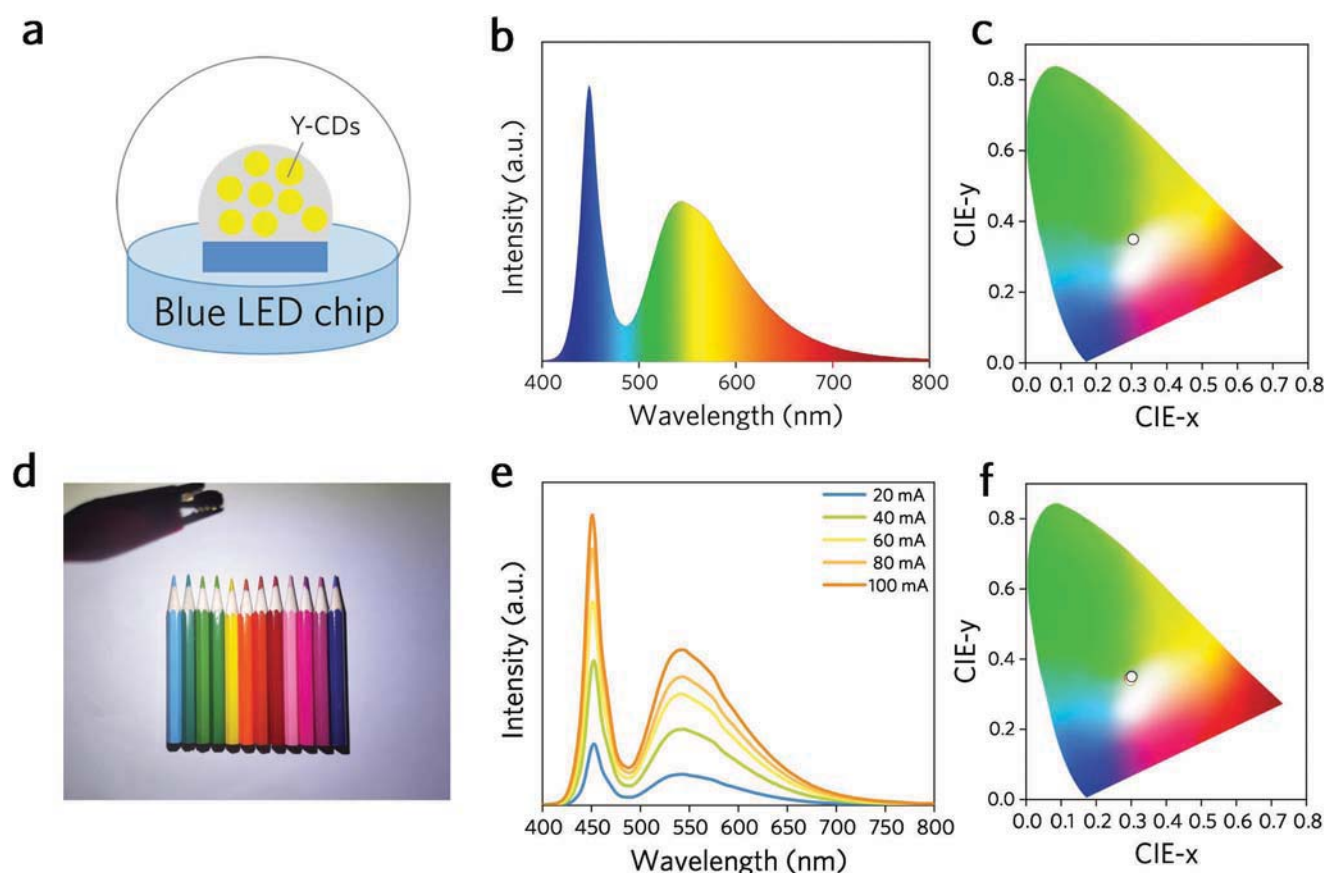


**Figure 5.** a) Schematic diagram of WLED. b) Emission spectrum of working WLED as shown in (d). c) The WLED's CIE color coordinate of (0.31, 0.35). d) Image of working WLED fabricated with Y-CDs and blue-emission chip. e,f) EL spectra and CIE color coordinates of WLED lamp under different drive currents from 20 to 100 mA, respectively.

is similar to that of the Y-CDs, except for the alicyclic bonds. Therefore, the relationship between piperazine and the AIE behavior of Y-CDs can be further affirmed.

Currently, the common assembly method of WLEDs for lighting is a combination of a blue-LED chip and YAG yellow phosphors, which are rare-earth-based fluorescent materials that are expensive and non-renewable. Y-CDs are also conducive to the construction of a single-component WLED with a blue InGaN LED chip, due to their advantages of solid-state yellow emission close to YAG phosphor and high PLQY. Meanwhile, the preparation of Y-CDs is low-cost and uses eco-friendly materials. Figure S15 (Supporting Information) also shows that Y-CDs have favorable optical stability and thermal stability. Next, to fabricate the WLED, potting adhesive and Y-CDs powder were mixed to form a uniform gel, and deposited on a commercial 450 nm InGaN LED whose emission is very close to the best excitation wavelength of Y-CDs powder (Figure 5a). As shown in Figure 5b, the electroluminescence (EL) spectrum of the obtained WLED displays two emission bands centered individually at 450 and 540 nm, which are attributed to the blue chip and Y-CDs powder, respectively. Meanwhile, its color coordinates are (0.31, 0.35), closer to sunlight (0.33, 0.33) (Figure 5c), which can be further proved by the image of the working WLED (Figure 5d). Other relevant parameters of the WLED were also measured (Table S3, Supporting Information). With increase of

the drive current from 20 to 100 mA (Figure 5e), the EL spectral intensities gradually enhance while the characteristic peaks are nearly unchanged. Moreover, the CRI and CIE color coordinate showed just slight changes (Figure 5f; Figure S16, Supporting Information), respectively. These results demonstrate that the obtained WLED exhibits reasonable stability. Therefore, together with the stability, low-cost preparation and high emission efficiency advantages of Y-CDs, they have potential applications in solid state displays and lighting.

Considering that Y-CDs are weakly emissive in water and strongly yellow emissive in ethanol, this prompts us to explore their potential applications in anti-counterfeiting and encryption as two-switch-mode ink. Treated by the as-prepared Y-CDs solution (Figure 6a), the filter papers are almost primrose yellow under white light and exhibit strong yellow-green fluorescence under 365 nm UV excitation. With the addition of water, the fluorescence turns to very weak yellow under 365 nm UV excitation. By adding ethanol, it shows the same optical characteristics as the contrast. Furthermore, the addition of water can turn on the weak yellow emission again. For information encryption and decryption applications of Y-CDs, riboflavin is used as interference. Both aqueous riboflavin and ethanol solution can show bright yellow-green fluorescence under 365 nm UV excitation, but the Y-CDs aqueous solution shows weak yellow emission. In Figure 6b, "S", "C", "A", and "U" are

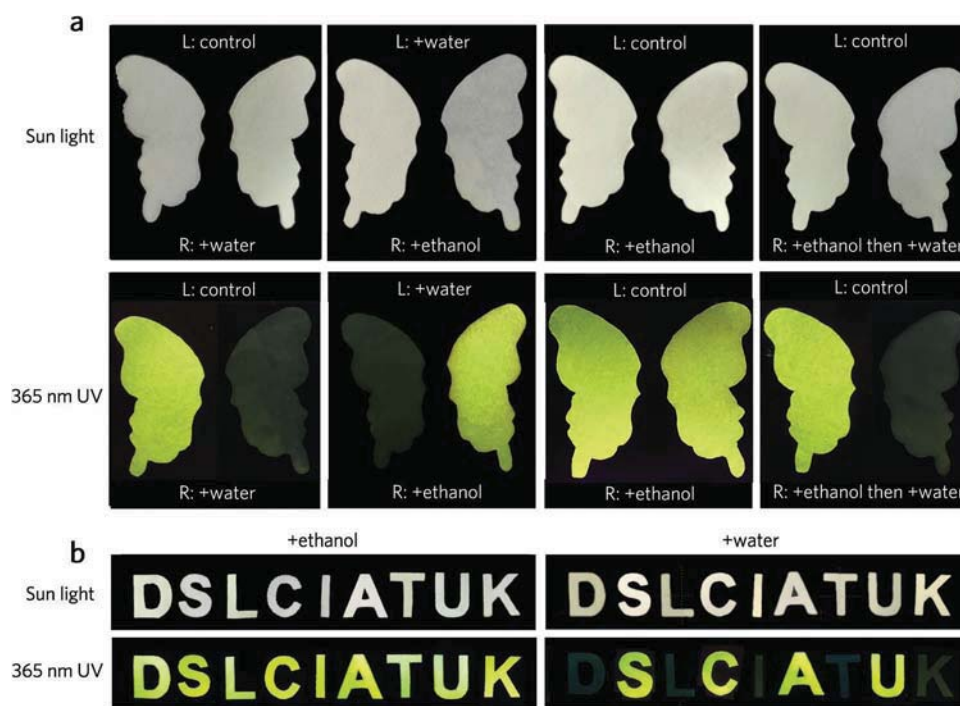


**Figure 6.** a) Photographs of filter papers with different treatment under variable irradiation. b) Information encryption application based on Y-CDs and riboflavin.

treated by riboflavin, while “I”, “K”, “D”, “L”, and “T” are treated by Y-CDs. Under the UV lamp, the wrong information “SICK ADULT” will be displayed with the ethanol treatment. The correct message “SCAU” appears only with water treatment.

AIE materials have important application value in the field of biological imaging, but most of the reported AIE-gens are soluble only in organic solvents, making them unsuitable for biological systems. Although a variety of AIE-based water-soluble nanoparticles have been developed, there are still some defects. For example, the low bond energy of non-covalent interaction might lead to the collapse of structures before reaching their destination. Therefore, based on the remarkable biocompatibility of CDs and the hydrophilicity of Y-CDs, we preliminarily studied the imaging behavior of Y-CDs in cells and legumes. First, the cell imaging behavior of HeLa cells incubated with Y-CDs was studied by Confocal Laser Scanning Microscopy (CLSM) under 458 nm excitation. As shown in Figure 7a, the yellow fluorescence signal area was mainly concentrated in the cytoplasm, but there is almost no signal in the nucleus. This phenomenon revealed that the HeLa cells absorbed Y-CDs mainly through endocytosis.<sup>[38]</sup> It is worth noting that relatively bright fluorescent signal points could be observed. It was speculated that the Y-CDs possibly aggregated in the cell membranes and lipid droplets. This is because in cells, the core of lipid droplets is composed of neutral fats, mainly including triglycerides and cholesterol esters, and there is a single layer of phospholipid molecules and various proteins wrapped around the core. However, compared with the traditional molecular rotor, AIE dyes contain more rotatable parts, which makes them more sensitive to a viscous environment. Meanwhile, our previous observation showed that the fluorescence intensity of the Y-CDs increased with the increase of solvent viscosity

(Figure 4g). This result indicated that Y-CDs could be used as excellent fluorescence dyes in biological imaging applications.

Next, mung bean was chosen as a model system to observe whether Y-CDs could be absorbed by plants and the imaging behavior of Y-CDs in bean sprouts. The mung bean seeds were grown in deionized water as the control group and in Y-CDs solution as experimental groups. After cultivation at room temperature for four days, the bean sprouts were harvested. As shown in Figure 7b, the stem of the group treated with Y-CDs are slightly longer than the control group. This is consistent with previous reports that carbon dots can promote the growth of bean sprouts.<sup>[39]</sup> There are many hydrophilic groups on the surface of the Y-CDs, so we speculated that it can promote the absorption of water and nutrients, thereby promoting the germination and growth of seeds.<sup>[40]</sup> In addition, Figure 7c shows that there is obvious yellow luminescence in the leaf, indicating the successful uptake of Y-CDs in the bean sprouts. Then, various parts of Y-CDs in the bean sprouts were studied by laser-scanning confocal fluorescence microscopy. It was found that the fluorescence signals of the Y-CDs exist in the longitudinal section of stems and cross-section of leaves (Figure 7d), which further verified that Y-CDs could be absorbed by bean sprouts. Meanwhile, most of the luminescence signals appear in the vascular system, which indicates that the transmission of Y-CDs occurs with the uptake of water.<sup>[40a]</sup> It is worth noting that relatively bright fluorescence signal points can also be observed, suggesting that Y-CDs aggregate in the inherently high lipophilic environment of bean sprouts and exhibit the AIE phenomenon. The results of the two preliminary experiments show that Y-CDs have potential application significance in biological imaging. And we will research the biological imaging capabilities of Y-CDs further.

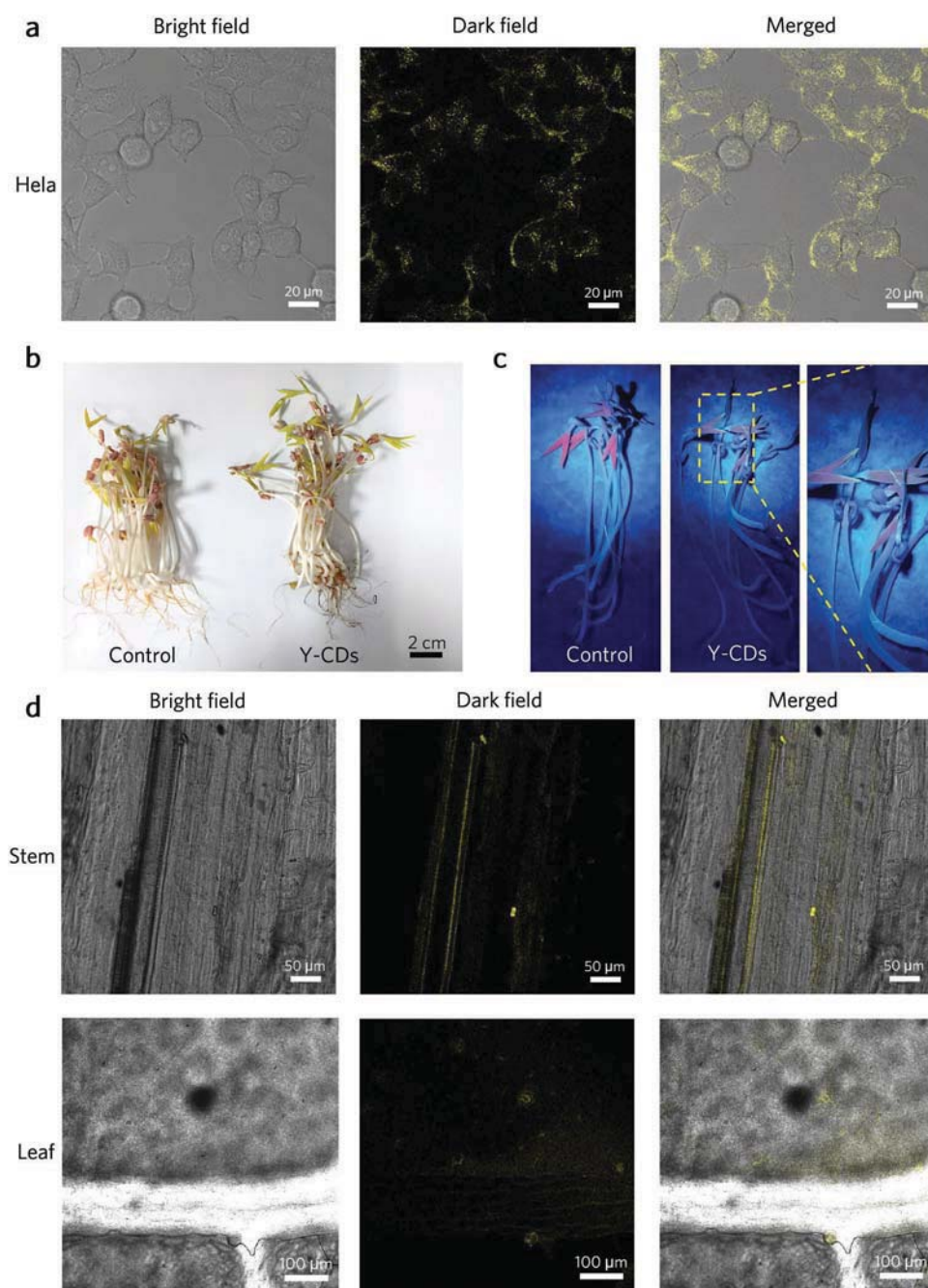


**Figure 7.** a) The bright field, dark field, and merged confocal images of HeLa cells incubated with Y-CDs solutions. b) Photographs of mung bean sprouts under daylight, including control (left), and Y-CDs-treated (right) sample. c) Photographs of mung bean sprouts under ultraviolet (365 nm) irradiation, including control (left), and Y-CDs-treated (right) sample. d) The bright field, dark field, and merged confocal images of longitudinal sections from stems and leaf cross-sections of mung bean sprouts incubated with Y-CDs solution.

### 3. Conclusion

In summary, we have synthesized high-efficiency hydrophilic yellow emissive Y-CDs with AIE characteristics, by one-pot microwave heating of trimellitic acid and piperazine. Through several characterization methods, it is concluded that Y-CDs mainly consist of graphite carbide cores and surface functional groups. In aqueous solutions, Y-CDs show weak yellow emission (PLQY = 6.14%), but significantly enhanced

(PLQY = 58.35%) in the solid state, like most reported AIE-gens. By calculating and comparing  $K_r$  and  $K_{nr}$  of the aqueous solution and powder, it is found that the  $K_{nr}$  is obviously lower in the solid state. This indicated that the aggregation of Y-CDs could lead to the suppression of surface groups motions and the reduction of the non-radiative rate, so as to obviously increase the PL efficiency of the Y-CDs powder. Moreover, the control experiments suggested that the AIE phenomenon of



Y-CDs was derived from the suppression of surface piperazine groups motions and decrease of the non-radiative rate. Based on the unique optical properties of Y-CDs, their applications in WLEDs, anti-counterfeiting, encryption, and bioimaging have been demonstrated. We hope that this work will not only provide a new way to prepare high-efficiency hydrophilic CDs with the AIE characteristic, but also promote the further development of CDs in practical applications.

## 4. Experimental Section

**Materials:** Piperazine, trimellitic acid, diethylenetriamine, citric acid, phthalic acid, and ethanol were purchased from Aladdin Chemicals Co., Ltd (Shanghai, China). Formamide, dimethyl sulfoxide (DMSO), and tetrahydrofuran (THF) were purchased from Shanghai Titan Technology Co., Ltd. with analytical reagent grade. The commercially available InGaN-LED chips with the emission wavelength centered at 450 nm were purchased from Shenzhen Looking Long Technology Co., Ltd. Potting adhesive was obtained from Shenzhen Huiruide Technology Co., Ltd. Dulbecco's modified Eagle's medium (DMEM), phosphate buffered saline (PBS) (pH = 7.4), fetal bovine serum (FBS), and trypsin solutions were acquired from Thermo Fisher. All reagents were used directly without further purification. Deionized (DI) water was used in the whole research.

**Synthesis of Y-CDs, Y-CDs1, and Y-CDs2:** With the assistance of ultrasonic treatment for a few minutes, trimellitic acid (1 g) and piperazine with three mass ratios (w/w = 3:2, 1:1, and 2:3) were dissolved in 10 mL deionized water in a 100 mL beaker. Then the beaker was placed in the center of the rotating plate of a household microwave oven (700 W) and heated steadily for 5 min. After cooling to room temperature, the crude product was dissolved in deionized water, which was filtered through 0.22  $\mu$ m pore sized membrane filters and then dialyzed with deionized water in a dialysis bag (500 Da) for purification. After the resulting yellow solution was freeze-dried, yellow powder of CDs was synthesized and named as Y-CDs1, Y-CDs, and Y-CDs2, respectively.

**Synthesis of C-CDs and P-CDs:** Piperazine (1 g), 1 g of citric acid, and 10 mL of deionized water were added into a 100 mL beaker, and ultrasonic treatment was carried out until they were dissolved. Then the beaker was put in the center of the rotating plate of the domestic microwave oven (700 W) and heated for 5 min. The crude product was cooled to room temperature and dissolved in deionized water. Then it was filtered by 0.22  $\mu$ m pore size membrane filters, and dialyzed by deionized water in a 500 Da dialysis bag. The light brown solution obtained was freeze-dried, and finally the powder of C-CDs was obtained. The preparation method of P-CDs was similar, that was, 1 g citric acid was replaced by 1 g phthalic acid.

**Synthesis of G-CDs:** Diethylenetriamine (1.5 g) and 1 g trimellitic acid were dissolved in 10 mL deionized water in the 100 mL beaker with the assistance of ultrasonic treatment for a few minutes. Then the beaker was placed in the center of the rotating plate of the domestic microwave oven (700 W) and heated steadily for 5 min. After cooling to room temperature, the crude product was dissolved in deionized water, which was filtered through 0.22  $\mu$ m pore sized membrane filtration and then dialyzed with deionized water in a dialysis bag (500 Da) for purification. The resulting yellow solution was freeze-dried, and finally a brown powder of G-CDs was obtained.

**Fabrication of White-Light-Emitting Diodes (WLEDs):** InGaN LED chips were purchased from Shenzhen Looking Long Technology Co., Ltd. The chips emitting 450 nm light with a working voltage of 3.0 V and a maximum driving power of 1 W were the excitation light source of the LED lamp. Y-CDs were mixed in potting adhesive, and the mixture was fully stirred until uniform. The mixed colloid was dropped onto the chip through distribution and then dried naturally for several hours. Finally, the lid of the WLED lamp bead was covered.

**Plant Growth:** Mung bean seeds with similar sizes were selected (30 seeds for each group) and arranged in culture dishes. Deionized water and Y-CDs solution (1 mg mL<sup>-1</sup>) were added into the above culture dishes, respectively, and cultured at room temperature for four days

without light. Deionized water for the control group and the Y-CDs solution for the experimental groups were renewed every day.

**Laser-Scanning Confocal Fluorescence Microscope Imaging:** HeLa cells were seeded on a confocal dish ( $\Phi$ : 20 mm, Biosharp brand). After culturing for 12 h, Y-CDs solution (20  $\mu$ g mL<sup>-1</sup>) was added to the cell culture system and incubated for 6 h. After washing with PBS solution three times, the cells were measured directly by laser-scanning confocal fluorescence microscopy ( $\lambda_{\text{ex}}$  = 458 nm, emission was collected at 484–628 nm). The mung beans were taken out and washed thoroughly with water. Then stem and leaf sections were cut to be analyzed by laser-scanning confocal fluorescence microscopy ( $\lambda_{\text{ex}}$  = 470 nm, emission was collected at 484–653 nm).

**Characterization:** The HR-TEM images were recorded using a JEOL-2010 electron microscope. The XRD pattern was collected using a XD-2X/M4600. Raman spectra were obtained by Renishaw through a micro spectrometer, and the excitation wavelength was 785 nm laser. FT-IR spectra were taken on a Nicolet Avatar 360 FT-IR spectrophotometer. X-ray photoelectron spectroscopy (XPS) was performed on a Kratos AXIS Ultra DLD X-ray photoelectron spectrometer with a monochromatic Al K $\alpha$  X-ray source. UV-vis absorption and transmittance spectra were carried out using a Hitachi UV-3900 spectrometer. The FL-7000 Hitachi fluorescence spectrofluorometer was used to record the PL spectra. The absolute PLQY and the PL decay curves were measured by FLS1000. The electroluminescence (EL) spectra were collected by an integrating sphere (Labsphere) equipped with an Ocean optics spectrograph under a working direct current. Confocal laser scanning microscopy (CLSM) characterizations were done using a confocal laser scanning biological microscope (TCS SP8 STED 3X, LEICA).

**Statistical Analysis:** The absorption and luminescence spectra presented in this work were all normalized at the position of the first excitonic peaks. The statistics of the carbon dots' sizes were based on sample sizes of at least 100 particles. All graphs and data analysis were performed using Advantage, Adobe Photoshop 2022, Excel 2016, Nano Measure, and OriginPro 2021 software.

## Supporting Information

Supporting Information is available from the Wiley Online Library or from the author.

## Acknowledgements

The present work was supported by the National Natural Science Foundations of China (12174119) and the Natural Science Foundation of Guangdong Province (2020A1515010443).

## Conflict of Interest

The authors declare no conflict of interest.

## Data Availability Statement

The data that support the findings of this study are available from the corresponding author upon reasonable request.

## Keywords

aggregation-induced emissions, anti-counterfeiting, bioimaging, carbon dots, solid state fluorescence

Received: June 27, 2022  
Revised: December 9, 2022  
Published online:



- [1] X. Zhang, Q. Zeng, Y. Xiong, T. Ji, C. Wang, X. Shen, M. Lu, H. Wang, S. Wen, Y. Zhang, X. Yang, X. Ge, W. Zhang, A. P. Litvin, A. V. Baranov, D. Yao, H. Zhang, B. Yang, A. L. Rogach, W. Zheng, *Adv. Funct. Mater.* **2020**, 30, 265.
- [2] J. Zhang, S.-H. Yu, *Mater. Today* **2016**, 19, 382.
- [3] B. Zhi, Y. Cui, S. Wang, B. P. Frank, D. N. Williams, R. P. Brown, E. S. Melby, R. J. Hamers, Z. Rosenzweig, D. H. Fairbrother, G. Orr, C. L. Haynes, *ACS Nano* **2018**, 12, 5741.
- [4] Z. Wang, Y. Liu, S. Zhen, X. Li, W. Zhang, X. Sun, B. Xu, X. Wang, Z. Gao, X. Meng, *Adv. Sci.* **2020**, 7, 1902688.
- [5] X. Zhang, H. Yang, Z. Wan, T. Su, X. Zhang, J. Zhuang, B. Lei, Y. Liu, C. Hu, *Adv. Opt. Mater.* **2020**, 8, 2000251.
- [6] Y. Chen, M. Zheng, Y. Xiao, H. Dong, H. Zhang, J. Zhuang, H. Hu, B. Lei, Y. Liu, *Adv. Mater.* **2016**, 28, 312.
- [7] D. Zhou, D. Li, P. Jing, Y. Zhai, D. Shen, S. Qu, A. L. Rogach, *Chem. Mater.* **2017**, 29, 1779.
- [8] S. Javanbakht, H. Namazi, *Carbohydr. Polym.* **2017**, 176, 220.
- [9] M. Park, H. Yoon, J. Lee, J. Kim, J. Lee, S. E. Lee, S. Yoo, S. Jeon, *Adv. Mater.* **2018**, 30, 1802951.
- [10] J. Luo, Z. Xie, J. W. Lam, L. Cheng, H. Chen, C. Qiu, H. S. Kwok, X. Zhan, Y. Liu, D. Zhu, B. Z. Tang, *Chem. Commun.* **2001**, 1740.
- [11] a) Y. Chen, J. W. Y. Lam, R. T. K. Kwok, B. Liu, B. Z. Tang, *Mater. Horiz.* **2019**, 6, 428; b) Y. Wang, J. Nie, W. Fang, L. Yang, Q. Hu, Z. Wang, J. Z. Sun, B. Z. Tang, *Chem. Rev.* **2020**, 120, 4534.
- [12] D. Ma, *Top. Curr. Chem.* **2021**, 379, 16.
- [13] J. Wu, W. Liu, J. Ge, H. Zhang, P. Wang, *Chem. Soc. Rev.* **2011**, 40, 3483.
- [14] R. T. Kwok, C. W. Leung, J. W. Lam, B. Z. Tang, *Chem. Soc. Rev.* **2015**, 44, 4228.
- [15] S. Xu, Y. Duan, B. Liu, *Adv. Mater.* **2020**, 32, 1903530.
- [16] A. Qin, J. W. Y. Lam, B. Z. Tang, *Prog. Polym. Sci.* **2012**, 37, 182.
- [17] Z. Xie, P. Sun, Z. Wang, H. Li, L. Yu, D. Sun, M. Chen, Y. Bi, X. Xin, J. Hao, *Angew. Chem., Int. Ed.* **2020**, 59, 9922.
- [18] H. Yang, Y. Liu, Z. Guo, B. Lei, J. Zhuang, X. Zhang, Z. Liu, C. Hu, *Nat. Commun.* **2019**, 10, 1789.
- [19] X. Xu, L. Mo, Y. Li, X. Pan, G. Hu, B. Lei, X. Zhang, M. Zheng, J. Zhuang, Y. Liu, C. Hu, *Adv. Mater.* **2021**, 33, 2104872.
- [20] Z. X. Liu, Z. L. Wu, M. X. Gao, H. Liu, C. Z. Huang, *Chem. Commun.* **2016**, 52, 2063.
- [21] a) L. Mo, X. Xu, Z. Liu, H. Liu, B. Lei, J. Zhuang, Z. Guo, Y. Liu, C. Hu, *Chem. Eng. J.* **2021**, 426, 130728; b) Y. Zheng, H. Wei, P. Liang, X. Xu, X. Zhang, H. Li, C. Zhang, C. Hu, X. Zhang, B. Lei, W. Y. Wong, Y. Liu, J. Zhuang, *Angew. Chem., Int. Ed. Engl.* **2021**, 60, 22253.
- [22] R. Liu, D. Wu, S. Liu, K. Koynov, W. Knoll, Q. Li, *Angew. Chem., Int. Ed.* **2009**, 48, 4598.
- [23] a) Z. Wang, F. Yuan, X. Li, Y. Li, H. Zhong, L. Fan, S. Yang, *Adv. Mater.* **2017**, 29, 1702910; b) X. Miao, D. Qu, D. Yang, B. Nie, Y. Zhao, H. Fan, Z. Sun, *Adv. Mater.* **2018**, 30, 1704740.
- [24] a) J. Yu, N. Song, Y.-K. Zhang, S.-X. Zhong, A.-J. Wang, J. Chen, *Sens. Actuators, B* **2015**, 214, 29; b) J. Feng, Y. Chen, Y. Han, J. Liu, C. Ren, X. Chen, *Anal. Chim. Acta* **2016**, 926, 107.
- [25] S. Qu, D. Zhou, D. Li, W. Ji, P. Jing, D. Han, L. Liu, H. Zeng, D. Shen, *Adv. Mater.* **2016**, 28, 3516.
- [26] a) Q. Fang, Y. Guan, M. Wang, L. Hou, X. Jiang, J. Long, Y. Chi, F. Fu, Y. Dong, *New J. Chem.* **2018**, 42, 8591; b) J. Liu, N. Wang, Y. Yu, Y. Yan, H. Zhang, J. Li, J. Yu, *Sci. Adv.* **2017**, 3, e1603171.
- [27] a) J. Chen, J.-S. Wei, P. Zhang, X.-Q. Niu, W. Zhao, Z.-Y. Zhu, H. Ding, H.-M. Xiong, *ACS Appl. Mater. Interfaces* **2017**, 9, 18429; b) Y. Dong, H. Pang, H. B. Yang, C. Guo, J. Shao, Y. Chi, C. M. Li, T. Yu, *Angew. Chem., Int. Ed.* **2013**, 52, 7800.
- [28] a) M. Wu, J. Zhan, B. Geng, P. He, K. Wu, L. Wang, G. Xu, Z. Li, L. Yin, D. Pan, *Nanoscale* **2017**, 9, 13195; b) Y. Li, W. Ho, K. Lv, B. Zhu, S. C. Lee, *Appl. Surf. Sci.* **2018**, 430, 380.
- [29] Z. Han, K. Wang, F. Du, Z. Yin, Z. Xie, S. Zhou, *J. Mater. Chem. C* **2018**, 6, 9631.
- [30] Y. Liu, M. Zhang, Y. Wu, R. Zhang, Y. Cao, X. Xu, X. Chen, L. Cai, Q. Xu, *Chem. Commun.* **2019**, 55, 12164.
- [31] E. Liu, D. Li, X. Zhou, G. Zhou, H. Xiao, D. Zhou, P. Tian, R. Guo, S. Qu, *ACS Sustainable Chem. Eng.* **2019**, 7, 9301.
- [32] X.-Q. Wang, W. Wang, W.-J. Li, Y. Qin, G.-Q. Yin, W.-L. Jiang, X. Li, S. Wu, H.-B. Yang, *Org. Chem. Front.* **2019**, 6, 1686.
- [33] W. Ji, L. Li, W. Song, X. Wang, B. Zhao, Y. Ozaki, *Angew. Chem., Int. Ed.* **2019**, 58, 14452.
- [34] S. Lin, M. Chen, Z. Wang, Y. Zhang, R. Yuan, X. Liang, W. Xiang, Y. Zhou, *Chem. Eng. J.* **2017**, 324, 194.
- [35] C. Yu, Z. Huang, W. Gu, Q. Wu, E. Hao, Y. Xiao, L. Jiao, W.-Y. Wong, *Mater. Chem. Front.* **2019**, 3, 1823.
- [36] X. M. Cai, Y. Lin, Y. Li, X. Chen, Z. Wang, X. Zhao, S. Huang, Z. Zhao, B. Z. Tang, *Nat. Commun.* **2021**, 12, 1773.
- [37] J. Chen, C. C. W. Law, J. W. Y. Lam, Y. Dong, S. M. F. Lo, I. D. Williams, D. Zhu, B. Z. Tang, *Chem. Mater.* **2003**, 15, 1535.
- [38] Z. Huang, X. Zhang, X. Zhang, C. Fu, K. Wang, J. Yuan, L. Tao, Y. Wei, *Polym. Chem.* **2015**, 6, 607.
- [39] A. Wang, F. Kang, Z. Wang, Q. Shao, Z. Li, G. Zhu, J. Lu, Y. Y. Li, *Adv. Sustainable Syst.* **2019**, 3, 1800132.
- [40] a) H. Wang, M. Zhang, Y. Song, H. Li, H. Huang, M. Shao, Y. Liu, Z. Kang, *Carbon* **2018**, 136, 94; b) E. Kou, Y. Yao, X. Yang, S. Song, W. Li, Y. Kang, S. Qu, R. Dong, X. Pan, D. Li, H. Zhang, B. Lei, *ACS Sustainable Chem. Eng.* **2021**, 9, 944.



Contents lists available at ScienceDirect

Chemical Engineering Journal

journal homepage: [www.elsevier.com/locate/cej](http://www.elsevier.com/locate/cej)

# Calcination temperature tuning of RTP and TADF with wide range of emission color from carbon dots confined in $\text{Al}_2\text{O}_3$

Jinkun Liu, Yimeng Luo, Zhun Ran, Fenglin Wang, Minhua Sun, Yangyang Luo, Jianle Zhuang, Xuejie Zhang, Bingfu Lei, Yingliang Liu, Chaofan Hu<sup>\*</sup>

Key Laboratory for Biobased Materials and Energy of Ministry of Education/Guangdong Provincial Engineering Technology Research Center for Optical Agriculture, College of Materials and Energy, South China Agricultural University, Guangzhou 510642, PR China

## ARTICLE INFO

### Keywords:

Carbon dots  
Phosphorescence  
Thermally activated delayed fluorescence  
Energy transfer

## ABSTRACT

The room temperature afterglow (RTA) of carbon dots (CDs) and their wide-ranging application prospects have attracted significant attention. However, most of the synthesis and regulation methods for multicolor CDs-based RTA materials are complex. Therefore, it is still a challenge to obtain a series of CDs-based RTA materials with broad and tunable emission wavelengths via a simple preparation method using the same organic precursor and matrix. In this study, a series of CDs@ $\text{Al}_2\text{O}_3$  materials with ultra-broad afterglow emission range (376 ~ 619 nm) were prepared by regulating the reaction temperature through a one-step calcination method. High-temperature consumption led to a decrease of surface functional groups and conjugation size of CDs, resulting in the gradually blue-shifted emission from red to UV region. We also discovered a unique phenomenon where the afterglow emission mode of the material shifted from room temperature phosphorescence (RTP) to thermally activated delayed fluorescence (TADF) as the temperature increased, attributed to the stabilization of the excited triplet state from the strengthened crystallinity of  $\text{Al}_2\text{O}_3$  matrix. Furthermore, a continuous emission at ~ 471 nm attributed to the oxygen defects of the matrix was observed. Multiple anti-counterfeiting, information encryption, and fingerprint detection are demonstrated based on the unique RTA properties of CDs@ $\text{Al}_2\text{O}_3$ .

## 1. Introduction

Room temperature afterglow (RTA), including room temperature phosphorescence (RTP) and thermally activated delayed fluorescence (TADF), has irreplaceable advantages in biological, optoelectronic, and energy-related fields with long-lived excitons from the dimension of time [1–7]. Inorganic phosphors synthesized with expensive and cytotoxic rare-earth elements under harsh synthetic conditions, and organic phosphorescent materials with complicated synthetic processes and instability, these two typical afterglow materials restrict their further practical applications with inherent drawbacks [8,9]. While carbon dots (CDs) have attracted increasing attention in recent years as a new type of emerging nanomaterials with low environmental toxicity, wide range of raw material sources, high photostability, and low preparation costs [10–12]. Based on the superior afterglow properties, CDs-based RTA materials are fascinating in information encryption, anti-counterfeiting, medical diagnostics, bioimaging, optoelectronic devices and other fields closely related to people's daily lives [13–19].

In order to promote the occurrence of RTP or TADF, sufficient intersystem crossing (ISC) processes and efficient radiation transitions are required [20–22]. On one hand, promoting intramolecular  $n-\pi^*$  configuration can enhance the spin-orbit coupling (SOC) between the singlet and triplet states, thereby promoting ISC processes [14,23]. Introducing elements containing lone pair electrons, such as N [24], O [25], P [26], F [27], etc., is a corresponding solution typically used. On the other hand, stabilizing lowest excited triplet state ( $T_1$ ) and reducing the non-radiative decay and quenching processes by embedding CDs into various matrixes (such as PVA [15], urea [28], cyanuric acid [29],  $\text{SiO}_2$  [30], zeolite [31],  $\text{B}_2\text{O}_3$  [32], etc.) or introducing polymer chains onto the surface of CDs to restrict molecular rotation [33]. To date, the achievable emission of CDs-based RTA materials have been gradually explored from common blue and green to orange and red, even full spectrum in several systems [32,34–43]. However, most of these materials still require specific combinations of CDs and matrix which involves multiple precursors and preparation steps to achieve particular effects. Recently, several strategies have been proposed to achieve multi-color

<sup>\*</sup> Corresponding author.

E-mail address: [thucf@scau.edu.cn](mailto:thucf@scau.edu.cn) (C. Hu).

<https://doi.org/10.1016/j.cej.2023.145597>

Received 1 July 2023; Received in revised form 5 August 2023; Accepted 21 August 2023

Available online 23 August 2023

1385-8947/© 2023 Published by Elsevier B.V.

afterglow in a single system. For example, Yang and co-workers changed the carbonization degree to regulate the RTP emission wavelengths of CDs from 485 to 558 nm [44]. Meng et al. present a strategy of amorphous – crystalline phase transition driven by thermally to achieve the RTP color tunable from green to orange-red [45]. Qiu et al. fabricated CDs composites by pyrolysis of citric acid and boric acid, the phosphorescence from blue to red ascribed to the increase particle size and oxidation degree of CDs [13]. Qu and co-workers realized RTP color from green to near-infrared based on aggregation-induced discoloration [46]. Unfortunately, the synthesis and regulation methods of these materials are complex, moreover, most of them show limited wavelength regions that remain to be extend to a wider range by an efficient guiding principle, which greatly limits their enormous potential applications. Additionally, the TADF emission of CDs is typically limited to the blue or green region, and the emission in the UV region has yet to be achieved, and the controllable conversion between RTP and TADF is difficult to achieve [22]. Therefore, to further improve the practicability of CDs-based RTA composites, an accurate, low-cost and easy large-scale preparation method within a single system is urgently needed to achieve broad and controllable modulation of RTA emission wavelength and lifetime.

In this study,  $\text{Al}_2\text{O}_3$  was used as a matrix to achieve RTA of CDs. The surface functional groups and conjugation size of CDs, the fixation ability and the content of defects of the matrix, were uniformly regulated through high-temperature treatment. A series of  $\text{CDs@Al}_2\text{O}_3$  composites were obtained, demonstrating the successful tuning of afterglow wavelength (619 nm ~ 376 nm), lifetime (60.6 ms ~ 520.6 ms), and luminescent mode (RTP or TADF). The characterization and analysis show that high-temperature consumption led to a decrease of

surface functional groups and conjugation size of CDs, resulting in the gradually blue-shifted emission wavelengths from red to UV region. The strengthened crystallinity of the  $\text{Al}_2\text{O}_3$  matrix stabilizes the triplet state of the CDs, thereby enabling adjustable lifetimes within a certain range and a transition from RTP to TADF. Our work realizes the maximum range of afterglow wavelength tuning in a single system by adjusting a single reaction parameter for CDs-based RTA materials, and it is also the first report on delayed fluorescence (DF) emission in the UV band. Furthermore, a continuous emission at ~ 471 nm attributed to the oxygen defects of the matrix was observed. Energy transfer process from CDs to the matrix because of the match energy gap between CDs and oxygen vacancy of  $\text{Al}_2\text{O}_3$ . Based on the outstanding RTA performance,  $\text{CDs@Al}_2\text{O}_3$  RTA materials offer considerable potential for applications in multiple anti-counterfeiting, information encryption and fingerprint detection.

## 2. Results and discussion

We developed an effective strategy for excited triple state stabilization and conjugation size reduction for in-situ preparation of  $\text{CDs@Al}_2\text{O}_3$  RTA materials. To obtain excellent optical performance in the CDs system, we chose 1,8-Naphthalimide (NA) as the precursor for CDs. Firstly, the selection of substances with abundant O and N atoms with a tendency of  $n-\pi^*$  transition as precursors can induce the generation of more triplet excitons by promoting the ISC process [47]. Secondly, aromatic precursors have large  $\pi$ -conjugation domains and high spin-orbit coupling [38], coupled with the imide structure which leads to an enhanced push-pull electron effect and an increase in intramolecular charge transfer (ICT) efficiency as a strong electron-

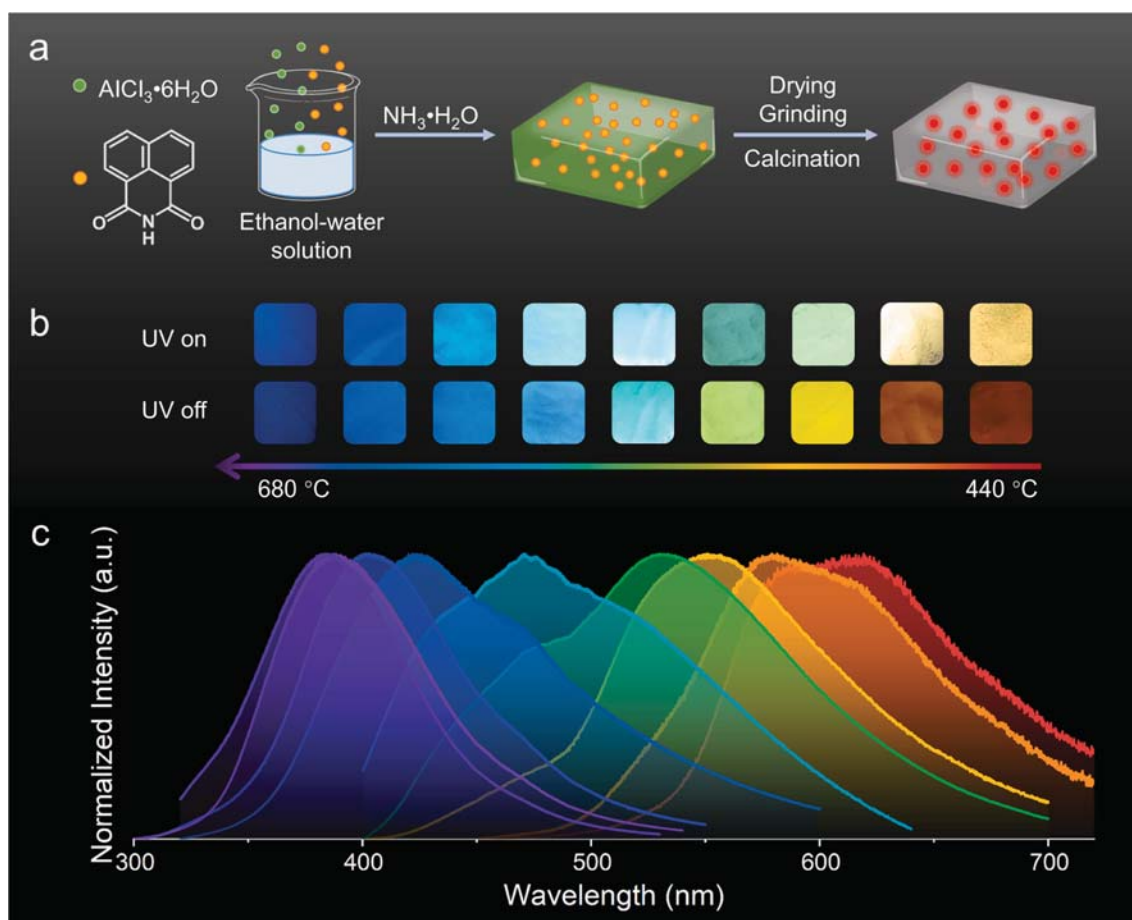


**Fig. 1.** a) Schematic representation of procedures for the preparation of  $\text{CDs@Al}_2\text{O}_3$  b) Images of the  $\text{CDs@Al}_2\text{O}_3$  powders before and after turning off the 365 nm UV lamp irradiation. c) Normalized afterglow spectra of  $\text{CDs@Al}_2\text{O}_3$  under ambient conditions.



withdrawing group [48], making CDs have small energy gaps, leading to long wavelength emission. Therefore, it is an ideal medium for preparing CDs-based RTA materials with adjustable optical performance. An effective  $\text{Al}_2\text{O}_3$ -assisted in-situ calcination strategy was further designed based on the above concept. Initially, as shown in Fig. 1a,  $\text{Al}^{3+}$  and NA were thoroughly mixed in an ethanol–water solution, the pH was adjusted to precipitate  $\text{Al}(\text{OH})_3$  while uniformly dispersing NA in the precipitation. The dried mixture was ground into powder for uniform reaction, and then  $\text{CDs@Al}_2\text{O}_3$  was synthesized by calcination at high temperature (440–680 °C). Based on different calcination temperatures, the obtained  $\text{CDs@Al}_2\text{O}_3$  composite materials were named  $\text{CDs@Al}_2\text{O}_3\text{-T}$  ( $T = 440, 470, 500, 530, 560, 590, 620, 650, 680$  °C). The high-temperature calcination process not only transformed loose  $\text{Al}(\text{OH})_3$  into rigid and dense  $\text{Al}_2\text{O}_3$ , but also resulted in the in-situ formation of luminescent CDs, which are completely embedded and fixed in the restricted space of  $\text{Al}_2\text{O}_3$  tightly. The resulting composite materials exhibited bright long-lived luminescence after removal of irradiation (Fig. 1b). As predicted, with the increasing calcination temperature, the long-lived luminescence could continuously blue-shift from red (619 nm) to the UV region (376 nm), with a tunable wide emission band up to 243 nm (Fig. 1c). The emission range is broader than that of the previously reported CD-based RTP materials which can adjust a single

reaction parameter to regulate the wavelength of afterglow in a single system (Table S1).

To better demonstrate the unique afterglow performance of  $\text{CDs@Al}_2\text{O}_3$ , several samples were chosen for further analysis. Firstly, a detailed structural characterization was carried out on the composite materials to understand the origin of their unique RTA properties. Transmission electron microscopy (TEM) images show that the formed CDs are uniformly dispersed in the  $\text{Al}_2\text{O}_3$  matrix (Fig. 2a–c and Fig. S1). The average particle size of the CDs decreases gradually with increasing pyrolysis temperature, i.e.,  $\text{CDs@Al}_2\text{O}_3\text{-440}$  is 2.58 nm,  $\text{CDs@Al}_2\text{O}_3\text{-560}$  is 2.46 nm,  $\text{CDs@Al}_2\text{O}_3\text{-680}$  is 2.21 nm. This is because the surface of the CDs is consumed during high temperature calcination, resulting in a smaller size. As a result, the CDs exhibit obvious size-dependent luminescence, which may be the reason for the shift of the afterglow peak from 619 nm to 376 nm. Specifically, the blue shift of the emission is due to the decrease in the electronic delocalization degree, leading to an increase in the energy gaps of CDs [49]. High-resolution transmission electron microscopy (HRTEM) images show that all these CDs possess crystalline structures with lattice fringe spacing of 0.21 nm, which is corresponding to the graphite (100) plane [50], and the crystal edges of  $\text{Al}_2\text{O}_3$  become clearer as the calcination temperature increases, indicating favorable crystallization at high temperature. X-ray diffraction

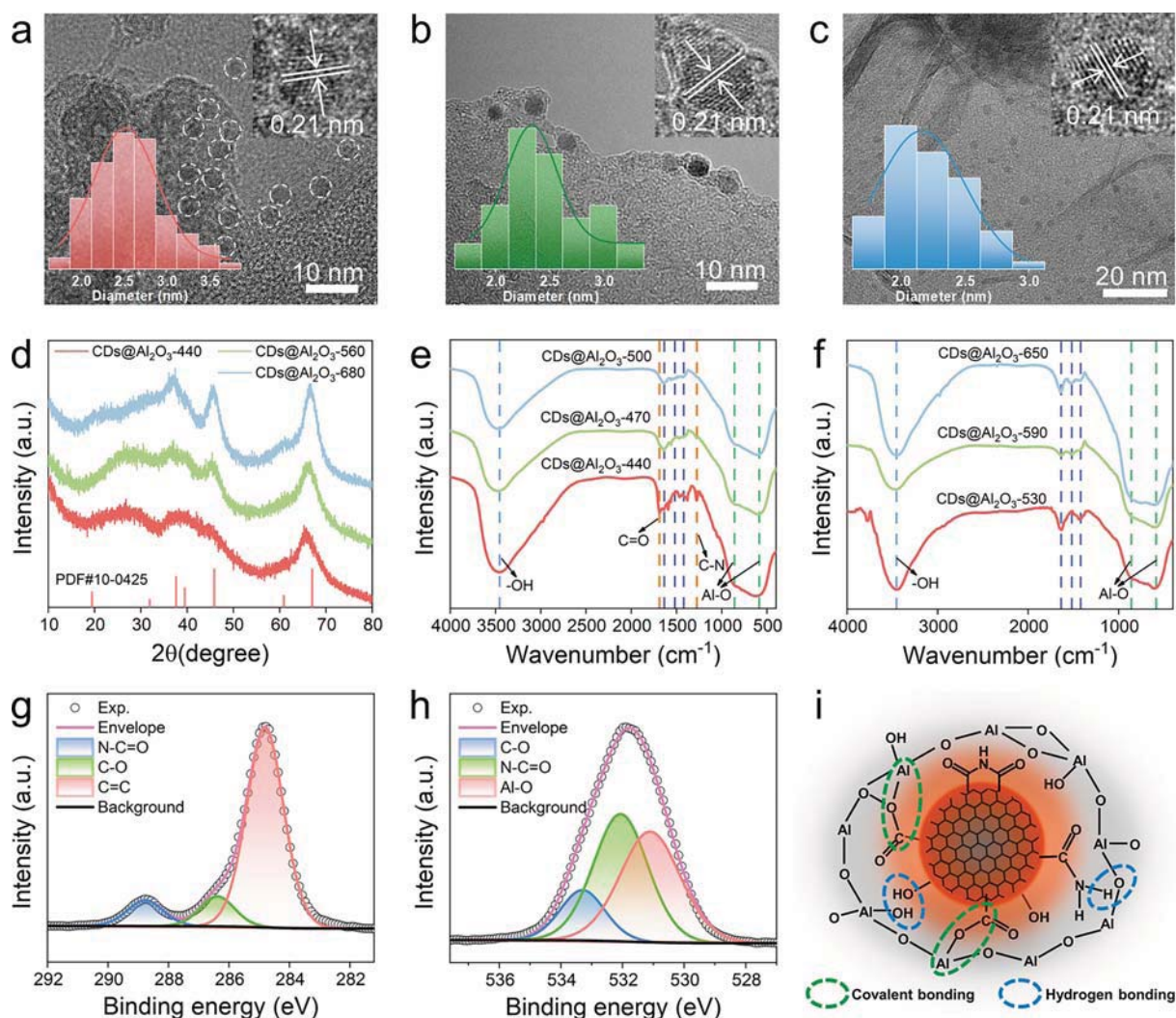


**Fig. 2.** TEM images of a)  $\text{CDs@Al}_2\text{O}_3\text{-440}$ , b)  $\text{CDs@Al}_2\text{O}_3\text{-560}$ , and c)  $\text{CDs@Al}_2\text{O}_3\text{-680}$ . Inset: HRTEM images and particle size distribution measured. d) XRD patterns of  $\text{CDs@Al}_2\text{O}_3\text{-440}$ ,  $\text{CDs@Al}_2\text{O}_3\text{-560}$ , and  $\text{CDs@Al}_2\text{O}_3\text{-680}$ . e) FT-IR spectrum of  $\text{CDs@Al}_2\text{O}_3\text{-440}$ ,  $\text{CDs@Al}_2\text{O}_3\text{-470}$ , and  $\text{CDs@Al}_2\text{O}_3\text{-500}$ . f) FT-IR spectra of  $\text{CDs@Al}_2\text{O}_3\text{-560}$ ,  $\text{CDs@Al}_2\text{O}_3\text{-620}$ , and  $\text{CDs@Al}_2\text{O}_3\text{-680}$ . High resolution XPS spectra and the corresponding fitting curves of g) C 1s and h) O 1s of  $\text{CDs@Al}_2\text{O}_3\text{-440}$ . i) Schematic of the proposed structure of  $\text{CDs@Al}_2\text{O}_3$ .



(XRD) patterns show distinct characteristic peaks of  $\gamma$ - $\text{Al}_2\text{O}_3$  at  $\sim 46^\circ$  and  $67^\circ$ , respectively, with two broad diffraction peaks, indicating the (440) diffraction of  $\gamma$ - $\text{Al}_2\text{O}_3$  (Fig. 2d and Fig. S2) [51]. It can be seen that with the increase of calcination temperature, the diffraction peaks of  $\gamma$ - $\text{Al}_2\text{O}_3$  become more and more obvious, continuously transforming from amorphous  $\text{Al}_2\text{O}_3$ .

Furthermore, Fourier transform infrared spectrum (FT-IR) and X-ray photoelectron spectrum (XPS) were used to study the chemical structure of the composite material. The FT-IR spectra (Fig. 2e, f and Fig. S3) show a wide and distinct O-H stretching vibration peak at  $3752$  to  $2705\text{ cm}^{-1}$  (blue line) [52]. The characteristic peaks of the aromatic ring skeleton vibrations are located at  $1639\text{ cm}^{-1}$ ,  $1518\text{ cm}^{-1}$ , and  $1420\text{ cm}^{-1}$  (purple line), and the intensities slightly decrease with increasing synthesis temperature, indicating a reduction in the conjugation size of CDs. The broad bands centered at  $860\text{ cm}^{-1}$  and  $586\text{ cm}^{-1}$  are caused by Al-O vibrations (green line) [53]. It is worth noting that the gradually disappearing stretching vibration absorption peaks at  $1684\text{ cm}^{-1}$  and  $1276\text{ cm}^{-1}$  are attributed to C=O and C-N, respectively, suggesting that the reserve of imide group may be an important reason for the red afterglow emission of CDs [47]. XPS scan results shown in Figs. S4–S8 reveal that all five composite materials are composed of C, O, Al, and N elements, the peaks at  $532.0$ ,  $400.1$ ,  $284.8$ , and  $74.4\text{ eV}$  correspond to

the characteristic peaks of O 1s, N 1s, C 1s, and Al 2p, respectively [54]. The three fitting peaks at  $284.8$ ,  $286.4$ , and  $288.8\text{ eV}$  in the high-resolution C 1s XPS represent the chemical bonds of C = C/C-C, C-O/C-N, and O-C = O, respectively (Fig. 2g and Figs. S3–S11) [44]. In the high-resolution O 1s spectrum, three binding energies at  $531.1$ ,  $532.0$ , and  $533.2\text{ eV}$  are observed, corresponding to Al-O, O = C-N, and C-O-C bonds (Fig. 2h and Figs. S3–S11) [55].

The aforementioned results indicate that the regular variation of the conjugation size and imide contents of CDs under high temperature enables the tuning of the material energy gaps. While the rigid and ordered  $\gamma$ - $\text{Al}_2\text{O}_3$  framework structure exerts a powerful constraint effect, the combination between CDs and  $\text{Al}_2\text{O}_3$  may occur through C-O-Al bonds, and large number of -OH groups contained in  $\text{Al}_2\text{O}_3$  may also form hydrogen bonds structures with the surface functional groups of CDs. All of these decrease the vibration and rotation of CDs, stabilize triplet excitons, and thus achieve efficient UV-red afterglow emission. Therefore,  $\text{Al}_2\text{O}_3$  not only serves as an ideal host for effectively dispersing CDs but also functions as a superior confinement matrix for fixing the triplet excited state. The structural relationship and possible chemical bonding between CDs and the  $\text{Al}_2\text{O}_3$  matrix are shown in Fig. 2i.

To investigate the extremely wide and adjustable RTA emission

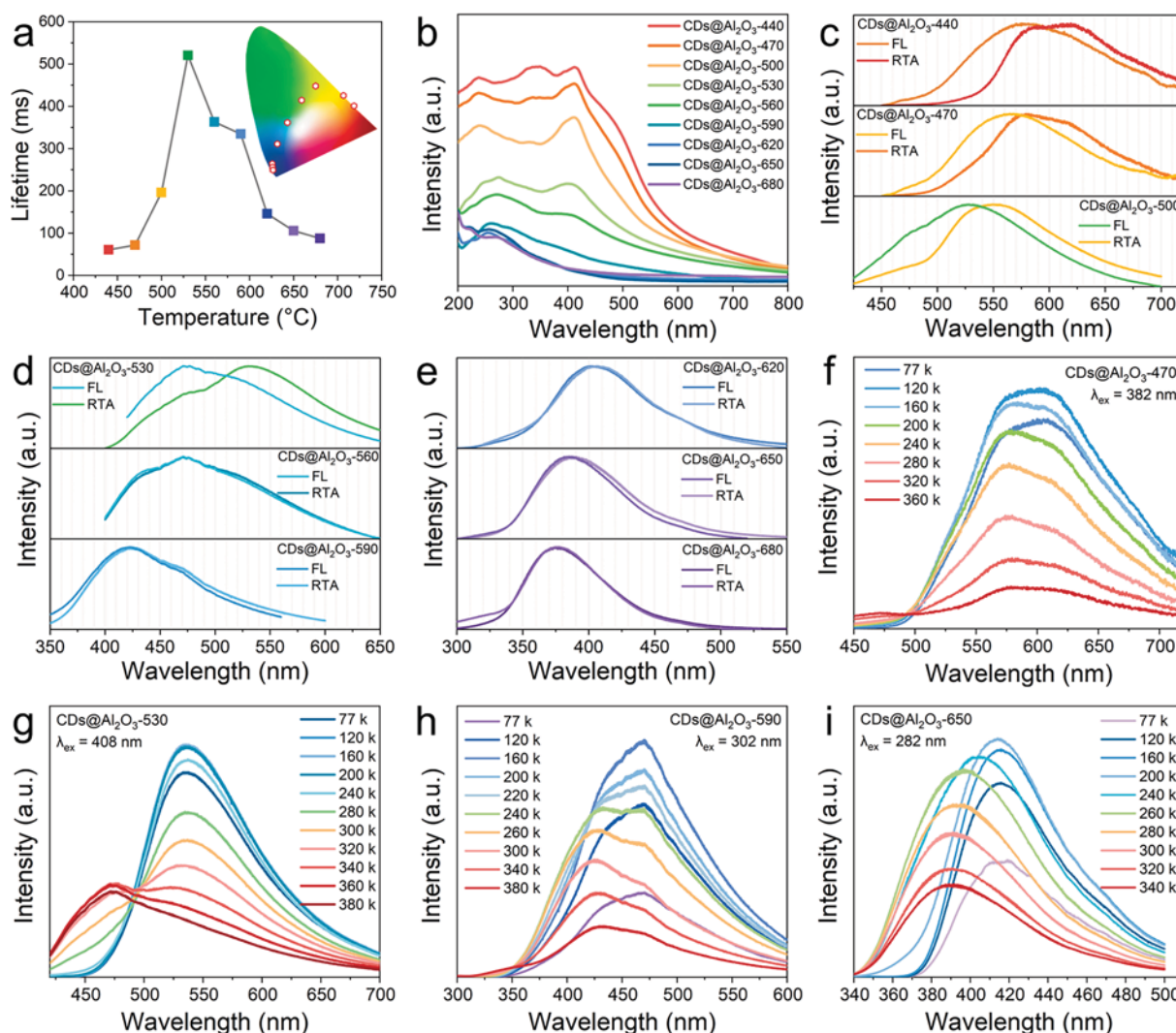


**Fig. 3.** a) Afterglow lifetime of CDs@Al<sub>2</sub>O<sub>3</sub> at room temperature. Inset: CIE coordinates of the afterglow emission of CDs@Al<sub>2</sub>O<sub>3</sub> composites under optimal excitation. b) UV-vis absorption spectra of CDs@Al<sub>2</sub>O<sub>3</sub>. Fluorescence (room temperature) and afterglow (77k) spectra for c) CDs@Al<sub>2</sub>O<sub>3</sub>-440, CDs@Al<sub>2</sub>O<sub>3</sub>-470, and CDs@Al<sub>2</sub>O<sub>3</sub>-500, d) CDs@Al<sub>2</sub>O<sub>3</sub>-530, CDs@Al<sub>2</sub>O<sub>3</sub>-560, and CDs@Al<sub>2</sub>O<sub>3</sub>-590, e) CDs@Al<sub>2</sub>O<sub>3</sub>-620, CDs@Al<sub>2</sub>O<sub>3</sub>-650, and CDs@Al<sub>2</sub>O<sub>3</sub>-680. Afterglow emission spectra at different temperature under optimal excitation of f) CDs@Al<sub>2</sub>O<sub>3</sub>-470, g) CDs@Al<sub>2</sub>O<sub>3</sub>-530, h) CDs@Al<sub>2</sub>O<sub>3</sub>-590, i) CDs@Al<sub>2</sub>O<sub>3</sub>-650.

wavelength properties, we further analyzed the photophysical properties of the samples. As shown in Fig. S9, the powder of the precursors showed no RTA emission and their fluorescence emission peaks were in blue and cyan region, which is different from CDs@Al<sub>2</sub>O<sub>3</sub>. The fluorescence and RTA emissions wavelength were less affected by the excitation wavelength, which may be attributed to the fact that the CDs were generated from a single precursor at a high temperature, resulting in the existence of only a single luminescent center in the CDs (Figs. S10 and S11). The corresponding CIE color coordinates of the afterglow emission of CDs@Al<sub>2</sub>O<sub>3</sub> composites under optimal excitation were (0.60, 0.40), (0.54, 0.45), (0.39, 0.51), (0.31, 0.43), (0.23, 0.30), (0.18, 0.19), (0.15, 0.08), (0.15, 0.06) and (0.15, 0.04), respectively (Fig. 3a). The decay curve from time-resolved afterglow spectra can be fitted well by a triexponential function (Fig. S12), from the decay components, the average lifetime was calculated according to the equation:

$$\tau_{avg} = \sum \alpha_i \tau_i^2 / \sum \alpha_i \tau_i$$

The average lifetime of the material calculated was 60.6–520.6 ms (Fig. 3a and Fig. S12), indicating long-lived emission features and adjustable characteristics within a certain range. With an increase in the calcination temperature, more ordered and denser  $\gamma$ -Al<sub>2</sub>O<sub>3</sub> matrixes were generated, which enhanced the protection capabilities for CDs. However, excessively high temperatures led to the consumption of CDs. The dynamic balance between the two components regulated the afterglow lifetime of the composite material, and the longest lifetime was observed when the calcination temperature is 530 °C. The UV–visible absorption spectra of the samples between 200 and 800 nm were measured and shown in Fig. 3b. It is apparent that the increase in calcination temperature caused blue shift of the absorption band, showing the narrowing of the CDs energy gaps, and indicating the smaller conjugation sizes were generated in the CDs. When the calcination temperature was low, the CDs composed of N- and O-doped aromatic carbon structures exhibit comprehensive absorption produced by  $\pi$ - $\pi^*$  and  $n$ - $\pi^*$  transitions, where the absorption peaks at  $\sim$  340 nm and  $\sim$  412 nm are considered to result from  $n$ - $\pi^*$  transitions of C = O and C-N bonds [16], and the absorption in the shorter wavelength region belongs to the  $\pi$ - $\pi^*$  transition of typical  $sp^2$  carbon in graphene-like structures, indicating that the short-wavelength afterglow is likely originating from the intrinsic emission of the carbonized core [54].

We compared the afterglow emission peak of each sample with the fluorescence emission peak at the same excitation wavelength (Fig. 3c–e). Interestingly, CDs@Al<sub>2</sub>O<sub>3</sub>-440, CDs@Al<sub>2</sub>O<sub>3</sub>-470, CDs@Al<sub>2</sub>O<sub>3</sub>-500, and CDs@Al<sub>2</sub>O<sub>3</sub>-530 showed typical RTP features with a relative fluorescence redshift and significant Stokes shift [56]. Starting from CDs@Al<sub>2</sub>O<sub>3</sub>-560, the fluorescence peaks almost overlapped with their afterglow peaks, indicating mainly TADF characteristics [27]. To verify the characteristic of mutual conversion between RTP and TADF and investigate the luminescence mechanism, model samples including CDs@Al<sub>2</sub>O<sub>3</sub>-470, CDs@Al<sub>2</sub>O<sub>3</sub>-530, CDs@Al<sub>2</sub>O<sub>3</sub>-560, CDs@Al<sub>2</sub>O<sub>3</sub>-590 and CDs@Al<sub>2</sub>O<sub>3</sub>-650 were selected for further analysis. Delayed photoluminescence measurements were performed in vacuum at different temperatures, and the differences of  $\Delta E_{ST}$  were analyzed to elucidate the different afterglow modes by minimizing vibration dissipation (Fig. 3f–i and Fig. S13). For the emission wavelength region larger than 500 nm, the emission intensity generally decreases with the increase of the testing temperature, which is a typical feature of RTP emission weakened by enhanced non-radiative transition with increasing temperature. From CDs@Al<sub>2</sub>O<sub>3</sub>-530 and CDs@Al<sub>2</sub>O<sub>3</sub>-560, it can be observed that while the phosphorescent peak decreases, the emission peak around 471 nm and the lower-wavelength shoulder peak gradually become more pronounced, indicating that the thermal activation energy can activate this afterglow emission, which is a characteristic of TADF materials. As for CDs@Al<sub>2</sub>O<sub>3</sub>-590 and CDs@Al<sub>2</sub>O<sub>3</sub>-650, the emission of the T<sub>1</sub> state at low temperatures increases with increasing temperature before decreasing again, which is an unusual phenomenon that may be due to

–NH groups on the surfaces of CDs being replaced by –OH at higher synthesis temperature, as –OH can ionize and form ionic bonds with Al [49,57]. When the testing temperature starts to rise, the enhanced ionic bonds stabilize the triplet state while the non-radiative transitions become stronger, the emission of the T<sub>1</sub> state reaches its maximum at a certain temperature in dynamic equilibrium. When the temperature is further increased, the thermal quenching effect takes the dominant position, the energy is dissipated by non-radiative transition, which reduces the luminescence intensity.

Stable excited triplet states and small  $\Delta E_{ST}$  are key factors in achieving TADF. The smaller  $\Delta E_{ST}$  facilitates the flow of electrons to achieve TADF through ISC and reverse intersystem crossing (RISC) between the lowest singlet (S<sub>1</sub>) and T<sub>1</sub>. At low temperatures (77 K), RISC cannot occur, and the afterglow emission of CDs@Al<sub>2</sub>O<sub>3</sub> corresponds to the T<sub>1</sub> state emission [58]. As the temperature rises, the wavelength of the afterglow emission changes, corresponding to delayed fluorescence of the S<sub>1</sub> state. By comparing the afterglow spectra at 77 K with the fluorescence spectra at room temperature, we calculated that the  $\Delta E_{ST}$  values of CDs@Al<sub>2</sub>O<sub>3</sub> are approximately 0.035 (CDs@Al<sub>2</sub>O<sub>3</sub>-470), 0.020 (CDs@Al<sub>2</sub>O<sub>3</sub>-530), 0.031 (CDs@Al<sub>2</sub>O<sub>3</sub>-560), 0.039 (CDs@Al<sub>2</sub>O<sub>3</sub>-590), and 0.027 (CDs@Al<sub>2</sub>O<sub>3</sub>-650) eV (Fig. S14 and Table S2). Obviously, the small and irregular differences in  $\Delta E_{ST}$  values are not the reason for the different photophysical processes of RTP and TADF. We attribute the true reason to the stabilization of the excited triplet state. Our results demonstrate that the Al<sub>2</sub>O<sub>3</sub> matrix plays a crucial role in enabling long-lived TADF behavior through RISC processes. The gradually strengthened crystalline structure of Al<sub>2</sub>O<sub>3</sub>, combined with the C-O-Al bonds and hydrogen bonds, suppresses the non-radiative decay of vibration and rotation and locks the triplet exciton on the CDs.

First-principles density functional theory (DFT) calculations has been used to further investigated the effect of the  $sp^2$  conjugation size or imide structure on RTA properties of CDs. As shown in Fig. 4, different configurations models based on the precursor were chosen for assessing. The calculation result indicates the corresponding energy of the LUMO-HOMO and the energy gaps of the models. As shown in Fig. 4a, when the imide groups decrease or replaced by amide groups, a trend of gradual decrease in turns (3.43 eV, 3.46 eV, 3.88 eV) in the energy gap was depicted, which may result from the electron-withdrawing groups that would contribute to an enhancement of smaller energy gaps in CDs [59]. The energy gaps of decreasing  $sp^2$  conjugation size in Fig. 4b were 2.42 eV, 3.05 eV and 3.84 eV, respectively, which indicated the same trend as the calculation result above that smaller conjugation size and higher-crystallinity carbon core decreased the vibration and enlarged the energy gaps of the CDs [49]. Hence, the energy gaps decrease with imide contents or increasing conjugation size play vital roles in the red-shift emission wavelength, which is further proves the luminescence mechanism.

In addition, the difference in emission fluctuation between 471 nm and the longer wavelength suggests that the centers of luminescence are distinct. Fluorescence and afterglow spectra of CDs@Al<sub>2</sub>O<sub>3</sub>-500, CDs@Al<sub>2</sub>O<sub>3</sub>-530, CDs@Al<sub>2</sub>O<sub>3</sub>-560, and CDs@Al<sub>2</sub>O<sub>3</sub>-590 all exhibit apparent emissions at 471 nm that do not observe the trend that emission wavelength dependent on calcination temperature; instead, only their intensities change (Fig. 2b and Figs. S10, S11, S15). As is well known, Al<sub>2</sub>O<sub>3</sub> is an insulator that it is difficult for electrons to transition from the conduction band to the valence band and emit visible light if it is not modified [60]. According to previous literature, Du et al. and Li et al. reported that blue luminescence in alumina films may arise from single-electron-occupied oxygen vacancies produced by the decomposition of oxalic acid impurities following high-temperature annealing [61,62]. Wang et al. prepared mesoporous alumina with afterglow emission by increasing the crystal defects through a porous structure [63]. Bai et al. reported the enhanced photoluminescence of Al<sub>2</sub>O<sub>3</sub> from CdSe quantum dots through energy transfer [64]. Therefore, the blue emission band near 471 nm of CDs@Al<sub>2</sub>O<sub>3</sub> likely originates from defect structures in the Al<sub>2</sub>O<sub>3</sub>.

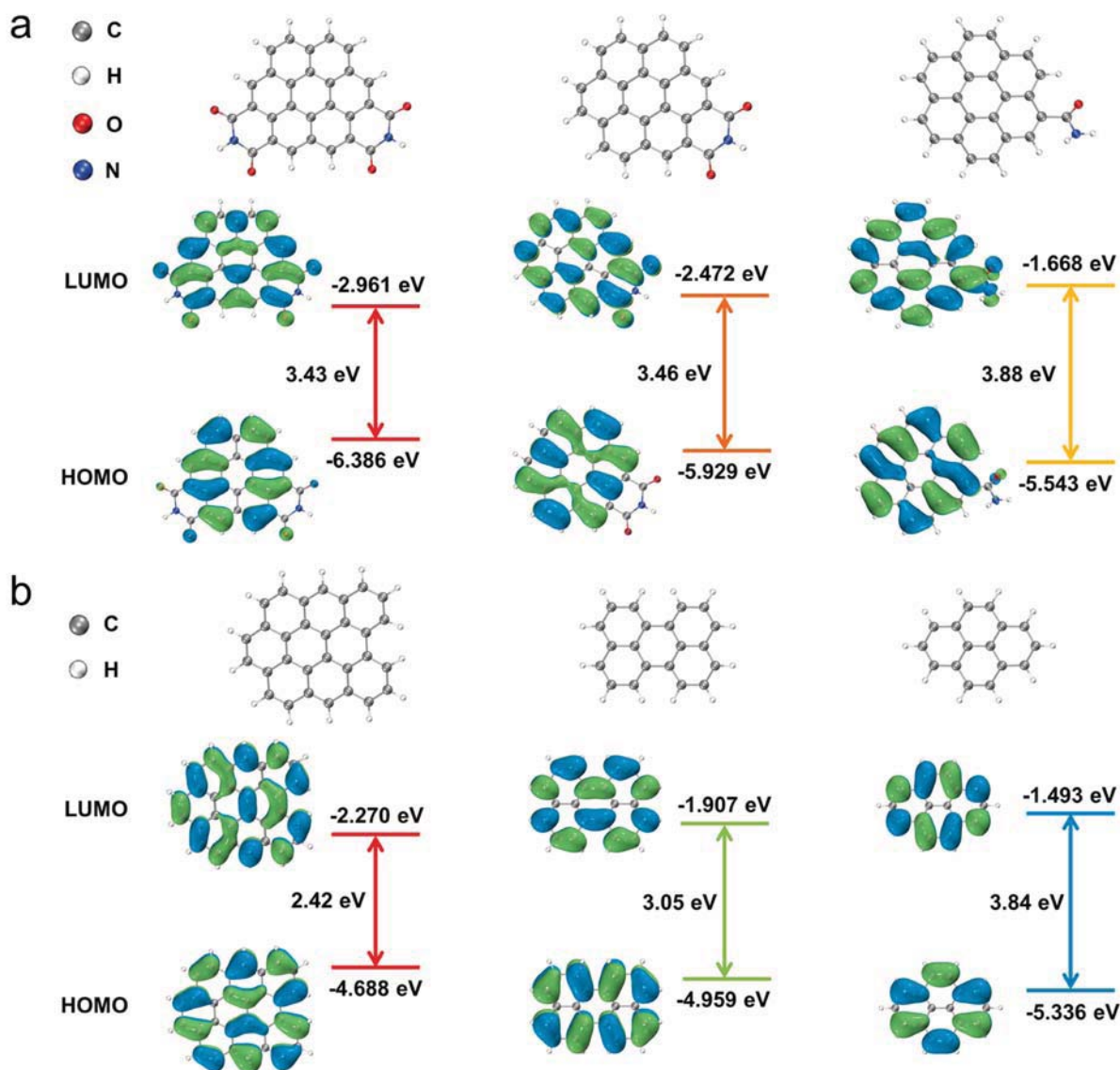


Fig. 4. The three configurations and the corresponding HOMO and LUMO of the CDs with different a) imide contents and b) conjugation size.

Furthermore, RTA can be observed in the CDs@Al<sub>2</sub>O<sub>3</sub> composite while the CDs-doped free Al<sub>2</sub>O<sub>3</sub> matrix almost no afterglow emission under the same excitation condition (Fig. 5a). The comparison shows that the characteristic luminescence of defects in Al<sub>2</sub>O<sub>3</sub> are activated by the formed CDs. Electron paramagnetic resonance spectrum (EPR) can accurately confirm the existence and state of oxygen vacancies in CDs@Al<sub>2</sub>O<sub>3</sub>. Signals were observed at  $g = 2.00477\text{--}2.00525$  (Fig. 5b and Table S2), which are believed to arise from the paramagnetic state of single-electron-occupied oxygen vacancies [65–67]. CDs@Al<sub>2</sub>O<sub>3</sub>-470, CDs@Al<sub>2</sub>O<sub>3</sub>-530, and CDs@Al<sub>2</sub>O<sub>3</sub>-560 all show evident signals, with the integral intensity being highest in CDs@Al<sub>2</sub>O<sub>3</sub>-560, indicating the presence of a large number of oxygen vacancies in these samples. Conversely, the signal of CDs@Al<sub>2</sub>O<sub>3</sub>-590 rapidly decreases, indicating a significant reduction in oxygen vacancies, consistent with the nearly disappearing emission peak at 471 nm in the afterglow spectrum. It should be noted that no significant relevant emission was observed in the afterglow spectra of CDs@Al<sub>2</sub>O<sub>3</sub>-440 and CDs@Al<sub>2</sub>O<sub>3</sub>-470 (Fig. 1c and Fig. S11), indicating that this emission is not an independent luminescence system from the carbon dots, the depths of trap centers of Al<sub>2</sub>O<sub>3</sub> cannot match the narrow energy gap of CDs at this point. When

the energy gap of CDs increases, the process of energy transfer becomes possible. The phenomenon has been reported that the matrix enhances the luminescence of CDs [34], or the energy transfer of CDs to luminescent molecules doped into the matrix [8,35], but there is no report on long-lasting luminescence in the matrix due to receiving the energy transfer from carbon dots, which is with significant importance for expanding the application scope of CDs-based materials. The consumption of CDs at high temperature causes the oxygen atoms in the Al<sub>2</sub>O<sub>3</sub> crystal network to break away, and the aluminum atoms are replaced by the carbon atoms on the CDs surface, thus forming more oxygen vacancy defects around the CDs and making the energy transfer process more efficient. As the calcination temperature increases, the atoms are arranged in order, and large number of crystallographic defects within Al<sub>2</sub>O<sub>3</sub> matrix are eliminated, leading to a decrease in the characteristic luminescence intensity. This implies that defect states of Al<sub>2</sub>O<sub>3</sub> do not participate as energy relay stations in achieving short-wavelength TADF. This further verifies that the appearance of delayed fluorescence is due to the stabilization of excited triplet states through the effects of strengthened crystallinity and densification of Al<sub>2</sub>O<sub>3</sub>, C-O-Al bonds and hydrogen bonds between CDs and Al<sub>2</sub>O<sub>3</sub>.



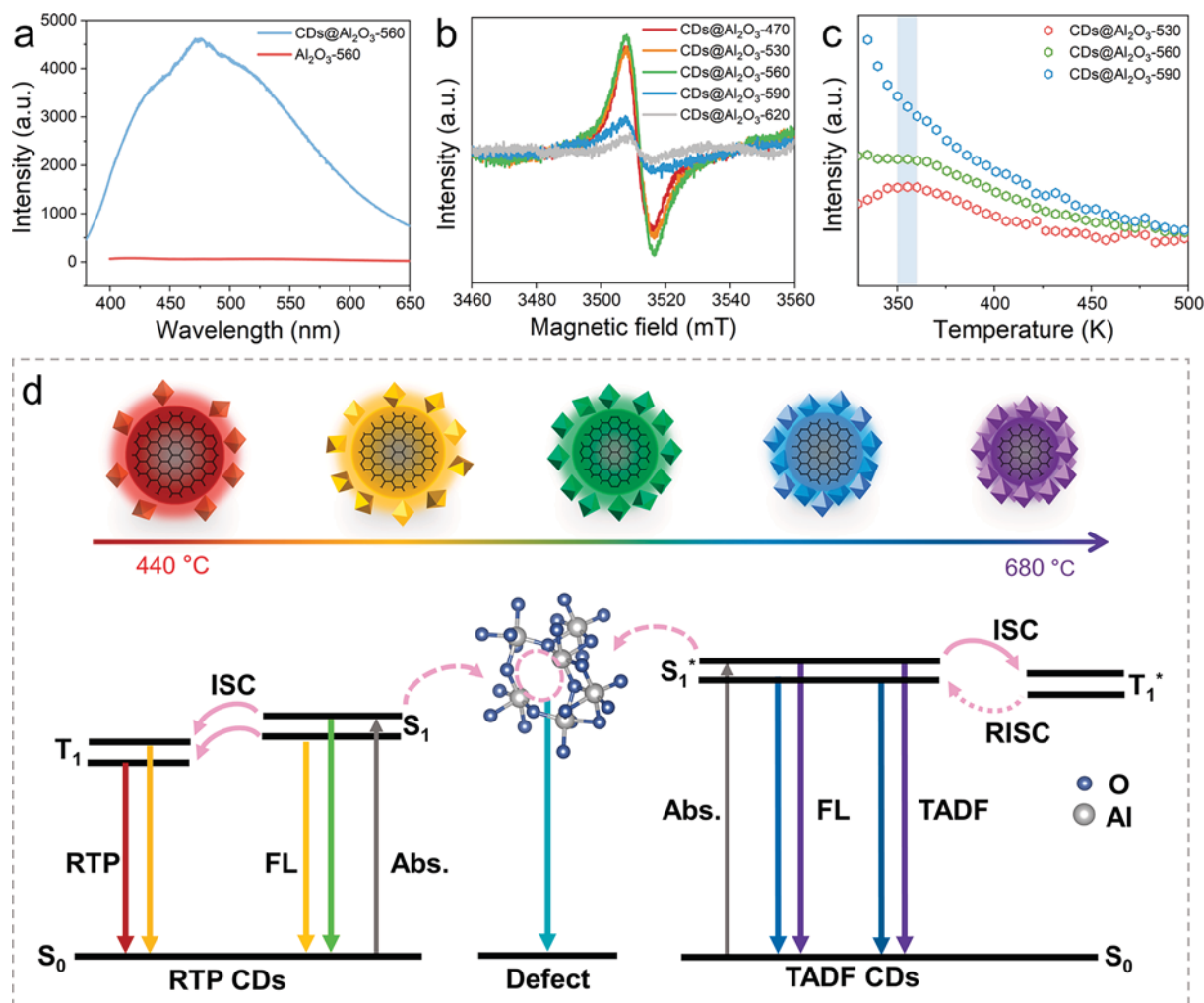


Fig. 5. a) Afterglow emission spectra of CDs@Al<sub>2</sub>O<sub>3</sub>-560 and Al<sub>2</sub>O<sub>3</sub>-560 powder at  $\lambda_{\text{ex}} = 280$  nm. b) EPR spectra of CDs@Al<sub>2</sub>O<sub>3</sub>-470, CDs@Al<sub>2</sub>O<sub>3</sub>-530, CDs@Al<sub>2</sub>O<sub>3</sub>-560, CDs@Al<sub>2</sub>O<sub>3</sub>-590, and CDs@Al<sub>2</sub>O<sub>3</sub>-650. c) TL curve spectra of CDs@Al<sub>2</sub>O<sub>3</sub>-560, CDs@Al<sub>2</sub>O<sub>3</sub>-590, and CDs@Al<sub>2</sub>O<sub>3</sub>-650. d) Schematic of the transition model of the multicolor afterglow CDs@Al<sub>2</sub>O<sub>3</sub>.

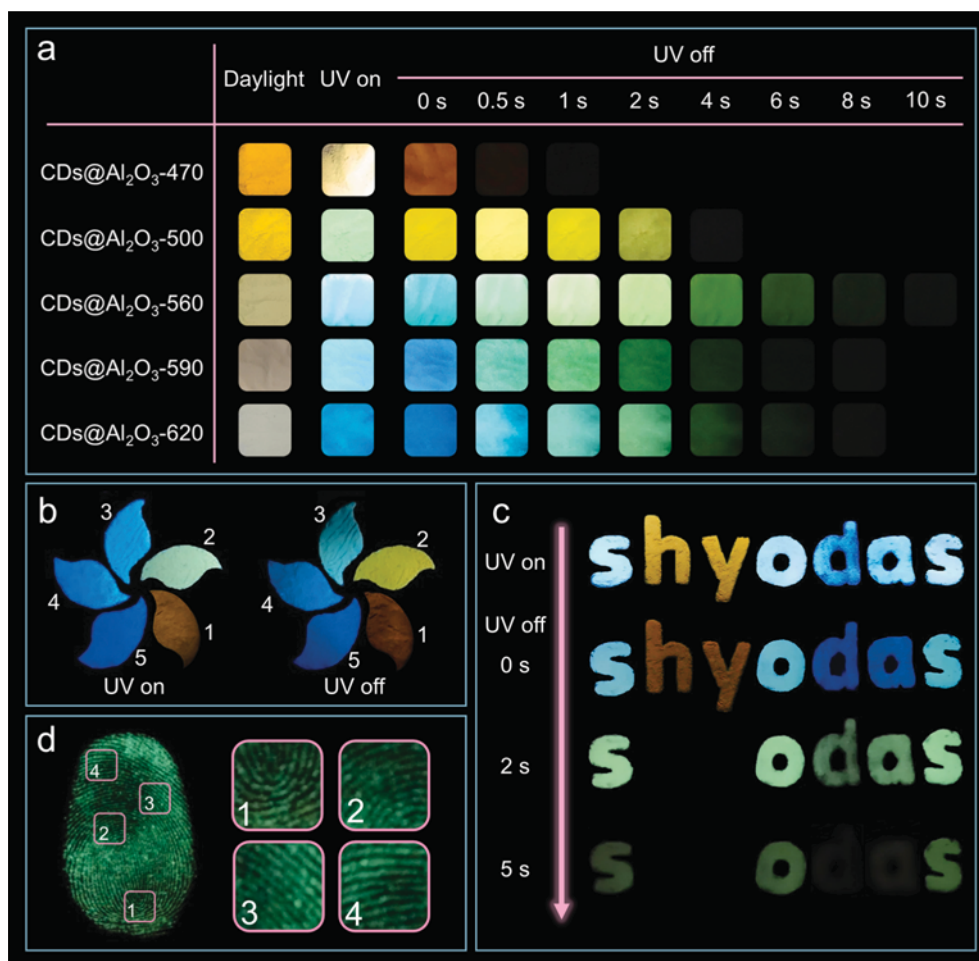
We further determined the trap depth of the material through thermoluminescence spectrum (TL) due to radiation transition caused by the thermal activation release of electrons trapped in the traps. The emission peak of CDs@Al<sub>2</sub>O<sub>3</sub>-530 and CDs@Al<sub>2</sub>O<sub>3</sub>-560 occurs at  $\sim 355$  K, with CDs@Al<sub>2</sub>O<sub>3</sub>-560 exhibiting a higher intensity, but there is no obvious peak of CDs@Al<sub>2</sub>O<sub>3</sub>-590, which corresponds to the sharp decrease in the oxygen vacancy signal peak in the EPR results for CDs@Al<sub>2</sub>O<sub>3</sub>-590 (Fig. 5c). According to the following formula for calculating the average defect depth:  $E = T_m / 500$  [68,69], the trap depth of the materials is estimated to be 0.71 eV. These results all further confirm that the 471 nm emission peak originates from oxygen vacancy defects in Al<sub>2</sub>O<sub>3</sub> via energy transfer.

Fig. 5d proposes possible mechanisms for these luminescent processes. When synthesized at a lower temperature, the conjugation size of CDs is larger, and the surface functional groups are better preserved, which favor the emission of long-wavelength RTP. The excitons first transitions from ground state ( $S_0$ ) to  $S_1$  after excitation. Due to the multiple constraints of the spatial confinement, covalent bonds, and hydrogen bonds of the Al<sub>2</sub>O<sub>3</sub> matrix on CDs, the excitons on the  $S_1$  can fall into  $T_1$  through ISC smoothly, and radiation transition of RTP is also benefited from the stabilizing of the triplet excited states. Large number of oxygen vacancies exist in the powder because of the lack of oxygen during the calcination process. When the energy gap of CDs adjusted by the calcination temperature approach to the oxygen vacancy defects

energy level of the Al<sub>2</sub>O<sub>3</sub> matrix, enabling energy transfer from CDs to the defects, and thus resulting in the observed the characteristic emission. The surface functional groups and the conjugation size decrease as the calcination temperature further increases, resulting in the corresponding increase of the energy gaps. Additionally, a considerable number of crystallographic defects within the Al<sub>2</sub>O<sub>3</sub> matrix are eliminated, which enhances the stabilization of the triplet states and promotes the RISC process from triplet states to singlet states, thereby generating TADF in the short wavelength range.

As shown in Fig. 6a, the multi-color luminescence of CDs@Al<sub>2</sub>O<sub>3</sub> can last up to 10 s under ambient conditions after illumination stops. Based on the modulated TADF/RTP luminescence wavelength and lifetime of CDs@Al<sub>2</sub>O<sub>3</sub> powder, we explored its potential applications in color multiple anti-counterfeiting, time-dependent information, and fingerprint detection. As shown in Fig. 6b, we illustrate a advanced security protection pattern composed of modes of fluorescence, RTP and TADF. Petals coded 1–5 represented by CDs@Al<sub>2</sub>O<sub>3</sub>-470, CDs@Al<sub>2</sub>O<sub>3</sub>-500, CDs@Al<sub>2</sub>O<sub>3</sub>-560, CDs@Al<sub>2</sub>O<sub>3</sub>-620, CDs@Al<sub>2</sub>O<sub>3</sub>-650, respectively. Upon the UV lamp, the pattern exhibits colorful fluorescence, which can be observed as the security protection mode. Once the UV lamp is switched off, it can be clearly observed that petals 1–3 show orange, yellow and cyan RTP that are different from the fluorescence, while petals 4–5 show blue TADF that are similar to their fluorescence emission under UV on. As shown in Fig. 6c, the pattern “shyodas” was fabricated with





**Fig. 6.** a) Photographs of CDs@Al<sub>2</sub>O<sub>3</sub>-470, CDs@Al<sub>2</sub>O<sub>3</sub>-500, CDs@Al<sub>2</sub>O<sub>3</sub>-560, CDs@Al<sub>2</sub>O<sub>3</sub>-590, and CDs@Al<sub>2</sub>O<sub>3</sub>-620 under daylight, before and after switching off 365 nm UV lamp. b) Patterns of anti-counterfeiting fabricated with the CDs@Al<sub>2</sub>O<sub>3</sub> for advanced color-switching anti-counterfeiting. c) Photographs of information encryption fabricated with CDs@Al<sub>2</sub>O<sub>3</sub>-470, CDs@Al<sub>2</sub>O<sub>3</sub>-560 and CDs@Al<sub>2</sub>O<sub>3</sub>-650. d) Photographs of visualized fingerprint detection, and the corresponding enlarged image.

CDs@Al<sub>2</sub>O<sub>3</sub>-560, CDs@Al<sub>2</sub>O<sub>3</sub>-470, CDs@Al<sub>2</sub>O<sub>3</sub>-470, CDs@Al<sub>2</sub>O<sub>3</sub>-560, CDs@Al<sub>2</sub>O<sub>3</sub>-650, CDs@Al<sub>2</sub>O<sub>3</sub>-650, respectively. When the UV light was turned on and off instantly, the “shyodas” code can be observed different color combinations as the first-level encrypted message. After the time extension for 2 s, the letters “h” and “y” vanished, the encrypted digital information was reorganized as “sodas”. With a five-second delay, the second-level encrypted message was again reorganized into “sos” showing multiple information encryption. In addition to the application in security protection, the CDs@Al<sub>2</sub>O<sub>3</sub> materials with long-lived RTA can regard as ideal agents for fingerprint detection to efficiently shield short-lived background fluorescence (Fig. 6d). In fact, in addition to being used as intelligent materials in the aforementioned application scenarios, the multi-adjustable residual luminescence characteristic of CDs@Al<sub>2</sub>O<sub>3</sub> indicate the great promise of CDs@Al<sub>2</sub>O<sub>3</sub> in antibacterial agents, bioimaging, display devices, and other areas by simply amplifying reaction system in proportion.

### 3. Conclusion

In summary, we herein report a unified control strategy for the surface functional groups and conjugation size of CDs, the fixation ability and the content of defects of the matrix, by solely adjusting the calcination temperature of the in-situ generated CDs@Al<sub>2</sub>O<sub>3</sub> RTA materials. Our results demonstrate the successful tuning of afterglow wavelength (619 nm ~ 376 nm), lifetime (60.6 ms ~ 520.6 ms), and luminescent mode (RTP or TADF). Furthermore, a continuous emission

at ~ 471 nm attribute to the oxygen defects of the matrix was observed. High temperature decreases the content of surface functional groups and conjugation size of CDs, increases the energy gap between the excited state and the ground state, thereby enabling adjustable RTA wavelength. Meanwhile, because of the strengthened crystallinity of the Al<sub>2</sub>O<sub>3</sub> matrix stabilizes the triplet state of the CDs, the RISC process between singlet and triplet states is promoted, resulting in adjustable lifetimes the transformation of luminescent mode from RTP to TADF. When the energy gap of the CDs matches with the oxygen vacancy of Al<sub>2</sub>O<sub>3</sub> allows characteristic luminescence at 471 nm of the defects to be achieved through energy transfer. Our work realizes the maximum range of afterglow wavelength tuning in a single system by adjusting a single reaction condition for CDs-based RTA materials, and is also the first report on DF emission in the UV band. This work provides a reasonable design strategy for red to UV RTA materials. Based on the outstanding RTA performance, CDs@Al<sub>2</sub>O<sub>3</sub> RTA materials offers considerable potential for applications in multiple anti-counterfeiting, information encryption and fingerprint detection.

### 4. Experimental section

#### 4.1. Materials

All reagents and solvents were commercially available and used without further purification. 1,8-Naphthalimide and ethanol were purchased from Aladdin Shanghai China. AlCl<sub>3</sub>·6H<sub>2</sub>O and NH<sub>3</sub>·H<sub>2</sub>O were

purchased from Macklin Chemical Reagent Co. Ltd (Shanghai, China). And the deionized water was supplied by a Water Purifier Nano pure water system (Master-E, Hitech-science tool, shanghai, China).

#### 4.2. Synthesis of CDs@Al<sub>2</sub>O<sub>3</sub>

First, 7.5 mmol AlCl<sub>3</sub>·6H<sub>2</sub>O and 0.25 mmol 1,8-Naphthalimide (NA) were thoroughly mixed in mixed solution of 8 mL H<sub>2</sub>O and 8 mL ethanol. Subsequently, NH<sub>3</sub>·H<sub>2</sub>O was added drop-wise into the mixed solution under stirring until precipitation generated completely. After aging for 3 h, the precipitation was washed with deionized water to remove most of the NH<sub>4</sub><sup>+</sup> and Cl<sup>-</sup>. After that, the mixture was dried at 80 °C for 10 h and ground into fine powders for uniform reaction.

The powders were calcined in air in a muffle furnace at different temperature (440–680 °C) for 150 min with a rate of 5 °C / min to obtain CDs@Al<sub>2</sub>O<sub>3</sub> composites. Based on different calcination temperatures, the obtained CDs@Al<sub>2</sub>O<sub>3</sub> composite materials were named CDs@Al<sub>2</sub>O<sub>3</sub>-T (T = 440, 470, 500, 530, 560, 590, 620, 650, 680 °C).

#### 4.3. Characterizations

The HR-TEM images were recorded using a JEOL-2010 electron microscope. The XRD pattern was collected using a XD-2×/M4600. FT-IR spectra were taken on a Nicolet Avatar 360 FT-IR spectrophotometer. X-ray photoelectron spectroscopy (XPS) was performed on a Kratos AXIS Ultra DLD X-ray photoelectron spectrometer with a monochromatic Al K $\alpha$  X-ray source. UV–vis absorption and transmittance spectra were carried out using a Hitachi UV-3900 spectrometer. The FL-7000 Hitachi fluorescence spectrofluorometer was used to record the temperature-dependent PL emission spectra, afterglow emission spectra, and afterglow decay curves. TL data were recorded using an FJ427A1 thermoluminescent dosimeter (CNNC Beijing Nuclear Instruments Factory) between the range of 330 and 500 K at a heating rate of 5 K s<sup>-1</sup>. The EPR spectra were recorded on an EPR spectrometer (Bruker A300) operating in the X-band frequencies ( $\approx$ 9.447 GHz) at RT.

#### 5. First-principles DFT calculations

Density functional theory (DFT) calculations were carried out with the B3LYP functional with the combination of the Grimme's D3 version of dispersion correction with Becke-Johnson (BJ) damping parameter. The basis set of 6-31G (d, p) were adopt for the geometry optimization and frequency calculations. The geometries were fully optimized without any structural constraints. The harmonic frequency calculations were carried out at the same level of theory to verify that all structures have no imaginary frequency. Frontier orbitals were visualized using the VMD package.

#### Declaration of Competing Interest

The authors declare that they have no known competing financial interests or personal relationships that could have appeared to influence the work reported in this paper.

#### Data availability

Data will be made available on request.

#### Acknowledgements

This work was supported by the National Natural Science Foundations of China (12174119), the Natural Science Foundation of Guangdong Province (2020A1515010443, 2023A1515012003).

#### Appendix A. Supplementary data

Supplementary data to this article can be found online at <https://doi.org/10.1016/j.cej.2023.145597>.

#### References

- [1] Y. Fan, S. Liu, M. Wu, L. Xiao, Y. Fan, M. Han, K. Chang, Y. Zhang, X.u. Zhen, Q. Li, Z. Li, Mobile phone flashlight-excited red afterglow bioimaging, *Adv. Mater.* 34 (18) (2022) 2201280.
- [2] W.B. Ma, Y.R. Su, Q.S. Zhang, C. Deng, L. Pasquali, W.J. Zhu, Y. Tian, P. Ran, Z. Chen, G.Y. Yang, G.J. Liang, T.Y. Liu, H.M. Zhu, P. Huang, H.Z. Zhong, K. W. Wang, S.Q. Peng, J.L. Xia, H.F. Liu, X. Liu, Y. Yang, Thermally activated delayed fluorescence (TADF) organic molecules for efficient X-ray scintillation and imaging, *Nat. Mater.* 21 (2) (2022) 210–, <https://doi.org/10.1038/s41563-021-01132-x>.
- [3] Y. Fu, H. Liu, B.Z. Tang, Z. Zhao, Realizing efficient blue and deep-blue delayed fluorescence materials with record-beating electroluminescence efficiencies of 43.4, *Nat. Commun.* 14(1) (2023) 2019–2019, <https://doi.org/10.1038/s41467-023-37687-3>.
- [4] H. Su, K. Hu, W.H. Huang, T. Wang, X.L. Zhang, B. Chen, H. Miao, X.P. Zhang, G. Q. Zhang, Functional Roles of Polymers in Room-Temperature Phosphorescent Materials: Modulation of Intersystem Crossing, Air Sensitivity and Biological Activity, *Angew. Chem. Int. Ed.* 62 (12) (2023) e202218712.
- [5] L.L. Liang, J.Y. Chen, K. Shao, X. Qin, Z.F. Pan, X.G. Liu, Controlling persistent luminescence in nanocrystalline phosphors, *Nat. Mater.* 22 (3) (2023) 289–304, <https://doi.org/10.1038/s41563-022-01468-y>.
- [6] C. Qian, Z.M. Ma, X.H. Fu, X. Zhang, Z.W. Li, H.W. Jin, M.X. Chen, H. Jiang, X. R. Jia, Z.Y. Ma, More than Carbazole Derivatives Activate Room Temperature Ultralong Organic Phosphorescence of Benzoinole Derivatives, *Adv. Mater.* 34 (19) (2022) e2200544.
- [7] Z. Li, Q. Pei, Y. Zheng, Z. Xie, M. Zheng, Carbon dots for long-term near-infrared afterglow imaging and photodynamic therapy, *Chem. Eng. J.* 467 (2023) 143384.
- [8] W.J. Zhao, Z.K. He, B.Z. Tang, Room-temperature phosphorescence from organic aggregates, *Nat. Rev. Mater.* 5 (12) (2020) 869–885, <https://doi.org/10.1038/s41578-020-0223-z>.
- [9] L.u. Yang, S. Gai, H.e. Ding, D. Yang, L. Feng, P. Yang, Recent Progress in Inorganic Afterglow Materials: Mechanisms, Persistent Luminescent Properties, Modulating Methods, and Bioimaging Applications, *Adv. Opt. Mater.* 11 (11) (2023), <https://doi.org/10.1002/adom.202202382>.
- [10] J. Liu, T. Kong, H.-M. Xiong, Mulberry-Leaves-Derived Red-Emissive Carbon Dots for Feeding Silkworms to Produce Brightly Fluorescent Silk, *Adv. Mater.* 34 (16) (2022) e2200152.
- [11] H. Hou, C.E. Banks, M. Jing, Y. Zhang, X. Ji, Carbon Quantum Dots and Their Derivative 3D Porous Carbon Frameworks for Sodium-Ion Batteries with Ultralong Cycle Life, *Adv. Mater.* 27 (47) (2015) 7861–7866, <https://doi.org/10.1002/adma.201503816>.
- [12] L. Ai, Z. Song, M. Nie, J. Yu, F. Liu, H. Song, B. Zhang, G.L.N. Waterhouse, S. Lu, Solid-state Fluorescence from Carbon Dots Widely Tunable from Blue to Deep Red through Surface Ligand Modulation, *Angew. Chem. Int. Ed.* 62 (12) (2023) e202217822.
- [13] Y. Ding, X. Wang, M. Tang, H. Qiu, Tailored Fabrication of Carbon Dot Composites with Full-Color Ultralong Room-Temperature Phosphorescence for Multidimensional Encryption, *Adv. Sci.* 9 (3) (2022) 2103833.
- [14] P. Long, Y. Feng, C. Cao, Y.u. Li, J. Han, S. Li, C. Peng, Z. Li, W. Feng, Self-Protective Room-Temperature Phosphorescence of Fluorine and Nitrogen Codoped Carbon Dots, *Adv. Funct. Mater.* 28 (37) (2018) 1800791.
- [15] K. Jiang, L. Zhang, J. Lu, C. Xu, C. Cai, H. Lin, Triple-Mode Emission of Carbon Dots: Applications for Advanced Anti-Counterfeiting, *Angew. Chem. Int. Ed.* 55 (25) (2016) 7231–7235.
- [16] Y. Zheng, H. Wei, P. Liang, X. Xu, X. Zhang, H. Li, C. Zhang, C. Hu, X. Zhang, B. Lei, W.-Y. Wong, Y. Liu, J. Zhuang, Near-Infrared-Excited Multicolor Afterglow in Carbon Dots-Based Room-Temperature Afterglow Materials, *Angew. Chem. Int. Ed.* 60 (41) (2021) 22253–22259.
- [17] Y.-C. Liang, Q. Cao, K.-K. Liu, X.-Y. Peng, L.-Z. Sui, S.-P. Wang, S.-Y. Song, X.-Y. Wu, W.-B. Zhao, Y. Deng, Q. Lou, L. Dong, C.-X. Shan, Phosphorescent Carbon-Nanodots-Assisted Forster Resonant Energy Transfer for Achieving Red Afterglow in an Aqueous Solution, *ACS Nano* 15 (10) (2021) 16242–16254, <https://doi.org/10.1021/acsnano.1c05234>.
- [18] L. Mo, H. Liu, Z. Liu, X. Xu, B. Lei, J. Zhuang, Y. Liu, C. Hu, Cascade Resonance Energy Transfer for the Construction of Nanoparticles with Multicolor Long Afterglow in Aqueous Solutions for Information Encryption and Bioimaging, *Adv. Opt. Mater.* 10 (10) (2022) 2102666.
- [19] Z. Song, Y. Shang, Q. Lou, J. Zhu, J. Hu, W. Xu, C. Li, X. Chen, K. Liu, C.-X. Shan, X. Bai, A Molecular Engineering Strategy for Achieving Blue Phosphorescent Carbon Dots with Outstanding Efficiency above 50%, *Adv. Mater.* 35 (6) (2023) e2207970.
- [20] Y. Sun, X. Zhang, J. Zhuang, H. Zhang, C. Hu, M. Zheng, B. Lei, Y. Liu, The room temperature afterglow mechanism in carbon dots: Current state and further guidance perspective, *Carbon* 165 (2020) 306–316, <https://doi.org/10.1016/j.carbon.2020.04.030>.
- [21] B. Wang, S. Lu, The light of carbon dots: From mechanism to applications, *Matter* 5 (1) (2022) 110–149, <https://doi.org/10.1016/j.matt.2021.10.016>.

- [22] M. Lei, J. Zheng, Y. Yang, L. Yan, X. Liu, B. Xu, Carbon dots-based delayed fluorescent materials: Mechanism, structural regulation and application, *Science* 25 (9) (2022) 104884.
- [23] Q.i. Feng, Z. Xie, M. Zheng, Colour-tunable ultralong-lifetime room temperature phosphorescence with external heavy-atom effect in boron-doped carbon dots, *Chem. Eng. J.* 420 (2021) 127647.
- [24] K. Jiang, Y. Wang, C. Cai, H. Lin, Conversion of Carbon Dots from Fluorescence to Ultralong Room-Temperature Phosphorescence by Heating for Security Applications, *Adv. Mater.* 30 (26) (2018) e1800783.
- [25] J. Tan, Q. Li, S. Meng, Y. Li, J. Yang, Y. Ye, Z. Tang, S. Qu, X. Ren, Time-Dependent Phosphorescence Colors from Carbon Dots for Advanced Dynamic Information Encryption, *Adv. Mater.* 33 (16) (2021) 2006781.
- [26] J. Shen, B. Xu, Z. Wang, J. Zhang, W. Zhang, Z. Gao, X. Wang, C. Zhu, X. Meng, Aggregation-induced room temperature phosphorescent carbonized polymer dots with wide-range tunable lifetimes for optical multiplexing, *J. Mater. Chem. C* 9 (21) (2021) 6781–6788, <https://doi.org/10.1039/d1tc01057c>.
- [27] L. Mo, X. Xu, Z. Liu, H. Liu, B. Lei, J. Zhuang, Z. Guo, Y. Liu, C. Hu, Visible-light excitable thermally activated delayed fluorescence in aqueous solution from F, N-doped carbon dots confined in silica nanoparticles, *Chem. Eng. J.* 426 (2021) 130728.
- [28] Q. Li, M. Zhou, Q. Yang, Q. Wu, J. Shi, A. Gong, M. Yang, Efficient Room-Temperature Phosphorescence from Nitrogen-Doped Carbon Dots in Composite Matrices, *Chem. Mater.* 28 (22) (2016) 8221–8227, <https://doi.org/10.1021/acs.chemmater.6b03049>.
- [29] Q. Li, M. Zhou, M. Yang, Q. Yang, Z. Zhang, J. Shi, Induction of long-lived room temperature phosphorescence of carbon dots by water in hydrogen-bonded matrices, *Nat. Commun.* 9 (2018), <https://doi.org/10.1038/s41467-018-03144-9>.
- [30] K. Jiang, Y. Wang, C. Cai, H. Lin, Activating Room Temperature Long Afterglow of Carbon Dots via Covalent Fixation, *Chem. Mater.* 29 (11) (2017) 4866–4873, <https://doi.org/10.1021/acs.chemmater.7b00831>.
- [31] J. Liu, N. Wang, Y. Yu, Y. Yan, H. Zhang, J. Li, J. Yu, Carbon dots in zeolites: A new class of thermally activated delayed fluorescence materials with ultralong lifetimes, *Sci. Adv.* 3 (5) (2017), <https://doi.org/10.1126/sciadv.1603171>.
- [32] W. Li, W. Zhou, Z. Zhou, H. Zhang, X. Zhang, J. Zhuang, Y. Liu, B. Lei, C. Hu, A Universal Strategy for Activating the Multicolor Room-Temperature Afterglow of Carbon Dots in a Boric Acid Matrix, *Angew. Chem. Int. Ed.* 58 (22) (2019) 7278–7283, <https://doi.org/10.1002/anie.201814629>.
- [33] S. Tao, S. Lu, Y. Geng, S. Zhu, S.A.T. Redfern, Y. Song, T. Feng, W. Xu, B. Yang, Design of Metal-Free Polymer Carbon Dots: A New Class of Room-Temperature Phosphorescent Materials, *Angew. Chem. Int. Ed.* 57 (9) (2018) 2393–2398, <https://doi.org/10.1002/anie.201712662>.
- [34] Y.H. Deng, D.X. Zhao, X. Chen, F. Wang, H. Song, D.Z. Shen, Long lifetime pure organic phosphorescence based on water soluble carbon dots, *Chem. Commun.* 49 (51) (2013) 5751–5753, <https://doi.org/10.1039/c3cc42600a>.
- [35] X.W. Dong, L.M. Wei, Y.J. Su, Z.L. Li, H.J. Geng, C. Yang, Y.F. Zhang, Efficient long lifetime room temperature phosphorescence of carbon dots in a potash alum matrix, *J. Mater. Chem. C* 3 (12) (2015) 2798–2801, <https://doi.org/10.1039/c5tc00126a>.
- [36] J. Hou, L. Wang, P. Zhang, Y. Xu, L. Ding, Facile synthesis of carbon dots in an immiscible system with excitation-independent emission and thermally activated delayed fluorescence, *Chem. Commun.* 51 (100) (2015) 17768–17771, <https://doi.org/10.1039/c5cc08152a>.
- [37] T. Yuan, F.L. Yuan, X.H. Li, Y.C. Li, L.Z. Fan, S.H. Yang, Fluorescence-phosphorescence dual emissive carbon nitride quantum dots show 25% white emission efficiency enabling single-component WLEDs, *Chem. Sci.* 10 (42) (2019) 9801–9806, <https://doi.org/10.1039/c9sc03492g>.
- [38] J. Zhu, X. Bai, X. Chen, H.e. Shao, Y. Zhai, G. Pan, H. Zhang, E.V. Ushakova, Y. u. Zhang, H. Song, A.L. Rogach, Spectrally Tunable Solid State Fluorescence and Room-Temperature Phosphorescence of Carbon Dots Synthesized via Seeded Growth Method, *Adv. Opt. Mater.* 7 (9) (2019) 1801599.
- [39] C. Lin, Y. Zhuang, W. Li, T.-L. Zhou, R.-J. Xie, Blue, green, and red full-color ultralong afterglow in nitrogen-doped carbon dots, *Nanoscale* 11 (14) (2019) 6584–6590, <https://doi.org/10.1039/c8nr09672d>.
- [40] Q. Lou, N. Chen, J. Zhu, K. Liu, C. Li, Y. Zhu, W. Xu, X. Chen, Z. Song, C. Liang, C.-X. Shan, J. Hu, Thermally Enhanced and Long Lifetime Red TADF Carbon Dots via Multi-Confinement and Phosphorescence Assisted Energy Transfer, *Adv. Mater.* 35 (20) (2023) e2211858, <https://doi.org/10.1002/adma.202211858>.
- [41] S.-Y. Song, K.-K. Liu, X. Mao, Q. Cao, N. Li, W.-B. Zhao, Y. Wang, Y.-C. Liang, J.-H. Zang, X. Li, Q. Lou, L. Dong, C.-X. Shan, Colorful Triplet Excitons in Carbon Nanodots for Time Delay Lighting, *Adv. Mater.* 35 (21) (2023) e2212286, <https://doi.org/10.1002/adma.202212286>.
- [42] Q.i. Feng, Z. Xie, M. Zheng, Room temperature phosphorescent carbon dots for latent fingerprints detection and in vivo phosphorescence bioimaging, *Sensors and Actuators B-Chemical* 351 (2022) 130976, <https://doi.org/10.1016/j.snb.2021.130976>.
- [43] S. Zong, B. Wang, X. Yin, W. Ma, J. Zhang, J. Li, Calcination-controlled fabrication of carbon dots@zeolite composites with multicolor fluorescence and phosphorescence, *Nano Res.* 15 (10) (2022) 9454–9460, <https://doi.org/10.1007/s12274-022-4558-1>.
- [44] C. Xia, S. Zhu, S.-T. Zhang, Q. Zeng, S. Tao, X. Tian, Y. Li, B. Yang, Carbonized Polymer Dots with Tunable Room-Temperature Phosphorescence Lifetime and Wavelength, *ACS Appl. Mater. Interfaces* 12 (34) (2020) 38593–38601, <https://doi.org/10.1021/acsami.0c11867>.
- [45] Z. Wang, J. Shen, B. Xu, Q. Jiang, S. Ming, L. Yan, Z. Gao, X. Wang, C. Zhu, X. Meng, Thermally Driven Amorphous-Crystalline Phase Transition of Carbonized Polymer Dots for Multicolor Room-Temperature Phosphorescence, *Adv. Opt. Mater.* 9 (16) (2021) 2100421, <https://doi.org/10.1002/adom.202100421>.
- [46] Q. Li, D. Cheng, H. Gu, D. Yang, Y. Li, S. Meng, Y. Zhao, Z. Tang, Y. Zhang, J. Tan, S. Qu, Aggregation-induced color fine-tunable carbon dot phosphorescence covering from green to near-infrared for advanced information encryption, *Chem. Eng. J.* 462 (2023), 142339, <https://doi.org/10.1016/j.cej.2023.142339>.
- [47] Z. Yan, T. Chen, L. Yan, X. Liu, J. Zheng, F.-D. Ren, Y. Yang, B. Liu, X. Liu, B. Xu, One-Step Synthesis of White-Light-Emitting Carbon Dots for White LEDs with a High Color Rendering Index of 97, *Adv. Sci.* 10 (12) (2023) e2206386, <https://doi.org/10.1002/adv.202206386>.
- [48] X. Xu, L. Mo, Y. Li, X. Pan, G. Hu, B. Lei, X. Zhang, M. Zheng, J. Zhuang, Y. Liu, C. Hu, Construction of Carbon Dots with Color-Tunable Aggregation-Induced Emission by Nitrogen-Induced Intramolecular Charge Transfer, *Adv. Mater.* 33 (49) (2021) 2104872, <https://doi.org/10.1002/adma.202104872>.
- [49] S.-Y. Song, K.-K. Liu, Q. Cao, X. Mao, W.-B. Zhao, Y. Wang, Y.-C. Liang, J.-H. Zang, Q. Lou, L. Dong, C.-X. Shan, Ultraviolet phosphorescent carbon nanodots, *Light: Sci. Appl.* 11 (1) (2022), <https://doi.org/10.1038/s41377-022-00837-1>.
- [50] Y. Chen, M. Zheng, Y. Xiao, H. Dong, H. Zhang, J. Zhuang, H. Hu, B. Lei, Y. Liu, A Self-Quenching-Resistant Carbon-Dot Powder with Tunable Solid-State Fluorescence and Construction of Dual-Fluorescence Morphologies for White Light Emission, *Adv. Mater.* 28 (2) (2016) 312–318, <https://doi.org/10.1002/adma.201503380>.
- [51] A.K. Patra, A. Dutta, A. Bhauik, Self-assembled mesoporous gamma-Al<sub>2</sub>O<sub>3</sub> spherical nanoparticles and their efficiency for the removal of arsenic from water, *J. Hazard. Mater.* 201 (2012) 170–177, <https://doi.org/10.1016/j.jhazmat.2011.11.056>.
- [52] J. He, Y. Chen, Y. He, X. Xu, B. Lei, H. Zhang, J. Zhuang, C. Hu, Y. Liu, Anchoring Carbon Nanodots onto Nanosilica for Phosphorescence Enhancement and Delayed Fluorescence Nascence in Solid and Liquid States, *Small* 16 (49) (2020), <https://doi.org/10.1002/sml.202005228>.
- [53] W. Ge, P. Zhang, X. Zhang, W. Gao, C. Lu, Y. Ge, Amorphous Alumina: A Bright Red Matrix for Flexible and Transparent Anti-counterfeiting, *ACS Sustain. Chem. Eng.* 9 (30) (2021) 10220–10226, <https://doi.org/10.1021/acssuschemeng.1c02541>.
- [54] Z. Song, Y. Liu, X. Lin, Z. Zhou, X. Zhang, J. Zhuang, B. Lei, C. Hu, Multiemissive Room-Temperature Phosphorescent Carbon Dots@ZnAl<sub>2</sub>O<sub>4</sub> Composites by Inorganic Defect Triplet-State Energy Transfer, *ACS Appl. Mater. Interfaces* 13 (29) (2021) 34705–34713, <https://doi.org/10.1021/acsami.1c07391>.
- [55] Z. Wan, Y. Li, Y. Zhou, D. Peng, X. Zhang, J. Zhuang, B. Lei, Y. Liu, C. Hu, High-Efficiency Solid-State Luminescence from Hydrophilic Carbon Dots with Aggregation-Induced Emission Characteristics, *Adv. Funct. Mater.* 33 (11) (2023), <https://doi.org/10.1002/adfm.202207296>.
- [56] Y. Sun, J. Liu, X. Pang, X. Zhang, J. Zhuang, H. Zhang, C. Hu, M. Zheng, B. Lei, Y. Liu, Temperature-responsive conversion of thermally activated delayed fluorescence and room-temperature phosphorescence of carbon dots in silica, *J. Mater. Chem. C* 8 (17) (2020) 5744–5751, <https://doi.org/10.1039/d0tc00507j>.
- [57] M. Xu, C. Dong, J. Xu, S.U. Rehman, Q. Wang, V.Y. Osipov, K. Jiang, J. Wang, H. Bi, Fluorinated carbon dots/carboxyl methyl cellulose sodium composite with a temperature-sensitive fluorescence/phosphorescence applicable for anti-counterfeiting marking, *Carbon* 189 (2022) 459–466, <https://doi.org/10.1016/j.carbon.2021.12.077>.
- [58] J. Liu, H. Zhang, N. Wang, Y. Yu, Y. Cui, J. Li, J. Yu, Template-Modulated Afterglow of Carbon Dots in Zeolites: Room-Temperature Phosphorescence and Thermally Activated Delayed Fluorescence, *ACS Mater. Lett.* 1 (1) (2019) 58–63, <https://doi.org/10.1021/acsmaterialslett.9b00073>.
- [59] B.H. Zhang, B.Z. Wang, E.V. Ushakova, B.C. He, G.C. Xing, Z.K. Tang, A.L. Rogach, S.N. Qu, Assignment of Core and Surface States in Multicolor-Emissive Carbon Dots, *Small* (2022) e2204158.
- [60] C. Zhang, J. Lin, Defect-related luminescent materials: synthesis, emission properties and applications, *Chem. Soc. Rev.* 41 (23) (2012) 7938–7961, <https://doi.org/10.1039/c2cs35215j>.
- [61] Y. Du, W. Cai, C. Mo, J. Chen, L. Zhang, X. Zhu, Preparation and photoluminescence of alumina membranes with ordered pore arrays, *Appl. Phys. Lett.* 74(20) (1999) 2951–2953.
- [62] Y. Li, G.H. Li, G.W. Meng, L.D. Zhang, F. Philipp, Photoluminescence and optical absorption caused by the F<sup>+</sup> centres in anodic alumina membranes, *J. Phys. Condens. Matter* 13 (11) (2001) 2691–2699.
- [63] J. Wang, N. Chen, G. Bian, X. Mu, N. Du, W. Wang, C.-G. Ma, S. Fu, B. Huang, T. Liu, Y. Yang, Q. Yuan, Solar-Driven Overproduction of Biofuels in Microorganisms, *Angew. Chem. Int. Ed.* 61 (32) (2022), <https://doi.org/10.1002/anie.202207132>.
- [64] Z. Bai, L. Hao, Z. Zhang, Z. Huang, S. Qin, Enhanced photoluminescence of corrugated Al<sub>2</sub>O<sub>3</sub> film assisted by colloidal CdSe quantum dots, *Nanotechnol.* 28 (20) (2017) 205206.
- [65] W. Shi, J. Yao, L. Bai, C. Lu, Defect-Stabilized Triplet State Excitons: Toward Ultralong Organic Room-Temperature Phosphorescence, *Adv. Funct. Mater.* 28 (52) (2018) 1804961.
- [66] H.-Y. Wang, L.u. Zhou, H.-M. Yu, X.-D. Tang, C. Xing, G. Nie, H. Akafzade, S.-Y. Wang, W. Chen, Exploration of Room-Temperature Phosphorescence and New Mechanism on Carbon Dots in a Polyacrylamide Platform and their Applications for Anti-Counterfeiting and Information Encryption, *Adv. Opt. Mater.* 10 (15) (2022) 2200678.
- [67] J. Yao, J. Kong, L. Kong, X. Wang, W. Shi, C. Lu, The phosphorescence nanocomposite thin film with rich oxygen vacancy: Towards sensitive oxygen

- sensor, Chin. Chem. Lett. 33 (8) (2022) 3977–3980, <https://doi.org/10.1016/j.ccl.2021.11.003>.
- [68] B.-M. Liu, R. Zou, S.-Q. Lou, Y.-F. Gao, L.i. Ma, K.-L. Wong, J. Wang, Low-dose X-ray-stimulated LaGaO<sub>3</sub>:Sb, Cr near-infrared persistent luminescence nanoparticles for deep-tissue and renewable in vivo bioimaging, Chem. Eng. J. 404 (2021) 127133.
- [69] P. Xiong, C. Zheng, M. Peng, Z. Zhou, F. Xu, K. Qin, Y. Hong, Z. Ma, Self-activated persistent luminescence from Ba(2)Zr(2)Si(3)O(12) for information storage, J. Am. Ceram. Soc. 103 (12) (2020) 6922–6931, <https://doi.org/10.1111/jace.17412>.



# Carbon Dots as a Protective Agent Alleviating Abiotic Stress on Rice (*Oryza sativa* L.) through Promoting Nutrition Assimilation and the Defense System

Yadong Li, Junmei Gao, Xiaokai Xu, Ying Wu, Jianle Zhuang, Xuejie Zhang, Haoran Zhang, Bingfu Lei, Mingtao Zheng,\* Yingliang Liu,\* and Chaofan Hu\*

Cite This: <https://dx.doi.org/10.1021/acsami.0c11724>

Read Online

ACCESS |

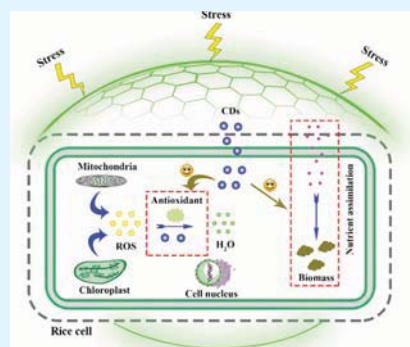
Metrics & More

Article Recommendations

Supporting Information

**ABSTRACT:** Abiotic stress severely threatens agriculture. Herein, we studied the effect of heteroatom-free carbon dots (CDs) on the alleviation of abiotic stresses in rice for the first time. During in vitro coincubation, suspended rice cells were exposed to 2,4-dichlorophenoxyacetate sodium (2,4-D-Na, 30  $\mu\text{g mL}^{-1}$ ), 2,4-dichlorophenoxyacetic acid (2,4-D, 5  $\mu\text{g mL}^{-1}$ ), NaCl (0.15  $\text{mol L}^{-1}$ ), and high light (2000 Lux), both with and without CDs (100  $\mu\text{g mL}^{-1}$ ). After a week, CDs significantly reduced the inhibition rate of 2,4-D-Na on the rice cell biomass from 48.16 to 27.44% and increased the biomass of rice cells exposed to 2,4-D, NaCl, and high light, by 4.12, 1.10, and 4.01 times that of the control (pure nutrient medium), respectively. Furthermore, the growth of CD-germinated rice seedlings was not obviously affected by 2,4-D-Na, 2,4-D, and NaCl. Further results showed that the CDs demonstrated an intrinsic free-radical scavenging property and could increase the peroxidase activity and the contents of phenolics and flavonoids in rice by 125.81, 39.60, and 47.63%, respectively. Furthermore, CDs improved the nutrient assimilation of rice cells under 2,4-D stress by 14.69%. With higher antioxidant capacity and sufficient nutrients, the CD-treated rice showed excellent resistance to abiotic stresses. This study suggested the great potential of CDs in protecting crops against abiotic stress.

**KEYWORDS:** carbon dots, abiotic stress, 2,4-dichlorophenoxyacetic acid, nutrition assimilation, antioxidant defense



## INTRODUCTION

In the wake of population growth and industrial development, agriculture is facing a severe challenge to increase food production.<sup>1</sup> However, more than 90% of the global land area is threatened by various abiotic stresses (drought, cold, salt, strong solar radiation, abuse of pesticides, etc.), which leads to about half of the crop yield loss worldwide.<sup>2</sup> The adverse environmental conditions are expected to be exacerbated because of the changing climate in the future.<sup>2</sup> An increase in the generation of various reactive oxygen species (ROS) and oxidative damage to proteins, lipids, carbohydrates, and DNA are common consequences of abiotic stresses on plants.<sup>3</sup> Although plants have evolved complex self-protective mechanisms to scavenge ROS, including enzymatic (superoxide dismutase, SOD; catalase, CAT; peroxidase, POD, etc.) and nonenzymatic (phenolic, flavonoid, ascorbate, and glutathione) antioxidant systems,<sup>4</sup> severe abiotic stress conditions can easily break the ROS/antioxidant homeostasis in plants, leading to oxidative damage.<sup>4</sup> Exogenous plant growth regulators (brassinosteroids,<sup>5</sup> melatonin,<sup>6,7</sup> etc.) and some specific beneficial microorganisms<sup>8,9</sup> can alleviate the abiotic stress on the crop. However, the efficacy of growth regulators is largely affected by the environmental conditions,<sup>10</sup> and

microorganisms usually have a low population or lack catabolic capacity under adverse environmental conditions.<sup>11</sup>

Recently, nanomaterials have been proved to counter abiotic stress-induced oxidative damage to plants as they can mimic the role of antioxidant enzymes.<sup>12</sup> However, the effect of several nanomaterials on plants is ambiguous and controversial because of their toxicity.<sup>12,13</sup> For example, titanium dioxide ( $\text{TiO}_2$ ) nanoparticles could improve the growth and the tolerance of bean plants under saline stress<sup>14</sup> but lead to a reduction in root growth in onions and radishes.<sup>15</sup> Carbon dots (CDs) are among the latest discovered carbon nanomaterials possessing low cost, biocompatibility, nontoxicity, water solubility, and chemical inertness. Recently, CDs have been reported to enhance the growth and photosynthesis of plants.<sup>16–18</sup> CDs can also be degraded to plant-hormone analogs and  $\text{CO}_2$  in rice plants in which the hormone analogs

Received: June 28, 2020

Accepted: July 2, 2020

Published: July 2, 2020

Scheme 1. Schematic Illustration of the Formation Mechanism of the CDs

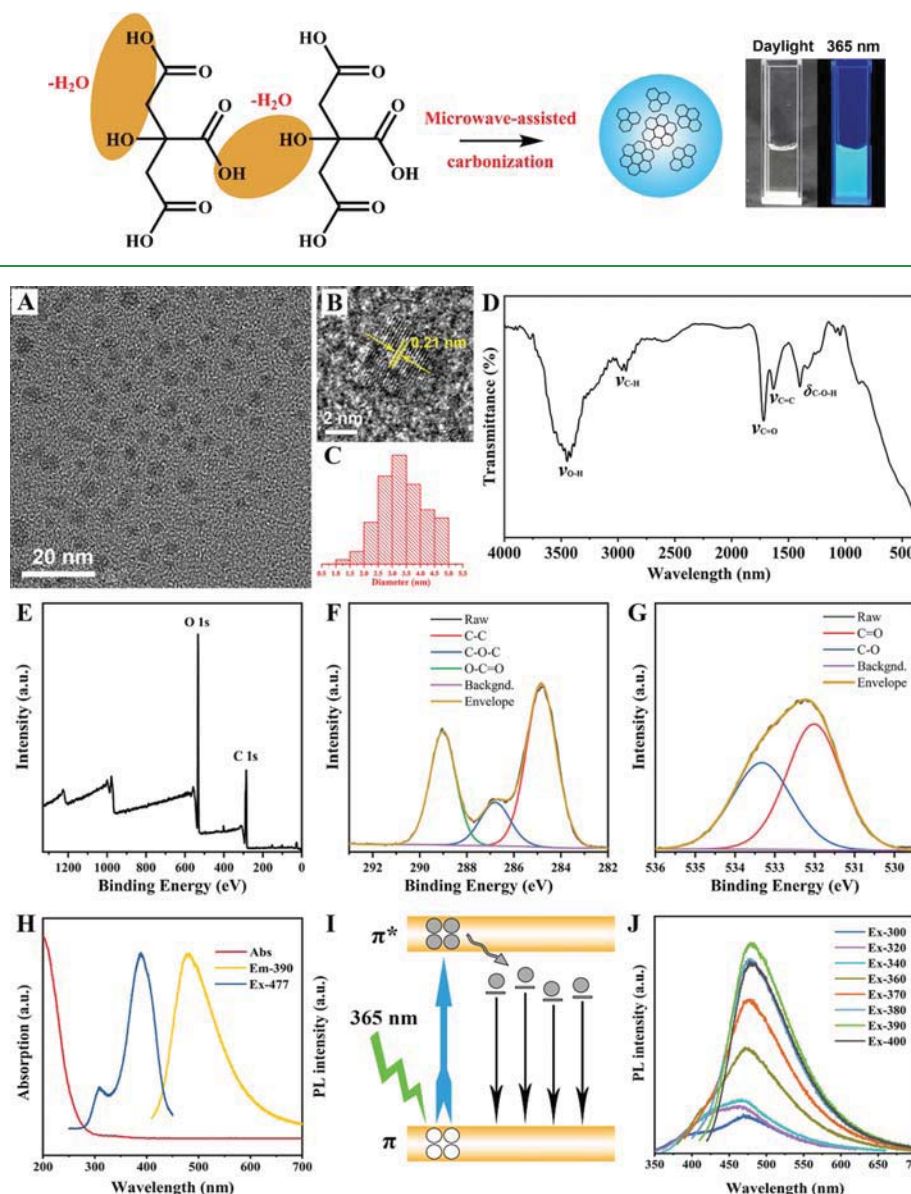


**Figure 1.** (A) HRTEM image, (B) lattice fringe image, (C) size distribution, (D) FTIR spectrum, (E) full XPS pattern, high-resolution XPS spectra of (F) C 1s and (G) O 1s, (H) UV/Vis absorbance (red line), FL excitation (blue line), and FL emission (yellow line) spectra, (I) representation of the FL mechanism, and (J) FL emission spectra at different excitation wavelengths of the prepared CDs.

can promote the growth and  $\text{CO}_2$  is converted into carbohydrates through the Calvin cycle of photosynthesis.<sup>16</sup> Furthermore, CDs are rich in defects and unpaired electrons on their surface, which can act as proton donors to quench free radicals.<sup>19–21</sup> Thus, CDs are a promising alternative to protect plants from abiotic stress by scavenging ROS. However, the CDs used to scavenge free radicals are doped with heteroatoms and it is difficult to distinguish whether CDs or heteroatoms play the key roles in scavenging free radicals. In addition, there is no literature about using heteroatom-free CDs for the in vivo protection of plants from abiotic stress.

In this study, stable and high-yield CDs without heteroatoms were prepared to protect the plant from abiotic stress. Rice (*Oryza sativa* L.) was used as a model because of its important

role in feeding more than half of the world's population.<sup>22</sup> Rice cell suspensions and rice seedlings were exposed to salt, light, and herbicides with different modes of action, including 2,4-dichlorophenoxyacetic acid (2,4-D), 2,4-D sodium salt (2,4-D-Na), 41% glyphosate isopropylamine (IPA) salt, and pendimethalin emulsifiable concentrate (PM-EC). This study indicated that CDs, an important part of the modern field of nanotechnology, may have a promising future as a novel plant protective agent against abiotic stress in agriculture.

## RESULTS AND DISCUSSION

**Preparation and Characterization of CDs.** Chemically stable CDs with a yield of up to 60.6% were prepared using citric acid (CA) by a microwave-assisted method as shown in

B

<https://dx.doi.org/10.1021/acsami.0c11724>  
ACS Appl. Mater. Interfaces XXXX, XXX, XXX–XXX

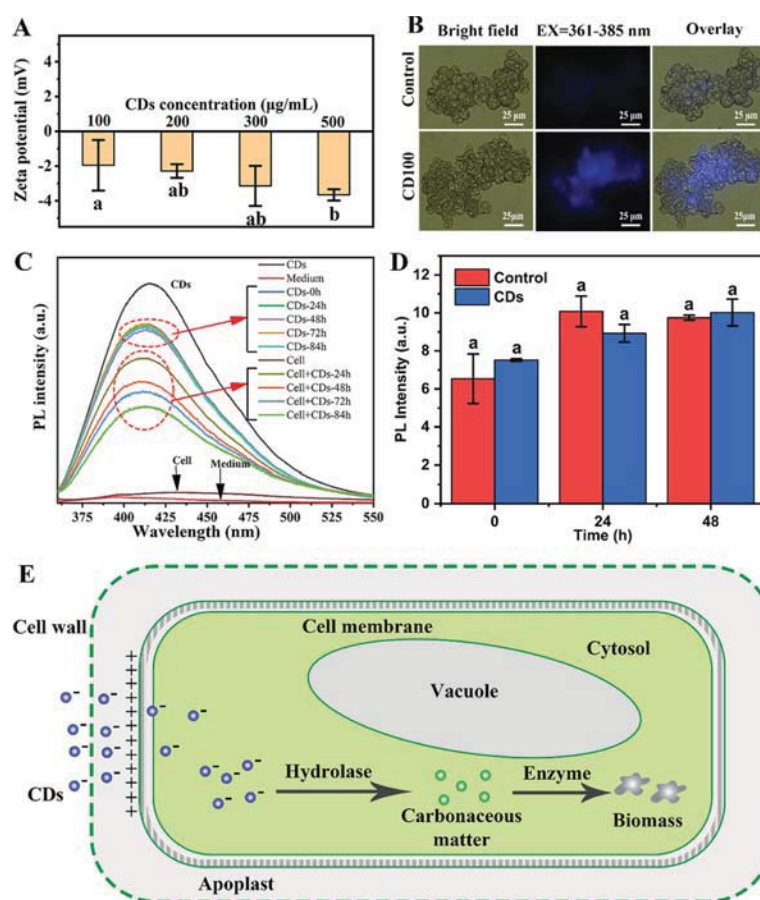


**Figure 2.** (A) Zeta potential of the CDs; (B) fluorescence images of rice cells from control and CD treatments; (C) fluorescence decay of the liquid medium incubated with and without rice cells; (D) fluorescence intensity of the cytoplasm of rice cells from control and CD treatments at an interval of 24 h; and (E) schematic showing the uptake and fate of CDs in rice cells. Error bars correspond to SD ( $n = 5$ ). Marked with the same letter indicating the insignificant difference ( $p < 0.05$ ).

**Scheme 1.** During the reaction, CA molecules underwent intermolecular/intramolecular dehydration between the hydroxyl and carboxyl groups and then were carbonized to form CDs.<sup>23</sup> Under the excitation of 365 nm light, the CDs emitted cyan fluorescence and the obtained CDs remained stable in water for more than 8 months without precipitation in an ambient environment. Such chemical stability contributes to their application in the biological field. High-resolution transmission electron microscopy (HRTEM) images showed that the CDs were tori-spherical and monodispersed nanoparticles with an average size of  $3.38 \pm 0.74$  nm (Figure 1A,C). A lattice spacing of 0.21 nm, discernable in Figure 1B, was attributed to the (100) in-plane lattice spacing of graphite.<sup>24</sup> The X-ray diffraction spectrum of the CDs showed a broad diffraction peak centered at a  $2\theta$  value of  $20.28^\circ$  (Figure S1), indicating the amorphous structure of the CDs.

Fourier transform infrared (FTIR) spectroscopy and X-ray photoelectron spectroscopy (XPS) were employed to further study the composition of the CDs. The strong and broad peak at  $3450\text{ cm}^{-1}$  in the FTIR spectrum resulted from the stretching vibration of  $-\text{OH}$ . The typical peaks around 2927, 1718, and  $1631\text{ cm}^{-1}$  were ascribed to the stretching vibration of  $\text{C}-\text{H}$ ,  $\text{C}=\text{O}$ , and  $\text{C}=\text{C}$ , and the peak at  $1400\text{ cm}^{-1}$  was assigned to the in-plane bending vibrations of  $-\text{OH}$  (Figure 1D).<sup>25</sup> XPS results (Figure 1E) showed the major elements of

carbon (C 1 s at 284 eV) and oxygen (O 1 s at 532 eV) in the CDs. The C 1 s band was deconvoluted into  $\text{sp}^2$  C in  $\text{C}-\text{C}$  at 284.83 eV,  $\text{sp}^3$  C in  $\text{C}-\text{O}$  at 286.8 eV, and  $\text{C}=\text{O}$  at 289.02 eV (Figure 1F).<sup>26</sup> The high-resolution O 1 s XPS spectrum confirmed the presence of  $\text{C}=\text{O}$  and  $\text{C}-\text{O}$  at 532.02 and 533.32 eV, respectively (Figure 1G).<sup>27</sup> These results suggested the presence of hydrophilic  $-\text{OH}$  and  $-\text{COOH}$  groups on the surface of the CDs, resulting in a hydrodynamic diameter of the CDs as large as 175.12 nm (Figure S2), thereby increasing the buoyant force and viscous force subjected by the CDs.<sup>28</sup> Therefore, the CDs could be kept in a stable colloidal state.

As shown in Figure 1H, the ultraviolet–visible (UV–vis) spectrum of CDs showed a strong absorption peak at 201 nm, which was assigned to the  $\pi \rightarrow \pi^*$  transition of  $\text{C}=\text{C}$  in the carbon core.<sup>29</sup> The radiative recombination of electron–hole pairs in such  $\text{sp}^2$  clusters mainly determined the fluorescence of the CDs (Figure 1I).<sup>23</sup> In addition, the CD solution exhibited emission at 477 nm with  $\lambda_{\text{max}}$  at 390 nm (Figure 1H). No shift was observed in the emission when the excitation wavelength changed from 280 to 420 nm (Figure 1J), indicating that the CDs possessed a uniform particle size and emission sites.<sup>30</sup> The quantum yields (QYs) of the obtained CDs were measured as about 1.97% using quinine sulfate as a reference (Figure S3).

C

<https://dx.doi.org/10.1021/acsami.0c11724>  
ACS Appl. Mater. Interfaces XXXX, XXX, XXX–XXX



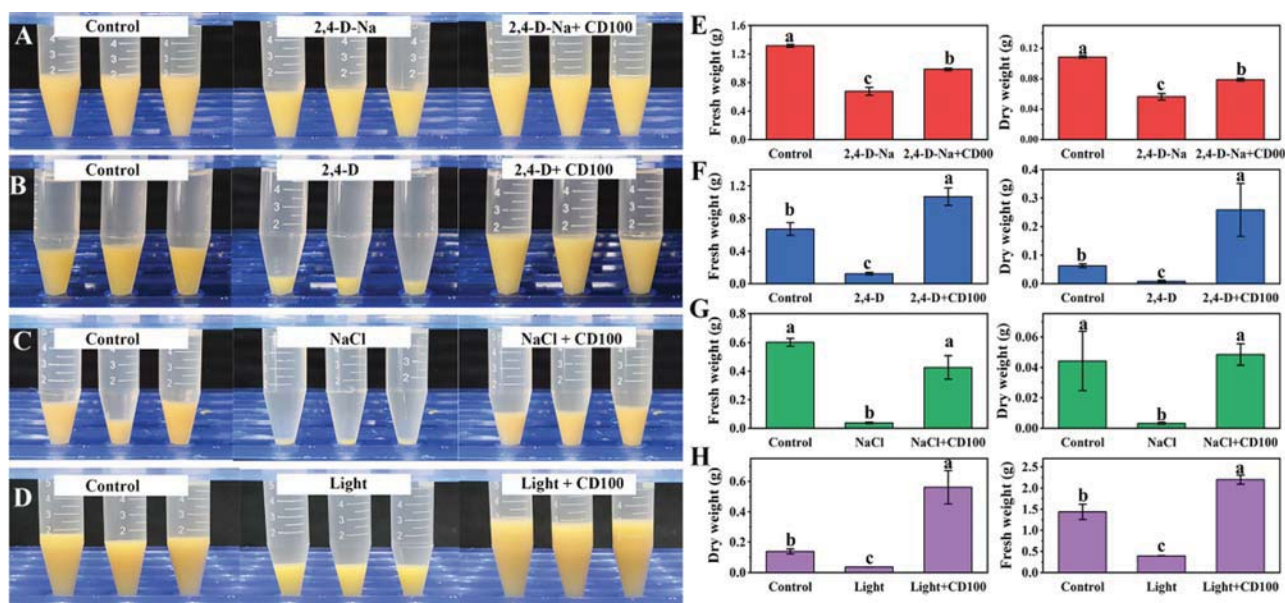


**Figure 3.** (A–D) Photographs of the biomass of rice cells exposed to 2,4-D-Na ( $30 \mu\text{g}\cdot\text{mL}^{-1}$ ), 2,4-D ( $5 \mu\text{g}\cdot\text{mL}^{-1}$ ), NaCl ( $0.15 \text{ M}$ ), and light ( $2000 \text{ LUX}$ ) stress in the presence and absence of CDs ( $100 \mu\text{g}\cdot\text{mL}^{-1}$ ); (E–H) corresponding fresh and dry weights of the rice cells from each treatment. Error bars correspond to SD ( $n = 3$ ). Marked with different letters indicating a significant difference ( $p < 0.05$ ).

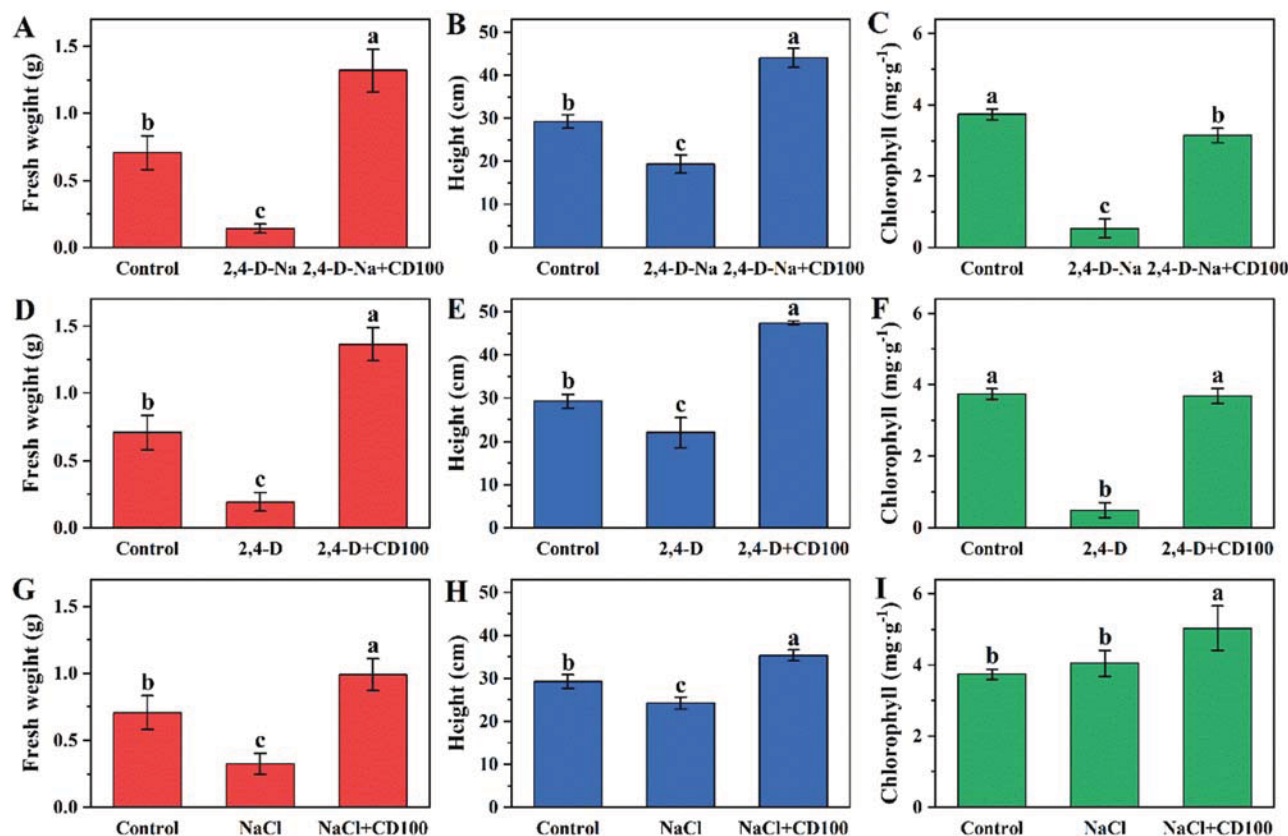


**Figure 4.** (A–I) Fresh weights, height, and chlorophyll content of rice seedlings exposed to 2,4-D-Na ( $30 \mu\text{g}\cdot\text{mL}^{-1}$ ), 2,4-D ( $5 \mu\text{g}\cdot\text{mL}^{-1}$ ), and NaCl ( $0.15 \text{ M}$ ) stress with and without CDs ( $\mu\text{g}\cdot\text{mL}^{-1}$ ). Error bars correspond to SD ( $n = 5$ ). Marked with different letters indicating a significant difference ( $p < 0.05$ ).

**Uptake of CDs in Rice Cells.** To avoid the complex environmental conditions, the suspended rice cell culture was

used as a model to investigate the effect of CDs on rice. First, the uptake of CDs by rice cells was studied by measuring the

D

<https://dx.doi.org/10.1021/acsami.0c11724>  
ACS Appl. Mater. Interfaces XXXX, XXX, XXX–XXX



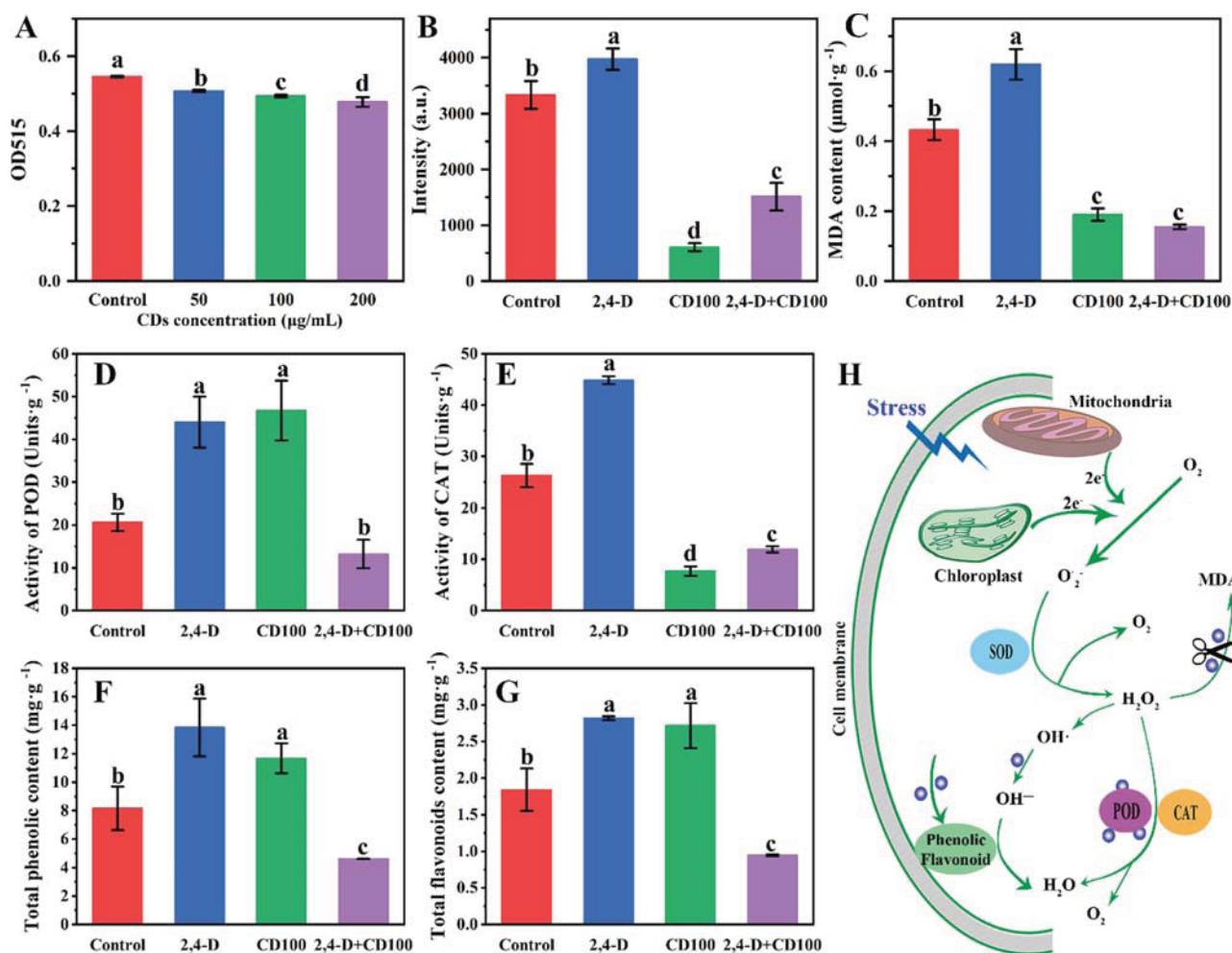


**Figure 5.** (A) Scavenging activity of CDs against free DPPH radicals; (B) fluorescence intensity of rice cells stained with the DCFH-DA probe; (C) MDA contents, (D and E) POD and CAT activities, and total contents of (F) phenolics and (G) flavonoids in the rice cells in different treatments; and (H) mechanisms of CDs promoting the antioxidant ability of the rice cells under abiotic stresses. Error bars are SD ( $n = 3$ ). Marked with different letters indicating a significant difference ( $p < 0.05$ ).

fluorescence signal in the rice cells and the liquid medium. As shown in Figure 2A, the prepared CDs ( $100\text{--}1000\text{ }\mu\text{g}\cdot\text{mL}^{-1}$ ) showed a negatively charged surface from  $-1.96$  to  $-4.65$  mV, contributing to the adsorption on the rice cell surface with a positively charged plasma membrane.<sup>31</sup> With a small size of  $3.38 \pm 0.74$  nm and hydrophilic  $-\text{OH}$  and  $-\text{COOH}$  groups, the CDs could be easily internalized into the rice cells.<sup>31–33</sup> Compared with the control group, the CD-treated ( $100\text{ }\mu\text{g}\cdot\text{mL}^{-1}$ ) rice cells showed a stronger fluorescence signal under the excitation of  $360\text{--}390$  nm with a fluorescence microscope (Figure 2B). Simultaneously, the fluorescence signal from the liquid medium containing rice cells decreased with time, while no significant changes were observed from the incubations without rice cells (Figure 2C). However, no obvious accumulation of the fluorescence signal was observed in the extracted cytoplasm from CD-treated rice cells in a 24 h interval (Figure 2D). Kang et al. previously reported that the horseradish peroxidase in rice plants could degrade CDs into plant-hormone analogs and  $\text{CO}_2$ , which contributed to plant growth.<sup>16</sup> Therefore, it could be inferred that the CDs were first adsorbed on the surface of the rice cells, and then gradually permeated into them. Finally, the CDs were

metabolized by rice cells for their growth (Figure 2E). The adsorption-permeation-degradation of the CDs by rice cells is a continuous process.

**Effect of CDs on Rice Cell Growth and Alleviation of Abiotic Stress.** According to a preliminary experiment (Figure S4),  $100\text{ }\mu\text{g}\cdot\text{mL}^{-1}$  of CDs was optimal for the growth of rice cells; hence, this dose was used in the following investigations. The intensities of different stresses obtained were as follows: salt stress ( $0.15\text{ M}$  of  $\text{NaCl}$ ), light stress ( $2000\text{ LUX}$ ), 2,4-D ( $5\text{ }\mu\text{g}\cdot\text{mL}^{-1}$ ), 2,4-D-Na ( $30\text{ }\mu\text{g}\cdot\text{mL}^{-1}$ ), glyphosate IPA salt ( $0.5\text{ }\mu\text{L}\cdot\text{mL}^{-1}$ ), and PM-EC ( $0.5\text{ }\mu\text{L}\cdot\text{mL}^{-1}$ ) (no data presented). After incubation for a week, CDs reduced the inhibition rates of 2,4-D-Na on the fresh and dry weights of rice cells from 48.52 and 48.16% to 25.16 and 27.38%, respectively (Figure 3A,E). For 2,4-D ( $5\text{ }\mu\text{g}\cdot\text{mL}^{-1}$ ), CDs not only completely alleviated its inhibition rates (81.80% in fresh weight and 87.22% in dry weight) on rice cells, but also increased the fresh and dry weights of rice cells by 59.40 and 312.30% compared with the control (Figure 3B,F). In addition, the salt stress significantly reduced the fresh and dry weights of the rice cells by 93.73 and 92.76%, respectively, which were completely alleviated by CDs (Figure 3C,G). Similar to 2,4-D

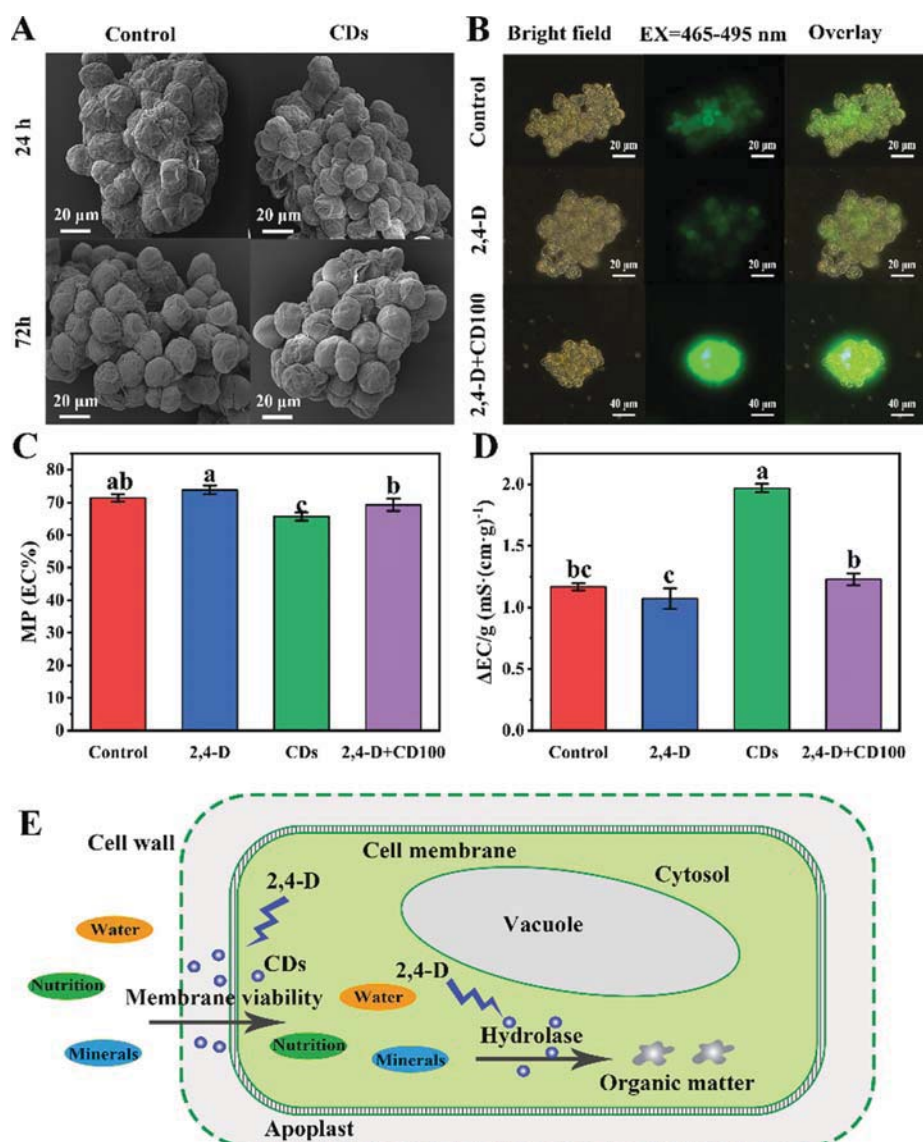


**Figure 6.** (A) SEM images of rice cells from control and CD exposure; (B) cell viabilities of the rice cells; (C) membrane permeability and (D) nutrition uptake rate of the rice cells; and (E) schematic showing the effect of CDs on the nutrition assimilation by rice cells. Error bars are SD ( $n = 5$ ). Marked with different letters indicating a significant difference ( $p < 0.05$ ).

stress, CDs completely alleviated the inhibition of high light stress (72.40% in fresh weight and 73.25% in dry weight) on rice cells and increased their fresh and dry weights by 53.06 and 300.86%, respectively, compared with the control (Figure 3D,H).

The alleviation of the CDs to 2,4-D-Na, 2,4-D, and NaCl was further investigated using rice seedlings. First, the rice seeds were germinated using deionized water and CDs at  $100 \mu\text{g mL}^{-1}$  and then exposed to 2,4-D-Na at  $30 \mu\text{g mL}^{-1}$ , 2,4-D at  $5 \mu\text{g mL}^{-1}$ , and NaCl at 0.15 M under greenhouse conditions for 3 weeks. The results showed that the CD-germinated rice seedlings showed an obvious tolerance to 2,4-D-Na, 2,4-D, and NaCl (Figure S5). As shown in Figure 4, 2,4-D-Na, 2,4-D, and NaCl treatments significantly decreased the fresh weight of the rice seedlings by 80.19, 72.76, and 54.01% and height by 33.88, 24.74, and 17.06% compared with the control. Furthermore, 2,4-D-Na and 2,4-D significantly decreased the chlorophyll content in the treated rice leaf by

85.75 and 86.80% compared with the control, and NaCl showed no obvious influence on it. However, the fresh weight and height of the CD-germinated rice seedlings were not only reduced by 2,4-D-Na, 2,4-D, and NaCl, but also significantly increased by 86.78 and 50.41% in 2,4-D-Na treatment, 92.80 and 62.22% in 2,4-D treatment, and 40.09 and 20.61% in NaCl treatment. For the chlorophyll content in rice seedlings, CDs completely protected it from the inhibition of 2,4-D and increased it by 49.85% compared with 2,4-D-Na treatment. Although NaCl did not significantly influence the chlorophyll content in rice seedlings, CDs increased it by 34.67% compared with the control.

Nevertheless, CDs showed insignificant alleviation on the glyphosate IPA salt ( $0.5 \mu\text{L mL}^{-1}$ ) and PM-EC ( $0.5 \mu\text{L mL}^{-1}$ ) stress (Figure S6). The different results might result from the different action models of these stresses on rice cell growth. Salt and high light stresses inhibited plant growth mainly through inducing overaccumulation of ROS.<sup>34,35</sup> Similarly,

F

<https://dx.doi.org/10.1021/acsami.0c11724>  
ACS Appl. Mater. Interfaces XXXX, XXX, XXX–XXX

ROS-mediated disequilibrium of the enzyme system in the plant was mainly responsible for the inhibition of 2,4-D and 2,4-D-Na in plant growth.<sup>36,37</sup> However, glyphosate IPA salt specifically inhibits the activity of 5-enolpyruvylshikimic-3-phosphate synthase, disturbing the shikimate pathway in the plant.<sup>38</sup> The mitotic sequence is the specific target of PM by inhibiting the production of the microtubule protein.<sup>39</sup> Therefore, we supposed that the alleviation of abiotic stress by CDs could depend on scavenging the intracellular ROS in rice cells. To prove this hypothesis, 2,4-D stress was used as a model to further understand the alleviation of abiotic stress by CDs.

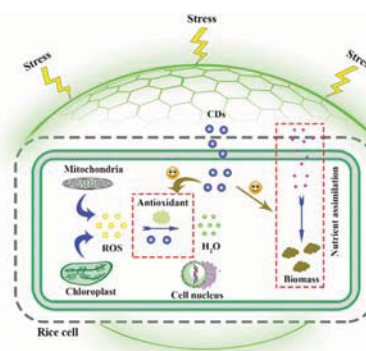
**ROS Content and the Antioxidant Defense System of Rice Cells.** Previous studies have demonstrated the properties of CDs to scavenge ROS because of the defects and unpaired electrons on their surface.<sup>19–21,40,41</sup> The CDs used in this study were rich in –OH active groups, that is, defects on their surface, which could scavenge free radicals by transferring free electrons from free radicals to the C–C backbone in the core. Figure 5A indicates that the CDs could intrinsically scavenge DPPH radicals in a concentration-dependent manner in the dark. Generally, abiotic stress can induce ROS in plants, leading to oxidative damage. Malondialdehyde (MDA), the product of lipid peroxidation, is usually used as a biomarker for the level of oxidative damage. To protect themselves from oxidative damage, plants have evolved a complex antioxidant defense system to scavenge ROS.<sup>2</sup> Therefore, the intracellular ROS (Figure S7 and Figure 5B), MDA contents (Figure 5C), and the antioxidant defense system of the CD-treated rice cells were investigated, including POD (Figure 5D) and CAT (Figure 5E) activities, and the total contents of phenolics (Figure 5F) and flavonoids (Figure 5G). 2', 7'-Dichlorofluorescein diacetate (DCFH-DA) was used as a fluorescent probe to visualize the ROS of treated rice cells based on the green fluorescence intensity.<sup>42</sup> As seen from the results, 2,4-D significantly increased the ROS content in rice cells by 19.28% compared to the control, resulting in a significant increase in MDA content by 43.17%. Then, the generated ROS activated the antioxidant defense system of rice by significantly enhancing the POD and CAT activities (112.90 and 70.76%) and the phenolics and flavonoid contents (69.60 and 53.14%) compared to the control. In contrast, CDs alone significantly decreased the ROS and MDA contents by 81.89 and 56.07% compared with the control group. Besides, CDs alone could significantly activate the antioxidant defense system of rice cells by increasing the POD activity and the phenolic and flavonoid contents in the rice cells by 125.81, 43.06, and 47.63%, respectively. This result indicated that CDs intrinsically contributed to the antioxidant defense system of rice to scavenge ROS. Therefore, with the incubation of 2,4-D and CDs, the rice cells showed much lower oxidative damage (ROS and MDA contents were decreased by 54.61 and 64.28%), which led to a weak antioxidant defense response (POD and CAT activities, and phenolic and flavonoid contents were decreased by 35.89, 54.42, 43.53, and 48.61%), compared with the control. These results proved our hypothesis that the CDs mitigated abiotic stress to rice primarily by scavenging ROS through their catalysis and enhancing the antioxidant defense of rice cells as shown in Figure 5H. Similar to our results, CDs have been previously reported to protect plants from drought and heavy metal cadmium stress by enhancing their antioxidant defense system.<sup>43,44</sup>

**Effect of CDs on the Assimilation of Nutrition by Rice Cells.** In addition to the antioxidant defense system of the plant, the active nutrient assimilation also contributes to the plant tolerance to abiotic stress.<sup>45</sup> The cell membrane plays a key role in nutrient assimilation and protects them from the external environment. Scanning electron microscopy (SEM) images (Figure 6A) showed a plumper and smoother surface of CD-treated rice cells, compared with those of the control after 24 and 72 h of incubation, suggesting more endocytosis in CD-treated cells. Interestingly, CDs did not affect the membrane/wall structure of the rice cells because no significant difference in surface morphology was observed compared with the control. Then, cell viability was investigated using an FDA probe, which can be easily hydrolyzed to a high-intensity green fluorescent molecule in plant cells with high viability.<sup>46</sup> The fluorescence intensity is proportional to cell viability. Compared with the control, 2,4-D ( $5 \mu\text{g}\cdot\text{mL}^{-1}$ ) decreased the cell viability, which was recovered above the control level by CDs (Figure 6B). Figure 6C shows the membrane permeability (MP) of the treated rice cells. Compared with the control, 2,4-D increased electrolyte leakage from rice cells, which was significantly decreased by CDs alone. In the incubation of CDs and 2,4-D, the electrolyte leakage rate from rice cells was significantly decreased compared with those in 2,4-D treatment. With higher cell viability and lower MP, CD-treated rice cells could have higher nutrient assimilation, which was determined by the decreased rate in the conductivity of the culture medium. The results showed that 2,4-D inhibited the nutritional assimilation rate of rice cells by 8.21%, while CDs significantly improved it by 68.55% compared to the control. Under the suppression of 2,4-D, CDs significantly increased the nutritional uptake of rice cells by 14.69% compared with the 2,4-D treatment (Figure 6D). Summarizing from the above results, the CDs could alleviate the inhibition of 2,4-D to the growth of rice cells by promoting their ability to assimilate nutrients (Figure 6E).

## CONCLUSIONS

In the present study, chemically stable and high-yield (60.6%) CDs were prepared using citric acid (CA) by a microwave-assisted method. The prepared CDs could effectively protect rice from the stresses of salt, high light, and herbicides of 2,4-D and 2,4-D-Na by improving the antioxidant defense system and increasing the nutrient assimilation of rice (Scheme 2). The CDs showed potential as a protective agent against abiotic stresses for crop plants in agriculture. Our results suggested

**Scheme 2. Model of CDs in Protecting Rice against the Inhibition of Abiotic Stress**





that the CDs were degraded after internalization by rice cells without accumulation. However, the CD-germinated rice seedling showed high resistance to the abiotic stresses even after 3 weeks. Therefore, the long residual action of the CDs on the resistance of rice seedlings needs further investigation for the molecular mechanism. Furthermore, because of the narrow profit margin of agriculture, much attention should be paid to the large-scale preparation of CDs with low cost. Additionally, the field testing and environmental risk assessment of CDs will be carried out in our future study.

## EXPERIMENTAL SECTION

**Materials.** Citric acid monohydrate (CA), quinine sulfate, fluorescein diacetate (FDA), trichloroacetic acid (TCA), thiobarbituric acid (TBA), tris(hydroxymethyl)aminomethane (Tris), and 2,2-diphenyl-1-picryl-hydrazyl (DPPH) were purchased from Shanghai Macklin Biochemical Co. Ltd. (Shanghai, China). 2', 7'-Dichloro-fluorescein diacetate (DCFH-DA), plant total phenolic kit, 2-thiobarbituric acid, and rutin were purchased from Shanghai Yuanye Biotechnology Co. Ltd. (Shanghai, China).

**Preparation and Characterization of CDs.** CDs were prepared using citric acid (CA) by a microwave-assisted method. Briefly, CA (2.1 g, 10 mmol) was dissolved in ultrapure water (20 mL) and heated using a domestic microwave oven under medium heat (350 W) until the formation of a yellow colloidal substance. Shaking was necessary at intervals to ensure a homogeneous reaction. The obtained CDs were redispersed in ultrapure water and purified by filtration (0.22  $\mu\text{m}$ ). After freeze-drying, the sample was dissolved in ultrapure water to 100 mg/mL and stored in an ambient environment.

A FEI Tecnai 12 transmission electron microscope, a Nicolet Avatar 360 FTIR spectrophotometer, an AXIS ULTRA DLD X-ray photoelectron spectrometer, an Ultima IV X-ray diffractometer, an F-7000 Hitachi fluorescence spectrophotometer, a PerkinElmer UV-vis spectrophotometer (Lambda 750), and a Malvern Zetasizer Nano ZSE were used to characterize the prepared CDs. The QY of CDs was determined using quinine sulfate (0.1 M  $\text{H}_2\text{SO}_4$  as a solvent, QY = 54%) as a reference according to the literature.<sup>47</sup>

### Abiotic Stress Treatment and Cultivation of Rice Materials.

Rice suspended cells and seedlings were cultured to investigate the alleviation of CDs to salt, high light, and herbicide stresses, including 2,4-dichlorophenoxyacetic acid (2,4-D) (99%), 2,4-D sodium salt (2,4-D-Na) (99%), 41% glyphosate IPA salt, and PM-EC. Preliminary experiments were conducted to determine the appropriate dose of CDs and the intensities of these stresses.

Suspended rice cell lines (*Oryza sativa* L. cv Nipponbare) were obtained from the College of Life Science, South China Agricultural University. The rice cells were incubated using sterile nutrient solution (Table 1S) with shaking (120 rpm) at 28 °C in the dark, which was subcultured at a 7 d interval by refreshing the nutrient solution.<sup>48</sup> The rice cells were exposed to NaCl at 0.15 M, light intensity at 2000 Lux, 2,4-D at 5  $\mu\text{g}\cdot\text{mL}^{-1}$ , 2,4-D-Na at 30  $\mu\text{g}\cdot\text{mL}^{-1}$ , IPA at 0.5  $\mu\text{L}\cdot\text{mL}^{-1}$ , and PM-EC at 0.5  $\mu\text{L}\cdot\text{mL}^{-1}$  with and without CDs at 100  $\mu\text{g}\cdot\text{mL}^{-1}$ . Rice cells cultured in pure nutrient solution were used as the control treatment. After a week, the rice cells from each treatment were harvested and measured for their fresh and dry weight. All treatments were replicated at least three times.

Rice seedlings were cultured in a greenhouse. First, rice seeds (Huahang 31) were sterilized using 75% ethyl alcohol for 20 min and cultured at about 30 °C in the dark using deionized water or CD solution at 100  $\mu\text{g}\cdot\text{mL}^{-1}$ . After 3 days, the germinated rice seeds were placed in light. At the 7th day, the deionized water- or CD-germinated rice seedlings were transplanted to square plastic pots containing a seedling raising substrate, which were pretreated with 1 L of NaCl at 0.15 M, 2,4-D at 5  $\mu\text{g}\cdot\text{mL}^{-1}$ , and 2,4-D-Na at 30  $\mu\text{g}\cdot\text{mL}^{-1}$ , respectively, 3 days before the transplant. The deionized water-germinated rice seedlings cultured by a pure seedling raising substrate were used as the control. All treatments were replicated at least three times. These seedlings were grown in a greenhouse under natural light

and temperature (about 35 °C during the day and 30 °C at night). After 3 weeks, these rice seedlings were collected and measured for their height, biomass, and chlorophyll content.<sup>49</sup>

**Uptake of CDs by Rice Cells.** The uptake of CDs by rice cells was characterized by the observation made using fluorescence microscopy and fluorescence decay of the liquid medium at an interval of 24 h. A mixture of CDs and liquid medium without rice cells was synchronously incubated as a reference. Furthermore, the cytoplasm was extracted for fluorescence measurements to determine the accumulation of CDs in the rice cells.

**Membrane Permeability and Nutrient Assimilation by Rice Cells.** The membrane permeability was estimated by electrolyte leakage as described by Alpaslan et al.<sup>50</sup> Rice cells (1 g) from each treatment were incubated in ultrapure water (10 mL) at 30 °C for 3 h. Then, the electrical conductivities of the supernatant were measured before ( $\text{EC}_1$ ) and after ( $\text{EC}_2$ ) boiling for 2 min. The MP was expressed as eq 1:

$$\text{MP (\%)} = (\text{EC}_1/\text{EC}_2) \times 100 \quad (1)$$

The uptake of nutrition by rice cells was determined by the decrease in electrical conductivities of the liquid medium caused by a unit gram of rice cells before and after incubation for a week ( $\Delta\text{EC/g}$ ).

**Viability of Rice Cells.** The cell viability was visualized using an FDA probe according to the method reported by Jones et al.<sup>51</sup> The treated rice cells (0.1 g) were stained with FDA (5  $\mu\text{g}\cdot\text{mL}^{-1}$ ) at room temperature for 5 min. An inverted fluorescence microscope (Nikon, ECLIPSE Ti2-U) equipped with a Nikon DS-Ri2 microscope camera was used to observe the stained cells with excitation wavelengths from 465 to 495 nm and emission wavelengths from 512 to 552 nm.

**In Vitro Free Radical Assay.** Antioxidant efficacy of the CDs was measured in vitro using DPPH following the protocol described by Wang et al. with some modifications.<sup>52</sup> DPPH can be easily reduced by antioxidants with the color changing from purple to yellow in the dark, leading to a decrease in absorbance at 515 nm. DPPH radical solution in ethanol (100  $\mu\text{mol}$ , 1.5 mL) was mixed with CD solution (final concentrations of 50, 100, and 200  $\mu\text{g}\cdot\text{mL}^{-1}$ ) and incubated in the dark for 1 h. Each incubation was repeated three times. Finally, the antioxidant activity of the CDs was measured according to the decrease of the absorption intensity at 515 nm.

**ROS Content.** The ROS contents in rice cells were visualized using the DCFH-DA probe as described by Bing et al.<sup>42</sup> The treated rice cells (0.1 g) were incubated with DCFH-DA (5  $\mu\text{mol}\cdot\text{L}^{-1}$ ) for 10 min at 28 °C in the dark. After washing with PBS, the cells were observed using a fluorescence microscope with excitation wavelengths from 465 to 495 nm and emission wavelengths from 512 to 552 nm. Then, the cytoplasm was extracted by sonication in an ice bath and centrifugation (3000 rpm, 5 min), and the supernatants were measured for their fluorescence intensity.

**Lipid Peroxidation and the Antioxidant Defense System in Rice Cells.** The treated rice cells (0.5 g) were ground with liquid nitrogen and homogenized in Tris-HCl buffer (pH = 7.4, 3 mL). Then, the supernatants were collected by centrifugation at 10000 rpm at 4 °C for 10 min and kept at 4 °C for the following measurements. Lipid peroxidation was measured in terms of MDA contents by following the method reported by Bartlewicz et al.<sup>9</sup> POD activity was determined by monitoring the increase rate of the absorbance at 470 nm in 3 min using a UV-vis spectrophotometer.<sup>6</sup> The activity of CAT was assayed by measuring the decomposition rate of hydrogen peroxide according to the absorbance at 240 nm in 2 min.<sup>11</sup> The total phenolic content was measured using a kit from Shanghai Yuanye Biotechnology Co. Ltd., according to the specification. The total flavonoid content was measured by the aluminum chloride colorimetric assay.<sup>53</sup> MDA, phenolic, and flavonoid contents were expressed as milligrams per gram of fresh cells. The activity of CAT was expressed as units per gram of fresh cells.

**Statistical Analysis.** Values presented in this manuscript were expressed as mean  $\pm$  standard deviation (SD). Statistical significance of all data was determined using a one-way analysis of variance



(ANOVA) and compared using Duncan's test at  $p < 0.05$  levels in SPSS 24.

## ■ ASSOCIATED CONTENT

### SI Supporting Information

The Supporting Information is available free of charge at <https://pubs.acs.org/doi/10.1021/acsami.0c11724>.

XRD spectra, hydrodynamic diameter, and quantum yield of CDs; growth of rice cells treated with CDs at different concentrations; rice seedling growth exposed to different stresses pretreated with and without CDs; alleviation of CDs to pendimethalin and glyphosate; fluorescence images of DCFH-DA stained rice cells treated with and without CDs; formulation of the rice liquid medium (PDF)

## ■ AUTHOR INFORMATION

### Corresponding Authors

**Mingtao Zheng** – Key Laboratory for Biobased Materials and Energy of Ministry of Education/Guangdong Provincial Engineering Technology Research Center for Optical Agriculture, College of Materials and Energy, South China Agricultural University, Guangzhou 510642, China; Guangdong Laboratory of Lingnan Modern Agriculture, Guangzhou 510642, China; [orcid.org/0000-0001-8083-8724](https://orcid.org/0000-0001-8083-8724); Email: [mtzheng@scau.edu.cn](mailto:mtzheng@scau.edu.cn)

**Yingliang Liu** – Key Laboratory for Biobased Materials and Energy of Ministry of Education/Guangdong Provincial Engineering Technology Research Center for Optical Agriculture, College of Materials and Energy, South China Agricultural University, Guangzhou 510642, China; Guangdong Laboratory of Lingnan Modern Agriculture, Guangzhou 510642, China; [orcid.org/0000-0003-1930-0700](https://orcid.org/0000-0003-1930-0700); Email: [tlilyl@scau.edu.cn](mailto:tlilyl@scau.edu.cn)

**Chaofan Hu** – Key Laboratory for Biobased Materials and Energy of Ministry of Education/Guangdong Provincial Engineering Technology Research Center for Optical Agriculture, College of Materials and Energy, South China Agricultural University, Guangzhou 510642, China; Guangdong Laboratory of Lingnan Modern Agriculture, Guangzhou 510642, China; [orcid.org/0000-0003-2311-8733](https://orcid.org/0000-0003-2311-8733); Email: [thucf@scau.edu.cn](mailto:thucf@scau.edu.cn)

### Authors

**Yadong Li** – Key Laboratory for Biobased Materials and Energy of Ministry of Education/Guangdong Provincial Engineering Technology Research Center for Optical Agriculture, College of Materials and Energy, South China Agricultural University, Guangzhou 510642, China; Guangdong Laboratory of Lingnan Modern Agriculture, Guangzhou 510642, China; [orcid.org/0000-0002-7166-3261](https://orcid.org/0000-0002-7166-3261)

**Junmei Gao** – Vocational Teachers College, Jiangxi Agricultural University, Nanchang 330045, China

**Xiaokai Xu** – Key Laboratory for Biobased Materials and Energy of Ministry of Education/Guangdong Provincial Engineering Technology Research Center for Optical Agriculture, College of Materials and Energy, South China Agricultural University, Guangzhou 510642, China; Guangdong Laboratory of Lingnan Modern Agriculture, Guangzhou 510642, China

**Ying Wu** – Key Laboratory for Biobased Materials and Energy of Ministry of Education/Guangdong Provincial Engineering Technology Research Center for Optical Agriculture, College of Materials and Energy, South China Agricultural University,

Guangzhou 510642, China; Guangdong Laboratory of Lingnan Modern Agriculture, Guangzhou 510642, China  
**Jianle Zhuang** – Key Laboratory for Biobased Materials and Energy of Ministry of Education/Guangdong Provincial Engineering Technology Research Center for Optical Agriculture, College of Materials and Energy, South China Agricultural University, Guangzhou 510642, China; Guangdong Laboratory of Lingnan Modern Agriculture, Guangzhou 510642, China; [orcid.org/0000-0002-4649-1939](https://orcid.org/0000-0002-4649-1939)

**Xuejie Zhang** – Key Laboratory for Biobased Materials and Energy of Ministry of Education/Guangdong Provincial Engineering Technology Research Center for Optical Agriculture, College of Materials and Energy, South China Agricultural University, Guangzhou 510642, China; Guangdong Laboratory of Lingnan Modern Agriculture, Guangzhou 510642, China; [orcid.org/0000-0002-4029-7000](https://orcid.org/0000-0002-4029-7000)

**Haoran Zhang** – Key Laboratory for Biobased Materials and Energy of Ministry of Education/Guangdong Provincial Engineering Technology Research Center for Optical Agriculture, College of Materials and Energy, South China Agricultural University, Guangzhou 510642, China; Guangdong Laboratory of Lingnan Modern Agriculture, Guangzhou 510642, China

**Bingfu Lei** – Key Laboratory for Biobased Materials and Energy of Ministry of Education/Guangdong Provincial Engineering Technology Research Center for Optical Agriculture, College of Materials and Energy, South China Agricultural University, Guangzhou 510642, China; Guangdong Laboratory of Lingnan Modern Agriculture, Guangzhou 510642, China

Complete contact information is available at: <https://pubs.acs.org/doi/10.1021/acsami.0c11724>

### Notes

The authors declare no competing financial interest.

## ■ ACKNOWLEDGMENTS

This work was supported by the National Natural Science Foundation of China (Grant No. 21571067).

## ■ REFERENCES

- (1) Zhao, C.; Liu, B.; Piao, S.; Wang, X.; Lobell, D. B.; Huang, Y.; Huang, M.; Yao, Y.; Bassu, S.; Ciais, P.; Durand, J.-L.; Elliott, J.; Ewert, F.; Janssens, I. A.; Li, T.; Lin, E.; Liu, Q.; Martre, P.; Müller, C.; Peng, S.; Peñuelas, J.; Ruane, A. C.; Wallach, D.; Wang, T.; Wu, D.; Liu, Z.; Zhu, Y.; Zhu, Z.; Asseng, S. Temperature Increase Reduces Global Yields of Major Crops in Four Independent Estimates. *Proc. Natl. Acad. Sci. U. S. A.* **2017**, *114*, 9326–9331.
- (2) Minhas, P. S.; Rane, J.; Pasala, R. K., Abiotic Stresses in Agriculture: An Overview. In *Abiotic Stress Management for Resilient Agriculture*, Minhas, P. S.; Rane, J.; Pasala, R. K., Eds. Springer Singapore: Singapore, 2017, pp 3–8.
- (3) Choudhury, F. K.; Rivero, R. M.; Blumwald, E.; Mittler, R. Reactive Oxygen Species, Abiotic Stress and Stress Combination. *Plant J.* **2017**, *90*, 856–867.
- (4) Zhu, J.-K. Abiotic Stress Signaling and Responses in Plants. *Cell* **2016**, *167*, 313–324.
- (5) Li, M.; Ahammed, G. J.; Li, C.; Bao, X.; Yu, J.; Huang, C.; Yin, H.; Zhou, J. Brassinosteroid Ameliorates Zinc Oxide Nanoparticles-Induced Oxidative Stress by Improving Antioxidant Potential and Redox Homeostasis in Tomato Seedling. *Front. Plant Sci.* **2016**, *7*, 615.
- (6) Jiang, C.; Cui, Q.; Feng, K.; Xu, D.; Li, C.; Zheng, Q. Melatonin Improves Antioxidant Capacity and Ion Homeostasis and Enhances Salt Tolerance in Maize Seedlings. *Acta. Physiol. Plant.* **2016**, *38*, 82.
- (7) Li, X.; Wei, J.-P.; Scott, R. E.; Liu, J.-W.; Guo, S.; Li, Y.; Zhang, L.; Han, W.-Y. Exogenous Melatonin Alleviates Cold Stress by

Promoting Antioxidant Defense and Redox Homeostasis in *Camellia Sinensis* L. *Molecules* **2018**, *23*, 165.

(8) Fuentes, A.; Almonacid, L.; Ocampo, J. A.; Arriagada, C. Synergistic Interactions between a Saprophytic Fungal Consortium and *Rhizophagus Irregularis* Alleviate Oxidative Stress in Plants Grown in Heavy Metal Contaminated Soil. *Plant Soil* **2016**, *407*, 355–366.

(9) Armada, E.; Probanza, A.; Roldán, A.; Azcón, R. Native Plant Growth Promoting Bacteria *Bacillus Thuringiensis* and Mixed or Individual Mycorrhizal Species Improved Drought Tolerance and Oxidative Metabolism in *Lavandula Dentata* Plants. *J. Plant Physiol.* **2016**, *192*, 1–12.

(10) Yasar, S.; Jaskani, M. J.; Asif, M.; Qasim, M. Application of Plant Growth Regulators in Ornamental Plants: a Review. *Pak. J. Agric. Sci.* **2017**, *54*, 327–333.

(11) Bartlewicz, J.; Pozo, M. I.; Honnay, O.; Lievens, B.; Jacquemyn, H. Effects of Agricultural Fungicides on Microorganisms Associated with Floral Nectar: Susceptibility Assays and Field Experiments. *Environ. Sci. Pollut. Res.* **2016**, *23*, 19776–19786.

(12) Khan, M. N.; Mobin, M.; Abbas, Z. K.; AlMutairi, K. A.; Siddiqui, Z. H. Role of Nanomaterials in Plants under Challenging Environments. *Plant Physiol. Biochem.* **2017**, *110*, 194–209.

(13) Chen, M.; Qin, X.; Zeng, G. Biodiversity Change behind Wide Applications of Nanomaterials? *Nano Today* **2017**, *17*, 11–13.

(14) Abdel Latif, A. A. H.; Srivastava, A. K.; El-sadek, M. S. A.; Kordrostami, M.; Tran, L.-S. P. Titanium Dioxide Nanoparticles Improve Growth and Enhance Tolerance of Broad Bean Plants under Saline Soil Conditions. *Land Degrad. Dev.* **2018**, *29*, 1065–1073.

(15) Pittol, M.; Tomacheski, D.; Simões, D. N.; Ribeiro, V. F.; Santana, R. M. C. Macroscopic Effects of Silver Nanoparticles and Titanium Dioxide on Edible Plant Growth. *Environ. Nanotechnol. Monit. Manag.* **2017**, *8*, 127–133.

(16) Li, H.; Huang, J.; Lu, F.; Liu, Y.; Song, Y.; Sun, Y.; Zhong, J.; Huang, H.; Wang, Y.; Li, S.; Lifshitz, Y.; Lee, S.-T.; Kang, Z. Impacts of Carbon Dots on Rice Plants: Boosting the Growth and Improving the Disease Resistance. *ACS Appl. Bio. Mater.* **2018**, *1*, 663–672.

(17) Li, W.; Wu, S.; Zhang, H.; Zhang, X.; Zhuang, J.; Hu, C.; Liu, Y.; Lei, B.; Ma, L.; Wang, X. Enhanced Biological Photosynthetic Efficiency Using Light-Harvesting Engineering with Dual-Emissive Carbon Dots. *Adv. Funct. Mater.* **2018**, *28*, 1804004.

(18) Li, Y.; Xu, X.; Wu, Y.; Zhuang, J.; Zhang, X.; Zhang, H.; Lei, B.; Hu, C.; Liu, Y. A Review on the Effects of Carbon Dots in Plant Systems. *Mater. Chem. Front.* **2020**, *4*, 437–448.

(19) Das, B.; Pal, P.; Dadhich, P.; Dutta, J.; Dhara, S. In Vivo Cell Tracking, Reactive Oxygen Species Scavenging, and Antioxidative Gene Down Regulation by Long-Term Exposure of Biomass-Derived Carbon Dots. *ACS Biomater. Sci. Eng.* **2019**, *5*, 346–356.

(20) Wang, H.; Xie, Y.; Na, X.; Bi, J.; Liu, S.; Zhang, L.; Tan, M. Fluorescent Carbon Dots in Baked Lamb: Formation, Cytotoxicity and Scavenging Capability to Free Radicals. *Food Chem.* **2019**, *286*, 405–412.

(21) Lu, F.; Yang, S.; Song, Y.; Zhai, C.; Wang, Q.; Ding, G.; Kang, Z. Hydroxyl Functionalized Carbon Dots with Strong Radical Scavenging Ability Promote Cell Proliferation. *Mater. Res. Express* **2019**, *6*, No. 065030.

(22) Sasaki, T.; Antonio, B.; Rice. In *Reference Module in Life Sciences*, Elsevier: 2017.

(23) Zhu, S.; Song, Y.; Zhao, X.; Shao, J.; Zhang, J.; Yang, B. The Photoluminescence Mechanism in Carbon Dots (Graphene Quantum Dots, Carbon Nanodots, and Polymer Dots): Current State and Future Perspective. *Nano Res.* **2015**, *8*, 355–381.

(24) Dong, Y.; Pang, H.; Yang, H. B.; Guo, C.; Shao, J.; Chi, Y.; Li, C. M.; Yu, T. Carbon-Based Dots Co-doped with Nitrogen and Sulfur for High Quantum Yield and Excitation-Independent Emission. *Angew. Chem., Int. Ed. Engl.* **2013**, *52*, 7954–7804.

(25) Gao, T.; Wang, X.; Yang, L.-Y.; He, H.; Ba, X.-X.; Zhao, J.; Jiang, F.-L.; Liu, Y. Red, Yellow, and Blue Luminescence by Graphene Quantum Dots: Syntheses, Mechanism, and Cellular Imaging. *ACS Appl. Mater. Interfaces* **2017**, *9*, 24846–24856.

(26) Liu, S.; Tian, J.; Wang, L.; Zhang, Y.; Qin, X.; Luo, Y.; Asiri, A. M.; Al-Youbi, A. O.; Sun, X. Hydrothermal Treatment of Grass: A Low-Cost, Green Route to Nitrogen-Doped, Carbon-Rich, Photoluminescent Polymer Nanodots as an Effective Fluorescent Sensing Platform for Label-Free Detection of Cu(II) Ions. *Adv. Mater.* **2012**, *24*, 2037–2041.

(27) Sevilla, M.; Fuertes, A. B. Chemical and Structural Properties of Carbonaceous Products Obtained by Hydrothermal Carbonization of Saccharides. *Chem. Eur. J.* **2009**, *15*, 4195–4203.

(28) Clark, B. D.; DeSantis, C. J.; Wu, G.; Renard, D.; McClain, M. J.; Bursi, L.; Tsai, A.-L.; Nordlander, P.; Halas, N. J. Ligand-Dependent Colloidal Stability Controls the Growth of Aluminum Nanocrystals. *J. Am. Chem. Soc.* **2019**, *141*, 1716–1724.

(29) Zhang, Y.; Liu, X.; Fan, Y.; Guo, X.; Zhou, L.; Lv, Y.; Lin, J. One-Step Microwave Synthesis of N-Doped Hydroxyl-Functionalized Carbon Dots with Ultra-High Fluorescence Quantum Yields. *Nanoscale* **2016**, *8*, 15281–15287.

(30) Saidi, W. A. Oxygen Reduction Electrocatalysis Using N-Doped Graphene Quantum-Dots. *J. Phys. Chem. Lett.* **2013**, *4*, 4160–4165.

(31) Wu, H.; Tito, N.; Giraldo, J. P. Anionic Cerium Oxide Nanoparticles Protect Plant Photosynthesis from Abiotic Stress by Scavenging Reactive Oxygen Species. *ACS Nano* **2017**, *11*, 11283–11297.

(32) Giraldo, J. P.; Landry, M. P.; Faltermeier, S. M.; McNicholas, T. P.; Iverson, N. M.; Boghossian, A. A.; Reuel, N. F.; Hilmer, A. J.; Sen, F.; Brew, J. A.; Strano, M. S. Plant Nanobionics Approach to Augment Photosynthesis and Biochemical Sensing. *Nat. Mater.* **2014**, *13*, 400–408.

(33) Schwab, F.; Zhai, G.; Kern, M.; Turner, A.; Schnoor, J. L.; Wiesner, M. R. Barriers, Pathways and Processes for Uptake, Translocation and Accumulation of Nanomaterials in Plants – Critical Review. *Nanotoxicology* **2016**, *10*, 257–278.

(34) Miller, G. A. D.; Suzuki, N.; Ciftci-Yilmaz, S.; Mittler, R. Reactive Oxygen Species Homeostasis and Signalling during Drought and Salinity Stresses. *Plant Cell Environ.* **2010**, *33*, 453–467.

(35) Asada, K. Production and Scavenging of Reactive Oxygen Species in Chloroplasts and Their Functions. *Plant Physiol.* **2006**, *141*, 391–396.

(36) Pazmiño, D. M.; Rodríguez-Serrano, M.; Romero-Puertas, M. C.; Archilla-Ruiz, A.; Del Río, L. A.; Sandalio, L. M. Differential Response of Young and Adult Leaves to Herbicide 2,4-Dichlorophenoxyacetic Acid in Pea Plants: Role of Reactive Oxygen Species. *Plant Cell Environ.* **2011**, *34*, 1874–1889.

(37) Romero-Puertas, M. C.; McCarthy, I.; Gómez, M.; Sandalio, L. M.; Corpas, F. J.; Del Río, L. A.; Palma, J. M. Reactive Oxygen Species-Mediated Enzymatic Systems Involved in the Oxidative Action of 2,4-Dichlorophenoxyacetic Acid\*. *Plant Cell Environ.* **2004**, *27*, 1135–1148.

(38) de María, N.; Becerril, J. M.; García-Plazaola, J. I.; Hernández, A.; de Felipe, M. R.; Fernández-Pascual, M. New Insights on Glyphosate Mode of Action in Nodular Metabolism: Role of Shikimate Accumulation. *J. Agric. Food Chem.* **2006**, *54*, 2621–2628.

(39) Appleby, A. P.; Valverde, B. E. Behavior of Dinitroaniline Herbicides in Plants. *Weed Technol.* **1989**, *3*, 198–206.

(40) Zhao, S.; Lan, M.; Zhu, X.; Xue, H.; Ng, T.-W.; Meng, X.; Lee, C.-S.; Wang, P.; Zhang, W. Green Synthesis of Bifunctional Fluorescent Carbon Dots from Garlic for Cellular Imaging and Free Radical Scavenging. *ACS Appl. Mater. Interfaces* **2015**, *7*, 17054–17060.

(41) Das, B.; Dadhich, P.; Pal, P.; Srivas, P. K.; Bankoti, K.; Dhara, S. Carbon Nanodots from Date Molasses: New Nanolights for the In Vitro Scavenging of Reactive Oxygen Species. *J. Mater. Chem. B* **2014**, *2*, 6839–6847.

(42) Bing, W.; Sun, H.; Yan, Z.; Ren, J.; Qu, X. Programmed Bacteria Death Induced by Carbon Dots with Different Surface Charge. *Small* **2016**, *12*, 4713–4718.

(43) Su, L.-X.; Ma, X.-L.; Zhao, K.-K.; Shen, C.-L.; Lou, Q.; Yin, D.-M.; Shan, C.-X. Carbon Nanodots for Enhancing the Stress Resistance of Peanut Plants. *ACS Omega* **2018**, *3*, 17770–17777.

- (44) Xiao, L.; Guo, H.; Wang, S.; Li, J.; Wang, Y.; Xing, B. Carbon Dots Alleviate the Toxicity of Cadmium Ions ( $\text{Cd}^{2+}$ ) toward Wheat Seedlings. *Environ. Sci. Nano* **2019**, *6*, 1493–1506.
- (45) Nazar, R.; Iqbal, N.; Syeed, S.; Khan, N. A. Salicylic Acid Alleviates Decreases in Photosynthesis under Salt Stress by Enhancing Nitrogen and Sulfur Assimilation and Antioxidant Metabolism Differentially in Two Mungbean Cultivars. *J. Plant Physiol.* **2011**, *168*, 807–815.
- (46) Fodor, E.; Ayaydin, F., Fluorescent Probes and Live Imaging of Plant Cells. In *Advances in Plant Ecophysiology Techniques*, Sánchez-Moreiras, A. M.; Reigosa, M. J., Eds. Springer International Publishing: Cham, 2018, pp 241–251.
- (47) Wu, P.; Li, W.; Wu, Q.; Liu, Y.; Liu, S. Hydrothermal Synthesis of Nitrogen-Doped Carbon Quantum Dots from Microcrystalline Cellulose for the Detection of  $\text{Fe}^{3+}$  Ions in an Acidic Environment. *RSC Adv.* **2017**, *7*, 44144–44153.
- (48) Cui, J.; Liu, T.; Li, F.; Yi, J.; Liu, C.; Yu, H. Silica Nanoparticles Alleviate Cadmium Toxicity in Rice Cells: Mechanisms and Size Effects. *Environ. Pollut.* **2017**, *228*, 363–369.
- (49) Shibghatallah, M. A. H.; Khotimah, S. N.; Suhandono, S.; Viridi, S.; Kesuma, T. Measuring Leaf Chlorophyll Concentration from Its Color: A Way in Monitoring Environment Change to Plantations. *AIP Conf. Proc.* **2013**, *1554*, 210–213.
- (50) Alpaslan, M.; Gunes, A. Interactive Effects of Boron and Salinity Stress on the Growth, Membrane Permeability and Mineral Composition of Tomato and Cucumber Plants. *Plant Soil* **2001**, *236*, 123–128.
- (51) Jones, K.; Kim, D. W.; Park, J. S.; Khang, C. H. Live-Cell Fluorescence Imaging to Investigate the Dynamics of Plant Cell Death during Infection by the Rice Blast Fungus *Magnaporthe Oryzae*. *BMC Plant Biol.* **2016**, *16*, 69.
- (52) Wang, L.; Li, Y.; Wang, Y.; Kong, W.; Lu, Q.; Liu, X.; Zhang, D.; Qu, L. Chlorine-Doped Graphene Quantum Dots with Enhanced Anti- and Pro-Oxidant Properties. *ACS Appl. Mater. Interfaces* **2019**, *11*, 21822–21829.
- (53) Ramborger, B. P.; Ortis Gularte, C. A.; Rodrigues, D. T.; Gayer, M. C.; Sigal Carriço, M. R.; Bianchini, M. C.; Puntel, R. L.; Denardin, E. L. G.; Roehrs, R. The Phytoremediation Potential of *Plectranthus Neochilus* on 2,4-Dichlorophenoxyacetic Acid and the Role of Antioxidant Capacity in Herbicide Tolerance. *Chemosphere* **2017**, *188*, 231–240.



# Time-Dependent Room-Temperature Afterglow of Carbon Dots Constructed by Trap-Induced Multiemission Centers

Zhun Ran, Hongjie Jia, Ziting Zhong, Hongwei Yang, Yinda Zhu, Yuqi Li, Jinkun Liu, Xuejie Zhang, Jianle Zhuang, Yingliang Liu, Bingfu Lei,\* and Chaofan Hu\*



Cite This: *Nano Lett.* 2025, 25, 6993–7002



Read Online

ACCESS |

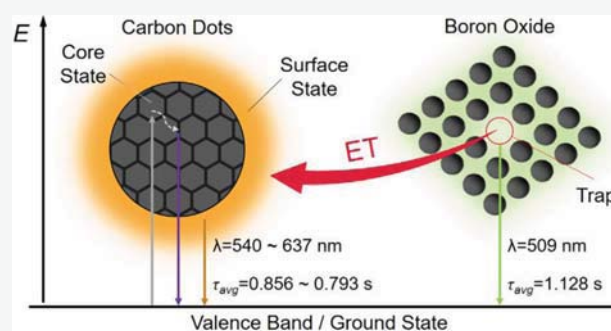
Metrics & More

Article Recommendations

Supporting Information

**ABSTRACT:** Traps, due to the ability to capture, store, and release charge carriers, have attracted significant attention in the construction of long afterglow materials. In this study, a one-step in situ calcination strategy was employed to fabricate carbon dot (CD)-based composites, and the traps were designed as one of the emission centers within the composite system. Upon removal of ultraviolet light, the materials showed a time-dependent afterglow color (TDAC), with the luminescent color gradually changing from orange to green. The study indicates that the dynamic afterglow results from the energy transfer from traps to the surface triplet state of the CDs. In addition, CDs generated during the in situ calcination process serve as dopants, increasing the number of original traps and facilitating the formation of new ones. Based on the TDAC characteristics, we demonstrate the applications in anti-counterfeiting and information encryption. This strategy offers new insights into the development of multicolor afterglow materials.

**KEYWORDS:** carbon dots, trap, time-dependent afterglow color, multiemission centers, energy transfer



Long afterglow luminescence refers to the ability of materials to maintain their luminescence after the excitation source has been removed.<sup>1–4</sup> Inorganic long afterglow materials have garnered sustained research interest because of their long luminescence duration and diverse applications.<sup>5–7</sup> Within the host matrix, lattice defects play a crucial role in influencing the migration of charge carriers.<sup>8,9</sup> This is mainly reflected in the fact that the defect-related traps store and release charge carriers through trapping and detrapping processes.<sup>10–13</sup> Presently, apart from the traps generated during the synthesis process, ion-doping strategies have been widely employed for trap regulation.<sup>14–16</sup> Recently, traps have also been utilized in the design of organic long afterglow materials, achieving persistent luminescence with a duration of more than 24 h.<sup>17</sup> Therefore, the rational utilization and regulation of traps in long afterglow luminescence represent significant research topics that are essential for further expanding practical applications in the field of optoelectronics.

In recent years, there has been intense discussion surrounding the afterglow luminescence of boric acid (BA). Zheng et al.<sup>18</sup> first reported that pure BA exhibited ultralong room-temperature phosphorescence (RTP) in the crystalline state. However, Wu and colleagues<sup>19</sup> presented contradictory experimental results. Their experiments demonstrated that pure BA exhibits neither fluorescence nor phosphorescence under solid state conditions, while the observed RTP in

commercial BA samples originates from trace impurities. This led several research groups to conduct validations on the afterglow of BA.<sup>20–22</sup> Unfortunately, these studies yielded conflicting conclusions, and the exact origin of the afterglow in pure BA remains inconclusive. In our previous study, we obtained ultralong afterglow emission by heat treatment of BA, with an afterglow lifetime of up to 1.87 s.<sup>23</sup> The results show that BA gradually dehydrates to form boron oxide (B<sub>2</sub>O<sub>3</sub>) as the temperature increases, which is consistent with Balci's findings.<sup>24</sup> We demonstrated that the afterglow originates from calcination-induced oxygen vacancy traps. Recently, Stagi et al.<sup>25</sup> also reported similar results, confirming that the afterglow of BA after heat treatment is related to the existence of traps. In 2019, our group for the first time used B<sub>2</sub>O<sub>3</sub> as a matrix to activate the room-temperature afterglow of carbon dots (CDs).<sup>26</sup> Following this, B<sub>2</sub>O<sub>3</sub> was utilized as a versatile matrix for the fabrication of pure organic long afterglow materials<sup>27,28</sup> and CD-based long afterglow materials.<sup>29–34</sup> However, in most reports, the B<sub>2</sub>O<sub>3</sub> matrix has primarily been

**Received:** February 2, 2025

**Revised:** April 15, 2025

**Accepted:** April 15, 2025

**Published:** April 18, 2025



ACS Publications

© 2025 American Chemical Society

6993

<https://doi.org/10.1021/acs.nanolett.5c00723>  
Nano Lett. 2025, 25, 6993–7002



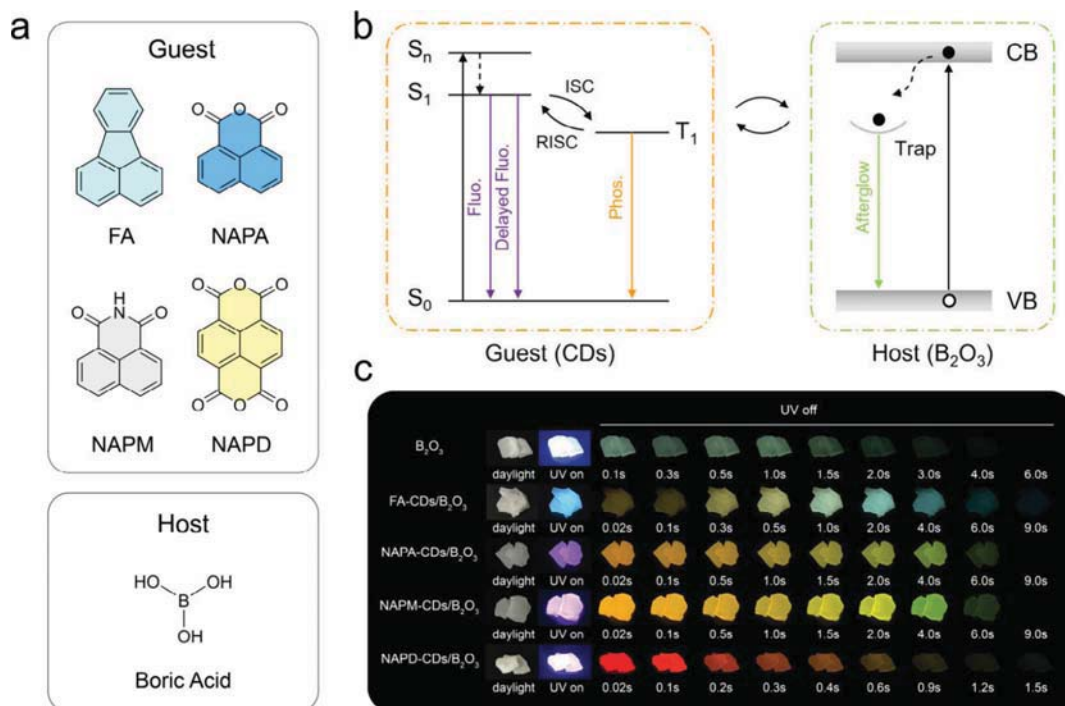


**Figure 1.** (a) The molecular structure of guest and host. (b) Proposed mechanism for TDAC materials. (c) Digital photograph of the four CD-based long afterglow materials under daylight, under 365 nm UV light, and after removing 365 nm UV light.

employed to protect triplet excitons, while the study of traps remains limited.

Time-dependent afterglow color (TDAC) materials provide multiple color changes in the time dimension, thus manifesting more advanced applications in the fields of anti-counterfeiting and information encryption.<sup>35–37</sup> Tan et al.<sup>38</sup> were the first to realize the TDAC of CD-based long afterglow materials by regulating the surface state and core state of CDs. Kang et al.<sup>39</sup> obtained color-tunable TDAC carbonized polymer dots (CPDs) by limiting the association of carboxyl dimers to form a red emission center. Zong et al.<sup>40</sup> realized the TDAC phenomenon at different temperatures by constructing the energy transfer between CDs and  $\text{Mn}^{2+}$ . Moreover, the construction of structural defects,<sup>41</sup> the assembly of double CDs in the matrix,<sup>42</sup> the introduction of functional groups,<sup>43</sup> and multiple surface states<sup>44</sup> have been utilized to obtain TDAC. Obviously, these works have demonstrated that the key to realizing TDAC is to build two or more emission centers within the system.

Here, we report the preparation of CD-based long afterglow materials with the TDAC phenomenon through the host–guest doping strategy. Upon removal of ultraviolet light, the afterglow color displays a gradual blue shift over time and persists for several seconds. The results indicate that the TDAC is composed of the radiative transition of triplet excitons of CDs and the trap luminescence of the  $\text{B}_2\text{O}_3$  matrix, accompanied by energy transfer. In addition, we demonstrate that the afterglow emission of  $\text{B}_2\text{O}_3$  originates from internal traps and CDs as “impurities” that create additional traps during the formation of  $\text{B}_2\text{O}_3$ . More importantly, these traps serve as energy donors and directly induce the TDAC emission of the CDs.

Unlike the design concepts of the reported CD-based long afterglow materials with TDAC, our goal is to utilize the host matrix with afterglow emission to develop TDAC composites.

Based on this, we chose naphthalene and its derivatives as carbon sources to prepare long wavelength CDs (with short lifetime) and chose BA to prepare a short wavelength matrix (with long lifetime) (Figure 1a,b). Due to the difference in lifetime and emission wavelength, this strategy facilitates the easy acquisition of TDAC. The preparation process is shown in Figure S1. It is important to note that the four precursors do not exhibit afterglow emission before the reaction but only fluorescence emission (Figure S2). Interestingly, compared with the green afterglow emitted by  $\text{B}_2\text{O}_3$ , the composite system with the addition of the carbon source exhibits the TDAC phenomenon upon turning off the 365 nm ultraviolet light.

Transmission electron microscopy (TEM) images show that four typical CDs are uniformly dispersed in the  $\text{B}_2\text{O}_3$  matrix, and their average particle sizes are 1.66, 2.42, 2.97, and 4.54 nm, respectively (Figure 2a–d). The high-resolution TEM image shows that all four CDs possess crystalline structures with a lattice fringe spacing of 0.21 nm, corresponding to the (100) crystal plane of graphitized carbon.<sup>45,46</sup> The X-ray diffraction (XRD) pattern shows good agreement with the simulated XRD pattern of  $\text{B}_2\text{O}_3$  and exhibits obvious  $\text{B}_2\text{O}_3$  characteristic peaks at  $\sim 14.5^\circ$  and  $27.8^\circ$ , respectively (Figure 4e). The Fourier transform infrared spectroscopy (FT-IR) spectra show peaks at 3218, 1440, and  $1195\text{ cm}^{-1}$ , assigned to the  $-\text{OH}$ ,  $\text{B}-\text{O}$ , and  $\text{B}-\text{O}-\text{H}$ , respectively. Additionally, the peaks at 1105, 1027, and  $927\text{ cm}^{-1}$  correspond to the  $\text{C}-\text{N}$ ,  $\text{B}-\text{O}-\text{C}$ , and  $\text{B}-\text{C}$  stretching vibrations, respectively (Figure 4f). Notably, compared with  $\text{B}_2\text{O}_3$ , the four CD-based long afterglow materials exhibit new stretching vibration peaks at  $927\text{ cm}^{-1}$  (B, C). The results of X-ray photoelectron spectroscopy (XPS) further confirm the experimental results of FT-IR. The full-scan XPS spectra reveal characteristic peaks of C 1s, O 1s, and B 1s with binding energies at 284, 533, and 194 eV, respectively (Figure 4d). The high-resolution C 1s

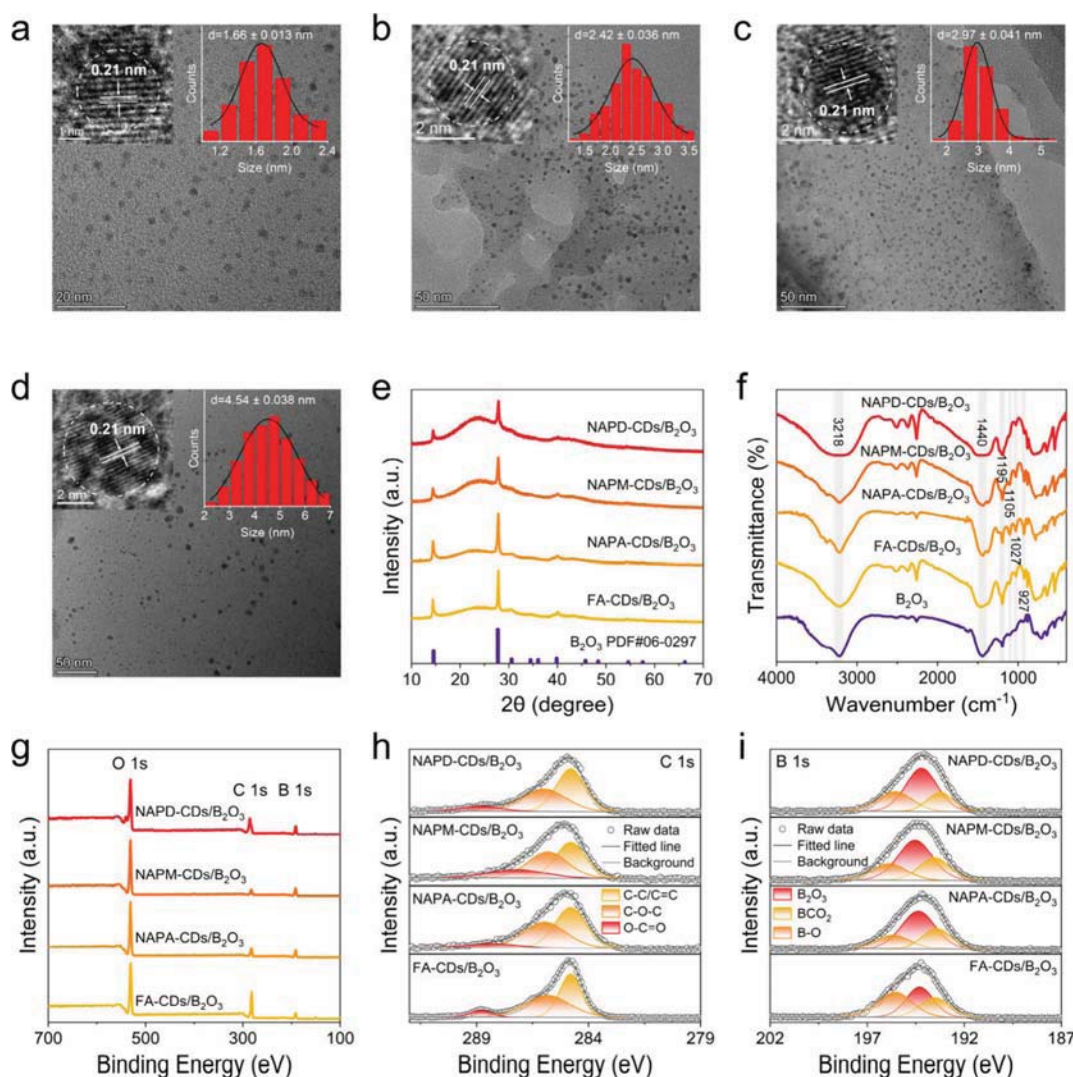


**Figure 2.** Morphology and chemical structure of the four CD-based long afterglow materials. (a–d) TEM image of FA-CDs/B<sub>2</sub>O<sub>3</sub> (a), NAPA-CDs/B<sub>2</sub>O<sub>3</sub> (b), NAPM-CDs/B<sub>2</sub>O<sub>3</sub> (c), and NAPD-CDs/B<sub>2</sub>O<sub>3</sub> (d). Inset: the high-resolution TEM image of CDs and the size of the particle distribution. (e) Powder XRD patterns of the four CD-based long afterglow materials. (f) FT-IR spectra of the B<sub>2</sub>O<sub>3</sub> and four CD-based long afterglow materials. (g) Full scan XPS spectra of the four CD-based long afterglow materials. (h, i) High-resolution C 1s (h) and B 1s (i) XPS spectra of the four CD-based long afterglow materials.

spectra have three peaks at 284.8, 285.9, and 288.8 eV, corresponding to C–C/C=C, C–O–C, and O–C=O bonds, respectively (Figure 4e). The high-resolution B 1s curve can be deconvoluted into three peaks at 193.4, 194.3, and 195.5 eV, belonging to BCO<sub>2</sub>, B<sub>2</sub>O<sub>3</sub>, and B–O, respectively (Figure 4f). The high-resolution O 1s spectra exhibited peaks at binding energies of 534.7 and 533.4 eV, corresponding to C–O and C=O, respectively (Figure S3). These results demonstrate that during the formation of CDs, the covalent coupling reaction occurs between CDs and B<sub>2</sub>O<sub>3</sub>, leading to the generation of new B–C bonds.

The photophysical properties of FA-CDs/B<sub>2</sub>O<sub>3</sub>, NAPA-CDs/B<sub>2</sub>O<sub>3</sub>, NAPM-CDs/B<sub>2</sub>O<sub>3</sub>, and NAPD-CDs/B<sub>2</sub>O<sub>3</sub> under steady state conditions were thoroughly investigated. As shown in Figure 3a–d, their afterglow emission spectra exhibit multiple emission characteristics, and the maximum emission wavelengths are 542, 540, 553, and 603 nm, respectively. The average lifetimes of FA-CDs/B<sub>2</sub>O<sub>3</sub>, NAPA-CDs/B<sub>2</sub>O<sub>3</sub>, NAPM-CDs/B<sub>2</sub>O<sub>3</sub>, and NAPD-CDs/B<sub>2</sub>O<sub>3</sub> are calculated to be 1.117,

0.878, 0.696, and 0.224 s (Figure 3e–h, Table S1). The corresponding Commission International d’Éclairage (CIE) coordinates are (0.31, 0.43), (0.41, 0.55), (0.44, 0.53), and (0.58, 0.38) (Figure 3i). Their afterglow quantum yields were determined to be 6.18%, 41.52%, 40.44%, and 5.26%, respectively (Figures S4–S7). Notably, as shown in Figure 2b, the fluorescence emission spectrum of NAPA-CDs/B<sub>2</sub>O<sub>3</sub> comprises a main emission peak at 389 nm and secondary emission peaks at 540 and 585 nm under the excitation of 365 nm. Interestingly, the peak positions of the secondary emission peaks coincide perfectly with those of the afterglow emission peaks and remain consistent even at 77 K (Figure S8). Therefore, we speculate that the fluorescence emission spectrum of NAPA-CDs/B<sub>2</sub>O<sub>3</sub> exhibits dual emission, which is composed of short wavelength fluorescence emission (389 nm) and long wavelength afterglow emission (540 and 585 nm). Upon normalizing the afterglow emission of the four CD-based long afterglow materials and B<sub>2</sub>O<sub>3</sub>, we found that they exhibit afterglow emission at 509 nm, indicating that B<sub>2</sub>O<sub>3</sub>



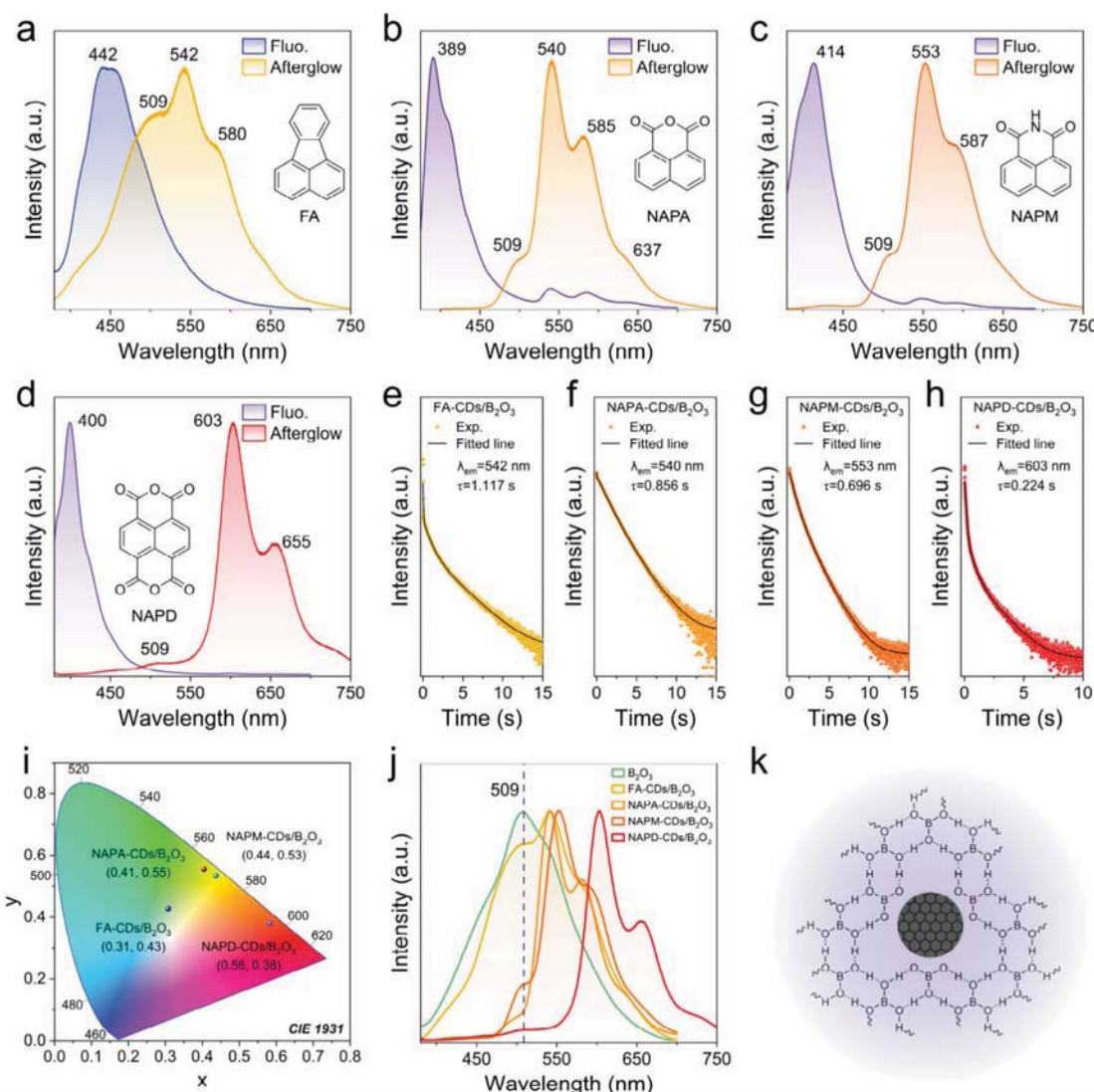


**Figure 3.** Photophysical properties of the four CD-based long afterglow materials. (a–d) Normalized fluorescence emission spectra and afterglow emission spectra of FA-CDs/B<sub>2</sub>O<sub>3</sub> (a), NAPA-CDs/B<sub>2</sub>O<sub>3</sub> (b), NAPM-CDs/B<sub>2</sub>O<sub>3</sub> (c), and NAPD-CDs/B<sub>2</sub>O<sub>3</sub> (d) acquired under 365 nm excitation. (e, f) Afterglow lifetimes of FA-CDs/B<sub>2</sub>O<sub>3</sub> (e), NAPA-CDs/B<sub>2</sub>O<sub>3</sub> (f), NAPM-CDs/B<sub>2</sub>O<sub>3</sub> (g), and NAPD-CDs/B<sub>2</sub>O<sub>3</sub> (h) acquired under 365 nm excitation. (i) CIE coordinates of RTP color of the four CD-based long afterglow materials. (j) Normalized afterglow emission spectra of the four CD-based long afterglow materials under 365 nm excitation. (k) Schematic of the proposed structure of the four CD-based long afterglow materials.

itself contributes to the afterglow in the composite system (Figure 3j). The above research proves that CD-based long afterglow materials prepared by a one-step calcination strategy have at least two emission centers, attributed to CDs and B<sub>2</sub>O<sub>3</sub>, which aligns with our expectations. Therefore, the B–C bond and the rigid host (B<sub>2</sub>O<sub>3</sub>) protect the triplet exciton of CDs from quenching by environmental factors and reduce non-radiative transitions, thereby obtaining effective afterglow emission (Figure 3k).<sup>47</sup>

In order to explore the origin of TDAC, we selected NAPA-CDs/B<sub>2</sub>O<sub>3</sub> with an obvious discoloration phenomenon for subsequent research. After comparing the afterglow emission spectra and digital photograph of NAPA-CDs/B<sub>2</sub>O<sub>3</sub> with different doping ratios, we chose NAPA-CDs/B<sub>2</sub>O<sub>3</sub> with a molar ratio of 1:6000 for photophysical experiments (Figure 4a, Figure S9). The afterglow emission spectra demonstrated that with the increase of excitation wavelength, NAPA-CDs/B<sub>2</sub>O<sub>3</sub> exhibits four emission peaks, corresponding to 509, 540,

585, and 637 nm, respectively (Figure 4b). We also studied the ultraviolet absorption spectra of CDs in aqueous solutions (Figure S10). The absorption bands at ~225 and ~295 nm are attributed to  $\pi$ – $\pi^*$  transitions of C=C bonds within the carbon core, and the ~343 nm absorption band is attributed to  $n$ – $\pi^*$  transitions of surface functional groups C=O.<sup>48,49</sup> The temperature-dependent afterglow spectra of NAPA-CDs/B<sub>2</sub>O<sub>3</sub> were measured (Figure 4c). As the temperature increases from 100 to 350 K, the afterglow emission intensity gradually increases, which is a characteristic of thermally activated delayed fluorescence materials.<sup>50,51</sup> However, at 400 K, the emission intensity sharply decreased, likely due to high temperatures damaging the internal structure (Figure S11). The afterglow lifetime decay curves of each emission peak under 365 nm excitation were further explored (Figure 4d, Figure S12, and Table S2). Under emission conditions of 509, 540, 585, and 637 nm, NAPA-CDs/B<sub>2</sub>O<sub>3</sub> possessed afterglow lifetimes of 1.128, 0.856, 0.810, and 0.793 s, respectively.

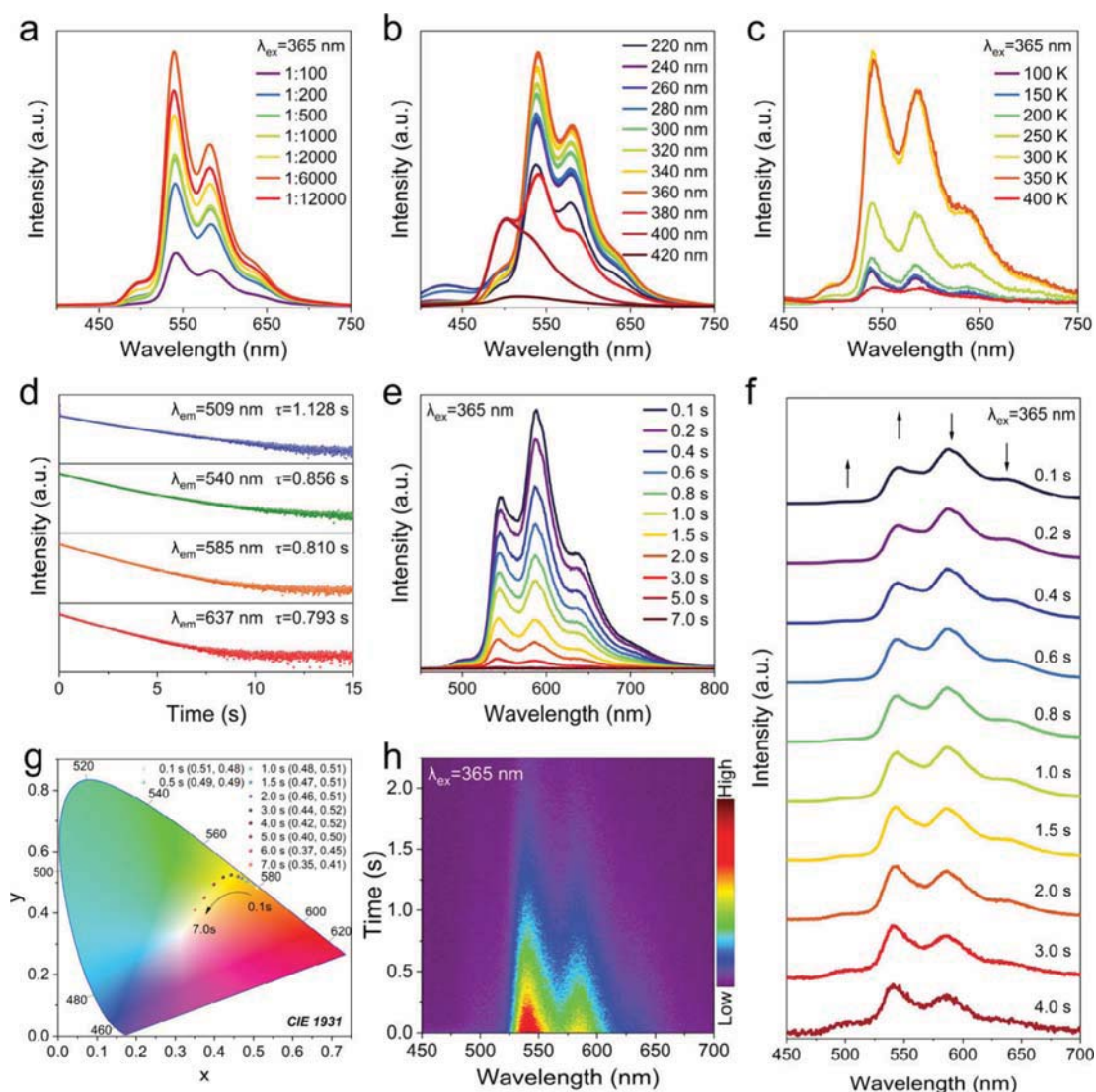


**Figure 4.** Afterglow properties of NAPA-CDs/B<sub>2</sub>O<sub>3</sub>. (a) Afterglow emission spectra of NAPA-CDs/B<sub>2</sub>O<sub>3</sub> with different doping proportions under excitation at 365 nm. (b) Afterglow emission spectra of NAPA-CDs/B<sub>2</sub>O<sub>3</sub> under different excitation wavelengths. (c) Temperature-dependent afterglow spectra from 100 to 400 K of NAPA-CDs/B<sub>2</sub>O<sub>3</sub> under excitation at 365 nm. (d) Room-temperature lifetime decay curves of NAPA-CDs/B<sub>2</sub>O<sub>3</sub> under excitation at 365 nm. (e) Time-resolved afterglow emission spectra of NAPA-CDs/B<sub>2</sub>O<sub>3</sub> after 365 nm irradiation. (f) Normalization time-resolved afterglow emission spectra of NAPA-CDs/B<sub>2</sub>O<sub>3</sub>. (g) CIE coordinates of the time-resolved afterglow spectra. (h) Time-dependent afterglow mapping of NAPA-CDs/B<sub>2</sub>O<sub>3</sub> excited by 365 nm.

Time-resolved emission spectroscopy (TRES) was used to measure the delayed emission spectra at different delay times (Figure 4e). At 0.1 s, the emission peak at 585 nm stood out prominently compared with other peaks, dominating the emission spectrum. As time elapsed, the emission peaks at 509 and 540 nm showed an increasing trend relative to those at 585 and 637 nm, reaching equilibrium at approximately 1.5 s for the two peaks (540 and 585 nm). Subsequently, the 540 nm emission became the dominant emission (Figure 4f). The CIE chromaticity diagram of the afterglow changes was plotted (Figure 4g), indicating a continuous shift in light emission color from orange (0.51, 0.48) to green (0.35, 0.41), consistent with human visual perception. The time-resolved afterglow spectra of NAPA-CDs/B<sub>2</sub>O<sub>3</sub> were recorded, showing afterglow emission bands in the range of 500–650 nm with signals lasting over 1 s (Figure 4h, Figure S13). Therefore, various experimental data demonstrated that the dynamic afterglow of

NAPA-CDs/B<sub>2</sub>O<sub>3</sub> is attributed to the competitive interactions and lifetime differences of multiple emission peaks.

Notably, we discovered an interesting photofluorochromic phenomenon in NAPA-CDs/B<sub>2</sub>O<sub>3</sub>. Under 365 nm ultraviolet irradiation, the luminescence of NAPA-CDs/B<sub>2</sub>O<sub>3</sub> obviously changed from blue to purple (Figure S14a). The fluorescence emission spectrum revealed that the fluorescence emission peak of NAPA-CDs/B<sub>2</sub>O<sub>3</sub> was independent of the excitation wavelength (Figure S14b). The temperature-dependent fluorescence spectra of NAPA-CDs/B<sub>2</sub>O<sub>3</sub> were studied, and the fluorescence intensity gradually decreased when heated from 100 to 400 K, which was caused by the increased nonradiative transition rate at high temperatures (Figure S14c). The fluorescence lifetime graph varying with temperature further validates these conclusions (Figure S14d). Additionally, the fluorescence emission spectra of NAPA-CDs/B<sub>2</sub>O<sub>3</sub> under ultraviolet irradiation were measured by



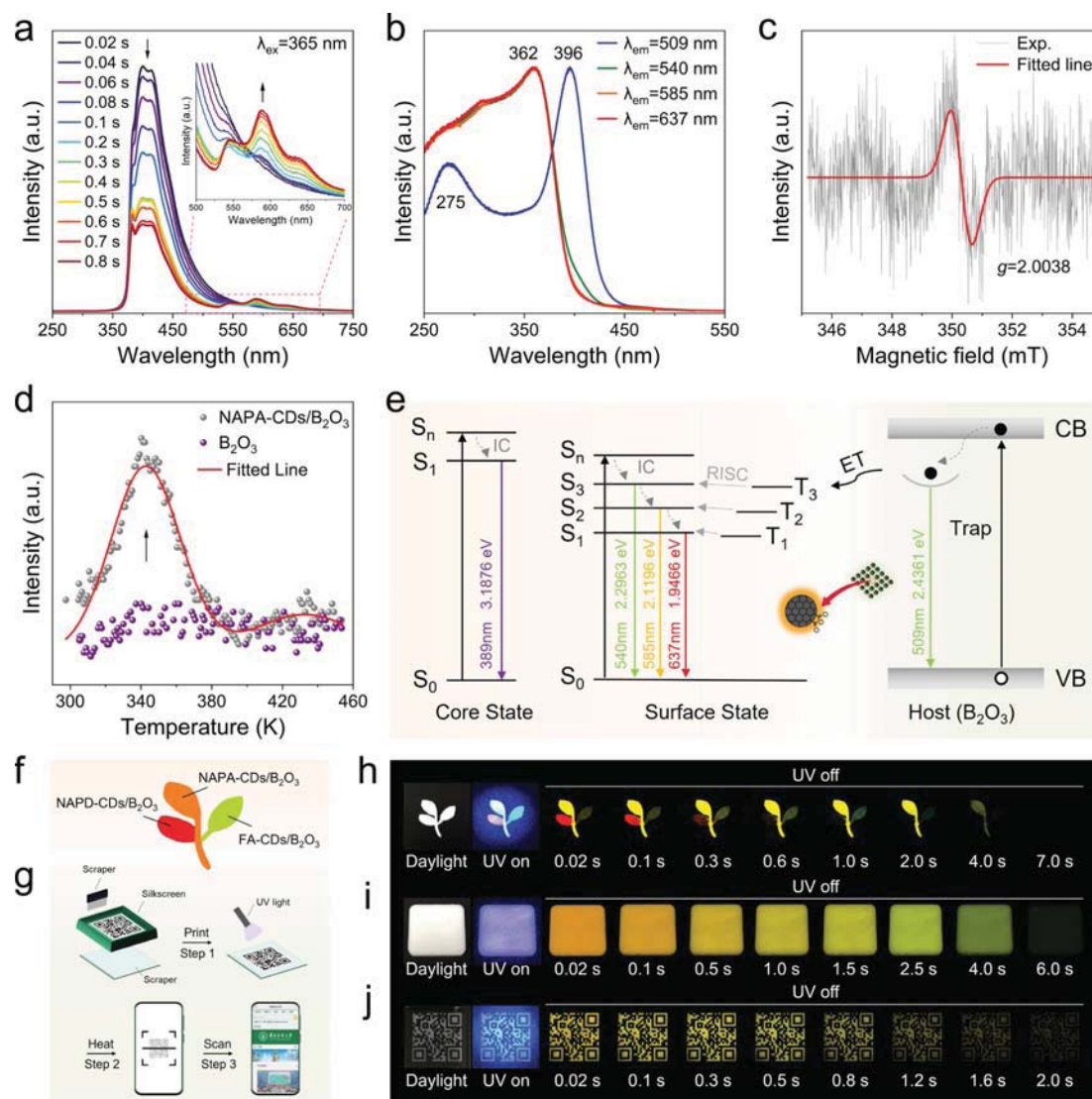


**Figure 5.** A possible afterglow emission mechanism of NAPA-CDs/B<sub>2</sub>O<sub>3</sub>. (a) Time-resolved fluorescence spectra of NAPA-CDs/B<sub>2</sub>O<sub>3</sub> after 365 nm irradiation. Inset: amplification at 500~700 nm. (b) Normalized afterglow excitation spectra of NAPA-CDs/B<sub>2</sub>O<sub>3</sub> measured at 509, 540, 585, and 637 nm. (c) ESR spectra of NAPA-CDs/B<sub>2</sub>O<sub>3</sub>. (d) TL curve spectra of B<sub>2</sub>O<sub>3</sub> and NAPA-CDs/B<sub>2</sub>O<sub>3</sub>. (e) Possible afterglow emission processes and energy level diagram of NAPA-CDs/B<sub>2</sub>O<sub>3</sub>. (f) Information encryption schematic diagram designed with FA-CDs/B<sub>2</sub>O<sub>3</sub>, NAPA-CDs/B<sub>2</sub>O<sub>3</sub>, and NAPA-CDs/B<sub>2</sub>O<sub>3</sub>. (g) Multimode anti-counterfeiting schematic diagram and screen-printing process based on the initial NAPA-CDs/B<sub>2</sub>O<sub>3</sub> powder. (h) Digital photograph of three time-dependent room-temperature afterglow materials under daylight, under 365 nm UV light, and after removing 365 nm UV light. (i) The composite film consisting of NAPA-CDs/B<sub>2</sub>O<sub>3</sub> powder embedded in the PDMS matrix was photographed under daylight, under 365 nm UV light, and after removing 365 nm UV light. (j) Digital photograph of the fabricated pattern based on PDMS films under daylight, under 365 nm UV light, and after removing 365 nm UV light.

using TRES (Figure 5a). The results showed that no long wavelength delayed fluorescence emission was detected at the initial stage of ultraviolet irradiation. With the increase of irradiation time, the long wavelength delayed fluorescence emission peak gradually increased, while the short wavelength fluorescence peak gradually decreased, resulting in a noticeable change in fluorescence color. As shown in the CIE chromaticity diagram (Figure S14e), the luminescence color shows a successive change from blue (0.167, 0.082) to purple (0.249, 0.153), which is consistent with the observation of the human eye. Overall, these findings indicate that the photo-fluorochromic phenomenon of NAPA-CDs/B<sub>2</sub>O<sub>3</sub> is closely related to the emission of delayed fluorescence.

We conducted a further investigation into the origin of TDAC. The normalized afterglow excitation spectra indicated that the excitation spectra of 540, 585, and 637 nm are basically consistent, suggesting that these emissions originate from the same emission center (Figure 5b, Figure S15a). However, the excitation spectrum at 509 nm displayed a completely different curve and is highly consistent with the excitation spectrum of B<sub>2</sub>O<sub>3</sub>, with optimal excitation at 396 nm (Figure S15b). The above studies show that there are two emission centers of CDs and B<sub>2</sub>O<sub>3</sub> in the system. The fluorescence lifetimes under excitation at 340 nm were measured to be 2.913, 14.598, and 28.402 ns for 389, 540, and 585 nm, respectively (Figure S16). According to Einstein's formula, the average lifetime of the excited states undergoing

spontaneous emission can be calculated, allowing the determination of the oscillator strength at these points (Table S3, eq S1).<sup>52</sup> The calculated results indicate that the oscillator strength at 540 nm ( $S_3$ ) is stronger than at 585 nm ( $S_2$ ), indicating the anti-Kasha radiation transition.<sup>53</sup> According to eq S2, the energy levels of the defect and surface states were calculated. The energy level of  $B_2O_3$  is 2.4361 eV, while the energy levels of surface states  $S_3$ ,  $S_2$ , and  $S_1$  are 2.2963, 2.1196, and 1.9466 eV, respectively. Furthermore, electron spin resonance (ESR) spectroscopy was utilized to investigate the presence and state of oxygen vacancies in NAPA-CDs/ $B_2O_3$ , finding a  $g$  value of 2.0038 corresponding to the center of the resonance field (Figure 5c). Thermoluminescence (TL) spectroscopy is widely used to investigate the trap characteristics of afterglow materials, and the TL curves of NAPA-CDs/ $B_2O_3$  and  $B_2O_3$  were measured (Figure 5d). The results show that both samples can release charge carriers to form thermoluminescence after thermal excitation. Notably, the thermoluminescence peaks for both NAPA-CDs/ $B_2O_3$  and  $B_2O_3$  occurred at approximately the same heating temperature of 344 K, indicating that the addition of CDs did not alter the type of traps within the matrix. The difference is that compared with  $B_2O_3$ , the thermal release peak of NAPA-CDs/ $B_2O_3$  shows a higher intensity, which means that the number of traps in NAPA-CDs/ $B_2O_3$  is significantly more than that in  $B_2O_3$ . According to the following formula for calculating the average trap depth:  $E_T = T_m/500$ ,<sup>54</sup> the estimated trap depth in NAPA-CDs/ $B_2O_3$  was determined to be 0.688 eV.

In conclusion, a possible luminescence mechanism is proposed (Figure 5e). Under 365 nm ultraviolet irradiation, the electrons in the core state rapidly radiate out at 389 nm. Meanwhile, the electrons in the surface states undergo intersystem crossing (ISC) to the excited triplet state, followed by reverse intersystem crossing (RISC) to the excited singlet state, and finally return to the ground state via delayed fluorescence, corresponding to the photofluorochromic phenomenon from blue to purple. Upon the cessation of irradiation, the electrons stored in the traps are released. Since the energy level difference between  $B_2O_3$  and the surface triplet states of CDs is very small, electrons can reach the surface triplet states of CDs and enhance their radiative transitions. Initially, energy transfer from the traps to the triplet states shows no selectivity, allowing charge carriers to populate the  $T_1$ ,  $T_2$ , and  $T_3$  energy levels. Due to the RISC and internal conversion (IC) processes occurring within the CDs, a small fraction of excitons reach the  $T_2$  and  $T_3$  energy levels, resulting in a relatively high initial emission intensity. Over time, the energy transfer efficiency decreases. However, compared with the  $T_2$  and  $T_3$  energy levels, the  $T_1$  energy level is closer to the trap energy level, causing it to gradually dominate in the later stage, which corresponds to the observed TDAC phenomenon.

Due to the unique TDAC emission, CD-based long afterglow materials with dynamic afterglow have a very broad application prospect in the fields of anti-counterfeiting and information encryption. The prepared materials can be ground into powder and sieved through a 200 mesh sieve, retaining a distinct TDAC phenomenon (Figure S17). A flower pattern was designed for advanced anti-counterfeiting (Figure 5f). Upon removal of 365 nm ultraviolet light, each part fades in chronological order and exhibits a TDAC (Figure 5h). In addition, we also embedded NAPA-CDs/ $B_2O_3$  into polydimethylsiloxane (PDMS) to produce a composite film that is waterproof and flexible (Figure S18). Upon removal of 365 nm

ultraviolet light, the composite film shows a bright orange afterglow, and the afterglow color gradually changes to green over time, which is consistent with the luminescence behavior observed in bulk and powder (Figure 5i). Following the approach depicted in Figure 5g, QR codes were printed on a glass sheet using screen printing technology. After UV irradiation is removed, an orange to green afterglow can be observed (Figure 5j).

In summary, we present a novel strategy to construct time-dependent afterglow color. Our results demonstrate that the formation of covalent bonds within the composite and the establishment of a rigid environment are critical for achieving long wavelength afterglow. In addition, during the formation of boron oxide, CDs act as dopants to create additional defects within the matrix, thereby increasing the trap concentration. Further research reveals that TDAC originates from energy transfer of traps to the surface states of CDs, rather than from the emission competition between CDs and boron oxide. Specifically, the energy level of the traps is closer to the long wavelength energy level of CDs, allowing the traps to provide electrons to induce TDAC of CDs. We have demonstrated the universality of this strategy, which will promote the development and application of TDAC materials. Although this study establishes a fundamental framework for TDAC materials, precisely controlling the type and depth of traps to regulate TDAC remains challenging. This challenge might be effectively addressed through machine-learning-assisted optimization of synthesis parameters.

## ■ ASSOCIATED CONTENT

### Supporting Information

The Supporting Information is available free of charge at <https://pubs.acs.org/doi/10.1021/acs.nanolett.5c00723>.

Video S1: the afterglow video of  $B_2O_3$  (MP4)

Video S2: the afterglow video of FA-CDs/ $B_2O_3$  (MP4)

Video S3: the afterglow video of NAPA-CDs/ $B_2O_3$  (MP4)

Video S4: the afterglow video of NAPM-CDs/ $B_2O_3$  (MP4)

Video S5: the afterglow video of NAPD-CDs/ $B_2O_3$  (MP4)

Video S6: the afterglow video of the PDMS composite film (MP4)

Experimental section including materials, preparation, and instruments; results and discussion including optical images, high-resolution O 1s XPS spectra, afterglow quantum yield, UV-vis absorption spectra, afterglow decay and fitting curve, 3D time-dependent afterglow mapping, fluorescence emission spectra, temperature-dependent fluorescence spectra, temperature-dependent fluorescence lifetime, CIE coordinates of the time-resolved fluorescence spectra, afterglow excitation spectra, fluorescence lifetime (PDF)

## ■ AUTHOR INFORMATION

### Corresponding Authors

Chaofan Hu – Key Laboratory for Biobased Materials and Energy of Ministry of Education/Guangdong Provincial Engineering Technology Research Center for Optical Agriculture, College of Materials and Energy, South China Agricultural University, Guangzhou 510642, China;



orcid.org/0000-0003-2311-8733; Email: [thucf@scau.edu.cn](mailto:thucf@scau.edu.cn)

**Bingfu Lei** – Key Laboratory for Biobased Materials and Energy of Ministry of Education/Guangdong Provincial Engineering Technology Research Center for Optical Agriculture, College of Materials and Energy, South China Agricultural University, Guangzhou 510642, China; orcid.org/0000-0002-6634-0388; Email: [tleibf@scau.edu.cn](mailto:tleibf@scau.edu.cn)

## Authors

**Zhun Ran** – Key Laboratory for Biobased Materials and Energy of Ministry of Education/Guangdong Provincial Engineering Technology Research Center for Optical Agriculture, College of Materials and Energy, South China Agricultural University, Guangzhou 510642, China; orcid.org/0009-0005-1655-7422

**Hongjie Jia** – Key Laboratory for Biobased Materials and Energy of Ministry of Education/Guangdong Provincial Engineering Technology Research Center for Optical Agriculture, College of Materials and Energy, South China Agricultural University, Guangzhou 510642, China

**Ziting Zhong** – Key Laboratory for Biobased Materials and Energy of Ministry of Education/Guangdong Provincial Engineering Technology Research Center for Optical Agriculture, College of Materials and Energy, South China Agricultural University, Guangzhou 510642, China

**Hongwei Yang** – Key Laboratory for Biobased Materials and Energy of Ministry of Education/Guangdong Provincial Engineering Technology Research Center for Optical Agriculture, College of Materials and Energy, South China Agricultural University, Guangzhou 510642, China; orcid.org/0009-0007-9365-4028

**Yinda Zhu** – Key Laboratory for Biobased Materials and Energy of Ministry of Education/Guangdong Provincial Engineering Technology Research Center for Optical Agriculture, College of Materials and Energy, South China Agricultural University, Guangzhou 510642, China

**Yuqi Li** – Key Laboratory for Biobased Materials and Energy of Ministry of Education/Guangdong Provincial Engineering Technology Research Center for Optical Agriculture, College of Materials and Energy, South China Agricultural University, Guangzhou 510642, China; MOE Key Laboratory of Laser Life Science and Guangdong Provincial Key Laboratory of Laser Life Science, College of Biophotonics, South China Normal University, Guangzhou 510631, China

**Jinkun Liu** – Key Laboratory for Biobased Materials and Energy of Ministry of Education/Guangdong Provincial Engineering Technology Research Center for Optical Agriculture, College of Materials and Energy, South China Agricultural University, Guangzhou 510642, China

**Xuejie Zhang** – Key Laboratory for Biobased Materials and Energy of Ministry of Education/Guangdong Provincial Engineering Technology Research Center for Optical Agriculture, College of Materials and Energy, South China Agricultural University, Guangzhou 510642, China; orcid.org/0000-0002-4029-7000

**Jianle Zhuang** – Key Laboratory for Biobased Materials and Energy of Ministry of Education/Guangdong Provincial Engineering Technology Research Center for Optical Agriculture, College of Materials and Energy, South China Agricultural University, Guangzhou 510642, China; orcid.org/0000-0002-4649-1939

**Yingliang Liu** – Key Laboratory for Biobased Materials and Energy of Ministry of Education/Guangdong Provincial Engineering Technology Research Center for Optical Agriculture, College of Materials and Energy, South China Agricultural University, Guangzhou 510642, China; orcid.org/0000-0003-1930-0700

Complete contact information is available at: <https://pubs.acs.org/10.1021/acs.nanolett.5c00723>

## Author Contributions

Z.R., B.L., and C.H. conceived the experiments. Z.R. synthesized all materials. Z.R., H.J., Z.Z., H.Y., Y.Z., Y.L., and J.L. conducted structure characterization. X.Z., J.Z., and Y.L. gave suggestions to optimize the system. Z.R., B.L., and C.H. wrote the first draft of the paper, and all authors contributed to revise the paper.

## Notes

The authors declare no competing financial interest.

## ACKNOWLEDGMENTS

This work was supported by the National Natural Science Foundation of China (12174119, 52172142, 12274144, and 52472160), and the Natural Science Foundation of Guangdong Province (2023A1515012003, 2025A1515010658).

## REFERENCES

- (1) Pan, Z.; Lu, Y.-Y.; Liu, F. Sunlight-activated long-persistent luminescence in the near-infrared from Cr<sup>3+</sup>-doped zinc gallagermanates. *Nat. Mater.* **2012**, *11* (1), 58–63.
- (2) Maldiney, T.; Bessière, A.; Seguin, J.; Teston, E.; Sharma, S. K.; Viana, B.; Bos, A. J. J.; Dorenbos, P.; Bessodes, M.; Gourier, D.; et al. The in vivo activation of persistent nanophosphors for optical imaging of vascularization, tumours and grafted cells. *Nat. Mater.* **2014**, *13* (4), 418–426.
- (3) Wang, Z.; Zhu, C.-Y.; Mo, J.-T.; Xu, X.-Y.; Ruan, J.; Pan, M.; Su, C.-Y. Multi-Mode Color-Tunable Long Persistent Luminescence in Single-Component Coordination Polymers. *Angew. Chem., Int. Ed.* **2021**, *60* (5), 2526–2533.
- (4) Matsuzawa, T.; Aoki, Y.; Takeuchi, N.; Murayama, Y. A New Long Phosphorescent Phosphor with High Brightness, SrAl<sub>2</sub>O<sub>4</sub>: Eu<sup>2+</sup>, Dy<sup>3+</sup>. *J. Electrochem. Soc.* **1996**, *143* (8), 2670.
- (5) Yang, R.; Yang, D.; Wang, M.; Zhang, F.; Ji, X.; Zhang, M.; Jia, M.; Chen, X.; Wu, D.; Li, X. J.; et al. High-Efficiency and Stable Long-Persistent Luminescence from Undoped Cesium Cadmium Chlorine Crystals Induced by Intrinsic Point Defects. *Adv. Sci.* **2023**, *10* (15), 2207331.
- (6) Li, Y.; Gecevicius, M.; Qiu, J. Long persistent phosphors—from fundamentals to applications. *Chem. Soc. Rev.* **2016**, *45* (8), 2090–2136.
- (7) Yang, X.; Waterhouse, G. I. N.; Lu, S.; Yu, J. Recent advances in the design of afterglow materials: mechanisms, structural regulation strategies and applications. *Chem. Soc. Rev.* **2023**, *52* (22), 8005–8058.
- (8) Lei, B.; Machida, K.-i.; Horikawa, T.; Hanzawa, H.; Kijima, N.; Shimomura, Y.; Yamamoto, H. Reddish Orange Long Lasting Phosphorescence of Ca<sub>2</sub>Si<sub>3</sub>N<sub>8</sub>: Eu<sup>2+</sup>, Tm<sup>3+</sup> Phosphor. *J. Electrochem. Soc.* **2010**, *157* (6), J196.
- (9) Cui, G.; Yang, X.; Zhang, Y.; Fan, Y.; Chen, P.; Cui, H.; Liu, Y.; Shi, X.; Shang, Q.; Tang, B. Round-the-Clock Photocatalytic Hydrogen Production with High Efficiency by a Long-Afterglow Material. *Angew. Chem., Int. Ed.* **2019**, *58* (5), 1340–1344.
- (10) Wang, S.; Liu, R.; Li, J.; Meng, C.; Liu, J.; Chen, J.; Cheng, P.; Wu, K. Blue Long Afterglow and Ultra Broadband Vis-NIR Emission from All-Inorganic Copper-Doped Silver Halide Single Crystals. *Angew. Chem., Int. Ed.* **2024**, *63* (2), No. e202403927.

- (11) Zhuang, Y.; Wang, L.; Lv, Y.; Zhou, T.-L.; Xie, R.-J. Optical Data Storage and Multicolor Emission Readout on Flexible Films Using Deep-Trap Persistent Luminescence Materials. *Adv. Funct. Mater.* **2018**, *28* (8), 1705769.
- (12) Ou, X.; Qin, X.; Huang, B.; Zan, J.; Wu, Q.; Hong, Z.; Xie, L.; Bian, H.; Yi, Z.; Chen, X.; et al. High-resolution X-ray luminescence extension imaging. *Nature* **2021**, *590* (7846), 410–415.
- (13) Lyu, T.; Dorenbos, P. Charge carrier trapping management in Bi<sup>3+</sup> and lanthanides doped Li(Sc,Lu)GeO<sub>4</sub> for x-ray imaging, anti-counterfeiting, and force recording. *Applied Physics Reviews* **2024**, *11* (1), 011415.
- (14) Xu, X.; Wang, Y.; Zeng, W.; Gong, Y.; Liu, B. Luminescent Properties of the Multicolor Afterglow Phosphors Ca<sub>3</sub>SnSi<sub>2</sub>O<sub>9</sub>: Re<sup>3+</sup> (Re = Pr, Tb, Sm). *J. Am. Ceram. Soc.* **2011**, *94* (11), 3632–3635.
- (15) Liang, L.; Chen, J.; Shao, K.; Qin, X.; Pan, Z.; Liu, X. Controlling persistent luminescence in nanocrystalline phosphors. *Nat. Mater.* **2023**, *22* (3), 289–304.
- (16) Zheng, W.; Li, X.; Liu, N.; Yan, S.; Wang, X.; Zhang, X.; Liu, Y.; Liang, Y.; Zhang, Y.; Liu, H. Solution-Grown Chloride Perovskite Crystal of Red Afterglow. *Angew. Chem., Int. Ed.* **2021**, *60* (46), 24450–24455.
- (17) Lin, C.; Wu, Z.; Ma, H.; Liu, J.; You, S.; Lv, A.; Ye, W.; Xu, J.; Shi, H.; Zha, B.; et al. Charge trapping for controllable persistent luminescence in organics. *Nat. Photonics* **2024**, *18* (4), 350–356.
- (18) Zheng, H.; Cao, P.; Wang, Y.; Lu, X.; Wu, P. Ultralong Room-Temperature Phosphorescence from Boric Acid. *Angew. Chem., Int. Ed.* **2021**, *60* (17), 9500–9506.
- (19) Wu, Z.; Roldao, J. C.; Rauch, F.; Friedrich, A.; Ferger, M.; Würthner, F.; Gierschner, J.; Marder, T. B. Pure Boric Acid Does Not Show Room-Temperature Phosphorescence (RTP). *Angew. Chem., Int. Ed.* **2022**, *61* (15), No. e202200599.
- (20) Zhang, Z.; Wang, Z.; Liu, X.; Shi, Y.-e.; Li, Z.; Zhao, Y. Modulating Emission of Boric Acid into Highly Efficient and Color-Tunable Afterglow via Dehydration-Induced Through-Space Conjugation. *Adv. Sci.* **2023**, *10* (15), 2300139.
- (21) Cao, P.; Wang, Y.; Zheng, H.; Wu, P. Unusual phosphorescence of boric acid: From impurity or clusterization-triggered emission? *Aggregate* **2024**, *5* (2), No. e468.
- (22) Song, Y.; Duan, X.; Jiang, Y.-n.; Ma, Y. B–O–O–B Impurity Induces Ultralong Room-Temperature Phosphorescence of Boric Acid. *J. Phys. Chem. Lett.* **2024**, *15* (26), 6890–6895.
- (23) Zhou, Z. S.; Jiang, K. F.; Chen, N. D.; Xie, Z. F.; Lei, B. F.; Zhuang, J. L.; Zhang, X. J.; Liu, Y. L.; Hu, C. F. Room temperature long afterglow from boron oxide: A boric acid calcined product. *Mater. Lett.* **2020**, *276*, 128226.
- (24) Balci, S.; Sezgi, N. A.; Eren, E. Boron Oxide Production Kinetics Using Boric Acid as Raw Material. *Ind. Eng. Chem. Res.* **2012**, *51* (34), 11091–11096.
- (25) Stagi, L.; Malfatti, L.; Zollo, A.; Livraghi, S.; Carboni, D.; Chiriu, D.; Corpino, R.; Ricci, P. C.; Cappai, A.; Carbonaro, C. M.; et al. Phosphorescence by Trapping Defects in Boric Acid Induced by Thermal Processing. *Adv. Opt. Mater.* **2024**, *12*, 2302682.
- (26) Li, W.; Zhou, W.; Zhou, Z. S.; Zhang, H. R.; Zhang, X. J.; Zhuang, J. L.; Liu, Y. L.; Lei, B. F.; Hu, C. F. A Universal Strategy for Activating the Multicolor Room-Temperature Afterglow of Carbon Dots in a Boric Acid Matrix. *Angew. Chem., Int. Ed.* **2019**, *58* (22), 7278–7283.
- (27) Guo, P.; Shi, Y.-e.; Shen, S.; Zhou, C.; Jiang, J.; Wang, Z. Achieving Efficient Room-Temperature Phosphorescence in the Host–Guest System through Covalent-Bond-Strengthened Hydrogen Bonding. *J. Phys. Chem. C* **2024**, *128* (17), 7169–7176.
- (28) Cheng, Y.; Fan, W.; He, R.; Meng, X.; Zhou, Q.; Ma, X.; Liu, Y.; Shi, Y.; Zheng, L.; Cao, Q. Naphthoic Acid Derivatives@Boric Acid Based Fast Photo-Activated Room-Temperature Phosphorescence Materials with Dynamic Changed Emission Color. *Adv. Opt. Mater.* **2024**, *12* (15), 2303017.
- (29) Zheng, Y.; Arkin, K.; Bei, Y.; Ma, X.; Shang, Q. Synergistic lifetime extension strategy based on Förster resonance energy transfer and TADF for carbon-dot-based room temperature afterglow. *Matter* **2023**, *6* (12), 4339–4356.
- (30) Liu, Y.; Cheng, D.; Wang, B.; Yang, J.; Hao, Y.; Tan, J.; Li, Q.; Qu, S. Carbon Dots-Inked Paper with Single/Two-Photon Excited Dual-Mode Thermochromic Afterglow for Advanced Dynamic Information Encryption. *Adv. Mater.* **2024**, *36* (31), 2403775.
- (31) Li, Q.; Zhao, Z.; Meng, S.; Li, Y.; Zhao, Y.; Zhang, B.; Tang, Z.; Tan, J.; Qu, S. Ultra-strong phosphorescence with 48% quantum yield from grinding treated thermal annealed carbon dots and boric acid composite. *SmartMat* **2022**, *3* (2), 260–268.
- (32) Gao, J.; Wu, X.; Jiang, X.; Li, M.; He, R.; Shen, W. Achieving purple light excitable high-efficiency temperature-responsive dual- and single-mode afterglow in carbon dots. *Carbon* **2023**, *208*, 365–373.
- (33) Ding, Y.; Wang, X.; Tang, M.; Qiu, H. Tailored Fabrication of Carbon Dot Composites with Full-Color Ultralong Room-Temperature Phosphorescence for Multidimensional Encryption. *Adv. Sci.* **2022**, *9* (3), 2103833.
- (34) Liu, X.; Liu, W.; Zuo, K.; Zheng, J.; Wang, M.; Liu, X. High Color Stability Blue-to-Violet Room Temperature Phosphorescent Carbon Dot Composites with Ultralong Lifetime for Information Encryption. *ACS Sustainable Chem. Eng.* **2023**, *11* (5), 1809–1819.
- (35) Wang, J.-X.; Fang, Y.-G.; Li, C.-X.; Niu, L.-Y.; Fang, W.-H.; Cui, G.; Yang, Q.-Z. Time-Dependent Afterglow Color in a Single-Component Organic Molecular Crystal. *Angew. Chem., Int. Ed.* **2020**, *59* (25), 10032–10036.
- (36) Li, Q.; Meng, S.; Li, Y.; Cheng, D.; Gu, H.; Zhao, Z.; Tang, Z.; Tan, J.; Qu, S. Surface ionization-induced tunable dynamic phosphorescence colors from carbon dots on paper for dynamic multimode encryption. *Carbon* **2022**, *195*, 191–198.
- (37) Zhang, L.; Chen, X.; Xin, M.; Yang, H.; Guo, D.; Hu, Y. Full-Color Dynamic Afterglow in Carbon Dot-Based Materials Regulated by Dual-Phosphorescence Resonance Energy Transfer. *Small* **2024**, *20* (52), 2406596.
- (38) Tan, J.; Li, Q.; Meng, S.; Li, Y.; Yang, J.; Ye, Y.; Tang, Z.; Qu, S.; Ren, X. Time-Dependent Phosphorescence Colors from Carbon Dots for Advanced Dynamic Information Encryption. *Adv. Mater.* **2021**, *33* (16), 2006781.
- (39) Kang, C.; Tao, S.; Yang, F.; Zheng, C.; Qu, Z.; Yang, B. Enabling Carbonized Polymer Dots with Color-tunable Time-dependent Room Temperature Phosphorescence through Confining Carboxyl Dimer Association. *Angew. Chem., Int. Ed.* **2024**, *63* (1), No. e202316527.
- (40) Zong, S.; Wang, B.; Zhang, J.; Yu, X.; Zhou, Y.; Chen, Y.; Zhang, T.; Li, J. Confinement Microenvironment Regulation of Carbon Dots in Zeolite for Multi-Mode Time-Dependent Phosphorescence Color Evolution. *Angew. Chem., Int. Ed.* **2025**, *64* (7), No. e202420156.
- (41) Shi, W.; Wang, R.; Liu, J.; Peng, F.; Tian, R.; Lu, C. Time-dependent Phosphorescence Color of Carbon Dots in Binary Salt Matrices through Activations by Structural Confinement and Defects for Dynamic Information Encryption. *Angew. Chem., Int. Ed.* **2023**, *62* (23), No. e202303063.
- (42) Zong, S.; Zhang, J.; Yin, X.; Li, J.; Qu, S. Time-Dependent and Excitation-Dependent Afterglow Color Evolution from the Assembly of Dual Carbon Dots in Zeolite. *Nano Lett.* **2024**, *24* (6), 1859–1866.
- (43) Sun, J.; Sun, Z.; Wang, Z.; Wang, N.; Han, Y.; Zhang, L.; Zhang, B.; Zhang, X. Ultra-Long-Lived Red TADF-CDs: Solid-State Synthesis, Time-Dependent Phosphorescence Color And Luminescent Mechanism. *Adv. Opt. Mater.* **2024**, *12* (12), 2302542.
- (44) Cui, S.; Wang, B.; Zan, Y.; Shen, Z.; Liu, S.; Fang, W.; Yan, X.; Li, Y.; Chen, L. Colorful, time-dependent carbon dot-based afterglow with ultralong lifetime. *Chem. Eng. J.* **2022**, *431*, 133373.
- (45) Ai, L.; Xiang, W. J.; Xiao, J. P.; Liu, H. M.; Yu, J. K.; Zhang, L. L.; Wu, X. T.; Qu, X. L.; Lu, S. Y. Tailored Fabrication of Full-Color Ultrastable Room-Temperature Phosphorescence Carbon Dots Composites with Unexpected Thermally Activated Delayed Fluorescence. *Adv. Mater.* **2024**, *36* (27), 2401220.
- (46) Zhang, T.; Wang, M.; Liu, L.; Li, Z.; Bi, H. Visible-Light Manipulated Reversible and Ultralong Phosphorescence of Carbon



Dots Through Dynamic Cross-Linking. *Adv. Funct. Mater.* **2024**, *34* (45), 2406672.

(47) Li, Z. Z.; Cao, S.; Zheng, Y. Y.; Song, L. Q.; Zhang, H. C.; Zhao, Y. L. Colorful Ultralong Room Temperature Phosphorescent Afterglow with Excitation Wavelength Dependence Based on Boric Acid Matrix. *Adv. Funct. Mater.* **2024**, *34* (3), 2306956.

(48) Ma, Y.; Wu, L.; Ren, X.; Zhang, Y.; Lu, S. Toward Kilogram-Scale Preparation of Full-Color Carbon Dots by Simply Stirring at Room Temperature in Air. *Adv. Funct. Mater.* **2023**, *33* (50), 2305867.

(49) Zhang, Q.; Xu, S.; Zhang, L.; Yang, L.; Jiang, C. Multiemitting Ultralong Phosphorescent Carbonized Polymer Dots via Synergistic Enhancement Structure Design. *Adv. Sci.* **2024**, *11* (18), 2400781.

(50) Xiao, Y.; Hu, W.; Liu, B.; Li, S.; Lü, C. Thermally Activated Delayed Fluorescence (TADF) Carbonized Polymer Dots for Efficient Red-Light-Induced Reversible Deactivation Radical Polymerization. *Macromolecules* **2025**, *58* (1), 97–108.

(51) Lei, M.; Zheng, J.; Yang, Y.; Yan, L.; Liu, X.; Xu, B. Carbon dots-based delayed fluorescent materials: Mechanism, structural regulation and application. *iScience* **2022**, *25* (9), 104884.

(52) Hilborn, R. C. Einstein coefficients, cross sections,  $f$  values, dipole moments, and all that. *Am. J. Phys.* **1982**, *50* (11), 982–986.

(53) Li, J.; Li, X.; Wang, G.; Wang, X.; Wu, M.; Liu, J.; Zhang, K. A direct observation of up-converted room-temperature phosphorescence in an anti-Kasha dopant-matrix system. *Nat. Commun.* **2023**, *14* (1), 1987.

(54) Shi, W. Y.; Yao, J.; Bai, L. Q.; Lu, C. Defect-Stabilized Triplet State Excitons: Toward Ultralong Organic Room-Temperature Phosphorescence. *Adv. Funct. Mater.* **2018**, *28* (52), 1804961.

# Multiemissive Room-Temperature Phosphorescent Carbon Dots@ZnAl<sub>2</sub>O<sub>4</sub> Composites by Inorganic Defect Triplet-State Energy Transfer

Zhijian Song, Yingliang Liu, Xiaomin Lin, Zhishan Zhou, Xuejie Zhang, Jianle Zhuang, Bingfu Lei, and Chaofan Hu\*



Cite This: <https://doi.org/10.1021/acsami.1c07391>



Read Online

ACCESS |



Metrics & More



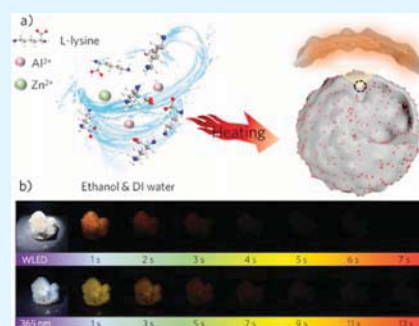
Article Recommendations



Supporting Information

**ABSTRACT:** Room-temperature phosphorescence (RTP) with carbon dots (CDs) can be exploited further if the mechanism of trap-state-mediated triplet-state energy transfer is understood and controlled. Herein, we developed an in situ calcination method for the preparation of a CDs@ZnAl<sub>2</sub>O<sub>4</sub> composite material that exhibits unique UV and visible light-excitable ultra-broad-band RTP. The ZnAl<sub>2</sub>O<sub>4</sub> matrix can protect the triplet emissions of CDs by the confinement effect and spin–orbit coupling. In addition, benefitting from the efficient energy transfer between the inorganic trap state and the triplet state of CDs, the special yellow to red RTP of CDs@ZnAl<sub>2</sub>O<sub>4</sub> composites can be realized. A slow-decaying phosphorescence at 570 nm with a lifetime of 1.05 s and a fast-decaying phosphorescence at 400 nm with a lifetime of 0.41 s were observed with UV irradiation of 290 nm, which originated from the surface and core triplet states of CDs, respectively. Based on the unique RTP performance, anti-counterfeiting and information encryption were successfully realized using the CDs@ZnAl<sub>2</sub>O<sub>4</sub> composites with LED light or UV light.

**KEYWORDS:** carbon dots, energy transfer, multiemission, inorganic matrix, phosphorescence



## 1. INTRODUCTION

Room-temperature phosphorescence (RTP) materials have shown more advantages over fluorescent materials in the applications of data storage, document encryption, anti-counterfeiting, time-resolved bioimaging, and so on. Nonetheless, traditional phosphorescent materials suffer from the following disadvantages: (i) upscaling of raw materials, (ii) complicated preparation and purification procedures, and (iii) exacting requirements on afterglow such as in a crystalline state as well as in a bulk form and rare to observe afterglow in aqueous solution and an oxygen atmosphere.<sup>1–4</sup> Recently, carbon dots (CDs), a novel member of nanoluminescent materials with unique optical properties, excellent biocompatibility, and easy preparation,<sup>5</sup> have become efficient alternatives to traditional phosphorescent materials and overcome many of the drawbacks. Significantly, CDs were embedded into various materials to obtain CDs-based RTP materials through structural confinement and chemical bonding (coordination,<sup>6–8</sup> covalent bonding,<sup>9–13</sup> and hydrogen bonds<sup>14,15</sup> between the rigid matrix and interior CDs. Specifically, the direct in situ incorporation of photoluminescent (PL) materials into inorganic materials requires a strong driving force between the coassembly of guest luminescent species and host inorganic matrices.<sup>16</sup> Fortunately, calcination is suitable

for the in situ generation of CDs and perfectly fixing them within the matrices.<sup>17,18</sup>

Almost all inorganic matrices have inherent internal defects, but their roles in the energy-transfer process in the CDs@inorganic-matrix composite have not been precisely discussed until recently. Lu and coworkers made remarkable progress in activating weak phosphorescence under visible light and developing ultralong and efficient CDs RTP materials by defect-stabilizing triplet-state excitons.<sup>7</sup> Recently, a core–satellite structure was achieved in our previous work from CDs-decorated amorphous silica, with an electron trap that can capture, store, and gradually release the electrons and provide more stabilized triplet excitons.<sup>19</sup> However, the reported CDs@inorganic-matrix materials can only present blue or green RTP (blue or green RTP), which limits the applications of the materials. Yu and coworkers made significant effort to simultaneously promote stability and enhance red phosphorescence efficiency of CDs-based composite materials realized

Received: April 21, 2021

Accepted: July 1, 2021



ACS Publications

© XXXX American Chemical Society

A

<https://doi.org/10.1021/acsami.1c07391>  
ACS Appl. Mater. Interfaces XXXX, XXX, XXX–XXX

by the energy transfer from CDs to red emissive  $\text{Mn}^{2+}$  doped in a zeolite matrix.<sup>20,21</sup> Utilization of phosphorescence resonance energy transfer between pure organic materials and long-wavelength dye provides a good solution to achieve red-shifted phosphorescence. Intermolecular interactions provide a feasible avenue for realizing RTP.<sup>22,23</sup> However, PL of CDs can be analyzed by combining the effect of intrinsic emission and surface group emission.<sup>24</sup> There is no literature to prove whether the energy-transfer process occurs on the surface or in the core triplet state of CDs. Therefore, it is still highly desirable to clarify the energy-transfer mechanism of CDs-based RTP materials.

Herein, we present a facile one-step calcination method for the in situ preparation of a  $\text{CDs@ZnAl}_2\text{O}_4$  composite material that exhibits unique UV and visible light-excitable ultra-broadband RTP. A  $\text{CDs@ZnAl}_2\text{O}_4$  composite is prepared by a calcination system by using small organic molecules and metallic nitrate as the precursors (Figure 1a). Intense green

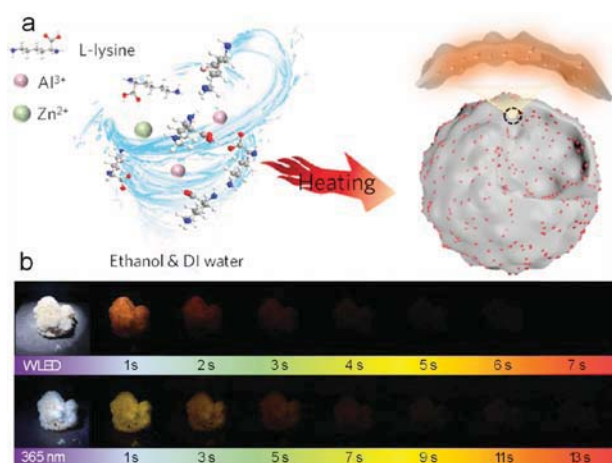


**Figure 1.** (a) Schematic for the preparation of  $\text{CDs@ZnAl}_2\text{O}_4$  powder via an in situ calcination method. (b) Digital photos of the  $\text{CDs@ZnAl}_2\text{O}_4$  composite before and after turning off the WLED and UV light (365 nm).

phosphorescence is obtained after UV irradiation, which lasts for about 13 s. In addition, a gradual phosphorescence from yellow to red can be seen, which lasts for about 7 s after white light-emitting diode (WLED) irradiation (Figure 1b). In addition, the average lifetimes of the phosphorescence at 400 and 570 nm are measured to be 0.41 and 1.05 s, respectively. The multiemissive RTP characteristic of  $\text{CDs@ZnAl}_2\text{O}_4$  composites mainly originates from various triplet states produced by different intersystem crossing routes owing to the matrix-assisted system and trap-stabilized triplet-state excitons.

## 2. RESULTS AND DISCUSSION

In this study, we proposed a universal strategy for in situ preparation of CDs-based phosphorescent materials. During the process of calcination and crystallization, CDs were formed and inlaid into the steadfast crystal structure of matrices, which met our expectations for restricting the CDs in nanospace.  $\text{CDs@ZnAl}_2\text{O}_4$  can be obtained with a variety of organic molecules such as glucose, L-lysine, L-cysteine, and cetyltrimethyl ammonium bromide (CTAB). This method can be readily applied to industrial-scale production. Moreover, our

experiment indicated the CDs-based phosphorescent materials synthesized with different small organic molecules in this way resulted in analogous CDs structures, showing similar phosphorescence peaks (Figures S1, S3a,b, and S7a).

The structure of  $\text{CDs@ZnAl}_2\text{O}_4$  was characterized using an X-ray diffractometer (XRD) to verify the generation of zinc aluminate. From the XRD pattern (Figures 2a and S3), several

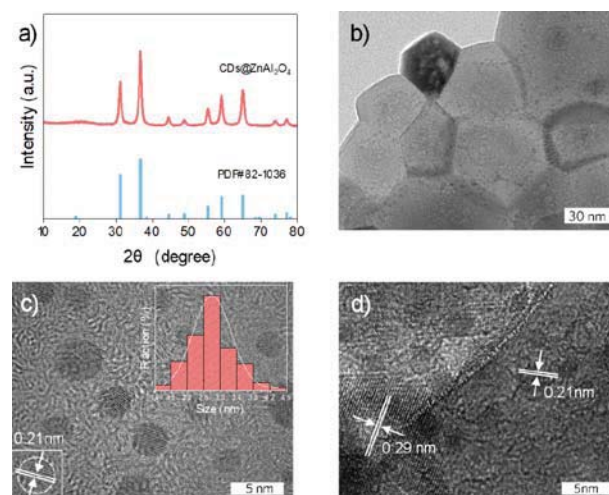


**Figure 2.** (a) XRD patterns of  $\text{ZnAl}_2\text{O}_4$  (blue line) and  $\text{CDs@ZnAl}_2\text{O}_4$  (red line). (b) TEM image. (c) HRTEM image treated with ammonia (insets show the CD image, a lattice distance of 0.21 nm, and the average size of CDs) and (d) HRTEM image of  $\text{CDs@ZnAl}_2\text{O}_4$ .

sharp bands centered at  $31.1^\circ$ ,  $36.6^\circ$ ,  $59.1^\circ$ , and  $65.0^\circ$  were observed, corresponding to the (220), (311), (511), and (440) lattice zinc aluminate (PDF#82-1036). High-resolution transmission electron microscopy (HRTEM) (Figure 2b–d) provided powerful and direct evidence for the well-dispersed crystalline CDs that were obtained with a relatively uniform size of about 2.8 nm embedded in a  $\text{ZnAl}_2\text{O}_4$  confined space. Significant lattice fringes of this composite were observed with lattice spacings of 0.21 and 0.29 nm, which were consistent with the (100) crystallographic facets of graphitic carbon and the (220) crystallographic facets of  $\text{ZnAl}_2\text{O}_4$ , respectively, indicating the sufficiently dense structure under high-temperature carbonization. As shown in Figures 2d and S3a,b, the typical crystalline structure of the  $\text{ZnAl}_2\text{O}_4$  matrix could remain the same even after embedding CDs, and amorphous graphite was synchronously reduced with the temperature increase. Scanning electron microscopy (SEM) images showed  $\text{CDs@ZnAl}_2\text{O}_4$  composed of grains with rounded shapes and a few ones that are larger in one direction (oval-like shape) (Figure 5).

The chemical structures of  $\text{CDs@ZnAl}_2\text{O}_4$  were analyzed using X-ray photoelectron spectroscopy (XPS) and Fourier transform infrared (FT-IR) spectroscopy. The Zn 2p<sub>1</sub>, Zn 2p<sub>3</sub>, O 1s, C 1s, and Al 2p peaks were identified at 1044.7, 1021.7, 531.4, 284.2, and 74.0 eV, respectively (Figures 3b and S8). To further identify the nature of CDs, the high-resolution spectrum of C 1s (Figure 3c) was deconvoluted into three peaks at 284.7, 285.1, and 289.0 eV, which originated from C=C, C–C/C–O, and C=O, respectively. The same result was observed in the high-resolution spectrum of O 1s (Figure 3d) with two peaks at 530.5 and 531.4 eV. These inferences



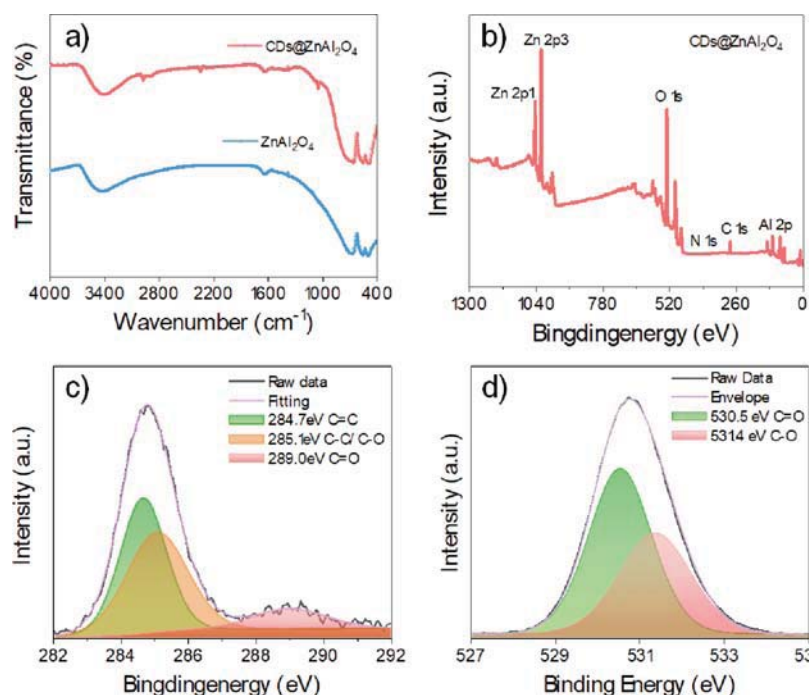


**Figure 3.** (a) FT-IR spectra of ZnAl<sub>2</sub>O<sub>4</sub> (blue line) and CDs@ZnAl<sub>2</sub>O<sub>4</sub> (red line). (b) XPS spectra of CDs@ZnAl<sub>2</sub>O<sub>4</sub>. (c) High-resolution XPS spectra of C 1s and fitting patterns. (d) High-resolution XPS spectra of O 1s and fitting patterns.

are further supported by FT-IR measurements (Figures 3a and S7), and broad and pronounced absorption peaks at 3689–3023 cm<sup>-1</sup> indicated the existence of many O–H groups. Meanwhile, the appearance of absorption peaks at 2978, 1646, and 1052 cm<sup>-1</sup>, associated with the C–H, O–H, and N–H stretching, is observed, which further indicates the presence of CDs. The peaks centered at 489 cm<sup>-1</sup> correspond to the stretching vibrations of the octahedral site of Zn–O, and two peaks centered at 553 and 659 cm<sup>-1</sup> correspond to the symmetric stretching vibrations of Al–O and to the symmetric bending vibration of Al–O, respectively.<sup>25</sup> High-angle annular dark-field scanning transmission electron microscopy (TEM) and SEM with the energy-dispersive spectroscopy (EDS) technique were also employed to characterize the presence of N, C, O, Al, and Zn elements in CDs@ZnAl<sub>2</sub>O<sub>4</sub> (Figures 4g,h and S6).

To systematically investigate the photophysical properties of CDs@ZnAl<sub>2</sub>O<sub>4</sub>, the absorption and fluorescence (FL) spectra of CDs@ZnAl<sub>2</sub>O<sub>4</sub> and ZnAl<sub>2</sub>O<sub>4</sub> had been explored (Figures 4a and S9a,c). Impressively, the UV–vis absorption spectrum displays a significant absorption enhancement in the entire visible light region, especially with an additional shoulder peak at 400 nm, which is assigned to the  $n \rightarrow \pi^*$  transitions due to the CDs with functional groups, proving that CDs@ZnAl<sub>2</sub>O<sub>4</sub> is capable of being excited by visible light. Fortunately, the similarity within their FL located at 470 nm indicates that the internal trap present in CDs@ZnAl<sub>2</sub>O<sub>4</sub> should be responsible for the FL. Figure 4b shows the intersection between the asymptotic linear fit and the photon energy axis that shows a good approximation of the optical band gap energy ( $E_g$ ) value. It corresponds well to the emission in the 390 nm (3.18 eV) region.<sup>26</sup> The FL excitation and emission spectra of CDs@ZnAl<sub>2</sub>O<sub>4</sub> show a maximum emission peak at 390 nm under 365 nm excitation and a shoulder peak at 470 nm. The maximum

and shoulder emission peaks correspond to the energy gap and trap-state energy gap of CDs@ZnAl<sub>2</sub>O<sub>4</sub>.

As shown in Figure 4d, when excited at 290 nm, a broad phosphorescence band ranging from 350 to 650 nm with multiple peaks (400, 470, and 570 nm) is found in its phosphorescence spectrum. In addition, from the three-dimensional (3D) scanning excitation-phosphorescence emission mapping shown in Figure S15, the phosphorescence spectra sharply changed when the excitation wavelength is altered from 280 to 420 nm, further giving three emission centers. As shown in Figure 4i, the multiple emission centers give multiple average lifetimes of 0.41, 0.81, and 1.05 s, respectively, with the emission peaks at 400, 470, and 570 nm, which can further identify the multiemission center of CDs@ZnAl<sub>2</sub>O<sub>4</sub>. As shown in Figure 4c, the excitation-dependent behavior of phosphorescence around the 550–625 nm region can be attributed to the presence of multiple triplet states in CDs@ZnAl<sub>2</sub>O<sub>4</sub>.<sup>27</sup> The excitation peak wavelength is rather close to the absorption band at 400 nm. Thus, relevant surface groups of CDs that absorb at 400 nm should be responsible for the excitation-dependent behavior of phosphorescence,<sup>28</sup> which is further confirmed by the fact that the phosphorescence lifetime decay curve of CDs@ZnAl<sub>2</sub>O<sub>4</sub> under UV irradiation of 400 nm can be fitted to a triexponential function (Figure S2). According to the following equation

$$\tau_{\text{avg}} = \frac{\sum A_i \tau_i^2}{\sum A_i \tau_i} \quad (1)$$

the fitted phosphorescence lifetime decay curves show that CDs@ZnAl<sub>2</sub>O<sub>4</sub> has an average lifetime of 1.05 s. Figure S14 also shows an average lifetime of 1.79 s under WLED irradiation.

Specifically, the RTP of CDs@ZnAl<sub>2</sub>O<sub>4</sub> gives Commission Internationale de l'Eclairage (CIE) coordinates of (0.28, 0.31),

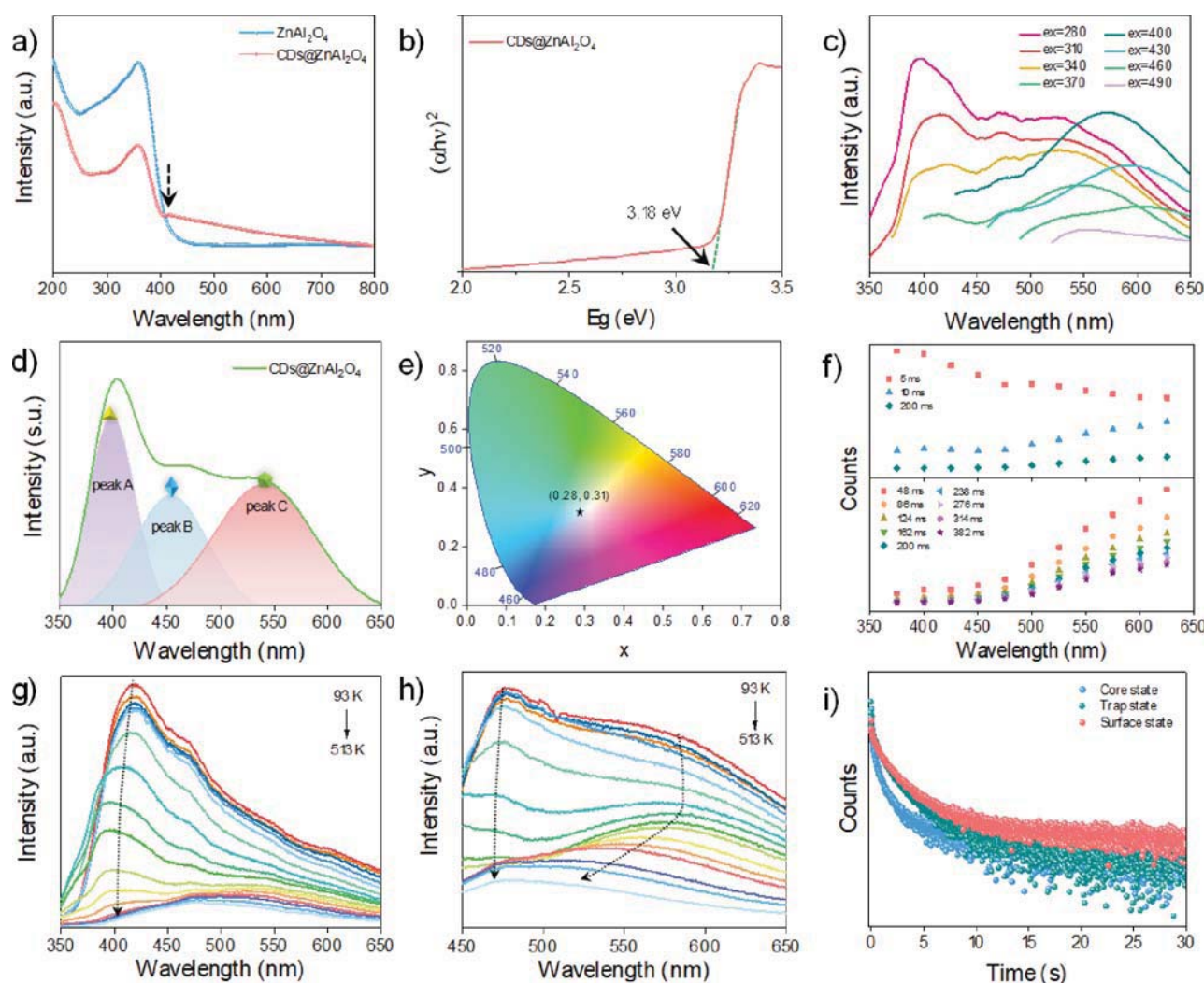


**Figure 4.** (a) Absorption of  $\text{ZnAl}_2\text{O}_4$  (blue line) and  $\text{CDs@ZnAl}_2\text{O}_4$  (red line). (b) UV-vis absorption spectra of  $\text{CDs@ZnAl}_2\text{O}_4$  after Kubelka–Munk unit conversion. (c) Wavelength-dependent phosphorescence spectra. (d) Phosphorescence spectra. (e) Calculated phosphorescence color coordinates in the CIE 1931 chromaticity diagram. (f) Time-resolved phosphorescence spectra. (g,h) Temperature-dependent phosphorescence intensity-resolved spectra of  $\text{CDs@ZnAl}_2\text{O}_4$  under irradiation of 290 and 400 nm, respectively. (i) Time-resolved decay curve of  $\text{CDs@ZnAl}_2\text{O}_4$  at room temperature, recorded at emission wavelengths of 400, 470, and 570 nm under irradiation of 290 nm.

as shown in Figure 4e, displaying a complex white phosphorescence. Note that the achievement of CDs-based RTP materials with white RTP is still challenging and had rarely been reported.<sup>29</sup> Moreover, the CIE coordinates evolve from (0.25, 0.25) to (0.28, 0.31) and then to (0.27, 0.33), with the variation of temperature (Figure S11). In other words, the RTP color can be modulated in the  $\text{CDs@ZnAl}_2\text{O}_4$  material by temperature adjustment, without adding any other qualifications.

The temperature-dependent phosphorescence in Figure 4g,h displays the main phosphorescence peak intensity of  $\text{CDs@ZnAl}_2\text{O}_4$  composites under UV irradiation of 290 and 400 nm. The phosphorescence intensity of  $\text{CDs@ZnAl}_2\text{O}_4$  is inversely proportional to the increase in temperature, suggesting a phosphorescence characteristic rather than delayed FL. It can be clearly seen that as the temperature increases, the long-wavelength emission gradually blue-shifts and sharply weakens, which can be better proved that the long-wavelength emission is attributed to the surface state of the CDs. When the

temperature increases from 303 to 513 K, the intensity of long-wavelength phosphorescence decreases significantly, but the phosphorescence at 470 nm does not decrease significantly (Figure S16). Hence, the phosphorescent center at 470 nm is different from the long-wavelength phosphorescent center. Distinctly, similar FL and phosphorescence peaks at 470 nm (2.64 eV) of the  $\text{CDs@ZnAl}_2\text{O}_4$  powder are observed (Figures 4d and S9), indicating that FL and phosphorescence should have been resulted from the same chemical structure O vacancy.<sup>26</sup> Figure S10 shows that the FL lifetime of  $\text{CDs@ZnAl}_2\text{O}_4$  composites is at the nanosecond level. However, Figure 4i shows the phosphorescent center at 470 nm with an average lifetime of 0.81 s, indicating that their phosphorescence derives from trapped charge carriers gradually released from isolated traps. Furthermore, green phosphorescence can be observed by the naked eye in the  $\text{CDs@ZnAl}_2\text{O}_4$  composite rather than the CDs-doped free  $\text{ZnAl}_2\text{O}_4$  matrix (Figure S9b,d). Comparison of the phosphorescence spectra of the CDs-doped free  $\text{ZnAl}_2\text{O}_4$  matrix and the  $\text{CDs@ZnAl}_2\text{O}_4$

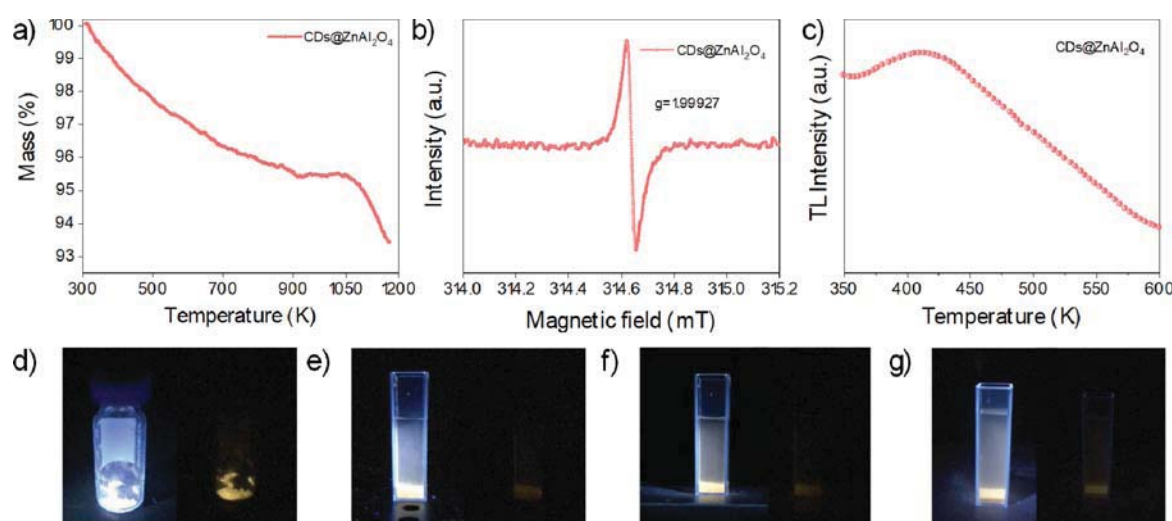


**Figure 5.** (a) TGA thermogram; (b) ESR spectrum; (c) TL curve spectra; (d) photos of the composites obtained from TGA; and (e) photos of the composites in hydrochloric acid, (f) in water, (g) and in caustic soda solution of CDs@ZnAl<sub>2</sub>O<sub>4</sub> over 100 days.

composite shows that the trap-state exciton emissions of ZnAl<sub>2</sub>O<sub>4</sub> are activated by the addition of CDs.<sup>30</sup> As the broad band shows persistent luminescence evidently due to defect(s) as obtained with R<sup>3+</sup> (e.g., La<sup>3+</sup>, Cr<sup>3+</sup>, and Pr<sup>3+</sup>)-doped inorganic matrices, the radiative process between the electron and hole trapping mechanisms should consider the energy level positions for R<sup>3+</sup> itself.<sup>31,32</sup> By analogy, for CD-based RTP materials, the RTP of CDs@ZnAl<sub>2</sub>O<sub>4</sub> originates from the ultralong lifetime triplet state of the filled CDs. For this, we have synthesized a series of CDs@ZnAl<sub>2</sub>O<sub>4</sub> with different doping concentrations of CDs by changing the molar amount of small organic molecules. Experiments show that, within a certain range, the phosphorescence intensity of these composites increases with an increase in the carbon doping concentration.

In our previous studies, we demonstrated a dual emission, which is due to the carbonized cores and the surface groups of CDs.<sup>33</sup> To reveal the principle of multiemissive RTP, we prepared a series of CDs@ZnAl<sub>2</sub>O<sub>4</sub> composites by executing temperature gradient experiments. Figure S12a,b shows that both quality and quantity of CDs changed with an increase in reaction temperature. When the reaction temperature increased from 500 to 700 °C, the phosphorescence intensity distinctly increased, while when the reaction temperature increased from 700 to 900 °C, the phosphorescence intensity gradually decreased. Curiously, when the reaction temperature was 800 °C, the phosphorescence peak at 400 nm shows a significant increase. This means that in this system, the crystallinity of CDs tends to increase, and the surface functional groups of the CDs will decrease accordingly. The crystalline degree of the ZnAl<sub>2</sub>O<sub>4</sub> matrix is crucial for the phosphorescence stability of CDs@ZnAl<sub>2</sub>O<sub>4</sub>. When the temperature increases, the crystallization degree of CDs@ZnAl<sub>2</sub>O<sub>4</sub> increases, and hence, the fine and close spatial structure can be formed to stabilize the vibration and rotation of CDs, thus protecting the triplet phosphorescence. In addition, if the reaction temperature is too low, there would be no effective protection, and if the temperature is too high, the CDs will be consumed. It is worth mentioning that the CDs@ZnAl<sub>2</sub>O<sub>4</sub> composite obtained by calcination at 900 °C has similar structures (Figures S3c and S4d–f), and almost no

signal can be detected except for an extremely inconspicuous phosphorescence peak at 400 nm (Figure S13), which can be attributed to a small number of CDs that have not been completely consumed. Therefore, we have reason to believe that small organic molecules undergo dehydration and carbonization during the calcination process. Small organic molecules form CDs, which are then embedded in the matrix. In the process of heat preservation, the unreacted small organic molecules are combined with oxygen to decompose, and the surface of the over-reacted CDs is consumed due to high temperature, thus obtaining CDs with uniform size distribution. We discovered that the RTP intensities of all CDs@ZnAl<sub>2</sub>O<sub>4</sub> composites, which are synthesized at different calcination temperatures, are quite different, indicating that the doping of CDs in the material had changed. These inferences are further supported by XRD (Figure S4f, inset) and HRTEM. It is in line with our expectations, which further proved that the surface groups of the CDs emit long-wavelength phosphorescence. At the same time, it can also be proved that the phosphorescent center at 400 nm is attributed to the carbonized cores of CDs.

There is no doubt that the wavelength of phosphorescence is related to the energy gap between the triplet excited and ground states. Obviously, achieving effective radiation transition under UV irradiation of 290 nm (4.27 eV) to the triplet-state emission at 550 nm (2.25 eV) is difficult. Fortunately, the emission peak at 470 nm (2.63 eV) is just located between the core and surface-state emissions of CDs, which facilitates the energy-transfer process between the ZnAl<sub>2</sub>O<sub>4</sub> matrix and CDs. In addition, the trap of CDs@ZnAl<sub>2</sub>O<sub>4</sub> contributes to reducing the energy gap for realizing the effective electron transition and to generate an effective RTP. With the possible RTP process as shown in Figure 6, we hypothesized that the ultraviolet light is received by CDs, which emitted phosphorescence from the triplet transition of the carbonized cores; The ultraviolet light is absorbed by the ZnAl<sub>2</sub>O<sub>4</sub> matrix, and the electrons transition from the valence band to the defect state and then recombine with the holes in the oxygen vacancy through the charge accompanying the blue emission; the other electrons that escaped from the defect state can be combined with surface states of CDs through radiation



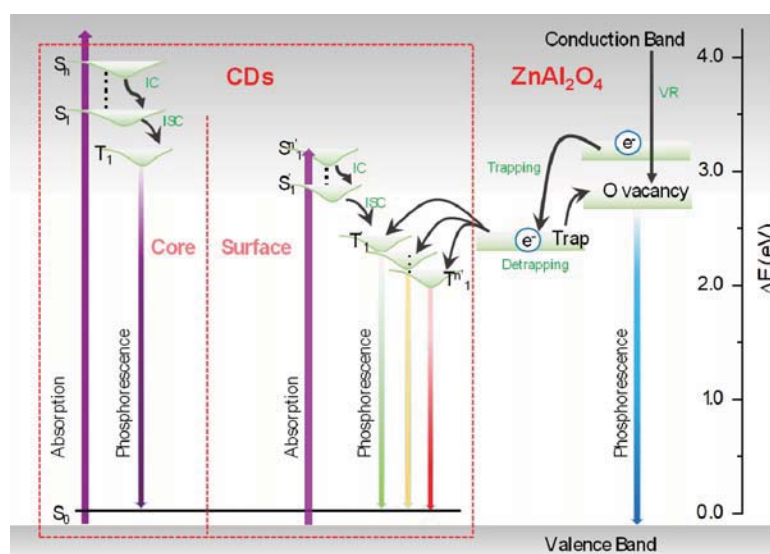


**Figure 6.** A scheme of energy band structure and possible RTP process for CDs@ZnAl<sub>2</sub>O<sub>4</sub>.

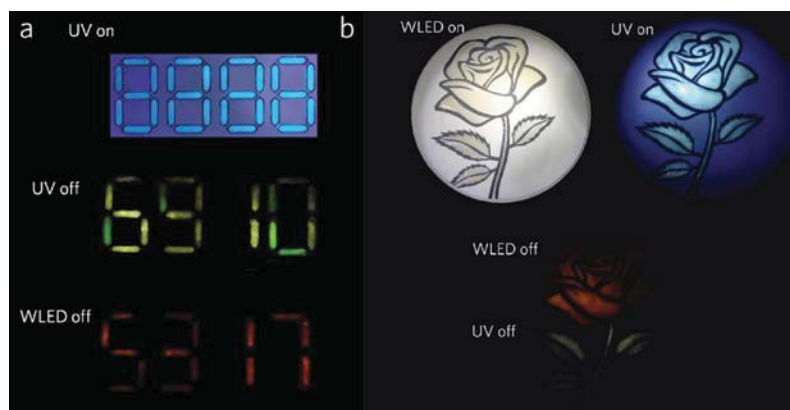


**Figure 7.** (a) Data encryption/decryption strategy. Real information “5317” was written by CDs@ZnAl<sub>2</sub>O<sub>4</sub>, fake information “8888” was overwritten by blue dye, and deceptive information “6910” was overwritten by CDs@SiO<sub>2</sub> that cannot be excited by the WLED. (b) Photographs of the flower pattern under turn-on and turn-off of UV (365 nm) light and the WLED.

transition that occurs in the different excited triplet states accompanied by yellow to red phosphorescence.<sup>7</sup> To better prove the strategy leading to the mediation of the trap we have identified, we have analyzed the evolution of our time-resolved PL (TRPL) spectrum on millisecond time scales. Figure 4f displays the main phosphorescence spectral components that contribute to the TRPL spectra of CDs@ZnAl<sub>2</sub>O<sub>4</sub> composites over the several milliseconds under UV irradiation of 290 nm. As Lian and co-workers expected, the PL lifetimes should be the same throughout the trap state emission band.<sup>34</sup> Moreover, the RTP duration is related to the photoexcitation time because of a charge-storage mechanism, but normal phosphorescence does not depend on the photoexcitation time.<sup>35</sup> In the delay time range of 5–400 ms, the TRPL spectra of the CDs@ZnAl<sub>2</sub>O<sub>4</sub> composites show an obvious spectral shape change and a faster short wavelength trap decay compared to the long-wavelength triplet. A dynamic Stokes shift of the TRPL spectra is observed from the short-wavelength region to the long-wavelength region due to the fast-decaying phosphorescence at short wavelengths, and the process of energy transfer is

observed from the gradual release of charge carriers from the trap state ones to the surface group triplet state.

To identify the type of trap centers, electron spin resonance (ESR) of CDs@ZnAl<sub>2</sub>O<sub>4</sub> was recorded and is shown in Figure 5b. An ESR signal at  $g = 1.9993$  is observed, which could be identified as an electron trapped around the oxygen vacancy.<sup>36</sup> As expressed by the thermoluminescence (TL) spectrum, a peak can be obtained at 389 K (Figure 5c). The depths of trap centers were researched by detecting the temperature-dependent phosphorescence emission spectra, and the related trap depth can be calculated by using the following formula:<sup>37,38</sup>

$$E = \frac{T_m}{500} \quad (2)$$

According to the above formula, the trap depth of CDs@ZnAl<sub>2</sub>O<sub>4</sub> is estimated to be 0.778 eV, which may be from traps caused by CDs doping.<sup>30</sup>

The stability of phosphorescence is vital for practical applications of RTP materials. CDs-based RTP materials are easily quenched by the dissolved oxygen and solvent-assisted relaxation. It is worth mentioning that CDs@ZnAl<sub>2</sub>O<sub>4</sub> exhibits

an ultrahigh optical stability under various conditions. The emission of CDs@ZnAl<sub>2</sub>O<sub>4</sub> is not quenched in three solvents with different pH values (1, 7, and 13) for more than 100 days, showing high solvent stability (Figure 5e–g). Therefore, it is difficult to separate CDs from CDs@ZnAl<sub>2</sub>O<sub>4</sub> by solution etching. It can also be observed from the thermogravimetric analyzer (TGA) thermogram (Figure 5a) that the content of CDs barely decreases until 800 °C, indicating that CDs@ZnAl<sub>2</sub>O<sub>4</sub> has high thermal stability. Such a high thermal stability is attributed to the confinement effect of the composite material. The external crystal structure can not only prevent the vibration and rotation of the CDs but also prevent the CDs from being destroyed. Impressively, when the sample is taken out from the TGA (Figure 5d), the phosphorescence is still present as well. As shown in Figure S17, the derivative thermogravimetry (DTG) curve of CDs@ZnAl<sub>2</sub>O<sub>4</sub> shows two separate steps of dehydration and consumption. The dehydration effect on the DTG curve corresponds to the binding of water molecules, and the consumption corresponds to the burning of internal CDs. When the calcination temperature is 500 °C, a sharp consumption can be detected, giving further evidence that it is difficult to achieve effective protection at low temperature, which is proved in Figure S3c.

Based on the advantages of the abovementioned CDs@ZnAl<sub>2</sub>O<sub>4</sub> powder, including extensive and effective ultraviolet and WLED excitation characteristics and high resistance to heat and humidity, Figure 7a shows an example of the data encryption/decryption strategy. Under irradiation of 365 nm, only digital combination 8888 can be recognized. After turning off the UV light, however, the RTP displays another deceptive information 6910, which can be clearly seen by the naked eye. When changing the excitation light to the WLED and turning off, the RTP displays the real information 5317. Furthermore, the ultralong lifetime of RTP facilitates multilevel security for luminescence graphics, which demonstrates the strong usability of tunable afterglow that could be easily achieved by changing light. In addition, a simple pattern (Figure 7b) of a flower was fabricated with CDs@ZnAl<sub>2</sub>O<sub>4</sub>. A red “petal” and green “leaves” were observed by the camera after removing the WLED and ultraviolet light, respectively.

### 3. CONCLUSIONS

In summary, a CDs@ZnAl<sub>2</sub>O<sub>4</sub> composite material was synthesized in situ by a universal one-step calcination method. The composite material exhibits unique UV to visible light excitable ultra-broad-band RTP and a special long-wavelength enduring red RTP with an ultralong lifetime of 1.05 s. To clarify the RTP mechanism of the CDs@ZnAl<sub>2</sub>O<sub>4</sub> composite, we constructed a model comprising gradual release charge carriers from the trap of ZnAl<sub>2</sub>O<sub>4</sub> as the donor and the oxygen vacancy or the surface groups of CDs as the acceptors. This strategy of employing inorganic defects to achieve steady phosphorescence of the triplet state of CDs would not only promote the development of the application of energy transfer in the photochemical field but also provide guidance for designing strategies for multiple functional phosphorescent materials.

### 4. EXPERIMENTAL SECTION

**4.1. Materials.** All reagents were used without purification. Reagent grade ethylenediamine, ethanolamine, ethylenediaminetetraacetic acid, anhydrous citric acid, aluminum nitrate, CTAB, urea,

polyacrylic acid, L-cysteine, ethyl silicate, and tetraethyl orthosilicate were bought from Aladdin Chemicals Co., Ltd. (Shanghai, China). D-glucose, L-lysine, and aspartic acid were purchased from Macklin Biochemical Co., Ltd. (Shanghai, China). Tetraphenylethylene, hydrochloric acid, and ethanol amine were purchased from Sinopharm Chemical Reagent Co., Ltd. (Shanghai, China). Zinc nitrate was purchased from Guangzhou Chemical Reagent Factory (Guangzhou, China). High-purity water was obtained from the HITECH purification system.

**4.2. Characterization.** TEM and HRTEM images were collected using a JEOL-2010 electron microscope. XRD of the as-prepared materials was performed using MSAL-XD2 (Cu K $\alpha$  radiation,  $\lambda$  = 0.154051 nm). The FT-IR spectra were measured using a Nicolet Avatar 360 FT-IR spectrophotometer. XPS spectra were obtained by employing an XPS (Axis Ultra DLD, Kratos). TL data were recorded using an FJ427A1 thermoluminescent dosimeter (CNNC Beijing Nuclear Instruments Factory) between the range of 330 and 600 K at a heating rate of 5 K s<sup>-1</sup>. The surface morphologies and particle sizes of the samples were analyzed by SEM (JSM-2010). The EPR spectra were recorded on an EPR spectrometer (Bruker A300) operating in the X-band frequencies ( $\approx$ 9.447 GHz) at RT. UV–vis absorption spectra were taken on a JASCO V-570 spectrophotometer. PL spectra and afterglow decay curves were recorded with an F-7000 Hitachi FL spectrofluorometer. The PL decay curves and time-resolved decay were recorded on an Edinburgh FLS1000 spectrophotometer. Temperature-dependent PL emission spectra, afterglow emission spectra, and afterglow decay curves were obtained by combining a heating apparatus (Oxford Instruments) with the same Hitachi F-7000 FL spectrophotometer.

**4.3. Synthesis.** Synthesis of CDs@ZnAl<sub>2</sub>O<sub>4</sub>: In brief, 0.01 mol of zinc nitrate, 0.02 mol of aluminium nitrate, and 0.04 mol of L-lysine were dissolved in 15 mL of DI water and 15 mL of ethanol in a 300 mL crucible with stirring at room temperature. Subsequently, the rotor was removed and the reaction mixture was transferred to a muffle furnace, followed by heating at a rate of 10 °C/min to a preset temperature of 700 °C under air, which was held for 4 h, during which the precursor materials gradually decomposed and inflated into a spherical-shaped porous foam. The final products were ground into powder.

### ■ ASSOCIATED CONTENT

#### Supporting Information

The Supporting Information is available free of charge at <https://pubs.acs.org/doi/10.1021/acsami.1c07391>.

Additional experimental details; phosphorescence spectra of CDs@ZnAl<sub>2</sub>O<sub>4</sub> synthesized with different types or doping concentrations of small organic molecules; time-resolved decay spectrum of CDs@ZnAl<sub>2</sub>O<sub>4</sub>; XRD patterns, HRTEM image and SEM image of CDs@ZnAl<sub>2</sub>O<sub>4</sub>; FT-IR spectra, XPS spectra, absorption, FL excitation and emission and phosphorescence spectra of the CDs@ZnAl<sub>2</sub>O<sub>4</sub> composite; FL decay curves; calculated phosphorescence color coordinates in the CIE 1931 chromaticity diagram; phosphorescence decay; and excitation-phosphorescence mapping, temperature-dependent intensity-resolved spectra, and TGA thermogram of CDs@ZnAl<sub>2</sub>O<sub>4</sub> (PDF)

### ■ AUTHOR INFORMATION

#### Corresponding Author

Chaofan Hu – Key Laboratory for Biobased Materials and Energy of Ministry of Education/Guangdong Provincial Engineering Technology Research Center for Optical Agriculture, College of Materials and Energy, South China Agricultural University, Guangzhou 510642, P. R. China;

orcid.org/0000-0003-2311-8733; Email: thucf@scau.edu.cn

## Authors

**Zhijian Song** — Key Laboratory for Biobased Materials and Energy of Ministry of Education/Guangdong Provincial Engineering Technology Research Center for Optical Agriculture, College of Materials and Energy, South China Agricultural University, Guangzhou 510642, P. R. China

**Yingliang Liu** — Key Laboratory for Biobased Materials and Energy of Ministry of Education/Guangdong Provincial Engineering Technology Research Center for Optical Agriculture, College of Materials and Energy, South China Agricultural University, Guangzhou 510642, P. R. China;

orcid.org/0000-0003-1930-0700

**Xiaomin Lin** — Key Laboratory for Biobased Materials and Energy of Ministry of Education/Guangdong Provincial Engineering Technology Research Center for Optical Agriculture, College of Materials and Energy, South China Agricultural University, Guangzhou 510642, P. R. China

**Zhishan Zhou** — Key Laboratory for Biobased Materials and Energy of Ministry of Education/Guangdong Provincial Engineering Technology Research Center for Optical Agriculture, College of Materials and Energy, South China Agricultural University, Guangzhou 510642, P. R. China

**Xuejie Zhang** — Key Laboratory for Biobased Materials and Energy of Ministry of Education/Guangdong Provincial Engineering Technology Research Center for Optical Agriculture, College of Materials and Energy, South China Agricultural University, Guangzhou 510642, P. R. China

**Jianle Zhuang** — Key Laboratory for Biobased Materials and Energy of Ministry of Education/Guangdong Provincial Engineering Technology Research Center for Optical Agriculture, College of Materials and Energy, South China Agricultural University, Guangzhou 510642, P. R. China;

orcid.org/0000-0002-4649-1939

**Bingfu Lei** — Key Laboratory for Biobased Materials and Energy of Ministry of Education/Guangdong Provincial Engineering Technology Research Center for Optical Agriculture, College of Materials and Energy, South China Agricultural University, Guangzhou 510642, P. R. China;

orcid.org/0000-0002-6634-0388

Complete contact information is available at:  
<https://pubs.acs.org/10.1021/acsami.1c07391>

## Notes

The authors declare no competing financial interest.

## ACKNOWLEDGMENTS

This work was supported by the National Natural Science Foundation of China (Grant nos. 21571067 and 51402207), the National Natural Science Foundation of China Joint Fund with Guangdong under Key Project (Grant no. U1501242), and the Natural Science Foundation of Guangdong Province (no. 2020A1515010443).

## REFERENCES

(1) Sun, Y.; Zhang, X.; Zhuang, J.; Zhang, H.; Hu, C.; Zheng, M.; Lei, B.; Liu, Y. The room temperature afterglow mechanism in carbon dots: Current state and further guidance perspective. *Carbon* **2020**, *165*, 306–316.

(2) Jiang, K.; Wang, Y.; Li, Z.; Lin, H. Afterglow of carbon dots: Mechanism, strategy and applications. *Mater. Chem. Front.* **2020**, *4*, 386–399.

(3) Tan, H.; Wang, T.; Shao, Y.; Yu, C.; Hu, L. Crucial Breakthrough of Functional Persistent Luminescence Materials for Biomedical and Information Technological Applications. *Front. Chem.* **2019**, *7*, 387.

(4) Li, J.; Wang, B.; Zhang, H.; Yu, J. Carbon Dots-in-Matrix Boosting Intriguing Luminescence Properties and Applications. *Small* **2019**, *15*, No. 1805504.

(5) Liu, J.; Li, R.; Yang, B. Carbon Dots: A New Type of Carbon-Based Nanomaterial with Wide Applications. *ACS Cent. Sci.* **2020**, *6*, 2179–2195.

(6) He, T.; Hu, W.; Shi, H.; Pan, Q.; Ma, G.; Huang, W.; Fan, Q.; Lin, X. Strong nonlinear optical phosphorescence from water-soluble polymer dots: Towards the application of two-photon bioimaging. *Dyes Pigm.* **2015**, *123*, 218–221.

(7) Shi, W.; Yao, J.; Bai, L.; Lu, C. Defect-Stabilized Triplet State Excitons: Toward Ultralong Organic Room-Temperature Phosphorescence. *Adv. Funct. Mater.* **2018**, *28*, No. 1809461.

(8) Su, Q.; Lu, C.; Yang, X. Efficient room temperature phosphorescence carbon dots: Information encryption and dual-channel pH sensing. *Carbon* **2019**, *152*, 609–615.

(9) Li, W.; Zhou, W.; Zhou, Z.; Zhang, H.; Zhang, X.; Zhuang, J.; Liu, Y.; Lei, B.; Hu, C. A Universal Strategy for Activating the Multicolor Room-Temperature Afterglow of Carbon Dots in a Boric Acid Matrix. *Angew. Chem., Int. Ed. Engl.* **2019**, *58*, 7278–7283.

(10) Liu, J.; Kang, X.; Zhang, H.; Liu, Y.; Wang, C.; Gao, X.; Li, Y. Carbon dot-based nanocomposite: Long-lived thermally activated delayed fluorescence for lifetime thermal sensing. *Dyes Pigm.* **2020**, *181*, No. 108576.

(11) Park, M.; Kim, H. S.; Yoon, H.; Kim, J.; Lee, S.; Yoo, S.; Jeon, S. Controllable Singlet-Triplet Energy Splitting of Graphene Quantum Dots through Oxidation: From Phosphorescence to TADF. *Adv. Mater.* **2020**, *32*, No. 2000936.

(12) Han, S.; Lian, G.; Zhang, X.; Cao, Z.; Wang, Q.; Cui, D.; Wong, C. P. Boron nitride dots In-situ embedded in a B<sub>2</sub>O<sub>3</sub> matrix with the long lifetime Room-Temperature phosphorescence in dry and wet states. *Chem. Eng. J.* **2021**, *417*, No. 129175.

(13) Li, W.; Wu, S.; Xu, X.; Zhuang, J.; Zhang, H.; Zhang, X.; Hu, C.; Lei, B.; Kaminski, C. F.; Liu, Y. Carbon Dot-Silica Nanoparticle Composites for Ultralong Lifetime Phosphorescence Imaging in Tissue and Cells at Room Temperature. *Chem. Mater.* **2019**, *31*, 9887–9894.

(14) Bao, X.; Ushakova, E. V.; Liu, E.; Zhou, Z.; Li, D.; Zhou, D.; Qu, S.; Rogach, A. On-Off Switching of the Phosphorescence Signal in a Carbon Dot/Polyvinyl alcohol Composite for the Multiple Data Encryption. *Nanoscale* **2019**, *11*, 14250–14255.

(15) Jiang, K.; Wang, Y.; Cai, C.; Lin, H. Conversion of Carbon Dots from Fluorescence to Ultralong Room-Temperature Phosphorescence by Heating for Security Applications. *Adv. Mater.* **2018**, *30*, No. 1800783.

(16) Liu, J.; Wang, N.; Yu, Y.; Yan, Y.; Yu, J. Carbon dots in zeolites: A new class of thermally activated delayed fluorescence materials with ultralong lifetimes. *Sci. Adv.* **2017**, *3*, No. 1603171.

(17) Sun, Y.; Liu, S.; Sun, L.; Wu, S.; Hu, G.; Pang, X.; Smith, A. T.; Hu, C.; Zeng, S.; Wang, W.; Liu, Y.; Zheng, M. Ultralong lifetime and efficient room temperature phosphorescent carbon dots through multi-confinement structure design. *Nat. Commun.* **2020**, *11*, No. 5591.

(18) Wang, C.; Chen, Y.; Xu, Y.; Ran, G.; He, Y.; Song, Q. Aggregation-Induced Room-Temperature Phosphorescence Obtained from Water-Dispersible Carbon Dot-Based Composite Materials. *ACS Appl. Mater. Interfaces* **2020**, *12*, 10791–10800.

(19) He, J.; Chen, Y.; He, Y.; Xu, X.; Lei, B.; Zhang, H.; Zhuang, J.; Hu, C.; Liu, Y. Anchoring Carbon Nanodots onto Nanosilica for Phosphorescence Enhancement and Delayed Fluorescence Nascence in Solid and Liquid States. *Small* **2020**, *16*, No. 2005228.



- (20) Wang, B.; Yu, Y.; Zhang, H.; Xuan, Y.; Chen, G.; Ma, W.; Li, J.; Yu, J. Carbon Dots in a Matrix: Energy-Transfer-Enhanced Room-Temperature Red Phosphorescence. *Angew. Chem., Int. Ed. Engl.* **2019**, *58*, 18443–18448.
- (21) Wang, B.; Mu, Y.; Zhang, H.; Shi, H.; Chen, G.; Yu, Y.; Yang, Z.; Li, J.; Yu, J. Red Room-Temperature Phosphorescence of CDs@Zeolite Composites Triggered by Heteroatoms in Zeolite Frameworks. *ACS Cent. Sci.* **2019**, *5*, 349–356.
- (22) Dang, Q.; Jiang, Y.; Wang, J.; Wang, J.; Zhang, Q.; Zhang, M.; Luo, S.; Xie, Y.; Pu, K.; Li, Q.; Li, Z. Room-Temperature Phosphorescence Resonance Energy Transfer for Construction of Near-Infrared Afterglow Imaging Agents. *Adv. Mater.* **2020**, *32*, No. 2006752.
- (23) Song, L.; Wang, X.; Zhang, M.; Jia, W.; Wang, Q.; Ye, W.; Wang, H.; Lv, A.; Ma, H.; Gu, L.; Shi, H.; An, Z.; Huang, W. A Single-Component Supramolecular Organic Framework with Efficient Ultralong Phosphorescence. *CCS Chem.* **2021**, 466–472.
- (24) Sarkar, S.; Gandla, D.; Venkatesh, Y.; Bangal, P. R.; Ghosh, S.; Yang, Y.; Misra, S. Graphene quantum dots from graphite by liquid exfoliation showing excitation-independent emission, fluorescence upconversion and delayed fluorescence. *Phys. Chem. Chem. Phys.* **2016**, *18*, 21278–21287.
- (25) Ramachandran, S.; Dash, C. S.; Thamilselvan, A.; Kalpana, S.; Sundararajan, M. Rapid Synthesis and Characterization of Pure and Cobalt Doped Zinc Aluminate Nanoparticles via Microwave Assisted Combustion Method. *J. Nanosci. Nanotechnol.* **2020**, *20*, 2382–2388.
- (26) Srinivas Reddy, G.; Sharma, H.; Bhaskar, P.; Manjunatha, M. Effect of type of fuel used and calcination temperature on the disorder-order transformation of zinc aluminate spinel during combustion synthesis. *Mater. Chem. Phys.* **2020**, *253*, No. 123388.
- (27) Gu, L.; Shi, H.; Bian, L.; Gu, M.; Ling, K.; Wang, X.; Ma, H.; Cai, S.; Ning, W.; Fu, L.; Wang, H.; Wang, S.; Gao, Y.; Yao, W.; Huo, F.; Tao, Y.; An, Z.; Liu, X.; Huang, W. Colour-tunable ultra-long organic phosphorescence of a single-component molecular crystal. *Nat. Photonics* **2019**, *13*, 406–411.
- (28) Jiang, K.; Gao, X.; Feng, X.; Wang, Y.; Li, Z.; Lin, H. Carbon Dots with Dual-Emissive, Robust and Aggregation-Induced Room Temperature Phosphorescence Characteristics. *Angew. Chem., Int. Ed. Engl.* **2019**, *59*, 1263–1269.
- (29) Joseph, J.; Anappara, A. A. Cool white, persistent room-temperature phosphorescence in carbon dots embedded in a silica gel matrix. *Phys. Chem. Chem. Phys.* **2017**, *19*, 15137–15144.
- (30) Diaz-Torres, L. A.; Gomez-Solis, C.; Oliva, J.; García, C. R.; Oliva, A. I.; Angeles-Chavez, C.; Hirata, G. A. Long-lasting green, yellow, and red phosphorescence of carbon dots embedded on ZnAl<sub>2</sub>O<sub>4</sub> nanoparticles synthesized by a combustion method. *J. Phys. D: Appl. Phys.* **2018**, *51*, No. 415104.
- (31) Xiong, P.; Peng, M.; Qin, K.; Xu, F.; Xu, X. Visible to Near-Infrared Persistent Luminescence and Mechanoluminescence from Pr<sup>3+</sup> Doped LiGaSO<sub>8</sub> for Energy Storage and Bioimaging. *Adv. Opt. Mater.* **2019**, *7*, No. 1901107.
- (32) Xiong, P.; Peng, M. Visible to near-infrared persistent luminescence from Tm<sup>3+</sup>-doped two-dimensional layered perovskite Sr<sub>2</sub>SnO<sub>4</sub>. *J. Mater. Chem. C* **2019**, *7*, 8303–8309.
- (33) Yang, H.; Liu, Y.; Guo, Z.; Lei, B.; Zhuang, J.; Zhang, X.; Liu, Z.; Hu, C. Hydrophobic carbon dots with blue dispersed emission and red aggregation-induced emission. *Nat. Commun.* **2019**, *10*, No. 1789.
- (34) Jin, T.; Lian, T. Trap state mediated triplet energy transfer from CdSe quantum dots to molecular acceptors. *J. Chem. Phys.* **2020**, *153*, No. 074703.
- (35) Nishimura, N.; Lin, Z.; Jinnai, K.; Kabe, R.; Adachi, C. Many Exciplex Systems Exhibit Organic Long-Persistent Luminescence. *Adv. Funct. Mater.* **2020**, *30*, No. 2000795.
- (36) Zhou, Z.; Jiang, K.; Chen, N.; Xie, Z.; Lei, B.; Zhuang, J.; Zhang, X.; Liu, Y.; Hu, C. Room temperature long afterglow from boron oxide: A boric acid calcined product. *Mater. Lett.* **2020**, *276*, No. 128226.
- (37) Liu, B.; Zou, R.; Lou, S.; Gao, Y.; Ma, L.; Wong, K.; Wang, J. Low-dose X-ray-stimulated LaGaO<sub>3</sub>:Sb,Cr near-infrared persistent luminescence nanoparticles for deep-tissue and renewable in vivo bioimaging. *Chem. Eng. J.* **2021**, *404*, No. 127133.
- (38) Xiong, P.; Zheng, C.; Peng, M.; Zhou, Z.; Xu, F.; Qin, K.; Hong, Y.; Ma, Z. Self-activated persistent luminescence from Ba<sub>2</sub>Zr<sub>2</sub>Si<sub>3</sub>O<sub>12</sub> for information storage. *J. Am. Ceram. Soc.* **2020**, *103*, 6922–6931.

# Multicolor Afterglow from Carbon Dots: Preparation and Mechanism

Zhun Ran, Jinkun Liu, Jianle Zhuang, Yingliang Liu, and Chaofan Hu\*

Carbon dots (CDs), as emerging long afterglow luminescent material, have attracted the attention of researchers and become one of the hot topics in long afterglow materials. In recent years, researchers have obtained a series of CDs-based long afterglow materials with different properties utilizing matrix-assisted and self-protective methods. To meet diverse application needs, the development of multicolor CDs-based long afterglow materials is a focus and challenge in this field. Most of the previously reported CDs-based long afterglow materials generally emit blue or green afterglow. Recently, some multicolor systems have been discovered, and the emission range can extend from ultraviolet to near-infrared. However, there is a lack of systematic and in-depth analysis regarding the preparation strategy and luminescence mechanism of multicolor afterglow from CDs-based long afterglow materials. Based on this, this review summarizes the preparation strategies of multicolor afterglow from raw materials and reaction parameters. Then, the luminescence mechanisms of multicolor afterglow are analyzed from seven factors, including carbonization degree, surface state, aggregation degree, temperature dependence, excitation dependence, multi-emission center, and energy transfer. Moreover, the applications of multicolor afterglow from CDs-based long afterglow materials are introduced. Finally, the problems and challenges in this field are discussed, and the future development directions are analyzed.

## 1. Introduction

Long afterglow materials can maintain persistent luminescence after the excitation source is removed.<sup>[1–4]</sup> Which have attracted significant attention due to their potential applications in the field of life medicine,<sup>[5,6]</sup> optical sensing,<sup>[7]</sup> illumination displays,<sup>[8,9]</sup> and security encryption.<sup>[10,11]</sup> According to the current research, long afterglow luminescent materials can be classified into inorganic and organic long afterglow materials. Inorganic long afterglow materials have attracted much attention due to their

excellent luminescence duration, which is usually achieved afterglow emission by doping rare earth metals, transition metals, and main group metals into the inorganic matrix. The preparation process is usually accompanied by high temperature sintering to obtain more internal thermal defects, thereby significantly enhancing the afterglow performance.<sup>[12–15]</sup> However, high calcination temperatures cause inhomogeneous particles, poorer surface morphology, higher production costs, and complicated practical operations.<sup>[16,17]</sup> Moreover, the use of expensive metals further restricts their applications. In recent years, organic long afterglow materials have become a new research hotspot due to their advantages such as easy availability of raw materials, various preparation methods, diverse structures, and low cost.<sup>[18–23]</sup> However, conventional organic afterglow materials exhibit extremely low luminescence efficiency due to the spin prohibition of the potential singlet-triplet states emission.<sup>[24]</sup> In addition, the quenching effect of the triplet excited states on oxygen and water makes it difficult

to achieve the desired afterglow performance of organic chromophores under environmental conditions.<sup>[25,26]</sup> In pursuit of effective afterglow emission, the current strategy is to modify the structure of compounds or chromophores by introducing special aromatic carbonyl and halogen atoms.<sup>[27,28]</sup> However, this approach to preparing organic long afterglow materials usually requires very complex chemical synthesis and special molecular design.<sup>[29]</sup>

In 2004, Xu et al.<sup>[30]</sup> isolated fluorescent carbon nanoparticles from single-walled carbon nanotubes. Two years later, Sun et al.<sup>[31]</sup> named these fluorescent carbon nanoparticles as carbon dots (CDs). With the advantages of wide source, simple preparation, low toxicity, excellent biocompatibility, and high quantum yields (QYs),<sup>[32,33]</sup> they have rapidly gained widespread attention and have been greatly applied in the fields of energy,<sup>[34]</sup> catalysis,<sup>[35,36]</sup> sensing,<sup>[37,38]</sup> optoelectronics,<sup>[39,40]</sup> and biomedicine.<sup>[41–44]</sup> In 2013, Deng et al.<sup>[45]</sup> discovered green room temperature phosphorescence (RTP) phenomenon in CDs dispersed into polyvinyl alcohol (PVA) matrix. CDs-based long afterglow materials have been extensively developed and have made significant progress. Here, we present a list of

Z. Ran, J. Liu, J. Zhuang, Y. Liu, C. Hu  
Key Laboratory for Biobased Materials and Energy of Ministry of Education/Guangdong Provincial Engineering Technology Research Center for Optical Agriculture  
College of Materials and Energy  
South China Agricultural University  
Guangzhou 510642, P. R. China  
E-mail: thucf@scau.edu.cn

The ORCID identification number(s) for the author(s) of this article can be found under <https://doi.org/10.1002/smt.202301013>

DOI: 10.1002/smt.202301013

**Table 1.** Summary of typical single-color afterglow from carbon dots.

Year	Afterglow color	Emission wavelength [nm]	Lifetime [ms]	Afterglow QYs [%]	Refs.
2013	Green	500	380	–	[45]
2017	Blue	430	350	–	[33]
2019	Red	620	1.814	5.7	[46]
2020	Yellow	560	183.6	4.2	[47]
2020	Orange	585	240.8	–	[48]
2021	Near-infrared	690	13.29	2.87	[49]
2022	Ultraviolet	348	15.8	16.2	[50]

representative studies for each color, and each study has outstanding contributions, not ranked in any order (Table 1). In 2017, Yu's group reported the achievement of deep blue delayed fluorescence was obtained by embedding CDs in zeolite matrix, with emission wavelength of 430 nm and lifetime of 350 ms.<sup>[33]</sup> In 2019, Yu's team utilized an energy transfer strategy to develop red emission from CDs-based long afterglow materials. They demonstrated that energy transfer occurs between CDs and Mn-doped zeolite matrix, and the zeolite matrix effectively stabilizes triplet excited states excitons and reduces nonradiative relaxation.<sup>[46]</sup> In 2020, Lin's group developed yellow room temperature phosphorescence CDs with aggregation-induced properties, and they found that the RTP emission gradually enhanced with the addition of poor solvents.<sup>[47]</sup> In 2020, Lin's group reported the use of L-aspartic acid as a precursor to achieve visible-light-excited matrix-free orange afterglow from CDs by one-step microwave heating.<sup>[48]</sup> In 2021, Lin's research group first reported CDs-based long afterglow materials with near-infrared phosphorescence emission. They demonstrated that the covalent bond formed between CDs and CA is critical for achieving near-infrared RTP and green thermally activated delayed fluorescence (TADF).<sup>[49]</sup> In 2022, Pan et al.<sup>[44]</sup> developed near-infrared phosphorescence CDs with a maximum emission of 700 nm and applied them in tumor therapy. In 2022, Shan's group used the strategy of structural confinement and reducing the size of the conjugate to achieve ultraviolet phosphorescence in CDs-based long afterglow materials for the first time.<sup>[50]</sup> By using keywords to search on the "Web of Science", the number of publications increases as the year progresses. As of September 18th, 2023, there are 263 papers published on this topic (Figure 1).

Compared with the single-color afterglow, multicolor afterglow has superior applications in display, imaging, information encryption, and anti-counterfeiting.<sup>[51–54]</sup> However, the construction of multicolor afterglow is a significant challenge. On the one hand, triplet excited states excitons are highly susceptible to inactivation by the external environment. On the other hand, according to the Kasha's rules, the emission level of a given singlet excited states or triplet excited states is only related to their lowest excited level, and irrelevant to the initial excited state.<sup>[55,56]</sup> At present, many reviews have summarized the research progress of CDs-based long afterglow materials.<sup>[57–68]</sup> However, most reviews only summarize the preparation methods of CDs-based long afterglow materials, the activation strategies of afterglow, and introduce related applications. Furthermore, only a few articles briefly mention multicolor afterglow as part of their com-

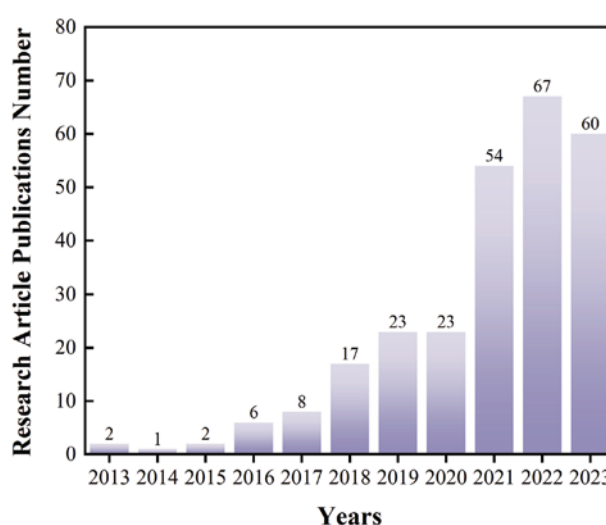


**Figure 1.** The summary of CDs-based long afterglow materials publication since 2013, analyzed via Web of Science up to September 18th, 2023. Search criteria: (TOPIC: (Carbonized Polymer Dots) OR TOPIC: (Carbon Dots) OR TOPIC: (Carbon Nanodots) OR TOPIC: (Graphene Quantum Dots)) AND (TOPIC: (Afterglow) OR TOPIC: (Phosphorescence) OR TOPIC: (Delayed Fluorescence)).

prehensive reviews focusing on other topics. For example, our research group comprehensively summarized the influence of self-protective structure and matrix-assisted system on the afterglow emission of CDs.<sup>[57]</sup> Lin's group explored the effect of heavy atom doping on afterglow emission and the strategy of self-protective CDs to achieve RTP emission.<sup>[58]</sup> Likewise, Shuang et al.<sup>[59]</sup> summarized the main methods for synthesizing RTP CDs, including matrix-assisted and self-protective. Cao et al.<sup>[61]</sup> outlined the classification and synthesis of CDs, and discussed two strategies for achieving RTP, including embedding CDs into matrix and doping with heteroatoms. Yang and co-workers have investigated the effect of doping with elements such as O, N, P, B, halogens, Metallic element, and heteroatoms on RTP CDs. Next, the effect of rigid structure on RTP emission has been summarized.<sup>[62]</sup> Xu et al.<sup>[63]</sup> explained the mechanism of delayed fluorescence from four aspects: Thermally activated delayed fluorescence, Triplet-triplet annihilation, Hot intersystem crossing, and Defect-induced delayed fluorescence. Yang's group summarized the polymer-structure-induced afterglow, which originates from the crosslinked polymer network formed during the carbonization process.<sup>[65]</sup> However, these reviews only focus on the preparation of CDs-based long afterglow materials, and do not mention multicolor afterglow. Huang's research team summarized the source and activation strategy of the afterglow of CDs in detail, and introduced afterglow from CDs with excitation-dependent and temperature-dependent. However, these two mechanisms do not fully encompass the regulation of multicolor afterglow.<sup>[60]</sup> Gong's group summarized the preparation strategies of CDs-based RTP materials from matrix-assisted methods and self-protective synthesis. Although multicolor afterglow is mentioned many times in this review, it is only presented as scattered examples throughout the text, and they are without a comprehensive summary of the sources of multicolor afterglow.<sup>[64]</sup> Yang et al.<sup>[66]</sup> introduced that doping of heteroatoms and/or



employing of energy-accepting matrix are advantages to generation of multiple RTP color and dynamic RTP properties. However, this approach can only generalize a small fraction of the multicolor afterglow from CDs. An's research team introduced the regulation of afterglow properties, including the regulation of luminescent color. However, they only explored the regulation of the afterglow color from the perspective of the luminescent center, and did not provide a comprehensive summary of the multicolor afterglow from CDs.<sup>[67]</sup> Zhou et al.<sup>[68]</sup> mentioned multicolor RTP CDs and lifetime-tunable RTP CDs. Unfortunately, multicolor regulation has not been systematically summarized, and the references listed in this article is only a small part. Overall, while these studies have contributed valuable insights into various aspects of afterglow emission in CDs, a comprehensive and systematic review encompassing the preparation strategy and luminescence mechanism of multicolor afterglow from CDs-based long afterglow materials is still lacking.

In this review, we summarize the multicolor CDs-based long afterglow materials from preparation strategy and luminescence mechanism. First, we introduce the effects of raw materials and reaction parameter on the luminescent color of CDs-based long afterglow materials. Then, we categorize the luminescence mechanism of multicolor afterglow from CDs-based long afterglow materials from seven factors, including carbonization degree, surface state, aggregation degree, temperature dependence, excitation dependence, multi-emission center, and energy transfer. It should be noted that these luminescence mechanisms will further guide us in designing more rational preparation schemes to achieve the desired multicolor afterglow. Next, we briefly introduce the applications of multicolor afterglow from CDs-based long afterglow materials in anti-counterfeiting, information security, WLED, and bioimaging. Finally, we provide our perspectives and guidance on the construction of multicolor afterglow, the performance optimization of afterglow emission, and the applications of CDs-based long afterglow materials. **Figure 2** compiles all the articles relevant to multicolor afterglow from CDs-based long afterglow materials, and the illustration represents one of the most representative works of that year.

## 2. Luminescence Mechanism of Afterglow from CDs

The luminescence mechanism of CDs can be elucidated by considering the luminescence mechanism of organic afterglow materials. According to the current study, the afterglow from CDs includes room temperature phosphorescence (RTP) and delayed fluorescence (DF), both of which can be explained by the Jablonski diagram (**Figure 3**).<sup>[75]</sup>

Effective capture and stable excitation of triplet excited states excitons are necessary for afterglow emission. On the one hand, singlet excited states must undergo intersystem crossing (ISC) to become triplet excited states. The introduction of heteroatoms or heavy atoms with lone pair electrons can effectively mix different molecular orbital configurations. This enhances the spin-orbit coupling (SOC), improves the efficiency of ISC, and increases the number of triplet excited states excitons.<sup>[76–80]</sup> On the other hand, due to the extreme instability of photogenerated radical anions and cations under water and oxygen conditions,

triplet excited states excitons are highly susceptible to rapid deactivation by environmental influences.<sup>[81]</sup> In addition, molecular vibrations exist in triplet excited states excitons, which necessitate the reduction of nonradiative leap constant ( $K_{nr}$ ) and the quenching rate constant ( $K_q$ ). Extensive studies have shown that CDs can easily form hydrogen bonds or covalent bonds with matrix, effectively reducing molecular vibrations.<sup>[82]</sup> Moreover, matrix acts as a barrier, preventing the contact of CDs with water, oxygen, acids, and bases, thereby further protecting CDs from quenching.

Therefore, a common strategy for fabricating CDs-based long afterglow materials is to dope or grow in situ heteroatom-rich carbon dots within a protective matrix. To date, both organic and inorganic matrices have been widely developed for the synthesis of CDs. For example, polyurethane(PU),<sup>[83]</sup> polyacrylamide(PAM),<sup>[84]</sup> polyvinyl alcohol(PVA),<sup>[45,85–87]</sup> polyacrylic acid,<sup>[88]</sup> urea/biuret,<sup>[89,90]</sup> cyanuric acid(CA),<sup>[91,92]</sup> dicyandiamide,<sup>[93]</sup> polyvinylpyrrolidone,<sup>[94]</sup> zeolite,<sup>[95]</sup> silica,<sup>[96–98]</sup> NaCl,<sup>[99]</sup> layered double hydroxides,<sup>[100,101]</sup> and aluminum sulfate.<sup>[102]</sup> Furthermore, matrix-free self-protective systems represented by condensation and polymerization reactions have been widely reported.<sup>[28,103]</sup> The basic process can be described as the formation of chain polymers from polymers or small molecule matrix at the beginning of the reaction. As the carbonization degree increases, the chain polymers intertwine and the center gradually carbonizes to form CDs.

## 3. Preparation Strategy for Multicolor Afterglow from CDs

At present, bottom-up has become the primary method for synthesizing CDs due to the abundant carbon sources and diverse synthetic strategies.<sup>[133]</sup> The general procedure for synthesizing CDs can be simplified as follows: 1) Dissolving the precursor in the solvent (solvent-free methods require the mixing of raw materials); 2) Heating the reaction mixture at high temperatures for carbonization; 3) Separation and purification. Therefore, careful design in the first and second steps is necessary to obtain CDs-based materials with multicolor afterglow. In this section, we categorize the preparation strategies into two types, including raw materials and reaction parameter. As shown in **Table 2**, the different preparation strategies for multicolor CDs-based long afterglow materials are summarized.

### 3.1. Raw Materials

Raw materials participate in chemical reactions as reactants, which can be summarized as precursor and solvent. Precursor is the starting materials for synthesizing CDs, and its basic structure and properties have an important impact on the afterglow emission. As discussed in the previous section, the matrix plays an important role in the preparation of CDs-based long afterglow materials. In addition to complexing with CDs to protect triplet excited states excitons activated afterglow, the matrix can also participate in the reaction of precursor as a reactant to regulate the afterglow color of CDs-based long afterglow materials. Moreover, the solvent not only plays the role of dissolving precursor, but also plays a crucial role in regulating the construction of multicolor afterglow through its chemical properties.

# Multicolor Afterglow from Carbon Dots

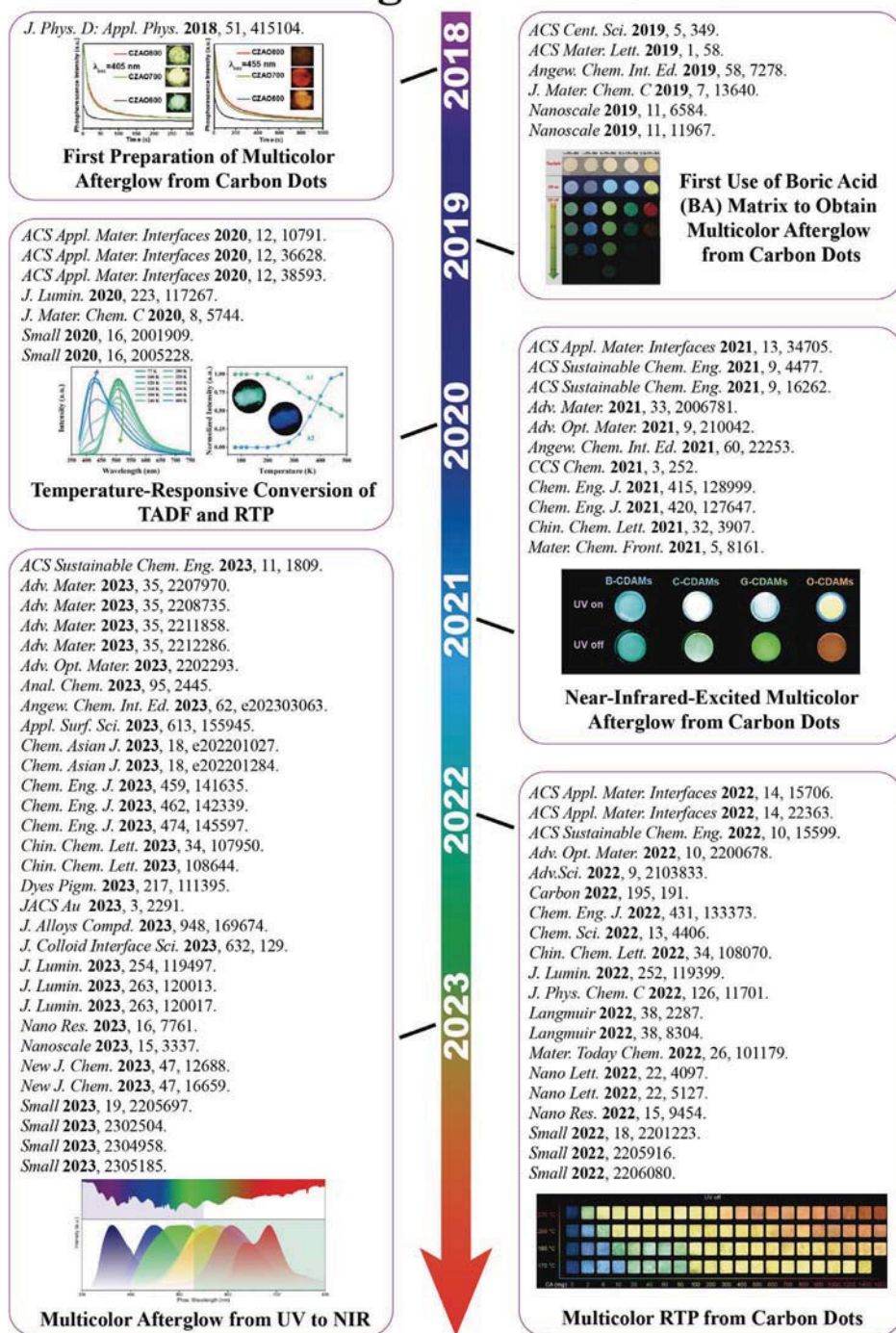


**Figure 2.** Recent advances of multicolor afterglow from carbon dots. Reproduced with permission.<sup>[69]</sup> Copyright 2018, IOP Publishing. Reproduced with permission.<sup>[70]</sup> Copyright 2019, Wiley-VCH. Reproduced with permission.<sup>[71]</sup> Copyright 2020, The Royal Society of Chemistry. Reproduced with permission.<sup>[72]</sup> Copyright 2021, Wiley-VCH. Reproduced with permission.<sup>[73]</sup> Copyright 2022, Wiley-VCH. Reproduced with permission.<sup>[74]</sup> Copyright 2023 Wiley-VCH.

## 3.1.1. Precursor

Precise regulation of precursors is the easiest way to achieve multicolor afterglow emission. On the one hand, the functional groups carried by the precursors are retained as chromophores

during the formation of CDs. On the other hand, the conjugated structure of the precursor is crucial, and CDs with different degrees of conjugation will be formed during the subsequent carbonization process, thereby affecting the change of the energy gap. Here, we follow the process of preparing CDs-based long

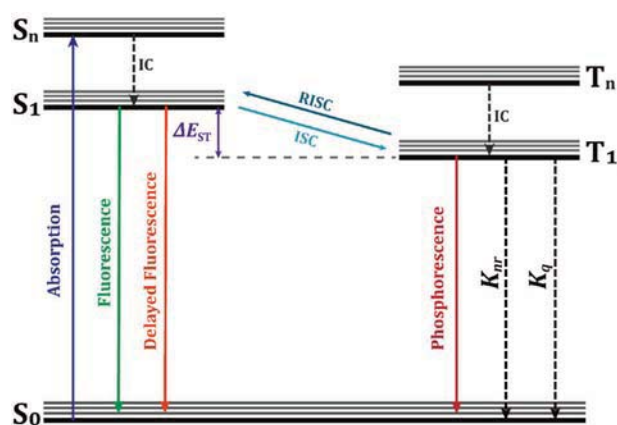


**Figure 3.** Simplified Jablonski diagram. IC = internal conversion, ISC = intersystem crossing, RISC = reverse intersystem crossing.

afterglow materials, which can be divided into one-step in situ and two-step composite preparation.

One-step method can be outlined as a one-step chemical reaction of precursors to prepare CDs-based long afterglow materials with multicolor by hydrothermal, solvothermal, microwave, and pyrolysis. Similar to the strategy of organic RTP materials to obtain multicolor emission through structural design, multicolor CDs-based long afterglow materials can be obtained by screening precursors.<sup>[134]</sup> It is worth noting that this strategy can precisely regulate the growth of CDs to a certain extent and obtain multicolor emission.<sup>[80,135]</sup> However, except for CDs with self-protective properties that emit afterglow at room temperature visible to the naked eye, the majority of CDs do not observe afterglow, even though the radiative leap of triplet excited states excitons is available. Based on this, embedding CDs with fluorescence emission into the matrix to achieve afterglow emission is one of the best strategies, and the emission wavelengths can be inherited or emitted at longer wavelengths. In short, two-step method to achieve multicolor afterglow, the first step is to prepare seed CDs under different reaction conditions, and the second step is to compound the seed CDs with the matrix to form CDs-based composite with afterglow emission. By using different raw materials to prepare CDs with different fluorescent colors, and then compounded with the matrix to obtain CDs composites with multicolor afterglow emission.

In the early stage of multicolor afterglow research, the selection of precursors with widely diverse chemical structures is an important way to obtain multicolor afterglow. In the process of forming CDs, the functional groups carried by the precursor can be retained and attached to the surface of CDs, which plays a role in regulating the luminescence color. In 2019, our group<sup>[70]</sup> for the first time used boric acid (BA) as a matrix to activate the room temperature afterglow of CDs. By using seed CDs obtained from different precursor, multicolor (blue, green, yellow-green, and orange) afterglow from CDs without heteroatom doping and heteroatom doping are obtained (Figure 4a). We propose that the glassy state formed by the boric acid can effectively protect the triplet excited states excitons of CDs and reduce the non-radiative leap processes. Using this idea, Cui et al.<sup>[104]</sup> obtained cyan, green, and orange afterglow via one-step melting treatment

of BA with three different chemical structures precursors. Similarly, Yu's team<sup>[105]</sup> reported a CDs-based long afterglow material using different organic templates as precursors to obtain green RTP and blue TADF in Zeolites matrix, respectively. In 2022, our group<sup>[111]</sup> reported bright green, yellow, and orange afterglow emission using  $Y(OH)_x F_{3-x}$  (denoted as YOHF) as a universal matrix. A recent study, Xu et al.<sup>[112]</sup> adopted the idea of MOF-limited domain and synthesized CDs@MOF by preparing seed CDs with different structures and properties. Their RTP color could be regulated from blue (478 nm) to red (631 nm). Further, this strategy can be extended to COF as well as HOF to activate multicolor afterglow from CDs. Additionally, multicolor afterglow has been reported in PVA,<sup>[113]</sup> CA,<sup>[114]</sup> PAM,<sup>[115]</sup> and  $SiO_2$ .<sup>[132]</sup>

The conjugated structure of the precursor also has an important influence on the multicolor afterglow. With the increase of the number of atoms in the conjugated chain, the separation of HOMO and LUMO gradually decreases. Therefore, the energy required to excite the electron leap is decreasing, which is very conducive to the construction of long wavelength and multicolor afterglow.<sup>[74]</sup> For instance, Tan et al.<sup>[106]</sup> used 2-Hydroxy-1,4-naphthoquinone, 2,5-dihydroxy-1,4-benzoquinone, and alizarin with urea for microwave heating and prepared CDs-based long afterglow materials showing green, yellow and red afterglow. They show that as the degree of conjugation of precursors increased, the degree of conjugation of chromophores on the surface of CDs also increased, reducing the energy gap between the lowest singlet and lowest triplet states, leading to a red shift in the afterglow emission wavelength (Figure 4b).

The number, location and type of functional groups contained in the precursor are important to help with the multicolor afterglow. Substances rich in C=O and C=N functional groups are generally considered to have the potential for multicolor afterglow emission, as these groups are considered prerequisites for the generation of multicolor afterglow from CDs-based long afterglow materials.<sup>[128,136,137]</sup> Moreover, the precursors have functional groups that can form hydrogen bonds and covalent bonds, which play a role in immobilizing chromophores, stabilizing excited triplet excitons, enhancing the ISC process, and realizing multicolor afterglow.<sup>[138]</sup> Wu et al.<sup>[107]</sup> screened m-phenylenediamine and folic acid, which contain abundant C=O and C=N functional groups as precursors, and obtained blue-green and green afterglow. Further studies show that the reason for the color difference might be caused by the differential effect of the C=N/C=O bond with the H-atom interaction force (Figure 4c). Furthermore, due to the differences in molecular structures, isomers have been widely used to prepare multicolor fluorescent CDs. Inspired by this concept, Qi et al.<sup>[109]</sup> prepared CDs-based long afterglow materials with yellow, yellow-green, and yellow-white afterglow by using microwave assisted heating method. The results show that the modulation of particle size, surface state and  $\pi-\pi$  interactions within CDs can be tuned by changing three PD precursors.

In general, different physical and chemical properties of products can be obtained by controlling the ratio of reactants. For the construction of multicolor afterglow of CDs, the luminescence color can be regulated by changing the proportion of precursors while keeping the precursor type constant. For instance, Feng et al.<sup>[110]</sup> prepared yellow-green and yellow CDs-based long



**Table 2.** Summary of different preparation strategies for multicolor CDs-based long afterglow materials.

Name	Raw materials	Reaction parameter	Afterglow color	Emission wavelength [nm]	Lifetime [ms]	Afterglow QYs [%]	Refs.
CDs/BA	7-Hydroxycoumarin, 3-chloro-4-hydroxy-benzaldehyde, 1,8-naphthalimide, boric acid	Heat, 220 °C, 5–10 min	Cyan, green, orange	494, 560, 608, 662	1740, 940, 300, 590	66.13, 23.65, 56.41, 31.66	[104]
CDs@SBT-1, CDs@SBT-2	(4-(2-aminoethyl)morpholine, 4,7,10-trioxo-1,13-tridecanediamine	Solvothermal, 170 °C, 7 d	Green, blue	525, 440	574, 153	–	[105]
rCDs	alizarin, 2-Hydroxy-1,4-naphthoquinone, 2,5-Dihydroxy-1,4-benzoquinone, urea	Microwave, 750 W, 4–5 min	Green, yellow-green, red	493, 535, 605	–, –, 211	–, –, 30	[106]
m-PD-CDs, FA-CDs	m-phenylenediamine, folic acid, ethanol	Solvothermal, 260 °C, 2 h	Blue-green, green	424, 504	–	–	[107]
CDs-1, CDs-2, CDs-3, CDs-4	Pyromellitic acid, trimelic acid, terephthalic acid, boric acid	Calcining, 200 °C, 10 min	Blue, violet, deep-blue	440, 407, 430	633, 1882, 2332	47, 57, 65	[108]
o-C-dots, m-C-dots, p-C-dots	o-phenylenediamine, m-phenylenediamine, p-phenylenediamine, boric acid, diethylenetriaminepentakis	Microwave, 800 W, 15 min	Yellow, yellow-green, yellowish-white	570, 550, 540	0.5, 153, 89	–	[109]
BD50	Citric acid, boric acid, water	Heat, 180 °C, 5 h	Yellow-green, yellow, blue, blue-green, yellow	512, 517, 424, 426, 444	1170, 1240, 2160, 2520, 2320	23.5, 17.4, 7.4, 7.8, 11.3	[110]
CDs/BA	CDs, boric acid, water	Heat, 180 °C, 5 h	Blue to orange	490 to 570	2260	17.5	[70]
CDs-g@YOHF, CDs-y@YOHF, CDs-o@YOHF	CDs, Y(NO <sub>3</sub> ) <sub>3</sub> ·6H <sub>2</sub> O, NaF, NaOH	Hydrothermal, 140 °C, 15 h	Bright green, yellow, orange	494, 549, 602	530, 370, 410	–	[111]
CDs@MOF	1,4-dicarboxybenzene, DMF, Zn(NO <sub>3</sub> ) <sub>2</sub> ·6H <sub>2</sub> O, CDs, water	Hydrothermal, 100 °C, 6 h	Blue, green, yellow, orange, red	478 to 631	1064.21, 375.55, 272.83, 169.74, 85.67	6.5 to 18.6	[112]
CNDs	CDs, polyvinyl alcohol, water	Heat, 95, 3 h	Blue, green, yellow, orange	435, 505, 560, 590	567, 1387, 726, 311	6.24, 12.32, 4.32, 2.03	[113]
CDs@CA	Cyanuric acid, CDs, water	Hydrothermal, 200 °C, 3 h	Deep blue, green, yellow, orange, red	416, 466, 550, 618, 618	1740, 977, 1680, 87, 31	23.2, 10.6, 13.7, 2.7, 1.3	[114]
CDs@PAM	CDs, polyacrylamide, water	Heat, 80 °C, 10 h	Blue, green, orange, red	476, 502, 586, 633	637, 583.81, 503.23, 478.97	–	[115]
B-CDs, G-CDs, Y-CDs, R-CDs	melamine, NaOH, maleic anhydride,	Heat, 200 °C, 10 h	UV, blue, green, yellow, red, NIR	300 to 800	15.8, 818.0, 239.7, 168.4, 426.4, 127.6	8.1, 6.0, 3.9	[74]
CDs@CA	Urea, water, m-phenylenediamine	Hydrothermal, 300 °C, 3 h	Deep-blue, Violet	430, 425	1806, 1640	17.7, 39.3	[116]
CNQDs	Urea, 1,4-benzenediboronic acid, 2-naphthaleneboronic acid	Pyrolysis, 200 °C, 3 h	Deep-blue, green	418, 530	6470, 1550	10.5, 8.99	[117]
B-CDs, C-CDs, G-CDs	Glutathione, water, m-phenylenediamine, p-phenylenediamine, Sodium alginate	Hydrothermal, 220 °C, 18 h	Blue, green, yellow	423, 490, 525	165.8, 284.5, 186.1	6.90, 21.62, 7.34	[118]
CDs/B <sub>2</sub> O <sub>3</sub>	CDs, boric acid, water	Heat, 180 °C, 5 h	Blue-green to orange-yellow	475 to 565	423.5, 325.3, 397.8, 318.1, 415.2	–	[119]

(Continued)

**Table 2.** (Continued)

Name	Raw materials	Reaction parameter	Afterglow color	Emission wavelength [nm]	Lifetime [ms]	Afterglow QYs [%]	Refs.
CD <sub>1</sub> @MCM-22P, CD <sub>2</sub> @ZSM-12	Hexamethylenimine, NaOH, sodium aluminate, water	Hydrothermal, 160 °C, 4 d/3 d	Blue, green	455, 530	790, 316.7	6.81, 3.45	[120]
CDs@Uet	Urea, ethanol, m-phenylenediamine, o-phenylenediamine, p-phenylenediamine	Solvothermal, 200 °C, 6 h	Deep-blue to red	463, 474, 481, 520, 528	1580, 1170, 1230, 2020, 1010	20.1, 16.5, 11.7, 13.7, 4.4	[121]
B-LTW, Y-LTW	Lignin, o-phenylenediamine, formamide, ethanol	Solvothermal, 200 °C, 10h	Green, red	505, 705	208.83, 146.06	–	[122]
B-CD composites	Citric acid, boric acid	Pyrolysis, 170 to 200 °C, 5h	Blue to red	466 to 638	113.90 to 581.76	0.42 to 13.74	[73]
CDs@SiO <sub>2</sub> -Raw, CDs@SiO <sub>2</sub> -550,	Silica, hexamethylenimine	Hydrothermal, calcining, 550 °C, 6 h	Blue-green to yellow	447, 469, 508, 525	252, 166, 451195	–	[123]
CDs@zeolite	H <sub>3</sub> PO <sub>4</sub> -DPA, Al(OH) <sub>3</sub> , Fumed Silica, TMA · 5H <sub>2</sub> O, TEABr, α-Lipoic Acid, DETA, EDA	Hydrothermal, 220 °C, 6 to 36h	–	–	2100, 1970, 1820, 1680, 1560, 1360, 1220, 620, 380	11.34, 11.69, 9.7, 9.68, 12.44, 12.71, 8.2, 7.3, 1.8	[124]
CPDs	1-[3-(Trimethoxy silyl) propyl] urea, Phosphoric acid	Microwave, 630w, 102 to 300s	Yellow, green, cyan, blue	550, 525, 505, 480	365 to 1065	59.41, 11.81, 44.82, 3.38	[125]
CDs@clay	Layered clay, Pyridine-2,6-dicarboxylic acid (DPA)	Calcining, 550 °C, 2 h	Blue, green	420, 517	1050, 608	1.08, 6.06	[126]
B-CDs	boric acid (BA),	Calcining, 260 °C, 12 h	Blue, green	417, 494	1043.56, 590.62	9.6	[127]
CDs-MS	1,3,5-benzenetricarboxylic acid (BTA)	Calcining, 350 °C, 3h	Green, yellow	–	701, 886	–	[128]
N, O-CDs@IP	1,2,4-triaminobenzene, KNO <sub>3</sub> , NaCl and 1,2,4-triaminobenzene	Calcining, 450, 5h	Cyan, green	482, 518	2040, 1150	24.7, 19.88	[129]
uCDs	KNO <sub>3</sub> , MgCl <sub>2</sub> , NaH <sub>2</sub> PO <sub>4</sub> , Glycine	Hydrothermal, 160 °C, 6 h	Yellow-green, orange	570610	91, 281	–	[130]
AB-CDC-1	Citric acid, ethylenediamine, urea	Pyrolysis, 200 to 260 °C, 10 h	Blue to red	462, 506, 487, 551, 605, 623	492, 746, 1106, 359.5, 80, 26	11.1, 16.6, 23.35, 19.4, 4.94, 4.32	[131]
B-CD@SiO <sub>2</sub> , R-CD@SiO <sub>2</sub> , Y-G-CD@SiO <sub>2</sub> , Y-CD@SiO <sub>2</sub>	L-arginine, boric acid (BA)	Hydrothermal, 200 °C, 2 to 6 h/ Calcining, 600 °C, 90 min	Blue, green, yellow, red	465, 500, 580, 680	252.41, 258.09, 1085.42, 2109.57	36.68, 5.55, 4.36, 15.88	[132]

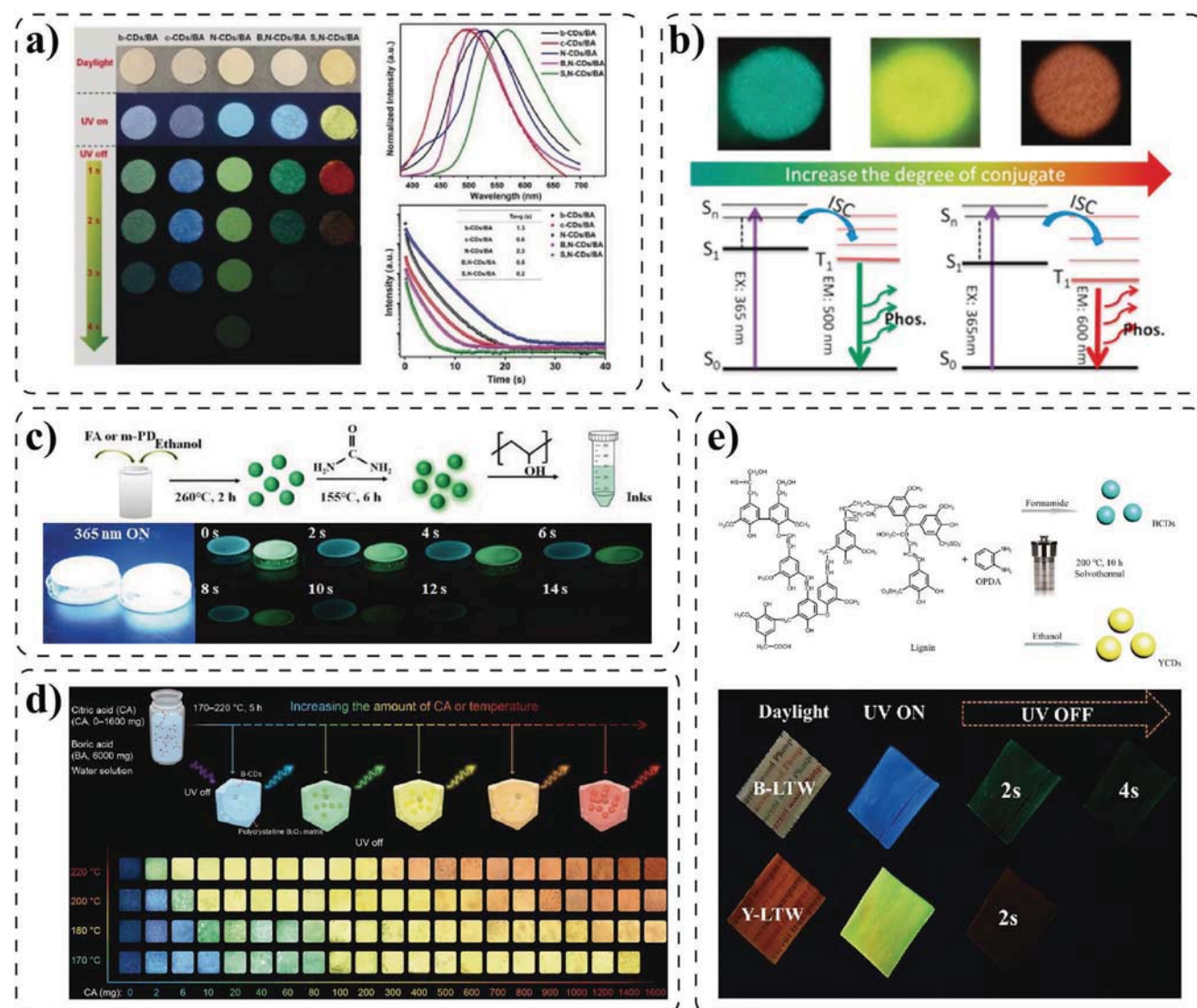


**Figure 4.** a) Digital photographs of CDs/BA composites before and after turning off 365 nm UV light, and afterglow emission spectra, afterglow decay curves and lifetimes of CDs/BA composites by excited at 350 nm. Reproduced with permission.<sup>[70]</sup> Copyright 2019, Wiley-VCH. b) Proposed mechanism for the long wavelength RTA emission of CD-based composites. Reproduced with permission.<sup>[106]</sup> Copyright 2020, Elsevier. c) Schematic illustration for the fabrication of CDs, and RTP decay photographs. Reproduced with permission.<sup>[107]</sup> Copyright 2021, Elsevier. d) Schematic representation of the fabrication process of B-CD composites with tunable full-color RTP, and Optical images of B-CD composites prepared from CA and BA at different reaction conditions. Reproduced with permission.<sup>[73]</sup> Copyright 2022, Wiley-VCH. e) Schematic of the LTW with daylight, UV on or off, and Schematic of the FL and RTP mechanisms. Reproduced with permission.<sup>[122]</sup> Copyright 2020, American Chemical Society.

afterglow materials by changing the citric acid content in the precursor. With the content of citric acid gradually increases, the content of B-C bonds in CDs decreases, resulting in a red shift of the emission wavelength. It is worth noting that by controlling the ratio of seed CDs to matrix, the luminescence color of CDs-based long afterglow materials can be further regulated. Qiu et al.<sup>[73]</sup> reported a strategy to achieve multicolor afterglow by controlling the citric acid feeding and the pyrolysis temperature. With the increase of the citric acid feeding and the pyrolysis temperature, the particle size of B-CDs gradually increased, and the afterglow emission color shifted from blue to red (Figure 4d). Recently, CDs with UV to NIR emission were developed by Shan et al.<sup>[74]</sup> who prepared seed CDs using imidazole and maleic anhydride. Sub-

sequently, the seed CDs and NaOH were compounded in the ratios of 1:6, 1:4, and 1:1 to obtain green, yellow, and red afterglow emissions.

### 3.1.2. Solvent

A large number of experimental data show that hydrothermal or solvothermal are the most commonly used approaches for preparing CDs. The solubility of the precursor in the solvent, as well as the boiling point, acidity, and polarity of the solvent, have significant effects on the dehydration and carbonization of the precursor.<sup>[139–142]</sup> Therefore, the type of solvent can lead to



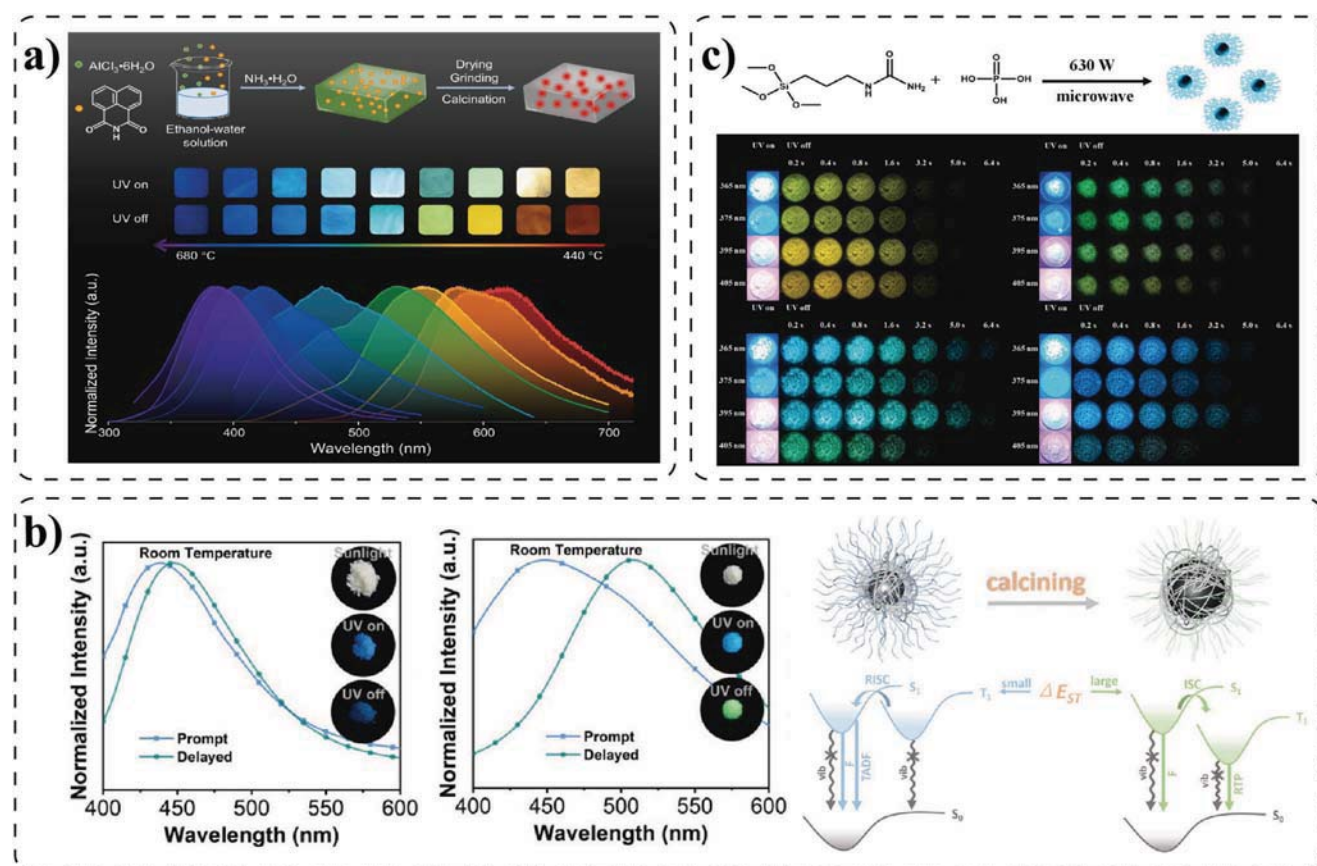


**Figure 5.** a) Schematic of CDs@Al<sub>2</sub>O<sub>3</sub> composites before and after turning off 365 nm UV light, and afterglow emission spectra. Reproduced with permission.<sup>[144]</sup> Copyright 2023, Elsevier. b) Normalized steady-state photoluminescence spectra and delayed photoluminescence spectra of CDs@SiO<sub>2</sub>-Raw and CDs@SiO<sub>2</sub>-550. Reproduced with permission.<sup>[123]</sup> Copyright 2022, American Chemical Society. c) Diagrammatic drawing of the synthesis process for multicolor RTP CPDs by microwave-assisted reactions under 630 W. Reproduced with permission.<sup>[125]</sup> Copyright 2022, American Chemical Society.

different graphitized core and surface functional groups, which will result in CDs with different afterglow emission wavelengths. For instance, Liu et al.<sup>[122]</sup> used formamide and ethanol as solvents to prepare two colors of the afterglow from CDs. The experimental results show that the particle size of CDs prepared using ethanol was significantly larger than formamide. However, ethanol as a solvent causes excessive carbonization of CDs, which reduces the N content in CDs and destroys the RTP luminescence center, thus causing a red shift of the emission wavelength and producing a red afterglow (705 nm) (Figure 4e).

### 3.2. Reaction Parameter

#### 3.2.1. Reaction Temperature

Temperature plays an important role in the synthesis of CDs, primarily in the dehydration condensation of precursors and the carbonation, which further affects the emission wavelength of afterglow.<sup>[143]</sup> In this section, we discuss the preparation of multicolor CDs-based long afterglow materials in two aspects: one-step heating and post-annealing.

One-step heating to regulate the luminescent color refers to changing the reaction temperature during the synthesis of CDs to control the degree of carbonization and the number of surface functional groups, thus obtaining CDs with different luminescent properties. Compared to the uncontrolled temperature in the microwave method, most CDs-based long afterglow materials are prepared by hydrothermal and solvothermal methods. Therefore, multicolor afterglow from CDs can be realized by regulating the temperature gradient during heating. Recently, our research group<sup>[144]</sup> successfully obtained multicolor afterglow in the range of 376–619 nm by using one-step in-situ calcination preparation strategy. The study demonstrates that the surface functional groups, conjugation degree and defects of CDs can be regulated by changing the calcination temperature. As the temperature increases from 440 °C to 680 °C, the luminescence color of CDs shifts from red to ultraviolet (Figure 5a).

Post-annealing is also an effective way to achieve multicolor afterglow.<sup>[145]</sup> The basic process can be summarized as the preparation of seed CDs by hydrothermal or microwave methods, followed by heat treatment. Multicolor afterglow can be achieved by further modifying CDs or changing the degree of carbonization of CDs. For example, Liu et al.<sup>[123]</sup> synthesized the seed CDs with blue afterglow emission by hydrothermal method,

and then calcined the seed CDs at different temperatures in the atmospheric atmosphere. Multicolor afterglow was obtained by adjusting the carbonization degree of CDs. Further studies show that seed CDs form small carbon cores and a large number of connected polymer chains during hydrothermal heating, demonstrating TADF emission. As the calcination temperature increases, the carbonization of CDs increases, forming larger carbon cores and a few polymer chains, resulting in RTP emission (Figure 5b).

### 3.2.2. Reaction Time

Under the different heating methods, the longer the reaction time, the higher the dehydration and carbonization of the precursors, which regulate the afterglow color of CDs. Liu et al.<sup>[125]</sup> reported a method to synthesize CDs by controlling the microwave time. Using 1-[3-(trimethoxy silyl) propyl] urea and phosphoric acid as raw materials, yellow, green, cyan, and blue afterglows were obtained by controlling the heating time with microwave-assisted method. In particular, the multicolor is attributed to the increase in microwave reaction time, the increase in the degree of carbonization of CDs, the weakening of the polymer structure, and the gradual decrease in the C=O bond on the surface, which reduces the ISC process and leads to the blue shift of the emission wavelength (Figure 5c).

## 4. Luminescence Mechanism of Multicolor Afterglow from CDs

In Section 3, we provide a detailed overview of the methods and strategies employed for achieving multicolor afterglow in CDs from the perspective of material preparation. However, the diversity of raw materials and reaction parameters results in luminescent colors that cannot be explained by a unified mechanism. In this section, we categorize and summarize the reported CDs-based long afterglow materials and provide an explanation of the multicolor emission from a mechanistic point of view. As shown in Table 3, the different luminescence mechanisms for multicolor CDs-based long afterglow materials are summarized.

### 4.1. Carbonization Degree

At present, CDs are considered to have a core-shell model structure consisting of graphitized carbon cores and various functional groups surfaces.<sup>[172]</sup> As discussed before, in the bottom-up-based carbonization process, temperature and time directly affect the carbonization degree of CDs, resulting in the change of emission wavelength. For example, Xia et al.<sup>[146]</sup> prepared blue-green to yellow CDs by hydrothermal method at 150 °C to 300 °C. As the carbonization temperature increased, the degree of conjugation of CDs increased and the emission band gap of the RTP emission center narrowed, which caused the RTP emission wavelength to shift from 485 nm to 558 nm (Figure 6a). Similarly, Shen et al.<sup>[147]</sup> used 1,3-diaminopropane and hydroxyethyl diphosphonic acid as precursors and successfully prepared yellow-green, yellow, and orange CDs by varying the hydrothermal heating temperature.

Further studies show that the multicolor afterglow may be attributed to the expansion of the conjugated  $sp^2$  structural domain with increasing hydrothermal temperature, resulting in a decrease in the energy gap.

Performing secondary or multiple carbonizations on the obtained CDs-based long afterglow materials is a feasible strategy for achieving multicolor afterglow. Wang et al.<sup>[148]</sup> reported a method based on a thermally driven amorphous-crystal topological phase transition to realize green, yellow-green, yellow, and orange-red multicolor CDs. It is shown that thermal annealing is the key factor to achieve multicolor afterglow. Polymer chains are further cross-linked, dehydrated, and carbonized under high temperature annealing, which gradually transformed from the amorphous state to the crystalline state. The conjugated  $\pi$  domain in CDs is continuously crystallized and expanded, the energy gap is constantly reduced, and the afterglow emission is red-shifted. It is worth noting that the polymer structure and the doping of heteroatoms are key to achieving afterglow emission, but not the cause of multicolor afterglow (Figure 6b).

Multicolor afterglow from CDs with different degrees of carbonization can be obtained by adjusting the type and ratio of precursors or solvents in raw materials. Yang's team<sup>[149]</sup> reported the synthesis of green to orange RTP CDs using different ratios of ethanol and  $H_2O$  as solvents, followed by the addition of equal amounts of sulfuric acids, under microwave conditions. Further studies show that sulfuric acids and ethanol are key to the synthesis of multicolor afterglow. The addition of sulfuric acids can make the precursor dehydrate and graphitize rapidly, and make the surface of CDs oxidize rapidly, increasing the number of C=O. Meanwhile, the addition of ethanol lowered the boiling point of the reaction. Therefore, with the increasing volume of ethanol, the accelerated dehydration of precursors and the increase in graphitization, the  $sp^2$  conjugation domain expands (Figure 6c).

### 4.2. Surface State

Compared with the stability of the carbon core state, the surface state of CDs is more affected by the environment. According to existing research, the surface state of CDs can be classified into surface chemical composition, surface functional group composition, and surface defects. Different surface states result in variations in the energy levels of CDs, ultimately affecting the changes in luminescent colors.<sup>[173,174]</sup> Therefore, the surface state of CDs is considered one of the reasons of multicolor luminescence.

The strategy of constructing carbon core state luminescence and surface state luminescence to achieve multicolor afterglow is feasible.<sup>[175]</sup> Compared to the stable carbon core state, the surface state is more influenced by the environment. Therefore, regulating the luminescence of the surface state can enable the switching from single emission center to dual emission centers, thereby achieving control over the emission color. In 2021, Qu's team<sup>[150]</sup> demonstrated a strategy based on the one-step hydrothermal preparation of dynamic phosphorescent CDs. Under excitation at 395 nm, it exhibited time-dependent phosphorescence ranging from orange to green. The results show that green phosphorescence is excited by light below 395 nm, and red phosphorescence is excited by light above 395 nm. The reason for the multicolor

**Table 3.** Summary of different luminescence mechanisms for multicolor CDs-based long afterglow materials.

Luminescence mechanism	Afterglow color	Emission wavelength [nm]	Lifetime [ms]	Afterglow QYs [%]	Refs.
Carbonization degree	Blue-green, green, yellow-green, yellow	485 to 558	61.4 to 466.5	–	[146]
Carbonization degree	Yellow-green, yellow, orange	–	–	–	[147]
Carbonization degree	Green, yellow-green, yellow, orange-red	443, 465, 483, 559	481, 511, 437, 426	8.7, 6.3, 3.2, 1.5	[148]
Carbonization degree	Blue, green, yellow	501, 517554	189.24, 92.85, 85.09	14.5, 10.7, 3.3	[149]
Surface state	Green, red	555, 630	348, 340	4.2, 3.2	[150]
Surface state	Blue, yellow-green,	480, 550	521, 729	0.8, 2.6	[151]
Aggregate degree	Blue, green, red	483 to 635	398, 347, 58	9.05, 4.4, 0.63	[152]
Aggregate degree	Green, yellow, orange, red, NIR	530, 555, 585, 625, 645, 750	1660, 1180, 16, 0.4	38.2, 20.8, 1.6, 0.51	[153]
Excitation dependence	Cyan to yellow	500, 535, 555, 575	750, 880, 750, 500	–	[136]
Excitation dependence	Green, yellow, orange-red	553, 606, 640	423.43, 257.12, 220.82	3.68, 4.33, 2.16	[154]
Excitation dependence	Blue, green	462, 518	712, 746	–	[155]
Temperature dependence	Blue, green	480, 507	1620 (green)	–	[71]
Temperature dependence	Yellow-green to red	–	–	–	[156]
Multi-emission center	Blue, green	402, 510	1100, 1240	–	[157]
Multi-emission center	Yellow to red	400, 570	410, 1050	–	[158]
Multi-emission center	Green, yellow	515, 560	419, 464	–	[159]
Multi-emission center	Blue to red	484, 522, 560, 617, 633	1052.23, 1222.39, 815.44, 392.01, 256.24	4.08, 0.52, 0.16, 0.21, 0.16	[160]
Energy transfer	Green, yellow, orange, red	510, 550, 580, 610	1610, 1250, 1210, 1130	–	[161]
Energy transfer	Green to orange	522, 520, 564, 590	1200, 1260, 990, 940	38.2, 28.8, 13.9, 15.8	[162]
Energy transfer	Green, yellow, orange, orange-red	505, 553, 575, 627	1650, 603.7, 784.7, 966	–	[163]
Energy transfer	Blue-green, green, yellow, orange, red	486 to 623	769.3, 766.4, 738.7, 797.5, 716.0	2.05, 2.32, 1.54, 1.38, 0.37	[164]
Energy transfer	Green to blue purple	–	–	–	[165]
Energy transfer	Blue, green, red	445, 550, 615	2030, 480, 400	50.17, –, –	[166]
Energy transfer	Blue, green, orange, red	463 to 614	232 to 1500	4.3, 5.5	[167]
Energy transfer	Green, orange, red	510, 575, 600	1440, 1110, 920	–	[168]
Energy transfer	Blue, green	440, 500	2150, 1890	–	[169]
Energy transfer	Red, green	620, 500	1.81, 22.32	5.7, 14.1	[46]
Energy transfer	Green, yellow, red	520, 565, 590	1261, 730, 585	11.31, 20.57, 20.66	[170]
Energy transfer	Blue, cyan, green, orange	425, 477, 506, 598	1820, 800, 1850, 120	–	[72]
Energy transfer	Blue, green, red	–	–	–	[171]

emission is attributed to the dual phosphorescence emission center constructed by the carbon core state and surface state. Because CDs inherit the nitrogen heterocyclic structure of levofloxacin during the hydrothermal process, they have carbon core triplet state with green phosphorescence emission. Meantime, the C=O formed in the hydrothermal treatment is in the surface triplet state with red phosphorescence emission. However, when reduced with NaBH<sub>4</sub>, the C=O content of CDs surface significantly decreased, causing the destruction of the surface state and only show green phosphorescence (Figure 7a). One year later, they obtained yellow-green to blue afterglow using folic acid as precursor through one-step hydrothermal method.<sup>[151]</sup> The results show that the presence of N-doped carbon core causes CDs to show yellow-green phosphorescence. However, upon the addition of sodium carbonate, the surface phenolic hydroxyl groups were ionized, and the CDs showed blue phosphorescence. They found

that the alkali-induced ionization of phenolic hydroxyl played a significant role in passivating surface defects, enhancing the ISC rate, and reducing nonradiative transitions. The ionization-induced delocalization effect of surface phenolic hydroxyl greatly facilitated n– $\pi^*$  transition by increasing the number of lone pair electrons, thereby reducing the singlet–triplet splitting and activating the blue phosphorescence of the surface state. Due to the different decay rates of the carbon core state and surface state, a unique time-dependent phosphorescence was generated (Figure 7b).

### 4.3. Aggregate Degree

In organic luminescence, aggregation can either decrease or enhance the emission of chromophores, corresponding to



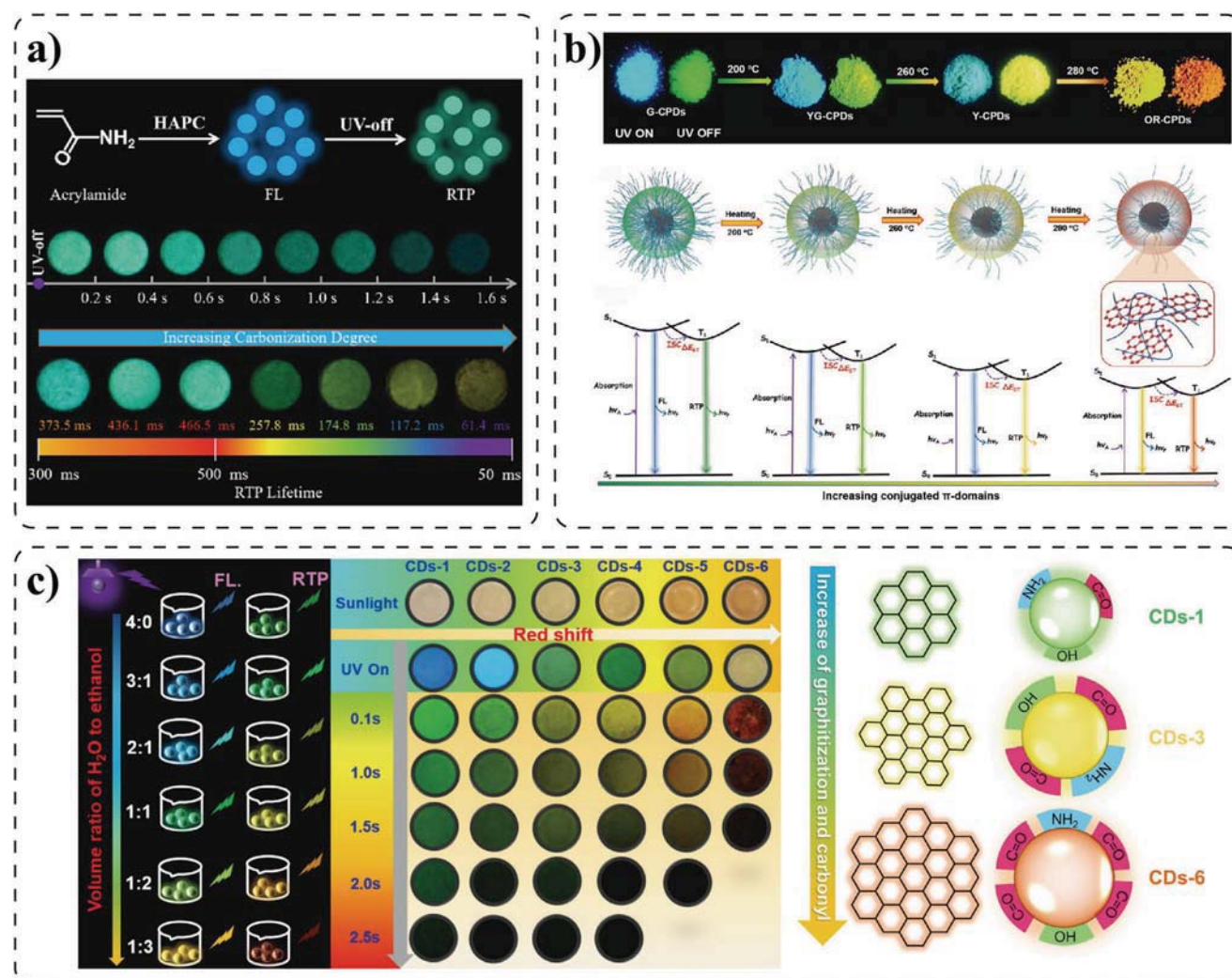


**Figure 6.** a) Optical image of carbonized polymer dots leading to multicolor luminescence with the increasing carbonization degree. Reproduced with permission.<sup>[146]</sup> Copyright 2020, American Chemical Society. b) Photographs of CPDs powders before and after turning off 365 nm UV light, and schematics of structural evolutions of CPDs accomplished upon post-annealing and the corresponding energy diagrams responsible for FL and RTP emissions. Reproduced with permission.<sup>[148]</sup> Copyright 2021, Wiley-VCH. c) Preparation of the multicolor CDs through adjusting the volume ratio of water to ethanol, and images of these CDs with sunlight, UV on or UV off. Reproduced with permission.<sup>[149]</sup> Copyright 2023, Elsevier.

the phenomena of aggregation-caused quenching (ACQ) and aggregation-induced emission (AIE), respectively.<sup>[176,177]</sup> However, the luminescence in solid state or concentrated solution is weakened or not, which hinders the application of ACQ effect.<sup>[178]</sup> In 2001, Tang et al.<sup>[179]</sup> discovered the AIE effect, which resulted in enhanced emission of chromophores in the aggregated state. Therefore, chromophores traditionally associated with ACQ effects can achieve luminescent applications through the concept of AIE. In recent years, researchers have observed aggregation phenomena in CDs, resulting in unique luminescent behaviors. For instance, our research group reported a hydrophobic CDs with AIE characteristics. In dispersed state, the carbon core exhibits blue emission from the conjugated  $\pi$ -domains. Upon aggregation of CDs, the  $\pi$ - $\pi$  stacking of the conjugated  $\pi$ -domains leads to quenching of the blue emission. However, the intramolecular rotation restriction caused by aggregation of surface fluorophores with S-S bonds results in red emission. Addi-

tionally, other reports on AIE fluorescence have been extensively summarized elsewhere and will not be elaborated here.<sup>[180–185]</sup>

Excitingly, the AIE effect has also been discovered in the construction of CDs-based long afterglow materials. In 2020, Jiang et al.<sup>[47]</sup> prepared yellow RTP TA-CDs using trimellitic acid as precursor. They demonstrated that the large conjugated structure formed by aggregation under hydrothermal treatment is the main reason for the emission of yellow RTP (Figure 8a). Such aggregation would not only stabilized triplet excited states, but also generated new triplet excited states, resulting in aggregation-induced yellow RTP. Recent studies have found that the degree of aggregation can regulate the energy levels, providing a new approach for multicolor emission of CDs-based long afterglow materials. Shan's team<sup>[152]</sup> adjusted the luminescent color of afterglow by controlling the amount of matrix involved in the one-step method. Blue, green, and red afterglow materials were prepared using citric acid and NaOH under microwave-assisted heating.

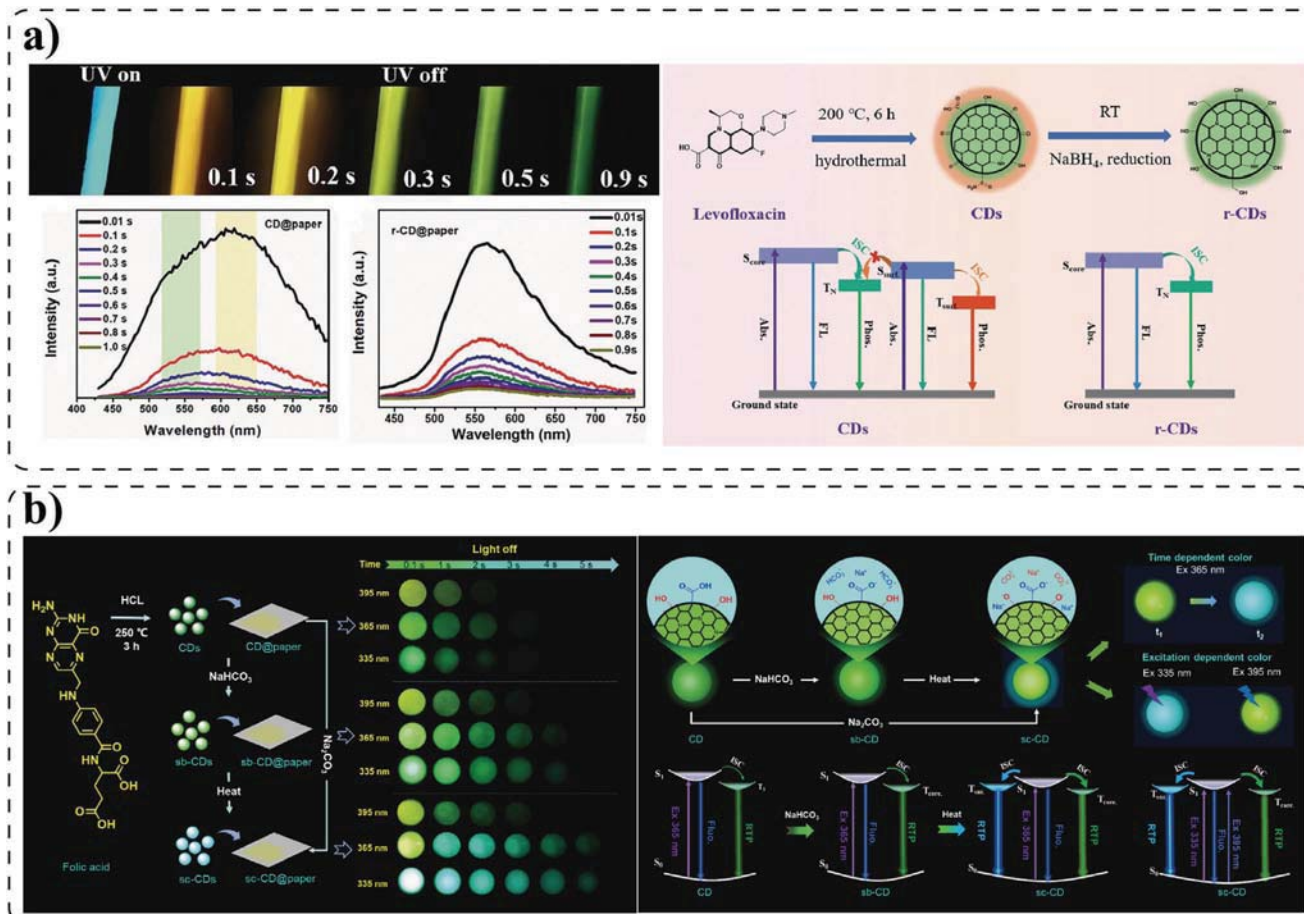


**Figure 7.** a) Digital photographs of CD@paper under 395 nm light irradiation and those taken from 0.1 to 0.9 s after turning off the 395 nm light, and possible phosphorescence emission processes for the CDs and r-CDs. Reproduced with permission.<sup>[150]</sup> Copyright 2021, Wiley-VCH. b) Possible photoluminescence emission processes and energy level diagram of CDs composite. Reproduced with permission.<sup>[151]</sup> Copyright 2022, Elsevier.

They found that the content of CDs in the monoclinic NaOH unit cell caused different degrees of aggregation of CDs, resulting in color changes. As the NaOH content decreased, more CDs nanoparticles were confined within a monoclinic NaOH unit cell. Theoretical calculations confirmed that the reduction of the energy gap between  $T_1$  and  $S_0$  could be achieved by altering the aggregation state of CDs, resulting in a red shift of phosphorescence emission (Figure 8b). Similarly, Qu's team<sup>[153]</sup> reported a aggregation-induced red shift CDs, and their luminescent colors can be regulated from green to near-infrared. They used hydrothermal lyxorine as seed CDs, followed by their combination with different amounts of boric acid. With the concentration of CDs increases, the content of CDs in boric acid increases, and the interaction range between CDs decreased, leading to generate new aggregation states, resulting in multicolor afterglow (Figure 8c).

#### 4.4. Excitation Dependence

Selective excitation is an important reason for the excitation dependence of CDs at different excitation wavelengths, which

is closely related to the various components generated during the preparation process. Due to the presence of different types of aggregates during the formation of CDs, this leads to the embedding of multiple discrete electronic states, which show a large excitation dependent shift in the emission spectra of CDs.<sup>[186]</sup> This behavior is macroscopically manifested by the fact that the particle size distribution of CDs is inhomogeneous, so that each component shows multicolor luminescence upon excitation at different wavelengths. Up to the available studies, excitation dependence induced by multiple triplet states is not a universal phenomenon. Here, we present CDs-based long afterglow materials with typical excitation dependence.

Jiang et al.<sup>[136]</sup> screened succinic acid and diethylenetriamine as precursors for hydrothermal reaction. By changing the excitation wavelength, the prepared MP-CDs have multicolor emission characteristics ranging from cyan to yellow (Figure 9a). They attributed this unique optical property of MP-CDs to the fact that C=O/C=N groups form different luminescent centers during hydrothermal processes. The luminescent centers change when the excitation wavelength changes. In view of the above inspiration, Li et al.<sup>[154]</sup> reported a strategy to achieve multicolor afterglow by



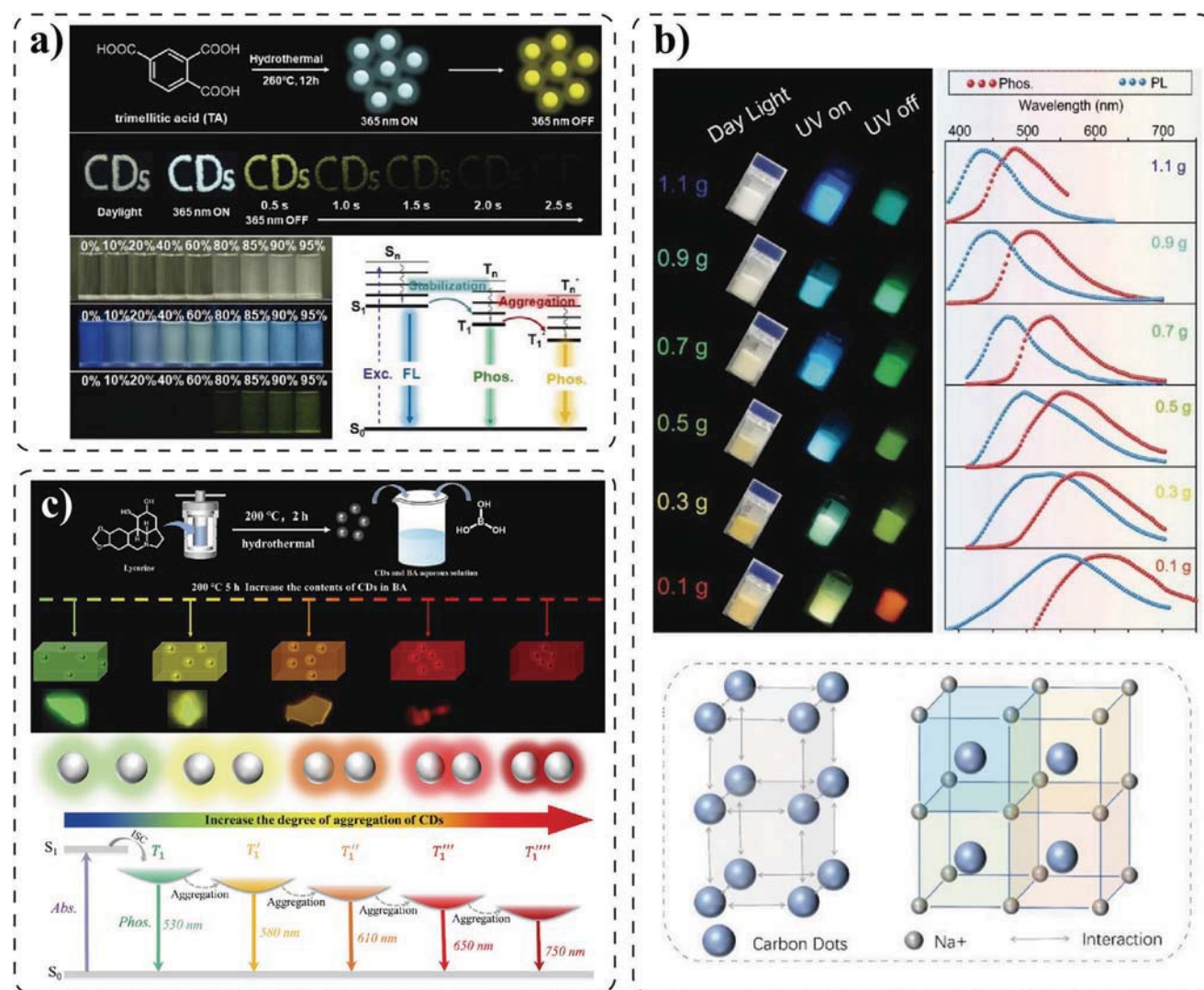


**Figure 8.** a) Illustration of the preparation procedure for TA-CDs, and photographs of the TA-CDs dispersion in THF with various amounts of water (0 to 95 %). Reproduced with permission.<sup>[47]</sup> Copyright 2020, Wiley-VCH. b) The optical pictures of the products obtained from the microwave-assisted citric acid with different massive NaOH. Reproduced with permission.<sup>[152]</sup> Copyright 2022, Wiley-VCH. c) Schematic illustration for the preparation of the CD@BA composites, and possible phosphorescence emission processes and energy level diagram. Reproduced with permission.<sup>[153]</sup> Copyright 2023, Elsevier.

post-treatment modification of seed CDs. The RTP can be color tunable from 553 to 640 nm range. They showed that the addition of acid further accelerated the carbonization and heteroatom doping of CDs, prompting the formation of multiple luminescent centers (Figure 9b).

Recently, CDs with extremely broad excitation regions have been widely reported, and they have typical excitation-dependent properties. For example, Yang's group<sup>[155]</sup> reported CDs-based long afterglow materials that can be excited by green light. Blue and green afterglow can be obtained under 254 and 365 nm. Surprisingly, even if the green light of 500 nm is used for excitation, the phosphorescence emission wavelength of 524 nm can still be obtained. They show that the multicolor phosphorescence emission originates from multiple chromophores aggregates with different excited states (Figure 9c).

#### 4.5. Temperature Dependence

In Section 2, we introduced the conditions for the generation of afterglow from CDs, while briefly discussing the mechanisms of RTP and DF. From the Jablonski diagram, we can conclude that due to the different HOMO energy levels of RTP and DF, the wavelengths of the emitted light upon the return of excited-state electrons to the ground state are distinct. This provides a new design approach for constructing CDs-based long afterglow materials with dual emission. In 2020, our research group<sup>[71]</sup> reported CDs-based long afterglow materials exhibiting temperature-responsive afterglow conversion characteristics. We selected rice husk and ethylenediamine as precursors to prepare CD@SiO<sub>2</sub> composite by one-step in-situ coating strategy. These materials exhibited green RTP at room temperature,



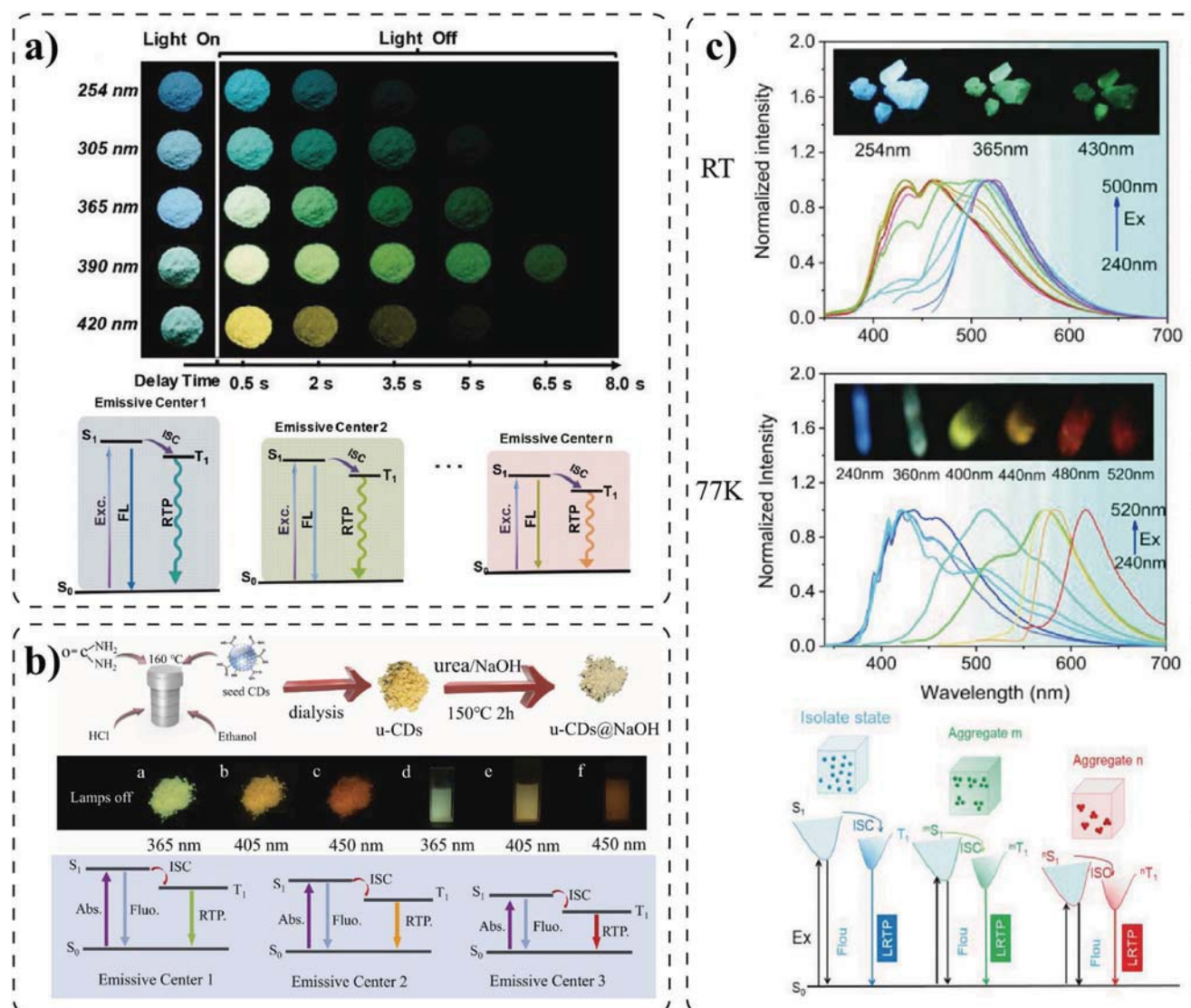


**Figure 9.** a) Schematic illustration of the preparation process for MP-CDs, and photographs of the MP-CDs powder under irradiation by lamps with different wavelength. Reproduced with permission.<sup>[136]</sup> Copyright 2020, Wiley-VCH. b) Schematic illustration of the formation of u-CDs@NaOH, and proposed mechanism for the enhanced multicolor RTP emission of u-CDs@NaOH. Reproduced with permission.<sup>[154]</sup> Copyright 2023, Elsevier. c) Photophysical properties of large sized m,p/CDs-ME crystal. Reproduced with permission.<sup>[155]</sup> Copyright 2022, American Chemical Society.

with a lifetime of up to 1.62 s, and also demonstrated excellent green emission in aqueous solutions. Interestingly, when heating CDs@SiO<sub>2</sub> from 77 to 480 K, the afterglow color gradually changed from green to blue. The study indicated that CDs@SiO<sub>2</sub> exhibited RTP emission at cryogenic temperature and room temperature. When the temperature gradually increases, RTP and DF coexist and compete with each other. At 480 K, DF emission became dominant, which can be attributed to the promotion of non-radiative transitions at high temperatures, thus weakening RTP emission (Figure 10a). Similarly, Shen et al.<sup>[187]</sup> used ciprofloxacin and boric acid (BA) as precursors to obtain CDs-based long afterglow materials with dual-mode emission when heated at 180 °C. The study revealed that the emission at 438 nm belongs to DF, while the emission at 490 nm belongs to RTP. As the ambient temperature gradually increases, the intensity of

phosphorescence emission weakened and the DF emission enhanced. Consequently, when the temperature of the CDs-based long afterglow material decreases from 323 K to 80 K, a color transition from deep blue to cyan is observed. In a recent study, Shan's team<sup>[156]</sup> employed a surface engineering strategy to modify seed CDs with urea, (3-aminopropyl) triethoxysilane, and NaOH to obtain temperature-dependent afterglow. The results showed that the afterglow color of uCDs@SiO<sub>2</sub>/NaOH changed from orange to bright red as the temperature gradually increased from 298 to 373 K. The delayed emission spectra showed that they had multiple emission peaks. When the temperature gradually increased, the delayed emission intensity at 600, 640, and 670 nm increased (corresponding to TADF), while the delayed emission intensity at 535 nm gradually decreased (corresponding to RTP). They demonstrated that the excitons are converted from triplet

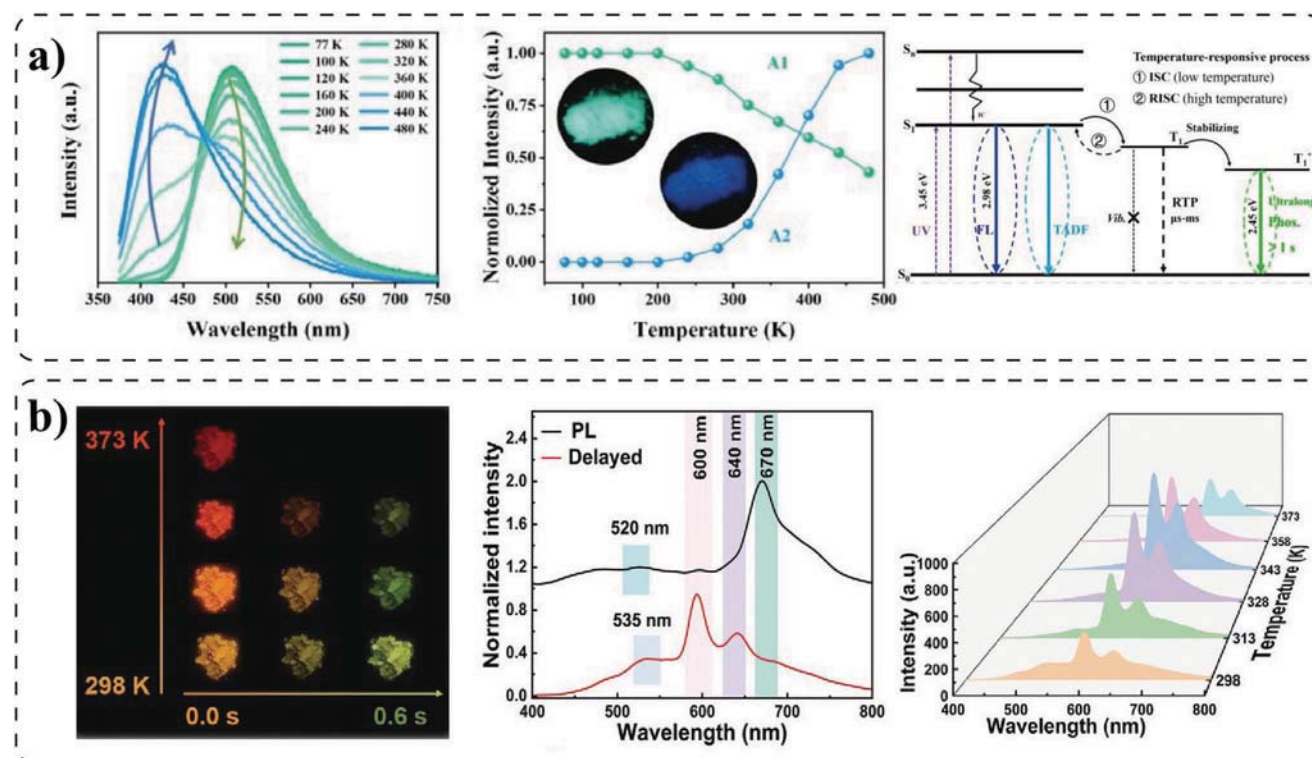


**Figure 10.** a) Temperature-dependent afterglow emission spectra of CDs@SiO<sub>2</sub>. Reproduced with permission.<sup>[71]</sup> Copyright 2020, Royal Society of Chemistry. b) PL spectrum and delayed emission spectrum of uCDs@SiO<sub>2</sub>/NaOH. Reproduced with permission.<sup>[156]</sup> Copyright 2023, Wiley-VCH.

excited states to singlet excited states via RISC process with the help of thermal activation at high temperature, resulting in red DF emission. However, only orange RTP emission can be generated at low temperatures. Interestingly, uCDs@SiO<sub>2</sub>/NaOH also exhibits time-dependent afterglow from orange to green after removing the excitation source, which is due to the differences in emission intensity and lifetime of multiple emission peaks in CDs at different times (Figure 10b).

#### 4.6. Multi-emission Center

Recently, the phenomenon of multicolor afterglow caused by multi-emission center has been reported in CDs-based long afterglow luminescence systems. Different from the luminescence of surface states and carbon core states, CDs-based long afterglow materials with multi-emission center all have the participation of matrix. In the second section, we introduce how the matrix can protect triplet excited states, thereby constructing an effective ISC to achieve afterglow emission. However, both organic matrix and inorganic matrix also exhibit afterglow emission. Therefore, during the process of constructing multicolor afterglow using CDs with matrix, the matrix can act as the second luminescence center in addition to the CDs emission. For example, Ren et al.<sup>[157]</sup> reported a method to achieve blue and green afterglow with folic acid as carbon source and cyanuric acid (CA) as matrix. They show that the multicolor afterglow originates from different emission modes, with dual emission of 402 nm (DF) and 454 nm (RTP) at 254 nm excitation wavelength. However, CA ex-

hibits afterglow emission at the excitation wavelength of 254 nm, which indicates the existence of at least two luminescent centers in FCQDs-CA (Figure 11a).

In addition, there can be energy transfer between multi-emission center. Our group<sup>[96]</sup> proposed the luminescence strategy of trap energy transfer, matrix defect luminescence has a stable or enhanced effect on carbon core states/surface states luminescence. When the electron is excited by light, some electrons can be captured and stored in the trap state. After turning off the light source, these electrons escape from the trap state and strive to T<sub>1</sub> or S<sub>1</sub>, forming RTP or DF emission (Figure 11b). Based on the above finding, our group<sup>[158]</sup> used aluminum nitrate and zinc nitrate as inorganic matrix raw materials, and small organic molecules as carbon sources to develop CDs@ZnAl<sub>2</sub>O<sub>4</sub> with UV and visible light excitation by one-step high-temperature in-situ calcination. We demonstrate that the phosphorescence of CDs@ZnAl<sub>2</sub>O<sub>4</sub> can be excited by a wide range of ultraviolet-blue light sources, which are attributed to multiple luminescent centers of CDs@ZnAl<sub>2</sub>O<sub>4</sub>, further explained as the intrinsic emission of the carbon dots core, the surface state emission of the surface functional groups, and the electronic defects of the matrix. In 2023, Lu et al.<sup>[159]</sup> reported the time-dependent phosphorescence ranging from yellow to green in NaCl matrix. The results show that doping with single metal ion (Na) only obtain green phosphorescence, while doping with dual metal ions (Na, Mg) can achieve yellow phosphorescence. They analyzed that the source of time-dependent phosphorescence is the dual effect of structural constraints and lattice defects in the inorganic salt matrix. The crystal structure of NaCl provides a rigid environment



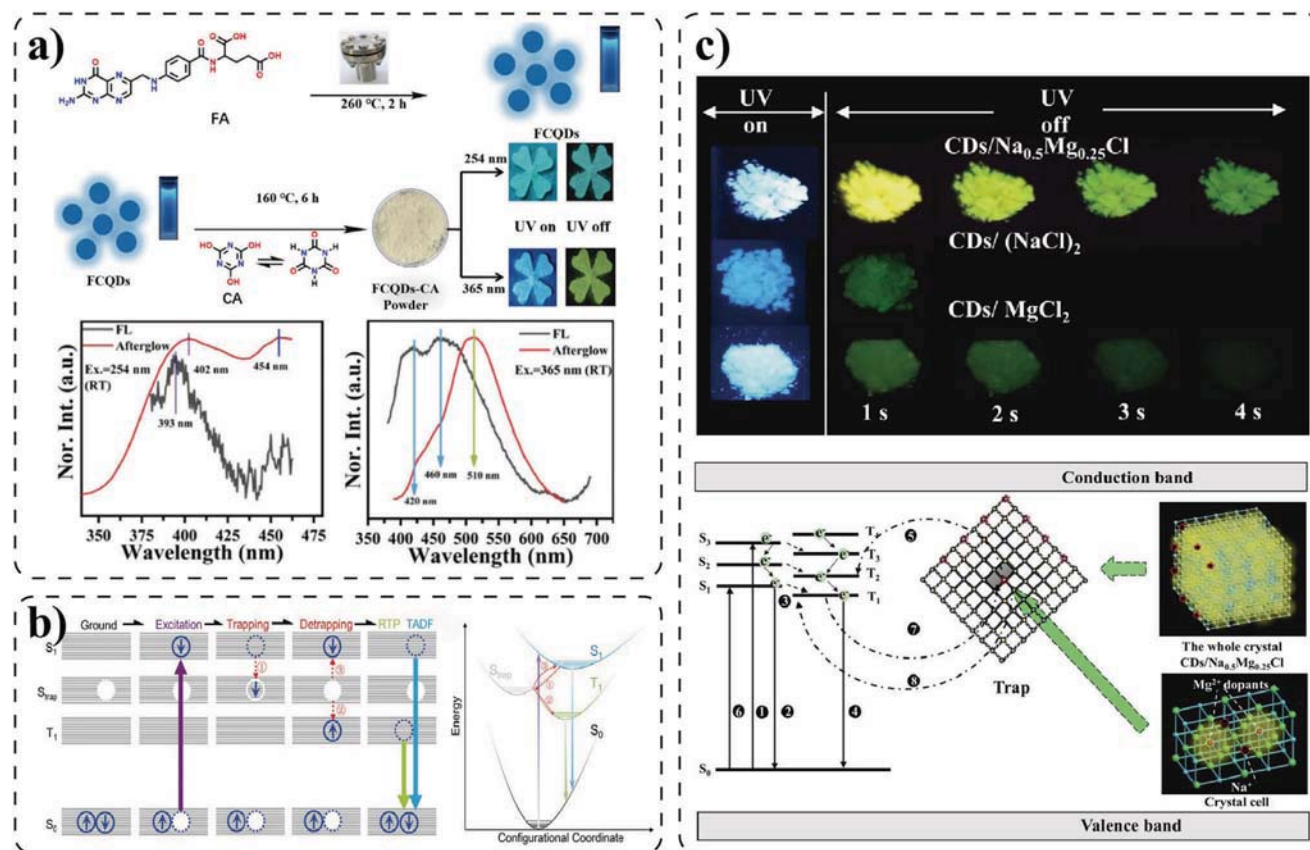


**Figure 11.** a) Synthesis procedure and phosphorescence emission spectra of FCQDs-CA. Reproduced with permission.<sup>[157]</sup> Copyright 2021, Royal Society of Chemistry. b) Mechanism of electron-trap-mediated long-lived emission in terms of Jablonski diagram and configuration coordinate curves. Reproduced with permission.<sup>[96]</sup> Copyright 2020, Wiley-VCH. c) Afterglow Photographs of CDs/ $\text{Na}_{0.5}\text{Mg}_{0.25}\text{Cl}$ , CDs/ $(\text{NaCl})_2$ , and CDs/ $\text{MgCl}_2$ , and schematic representation of afterglow mechanism. Reproduced with permission.<sup>[159]</sup> Copyright 2023, Wiley-VCH.

for triplet excited states excitons, thereby activating green RTP in CDs. It is worth noting that by embedding  $\text{Mg}^{2+}$  into the NaCl crystal to replace  $\text{Na}^+$ , the NaCl crystal structure expands and lattice defects increase. These defects serve as trap centers for excitons, facilitating their capture and transfer (Figure 11c).

#### 4.7. Energy Transfer

The strategy to achieve multicolor luminescence by constructing intermolecular energy transfer has been widely reported in recent years.<sup>[188,189]</sup> Therefore, the strategy of achieving multicolor afterglow by constructing energy transfer strategy has become a new research focus. It is noted that CDs in the energy transfer system can serve not only as an energy donor, but also as an energy acceptor. In this section, we divide the description into non-radiative energy transfer and radiative energy transfer.

##### 4.7.1. Non-radiative Energy Transfer

Non-radiative energy transfer of CDs includes Förster resonance energy transfer (FRET) and Dexter charge transfer (DCT).<sup>[190,191]</sup> The fundamental process occurs at the nanoscale and involves

the non-radiative transfer of energy or charge between the donor and the acceptor.<sup>[192]</sup> The luminescence color and lifetime of CDs can be changed by rational construction of energy donors and energy acceptors.

FRET has been proven to be an important method for preparing multicolor luminescent materials.<sup>[193–196]</sup> The basic process is that the excited donor transfers energy to the ground state acceptor via long-range dipole-dipole interaction.<sup>[197]</sup> In the study of fluorescent materials, FRET is used to construct long wavelength multicolor emission, as this strategy is easily achievable and yields good results.<sup>[198,199]</sup> As a multicolor luminescence strategy, using CDs with afterglow emission as energy donors and fluorescent dyes as energy acceptors, implantation of RET into the system is an effective strategy to obtain CDs with tunable afterglow color and lifetime.

Amorphous silica is widely used in the preparation of aqueous CDs-based long afterglow materials. The stable covalent bond and network structure can perfectly isolate the quenching effect of water and oxygen on CDs, which is the best host for FRET.<sup>[97,98]</sup> Shan's group<sup>[200]</sup> confined CNDs and RhB to amorphous silica, and obtain an emission wavelength of 600 nm with FRET efficiency as high as 99.2%. Based on this, our group<sup>[161]</sup> co-assembled CDs and organic fluorescent dyes into sub-20 nm monodispersed silica nanoparticles. We constructed several



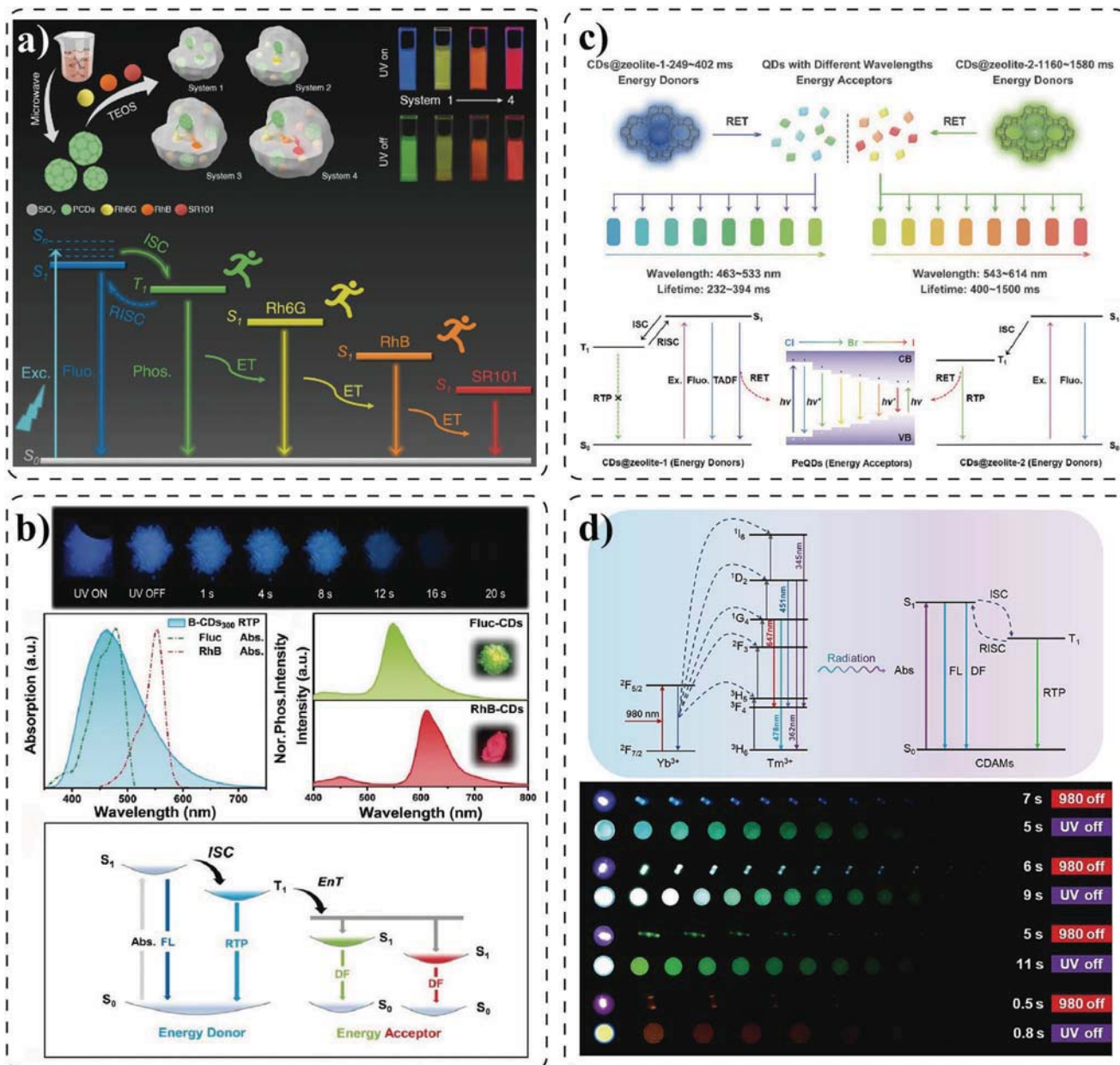


**Figure 12.** a) Schematic illustration of procedures for the preparation of PCDs and system 1-4, and proposed possible afterglow mechanism of system 4 in aqueous environment. Reproduced with permission.<sup>[161]</sup> Copyright 2022, Wiley-VCH. b) Blue phosphorescence emission of B-CDs<sub>300</sub> and absorption spectra of Fluc and RhB, afterglow emission of Fluc-CDs and RhB-CDs complexes, and simplified Jablonski diagram for FRET processes. Reproduced with permission.<sup>[166]</sup> Copyright 2023, Wiley-VCH. c) Schematic diagram of RET process from CDs@zeolite composites to QDs, and afterglow images of 16 kinds of PeQDs with CDs@zeolite composites as energy donors. Reproduced with permission.<sup>[167]</sup> Copyright 2023, Wiley-VCH. d) Simplified schematic illustration of activating the multicolor afterglow of CDAMs under the NIR CW laser excitation. Reproduced with permission.<sup>[72]</sup> Copyright 2021, Wiley-VCH.

cascade resonance energy transfer nanosystems and obtained green (PCDs), yellow (Rh6G), orange (RhB), and red (SR101) water-phase CDs-based afterglow composites. The energy transfer efficiency reached 70.5% and the afterglow lifetime reached 1.13 s (Figure 12a). Cheng et al.<sup>[162]</sup> and Li et al.<sup>[163]</sup> obtained multicolor afterglow using the above strategy, respectively.

Referring to amorphous silica encapsulated CDs and fluorescent dyes, organic matrices can be used as encapsulation

hosts, and then achieve multicolor afterglow by FRET. For example, Jin and co-workers<sup>[164]</sup> constructed RhB/CDs/PVA system by FRET design to achieve tunable emission wavelengths from 486 to 623 nm with a maximum transfer efficiency of 59.93%. Li et al.<sup>[165]</sup> used the same method to achieve multicolor afterglow from blue to green. In addition, urea is often used as self-protecting carbon dots to achieve RTP emission, which was widely reported in previous studies. In 2022, Song et al.<sup>[166]</sup>

obtained blue RTP and lifetime of 2.03 s by urea bath method. They used FRET strategy to achieve energy transfer from B-CDs to Fluc and RhB, and obtained green and red afterglow (Figure 12b). By simply changing the content of B-CDs, Fluc and RhB, these high QYs CDs can achieve white afterglow emission with color temperature tunable.

Recently, perovskite quantum dots have the advantages of narrower emission band spectrum, wider color gamut, and higher QYs, which make them more attention for display applications.<sup>[201–203]</sup> Yu and co-workers<sup>[167]</sup> developed a time-dependent polychrome stereoscopic luminescence system based on FRET. They used two kinds of CDs@zeolite as energy donors, and multicolor fluorescent perovskite quantum dots (PeQDs) with fixed band gaps as energy acceptors. The afterglow emission wavelengths were obtained from 463 to 614 nm, the afterglow life was tuned from 232 to 1500 ms, and the maximum FRET efficiency can reach 95% (Figure 12c).

#### 4.7.2. Radiative Energy Transfer

Despite the extensive practical application of non-radiative energy transfer in the design of multicolor afterglow from CDs-based long afterglow materials. However, when the distance between the donor and acceptor is small enough and the energy levels are matched with each other, the energy can be effectively transferred.<sup>[189,204]</sup> As discussed in the previous section, a strategy to achieve non-radiative energy transfer is to encapsulate CDs with other materials in the nanoscale range. It is worth noting that radiation energy transfer only requires overlap in the donor–acceptor spectrum area. Therefore, the conditions for satisfying non-radiative energy transfer are harsh. In view of this, our group<sup>[72]</sup> developed a general strategy based on efficient radiative energy transfer. Through the upconversion luminescence (UCL) material, the near-infrared light is skillfully converted into ultraviolet or visible light to realize the multicolor afterglow of CDs (Figure 12d). Yb<sup>3+</sup> as the sensitizer absorbed the 980 nm NIR light and transferred energy to the <sup>1</sup>I<sub>6</sub>, <sup>1</sup>D<sub>2</sub>, and <sup>1</sup>G<sub>4</sub> levels of the Tm<sup>3+</sup>. With the radiative transition of <sup>1</sup>I<sub>6</sub>, <sup>1</sup>D<sub>2</sub>, and <sup>1</sup>G<sub>4</sub> energy levels, the released photons are absorbed by CDs, resulting in afterglow emission. In addition, Wu et al.<sup>[171]</sup> adopted the same strategy to achieve multicolor afterglow under 980 nm excitation by one-step in situ introduction of upconversion luminescence into CDs composites.

## 5. Applications

Multicolor CDs-based long afterglow materials possess a wide color gamut and long lifetime, making them superior applications than fluorescence. In this section, we present typical applications of multicolor CDs-based long afterglow materials.

Due to the frequent cases of counterfeiting and falsifying, anti-counterfeiting and information security have become new global challenges to deal with, making the development of novel anti-counterfeiting technologies particularly important.<sup>[205,206]</sup> However, multicolor CDs-based long afterglow materials can carry more encrypted information, enabling anti-counterfeiting techniques with multilevel luminescence. They are more advanced

than single- or dual-layer luminescent anti-counterfeiting modes, as well as more difficult to counterfeit.<sup>[207]</sup> Our group<sup>[70]</sup> used the prepared multicolor CDs/BA composites for anti-counterfeiting and information encryption applications, and the bamboo prints show up from the panda's hand when the UV lamp is turned off. "SCAU" becomes "SAU" with color emission. In addition, "TFRAULSE" is a mixture of "TRUE" and "FALSE," When the light source is turned off, the mixture presents the valid information "TRUE" and "FALS" (Figure 13a). As a novel information encryption scheme, Yu's group<sup>[167]</sup> presents a time-dependent polychrome stereoscopic luminescence system based on FRET. After UV excitation, the luminescent images show different colors when viewed from the top, bottom, and side. Remarkably, when viewed from the side, the system shows five afterglow colors corresponding to color bar codes, which successfully achieves the encryption of 4D information in time and space (Figure 13b).

White light-emitting diodes (WLEDs) require continuous and broad spectra to achieve full coverage of visible light.<sup>[208]</sup> However, single fluorescent or afterglow does not provide full coverage. At present, white light emission is mainly achieved through the combination of different luminescent components.<sup>[209]</sup> Therefore, multicolor CDs-based long afterglow materials are used as components to achieve white light emission, which gives a new idea for the development of WLEDs. Bai and co-workers<sup>[166]</sup> prepared CDs-based long afterglow materials with white afterglow emission using the FRET strategy. The CIE coordinates of CDs-based long afterglow materials could be tuned from (0.30, 0.30) to (0.41, 0.37), and the correlated color temperature (CCT) could be tuned from 7964 to 3203 K (Figure 13c).

With the rapid development of medical technology, cancer treatment has become the most concerned topic in the medical field. The use of visible or near-infrared excited luminescent materials in optical bioimaging for real-time targeted imaging of tumors has positive implications for subsequent treatment.<sup>[210,211]</sup> However, fluorescence imaging requires real-time light excitation, which is easily disturbed by tissue self-illuminating phenomenon, resulting in low signal-to-noise ratio and low imaging depth.<sup>[212]</sup> Therefore, multicolor CDs-based long afterglow materials have shown excellent applications as bioimaging agents for in vivo or in vitro imaging. Our group<sup>[161]</sup> used prepared green, yellow, orange, and red-emitting CDs for bioimaging. The control group did not show an effective signal due to the interference of blue fluorescence and scattered light. However, the experimental group injected with the afterglow agent can show green, yellow, orange, and red afterglow signals (Figure 13d). Because of the high signal-to-noise ratio, the afterglow signal is easier to capture than the fluorescence signal.

## 6. Summary and Outlook

In the past few years, multicolor CDs-based long afterglow materials have been extensively explored and showed great potential in the applications of information encryption, anti-counterfeiting, display and imaging. Here, we present an overview of multicolor CDs-based long afterglow materials from the two dimensions of preparation strategy and luminescence mechanism. The different raw materials and reaction parameters in

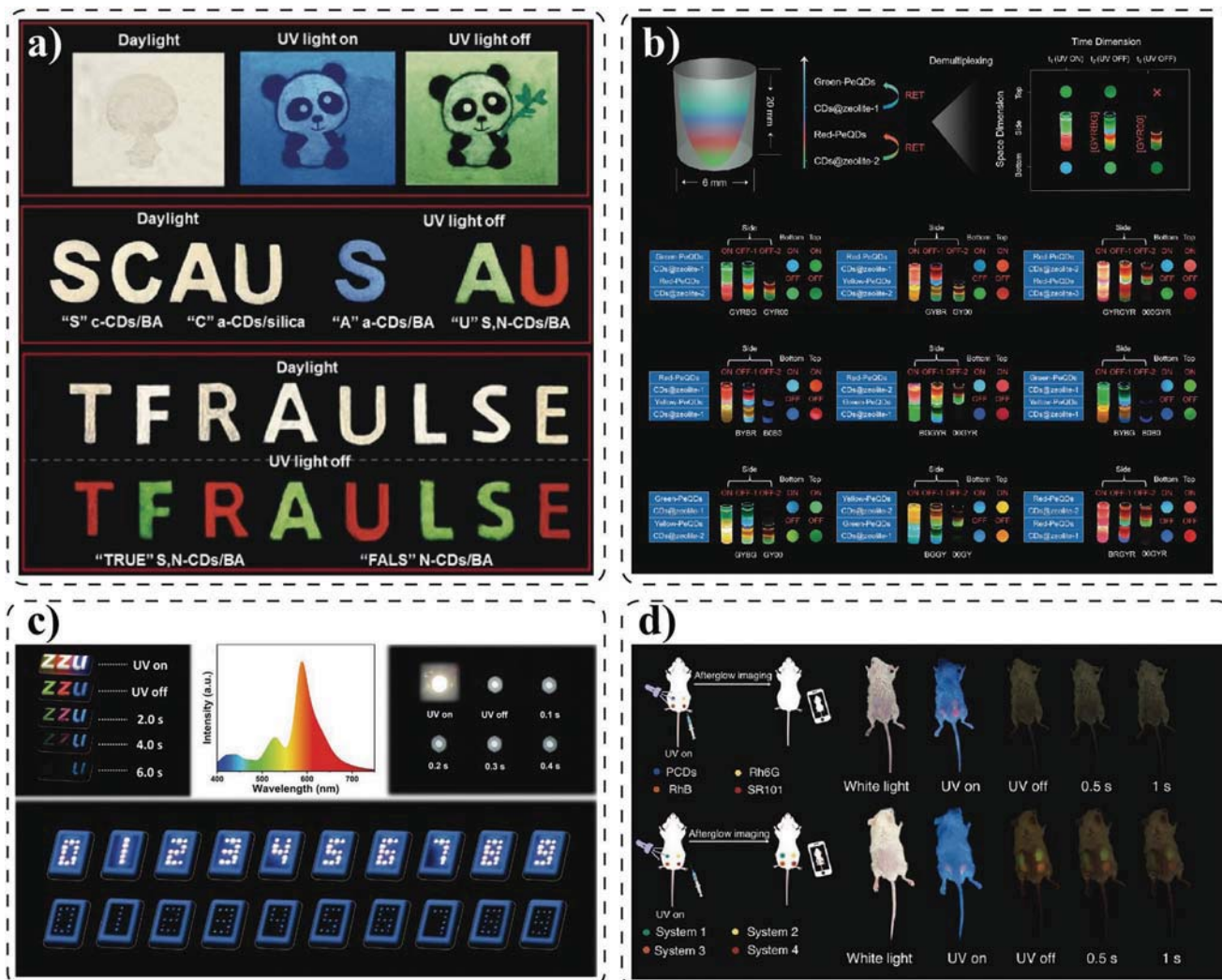


**Figure 13.** a) Digital photographs of anti-counterfeiting and information encryption made from CDs/BA composites. Reproduced with permission.<sup>[170]</sup> Copyright 2019, Wiley-VCH. b) Illustration of time-dependent polychrome stereoscopic luminescence system based on RET and application. Reproduced with permission.<sup>[167]</sup> Copyright 2023, Wiley-VCH. c) Demonstration of white light illumination. Reproduced with permission.<sup>[166]</sup> Copyright 2023, Wiley-VCH. d) Photographs of mice of control group injected subcutaneously with commercial fluorescent dyes, and the mice of treated group injected subcutaneously. Reproduced with permission.<sup>[161]</sup> Copyright 2022, Wiley-VCH.

the preparation strategy directly influence the afterglow color of CDs-based long afterglow materials, while subsequent purification no longer affects the luminescent color. Therefore, the luminescence mechanism of multicolor afterglow from CDs-based long afterglow materials obtained by various preparation strategies is also different. We summarized seven types of luminescence mechanisms of CDs-based long afterglow materials, aiming to provide relevant assistance to researchers in the design and construction of multicolor afterglow. By utilizing these techniques, the luminescence color of CDs-based long afterglow materials can be regulated, which is very friendly to the development of multicolor or full-color afterglow from CDs-based long afterglow materials. However, there are still problems and challenges that need to be solved urgently. Here we will discuss the existing issues and offer feasible solutions.

- 1) The luminescence mechanism of CDs-based long afterglow materials with multicolor characteristics is still unclear. While it is generally believed that the functional groups and energy gaps of C=O/C=N are the sources of different luminescent colors of CDs, but this has not been fully verified. Despite several mechanisms being proposed, a unified and systematic explanation has not been established, requiring further research.
- 2) Achieving full-color coverage of luminescent colors is still a key issue. Although three-color or multicolor afterglows have been developed, most of them are limited to blue and green, which greatly limits the application of CDs. In addition, red or near-infrared afterglow with long wavelength emission and violet or ultraviolet afterglow with short wavelength emission need to be further developed. Nowadays, it is considered that precursors with a large conjugated structures are a feasible



strategy to obtain long wavelength afterglow. Notably, using energy transfer strategy has been validated as a feasible approach for achieving long or short wavelength emission.

- 3) It is a challenge to prepare CDs with high QYs and long afterglow lifetime. In terms of lifetime and QYs, CDs-based afterglow materials do not possess advantages compared to traditional rare earth-doped inorganic persistent luminescent materials and pure organic room temperature phosphorescent materials.<sup>[213]</sup> According to the data in Tables 2 and 3, the lifetime of CDs does not exceed 5 s, and the afterglow QYs is generally low. Therefore, the lifetime and afterglow time of CDs-based afterglow materials need to be studied in depth.
- 4) There are still few CDs-based long afterglow materials that exhibit multicolor responses to external stimuli such as temperature, mechanical stress, light, and solution. By constructing an effective synthetic strategy to obtain CDs with AIE properties, it might be possible to achieve multicolor responses afterglow.
- 5) It is necessary to develop and explore the applications of multicolor CDs-based long afterglow materials. For example, CDs have been well verified in biological imaging. However, there are few reports on photodynamic therapy based on CDs-based long afterglow materials. In addition, new applications need to be developed to expand the application scenarios of CDs-based long afterglow materials.

## Acknowledgements

This work was supported by the National Natural Science Foundation of China (12174119), the Natural Science Foundation of Guangdong Province (2020A1515010443, 2023A1515012003).

## Conflict of Interest

The authors declare no conflict of interest.

## Keywords

carbon dots, multicolor, afterglow, room temperature phosphorescence, delayed fluorescence

Received: August 5, 2023  
Revised: September 26, 2023  
Published online:

- [1] Z. Pan, Y.-Y. Lu, F. Liu, *Nat. Mater.* **2012**, *11*, 58.
- [2] X. Ou, X. Qin, B. Huang, J. Zan, Q. Wu, Z. Hong, L. Xie, H. Bian, Z. Yi, X. Chen, Y. Wu, X. Song, J. Li, Q. Chen, H. Yang, X. Liu, *Nature* **2021**, *590*, 410.
- [3] L. Liang, J. Chen, K. Shao, X. Qin, Z. Pan, X. Liu, *Nat. Mater.* **2023**, *22*, 289.
- [4] P. Alam, T. S. Cheung, N. L. C. Leung, J. Zhang, J. Guo, L. Du, R. T. K. Kwok, J. W. Y. Lam, Z. Zeng, D. L. Phillips, H. H. Y. Sung, I. D. Williams, B. Z. Tang, *J. Am. Chem. Soc.* **2022**, *144*, 3050.
- [5] K. Y. Zhang, Q. Yu, H. Wei, S. Liu, Q. Zhao, W. Huang, *Chem. Rev.* **2018**, *118*, 1770.
- [6] Q. Miao, C. Xie, X. Zhen, Y. Lyu, H. Duan, X. Liu, J. V. Jokerst, K. Pu, *Nat. Biotechnol.* **2017**, *35*, 1102.

- [7] H. Chen, Y. Sun, M. Liu, F. Li, Q. Peng, H. Huang, *Angew. Chem., Int. Ed.* **2023**, *62*, e202302629.
- [8] Y. Shi, R. Lei, F. Li, S. Li, X. Tao, P. Yang, X. Chen, Q. Zhao, Z. L. Wang, *ACS Energy Lett.* **2021**, *6*, 3132.
- [9] Y.-Y. Hu, X.-Y. Dai, X. Dong, M. Huo, Y. Liu, *Angew. Chem., Int. Ed.* **2022**, *61*, e202213097.
- [10] Z. Wang, Y. Zhang, C. Wang, X. Zheng, Y. Zheng, L. Gao, C. Yang, Y. Li, L. Qu, Y. Zhao, *Adv. Mater.* **2020**, *32*, 1907355.
- [11] H. Ju, H. Zhang, L. X. Hou, M. Zuo, M. Du, F. Huang, Q. Zheng, Z. L. Wu, *J. Am. Chem. Soc.* **2023**, *145*, 3763.
- [12] Z. Xia, A. Meijerink, *Chem. Soc. Rev.* **2017**, *46*, 275.
- [13] G. W. Xiao, B. Zhou, X. Y. Fang, D. P. Yan, *Research* **2021**, *2021*, 9862327.
- [14] L. Yang, S. Gai, He Ding, D. Yang, L. Feng, P. Yang, *Adv. Opt. Mater.* **2023**, *11*, 2202382.
- [15] M. D. Mehare, C. M. Mehare, H. C. Swart, S. J. Dhoble, *Prog. Mater. Sci.* **2023**, *133*, 101067.
- [16] Y. Li, M. Gecevicius, J. Qiu, *Chem. Soc. Rev.* **2016**, *45*, 2090.
- [17] H. Terraschke, C. Wickleder, *Chem. Rev.* **2015**, *115*, 11352.
- [18] L. Cao, K. Klimes, Y. Ji, T. Fleetham, J. Li, *Nat. Photonics* **2020**, *15*, 230.
- [19] J. Jin, H. Jiang, Q. Yang, L. Tang, Y. Tao, Y. Li, R. Chen, C. Zheng, Q. Fan, K. Y. Zhang, Q. Zhao, W. Huang, *Nat. Commun.* **2020**, *11*, 842.
- [20] C. Chen, Z. Chi, K. C. Chong, A. S. Batsanov, Z. Yang, Z. Mao, Z. Yang, B. Liu, *Nat. Mater.* **2021**, *20*, 175.
- [21] D. Li, Y. Yang, J. Yang, M. Fang, B. Z. Tang, Z. Li, *Nat. Commun.* **2022**, *13*, 347.
- [22] Y. Tao, C. Liu, Y. Xiang, Z. Wang, X. Xue, P. Li, H. Li, G. Xie, W. Huang, R. Chen, *J. Am. Chem. Soc.* **2022**, *144*, 6946.
- [23] J.-A. Li, L. Zhang, C. Wu, Z. Huang, S. Li, H. Zhang, Q. Yang, Z. Mao, S. Luo, C. Liu, G. Shi, B. Xu, *Angew. Chem., Int. Ed.* **2023**, *62*, e202217284.
- [24] G. Baryshnikov, B. Minaev, H. Ågren, *Chem. Rev.* **2017**, *117*, 6500.
- [25] Y. Gong, G. Chen, Q. Peng, W. Z. Yuan, Y. Xie, S. Li, Y. Zhang, B. Z. Tang, *Adv. Mater.* **2015**, *27*, 6195.
- [26] W. Zhao, Z. He, B. Z. Tang, *Nat. Rev. Mater.* **2020**, *5*, 869.
- [27] O. Bolton, K. Lee, H. J. Kim, K. Y. Lin, J. Kim, *Nat. Chem.* **2011**, *3*, 205.
- [28] S. Tao, S. Lu, Y. Geng, S. Zhu, S. A. T. Redfern, Y. Song, T. Feng, W. Xu, B. Yang, *Angew. Chem., Int. Ed.* **2018**, *57*, 2393.
- [29] Y. Liang, C. Xu, H. Zhang, S. Wu, J.-A. Li, Y. Yang, Z. Mao, S. Luo, C. Liu, G. Shi, F. Sun, Z. Chi, B. Xu, *Angew. Chem., Int. Ed.* **2023**, *135*, e202217616.
- [30] X. Xu, R. Ray, Y. Gu, H. J. Ploehn, L. Gearheart, K. Raker, W. A. Scrivens, *J. Am. Chem. Soc.* **2004**, *126*, 12736.
- [31] Y.-P. Sun, B. Zhou, Y. Lin, W. Wang, K. A. S. Fernando, P. Pathak, M. J. Mezziani, B. A. Harruff, X. Wang, H. Wang, P. G. Luo, H. Yang, M. E. Kose, B. Chen, L. M. Veca, S.-Y. Xie, *J. Am. Chem. Soc.* **2006**, *128*, 7756.
- [32] S. Y. Lim, W. Shen, Z. Gao, *Chem. Soc. Rev.* **2015**, *44*, 362.
- [33] J. Liu, N. Wang, Y. Yu, Y. Yan, H. Zhang, J. Li, J. Yu, *Sci. Adv.* **2017**, *3*, e1603171.
- [34] H. Wu, S. Lu, B. Yang, *Acc. Mater. Res.* **2022**, *3*, 319.
- [35] J. Liu, Y. Liu, N. Liu, Y. Han, X. Zhang, H. Huang, Y. Lifshitz, S.-T. Lee, J. Zhong, Z. Kang, *Science* **2015**, *347*, 970.
- [36] X. Yang, L. Sheng, Y. Ye, J. Sun, Z. Li, X. Ning, J. Cao, X. Sun, *J. Mater. Sci. Technol.* **2023**, *150*, 11.
- [37] J. Lin, X. Huang, E. Kou, W. Cai, H. Zhang, X. Zhang, Y. Liu, W. Li, Y. Zheng, B. Lei, *Biosens. Bioelectron.* **2023**, *219*, 114848.
- [38] T. Rasheed, *TrAC, Trends Anal. Chem.* **2023**, *158*, 116841.
- [39] Z. Chen, Y. Liu, Z. Kang, *Acc. Chem. Res.* **2022**, *55*, 3110.
- [40] Z. Yan, T. Chen, L. Yan, X. Liu, J. Zheng, F.-D. Ren, Y. Yang, B. Liu, X. Liu, B. Xu, *Adv. Sci.* **2023**, *10*, 2206386.

- [41] S. Zhao, S. Sun, K. Jiang, Y. Wang, Y. Liu, S. Wu, Z. Li, Q. Shu, H. Lin, *Nano-Micro Lett.* **2019**, 11, 32.
- [42] L. Đorđević, F. Arcudi, M. Cacioppo, M. Prato, *Nat. Nanotechnol.* **2022**, 17, 112.
- [43] Y. Wang, X. Li, S. Zhao, B. Wang, X. Song, J. Xiao, M. Lan, *Coord. Chem. Rev.* **2022**, 470, 214703.
- [44] B. Geng, J. Hu, Y. Li, S. Feng, D. Pan, L. Feng, L. Shen, *Nat. Commun.* **2022**, 13, 5735.
- [45] Y. Deng, D. Zhao, X. Chen, F. Wang, H. Song, D. Shen, *Chem. Commun.* **2013**, 49, 5751.
- [46] B. Wang, Y. Mu, H. Zhang, H. Shi, G. Chen, Y. Yu, Z. Yang, J. Li, J. Yu, *ACS Cent. Sci.* **2019**, 5, 349.
- [47] K. Jiang, X. Gao, X. Feng, Y. Wang, Z. Li, H. Lin, *Angew. Chem., Int. Ed.* **2020**, 59, 1263.
- [48] S. Z. Hu, K. Jiang, Y. C. Wang, S. Wang, Z. J. Li, H. W. Lin, *Nanomaterials* **2020**, 10, 464.
- [49] Y. Wang, K. Jiang, J. Du, L. Zheng, Y. Li, Z. Li, H. Lin, *Nano-Micro Lett.* **2021**, 13, 198.
- [50] S. Y. Song, K. K. Liu, Q. Cao, X. Mao, W. B. Zhao, Y. Wang, Y. C. Liang, J. H. Zang, Q. Lou, L. Dong, C. X. Shan, *Light: Sci. Appl.* **2022**, 11, 146.
- [51] X. Zhang, C. Yin, J. You, R. Li, J. Zhang, Y. Cheng, Y. Wang, J. Zhang, *Research* **2023**, 6, 0029.
- [52] Y. Wang, H. Wu, W. Hu, J. F. Stoddart, *Adv. Mater.* **2022**, 34, 2105405.
- [53] L. Gu, H. Wu, H. Ma, W. Ye, W. Jia, H. Wang, H. Chen, N. Zhang, D. Wang, C. Qian, Z. An, W. Huang, Y. Zhao, *Nat. Commun.* **2020**, 11, 944.
- [54] X. Dou, T. Zhu, Z. Wang, W. Sun, Y. Lai, K. Sui, Y. Tan, Y. Zhang, W. Z. Yuan, *Adv. Mater.* **2020**, 32, 2004768.
- [55] N. Gan, X. Zou, Y. Zhang, L. Gu, Z. An, *Appl. Phys. Rev.* **2023**, 10, 021313.
- [56] G. N. Lewis, M. Kasha, *J. Am. Chem. Soc.* **1944**, 66, 2100.
- [57] Y. Sun, X. Zhang, J. Zhuang, H. Zhang, C. Hu, M. Zheng, B. Lei, Y. Liu, *Carbon* **2020**, 165, 306.
- [58] K. Jiang, Y. Wang, Z. Li, H. Lin, *Mater. Chem. Front.* **2020**, 4, 386.
- [59] J. Jia, W. Lu, Y. Gao, L. Li, C. Dong, S. Shuang, *Talanta* **2021**, 231, 122350.
- [60] C. Peng, X. Chen, M. Chen, S. Lu, Y. Wang, S. Wu, X. Liu, W. Huang, W. Huang, *Research* **2021**, 2021, 6098925.
- [61] X. Wei, J. Yang, L. Hu, Y. Cao, J. Lai, F. Cao, J. Gu, X. Cao, *J. Mater. Chem. C* **2021**, 9, 4425.
- [62] H.-X. Kang, J.-X. Zheng, X.-G. Liu, Y.-Z. Yang, *New Carbon Mater.* **2021**, 36, 649.
- [63] M. Lei, J. Zheng, Y. Yang, L. Yan, X. Liu, B. Xu, *iScience* **2022**, 25, 104884.
- [64] J. Li, Y. Wu, X. Gong, *Chem. Sci.* **2023**, 14, 3705.
- [65] C. Zheng, S. Tao, B. Yang, *Small Struct.* **2023**, 4, 2200327.
- [66] K. Wang, L. Qu, C. Yang, *Small* **2023**, 19, 2206429.
- [67] H. X. Shi, Y. Wu, J. H. Xu, H. F. Shi, Z. F. An, *Small* **2023**, 19, 2207104.
- [68] S. Zhou, F. Wang, N. Feng, A. Xu, X. Sun, J. Zhou, H. Li, *Small* **2023**, 19, 2301240.
- [69] L. A. Diaz-Torres, C. Gomez-Solis, J. Oliva, C. R. García, A. I. Oliva, C. Angeles-Chavez, G. A. Hirata, *J. Phys. D: Appl. Phys.* **2018**, 51, 415104.
- [70] W. Li, W. Zhou, Z. Zhou, H. Zhang, X. Zhang, J. Zhuang, Y. Liu, B. Lei, C. Hu, *Angew. Chem., Int. Ed.* **2019**, 58, 7278.
- [71] Y. Sun, J. Liu, X. Pang, X. Zhang, J. Zhuang, H. Zhang, C. Hu, M. Zheng, B. Lei, Y. Liu, *J. Mater. Chem. C* **2020**, 8, 5744.
- [72] Y. Zheng, H. Wei, P. Liang, X. Xu, X. Zhang, H. Li, C. Zhang, C. Hu, X. Zhang, B. Lei, W.-Y. Wong, Y. Liu, J. Zhuang, *Angew. Chem., Int. Ed.* **2021**, 60, 22253.
- [73] Y. Ding, X. Wang, M. Tang, H. Qiu, *Adv. Sci.* **2022**, 9, e2103833.
- [74] S.-Y. Song, K.-K. Liu, X. Mao, Q. Cao, N. Li, W.-B. Zhao, Y. Wang, Y.-C. Liang, J.-H. Zang, X. Li, Q. Lou, L. Dong, C.-X. Shan, *Adv. Mater.* **2023**, 35, 2212286.
- [75] A. Jablonski, *Nature* **1933**, 131, 839.
- [76] K. Jiang, Y. Wang, X. Gao, C. Cai, H. Lin, *Angew. Chem., Int. Ed.* **2018**, 57, 6216.
- [77] M. A. El-Sayed, *J. Chem. Phys.* **1963**, 38, 2834.
- [78] M. A. El-Sayed, *Acc. Chem. Res.* **1968**, 1, 8.
- [79] M. S. Kwon, Y. Yu, C. Coburn, A. W. Phillips, K. Chung, A. Shanker, J. Jung, G. Kim, K. Pipe, S. R. Forrest, J. H. Youk, J. Gierschner, J. Kim, *Nat. Commun.* **2015**, 6, 8947.
- [80] Z. An, C. Zheng, Y. Tao, R. Chen, H. Shi, T. Chen, Z. Wang, H. Li, R. Deng, X. Liu, W. Huang, *Nat. Mater.* **2015**, 14, 685.
- [81] R. Kabe, C. Adachi, *Nature* **2017**, 550, 384.
- [82] Q. Peng, H. Ma, Z. Shuai, *Acc. Chem. Res.* **2021**, 54, 940.
- [83] J. Tan, J. Zhang, W. Li, L. Zhang, D. Yue, *J. Mater. Chem. C* **2016**, 4, 10146.
- [84] Y. Zhai, P. Wang, X. Zhang, S. Liu, J. Li, Z. Chen, S. Li, *Chin. Chem. Lett.* **2022**, 33, 783.
- [85] J. Zhu, X. Bai, J. Bai, G. Pan, Y. Zhu, Y. Zhai, H. Shao, X. Chen, B. Dong, H. Zhang, H. Song, *Nanotechnology* **2018**, 29, 085705.
- [86] K. Jiang, Y. Wang, C. Cai, H. Lin, *Adv. Mater.* **2018**, 30, 1800783.
- [87] Z. Tian, D. Li, E. V. Ushakova, V. G. Maslov, D. Zhou, P. Jing, D. Shen, S. Qu, A. L. Rogach, *Adv. Sci.* **2018**, 5, 1800795.
- [88] H. Gou, Y. Liu, G. Zhang, Q. Liao, X. Huang, F. Ning, C. Ke, Z. Meng, K. Xi, *Nanoscale* **2019**, 11, 18311.
- [89] Q. Li, M. Zhou, Q. Yang, Q. Wu, J. Shi, A. Gong, M. Yang, *Chem. Mater.* **2016**, 28, 8221.
- [90] C. Lin, Y. Zhuang, W. Li, T.-L. Zhou, R.-J. Xie, *Nanoscale* **2019**, 11, 6584.
- [91] Y. F. Gao, H. L. Zhang, Y. Jiao, W. J. Lu, Y. Liu, H. Han, X. J. Gong, S. M. Shuang, C. Dong, *Chem. Mater.* **2019**, 31, 7979.
- [92] L. Ding, X. Jin, Y. Gao, J. Wu, T. Ai, H. Zhou, X. Chen, X. Zhang, W. Chen, *Adv. Opt. Mater.* **2023**, 11, 2202349.
- [93] M. Fu, L. Lin, X. Wang, X. Yang, *J. Colloid Interface Sci.* **2023**, 639, 78.
- [94] Y. Liu, X. Huang, Z. Niu, D. Wang, H. Gou, Q. Liao, K. Xi, Z. An, X. Jia, *Chem. Sci.* **2021**, 12, 8199.
- [95] X. Yu, K. Liu, H. Zhang, B. Wang, W. Ma, J. Li, J. Yu, *Small* **2021**, 17, e2103374.
- [96] J. He, Y. Chen, Y. He, X. Xu, B. Lei, H. Zhang, J. Zhuang, C. Hu, Y. Liu, *Small* **2020**, 16, e2005228.
- [97] Y.-C. Liang, S.-S. Gou, K.-K. Liu, W.-J. Wu, C.-Z. Guo, S.-Y. Lu, J.-H. Zang, X.-Y. Wu, Q. Lou, L. Dong, Y.-F. Gao, C.-X. Shan, *Nano Today* **2020**, 34, 100900.
- [98] Y. Sun, S. Liu, L. Sun, S. Wu, G. Hu, X. Pang, A. T. Smith, C. Hu, S. Zeng, W. Wang, Y. Liu, M. Zheng, *Nat. Commun.* **2020**, 11, 5591.
- [99] H. Liu, F. Wang, Y. Wang, J. Mei, D. Zhao, *ACS Appl. Mater. Interfaces* **2017**, 9, 18248.
- [100] R. X. Wang, Y. J. Zhu, Z. J. Xia, K. X. Liang, L. W. Kong, J. Liu, W. Y. Shi, C. Lu, *J. Mater. Chem. C* **2022**, 10, 17182.
- [101] L. Q. Bai, N. Xue, X. R. Wang, W. Y. Shi, C. Lu, *Nanoscale* **2017**, 9, 6658.
- [102] J. Joseph, A. A. Anappara, *ChemistrySelect* **2017**, 2, 4058.
- [103] S. Tao, C. Zhou, C. Kang, S. Zhu, T. Feng, S.-T. Zhang, Z. Ding, C. Zheng, C. Xia, B. Yang, *Light Sci. Appl.* **2022**, 11, 56.
- [104] S. Cui, B. Wang, Y. Zan, Z. Shen, S. Liu, W. Fang, X. Yan, Y. Li, L. Chen, *Chem. Eng. J.* **2022**, 431, 133373.
- [105] J. Liu, H. Zhang, N. Wang, Y. Yu, Y. Cui, J. Li, J. Yu, *ACS Mater. Lett.* **2019**, 1, 58.
- [106] J. Tan, Z. Yi, Y. Ye, X. Ren, Q. Li, *J. Lumin.* **2020**, 223, 117267.
- [107] Y. Wu, X. Fang, J. Shi, W. Yao, W. Wu, *Chin. Chem. Lett.* **2021**, 32, 3907.
- [108] X. Liu, W. Liu, K. Zuo, J. Zheng, M. Wang, X. Liu, *ACS Sustainable Chem. Eng.* **2023**, 11, 1809.

- [109] H. Qi, X. Cui, H. Zhang, Y. Tong, M. Qian, W. Zhou, S. Ding, H. Qi, *Chem. Asian J.* **2023**, 18, e202201284.
- [110] Q. Feng, Z. G. Xie, M. Zheng, *Chem. Eng. J.* **2021**, 420, 127647.
- [111] P. Liang, Y. Zheng, X. Zhang, H. Wei, X. Xu, X. Yang, H. Lin, C. Hu, X. Zhang, B. Lei, W. Y. Wong, Y. Liu, J. Zhuang, *Nano Lett.* **2022**, 22, 5127.
- [112] B. Xu, Z. Wang, J. Shen, J. Li, Y. Jia, T. Jiang, Z. Gao, X. Wang, X. Meng, *J. Phys. Chem. C* **2022**, 126, 11701.
- [113] Q. Cao, K.-K. Liu, Y.-C. Liang, S.-Y. Song, Y. Deng, X. Mao, Y. Wang, W.-B. Zhao, Q. Lou, C.-X. Shan, *Nano Lett.* **2022**, 22, 4097.
- [114] Y. Zheng, Q. Zhou, Y. Yang, X. Chen, C. Wang, X. Zheng, L. Gao, C. Yang, *Small* **2022**, 18, e2201223.
- [115] H. Y. Wang, L. Zhou, H. M. Yu, X. D. Tang, C. Xing, G. C. Nie, H. Akafzade, S. Y. Wang, W. Chen, *Adv. Opt. Mater.* **2022**, 10, 2200678.
- [116] W. Wang, J.-A. Li, S. Ma, Z. Chai, S. Huang, Y. Zhao, S. Wang, Y. Chen, F. Azad, H. Chen, D. Yue, B. Xu, S. Su, *J. Lumin.* **2022**, 252, 119399.
- [117] B. Han, X. Lei, D. Li, Q. Liu, Y. Chen, J. Wang, G. He, *Adv. Opt. Mater.* **2023**, 11, 2202293.
- [118] H. Zhang, L. Sun, X. Guo, J. Xu, X. Zhao, Y. Xia, *Appl. Surf. Sci.* **2023**, 613, 155945.
- [119] W. He, X. Sun, X. Cao, *ACS Sustainable Chem. Eng.* **2021**, 9, 4477.
- [120] J. Wen, Z. Zeng, B. Wang, J. Hong, Y. Chen, J. Zhang, J. Li, J. Jiang, *Nano Res.* **2023**, 16, 7761.
- [121] W. Wang, Q. Chang, L. Li, J.-A. Li, D. Yue, S. Su, *J. Lumin.* **2023**, 263, 120017.
- [122] Y. Liu, H. Yang, C. Ma, S. Luo, M. Xu, Z. Wu, W. Li, S. Liu, *ACS Appl. Mater. Interfaces* **2020**, 12, 36628.
- [123] Y. Liu, X. Kang, Y. Xu, Y. Li, S. Wang, C. Wang, W. Hu, R. Wang, J. Liu, *ACS Appl. Mater. Interfaces* **2022**, 14, 22363.
- [124] X. Yu, K. Liu, H. Zhang, B. Wang, G. Yang, J. Li, J. Yu, *CCS Chem.* **2021**, 3, 252.
- [125] Y. Liu, C. Zheng, B. Yang, *Langmuir* **2022**, 38, 8304.
- [126] Y. Deng, P. Li, H. Jiang, Xu Ji, H. Li, *J. Mater. Chem. C* **2019**, 7, 13640.
- [127] T. Li, C. Wu, M. Yang, B. Li, X. Yan, X. Zhu, H. Yu, M. Hu, J. Yang, *Langmuir* **2022**, 38, 2287.
- [128] C. Wang, Y. Chen, T. Hu, Y. Chang, G. Ran, M. Wang, Q. Song, *Nanoscale* **2019**, 11, 11967.
- [129] Z. Chen, X. Liang, D. He, M. Hu, L. Wen, *New J. Chem.* **2023**, 47, 12688.
- [130] C. Li, H. Liang, S. Bai, J. Zhu, Z. Chen, G. Yang, Y. Zhu, *J. Lumin.* **2023**, 254, 119497.
- [131] X. Wang, S. Wang, Y. Huang, L. Huang, J. Sun, Z. Lin, *Chem. Asian J.* **2023**, 18, e202201027.
- [132] Y. Zhang, M. Li, S. Lu, *Small* **2022**, 19, 2206080.
- [133] J. Liu, R. Li, B. Yang, *ACS Cent. Sci.* **2020**, 6, 2179.
- [134] H. Zhang, Z. Zhao, A. T. Turley, L. Wang, P. R. McGonigal, Y. Tu, Y. Li, Z. Wang, R. T. K. Kwok, J. W. Y. Lam, B. Z. Tang, *Adv. Mater.* **2020**, 32, 2001457.
- [135] L. Ai, Z. Song, M. Nie, J. Yu, F. Liu, H. Song, B. Zhang, G. I. N. Waterhouse, S. Lu, *Angew. Chem., Int. Ed.* **2023**, 135, e202217822.
- [136] K. Jiang, S. Hu, Y. Wang, Z. Li, H. Lin, *Small* **2020**, 16, e2001909.
- [137] P. Long, Y. Feng, C. Cao, Y. Li, J. Han, S. Li, C. Peng, Z. Li, W. Feng, *Adv. Funct. Mater.* **2018**, 28, 1800791.
- [138] J. Zhao, W. Wu, J. Sun, S. Guo, *Chem. Soc. Rev.* **2013**, 42, 5323.
- [139] N. Basu, D. Mandal, *J. Phys. Chem. C* **2018**, 122, 18732.
- [140] X. Shi, Y. Hu, H.-M. Meng, J. Yang, L. Qu, X.-B. Zhang, Z. Li, *Sens. Actuators, B* **2020**, 306, 127582.
- [141] W. Wang, J. Wu, Y. Xing, Z. Wang, *Sens. Actuators, B* **2022**, 360, 131645.
- [142] Z. He, Y. Sun, C. Zhang, J. Zhang, S. Liu, K. Zhang, M. Lan, *Carbon* **2023**, 204, 76.
- [143] J. Li, X. Gong, *Small* **2022**, 18, e2205099.
- [144] J. Liu, Y. Luo, Z. Ran, F. Wang, M. Sun, Y. Luo, J. Zhuang, X. Zhang, B. Lei, Y. Liu, C. Hu, *Chem. Eng. J.* **2023**, 474, 145597.
- [145] C. Xia, S. Zhu, T. Feng, M. Yang, B. Yang, *Adv. Sci.* **2019**, 6, 1901316.
- [146] C. Xia, S. Zhu, S.-T. Zhang, Q. Zeng, S. Tao, X. Tian, Y. Li, B. Yang, *ACS Appl. Mater. Interfaces* **2020**, 12, 38593.
- [147] J. Shen, B. Xu, S. Chen, Y. Jia, J. Li, T. Jiang, Z. Gao, X. Wang, C. Zhu, H. Shi, Z. Wang, *ACS Sustainable Chem. Eng.* **2022**, 10, 15599.
- [148] Z. F. Wang, J. Shen, B. Xu, Q. L. Jiang, S. L. Ming, L. T. Yan, Z. H. Gao, X. Wang, C. F. Zhu, X. G. Meng, *Adv. Opt. Mater.* **2021**, 9, 210042.
- [149] L. Gan, Y. Zhu, X. Yang, *Chem. Eng. J.* **2023**, 459, 141635.
- [150] J. Tan, Q. Li, S. Meng, Y. Li, J. Yang, Y. Ye, Z. Tang, S. Qu, X. Ren, *Adv. Mater.* **2021**, 33, 2006781.
- [151] Q. Li, S. Meng, Y. Li, D. Cheng, H. Gu, Z. Zhao, Z. Tang, J. Tan, S. Qu, *Carbon* **2022**, 195, 191.
- [152] Z. Z. Ding, C. L. Shen, J. F. Han, G. S. Zheng, Q. C. Ni, R. W. Song, K. K. Liu, J. H. Zang, L. Dong, Q. Lou, C. X. Shan, *Small* **2022**, 19, 2205916.
- [153] Q. Li, D. Cheng, H. Gu, D. Yang, Y. Li, S. Meng, Y. Zhao, Z. Tang, Y. Zhang, J. Tan, S. Qu, *Chem. Eng. J.* **2023**, 462, 142339.
- [154] C. Li, X. Zhao, C. Li, J. Hu, J. Zhu, Q. Lou, N. Chen, Z. Song, X. Chen, G. Pan, *J. Alloys Compd.* **2023**, 948, 169674.
- [155] Y. Zheng, Z. Wang, J. Liu, Y. Zhang, L. Gao, C. Wang, X. Zheng, Q. Zhou, Y. Yang, Y. Li, H. Tang, L. Qu, Y. Zhao, C. Yang, *ACS Appl. Mater. Interfaces* **2022**, 14, 15706.
- [156] Q. Lou, N. Chen, J. Zhu, K. Liu, C. Li, Y. Zhu, W. Xu, Xu Chen, Z. Song, C. Liang, C.-X. Shan, J. Hu, *Adv. Mater.* **2023**, 35, 2211858.
- [157] Y. Zhu, J. Bai, Z. Huang, G. Yuan, Lu Zhang, X. Wang, L. Ren, *Mater. Chem. Front.* **2021**, 5, 8161.
- [158] Z. Song, Y. Liu, X. Lin, Z. Zhou, X. Zhang, J. Zhuang, B. Lei, C. Hu, *ACS Appl. Mater. Interfaces* **2021**, 13, 34705.
- [159] W. Shi, R. Wang, J. Liu, F. Peng, R. Tian, C. Lu, *Angew. Chem., Int. Ed.* **2023**, 62, e202303063.
- [160] H. Shi, Z. Niu, H. Wang, W. Ye, K. Xi, X. Huang, H. Wang, Y. Liu, H. Lin, H. Shi, Z. An, *Chem. Sci.* **2022**, 13, 4406.
- [161] L. Mo, H. Liu, Z. Liu, X. Xu, B. Lei, J. Zhuang, Y. Liu, C. Hu, *Adv. Opt. Mater.* **2022**, 10, 2102666.
- [162] Q. Cheng, Z. Chen, L. Hu, Y. Song, S. Zhu, R. Liu, H. Zhu, *Chin. Chem. Lett.* **2022**, 34, 108070.
- [163] T. Li, X. Li, Y. Zheng, P. Zhu, C. Zhang, K. Zhang, J.-J. Xu, *Anal. Chem.* **2023**, 95, 2445.
- [164] K. Jin, X. Ji, J. Zhang, Q. Mi, J. Wu, J. Zhang, *Mater. Today Chem.* **2022**, 26, 101179.
- [165] L. Yang, Q. Zhang, Y. Huang, C. Luo, Z. Quan, H. Li, S. Sun, Y. Xu, *J. Colloid Interface Sci.* **2023**, 632, 129.
- [166] Z. Song, Y. Shang, Q. Lou, J. Zhu, J. Hu, W. Xu, C. Li, X. Chen, K. Liu, C. X. Shan, X. Bai, *Adv. Mater.* **2023**, 35, 2207970.
- [167] X. Yu, K. Liu, B. Wang, H. Zhang, Y. Qi, J. Yu, *Adv. Mater.* **2023**, 35, 2208735.
- [168] W.-H. Lv, Q. Cao, S.-Y. Song, Y.-C. Liang, R. Zhou, K.-K. Liu, C.-X. Shan, *Small* **2023**, 19, 2302504.
- [169] Z. Zhou, Z. Song, J. Liu, B. Lei, J. Zhuang, X. Zhang, Y. Liu, C. Hu, *Adv. Opt. Mater.* **2022**, 10, 2100704.
- [170] Y. Sun, L. Jiang, Y. Chen, Y. Liu, *Chin. Chem. Lett.* **2023**, 108644.
- [171] Y. Wu, X. Chen, P. Guo, E. Xue, B. Tian, K. Zheng, J. Liang, W. Wu, *J. Lumin.* **2023**, 263, 120013.
- [172] R. Bhuyan, B. Kommula, L. Bishwal, S. Mandal, S. Bhattacharyya, *J. Phys. Chem. C* **2022**, 126, 16377.
- [173] H. Ding, X. H. Li, X. B. Chen, J. S. Wei, X. B. Li, H. M. Xiong, *J. Appl. Phys.* **2020**, 127, 231101.
- [174] Z. Zhu, Y. Zhai, Z. Li, P. Zhu, S. Mao, C. Zhu, D. Du, L. A. Belfiore, J. Tang, Y. Lin, *Mater. Today* **2019**, 30, 52.
- [175] H. A. Nguyen, I. Srivastava, D. P. J. Pan, M. Gruebele, *ACS Nano* **2020**, 14, 6127.



- [176] H. Wang, E. Zhao, J. W. Y. Lam, B. Z. Tang, *Mater. Today* **2015**, *18*, 365.
- [177] W. B. Wu, B. Liu, *Natl. Sci. Rev.* **2021**, *8*, nwaa222.
- [178] J. Mei, N. L. C. Leung, R. T. K. Kwok, J. W. Y. Lam, B. Z. Tang, *Chem. Rev.* **2015**, *115*, 11718.
- [179] J. Luo, Z. Xie, J. W. Y. Lam, L. Cheng, B. Z. Tang, H. Chen, C. Qiu, H. S. Kwok, X. Zhan, Y. Liu, D. Zhu, *Chem. Commun.* **2001**, 1740.
- [180] C. Kang, S. Tao, F. Yang, B. Yang, *Aggregate* **2022**, *3*, e169.
- [181] Y. Ru, G. I. N. Waterhouse, S. Lu, *Aggregate* **2022**, *3*, e296.
- [182] X. K. Xu, L. Q. Mo, Y. D. Li, X. Q. Pan, G. Q. Hu, B. F. Lei, X. J. Zhang, M. T. Zheng, J. L. Zhuang, Y. L. Liu, C. F. Hu, *Adv. Mater.* **2021**, *33*, 2104872.
- [183] Z. Wan, Y. Li, Y. Zhou, D. Peng, X. Zhang, J. Zhuang, B. Lei, Y. Liu, C. Hu, *Adv. Funct. Mater.* **2023**, *33*, 2207296.
- [184] H. Wang, L. Ai, H. Song, Z. Song, X. Yong, S. Qu, S. Lu, *Adv. Funct. Mater.* **2023**, *33*, 2303756.
- [185] J. Li, F. Zhao, F. Nan, J. Wang, Y. Zhang, K. Liang, X. Xue, T. Chen, L. Kong, J. Ge, P. Wang, *Chin. J. Chem.* **2023**, *41*, 1950.
- [186] A. Sharma, T. Gadly, A. Gupta, A. Ballal, S. K. Ghosh, M. Kumbhakar, *J. Phys. Chem. Lett.* **2016**, *7*, 3695.
- [187] K. Shen, P. Li, J. Lin, Z. Wang, G. Cai, X. Ming, Y. Liu, C. Gao, Z. Xu, *Carbon* **2023**, *208*, 160.
- [188] J.-S. Huang, T. Goh, X. Li, M. Y. Sfeir, E. A. Bielinski, S. Tomasulo, M. L. Lee, N. Hazari, A. D. Taylor, *Nat. Photonics* **2013**, *7*, 479.
- [189] L. Ma, Q. Xu, S. Sun, B. Ding, Z. Huang, X. Ma, He Tian, *Angew. Chem., Int. Ed.* **2022**, *61*, e202115748.
- [190] D. L. Dexter, *J. Chem. Phys.* **1953**, *21*, 836.
- [191] K. Sudha, S. Sundharamurthi, S. Karthikaikumar, K. Abinaya, P. Kalimuthu, *J. Phys. Chem. C* **2017**, *121*, 5941.
- [192] C. Bradac, Z. Q. Xu, I. Aharonovich, *Nano Lett.* **2021**, *21*, 1193.
- [193] E. A. Jares-Erijman, T. M. Jovin, *Nat. Biotechnol.* **2003**, *21*, 1387.
- [194] A. Ajayaghosh, V. K. Praveen, C. Vijayakumar, *Chem. Soc. Rev.* **2008**, *37*, 109.
- [195] W. R. Algar, N. Hildebrandt, S. S. Vogel, I. L. Medintz, *Nat. Methods* **2019**, *16*, 815.
- [196] A. Cravcenko, M. Hertzog, C. Ye, M. N. Iqbal, U. Mueller, L. Eriksson, K. Borjesson, *Sci. Adv.* **2019**, *5*, eaaw5978.
- [197] L. Yuan, W. Lin, K. Zheng, S. Zhu, *Acc. Chem. Res.* **2013**, *46*, 1462.
- [198] S. Kuila, S. J. George, *Angew. Chem., Int. Ed.* **2020**, *59*, 9393.
- [199] Q. Dang, Y. Jiang, J. Wang, J. Wang, Q. Zhang, M. Zhang, S. Luo, Y. Xie, K. Pu, Q. Li, Z. Li, *Adv. Mater.* **2020**, *32*, 2006752.
- [200] Y.-C. Liang, Q. Cao, K.-K. Liu, X.-Y. Peng, L.-Z. Sui, S.-P. Wang, S.-Yu Song, X.-Y. Wu, W.-B. Zhao, Y. Deng, Q. Lou, L. Dong, C.-X. Shan, *ACS Nano* **2021**, *15*, 16242.
- [201] H. Moon, C. Lee, W. Lee, J. Kim, H. Chae, *Adv. Mater.* **2019**, *31*, 1804294.
- [202] B. Liu, Y. Guo, Q. Su, Y. Zhan, Z. Chen, Y. Li, B. You, X. Dong, S. Chen, W.-Y. Wong, *Adv. Sci.* **2022**, *9*, 2104488.
- [203] A. Azam, J. Yang, W. Li, J.-K. Huang, S. Li, *Prog. Mater. Sci.* **2023**, *132*, 101042.
- [204] L. Wu, C. Huang, B. P. Emery, A. C. Sedgwick, S. D. Bull, X.-P. He, H. Tian, J. Yoon, J. L. Sessler, T. D. James, *Chem. Soc. Rev.* **2020**, *49*, 5110.
- [205] W. Ren, G. Lin, C. Clarke, J. Zhou, D. Jin, *Adv. Mater.* **2020**, *32*, 1901430.
- [206] A. Abdollahi, H. Roghani-Mamaqani, B. Razavi, M. Salami-Kalajahi, *ACS Nano* **2020**, *14*, 14417.
- [207] X. Ma, M. Zhou, L. Jia, G. Ling, J. Li, W. Huang, D. Wu, *Mater. Horiz.* **2023**, *10*, 107.
- [208] Z. Wu, D. Ma, *Mater. Sci. Eng., R* **2016**, *107*, 1.
- [209] Y. Shi, W. Su, F. Yuan, T. Yuan, X. Song, Y. Han, S. Wei, Y. Zhang, Y. Li, X. Li, L. Fan, *Adv. Mater.* **2023**, 2210699.
- [210] S. Yang, W. Dai, W. Zheng, J. Wang, *Coord. Chem. Rev.* **2023**, *475*, 214913.
- [211] X. Li, C. Yin, S. S. Liew, C.-S. Lee, K. Pu, *Adv. Funct. Mater.* **2021**, *31*, 2106154.
- [212] Y. Jiang, K. Pu, *Chem. Rev.* **2021**, *121*, 13086.
- [213] Lu Yang, S. Gai, He Ding, D. Yang, L. Feng, P. Yang, *Adv. Opt. Mater.* **2023**, *11*, 2202382.



**Zhun Ran** is a master student at Key Laboratory for Biobased Materials and Energy of Ministry of Education/Guangdong Provincial Engineering Technology Research Center for Optical Agriculture, College of Materials and Energy, South China Agricultural University. His current research interests are synthesis and applications of carbon dots-based long afterglow materials.



**Chaofan Hu** received his B.S. degree from Hebei Polytechnic University in 2007 and M.S. degree from South China Normal University in 2010 and obtained his Ph.D. degree from Jinan University in 2013 and then joined Taiyuan University of Technology as a lecturer. Currently, he is an associate professor at South China Agricultural University. His research interests include the synthesis of luminescent nanomaterials and their bio-applications.

# Energy Transfer Mediated Enhancement of Room-Temperature Phosphorescence of Carbon Dots Embedded in Matrixes

Zhishan Zhou, Zhijian Song, Jinkun Liu, Bingfu Lei, Jianle Zhuang, Xuejie Zhang, Yingliang Liu,\* and Chaofan Hu\*

Energy transfer (EnT) is a commonly used study method in the research of organic luminescent materials, but rarely reported in carbon dots (CDs) related work. In this work, an efficient EnT mediated method for enhancing room temperature phosphorescence (RTP) of CDs through embedding pure phosphorescent CDs into afterglow matrixes is brought up for the first time. In such design system, the emission intensity, phosphorescence lifetime, and emission time of CDs are prolonged significantly, and all the CD-based materials emit more than 20 s phosphorescence visible to eye after the ultraviolet excitation. The overlap between the phosphorescence excitation spectra of CDs and the afterglow emission spectra of afterglow matrixes reveal the possibility of the EnT from matrixes to CDs, and the phosphorescence emission and lifetimes spectra of CDs, matrixes, and CDs@matrix further verify the presence of EnT process. Besides, phosphorescent CDs embedded in nonafterglow emission matrixes are also synthesized for analysis and comparison. To employ the outstanding characteristics of the compound of pure phosphorescent CDs and afterglow matrix, advanced information encryption/decryption and rapid fingerprint detection applications are designed. This EnT mediated enhancing RTP strategy provides a new design route to construct the CD-based material with long phosphorescence emission and high emission intensity.

## 1. Introduction

To date, great effort has been devoted to the origins of afterglow emission in carbon dots (CDs), and evidence proves that the

phosphorescence emission related to the triplet transition.<sup>[1]</sup> Generally, phosphorescence is difficult to be observed from pure CDs at room temperature due to the vibrational dissipation of the molecular and oxygen-quenching of the triplet excitons. However, some special self-protective CDs (without matrix protection) with room temperature phosphorescence (RTP) have been developed these years. Articles reported that the effect mechanism to achieve the RTP emission of these pure CDs is mainly reflected in two aspects: 1) Doping heteroatoms such as N, P, and halogens to reduce the energy gap ( $\Delta E_{ST}$ ) and promote the  $n-\pi^*$  transitions, and consequently facilitate the generation of triplet excitons.<sup>[2]</sup> 2) The formed intraparticle and interparticle hydrogen bonds and covalently crosslinked framework of CDs played a significant role in stabilizing triplet states which greatly suppressed non-radiative transitions.<sup>[3]</sup> Considering the excellent water solubility and easy handle, nonmatrix CDs express good potential in ink printing for anticounterfeiting and information encryption/decryption.<sup>[3b,4]</sup>

which is of great significance to the development of CDs. Unfortunately, it has been noticed that pure CDs have very poor stability under ambient conditions,<sup>[5]</sup> whose afterglow emission totally quenched by oxygen or moisture unless stored in a dryer, which is very unfavorable for practical application.

In order to obtain stable RTP, hybrid systems of CDs in various solid matrix (e.g., boric acid,<sup>[6]</sup> urea,<sup>[7]</sup> aluminum sulfate ( $Al_2(SO_4)_3$ ),<sup>[8]</sup> polyvinyl alcohol (PVA),<sup>[9]</sup> silica gel,<sup>[10]</sup> etc.) were usually constructed. Previous study revealed that three key reasons may be responsible for the RTP of CDs@matrix system. 1) The structure confinement effects of matrixes on CDs can protect the triplet states of CDs and suppress the nonradiative deactivation. 2) The addition of heteroatom doping may facilitate spin-orbit coupling and promote the intersystem crossing (ISC) process. 3) The formed bonding effects (e.g., hydrogen bonds, covalent bonds, etc.) between matrixes and CDs can stabilize the triplet state and greatly inhibit the nonradiative transition. Supplementally, a novel energy transfer (EnT) strategy has been developed to generate afterglow emission, which is

Z. Zhou, Z. Song, J. Liu, B. Lei, J. Zhuang, X. Zhang, Y. Liu, C. Hu  
Key Laboratory for Biobased Materials and Energy of Ministry of Education  
Guangdong Provincial Engineering Technology Research Center for Optical Agriculture  
College of Materials and Energy  
South China Agricultural University  
Guangzhou 510642, China  
E-mail: tliuyl@scau.edu.cn; thucf@scau.edu.cn

Z. Zhou, Z. Song, J. Liu, B. Lei, J. Zhuang, X. Zhang, Y. Liu, C. Hu  
Guangdong Laboratory of Lingnan Modern Agriculture  
Guangzhou 510642, China

 The ORCID identification number(s) for the author(s) of this article can be found under <https://doi.org/10.1002/adom.202100704>.

DOI: 10.1002/adom.202100704



very common in the research of organic luminescent materials, but rarely reported in CDs related work. To date, EnT has been mainly utilized in constructing the donor (CDs)—acceptor (matrix) system to produce tunable multicolor especially red phosphorescence.<sup>[11]</sup> In addition, enhanced phosphorescence can be obtained through defects-assist stabilizing triplet state excitons of CDs.<sup>[5,12]</sup> However, the fabrication of CD-based afterglow materials with ultralong phosphorescence lifetime or long-wavelength afterglow emission originates from CDs remains a challenge.

According to the Dexter's EnT theory, the possibility of energy transfer is proportional to the spectral overlap integral, which means that the realize of a high EnT rate constant decided by the predesign of suitable donor afterglow matrixes and acceptor phosphorescent CDs.<sup>[13]</sup> Our previous work reported activated multicolor RTP of CDs in boron oxide ( $B_2O_3$ ) matrix and blue afterglow emission of  $B_2O_3$  generated from oxygen traps.<sup>[6,14]</sup> Gogoi et al. reported green phosphorescence associated with triplet excitons in urea heated product.<sup>[15]</sup> Inspired by the donor–acceptor emission mechanism, we try to construct a system based on EnT through encapsulating nonmatrix phosphorescent CDs in afterglow matrixes to prepare CDs exhibiting long RTP. Thus, in this work,  $B_2O_3$  (and urea) was preselected as the donor in the process of EnT to provide secondary protection for the phosphorescence of CDs. To understand the EnT enhanced phosphorescence mechanism, the pure CDs were embedded into other two matrixes without

afterglow emission (PVA and  $Al_2(SO_4)_3$ ), respectively. The analysis revealed that afterglow matrixes are beneficial for rigiding, enhancing, and prolonging the phosphorescence, because it can not only prevent the oxygen and water diffusion but also enhance the phosphorescence behavior of CDs by EnT.

In this work, self-protective phosphorescent CDs reported by Lin et al. were embedded into  $B_2O_3$ .<sup>[16]</sup> The synthesis process of P-CDs@ $B_2O_3$  is shown in **Figure 1a**. Surprisingly, as shown in **Figures 1a** and **2g**, after the incorporation of P-CDs into  $B_2O_3$ , the P-CDs@ $B_2O_3$  exhibits brighter phosphorescence than the P-CDs, with a phosphorescence lifetime of 2.15 s (up to 24 s by the naked eye and color from green to cyan and then to blue) under the excitation of 365 nm. Moreover, a yellow-green phosphorescence emission of up to 5 s of P-CDs@ $B_2O_3$  solid was activated by visible light (electric torch light).

## 2. Results and Discussion

After the heating treatment, P-CDs are successfully dispersed in  $B_2O_3$  matrix, which was supported by the transmission electron microscopy (TEM) shown in **Figure 2a**. The high-resolution transmission electron microscopy (HRTEM) shown in **Figure 2b** reveals the P-CDs@ $B_2O_3$  and P-CDs have crystalline structures with the same lattice spacing to be 0.21 nm attributing to the (100) facet of graphite.<sup>[2b]</sup> The Fourier transform-infrared (FT-IR) spectrum of P-CDs@ $B_2O_3$  and P-CDs were

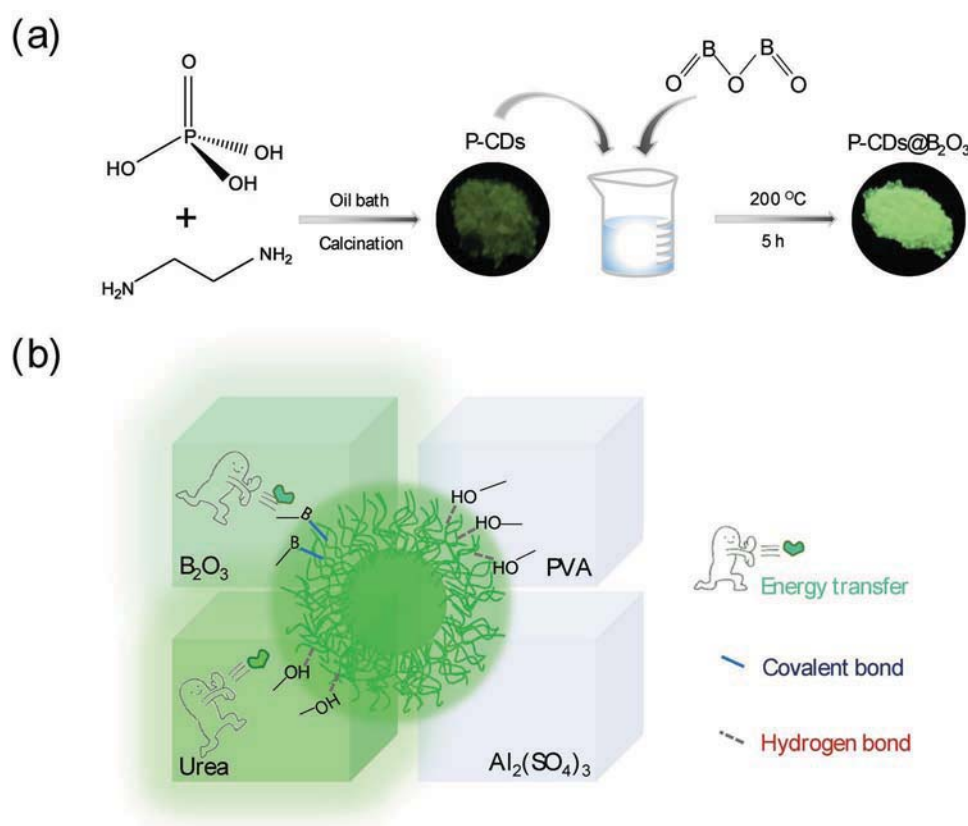


**Figure 1.** a) Schematic illustration for the preparation of P-CDs@ $B_2O_3$ , and the phosphorescence properties of P-CDs and P-CDs@ $B_2O_3$  under 365 nm UV light off. b) Schematic representation of the photophysical chemistry interaction of P-CDs in matrixes ( $B_2O_3$ , urea, PVA,  $Al_2(SO_4)_3$ ).

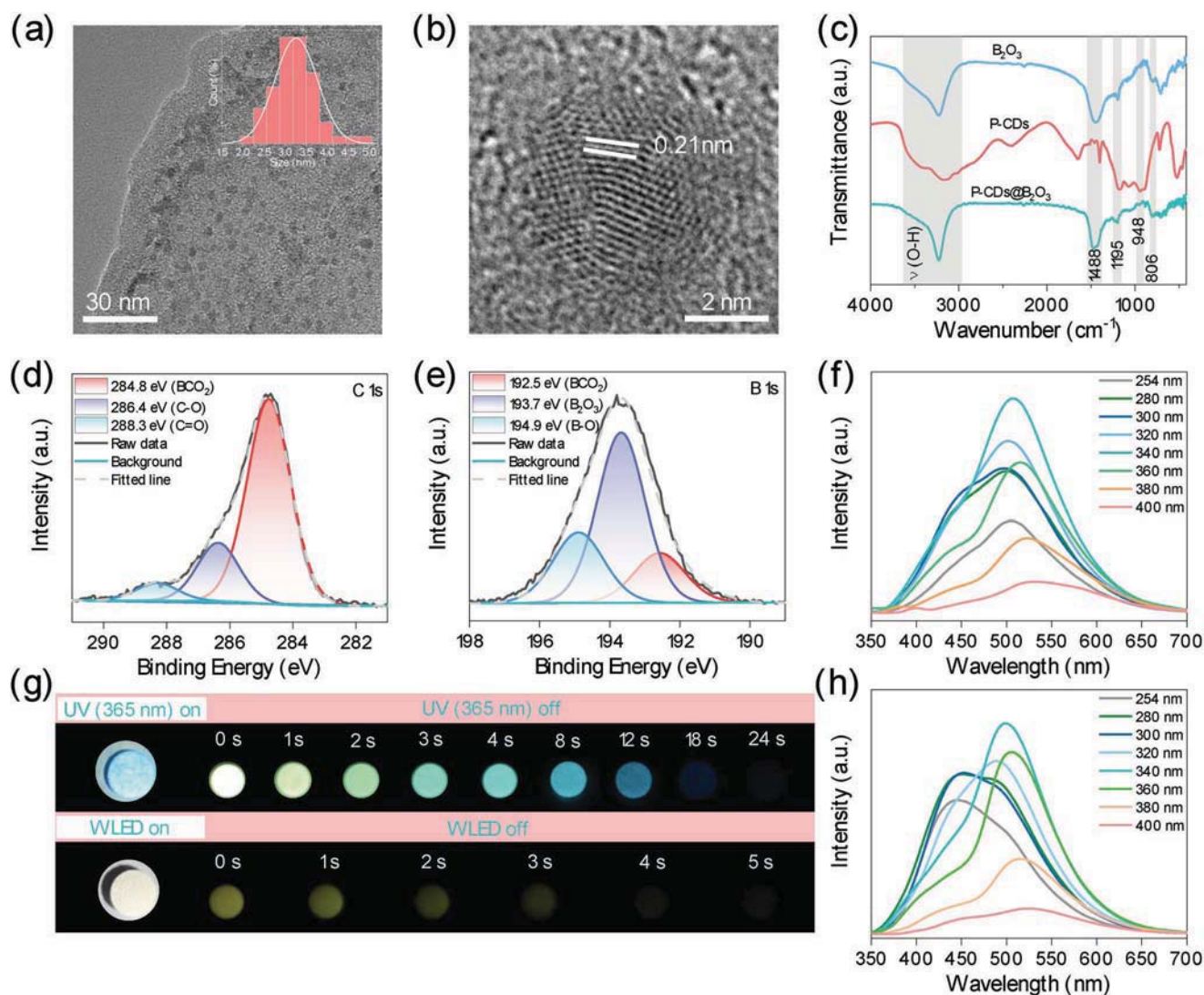


**Figure 2.** a) TEM images of the P-CDs@B<sub>2</sub>O<sub>3</sub> (insets showing the particle size distributions). b) HRTEM images of the P-CDs@B<sub>2</sub>O<sub>3</sub>. c) FT-IR spectra of B<sub>2</sub>O<sub>3</sub>, P-CDs, and P-CDs@B<sub>2</sub>O<sub>3</sub>, respectively. d,e) XPS high-resolution C 1s and B 1s spectra of P-CDs@B<sub>2</sub>O<sub>3</sub>, respectively. f) Afterglow emission spectra of P-CDs powder under  $\lambda_{\text{ex}}$  from 254 to 400 nm. g) Photographs of P-CDs@B<sub>2</sub>O<sub>3</sub> before and after turning off 365 nm UV light or WLED. h) Afterglow emission spectra of P-CDs@B<sub>2</sub>O<sub>3</sub> under different excitation wavelength.

examined (Figure 2c; and Figure S1, Supporting Information). The absorption peak located at 1467 and 1488 cm<sup>-1</sup> can be attributed to the stretching vibration of –OH and B–O, respectively.<sup>[17]</sup> The characteristic absorption peak at 1195 cm<sup>-1</sup> correspond to oxygen atom asymmetrically stretched which connects the trigonal boron atoms.<sup>[18]</sup> The emergence of new peak located at 948 cm<sup>-1</sup> indicates the formation of the boron-carbon covalent bond connecting the B<sub>2</sub>O<sub>3</sub> and P-CDs.<sup>[18]</sup> The X-ray photoelectron spectroscopy (XPS) analysis is consistent with these results. The XPS C 1s spectra of P-CDs@B<sub>2</sub>O<sub>3</sub> (Figure 2d) shows three peaks at 284.8, 286.4, and 288.3 eV for C=C, C–O, and O–C=O bonds, respectively.<sup>[19]</sup> The XPS B 1s spectra (Figure 2e) exhibits three binding energies at 192.5, 193.7, and 194.9 eV that can be assigned to BCO<sub>2</sub>, B<sub>2</sub>O<sub>3</sub>, and B–O, respectively.<sup>[20]</sup> The above results indicate that P-CDs were successfully embedded in B<sub>2</sub>O<sub>3</sub> matrix through boron-carbon covalent bond, which is identified as an effective

measure to stable triplet excitons to suppress inactivation from molecular collision.<sup>[21]</sup> The above results indicate the nanoscale combination of the P-CDs and B<sub>2</sub>O<sub>3</sub> matrix.

Subsequently, photophysical properties of the P-CDs@B<sub>2</sub>O<sub>3</sub> were fully investigated. The P-CDs@B<sub>2</sub>O<sub>3</sub> show two fluorescence emission peaks similar to P-CDs (Figure S2c,i, Supporting Information). Figure 2f,h shows the afterglow emission of P-CDs and P-CDs@B<sub>2</sub>O<sub>3</sub> under the excitation from 254 to 400 nm. Similar afterglow emissions were observed in P-CDs and P-CDs@B<sub>2</sub>O<sub>3</sub>. All two afterglow emission peaks were exhibited in P-CDs and P-CDs@B<sub>2</sub>O<sub>3</sub>, one peaked at about 440 nm with few excitation-wavelength-dependent and the other peak showed redshift with the excitation wavelength increased. The short-wavelength afterglow emission peak ( $\approx$ 440 nm) can be efficiently excited by high-energy light but becomes weak under the excitation of long-wavelength light. The long-wavelength afterglow emission peak at  $\approx$ 500 nm under the

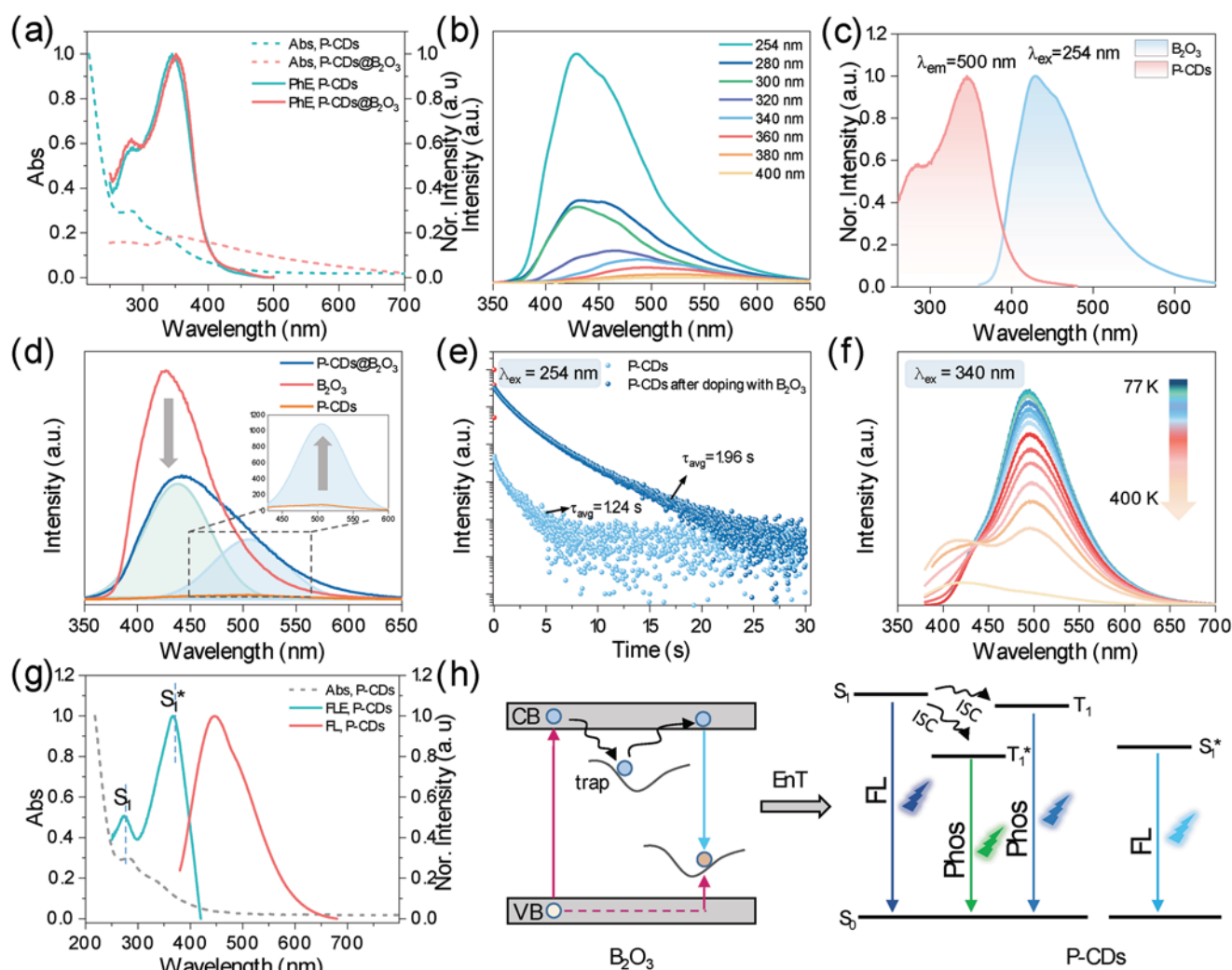


**Figure 3.** a) The UV-vis absorbance curves (dotted curves), the normalized phosphorescence excitation spectra (full lines) of the P-CDs and P-CDs@B<sub>2</sub>O<sub>3</sub>. b) The afterglow emission curves of B<sub>2</sub>O<sub>3</sub> under different excitation wavelength. c) The phosphorescence excitation curve of the P-CDs and afterglow emission curve of B<sub>2</sub>O<sub>3</sub> at  $\lambda_{\text{ex}} = 254$  nm. d) Phosphorescence emission spectra of P-CDs, B<sub>2</sub>O<sub>3</sub>, and P-CDs@B<sub>2</sub>O<sub>3</sub> powder at  $\lambda_{\text{ex}} = 254$  nm. e) Time-resolved decay spectra of P-CDs and P-CDs@B<sub>2</sub>O<sub>3</sub> at room temperature with  $\lambda_{\text{ex}} = 254$  nm and  $\lambda_{\text{em}} = 500$  nm. f) Afterglow emission spectra of the P-CDs@B<sub>2</sub>O<sub>3</sub> at different temperature under 340 nm excitation. g) The UV-vis absorbance curves (dotted curves), normalized fluorescence excitation (green full line), and emission (red full line) curves of P-CDs. h) Schematic illustration of afterglow energy transfer from the B<sub>2</sub>O<sub>3</sub> donor to the P-CDs acceptor in P-CDs@B<sub>2</sub>O<sub>3</sub>.

optimal excitation wavelength of 340 nm. The excitation curves of the two peaks were also measured shown in Figure S2d (Supporting Information). As seen in Figure 3a, absorbance maxima at about 280 nm and a broad band from 320 to 500 nm were observed in both the UV-vis curves of P-CDs@B<sub>2</sub>O<sub>3</sub> and P-CDs, which may be attributed to the  $\pi \rightarrow \pi^*$  and  $n \rightarrow \pi^*$  transition of subfluorophores of P-CDs.<sup>[16]</sup> Combined with the similar emission and excitation curve of the P-CDs and P-CDs@B<sub>2</sub>O<sub>3</sub> with identical optimal excitation wavelength at  $\approx 340$  nm, it can conclude that the afterglow emission of P-CDs@B<sub>2</sub>O<sub>3</sub> and P-CDs arise from the same luminescence center of P-CDs. In other words, the phosphorescence emission of P-CDs@B<sub>2</sub>O<sub>3</sub> mainly raise from excited triplet species in P-CDs. The afterglow emission curves of B<sub>2</sub>O<sub>3</sub> excited by different wavelength were shown in Figure 3b, showing the optimal afterglow emission under the 300 nm excitation. In order to directly verify the

feasibility of EnT from B<sub>2</sub>O<sub>3</sub> to P-CDs, the afterglow emission curve of B<sub>2</sub>O<sub>3</sub> and the excitation curve of P-CDs were investigated (Figure 3c). The overlap region (360–480 nm) confirms the possibility of EnT occurring. In order to clearly reflect the energy transfer process, selective excitation should be ensured. As shown in Figure S2a (Supporting Information), the afterglow excitation curves of B<sub>2</sub>O<sub>3</sub> and P-CDs illustrate that the B<sub>2</sub>O<sub>3</sub> was highly excited by 254 nm for the optimal afterglow emission, but the emission intensity of P-CDs under the excitation of 254 nm is very weak. The energy transfer also can be verified by the increased lifetime and intensity of the energy acceptor. This approach is usually applied to the composite system to demonstrate the energy transfer process.<sup>[22]</sup> Therefore, the afterglow emission curves of P-CDs, P-CDs@B<sub>2</sub>O<sub>3</sub>, and B<sub>2</sub>O<sub>3</sub> under the excitation of 254 nm were investigated. Compared to the B<sub>2</sub>O<sub>3</sub>, the afterglow peak of P-CDs@B<sub>2</sub>O<sub>3</sub> was diminished



in the range of 380–480 nm (Figure 3d), which exactly corresponds to the region of EnT (360–480 nm), further indicating the afterglow EnT from  $B_2O_3$  donor to P-CDs acceptor. As shown in Figure 3e, the lifetime of P-CDs in  $B_2O_3$  increase obviously compared with P-CDs, which also comply the change rule of the energy acceptor. The EnT process results in a longer phosphorescence lifetime of P-CDs@ $B_2O_3$  (1.96 s) than that of P-CDs (1.24 s). The lifetime of  $B_2O_3$  before and after doping with P-CDs were also measured (Figure S3a, Supporting Information). Unexpectedly, the lifetime of  $B_2O_3$  does not decrease after doping with P-CDs, which is not the same as the most literatures reported. The addition of CDs will cause more structural defects in  $B_2O_3$ , which makes  $B_2O_3$  exhibit longer lifetime and intensity. It is proved that the RTP of  $B_2O_3$  originates from its structural defects in our previously published work.<sup>[14]</sup> In addition, the formation of boron carbon bonds (covalent bonds) between CDs and  $B_2O_3$  may further influent the lifetime of the afterglow.<sup>[6]</sup>

To confirm the energy level diagram of P-CDs@ $B_2O_3$ , afterglow features were further investigated. The temperature-dependent afterglow spectrum of P-CDs@ $B_2O_3$  was shown in Figure 3f. With the temperature increased from 77 to 375 K, under the excitation of 340 nm, both the emission intensity at  $\approx 440$  and  $\approx 500$  nm decreased, but the intensity increased in the range of 380–435 nm. In order to understand the increased curves, the temperature-dependent afterglow spectrum of P-CDs and  $B_2O_3$  were explored. As shown in Figure S2e (Supporting Information), the intensities of afterglow emission of P-CDs peaked at  $\approx 440$  and  $\approx 500$  nm declined integrally with the temperature increased, corresponding well to the phosphorescence characteristic with higher nonradiative deactivation at elevated temperatures. Under the 340 nm excitation, the afterglow emission band of  $B_2O_3$  in the range of 360–450 nm increased with the temperature increased (Figure S2f, Supporting Information). Combined with the temperature response spectrum of  $B_2O_3$ , it can conclude that the increased curves in the range of 380–435 nm of P-CDs@ $B_2O_3$  were caused by  $B_2O_3$ . Under the excitation of 340 nm, the normalized phosphorescence emission spectra of P-CDs and P-CDs@ $B_2O_3$  investigated at room temperature were shown in Figure S2h (Supporting Information), the almost complete overlap of the two curves illustrates that the phosphorescence emission of the P-CDs@ $B_2O_3$  at room temperature is derived from P-CDs, and the role of  $B_2O_3$  is reflected as an energy donor in the CDs@matrix system. Thanks to the  $B_2O_3$ , the P-CDs@ $B_2O_3$  still exhibited blue afterglow (originates from  $B_2O_3$ ) at 125 °C. According to the temperature-dependent afterglow spectrum of P-CDs@ $B_2O_3$ , the features of peaks at 440 and 500 nm correspond to phosphorescence (originates from P-CDs). The existence of  $S_1$  (first excited singlet states) on the core and  $S_1^*$  (lower singlet states) on the surface of the P-CDs is reported by Lin,<sup>[16]</sup> and it is evidenced to the matching of absorption and fluorescence excitation spectra in Figure 3g. In addition, two phosphorescence emission centers concluded by temperature-dependent afterglow spectrum of P-CDs indicating that a portion of electrons jump to  $T_1$  from  $S_1$  by ISC for 440 nm emission, and other electrons jump to side energy levels ( $T_1^*$ ) for 500 nm emission. According to the article of the self-afterglow of  $B_2O_3$ , the afterglow emission was caused

by oxygen vacancies. The free electrons jump out from the traps (oxygen vacancies) to combine with the holes to generate afterglow. Above all, the EnT strategy in the P-CDs@ $B_2O_3$  system is demonstrated in Figure 3h. This schematic diagram depicts the relevant processes of optical physics and the energy levels. Comparing the low temperature (77 K) fluorescence and phosphorescence spectra of P-CDs@ $B_2O_3$  (Figure S3b, Supporting Information), the  $\Delta E_{ST}$  between the  $T_1$  and  $S_1$  was calculated to be 0.305 eV, and the  $\Delta E_{ST}$  between the  $T_1^*$  and  $S_1$  was calculated to be 0.643 eV.

It was mentioned above that the P-CDs@ $B_2O_3$  emit phosphorescence from green to blue after the 365 nm excitation. In order to understand the interesting phenomena, the phosphorescence behaviors of P-CDs@ $B_2O_3$  were explored. As shown in Figure 2h, the P-CDs@ $B_2O_3$  exhibit two phosphorescence emission peaks at about 440 and 500 nm, and the afterglow emission curves of P-CDs, P-CDs@ $B_2O_3$ , and  $B_2O_3$  under the 365 nm excitation were displayed in Figure S2b (Supporting Information). Under the 365 nm excitation, the phosphorescence lifetime of peak at 440 nm of P-CDs@ $B_2O_3$  was calculated to be 2.15 s, and the peak at 500 nm possessed a shorter lifetime of 1.89 s (Figure S2g, Supporting Information). Furthermore, it has been concluded in the previous discussion that the phosphorescence emission of the P-CDs@ $B_2O_3$  at room temperature is derived from P-CDs rather than  $B_2O_3$ . Therefore, the two peaks with different lifetimes results in time-resolved afterglow emission of P-CDs@ $B_2O_3$  (Figure 2g). The ultralong afterglow emission of 24 s from the P-CDs@ $B_2O_3$  was displayed in Figure 2g; and Video S1 in the Supporting Information. Unlike the RTP CDs commonly reported, when P-CDs@ $B_2O_3$  was excited by electric torch light, an interesting yellow-green afterglow emission of up to 5 s was observed. Compared to ultraviolet light, visible light is ubiquitous and safer, so luminescent material with phosphorescence excited by electric torch light has received widespread applications.<sup>[23]</sup> In the P-CDs@ $B_2O_3$  composite system, boron atoms with vacant p orbit attracting  $\pi$  transition are introduced to form more p  $n-\pi^*$  conjugated system, resulting in a broadband ultraviolet absorption of the P-CDs@ $B_2O_3$ . And the ultrawide ultraviolet absorption band from 280 to 700 nm causes the visible-light-excited afterglow feature of the P-CDs@ $B_2O_3$  (Figure 3a).

In order to verified the EnT mediated enhancement of RTP of nonmatrix CDs, P-CDs were dispersed in urea, another matrix with phosphorescence emission.<sup>[15]</sup> The phosphorescence emission spectra of heated urea under the different excitation wavelength were shown in Figure S4a (Supporting Information), and the curves show that urea heated product exhibit optimum phosphorescence under the 300 nm excitation. The overlap area of the emission spectrum (urea) and the excitation spectrum (P-CDs) declares the possibility of the energy transfer from urea to P-CDs (Figure S4b, Supporting Information). The phosphorescence emission spectra of P-CDs@Urea were shown in Figure S4c (Supporting Information). The afterglow emission spectra for P-CDs, P-CDs@Urea, and urea under the excitation of 300 nm were shown in Figure S4d (Supporting Information). Compared to the urea, the afterglow emission peak of P-CDs@Urea ranging from 350 to 405 nm was diminished, indicating the phosphorescence EnT from urea donor to P-CDs acceptor. The energy transfer process results in a longer

**Table 1.** Summarized phosphorescence lifetimes. (P-CDs was taken out of the dryer and tested immediately).

Afterglow material	Excitation [nm]	Emission [nm]	$\tau_1$ [s]	$\tau_2$ [s]	$\tau_3$ [s]	$\tau_{avg}$ [s]
P-CDs			0.28	0.93	0.05	1.23
P-CDs@B <sub>2</sub> O <sub>3</sub>			0.68	1.77	3.27	1.89
P-CDs@Urea	365	500	0.58	1.62	3.47	1.85
P-CDs@PVA			0.73	1.62	2.91	1.55
P-CDs@Al <sub>2</sub> (SO <sub>4</sub> ) <sub>3</sub>			0.63	1.57	2.93	1.64

phosphorescence lifetime to be 1.87 s of P-CDs after doping with urea. Under the excitation of 365 nm, the phosphorescence decay lifetimes of P-CDs and P-CDs@Urea were also summarized in **Table 1** with average lifetimes of 1.85 and 1.23 s for the P-CDs@Urea and P-CDs, demonstrating the feasibility of EnT enhanced RTP of pure CDs. P-CDs@Urea showed 22 s afterglow (**Figure 4**).

To understand the EnT enhanced phosphorescence mechanism, the P-CDs were embedded into PVA and Al<sub>2</sub>(SO<sub>4</sub>)<sub>3</sub> matrixes (without afterglow emission), respectively. The optical properties of them were shown in Figure S5a–d (Supporting Information). It shows that PVA and Al<sub>2</sub>(SO<sub>4</sub>)<sub>3</sub> exhibit no afterglow. Considering the moisture absorption and oxygen susceptibility of the pure afterglow CDs, we hypothesized that the substrate without afterglow emission would appropriately

enhance the phosphorescence properties of the CDs, thus, P-CDs were also embedded into PVA and Al<sub>2</sub>(SO<sub>4</sub>)<sub>3</sub>, respectively. The phosphorescence lifetimes of P-CDs@PVA and P-CDs@Al<sub>2</sub>(SO<sub>4</sub>)<sub>3</sub> were summarized in Table 1. And the digital photos of phosphorescence emission were shown in Figure 4. The P-CDs@PVA has the afterglow lifetime up to 1.55 with 18 s phosphorescence emission time, and P-CDs@Al<sub>2</sub>(SO<sub>4</sub>)<sub>3</sub> has the afterglow lifetime up to 1.64 with 20 s phosphorescence emission time, which are longer than P-CDs but shorter than P-CD in B<sub>2</sub>O<sub>3</sub> or urea. Considering the moisture and oxygen resistance of the matrix, the phosphorescence of the P-CDs enhanced after being embedded into a nonafterglow emission matrix.

To prove the universality of EnT strategy, we designed a series of CDs@matrix composites by incorporating pure phosphorescent CDs into the B<sub>2</sub>O<sub>3</sub>, urea, PVA, and Al<sub>2</sub>(SO<sub>4</sub>)<sub>3</sub>. The N-CDs<sup>[24]</sup> and E-CDs<sup>[3b]</sup> were prepared according to methods reported. The phosphorescence emission spectra and decay curve of N-CDs were shown in Figure S6a,b (Supporting Information). And the phosphorescence emission spectra and decay curve of E-CDs were shown in Figure S7a,b (Supporting Information). The afterglow lifetimes of the composite materials were summarized in Tables S1 and S2 (Supporting Information). As shown in Figure 4, the afterglow emission time is far longer than the N-CDs and E-CDs itself reported.<sup>[3b,24]</sup> All the pure CDs embedded in B<sub>2</sub>O<sub>3</sub> or urea emit more than 20 s RTP, and the N-CDs@B<sub>2</sub>O<sub>3</sub> emit afterglow of up to 30 s. As for

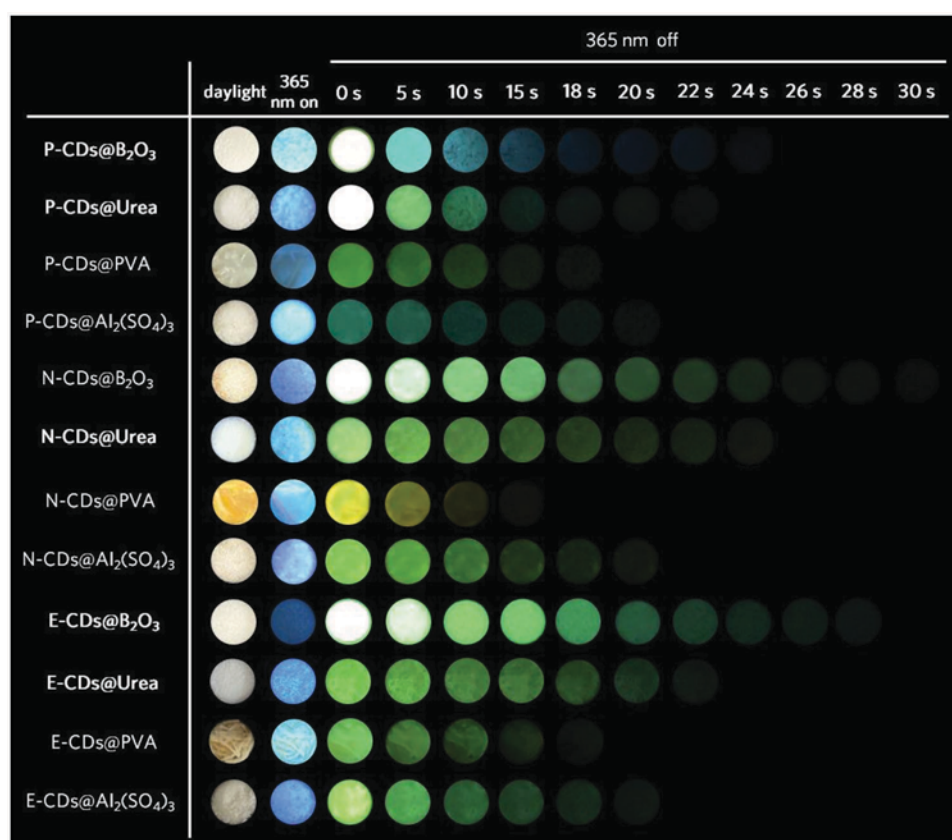


**Figure 4.** Luminescence photographs of a series of composites under a 365 nm UV irradiation and at different time intervals after the removal of 365 nm ultraviolet lamp.

P-CDs, N-CDs, E-CDs, when they were embedded in these four matrixes, the phosphorescence emission time complied with the following rules:  $B_2O_3 > \text{urea} > Al_2(SO_4)_3 > \text{PVA}$ . Nonafterglow emission matrixes also prolonged the phosphorescence emission time of CDs, but less efficient than the matrixes with afterglow emission.

Combined with literatures, the mechanism of secondary protection by these four matrixes for the enhanced phosphorescence behaviors of CDs was proposed in Figure 1b. First of all, as energy donors, the surrounding afterglow matrixes ( $B_2O_3$ , urea) plays primarily important roles in enhancing the phosphorescence emission intensity and lifetime of CDs (energy acceptors). The afterglow energy transfer from the matrixes to CDs availably generates significantly prolonged phosphorescence emission time much longer than that of the compound of CDs and nonafterglow emission matrixes. The boron carbon bonds (covalent bonds) between CDs and  $B_2O_3$  help to lock the species of triplet of CDs, and the emerging glassy state greatly rigidify the molecules, thereby reducing the nonradiative deactivation. The formed hydrogen bonds between CDs and urea play roles in suppressing the intramolecular motions and rigidifying triplet species of CDs, which is similar to the covalent bond between CDs and  $B_2O_3$ . However, compared to covalent bonds, the hydrogen bonds express weaker in this term, and the structure of urea is not as hard as  $B_2O_3$ , thus, (P, N, E)-CDs@ $B_2O_3$  exhibit longer phosphorescence than (P, N, E)-CDs@Urea.

Likewise, the formed hydrogen bonds between PVA matrixes and CDs strengthen the phosphorescence emission of CDs when pure phosphorescent CDs were embedded in PVA matrixes. Eventually, all these four matrixes can act as oxygen and water barriers, preventing triplet excitons quenching and reducing energy inactivation, thus further enhancing the phosphorescence emission of CDs.

The photographs of phosphorescence behaviors of P-CDs and P-CDs@ $B_2O_3$  under room temperature (RT, 25 °C) and 120 °C have been taken (Figure 5a). The P-CDs powders emit blue fluorescence and weak green phosphorescence at RT, when the temperature up to 120 °C, the P-CDs are burnt and the fluorescence and phosphorescence disappear. The P-CDs@ $B_2O_3$  emit blue phosphorescence at 120 °C, thanks to the afterglow of  $B_2O_3$ , which is in accordance with the temperature-dependent afterglow emission spectra. Since the ultralong and visible-light-excited RTP properties of P-CDs@ $B_2O_3$ , an encrypted information protection mechanism was constructed. As shown in Figure 5b, alphabetic codes of "S" "C" "A" "U" were stacked, wherein the "S" "A" were marked by P-CDs@ $B_2O_3$ , the "C" "U" were covered with P-CDs. The encryption model shows yellow phosphorescence passwords "S" "A" following visible-light excitation. Under the 365 nm UV irradiation, the blue patterns of "S" "C" "A" "U" are seen. Once stopping the excitation source, the green phosphorescence alphabets of "S" "C" "A" "U" are shown. As time goes on to 7 s, because of the different

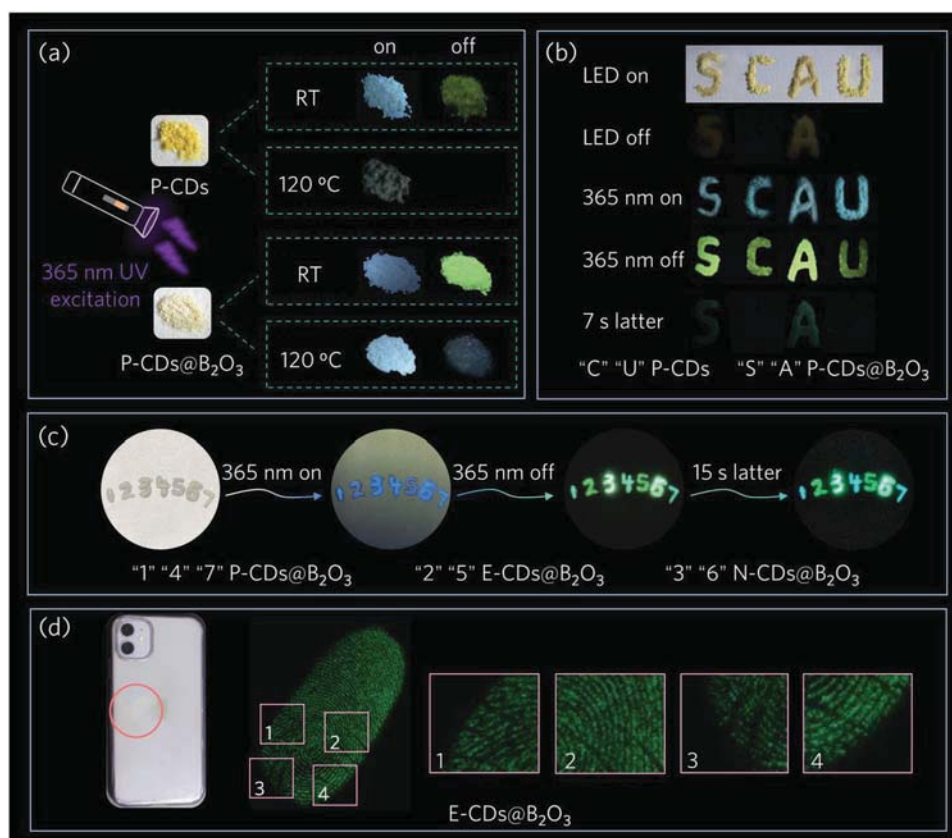


**Figure 5.** a) Photographs of P-CDs and P-CDs@ $B_2O_3$  under RT, 120 °C, respectively. b) Security protection application made from P-CDs and P-CDs@ $B_2O_3$ . c) Time-resolved information encryption/decryption application made from P-CDs@ $B_2O_3$ , E-CDs@ $B_2O_3$ , and N-CDs@ $B_2O_3$ . d) Photographs of E-CDs@ $B_2O_3$ -stained fingerprints on the back of phone, the phosphorescence fingerprint, and the enlarged image of the corresponding pink rectangles.



phosphorescence emission time from P-CDs and P-CDs@B<sub>2</sub>O<sub>3</sub>, only encrypted passwords of “S” “A” are finally left. Furthermore, since the unique time-responsive color-changed afterglow characteristics of P-CDs@B<sub>2</sub>O<sub>3</sub>, advanced information encryption was proposed. As shown in Figure 5c, “1” “4” “7” were marked by P-CDs@B<sub>2</sub>O<sub>3</sub>, “2” “5” by E-CDs@B<sub>2</sub>O<sub>3</sub>, and “3” “6” were covered with N-CDs@B<sub>2</sub>O<sub>3</sub>. The digital code is faint yellow under the daylight and exhibits blue fluorescence under the excitation of 365 nm UV lamp. Once switching off the lamp, green codes “1” “2” “3” “4” “5” “6” “7” are observed. The encrypted codes are hidden and cannot be identified in all alphabetic code, either under the UV light or when the UV light is turned off. Encrypted password codes “1” “4” “7” emitting blue phosphorescence are recognized after switching off the excitation source for 15 s. These results indicate the potential of the synthesized P-CDs@B<sub>2</sub>O<sub>3</sub> in the field of information protection and encryption/decryption.

Fingerprints have become one of the important information for identity verification, which have been utilized in forensic examination, entry-exit inspection, and medical diagnosis, however, fingerprints are generally difficult to observe with the naked eye, thus, visualization techniques are required for detection.<sup>[25]</sup> Compared with fluorescence emission of CDs, phosphorescence is more suitable for fingerprint detection which can shield background luminescence signal. Taking advantages of ultrabright and ultralong phosphorescence emission, the as-fabricated E-CDs@B<sub>2</sub>O<sub>3</sub> were expected to be applied in rapid fingerprint detection. The finger first pressed on the back of the mobile phone, the E-CDs@B<sub>2</sub>O<sub>3</sub> powders were carefully and evenly spread on the fingerprint and hold for a few seconds, a phosphorescent fingerprint was obtained after removing excess powders. As presented in Figure 5d, the fingerprint pattern was clearly revealed by the strong phosphorescence emission and was of high-quality, and some unique texture details can be well observed after magnifying some specific areas.

### 3. Conclusion

In summary, an efficient energy transfer mediated method for greatly enhanced phosphorescence of CDs through embedding pure phosphorescent CDs into afterglow matrix is reported for the first time. In such CDs embedded in B<sub>2</sub>O<sub>3</sub> or urea composites system, all materials prepared emit more than 20 s RTP, and the N-CDs@B<sub>2</sub>O<sub>3</sub> emit phosphorescence of up to 30 s. Moreover, studies revealed that nonafterglow-emission matrix could also enhance the phosphorescence emission time of CDs because of being an oxygen and water barrier. We simply designed a time-resolved alphabetic security code application by using P-CDs and P-CDs@B<sub>2</sub>O<sub>3</sub>. The P-CDs@B<sub>2</sub>O<sub>3</sub> emits time-resolved afterglow emission and color from green to cyan and then to blue, thus, an advanced information encryption/decryption application was proposed. In addition, thanks to the strong and ultralong phosphorescence emission, the E-CDs@B<sub>2</sub>O<sub>3</sub> were expected to exploit to rapid fingerprint detection. This work not only synthesized a series of long afterglow emission CD-based materials, but also broaden the path for the development of long-lived phosphorescent CDs, which further increased the possibilities for the CD-based long

afterglow materials comparable to the traditional long afterglow materials.

### Supporting Information

Supporting Information is available from the Wiley Online Library or from the author.

### Acknowledgements

Z.Z. and Z.S. contributed equally to this work. The authors acknowledge the financial support from the National Natural Science Foundations of China (Grant Nos. 21571067, 12174119, and 51402207), the National Natural Science Foundation of China Joint Fund with Guangdong under Key Project (Grant No. U1501242), and the Natural Science Foundation of Guangdong Province (No. 2020A151010443).

### Conflict of Interest

The authors declare no conflict of interest.

### Data Availability Statement

The data that supports the findings of this study are available in the supplementary material of this article.

### Keywords

afterglow matrixes, carbon dots, energy transfer, room temperature phosphorescence, secondary protection

Received: April 7, 2021

Revised: July 22, 2021

Published online:

- [1] a) Y. Sun, X. Zhang, J. Zhuang, H. Zhang, C. Hu, M. Zheng, B. Lei, Y. Liu, *Carbon* **2020**, 165, 306; b) K. Jiang, Y. Wang, Z. Li, H. Lin, *Mater. Chem. Front.* **2020**, 4, 386.
- [2] a) Z. X. Liu, J. Q. Wang, Y. Mu, Q. Wei, J. H. Li, G. M. Wang, *Inorg. Chem.* **2020**, 59, 17870; b) L. Peng, Y. Feng, C. Cao, Y. Li, J. Han, S. Li, C. Peng, Z. Li, W. Feng, *Adv. Funct. Mater.* **2018**, 28, 1800791.
- [3] a) S. Tao, S. Lu, Y. Geng, S. Zhu, S. A. T. Redfern, Y. Song, T. Feng, W. Xu, B. Yang, *Angew. Chem., Int. Ed. Engl.* **2018**, 57, 2393; b) K. Jiang, Y. Wang, X. Gao, C. Cai, H. Lin, *Angew. Chem., Int. Ed. Engl.* **2018**, 57, 6216.
- [4] Q. Su, C. Lu, X. Yang, *Carbon* **2019**, 152, 609.
- [5] J. He, Y. Chen, Y. He, X. Xu, B. Lei, H. Zhang, J. Zhuang, C. Hu, Y. Liu, *Small* **2020**, 16, 2005228.
- [6] W. Li, W. Zhou, Z. Zhou, H. Zhang, X. Zhang, J. Zhuang, Y. Liu, B. Lei, C. Hu, *Angew. Chem., Int. Ed. Engl.* **2019**, 58, 7278.
- [7] C. Lin, Y. Zhuang, W. Li, T. L. Zhou, R. J. Xie, *Nanoscale* **2019**, 11, 6584.
- [8] J. Joseph, A. A. Anappara, *ChemistrySelect* **2017**, 2, 4058.
- [9] Z. Tian, D. Li, E. V. Ushakova, V. G. Maslov, D. Zhou, P. Jing, D. Shen, S. Qu, A. L. Rogach, *Adv. Sci.* **2018**, 5, 1800795.
- [10] J. Joseph, A. A. Anappara, *Phys. Chem. Chem. Phys.* **2017**, 19, 15137.

- [11] a) B. Wang, Y. Mu, H. Zhang, H. Shi, G. Chen, Y. Yu, Z. Yang, J. Li, J. Yu, *ACS Cent. Sci.* **2019**, *5*, 349; b) B. Wang, Y. Yu, H. Zhang, Y. Xuan, G. Chen, W. Ma, J. Li, J. Yu, *Angew. Chem., Int. Ed. Engl.* **2019**, *58*, 18443; c) C. Shi, J. Yao, X. Wang, X. Wen, W. Shi, C. Lu, *J. Mater. Chem. C* **2019**, *7*, 14170.
- [12] W. Shi, J. Yao, L. Bai, C. Lu, *Adv. Funct. Mater.* **2018**, *28*, 1809461.
- [13] Y. Wei, Z. Cheng, J. Lin, *Chem. Soc. Rev.* **2019**, *48*, 310.
- [14] Z. Zhou, K. Jiang, N. Chen, Z. Xie, B. Lei, J. Zhuang, X. Zhang, Y. Liu, C. Hu, *Mater. Lett.* **2020**, *276*, 128226.
- [15] K. Patir, S. K. Gogoi, *Chem. – Asian J.* **2019**, *14*, 2573.
- [16] K. Jiang, Y. Wang, C. Cai, H. Lin, *Adv. Mater.* **2018**, *30*, 1800783.
- [17] X. Liu, S. Ye, Y. Qiao, G. Dong, Q. Zhang, J. Qiu, *Chem. Commun.* **2009**, 4073.
- [18] M. G. Rodríguez, O. V. Kharissova, U. Ortiz-Méndez, *Rev. Adv. Mater. Sci.* **2004**, *7*, 55.
- [19] S. Zhou, X. Zheng, X. Yu, J. Wang, J. Weng, X. Li, B. Feng, M. Yin, *Chem. Mater.* **2007**, *19*, 247.
- [20] Z. Ling, G. Wang, M. Zhang, X. Fan, C. Yu, J. Yang, N. Xiao, J. Qiu, *Nanoscale* **2015**, *7*, 5120.
- [21] a) Y. F. Gao, H. L. Zhang, Y. Jiao, W. J. Lu, Y. Liu, H. Han, X. J. Gong, S. M. Shuang, C. Dong, *Chem. Mater.* **2019**, *31*, 7979; b) Q. Huang, H. Gao, S. Yang, D. Ding, Z. Lin, Q. Ling, *Nano Res.* **2020**, *13*, 1035; c) Y. Gao, H. Zhang, S. Shuang, C. Dong, *Adv. Opt. Mater.* **2020**, *8*, 1901557.
- [22] a) X. He, J. Lin, W. Zhai, Y. Huang, Q. Li, C. Yu, J. Liang, L. Li, Y. Fang, Z. Liu, C. Tang, *J. Chem. Phys. C* **2017**, *121*, 19915; b) M. Park, H. Yoon, J. Lee, J. Kim, J. Lee, S. E. Lee, S. Yoo, S. Jeon, *Adv. Mater.* **2018**, *30*, 1802951.
- [23] S. Lian, Y. Qi, C. Rong, L. Yu, A. Zhu, D. Yin, S. Liu, *J. Phys. Chem. C* **2010**, *114*, 7196.
- [24] Y. Chen, J. He, C. Hu, H. Zhang, B. Lei, Y. Liu, *J. Mater. Chem. C* **2017**, *5*, 6243.
- [25] P. Hazarika, D. A. Russell, *Angew. Chem., Int. Ed. Engl.* **2012**, *51*, 3524.

## RESEARCH ARTICLE

# Cascade Resonance Energy Transfer for the Construction of Nanoparticles with Multicolor Long Afterglow in Aqueous Solutions for Information Encryption and Bioimaging

Luoqi Mo, Hao Liu, Zhiming Liu, Xiaokai Xu, Bingfu Lei, Jianle Zhuang, Yingliang Liu, and Chaofan Hu\*

There are still huge challenges in the development of carbon dots (CDs) based long afterglow materials with multicolor emissions, especially in aqueous solutions. This work reports a novel strategy of achieving of multicolor long afterglow in aqueous solution by incorporating phosphorescent CDs and fluorescent dyes into sub-20 nm monodispersed silica nanoparticles. The silica matrix not only stabilizes the triplet excitons of CDs but also facilitates the efficient cascade Förster resonance energy transfer between the phosphorescent donor (CDs) and the energy acceptor (fluorescent dyes), which enables intensive multicolor long afterglow with adjustable wavelength from 510 to 610 nm and the largest Stokes shift of 255 nm. Based on these multicolor long afterglow nanoparticles, some time-resolved, color multiple information encryptions are designed. By eliminating background noise, the signal-to-noise ratio of *in vivo* afterglow imaging is as high as 155.1 in the *in vivo* imaging system. Interestingly, the afterglow signal in mice can be easily and conveniently collected by the camera of cell phones, which may make *in vivo* bioimaging portable and inexpensive. This study will provide new ideas for the synthesis of multicolor CDs-based long afterglow materials in solutions.

## 1. Introduction

In recent years, room temperature phosphorescence (RTP) has received increasing interest due to the elimination of background noise, long-lived emission, and large Stokes shift, allowing its application in anti-counterfeiting, bioimaging, and optoelectronic devices.<sup>[1,2]</sup> Carbon dots (CDs), an emerging

0D luminescent material, are expected to become a candidate for traditional phosphorescent materials such as metal-organic complexes and organics due to their excellent biocompatibility, photostability, and raw materials versatility.<sup>[3–6]</sup>

So far, solid CDs-based RTP has made great progress in long lifetime, multicolor emission, and dynamic changes,<sup>[7–13]</sup> but the interruption of phosphorescence or poor dispersion of the materials in water still limits their practical application in anti-counterfeiting and biological imaging.<sup>[14]</sup> Therefore, developing CDs-based RTP materials with good dispersion and maintaining intensive phosphorescence in aqueous environment, remains a challenging task, which has aroused great interest among researchers. For instance, CDs are covalently connected with nanosilica at high temperatures,<sup>[15]</sup> or utilizing bound water to construct hydrogen-bonded networks between CDs and cy-

nuric acid to achieve CDs-based afterglow in aqueous environments.<sup>[16]</sup> Our group incorporated CDs into amorphous silica via the conventional Stöber synthesis route to achieve ultra-long lifetime RTP in water and realized the first CDs-based phosphorescence bioimaging in cells and plants.<sup>[17]</sup> Moreover, we have recently achieved the first visible-light excitable delayed fluorescence and the nanoparticles monodispersed in water through an improved sol-gel process.<sup>[18]</sup> Obviously, silica plays an important role in the development of CDs-based afterglow in water. In the CDs@SiO<sub>2</sub> assembly, the amorphous silica plays a dual role in suppressing the non-radiative transition of triplet excitons and conferring excellent hydrophilic properties to the hybridization systems by the abundant silica hydroxyl groups.<sup>[19,20]</sup> However, the current CDs-based afterglow color in aqueous solution is limited to blue and green, due to the complexity of multi-color afterglow CDs preparation<sup>[21]</sup> and the dependence of multicolor afterglow on solid matrices,<sup>[22]</sup> which restricts the penetration depth of afterglow for bioimaging. Therefore, it is crucial to explore new strategies to develop multicolor CDs-based afterglow in water.

Förster resonance energy transfer (FRET) between singlet states of chromophores in multi-fluorophore assemblies has been extensively studied to obtain wavelength-tunable

L. Mo, X. Xu, B. Lei, J. Zhuang, Y. Liu, C. Hu  
Key Laboratory for Biobased Materials and Energy of Ministry of Education Guangdong Provincial Engineering Technology Research Center for Optical Agriculture  
College of Materials and Energy  
South China Agricultural University  
Guangzhou 510642, P. R. China  
E-mail: thucf@scau.edu.cn

L. Mo, H. Liu, Z. Liu  
Guangdong Provincial Key Laboratory of Laser Life Science  
College of Biophotonics  
South China Normal University  
Guangzhou 510631, P. R. China

 The ORCID identification number(s) for the author(s) of this article can be found under <https://doi.org/10.1002/adom.202102666>.

DOI: 10.1002/adom.202102666



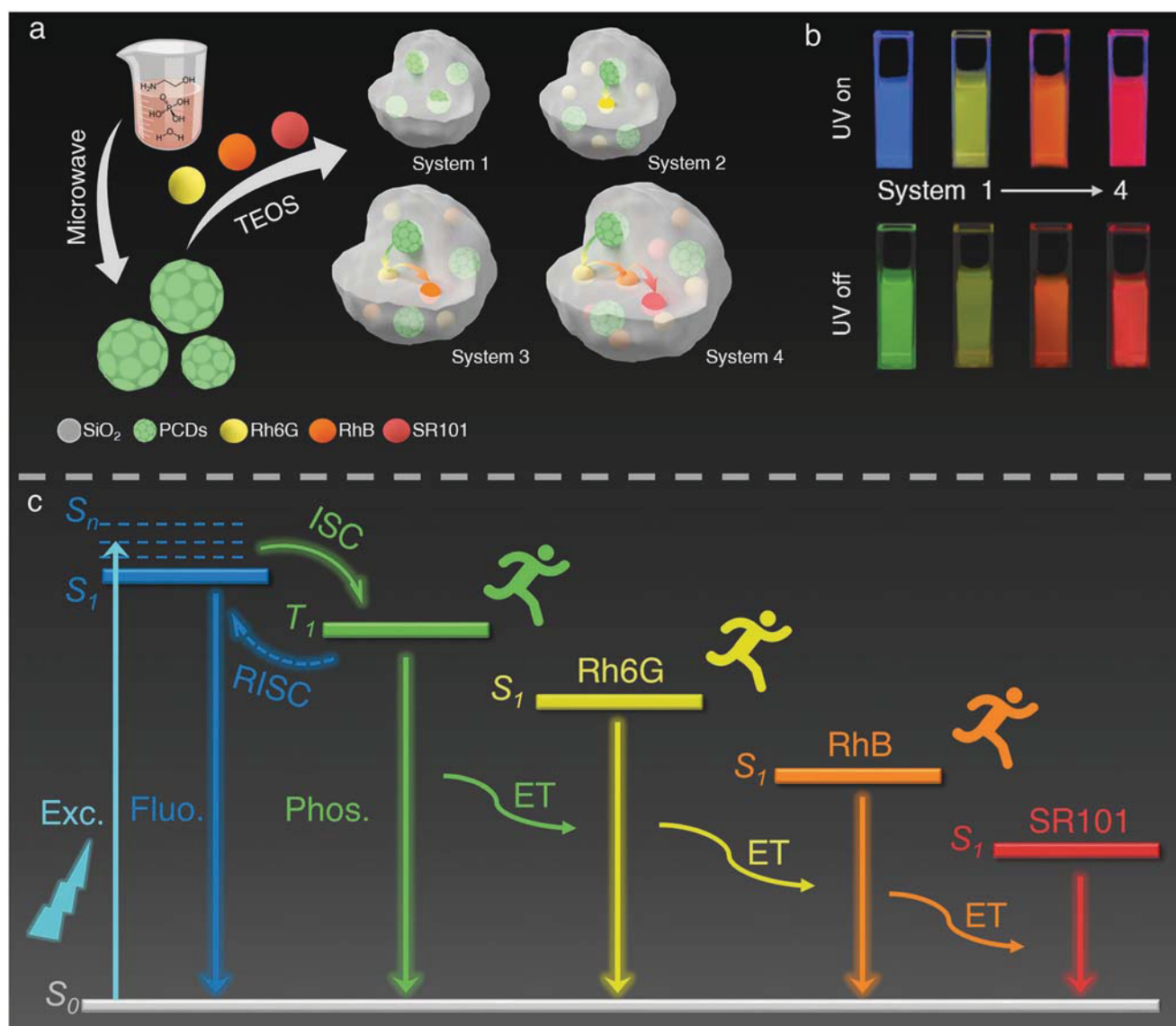


**Figure 1.** a) Schematic illustration of procedures for the preparation of PCDs and system 1–4. b) The fluorescence and afterglow images of multicolor afterglow systems under 365 nm light irradiation in water. c) Proposed possible afterglow mechanism of system 4 in aqueous environment.

fluorescent materials.<sup>[23–25]</sup> Here we are inspired that energy transfer might occur between the long-lived triplet state of the phosphorescent donor (CDs) and the short-lived singlet states of acceptor (organic fluorescent dyes) to develop adjustable wavelength delayed fluorescence.<sup>[26–28]</sup> Recently, several studies have demonstrated the accessibility of energy transfer between triplet and singlet states in polymer matrix.<sup>[29–31]</sup> However, these systems are solid-state and contain only one-step direct energy transfer, which limits the afterglow wavelength variation range. Cascade resonance energy transfer has recently received rising interest in artificial light-harvesting systems because of its ability to achieve tunable fluorescence with broad-spectra compared to one-step FRET.<sup>[32–34]</sup> According to our previous work, amorphous silica could function as an ideal host for loading CDs and fluorescent dyes to achieve energy transfer from the donor triplet state to the acceptor singlet state in aqueous

environment. Herein, we constructed four systems with multicolor long afterglow from green through yellow, orange to red based on the cascade FRET between phosphorescent CDs and fluorescent dyes in amorphous silica, as shown in **Figure 1**. These multicolor long afterglow systems exhibit great application potential in time-resolved, color multiple information encryption, and time-resolved bioimaging in vivo/vitro based on the rare intensive multicolor long afterglow and different decay rates in aqueous environment.

## 2. Results and Discussion

The reported phosphorus, nitrogen co-doped CDs (PCDs) encapsulated in amorphous silica network showed strong phosphorescence, which makes PCDs a remarkable

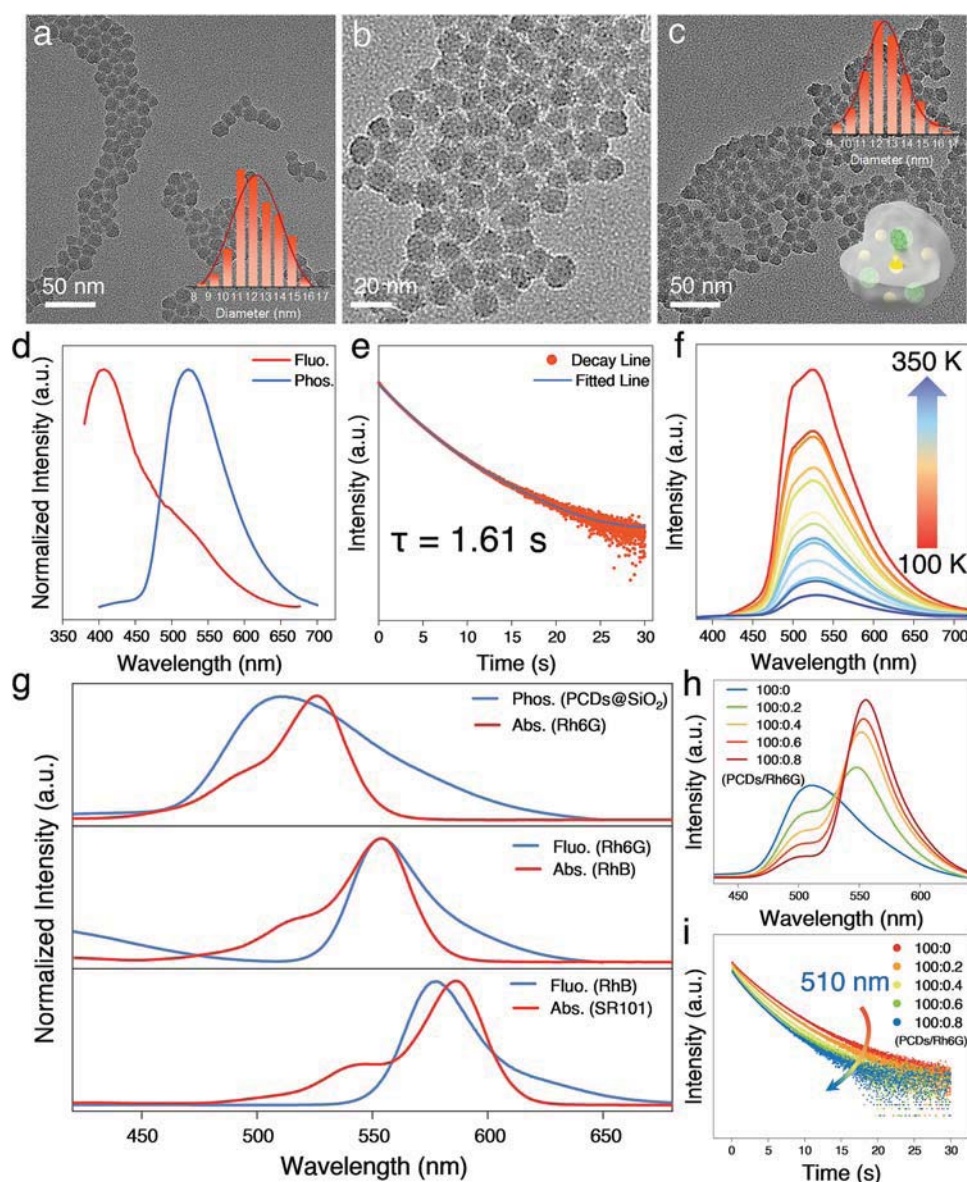


**Figure 2.** a) TEM image (inset showing the particle size distribution) of system 1. b) HR-TEM image of system 1. c) TEM image of system 2, inset: Showing the particle size distribution. d) The normalized fluorescence and phosphorescence spectra of system 1 in water under 355 nm excitation. e) Phosphorescence decay curve and lifetimes of aqueous system 1 monitored at 510 nm. f) Phosphorescence spectra of solid-state system 1 at different temperatures. g) Overlapping images of the phosphorescence spectra of system 1, fluorescence spectra of Rh6G, RhB, and the UV-vis absorption spectra of Rh6G, RhB, SR101, respectively. h) Afterglow spectra and i) afterglow decay of system 2 monitored at 510 nm with different wt% Rh6G excited at 355 nm.

phosphorescence donor in water.<sup>[19]</sup> However, the network structure of amorphous silica will influence the stability and biocompatibility of the material in aqueous environment. In this study, sub-20 nm monodisperses CDs-silica composite nanoparticles (PCDs@SiO<sub>2</sub>, system 1) with well-defined spherical morphology were obtained by improved sol-gel process (Figure 2a). The high-resolution transmission electron microscopy (HR-TEM) reveals that the PCDs have an average particle size of 2.27 nm and own an interplanar spacing of 0.21 nm attributed to the (001) facet of graphite (Figure S1, Supporting Information).<sup>[9]</sup> The fluorescence of system 1 in water is similar to that of PCDs with the optimal emission at 400 nm and decay rate of

5.19 ns, demonstrating that the optical properties of PCDs are preserved in system 1 (Figure S2, Supporting Information). In the afterglow spectra of system 1, system 1 nanoparticles exhibited intensive green emission at 510 nm with a lifetime of 1.61 s in the aqueous environment, as shown in Figure 2d,e. Through the temperature-dependent afterglow spectra, the afterglow properties of system 1 was determined to be phosphorescent, where the emission of the afterglow decreases with increasing temperature (Figure 2f). In addition, the excitation of phosphorescence is comparable to the absorption peak at 340 nm attributed to  $n-\pi^*$  transitions of C=O/C=N in PCDs,<sup>[35]</sup> hence the origin of phosphorescence can be inferred from the  $n-\pi^*$

transitions of PCDs (Figure S3a, Supporting Information). The energy gap ( $\Delta E_{ST}$ ) of system 1 between the singlet state ( $S_1$ ) and the triplet state ( $T_1$ ) is calculated as 0.72 eV by measuring the fluorescence and phosphorescence spectra at low temperature (77 K) under excitation at 355 nm (Figure S3b, Supporting Information). As shown in Figure 2b, HR-TEM of system 1 clearly shows that the PCDs are immobilized on the amorphous silica, which can effectively stabilize the excitons located in the triplet state of PCDs. Furthermore, the Fourier transform infrared spectra indicated that system 1 has a new absorption peak at 1240  $\text{cm}^{-1}$  attributed to the C–Si stretching vibration compared to free PCDs and silica, providing clear evidence that PCDs is embedded in amorphous silica by Si–C covalent bonds (Figure S4, Supporting Information).<sup>[19]</sup> Zeta potential measurements gave a relatively high negative  $\xi$ -potential (–30.6 mV), revealing the strong electrostatic repulsion around the nanoparticle surface prevents their agglomeration to improve the stability of nanoparticles in aqueous solutions. As a result, there was no significant aggregation of system 1 observed despite storage at room temperature for several weeks. Therefore, system 1 is an ideal donor for the construction of energy transfer system to develop long-lived wavelength-tunable afterglow because of its intensive long-lived phosphorescence emission and stable structure in the water.

As the FRET process originates from dipole-dipole interactions, certain criteria need to be met to occur. First, the process requires enough spectral overlap between donor emission and acceptor absorption. Second, the distance between donor and acceptor needs to be less than  $\approx 10$  nm. Finally, the dipoles of donor and acceptor should be orientated favorably toward each other.<sup>[36]</sup> Rhodamine 6G (Rh6G) is expected to be a promising acceptor for system 1 since its absorption band overlaps well with the phosphorescence emission of system 1, which meets the first point of the effective FRET requirements (Figure 2g). Meanwhile, phosphorescent PCDs and Rh6G are easily encapsulated simultaneously into amorphous silica during the hydrolysis of tetraethyl orthosilicate, where the donor and acceptor are close enough to trigger efficient FRET. An effective one-step energy transfer system (PCDs/Rh6G@SiO<sub>2</sub>, system 2) triggered by phosphorescence was successfully constructed. The TEM images of system 2 nanoparticles showed quasi-sphere structures with a diameter of about 13 nm (Figure 2c). Subsequently, the afterglow behavior of system 2 was studied to determine the occurrence of energy transfer from the triplet state of PCDs to the singlet state of Rh6G. As shown in Figure 2h, the afterglow intensity of PCDs (donor) at 510 nm gradually decreased, while the afterglow emission of Rh6G (acceptor) at 550 nm increased when excited at 355 nm. The phosphorescence lifetime of the donor PCDs monitored at 510 nm decreased from 1.61 to 1.26 s accompanied by an increase in acceptor doping (Figure 2i). The above discussion proved that FRET occurs between the triplet state of donor PCDs and the singlet state of acceptor Rh6G. Importantly, the color of the afterglow changed from green (system 1) to yellow (system 2) due to the increase of the afterglow intensity ratio (550/510 nm) to 6.8 when the mass ratio of donor/acceptor was 125:1 (Figure S5, Supporting Information). The system 2 afterglow lifetime monitored at 550 nm was tested to be 1.25 s (Figure S6a, Supporting Information) and the yellow afterglow could be observed by the naked eye for about

8 s. Thus, we obtained the delayed fluorescence of Rh6G at 550 nm through the one-step FRET process compared to the instantaneous fluorescence lifetime of 6.1 ns (Figure S6b, Supporting Information). The energy transfer efficiency was calculated to be 72.2% at the mass ratio of donor/acceptor = 125:1, according to the following equation where  $\langle I_{DA} \rangle$  is the afterglow intensity of donor in presence of acceptor and  $\langle I_D \rangle$  is the afterglow intensity of donor without any acceptor:<sup>[32]</sup>

$$\Phi_{ET} = 1 - \frac{I_{DA}}{I_D} \quad (1)$$

Although we achieved the first CDs-based yellow long afterglow in aqueous solution, this still could not adequately meet the need for multicolor long afterglow development for bioimaging and anti-counterfeiting.

We further investigated the possibility of fabricating broad-spectra tunable long afterglow nanoparticles by cascade FRET strategy. After a rigorous screening process, Rhodamine B (RhB) was selected as a suitable acceptor for system 2 because the absorption band of RhB is close to the fluorescence of Rh6G (Figure 2g). The second acceptor RhB (acceptor II), PCDs, and Rh6G (acceptor I) were co-encapsulated into amorphous silica to form system 3 executing the two-step FRET of the afterglow. The morphology of system 3 shows monodisperses spheres with a diameter of about 13 nm (Figure 3a). The afterglow emission intensity at 550 nm ascribed to Rh6G decreased, while the optimal afterglow emission of system 3 gradually red-shifts to 580 nm with increasing doping of the second acceptor RhB (Figure 3b). The afterglow intensity ratio (580 nm/550 nm) of system 3 reached 8.1 at the mass ratio of donor/acceptor I/acceptor II = 125:1:1, making the afterglow color change from yellow to orange (Figure S7a, Supporting Information). These observations indicate that an afterglow cascade FRET process takes place from phosphorescence PCDs to RhB, and Rh6G may function as a key bridge to realize this two-step energy transfer. To confirm the crucial role of Rh6G as a bridge for two-step energy transfer, the afterglow decay rate at 550 nm was tested. The afterglow decay at 550 nm shortens from 1.25 to 1.07 s with increasing concentration of the second acceptor RhB doping (Figure 3c), demonstrating that FRET happens between the relay acceptor (Rh6G) and final acceptor (RhB). The energy transfer efficiency was calculated to be 83.7% with a mass ratio of PCDs/Rh6G/RhB = 125:1:1. System 3 has an afterglow lifetime of 1.21 s at 580 nm (Figure S7b, Supporting Information), which can be observed by the naked eye for 6 s. As shown in Figure S7c, Supporting Information, RhB in system 3 exhibits distinct delayed fluorescence characteristics at 580 nm compared to the short fluorescence lifetime of RhB solution ( $\approx 3.1$  ns). The green phosphorescence of system 1 was successfully tuned to orange long afterglow by two-step FRET in aqueous environments.

To further demonstrate the reliability of cascade FRET in modulating afterglow emission in a broad wavelength range, a red long afterglow emission system 4 was constructed by a three-step FRET process. Sulforhodamine 101 (SR101) was chosen as the acceptor for system 3 because the absorption of SR101 is comparable to the fluorescence of RhB (Figure 2g). System 4 still maintains quasi-spherical morphology with a



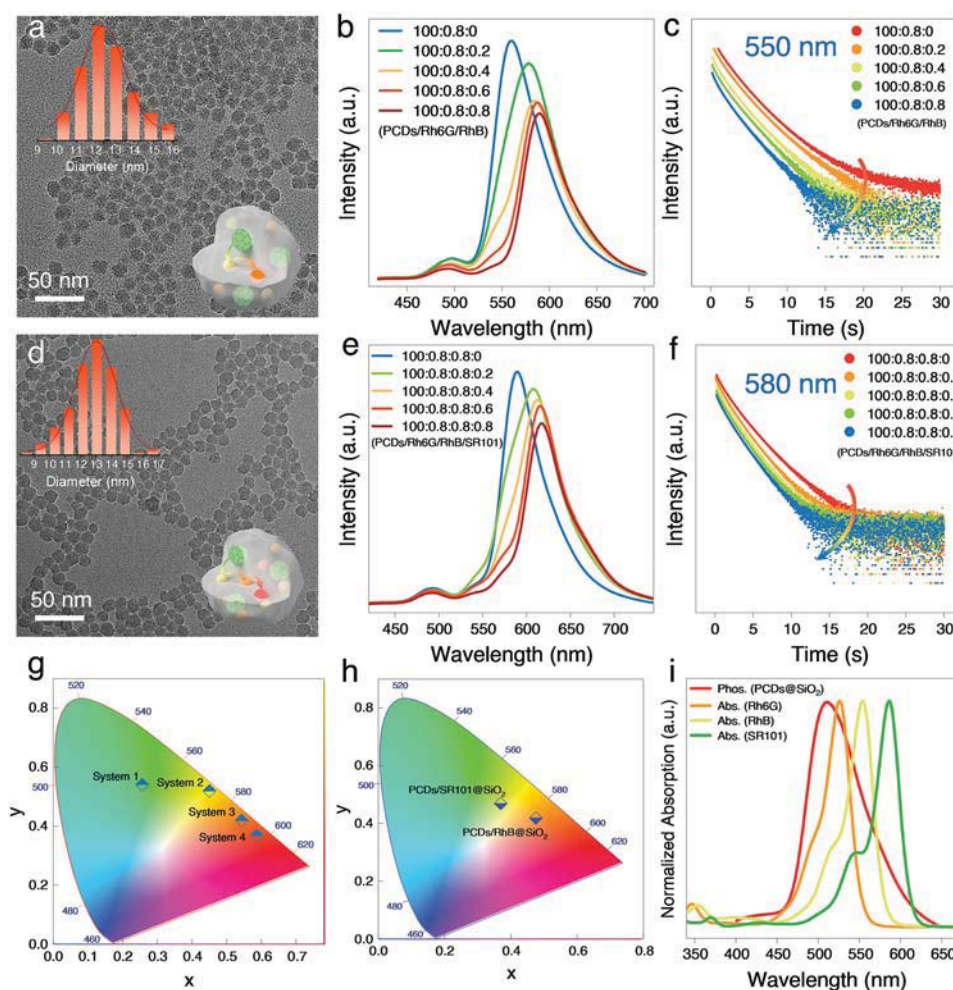


**Figure 3.** a) TEM image of system 3 (inset showing the particle size distribution). b) Afterglow spectra and c) afterglow decay monitored at 550 nm of system 3 with different wt% RhB excited at 355 nm. d) TEM image of system 4 (inset showing the particle size distribution). e) Afterglow spectra and f) afterglow decay monitored at 580 nm of system 4 with different wt% SR101 excited at 355 nm. Trajectory of afterglow color change in CIE coordinate diagram for g) cascade energy transfer and h) one-step energy transfer. i) The normalized phosphorescence spectra of system 1 and the UV-vis absorption spectra of Rh6G, RhB, and SR101.

diameter of about 13 nm (Figure 3d). Figure 3e shows that as the doping of SR101 in system 4 increases, the afterglow emission red-shifts to 610 nm under 355 nm excitation. The Stokes shift is up to 255 nm. At the mass ratio of PCDs/Rh6G/RhB/SR101 = 125/1/1/1, the afterglow emission intensity ratio (610 nm/580 nm) is 4.3 (Figure S8a, Supporting Information) and the energy transfer efficiency is calculated to be 70.5%. The afterglow color varies from orange (system 3) to red (system 4) in water. Further, the afterglow lifetime of 580 nm decreases sharply from 1.21 s of system 3 to 0.99 s of system 4 (Figure 3f), confirming the FRET process. In this three-step FRET process, Rh6G and RhB act as a critical relay to harvest excitation energy from the triplet state of PCDs and then transfer the energy to SR101. At last, the afterglow lifetime at 610 nm is 1.13 s (Figure S8b, Supporting Information), and the visual lasts 4 s. The average lifetime of SR101 increases from 3.2 ns to 1.13 s (Figure S8c, Supporting Information) and achieves the longest-lived red afterglow emission in

aqueous solution through cascade energy transfer (Table S1, Supporting Information).

The 3D afterglow spectra of the system 1–4 show that the excitation centers of the afterglow are fixed at about 355 nm, and the emission centers of the afterglow are red-shifted from 510 to 610 nm (from system 1 to system 4), which further confirms that the long-lived phosphorescence of system 1 is the origin of delayed fluorescence of system 2–4 (Figure S9, Supporting Information). Similarly, the color coordinates of system 1–4 are regularly red-shifted on the CIE 1931 chromaticity coordinates (from green to red) by cascade resonance energy transfer (Figure 3g). The afterglow intensities of argon-purged solutions of systems 1–4 was not significantly improved, demonstrating that the silica network can effectively protect triplet excitons and enable the energy transfer process, as shown in Figure S10, Supporting Information. In addition, the fluorescence spectra of the organic dyes well matched the corresponding afterglow spectra, demonstrating that the optical properties of the organic dyes were preserved after being immobilized on silica,

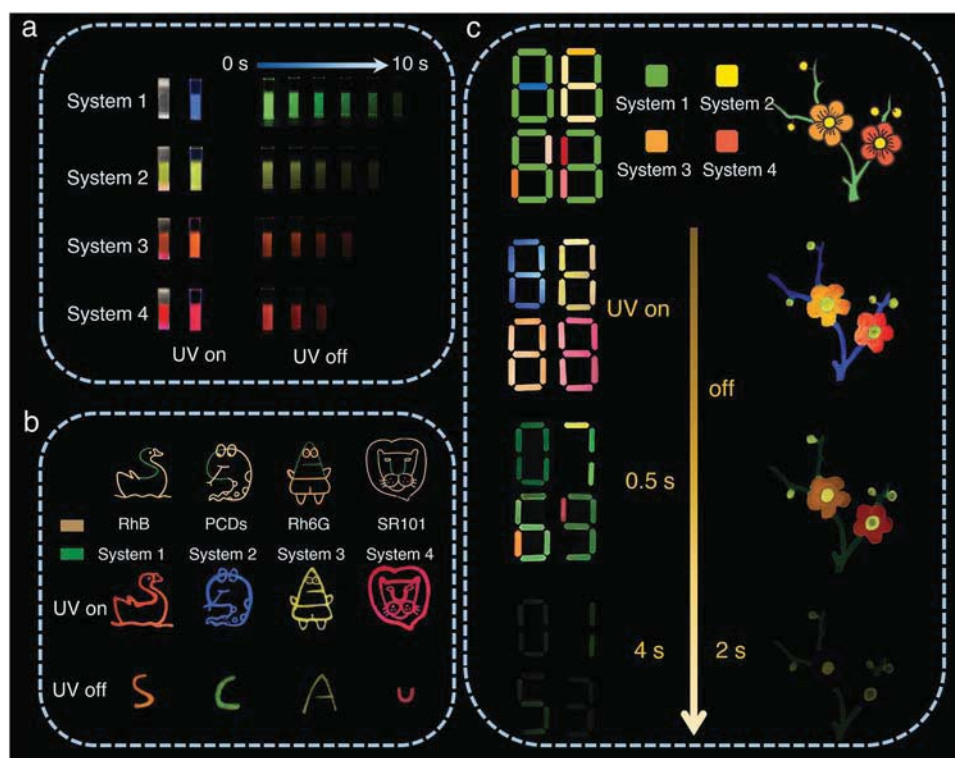


**Figure 4.** a) Photographs of afterglow systems (system 1–4) aqueous solution at different delay times after 365 nm irradiation, respectively. b) Digital photograph with the colored encrypted pattern. c) Multilevel, dynamic afterglow colored figures and graphics for advanced dynamic information encryption.

as shown in Figure S11, Supporting Information. To verify the necessity of cascade resonance energy transfer to develop tunable multicolor CDs-based afterglow, two other one-step energy transfer systems (PCDs/RhB@SiO<sub>2</sub> and PCDs/SR101@SiO<sub>2</sub>) were constructed. Regrettably, the afterglow emission enhancement in 580 nm (RhB) and 610 nm (SR101) are weak making the afterglow emission intensity ratio (580 nm/510 nm and 610 nm/510 nm) are 2.7 and 0.8, respectively, at the mass ratio of donor/acceptor = 125/1 in the two one-step FRET systems (Figures S12 and S13, Supporting Information) because the overlap integral between acceptor absorption and donor phosphorescence emission is gradually reduced (Figure 3i). The afterglow colors of PCDs/RhB@SiO<sub>2</sub> assembly and PCDs/SR101@SiO<sub>2</sub> assembly were in yellow-orange and yellow-green regions in the CIE 1931 chromaticity coordinates respectively, which is clearly different from the afterglow colors of those cascaded energy transfer systems (Figure 3h). The above discussion indicates the necessity of cascade resonance energy transfer for the development of CDs-based multicolor long afterglow in water. In addition, the relatively high negative  $\xi$ -potential of systems 1–4 ensures their stability in solution and offers the possibility of further applications, as shown in Figure S14, Supporting Information.

The multicolor afterglow systems were used as encrypted security ink in information encryption and anti-counterfeiting based on their unique optical properties. As shown in Figure 4b, the corresponding commercial fluorescent dyes and long afterglow systems made up four cartoon patterns, showing the four color cartoon patterns under the excitation of 365 nm UV

light. Interestingly, the pattern disappeared and transformed to four colored letters “SCAU” as the excitation light source was withdrawn. These multicolor long afterglow systems have different lifetimes, which facilitates the development of time-dependent, color multiple advanced encryptions (Figure 4a and Table S2, Supporting Information). Multilevel, dynamic digital and graphical encryption were designed based on different lifetimes between systems (Figure 4c). In digital encryption, the message was identified as “8888” under the radiation of the UV light, which was reorganized as “0769” when the 365 nm light was just turned off. After a delay time of 4 s, the message was again reorganized into second-level message “0153,” because system 1 has the longest lifetime. Similarly, systems 1–4 form a plum blossom for dynamic pattern encryption. The fluorescence image of the plum blossom showed blue branches, but the branches transformed into green phosphorescence when the excitation source was just turned off. With a two-second delay, the second level of image information was displayed, showing the disappearance of the orange and red plum blossoms, retaining the green branches and yellow buds.

These multicolor long afterglow systems exhibited excellent biocompatibility with up to 250  $\mu\text{g mL}^{-1}$  by CCK-8 assessed the cell viability of human hepatocellular carcinoma cells (HepG2). In addition, the afterglow intensity of the systems remained over 90% after 2 h of xenon irradiation, which demonstrates their potential in bioimaging (Figure S15, Supporting Information). HepG2 cells were first used to verify the afterglow imaging potential in vitro. Bright multicolor fluorescent signals were captured in HepG2 incubated with systems 1–4 (0.8 wt%



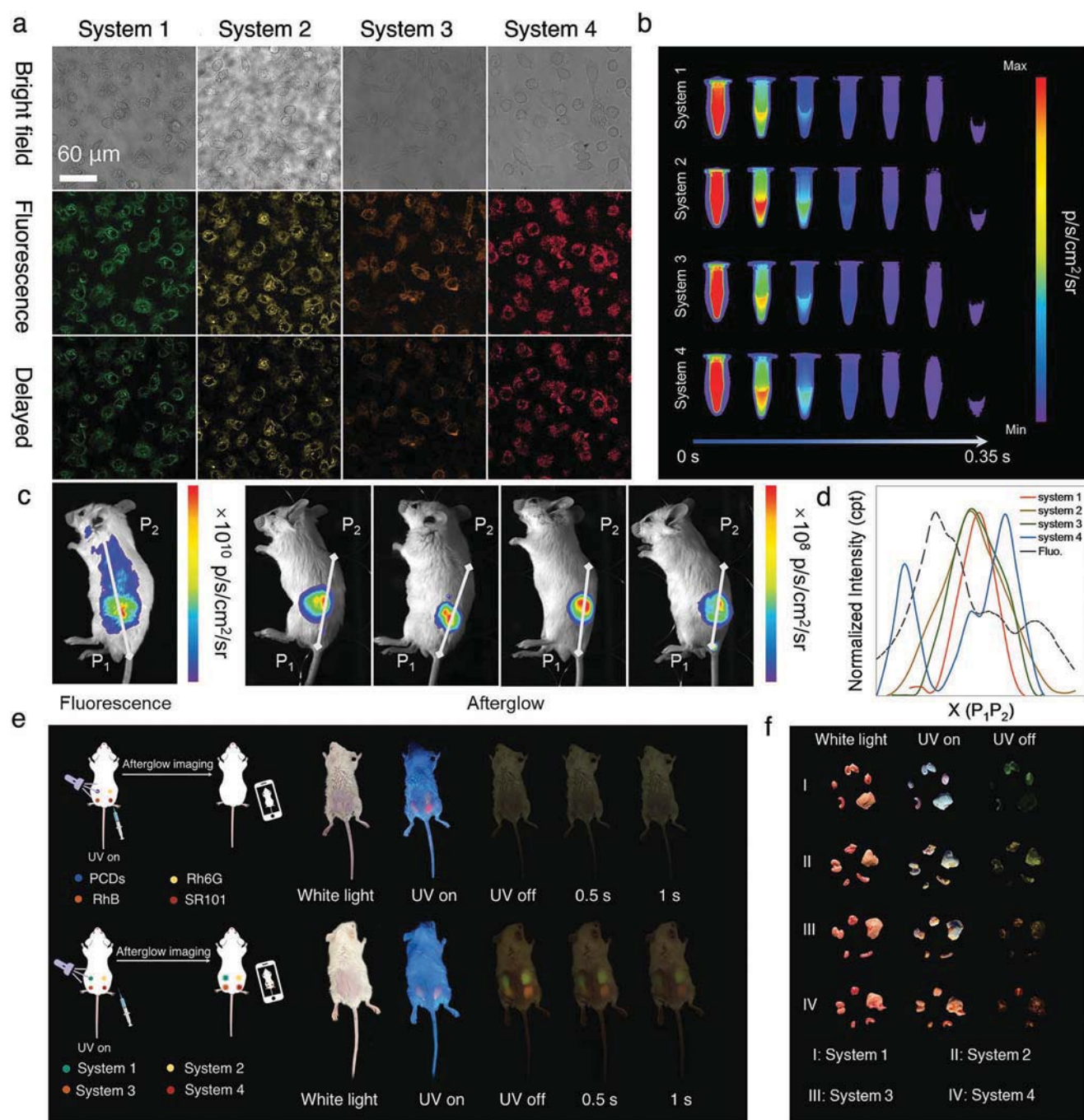


**Figure 5.** a) The confocal images of HepG2 cells incubated with 200  $\mu\text{g mL}^{-1}$  system 1–4 (0.8 wt% acceptor), including bright field, fluorescence images and delayed fluorescence images (time-gated at 8.5–12 ns). b) The afterglow decay of system 1–4 on IVIS system. c) In vivo fluorescence and afterglow imaging of living mice after subcutaneous injection SR101 and system 1–4. d) Variation of signal intensity from P<sub>1</sub> to P<sub>2</sub>. e) Photographs of mice of control group injected subcutaneously with commercial fluorescent dyes, and the mice of treated group injected subcutaneously with system 1–4 under UV lamps turned on and off, respectively. f) Digital photographs of mice isolated organs incubated system 1–4 under white light, UV, and UV off, respectively.

acceptor) under excitation of a 405 nm laser, as shown in Figure 5a. However, owing to the influence of stray light and autofluorescence, the fluorescence image of HepG2 without time gate has high background signal. When a time gating of 8.5–12 ns is setting, the fluorescence image of HepG2 exhibits

relatively low background signals as a result of the shielding of the short-lived background signals. As a control, no significant fluorescent signal was collected in HepG2 incubated with PCDs when the gating time was 8.5–12 ns for the short fluorescence lifetime of PCDs (Figure S16, Supporting Information).



Moreover, the afterglow agents (System 1–4) in the in vivo imaging system (IVIS) exhibited afterglow decay of 0.35 s in bioluminescence mode demonstrating the possibility of System 1–4 for in vivo imaging (Figure 5b). To verify the performance of the afterglow agents in eliminating background fluorescence, system 1–4 (1 mg mL<sup>-1</sup>, 100 µL) was injected subcutaneously into mice without hair removal, respectively. Afterglow decay images of the living mice injected afterglow agents were then captured on IVIS under bioluminescence mode instantly after UV irradiation (365 nm). As shown in Figure S17, Supporting Information, the afterglow agents (system 1–4) in mice exhibited high signal-to-noise ratio and 0.2 s afterglow decay. As a control, fluorescent signals were detected in mice that had been injected subcutaneously with SR101 fluorescent agent. Fluorescent images of mice exhibit high background noise and low signal-to-noise ratio compared to afterglow images of mice due to strong autofluorescence of mice (Figure 5c). To quantify the signal-to-noise ratio, the variation in signal intensity over a distance (from P<sub>1</sub> to P<sub>2</sub>) is measured on the fluorescence and afterglow images of the mice. Apparently, the signal intensity of afterglow images in the site without signaling agent decreases rapidly, however, on fluorescent images there is a clear signal plateau due to strong autofluorescence (Figure 5d). As a result, the signal-to-noise ratio for the in vivo afterglow imaging are as high as 155.1 despite using mice without hair removal which is 81.5-fold higher than fluorescence dyes. Interestingly, the afterglow signal in mice can be easily captured by the camera of cell phone without the assistance of IVIS due to the high signal-to-noise ratio. As shown in Figure 5e, 100 µL of system 1–4 (1 mg mL<sup>-1</sup>) were injected into four different subcutaneous parts of a mouse as the treated group, while 100 µL (100 µg mL<sup>-1</sup>) of four different fluorescent dyes (PCDs, Rh6G, RhB, and SR101) were injected into the subcutaneous of another mouse as a control. The fluorescence signals in the treated and control groups was not clear under UV irradiation (20 W) due to interference from apparent blue autofluorescence and scattered light. However, mice injected with system 1–4 after ceasing excitation showed marked green, yellow, orange, and red afterglow signals due to the absence of background light interference. On the contrary, no fluorescence signal was collected in the control group after the excitation was removed, because the fluorescence lifetime of those common fluorescent dyes was nanoseconds. In addition, the capability of these afterglow systems to image biological organs has also been verified. After incubation of four groups of mice isolated organs with different afterglow systems (1 mg mL<sup>-1</sup>) for 3 h, obvious afterglow signals were collected in the connective tissue of the organs, indicating that multicolor afterglow systems could penetrate the organs and maintain the afterglow properties (Figure 5f). Afterglow imaging allows in vivo bioimaging to happen in a portable and inexpensive way. Finally, the main organs (heart, liver, lungs, kidneys, and spleen) of mice subcutaneously injected with afterglow systems were collected on days 0, 3, 5, and 7 for pathological analysis to determine the toxicity of systems in vivo. Based on H&E stained images (Figure S18, Supporting Information), no significant cellular structural changes or inflammatory lesions in major organs were observed, indicating the potential of multicolor long afterglow systems for bioimaging applications because of its good biocompatibility in vivo.

### 3. Conclusion

In summary, the CDs-based multicolor long afterglow systems (green, yellow, orange, and red) were developed for the first time in aqueous solution through cascade FRET. Amorphous silica encapsulates the PCDs by covalent bonding, where the triplet state of the PCDs is effectively protected to produce intensive phosphorescence in the water. After simultaneous encapsulation of the fluorescent dyes and PCDs during TEOS hydrolysis, the multicolor long afterglow system was successfully fabricated by cascade FRET process including one-step, two-step, and three-step energy transfer from the triplet state of the PCDs to the singlet state of the acceptors. As a result, the long red afterglow with a large Stokes shift of 255 nm was produced under UV excitation. In addition, these long afterglow systems have homogeneous morphology and monodisperse properties in aqueous solution. Based on the difference afterglow decay between afterglow systems, time-resolved, color multiple advanced encryptions were developed. And these multicolor long afterglow systems exhibit good biocompatibility and high signal-to-noise ratios in afterglow imaging in vivo/ vitro making portable, inexpensive IVISs possible. Importantly, the implementation of multicolor long afterglow by cascade FRET presented here provides new ways to develop CDs-based wavelength-tunable long persistent fluorescence avoiding complex CDs material design and synthesis.

### Supporting Information

Supporting Information is available from the Wiley Online Library or from the author.

### Acknowledgements

L.M., H.L., and Z.L. contributed equally to this work. The present work was supported by the National Natural Science Foundations of China (21571067, 12174119, 62175071, and 32071399), the Natural Science Foundation of Guangdong Province (2020A1515010443, 2021A1515011988), and the Science and Technology Program of Guangzhou (2019050001). The animal experiments were performed according to the guidelines of protocols for Care and Use of Laboratory Animal Center and approved by the Animal Ethics Committee of South China Normal University (SCNU-BIP-2021-045).

### Conflict of Interest

The authors declare no conflict of interest.

### Data Availability Statement

The data that support the findings of this study are available from the corresponding author upon reasonable request.

### Keywords

bioimaging, carbon dots, cascade resonance energy transfer, information encryption, multicolor afterglow

Received: December 7, 2021  
Revised: February 8, 2022  
Published online:

- [1] K. Y. Zhang, Q. Yu, H. Wei, S. Liu, Q. Zhao, W. Huang, *Chem. Rev.* **2018**, *118*, 1770.
- [2] M. Luo, X. Li, L. Ding, G. Baryshnikov, S. Shen, M. Zhu, L. Zhou, M. Zhang, J. Lu, H. Agren, X. D. Wang, L. Zhu, *Angew. Chem., Int. Ed.* **2020**, *59*, 17018.
- [3] Y. Liu, X. Huang, Z. Niu, D. Wang, H. Gou, Q. Liao, K. Xi, Z. An, X. Jia, *Chem. Sci.* **2021**, *12*, 8199.
- [4] S. Tao, S. Lu, Y. Geng, S. Zhu, S. A. T. Redfern, Y. Song, T. Feng, W. Xu, B. Yang, *Angew. Chem., Int. Ed.* **2018**, *57*, 2393.
- [5] Z. Hu, H. Dai, X. Wei, D. Su, C. Wei, Y. Chen, F. Xie, W. Zhang, R. Guo, S. Qu, *RSC Adv.* **2020**, *10*, 17266.
- [6] D. Li, E. V. Ushakova, A. L. Rogach, S. Qu, *Small* **2021**, *17*, 2102325.
- [7] Y. Deng, P. Li, H. Jiang, X. Ji, H. Li, *J. Mater. Chem. C* **2019**, *7*, 13640.
- [8] Z. Han, P. Li, Y. Deng, H. Li, *Chem. Eng. J.* **2021**, *415*, 128999.
- [9] K. Jiang, S. Hu, Y. Wang, Z. Li, H. Lin, *Small* **2020**, *16*, 2001909.
- [10] Y. Sun, S. Liu, L. Sun, S. Wu, G. Hu, X. Pang, A. T. Smith, C. Hu, S. Zeng, W. Wang, Y. Liu, M. Zheng, *Nat. Commun.* **2020**, *11*, 5591.
- [11] J. Tan, Q. Li, S. Meng, Y. Li, J. Yang, Y. Ye, Z. Tang, S. Qu, X. Ren, *Adv. Mater.* **2021**, *33*, 2006781.
- [12] Z. Zhou, E. V. Ushakova, E. Liu, X. Bao, D. Li, D. Zhou, Z. Tan, S. Qu, A. L. Rogach, *Nanoscale* **2020**, *12*, 10987.
- [13] X. Bao, E. V. Ushakova, E. Liu, Z. Zhou, D. Li, D. Zhou, S. Qu, A. L. Rogach, *Nanoscale* **2019**, *11*, 14250.
- [14] M. Cui, M. Li, J. Wang, R. Chen, Z. Xu, J. Wang, J. Han, G. Hu, R. Sun, X. Jiang, B. Song, Y. He, *Angew. Chem., Int. Ed.* **2021**, *60*, 15490.
- [15] K. Jiang, Y. Wang, C. Cai, H. Lin, *Chem. Mater.* **2017**, *29*, 4866.
- [16] Q. Li, M. Zhou, M. Yang, Q. Yang, Z. Zhang, J. Shi, *Nat. Commun.* **2018**, *9*, 734.
- [17] W. Li, S. Wu, X. Xu, J. Zhuang, H. Zhang, X. Zhang, C. Hu, B. Lei, C. F. Kaminski, Y. Liu, *Chem. Mater.* **2019**, *31*, 9887.
- [18] L. Mo, X. Xu, Z. Liu, H. Liu, B. Lei, J. Zhuang, Z. Guo, Y. Liu, C. Hu, *Chem. Eng. J.* **2021**, *426*, 130728.
- [19] Y.-C. Liang, S.-S. Gou, K.-K. Liu, W.-J. Wu, C.-Z. Guo, S.-Y. Lu, J.-H. Zang, X.-Y. Wu, Q. Lou, L. Dong, Y.-F. Gao, C.-X. Shan, *Nano Today* **2020**, *34*, 100900.
- [20] J. He, Y. Chen, Y. He, X. Xu, B. Lei, H. Zhang, J. Zhuang, C. Hu, Y. Liu, *Small* **2020**, *16*, 2005228.
- [21] J. Zhu, X. Bai, X. Chen, H. Shao, Y. Zhai, G. Pan, H. Zhang, E. V. Ushakova, Y. Zhang, H. Song, A. L. Rogach, *Adv. Opt. Mater.* **2019**, *7*, 1801599.
- [22] W. Li, W. Zhou, Z. Zhou, H. Zhang, X. Zhang, J. Zhuang, Y. Liu, B. Lei, C. Hu, *Angew. Chem., Int. Ed.* **2019**, *58*, 7278.
- [23] A. Ajayaghosh, V. K. Praveen, C. Vijayakumar, *Chem. Soc. Rev.* **2008**, *37*, 109.
- [24] W. R. Algar, N. Hildebrandt, S. S. Vogel, I. L. Medintz, *Nat. Methods* **2019**, *16*, 815.
- [25] K. E. Sapsford, L. Berti, I. L. Medintz, *Angew. Chem., Int. Ed.* **2006**, *45*, 4562.
- [26] A. Cravencen, M. Hertzog, C. Ye, M. N. Iqbal, U. Mueller, L. Eriksson, K. Börjesson, *Sci. Adv.* **2019**, *5*, eaaw5978.
- [27] D. Wasserberg, S. C. Meskers, R. A. Janssen, *J. Phys. Chem. A* **2007**, *111*, 1381.
- [28] Q. Dang, Y. Jiang, J. Wang, J. Wang, Q. Zhang, M. Zhang, S. Luo, Y. Xie, K. Pu, Q. Li, Z. Li, *Adv. Mater.* **2020**, *32*, 2006752.
- [29] S. Garain, B. C. Garain, M. Eswaramoorthy, S. K. Pati, S. J. George, *Angew. Chem., Int. Ed.* **2021**, *60*, 19720.
- [30] S. Kuila, S. J. George, *Angew. Chem., Int. Ed.* **2020**, *59*, 9393.
- [31] Y. C. Liang, Q. Cao, K. K. Liu, X. Y. Peng, L. Z. Sui, S. P. Wang, S. Y. Song, X. Y. Wu, W. B. Zhao, Y. Deng, Q. Lou, L. Dong, C. X. Shan, *ACS Nano* **2021**, *15*, 16242.
- [32] M. Hao, G. Sun, M. Zuo, Z. Xu, Y. Chen, X. Y. Hu, L. Wang, *Angew. Chem., Int. Ed.* **2020**, *59*, 10095.
- [33] T. Xiao, L. Zhang, H. Wu, H. Qian, D. Ren, Z. Y. Li, X. Q. Sun, *Chem. Commun.* **2021**, *57*, 5782.
- [34] Q. Song, X. Yan, H. Cui, M. Ma, *ACS Nano* **2020**, *14*, 3696.
- [35] Q. Feng, Z. Xie, M. Zheng, *Chem. Eng. J.* **2021**, *420*, 127647.
- [36] A. J. P. Teunissen, C. Perez-Medina, A. Meijerink, W. J. M. Mulder, *Chem. Soc. Rev.* **2018**, *47*, 7027.

# Self-Quenching-Resistant Red Emissive Carbon Dots with High Stability for Warm White Light-Emitting Diodes with a High Color Rendering Index

Xiaoqin Zhang, Haiyao Yang, Zhijun Wan, Ting Su, Xuejie Zhang, Jianle Zhuang, Bingfu Lei, Yingliang Liu,\* and Chaofan Hu\*

Due to the excellent characteristics of energy-saving, environmentally friendly and long-life, the solid-state lighting based on white light-emitting diodes (WLEDs) is an emerging technology to replace traditional lighting solutions. However, the lack of red component of the most established method for fabricating commercial WLEDs results in high correlated color temperature (CCT) and low color rendering index (CRI). Herein, red-emitting carbon dots (R-CDs) with self-quenching-resistant property are synthesized using melamine and dithiosalicylic acid as precursors. In addition, R-CDs exhibit high thermal and photostability under high temperature and strong blue light irradiation. On the basis of the unique features of R-CDs, a WLED is fabricated by combining a blue-LED chip with commercial  $\text{Ce}^{3+}:\text{Y}_3\text{Al}_5\text{O}_{12}$  and R-CDs phosphors, which exhibits warm white light with a color coordinate of (0.41, 0.38), a high CRI of 92.7 and a CCT of 3827 K. Besides, the WLED exhibits good optical stability upon the increase of drive current from 20 to 100 mA. The results suggest R-CDs can be used as a color converter to fabricate high-quality warm WLEDs.

## 1. Introduction

White light-emitting diode (WLED) is a popular lighting mode, replacing the traditional lighting sources, since they are long-lived, eco-friendly and energy-saving.<sup>[1–4]</sup> Currently, the normal

way to assemble WLED for lighting is combination of a blue-LED chip and  $\text{YAG}:\text{Ce}^{3+}$  phosphors, which have distinct advantages such as simple manufacture, lowest cost and highest efficiency of all the WLEDs combination methods. People have strict requirements on the color quality of lighting sources, mainly in the correlated color temperature (CCT), color coordinates (CIE), color rendering index (CRI), white light uniformity, etc.<sup>[5,6]</sup> But the biggest disadvantage of blue chips and  $\text{YAG}:\text{Ce}^{3+}$  phosphors is that the color rendering is low. The maximum is only  $\approx 75$ .<sup>[7]</sup> The main reason is that the luminosity of the phosphor in the red region is mainly weak. In order to solve this problem, the researchers proposed synthetic red phosphors to supplement the lack of red light, such as rare earth-activated sulfide red phosphor ( $\text{CaS}:\text{Eu}^{2+}$ ;  $\text{Ca}_{1-x}\text{Sr}_x\text{S}:\text{Eu}$ , etc.), semiconductor quantum dots, and so on.<sup>[8,9]</sup>

However, their stability is relatively poor.

As the temperature of the LED working device rises, the luminance of the phosphor decreases and color shift occurs. Therefore, exploring alternative luminescent materials is a significant research direction to promote the development of WLEDs.

Carbon dots (CDs), an emerging class of carbon-based luminescent nanomaterials, have attracted more and more attention and interest in recent years owing to their outstanding properties, such as chemical stability,<sup>[10,11]</sup> photostability,<sup>[12–14]</sup> biocompatibility,<sup>[15,16]</sup> and low toxicity.<sup>[17–19]</sup> Because of those distinct merits, CDs could be able to apply in extensive fields, such as drug delivery,<sup>[20,21]</sup> solar cell,<sup>[22]</sup> optoelectronic devices,<sup>[23,24]</sup> bioimaging,<sup>[25,26]</sup> and so on. Innumerable explorations in WLEDs filed are emerging repeatedly because of remarkable optical characteristic of CDs, such as strong UV absorption, tunable fluorescence emission, high thermal stability, and photostability.<sup>[27]</sup> Acquiring fluorescence emission across the entire visible spectrum has been admitted as a key of WLEDs.<sup>[28]</sup> However, efficient long-wavelength (orange and red light regions) emissive CDs are very scarce due to lack of effective synthesized method and blur luminescence mechanism.<sup>[29]</sup> Traditional methods are available to obtain long-wavelength-emission CDs through complex material design, multistep purification, and bandgap engineering.<sup>[30]</sup> Although the researchers synthesized long-wavelength emission CDs, they

X. Zhang, Z. Wan, T. Su, Dr. X. Zhang, Dr. J. Zhuang, Prof. B. Lei, Prof. Y. Liu, Dr. C. Hu  
Key Laboratory for Biobased Materials and Energy of Ministry of Education/Guangdong Provincial Engineering Technology Research Center for Optical Agriculture  
College of Materials and Energy  
South China Agricultural University  
Guangzhou 510642, China  
E-mail: tliuyi@scau.edu.cn; thucf@scau.edu.cn

X. Zhang, Dr. X. Zhang, Dr. J. Zhuang, Prof. B. Lei, Prof. Y. Liu, Dr. C. Hu  
Guangdong Laboratory of Lingnan Modern Agriculture  
Guangzhou 510642, China

H. Yang  
College of Biophotonics  
South China Normal University  
Guangzhou 510631, China

 The ORCID identification number(s) for the author(s) of this article can be found under <https://doi.org/10.1002/adom.202000251>.

DOI: 10.1002/adom.202000251



had to face the dilemma: the CDs have low photoluminescence quantum yield (PLQY) and poor stability.<sup>[31]</sup> For example, Wang et al. reported the design and implementation of solid white-light-emitting phosphors (WCDs@PS), which combine blue and orange emissive CDs (BCDs and OCDs) assisted by polystyrene (PS).<sup>[32]</sup> However, when the temperature is raised from 20 to 80 °C, the intensity of the red emission region is attenuated results corresponding CIE coordinates were changed from (0.35, 0.29) to (0.32, 0.23), inferring that the instability of red CDs will have an undesirable influence on the performance of WLEDs. In addition, for light-emitting devices, the CDs must be illuminated in solid state.<sup>[33]</sup> However, solid-state CDs exhibit weak even no photoluminescence due to aggregation-induced luminescence quenching because of the Forster resonance energy transfer (FRET). Many studies reported that CDs must be homogeneously doping into matrixes, such as polymers (PVA, PVP, PMMA),<sup>[34–36]</sup> natural polymers (starch, cellulose),<sup>[37,38]</sup> small molecules (silane, boric acid, urea),<sup>[39,40]</sup> and so on, to achieve solid-state luminescence. The concentration of the CDs-doped matrix is limited because over-loading is still affected by FRET. For instance, Yuan et al. reported highly fluorescent CDs with red emission using perylene as the precursor, and doping them into methyltriethoxysilane (MTES) to obtain solid state fluorescence CDs.<sup>[41]</sup> Apart from this, the optimal loading concentration has been studied, the result indicating that the photoluminescence (PL) intensity of R-CDs/MTES gel glasses was significantly enhanced as the concentration of CDs increases from 0.003% to 0.03% but decreases at 0.1%. Nowadays, the PLQY of blue-green-light CDs can reach 99%,<sup>[42]</sup> the PLQY of red-emitting CDs is far less than that of blue-green-light CDs, and the concentration of CDs loaded into the matrix is limited, which causing that the lack of red light region is still a problem in the preparation of WLEDs. Hence, it is meaningful to synthesize red solid-state fluorescence of CDs with high stability and no doping into matrixes.

In our previous work, we synthesized a two-switch-mode luminescence carbon dots (R-CDs) that emits blue light in a dispersed state and red emission in solid state.<sup>[43]</sup> R-CDs exhibit similar PL characteristics as the reported blue-emission CDs in the dispersed state. In solid state, the CDs turn off of the blue emission, since the carbonized cores suffer from  $\pi$ - $\pi$  stacking interactions. But, the red solid-state luminescence of the CDs is derived from the radiation transitions produced by the intramolecular motion-limited effects of the surface groups upon aggregation. The symmetrical heterocycles about their disulfide bonds axes on the surface of R-CDs suffer from the restriction of intramolecular rotation (RIR), resulting in red aggregation induced emission. The anti-self-quenching R-CDs without doping matrix emits 620 nm excited at 560 nm excitation with the absolute PLQY of 12.7%. Besides, it has excellent thermal and photostability. Using the red solid-state luminescence properties of CDs could be directly packaged WLED combined with the 460 nm emitting blue chips and YAG:Ce<sup>3+</sup> commercial yellow phosphors. The R-CDs could act as a light conversion agent, absorbed the yellow-green light emitted by YAG:Ce<sup>3+</sup>, and emitted red light at the same time. By adjusting the amount of R-CDs added, an LED lamp with warm white light emission is achieved, with a high CRI of 92.7 and the CCT of 3827 K.

## 2. Result and Discussion

Transmission electron microscopy (TEM) shows the as-prepared R-CDs to be dispersed without aggregation and the inset high-resolution TEM (HRTEM) image shows the circular shape of the R-CDs, with visible crystalline lattice fringes (Figure 1a). The interlayer spacing of 0.21 nm corresponds to the graphene (100) planes reveals that the R-CDs contain graphite-like structures. Their diameters in the range from 2 to 5.8 nm were calculated from TEM image (Figure 1b). Moreover, in the X-ray diffraction (XRD) (Figure 1c) pattern, there is an apparent peak at  $\approx 25^\circ$ , which is attributed to an interlayer spacing of 0.34 nm, while the peak near  $41^\circ$  represents the 0.21 interlayer spacing.

The chemical composition of the R-CDs was examined by Fourier transform infrared (FT-IR) spectra and X-ray photoelectron spectra (XPS). The FT-IR spectra (Figure 1d) displays that the surface of the R-CDs contains O–H and N–H (3050–3650 cm<sup>−1</sup>),  $\text{C}=\text{C}$ –H (3040–3010 cm<sup>−1</sup>), S–H (2650 cm<sup>−1</sup>), amide carbonyl (1682 cm<sup>−1</sup>), C=C (1469 cm<sup>−1</sup>), C–N (1407 cm<sup>−1</sup>), C–S (685 cm<sup>−1</sup>), S–S (491 cm<sup>−1</sup>), C–NH (1261 cm<sup>−1</sup>), and C–O (1124 cm<sup>−1</sup>) functional groups or chemical bonds. Furthermore, the raw materials: dithiosalicylic acid (DTSA) and melamine (MA) contain the peaks of O–H and N–H (3050–3650 cm<sup>−1</sup>), which were higher than the R-CDs' peaks. After dehydration and amidation, the infrared signals of the hydroxyl groups and carboxyl groups are weakened, indicating that the hydrophilic groups of the red CDs are reduced to enhance their hydrophobicity. The full XPS scan (Figure 1e) shows the existence of all the constituting element of C 1s, N 1s, O 1s, and S 2p, with four peaks at 284, 400, 531, and 164 eV, and the atomic ratios were calculated to 70.40%, 16.39%, 4.47%, and 8.37%, respectively. The C 1s spectrum (Figure 1f) can be fitted into three peaks for sp<sup>2</sup> C (C–C/C=C) at 284.71 eV, sp<sup>3</sup> C(C–N) at 285.55 eV, C=O/C=N at 289.00 eV. The O 1s spectrum (Figure 1g) consists of two peaks of C=O at 531.75 eV, C–O at 533.80 eV. For N 1s, the XPS spectra (Figure 1h) can be converted into pyridinic N (399.42 eV) and pyrrolic N (400.70 eV). The S 2p spectrum (Figure 1i) contains three kinds of S species associated with S–H at 163.66 eV, S–C at 164.68 eV, and S–S at 165.32 eV. So it means that S and N elements have been incorporated into the R-CDs. Based on the chemical structures of the starting materials and product results, a possible growth mechanism for the R-CDs is illustrated in (Figure 2a). Under the solvothermal condition, dehydrolysis process happened between DTSA and MA to form a nanoscale graphite-like core and a large number of groups on the surface.

In detail, the UV–vis absorption, PL excitation, and emission of the CDs powder were measured to access their optical properties. In Figure 3a, the UV–vis absorption of R-CDs powder has three peaks at 245, 350, and 570 nm in n, respectively (Figure 3a, purple line). The peak at 245 nm results from  $\pi$ - $\pi^*$  transitions of the C=C in the core of the R-CDs, while the peak at 350 nm is attributed to the n- $\pi^*$  transitions of the C=N and C=O structures. In addition, a distinct absorption band from 530 to 600 nm was also observed in the lower-energy region. The absorption characteristic is usually considered to originate from the defect states caused by the functional groups on the CDs surfaces. Significantly, the PL spectra of the R-CDs show

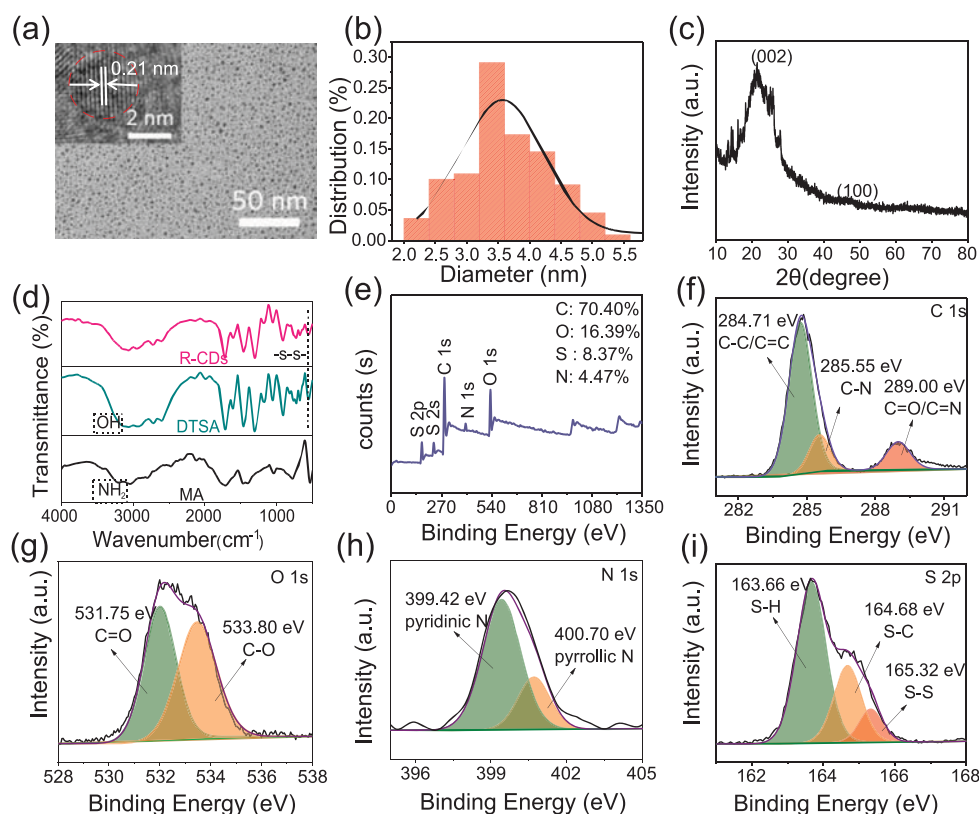


**Figure 1.** a) TEM image of the R-CDs. Inset: high-resolution TEM (HR-TEM) image of R-CDs. b) Particle size distribution measured by TEM. c) FT-IR spectrum of R-CDs, DTSA, and MA. d) XPS spectra of R-CDs. e) High-resolution XPS spectra of C 1s (f), O 1s (g), N 1s (h), and S 2p (i).

the maximum emission peak located at near 620 nm (Figure 3a, red line), and a broad excitation peak with maximum near 560 nm located in the region at 530–600 nm (Figure 3a, green

line). The maximum peak of the excited wavelength corresponds to the last peak in the UV–vis absorption spectrum, indicating that the red fluorescence emission is mainly caused

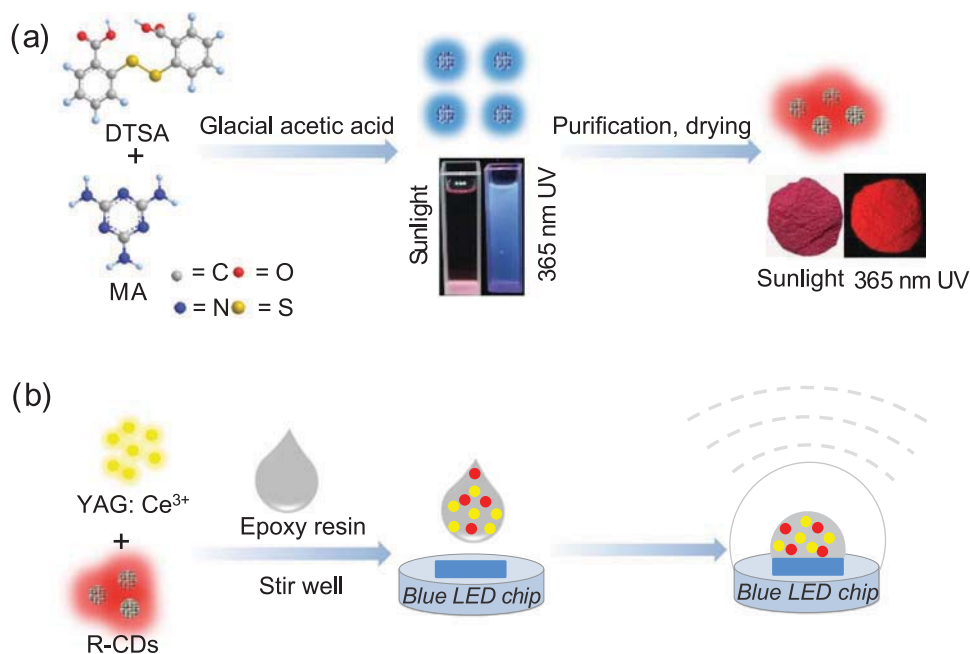


**Figure 2.** a) Formation of R-CDs monomers and their aggregates. b) Fabrication of WLEDs based on YAG:Ce<sup>3+</sup> and R-CDs.

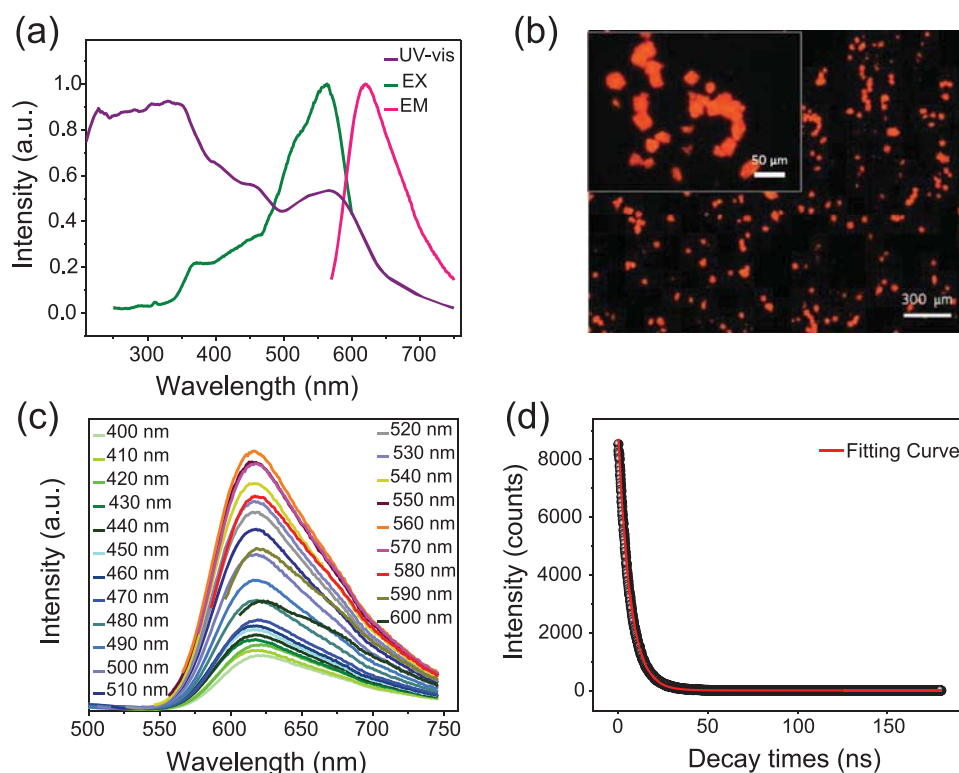


**Figure 3.** a) UV-vis absorption, PL excitation (EX) and emission (EM) spectra of R-CDs powder. b) The fluorescence image of R-CDs at an excitation wavelength of 565 nm. c) PL emission spectra of R-CDs powder at different excitation wavelength. d) Fluorescence decay curve of R-CDs powder.

by excitons in the surface state being excited. Moreover, the self-absorption of R-CDs is not serious because of small overlap between excitonic absorption and emission spectrum, which is beneficial for efficient fluorescence emission. As shown by the fluorescence image in Figure 3b, the CDs presents red fluorescence in solid-state at an excitation wavelength of 565 nm, which corresponds to the PL spectrum shown above. Furthermore, it is interesting to find that the PL peak of R-CDs located at 620 nm constantly unchanged with the excitation wavelength in the range from 400 to 600 nm, revealing that R-CDs exhibits excitation-wavelength-independent PL behavior in solid station (Figure 3c). Some studies been proposed that the excitation-wavelength-independent behavior is associated with a single type of chromophoric structure related to the surface molecular groups.<sup>[44]</sup> Thus, the corresponding luminescent mechanism may be ascribed to the surface molecular state fluorescence.<sup>[45,46]</sup>

It is worth noting that the absolute PLQY of R-CDs powder can be calculated as 12.7%, which is benefit to prepare LEDs effectively. The fluorescence decay lifetime of R-CDs was measured under the max excitation of 560 nm by using a multidimensional time-correlated single photon counting (TCSPC) method.<sup>[47]</sup> As depicted in Figure 3d, the decay trace of R-CDs was fitted using single exponential function in Equation (1)

$$y = A_1 \cdot \exp(-x/t_1) + y_0 \quad (1)$$

The average lifetime of R-CDs is calculated to be 6.60 ns, revealing the singlet state nature of PL emission and one radiative transition channels accounting for the emission.

Stability (thermal and photostability) should be evaluated because these properties of the CDs are essential for their application in the preparation of optical devices.<sup>[48]</sup> When the WLEDs are working, the temperature of the chips can reach about 150 °C. At this temperature, if the PL intensity of the phosphor is maintained at 80% or more of the intensity at room temperature, it is considered to exhibit better thermal stability. However, the stability of the CDs with red emission is relatively poor, and it is easy to be quenched under high temperature conditions and strong light radiation. Zhan et al. reported a one-step synthesis of multiple-color-emissive solid-state silica-coated CDs (silica/CDs) composites with emission from blue to orange.<sup>[49]</sup> They evaluated thermal quenching behaviors of silica/CDs composites from 20 to 100 °C, and the result shows that the relative PL intensity of B-silica/CDs, Y-silica/CDs, and O-silica/CDs only retains 83%, 99%, 63% of those at 20 °C, respectively. In addition, Wang et al. successfully prepare red emission carbon quantum dots with QY of 53% and high stability of maintaining 80% approximately at 160 °C, which is recognized by the researchers as excellent luminous efficiency and stability.<sup>[50]</sup> Since most of the red-emission CDs have luminescent centers derived from surface states, they are more susceptible to environmental factors and cause the PL intensity decreased. The luminescent center of the R-CDs we prepare is also derived from functional groups of surface, but they are not easily damaged by the high temperature environment due to RIR upon aggregation. Under the test conditions at the maximum excitation wavelength ( $\lambda_{\text{ex}} = 560$  nm), variable temperature spectroscopy image (Figure 4a) shows that the



fluorescence intensity of R-CDs remained stable as the temperature increased from 25 to 155 °C. When the temperature reached 155 °C, the PL intensity was as high as 97% of the PL intensity at 25 °C (Figure 4b). In addition, the high-temperature insulation test was carried out, then the R-CDs were kept in the heat preservation environment at 155 and 145 °C for 3 h, and the PL intensity was tested once every 30 min. The results show that the PL intensities remain nearly unchanged, indicating high thermal stability of R-CDs (Figure 4c,d). To further estimate the thermal stability of R-CDs, we conducted thermogravimetric analyzer in the air atmosphere at a heating rate of 10 °C min<sup>-1</sup> as shown in Figure S1 of the Supporting Information.

The thermogram reveals that R-CDs have a decomposition point of 280 °C, demonstrating that the materials can keep outstanding thermal stability in a large temperature range. Moreover, its photostability was also assessed. The evaluation of the antilight bleaching properties of the luminescent material is generally carried out under a xenon arc lamp simulating the full spectrum of sunlight. Since the final application of the R-CDs is used in the preparation of LED lamps, it is mainly subject to illumination from InGaN blue chip emitting 460 nm. Therefore, it is reasonable to use a high intensity blue light for its photostability test. The R-CDs were continuously irradiated for 24 h under 460 nm blue light and the fluorescence intensity

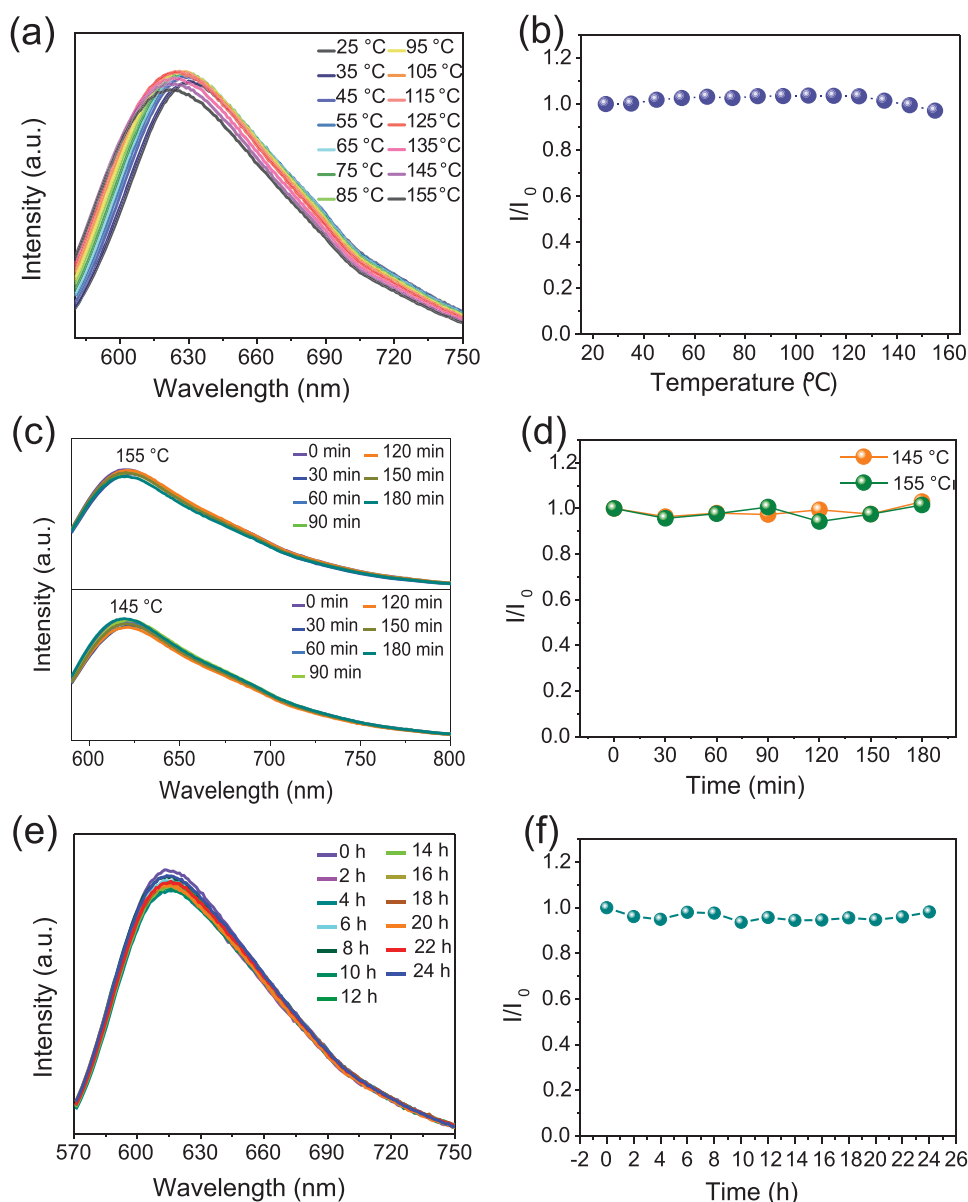


**Figure 4.** a) PL spectra of R-CQDs phosphors at different temperatures from 25 to 155 °C, under excitation at 560 nm. b) The integrated PL intensity of R-CQD phosphors at different temperatures. c) PL spectrum of R-CDs at a temperature of 145 °C for 180 min (ex = 560 nm) and PL spectrum of R-CDs at a temperature of 155 °C for 180 min (ex = 560 nm). d) The integrated PL intensity of R-CQD phosphors at 145 and 155 °C for different time. e) The photostability of R-CQDs under continuous radiation with a blue lamp for 24 h, under excitation at 560 nm. f) The integrated PL intensity of R-CQD phosphors at different times.

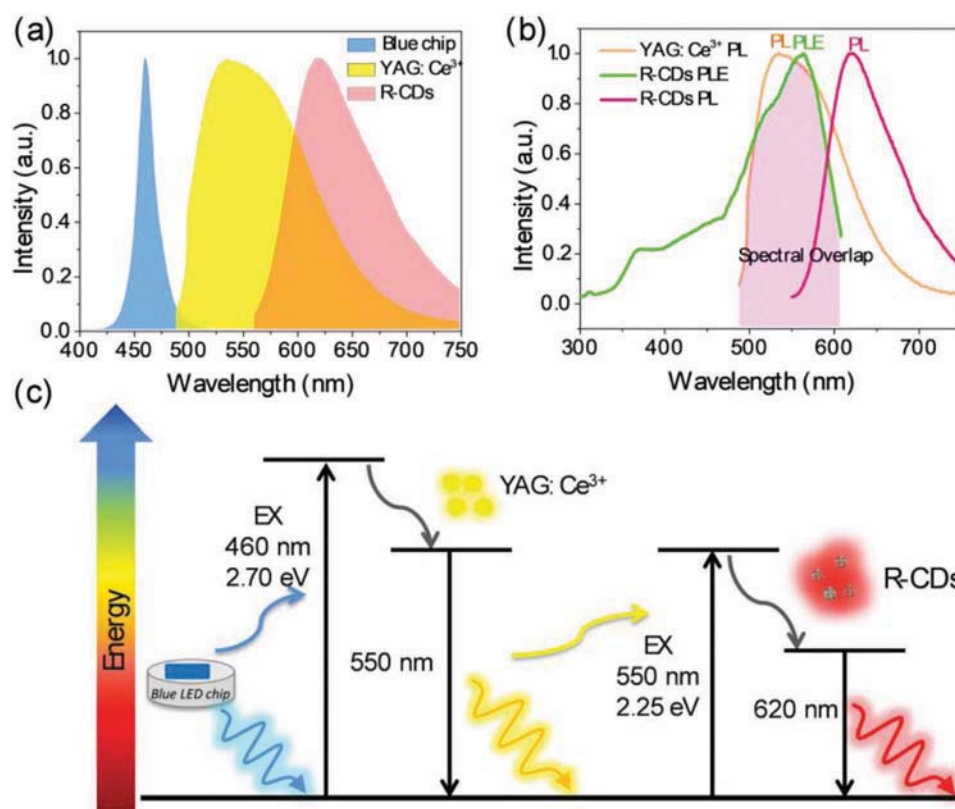


**Figure 5.** a) The emission spectra of blue chips, YAG:Ce<sup>3+</sup>, R-CDs at their max exciting wavelength, respectively. b) PL spectra of YAG:Ce<sup>3+</sup> under excitation of 460 nm, R-CDs' PLE spectra of emission at 620 nm and PL spectra of excitation at 560 nm. c) The energy levels diagram of blue chips, YAG:Ce<sup>3+</sup> and R-CDs.

test was performed with a 1 h interval. The fluorescence intensity of R-CDs shows no obvious decay (Figure 4c,d), demonstrating the excellent photostability of R-CDs.

As can be seen from Figure 2b, to fabricate the WLEDs, a mixture of yellow-emitting YAG:Ce<sup>3+</sup> phosphors and R-CDs were uniformly dispersed in epoxy resin silicone and deposited on commercial InGaN blue chips. As shown in Figure 5a, the blue light emitted by the blue chips, the yellow light emitted by the YAG:Ce<sup>3+</sup>, and the red light emitted by the R-CDs substantially fill the entire visible region at their max exciting wavelength, respectively. The PL spectrum of as fabricated warm WLED lamp obviously consists of three emission bands. R-CDs exhibited broader FWHM than traditional rare-earth phosphors and semiconductor quantum dots (QDs), leading to substantial spectra overlap among their long-wavelength emissions, which is beneficial for fabricating WLEDs with high CRI and low CCT. Figure 5b shows that the optimal emission center of YAG:Ce<sup>3+</sup> is around 560 nm, which is very close to the best excitation wavelength of R-CDs powder. It can be seen from Figure 5b that the emission curve of YAG:Ce<sup>3+</sup> has a large overlap with the excitation curve of R-CDs, indicating that the R-CDs powder can absorb the yellow light emitted by YAG:Ce<sup>3+</sup> well, and finally emit red fluorescence at about 620 nm. Energy levels diagram (Figure 5c) is used to simulate the energy transfer relationship between the blue chip, YAG:Ce<sup>3+</sup>, and R-CDs, which indicate that both YAG:Ce<sup>3+</sup> and R-CDs can be used as light-transfer agents.<sup>[51]</sup> Due to the existence of energy

transfer between InGaN chips, YAG:Ce<sup>3+</sup> and R-CDs, eventually the LEDs realized the emission of white light.

Initially, we used the most common regulation methods, that is, controlling the total mass of YAG:Ce<sup>3+</sup> and R-CDs, but changing their mass ratio from 10:0 to 10:4. As can be seen from Table 1, the WLEDs prepared by this regulation method cannot achieve low CCT and high CRI at the same time, which is mainly because the R-CDs need to absorb yellow light emitted by YAG:Ce<sup>3+</sup> to be converted into red fluorescence. When the mass of YAG:Ce<sup>3+</sup> is decreased and the mass of R-CDs is increased, the light in the yellow emission region is absorbed in a large amount to cause yellow light deficiency. Therefore, in order to obtain WLEDs with low CCT and high index characteristics, it is necessary to ensure a sufficient amount of YAG:Ce<sup>3+</sup> to drive the emission of R-CDs

**Table 1.** CIE color coordinates (x, y), CRI, CCT, luminous efficacy, mass, and mass ratios (YAG:Ce<sup>3+</sup> phosphors:R-CDs phosphors) of WLEDs 1–5 by controlling the total mass of YAG:Ce<sup>3+</sup> and R-CDs.

Number	Mass [mg]	Mass ratio	CIE (x,y)	CCT [K]	CRI
1	170: 0	10: 0	(0.35, 0.40)	5631	68.6
2	154: 16	10: 1	(0.35, 0.36)	4813	85.3
3	142: 28	10: 2	(0.36, 0.33)	5625	91.8
4	131: 39	10: 3	(0.35, 0.29)	6817	77.3
5	121: 49	10: 4	(0.35, 0.26)	8813	63.0

**Table 2.** CIE color coordinates ( $x$ ,  $y$ ), CRI, CCT, luminous efficacy, mass, and mass ratios (YAG:Ce<sup>3+</sup> phosphors:R-CDs phosphors) of WLEDs 1–4 by fixing the quality of YAG:Ce<sup>3+</sup>.

Number	Mass [mg]	Mass ratio	CIE [ $x$ , $y$ ]	CCT [K]	CRI
1	150: 0	10: 0	(0.33, 0.38)	6445	71.8
2	150: 15	10: 1	(0.35, 0.37)	5898	82.8
3	150: 30	10: 2	(0.38, 0.37)	4128	89.0
4	150: 45	10: 3	(0.41, 0.38)	3817	92.7

and supplement the light of the yellow band. Further, we have adjusted the control methods to fabricate the WLEDs. By regulating the mass ratio of YAG and R-CDs, that is, the quality of the fixed YAG:Ce<sup>3+</sup>, and sequentially increasing the amount of R-CDs incorporated, it is possible to realize the WLEDs from white light to warm white light (Table 2, Figure 6d). Besides, it can be observed that when the mass of R-CDs increases, the PL intensity of the blue region is weakened, which is beneficial to the health of the human eyes. Because short-wavelength blue light can directly penetrate the lens to reach the macula of the retina, leading to the decline of epithelial cells of the retinal pigment, which leads to a lack of nutrients in the light-sensitive cells and cause visual impairment, which is irreversible. Therefore, increasing the amount of R-CDs can

reduce the blue light emission of WLEDs, making it more eyes-protecting.<sup>[52]</sup>

It can be known from Table 2 that when the mass ratio of YAG to R-CDs is 10:3, a warm WLED is obtained, and its CCT and CRI are 3817 K and (0.4142, 0.3799), respectively, indicating that the warm WLED lamp produced a high-quality lighting. Notably, the warm WLED lamp features CRI of 92.7, which presents that Ra values significantly is better than rare-earth-based and inorganic semiconductor QDs-based warm WLEDs. Compared with WLEDs based on YAG:Ce<sup>3+</sup> phosphors, the CRI of WLED were increased from 71.8 to 92.7 by adding R-CDs phosphors (Figure 7b,e). As shown in Figure 7a,d, two photographs of the rainbow sugars are taken under different light sources. It is obvious that the warm WLED lamp is more capable of showing the true colors of the rainbow sugars than the WLED lamp based on only YAG:Ce<sup>3+</sup> phosphors. Besides, the warm WLED lamp makes our eyes more comfortable, avoiding too much radiation of short-wavelength-emission light. The luminous efficacy of the warm WLEDs is 60.66 lm w<sup>-1</sup>.

As shown in Figure 8a, the electroluminescence (EL) intensity of the warm WLED lamp increased with increasing the drive current from 20 to 100 mA. The CIE color coordinate, CCT, and CRI showed minor changes from (0.38, 0.41) to (0.37, 0.40), 4192 to 4325 K, and 88.06 to 90.04, respectively, upon

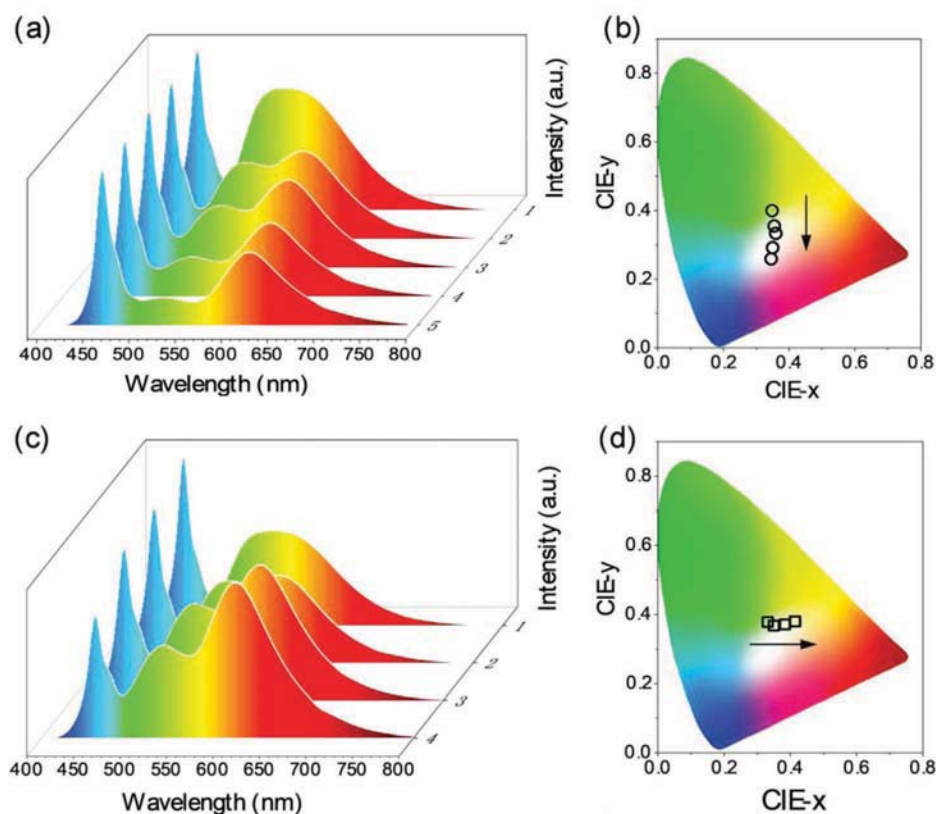


**Figure 6.** a) EL spectra of blue-LED chips coated with a mixture of YAG:Ce<sup>3+</sup> and R-CDs phosphors with various mass ratios by controlling the total mass of YAG:Ce<sup>3+</sup> and R-CDs. b) CIE of Blue-LED chips coated with a mixture of YAG:Ce<sup>3+</sup> and R-CDs phosphors with various mass ratios by controlling the total mass of YAG:Ce<sup>3+</sup> and R-CDs. c) EL spectra of Blue-LED chips coated with a mixture of YAG:Ce<sup>3+</sup> and R-CDs phosphors with various mass ratios by fixing the quality of YAG:Ce<sup>3+</sup>. d) CIE of blue-LED chips coated with a mixture of YAG:Ce<sup>3+</sup> and R-CDs phosphors with various mass ratios by fixing the quality of YAG:Ce<sup>3+</sup>.



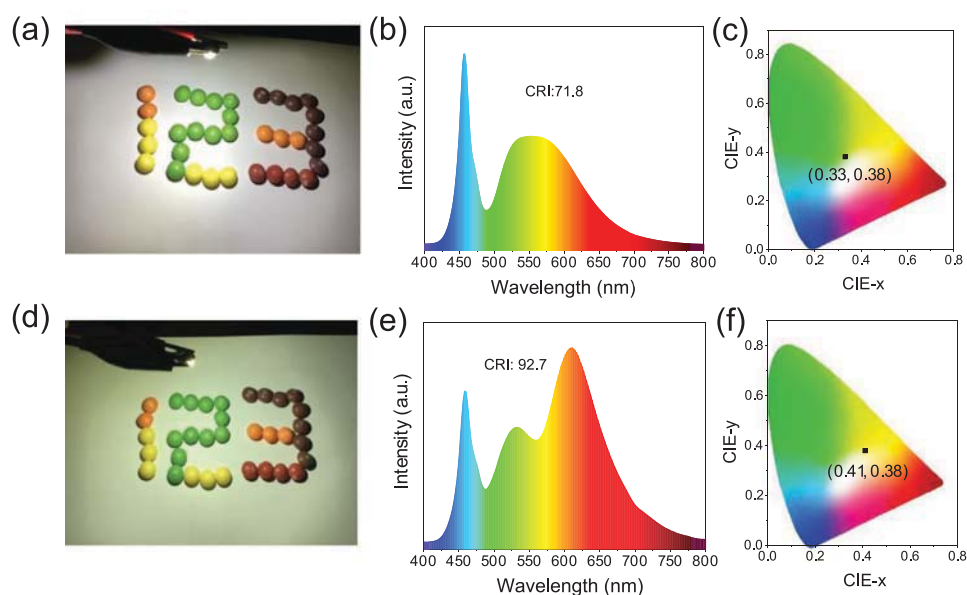


**Figure 7.** a) Image of working WLED fabricated only with YAG:Ce<sup>3+</sup> and blue-emission chip. b) Emission spectrum of working WLED with CRI of 71.75 as shown in (a). c) The WLED's CIE color coordinate of (0.33, 0.38). d) Image of working warm WLED fabricated only with R-CDs, YAG:Ce<sup>3+</sup>, and blue-emission chip. e) Emission spectrum of working warm WLED with CRI of 92.7 as shown in (d). f) The warm WLED's CIE color coordinate of (0.41, 0.38).

the increase of drive current from 20 to 100 mA (Figure 8b–d). These results strongly demonstrate that the warm white light generated from the warm WLED lamp has high color chromatics stability against the increase of drive current, which is

consistent with the high thermal stability and photostability of our R-CDs phosphors. The R-CDs phosphors have great potential in high performance WLEDs-based illumination applications.

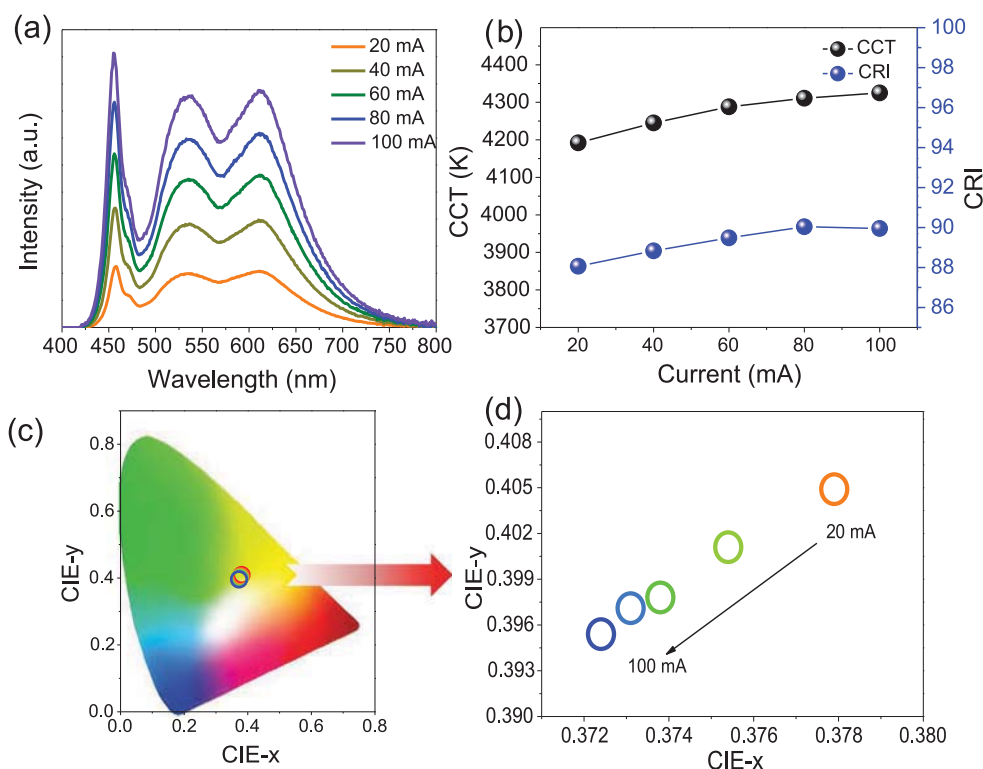


**Figure 8.** a) EL spectra of the warm WLED lamp under different drive currents from 20 to 100 mA. b) CCT and CRI values of the warm WLED lamp at different current. c,d) CIE color coordinates of the warm WLED lamp under different drive currents.

### 3. Conclusion

Based on our previous work, red emissive CDs that does not dope into matrixes to resist aggregation-caused-quenching was synthesized. Theirs thermal and photostability were further studied. When the test ambient temperature reaches 155 °C, its luminous intensity can still maintain 97% of the luminous intensity at room temperature. When it was continuously irradiated for 24 h under a 460 nm blue light, its luminous intensity remained stable. It shows that its thermal stability and photostability are very excellent, which lays the foundation for assembling LEDs. In view of the solid red luminescence characteristics of R-CDs, it can be used to solve the problem that WLED faces, that is, the lack part of the red light region, thereby increasing the CRI. Therefore, we have done a series of comparative experiments, fabrication of blue emission chips and YAG:Ce<sup>3+</sup> phosphors by using the most common WLEDs assembly method on the market, further to achieve a significant increase in CRI by adding different mass of R-CDs. Compared with the YAG:Ce<sup>3+</sup> phosphors-based WLEDs, the application of the R-CDs phosphors in color conversion agent is able to obviously enhance the CRI of WLEDs from 71.8 to 92.7. The R-CDs can be processed in various forms to meet the requirements of different applications based on its excellent characteristics of emitting long-wavelength fluorescence, high thermal stability, and photostability. We propose a synthesis method for such a solid-state luminescent material based on R-CDs, and hope to have a wider application in many other fields.

### 4. Experimental Section

**Materials and Chemicals:** The commercially available InGaN-LED chips with the emission wavelength centered at 460 nm were obtained from Huangzhi lighting accessories firm (Xixiang, Baoan district, Shenzhen). MA and DTSA were acquired from Shanghai Adamas Reagent Co., Ltd. Acetic acid was obtained from Guangdong Guanghua Sci-Tech Co., Ltd. A and B glue (epoxy resin), commercial YAG:Ce<sup>3+</sup> phosphors were purchased from Huangzhi lighting accessories firm (Xixiang, Baoan district, Shenzhen). All of the reagents and materials were of analytical grade and used as received without further purification. Deionized water was produced through a Millipore water purification system (Milli-Q, Millipore) and used in all experiments.

**Instruments and Measurements:** UV–vis absorption spectra of the solid-state samples were recorded on a Shimadzu UV-2550 ultraviolet-visible spectrophotometer. Hitachi FL7000 fluorescence spectrophotometer instrument apparatus was used to record the PL spectra. The samples were excavated by a picosecond diode laser (the excitation wavelengths were set to be 560 nm), and the fluorescence lifetime data was collected by the TCSPC system. The XRD pattern was collected using a XD-2 × / M4600. The HR-TEM images were performed using a JEOL-2010 electron microscope. FT-IR spectra were taken on a Nicolet Avatar 360 FT-IR spectrophotometer. XPS experiments were performed by a Kratos AXIS Ultra DLD X-ray photoelectron spectrometer with a monochromatic Al K $\alpha$  X-ray source. The absolute PLQY was measured by FLS1000. The EL spectra were measured by an integrating sphere (Labsphere) equipped with an Ocean optics spectrograph under an operating direct current.

**Synthesis of R-CDs:** R-CDs were synthesized according to the previously published method. Typically, 544 mg of DTSA and 201.6 mg of MA dissolved in 40 mL acetic acid with ultrasonic treatment, then the solution was transferred into an 80 mL Teflon reactor and reacted at 180 °C for 10 h. After completion, it was naturally cooled to room temperature, and the product was poured into 1 L of boiling water for

washing, suction filtration, and the solid was collected, and dried at 60 °C for 30 min to obtain R-CDs powder.

**Fabrication of LEDs:** InGaN LED chips were purchased from Shen Zhen Huangzhi lighting accessories CO., Ltd. The chips, which emitted 460 nm light at the operation voltage of 3.0 V, and whose maximum power of the drive is 1 W, were the excitation light source of the LED lamp. The YAG:Ce<sup>3+</sup> commercial phosphor powder was controlled to be unchanged at 150 mg, and the mass of the R-CDs powder was adjusted to 0, 15, 30, and 45 mg, respectively. They were mixed in a total volume of 1 mL of epoxy resin A.B glue (the mixing ratio of A.B glue was 1:1), and the mixture was thoroughly stirred until homogeneous. The mixed colloid is dropped onto the chip by dispensing, and after it is naturally left to be air-dried for several hours. Finally, the lid of the LED lamp bead is covered.

### Supporting Information

Supporting Information is available from the Wiley Online Library or from the author.

### Acknowledgements

The present work was supported by the National Natural Science Foundations of China (Grant Nos. 21571067 and 51402207), the National Natural Science Foundation of China Joint Fund with Guangdong under Key Project (Grant No. U1501242), and the Natural Science Foundation of Guangdong Province (2020A1515010443).

### Conflict of Interest

The authors declare no conflict of interest.

### Keywords

carbon dots, high photostability, high thermal stability, red emission, self-quenching-resistant, white light-emitting diodes

Received: February 13, 2020

Revised: April 26, 2020

Published online:

- [1] X.-F. Wang, G.-G. Wang, J.-B. Li, Z. Liu, W.-F. Zhao, J.-C. Han, *Chem. Eng. J.* **2018**, 336, 406.
- [2] Y. Jin, M. H. Fang, M. Grinberg, S. Mahlik, T. Lesniewski, M. G. Brik, G. Y. Luo, J. G. Lin, R. S. Liu, *ACS Appl. Mater. Interfaces* **2016**, 8, 11194.
- [3] B. Wang, H. Lin, F. Huang, J. Xu, H. Chen, Z. Lin, Y. Wang, *Chem. Mater.* **2016**, 28, 3515.
- [4] M. Peng, X. Yin, P. A. Tanner, M. G. Brik, P. Li, *Chem. Mater.* **2015**, 27, 2938.
- [5] S. Lin, M. Chen, Z. Wang, Y. Zhang, R. Yuan, X. Liang, W. Xiang, Y. Zhou, *Chem. Eng. J.* **2017**, 324, 194.
- [6] S. Qu, D. Zhou, D. Li, W. Ji, P. Jing, D. Han, L. Liu, H. Zeng, D. Shen, *Adv. Mater.* **2016**, 28, 3516.
- [7] R. Zhang, H. Lin, Y. Yu, D. Chen, J. Xu, Y. Wang, *Laser Photonics Rev.* **2014**, 8, 158.
- [8] M. Zhu, Y. Pan, Y. Huang, H. Lian, J. Lin, J. Mater. Chem. C **2018**, 6, 491.
- [9] X. Huang, S. Wang, B. Li, Q. Sun, H. Guo, *Opt. Lett.* **2018**, 43, 1307.

- [10] B. B. Chen, M. L. Liu, L. Zhan, C. M. Li, C. Z. Huang, *Anal. Chem.* **2018**, 90, 4003.
- [11] T. Gao, X. Wang, L. Y. Yang, H. He, X. X. Ba, J. Zhao, *ACS Appl. Mater. Interfaces* **2017**, 9, 24846.
- [12] Y. Zhang, Y. Nie, R. Zhu, D. Han, H. Zhao, Z. Li, *Talanta* **2019**, 204, 74.
- [13] G. Gao, Y.-W. Jiang, H.-R. Jia, J. Yang, F.-G. Wu, *Carbon* **2018**, 134, 232.
- [14] N. Zhou, Z. Hao, X. Zhao, S. Maharjan, S. Zhu, Y. Song, B. Yang, L. Lu, *Nanoscale* **2015**, 7, 15635.
- [15] X. Ye, Y. Xiang, Q. Wang, Z. Li, Z. Liu, *Small* **2019**, 15, 1901673.
- [16] T. Malina, K. Poláková, J. Skopalík, V. Milotová, K. Holá, M. Havrdová, K. B. Tománková, V. Čmiel, L. Šefc, R. Zbořil, *Carbon* **2019**, 152, 434.
- [17] W. Lu, Y. Jiao, Y. Gao, J. Qiao, M. Mozneb, S. Shuang, C. Dong, C. Z. Li, *ACS Appl. Mater. Interfaces* **2018**, 10, 42915.
- [18] Y. Liu, J. Liu, J. Zhang, X. Li, F. Lin, N. Zhou, B. Yang, L. Lu, *Biomater. Sci.* **2019**, 7, 1574.
- [19] S. K. Kailasa, S. Ha, S. H. Baek, L. M. T. Phan, S. Kim, K. Kwak, *Mater. Sci. Eng., C* **2019**, 98, 834.
- [20] T. Feng, X. Ai, G. An, P. Yang, Y. Zhao, *ACS Nano* **2016**, 10, 4410.
- [21] X. W. Hua, Y. W. Bao, F. G. Wu, *ACS Appl. Mater. Interfaces* **2018**, 10, 10664.
- [22] L. Liu, X. Yu, Z. Yi, F. Chi, H. Wang, Y. Yuan, *Nanoscale* **2019**, 11, 15083.
- [23] F. Yuan, T. Yuan, L. Sui, Z. Wang, Z. Xi, Y. Li, X. Li, L. Fan, Z. Tan, A. Chen, M. Jin, S. Yang, *Nat. Commun.* **2018**, 9, 2249.
- [24] T. Feng, Q. Zeng, S. Lu, X. Yan, J. Liu, S. Tao, M. Yang, B. Yang, *ACS Photonics* **2018**, 5, 502.
- [25] S. Zhu, Q. Meng, L. Wang, J. Zhang, Y. Song, H. Jin, K. Zhang, H. Sun, H. Wang, B. Yang, *Angew. Chem., Int. Ed.* **2013**, 52, 3953.
- [26] Y. Wen, Q. Jia, F. Nan, X. Zheng, W. Liu, J. Wu, H. Ren, J. Ge, P. Wang, *Chem. Asian. J.* **2019**, 14, 2162.
- [27] Z. Zhou, P. Tian, X. Liu, S. Mei, D. Zhou, D. Li, P. Jing, W. Zhang, R. Guo, S. Qu, A. L. Rogach, *Adv. Sci.* **2018**, 5, 1800369.
- [28] T. Meng, T. Yuan, X. Li, Y. Li, L. Fan, S. Yang, *Chem. Commun.* **2019**, 55, 6531.
- [29] H. Ding, S. B. Yu, J. S. Wei, H. M. Xiong, *ACS Nano* **2016**, 10, 484.
- [30] Y. He, J. He, Z. Yu, H. Zhang, Y. Liu, G. Hu, M. Zheng, H. Dong, J. Zhuang, B. Lei, *J. Mater. Chem. C* **2018**, 6, 2495.
- [31] Y. Liu, W. Duan, W. Song, J. Liu, C. Ren, J. Wu, *ACS Appl. Mater. Interfaces* **2017**, 9, 12663.
- [32] C. Wang, T. Hu, Y. Chen, Y. Xu, Q. Song, *ACS Appl. Mater. Interfaces* **2019**, 11, 22332.
- [33] D. Wang, W. U. Khan, Y. Wang, *Chem. Asian. J.* **2019**, 14, 286.
- [34] C. Sun, Y. Zhang, K. Sun, C. Reckmeier, T. Zhang, X. Zhang, J. Zhao, C. Wu, W. W. Yu, A. L. Rogach, *Nanoscale* **2015**, 7, 12045.
- [35] Y. Zhai, Y. Wang, D. Li, D. Zhou, P. Jing, D. Shen, S. Qu, J. Colloid Interface Sci. **2018**, 528, 281.
- [36] Y. Li, P. Miao, W. Zhou, X. Gong, X. Zhao, *J. Mater. Chem. A* **2017**, 5, 21452.
- [37] S. Javanbakht, H. Namazi, *Carbohydr. Polym.* **2017**, 176, 220.
- [38] H. Tetsuka, A. Nagoya, R. Asahi, *J. Mater. Chem. C* **2015**, 3, 3536.
- [39] D. Zhou, D. Li, P. Jing, Y. Zhai, D. Shen, S. Qu, A. L. Rogach, *Chem. Mater.* **2017**, 29, 1779.
- [40] M. Park, H. Yoon, J. Lee, J. Kim, J. Lee, S. E. Lee, S. Yoo, S. Jeon, *Adv. Mater.* **2018**, 30, 1802951.
- [41] B. Yuan, S. Guan, X. Sun, X. Li, H. Zeng, Z. Xie, *ACS Appl. Mater. Interfaces* **2018**, 10, 16005.
- [42] Y. Zhang, X. Liu, Y. Fan, X. Guo, L. Zhou, Y. Lv, *Nanoscale* **2016**, 8, 15281.
- [43] H. Yang, Y. Liu, Z. Guo, B. Lei, J. Zhuang, X. Zhang, Z. Liu, C. Hu, *Nat. Commun.* **2019**, 10, 1789.
- [44] B. Wang, J. Li, Z. Tang, B. Yang, S. Lu, *Sci. Bull.* **2019**, 64, 1285.
- [45] X. Wei, S. Mei, D. Yang, G. Zhang, F. Xie, W. Zhang, R. Guo, *Nanoscale Res. Lett.* **2019**, 14, 172.
- [46] S. Mei, X. Wei, Z. Hu, C. Wei, D. Su, D. Yang, G. Zhang, W. Zhang, R. Guo, *Opt. Mater.* **2019**, 89, 224.
- [47] Y. Ding, F. Zhang, J. Xu, Y. Miao, Y. Yang, X. Liu, B. Xu, *RSC Adv.* **2017**, 7, 28754.
- [48] Y. H. Kim, P. Arunkumar, B. Y. Kim, S. Unithrattil, E. Kim, S. H. Moon, J. Y. Hyun, K. H. Kim, D. Lee, J. S. Lee, W. B. Im, *Nat. Mater.* **2017**, 16, 543.
- [49] Y. Zhan, B. Shang, M. Chen, L. Wu, *Small* **2019**, 15, 1901161.
- [50] Z. Wang, F. Yuan, X. Li, Y. Li, H. Zhong, L. Fan, *Adv. Mater.* **2017**, 29, 37.
- [51] J. Hou, L. Wang, P. Zhang, Y. Xu, L. Ding, *Chem. Commun.* **2015**, 51, 17768.
- [52] S. J. Park, H. K. Yang, B. K. Moon, *Nano Energy* **2019**, 60, 87.



## PAPER



Cite this: *J. Mater. Chem. C*, 2020, **8**, 11563

## pH-Responsive carbon dots with red emission for real-time and visual detection of amines†

Xiaoqin Zhang,<sup>a</sup> Chongyuan Chen,<sup>a</sup> Dongping Peng,<sup>a</sup> Yizi Zhou,<sup>a</sup> Jianle Zhuang,<sup>ab</sup> Xuejie Zhang,<sup>ab</sup> Bingfu Lei,<sup>ab</sup> Yingliang Liu<sup>ab\*</sup> and Chaofan Hu<sup>ab</sup>

Biogenic amines (BAs) from rotten food cause serious harm to sensitive people. Therefore, the development of a smart label that can intuitively monitor the degree of food decay in real-time is of great significance in food safety. Herein, we report the synthesis of pH-responsive carbon dots with red emission (R-CDs) by the solvothermal treatment of citric acid and urea. The fluorescence intensity of R-CDs gradually increased as the pH of the solution increased from 1 to 12. We studied the mechanisms of pH response and found that H-aggregation occurred when R-CDs were in acidic solution and caused quenching; when they were distributed in alkaline solution, the Fermi level shift caused reduced self-absorption and enhanced red fluorescence emission. The intense red emission of R-CDs is beneficial for the visual detection of alkaline organic amines and BAs derived from rotten shrimp to achieve food safety detection. Moreover, the R-CDs can be used as a promising pH-sensitive fluorescent ink, which has broad prospects and significance in anticounterfeiting and information encryption.

Received 31st May 2020,  
Accepted 8th July 2020

DOI: 10.1039/d0tc02597f

rsc.li/materials-c

## Introduction

Food and food safety are closely related to life. However, biogenic amines (BAs) are formed during the storage and processing of certain foods, such as meat, seafood, wine, etc., and the excessive intake of BA can cause adverse physiological reactions such as headaches, abdominal cramps, and vomiting, especially in sensitive individuals. That is why, from the perspective of human health and food safety, it is very important to develop a fast, convenient and reliable method for the determination of the BAs content in food.<sup>1–3</sup> Traditionally, there are many methods for detecting BAs, such as chromatography,<sup>4,5</sup> electrophoresis<sup>6,7</sup> and conductive polymer materials.<sup>8</sup> The inevitable difficulties of these methods include complex separation methods and expensive instruments, which hinder the determination of BAs. As a result, many sensors have been developed to solve this dilemma in BAs analysis. Optical sensors are among the proposed solutions because of their high selectivity and sensitivity. Several optical sensors, including organic molecules<sup>9–11</sup> and metal nanoparticles,<sup>12–14</sup> have been reported for detecting BAs. Chromogenic

probes are used in organic solutions, or inorganic/aqueous solutions, and these strict conditions limit the detection of biogenic amines. Metal nanoparticles may contaminate food, which would be harmful to human health after human intake. Therefore, it is of great significance to synthesize an emerging, non-toxic, low-cost, biogenic amine-responsible optical material.

Carbon dots (CDs) are a new class of carbon-based nanomaterials that have attracted much attention. Due to their excellent properties, such as chemical stability,<sup>15,16</sup> photostability,<sup>17–19</sup> biocompatibility,<sup>20,21</sup> and low toxicity,<sup>22–24</sup> CDs can be applied to a wide range of fields, such as drug delivery,<sup>25,26</sup> solar cells,<sup>27</sup> photovoltaic devices,<sup>28,29</sup> biological imaging, and so on.<sup>30,31</sup> Especially in the application of pH sensors, CDs have aroused great interest due to the simple synthesis, easy detection, fast response and high sensitivity.<sup>32–34</sup> In general, most of the effects of CD-based pH responses are mainly divided into two types, namely, single photoluminescence (PL) intensity changes<sup>35–37</sup> and ratio fluorescence changes.<sup>38–40</sup> The mechanism of pH response is also considered to be the protonation and deprotonation of the anticounterfeiting functional groups on the surfaces of the CDs.<sup>41</sup> The emission mechanism of CD is affected by many factors such as the quantum size effect, surface states, and molecular states. The topic of the PL mechanisms of CDs-based materials is still controversial, and the same is true for PL mechanisms of pH-sensitive CDs, mainly because the complex and unknown structures of these nanomaterials are not clear.<sup>42</sup> Therefore, it is of great significance

<sup>a</sup> Key Laboratory for Biobased Materials and Energy of Ministry of Education/ Guangdong Provincial Engineering Technology Research Center for Optical Agriculture, College of Materials and Energy, South China Agricultural University, Guangzhou, 510642, China. E-mail: thucf@scau.edu.cn, tliuyi@scau.edu.cn

<sup>b</sup> Guangdong Laboratory of Lingnan Modern Agriculture, Guangzhou, 510642, China

† Electronic supplementary information (ESI) available. See DOI: 10.1039/d0tc02597f

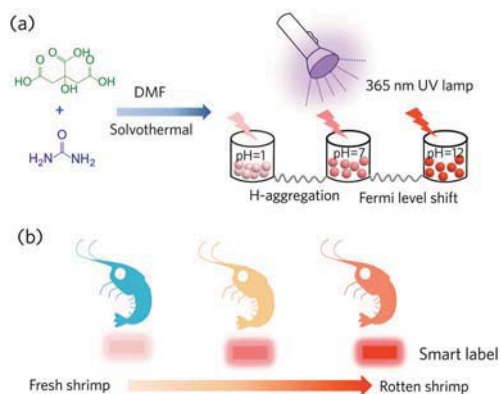


Fig. 1 (a) The formation of R-CDs monomers. (b) Filter paper with adsorbed R-CDs was used to detect the degree of shrimp freshness. (The state of the shrimp on different days is from left to right.)

to explore the emission mechanism of CDs in both emission intensity and peak position with pH-dependence.

In this work, we synthesized pH-responsive CDs with red emission by using citric acid and urea as precursors and the fluorescence intensity of the R-CDs also gradually increased as the pH of the solution increased from 1 to 12 (Fig. 1a). A new mechanism based on H-aggregation and the Fermi level shift is proposed to illustrate the pH-responsive emission of R-CDs. Unlike the narrow response range of the most reported pH-sensitive CDs, R-CDs exhibited a large pH-response range, especially in the alkaline range, and the distinct red emission obviously achieved an excellent visualization effect. Since organic amines are alkaline, the R-CDs emit red light more obviously in alkaline conditions, which is more beneficial for achieving visual detection effects. R-CDs have the advantages of non-toxicity, low-cost and large pH-responsive range. Moreover, as biogenic amine-responding optical materials, R-CDs can achieve visualization effects without any expensive instruments; the production of BAs is mainly due to the decomposition of proteins by microorganisms. Shrimp is suitable as the tested material because of rich protein. There is about 20% protein in 100 g of shrimp. Therefore, R-CDs were applied to test the freshness of shrimp because shrimp decay will produce many different organic amines (Fig. 1b). Further, the pH-sensitive R-CDs can be used for “anti-counterfeit ink”. We have expanded the application of pH-sensitive R-CDs, hoping that they will have broad prospects in food safety and information encryption.

## Experimental section

### Materials and chemicals

Citric acid (99.5%) was purchased from Aladdin Reagent Co. Ltd. Urea (99%) was obtained from Xilong Chemical Co. Ltd. *N,N*-Dimethylformamide (99.5%) was acquired from Shanghai Titan Scientific Co., Ltd. All of the reagents and materials were used as received without further purification. Deionized water was produced using a Millipore water purification system (Milli-Q, Millipore) that was used in all experiments.

### Instruments and measurements

UV-Vis absorption spectra of the samples were recorded on a Shimadzu UV-2550 ultraviolet-visible spectrophotometer. A Hitachi FL7000 fluorescence spectrophotometer instrument was used to record the PL spectra. The samples were excited by a picosecond diode laser (the excitation wavelengths were set to 550 nm), and the fluorescence lifetime data were collected by the time-correlated single-photon counting (TCSPC) system. The XRD pattern was collected using an XD-2X/M4600. The HR-TEM images were performed using a JEOL-2010 electron microscope. FT-IR spectra were obtained on a Nicolet Avatar 360 FT-IR spectrophotometer. X-ray photoelectron spectroscopy (XPS) was conducted on a Thermo Scientific™ K-Alpha™+ spectrometer equipped with a monochromatic Al K $\alpha$  X-ray source (1486.6 eV) operating at 100 W. Samples were analyzed under vacuum ( $P < 10^{-8}$  mbar) with a pass energy of 150 eV (survey scans) or 25 eV (high-resolution scans). The experimental peaks were fitted with Avantage software. The absolute quantum yield (QY) was measured using an FLS1000.

### Synthesis of CDs with red emission

CDs with red emission were synthesized with some modifications, according to the method by Qu and his partners.<sup>43</sup> In detail, 3 g of citric acid and 6 g of urea were added to 30 mL *N,N*-dimethylformamide with ultrasonic treatment for 20 minutes until completely dissolved. Afterward, the mixture was transferred to a 100 mL Teflon reactor and reacted at 160 °C for 6 h. After completion, the obtained dark brown solution was mixed with 60 mL of KOH aqueous solution (50 mg mL<sup>-1</sup>), stirred for 1 min, and then centrifuged at 16 000 rpm for 10 min. The precipitate was collected, dissolved in water, and centrifuged twice (16 000 rpm, 10 min) to wash away residual salts and base, followed by freeze-drying to give the dark product of CDs.

### Preparation pH-responsive filter papers treated with R-CDs

A homogeneous solution with a concentration of 0.1 mg mL<sup>-1</sup> was prepared by dissolving R-CDs in water and the pH was adjusted to 2.5 by adding a little hydrochloric acid solution. The cut filter papers were then immersed in the R-CDs solution, allowed to stand for 5 minutes, picked up, and dried in an oven at 60 °C.

### Preparation and detection of amine solutions

Commercial ammonia was diluted with different quantities of deionized water to obtain a series of ammonia solutions with known concentrations. The pH-responsive filter papers were immersed in the ammonia solutions for one minute. After they were removed from the solutions and dried, the fluorescence of the filter papers was recorded as soon as possible. The preparation and detection processes of other amine solutions were the same as that of ammonia.

### Detection of shrimp freshness

Fresh shrimp were purchased from the market, rinsed with deionized water and the excess water was removed with a fan.

The shrimp were placed in 9 cm disposable plastic Petri dishes and the filter papers were also affixed to the Petri dishes and sealed with tape.

#### Detection of the ammonia nitrogen content in the shrimp meat infused with Nessler's reagent

Here, 0 mL, 0.50 mL, 1.00 mL, 2.00 mL, 4.00 mL, 8.00 mL, 10.00 mL of ammonium standard solution ( $10 \mu\text{g mL}^{-1}$ ) were taken in 50 mL volumetric flasks, respectively, and water was added and made up to the mark. Then, 1 mL of sodium methyl tartrate solution and 1.5 mL of Nessler's reagent were added to the solution in sequence and allowed to stand for 10 minutes. The absorbance was measured, using water as a reference, at a wavelength of 420 nm. The shell, head and tendons were removed from all the shrimp. The shrimp meat was cut and stirred evenly, then 5 g of shrimp meat was poured into a beaker and 10 times the amount of water was added, followed by shaking and soaking for 30 minutes, then filtering to obtain the meat infusion. The meat infusion was taken into a cuvette, then 1 mL of sodium methyl tartrate solution and 1.5 mL of Nessler's reagent were added and allowed to stand for 10 minutes. The absorbance was determined and the phenomenon of meat

infusion at different temperatures and for different numbers of days was observed.

#### Applications of R-CDs in anti-counterfeiting

The filter paper treated with R-CDs solution at pH 2.5 was cut into a symmetrical rabbit shape and showed a faint red emission. By changing the acidity and alkalinity of the rabbit's contact environment, the degree of red emission can be changed.

## Results and discussion

The R-CDs were synthesized through the simple solvothermal treatment of citric acid and urea. After impurity-removal treatment, the obtained product was characterized by transmission electron microscopy (TEM), high-resolution TEM (HRTEM), and X-ray diffraction (XRD) to prove the successful synthesis of the CD. Fig. 2a shows that the as-synthesized R-CDs had a circular shape, were well dispersed and displayed a uniform size. The inset high-resolution TEM (HRTEM) image shows an interplanar spacing of 0.21 nm, corresponding to the (100) lattice space of graphite. Judging from the randomly selected 100 individual particles, the sizes of R-CDs were mainly

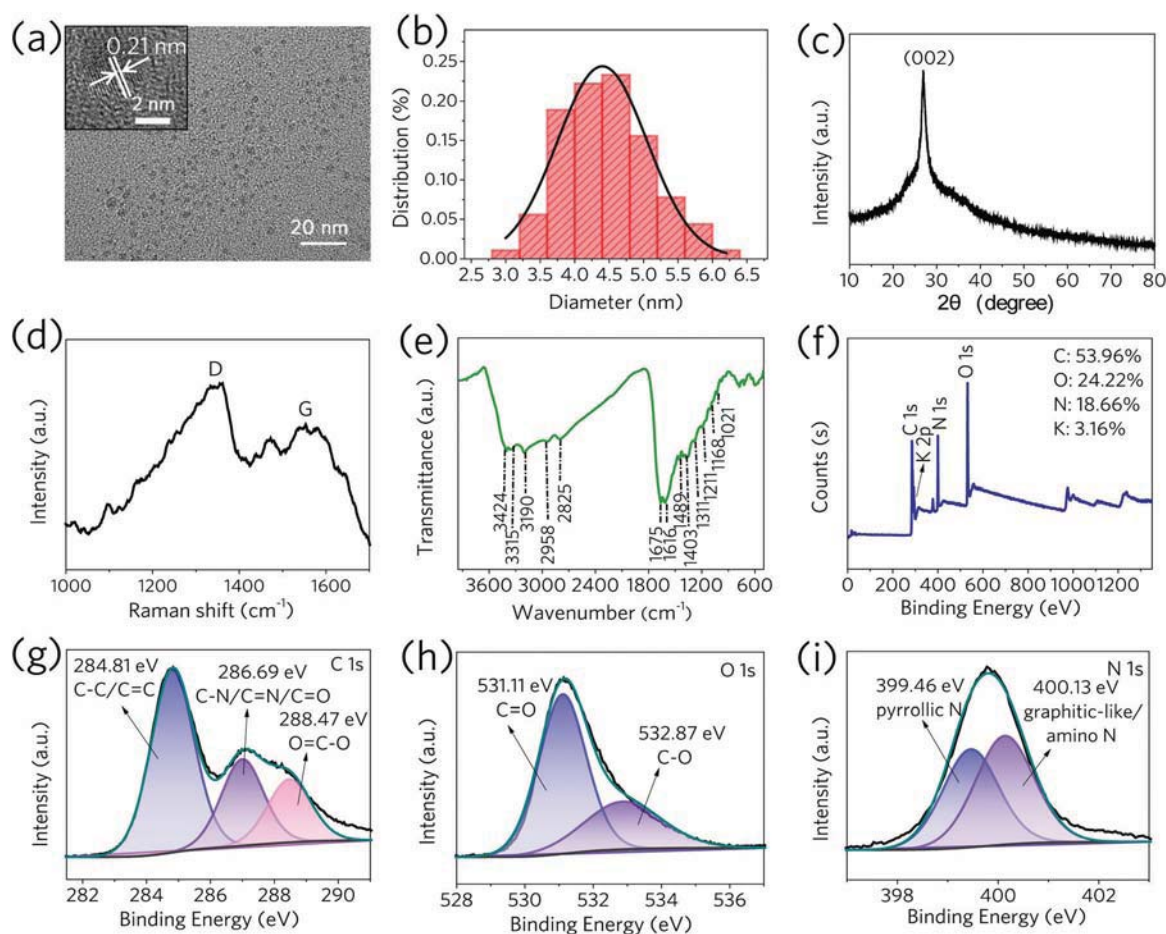


Fig. 2 (a) TEM image of the R-CDs. Inset: High-resolution TEM (HR-TEM) image of R-CDs. (b) Particle size distribution measured by TEM. (c) X-ray diffraction (XRD) pattern of the R-CDs. (d) Raman spectrum of the R-CDs. (e) FT-IR spectrum of the R-CDs, DTSA and MA. (f) XPS spectrum of R-CDs. High-resolution XPS spectra of C 1s (g), O 1s (h), N 1s (i).



in the range from 2.8–6.4 nm with an average diameter of 4.5 nm. In Fig. 2c, the X-ray diffraction (XRD) pattern of R-CD shows a prominent peak centered at around  $26^\circ$  for its (002) plane, and a strong and narrow peak attributed to the graphite structure of R-CDs. There are two peaks of  $1328\text{ cm}^{-1}$  (D band) and  $1567\text{ cm}^{-1}$  (G band) shown on the Raman spectrum, referring to disordered structures or defects and  $\text{sp}^2$  carbon networks in the carbon materials, respectively (Fig. 2d). The intensity ratio  $I_{\text{D}}/I_{\text{G}}$  was calculated to be 1.06, demonstrating a high degree of graphitization, which is consistent with the TEM and XRD results.

By analysing the Fourier transform infrared (FTIR) spectrum, the functional groups on the surface of R-CDs can be identified to further understand its characteristics. As shown in Fig. 2e, the R-CDs sample possessed abundant hydrophilic groups such as O–H ( $3424\text{ cm}^{-1}$ ), amino/amide N–H bonds ( $3315$  and  $3145\text{ cm}^{-1}$ ) on their surfaces, thereby ensuring their good solubility in water. The stretching vibrations of C–C ( $1616\text{ cm}^{-1}$ ), C–N ( $1403\text{ cm}^{-1}$ ), and C=N ( $1489\text{ cm}^{-1}$ ) bonds were observed from the FTIR spectrum, indicating that the polyaromatic structures were formed in R-CDs during the reaction process, which resulted in a dehydration reaction between CA and urea, forming a highly graphitized structure. The vibrational absorption band of C–H located at  $2958$  and  $2825\text{ cm}^{-1}$  and the strong band at  $1675\text{ cm}^{-1}$  could be related to the amide carbonyl. Moreover, from the FTIR spectrum, R-CDs contain C–N ( $1311\text{ cm}^{-1}$ ), C–O–C ( $1168\text{ cm}^{-1}$ ), and C–O ( $1211$  and  $1022\text{ cm}^{-1}$ ) groups. The chemical composition and speciation of O-CDs were also examined by X-ray photoelectron spectroscopy (XPS). As shown in Fig. 2f, the XPS full-survey spectrum contains four peaks at  $284.8\text{ eV}$ ,  $531.1\text{ eV}$ ,  $400.0\text{ eV}$  and K 2p  $292.9\text{ eV}$ , revealing that R-CDs were mainly composed of C, O, N, and K elements, and the atomic ratios were 53.96%, 24.22%, 18.66%, and 3.16%, respectively. Since the N-rich precursors participated in the synthesis reaction, there was a high content of N element in the resulting products. The high-resolution spectrum of C 1s (Fig. 2g) can be decomposed into three peaks, the binding energy of  $284.81\text{ eV}$  corresponds to C–C/C=C,  $286.69\text{ eV}$  corresponds to C–N/C=N/C=O, and  $288.47\text{ eV}$  corresponds to O=C–O. The O 1s spectrum (Fig. 2h) exhibits two peaks at  $531.11$  and  $532.87\text{ eV}$ , respectively, which correspond to C=O and C–O groups. The high-resolution spectrum of N 1s (Fig. 2i) can be decomposed into two peaks with binding energies of  $399.46$  and  $400.13\text{ eV}$ , respectively, which correspond to pyrrolic N and graphitic-like/amino N groups. By combining all these characterization data and analyses, the R-CDs could be considered to be composed of a graphite-like skeleton/core, on which they are covered with abundant amino and hydroxyl functional groups. Various functional groups on the surface of R-CDs not only enhanced water solubility, but were also the basis of long-wavelength PL emission performance.<sup>44,45</sup>

The optical properties of R-CDs were further evaluated by UV-visible absorption, PL excitation and emission. Fig. 3a shows the UV-vis spectrum (dotted line), with a broad absorption from 300 to 600 nm, and a dominant band at  $\lambda_{\text{max}} \approx 550\text{ nm}$ .

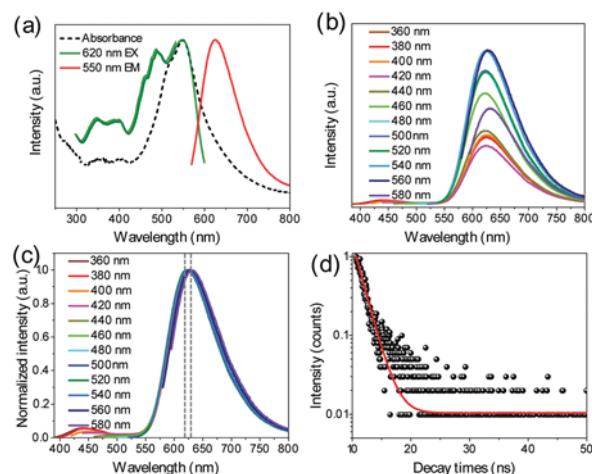


Fig. 3 (a) UV-vis absorption, PL excitation (EX) and emission (EM) spectra of R-CDs in water. (b) PL emission spectra of R-CDs in water at different excitation wavelengths. (c) Normalized PL emission spectra of R-CDs in water at different excitation wavelengths. (d) Fluorescence decay curve of R-CDs.

Their absorption in the UV region (300–400 nm) corresponds to  $n\text{--}\pi^*$  transitions of the C=N and C=O groups. Unexpectedly, the absorption in the visible region (440–600 nm) has two peaks, the main peak at about 550 nm and the shoulder peak at about 500 nm. One peak is caused by the defect states from the functional groups on the CDs surfaces, and the other peak is caused by the large amount of graphitic-like N that exists in R-CDs.<sup>46</sup> It can be speculated that both of the above were by the narrowing electron-transfer slit, resulting in long-wavelength PL emission. The PL excitation spectrum (Fig. 3a green line) of the R-CDs overlapped with the absorption spectrum in the long-wavelength region to some extent, indicating that sufficient graphitic-like N and surface structures and states contributed to the intense red emission. Fig. 3a (red line) reveals that the PL emission spectrum of R-CDs is located at approximately 620 nm. Fig. 3b shows that the PL peak of R-CDs at 620 nm varied slightly with the excitation wavelength in the range of 360 to 580 nm, indicating that R-CDs exhibit weak excitation-wavelength-dependent PL behavior. It was observed that the maximum PL emission peak was red-shifted from 621 to 629 nm though normalizing all the emission spectra (Fig. 3c), indicating that the R-CDs have more than one luminescence center.<sup>47,48</sup> Therefore, it could be inferred that the R-CDs have two fluorescent emission centers, derived from the rich graphitic-like N structures in the core and the defect states from the surface functional groups. The time-resolved PL spectrum (Fig. 3d) shows that R-CDs had double-exponential emission in aqueous solution, and the average lifetime was 1.56 ns when excited by 550 nm. Furthermore, the absolute QY of R-CDs in water was as high as 10.6%, which achieved a good level among the reported QYs of R-CDs in water.<sup>49,50</sup>

Based on the different PL intensities of the R-CDs at different pH values, efforts were made to further understand the optical properties of R-CD in aqueous solution at pH 1–12. As shown in Fig. 4a, the R-CDs showed great differences in

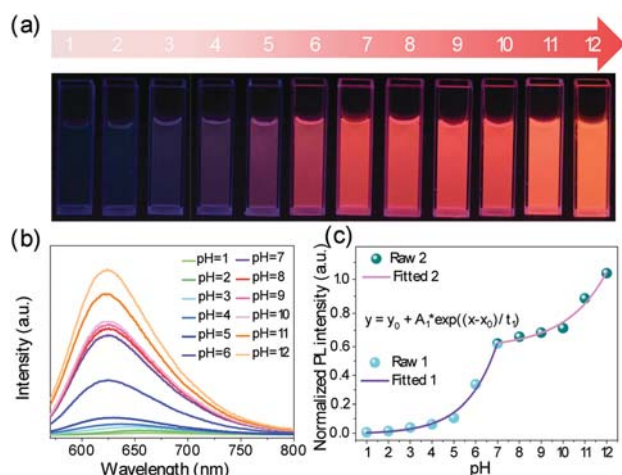


Fig. 4 (a) Photographs of R-CDs solutions with pH values ranging from 1 to 12 under UV light of 365 nm. (b) PL spectra of R-CDs as pH values increased from 1 to 12 at 550 nm excitation. (c) A fitted plot of normalized PL intensities and pH values; the inset displays the fitting equation.

brightness under UV light: it can be initially judged that the PL intensity is weak in an acidic environment and strong in an alkaline environment. The emission peaks of R-CDs ( $\lambda_{\text{ex}} = 550 \text{ nm}$ ) in solutions with different pH values had slight differences (Fig. 4b), while the PL intensities showed an increasing trend when the pH increased from 1 to 7, and there was another sharp increasing trend when the pH reached 7–12. Moreover, to evaluate the relationship between the PL emission intensity of R-CDs and pH values, and determine whether they can be used as indicators, the normalized PL intensity as a function of pH was analysed in detail. As illustrated in Fig. 4c, the normalized PL intensities under different pH conditions presented a curve change that fit two similar exponential growths, respectively, in acidic and alkaline environments. Two non-linear curves were fit with the same exponential growth function:  $y = y_0 + A_1 \times \exp((x - x_0)/t)$ , where  $y_0$ ,  $A_1$ ,  $x_0$  and  $t$  are constants,  $x$  is the pH value, and  $y$  represents the corresponding normalized PL intensity. As a result, the plot for the acidic environment (pH = 1–7) was well fitted to  $y = -0.0061 + 0.0075 \times \exp((x - 0.8457)/1.3868)$ , and the other plot for the alkaline environment (pH = 7–12) was well fitted to  $y = 0.5948 + 0.0100 \times \exp((x - 4.9184)/1.8635)$ , indicating that R-CDs are theoretically expected to detect pH values in the range of 1–12. More importantly, as shown in Fig. S1 (ESI<sup>†</sup>), when the pH was cycled in the range of 2–12, the fluorescence response and brightness dependence of R-CDs are reversible. The dependence of pH-induced changes in fluorescence intensity brings the benefits of continuous pH monitoring in practical applications, enabling real-time and visual inspection.

The UV-vis absorption, PL excitation, and PL emission spectra of R-CDs at different pH values demonstrated the optical properties and mechanism. The PL spectra of the R-CDs indicated an emission peak at 620 nm excited at 550 nm with a pH of 7–12, but the emission peak was red-shifted from approximately 625 nm to 650 nm when the pH

changed from 6 to 1 (Fig. 5a). Fig. 5b shows that the PLE spectra of the R-CDs have two main excitation peaks, one located at about 550 nm and the other is a shoulder peak at about 500 nm. Similarly, the main excitation peak at around 550 nm was redshifted to 570 nm when the pH went from 6 to 1, indicating that the red emission of R-CDs was primarily caused by the main excitation peak. UV-vis absorption spectra exhibited that there were two peaks in the visible region, where the peak position was almost unchanged in neutral and alkaline aqueous solutions, but a blue-shift (500 nm to 457 nm) was observed from pH 6 to 1. Since the CDs can be regarded as the core of the conjugated structures covered with many functional groups on the surface, these conjugated structures can form aggregates through the  $\pi$ - $\pi$  stacking effect, which results in spectral shifts. In general, H aggregation leads to a blue shift in the absorption spectrum.<sup>51,52</sup> Thus, the blue shift of the absorption peak is mainly due to the H-aggregation of R-CDs in the acidic environment to form large aggregates, leading to fluorescence quenching. Furthermore, the aggregation and dispersion of the R-CDs at different pH values were directly observed through TEM images (Fig. 5d–i). The R-CDs were severely aggregated at pH 2 and relatively dispersed at neutral and alkaline pH, which corresponds to the quenching of R-CDs at by H-aggregation.

It is worth noting that there were no changes in the peak positions of the PLE spectrum, PL spectrum, and UV-visible absorption spectrum of R-CDs in neutral and alkaline aqueous solutions. However, the intensity of red emission still gradually increased with increasing pH values, as mentioned above. On varying the pH from 1 to 12, the zeta potential of R-CDs dramatically changed from 0.123 mV to  $-47.3 \text{ mV}$ , which corresponds to the protonation and deprotonation of the surface functional groups of R-CDs (Fig. S2, ESI<sup>†</sup>). The presence of electrostatic doping/charging on the R-CDs surface and the shift in the Fermi level resulted in the reduction of long-wavelength electron transitions.<sup>43</sup> In Fig. S3a–c (ESI<sup>†</sup>) the excitation spectra overlap well with the UV-visible spectra, which facilitates the red emission of R-CDs at pH 8, 10 and 12. As the pH increases (8–12), the absorption in the long-wavelength region gradually decreases, leading to smaller self-absorption and enhancing the output red emission of the R-CDs (Fig. S3d, ESI<sup>†</sup>). Hence, the mechanisms have been discovered in which the fluorescence intensity of R-CDs gradually increases from acidic to alkaline medium. Fig. 5j shows that the R-CDs became less fluorescent due to H-aggregation in an acidic environment, while the Fermi level shifted in alkaline conditions, causing fluorescence enhancement.

Rotten seafood releases a large amount of BAs because the rich protein decomposes into amino acids that are eventually degraded by microorganisms. Considering that the R-CDs with higher fluorescence intensity and obvious fluorescence response under alkaline conditions match the pH range of BAs, it is not difficult to envisage the advantages of R-CDs in the monitoring of BAs. Hence, it provides a more convenient and lower-cost option in monitoring food decay. BAs are a generic term for a class of nitrogen-containing low molecular weight organic

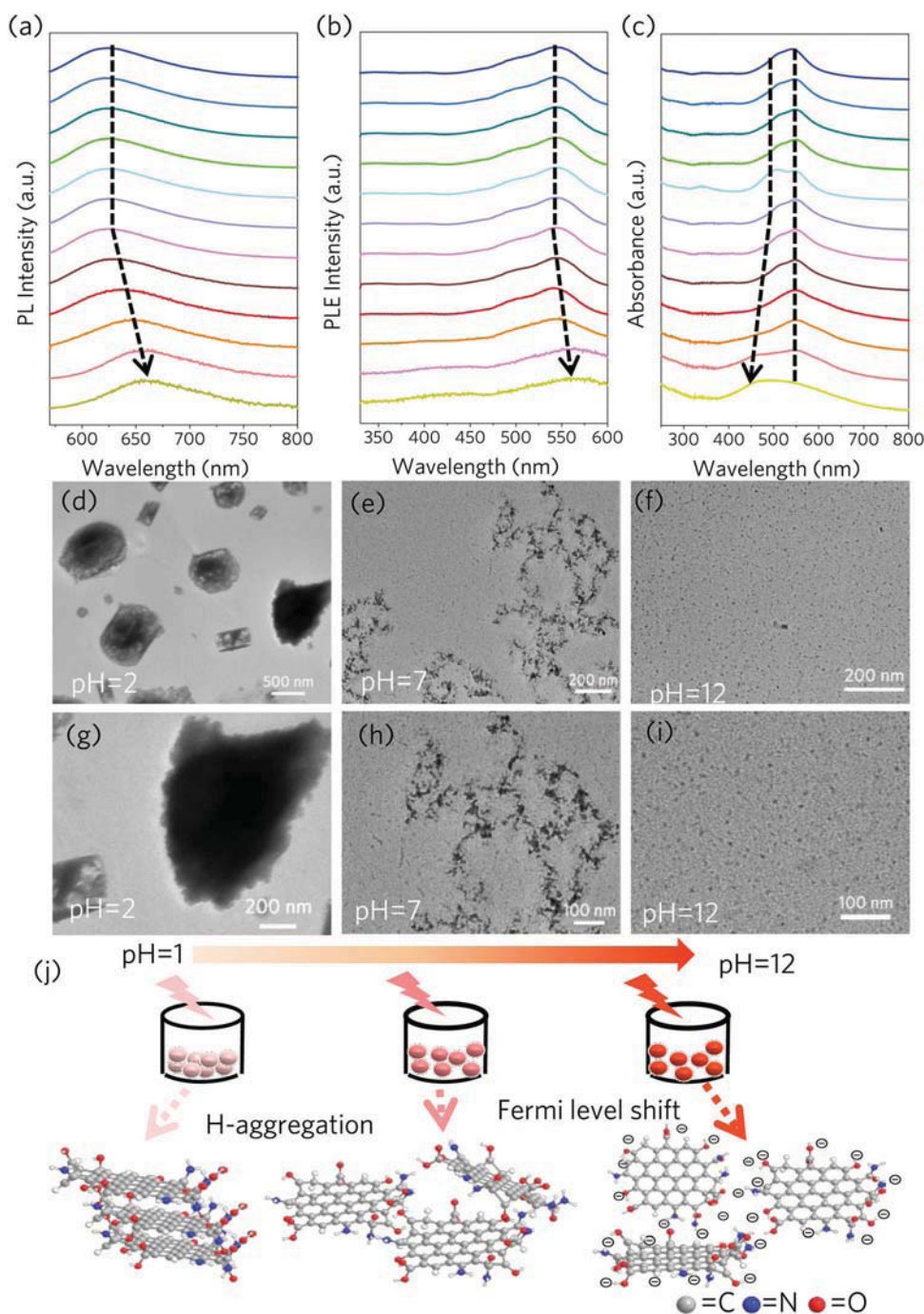


**Fig. 5** (a) PL spectra of R-CDs as the pH increased from 1 to 12 at 550 nm excitation. (b) PLE spectra of R-CDs as the pH increased from 1 to 12 at 620 nm emission. (c) UV-vis absorption of R-CDs as the pH increased from 1 to 12. (d) and (g) TEM image of the R-CDs at pH 2. (e) and (h) TEM image of the R-CDs at pH 7. (f) and (i) TEM image of the R-CDs at pH 12. (j) The mechanisms of R-CDs at different pH values.

compounds produced by organisms.  $\text{NH}_3$ ,  $\text{NH}_4\text{Et}_2$ , 1,4-butanediamine, histamine,  $\text{NEt}_3$ , and other organic amines are the important components of BAs. Therefore, to assess whether R-CDs are sensitive to BAs, several organic amines were selected for detection. There are several pictures of organic amines in a range of concentrations (101–105 ppm) detected by smart labels (pH-responsive filter papers treated with R-CDs), followed by pyrrolidine,  $\text{NEt}_3$ , ethylenediamine, morphine, histamine,

$\text{NH}_4\text{Et}_2$ , 1,4-butanediamine,  $\text{NH}_3$ , respectively (Fig. 6). The smart label paper enhanced the intensity of the red emission as the concentration of organic amines increased, as indicated by the white arrows. The control tags were treated with R-CDs solution at pH 2.5 and not with the organic amine solution. In addition, the pH values of organic amines with different concentrations were tested in real-time. Amino groups are basic groups that can absorb protons, so as the concentration of organic amines



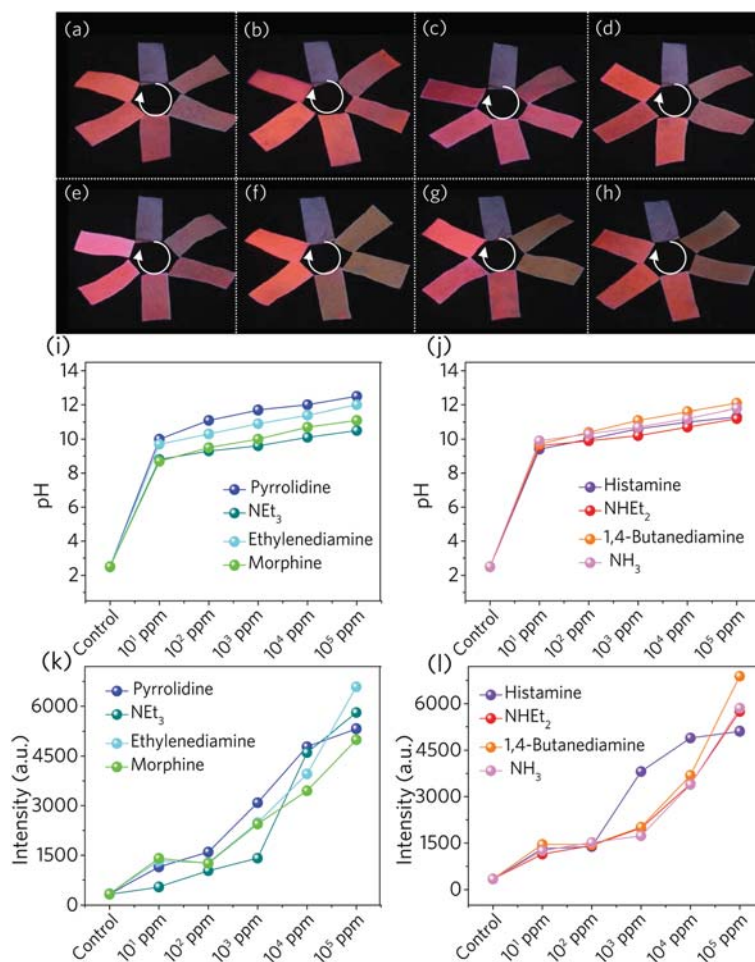


**Fig. 6** Detection of different concentrations (101–105 ppm) of amine solutions with pH-responsive filter papers, followed by (a) pyrrolidine, (b)  $\text{NEt}_3$ , (c) ethylenediamine, (d) morphine, (e) histamine, (f)  $\text{NH}_4\text{Et}_2$ , (g) 1,4-butanediamine, (h)  $\text{NH}_3$ , respectively. (i) pH of amines at different concentrations, including pyrrolidine,  $\text{NEt}_3$ , ethylenediamine and morphine. (j) pH of amines at different concentrations, including histamine,  $\text{NH}_4\text{Et}_2$ , 1,4-butanediamine,  $\text{NH}_3$ . (k) Correlation between the red emission intensity of filter papers and commercial amine concentrations, including pyrrolidine,  $\text{NEt}_3$ , ethylenediamine and morphine. (l) Correlation between the red emission intensity of filter papers and commercial amine concentration, histamine,  $\text{NH}_4\text{Et}_2$ , 1,4-butanediamine,  $\text{NH}_3$ .

increased, the pH increased accordingly (Fig. 6i and j). As shown in Fig. 6k and l, the luminous intensity of the smart labels increased with increasing concentrations of organic amines. However, since there was no significant linear relationship between the intensity and pH values, further quantitative analysis was not possible. Nevertheless, because of obvious changes at different pH values the smart labels were still used and did not affect our judgment.

Since the R-CDs have an obvious response to low concentrations of organic amines, shrimp were selected as the monitoring objects to test whether R-CDs are suitable as smart labels for detecting seafood freshness. A slight red colour represents freshness and the more visible the red emission, the higher the degree of decay. As shown in Fig. 7a, a piece of pH-responsive filter paper treated with R-CDs was fixed inside each sealed packaging container of the shrimp and stored at 4 °C and room temperature for 1–3 days. When stored at room temperature for only one day, the red fluorescence intensity of the filter paper

became higher than before. On the third day, it was observed that the red fluorescence of the filter paper had become particularly noticeable under UV light. However, when fresh shrimp were stored in a refrigerator at 4 °C for three days, there was no significant change in the fluorescence intensity of the filter paper. To verify that the red emission enhancement of smart tags was caused by volatile BAs, we measured the ammonia nitrogen content of shrimp stored at different temperatures by using Nessler's reagent. Nessler's reagent is a solution of mercury dichloride–potassium-iodide–potassium hydroxide ( $\text{HgCl}_2$ –KI–KOH). Iodine and mercury ions react with ammonia to form a reddish-brown complex under strongly alkaline conditions. The more such red-brown complexes are produced, the solution becomes more turbid, and the corresponding ammonia nitrogen content is greater, which is used to simply judge the BAs of the meat infusion. The shrimp meat infusion became more and more turbid as the number of days increased at room temperature. The trend changed from transparent to

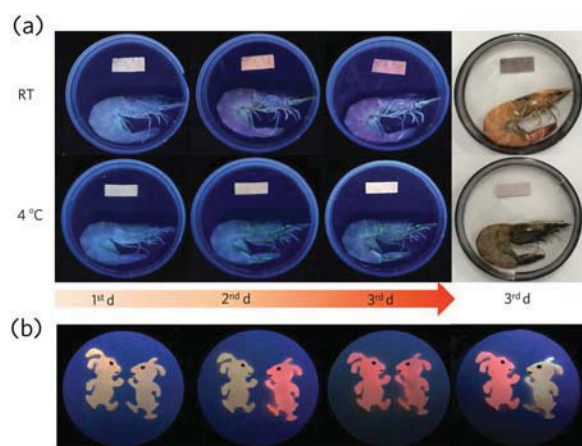


Fig. 7 (a) Monitoring of the freshness of shrimp by using the smart label. Images of the CDs-based fluorescent material with red fluorescence as a smart trademark for monitoring the freshness of shrimps stored at different temperatures (RT: room temperature). (b) Applications of R-CDs in anti-counterfeiting: schematic illustration of information protection (encryption and decryption) processes by touching different pH solutions.

slightly yellow to dark yellow, corresponding to the first day to the third day (Fig. S4a, ESI†). At room temperature, the meat infusion on the first day was clear and transparent, meaning the shrimp were fresh. The meat infusion on the second day was yellow, meaning the shrimp had rotted. The rotting on the third day was more severe. However, the meat infusion of shrimp stored at 4 °C for three days was still transparent under the titration with Nessler's reagent (Fig. S4b, ESI†). The degree of turbidity of the meat infusion reflects the ammonia nitrogen content of the shrimp. It was determined that the quantity of ammonia nitrogen produced by 5 g of shrimp at room temperature increased significantly with the number of days, from 7.72 µg on the first day to 113.44 µg on the third day. After three days at 4 °C, the quantity of ammonia nitrogen did not change much, only from 7.76 µg to 12.34 µg (Fig. S4d, ESI†). This further illustrates that the absorption of organic amines by the filter paper causes the R-CDs to be in an alkaline environment and causes enhanced red emission. Therefore, the decay of the shrimp caused the release of BAs, which left the R-CDs in an alkaline environment, resulting in the enhanced emission of red light.

Based on the pH sensitivity of R-CDs, we also tried to apply them to information encryption. A symmetrical rabbit-shaped filter paper treated with R-CDs solution at pH 2.5, showed a faint red emission. The rabbit-shaped filter paper on the right was immersed in the aqueous solution at pH 12 for a few seconds, then removed and dried, and red light was observed under a UV lamp (365 nm). The rabbit-shaped filter paper on the left was then treated in the same way; both sides emitted red light. The rabbit-shaped filter paper on the right was immersed in an aqueous solution at pH 2.5, and it was found that it emitted weak red light, and the left still emitted strong red light. Therefore, the pH-sensitive R-CDs can be used as “anti-counterfeiting ink”, which has great prospects and significance in information encryption.

## Conclusions

In summary, R-CDs with bright red PL emission were synthesized by solvothermal-assisted treatment of CA and urea in DMF at 160 °C within 6 h. R-CDs exhibited pH-sensitive PL intensity that changed from slight red light to strong red light as the pH values increased. The mechanisms of the changes in the luminous intensity caused by pH were studied. The low intensity of R-CDs in acidic solution was mainly due to the self-quenching of R-CDs by H-aggregation. In the alkaline solution, because the electron-rich hydroxide radicals are on the R-CDs surfaces, the Fermi level of the surface is reduced, thereby reducing the absorption in the long-wavelength band, which reduces the self-absorption between absorption and emission. Based on the pH sensitivity of R-CDs, it was applied to food safety testing. By immersing the filter papers in R-CDs solution, we developed smart labels with excellent amine sensing. Such a promising response capability provides a great opportunity to quickly and accurately detect BAs in real-time with the naked eyes. We further applied smart tags to detect BAs from rotten shrimp, which is of great significance for ensuring food safety and has practical application value in the food industry. Based on its pH sensitivity, R-CDs solutions have also been tested for use as “anti-counterfeit ink”, to further develop applications and enhance the practical application value.

## Conflicts of interest

There are no conflicts to declare.

## Acknowledgements

The present work was supported by the National Natural Science Foundations of China (Grant No. 21571067, 51402207), the National Natural Science Foundation of China Joint Fund with Guangdong under Key Project (Grant No. U1501242) and the Natural Science Foundation of Guangdong Province (2020A1515010443).

## References

- 1 F. Bedia Erim, *TrAC, Trends Anal. Chem.*, 2013, **52**, 239–247.
- 2 C. Schaude, C. Meindl, E. Frohlich, J. Attard and G. J. Mohr, *Talanta*, 2017, **170**, 481–487.
- 3 R. Jia, W. Tian, H. Bai, J. Zhang, S. Wang and J. Zhang, *Nat. Commun.*, 2019, **10**, 795.
- 4 A. A. Tameem, B. Saad, A. Makahleh, A. Salhin and M. I. Saleh, *Talanta*, 2010, **82**, 1385–1391.
- 5 S. Jia, Y. P. Kang, J. H. Park, J. Lee and S. W. Kwon, *Food Chem.*, 2012, **132**, 1185–1190.
- 6 L. K. Fiddes, J. Chang and N. Yan, *Sens. Actuators, B*, 2014, **202**, 1298–1304.
- 7 S. Hernandez-Cassou and J. Saurina, *J. Chromatogr. B: Anal. Technol. Biomed. Life Sci.*, 2011, **879**, 1270–1281.

- 8 N. S. Yurova, A. Danchuk, S. N. Mobarez, N. Wongkaew, T. Rusanova, A. J. Baeumner and A. Duerkop, *Anal. Bioanal. Chem.*, 2018, **410**, 1111–1121.
- 9 C. F. Chow, M. H. Lam and W. Y. Wong, *Anal. Chem.*, 2013, **85**, 8246–8253.
- 10 M. A. Sahudin, M. S. Su'ait, L. L. Tan, Y. H. Lee and N. H. Abd Karim, *Anal. Bioanal. Chem.*, 2019, **411**, 6449–6461.
- 11 K. M. A. El-Nour, E. T. A. Salam, H. M. Soliman and A. S. Orabi, *Nanoscale Res. Lett.*, 2017, **12**, 231.
- 12 Q. Liu, S. Mukherjee, R. Huang, K. Liu, T. Liu, K. Liu, R. Miao, H. Peng and Y. Fang, *Chem. – Asian J.*, 2019, **14**, 2751–2758.
- 13 L. González-Ceballos, B. Melero, M. Trigo-López, S. Vallejos, A. Muñoz, F. C. García, M. A. Fernandez-Muiño, M. T. Sancho and J. M. García, *Sens. Actuators, B*, 2020, **304**, DOI: 10.1016/j.snb.2019.127249.
- 14 Y. Zhang, H. Yang, H. Ma, G. Bian, Q. Zang, J. Sun, C. Zhang, Z. An and W. Y. Wong, *Angew. Chem., Int. Ed.*, 2019, **58**, 8773–8778.
- 15 B. B. Chen, M. L. Liu, L. Zhan, C. M. Li and C. Z. Huang, *Anal. Chem.*, 2018, **90**, 4003–4009.
- 16 T. Gao, X. Wang, L. Y. Yang, H. He, X. X. Ba, J. Zhao, F. L. Jiang and Y. Liu, *ACS Appl. Mater. Interfaces*, 2017, **9**, 24846–24856.
- 17 Y. Zhang, Y. Nie, R. Zhu, D. Han, H. Zhao and Z. Li, *Talanta*, 2019, **204**, 74–81.
- 18 G. Gao, Y.-W. Jiang, H.-R. Jia, J. Yang and F.-G. Wu, *Carbon*, 2018, **134**, 232–243.
- 19 N. Zhou, Z. Hao, X. Zhao, S. Maharjan, S. Zhu, Y. Song, B. Yang and L. Lu, *Nanoscale*, 2015, **7**, 15635–15642.
- 20 X. Ye, Y. Xiang, Q. Wang, Z. Li and Z. Liu, *Small*, 2019, **15**, e1901673.
- 21 T. Malina, K. Poláková, J. Skopalík, V. Milotová, K. Holá, M. Havrdová, K. B. Tománková, V. Čmiel, L. Šefc and R. Zbořil, *Carbon*, 2019, **152**, 434–443.
- 22 W. Lu, Y. Jiao, Y. Gao, J. Qiao, M. Mozneb, S. Shuang, C. Dong and C. Z. Li, *ACS Appl. Mater. Interfaces*, 2018, **10**, 42915–42924.
- 23 Y. Liu, J. Liu, J. Zhang, X. Li, F. Lin, N. Zhou, B. Yang and L. Lu, *Biomater. Sci.*, 2019, **7**, 1574–1583.
- 24 S. K. Kailasa, S. Ha, S. H. Baek, L. M. T. Phan, S. Kim, K. Kwak and T. J. Park, *Mater. Sci. Eng., C*, 2019, **98**, 834–842.
- 25 T. Feng, X. Ai, G. An, P. Yang and Y. Zhao, *ACS Nano*, 2016, **10**, 4410–4420.
- 26 X. W. Hua, Y. W. Bao and F. G. Wu, *ACS Appl. Mater. Interfaces*, 2018, **10**, 10664–10677.
- 27 L. Liu, X. Yu, Z. Yi, F. Chi, H. Wang, Y. Yuan, D. Li, K. Xu and X. Zhang, *Nanoscale*, 2019, **11**, 15083–15090.
- 28 F. Yuan, T. Yuan, L. Sui, Z. Wang, Z. Xi, Y. Li, X. Li, L. Fan, Z. Tan, A. Chen, M. Jin and S. Yang, *Nat. Commun.*, 2018, **9**, 2249.
- 29 T. Feng, Q. Zeng, S. Lu, X. Yan, J. Liu, S. Tao, M. Yang and B. Yang, *ACS Photonics*, 2017, **5**, 502–510.
- 30 S. Zhu, Q. Meng, L. Wang, J. Zhang, Y. Song, H. Jin, K. Zhang, H. Sun, H. Wang and B. Yang, *Angew. Chem., Int. Ed.*, 2013, **52**, 3953–3957.
- 31 Y. Wen, Q. Jia, F. Nan, X. Zheng, W. Liu, J. Wu, H. Ren, J. Ge and P. Wang, *Chem. – Asian J.*, 2019, **14**, 2162–2168.
- 32 X. Jin, X. Sun, G. Chen, L. Ding, Y. Li, Z. Liu, Z. Wang, W. Pan, C. Hu and J. Wang, *Carbon*, 2015, **81**, 388–395.
- 33 W. Shi, X. Li and H. Ma, *Angew. Chem., Int. Ed.*, 2012, **51**, 6432–6435.
- 34 R. Kumari, K. Pal, P. Karmakar and S. K. Sahu, *ACS Appl. Nano Mater.*, 2019, **2**, 5900–5909.
- 35 B. Shi, Y. Su, L. Zhang, R. Liu, M. Huang and S. Zhao, *Biosens. Bioelectron.*, 2016, **82**, 233–239.
- 36 Y. Z. Fan, Q. Tang, S. G. Liu, Y. Z. Yang, Y. J. Ju, N. Xiao, H. Q. Luo and N. B. Li, *Appl. Surf. Sci.*, 2019, **492**, 550–557.
- 37 B. Kong, A. Zhu, C. Ding, X. Zhao, B. Li and Y. Tian, *Adv. Mater.*, 2012, **24**, 5844–5848.
- 38 Y. Wang, L. Lu, H. Peng, J. Xu, F. Wang, R. Qi, Z. Xu and W. Zhang, *Chem. Commun.*, 2016, **52**, 9247–9250.
- 39 J. Shangguan, D. He, X. He, K. Wang, F. Xu, J. Liu, J. Tang, X. Yang and J. Huang, *Anal. Chem.*, 2016, **88**, 7837–7843.
- 40 S. Hu, X. Meng, F. Tian, W. Yang, N. Li, C. Xue, J. Yang and Q. Chang, *J. Mater. Chem. C*, 2017, **5**, 9849–9853.
- 41 X. Jia, J. Li and E. Wang, *Nanoscale*, 2012, **4**, 5572–5575.
- 42 P. Yang, Z. Zhu, T. Zhang, W. Zhang, W. Chen, Y. Cao, M. Chen and X. Zhou, *Small*, 2019, **15**, e1902823.
- 43 S. Qu, D. Zhou, D. Li, W. Ji, P. Jing, D. Han, L. Liu, H. Zeng and D. Shen, *Adv. Mater.*, 2016, **28**, 3516–3521.
- 44 Y. Liu, H. Gou, X. Huang, G. Zhang, K. Xi and X. Jia, *Nanoscale*, 2020, **12**, 1589–1601.
- 45 B. Wang, J. Li, Z. Tang, B. Yang and S. Lu, *Sci. Bull.*, 2019, **64**, 1285–1292.
- 46 K. Hola, M. Sudolska, S. Kalytchuk, D. Nachtigallova, A. L. Rogach, M. Otyepka and R. Zboril, *ACS Nano*, 2017, **11**, 12402–12410.
- 47 Y. Chen, M. Zheng, Y. Xiao, H. Dong, H. Zhang, J. Zhuang, H. Hu, B. Lei and Y. Liu, *Adv. Mater.*, 2016, **28**, 312–318.
- 48 S. Paulo-Mirasol, E. Martinez-Ferrero and E. Palomares, *Nanoscale*, 2019, **11**, 11315–11321.
- 49 Z. Xu, C. Wang, K. Jiang, H. Lin, Y. Huang and C. Zhang, *Part. Part. Syst. Charact.*, 2015, **32**, 1058–1062.
- 50 Y. Liu, W. Duan, W. Song, J. Liu, C. Ren, J. Wu, D. Liu and H. Chen, *ACS Appl. Mater. Interfaces*, 2017, **9**, 12663–12672.
- 51 D. Qu, D. Yang, Y. Sun, X. Wang and Z. Sun, *J. Phys. Chem. Lett.*, 2019, **10**, 3849–3857.
- 52 J. S. Anjali Devi, R. S. Aparna, R. R. Anjana, J. Nebu, S. M. Anju and S. George, *J. Phys. Chem. A*, 2019, **123**, 7420–7429.



# Efficient Preparation of Hydrophilic Boron Nitride Nanosheets for Human Heat Dissipation Applications

Chunjin Chen, Baiqing Yu, Hongjie Jia, Zhun Ran, Jianle Zhuang, Xuejie Zhang, Bingfu Lei, Yingliang Liu, and Chaofan Hu\*



Cite This: <https://doi.org/10.1021/acsanm.4c01100>



Read Online

ACCESS |

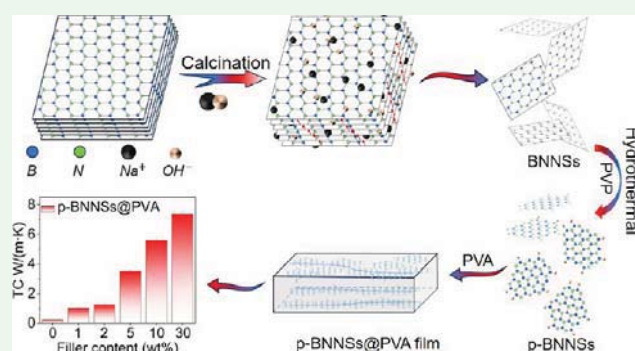
Metrics & More

Article Recommendations

Supporting Information

**ABSTRACT:** Hexagonal boron nitride (h-BN) is commonly used as a polymer filler to produce wearables with outstanding heat dissipation properties and excellent biocompatibility. However, the poor interfacial compatibility of h-BN in polymers, resulting from the chemical inertness of boron nitride and the low stripping efficiency of h-BN, limits its performance in thermal conductivity (TC) applications. To address these issues, we innovatively introduced a solid-phase molten salt method combined with a hydrothermal exfoliation strategy in this work to obtain poly(*N*-vinyl-2-pyrrolidone) stabilized hydrophilic boron nitride nanosheets (p-BNNSs). Notably, the method is simple and efficient, and the prepared p-BNNSs have fewer layers and higher hydrophilicity. The TC of the 30 wt % p-BNNSs@PVA films reached  $7.38 \text{ W m}^{-1} \text{ K}^{-1}$ , representing a 3244% enhancement compared to pure PVA films. The nanofiber film was fabricated using electrospinning with the optimal filling ratio, successfully facilitating heat conduction on human skin. Finally, it is proposed that the use of nanofiber films as advanced medical films offers a practical solution to the negative impact of hot weather on wound healing.

**KEYWORDS:** hydrophilic boron nitride nanosheets, exfoliation, thermal conductivity, electrospinning, medical films



## INTRODUCTION

Hexagonal boron nitride (h-BN) is considered a typical two-dimensional material and is often referred to as “white graphene” due to its hexagonal crystal system, similar lattice constants, and white color.<sup>1–3</sup> However, compared to graphene, h-BN has greater stability. It can remain stable in air at 800 °C and does not react with acids and bases at room temperature. Due to its wide bandgap of 5.9 eV, h-BN is electrically insulating and exhibits strong ultraviolet absorption.<sup>4,5</sup> h-BN is often utilized as a polymer filler to enhance the thermal conductivity (TC) of polymers owing to the high TC up to  $400 \text{ W m}^{-1} \text{ K}^{-1}$ .<sup>6–9</sup>

However, the chemical inertness and hydrophobic nature of h-BN make it an insufficiently compatible filler with polymers for building an effective TC network.<sup>10</sup> This greatly restricts the potential application of h-BN in TC. Therefore, it is especially important to exfoliate and functionalize h-BN.<sup>11</sup> By exfoliating h-BN into boron nitride nanosheets (BNNSs) with a small number of layers and introducing hydrophilic functional groups (–OH, –NH<sub>2</sub>, etc.) on its surface, the interlayer interaction force is weakened.<sup>12,13</sup> This enlarges the aspect ratio and specific surface area, effectively reducing phonon scattering and constructing a more efficient TC network, resulting in higher TC.<sup>14,15</sup> Common exfoliation methods include ball milling,<sup>16</sup> liquid-phase sonication,<sup>17</sup>

Hummer’s method,<sup>12</sup> microwave method,<sup>18</sup> etc. Each of these methods has its own advantages and disadvantages. For example, although ball milling has been proven to be one of the best methods to exfoliate h-BN, ball milling is often accompanied by a large amount of interpolant consumption (basically 5–60 times that of h-BN). In addition, the ball milling process reduces the transverse dimensions of BNNSs and is prone to introduce defects that adversely affect the application of BNNSs.<sup>19</sup> Liquid-phase sonication is a simple and economical method to achieve the exfoliation of h-BN through the ultrasonic cavitation effect, and it is possible to select solvents with similar surface tensile energy to h-BN through Hansen Dissolution Parameter Theory (HSP) [e.g., *N*-methylpyrrolidone (NMP), *N,N*-dimethylformamide (DMF), and isopropanol (IPA)] to achieve effective exfoliation efficiency. But the use of polar organic solvents is prone to environmental pollution, and the exfoliation mechanism still needs further study.<sup>7</sup> Another important factor

**Received:** February 23, 2024

**Revised:** April 16, 2024

**Accepted:** April 24, 2024

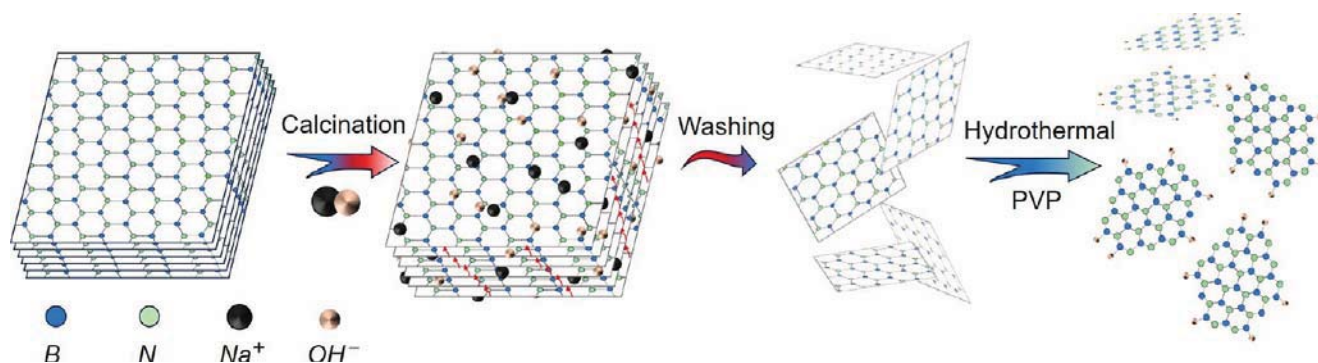


Figure 1. Flowchart of the preparation of p-BNNSs.

in improving the TC of polymer composites is to create a continuous TC network by controlling the distribution of boron nitride in the polymer matrix, for example, through electrospinning. Electrospinning allows for the alignment of boron nitride along the shear flow during the spinning process, resulting in a highly oriented microstructure in the axial direction of the film.<sup>20</sup> This further enhances the TC of the p-BNNSs@PVA films.

In this paper, we present a simple and cost-effective method for achieving the exfoliation and functionalization of h-BN to produce hydrophilic boron nitride nanosheets (p-BNNSs) with a few layers. The process is primarily divided into two steps. First, the intercalation and exfoliation of h-BN are achieved using the solid-phase molten salt method under high-temperature conditions. This results in an increase in the h-BN layer spacing, and alkali ions are inserted into the layer to strip h-BN, thereby obtaining BNNSs. Then, p-BNNSs are obtained by using a small amount of polyvinylpyrrolidone (PVP) as a dispersing agent in a hydrothermal reaction with BNNSs. Under the influence of PVP and high pressure, the stripping energy of BNNSs was reduced, leading to further exfoliation and the grafting on the surface. To confirm the effectiveness of the method, the morphology, components, hydrophilicity, and UV absorption of p-BNNSs were evaluated. Moreover, p-BNNSs can be well-dispersed in PVA in a tightly ordered arrangement, forming a completely TC network. The p-BNNSs@PVA films showed a high TC of  $7.38 \text{ W m}^{-1} \text{ K}^{-1}$  with a p-BNNSs content of 30 wt %. To enhance the TC of the films, the mechanical properties and TC of the p-BNNSs@PVA film were used as a reference to determine the optimal doping ratio for preparing the p-BNNSs@PVA nanofiber film through electrospinning and to realize the TC test on the human skin. Finally, it is proposed to utilize the nanofiber film as a pharmaceutical film, which will improve the pharmaceutical film's capacity to quickly dissipate heat, inhibit bacteria, and provide protection against ultraviolet rays.

## RESULTS AND DISCUSSION

**Morphology and Structure Characterization of p-BNNSs.** Figure 1 depicts the flowchart of the two-step approach for stripping and functionalizing p-BNNSs. The first step involves the solid-phase molten-salt method, which utilizes alkali-metal ions to shear and intercalate under high-temperature conditions, achieving the stripping of h-BN. This method differs from the conventional alkali thermal stripping method in that it does not require a reaction still to create high-pressure reaction conditions, but only high-temperature conditions.<sup>21</sup> Additionally, the amount of alkali used in this

method is greatly reduced. It is well-known that h-BN chemically interacts with NaOH at high temperatures, resulting in the loss of boron nitride ( $\text{BN} + 3\text{NaOH} \rightarrow \text{Na}_3\text{BO}_3 + \text{NH}_3$ ). So as to reduce the consumption of h-BN and improve the stripping effect of BNNSs, the reaction temperature, time, and amount of alkali in the solid-phase molten salt method were adjusted. The optimal conditions were determined to be calcined at  $600^\circ\text{C}$  for 2 h with a mass ratio of NaOH to h-BN of 2:1. During the solid-phase molten salt method, h-BN undergoes thermal expansion, increasing the interlayer spacing. Additionally, alkali ions continuously infiltrate the interlayers of boron nitride due to thermal movement, facilitating the exfoliation of h-BN through interpolation and shearing. As shown in Figure 2a, the untreated h-BN has large lateral sizes ( $2\text{--}6 \mu\text{m}$ ) and substantial layer accumulations with thicknesses ranging from tens to hundreds of nanometers (Figure 2g,j). The BNNSs obtained by using the solid-phase molten salt method have reduced lateral sizes of about  $2 \mu\text{m}$ . It is evident that the BNNSs curl under the intercalation of alkali ions during the stripping process (Figure 2b). Additionally, Figure 2h,k demonstrate that the thickness of the BNNSs is significantly reduced to only about  $4\text{--}5 \text{ nm}$ . It is evident that the solid-phase molten salt method, conducted under these experimental conditions, produces a better stripping effect, resulting in a 73.4% yield of BNNSs. The second step of functionalization is based on the first step, in which BNNSs and PVP are codispersed in water for a hydrothermal reaction to achieve further functionalization of BNNSs (Figure 1). Using PVP as the hydrophilic modifier can effectively enhance the hydrothermal effect of BNNSs. This is evident from the SEM images that the resulting p-BNNSs do not exhibit obvious agglomeration (Figure 2c). Furthermore, the thickness of the p-BNNSs is further reduced to only 3 nm after additional hydrothermal stripping (Figure 2i,l). Figure 2d depicts the TEM image of h-BN. The darker color indicates a larger thickness of h-BN. In contrast, the corresponding TEM image of p-BNNSs (Figure 2e) appears almost transparent, suggesting a less-layered structure of the nanosheets. The high-magnification image (Figure 2f) at its center reveals the layered structure of p-BNNSs, with the figure showing that the number of p-BNNSs layers is 9, consistent with the thickness shown in the AFM image (Figure 2i,l). The HRTEM image in the inset shows that the interlayer thickness of p-BNNSs is  $0.36 \text{ nm}$ , which is attributed to the increased interlayer spacing resulting from the high-temperature expansion and ion intercalation. The water contact angles of h-BN and p-BNNSs were measured after compressing the tablets. It was found that the contact angle of h-BN was  $105.92^\circ$ , indicating hydrophobicity,



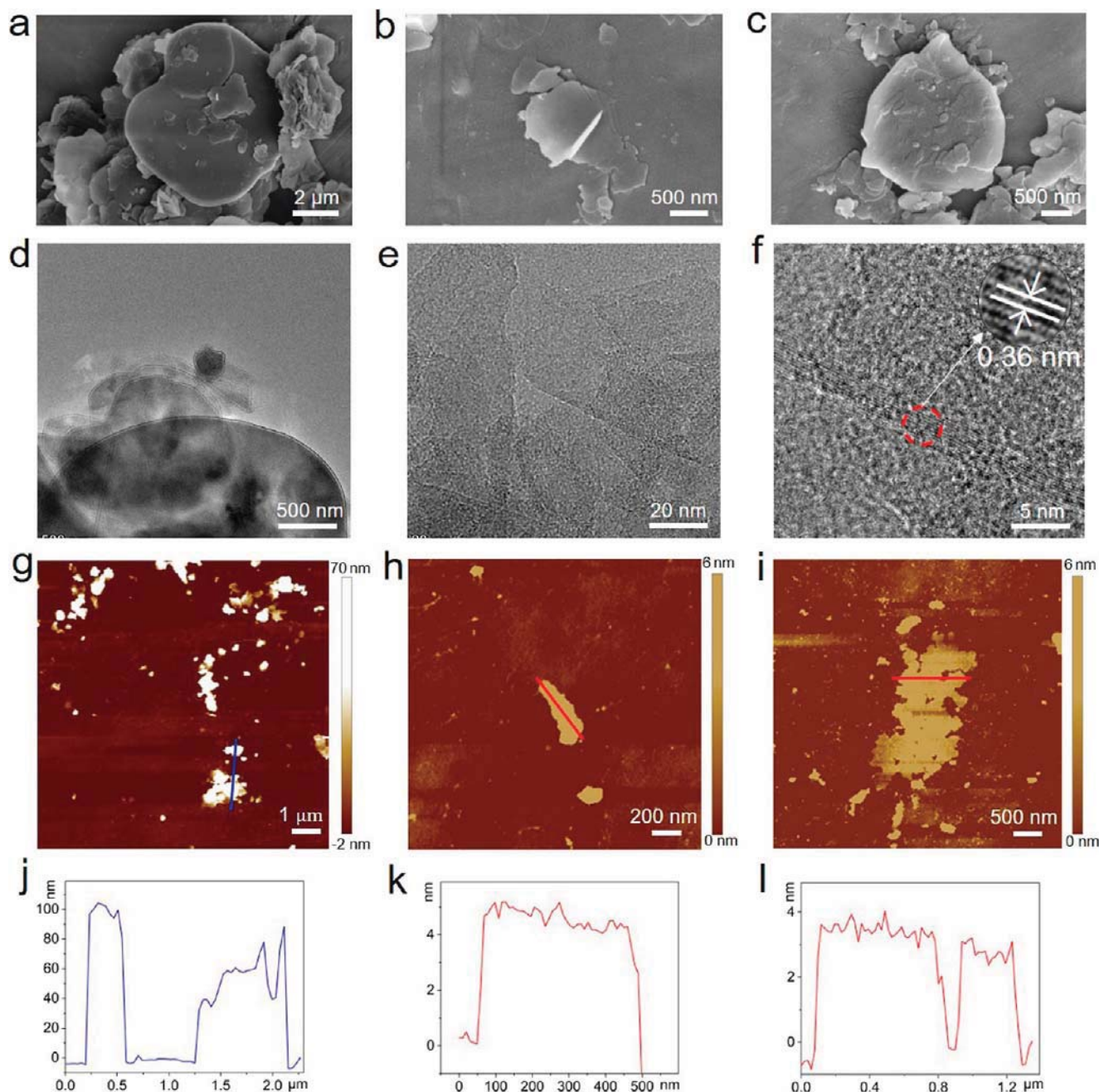


**Figure 2.** Morphology characterization of h-BN, BNNSs, and p-BNNSs. (a) SEM images of pristine h-BN, sized at 2–6 μm. (b) SEM images of BNNSs. (c) SEM images of p-BNNSs. (d) TEM image of h-BN. (e,f) TEM image of p-BNNSs. Inset: HRTEM image within the circle. (g) AFM image of h-BN; the inset shows the corresponding height profile. (h,i) AFM image of BNNSs and p-BNNSs. (j–l) Corresponding thickness distribution curves.

while the contact angle of p-BNNSs was only 32.69°, indicating good hydrophilicity (Figure S1). Further, 2 mg/mL of h-BN and p-BNNS dispersions were prepared separately and ultrasonically dispersed for 10 min. The dispersion was then observed. As shown in Figure S2, h-BN was not well dispersed in the water after sonication due to its hydrophobic nature, and a significant amount remained suspended on the water surface. After resting for 1 day, h-BN was found to have settled. In contrast, p-BNNSs were well dispersed in water and maintained a good suspension stability even after 5 days. In conclusion, microscopic testing and macroscopic observation of p-BNNSs can effectively demonstrate that p-BNNSs have

been exfoliated into boron nitride nanosheets with a small number of layers, high aspect ratios, and good hydrophilicity and suspension stability.

The crystal structures of h-BN and p-BNNSs were further tested by XRD and Raman. As shown in Figure 3a, the peaks of h-BN at 26.72, 41.59, 43.82, 50.18, and 55.14° correspond to the (002), (100), (101), (102), and (104) crystal planes of h-BN, which are of a typical hexagonal crystal structure. The position of the diffraction peaks of p-BNNSs corresponds to that of h-BN, but the intensity of the characteristic peaks at the (002) crystal plane is significantly reduced and the width is increased, which is attributed to the significant reduction of the



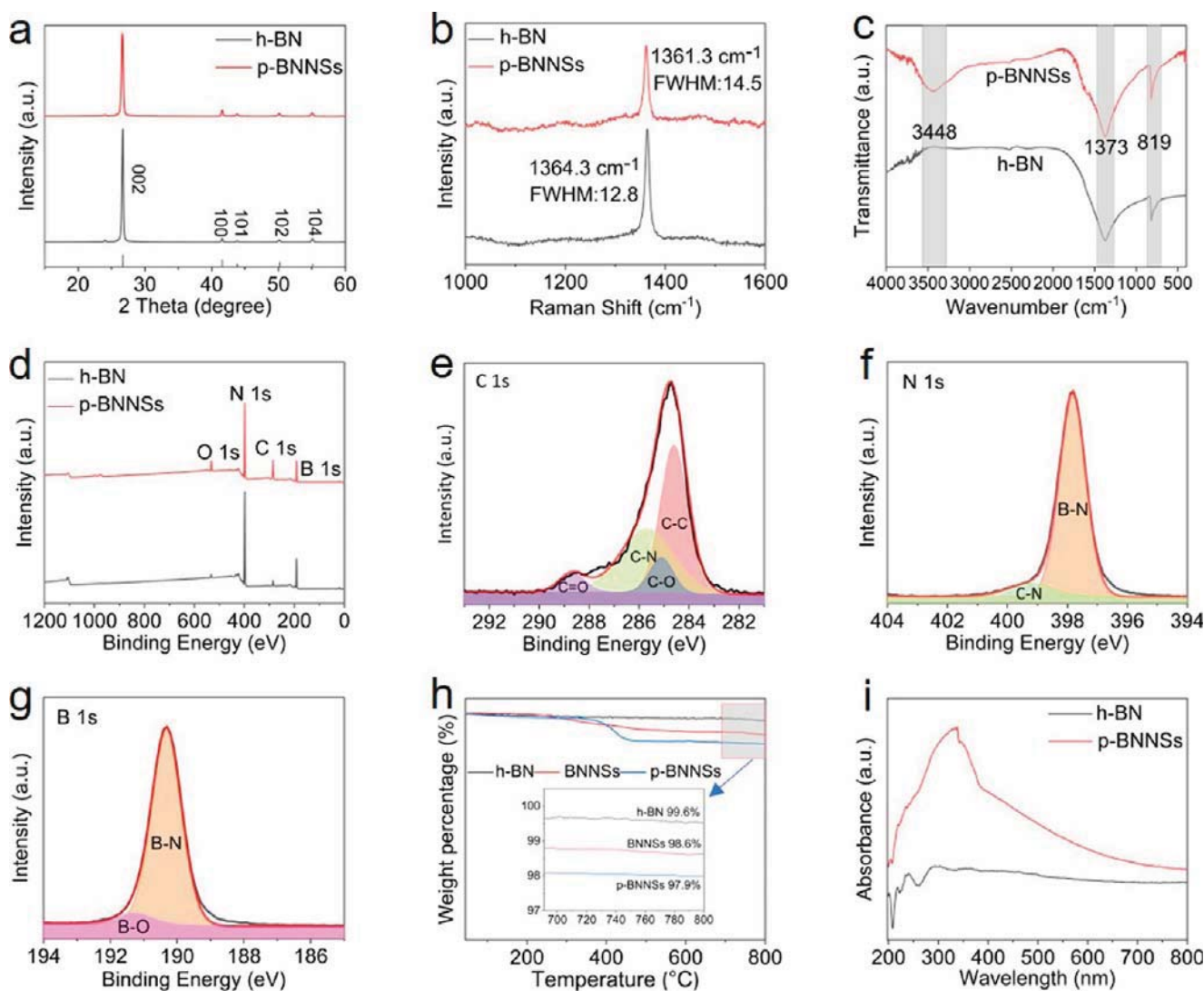


**Figure 3.** Composition and structural characterization of BN. (a) XRD patterns, (b) Raman spectra, and (c) FT-IR spectra of h-BN and p-BNNSs. (d) Full XPS spectrum of h-BN and p-BNNSs. (e–g) C 1s, N 1s, B 1s spectra of p-BNNSs. (h) TGA results of h-BN, BNNSs, and p-BNNSs. (i) UV-vis absorption curves of h-BN and p-BNNSs.

size and thickness of the p-BNNSs after exfoliation and functionalization and the reduction of the degree of extension/ordered stacking in the *c*-direction.<sup>19,22</sup> Figure 3b shows the Raman spectra of the h-BN and p-BNNSs. h-BN's band at 1364.3  $\text{cm}^{-1}$  belongs to the B–N high-frequency vibrational mode ( $E_{2g}$ ), whereas the corresponding peak of p-BNNSs are slightly red-shifted to 1361.3  $\text{cm}^{-1}$ , indicating that the interlayer interactions of p-BNNSs are weakened and it has been exfoliated into boron nitride nanosheets with only few layers.<sup>23</sup> Moreover, their half-peak full width increased from 12.8 to 14.5, further indicating that the crystallinity of p-BNNSs was reduced and the crystal size and thickness decreased.<sup>24</sup> To further test the functionalization effect of p-BNNSs, the FTIR spectra of h-BN and p-BNNSs were tested (Figure 3c), and they both had strong absorption peaks at 819 and 1373  $\text{cm}^{-1}$ , which were attributed to the out-of-plane bending vibration of B–N–B and the in-plane stretching vibration of B–N,<sup>25</sup> but the peaks of p-BNNSs were significantly narrower than those of h-BN, which might be due to the fact that p-BNNSs has a smaller thickness.<sup>26</sup> But unlike the spectrum of h-BN, p-BNNSs have a strong

absorption peak at 3448  $\text{cm}^{-1}$  from the –OH stretching vibration, indicating that p-BNNSs were successfully grafted with –OH after functionalization. Next, we used XPS to characterize the elemental composition and structure of h-BN and p-BNNSs, and Figure 3d shows the full-scan photoelectron spectra, with peaks at approximately 191, 285, 398, and 532 eV corresponding to the elements B, C, N, and O, respectively,<sup>27</sup> where the trace C and O elements in h-BN are supposed to originate from moisture and C impurities in the air. But from the full spectrum of p-BNNSs, it can be seen that there is a significant increase in its O element content, with the atomic ratio calculated to be 4.51%, which is attributed to the fact that the hydroxyl group binds to the B element through covalent bonding and is successfully grafted on the surface of p-BNNSs. The content of the C element in p-BNNSs also increased significantly, which mainly came from the test background pollution and the C residue in the hydrothermal process. In Figure 3e, the high-resolution XPS spectrum of C 1s is mainly divided into four peaks of 284.6, 285.1, 285.7, and 288.8 eV, which belong to C–C, C–O, C–N, and C=O respectively,<sup>27</sup> where the presence of C=O bonds mainly originates from the

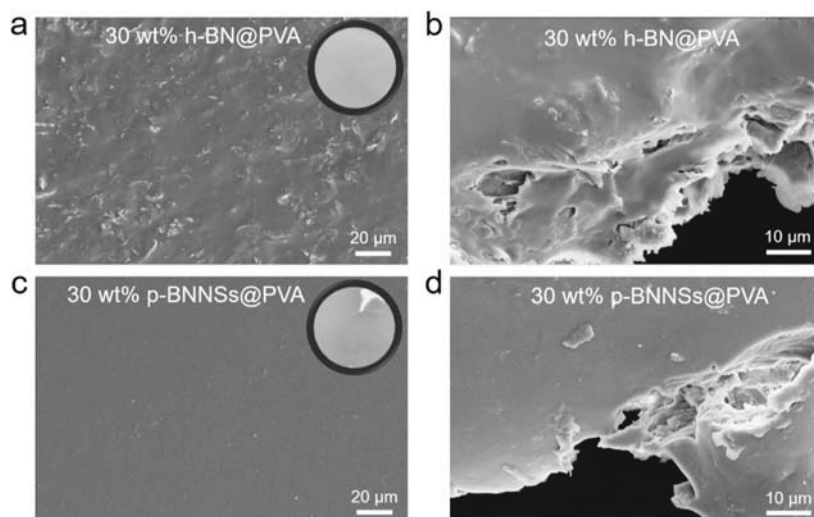


**Figure 4.** Characterization of p-BNNSs@PVA films. (a) Surface morphology of the 30 wt % h-BN@PVA film under SEM; the inset shows the 30 wt % h-BN@PVA film. (b) Morphology of the 30 wt % h-BN@PVA film at fracture. (c) Surface morphology of the 30 wt % p-BNNSs@PVA film under SEM; the inset shows the 30 wt % p-BNNSs@PVA film. (d) Morphology of the 30 wt % p-BNNSs@PVA film at fracture.

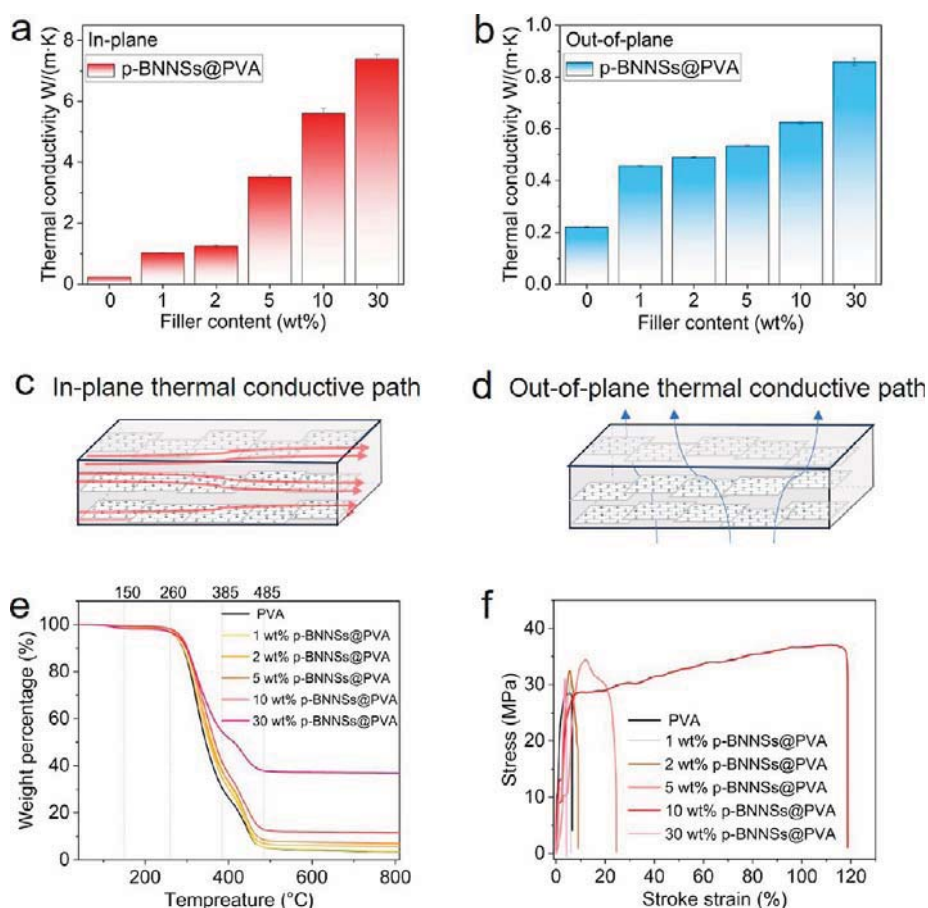


**Figure 5.** TC and mechanical properties of p-BNNSs@PVA films. (a) In-plane TC of p-BNNSs@PVA films. (b) Out-of-plane TC of p-BNNSs@PVA films. (c) Schematic of the in-plane TC path of p-BNNSs@PVA films. (d) Schematic of the out-of-plane TC path of p-BNNSs@PVA films. (e) TGA curves of p-BNNSs@PVA films with different doping concentrations. (f) Stress–strain curves of p-BNNSs@PVA films.

residual PVP in the hydrothermal reaction. The N 1s spectral band (Figure 3f) has two characteristic peaks at 397.8 and 399.4 eV, respectively, corresponding to the B–N and C–N bonds, where the presence of the C–N bond corresponds to

the one in the C 1s spectral band. In addition, the fitting curve of B 1s shows (Figure 3g) that in addition to the B–N bond at 190.3 eV, there is also a weaker peak at 191.4 eV, which is a characteristic peak of the B–O bond, and the presence of the

B–O bond further suggests that –OH was successfully grafted on the surface of p-BNNSs.<sup>12</sup> After that, thermogravimetric analysis of h-BN, BNNSs, and p-BNNSs was carried out under a nitrogen atmosphere to study their thermal stability, and Figure 3h shows their TGA curves, from which it can be seen that the boron nitride, whether treated or not, exhibits good thermal stability. The mass loss of h-BN from room temperature to 800 °C is little and that 0.4% mass loss should be originated from water vapor. The residual mass of BNNSs after heating is 98.6% of the original mass, which indicates that a small amount of hydroxyl group is introduced at the stage of the solid-phase molten-salt method while NaOH strips BNNSs. The residual mass of p-BNNSs is 97.9%, which indicates that the hydroxyl grafting rate is 2.1% after exfoliation and functionalization of p-BNNSs.<sup>10</sup> Finally, the UV absorption properties of h-BN and p-BNNSs were tested (Figure 3i);<sup>28</sup> as we can see from the figure, p-BNNSs have significantly improved UV absorption properties compared to h-BN, with good absorption properties in the whole UV band. The above data analysis provides strong and valuable evidence that p-BNNSs have been exfoliated into boron nitride nanosheets with fewer layers and successfully grafted with hydroxyl functional groups for the functionalization of p-BNNSs.

**Composition and Morphology of p-BNNSs@PVA Films.** In the production of polymer films using water as a solvent, the size, thickness, and hydrophilicity of the filler, along with its compatibility with the polymer and dispersion conditions, will affect the properties of the resulting films. Figure 4a depicts the surface morphology of a 30 wt % h-BN@PVA film under SEM. It is evident that the surface of the film is not flat and contains numerous protrusions. This is attributed to the large size and thickness of h-BN, which is hydrophobic and fails to form cross-links with PVA during composite film preparation. Consequently, it tends to accumulate in the PVA, leading to disordered distribution and an increased number of protrusions and defects in the polymer films.<sup>6,29</sup> The SEM image of the 30 wt % h-BN@PVA film at the fracture (Figure 4b) also reveals the presence of numerous defects and cavities within the film as well as h-BN particles stacked together. Figure 4c depicts the surface morphology of p-BNNSs@PVA films filled with the same mass fraction. p-BNNSs@PVA films have a flat and smooth surface compared with h-BN-filled films. The thin surface in the inset even appears to be reflective, which is attributed to the fact that the p-BNNSs have been exfoliated and functionalized to become hydrophilic boron nitride nanosheets with only a small number of layers. During the film preparation process, the p-BNNSs can cross-link well with PVA and are uniformly dispersed in PVA in a tightly ordered arrangement. Similarly, in the image at the fracture (Figure 4d), the p-BNNSs@PVA film is very dense and does not show defects and cavities inside the film. p-BNNSs exhibit strong in-plane orientation in PVA, which significantly enhances the TC of PVA films.

**Thermal Conductivity and Mechanical Properties of p-BNNSs@PVA Films.** The TC of pure PVA as well as PVA films with 1, 2, 5, 10, and 30 wt % p-BNNSs was initially measured and calculated. Figure 5a depicts the in-plane TC diagram. The picture illustrates that incorporating p-BNNSs into PVA as a filler effectively enhances the TC of the PVA film. Moreover, with the increase in p-BNNSs content, the in-plane TC of p-BNNSs@PVA films also increased rapidly. The in-plane TC of 30 wt % p-BNNSs@PVA films even reached

7.38 W m<sup>-1</sup> K<sup>-1</sup>, which was 33.44 times that of the pure PVA films. This is attributed to the fact that p-BNNSs, as a thermally conductive filler, forms a tightly ordered arrangement when cross-linked with PVA, thus constructing a good TC network. This network effectively enhances phonon scattering, allowing heat to be rapidly conducted out and resulting in high TC. The in-plane TC paths of the p-BNNSs@PVA films are depicted in Figure 5c. The p-BNNSs@PVA films were analyzed by XRD, and the degree of orientation ( $\delta$ ) of the p-BNNSs was calculated (Figure S6). The  $\delta$  of the films, at only 0.356%, indicates a highly horizontal orientation distribution of p-BNNSs in PVA.<sup>30</sup> Figure 5b illustrates the out-of-plane TC plots of p-BNNSs@PVA films, demonstrating a significant increase in their out-of-plane TC with the introduction of p-BNNSs. Specifically, the out-of-plane TC was enhanced by a factor of 3.89 at a p-BNNSs content of 30 wt %. Figure 5d depicts the path diagram of the out-of-plane TC of the p-BNNSs@PVA films. The ordered stacking of p-BNNSs layers provides paths for phonon scattering, thus improving the out-of-plane TC of p-BNNSs@PVA films. Subsequently, the TGA curves of p-BNNSs@PVA films under a nitrogen atmosphere are provided in Figure 5e. The thermal degradation of p-BNNSs@PVA films is similar to that of the pure PVA film, exhibiting three stages of mass loss. The mass loss below 150 °C mainly originates from the water adsorbed in the film, while the mass loss between 260 and 385 °C is due to the breakage of PVA chains and pyrolysis of functional groups. The combustion of the remaining carbonaceous material in the film at 385–485 °C results in further weight loss.<sup>31</sup> Comparing with the pure PVA film, it is evident that the thermal stability of the p-BNNSs@PVA film is significantly improved. As the amount of p-BNNSs increases, the thermal stability of the p-BNNSs@PVA film also improves.

The introduction of p-BNNSs also significantly improves their mechanical properties. To evaluate the mechanical properties of p-BNNSs@PVA films, mechanical samples with different doping concentrations of p-BNNSs@PVA were fabricated separately (Figure S3), and tensile tests were conducted. The stress–strain curves were obtained from these tests (Figure 5f). From the figure, it is evident that pure PVA films can withstand a maximum stress of only 28.36 MPa and a strain of 6.54%. However, with an increase in the p-BNNSs content, the maximum stress and strain that p-BNNSs@PVA films can withstand initially increase and then decrease. The maximum values were observed when the p-BNNSs content was 10 wt %. The maximum stress of 10 wt % p-BNNSs@PVA films reached 37.09 MPa, and the elongation at break was 118.64%, resulting in a 30.78% increase in tensile strength and a 17.14-fold increase in tensile flexibility compared to pure PVA films. The compactness and stronger interfacial interactions of p-BNNSs@PVA films explain the observed behavior.<sup>32</sup> Nevertheless, as the p-BNNSs content increased to 30 wt %, the stress and strain of the resulting films decreased dramatically to 31.00 MPa and 4.18%, respectively. Figure S5 shows the stress–strain curves of PVA films with 10, 20, 25, and 30% loading contents. As shown in Figure S5, the strain–stress of the film is optimal at a content of 10% and decreases gradually as the content continues to increase. This decrease was attributed to the high p-BNNSs content affecting the cross-linking network of PVA and the intrinsic brittleness of hexagonal boron nitride.<sup>6</sup> The high hydrophilicity of p-BNNSs, its fewer layers, and larger aspect ratio enable it to cross-link with PVA, resulting in a tightly ordered arrangement.



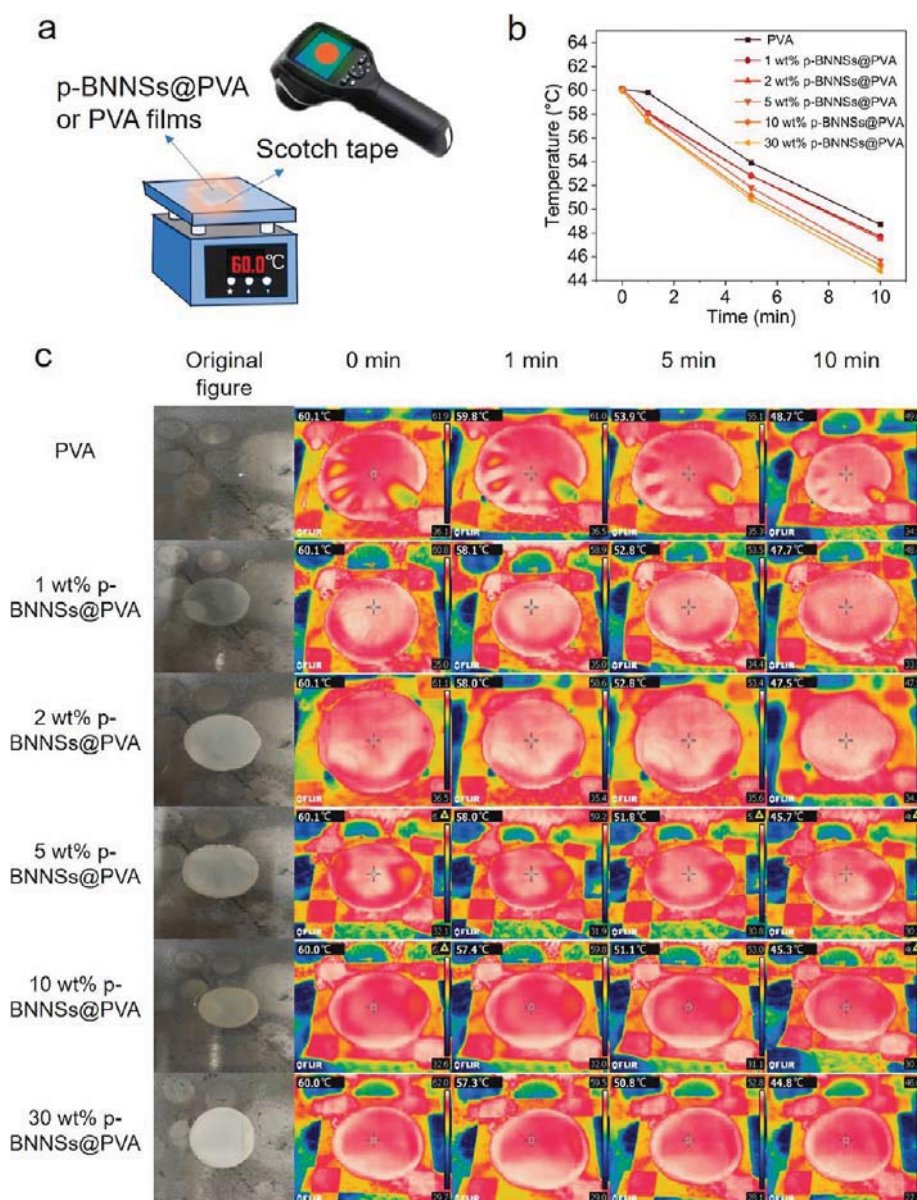


**Figure 6.** Thermal dissipation of p-BNNSs@PVA films. (a) Schematic diagram for the characterization of thermal management of p-BNNSs@PVA films. (b) Surface temperature of p-BNNSs@PVA (0, 1, 2, 5, 10, and 30 wt %) films with different mass fractions as a function of time. (c) Corresponding infrared thermography images.

This arrangement provides phonon scattering paths, greatly increasing the TC and mechanical properties of the p-BNNSs@PVA films.

**Heat Dissipation Performance of p-BNNSs@PVA Films.** The TC test described above demonstrates that p-BNNSs@PVA films exhibit excellent TC, and the TC of the composite films increases with the higher p-BNNSs doping concentration. To further confirm the TC of p-BNNSs@PVA films, the films' actual heat dissipation capability was tested by using infrared thermography. As depicted in Figure 6a, pure PVA films and p-BNNSs@PVA films with varying mass fractions were attached to a heating table using transparent adhesive tape. Subsequently, they were heated to 60 °C, and the surface temperatures of the films at the same location were recorded 1, 5, and 10 min after the heating was turned off using an infrared thermography camera to assess the heat dissipation properties of the films. Figure 6b illustrates the

surface temperatures of p-BNNSs@PVA films with different mass fractions during the same time period after cessation of heating. As shown in the line graphs of films, the surface temperatures of pure PVA, 1, 2, 5, 10, and 30 wt % p-BNNSs@PVA films decreased from 60 to 48.7, 47.7, 47.5, 45.7, 45.3, and 44.8 °C, respectively. The rate at which heat dissipates from the film directly correlates with its TC. A higher TC results in a faster heat dissipation rate. The inclusion of p-BNNSs can notably enhance the heat dissipation rate of PVA films, and this rate increases with higher doping amounts. When the mass fraction of p-BNNSs reaches 30 wt %, the heat dissipation rate of p-BNNSs@PVA films reaches its maximum. After the heating is stopped for 10 min, the surface temperature of the films is reduced by 15.2 °C, whereas that of the pure PVA films is only reduced by 11.4 °C. The infrared thermogram captured by the thermal imager (Figure 6c) reveals that the surface temperature of the pure PVA film is not

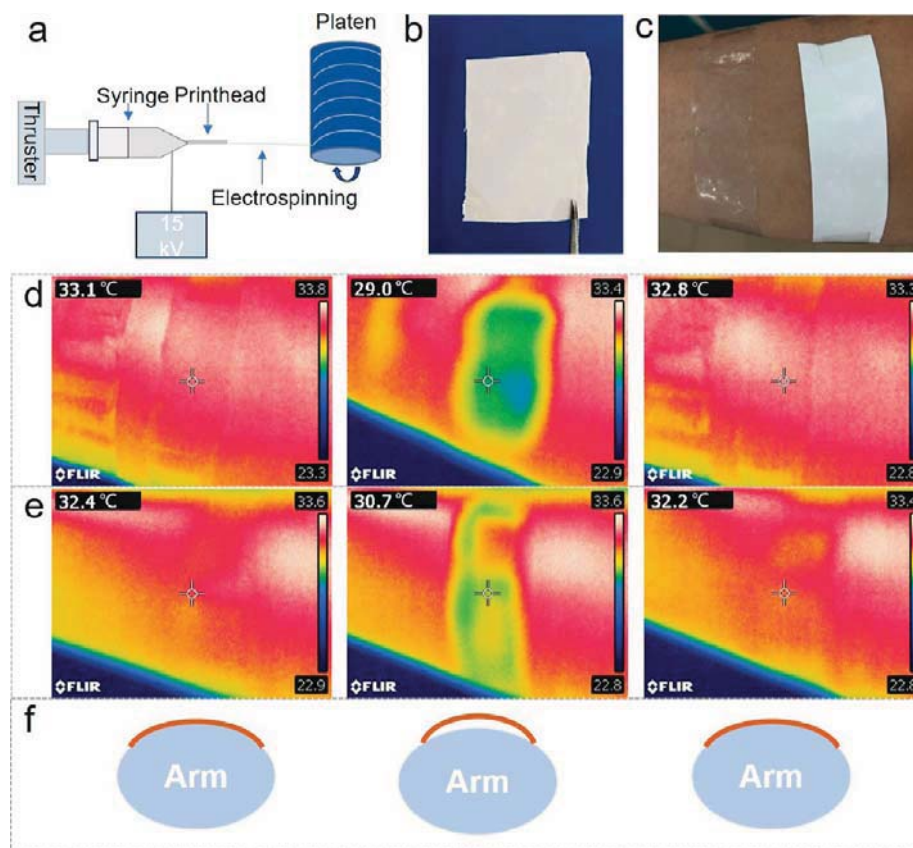


**Figure 7.** Thermal cooling properties of p-BNNSs@PVA nanofiber films. (a) Schematic diagram of p-BNNSs@PVA nanofiber films. (b) Thin films prepared by electrospinning. (c) Pure PVA film and nanofiber film were applied to the human arm. (d) Infrared thermography images of nanofiber film during contact-detachment-contact with skin. (e) Infrared thermography images of pure PVA Films during contact-detachment-contact with skin. (f) Schematic diagram of cyclic contact-detachment-contact between film and skin.

evenly distributed. In contrast, the surface temperature of the p-BNNSs@PVA films quickly achieves a uniform distribution, with the entire film exhibiting nearly the same surface temperature. This observation suggests that heat can efficiently diffuse within p-BNNSs@PVA films, indicating their high TC.

**Thermal Conductive Applications of p-BNNSs@PVA Nanofiber Films.** Considering the thermodynamic properties of p-BNNSs@PVA films, it was concluded that 10 wt % p-BNNSs@PVA films had the best performance, which not only had good TC ( $5.61 \text{ W m}^{-1} \text{ K}^{-1}$ ) but also good tensile resistance and toughness ( $37.09 \text{ MPa}$ ), so the same doping concentration was used to prepare p-BNNSs@PVA nanofiber films by electrospinning, as shown in Figure 7a, which is a simple schematic diagram of the electrospinning. Figure 7b shows the demonstration of the film, which is characterized by lightness, softness, and smoothness. The p-BNNSs@PVA nanofiber films have higher TC ( $6.04 \text{ W m}^{-1} \text{ K}^{-1}$ ) compared to that of p-BNNSs@PVA films, although their mechanical strength is reduced (Figure S7). The actual TC of the nanofiber film on human skin was then evaluated using a thermal imager. As shown in Figure 7c, the nanofiber film and the pure PVA film were attached to the human arm with transparent adhesive tape, and the cyclic contact and separation of the film from the skin were controlled by adjusting the tightness of the tape. During the cycling process, the surface temperature change of the film within 2 s was recorded with a thermal imager (Figure 7d). The temperature of the nanofiber film in contact with the skin rapidly increased

to  $33.1^\circ\text{C}$ , and then the tape was loosened, the nanofiber film was separated from the skin, and the surface temperature of the film cooled to  $29.0^\circ\text{C}$  within 2 s. The surface temperature of the nanofiber film was recorded by a thermal imager during the cycling process. When the tape was tightened again to bring the nanofiber film into contact with the skin again, the surface temperature of the film then increased to  $32.8^\circ\text{C}$  immediately. Figure 7f shows a schematic diagram of the cyclic contact-detachment-contact between the film and the arm. However, when the pure PVA film was used instead (Figure 7e), the pure PVA film was  $32.4^\circ\text{C}$  after contact with the skin, and the temperature remained at  $30.7^\circ\text{C}$  for 2 s after separation from the skin and slowly increased to  $32.2^\circ\text{C}$  for 2 s after close contact with the skin again. The calculation shows that the warming rate of nanofiber film in contact with skin is  $1.9^\circ\text{C/s}$ , while the warming rate of pure PVA film is only  $0.75^\circ\text{C/s}$ . Figure S8 demonstrates that when the nanofiber film has a larger contact area with the skin, heat exchange with the skin occurs more rapidly, leading to a higher heat dissipation efficiency.

Compared to pure PVA film, nanofiber film in contact with human skin or air exhibits higher heat exchange efficiency, which can effectively enhance the dispersion of body heat and create a comfortable temperature environment for individuals. Additionally, leveraging the exceptional mechanical properties and high TC of p-BNNSs@PVA films, along with the antimicrobial and UV-absorbing properties of p-BNNSs (Figure S4), it is suggested to incorporate p-BNNSs into



pharmaceutical-grade poly(vinyl alcohol) at a mass fraction of 10%. Subsequently, p-BNNSs@PVA nanofiber films can be prepared through electrospinning to serve as a novel medical film.<sup>33</sup> p-BNNSs can enhance its UV absorption, antimicrobial, TC, and mechanical properties beyond those of the original poly(vinyl alcohol) medical film. The new medical film prepared using electrospinning technology has several advantages: (1) it is lightweight, thin, and soft, providing gentle contact with the skin, which can enhance patient comfort. (2) The nanofiber film has a large specific surface area and porosity, which can facilitate air exchange and promote wound healing. (3) It has good ultraviolet absorption properties, which can attenuate the patient's wound when exposed to ultraviolet irradiation. (4) The incorporation of boron nitride with antibacterial properties into the pharmaceutical film can inhibit bacterial damage to the wound. (5) Nanofiber film exhibits superhigh TC, which can significantly enhance heat dissipation from the wound. Especially in today's context of global warming and the increasing greenhouse effect, the incorporation of p-BNNSs into pharmaceutical-grade poly(vinyl alcohol) and the production of new pharmaceutical films using electrospinning technology offer a viable solution to mitigate the adverse effects of hot weather on wound healing.

## CONCLUSIONS

In conclusion, this paper proposes an innovative method for the preparation of hydrophilic boron nitride nanosheets using solid-phase and hydrothermal methods to exfoliate and functionalize h-BN. The method is simple and cost-effective. The prepared p-BNNSs have a small number of layers and maintain a good aspect ratio. Its strong hydrophilicity allows it to be suspended and stabilized in water for more than 5 days. Moreover, the resulting p-BNNSs@PVA films exhibit excellent TC and mechanical properties, even with an in-plane TC of  $7.38 \text{ W m}^{-1} \text{ K}^{-1}$ , which is 3244% higher than that of pure PVA films, and the tensile resistance is 30.78% higher. Then, the nanofiber membrane created through electrospinning with the optimal doping ratio exhibited excellent performance in dissipating heat from the human body. Finally, p-BNNSs were proposed to be incorporated into pharmaceutical-grade poly(vinyl alcohol), and the p-BNNSs@PVA nanofiber film was utilized as a novel medical film. Given its properties, it proved to be an effective solution to the challenge of impeding patients' wound healing in hot weather.

## EXPERIMENTAL SECTION

**Materials.** Hexagonal boron nitride (h-BN sized at 2–6  $\mu\text{m}$ ) was provided by Jiupeng New Material Co. Sodium hydroxide (NaOH), polyvinylpyrrolidone (PVP), and poly(vinyl alcohol) (PVA) were purchased from Shanghai Macklin Biochemical Co., Ltd. All chemicals are supplied by the merchant, and no further purification was required.

**Preparation of p-BNNSs.** The preparation of p-BNNSs was mainly divided into two steps; the first step was the solid-phase molten salt method. First, 1 g of h-BN and 2 g of NaOH were weighed according to the mass ratio of 1:2, and then 10 mL of cosolvents of deionized water and ethanol (water/ethanol = 1:1) were added and ultrasonically stirred for 10 min, so that the h-BN and NaOH were uniformly dispersed in the water–ethanol mixture solvents and were fully in contact with each other. After sonication, the mixture was dried in an oven at 80 °C for 12 h to evaporate ethanol and water. Afterward, the mixture was transferred to a muffle furnace at 600 °C for calcination at high temperature for 2 h. At the

end of the calcination, the mixture was washed with water by vacuum filtration to remove NaOH, and BNNSs were obtained by drying. Next, the products are subjected to a second treatment using a liquid-phase hydrothermal reaction method. First, 0.5 g of BNNSs prepared in the first step and 0.25 g of PVP were dispersed in 50 mL of water and subjected to a hydrothermal reaction at 150 °C for 10 h. After the reaction, the residual PVP was removed by vacuum filtration and dried to obtain final p-BNNSs. After the reaction, the residual PVP was removed by vacuum filtration and dried to obtain the final p-BNNSs.

**Preparation of p-BNNSs@PVA Films.** Preparation of p-BNNSs@PVA films was performed by a simple casting method. First, the appropriate amount of p-BNNSs was weighed and dispersed in 50 mL of water using ultrasonic stirring for 5 min to obtain the p-BNNS dispersion solution. The solution was then heated and stirred at 80 °C using an oil bath method. During the heating and stirring process, 4 g of PVA was added to the p-BNNS dispersion. After the 4 h oil bath refluxing process, the resulting p-BNNSs@PVA slurry was poured into preprepared PTFE molds and evenly spread with a spatula. It was then left at room temperature for 10 h to allow for the complete cross-linking of p-BNNSs and PVA, achieving self-assembly. Finally, the film was placed in an oven at 60 °C and dried for 10 h to obtain the final p-BNNSs@PVA film. The p-BNNSs content in the prepared p-BNNSs@PVA films varied at 0, 1, 2, 5, 10, and 30 wt %, respectively. Similarly, h-BN@PVA films were prepared by using untreated h-BN by the same method.

**Preparation of the p-BNNSs@PVA Nanofiber Film.** 0.111 g of p-BNNSs and 1 g of PVA were dispersed into 10 mL of water, and then the mixture was stirred at 80 °C for 5 h to dissolve the PVA and let the p-BNNSs uniformly disperse in the PVA solution to form the spinning solution. After that, the spinning solution was injected by a syringe pump and spun under 15 kV voltage.

**Characterization.** The morphology and structure of h-BN, BNNSs, and p-BNNSs were characterized by field emission scanning electron microscopy (SEM Verios 460), and the surfaces of the h-BN@PVA film and p-BNNSs@PVA film were observed comparatively. Atomic force microscopy (AFM, Park XE7, Korea) was used to observe the morphology and thickness of the h-BN, BNNSs and p-BNNSs. The microstructure of p-BNNSs was observed by transmission electron microscopy (TEM Talos F200S). The crystal structures of h-BN and p-BNNSs were characterized using X-ray diffractometry (XRD Ultima IV) in the  $2\theta$  range from 10 to 80°. FT-IR spectra of p-BNNSs were recorded by using a Fourier transform infrared spectrometer (FT-IR Nicolet IS10). The Raman scattering spectra were measured with a Raman spectrometer (Raman Alpha 300R) under a 523 nm laser excitation. The UV absorption properties of p-BNNSs were measured by using a UV–visible spectrophotometer (UV–vis–UV-2550). X-ray photoelectron spectroscopy (XPS, Thermo Fisher Nexsa) was used to analyze the elemental composition and content of the p-BNNSs surface. Thermogravimetric analysis of h-BN, BNNSs, and p-BNNSs was conducted using a thermogravimetric analyzer (TGA TG209F1LibraTM). The water contact angles of p-BNNSs were measured by a contact angle meter (JC2000C1). The heat dissipation of p-BNNSs@PVA films with different mass fractions after heating to 60 °C was observed by using a heating table and a thermal imager. The density ( $\rho$ ), thermal diffusion coefficient ( $\alpha$ ), and specific heat capacity ( $C_p$ ) of the films were measured using an analytical balance (CPA225D), a TC meter (NETZSCH-LFA 467HT), and a differential scanning calorimeter (NETZSCH-DSC214), respectively, and the thermal conductivities of the films were then calculated according to the formula  $\text{TC} = \alpha \cdot C_p \cdot \rho$ . Stress–strain curves of p-BNNSs@PVA were measured by a universal testing machine (UTM4204).

## ASSOCIATED CONTENT

### Supporting Information

The Supporting Information is available free of charge at <https://pubs.acs.org/doi/10.1021/acsnm.4c01100>.



Water contact angle of h-BN and p-BNNSs; dispersion of h-BN and p-BNNSs in water at different times; mechanical spline of p-BNNSs@PVA with different doping concentrations; UV-vis absorption spectra of 10 wt % p-BNNSs@PVA films; stress-strain curves of 20 and 25 wt % p-BNNSs@PVA films; XRD patterns of p-BNNSs@PVA films; stress-strain curves and TC of the nanofiber films; heat dissipation of the pure PVA film and nanofiber film on EP; and some of the nanofiber membranes for heat dissipation on the EP (PDF)

## AUTHOR INFORMATION

### Corresponding Author

**Chaofan Hu** – Key Laboratory for Biobased Materials and Energy of Ministry of Education/Guangdong Provincial Engineering Technology Research Center for Optical Agriculture, College of Materials and Energy, South China Agricultural University, Guangzhou 510642, P. R. China; [orcid.org/0000-0003-2311-8733](https://orcid.org/0000-0003-2311-8733); Email: [thucf@scau.edu.cn](mailto:thucf@scau.edu.cn)

### Authors

**Chunjin Chen** – Key Laboratory for Biobased Materials and Energy of Ministry of Education/Guangdong Provincial Engineering Technology Research Center for Optical Agriculture, College of Materials and Energy, South China Agricultural University, Guangzhou 510642, P. R. China

**Baiqing Yu** – Key Laboratory for Biobased Materials and Energy of Ministry of Education/Guangdong Provincial Engineering Technology Research Center for Optical Agriculture, College of Materials and Energy, South China Agricultural University, Guangzhou 510642, P. R. China

**Hongjie Jia** – Key Laboratory for Biobased Materials and Energy of Ministry of Education/Guangdong Provincial Engineering Technology Research Center for Optical Agriculture, College of Materials and Energy, South China Agricultural University, Guangzhou 510642, P. R. China

**Zhun Ran** – Key Laboratory for Biobased Materials and Energy of Ministry of Education/Guangdong Provincial Engineering Technology Research Center for Optical Agriculture, College of Materials and Energy, South China Agricultural University, Guangzhou 510642, P. R. China; [orcid.org/0009-0005-1655-7422](https://orcid.org/0009-0005-1655-7422)

**Jianle Zhuang** – Key Laboratory for Biobased Materials and Energy of Ministry of Education/Guangdong Provincial Engineering Technology Research Center for Optical Agriculture, College of Materials and Energy, South China Agricultural University, Guangzhou 510642, P. R. China; [orcid.org/0000-0002-4649-1939](https://orcid.org/0000-0002-4649-1939)

**Xuejie Zhang** – Key Laboratory for Biobased Materials and Energy of Ministry of Education/Guangdong Provincial Engineering Technology Research Center for Optical Agriculture, College of Materials and Energy, South China Agricultural University, Guangzhou 510642, P. R. China; [orcid.org/0000-0002-4029-7000](https://orcid.org/0000-0002-4029-7000)

**Bingfu Lei** – Key Laboratory for Biobased Materials and Energy of Ministry of Education/Guangdong Provincial Engineering Technology Research Center for Optical Agriculture, College of Materials and Energy, South China Agricultural University, Guangzhou 510642, P. R. China; [orcid.org/0000-0002-6634-0388](https://orcid.org/0000-0002-6634-0388)

**Yingliang Liu** – Key Laboratory for Biobased Materials and Energy of Ministry of Education/Guangdong Provincial

Engineering Technology Research Center for Optical Agriculture, College of Materials and Energy, South China Agricultural University, Guangzhou 510642, P. R. China; [orcid.org/0000-0003-1930-0700](https://orcid.org/0000-0003-1930-0700)

Complete contact information is available at: <https://pubs.acs.org/10.1021/acsanm.4c01100>

### Author Contributions

C.C. conceived and designed experiments, fabricated samples, and conducted/analyzed most of the characterizations, and wrote and revised the article. B.Y. was in charge of electrospinning experiments, revised the article. H.J. was responsible for the analysis of XPS data. Z.R. helped with the infrared thermal imaging tests. J.Z. and X.Z. supervised the writing and provided advice. B.L. supervised the writing and provided resources. Y.L. was responsible for project, acquired the funding for research, supervised the writing, and provided resources. C.H. proposed the experimental plan, directed the writing, acquired the funding for research, and provided resources. All authors have given approval to the final version of the manuscript.

### Notes

The authors declare no competing financial interest.

## ACKNOWLEDGMENTS

This work was supported by the National Natural Science Foundation of China (12174119, 52172142), the Natural Science Foundation of Guangdong Province (2023A1515012003).

## REFERENCES

- (1) Kim, S. M.; Hsu, A.; Park, M. H.; Chae, S. H.; Yun, S. J.; Lee, J. S.; Cho, D.-H.; Fang, W.; Lee, C.; Palacios, T.; Dresselhaus, M.; Kim, K. K.; Lee, Y. H.; Kong, J. Synthesis of Large-Area Multilayer Hexagonal Boron Nitride for High Material Performance. *Nat. Commun.* **2015**, *6*, 8662.
- (2) Weng, Q.; Wang, X.; Wang, X.; Bando, Y.; Golberg, D. Functionalized Hexagonal Boron Nitride Nanomaterials: Emerging Properties and Applications. *Chem. Soc. Rev.* **2016**, *45* (14), 3989–4012.
- (3) Luo, W.; Wang, Y.; Hitz, E.; Lin, Y.; Yang, B.; Hu, L. Solution Processed Boron Nitride Nanosheets: Synthesis, Assemblies and Emerging Applications. *Adv. Funct. Mater.* **2017**, *27* (31), 1701450.
- (4) Yu, K. M.; Zou, K.; Lang, H. J.; Peng, Y. T. Nanofriction Characteristics of h-BN with Electric Field Induced Electrostatic Interaction. *Friction* **2021**, *9* (6), 1492–1503.
- (5) Li, L. H.; Chen, Y. Atomically Thin Boron Nitride: Unique Properties and Applications. *Adv. Funct. Mater.* **2016**, *26* (16), 2594–2608.
- (6) An, L.; Gu, R.; Zhong, B.; Wang, J.; Zhang, J.; Yu, Y. Quasi-Isotropically Thermal Conductive, Highly Transparent, Insulating and Super-Flexible Polymer Films Achieved by Cross Linked 2D Hexagonal Boron Nitride Nanosheets. *Small* **2021**, *17* (46), 2101409.
- (7) An, L.; Yu, Y.; Cai, Q.; Mateti, S.; Li, L. H.; Chen, Y. I. Hexagonal Boron Nitride Nanosheets: Preparation, Heat Transport Property and Application as Thermally Conductive Fillers. *Prog. Mater. Sci.* **2023**, *138*, 101154.
- (8) Guo, H.; Niu, H.; Zhao, H.; Kang, L.; Ren, Y.; Lv, R.; Ren, L.; Maqbool, M.; Bashir, A.; Bai, S. Highly Anisotropic Thermal Conductivity of Three-Dimensional Printed Boron Nitride-Filled Thermoplastic Polyurethane Composites: Effects of Size, Orientation, Viscosity, and Voids. *ACS Appl. Mater. Interfaces* **2022**, *14* (12), 14568–14578.
- (9) Han, J.; Du, G.; Gao, W.; Bai, H. An Anisotropically High Thermal Conductive Boron Nitride/Epoxy Composite Based on

Nacre-Mimetic 3D Network. *Adv. Funct. Mater.* **2019**, 29 (13), 1900412.

(10) Wu, N.; Yang, W.; Che, S.; Sun, L.; Li, H.; Ma, G.; Sun, Y.; Liu, H.; Wang, X.; Li, Y. Green Preparation of High-Yield and Large-Size Hydrophilic Boron Nitride Nanosheets by Tannic Acid-Assisted Aqueous Ball Milling for Thermal Management. *Composites, Part A* **2023**, 164, 107266.

(11) Martinez-Jimenez, C.; Chow, A.; Smith McWilliams, A. D.; Marti, A. A. Hexagonal Boron Nitride Exfoliation and Dispersion. *Nanoscale* **2023**, 15 (42), 16836–16873.

(12) Jing, L.; Li, H.; Tay, R. Y.; Sun, B.; Tsang, S. H.; Cometto, O.; Lin, J.; Teo, E. H. T.; Tok, A. I. Y. Biocompatible Hydroxylated Boron Nitride Nanosheets/Poly(Vinyl Alcohol) Interpenetrating Hydrogels with Enhanced Mechanical and Thermal Responses. *ACS Nano* **2017**, 11 (4), 3742–3751.

(13) Jiang, H.; Cai, Q.; Mateti, S.; Yu, Y.; Zhi, C.; Chen, Y. Boron Nitride Nanosheet Dispersion at High Concentrations. *ACS Appl. Mater. Interfaces* **2021**, 13 (37), 44751–44759.

(14) Zhou, Y.; Xu, L.; Liu, M.; Qi, Z.; Wang, W.; Zhu, J.; Chen, S.; Yu, K.; Su, Y.; Ding, B.; Qiu, L.; Cheng, H.-M. Viscous Solvent-Assisted Planetary Ball Milling for the Scalable Production of Large Ultrathin Two-Dimensional Materials. *ACS Nano* **2022**, 16, 10179–10187.

(15) Li, Y. W.; Huang, T. Q.; Chen, M.; Wu, L. M. Simultaneous Exfoliation and Functionalization of Large-Sized Boron Nitride Nanosheets for Enhanced Thermal Conductivity of Polymer Composite Film. *Chem. Eng. J.* **2022**, 442, 136237.

(16) Chen, S.; Xu, R.; Liu, J.; Zou, X.; Qiu, L.; Kang, F.; Liu, B.; Cheng, H.-M. Simultaneous Production and Functionalization of Boron Nitride Nanosheets by Sugar-Assisted Mechanochemical Exfoliation. *Adv. Mater.* **2019**, 31 (10), 1804810.

(17) Elo, T.; Singh Parihar, V.; Nag, R.; Bera, A.; Layek, R. Scalable Synthesis of Highly Exfoliated, Water-Dispersible Boron Nitride Nanosheets for Nano-Fibrillated Cellulose Membrane Toughening. *Chem. Eng. Sci.* **2023**, 276, 118820.

(18) Liu, Z.; Wang, Y. B.; Wang, Z. Y.; Yao, Y. G.; Dai, J. Q.; Das, S.; Hu, L. B. Solvo-Thermal Microwave-Powered Two-Dimensional Material Exfoliation. *Chem. Commun.* **2016**, 52 (33), 5757–5760.

(19) Lei, W.; Mochalin, V. N.; Liu, D.; Qin, S.; Gogotsi, Y.; Chen, Y. Boron Nitride Colloidal Solutions, Ultralight Aerogels and Free-standing Membranes Through One-Step Exfoliation and Functionalization. *Nat. Commun.* **2015**, 6, 8849.

(20) Lu, W.; Deng, Q.; Liu, M.; Ding, B.; Xiong, Z.; Qiu, L. Coaxial Wet Spinning of Boron Nitride Nanosheet-Based Composite Fibers with Enhanced Thermal Conductivity and Mechanical Strength. *Nano-Micro Lett.* **2024**, 16 (1), 25.

(21) Li, X. L.; Hao, X. P.; Zhao, M. W.; Wu, Y. Z.; Yang, J. X.; Tian, Y. P.; Qian, G. D. Exfoliation of Hexagonal Boron Nitride by Molten Hydroxides. *Adv. Mater.* **2013**, 25 (15), 2200–2204.

(22) Thangasamy, P.; Sathish, M. Supercritical Fluid Processing: a Rapid, One-Pot Exfoliation Process for the Production of Surfactant-Free Hexagonal Boron Nitride Nanosheets. *CrystEngComm* **2015**, 17 (31), 5895–5899.

(23) Xiao, F.; Naficy, S.; Casillas, G.; Khan, M. H.; Katkus, T.; Jiang, L.; Liu, H.; Li, H.; Huang, Z. Edge-Hydroxylated Boron Nitride Nanosheets as an Effective Additive to Improve the Thermal Response of Hydrogels. *Adv. Mater.* **2015**, 27 (44), 7196–7203.

(24) Ma, Z.-S.; Wu, P.-R.; Liu, Z.; Cheng, Z.-L. Hydrothermal Exfoliation of Boron Nitride into Few-Layer Nanosheets in Mixed NaOH/KOH Solution. *Mater. Lett.* **2019**, 240, 108–112.

(25) Ji, J.; Duan, H.; Zhou, Z.; Liu, C.; Wang, D.; Yan, S.; Yang, S.; Bai, W.; Xue, Y.; Tang, C. Highly Dispersed and Functionalized Boron Nitride Nanosheets Contribute to Ultra-Stable Long-Life All-Solid-State Batteries. *J. Mater. Chem. A* **2023**, 11 (21), 11298–11309.

(26) Hu, X.; Liu, J.; He, Q.; Meng, Y.; Cao, L.; Sun, Y.-P.; Chen, J.; Lu, F. Aqueous Compatible Boron Nitride Nanosheets for High-Performance Hydrogels. *Nanoscale* **2016**, 8 (7), 4260–4266.

(27) Yang, M.; Hu, D.; Guo, Y.; Zhao, X.; Ma, W. Glucose-Assisted Exfoliation of Hexagonal Boron Nitride Nanosheets and Modification

with Hyperbranched Polymers for Thermally Conductive Epoxy Composites: Implications for Thermal Management. *ACS Appl. Nano Mater.* **2022**, 5 (11), 16315–16324.

(28) Grudin, D. V.; Ermolaev, G. A.; Baranov, D. G.; Toksumakov, A. N.; Voronin, K. V.; Slavich, A. S.; Vyshnevyy, A. A.; Mazitov, A. B.; Kruglov, I. A.; Ghazaryan, D. A.; Arsenin, A. V.; Novoselov, K. S.; Volkov, V. S. Hexagonal Boron Nitride Nanophotonics: a Record-Breaking Material for the Ultraviolet and Visible Spectral Ranges. *Mater. Horiz.* **2023**, 10 (7), 2427–2435.

(29) Liu, J.; Feng, H.; Dai, J.; Yang, K.; Chen, G.; Wang, S.; Jin, D.; Liu, X. A Full-Component Recyclable Epoxy/BN Thermal Interface Material with Anisotropy High Thermal Conductivity and Interface Adaptability. *Chem. Eng. J.* **2023**, 469, 143963.

(30) Yuan, C.; Duan, B.; Li, L.; Xie, B.; Huang, M.; Luo, X. Thermal Conductivity of Polymer-Based Composites with Magnetic Aligned Hexagonal Boron Nitride Platelets. *ACS Appl. Mater. Interfaces* **2015**, 7 (23), 13000–13006.

(31) Zhang, H.; Xu, S. Improvement of "Point-Plane"-Like Hetero-Structured Fillers on Thermal Conductivity of Poly(Vinyl Alcohol) Composites. *Polym. Compos.* **2023**, 44 (7), 4201–4214.

(32) Liu, B.; Zeng, J.; Li, P.; Li, J.; Wang, B.; Xu, J.; Gao, W.; Chen, K. Flexible Nanocellulose-Based Layered Films by Crosslinking Phosphorus Lignin Nanoparticles and Functionalized Boron Nitride Nanosheets for Flame-Resistant and Thermal Conductivity Applications. *J. Mater. Chem. A* **2023**, 11 (44), 24057–24071.

(33) Wilkinson, A. C.; Ishida, R.; Kikuchi, M.; Sudo, K.; Morita, M.; Crisostomo, R. V.; Yamamoto, R.; Loh, K. M.; Nakamura, Y.; Watanabe, M.; Nakauchi, H.; Yamazaki, S. Long-Term Ex Vivo Haematopoietic-Stem-Cell Expansion Allows Nonconditioned Transplantation. *Nature* **2019**, 571 (7763), 117–121.

# 前驱体结构调控策略制备碳点基 多色室温磷光材料

刘金坤<sup>1</sup>, 冉 准<sup>1</sup>, 刘青青<sup>2</sup>, 刘应亮<sup>1</sup>, 庄健乐<sup>1</sup>, 胡超凡<sup>1</sup>

(1. 华南农业大学材料与能源学院, 生物基材料与能源教育部重点实验室/广东省光学农业工程技术研究中心, 广州 510642; 2. 广东第二师范学院化学与材料科学学院, 广州 510303)

**摘要** 提出了一种简单易行的前驱体分子结构调控策略, 以  $\text{Al}_2\text{O}_3$  作为基质、不同结构的小分子为有机前驱体, 通过原位煅烧法制备了磷光发射颜色覆盖可见光区的碳点基复合材料. 通过透射电子显微镜、傅里叶变换红外光谱、X 射线衍射和 X 射线电子能谱证明了碳点成功生长在  $\text{Al}_2\text{O}_3$  基质内部. 荧光光谱测试结果表明, 4 种  $\text{CDs@Al}_2\text{O}_3$  复合材料的磷光颜色分别为蓝色(454 nm)、绿色(520 nm)、橙色(572 nm)和红色(632 nm), 平均寿命分别为 130.6, 293.6, 498.6 和 539.0 ms. 随着前驱体中  $\pi$  共轭度及含氧官能团数量的增加, 碳点激发态与基态之间的能隙变小, 引起磷光发射波长红移, 从而实现多色磷光发射的调控. 基于该材料多色室温磷光特性, 初步探究了其在防伪和信息加密方面的应用效果.

**关键词** 碳点; 室温磷光; 长余辉; 氧化铝

中图分类号 O631

文献标志码 A

doi: 10.7503/cjcu20240412

## Preparation of Carbon Dot-based Multicolor Room-temperature Phosphorescent Materials via Precursor Structure Regulation Strategies

LIU Jinkun<sup>1</sup>, RAN Zhun<sup>1</sup>, LIU Qingqing<sup>2\*</sup>, LIU Yingliang<sup>1</sup>,  
ZHUANG Jianle<sup>1</sup>, HU Chaofan<sup>1\*</sup>

(1. Key Laboratory for Biobased Materials and Energy of Ministry of Education/Guangdong Provincial Engineering Technology Research Center for Optical Agriculture, College of Materials and Energy, South China Agricultural University, Guangzhou 510642, China;  
2. College of Chemistry and Materials Science, Guangdong University of Education, Guangzhou 510303, China)

**Abstract** In this paper, a simple precursor molecular structure regulation strategy was presented, and carbon dot-based composites with phosphorescent emission colors covering the visible light spectrum were prepared through an *in situ* calcination method using  $\text{Al}_2\text{O}_3$  as a matrix and various small molecules as organic precursors. Transmission electron microscopy, Fourier-transform infrared spectroscopy, X-ray diffraction, and X-ray photoelectron spectroscopy confirmed the successful growth of carbon dots within the  $\text{Al}_2\text{O}_3$  matrix. Fluorescence spectroscopy tests

收稿日期: 2024-09-02. 网络首发日期: 2024-11-19.

联系人简介: 胡超凡, 男, 博士, 副教授, 主要从事碳基发光材料的制备及应用研究. E-mail: thucf@scau.edu.cn

刘青青, 女, 博士, 讲师, 主要从事发光材料及其在分析化学中的应用研究. E-mail: lqingqing04@gdei.edu.cn

基金项目: 广东省普通高校青年创新人才项目(批准号: 2019KQNCX097)、国家自然科学基金(批准号: 12174119, 52172142)和广东省自然科学基金(批准号: 2023A1515012003, 2022A1515011958)资助.

Supported by the Foundation for Young Talents in Higher Education of Guangdong Province, China(No.2019KQNCX097), the National Natural Science Foundation of China(Nos.12174119, 52172142) and the Natural Science Foundation of Guangdong Province, China(Nos.2023A1515012003, 2022A1515011958).



indicated that the phosphorescent colors of the four CDs@Al<sub>2</sub>O<sub>3</sub> composites were blue (454 nm), green (520 nm), orange (572 nm), and red (632 nm), with average lifetimes of 130.6, 293.6, 498.6, and 539.0 ms, respectively. The observed redshift in phosphorescent emission wavelength attributed to the decrease in the energy gap between the excited state and ground state of the carbon dots with increasing  $\pi$ -conjugation and number of oxygen-containing functional groups in the precursor, which achieved the modulation of multicolor phosphorescent emissions. Based on the multicolor room-temperature phosphorescent characteristics of this material, its applications in anti-counterfeiting and information encryption was preliminarily explored.

**Keywords** Carbon dots; Room temperature phosphorescence; Long afterglow; Al<sub>2</sub>O<sub>3</sub>

近年来,碳点(CDs)作为一种新型的纳米发光材料,具有原料来源广泛、环境毒性低、光稳定性高和制备成本低等特点<sup>[1-4]</sup>,在室温磷光材料领域引起了极大关注.基于碳点基室温磷光材料优越的余辉性能,其在信息加密、防伪、医学诊断和生物成像等与人们日常生活密切相关的领域已经得到了广泛应用<sup>[5-8]</sup>.然而,由于三重态与基态的能级差太窄难以稳定进行辐射跃迁,导致磷光发射的颜色范围经常被限制在蓝绿光区,对于更长波长的磷光发射较难实现<sup>[9-12]</sup>.这在很大程度上阻碍了碳点基多色室温长余辉材料的进一步大规模开发和应用.

目前,研究人员提出了一些可行策略来实现碳点的多色磷光发射,碳点基室温磷光材料的磷光发射逐渐从常见的蓝、绿色到橙、红色.如我们<sup>[5]</sup>曾通过用氧化硼对不同种类的碳点进行包覆,实现了碳点多色磷光发射.Yang等<sup>[13]</sup>通过调整碳点的碳化程度,将碳点的室温磷光发射波长从485 nm调节到558 nm.Li等<sup>[14]</sup>基于聚集诱导的分裂能级策略,制备出了从绿色到近红外室温磷光发射的CDs@B<sub>2</sub>O<sub>3</sub>复合材料.Yu等<sup>[15]</sup>以Mn掺杂的八面体沸石为基质制备了碳点基红色室温磷光复合材料,碳点(供体)和Mn<sup>2+</sup>之间的光谱重叠较大且距离较近,有利于能量转移到受体离子而产生红色余辉.我们<sup>[16]</sup>还基于单分散二氧化硅纳米颗粒中余辉发射的碳点(供体)和荧光染料(受体)之间的联级能量传递,开发了4种具有从绿色到黄色、橙色、红色的多色液相余辉系统.然而,其中的大多数材料需要特定的碳点与基质的组合才达到特定的发射波长,这不可避免地涉及到多种前驱体的筛选以及复杂的制备步骤<sup>[1,17-19]</sup>.更有策略性地制备具有长波长发射乃至可见光区全光谱发射的碳点基室温长余辉材料仍然是一个主要困难<sup>[20]</sup>.同时,对碳点基材料余辉的性能调控,有助于深入认识碳点磷光性能的形成和调控机制,并推动拓展其在实际应用需求的发展.

选择化学结构广泛多样的前驱体是获得多色余辉的重要途径,前驱体中所含官能团的数量、位置和类型对于产生多色余辉具有很重要的影响<sup>[11]</sup>.其中,富含C=O等官能团通常被认为是使碳点基长余辉材料具有多色余辉发射潜力的先决条件<sup>[18,21,22]</sup>,将能产生 $n-\pi^*$ 电荷跃迁的杂原子掺杂到碳点中,使碳点形成丰富的表面态的同时,可以有效地促进自旋-轨道耦合,有利于通过系间窜越(ISC)过程产生更多的三重态激子.Tan等<sup>[23]</sup>研究表明,前驱体的共轭结构对多色余辉也有重要影响,随着共轭链中原子个数的增加,激发电子跃迁的能量也随之降低,进而获得长波长发射.

本文分别以均苯四甲酸酐、1-萘甲酸、1,8-萘二甲酸酐和1,4,5,8-萘四甲酸酐为碳点前驱体,Al<sub>2</sub>O<sub>3</sub>作为基质包覆碳点,原位制备了4种磷光发射颜色覆盖可见光区的碳点基复合材料.对复合材料的结构形貌、化学结构进行了表征,研究了其光学性能,并探索了其在多色防伪和信息加密方面的应用.

## 1 实验部分

### 1.1 试剂与仪器

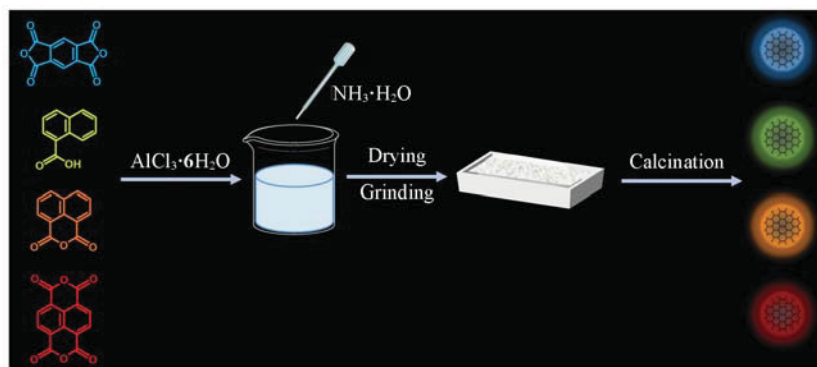
六水合氯化铝(AlCl<sub>3</sub>·6H<sub>2</sub>O)、无水乙醇、均苯四甲酸酐、1-萘甲酸、1,8-萘二甲酸酐、1,4,5,8-萘四甲酸酐、氨水和硼酸购自上海麦克林生化科技股份有限公司.所用试剂均为分析纯,实验用水为去离子水(电阻率18.2 M $\Omega$ ·cm).

FEI Talos F200S型透射电子显微镜(TEM,美国赛默飞公司);Ultima IV型X射线衍射仪(XRD,

日本株式会社理学公司); Nicolet Avatar 360 型傅里叶变换红外光谱仪 (FTIR, 美国 Nicolet 公司); Thermo Scientific Escalab 250Xi 型 X 射线光电子能谱仪 (XPS, 美国赛默飞公司); 日立 F7000 型荧光光谱仪 (PL, 日本 Hitachi 公司); Edinburgh Instruments FLS 1000 型荧光光谱仪 (PL, 英国爱丁堡仪器公司); Shimadzu UV-2550 型紫外-可见分光光度计 (UV-Vis, 日本岛津公司)。

## 1.2 实验过程

首先, 分别将 0.02 g 的均苯四甲酸酐、1-萘甲酸、1,8-萘二甲酸酐和 1,4,5,8-萘四甲酸酐放置到 4 个烧杯中, 分别加入 7.5 mmol 六水合氯化铝、8 mL 去离子水和 8 mL 乙醇, 超声 5 min 至分散溶解均匀。随后, 在搅拌中加入氨水直至沉淀完全生成, 静置陈化 3 h。将沉淀用去离子水洗涤 2 次, 去除绝大部分的  $\text{NH}_4^+$ ,  $\text{Cl}^-$  之后, 保留得到的固体, 将其置于 80 °C 鼓风干燥箱中干燥 10 h。将充分干燥后的块体充分磨成细粉末后置于瓷舟中, 然后转移到马弗炉中, 在空气氛围中以 5 °C/min 的速率加热至预设温度 450 °C, 保持 150 min。根据其展示出的余辉颜色分别将它们分别命名为 B-CDs@ $\text{Al}_2\text{O}_3$ , G-CDs@ $\text{Al}_2\text{O}_3$ , O-CDs@ $\text{Al}_2\text{O}_3$  和 R-CDs@ $\text{Al}_2\text{O}_3$ 。制备过程如 Scheme 1 所示。



Scheme 1 Schematic representation of procedures for the preparation of B-CDs@ $\text{Al}_2\text{O}_3$ , G-CDs@ $\text{Al}_2\text{O}_3$ , O-CDs@ $\text{Al}_2\text{O}_3$  and R-CDs@ $\text{Al}_2\text{O}_3$

## 2 结果与讨论

### 2.1 复合材料的表征

使用 TEM 和 XRD 测定了 4 种碳点基复合材料的结构和形貌。如图 1(A)~(D) 所示, 4 种复合材料中均生成了分散良好的球形或准球形结构的纳米尺寸的碳点。

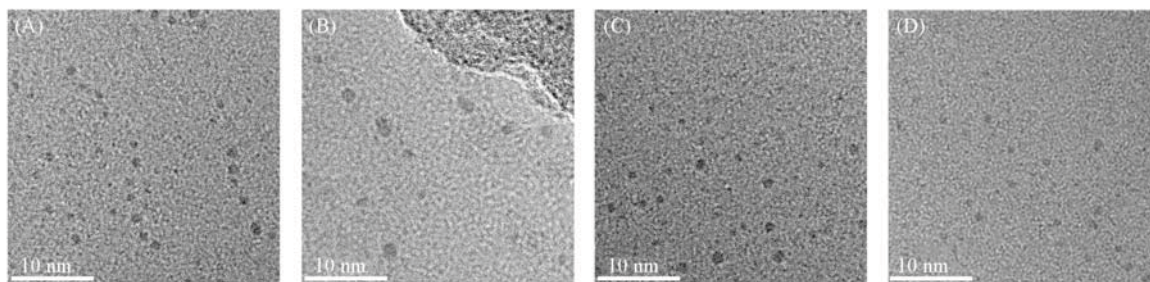


Fig. 1 TEM images of B-CDs@ $\text{Al}_2\text{O}_3$  (A), G-CDs@ $\text{Al}_2\text{O}_3$  (B), O-CDs@ $\text{Al}_2\text{O}_3$  (C) and R-CDs@ $\text{Al}_2\text{O}_3$  (D)

在图 2 的 XRD 谱图中, 在  $2\theta=37.60^\circ$ ,  $39.50^\circ$ ,  $45.39^\circ$  和  $67.00^\circ$  等处出现了明显的衍射峰, 表明了  $\gamma\text{-Al}_2\text{O}_3$  的形成<sup>[24]</sup>。而谱图中并未显示明显的碳点相关的石墨峰, 这也一定程度上表明了碳点的无定形性质<sup>[25,26]</sup>。以上结果可充分说明, 在煅烧后碳点在  $\text{Al}_2\text{O}_3$  基质中的原位形成, 并且嵌入其中, 由此得到了 CDs@ $\text{Al}_2\text{O}_3$  复合材料。

进一步采用 FTIR 和 XPS 研究了 4 种 CDs@ $\text{Al}_2\text{O}_3$  复合材料的化学结构。如图 3 所示, 以 860 和  $586\text{ cm}^{-1}$  (绿色虚线) 为中心的宽频带是由 Al—O 振动引起的<sup>[27]</sup>。1639, 1518,  $1420\text{ cm}^{-1}$  处 (紫色虚线) 为

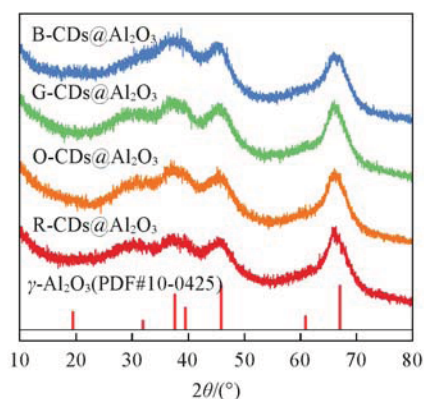


Fig. 2 XRD patterns of B-CDs@Al<sub>2</sub>O<sub>3</sub>, G-CDs@Al<sub>2</sub>O<sub>3</sub>, O-CDs@Al<sub>2</sub>O<sub>3</sub> and R-CDs@Al<sub>2</sub>O<sub>3</sub>

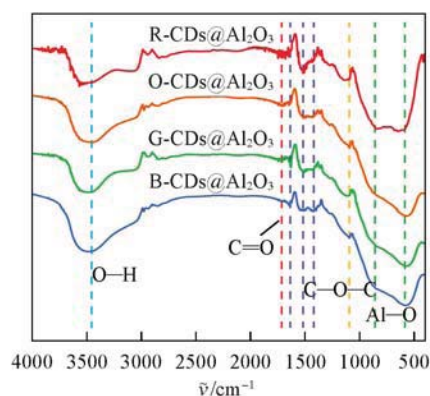


Fig. 3 FTIR spectra of B-CDs@Al<sub>2</sub>O<sub>3</sub>, G-CDs@Al<sub>2</sub>O<sub>3</sub>, O-CDs@Al<sub>2</sub>O<sub>3</sub> and R-CDs@Al<sub>2</sub>O<sub>3</sub>

芳环骨架振动特征峰, 对应了各个前驱体小分子的苯环或萘环结构<sup>[28]</sup>. 在 1093 cm<sup>-1</sup> 处(红色虚线)的吸收峰归属于 O—C—O 伸缩振动<sup>[29]</sup>, 在 1714 cm<sup>-1</sup> 处(红色虚线)的吸收峰则为 C=O 伸缩振动<sup>[30]</sup>, 这意味着生成的碳点继承了前驱体对应的官能团, 并在高温煅烧后得以保留. 3752~2705 cm<sup>-1</sup> 范围内有宽而明显的 O—H 伸缩振动峰<sup>[31]</sup>.

XPS 扫描结果显示, B-CDs@Al<sub>2</sub>O<sub>3</sub>, G-CDs@Al<sub>2</sub>O<sub>3</sub>, O-CDs@Al<sub>2</sub>O<sub>3</sub>, R-CDs@Al<sub>2</sub>O<sub>3</sub> 4 种复合材料均由 C, O 和 Al 元素组成, 在 532.0, 284.8 和 74.4 eV 处的特征峰分别对应 O<sub>1s</sub>, C<sub>1s</sub> 和 Al<sub>2p</sub> [图 4(A<sub>1</sub>)~(D<sub>1</sub>)]<sup>[32]</sup>. C<sub>1s</sub> 高分辨 XPS 谱图中, 约 284.8, 286.4 和 288.8 eV 处的 3 个拟合峰分别代表 C=C, C—O 和

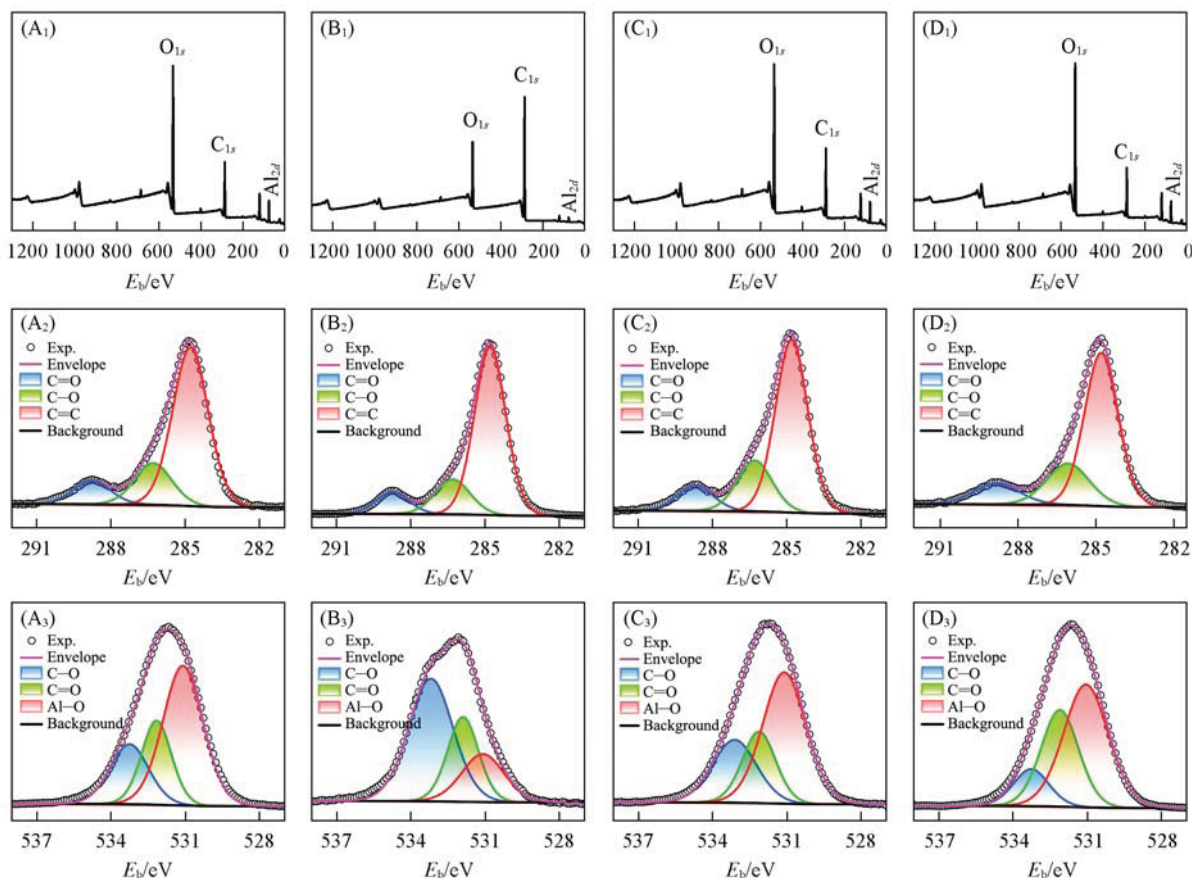


Fig. 4 Survey(A<sub>1</sub>—D<sub>1</sub>), C<sub>1s</sub>(A<sub>2</sub>—D<sub>2</sub>) and O<sub>1s</sub>(A<sub>3</sub>—D<sub>3</sub>) XPS spectra of B-CDs@Al<sub>2</sub>O<sub>3</sub>(A<sub>1</sub>—A<sub>3</sub>), G-CDs@Al<sub>2</sub>O<sub>3</sub>(B<sub>1</sub>—B<sub>3</sub>), O-CDs@Al<sub>2</sub>O<sub>3</sub>(C<sub>1</sub>—C<sub>3</sub>) and R-CDs@Al<sub>2</sub>O<sub>3</sub>(D<sub>1</sub>—D<sub>3</sub>)



C=O 化学键[图 4(A<sub>2</sub>)~(D<sub>2</sub>)]<sup>[13]</sup>. 在 O<sub>1s</sub> 的高分辨率 XPS 谱中, 在 531.1, 532.0 和 533.2 eV 处的结合能, 可分别对应 Al—O, O=C 与 C—O[图 4(A<sub>3</sub>)~(D<sub>3</sub>)]<sup>[33]</sup>. 由于使用的前驱体小分子在结构及官能团上都具有高度的相似性, 所以制备得到的复合材料在化学环境上也非常相似, 得到类似的表征分析结果.

上述结果表明, 经过高温煅烧后, 小分子充分聚合碳化形成碳点, 并被紧密锁定在 Al(OH)<sub>3</sub> 脱水形成致密的 Al<sub>2</sub>O<sub>3</sub> 中, 成功制备了具有余辉特性的 CDs@Al<sub>2</sub>O<sub>3</sub> 复合材料. 碳点表面的官能团促进了高效的  $n-\pi^*$  转变, 从而增强了单重态到三重态的 ISC 过程<sup>[34,35]</sup>. 同时,  $\gamma$ -Al<sub>2</sub>O<sub>3</sub> 的刚性框架结构对碳点有着强大的空间限制作用, 限制分子的振动和旋转, 同时将碳点与周围环境的猝灭剂隔绝, 有效地抑制了非辐射跃迁并稳定了激发三重态<sup>[36]</sup>.

## 2.2 复合材料的光学性能

对样品的光物理性质进行了分析. 如图 5(A) 所示, 4 种 CDs@Al<sub>2</sub>O<sub>3</sub> 复合材料的余辉最佳发射峰值分别为 454 nm (B-CDs@Al<sub>2</sub>O<sub>3</sub>), 520 nm (G-CDs@Al<sub>2</sub>O<sub>3</sub>), 572 nm (O-CDs@Al<sub>2</sub>O<sub>3</sub>), 632 nm (R-CDs@Al<sub>2</sub>O<sub>3</sub>), 其最佳激发下的余辉发射的对应 CIE 颜色坐标分别为 (0.29, 0.38), (0.18, 0.20), (0.48, 0.47) 和 (0.54, 0.46)[图 5(B)], 实现了在可见光区域的蓝色、绿色、橙色和红色余辉的覆盖.

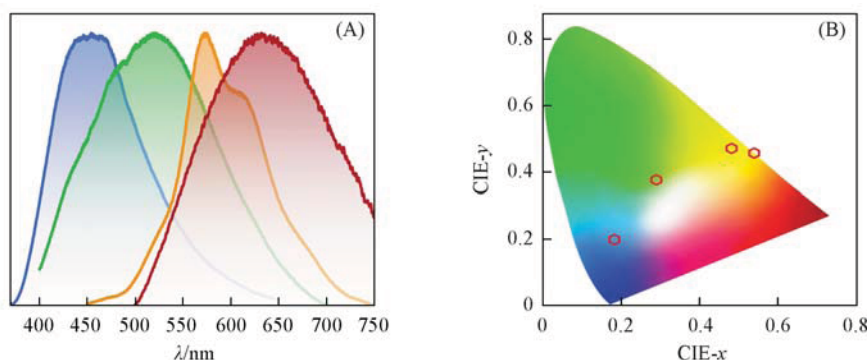
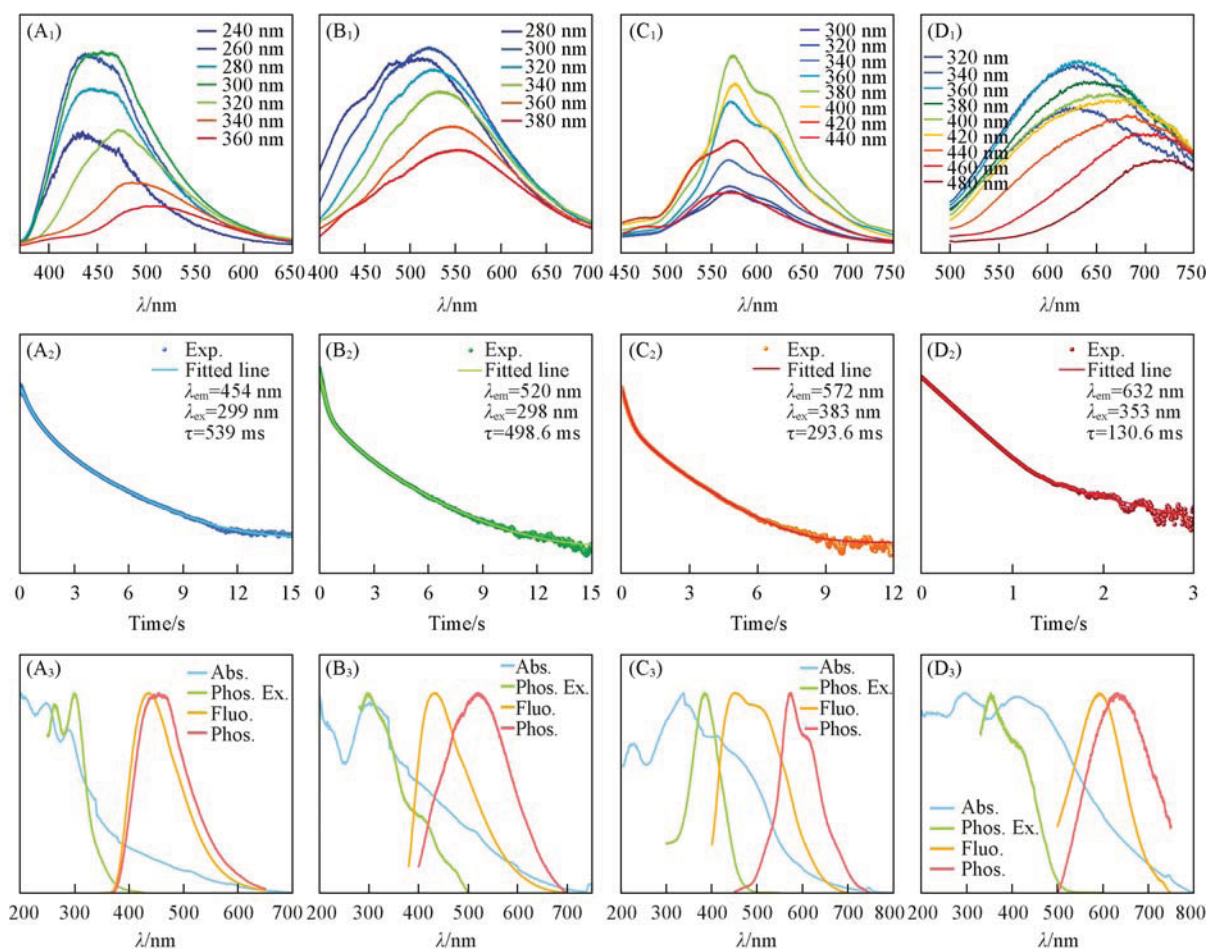


Fig. 5 Normalized afterglow spectra(A) and CIE coordinates(B) of B-CDs@Al<sub>2</sub>O<sub>3</sub>, G-CDs@Al<sub>2</sub>O<sub>3</sub>, O-CDs@Al<sub>2</sub>O<sub>3</sub> and R-CDs@Al<sub>2</sub>O<sub>3</sub>

测定了 4 种 CDs@Al<sub>2</sub>O<sub>3</sub> 复合材料在不同激发光源激发下的磷光发射光谱, 结果表明, CDs@Al<sub>2</sub>O<sub>3</sub> 复合材料的余辉光谱均表现出激发波长依赖性[图 6(A<sub>1</sub>)~(D<sub>1</sub>)]. 这可能是由于其存在多个三重态激发态, 时间分辨衰减曲线呈三指数衰变特征也证实了这一点[图 6(A<sub>2</sub>)~(D<sub>2</sub>)]. B-CDs@Al<sub>2</sub>O<sub>3</sub> 的平均寿命为 539.0 ms, G-CDs@Al<sub>2</sub>O<sub>3</sub> 的平均寿命为 498.6 ms、O-CDs@Al<sub>2</sub>O<sub>3</sub> 的平均寿命为 293.6 ms、R-CDs@Al<sub>2</sub>O<sub>3</sub> 的平均寿命为 130.6 ms, 表明它们都具有长寿命余辉发射的特征. 而导致其室温磷光寿命逐渐缩短的原因可能是: 由于碳点的磷光发光中心 T<sub>1</sub> 至 S<sub>0</sub> 之间的能隙变小, 三重态激子的非辐射跃迁增强. 为了确定 4 种 CDs@Al<sub>2</sub>O<sub>3</sub> 复合材料的余辉发射模式, 对其紫外-可见光吸收光谱、最佳余辉激发谱、最佳余辉发射谱及其同一波长激发的荧光发射谱进行了归一化处理, 并在同一张图中展示. 整体来说, 4 种 CDs@Al<sub>2</sub>O<sub>3</sub> 复合材料的主要吸收波长与余辉激发波长基本处在同一位置, 且吸收的波长范围更广, 而荧光与余辉的发射峰相对于前面两者依次红移, 符合各自波长对应的能量依次递减的规律, 因此, 可以确定 4 种 CDs@Al<sub>2</sub>O<sub>3</sub> 复合材料的余辉发射模式均为磷光发射<sup>[37]</sup>.

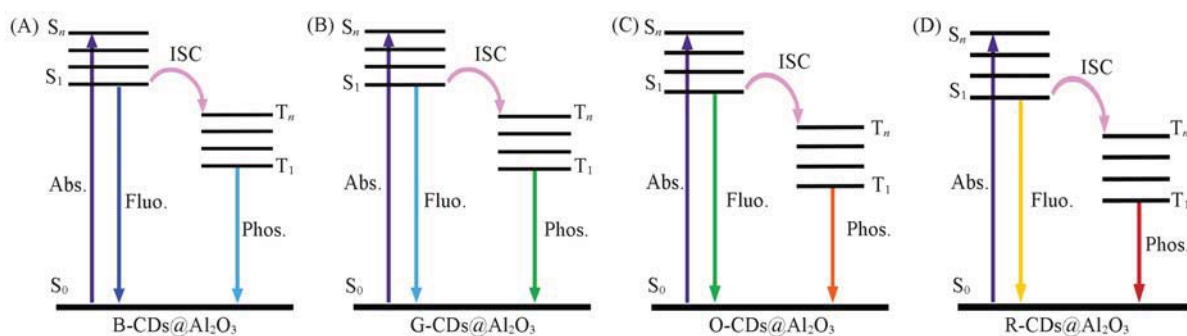
如图 6(A<sub>3</sub>) 所示, B-CDs@Al<sub>2</sub>O<sub>3</sub> 的最佳发射余辉峰为 454 nm, 最佳发射荧光峰为 434 nm, 余辉最佳激发峰为 300 nm, 而吸收光谱中 250 和 290 nm 附近的两个吸收峰为 C=C 的  $\pi-\pi^*$  跃迁导致, 在约 340 nm 处的肩峰为 C=O 的  $n-\pi^*$  跃迁引起的<sup>[38]</sup>. 如图 6(B<sub>3</sub>) 所示, G-CDs@Al<sub>2</sub>O<sub>3</sub> 的最佳发射余辉峰为 520 nm, 最佳发射荧光峰为 433 nm, 余辉最佳激发峰为 297 nm, 而吸收光谱中 310 nm 附近的两个吸收峰为 C=C 的  $\pi-\pi^*$  跃迁导致, 在约 380 nm 处的肩峰为 C=O 的  $n-\pi^*$  跃迁引起的. 如图 6(C<sub>3</sub>) 所示, O-CDs@Al<sub>2</sub>O<sub>3</sub> 的最佳发射余辉峰为 572 nm, 最佳发射荧光峰为 450 nm, 余辉最佳激发峰为 385 nm, 而吸收光谱中 220~230 nm 范围内出现的吸收峰为 C=C 的  $\pi-\pi^*$  跃迁导致, 在约 340、410 nm 处的峰及



**Fig. 6** Afterglow emission spectra(A<sub>1</sub>—D<sub>1</sub>), room temperature lifetime decay curves(A<sub>2</sub>—D<sub>2</sub>), normalized UV - Vis absorption, phosphorescence excitation, fluorescence and phosphorescence emission spectra (A<sub>3</sub>—D<sub>3</sub>) of B-CDs@Al<sub>2</sub>O<sub>3</sub>(A<sub>1</sub>—A<sub>3</sub>), G-CDs@Al<sub>2</sub>O<sub>3</sub>(B<sub>1</sub>—B<sub>3</sub>), O-CDs@Al<sub>2</sub>O<sub>3</sub>(C<sub>1</sub>—C<sub>3</sub>) and R-CDs@Al<sub>2</sub>O<sub>3</sub>(D<sub>1</sub>—D<sub>3</sub>)

440~500 nm 范围内的宽带吸收为 C=O 的  $n-\pi^*$  跃迁引起的. 如图 6(D<sub>3</sub>) 所示, R-CDs@Al<sub>2</sub>O<sub>3</sub> 的最佳发射余辉峰为 632 nm, 最佳发射荧光峰为 593 nm, 余辉最佳激发峰为 353 nm, 而吸收光谱中 200~250 nm 及 295 nm 附近出现的吸收峰为 C=C 的  $\pi-\pi^*$  跃迁导致, 在约 410 和 460 nm 处组成的宽吸收峰为 C=O 的  $n-\pi^*$  跃迁引起的. 从 4 种 CDs@Al<sub>2</sub>O<sub>3</sub> 复合材料的余辉激发光谱可以明显看出, 它们均表现出  $\pi-\pi^*$  跃迁产生的吸收, 同时余辉发射波长越长的 CDs@Al<sub>2</sub>O<sub>3</sub> 复合材料,  $n-\pi^*$  跃迁引起的吸收峰的范围也越宽, 且红移的趋势明显, 表明了碳点的能隙变窄.

综上所述, 经过高温热解, 碳点形成并被紧密锁定在刚性致密的氧化铝中, 成功制备了具有全可见光谱室温磷光特性的 CDs@Al<sub>2</sub>O<sub>3</sub> 复合材料. 根据以上的分析, 提出了一个合理的机制来解释在该体系中观察到的多色余辉(Scheme 2). 在入射光的激发下, 基态电子被提升到激发态, 随后通过能带内的非辐射振动弛豫跃迁到最低激发态. 碳点通过空间限制、氢键等与 Al<sub>2</sub>O<sub>3</sub> 紧密结合, 抑制分子内振动旋转并有效地隔绝了水、氧等猝灭剂, 从而稳定了三重态激子, 使磷光不被猝灭(见本文支持信息, 图 S1 和图 S2)<sup>[39,40]</sup>. 此外, 含氧官能团的存在表现出吸电子特性, 导致形成了  $p-\pi$  共轭体系<sup>[39]</sup>. 这种相互作用减小了最低激发单重态和三重态之间的能隙, 促进了系间窜越过程. 由于不同的前驱体共轭尺寸与含氧官能团的数量增加, 这两个关键因素都能影响调节碳点的结构, 降低了激发态与基态之间的能隙, 使得 CDs@Al<sub>2</sub>O<sub>3</sub> 复合材料的磷光发射波长红移, 从而实现发光波长可调的室温磷光性能.



Scheme 2 Schematic of the transition model of B-CDs@Al<sub>2</sub>O<sub>3</sub>(A), G-CDs@Al<sub>2</sub>O<sub>3</sub>(B), O-CDs@Al<sub>2</sub>O<sub>3</sub>(C) and R-CDs@Al<sub>2</sub>O<sub>3</sub>(D)

### 2.3 策略的普适性

为了证明合成策略的普遍性,采用上述4种前驱体小分子,以氧化铝为作为基质,通过一步加热的办法合成了一系列CD@B<sub>2</sub>O<sub>3</sub>复合材料.正如预期的那样,所有的相应复合材料都表现出长寿命室温磷光现象,且展示出了与对应的CDs@Al<sub>2</sub>O<sub>3</sub>复合材料同样的余辉颜色(图7).关闭激发光源后,CD@B<sub>2</sub>O<sub>3</sub>的磷光颜色从蓝色变为红色,其磷光发射波长分别为436, 508, 540和604 nm,平均寿命分别为612, 623, 596和155 ms(见本文支持信息图S3).因此,该策略为制备具有全可见光区颜色可调的碳点基室温磷光材料提供了一个有普适性意义的方向.

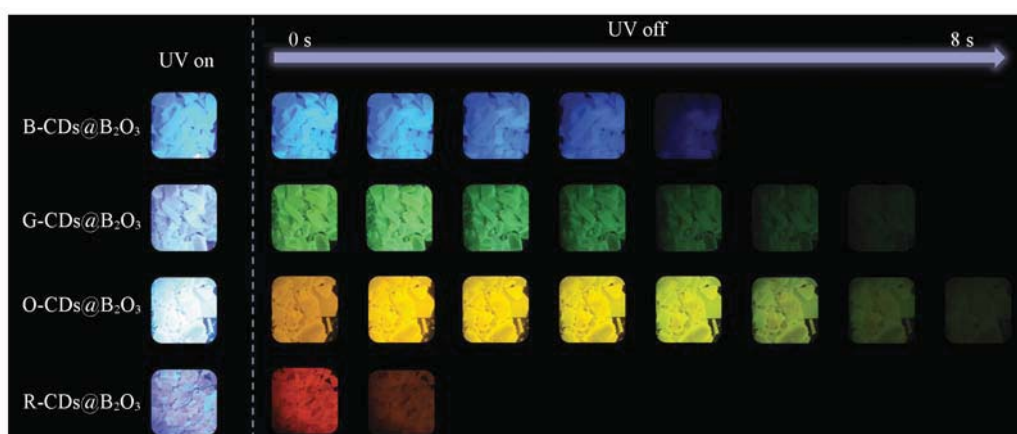
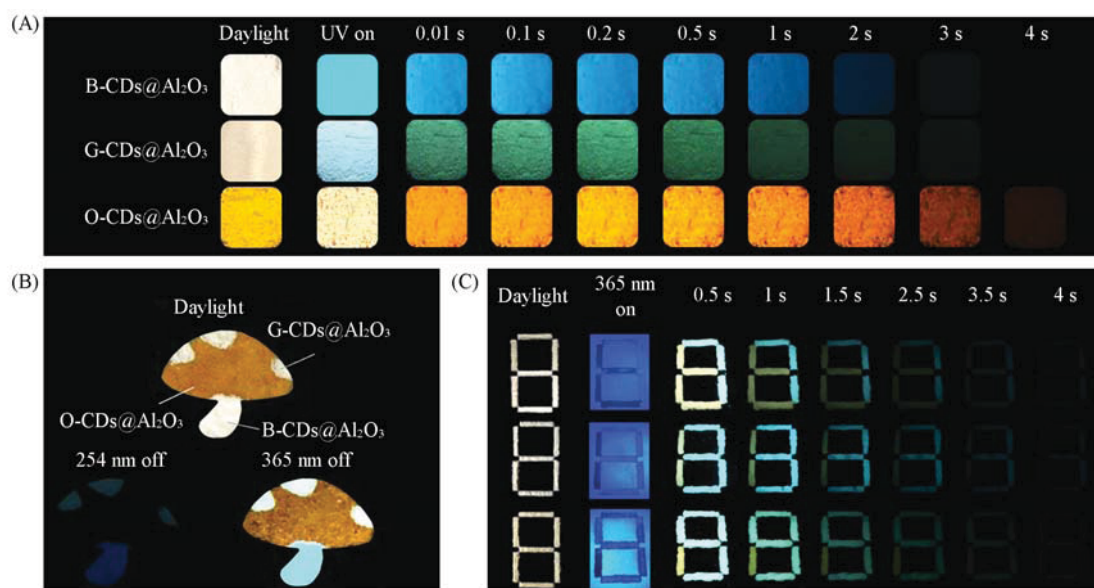


Fig. 7 Photographs of B-CDs@B<sub>2</sub>O<sub>3</sub>, G-CDs@B<sub>2</sub>O<sub>3</sub>, O-CDs@B<sub>2</sub>O<sub>3</sub> and R-CDs@B<sub>2</sub>O<sub>3</sub> under and switching off UV lamp

### 2.4 CDs@Al<sub>2</sub>O<sub>3</sub>复合材料的实物发光效果及应用

如图8(A)所示,停止激发光源照射后,在环境条件下CDs@Al<sub>2</sub>O<sub>3</sub>的多色发光最长可以持续4 s以上.然而,R-CDs@Al<sub>2</sub>O<sub>3</sub>的余辉持续时间及发射强度不足以进行观测.基于CDs@Al<sub>2</sub>O<sub>3</sub>粉末的余辉波长可调的优异特性,探索了其在多重防伪和信息加密方面的潜在应用.图8(B),展示了一种高级防伪模式,分别用B-CDs@Al<sub>2</sub>O<sub>3</sub>, O-CDs@Al<sub>2</sub>O<sub>3</sub>, G-CDs@Al<sub>2</sub>O<sub>3</sub>的粉末制作为蘑菇的菌柄、菌盖和上面的斑点.在日光下,该图案为黄色菌盖、白色菌柄和斑点的图案.254 nm的紫外光灯激发后关闭,由于254 nm的光源不能很好地激发O-CDs@Al<sub>2</sub>O<sub>3</sub>,所以图案只显示了蓝色的B-CDs@Al<sub>2</sub>O<sub>3</sub>菌柄和青绿色的G-CDs@Al<sub>2</sub>O<sub>3</sub>斑点.365 nm的紫外光灯激发后关闭,图案显示了橙黄色的O-CDs@Al<sub>2</sub>O<sub>3</sub>菌盖,而由于激发依赖的特性,B-CDs@Al<sub>2</sub>O<sub>3</sub>菌柄和G-CDs@Al<sub>2</sub>O<sub>3</sub>斑点变为了青绿色和黄绿色.如图8(C)所示,分别用B-CDs@Al<sub>2</sub>O<sub>3</sub>和G-CDs@Al<sub>2</sub>O<sub>3</sub>制作了信息加密功能的数字编码.在日光下和365 nm紫外光灯打开时,该图案数字编码为黄白色体色及蓝色荧光的“888”干扰信息,在关闭激发光源后,可以观察到不同的颜色组合的加密消息,即B-CDs@Al<sub>2</sub>O<sub>3</sub>粉末组成的青绿色“973”数字编码.





**Fig. 8** Photographs of B-CDs@Al<sub>2</sub>O<sub>3</sub>, G-CDs@Al<sub>2</sub>O<sub>3</sub> under daylight, before and after switching off 254 nm UV lamp, and photographs of O-CDs@Al<sub>2</sub>O<sub>3</sub> under daylight, before and after switching off 365 nm UV lamp(A), patterns of anti-counterfeiting fabricated with the CDs@Al<sub>2</sub>O<sub>3</sub> for advanced color-switching anti-counterfeiting(mushroom composed of B-CDs@Al<sub>2</sub>O<sub>3</sub>, G-CDs@Al<sub>2</sub>O<sub>3</sub> and O-CDs@Al<sub>2</sub>O<sub>3</sub>(B), photographs of coding for data encryption under daylight, 365 nm UV light and after removing 365 nm UV light(the numbers “973” composed of B-CDs@Al<sub>2</sub>O<sub>3</sub> and G-CDs@Al<sub>2</sub>O<sub>3</sub>)(C)

### 3 结 论

提出一种简单通用的前驱体分子结构调控策略, 原位制备了一系列全色余辉发射的 CDs@Al<sub>2</sub>O<sub>3</sub> 室温磷光材料. 结果表明, 随着前驱体中芳香族基团  $\pi$  共轭度从苯到萘及含氧官能团数量的增加, 降低了碳点激发态与基态之间的能隙, 两种因素之间的动态平衡调节了复合材料的余辉颜色, 磷光发射波长红移, 从而实现多色磷光发射的调控. 碳点通过空间限制、共价键、氢键的多重限域作用与 Al<sub>2</sub>O<sub>3</sub> 紧密结合, 抑制分子内振动旋转并有效地隔绝了水、氧等猝灭剂, 从而稳定了三重态激子, 使磷光不被猝灭. 4 种 CDs@Al<sub>2</sub>O<sub>3</sub> 复合材料的余辉颜色为蓝色、绿色、橙色和红色, 发射波长覆盖 454~632 nm, 平均寿命为 130.6~539.0 ms. 最后因其多色发光效果探索了防伪和信息保护加密方面的应用. 本研究通过简单调整前驱体结构, 可以很容易实现磷光行为的灵活调节, 对全色室温磷光发射碳点基复合材料提供了新的视角. 其出色的发光效果也在多重防伪、信息加密中得到重要的应用.

支持信息见 <http://www.cjcu.jlu.edu.cn/CN/10.7503/cjcu20240412>.

### 参 考 文 献

- [1] Liu H. X., Zhong X., Pan Q., Zhang Y., Deng W. T., Zou G. Q., Hou H. S., Ji X. B., *Coord. Chem. Rev.*, **2024**, 498, 215468
- [2] Đorđević L., Arcudi F., Cacioppo M., Prato M., *Nat. Nanotechnol.*, **2022**, 17(2), 112—130
- [3] Sun Y. Q., Liu S. T., Sun L. Y., Wu S. S., Hu G. Q., Pang X. L., Smith A., Hu C. F., Zeng S. S., Wang W. X., *Nat. Commun.*, **2020**, 11(1), 5591
- [4] Wareing T., Gentile P., Phan A., *ACS Nano*, **2021**, 15(10), 15471—15501
- [5] Li W., Zhou W., Zhou Z. S., Zhang H. R., Zhang X. J., Zhuang J. L., Liu Y. L., Lei B. F., Hu C. F., *Angew. Chem. Int. Ed.*, **2019**, 131(22), 7356—7361
- [6] Li J., Zhou H., Jin S., Xu B., Teng Q., Li C. H., Li J. S., Li Q. J., Gao Z. H., Zhu C. F., *Adv. Mater.*, **2024**, 36(24), 2401493
- [7] Geng B. J., Hu J. Y., Li Y., Feng S. N., Pan D. Y., Feng L. Y., Shen L. X., *Nat. Commun.*, **2022**, 13(1), 5735
- [8] Yu X. W., Liu K. K., Wang B. L., Zhang H. Y., Qi Y. Y., Yu J. H., *Adv. Mater.*, **2023**, 35(6), 2208735
- [9] Wang B. Y., Lu S. Y., *Matter*, **2022**, 5(1), 110—149



- [10] Ran Z., Liu J. K., Zhuang J. L., Liu Y. L., Hu C. F., *Small Methods*, **2024**, 8(1), 2301013
- [11] Zhou S. J., Wang F. X., Feng N., Xu A. X., Sun X. F., Zhou J., Li H. G., *Small*, **2023**, 19(33), 2301240
- [12] Lou Q., Chen N., Zhu J. Y., Liu K. K., Li C., Zhu Y. S., Xu W., Chen X., Song Z. J., Liang C. H., *Adv. Mater.*, **2023**, 35(20), 2211858
- [13] Xia C. L., Zhu S. J., Zhang S. T., Zeng Q. S., Tao S. Y., Tian X. Z., Li Y. F., Yang B., *ACS Appl. Mater. Interfaces*, **2020**, 12(34), 38593—38601
- [14] Li Q. J., Cheng D. K., Gu H. L., Yang D. Q., Li Y. C., Meng S., Zhao Y. Y., Tang Z. K., Zhang Y. B., Tan J., *Chem. Eng. J.*, **2023**, 462, 142339
- [15] Wang B. L., Mu Y., Zhang H. Y., Shi H. Z., Chen G. R., Yu Y., Yang Z. Q., Li J. Y., Yu J. H., *ACS Cent. Sci.*, **2019**, 5(2), 349—356
- [16] Mo L. Q., Liu H., Liu Z. M., Xu X. K., Lei B. F., Zhuang J. L., Liu Y. L., Hu C. F., *Adv. Opt. Mater.*, **2022**, 10(10), 2102666
- [17] He Z. G., Sun Y. D., Zhang C., Zhang J., Liu S. J., Zhang K., Lan M. H., *Carbon*, **2023**, 204, 76—93
- [18] Zhang Y. Q., Chen L., Liu B., Yu S. P., Yang Y. Z., Liu X. G., *Adv. Funct. Mater.*, **2024**, 34(25), 2315366
- [19] Ding Z. Z., Shen C. L., Han J. F., Zheng G. S., Ni Q. C., Song R. W., Liu K. K., Zang J. H., Dong L., Lou Q., *Small*, **2023**, 19(31), 2205916
- [20] Wang B. Y., Waterhouse G., Lu S. Y., *Trends Chem.*, **2023**, 5(1), 76—87
- [21] Kumari R., Kumar A., Negi K., Sahu S., *ACS Appl. Nano Mater.*, **2023**, 6(2), 918—929
- [22] Shi H. X., Niu Z. J., Wang H., Ye W. P., Xi K., Huang X., Wang H. L., Liu Y. F., Lin H. W., Shi H. F., An Z. F., *Chem. Sci.*, **2022**, 13(15), 4406—4412
- [23] Tan J., Yi Z. Z., Ye Y. X., Ren X. D., Li Q. J., *J. Lumin.*, **2020**, 223, 117267
- [24] Patra A., Dutta A., Bhaumik A., *J. Hazard. Mater.*, **2012**, 201, 170—177
- [25] Sun W. X., Zhang Y. Q., Yin G. C., Lu S. Y., *Adv. Funct. Mater.*, **2024**, 34(37), 2402346
- [26] Liu Y. P., Wang B. Z., Zhang Y. S., Guo J., Wu X. Y., OuYang D. F., Chen S., Chen Y. Q., Wang S. P., Xing G. C., *Adv. Funct. Mater.*, **2024**, 2401353
- [27] Ge W. Y., Zhang P. F., Zhang X. M., Gao W. X., Lu C. H., Ge Y., *ACS Sustainable Chem. Eng.*, **2021**, 9(30), 10220—10226
- [28] Ai L., Song Z. Q., Nie M. J., Yu J. K., Liu F. K., Song H. Q., Zhang B., Waterhouse G., Lu S. Y., *Angew. Chem. Int. Ed.*, **2023**, 62(12), e202217822
- [29] Li C. C., Zhao X. Y., Li C., Hu J. H., Zhu J. Y., Lou Q., Chen N., Song Z. J., Chen X., Pan G. C., *J. Alloys Compd.*, **2023**, 948, 169674
- [30] Arcudi F., Đorđević L., Prato M., *Angew. Chem. Int. Ed.*, **2017**, 129(15), 4234—4237
- [31] He J. L., Chen Y. H., He Y. L., Xu X. K., Lei B. F., Zhang H. R., Zhuang J. L., Hu C. F., Liu Y. L., *Small*, **2020**, 16(49), 2005228
- [32] Song Z. J., Liu Y. L., Lin X. M., Zhou Z. S., Zhang X. J., Zhuang J. L., Lei B. F., Hu C. F., *ACS Appl. Mater. Interfaces*, **2021**, 13(29), 34705—34713
- [33] Wan Z. J., Li Y. M., Zhou Y. Z., Peng D. P., Zhang X. J., Zhuang J. L., Lei B. F., Liu Y. L., Hu C. F., *Adv. Funct. Mater.*, **2023**, 33(11), 2207296
- [34] Han Y., Li M., Lai J. W., Li W. T., Liu Y. J., Yin L. Q., Yang L. Q., Xue X. G., Vajtai R., Ajayan P., *ACS Sustainable Chem. Eng.*, **2019**, 7(24), 19918—19924
- [35] Wang B. Y., Wang H. W., Hu Y. S., Waterhouse G., Lu S. Y., *Nano Lett.*, **2024**, 24(9), 2904—2911
- [36] Liu J. K., Luo Y. M., Ran Z., Wang F. L., Sun M. H., Luo Y. Y., Zhuang J. L., Zhang X. J., Lei B. F., Liu Y. L., Hu C. F., *Chem. Eng. J.*, **2023**, 474, 145597
- [37] Zhou Z. S., Song Z. J., Liu J. K., Lei B. F., Zhuang J. L., Zhang X. J., Liu Y. L., Hu C. F., *Adv. Opt. Mater.*, **2022**, 10(1), 2100704
- [38] Wu Y. C., Sun L. L., Han H. H., He X. P., Cao W. G., James T., *Chem. Sci.*, **2024**, 15(2), 757—764
- [39] Liang P., Zheng Y. H., Zhang X. C., Wei H. P., Xu X. K., Yang X. F., Lin H. H., Hu C. F., Zhang X. J., Lei B. F., *Nano Lett.*, **2022**, 22(13), 5127—5136
- [40] Lu D., Lu K., Wen H. T., Wei Z., Bianco A., Wang G. G., Zhang H. Y., *Small*, **2023**, 19(31), 2207046

(Ed.: V, K, S)



# Room temperature long afterglow from boron oxide: A boric acid calcined product

Zhishan Zhou<sup>a,b</sup>, Kaifan Jiang<sup>a</sup>, Niandi Chen<sup>a</sup>, Zifeng Xie<sup>a</sup>, Bingfu Lei<sup>a,b</sup>, Jianle Zhuang<sup>a,b</sup>, Xuejie Zhang<sup>a,b</sup>, Yingliang Liu<sup>a,b,\*</sup>, Chaofan Hu<sup>a,b,\*</sup>

<sup>a</sup> Key Laboratory for Biobased Materials and Energy of Ministry of Education/Guangdong Provincial Engineering Technology Research Center for Optical Agriculture, College of Materials and Energy, South China Agricultural University, Guangzhou 510642, China

<sup>b</sup> Guangdong Laboratory of Lingnan Modern Agriculture, Guangzhou 510642, China

## ARTICLE INFO

### Article history:

Received 2 April 2020

Received in revised form 23 June 2020

Accepted 25 June 2020

Available online 29 June 2020

### Keywords:

Boron oxide

Boric acid

Defects

Afterglow

Phosphorescence

Luminescence

## ABSTRACT

Afterglow materials are of increasing importance. Here we report for the first time an intense long-lasting blue afterglow observed in a metal-activator-free boric acid calcined product. It was found that the afterglow intensity varied with the calcination temperature and reaches a maximum at around 250 °C, with a high phosphorescence lifetime of 1.87 s under 254 nm excitation (more than 25 s to the naked eye). Defects formed during the calcination process are associated with oxygen vacancies, which store the energy and are thought to be the origin of the afterglow. The as-prepared boric acid calcined product serves well as an afterglow material for anti-counterfeiting and time-resolved information protection.

© 2020 Elsevier B.V. All rights reserved.

## 1. Introduction

Recently, afterglow materials have been widely used in sensing [1], light emitting diodes [2], and information security [3], etc. Superior afterglow materials are mostly metal-doped inorganic solids and organometallic compounds relying on various rare earth or transition metal ions as activators. They have high luminescence efficiency, and the afterglow can persist dozens of hours, such as the  $\text{SrAl}_2\text{O}_4:\text{Eu,Dy}$ . However, it needs to be calcined above 1000 °C and consumes rare-earth elements, which lead to high cost and high biological toxicity inevitably [4]. In contrast, the organic phosphorescent materials possess lots of merits, such as low toxicity, easy synthesis, and excellent stability. However, it is difficult to achieve long phosphorescence lifetime or high luminescence efficiency, because of the intense non-radiative transitions. At present, most organic phosphorescent materials exhibit afterglow with lifetime of sub-second [5]. Boron oxide is a useful material in the glass industry, which can improve the heat resistance, transparency of glass products, and the mechanical strength. It have been reported that adding  $\text{H}_3\text{BO}_3$  can prolong the green afterglow

of  $\text{SrAl}_2\text{O}_4:\text{Dy}^{3+}$ , and boron oxide was the key [6]. Qi et al. also reported an intensity tuneable afterglow of  $\text{ZnGa}_2\text{O}_4$  phosphor with different incorporated concentrations of  $\text{B}_2\text{O}_3$  [7]. In this article, we report an intense phosphorescence observed in a metal-activator-free boric acid calcined product. It is worth mentioning that compared with the metal-activator-free  $\text{SiO}_2$  nanotubes reported by Mou et al,  $\text{B}_2\text{O}_3$  exhibits longer lifetime and better stability [8].

## 2. Materials and methods

The synthesis process is shown in Fig. S1. 3 g boric acid was placed in a porcelain crucible and put in a muffle furnace and reacted at 100–500 °C for 5 h under air atmosphere. After cooling down to room temperature naturally, a series of products were obtained (named BA-X, X = 100, 150, 180, 200, 250, 300, 400, 500). The heating rate for the calcination process was 5 °C/min.

The thermogravimetric analysis was carried out in a DTG-60 (Shimadzu). The X-ray diffractometer (XRD) of as-prepared materials was examined by MSAL-XD2 (Cu-K $\alpha$  radiation,  $\lambda = 0.154051$  nm). Fluorescence and phosphorescence spectra were recorded with an F-7000 Hitachi fluorescence spectrofluorometer. Temperature-dependent afterglow spectra were conducted by the same Hitachi

\* Corresponding authors at: Guangdong Laboratory of Lingnan Modern Agriculture, Guangzhou 510642, China.

E-mail addresses: [tliuyl@scau.edu.cn](mailto:tliuyl@scau.edu.cn) (Y. Liu), [thucf@scau.edu.cn](mailto:thucf@scau.edu.cn) (C. Hu).



F-7000 fluorescence spectrophotometer in conjunction with a heating apparatus (Oxford Instruments).

### 3. Results and discussion

Among the as-synthesised samples, BA-100, BA-150, and BA-180 still remained in powder form, and almost no obvious afterglow was observed by the eye. Products reacted above 180 °C transformed into an amorphous glassy state. The afterglow became stronger as the temperature of calcination treatment rose from 180 °C to 250 °C, but dropped distinctly during the treatment at 300 °C and 400 °C. No phosphorescence was observed in BA-500. TGA analysis demonstrated a rapid weight loss of boric acid during the dehydration process at a temperature higher than 100 °C (Fig. 1a), which is consistent with the literature [9], and the weight loss of 45.24% is also consistent with the reported values [10]. The dehydration of boric acid takes place with two reactions: boric acid to metaboric acid (R1) and metaboric acid to boron oxide (R2). DTA analysis indicated that the dehydration started at around 97.5 °C, and R1 was completed at around 143.5 °C. The results of XRD and DTA analyses is consistent, BA-100 is composed of metaboric acid and boric acid, while BA-150 is only composed of metaboric acid. R2 starts as the temperature is increased. Theoretically, metaboric acid has transformed into boron oxide at 180 °C, but from the

XRD, there are no peaks of boron oxide in BA-180 because of the machine detection limit (Fig. 1c). The product is completely composed of boron oxide above 250 °C. In addition, the XRD shows that the characteristic peak due to the amorphous state becomes more obvious with an increase of temperature.

Optical spectra results are consistent with the intensity of afterglow observed by the eye. The afterglow of BA-X becomes stronger as the temperature of calcination reaction rises from 150 °C to 250 °C, but the intensity dropped distinctly above 300 °C (Fig. 1b). It is speculated that the boron oxide exhibits an afterglow but the degree of the amorphous state affects the intensity of the afterglow. R2 was finished completely at 250 °C, in which BA-250 is composed of boron oxide only. Besides, the amorphous degree of BA-250 is lower than the samples calcined at higher temperatures, so it is brighter than other samples which is consistent with the fact that the higher the disordered state is, the weaker the afterglow intensity is. Accordingly, it is reasonable to infer that the BA-500 is so amorphous that it exhibits no afterglow. BA-250 shows the strongest luminescence, so the following discussion takes BA-250 as an example.

The decay curves of BA-250 were fitted by a tri-exponential function, suggesting the average lifetime was 1.87 s (Ex. = 254 nm, Em. = 432 nm). And the fraction of each component in the tri-exponential decay can be evaluated by Formula (1) [11]:

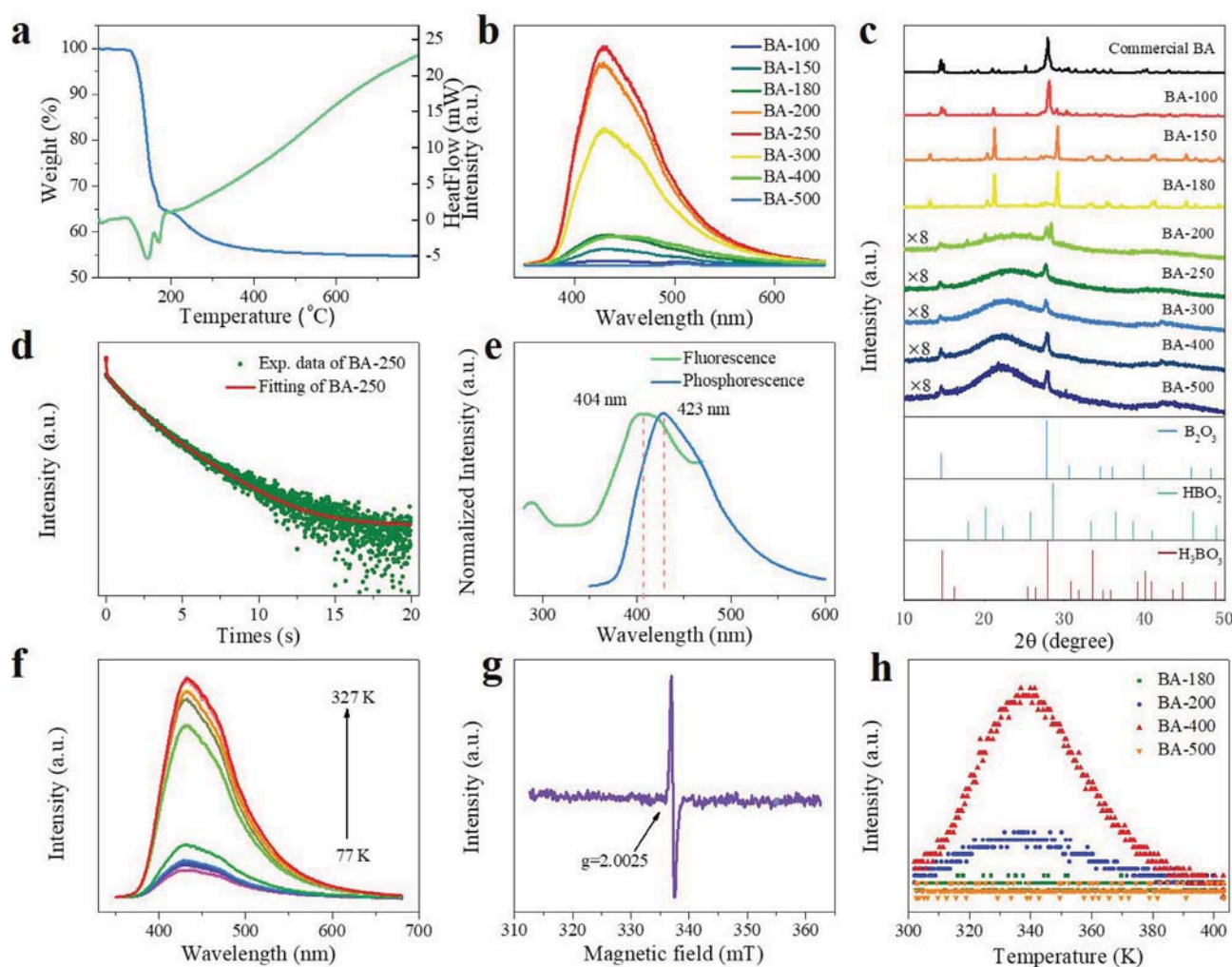


**Fig. 1.** a) TGA and DTA curves of boric acid; b) Phosphorescence emission spectra of BA-X excited by 254 nm; c) XRD; d) Phosphorescence lifetime decay curve of BA-250 excited by 254 nm and emitting at 432 nm; e) Photoluminescence spectra of BA-250 excited by 254 nm; f) Temperature response afterglow spectra of 250-BA excited by 254 nm; g) EPR spectra; h) Thermally stimulated luminescence glow curves.

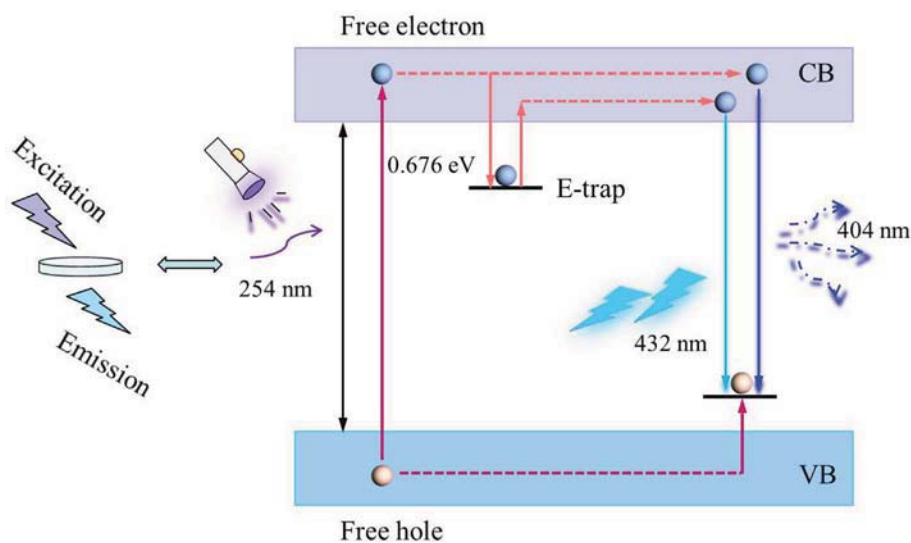


Fig. 2. The schematic of the afterglow process.

$$S_i = \frac{A_i \cdot \tau_i}{\sum_i A_i \cdot \tau_i} \times 100 \quad (1)$$

$A_i$  is the amplitude of the exponential decay, and  $\tau_i$  is the lifetime. The contributions of medium ( $\tau_1$ ) and slow ( $\tau_2$ ) components of BA-250 have a higher weight in the decay process. The fitting results of the attenuation parameters and the fraction of each component are shown in Table S1. There are two origins of afterglow; one is related to the triplet transition of organic matter and the other to the defects of inorganic matter. With the temperature increased from 77 K to 327 K (Fig. 1f), the intensity of the afterglow of BA-250 increased. Boron oxide, which contains no carbon atoms, is a pure inorganic compound, so the triplet mechanism is beyond the range of consideration. Electron paramagnetic resonance spectroscopy (EPR) proves that defects cause the afterglow of the sample (Fig. 1g). From the pattern, the centre of the resonance field corresponds to  $g$  value 2.0025, which is in the range of 2.000–2.003 ascribed to the oxygen vacancy [12]. The external thermal interference will promote the release of electrons from the traps, shown by an increase in the afterglow intensity. From Fig. 1h, a band with maxima at 338 K in BA-200 and BA-400 indicates the existence of trapping states, but no signal peak from the curve of BA-180 and BA-500.

The depths of trap centres can be calculated by Formula (2) [13].

$$E = T_m/500 \quad (2)$$

$T_m$  is the temperature at which the glow curve reaches its maximum. The trap depth of the product is estimated to be roughly 0.676 eV.

EPR spectra of BA-180, BA-200, BA-400, and BA-500 are shown in Fig. S7. As expected, the BA-180 did not show any EPR signal, indicating the absence of traps. Surprisingly, the EPR of BA-500 showed the oxygen vacancy signal. It means that the traps of boron oxide did not disappear even at 500 °C. However, BA-500 exhibits no afterglow because of its highly amorphous state, so no signal peak from the thermally stimulated luminescence glow curve of BA-500.

A possible whole exciton transfer process for activating the afterglow could be proposed as follows (Fig. 2). Under ultraviolet irradiation, free holes and free electrons are respectively formed in the valence band (VB) and conduction band (CB), then a portion of the free holes and free electrons cross the band to combine for

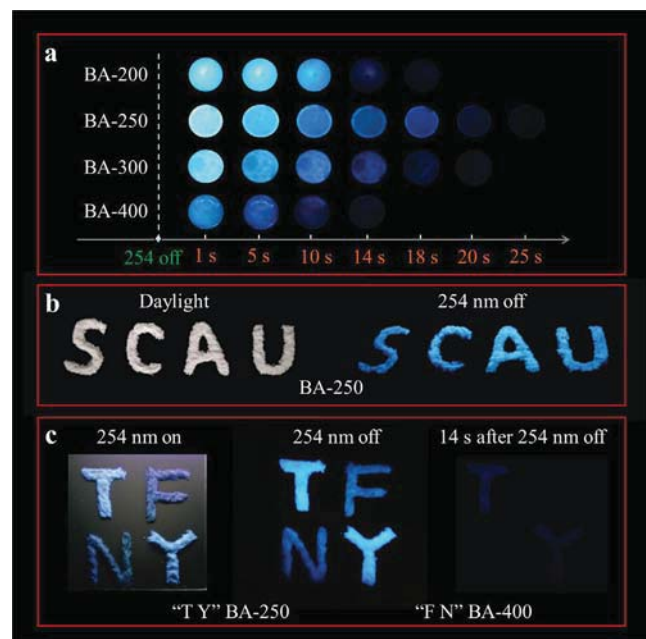


Fig. 3. Digital photos of a) afterglow, b) BA-250 in anti-counterfeiting application and c) information encryption made from BA-250 and BA-400. UV light: 254 nm.

fluorescence generation. Meanwhile, other free electrons can be captured by the electron traps (E-trap). After removal of the excitation light, the trapped electrons can be released with the help of thermal disturbances, and still pass through the lower energy band of CB though they lose a little bit of energy, then combine with the hole to excite an afterglow emission.

As shown in Fig. 3a, the afterglow varies from 14 s to 25 s. We simply demonstrated a security protection pattern using BA-250. After removal of the 254 nm UV irradiation, a blue “SCAU” could be clearly visualised. The application of time-resolved information encryption using BA-250 and BA-400 has also been proved (Fig. 3c). When turned off the Ultraviolet lamp, the bright blue pattern “TFNY” can be seen. After turning off the light for 14 s, the pattern turned into dark blue “TY”, so the information can be decrypted.

In summary, we presented an effective strategy to develop long-lasting afterglow through calcining boric acid without doping

any rare earth ions. The BA-250 shows the ultra-long lifetime to be 1.87 s (25 s to eye). EPR proved that the afterglow of the materials was caused by oxygen vacancies, and the amorphous state weakened the afterglow emission. This route offers an effective approach for novel afterglow materials, showing an important application in the field of anti-counterfeiting and information encryption.

#### CRediT authorship contribution statement

**Zhishan Zhou:** Writing - original draft, Formal analysis. **Kaifan Jiang:** Methodology. **Niandi Chen:** Investigation. **Zifeng Xie:** Data curation. **Bingfu Lei:** Conceptualization. **Jianle Zhuang:** Resources. **Xuejie Zhang:** Data curation. **Yingliang Liu:** Funding acquisition, Validation. **Chaofan Hu:** Supervision, Writing - review & editing.

#### Declaration of Competing Interest

The authors declare that they have no known competing financial interests or personal relationships that could have appeared to influence the work reported in this paper.

#### Acknowledgments

The present work was supported by the National Natural Science Foundations of China (Grant Nos. 21571067, 51402207),

the National Natural Science Foundation of China Joint Fund with Guangdong under Key Project (Grant Nos. U1501242).

#### Appendix A. Supplementary data

Supplementary data to this article can be found online at <https://doi.org/10.1016/j.matlet.2020.128226>.

#### References

- [1] F. Bunge, S. van den Driesche, M. Waespy, et al., *Sens. Actuat. B-Chem.* 289 (2019) 24–31.
- [2] J.S. Wang, C.F. Jiang, C. Liu, et al., *Mater. Lett.* 233 (2018) 149–152.
- [3] K. Jiang, Y.H. Wang, X.L. Gao, et al., *Angewan. Chem.-International Ed.* 57 (2018) 6216–6220.
- [4] Y. Li, M. Gecevicius, J.R. Qiu, et al., *Chem. Soc. Rev.* 45 (2016) 2090–2136.
- [5] H.L. Ma, A.Q. Lv, L.S. Fu, et al., *Ann. Phys.* 531 (2019) 1800482.
- [6] B.G. Zhai, L. Yang, Q.L. Ma, et al., *J. Lumin.* 181 (2017) 78–87.
- [7] R.X. Zhong, Z.R. Liu, J.Q. Qi, *Adv. Mater. Res.* 690 (2013) 627–631.
- [8] H.J. Chang, Y.F. Chen, H.P. Lin, et al., *Appl. Phys. Lett.* 78 (2001) 996–998.
- [9] S. Balci, N.A. Sezgi, E. Eren, *Indust. Eng. Chem. Res.* 51 (2012) 11091–11096.
- [10] F. Sevim, F. Demir, M. Bilen, et al., *Korean J. Chem. Eng.* 23 (2006) 736–740.
- [11] R.E. Rojas-Hernandez, F. Rubio-Marcos, A. Serrano, et al., *Nanomaterials* 9 (2019) 1473.
- [12] A. Khampuanbut, S. Santalelat, A. Pankiew, et al., *J. Colloid Interface Sci.* 560 (2020) 213–224.
- [13] W.Y. Shi, J. Yao, L.Q. Bai, et al., *Adv. Funct. Mater.* 28 (2018) 1804961.



# Morphology-controlled Synthesis of Molybdenum Oxide with Tunable Plasmon Absorption for Photothermal Therapy of Cancer

Xiaoqin Zhang,<sup>[a]</sup> Hongru Zu,<sup>[a, d]</sup> Yanxian Guo,<sup>[b]</sup> Qingqing Liu,<sup>\*,[c]</sup> Zhiming Liu,<sup>\*,[b]</sup> and Chaofan Hu<sup>\*,[a, e]</sup>

**Abstract:** Semiconductor nanocrystals showing surface plasmonic absorption features can be used as prospective substitutes for noble metallic nanoparticles. Herein, a creative one-pot hydrothermal route without template is used to synthesize plasmonic oxygen deficiency molybdenum oxide ( $\text{MoO}_{3-x}$ ) nanoparticles. The morphologies of as-prepared  $\text{MoO}_{3-x}$  nanomaterials arranged from amorphous to crystalline with the reaction temperature varied from 160 °C, 180 °C to 200 °C, namely  $\text{MoO}_{3-x}$  quantum dots (QDs),  $\text{MoO}_{3-x}$  nano-sheets, and  $\text{MoO}_2$  nanospheres. Simultaneously, in the near-infrared region (NIR),  $\text{MoO}_{3-x}$  nanomaterials exhibit gradually

enhanced localized surface plasmon resonance (LSPR) absorption, of which  $\text{MoO}_2$  nanospheres exhibit intense NIR absorption with a photothermal conversion efficiency up to 72.5% under 808 nm NIR laser irradiation. Moreover, the toxicity and cancer therapy efficacy of  $\text{MoO}_2$  nanospheres have been systematically assessed *in vitro* and *in vivo*, respectively. The results revealed that  $\text{MoO}_2$  nanospheres exhibit low toxicity and high therapeutic efficiency, making it an promising and effective photothermal agent in photothermal therapy

## 1. Introduction

In the last few decades, cancer remains one of the killers of human health.<sup>[1]</sup> Traditional treatments for cancer are including surgical excision, radiotherapy and chemotherapy. Nowadays, there are some developments in nanomaterials and nano-technology, and currently therapies based on them consist of photodynamic therapy (PDT) and photothermal therapy (PTT).<sup>[2–6]</sup> For PDT, reactive oxygen species (ROS) play important role in eradicating malignant tumors. Light of appropriate wavelength is injected from the outside and irradiates on the

photosensitizer (PS) located at tumor sites, and the photochemical reaction will cause the release of ROS from tissue oxygen.<sup>[3,7]</sup> When the laser is provided, the ROS generates as soon as possible, thus PDT has obvious therapeutic effect in treatment early, while as the time goes by, the PS could be photodegradable and tissue oxygen is also severely depleted, both of which will reduce the effect of treatment.<sup>[8]</sup> Furthermore, most of PSs with the largest absorption band in the visible region<sup>[9]</sup> has the disadvantage of poor water-solubility,<sup>[10]</sup> which strongly restricts the prospects for PDT to clinical applications. Thus, it is obvious that the therapeutic efficiency of PDT decreases with the irradiation time prolonged, while the PTT treatment just the opposite. The principle of PTT is absorbance and conversion NIR light into heat in tumor to causes cancer cells to die. Hyperthermia effect of heat accumulation over time can cause protein degeneration, rupture of membranes, and eventually destroy pathological tissue. Meanwhile, PTT combined with chemotherapy to achieve synergistic treatment manner,<sup>[11–13]</sup> which not only enhances the cell's uptake of the drug, but also controls the triggering of the release of drug molecules from drug carriers. A variety of NIR photo-absorbing agents have received a new discovery in the PTT including two-dimensional transition metal sulfide ( $\text{MoS}_2$  and  $\text{WS}_2$ ),<sup>[14]</sup> nonstoichiometric metal chalcogenides ( $\text{WO}_x$ ,  $\text{Cu}_{2-x}\text{Se}$ ,  $\text{Cu}_{2-x}\text{S}$ ),<sup>[15–18]</sup> noble metal (Au, Pt) nanomaterials,<sup>[19–21]</sup> carbon-based nanomaterials,<sup>[22–26]</sup> conducting polymers,<sup>[27]</sup> and so on. Nowadays, the discoveries of localized surface plasmon resonance (LSPR) nanomaterials have gradually attracted the attention of the scientific community. The  $\text{MoO}_{3-x}$  nanomaterials are applied as PTT reagents thanks to their characteristics of easy synthesis, low cost, low toxicity and good photothermal properties.<sup>[28–30]</sup>

Research work have indicated that molybdenum oxide ( $\text{MoO}_3$ ) has various forms: one of them is the thermodynamic

[a] X. Zhang, H. Zu, Dr. C. Hu  
Key Laboratory for Biobased Materials and  
Energy of Ministry of Education/Guangdong Provincial Engineering Technol-  
ogy  
Research Center for Optical Agriculture  
College of Materials and Energy  
South China Agricultural University  
Guangzhou 510642, Guangdong (People's Republic of China)  
E-mail: thucf@scau.edu.cn

[b] Y. Guo, Dr. Z. Liu  
College of Biophoton  
MOE Key Laboratory Laser Life Science  
South China Normal University  
Guangzhou 510631, Guangdong (People's Republic of China)  
E-mail: liuzm@scnu.edu.cn

[c] Dr. Q. Liu  
Department of Chemistry  
Guangdong Education University  
Guangzhou 510303, Guangdong (People's Republic of China)  
E-mail: lqingqing04@gdei.edu.cn

[d] H. Zu  
College of Biomedical Engineering  
Taiyuan University of Technology  
Taiyuan 030024, Shanxi (People's Republic of China)

[e] Dr. C. Hu  
Guangdong Laboratory of Lingnan Modern Agriculture  
Guangzhou 510642, Guangdong (People's Republic of China)

and stable phase of orthorhombic  $\alpha$ - $\text{MoO}_3$ ,<sup>[11–13]</sup> and the others are metastable phases of monoclinic  $\beta$ - $\text{MoO}_3$ ,<sup>[31]</sup> hexagonal  $\text{h-MoO}_3$ .<sup>[32,33]</sup> The conversion of the stoichiometric  $\text{MoO}_3$  into non-stoichiometric oxygen deficiency molybdenum oxide ( $\text{MoO}_{3-x}$ ) since that the becoming of heterovalent heteroatoms or lattice vacancies or lattice vacancies<sup>[34,35]</sup> have excellent advantages, such as electrical conductivity, catalytic properties, optical properties and so on, to be achieved by controlling and adjusting the valence state of molybdenum element<sup>[36,37]</sup> which will be applied in various science fields. Furthermore, increased with oxygen hole, the color of  $\text{MoO}_{3-x}$  arrange from blank to obvious blue with a valid LSPR absorption in NIR.<sup>[38,39]</sup> Thus, the  $\text{MoO}_{3-x}$  nanomaterials were applied in photothermal removal of cancer.<sup>[40–42]</sup>

The convenient way to obtain  $\text{MoO}_{3-x}$  nanomaterials is to separate from bulk oxide<sup>[17]</sup>  $\text{MoO}_3$  powders with an exfoliation process, which is time consuming and low yield. Generally, the extraction of  $\text{MoO}_{3-x}$  nanoparticles can be classified as two categories: hydrothermal and chemical exfoliation.<sup>[43]</sup> For instance, Song et al.<sup>[44]</sup> has achieved success in preparation of molybdenum oxide nanosheets by one pot hydrothermal method. But nanosheets obtained have poor hydrophilicity, which need to be modified by polyethylene glycol (PEG) to improve solubility. Xiao et al.<sup>[41]</sup> reported a research work about the synthesis of strong photoluminescence  $\text{MoO}_{3-x}$  quantum dots via hydrogen peroxide ( $\text{H}_2\text{O}_2$ ) as the oxidant to inserted into molybdenum disulfide ( $\text{MoS}_2$ ) powder. Compared with other papers, this method is without an external stimulus. However, they have a poor absolute fluorescence quantum yield is only 2.55%. Bao et al.<sup>[45]</sup> reported poly-(ethylene glycol) functionalized oxygen deficiency molybdenum oxide ( $\text{MoO}_{3-x}$ ) hollow nanospheres (HNSs) synthesized by hydrothermal method. Thanks to their high specific surface area and the available pore, the hollow spherical structure can be used as a

drug carrier. Lu et al.<sup>[18]</sup> reported that  $\text{MoO}_3$  quantum dots (QDs) were prepared in high yield by combining intercalation, thermal exfoliation and sonication process. However, the above mentioned requires high-temperature reaction conditions and extended processing time. Herein, it is very important to synthesize the excellent  $\text{MoO}_{3-x}$  nanoparticle by a simple and convenient way.

Here, we demonstrate an innovative one-pot hydrothermal method without template to fabricate water-soluble  $\text{MoO}_{3-x}$  nanoparticles. It was uncomplicated to add a certain quality of polyvinyl pyrrolidone (PVP) into the ammonium molybdate (( $\text{NH}_4$ )<sub>6</sub> $\text{Mo}_7\text{O}_{24}\cdot 4\text{H}_2\text{O}$ ) solution in the presence of hydrochloric acid (HCl). The acquired  $\text{MoO}_{3-x}$  nanoparticles were characterized have three morphologies with different reaction temperature. A key advantage is that with the temperature changed the plasmon peak red shifting, in which  $\text{MoO}_2$  nanospheres with an optimal absorbance peak. The toxicity of  $\text{MoO}_2$  nanospheres and the efficacy of cancer treatment effect have been relatively systematically assessed *in vitro* and *in vivo*. Thus, nanoparticles have confirmed to be a recommendable and appropriate candidate to PTT of cancer.

## 2. Results and Discussion

### 2.1. Preparation and analysis of $\text{MoO}_{3-x}$ nanomaterials

Different morphology  $\text{MoO}_{3-x}$  nanoparticles were prepared via one-pot hydrothermal treatment by making use of ammonium molybdate tetrahydrate (( $\text{NH}_4$ )<sub>6</sub> $\text{Mo}_7\text{O}_{24}\cdot 4\text{H}_2\text{O}$ ) as the Mo precursor and polyvinyl pyrrolidone K30 (PVP K30) as reductant. Different color and morphologies of  $\text{MoO}_{3-x}$  nanoparticles could be obtained by controlling the reaction temperature at 160 °C, 180 °C, 200 °C for 12 h (Figure 1). When the temperature at

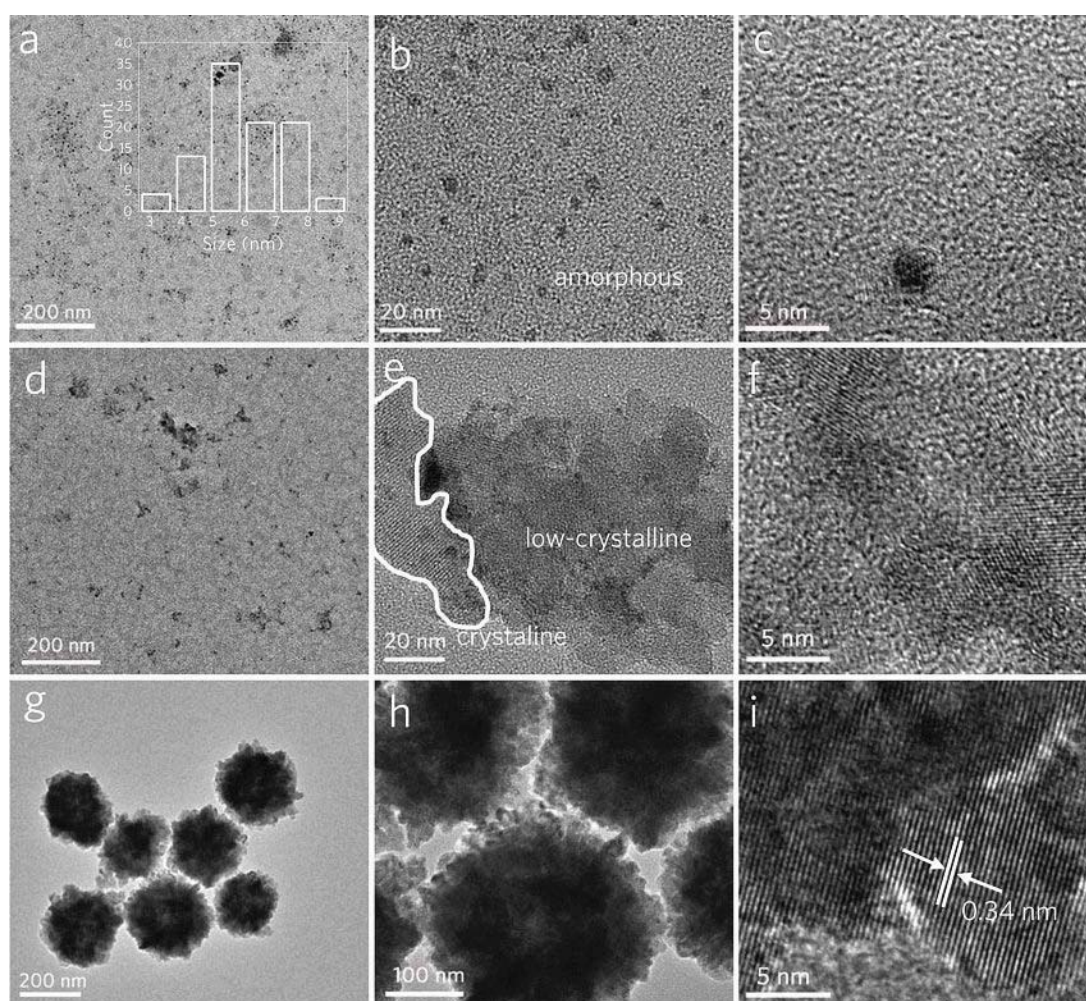


Figure 1. Schematic illustration describing the hydrothermal treatment synthesis process.

160 °C, transmission electron microscopy (TEM) images displayed that  $\text{MoO}_{3-x}$  nanoparticles in the form of quantum dots (QDs) and the average size of  $\text{MoO}_{3-x}$  QDs are about 6.51 nm observed from in Figure 2a. Furthermore, the high resolution transmission electron microscopy (HRTEM) images indicated that the  $\text{MoO}_{3-x}$  QDs are amorphous states in Figure 2c, which two typical nano-QDs were selected from Figure 2b. Meanwhile, a fraction of QDs appeared aggregation in this process. Subsequently,  $\text{MoO}_{3-x}$  quantum dots ( $\text{MoO}_{3-x}$  QDs) piled up together forming nanosheets (Figure 2d) when the temperature raised to 180 °C, which including crystalline and low-crystalline two states (Figure 2e). In Figure 2f, HRTEM images of crystalline  $\text{MoO}_{3-x}$  nanosheets gave a clear lattice fringe. Next, when the temperature increases to 200 °C, the nanosheets form into nanospheres (Figure 2g). As is shown in Figure 2h, there are clearly nanosheets at the edge of nanospheres and the obvious lattice fringes with spacing of 0.34 nm in the HRTEM micrograph can be considered as the  $(-1, 1, 1)$  crystal planes in Figure 2i, indicating a definite crystalline nature.

X-ray diffraction (XRD) patterns and Raman illustrated that the structure of the obtained products. The  $\text{MoO}_{3-x}$  QDs and nanosheets with a broad peak are poor crystallinity. Since of

confine dimensions, the intensity of XRD diffraction of  $\text{MoO}_{3-x}$  QDs and  $\text{MoO}_{3-x}$  nanosheets are too weak, which not be capable to specifically considered as Mo species. Nevertheless, they are similar to  $\text{Mo}_9\text{O}_{26}$  (JCPDs no. 12-0753, Figure 3a). However, as shown in Figure 3a, all peaks of  $\text{MoO}_2$  nanospheres can be able to correspond to the standard  $\text{MoO}_2$  (JCPDS No. 32-0671), and there are no unnecessary mismatched peaks, evidencing that the product is pure. Next, in order to verify that  $\text{MoO}_{3-x}$  nanoparticles were synthesized successfully, Fourier transform infrared spectroscopy (FT-IR) was performed. In Figure 3b, the peaks at 941, 941, and 953  $\text{cm}^{-1}$  are the characteristic of stretching vibrations of  $\text{Mo}=\text{O}$ , which represent  $\text{MoO}_{3-x}$ ,  $\text{MoO}_{3-x}$  nanosheets and  $\text{MoO}_2$  nanospheres. The stretching vibrations of  $\text{Mo}-\text{O}-\text{Mo}$  is located in the region 800–500  $\text{cm}^{-1}$ .<sup>[46–48]</sup> Furthermore, optical absorption in the NIR area was detected by UV-vis spectra. The synthesized product showed an NIR absorption band from 600 nm to 900 nm. Meanwhile, the absorption peak underwent a red shift from 160 °C to 200 °C (Figure 3c). When the synthesis temperature is 200 °C, the optimal absorption peak at about 900 nm, so as to the prepared nanospheres have a chance to apply to photothermal therapy.



**Figure 2.** (a) (d) (g) TEM images and (b) (c), (e) (f), (h) (i) HRTEM images which synthesized at the temperature of 160 °C, 180 °C and 200 °C respectively.



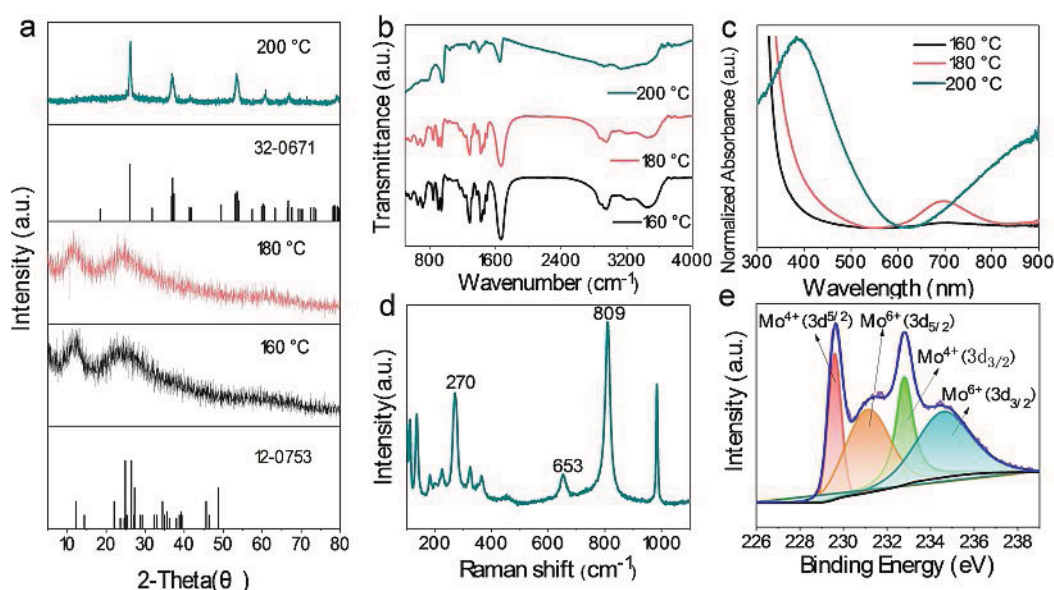


**Figure 3.** (a) XRD pattern of products. (b) FT-IR spectrum. (c) UV-Vis NIR spectrum. (d) Raman spectra of MoO<sub>2</sub> nanospheres. (e) Mo 3d spectrum of MoO<sub>2</sub> nanospheres.

Next, further characterization of MoO<sub>2</sub> nanospheres are by Raman and X-ray photoelectron spectroscopy (XPS). Strong Raman peaks at 270 cm<sup>-1</sup> represent the wagging mode of the double bond Mo=O, 653 cm<sup>-1</sup> is the Mo<sub>3</sub>-O stretching mode, 809 cm<sup>-1</sup> the stretching mode of Mo<sub>2</sub>-O, and 983 cm<sup>-1</sup> is Mo<sup>6+</sup>-O stretching mode respectively (Figure 3d). Component and valence of nanospheres was measured by XPS. In the XPS full spectrum, it exhibits that the materials obtained include C, O, N, and Mo elements (Figure S1). As for the signal of C 1s (284.8 eV), N 1s (401 eV), they may be attributed the PVP decoration. O 1s is at 531 eV, probably owing to the hydrophilic PVP carbon chain contains hydroxyl groups. In the meantime, in Figure 3e the Mo 3d spectra consist of a typical four-peak shape: a pair of strong peaks and a pair of weak peaks. The oxidation state of Mo<sup>4+</sup> is a pair of strong peaks at 229.71 and 232.91 eV,<sup>[49]</sup> while the characteristic peaks of Mo<sup>6+</sup> are a pair of weak peaks at 231.55 and 234.88 eV owing to the slight surface oxidation of MoO<sub>2</sub> nanospheres.<sup>[50,51]</sup>

In order to explore the effect of reaction time on the high temperature redox process, we have synthesized MoO<sub>3-x</sub> samples with different reaction time at 200 °C. As shown in Figure S2, X-ray diffraction (XRD) patterns of the obtained products with 6 h hydrothermal treatment display an amorphous state. At the reaction time of 12 and 24 h, MoO<sub>2</sub> has been successfully synthesized confirmed by the XRD patterns, which demonstrates that the redox process requires sufficient reaction time.

## 2.2. Photothermal features of MoO<sub>2</sub> nanospheres

Based on MoO<sub>2</sub> nanospheres with NIR absorption properties, the photothermal transformation performance is measured by

using 808 nm lasers. Adjusting the power density of the laser of 2.5 W/cm<sup>2</sup>, the temperatures of different concentrations of MoO<sub>2</sub> nanosphere aqueous solutions were recorded under a continuous irradiation laser. Figure 4a describes the typical thermal profiles of MoO<sub>2</sub> nanospheres dispersed in water. The nanospheres exhibit obvious concentration-dependent NIR photothermal effects. The temperature increases of the 100 µg/mL MoO<sub>2</sub> nanosphere aqueous dispersion changes from 25.6 °C to 89.8 °C after the irradiation of 5 min (Figure 4b). After that, photothermal cycling stability was examined. MoO<sub>2</sub> solution was irradiated by NIR for 5 minutes, followed by natural cooling for another 6 minutes in each cycle (Figure 4c). After the five cycles, the temperatures changes can be negligible, suggesting MoO<sub>2</sub> nanosphere have a good photostability (Figure S3). The photothermal conversion efficiency of MoO<sub>2</sub> nanospheres were recorded on the basis of literature method.<sup>[52]</sup> The following equation is used to evaluate the photothermal conversion efficiency  $\eta_T$ :

$$\eta_T = \frac{hS(T_{max} - T_{amb}) - Q_0}{I(1 - 10^{-A_\lambda})} \quad (1)$$

where  $h$ ,  $S$  represents the heat transfer coefficient and the surface area of the container respectively, and the value of  $hS$  can be calculated from equation (2). The  $T_{max}$  manifests the maximum system temperature and  $T_{amb}$  means ambient surrounding temperature. In accordance with Figure 4b,  $T_{max} - T_{amb}$  was computed to 64.2 °C.  $I$  signifies the laser power and  $A_\lambda$  means the absorbance (0.9631) with excitation wavelength of 808 nm. The heat input rate is expressed by  $Q_0$ , and its value is approximately 11.88 mW. The method to determine the lumped quantity  $hS$  is to measure the temperature decline rate after

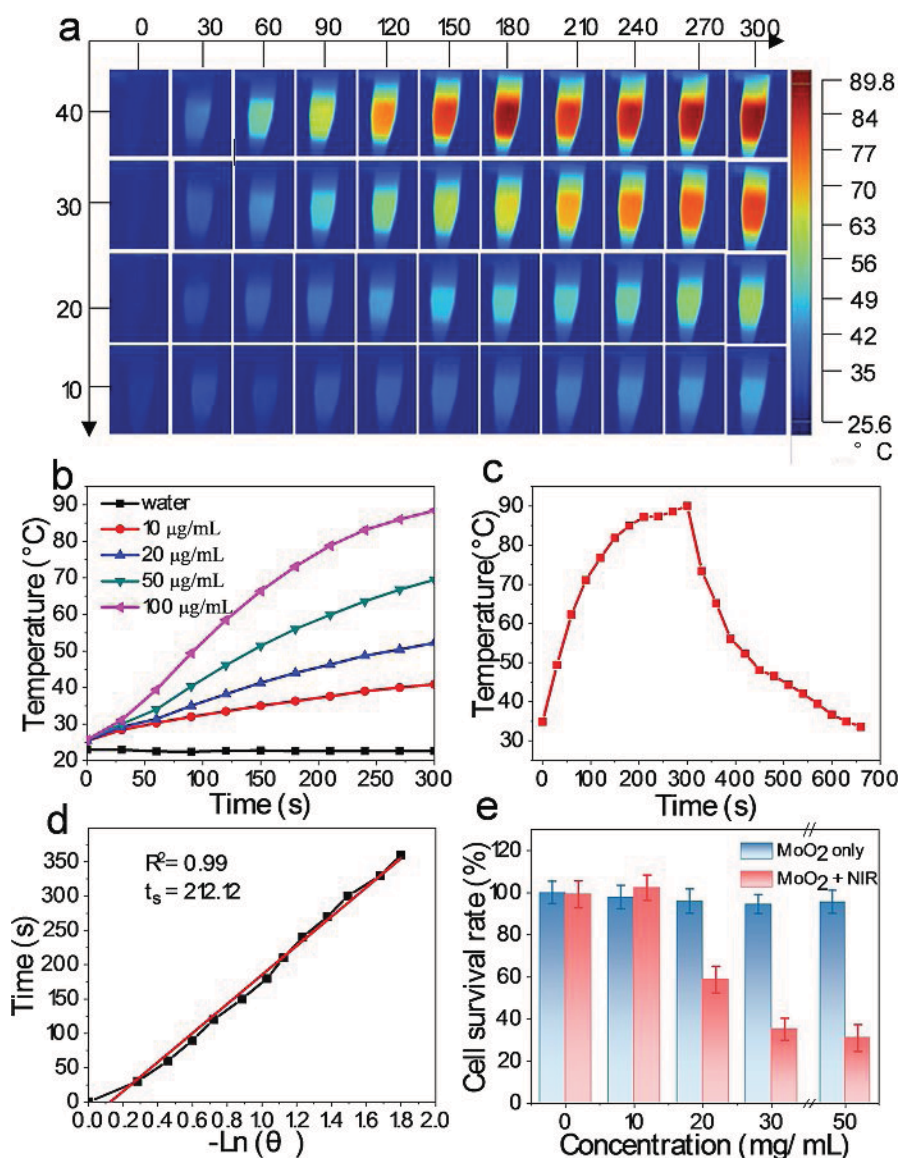


**Figure 4.** (a) Infrared thermographic images. (b) Temperature elevation of pure water and the aqueous dispersion MoO<sub>2</sub> nanospheres of different concentrations irradiated by 808 nm laser. (c) Photothermal effect of 100 µg/mL MoO<sub>2</sub> nanospheres upon being irradiated for 5 min and shutting down the laser. (d) Time constant for heat convert from the system is estimated to be  $\tau_s = 212.12$  s via using the liner date of the cooling period of panel (c) versus negative natural logarithm of driving force temperature. (e) Cell viability of HepG2 cells incubated with different MoO<sub>2</sub> nanospheres concentration for 24 h with or without 5 min laser irradiations at the wavelength of 808 nm. Data are expressed as mean  $\pm$  SD.

taking the light source away. The value of  $hS$  is obtained in the light of the following equation:

$$\tau_s = \frac{m_{DCD}}{hS} \quad (2)$$

where  $\tau_s$  is the sample system time constant is 212.12 s ( $R^2 = 0.991$ ),  $m_D$  means the mass (0.2 mg) and  $C_D$  is heat capacity (4.2 J/g) of deionized water taken use of solvent. Thence, from the above equation, the heat conversion efficiency of MoO<sub>2</sub> nanospheres at 808 nm laser is calculated to be 72.5%. Therefore, MoO<sub>2</sub> have characteristics of intensive optical absorbance

in the NIR region and high photothermal transformation capability, indicating that it is potential and feasible as a PTT.

### 2.3. In vitro photothermal ablation of cancer cells

Moreover, HepG2 liver cancer cells were nurtured with MoO<sub>2</sub> nanospheres in a 96-well plate to research cytotoxicity *in vitro*. As far as we are concerned, biocompatibility of a nanomaterial is the crucially important factor for biomedical applications. Tiny changes of the cell viabilities are observed after the cells were handled with different concentrations of MoO<sub>2</sub> nanospheres for 24 h, demonstrating the low cytotoxicity of this kind

of nanomaterial in a certain extent (Figure 4e). In addition, the cells were coloured with Hoechst 33258 and propidium iodide (PI). For more rigorous experiments, they were compartmentalized into four groups, namely the control group, NIR only, MoO<sub>2</sub> nanospheres only and MoO<sub>2</sub> nanospheres combined with NIR laser. As shown in Figure 5, bright field images displayed the cells morphology. Hoechst 33258 stained images stand for all cells, where the blue spots are the nucleus. Dead cells are stained with propidium iodide (PI), the image shows red. The merge images are overlay images of Hoechst staining and PI staining. In comparison, it was a significant downward of the group of MoO<sub>2</sub> nanospheres + NIR cell viabilities (Figure 4e). All cells irradiated by the laser were inactivated, while the unirradiated cells showed blue fluorescence, which indicates that the MoO<sub>2</sub> nanospheres are expected to perform NIR laser ablation of cancer cells *in vitro*.

#### 2.4. Phototherapeutic studies in vivo

Furthermore, to further confirm the PTT performance of MoO<sub>2</sub> nanospheres in vivo, 4T1 tumor-bearing mice were intratumorally injected 200  $\mu$ L PBS or MoO<sub>2</sub> nanospheres (100  $\mu$ g/mL) 24 h before treatment. Next, 808 nm (2.5 W/cm<sup>2</sup>) laser was used to irradiate the site of tumor for 2 min and IR thermal camera was applied to monitor the surface temperature of the body. As shown in Figure 6a, the temperature of treatment group varies

from 25.6°C to 70°C, increasing by 44.4°C, which is much higher than slightly elevated temperature of the control group, indicating a significantly thermal heating effect compared with that of NIR irradiation alone. Then, the phototherapeutic effect of MoO<sub>2</sub> nanospheres was detected *in vivo*. When the tumors of mice injected intratumorally grew to 200 mm<sup>3</sup>, they were divided into four groups at random (five per group): control group, NIR only group, MoO<sub>2</sub> nanospheres only group and MoO<sub>2</sub> nanospheres plus NIR group, respectively. After treatment for 16 days, it is worth noting that the tumor volume changes in the MoO<sub>2</sub> nanospheres plus NIR group are significantly different from that of the group of control, NIR only and MoO<sub>2</sub> only (Figure 6b). During the 16-day observation period, the body weights of mice in all groups changed subtly, demonstrating that the MoO<sub>2</sub> nanospheres has no acute toxicity (Figure 6c). Moreover, the tumor growth curve in MoO<sub>2</sub> plus NIR laser group also show an effective suppression on the growth of mice tumor after treatment, while the tumors in other groups grow at a fast rate (Figure 6d). Finally, the mice were killed and the tumor tissues and major organs including lung, liver, spleen, kidney and heart were extracted for routine hematoxylin and eosin (H&E) staining assay. Visible from Figure 7, the tissue sections of tumors represent a reduction in cells volume and deepen staining after H&E staining without inflammation accompanied, indicating that apoptosis is the main way to eliminate tumors under a integration of MoO<sub>2</sub> nanospheres and laser irradiation. Meanwhile, the major organs *via* histological

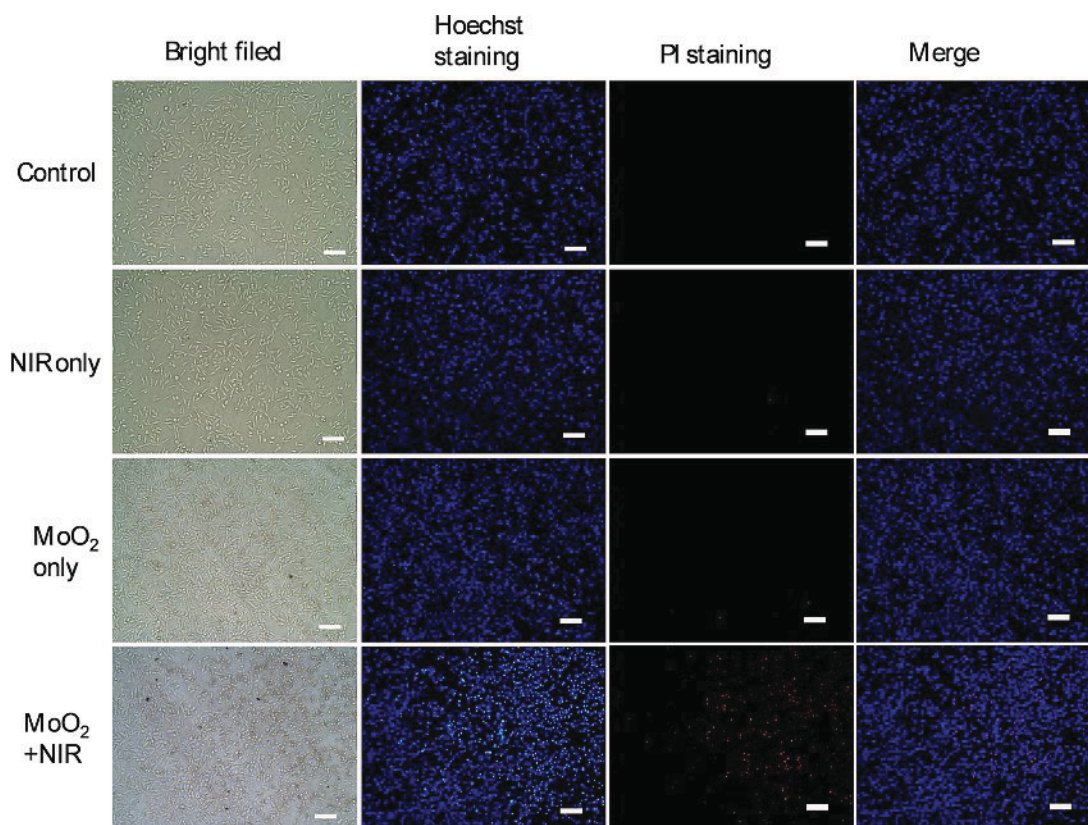
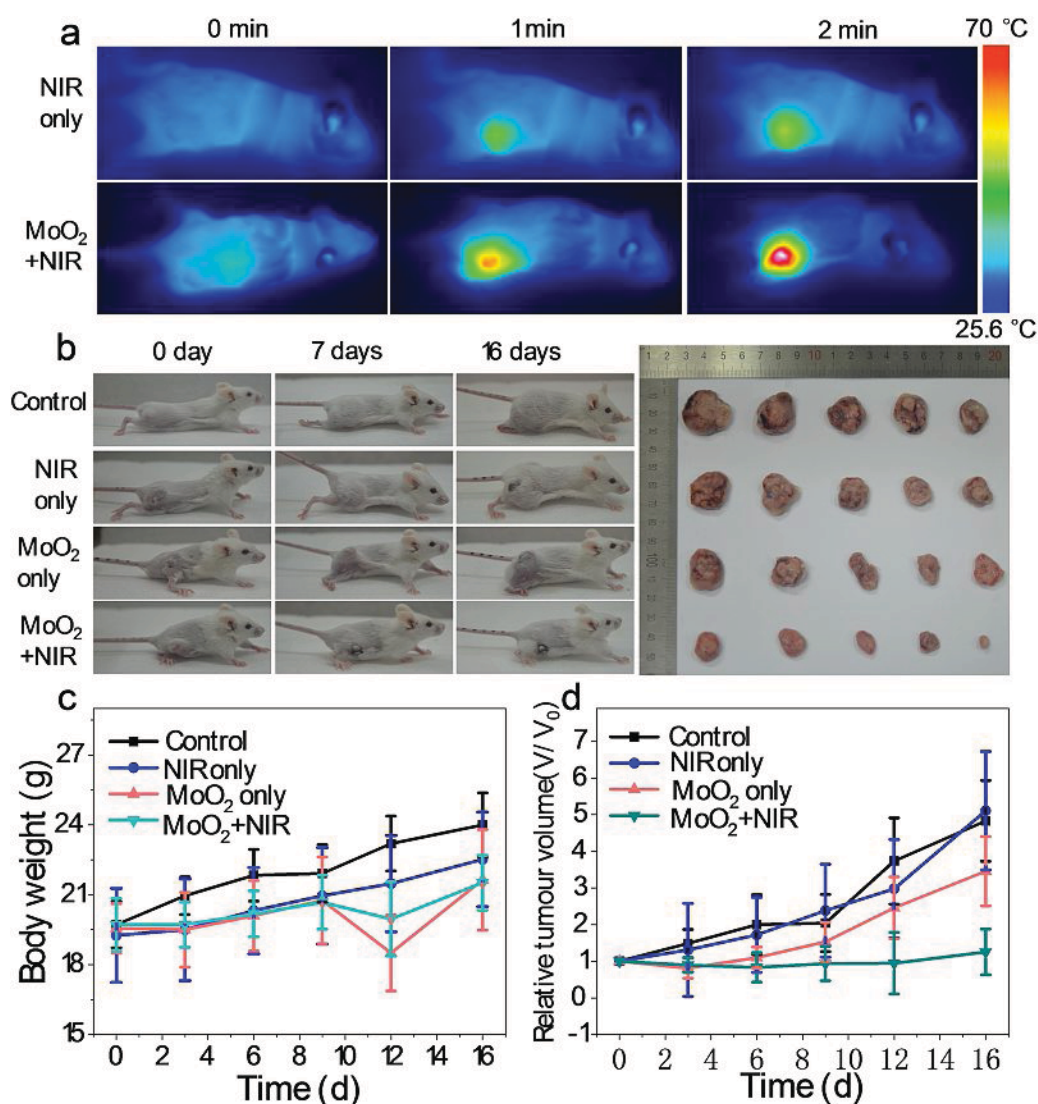


Figure 5. Fluorescence microscopy images of HepG2 cells with various treatments. (scale bar: 50  $\mu$ m)





**Figure 6.** (a) Thermographic image of 4T1 tumor-bearing mice injected with MoO<sub>2</sub> nanospheres or PBS with radiation of 808 nm NIR laser. (b) Volume variation of tumors after 808 nm laser irradiation for 2 min and representative photos of mice and tumors under various treatments after 16 days. (c) (d) Quantitative measurement body weight and tumor volume in mice after various treatments respectively.

analysis display no lesion, such as necrosis, inflammatory and hydropic degeneration in the sectioned tissues, noting that MoO<sub>2</sub> nanospheres can be used as photothermal agents to relieve the cancer.

### 3. Conclusion

In summary, we firstly synthesized different morphology MoO<sub>3-x</sub> nanoparticles with good biocompatibility via one-pot hydrothermal treatment by using (NH<sub>4</sub>)<sub>6</sub>Mo<sub>7</sub>O<sub>24</sub>·4H<sub>2</sub>O as the Mo precursor and PVP K30 as reductant. When the temperature varied from 160 °C, 180 °C to 200 °C, the morphology represented QDs, nanosheets and nanospheres, in which stable MoO<sub>2</sub> nanospheres with a good crystal from and a intense LSPR absorption in the NIR region, have potential to applied as NIR PTT nanoagents *in vivo* and *in vitro*. Moreover, the MoO<sub>2</sub> nano-

spheres we obtained possess high photothermal conversion efficiency ( $\eta = 72.5\%$ ). This provided new possibilities for MoO<sub>2</sub>-guided PTT in the field of biomedicine.

### Experimental section

#### Materials and Chemicals

Polyvinyl pyrrolidone K30 (PVP K30), Ammonium molybdate tetrahydrate ((NH<sub>4</sub>)<sub>6</sub>Mo<sub>7</sub>O<sub>24</sub>·4H<sub>2</sub>O), Hydrochloric acid (HCl, 36%) were purchased from shanghai bo biological technology co., Ltd, Macklin Regent Co., Ltd and Zhuhai hua cheng da chemical co., Ltd respectively. The purity of all reagents is AR grade, the ultrapure water used in the experiment was produced with a Milli-Q system.

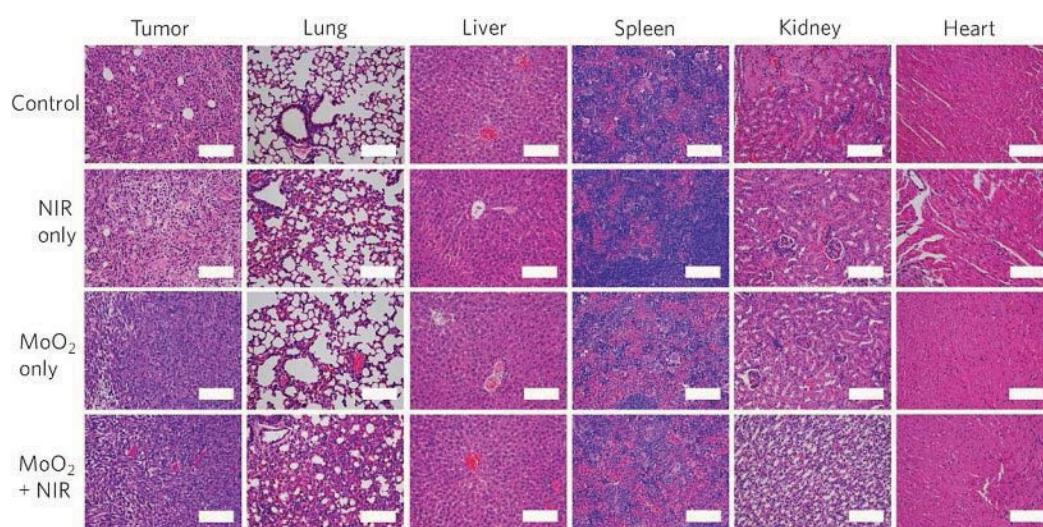


**Figure 7.** Histology staining of tumor and major organs collected from different groups of mice after 16 days treatment (scale bar: 50  $\mu$ m).

### Synthesis of $\text{MoO}_{3-x}$ nanoparticles

The configuration of the PVP solution is to weigh 3.76 g of PVP in 16 ml of water, and the configuration of another mixed solution is to add 2 mmol of ammonium molybdate and a solution of 2.4 mL of hydrochloric acid (1 mol/L) to 26 mL of deionized water. And then the two mixed solutions were stirred evenly. Subsequently, the mixture was poured in an autoclave (100 mL) and heated at 160 °C, 180 °C, and 200 °C for 12 h. After the reaction, the autoclave was taken out from the oven and waiting for a period of cooling down room temperature, the substance in the autoclave was followed by centrifugation, dialysis and freeze-drying to obtain product.

In order to further explore the effect of reaction time on the high temperature redox process, we have synthesized  $\text{MoO}_{3-x}$  samples by using above method with different reaction time (6 h, 12 h and 24 h) at 200 °C.

### Instruments and Equipments

JEOL-2010 electron microscope was used to take the HR-TEM images. The XRD pattern was recorded using a XD-2 $\times$ /M4600. The FT-IR spectra were obtained on a Nicolet 6700 FT-IR spectrometer. The X-ray photoelectron spectroscopy (XPS) was performed on a Thermo Scientific<sup>TM</sup> K-Alpha<sup>TM</sup>+ spectrometer. A Hitachi UV-Vis absorption spectra were recorded on a Shimadzu UV-2550 ultraviolet-visible spectrophotometer.

### Assessment of Photothermal Performance

The procedure for measuring the photothermal conversion performance is that  $\text{MoO}_2$  nanospheres aqueous dispersions with different concentrations (0, 10, 20, 50, 100  $\mu$ g/mL) was set into a cuvette with irradiation of 808 nm laser for 5 minutes.

The portable optical power meter is applied to independently calibrate the output power density of the 808 nm semiconductor laser device. The calibration value is 2.5 W/cm<sup>2</sup>. A thermocouple with an exactness of  $\pm 0.1$  °C was inserted into the aqueous dispersion solution to measure the temperature and the temperature was recorded every 30 s.

### Cell preparation

HepG2 liver cancer cells or mouse mammary carcinoma 4T1 cells were grown in 25 mL culture flasks in succession, cultivated by adding RPMI-1640 medium with 10% FBS, 100 mg/mL streptomycin, and 100 U/mL penicillin 10% heat-inactivated fetal bovine. It was then placed in a humid incubator with 5% CO<sub>2</sub> at 37 °C.

### In vitro cytotoxicity of the $\text{MoO}_2$ nanospheres

Using the MTT assay to estimate the cytotoxicity in vitro, which the cell line HepG2 liver cancer cells. There are  $1 \times 10^4$  cells per well HepG2 cells planted into a 96-well plate were cultured 24 h in an incubator on the premise that cells culture medium was placed at 37 °C and 5% CO<sub>2</sub>. Next, the complete medium was poured then a series of  $\text{MoO}_2$  nanospheres containing different of concentrations, and the cells were hatched out at 37 °C with 5% CO<sub>2</sub> for additional 24 h. Then the previous complete medium was changed to fresh medium with adding 5 mg/mL MTT (10  $\mu$ L), followed by incubating at 37 °C and 5% CO<sub>2</sub> for further 4 h. The next procedure was to add 100  $\mu$ L DMSO in order to lyse the cells. The spectrophotometric absorbance of formazan was performed using a Microplate Reader at 490 nm. Each of treatment group was done four replicates.

## In vivo toxicity of MoO<sub>2</sub> nanospheres

Twenty healthy female mice (5 weeks old, about 20 g) were obtained from the Experimental Animal Center of Southern Medical University and operated according to the protocol given official approval by the Animal Care and Use Committee of South China Normal University. A week later, the mice were subcutaneous injected 4T1 cells, then were divided into 4 groups with 5 mice in each group at random until the tumors grew to 200 mm<sup>3</sup>: PBS control, NIR only (808 nm laser, 2 min), MoO<sub>2</sub> only and MoO<sub>2</sub>+NIR (808 nm laser, 2 min) respectively. Next, 200 µL of PBS or MoO<sub>2</sub> nanospheres (100 µg/mL) were injected separately into the mice via intratumorally injected manner. Measuring the tumor volume to achieve evaluating the therapeutic effectiveness of each group, whose calculation formula is  $(V) = \text{length} \times \text{width}^2$ . The calculation formula of relative tumor volume is  $V/V_0$ , where  $V_0$  is the beginning tumor volume before treatment and  $V$  is the body weight recorded on 3 days, 6 days, 9 days, 12 days and 16 days.

## Histology staining

Histology staining refers to tumors and major organs excised from all groups, including lung, liver, spleen, kidney and heart. Subsequently, the tumors and organs were processed with 4% paraformaldehyde solution and paraffin. Hematoxylin and eosin (H&E) were utilized to stain the tumor tissues and organs, which observed by fluorescence microscope.

## Acknowledgments

The present work was supported by the National Natural Science Foundations of China (Grant No. 51402207, 21571067, 11874021) and the Natural Science Foundation of Guangdong Province (2020A1515010443). The funding information also has been revised in f202000311\_funding Excel.

## Conflict of Interest

The authors declare no conflict of interest.

**Keywords:** Molybdenum oxide · Surface plasmon resonance · Near-infrared light · Photothermal therapy · Cancer

- [1] H. W. Yang, M. Y. Hua, T. L. Hwang, K. J. Lin, C. Y. Huang, R. Y. Tsai, C. C. Ma, P. H. Hsu, S. P. Wey, P. W. Hsu, P. Y. Chen, Y. C. Huang, Y. J. Lu, T. C. Yen, L. Y. Feng, C. W. Lin, H. L. Liu, K. C. Wei, *Adv. Mater.* **2013**, *25*, 3605.
- [2] M. E. Werner, S. Karve, R. Sukumar, N. D. Cummings, J. A. Copp, R. C. Chen, T. Zhang, A. Z. Wang, *Biomaterials* **2011**, *32*, 8548.
- [3] J. H. Fang, Y. H. Lai, T. L. Chiu, Y. Y. Chen, S. H. Hu, S. Y. Chen, *Adv. Healthcare Mater.* **2014**, *3*, 1250.
- [4] Z. Xiao, C. Ji, J. Shi, E. M. Pridgen, J. Frieder, J. Wu, O. C. Farokhzad, *Angew. Chem. Int. Ed. Engl.* **2012**, *51*, 11853.
- [5] T. Liu, C. Wang, X. Gu, H. Gong, L. Cheng, X. Shi, L. Feng, B. Sun, Z. Liu, *Adv. Mater.* **2014**, *26*, 3433.

- [6] J. E. Dahlman, C. Barnes, O. Khan, A. Thiriot, S. Jhunjunwala, T. E. Shaw, Y. Xing, H. B. Sager, G. Sahay, L. Speciner, A. Bader, R. L. Bogorad, H. Yin, T. Racie, Y. Dong, S. Jiang, D. Seedorf, A. Dave, K. S. Sandu, M. J. Webber, T. Novobrantseva, V. M. Ruda, A. K. R. Lytton-Jean, C. G. Levins, B. Kalish, D. K. Mudge, M. Perez, L. Abezgauz, P. Dutta, L. Smith, K. Charisse, M. W. Kieran, K. Fitzgerald, M. Nahrensdorf, D. Danino, R. M. Tuder, U. H. von Andrian, A. Akinc, A. Schroeder, D. Panigrahy, V. Kotlianski, R. Langer, D. G. Anderson, *Nat. Nanotechnol.* **2014**, *9*, 648.
- [7] D. Ding, W. Guo, C. Guo, J. Sun, N. Zheng, F. Wang, M. Yan, S. Liu, *Nanoscale* **2017**, *9*, 2020.
- [8] S. Wang, P. Huang, L. Nie, R. Xing, D. Liu, Z. Wang, J. Lin, S. Chen, G. Niu, G. Lu, X. Chen, *Adv. Mater.* **2013**, *25*, 3055.
- [9] J. F. Lovell, C. S. Jin, E. Huynh, T. D. MacDonald, W. Cao, G. Zheng, *Angew. Chem. Int. Ed. Engl.* **2012**, *51*, 2429.
- [10] H. Peng, L. Jing, W. Can, W. Xiansong, Z. Chunlei, Z. Xuejiao, G. Shouwu, D. Cui, *Theranostics* **2011**, *1*, 240.
- [11] O. Lupan, V. Cretu, M. Deng, D. Gedamu, I. Paulowicz, S. Kaps, Y. K. Mishra, O. Polonsky, C. Zamponi, L. Kienle, V. Trofim, I. Tiginyanu, R. Adelung, *J. Phys. Chem. C* **2014**, *118*, 15068.
- [12] G. P. Nagabhushana, D. Samrat, G. T. Chandrappa, *RSC Adv.* **2014**, *4*, 56784.
- [13] B. Kannan, R. Pandeewari, B. G. Jeyaprakash, *Ceram. Int.* **2014**, *40*, 5817.
- [14] Y. Zhang, Q. Zhao, W. Zhu, L. Zhang, J. Han, Q. Lin, F. Ai, *Pharm. Res.* **2015**, *32*, 2372.
- [15] S. Z. Butler, S. M. Hollen, L. Cao, Y. Cui, J. A. Gupta, H. R. Gutiérrez, T. F. Heinz, S. S. Hong, J. Huang, A. F. Ismach, *ACS Nano* **2013**, *7*, 2898.
- [16] D. Jariwala, V. K. Sangwan, L. J. Lauhon, T. J. Marks, M. C. Hersam, *Acs Nano* **2014**, *8*, 1102.
- [17] J. N. Coleman, M. Lotya, A. O. Neill, S. D. Bergin, P. J. King, U. Khan, K. Young, A. Gaucher, S. De, R. J. Smith, I. V. Shvets, S. K. Arora, G. Stanton, H. Y. Kim, K. Lee, G. T. Kim, G. S. Duesberg, T. Hallam, J. J. Boland, J. J. Wang, J. F. Donegan, J. C. Grunlan, G. Moriarty, A. Shmeliov, R. J. Nicholls, J. M. Perkins, E. M. Grieveson, K. Theuvsen, D. W. McComb, P. D. Nellist, V. Nicolosi, *Science* **2011**, *311*, 568.
- [18] X. Lu, R. Wang, F. Yang, W. Jiao, W. Liu, L. Hao, X. He, *J. Mater. Chem. C* **2016**, *4*, 6720.
- [19] W. Yin, L. Yan, J. Yu, G. Tian, L. Zhou, X. Zheng, X. Zhang, Y. Yong, J. Li, Z. Gu, *ACS Nano* **2014**, *8*, 6922.
- [20] J. Li, Z. Lyv, Y. Li, H. Liu, J. Wang, W. Zhan, H. Chen, H. Chen, X. Li, *Biomaterials* **2015**, *51*, 12; C. Liang, S. Diao, C. Wang, H. Gong, T. Liu, G. Hong, X. Shi, H. Dai, Z. Liu, *Adv. Mater.* **2014**, *26*, 5646.
- [21] C. Liang, S. Diao, C. Wang, H. Gong, T. Liu, G. Hong, et al. *Adv. Mater.* **2014**, *26*, 5646.
- [22] F. Zhou, S. Wu, B. Wu, W. R. Chen, D. Xing, *Small* **2011**, *7*, 2727.
- [23] F. Li, X. Zhao, H. Wang, R. Zhao, T. Ji, H. Ren, G. J. Anderson, G. Nie, J. Hao, *Adv. Funct. Mater.* **2015**, *25*, 788.
- [24] J. Liu, J. Han, Z. Kang, R. Golamally, N. Xu, H. Li, X. Han, *Nanoscale* **2014**, *6*, 5770.
- [25] X. Liu, Q. Wang, C. Li, R. Zou, B. Li, G. Song, K. Xu, Y. Zheng, J. Hu, *Nanoscale* **2014**, *6*, 4361.
- [26] J. Mou, P. Li, C. Liu, H. Xu, L. Song, J. Wang, K. Zhang, Y. Chen, J. Shi, H. Chen, *Small* **2015**, *11*, 2275.
- [27] S. Wang, A. Riedinger, H. Li, C. Fu, H. Liu, L. Li, T. Liu, L. Tan, M. J. Barthel, G. Pugliese, F. De Donato, M. Scotto D'Abbasco, X. Meng, L. Manna, H. Meng, T. Pellegrino, *ACS Nano* **2015**, *9*, 1788.
- [28] P. Huang, J. Lin, W. Li, P. Rong, Z. Wang, S. Wang, X. Wang, X. Sun, M. Aronova, G. Niu, R. D. Leapman, Z. Nie, X. Chen, *Angew. Chem. Int. Ed. Engl.* **2013**, *52*, 13958.
- [29] Z. Zhang, J. Wang, X. Nie, T. Wen, Y. Ji, X. Wu, Y. Zhao, C. Chen, *J. Am. Chem. Soc.* **2014**, *136*, 7317.
- [30] L. Cheng, J. Liu, X. Gu, H. Gong, X. Shi, T. Liu, C. Wang, X. Wang, G. Liu, H. Xing, W. Bu, B. Sun, Z. Liu, *Adv. Mater.* **2014**, *26*, 1886.
- [31] R. Shimizu, K. Yamamoto, T. Suzuki, T. Ohsawa, S. Shiraki, T. Hitosugi, *Thin Solid Films* **2015**, *595*, 153.
- [32] V. Kumar, X. Wang, P. S. Lee, *Nanoscale* **2015**, *7*, 11777.
- [33] J. Guo, Y. Zhao, J. Zhao, J. Wu, Y. Song, Y. Tan, F. Wang, X. Hao, Y. Lu, F. Bao, *Eur. J. Inorg. Chem.* **2014**, *2014*, 3322.
- [34] H. Cheng, T. Kamegawa, K. Mori, H. Yamashita, *Angew. Chem. Int. Ed. Engl.* **2014**, *53*, 2910.
- [35] S. D. Lounis, E. L. Runnerstrom, A. Llodes, D. J. Milliron, *J. Phys. Chem. Lett.* **2014**, *5*, 1564.
- [36] M. L. Bhaisare, K. H. Sharma, J. Y. Lee, D. R. Hang, H. F. Wu, *New J. Chem.* **2016**, *40*, 8954.
- [37] G. Song, J. Shen, F. Jiang, R. Hu, W. Li, L. An, R. Zou, Z. Chen, Z. Qin, J. Hu, *ACS Appl. Mater. Interfaces* **2014**, *6*, 3915.



- [38] W. Fang, S. Tang, P. Liu, X. Fang, Gong, J. Gong, N. Zheng, *Small* **2012**, *8*, 3816.
- [39] D. Ding, W. Huang, C. Song, M. Yan, C. Guo, S. Liu, *Chem Commun (Camb)* **2017**, *53*, 6744.
- [40] H. Yu, Z. Zhuang, D. Li, Y. Guo, Y. Li, H. Zhong, H. Xiong, Z. Liu, Z. Guo, *J Mater. Chem. B* **2020**, *8*, 1040.
- [41] Y. Li, J. Wu, G. R. Williams, S. Niu, J. Zhou, Y. Yang, X. Zhang, Z. Fu, D. Li, L.-M. Zhu, *ACS Appl. Bio Mater.* **2019**, *2*, 4356.
- [42] Y. Li, Z. Miao, Z. Shang, Y. Cai, J. Cheng, X. Xu, *Adv. Funct. Mater.* **2019**, *30*, 1906311.
- [43] L. Niu, J. N. Coleman, H. Zhang, H. Shin, M. Chhowalla, Z. Zheng, *Small* **2016**, *12*, 272.
- [44] G. Song, J. Hao, C. Liang, T. Liu, M. Gao, L. Cheng, J. Hu, Z. Liu, *Angew. Chem. Int. Ed. Engl.* **2016**, *55*, 2122.
- [45] S. J. Xiao, X. J. Zhao, P. P. Hu, Z. J. Chu, C. Z. Huang, L. Zhang, *ACS Appl. Mater. Interfaces* **2016**, *8*, 8184.
- [46] T. Bao, W. Yin, X. Zheng, X. Zhang, J. Yu, X. Dong, Y. Yong, F. Gao, L. Yan, Z. Gu, Y. Zhao, *Biomaterials* **2016**, *76*, 11.
- [47] W. Han, P. Yuan, Y. Fan, H. Liu, X. Bao, *J. Mater. Chem.* **2012**, *22*, 12121.
- [48] A. Chithambararaj, A. C. Bose, *J. Alloys Compd.* **2011**, *509*, 8105.
- [49] J. Park, I. Choi, M. J. Lee, M. H. Kim, T. Lim, K. H. Park, J. Jang, S. M. Oh, S. K. Cho, J. J. Kim, *Electrochim. Acta* **2014**, *132*, 338.
- [50] S. Geng, Y. Liu, Y. S. Yu, W. Yang, H. Li, *Nano Res.*, **2019**, *13*, 121.
- [51] X. Xie, L. Lin, R.-Y. Liu, Y.-F. Jiang, Q. Zhu, A.-W. Xu, *J. Mater. Chem. A*, **2015**, *3*, 8055.
- [52] M. M. Alsaif, K. Latham, M. R. Field, D. D. Yao, N. V. Medhekar, G. A. Beane, R. B. Kaner, S. P. Russo, J. Z. Ou, K. Kalantarzadeh, *Adv. Mater.* **2014**, *26*, 3931.

---

Manuscript received: May 20, 2020  
 Revised manuscript received: July 5, 2020  
 Accepted manuscript online: July 6, 2020  
 Version of record online: July 28, 2020

---



Contents lists available at ScienceDirect

Journal of Hazardous Materials

journal homepage: [www.elsevier.com/locate/jhazmat](http://www.elsevier.com/locate/jhazmat)

## Research paper

## Carbon dots as light converter for plant photosynthesis: Augmenting light coverage and quantum yield effect

Yadong Li<sup>a,b</sup>, Xiaoqin Pan<sup>a,b</sup>, Xiaokai Xu<sup>a,b</sup>, Ying Wu<sup>a,b</sup>, Jianle Zhuang<sup>a,b</sup>, Xuejie Zhang<sup>a,b</sup>, Haoran Zhang<sup>a,b</sup>, Bingfu Lei<sup>a,b,\*</sup>, Chaofan Hu<sup>a,b,\*</sup>, Yingliang Liu<sup>a,b,\*</sup><sup>a</sup> Key Laboratory for Biobased Materials and Energy of Ministry of Education/Guangdong Provincial Engineering Technology Research Center for Optical Agriculture, College of Materials and Energy, South China Agricultural University, Guangzhou 510642, China<sup>b</sup> Guangdong Laboratory of Lingnan Modern Agriculture, Guangzhou 510642 China

## ARTICLE INFO

Editor: Dr. Navid B. Saleh

## Keywords:

Carbon dots  
Quantum yield  
Surface chemistry  
Photosynthesis  
Light conversion

## ABSTRACT

Carbon dots (CDs) with gradient-changed quantum yield (QY) were prepared by regulating the graphitic N and hydroxyl group contents. Then, the QY effect of CDs on plant photosynthesis was studied using chloroplasts and rice plants. After incubation for 2 h in the dark, CDs entered into the chloroplasts and converted ultraviolet radiation to photosynthetically active radiation. By this mechanism, CD1:0.2 (300  $\mu\text{g}\cdot\text{mL}^{-1}$ ) with a moderate QY of 46.42% significantly increased the photosynthetic activity of chloroplast (200  $\mu\text{g}\cdot\text{mL}^{-1}$ ) to reduce DCPIP and ferricyanide by 43.77% and 25.45%, respectively. After spraying on rice seedlings, CD1:0.2 (300  $\mu\text{g}\cdot\text{mL}^{-1}$ ) was evenly distributed in the leaves and resulted in maximum increases in the electron transport rate and photosynthetic efficiency of photosystem II by 29.81% and 29.88%, respectively. Furthermore, CD1:0.2 significantly increased the chlorophyll content and RuBisCO carboxylase activity of rice by 64.53% and 23.39%, respectively. Consequently, significant increases were observed in the growth of CD1:0.2-treated rice, including 18.99%, 64.31%, and 61.79% increases in shoot length, dry weights of shoot and root. These findings contribute to the exploitation of solar energy and agricultural production using CDs in the future.

## 1. Introduction

Agriculture supplies food to humanity and raw materials to industry. Due to the ever-increasing population and industry, global agricultural production is estimated to be increased by 70% by 2050 (van Esse et al., 2020). Fertilizers and pesticides have been increasingly used to ensure agricultural production, which brings about severe pollution to the environment (Wang et al., 2019; Liao et al., 2020). Although the advances in genetic engineering and agronomic techniques show great potential to increase crop production (Bailey-Serres et al., 2019; Singh et al., 2019), they are time-consuming, labor-intensive, and high-cost. Furthermore, genetically modified foods raise notable social concerns due to the unknown risk of long-term exposure (Zhang et al., 2016; Pham and Mandel, 2019). It has been commonly estimated that more than 90% of crop biomass is produced by photosynthesis, in which  $\text{CO}_2$  and water are synthesized into energy-rich organic matter by absorbing solar energy (Wu et al., 2019). However, due to the narrow absorption coverage (400–700 nm), the utilization efficiency of solar energy by

photosynthesis is less than 10%, which severely limits the improvement of plant photosynthetic efficiency (Grayson et al., 2017; Li et al., 2018; Pessarakli, 2016). Moreover, ultraviolet (UV) radiation (200–400 nm) in sunlight can induce reactive oxygen species (ROS) in the plants, which damage DNA, proteins, and cell membranes (Pathak et al., 2020; Radyukina et al., 2017). Thus, augmenting the light coverage of plant photosynthesis and reducing the toxic UV radiation are essential to food production.

The rapid development of nanotechnology allows us to explore novel materials in biological systems to enhance photosynthesis (Guo et al., 2020; Li et al., 2018; Pan et al., 2020). Fluorescent carbon dots (CDs) are an emerging star material in the carbon-based material family. Compared to other fluorescent materials, such as organic dye molecules, fluorescent protein, and semiconductor quantum dot, CDs exhibit outstanding properties, including resistance to photobleaching, biocompatibility, low toxicity, and low cost (Han et al., 2018; Xiao et al., 2019). Thus, CDs have been widely used in photocatalysis (Han et al., 2018), biomedicine (Jaleel and Pramod, 2018), biosensors (Sharma and

\* Corresponding authors at: Key Laboratory for Biobased Materials and Energy of Ministry of Education/Guangdong Provincial Engineering Technology Research Center for Optical Agriculture, College of Materials and Energy, South China Agricultural University, Guangzhou 510642, China

E-mail addresses: [tleibf@scau.edu.cn](mailto:tleibf@scau.edu.cn) (B. Lei), [thucf@scau.edu.cn](mailto:thucf@scau.edu.cn) (C. Hu), [tliuyl@scau.edu.cn](mailto:tliuyl@scau.edu.cn) (Y. Liu).

<https://doi.org/10.1016/j.jhazmat.2020.124534>

Received 2 April 2020; Received in revised form 29 October 2020; Accepted 8 November 2020

Available online 11 November 2020

0304-3894/© 2020 Elsevier B.V. All rights reserved.

Das, 2019), and the environment (Han et al., 2018; Nayak et al., 2020). Recently, CDs are reported to be beneficial to plant growth, resistance, and photosynthesis (Li et al., 2020a, 2020b). With highly tunable fluorescence emission under UV radiation (Molaei, 2020), CDs are promising to engineer nanobiohybrids with plants to augment the photosynthesis by light conversion. Previously, CDs have been demonstrated to transfer energy to the chloroplast and accelerate the electron transfer in photosystem II (PS II) (Li et al., 2018; Chandra et al., 2014; Wang et al., 2018). However, the direct energy transfer to chloroplast may disturb the normal physiology of the thylakoid (Pankratov et al., 2019; Lu et al., 2017). Given the critical role of the light intensity in photosynthesis (Lu et al., 2017), the quantum yield (QY) may be a crucial factor of CDs that influences the plant photosynthesis. Unfortunately, the preparation of CDs with gradient-tunable QYs remains a challenge, although various methods have been developed to enhance the QY of CDs (Zhang et al., 2016; Sun et al., 2015).

In this study, CDs with gradient-tunable QYs were successfully prepared, and the underlying mechanism was demonstrated. Then, CDs with QYs of 15.13%, 46.42%, and 90.59% were employed to study their effect on plant photosynthesis using isolated chloroplasts and rice plants. Finally, the growth of rice seedlings exposed to CDs was measured. This study demonstrates that moderate QY is essential for CDs to enhance the photosynthesis and growth of plants, indicating the great potential of CDs to increase agricultural production in the future.

## 2. Experimental section

### 2.1. Preparation of CDs

CDs with different QYs were prepared by one-pot microwave-assisted pyrolysis using citric acid (CA) and ethanolamine (EA). Briefly, CA (10 mM) and EA (0.05 mM, 0.2 mM, 0.8 mM, 1.5 mM or 2 mM) were dissolved in 20 mL ultrapure water by sonication for 30 min. These samples were heated in a domestic microwave oven under medium heat (350 W). The reaction went through rapid water removal and carbonization processes. Shaking every five minutes was necessary to avoid an uneven reaction. The formation of a black-brown colloidal substance indicated the generation of CDs, followed by another 5 min heating for full carbonization. The obtained samples were dissolved into ultrapure water, filtrated (0.22  $\mu$ m) and stored at room temperature. According to the molar ratios between CA and EA, these CDs were denoted as CD1:0.05, CD1:0.2, CD1:0.8, CD1:1.5, and CD1:2. The QYs of the CDs were determined using quinine sulfate (0.1 M H<sub>2</sub>SO<sub>4</sub> as the solvent, QY=54%) as a reference according to a literature method (Wu et al., 2017).

### 2.2. Characterization of CDs

The morphology of the CDs was observed using an FEI Tecnai 12 transmission electron microscope (TEM). The component of the CDs was analyzed by a Nicolet Avatar 360 FTIR spectrophotometer and AXIS ULTRA DLD X-ray photoelectron spectroscopy (XPS). F-7000 Hitachi and FLS 1000-STM fluorescence spectrophotometers were used to investigate the fluorescence spectrum and lifetime of the CDs. The UV-Vis absorption spectra of the CDs were measured using a Perkins Elmer UV-Vis spectrophotometer (Lambda 750).

### 2.3. Isolation of chloroplasts

With similar structure and function among different plants, the chloroplast isolated from lettuce (*Lactuca sativa* L.) was used as a model (Li et al., 2018), because its large leaves are rich in chloroplasts. Briefly, lettuce leaves (10 g) were ground using an electric blender for 10 s in 20 mL of sucrose phosphate buffer (0.4 M sucrose, 10 mM KCl, 30 mM Na<sub>2</sub>HPO<sub>4</sub>·12H<sub>2</sub>O, 20 mM KH<sub>2</sub>PO<sub>4</sub>, pH 6.2) under ice-cold condition. The slurry was filtered through 4-layers of gauze and centrifuged at

1000 rpm at 4 °C for 3 min to remove the cell debris. After second centrifugation at 3000 rpm for 3 min at 4 °C, the precipitate was collected and resuspended in the above buffer as chloroplast stock suspension. The obtained chloroplast was a mixture of broken chloroplasts (Type C), i.e., thylakoids, along with some intact ones (Li et al., 2018; Wang et al., 2017). The concentration of the chloroplast suspension was expressed by chlorophyll content. 100  $\mu$ L of chloroplast suspension was intensively mixed with 4.9 mL of acetone, followed by centrifugation at 3000 rpm for 3 min to remove the debris. Then, the absorbance of the supernatant was measured at 652 nm, and the chlorophyll concentration (mg·mL<sup>-1</sup>) was calculated by the following equation (Yuan et al., 2013):

$$C(\text{mg}\cdot\text{mL}^{-1}) = \frac{OD_{652} \times 50}{34.5} \quad (1)$$

where  $C$  represents the chlorophyll concentration, and  $OD_{652}$  is the absorbance at 652 nm.

### 2.4. Interaction between CD and chloroplast

CD1:0.05, CD1:0.2 and CD1:0.8 were used to investigate their effect on photosynthesis. Firstly, chloroplast suspensions were mixed with CDs and incubated in the dark at 4 °C for 2 h. Then, the formed composites (CD1:0.05@Chl, CD1:0.2@Chl and CD1:0.8@Chl) were collected by centrifugation at 3000 rpm for 3 min at 4 °C. Then, the morphologies of these composites were observed by an FEI Verios 460 scanning electron microscope (SEM) and an FEI Tecnai 12 TEM according to the standard protocol (Chandra et al., 2014). Furthermore, the UV-Vis spectra, fluorescence emission spectra, and fluorescence lifetime of these composites were measured using Perkin Elmer UV-Vis spectrophotometer (Lambda 750), F-7000 Hitachi, and FLS 1000-STM fluorescence spectrophotometer, respectively.

### 2.5. Hill reaction

Hill reaction was performed as described in our previous report (Li et al., 2018). Firstly, a preliminary experiment was carried out for the optimal concentration ratio between CDs and chloroplasts. The suspensions of CD@Chl (200  $\mu$ g chlorophyll per mL suspension) were mixed thoroughly with 2,6-dichlorophenolindophenol (DCPIP, 360  $\mu$ M) in the dark, and then radiated under 600 LUX light at room temperature. The absorbance of the mixtures at 600 nm was recorded at an interval of 1 min using a Perkin Elmer UV-Vis spectrophotometer (Lambda 750). A standard curve (Fig. S1) with a correlation coefficient of 0.9989 was used to match the reduced DCPIP. Three replications were evaluated for each treatment, and CDs and chloroplast alone were measured as control treatments. The DCPIP reduction reflected Hill activity of the chloroplasts.

### 2.6. Ferricyanide reduction

Ferricyanide reduction was measured by the spectrophotometric method (Li et al., 2018). According to Hill reaction, the concentration ratio between CDs and chloroplasts was set at 3:2. Chloroplast or CD@Chl suspensions (75  $\mu$ g CDs:50  $\mu$ g chlorophyll per mL suspension) was mixed with potassium ferricyanide (final concentration of 250  $\mu$ M) at room temperature in the dark. After irradiation under a xenon lamp (3000 LUX) for 2 min or a portable ultraviolet analyzer (365 nm, 16 W) for 5 min, trichloroacetic acid (final concentration of 2%) was added to stop the reaction. Then, the supernatant was collected to measure the absorbance at 420 nm after centrifugation at 3000 rpm for 3 min. A standard curve (Fig. S2) with a correlation coefficient of 0.9877 was used to match the concentration of the reduced potassium ferricyanide. Three replications were evaluated for each treatment. The CDs and chloroplasts alone at the same concentrations were measured as control treatments. The actual ferricyanide reduction ( $A$ ) by chloroplast or



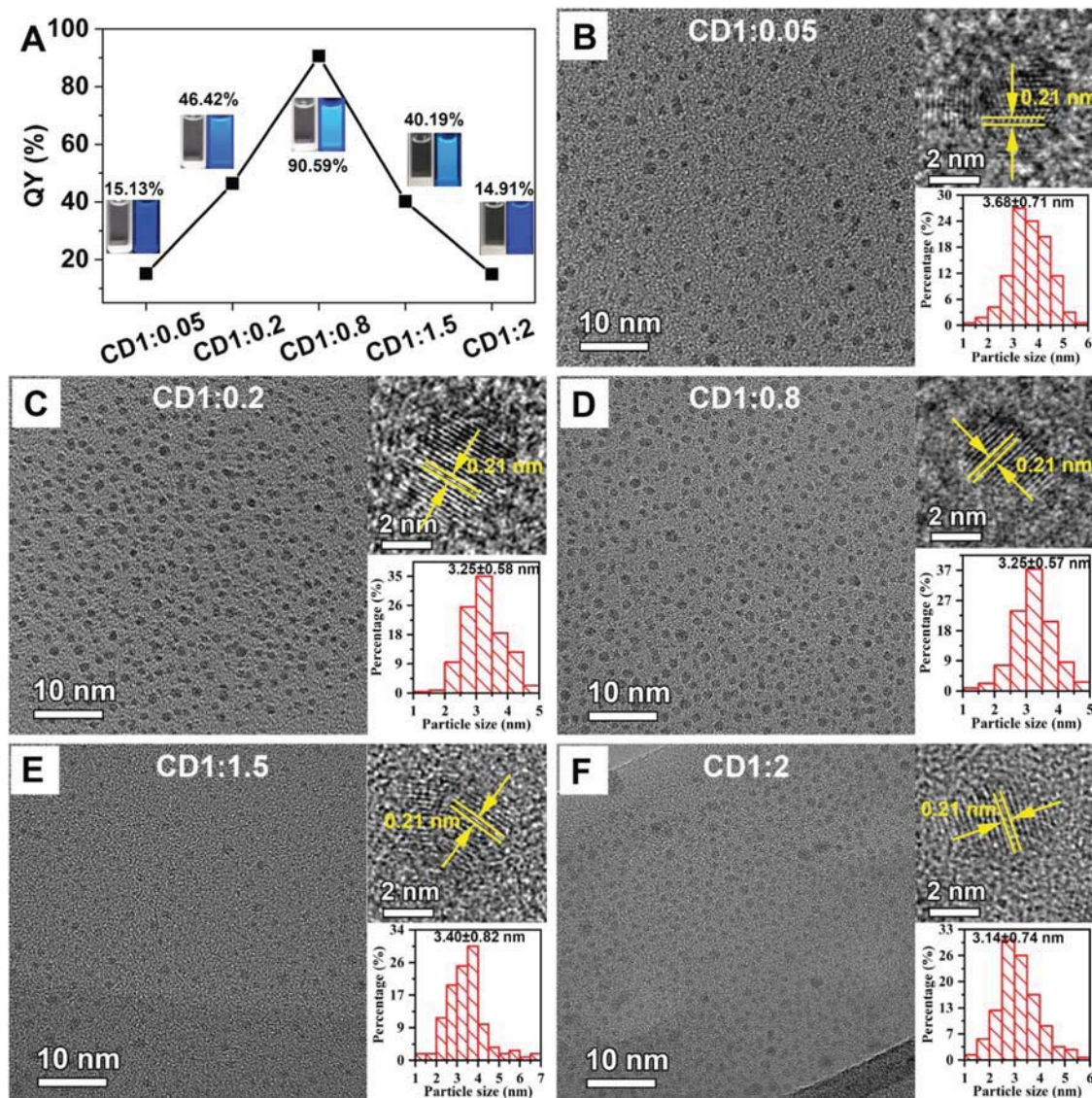


Fig. 1. (A) QYs as a function of molar ratio of the corresponding reactants; (B–F) TEM images (left), HR-TEM images (upper right) and size distribution histograms (bottom right) of CD1:0.05, CD1:0.2, CD1:0.8, CD1:1.5 and CD1:2.

CD@Chl was calculated by the following formula:

$$A(\mu M) = A_t - A_0 \quad (2)$$

where  $A_t$  represents the ferricyanide reduction in the treatments of chloroplast or CD@Chl, and  $A_0$  represents that in the treatments of CDs alone.

## 2.7. Rice plant cultivation

Rice seedlings were cultured by hydroponics, as described in our previous report (Li et al., 2018). Firstly, rice seeds were surface-sterilized using 75% ethanol for 20 min and rinsed with ultra-pure water. Then, the seeds were placed on a germination tray at 30 °C in the dark. After three days, the germinated seedlings were transferred to a greenhouse with a day/night temperature regime of 27 °C (14 h):23 °C (10 h) and a light intensity of 400  $\mu\text{mol m}^{-2} \text{s}^{-1}$ . The light source used for the cultivation of rice seedlings was composed of 6.58% of 345–400 nm, 48.66% of 400–495 nm, and 42.68% of 495–780 nm (Fig. S3, Table S1). On the 7th day, the rice seedlings were transplanted to pots with a density of 20 seedlings per pot. A specified nutrient solution (Table S2) was used to culture the seedlings and refreshed once a

week. The rice seedlings at the three-leaf stage were sprayed with CDs aqueous solutions ( $300 \mu\text{g}\cdot\text{mL}^{-1}$ ) three times a week with a dose of 5  $\text{mL}\cdot\text{pot}^{-1}$ . Shaking of the rice leaves should be avoided until the liquid drops dried. Deionized water was synchronously sprayed as a control group, and three replications were carried out for each treatment. After three weeks, the growth parameters (shoot and root lengths, total fresh and dry weights) of the rice seedlings were recorded. Another group of rice seedlings were cultured under pure UV radiation (450 LUX) and treated with CD1:0.2 to determine the light conversion of CD1:0.2 in photosynthesis.

## 2.8. Chlorophyll fluorescence measurements

Chlorophyll fluorescence of the CDs-treated rice leaves was measured using the Imaging PAM fluorometer system (Walz, Germany). Before the measurement, the rice seedlings were adapted to darkness for 30 min for the equilibrium of photosynthetic system II (PS II) redox states. The measurement was carried out using the penultimate leaves from each rice seedlings under photosynthetic active radiation (PAR) of 0, 1, 36, 111, 231, 396, 461, 531, 611, 701, and 801  $\mu\text{mol m}^{-2} \text{s}^{-1}$ . The electron transport rates (ETR) and actual photosynthetic efficiency Y(II)

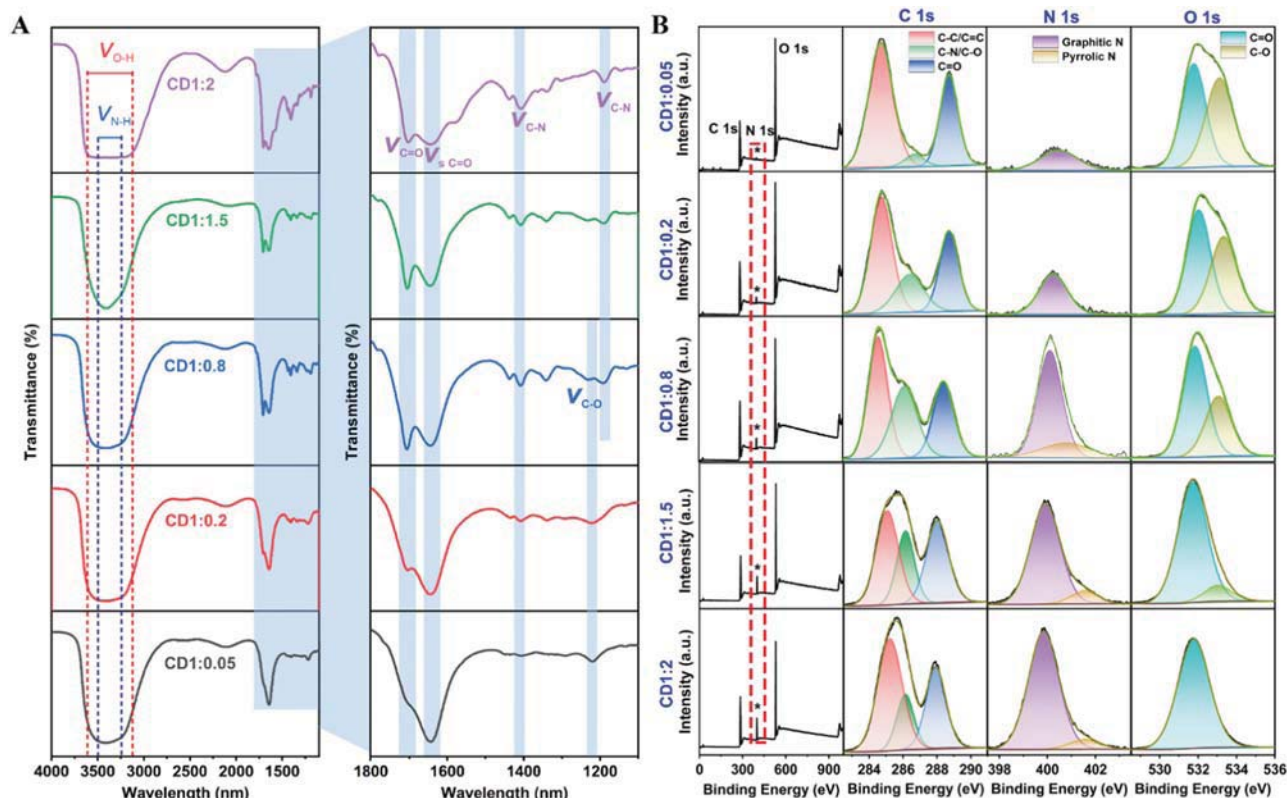


Fig. 2. (A) FTIR spectra, (B) full XPS patterns and high-resolution XPS spectra of C 1s, N 1s and O 1s of CD1:0.05, CD1:0.2, CD1:0.8, CD1:1.5 and CD1:2.

in PS II were measured at twelve random points on each rice leaf. The rice leaves sprayed with deionized water were measured as a control, and three rice leaves were measured for each treatment.

## 2.9. Rubisco activity

Carboxylase activity of RuBisCO (EC 4.1.1.39) of the treated rice seedlings was determined by a Plant Rubisco test kit (Shanghai SinoBest Biotechnology Co., Ltd. China). 0.1 g fresh leaves of the rice seedlings were ground using liquid nitrogen and homogenized into 1 mL of Tris-HCl buffer (50 mM, pH 7.6) under ice bath. Then, the slurries were centrifuged at 10,000 g at 4 °C for 10 min. The supernatants were collected as crude enzyme extract to measure the carboxylase activity of RuBisCO according to the kit instructions. In the reaction, RuBisCO catalyzed the Ribulose 1, 5-diphosphate (RuBP) and CO<sub>2</sub> to produce 3-phosphoglyceric acid (PGA). Catalyzed by glyceraldehyde-3-phosphate dehydrogenase and phosphoglycerate kinase, PGA was converted to glyceraldehyde-3-phosphate, and NADH was oxidized. The oxidation of NADH was measured by recording the decrease in absorbance at 340 nm within 2 min. The carboxylase activity of RuBisCO was calculated in terms of nmoles of NADH oxidized by 1 g of rice tissue in 1 min (Shabnam et al., 2017). Three biological replications were evaluated for each treatment. The rice seedlings sprayed with deionized water were measured as a control treatment.

## 2.10. Statistical analysis

Values presented in this manuscript were expressed as means  $\pm$  standard deviation (SD). Statistical significance of all data was determined using a one-way analysis of variance (ANOVA) and compared using Duncan's test at  $p < 0.05$  levels in SPSS 24.

## 3. Results and discussion

### 3.1. Morphology and chemical structure of CDs

CD1:0.05, CD1:0.2, CD1:0.8, CD1:1.5 and CD1:2 with QYs of 15.13%, 46.42%, 90.59%, 40.19% and 14.91%, respectively, were prepared using citric acid (CA) and ethanolamine (EA) at different molar ratios (Figs. 1A and S4). Fig. 1B–F show that the five CDs are torispherical and uniformly distributed with a lattice spacing of 0.21 nm, corresponding to the in-plane lattice spacing of graphite (100 facet) (Dong et al., 2013). Their average sizes are revealed as  $3.68 \pm 0.71$  nm (CD1:0.05),  $3.25 \pm 0.58$  nm (CD1:0.2),  $3.25 \pm 0.57$  nm (CD1:0.8),  $3.40 \pm 0.82$  nm (CD1:1.5) and  $3.14 \pm 0.74$  nm (CD1:2). The irregular changes in the size of CDs indicate that their gradient-changed QYs are attributed to surface chemistry rather than the dimensional variation.

The chemical components of these CDs were studied by FTIR and XPS spectra. Fig. 2A shows that all the CDs exhibit stretching vibrations of hydroxyl groups and N-H bonds from  $3200\text{ cm}^{-1}$  to  $3700\text{ cm}^{-1}$  (Zhang et al., 2016). Besides, there are two peaks around  $1643\text{ cm}^{-1}$  and  $1704\text{ cm}^{-1}$ , which are ascribed to the stretching vibration of C=O. The latter peak increases from CD1:0.05 to CD1:0.8 and then remains nearly unchanged in CD1:1.5 and CD1:2, as a result of the increased amidation between amino groups in EA and carboxyl groups in CA. Similar changes are also observed in the C-N peak at  $1407\text{ cm}^{-1}$  from CD1:0.05 to CD1:2. This reaction should occur during sonication (Fig. S5). Furthermore, an in-plane bending vibration of tertiary alcohol groups around  $1218\text{ cm}^{-1}$  is detected in CD1:0.05 and CD1:0.2, while CD1:0.8, CD1:1.5, and CD1:2 show a peak of C-N in secondary amine at  $1190\text{ cm}^{-1}$ . Such structural changes indicate that the hydroxyl groups on the formed CDs surface are gradually transformed to secondary amine in CD1:0.8, CD1:1.5, and CD1:2.

X-ray photoelectron spectroscopy (XPS) was carried out to study further the composition of these CDs (Fig. 2B). All CDs show three dominant peaks at 285 eV, 400 eV, and 533 eV, corresponding to C 1s, N



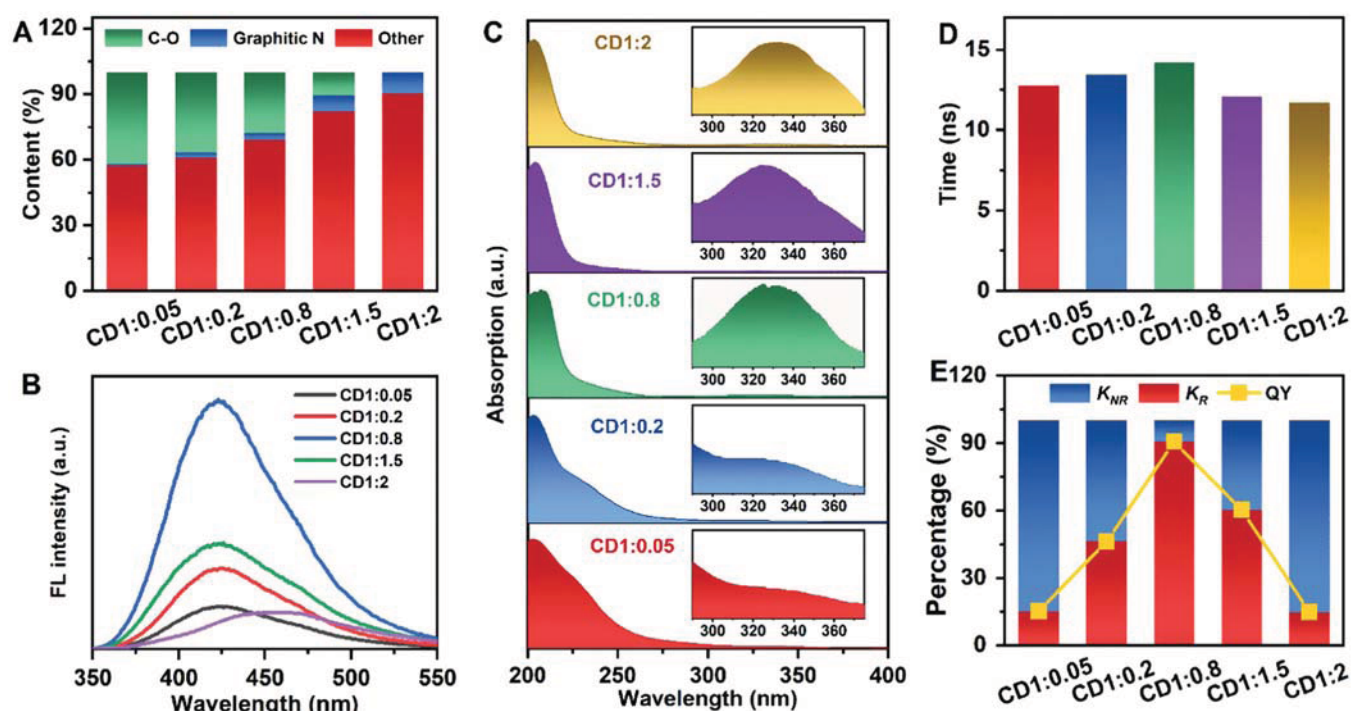


Fig. 3. (A) Graphitic N and C–O bond contents of the CDs as a function of the molar ratio of CA and EA; (B) FL spectra excited by 340 nm; (C) UV–Vis spectra, (D) lifetimes and (E)  $K_R$ ,  $K_{NR}$  ratios and QYs of CD1:0.05, CD1:0.2, CD1:0.8, CD1:1.5 and CD1:2.

1s, and O 1s, respectively. It is evident that the intensity of the N 1s peak gradually increases from CD1:0.05 to CD1:2. All C 1s XPS spectra are divided into  $sp^2$  C–C at 284.8 eV, C–N/C–O at 286.5 eV, and O–C=O at 288.8 eV (Liu et al., 2012). The N 1s peak is deconvoluted into only graphitic N in CD1:0.05 and CD1:0.2, and pyrrolic N is also detected in CD1:0.8, CD1:1.5, and CD1:2 (Zhang et al., 2016). The O 1s band reveals two different types of oxide state, C–O at 532.0 eV and C=O at 533.3 eV (Sevilla and Fuertes, 2009). It can be seen that the intensity of graphitic N peak increases from CD1:0.05 to CD1:2, while that of C–O peak decreases from CD1:0.05 to CD1:1.5 and disappears in CD1:2 (Fig. 2B). The corresponding contents of graphitic N and C–O in the CDs are displayed in Fig. 3A. Since the amino group tends to react with the carboxyl group more than with the hydroxyl group, the C–O bonds in the CDs are mainly in the C–OH state (Zhang et al., 2016). Therefore, the changed QYs of the as-prepared CDs are the result of the coordination between the graphitic N and hydroxyl groups in the CDs.

### 3.2. Optical characterization of CDs

To further investigate the mechanism underlying the gradient-changed QYs, the optical characterizations of the CDs were analyzed. Fig. 3B shows the fluorescence (FL) emission spectra of the CDs under the maximum excitation wavelength of 340 nm. CD1:0.05, CD1:0.2, CD1:0.8, and CD1:1.5 exhibit a maximum FL emission around 425 nm, which red-shifts to 462 nm in CD1:2 due to the excess amino moieties (Zhu et al., 2012). No excitation-independence is observed in the FL emissions of all CDs (Fig. S6), indicating their homogeneous emissive sites (Saidi, 2013; Liu et al., 2014). Fig. 3C shows two absorption peaks at 228 nm and 330 nm in the UV–Vis spectrums of the five CDs. The former one is assigned to the  $\pi$ - $\pi^*$  transition of aromatic C=C in the carbon core, and the latter one reveals the  $n$ - $\pi^*$  transition of the p- $\pi$  orbit between the graphitic N/C–O and the conjugate structure due to trapping excited-state energy (Zhang et al., 2016; Sun et al., 2015). It has been reported that  $\pi$ - $\pi^*$  transition leads to negligible FL signal in CDs, while  $n$ - $\pi^*$  transition can result in strong FL emission (Dong et al., 2013). Fig. 3C shows that the  $\pi$ - $\pi^*$  transition gradually decreases from CD1:0.05

to CD1:2, while the  $n$ - $\pi^*$  transition increases from CD1:0.05 to CD1:0.8, and then remains unchanged in CD1:1.5 and CD1:2. These changes are consistent with the graphitic N contents in these CDs, indicating that graphitic N is responsible for the utilization of the photon in the as-prepared CDs (Tang et al., 2013).

Theoretically, QY of CDs is determined by the ratio between the radiative transition ( $K_R$ ) and non-radiative transition ( $K_{NR}$ ) of the excited electrons, which are calculated from the lifetime ( $\tau$ ) and QY ( $\Phi$ ) using the formulae (Zhang et al., 2016):

$$\tau = (K_R + K_{NR})^{-1} \quad (3)$$

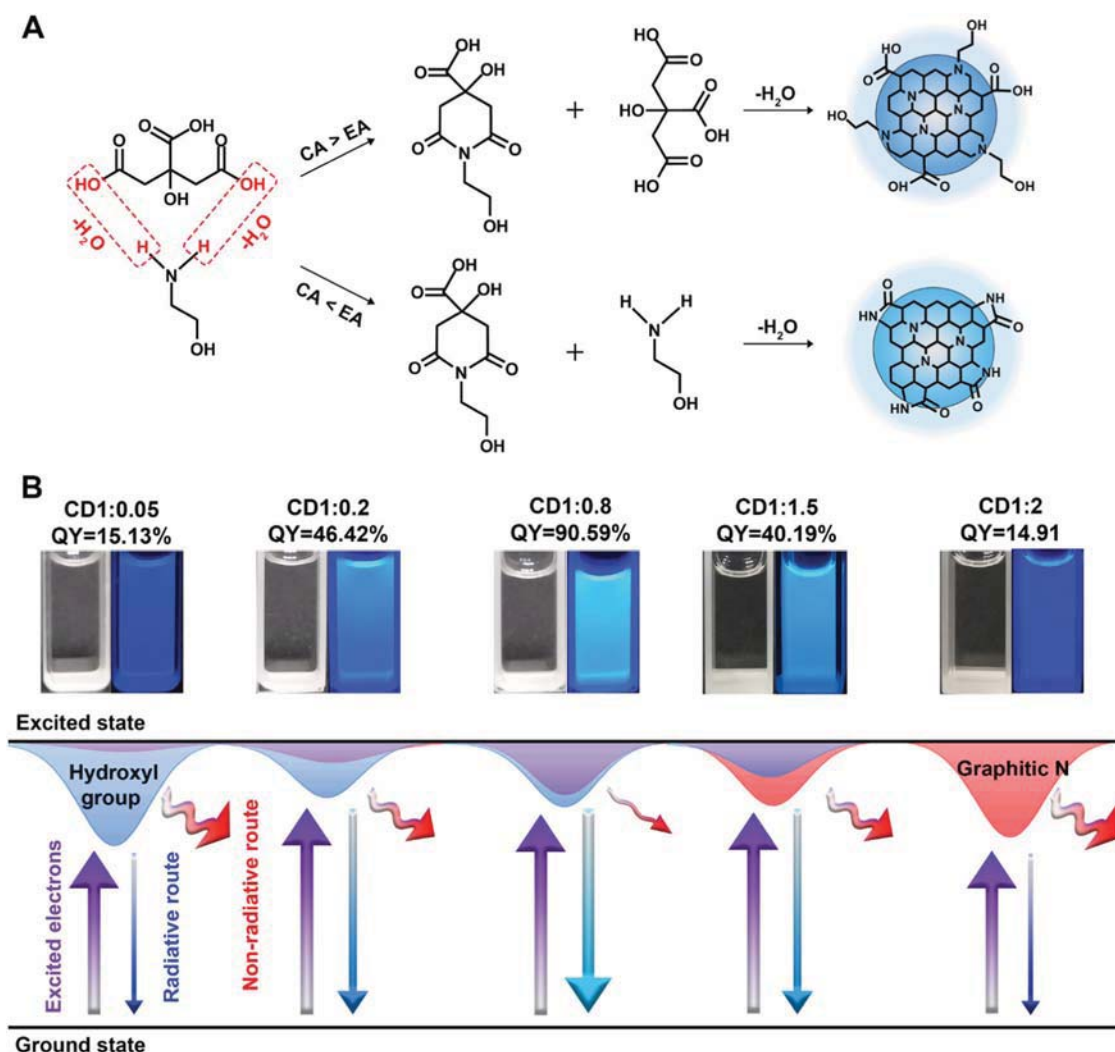
$$\Phi = K_R(K_R + K_{NR})^{-1} \quad (4)$$

The FL lifetimes decay profiles of CD1:0.05, CD1:0.2, CD1:0.8, CD1:1.5, and CD1:2 are shown in Fig. S7, and their lifetimes ( $\tau$ ) are fitted as 12.77 ns, 13.45 ns, 14.23 ns, 12.06 ns, and 11.71 ns, respectively (Fig. 3D). As expected, the ratio between  $K_R$  and  $K_{NR}$  increases from CD1:0.05 to CD1:0.8, and then declined in CD1:1.5 and CD1:2 (Fig. 3G), which is consistent with changes of their QYs.

### 3.3. Mechanisms of the CDs formation and changed QY

Summarizing the above results, the reaction process and the FL mechanism of the CDs are illustrated in Scheme 1. For CD1:0.05 and CD1:0.2, the amino groups in EA react with the carboxyl groups in CA during sonication and formed graphitic N in CDs after microwave pyrolysis. In the formation of CD1:0.8, CD1:1.5, and CD1:2, the excess amino groups will further react with the residual hydroxyl groups in CDs to produce secondary amine. These changes in the surface chemistry of the CDs determine their QYs. The carboxyl group in CDs always induce non-radiative recombination of localized electron-hole pairs and hold back the intrinsic state emission (Mei et al., 2010; Zhu et al., 2015). In this study, the carboxyl groups in CA were converted to graphitic N, which could introduce new energy levels in CDs and form  $\pi$  bonds in the plane. Thereby, the QY of CDs was increased from CD1:0.05 to CD1:0.8 by increasing the utilization of photons and decreasing the energy losses





Scheme 1. Schematic representation illustrating (A) the preparation of the CD samples and (B) their PL mechanism.

by molecular vibrations (Sun et al., 2015; Tang et al., 2013). Furthermore, the hydroxyl group, an electron donor, contributes to the integrity of the  $\pi$  conjugated system in CDs and can reduce non-radiative recombination of localized electron-hole pairs (Zhang et al., 2016; Feng et al., 2014). Therefore, the destruction of the hydroxyl group by the excess amino groups from CD1:0.8 to CD1:2 reduced their QYs.

### 3.4. QY effect of CDs on the photosynthesis of chloroplasts

CD1:0.05, CD1:0.2 and CD1:0.8 with QYs of 15.13%, 46.42%, and 90.59% were used to investigate their effect on plant photosynthesis. Firstly, the composites of CDs and the extracted chloroplasts (CD1:x@Chl) were prepared. Fig. 4A–D shows the SEM and TEM images of the chloroplasts and CD1:0.2@Chl. A large number of particles are observed on the surface and in the chamber of CD1:0.2@Chl, including the thylakoid. Interestingly, CD1:0.2 does not change the external and internal morphology of the chloroplasts. Under the excitation of 361–389 nm and 515–565 nm, the CD1:0.2@Chl shows blue and red FL emission, which originate from the CD1:0.2 and the chlorophyll molecule on thylakoid, respectively. (Fig. 4F and G). After overlaying the two images, the blue FL is completely around the red FL emission (Fig. 4H), indicating the uniform distribution of CD1:0.2 in the chloroplast. However, no significant changes are observed in the FL lifetimes of the CDs before and after the conjugation with chloroplasts (Figs. S8A–C). Therefore, there is no energy transfer between CDs and chloroplasts

(Wang et al., 2017). With a complete overlap of the CDs' FL emission and the absorbance spectra of chlorophyll from 370 nm to 500 nm (Fig. S8D), these CD1:x@Chl composites show an increasing absorption spectrum from 300 nm to 370 nm (Fig. 5A) and a new FL emission from 370 nm to 550 nm in a QY-dependent manner (Fig. 5B) compared to the chloroplast. However, the FL emission intensities of the CDs are remarkably decreased after conjugated to the chloroplast (Figs. S8D and 5B). Therefore, it is inferred that the blue FL emission of CDs in chloroplasts is reabsorbed by chlorophyll for photosynthesis.

Hill reaction was carried out to determine the photosynthetic activities of these CD1:x@Chl composites based on the reduction of DCPIP under xenon lamp radiation. Through a preliminary experiment (Fig. S9), CD1:x@Chl prepared from 300  $\mu\text{g}\cdot\text{mL}^{-1}$  of CDs and 200  $\mu\text{g}\cdot\text{mL}^{-1}$  of chloroplasts was used in the measurement. Fig. 5C shows that the three CDs alone cannot reduce DCPIP. On the contrary, CD1:0.2 @Chl shows higher Hill activity than the chloroplast alone with a maximum increase of 43.77% in the first minute. However, CD1:0.05 inhibits the Hill activity of chloroplasts, and CD1:0.8 leads to no significant influence. Ferricyanide reduction was further conducted to determine the photosynthetic activities of these CD1:x@Chl composites (Fig. 5D). After white light radiation by a xenon lamp (3000 LUX) for 2 min, CD1:0.05@Chl induced an insignificant increase in the ferricyanide reduction compared to the chloroplast alone, while CD1:0.2@Chl exhibited a significant increase of 25.45%. However, a significant decrease of 28.48% was observed in CD1:0.8@Chl to reduce

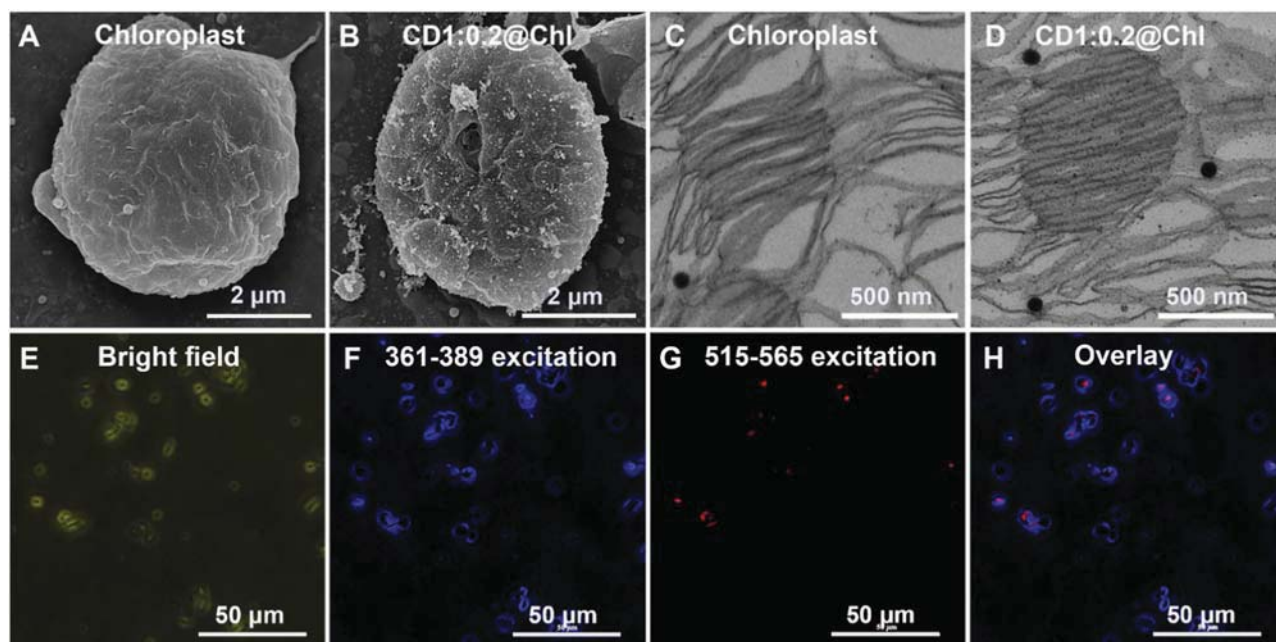


**Fig. 4.** SEM (A and B) and TEM (C and D) images of chloroplast alone and CD1:0.2@Chl; Fluorescent images of CD1:0.2@Chl: (E) bright field, (F) 361–389 excitation, (G) 515–565 excitation and (H) overlaid image of F and G.

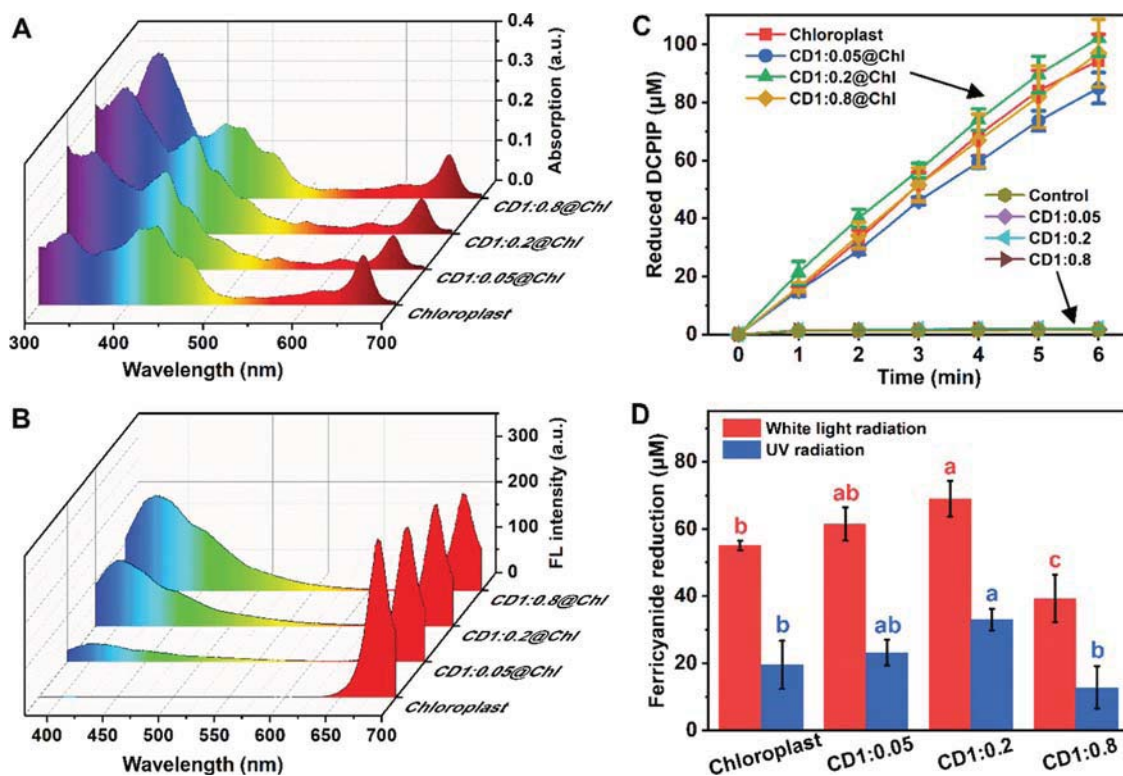


**Fig. 5.** UV–Vis absorbance (A), FL spectra (B), Hill activity (C), and ferricyanide reduction under white light and UV radiation (D) of chloroplast, CD1:0.05@Chl, CD1:0.2@Chl and CD1:0.8@Chl. Error bars correspond to standard deviation (n = 3). Marked with different letters indicate a significant difference ( $p < 0.05$ ).

ferricyanide than the chloroplast. These results coincide with the DCPIP reduction that CD1:0.2 with moderate QY of 46.42% is the most beneficial to chloroplast photosynthesis by converting UV to PAR. The light conversion of the CDs in photosynthesis of the chloroplast was directly demonstrated by the ferricyanide reduction under pure UV radiation. CD1:0.2@Chl exhibited a significant increase of 69.30% in the ferricyanide reduction, while no significant changes were observed in

CD1:0.05@Chl and CD1:0.8@Chl compared with chloroplast alone (Fig. 5D). The insignificant influence even inhibition of CD1:0.05 and CD1:0.8 on the photosynthetic activities of chloroplast may be due to their too low or high QYs. CD1:0.05 with a low QY of 15.13% possibly interferes with the light absorption of the chloroplast, and CD1:0.8 with QY as high as 90.59% may cause photoinhibition to the chloroplasts (Gao et al., 2019).



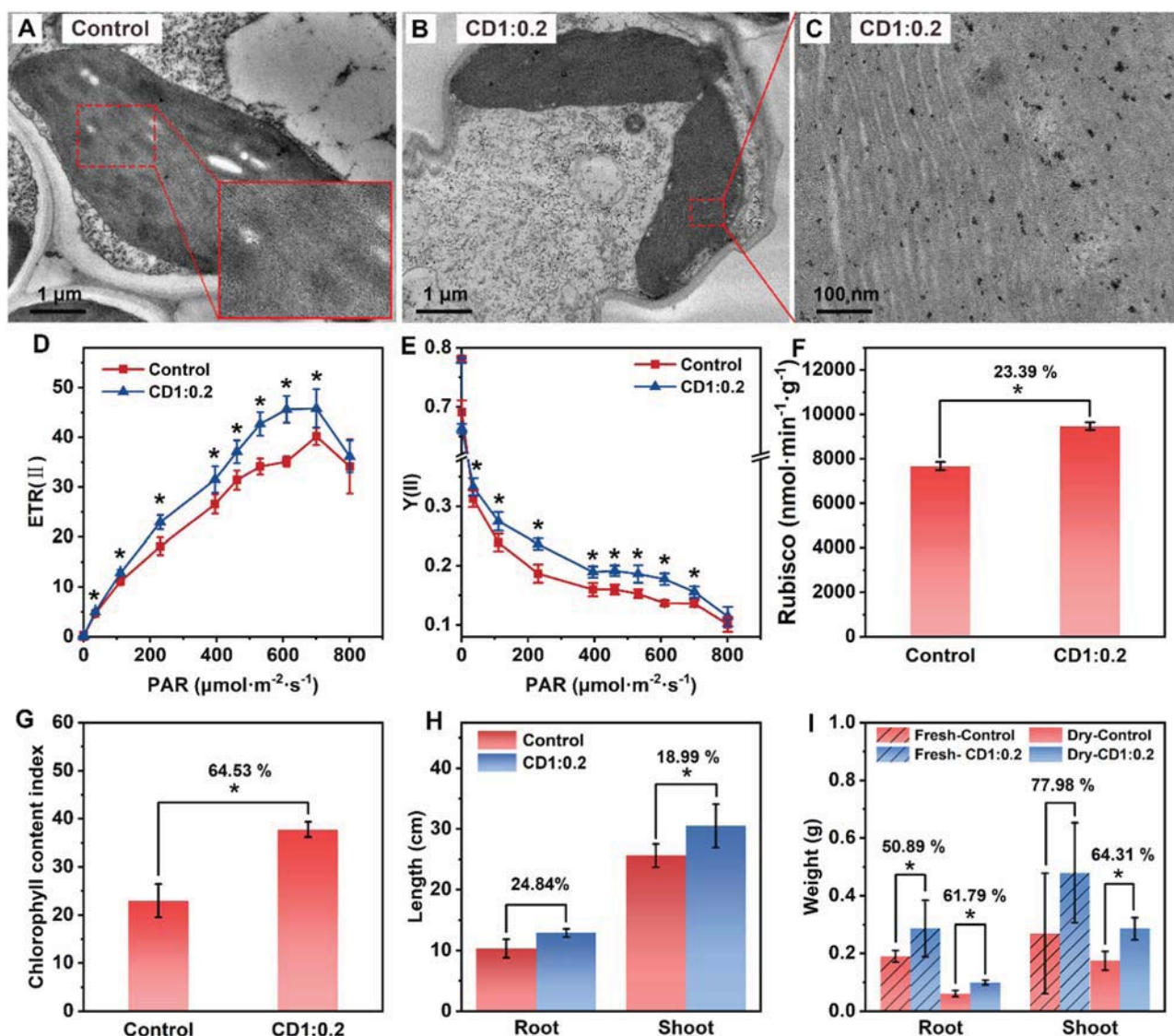


**Fig. 6.** TEM images of rice leaf samples from (A) control and (B) CD1:0.2 treatments; (C) the amplified image of the chloroplast in leaf from CD1:0.2 treatment; (D) the electron transport rates (ETR), (E) Y(II), (F) Rubisco activity, (G) chlorophyll content index, (H) root and shoot length, (I) fresh and dry weight of root and shoot of the rice seedlings in control and CD1:0.2 treatments. Error bars correspond to the standard deviation ( $n \geq 3$ ). Marked with an asterisk (\*) indicates a significant difference ( $p < 0.05$ ).

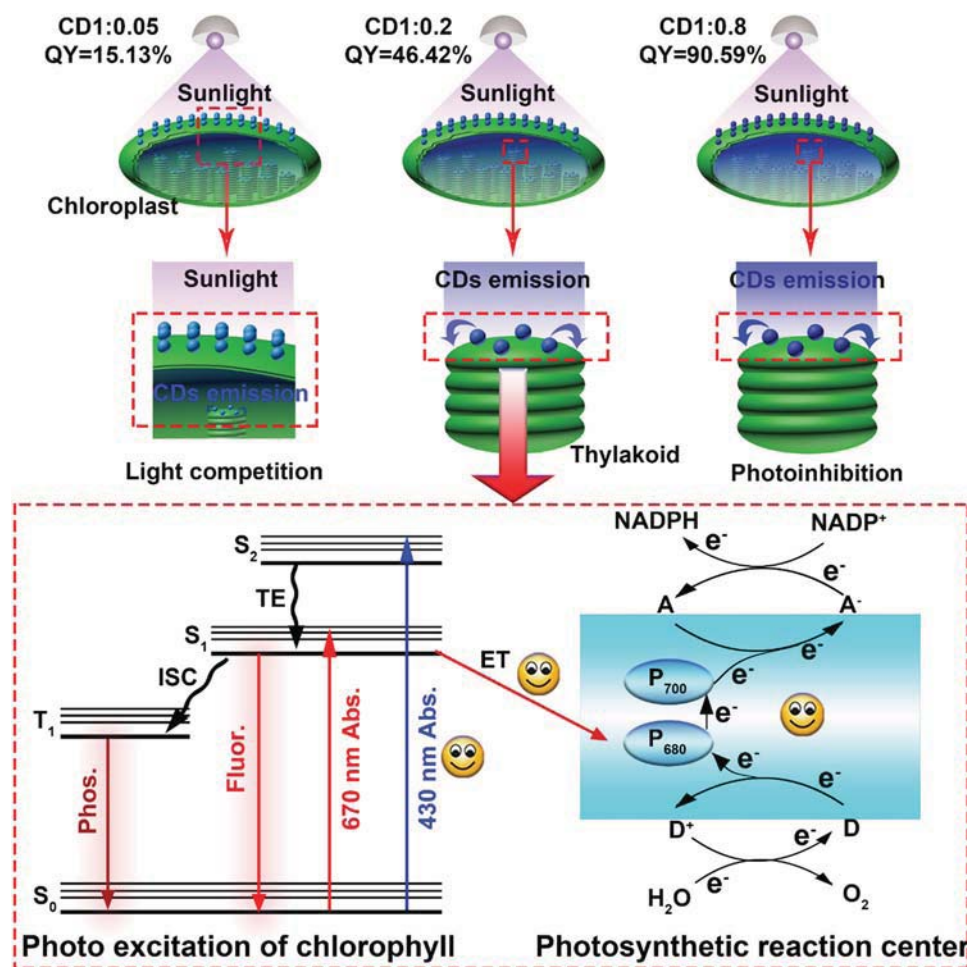
Previously, Sourov et al. demonstrated that CDs could conjugate to the chloroplast and transfer energy to the latter, thereby accelerating the electron transport rate in PS II (Chandra et al., 2014). However, the present results suggest that CDs just act as a light converter from UV radiation to PAR in the chloroplasts without energy transfer. This action model of CDs induces a weaker influence on the photosynthetic physiology of chloroplasts. UV radiation in the sunlight is detrimental to the plant photosynthesis by causing reactive oxygen species (ROS) (Booij-James et al., 2000; Kataria et al., 2014; Stapleton, 1992). In this study, the toxic UV radiation can be converted to PAR by CDs, realizing the harmless use of UV in photosynthesis.

### 3.5. Effect of CD1:0.2 on the photosynthesis and growth of rice seedlings

Subsequently, rice was used as a model to investigate the effect of CD1:0.2 ( $300 \mu\text{g}\cdot\text{mL}^{-1}$ ) on plant photosynthesis and growth. TEM was employed to observe the distribution of CD1:0.2 in rice leaves. Compared with the control (Fig. 6A), a large number of black particle clusters are observed in the cytoplasm and chloroplasts from CD1:0.2-treated rice leaf (Fig. 6B and C), indicating the uniform distribution of

CD1:0.2 in rice leaves. This result is consistent with the distribution of CD1:0.2 in chloroplasts. The agglomeration should result from the high ionic strength of the cytoplasm (Li et al., 2016; Su et al., 2018). Then, the ETR and actual photosynthetic efficiency Y(II) of PS II of the rice leaves were measured *in situ* by chlorophyll fluorescence measurements under increasing PAR. Compared with the control group, CD1:0.2 significantly increased the ETR and Y(II) of the rice under PAR from 36 to  $701 \mu\text{mol}\cdot\text{m}^{-2}\cdot\text{s}^{-1}$  (Fig. 6D and E), showing the maximum increases of 29.81% and 29.88% under  $611 \mu\text{mol}\cdot\text{m}^{-2}\cdot\text{s}^{-1}$ , respectively. Then, the carboxylase activity of RuBisCO in the rice seedlings was measured to investigate the effect of the CD1:0.2 on  $\text{CO}_2$  assimilation. As shown in Fig. 6F, CD1:0.2 significantly increases the carboxylase activity of RuBisCO of the rice seedlings by 23.39% compared to the control. Finally, CD1:0.2 significantly increases the chlorophyll content and shoot length of the rice seedlings by 64.53% and 18.99% (Fig. 6G and H), respectively. Furthermore, CD1:0.2 also leads to 64.31% increase in the dry weight of rice shoot, and 50.89% and 61.79% increases in the fresh and dry weights of rice root compared with the control (Fig. 6I). These results suggest the promotion of CD1:0.2 on the growth of rice as a light converter for the photosynthesis. To directly demonstrate the light





**Scheme 2.** Schematic representation illustrating the effect of the CDs on the photosynthesis and the underlying mechanism. Phos.: Phosphorescence, Fluor.: Fluorescence, Abs.: Absorption, TE: Thermal energy, ET: Energy transfer, P680 and P700: Reaction center pigments in PS II and PS I, respectively.

conversion of CD1:0.2, pure UV radiation was used to culture the rice seedlings treated with and without CD1:0.2. After 10 days of exposure, CD1:0.2 not only successfully protects the rice seedling from UV light, because no brown spots are observed on the CD1:0.2 treated rice leaves compared to the control (Fig. S10A and B), but also increases the growth of the rice seedlings (Fig. S10C and D). Subsequently, the photosynthetic and growth parameters of the rice seedling were measured. Under PAR from 281 to 1251  $\mu\text{mol}\cdot\text{m}^{-2}\cdot\text{s}^{-1}$ , CD1:0.2 significantly increased the  $F_v/F_m$  and ETR of the rice seedlings, with maximum increases of 42.22% and 76.91% at 396  $\mu\text{mol}\cdot\text{m}^{-2}\cdot\text{s}^{-1}$  (Fig. S11A and B), respectively. Furthermore, significant increases of 28.66%, 26.99%, 26.37%, and 20.45% are observed in the fresh weights and dry weights of the shoot and root of the CD1:0.2-treated rice seedlings (Fig. S11D and E), respectively. These results demonstrate the light conversion of CD1:0.2 in the photosynthesis of rice seedlings.

By exposure to the root, Kang et al. demonstrated that CDs could increase the root vigor and nutrient assimilation of the plants, thereby promoting their growth (Wang et al., 2018; Li et al., 2019). In this study, foliage spray of the CDs can minimize the interference from the nutrient assimilation. Therefore, to a certain extent, the CD1:0.2-enhanced growth of rice seedling results from the improvement in the photosynthesis. Similar distribution of CD1:0.2 was observed in isolated chloroplasts and rice leaves, suggesting the similar functions. Photosynthesis is a complex physiological process of plants, which includes light reaction and carbon assimilation, accompanied by the energy conversion from light energy to electric energy and to chemical energy (Pessarakli, 2016). Finally, the production of photosynthesis is stored in the plant as

stable chemical energy in the form of biomass. In this study, when light reaches the chloroplast, the internalized CD1:0.2 with a moderate QY of 46.42% converts UV radiation into PAR, which is captured by the chlorophyll in rice leaves, thereby increasing the ETR and Y(II) in light reaction of photosynthesis. Consequently, more assimilatory powers (ATP and NADPH) are produced for the following carbon assimilation. Under high light over the saturation point, the limited  $\text{CO}_2$  assimilation capacity usually inhibits the plant photosynthesis, because excess electrons produced in light reaction induce the generation of reactive oxygen species (Gao et al., 2019). RuBisCO is a key enzyme that control the carbon assimilation in photosynthesis, and its activity influences the photosynthetic rate directly (Wang et al., 2018; Li et al., 2019). The treatment of CD1:0.2 increased the carboxylase activity of RuBisCO in rice seedlings, which can promote the carbon assimilation. Therefore, to a certain extent, more PAY can be converted into chemical energy in CD1:0.2-treated rice seedlings, thereby promoting the growth of rice seedlings.

The toxicity of nanomaterials is a common concern in the biological field (Chen et al., 2018). A previous study has reported the concentration-dependent phytotoxicity of CDs, in which CDs exceeding 125  $\text{mg}\cdot\text{L}^{-1}$  significantly reduced the growth of the *Arabidopsis* (Chen et al., 2018). Besides, the effect of nanomaterials commonly depends on the plant species (Zhang et al., 2019). In our previous study, the CDs prepared from citric acid enhanced the resistance of rice plants against abiotic stress (Li et al., 2020a). Furthermore, the beneficial effects of CDs on different plants have been reported, including growth, photosynthesis, and resistance (Li et al., 2020b). In this study, the CDs entered

into the extracted chloroplast and the rice leaf cells without changes in the external and internal morphology. Moreover, the exposure of CD1:0.2 at 300  $\mu\text{g}\cdot\text{L}^{-1}$  to rice seedlings increased their growth. Therefore, the CDs in this study can be toxic-free to the rice at the used dose.

#### 4. Conclusion

In this study, different CDs with tunable QYs were prepared by tuning the amount of N precursor in the reaction. These CDs showed a gradient increase in graphite N and a decrease in hydroxyl groups, which led to their gradient-tunable QYs. After conjugating to the chloroplasts, the CDs can convert UV radiation (300–370 nm) to PAR (370–500 nm) without energy transfer to the chloroplasts. By this mechanism, CDs with QY of 46.42% (CD1:0.2) remarkably improved the photosynthesis of chloroplasts. Then, the promotion effect of CD1:0.2 on photosynthesis was further determined on rice plants, which finally resulted in a significant increase in plant growth. The action model of the CDs was visually described in Scheme 2. This study opens a new way to increase agricultural production in the world, especially in areas without adequate sunlight. However, before practical applications, some issues need to be resolved: (1) the synergistic effect of the QY and the dose of the CDs on the plant photosynthesis, (2) the large-scale preparation of the CDs with low cost, and (3) the environmental risk assessment of the CDs.

#### CRedit authorship contribution statement

**Yadong Li:** Methodology, Software, Formal analysis, Investigation, Writing - original draft, Visualization, Project administration. **Xiaoqin Pan:** Methodology, Validation, Investigation, Formal analysis. **Xiaokai Xu:** Methodology, Investigation, Formal analysis. **Ying Wu:** Methodology, Investigation. **Jianle Zhuang:** Visualization, Formal analysis. **Xuejie Zhang:** Software, Formal analysis. **Haoran Zhang:** Formal analysis, Data curation. **Bingfu Lei:** Formal analysis, Resources, Project administration, Writing - review & editing. **Chaofan Hu:** Conceptualization, Resources, Writing - review & editing. **Yingliang Liu:** Conceptualization, Resources, Supervision, Funding acquisition.

#### Declaration of Competing Interest

The authors declare that they have no known competing financial interests or personal relationships that could have appeared to influence the work reported in this paper.

#### Acknowledgments

This work was supported by the National Natural Science Foundation of China (Grant No. 21571067, 21671070).

#### Appendix A. Supporting information

Supplementary data associated with this article can be found in the online version at doi:10.1016/j.jhazmat.2020.124534.

#### References

- Bailey-Serres, J., Parker, J.E., Ainsworth, E.A., Oldroyd, G.E.D., Schroeder, J.I., 2019. Genetic strategies for improving crop yields. *Nature* 575, 109–118.
- Booij-James, I.S., Dube, S.K., Jansen, M.A.K., Edelman, M., Mattoo, A.K., 2000. Ultraviolet-B radiation impacts light-mediated turnover of the photosystem II reaction center heterodimer in *Arabidopsis* mutants altered in phenolic metabolism. *Plant Physiol.* 124, 1275–1284.
- Chandra, S., Pradhan, S., Mitra, S., Patra, P., Bhattacharya, A., Pramanik, P., Goswami, A., 2014. High throughput electron transfer from carbon dots to chloroplast: a rationale of enhanced photosynthesis. *Nanoscale* 6, 3647–3655.
- Chen, J., Liu, B., Yang, Z., Qu, J., Xun, H., Dou, R., Gao, X., Wang, L., 2018. Phenotypic, transcriptional, physiological and metabolic responses to carbon nanodot exposure in *Arabidopsis thaliana* (L.). *Environ. Sci. Nano* 5, 2672–2685.
- Chen, M., Zhou, S., Zhu, Y., Sun, Y., Zeng, G., Yang, C., Xu, P., Yan, M., Liu, Z., Zhang, W., 2018. Toxicity of carbon nanomaterials to plants, animals and microbes: recent progress from 2015-present. *Chemosphere* 206, 255–264.
- Dong, Y., Pang, H., Yang, H.B., Guo, C., Shao, J., Chi, Y., Li, C.M., Yu, T., 2013. Carbon-based dots co-doped with nitrogen and sulfur for high quantum yield and excitation-independent emission. *Angew. Chem. Int. Ed.* 52, 7800–7804.
- Feng, Y., Zhao, J., Yan, X., Tang, F., Xue, Q., 2014. Enhancement in the fluorescence of graphene quantum dots by hydrazine hydrate reduction. *Carbon* 66, 334–339.
- Gao, Y.-b., Zheng, W.-w., Zhang, C., Zhang, L.-l., Xu, K., 2019. High temperature and high light intensity induced photoinhibition of bayberry (*Myrica rubra* Sieb. et Zucc.) by disruption of D1 turnover in photosystem II. *Sci. Hortic.* 248, 132–137.
- Grayson, K.J., Faries, K.M., Huang, X., Qian, P., Dilbeck, P., Martin, E.C., Hitchcock, A., Vasilev, C., Yuen, J.M., Niedzwiedzki, D.M., Leggett, G.J., Holten, D., Kirmaier, C., Neil Hunter, C., 2017. Augmenting light coverage for photosynthesis through YFP-enhanced charge separation at the *Rhodobacter sphaeroides* reaction centre. *Nat. Commun.* 8, 13972.
- Guo, Z., Richardson, J.J., Kong, B., Liang, K., 2020. Nanobiohybrids: materials approaches for bioaugmentation. *Sci. Adv.* 6, eaaz0330.
- Han, M., Zhu, S., Lu, S., Song, Y., Feng, T., Tao, S., Liu, J., Yang, B., 2018. Recent progress on the photocatalysis of carbon dots: classification, mechanism and applications. *Nano Today* 19, 201–218.
- Jaleel, J.A., Pramod, K., 2018. Artful and multifaceted applications of carbon dot in biomedicine. *J. Control. Release* 269, 302–321.
- Kataria, S., Jajoo, A., Guruprasad, K.N., 2014. Impact of increasing Ultraviolet-B (UV-B) radiation on photosynthetic processes. *J. Photochem. Photobiol. B* 137, 55–66.
- Li, H., Huang, J., Liu, Y., Lu, F., Zhong, J., Wang, Y., Li, S., Lifshitz, Y., Lee, S.-T., Kang, Z., 2019. Enhanced RuBisCO activity and promoted dicotyledons growth with degradable carbon dots. *Nano Res.* 12, 1585–1593.
- Li, W., Zheng, Y., Zhang, H., Liu, Z., Su, W., Chen, S., Liu, Y., Zhuang, J., Lei, B., 2016. Phytotoxicity, uptake, and translocation of fluorescent carbon dots in mung bean plants. *ACS Appl. Mater. Interfaces* 8, 19939–19945.
- Li, W., Wu, S., Zhang, H., Zhang, X., Zhuang, J., Hu, C., Liu, Y., Lei, B., Ma, L., Wang, X., 2018. Enhanced biological photosynthetic efficiency using light-harvesting engineering with dual-emissive carbon dots. *Adv. Funct. Mater.* 28, 1804004.
- Li, Y., Jin, Q., Yang, D., Cui, J., 2018. Molybdenum sulfide induce growth enhancement effect of rice (*Oryza sativa* L.) through regulating the synthesis of chlorophyll and the expression of aquaporin gene. *J. Agric. Food Chem.* 66, 4013–4021.
- Li, Y., Gao, J., Xu, X., Wu, Y., Zhuang, J., Zhang, X., Zhang, H., Zheng, M., Liu, Y., Hu, C., 2020. Carbon dots as protective agent alleviating abiotic stresses on rice (*Oryza sativa* L.) through promoting nutrition assimilation and defense system. *ACS Appl. Mater. Interfaces* 12, 33575–33585.
- Li, Y., Xu, X., Wu, Y., Zhuang, J., Zhang, X., Zhang, H., Lei, B., Hu, C., Liu, Y., 2020. A review on the effects of carbon dots in plant systems. *Mater. Chem. Front.* 4, 437–448.
- Liao, J.-Y., Fan, C., Huang, Y.-Z., Pei, K.J.-C., 2020. Distribution of residual agricultural pesticides and their impact assessment on the survival of an endangered species. *J. Hazard. Mater.* 389, 121871.
- Liu, S., Tian, J., Wang, L., Zhang, Y., Qin, X., Luo, Y., Asiri, A.M., Al-Youbi, A.O., Sun, X., 2012. Hydrothermal treatment of grass: a low-cost, green route to nitrogen-doped, carbon-rich, photoluminescent polymer nanodots as an effective fluorescent sensing platform for label-free detection of Cu(II) ions. *Adv. Mater.* 24, 2037–2041.
- Liu, Y., Xiao, N., Gong, N., Wang, H., Shi, X., Gu, W., Ye, L., 2014. One-step microwave-assisted polyol synthesis of green luminescent carbon dots as optical nanoprobe. *Carbon* 68, 258–264.
- Lu, T., Meng, Z., Zhang, G., Qi, M., Sun, Z., Liu, Y., Li, T., 2017. Sub-high temperature and high light intensity induced irreversible inhibition on photosynthesis system of tomato plant (*Solanum lycopersicum* L.). *Front. Plant Sci.* 08.
- Mei, Q., Zhang, K., Guan, G., Liu, B., Wang, S., Zhang, Z., 2010. Highly efficient photoluminescent graphene oxide with tunable surface properties. *Chem. Commun.* 46, 7319–7321.
- Molaei, M.J., 2020. The optical properties and solar energy conversion applications of carbon quantum dots: a review. *Sol. Energy* 196, 549–566.
- Nayak, S., Prasad, S.R., Mandal, D., Das, P., 2020. Carbon dot cross-linked polyvinylpyrrolidone hybrid hydrogel for simultaneous dye adsorption, photodegradation and bacterial elimination from waste water. *J. Hazard. Mater.* 392, 122287.
- Pan, X.Q., Li, D.N., Fang, Y.P., Liang, Z.H., Zhang, H.R., Zhang, J.Z., Lei, B.F., Song, S.W., 2020. Enhanced photogenerated electron transfer in a semiartificial photosynthesis system based on highly dispersed titanium oxide nanoparticles. *J. Phys. Chem. Lett.* 11, 1822–1827.
- Pankratov, D., Zhao, J., Nur, M.A., Shen, F., Leech, D., Chi, Q., Pankratova, G., Gorton, L., 2019. The influence of surface composition of carbon nanotubes on the photobioelectrochemical activity of thylakoid bioanodes mediated by osmium-complex modified redox polymer. *Electrochim. Acta* 310, 20–25.
- Pathak, J., Rajneesh, Ahmed, H., Singh, D.K., Singh, P.R., Kumar, D., Kannaujiya, V.K., Singh, S.P., Sinha, R.P., 2020. Oxidative stress and antioxidant defense in plants exposed to ultraviolet radiation. In: Hasanuzzaman, M., Fotopoulos, V., Nahar, K., Fujita, M. (Eds.), *Reactive Oxygen, Nitrogen and Sulfur Species in Plants*. Wiley Online Library, pp. 371–420.
- Pessarakli, M., 2016. *Handbook of Photosynthesis*, Third ed. CRC Press, Boca Raton.
- Pham, N., Mandel, N., 2019. What influences consumer evaluation of genetically modified foods? *J. Public Policy Mark.* 38, 263–279.
- Radyukina, N.L., Ivanov, Y.V., Mapelli, S., Mikheeva, L.E., Karbysheva, E.A., 2017. Effects of medium-wave ultraviolet radiation on levels and spectrum of polyamines in leaves and roots of wild-growing plants. *Mosc. Univ. Biol. Sci. Bull.* 72, 155–158.

- Saidi, W.A., 2013. Oxygen reduction electrocatalysis using N-doped graphene quantum-dots. *J. Phys. Chem. Lett.* 4, 4160–4165.
- Sevilla, M., Fuertes, A.B., 2009. Chemical and structural properties of carbonaceous products obtained by hydrothermal carbonization of saccharides. *Chem. Eur. J.* 15, 4195–4203.
- Shabnam, N., Sharmila, P., Govindjee, Kim, H., Pardha-Saradhi, P., 2017. Differential response of floating and submerged leaves of longleaf pondweed to silver ions. *Front. Plant Sci.* 8, 1052.
- Sharma, A., Das, J., 2019. Small molecules derived carbon dots: synthesis and applications in sensing, catalysis, imaging, and biomedicine. *J. Nanobiotechnol.* 17, 92.
- Singh, M.K., Singh, S.P., Singh, B., 2019. Agro-techniques for baby corn production. In: Hasanuzzaman, M. (Ed.), *Agronomic Crops*. Springer, Singapore, pp. 261–272.
- Stapleton, A.E., 1992. Ultraviolet radiation and plants: burning questions. *Plant Cell* 4, 1353–1358.
- Su, L.-X., Ma, X.-L., Zhao, K.-K., Shen, C.-L., Lou, Q., Yin, D.-M., Shan, C.-X., 2018. Carbon nanodots for enhancing the stress resistance of peanut plants. *ACS Omega* 3, 17770–17777.
- Sun, J., Yang, S., Wang, Z., Shen, H., Xu, T., Sun, L., Li, H., Chen, W., Jiang, X., Ding, G., Kang, Z., Xie, X., Jiang, M., 2015. Ultra-high quantum yield of graphene quantum dots: aromatic-nitrogen doping and photoluminescence mechanism. Part. Part. Syst. Charact. 32, 434–440.
- Tang, L., Ji, R., Li, X., Teng, K.S., Lau, S.P., 2013. Energy-level structure of nitrogen-doped graphene quantum dots. *J. Mater. Chem. C* 1, 4908–4915.
- van Esse, H.P., Reuber, T.L., van der Does, D., 2020. Genetic modification to improve disease resistance in crops. *New Phytol.* 225, 70–86.
- Wang, H., Zhang, M., Song, Y., Li, H., Huang, H., Shao, M., Liu, Y., Kang, Z., 2018. Carbon dots promote the growth and photosynthesis of mung bean sprouts. *Carbon* 136, 94–102.
- Wang, X., Fan, J., Xing, Y., Xu, G., Wang, H., Deng, J., Wang, Y., Zhang, F., Li, P., Li, Z., 2019. Chapter three – the effects of mulch and nitrogen fertilizer on the soil environment of crop plants. In: Sparks, D.L. (Ed.), *Advances in Agronomy*. Academic Press, pp. 121–173.
- Wang, Y., Li, S., Liu, L., Lv, F., Wang, S., 2017. Conjugated polymer nanoparticles to augment photosynthesis of chloroplasts. *Angew. Chem. Int. Ed.* 56, 5308–5311.
- Wu, A., Hammer, G.L., Doherty, A., von Caemmerer, S., Farquhar, G.D., 2019. Quantifying impacts of enhancing photosynthesis on crop yield. *Nat. Plants* 5, 380–388.
- Wu, P., Li, W., Wu, Q., Liu, Y., Liu, S., 2017. Hydrothermal synthesis of nitrogen-doped carbon quantum dots from microcrystalline cellulose for the detection of  $\text{Fe}^{3+}$  ions in an acidic environment. *RSC Adv.* 7, 44144–44153.
- Xiao, L., Guo, H., Wang, S., Li, J., Wang, Y., Xing, B., 2019. Carbon dots alleviate the toxicity of cadmium ions ( $\text{Cd}^{2+}$ ) toward wheat seedlings. *Environ. Sci. Nano* 6, 1493–1506.
- Yuan, H., Liu, L., Lv, F., Wang, S., 2013. Bioluminescence as a light source for photosynthesis. *Chem. Commun.* 49, 10685–10687.
- Zhang, C., Wohlhueter, R., Zhang, H., 2016. Genetically modified foods: a critical review of their promise and problems. *Food Sci. Hum. Wellness* 5, 116–123.
- Ma, Y., Zhang, P., Xie, C., Guo, Z., He, X., Valsami-Jones, E., Lynch, I., Luo, W., Zheng, L., Zhang, Z., 2019. Plant species-dependent transformation and translocation of ceria nanoparticles. *Environ. Sci. Nano* 6, 60–67.
- Zhang, Y., Liu, X., Fan, Y., Guo, X., Zhou, L., Lv, Y., Lin, J., 2016. One-step microwave synthesis of N-doped hydroxyl-functionalized carbon dots with ultra-high fluorescence quantum yields. *Nanoscale* 8, 15281–15287.
- Zhu, S., Zhang, J., Tang, S., Qiao, C., Wang, L., Wang, H., Liu, X., Li, B., Li, Y., Yu, W., Wang, X., Sun, H., Yang, B., 2012. Surface chemistry routes to modulate the photoluminescence of graphene quantum dots: from fluorescence mechanism to up-conversion bioimaging applications. *Adv. Funct. Mater.* 22, 4732–4740.
- Zhu, S., Song, Y., Zhao, X., Shao, J., Zhang, J., Yang, B., 2015. The photoluminescence mechanism in carbon dots (graphene quantum dots, carbon nanodots, and polymer dots): current state and future perspective. *Nano Res.* 8, 355–381.





# Effects and mechanisms of proanthocyanidins-derived carbon dots on alleviating salt stress in rice by multi-omics analysis

Baoyan Guo<sup>a</sup>, Fengqiong Chen<sup>a</sup>, Guo Liu<sup>b</sup>, Wentao Li<sup>a</sup>, Wei Li<sup>a</sup>, Jianle Zhuang<sup>a</sup>,  
Xuejie Zhang<sup>a</sup>, Lashuang Wang<sup>c</sup>, Bingfu Lei<sup>a,\*</sup>, Chaofan Hu<sup>a,\*</sup>, Yingliang Liu<sup>a,\*</sup>

<sup>a</sup> Key Laboratory for Biobased Materials and Energy of Ministry of Education/Guangdong Provincial Engineering Technology Research Center for Optical Agriculture, College of Materials and Energy, South China Agricultural University, Guangzhou 510642, China

<sup>b</sup> College of Horticulture, South China Agricultural University, Guangzhou 510642, China

<sup>c</sup> Guangdong Tianzi Natural Inc, Guangzhou 510642, China

## ARTICLE INFO

### Keywords:

Carbon dots  
Proanthocyanidins  
Rice seedlings  
Salt stress  
Metabolome  
Transcriptome

## ABSTRACT

Carbon dots (CDs) with different structures were prepared by electrolysis (PE-CDs) and hydrothermal (PH-CDs) methods using proanthocyanidins as precursors. The smaller size and lower zeta potential enabled the PE-CDs treated rice seedlings to exhibit greater resistance to salt stress. The fresh weight of rice seedlings under salt stress was significantly increased by spraying CDs every other day for two weeks. PE-CDs treated group exhibited a faster electron transport rate, and the SOD activity and flavonoid content were 2.5-fold and 0.23-fold higher than those of the salt stress-treated group. Furthermore, the metabolomics and transcriptomics analysis revealed that the PsaC gene of photosystem I was significantly up-regulated under PE-CDs treatment, which accelerated electron transfer in photosystem I. The up-regulation of BX1 and IGL genes encoding indole synthesis allowed rice to enhance stress tolerance through tryptophan and benzoxazine biosynthesis pathways. These findings offer help in purposefully synthesizing CDs and boosting food production.

## 1. Introduction

Abiotic stresses result in significant crop losses globally each year. Nano-engineered materials can mitigate abiotic stresses and improve yield (Do Espirito Santo Pereira, Caixeta Oliveira, Fernandes Fraceto, & Santaella, 2021). However, the poor water solubility and biocompatibility, and the complexity and costly preparation process have limited their application (Chaudhary, Singh, Singh, & Rath, 2024).

CDs, as a new type of nanomaterials, are characterized by simple preparation methods, wide sources of precursors, excellent water solubility and biocompatibility, and adjustable surface functional groups. Recent studies demonstrate its excellent ability in promoting plant growth and mitigating abiotic stress on crops (Guo et al., 2022). N-CDs alleviated the photosynthesis defect in mterf5 mutants with defective PSII function by targeting Cyt-b6f and PQs, which are located between photosystems PSII and PSI, resulting in an enhancement of photosynthetic efficiency by 24.29%, and consequently, an increase in apple soluble sugar content by 11.43% (Jing et al., 2024).

Oxidative damage due to accumulation of reactive oxygen species

(ROS) in cells significantly impacts plant growth. Carboxy and amino groups on the surface of CDs have been reported to have free radical scavenging properties due to their ability to act as electron donors and acceptors (Das et al., 2014). CDs protect plants from abiotic stresses by scavenging free radicals and increasing antioxidant enzyme activity. *Salvia Miltiorrhiza*-derived CDs were proved to have stronger antioxidant properties than the precursors, scavenging DPPH<sup>•</sup>, O<sub>2</sub><sup>•−</sup>, and <sup>•</sup>OH with high efficiencies of 88.9%, 95.6%, and 71.4%, respectively. This CDs was effective in mitigating oxidative damage in Italian lettuce under salt stress, with a 92.2% decrease in MDA content compared to the control (Li et al., 2021). Nitrogen and sulfur co-doped CDs were found to have 80% scavenging rate of <sup>•</sup>OH at 0.55 mg/mL. The antioxidant effect on KMnO<sub>4</sub> was comparable to that of VC at the same concentration. The CDs could also enhance the antioxidant defense enzyme activities of tomato seedlings to enhance the drought resistance (Kou et al., 2021). Thus, having antioxidant properties is essential for CDs to mitigate abiotic stresses. In addition, the size and zeta potential of CDs are key factors because crops have size limitations on the particles that can be accessed (Wang et al., 2022). The hydrodynamic size limits for efficient

\* Corresponding authors.

E-mail addresses: [tleibf@scau.edu.cn](mailto:tleibf@scau.edu.cn) (B. Lei), [thucf@scau.edu.cn](mailto:thucf@scau.edu.cn) (C. Hu), [tliuyi@scau.edu.cn](mailto:tliuyi@scau.edu.cn) (Y. Liu).

<https://doi.org/10.1016/j.fochx.2024.101422>

Received 16 January 2024; Received in revised form 17 April 2024; Accepted 25 April 2024

Available online 1 May 2024

2590-1575/© 2024 The Authors. Published by Elsevier Ltd. This is an open access article under the CC BY-NC-ND license (<http://creativecommons.org/licenses/by-nc-nd/4.0/>).

nanoparticle transport in cotton and maize leaf cells have been reported to be 20 nm and 11 nm, respectively, and foliar delivery of positively charged nanoparticle in chloroplasts was more efficient (Hu et al., 2020). However, there are limited reports on the kinetics of CDs uptake by plants, the relationship between the structure of CDs and their mitigation of abiotic stresses in crops is not well understood at present. The molecular mechanisms of how CDs mitigate abiotic stresses in crops have been reported. Application of CDs in soil resulted in up-regulation of GmNRT, GmAMT, GmLB, and GmAQP gene expression in drought-stressed soybean roots, enhancing N transport and water uptake, which in turn promoted soybean growth and nutritional quality (Ji et al., 2023). PNDs enhanced drought tolerance in maize by regulating photosynthesis-related genes and synthesis genes of signaling molecules (Wang et al., 2022). However, there is a lack of in-depth studies on the role of CDs in alleviating salt stresses in rice seedlings at molecular level.

In this study, CDs were prepared by hydrothermal and electrolytic methods, respectively, using proanthocyanidins (PCs) (natural substances with strong antioxidant properties) as precursors, and the resulting CDs inherited the antioxidant properties of the precursors and possessed the ability to alleviate salt stress. In addition, the size and zeta potential of CDs were different due to the different preparation methods. The enhanced effects of two CDs on salt stress tolerance in rice were compared, and the stress mitigation abilities of CDs structures on antioxidant defense system, photosynthesis, osmoregulation, and nutrient uptake in rice seedlings were explored. The underlying mechanism responsible for the enhanced salt stress resistance was elucidated by metabolomics and transcriptomics analysis. This will provide a theoretical foundation for the structural design of functional CDs to improve crop resistance, yield and alleviate food shortage. Furthermore, novel target genes for CDs to alleviate salt stress in rice seedlings were also identified, revealing a new mechanism for CDs to alleviate plant stress.

## 2. Material and methods

### 2.1. Synthesis and characterization of CDs

PCs with a purity of 95% derived from pine bark extract were supplied by Guangdong Tianzi Natural Inc. Anhydrous ethanol was purchased from Aladdin Industries, Inc. PCs were used as precursors to prepare CDs by hydrothermal and electrolytic methods, respectively. Namely, 0.6 g PCs was mixed with 15 mL anhydrous ethanol and 45 mL water and sonicated for 30 min, then transferred into a Teflon-lined reaction kettle and placed in an oven at 200 °C/10 h, followed by filtration through filter paper and then 0.22 µm filter membrane, dialyzed with a dialysis bag (MW = 1000 Da, Solarbio, China) for 8 h, and lyophilized to obtain solid CDs. The specific step of preparing CDs by electrolysis involved weighing 1 g PCs and adding them to a beaker containing 300 mL of water. Two parallel graphite rods were used as electrodes, and a DC voltage of 60 V was applied at room temperature while magnetic stirring was conducted until one electrode was completely electrolyzed. The resulting solution was filtered, dialyzed in a dialysis bag (MW = 1000 Da, Solarbio, China) for 8 h, and then freeze-dried.

The morphology of the CDs was observed using an FEI Tecnai 12 transmission electron microscope (TEM). Functional groups on the surface of CDs were detected using a Nicolet Avatar 360 FTIR spectrophotometer. Structural characterization of the CDs was demonstrated using an Xpert Pro MPD X-ray diffractometer (XRD). A Renishaw Evolution device with a 532 nm laser as the excitation source was used to determine the Raman spectra of the CDs. A laser particle size analyzer (Zetasizer Nano ZSE) was used to determine the zeta potential. XPS analysis was also carried out using a Thermo SCIENTIFIC Nexsa spectrometer, with the source of ionizing radiation being AlK $\alpha$  radiation (1486.68 eV). A pass energy of 200 eV was used for the measurement spectra and 50 eV for the high-resolution spectra. The 1,1-Diphenyl-2-picrylhydrazyl (DPPH) scavenging activity, superoxide anion radical

(O $_2^{\bullet-}$ ) scavenging activity, and potassium permanganate (KMnO $_4$ ) reduction rate were used to assess the antioxidant qualities of CDs. After combining 100 µL of CDs solution with an equal amount of 1 mM KMnO $_4$  or 100 µg/mL DPPH, the mixture's absorbance at 515 or 517 nm was measured after half an hour in the absence of light. The control solution was the one without CDs. The following formula was used to compute the KMnO $_4$  reduction rate or DPPH scavenging activity: (A1-A2) / A1  $\times$  100% (1), where A1 and A2 stand for the absorbance values at 515 nm or 517 nm for the mixture of the control group and CDs treatment group with varied concentrations, respectively. Nitrotriazolium blue chloride (NBT) was used to measure the O $_2^{\bullet-}$  scavenging activity of CDs. First, a 0.05 M phosphate buffer (pH = 7.8) was used to prepare all of the reagents. Next, to create mother liquor (ready for use), 30 mL of buffer solution, 6 mL of 130 mM methionine solution, 6 mL of 750 µM NBT, 6 mL of 100 µM EDTA-Na $_2$ , 6 mL of 20 µM riboflavin, and 5 mL of distilled water were combined. Mother liquor was combined with CDs solution at varying concentrations in an equal volume; the CDs-free mixture served as the control. After 30 min of treatment at 4000 Lux, the mixture's absorbance value was measured at 560 nm. Eq. (1) was utilized to calculate the O $_2^{\bullet-}$  scavenging activity.

### 2.2. Cultivation of rice and salt stress treatment

Rice seeds ('Huahang 31') were disinfected with 75% ethanol and later germinated under darkness by laying flat in germination trays containing Hoagland's nutrient solution. Three days later, the germinated trays were transferred to the greenhouse for incubation (22–30 °C, 70% relative humidity, 400 µmol m $^{-2}$ ·s $^{-1}$  light intensity with a 16 h light/8 h dark regime). Seven days later, homogeneous rice seedlings were transplanted into pots containing nutrient solution with 12 seedlings per pot. On the second day after transplanting, the nutrient solution was replaced with a nutrient solution containing 50 mmol NaCl and CDs solution was sprayed to ensure that all leaves were covered with droplets and there was no runoff. Each pot of rice seedlings was sprayed with 5 mL of CDs solution each time. Each treatment was replicated six times and ultra-pure water was sprayed as a control. The foliar spray was conducted every two days for two weeks. Based on the pre-experiment (Detailed data was shown in SI Fig. S1), the optimal concentration of CDs under salt stress was used as the concentration of CDs for each group of foliar spray. That is, PH-CDs were 10 µg/mL, PE-CDs were 30 µg/mL. The group without salt stress treatment was recorded as Non—S, the salt stress treatment group sprayed water was recorded as S, and the salt stress treatment group sprayed optimal concentration of PH-CDs and PE-CDs was recorded as PH-CDs and PE-CDs. The top two leaves of rice seedlings from each treatment were collected and their height, fresh weight, and chlorophyll content were measured.

Photosynthetic parameters of rice seedlings were tested by chlorophyll fluorometry (Phyto = PAM ED, Walz, Germany). Prior to the test, all rice seedlings were kept in darkness for the whole night in order to achieve equilibrium in their photosynthetic processes. The test leaf, which was the second leaf from the top of the rice seedlings, was cut, covered with damp gauze, and put on a platform. The effective radiation and light intensities that were measured were 0, 1, 21, 36, 56, 81, 111, 146, 231, 336, 461, 611, and 801 µmol·m $^{-2}$ ·s $^{-1}$ . Ten test sites were chosen for every rice leaf, and six leaves were evaluated for each treatment.

### 2.3. Regulation of antioxidant defense system in salt-stressed rice seedlings by CDs

Determination of antioxidant defense system indicators in rice seedlings according to the method described in the literature (Li et al., 2020). Using the nitrogen blue tetrazolium (NBT) photoreduction method, the superoxide dismutase (SOD) activity was measured and expressed as the change in absorbance value at 560 nm. The guaiacol method was used to measure the peroxidase (POD) activity. A UV-Vis

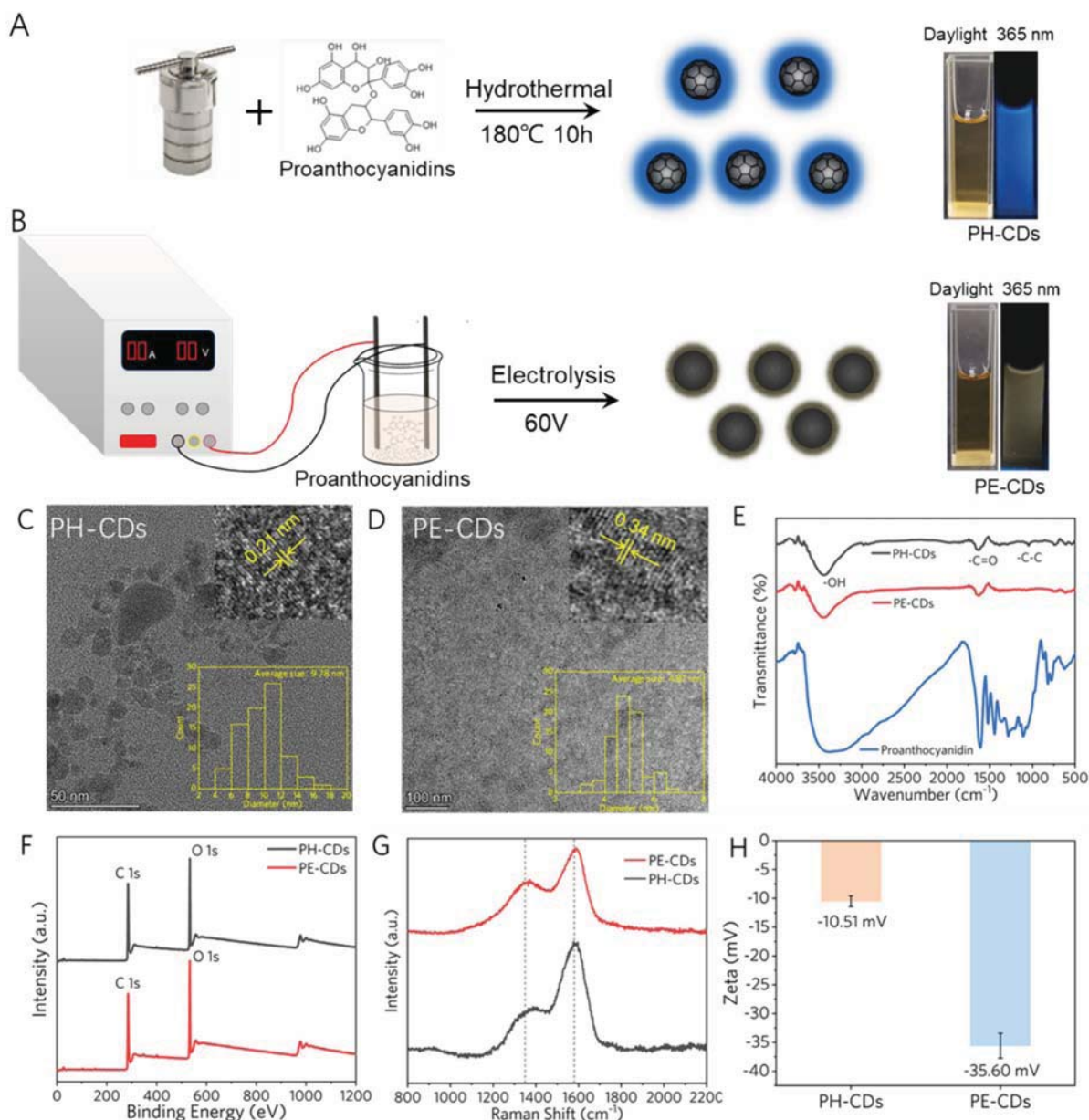


**Fig. 1.** Schematic of the synthesis of (A) PH-CDs and (B) PE-CDs. TEM images of PH-CDs (C) and PE-CDs (D). (E) FTIR of CDs compared with PCs. XPS (F), Raman spectrum (G) and Zeta potential (H) of CDs.

spectrophotometer was used to track the rate of increase in absorbance at 470 nm during a 3-min period. Using the test group without CDs as control. The rate of hydrogen peroxide breakdown was measured using the absorbance at 240 nm after two minutes to identify the presence of catalase (CAT) activity. The forinthenol method was used to determine the total plant phenol content, whereas the aluminum chloride colorimetric method was used to assess the flavonoid content. The standard curve of polyphenol content was plotted with the absorbance change under the gradient gallic acid concentration ( $y = 8.4366x + 0.0767$ ,  $R^2 = 0.9966$ ), and the standard curve of flavonoid content was plotted with the absorbance change under the gradient rutin concentration ( $y = 0.352x + 0.0395$ ,  $R^2 = 0.9997$ ). Using the thiobarbituric acid method, the amount of Malondialdehyde (MDA) in rice was measured in order to determine the degree of peroxidation.

#### 2.4. Regulation of osmoregulatory substances by CDs in salt-stressed rice seedlings

The colorimetric method was used to determine the content of betaine, free proline and soluble protein by using Rays salt, ninhydrin and Thomas Brilliant Blue, respectively. The content of soluble sugar was determined by the method using anthranilone sulfate. The standard curve was plotted according to the absorbance values of the standard solutions of proline ( $y = 0.0279x - 0.0091$ ,  $R^2 = 0.9901$ ) and betaine ( $y = 0.0318x + 0.0442$ ,  $R^2 = 0.9937$ ) at different concentrations, and the concentration of the samples was calculated from the standard curve. For soluble sugar and soluble protein determination, standard curves were plotted with glucose standard solution ( $y = 0.004x - 0.0203$ ,  $R^2 = 0.991$ ) and bovine serum albumin standard solution ( $y = 0.0067x + 0.0451$ ,  $R^2 = 0.993$ ), respectively.



## 2.5. Regulation of mineral nutrition by CDs in salt-stressed rice seedlings

Determination of total nitrogen content of plants was performed by sulfuric acid-hydrogen peroxide digestion, Kjeldahl method. The molybdenum antimony anti-colorimetric method was used to determine the total phosphorus content of plants. The contents of potassium (K), calcium (Ca), magnesium (Mg), manganese (Mn), iron (Fe), zinc (Zn) and copper (Cu) in rice seedlings were determined by flame atomic absorption spectrophotometry (Z-2300, Hitachi, Japan). Every eight samples, a quality control sample was done to assess stability.

## 2.6. Metabolomic profiling

The harvested rice seedling leaves were ground into powder under the protection of liquid nitrogen, and then vacuum freeze-dried for 24 h. 0.2000 g of the sample powder was weighed and dissolved in 1.2 mL of 70% ice methanol (4 °C) solution, and then extracted by ultrasonic extraction for 30 min, centrifuged at 12000 rpm for 10 min, and filtered through a 0.22 µm filter to obtain the supernatant. After that, the supernatant was examined using an Accela UHPLC system that was fitted with a heated electrospray ionization source and an LTQ-Orbitrap Velos mass spectrometer (Thermo Scientific, Bremen, Germany). Both positive and negative ion source modes were used for data gathering. Utilizing a Shim-pack Scepter column (2.1 × 150 mm, 1.9 µm Shimadzu, Japan), 45 °C was the column temperature and 0.3 mL/min was the flow rate. A (0.1% formic acid in water) and B (0.1% formic acid in acetonitrile) were present in the mobile phase of positive ion modes. A (5 mM ammonium acetate in water) and B (5 mM ammonium acetate in acetonitrile) were included in the negative ion mode mobile phase. The gradient elution conditions were 0–1 min, 2% B; 1–7 min, 2–40% B; 7–11 min, 40 to 95% B; 11–12.5 min, 95% B; 12.5–13.5 min, 95–2% B; 13–15 min, 2% B. The arbitrary unit of sheath gas was maintained at 60. Thirty arbitrary units of aux gas were maintained. For positive ionization mode, the spray voltage was 4 KV, while for negative ionization mode, it was −3.50 KV. The capillary temperature was maintained at 380 °C, while the probe heater temperature was maintained at 350 °C. The range of mass was 70–1050 *m/z*. Every ten samples, a quality control sample is done to assess stability. Following data transformation and analysis using the open-source program MS-DIAL (version 4.92, Japan), the data were filtered, standardized, and then subjected to multivariate analysis using MetaboAnalyst 5.0 for orthogonal partial least-squares discriminant analysis (OPLS-DA). The rationale behind the split was attributed to the variable significance in projection (VIP) value exceeding 1.5.

## 2.7. Transcriptomic profiling

The rice seedlings were removed after 2 weeks treatment and immediately placed in liquid nitrogen, preserved in dry ice and shipped to Shanghai Parsonage for reference genome transcriptome sequencing on an Illumina sequencer. The raw data were obtained and the samples were sequenced online. The 3' endband splice sequences were eliminated using Fastp (0.22.0), and the reads that had an average quality score below Q20 were eliminated to create the clean data. High quality analyses were then performed using the clean data. NCBI provided the reference genome database. Fragments Per Kilo bases per Million fragments (FPKM) was used to standardize the expression. With DESeq (v1.38.3), a differential expression analysis between comparison groups was carried out. The regulation of the differentially expressed genes was as follows: significance *P*-value < 0.05, expression difference fold |log<sub>2</sub>-FoldChange (FC)| > 1. The GO and KEGG pathway enrichment analyses were carried out with topGO (v2.50.0) and clusterProfiler (v4.6.0) software, respectively, with a focus on GO terms and KEGG pathways with *P*-value < 0.05.

## 2.8. Statistical analysis

All experiments were conducted three duplicates for each treatment. And the results were reported as mean ± standard deviation. The data were analyzed by ANOVA and LSD (*P* < 0.05) using SPSS statistical software.

## 3. Results and discussion

### 3.1. Characterization of CDs

PH-CDs was composed of PCs molecules polymerized to form macromolecules, and then carbonized to form CDs (Fig. 1A). The formation of PE-CDs may be the grafting of the decomposed PCs molecules in the electrolyte on the surface of the carbon core exfoliated from the carbon rod (Fig. 1B). Fig. 1C and D showed the TEM of CDs. PH-CDs and PE-CDs appeared as spherical nanoparticles with lattice spacing of  $0.21 \pm 0.025$  nm and  $0.34 \pm 0.026$  nm, and average particle sizes of  $9.78 \pm 2.45$  nm and  $4.87 \pm 0.65$  nm, respectively. The size of PE-CDs was smaller, which was in agreement with other reports that CDs prepared by electrolysis have dimensions of 2 to 6 nm (Zhang et al., 2019). CDs have capability to penetrate plant tissues through roots or aerial organs and tissues (e.g. cuticle, stomata, stomata). The uptake and transport must cross a series of chemical and physiological barriers that govern the size exclusion limit (Wang, Lombi, Zhao, & Kopittke, 2016). We suspect that the smaller size and enhanced affinity facilitates the movement of CDs into and out of plant tissues for their function.

Subsequently, the surface functional groups of CDs were characterized by FTIR. As shown in Fig. 1E, compared with PCs, the PH-CDs exhibited fewer FTIR peaks, showing a -OH stretching vibration peak at  $3450\text{ cm}^{-1}$ , a C=O peak at  $1650\text{ cm}^{-1}$ , and a faint -C-C peak at  $1050\text{ cm}^{-1}$ . The FTIR spectra of the two CDs were similar. XPS spectra showed that PH-CDs and PE-CDs were composed of C and O (Fig. 1F), the high-resolution C 1s spectra (Fig. S2) confirmed the existence of C=O, C = C/C-C, C—O, and the high-resolution O 1s spectra (Fig. S2) confirmed the existence of C—O and C=O (Yao et al., 2022). In the high-resolution O 1s spectrum, the area corresponding to C=O unit moiety in PH-CDs was larger than that in PE-CDs. However, the area associated with C—O unit moiety was lower in PH-CDs than in PE-CDs, indicating that the electrolysis method introduces more oxygen atoms. PE-CDs also contained more oxygen (34%) than PH-CDs (31%). In the Raman spectrum (Fig. 1G), the D band located at  $1351\text{ cm}^{-1}$  was attributed to the functional groups on the surface of the CDs, indicating sp<sup>3</sup> hybridized disordered carbon. The G band located at  $1580\text{ cm}^{-1}$  represented the sp<sup>2</sup> carbon structure, which was related to the graphite morphology. The ID/IG indicated the contribution of disordered surface states to the structure. The ID/IG was 0.35 for PH-CDs and 0.83 for PE-CDs, indicating more functional group modifications on the surface of PE-CDs with more oxygen-containing functional groups. The findings from Raman spectrum were consistent with those obtained from XPS.

The XRD patterns of the CDs were shown in Fig. S3, revealing two diffraction peaks at  $24.5^\circ$  and  $42^\circ$ , corresponding to the (002) and (100) crystal planes of graphite, respectively (Li et al., 2021). The zeta potential of the CDs was shown in Fig. 1H. Compared to PH-CDs, the zeta potential of PE-CDs was notably lower at −35.60 mV. The surface of PE-CDs prepared by electrolysis was rich in carboxyl and hydroxyl groups, as well as grafted with PCs-breaking groups. These hydrophilic groups contributed to the formation of high negative zeta potential. It has been reported that positively or negatively charged nanoparticles with zeta potentials higher than 20 or 30 mV were more likely to be taken up by plant cell or chloroplast membranes, whereas more neutral nanomaterials were unable to penetrate plant lipid bilayers (Hu et al., 2020). The surface of plant leaves is formed by a waxy layer of cuticles containing nano-scale (~2 nm) hydrophilic pores and micron-scale stomata (Lv, Christie, & Zhang, 2019). Nanomaterials are mainly delivered to plants through the cuticle and stomata. Furthermore, inside the leaf, the

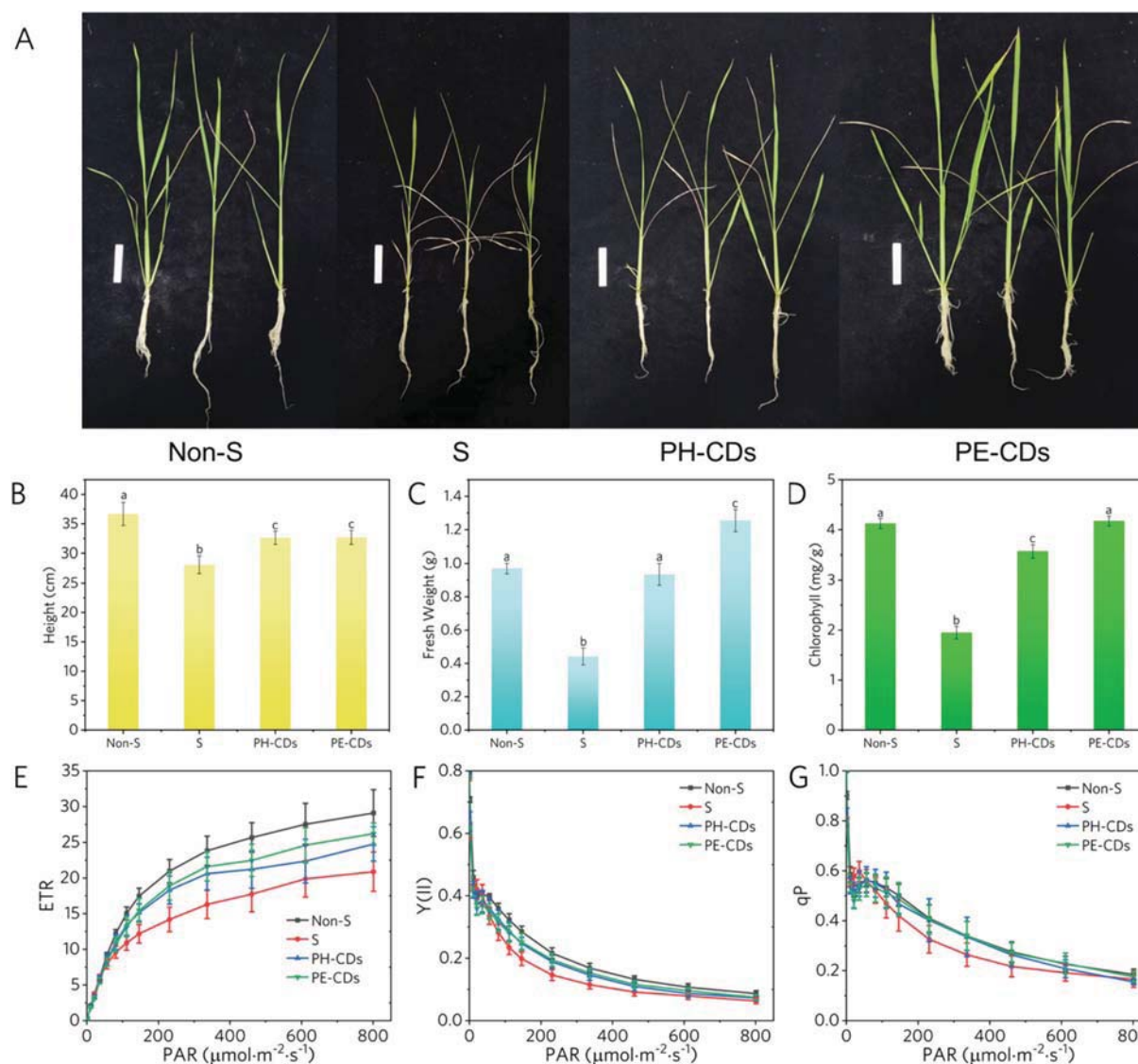


**Fig. 2.** Growth status of rice at seedling stage under different CDs treatments. Photos (A), height (B), fresh weight (C), and chlorophyll content (C) of rice seedlings under different treatments. Photosynthesis parameters include (E) ETR, (F) Y(II), and (G) qP. The group without salt stress treatment was recorded as Non—S, the salt stress treatment group sprayed water was recorded as S, and the salt stress treatment group sprayed optimal concentration of PH-CDs and PE-CDs was recorded as PH-CDs and PE-CDs. The error bars were standard deviations ( $n \geq 6$ ). Different letters marked indicate significant differences between treatments ( $p < 0.05$ ).

cell wall is a biological barrier with hydrophobicity and hydrophilicity, with a reported pore size of  $<13$  nm (Albersheim, Darvill, Roberts, Sederoff, & Staehelin, 2010) and a non-uniformly distributed negative charge (Fritz, 2007). A higher absolute value of the Zeta potential enhances the penetration of CDs into the chloroplasts through the plant cells (Wang et al., 2022).

### 3.2. The antioxidant properties of CDs

The antioxidant properties of the CDs were characterized by the  $\text{KMnO}_4$  degradation rate, DPPH scavenging activity and  $\text{O}_2^{\cdot-}$  scavenging activity, as shown in Fig. S4. PH-CDs showed the highest antioxidant activity, followed by PE-CDs. At a concentration of  $50 \mu\text{g/mL}$ , the  $\text{KMnO}_4$  degradation rate and  $\text{O}_2^{\cdot-}$  scavenging activity of PH-CDs were 2.34 times and 4.94 times greater than that of ascorbic acid (VC), respectively. The exact structural type of the CDs and the type of free radical are significantly influence their antioxidant properties. Three general methods exist for scavenging free radicals: electron transfer, hydrogen transfer, and production of free radical adducts at the carbon site of  $\text{SP}^2$  (Gázquez, Cedillo, & Vela, 2007). When it happens, radical

scavenging can be the result of one or more of the aforementioned actions working together. The abundant hydroxyl, carboxyl, and amino groups on the CDs surface promoted the occurrence of hydrogen transfer pathways. Unpaired electrons on the surface of CDs can be delocalized either by resonance within the aromatic domain or by chemical bond rearrangement. The oxidation level of PE-CDs was higher than PH-CDs, resulting in more C-OH and C=O groups than C-O-C groups. Therefore, PH-CDs exhibited the stronger antioxidant properties. PH-CDs and PE-CDs inherited the abundant phenolic hydroxyl groups of the precursor and thus possessed antioxidant capacity. DPPH was a stable N-centered radical with its nitrogen having two lone pair electrons surrounded by three benzene rings, it readily accepted the hydrogen radical and forms a stable complex (Ionita, 2021). The effect of the CDs on DPPH radical scavenging was not as good as that of VC, indicating that the CDs had a poor hydrogen supply capacity. This finding is consistent with previous studies by other researchers (Ruiz, Yate, García, Cabanero, & Grande, 2017).

### 3.3. CDs promoted the growth and development of salt-stressed rice seedlings

As shown in Fig. 2A-D, CDs treatments significantly enhanced the salt stress resistance of rice seedlings, leading to an increase in the height of salt-stressed seedlings. The fresh weight of PE-CDs treatments was significantly higher by 28.87% than that of Non-S, while the chlorophyll content was not significantly different from that of Non-S. The PH-CDs treatments also enhanced the fresh weight and chlorophyll content of rice seedlings, but were slightly inferior to that of PE-CDs. PH-CDs showed the strongest antioxidant activity, but PE-CDs showed the best effect in alleviating salt stress in rice seedlings. The possible reasons are that PE-CDs were smaller and more electronegative, facilitating their entry into plant cells through the pores on the leaf surface when sprayed. As shown in the Fig. 2E-G, with the increase of photosynthetic effective radiation (PAR) in rice leaves, the CDs treatment group exhibited higher relative electron transfer rate (ETR), actual photosynthetic efficiency (Y (II)) and photochemical burst capacity (qP) compared with the S group, where the ETR of the PE-CDs group was higher than that the PH-CDs.

### 3.4. Spraying CDs increased the ability of antioxidant defense system in rice seedlings under salt stress

As shown in Fig. S5. After two weeks of salt stress, the activities of SOD and CAT, and the contents of total polyphenols and flavonoids in rice seedlings (S) were significantly lower than those in Non-S. Upon the treatment with CDs, these parameters showed a significant increase, indicating the potential of CDs to enhance the antioxidant defense system of rice seedlings under salt stress. POD activity was significantly increased after salt stress compared with Non-S, whereas CDs treatment reduced this increase, with PE-CDs treatment showing the greatest reduction. The activities of scavenging enzymes in plants increased under mild and moderate stress. As the duration of stress increased, the enzyme activities decreased to different degrees. The activities of SOD and CAT decreased earlier, and the activity of POD decreased later.

Different results were reported due to different durations of salt stress exposure. For example, after 3 days of salt stress treatment, the SOD activity of rice seedlings was notably higher than that of the

untreated group, and the enzyme activity was significantly increased by the co-treatment of exogenous calcium and salt stress (Rahman, Nahar, Hasanuzzaman, & Fujita, 2016). At 3 days of salt stress treatment, the stress response of rice seedlings was still ongoing, and the stress stimulus produced more SOD. Our results showed that rice seedlings had lower SOD activity than the untreated group after 2 weeks of salt stress, probably because by this time the excess ROS in the seedlings had been cleared by the defense system or the salt-stressed seedlings were in a dying state. In addition, different parts of rice exhibit varied responses to salt stress. For example, after germination, the change trend of CAT content in root and shoot was opposite after salt stress treatment for 14 days (Mekawy, Abdelaziz, & Ueda, 2018). That was, compared with the control, CAT activity was significantly increased in root and decreased in shoot after salt stress treatment. The trend of CAT activity in the shoot of rice seedlings was consistent with our results. The trends of total flavonoids and total polyphenols in our results were consistent with other reports (Rahman et al., 2023).

Oxidative stress caused by salt stress led to lipid peroxidation in rice seedlings, as indicated by MDA content. As shown in Fig. S5F, the MDA content increased by 2 times after salt stress treatment compared with normal growing rice seedlings. MDA content was significantly decreased by 62.22% and 55.34% after treatment with PE-CDs and PH-CDs, respectively. These results indicated that rice seedlings subjected to CDs treatment suffered only slight oxidative damage. Similar results were reported by others (Basit et al., 2023).

### 3.5. Effect of CDs on osmotic regulatory substances in salt-stressed rice seedlings

Under high salt, cells synthesize e.g. proline, betaine, soluble sugars, soluble proteins, etc. as osmotic regulators to induce water transport across the membrane in a direction favorable to cell growth. The content of osmotic regulators is low under normal growth conditions and increases under stress. The amount of proline content reflected, to some extent, the degree of plant stress. As shown in Fig. S6A, the proline content significantly increased under salt stress, whereas it decreased by 33.25% and 12.54% after PH-CDs and PE-CDs treatments, respectively, indicating a lower stress degree. The results for betaine content were

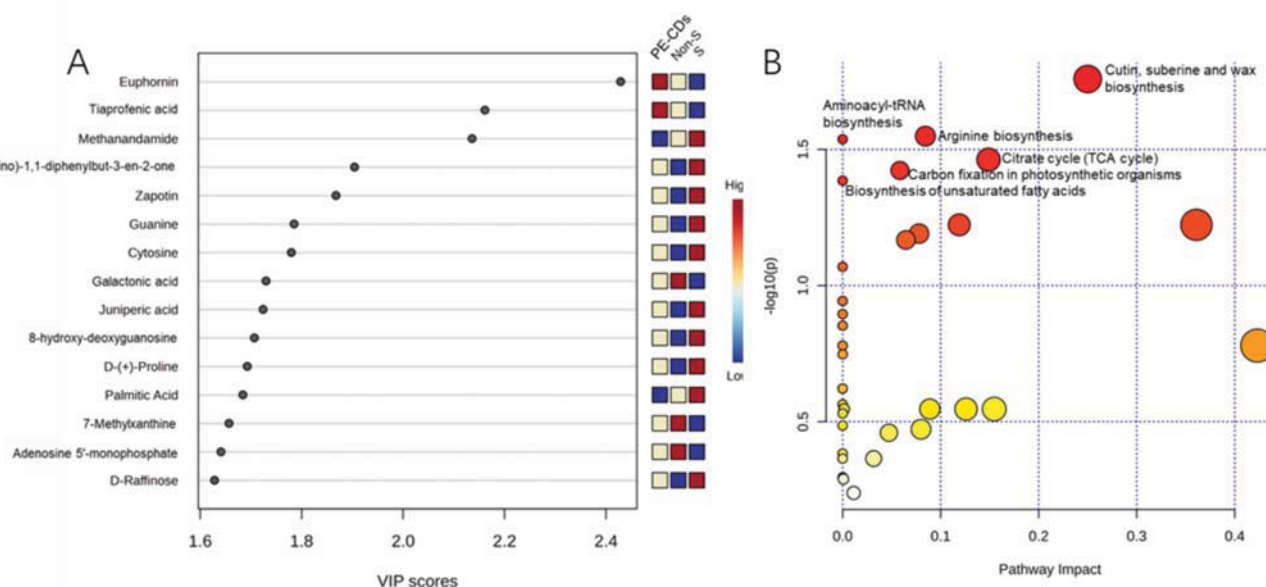


Fig. 3. Changes in metabolites of rice seedlings in different treatments. (A) VIP scores of responsible metabolites leading to isolation. (B) Metabolic pathway enrichment analysis of metabolites in rice seedlings under different treatments. Bubble size indicated the pathway impacts, and bubble color depth indicated the *P* value.



similar to those for proline. Soluble sugars are the main products of photosynthesis in higher plants and are involved in osmoregulation when plants are subjected to salt stress, and their content will increase (Boriboonkaset et al., 2013). Salt stress stimulated rice to produce more soluble sugars, and the spraying of PH-CDs could alleviate the stress degree, so the soluble sugar content was lower than S, while PE-CDs could stimulate plants to produce more soluble sugars to maintain and balance the osmotic pressure of rice cells when the stress persisted. Previous studies reported that rice varieties with higher salt tolerance showed a greater increase in soluble sugar content after salt stress (Lu et al., 2017). The soluble protein content of rice seedling under salt stress was significantly higher in the CDs-treated group compared to the S group, indicating that CDs treatments promoted rice seedlings to produce more soluble proteins and maintain osmotic pressure. The results were consistent with previous study (Huang et al., 2023).

### 3.6. Effect of CDs on mineral nutrition of salt-stressed rice seedlings

Excess salt in soil induces osmotic stress in plants by reducing the water potential that limits water uptake, while excess uptake of  $\text{Na}^+$  and  $\text{Cl}^-$  leads to ionic stress by affecting the uptake and distribution of essential elements, thereby interfering with various metabolic processes.

The results in Fig. S7 indicate that salt stress significantly reduced the content of most mineral elements (Ca, Fe, N, Cu, K, Mg) in rice seedlings. A similar report indicated that salt stress reduced trace element concentrations ( $\text{Fe}^{2+}$ ,  $\text{K}^+$ ,  $\text{Mg}^{2+}$ ) in rice roots and shoots (Farooq et al., 2022). The uptake of the above elements was increased by CDs treatment. Differently, Zn content was elevated under salt stress and decreased after CDs treatment, as previously reported (Villora, Moreno, Pulgar, & Romero, 2000). Fe is a cofactor of heme and methemoglobin and plays an important role in electron transfer in respiration, and the content of active Fe was positively correlated with the activities of POD and CAT (Mehrabanjoubani et al., 2019). Interestingly, under salt stress, spraying CDs resulted in a significant increase in Fe uptake by rice seedlings. Fe content was increased by 36.39% and 29.29% in PH-CDs and PE-CDs treated groups, respectively, compared to Non-S. The POD and CAT activities of CDs-treated rice seedlings increased under salt stress, which may be related to the increase in elemental Fe content. According to the results, CDs treatment plays an important role in alleviating the uptake of mineral elements under salt stress.

### 3.7. Changes of metabolic substances in CDs-treated rice seedlings

The growth-promoting effects of PE-CDs on rice under salt stress have been demonstrated through physiological and biochemical perspectives. To further understand the molecular mechanism, we conducted non-targeted metabolomic analysis. First, supervised multivariate analysis (partial least squares discriminant analysis, PLS-DA) was conducted on metabolomic data from normal-growing (Non-S), salt-stressed (S), and PE-CDs-treated rice seedlings under salt stress (PE-CDs). As shown in Fig. S8, there was a clear separation between three groups, indicating that the metabolite profiles of rice seedlings changed under different treatments. Fig. 3A displayed the key contributing metabolites that contributed to the separation in the PLS-DA analysis. The top 15 ranked metabolites with VIP > 1.5 mainly included flavonoids, nucleic acids, amino acids, organic acids, sugars, fatty acids, and other compounds. The metabolites were screened by  $P < 0.05$  and  $|\log_2\text{Fold Change}| \geq 1$ , as shown in Table S1.

Nucleic acid-based metabolites were significantly up-regulated under S treatment compared to Non-S, but this up-regulation was reduced with PE-CDs treatment. It indicated that the degradation of DNA and RNA in rice seedling tissues was accelerated under salt stress, but this effect was mitigated by PE-CDs. The same pattern was also observed for proline and L-phenylalanine, which are metabolites of amino acids. The results were consistent with the previous physiological index. L-Aspartic acid plays a crucial role in protein synthesis and is also

involved in nucleotide formation, as well as being an important component of the tricarboxylic acid cycle and glycolysis (Han et al., 2021). L-Aspartic acid was significantly down-regulated under salt stress compared with Non-S. It indicated that many biosynthetic processes in rice seedlings were enhanced under salt stress, and more L-Aspartic acid was involved in the synthesis, resulting in a significant down-regulation, whereas PE-CDs treatment was significantly up-regulated compared with S, which again proved that the PE-CDs treatment mitigated the salt stress degree. Polyphenols and flavonoids play a crucial role in scavenging ROS. After treatment with S, several flavonoid metabolites were significantly down-regulated, indicating that salt stress disrupted the redox balance of rice seedlings and caused oxidative damage, whereas after PE-CDs treatment, these flavonoids were up-regulated, suggesting that PE-CDs played a positive role in maintaining the redox balance and reducing oxidative damage. This finding aligns with the previously determined trends in total polyphenol and total flavonoid contents. Citric acid and malic acid, important substances in the tricarboxylic acid cycle, were significantly down-regulated in salt-stressed seedlings, indicating that salt stress caused damage and affected the physiological and metabolic processes of seedlings. In contrast, there was no difference between PE-CDs and Non-S, indicating that PE-CDs alleviated this injury, which was consistent with the growth indexes (height, fresh weight, etc.) measured in the previous period. The accumulation of D-Raffinose was reported to be positively correlated with plant drought tolerance (Li, Zhang, et al., 2020). D-Raffinose showed significant up-regulation under salt stress, indicating a strong stress response. However, after treatment with PE-CDs, D-Raffinose was significantly down-regulated compared to S, suggesting that PE-CDs alleviated the degree of salt stress. A similar trend was observed in 16-Hydroxyhexadecanoic acid, a key substance in plant keratin synthesis (Bian et al., 2022).

The analysis of enriched metabolic pathways identified six pathways that were screened at  $P < 0.05$  (Fig. 3B), namely: Cutin, suberine and wax biosynthesis, arginine biosynthesis, aminoacyl-tRNA biosynthesis, citrate cycle (TCA cycle), carbon fixation in photosynthetic organisms, and biosynthesis of unsaturated fatty acids. Cutin, suberine, and wax biosynthesis are linked to promoting plant growth (Ge et al., 2022). By integrating the metabolome with pre-physiological and biochemical indices, we discovered that PE-CDs can improve the antioxidant defense system in plants, remove ROS, protect photosynthesis, and alleviate ongoing salt stress.

### 3.8. Changes of transcriptional gene in CDs-treated rice seedlings

Metabolomics analysis identified molecular change events under salt stress that were alleviated by PE-CDs. These changes partially explain the improved stress tolerance by spraying PE-CDs. However, genes related to photosynthesis and the defense system were still absent. We then conducted transcriptomics analysis on rice seedlings to gain a more comprehensive understanding of how PE-CDs enhance stress tolerance.

The PCA results (Fig. S9A) demonstrated a distinct separation of each treatment group, indicating significant changes in transcriptome genes in both salt-stressed rice seedlings sprayed with PE-CDs and those without. Differentially expressed genes (DEGs) were counted and the screening conditions: expression difference fold  $|\log_2\text{Fold Change}| > 1$ ,  $P\text{-value} < 0.05$ . As shown in Fig. S9B–D, compared with Non-S, there were 3773 DEGs in S, while after PE-CDs treatment, the number of DEGs decreased to 2630. The number of down-regulated genes (719) was greater than the number of up-regulated genes (392) after PE-CDs treatment compared to S. GO enrichment analysis of DEGs (Fig. S10) revealed that compared to Non-S, the up-regulated genes in S were significantly enriched in oxidoreductase activity, defense response, toxin metabolic process, secondary metabolic process and other terms. The down-regulated genes were significantly enriched under the terms related to photosynthesis. In contrast, the top 20 terms in the group sprayed with PE-CDs under salt stress were significantly up-regulated, including oxidoreductase activity, transcription factor activity, defense

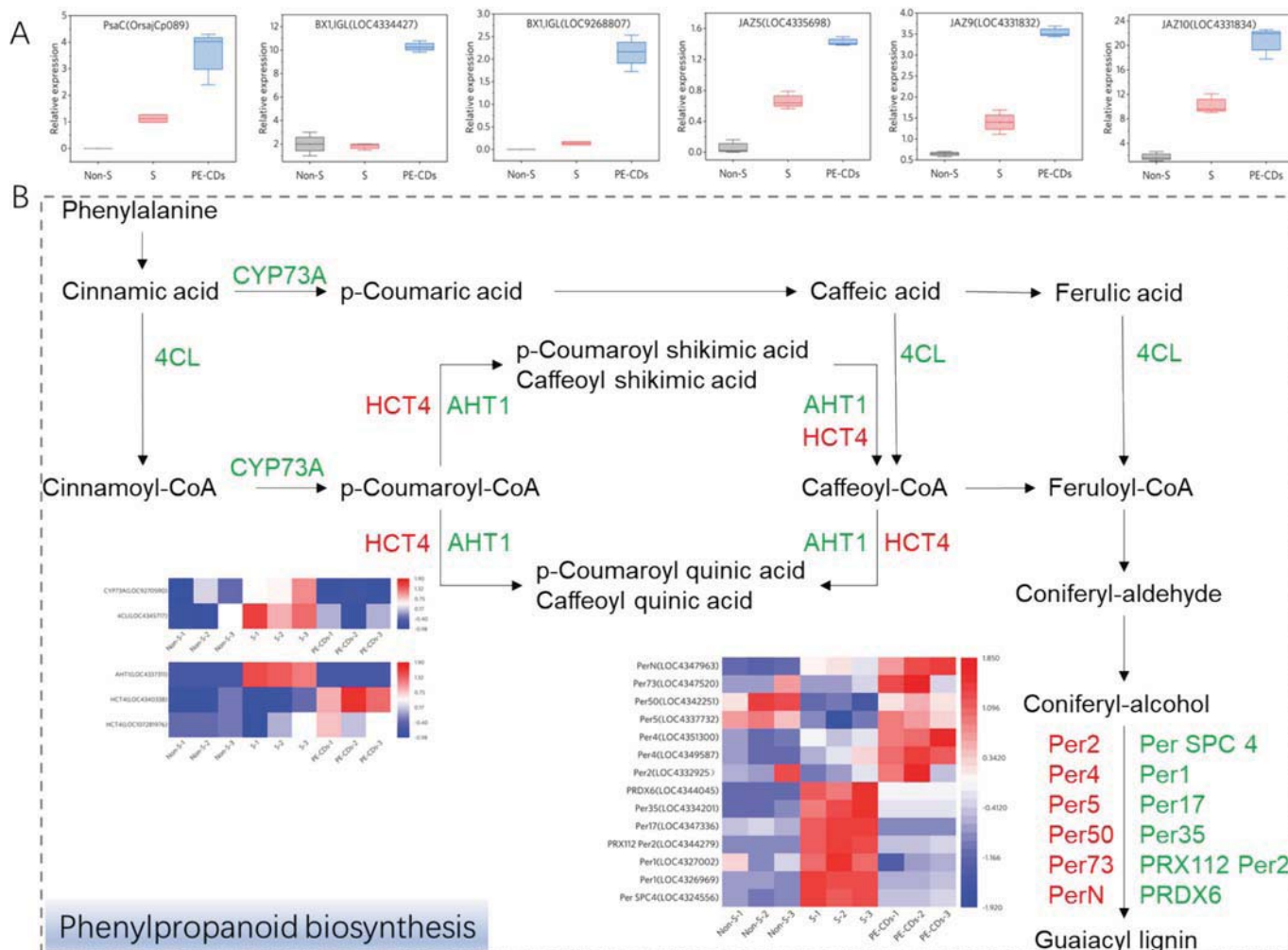


**Fig. 4.** Transcriptome analysis of rice seedlings under different treatments. (A) The relative expression levels of upregulated genes. (B) DEGs associated with Phenylpropanoid biosynthesis. Red and green colors represented genes up- and down-regulated, respectively, after treatment with PE-CDs compared to S. The embedded heatmap showed the expression levels of the relevant DEGs. (For interpretation of the references to color in this figure legend, the reader is referred to the web version of this article.)

response, etc.

The KEGG database pathway analysis was performed for DEGs (Fig. S11). Compared to Non-S, S treatment significantly down-regulated genes in photosynthesis-related pathways. Compared to Non-S, the DEGs in PE-CDs treatment were enriched in metabolism of terpenoids and polyketides, biosynthesis of other secondary metabolites, carbohydrate, lipid, amino acids metabolic pathways, and signal transduction pathways.

PsaC is an important constitutive subunit of photosystem I and is involved in electron transfer in ferredoxin (Yang et al., 2017). Photosystem I is high in iron and is significantly affected by iron deficiency, and studies have shown that PsaC is reduced substantially in iron deficiency (Yadavalli, Neelam, Rao, Reddy, & Subramanyam, 2012). Results (Fig. 4A) showed that the PsaC gene expression was significantly up-regulated in PE-CDs treatment compared with S. Combined with the physiological results, this indicated that the PE-CDs treatment accelerated the ETR in the photosystem, significantly increased the uptake of Fe, elevated the chlorophyll content, and enhanced photosynthesis under salt stress in the rice seedlings, thereby alleviating the salt stress and promoting the growth of rice. The BX1 and IGL genes encode enzymes that convert indole-3-glycerolphosphate to indole, a volatile defense signaling compound and a precursor for the biosynthesis of tryptophan and defense-related benzoxazinoid (Richter et al., 2021). The BX1 and IGL genes expression were significantly up-regulated in PE-

CDs compared to S. It suggested that PE-CDs treatment enhanced the rice defense system by up-regulating this gene and releasing defense signals while synthesizing large amounts of tryptophan. The JAZ protein negatively regulates the production of jasmonic acid, which is an important signaling molecule for abiotic stress, inducing costly defense responses. Increased rice investment in defense leads to reduced growth, so jasmonic acid-induced responses are down-regulated when defense is not required (Wasternack, 2017). As shown in Fig. 4A, the gene encoding the JAZ protein was significantly up-regulated in the PE-CDs compared to S, leading to a decrease in the synthesis of jasmonic acid, which in turn led to a decrease in jasmonic acid-induced investment in defense, and an increase in the amount of rice growth. It indicated that PE-CDs treatment reduced the salt stress degree and regulated defense investment and rice seedlings growth through the jasmonic acid signaling pathway.

Lignin and flavonoids are products of the phenylpropanoid metabolic pathway, which affects plant clearance of ROS and tolerance to abiotic stresses (Chen, Su, Zhang, Zhan, & Zeng, 2020). As shown in Fig. 4B, HCT4 genes and peroxidase-related (Per) genes were up-regulated after PE-CDs treatment compared with S treatment, indicating that these genes played a positive role in alleviating salt stress in rice. And 4CL genes were down-regulated in this pathway, which is consistent with the reported results (Xu et al., 2021). Diterpenoid biosynthesis has been reported to contribute to the tolerance of rice

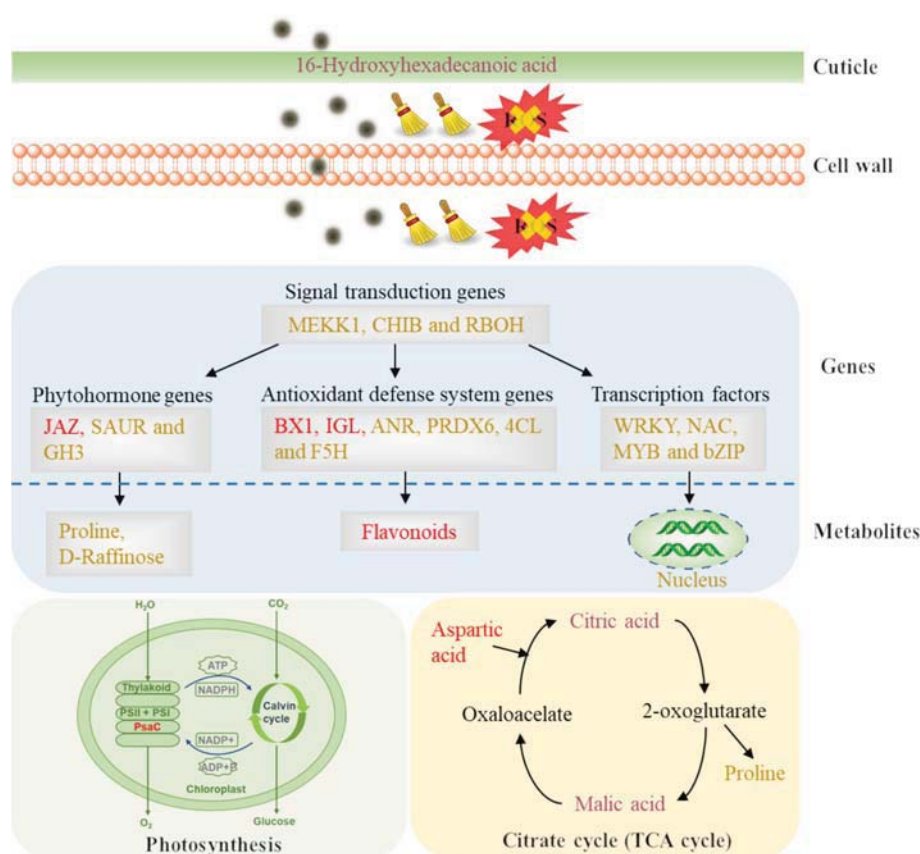


**Fig. 5.** Schematic diagram of the molecular mechanism for PE-CDs mitigated salt stress in rice seedlings. Red color represents up-regulated genes or metabolites. Gold font represents genes or metabolites that are up-regulated compared to Non-S and down-regulated compared to S. Purple font represents no significant difference in PE-CDs treatment compared to Non-S. (For interpretation of the references to color in this figure legend, the reader is referred to the web version of this article.)

seedlings to salinity stress (Li, Ma, Tai, Qiu, & Yang, 2020). An analysis of the pathway was shown in SI.

Phytohormone signaling networks regulate defense responses to help crops resist stresses. MEKK1, CHIB and RBOH genes are stress responsive genes in the MAPK signaling pathway, which play an important role in stress tolerance. Transcription factors are signaling endpoints that repress or activate the expression of target genes under different stresses. Detailed analysis on phytohormone signaling networks and transcription factors was shown in SI. Fig. 5 illustrated the possible molecular mechanisms of PE-CDs in alleviating salt stress in rice seedlings.

#### 4. Conclusion

The CDs prepared by both methods inherited the antioxidant properties of the precursors. The smaller size and lower zeta potential of PE-CDs were important factors contributing to their effectiveness. The electron donor-acceptor characteristics of PE-CDs enhanced the photosynthetic electron transport in photosynthesis. Furthermore, the photosynthesis of rice was promoted by up-regulation of the PsaC gene expression of PSI, and the defense system was enhanced by up-regulation of the BX1 and IGL genes expression. PE-CDs effectively mitigated the salt stress in rice seedlings, leading to the restoration of their fresh weight and chlorophyll content to the normal. The spraying of PE-CDs can help rice grow in salty soils, thereby expanding the global agricultural area and promoting environmental sustainability. However, field trials and the impact of CDs on the entire life cycle of crops also need further research.

#### CRediT authorship contribution statement

**Baoyan Guo:** Writing – review & editing, Writing – original draft, Validation, Investigation, Formal analysis, Data curation, Conceptualization. **Fengqiong Chen:** Writing – original draft, Software, Methodology, Formal analysis, Data curation, Conceptualization. **Guo Liu:** Writing – review & editing, Validation, Software, Resources, Methodology, Investigation, Data curation. **Wentao Li:** Validation, Methodology, Formal analysis, Data curation. **Wei Li:** Writing – original draft, Visualization, Software, Conceptualization. **Jianle Zhuang:** Writing – original draft, Visualization, Supervision, Project administration, Methodology, Formal analysis, Conceptualization. **Xuejie Zhang:** Software, Methodology, Investigation, Formal analysis. **Lashuang Wang:** Writing – original draft, Resources. **Bingfu Lei:** Writing – review & editing, Supervision, Project administration, Funding acquisition. **Chaofan Hu:** Writing – review & editing, Writing – original draft, Supervision. **Yingliang Liu:** Writing – review & editing, Writing – original draft, Visualization, Supervision, Resources, Project administration, Investigation, Funding acquisition, Conceptualization.

#### Declaration of competing interest

The authors declare no competing financial interest.

#### Data availability

Data will be made available on request.



## Acknowledgements

This work was financially supported by the National Natural Science Foundation of China (Grant No. 12174119 and 52172142), Science and Technology Program of Guangzhou, China (Grant No. 202103000059).

## Appendix A. Supplementary data

Supplementary data to this article can be found online at <https://doi.org/10.1016/j.fochx.2024.101422>.

## References

- Albersheim, P., Darvill, A., Roberts, K., Sederoff, R., & Staehelin, A. (2010). *Plant cell walls: From chemistry to biology*. New York: Garland Science, Taylor and Francis Group, LLC.
- Basit, F., Ulhassan, Z., Mou, Q., Nazir, M. M., Hu, J., Hu, W., ... Guan, Y. (2023). Seed priming with nitric oxide and/or spermine mitigate the chromium toxicity in rice (*Oryza sativa*) seedlings by improving the carbon-assimilation and minimising the oxidative damages. *Functional Plant Biology*, 50, 121–135. <https://doi.org/10.1071/FP21268>
- Bian, X., Yao, L., Si, E., Meng, Y., Li, B., Ma, X., Yang, K., Lai, Y., Shang, X., Li, C., Wang, J., & Wang, H. (2022). Characterization of glossy spike mutants and identification of candidate genes regulating cuticular wax synthesis in barley (*Hordeum vulgare* L.). *International Journal of Molecular Sciences*, 23, 13025. <https://doi.org/10.3390/ijms232113025>
- Boriboonkaset, T., Theerawitaya, C., Yamada, N., Pichakum, A., Supaibulwatana, K., Cha-um, S., Takabe, T., & Kirdmanee, C. (2013). Regulation of some carbohydrate metabolism-related genes, starch and soluble sugar contents, photosynthetic activities and yield attributes of two contrasting rice genotypes subjected to salt stress. *Protoplasma*, 250, 1157–1167. <https://doi.org/10.1007/s00709-013-0496-9>
- Chaudhary, M., Singh, P., Singh, G. P., & Rath, B. (2024). Structural features of carbon dots and their agricultural potential. *ACS Omega*, 9, 4166–4185. <https://doi.org/10.1021/acsomega.3c04638>
- Chen, X., Su, W., Zhang, H., Zhan, Y., & Zeng, F. (2020). Fraxinus mandshurica 4-coumarate-CoA ligase 2 enhances drought and osmotic stress tolerance of tobacco by increasing coniferyl alcohol content. *Plant Physiology and Biochemistry*, 155, 697–708. <https://doi.org/10.1016/j.plaphy.2020.08.031>
- Das, B., Dadhich, P., Pal, P., Srivas, P. K., Bankoti, K., & Dhara, S. (2014). Carbon nanodots from date molasses: New nanolights for the in vitro scavenging of reactive oxygen species. *Journal of Materials Chemistry B*, 2, 6839–6847. <https://doi.org/10.1039/C4TB01020E>
- Do Espírito Santo Pereira, A., Caixeta Oliveira, H., Fernandes Fraceto, L., & Santaella, C. (2021). Nanotechnology potential in seed priming for sustainable agriculture. *Nanomaterials*, 11, 267. <https://doi.org/10.3390/nano11020267>
- Farooq, M., Asif, S., Jang, Y., Park, J., Zhao, D., Kim, E., & Kim, K. (2022). Effect of different salts on nutrients uptake, gene expression, antioxidant, and growth pattern of selected rice genotypes. *Frontiers in Plant Science*, 13, Article 895282. <https://doi.org/10.3389/fpls.2022.895282>
- Fritz, E. (2007). Measurement of cation exchange capacity (CEC) of plant cell walls by X-ray microanalysis (EDX) in the transmission electron microscope. *Microscopy and Microanalysis*, 13, 233–244. <https://doi.org/10.1017/S1431927607070420>
- Gázquez, J. L., Cedillo, A., & Vela, A. (2007). Electrodonating and electroaccepting powers. *Journal of Physical Chemistry A*, 111, 1966–1970. <https://doi.org/10.1021/jp065459f>
- Ge, S., Qin, K., Ding, S., Yang, J., Jiang, L., Qin, Y., & Wang, R. (2022). Gas chromatography–mass spectrometry metabolite analysis combined with transcriptomic and proteomic provide new insights into revealing cuticle formation during pepper development. *Journal of Agricultural and Food Chemistry*, 70, 12383–12397. <https://doi.org/10.1021/acs.jafc.2c04522>
- Guo, B., Liu, G., Li, W., Hu, C., Lei, B., Zhuang, J., Zheng, M., & Liu, Y. (2022). The role of carbon dots in the life cycle of crops. *Industrial Crops and Products*, 187, Article 115427. <https://doi.org/10.1016/j.indcrop.2022.115427>
- Han, M., Zhang, C., Suglo, P., Sun, S., Wang, M., & Su, T. (2021). L-aspartate: An essential metabolite for plant growth and stress acclimation. *Molecules*, 26, 1887. <https://doi.org/10.3390/molecules26071887>
- Hu, P., An, J., Faulkner, M. M., Wu, H., Li, Z., Tian, X., & Giraldo, J. P. (2020). Nanoparticle charge and size control foliar delivery efficiency to plant cells and organelles. *ACS Nano*, 14, 7970–7986. <https://doi.org/10.1021/acsnano.9b09178>
- Huang, X., Zheng, D., Feng, N., Huang, A., Zhang, R., Meng, F., Jie, Y., Mu, B., Mu, D., & Zhou, H. (2023). Effects of prohexadione calcium spraying during the booting stage on panicle traits, yield, and related physiological characteristics of rice under salt stress. *PeerJ*, 11, Article e14673. <https://doi.org/10.7717/peerj.14673>
- Ionita, P. (2021). The chemistry of DPPH: free radical and congeners. *International Journal of Molecular Sciences*, 22, 1545. <https://doi.org/10.3390/ijms22041545>
- Ji, Y., Yue, L., Cao, X., Chen, F., Li, J., Zhang, J., Wang, C., Wang, Z., & Xing, B. (2023). Carbon dots promoted soybean photosynthesis and amino acid biosynthesis under drought stress: Reactive oxygen species scavenging and nitrogen metabolism. *Science of the Total Environment*, 856, Article 159125. <https://doi.org/10.1016/j.scitotenv.2022.159125>
- Jing, X., Liu, Y., Liu, X., Zhang, Y., Wang, G., Yang, F., Zhang, Y., Chang, D., Zhang, Z., You, C., Zhang, S., & Wang, X. (2024). Enhanced photosynthetic efficiency by nitrogen-doped carbon dots via plastoquinone-involved electron transfer in apple. *Horticulture Research*, 11, 1–12. <https://doi.org/10.1093/hr/uhae016>
- Kou, E., Yao, Y., Yang, X., Song, S., Li, W., Kang, Y., ... Lei, B. (2021). Regulation mechanisms of carbon dots in the development of lettuce and tomato. *ACS Sustainable Chemistry & Engineering*, 9, 944–953. <https://doi.org/10.1021/acssuschemeng.0c08308>
- Li, Q., Ma, C., Tai, H., Qiu, H., & Yang, A. (2020). Comparative transcriptome analysis of two rice genotypes differing in their tolerance to saline-alkaline stress. *PLoS One*, 15, Article e243112. <https://doi.org/10.1371/journal.pone.0243112>
- Li, T., Zhang, Y., Liu, Y., Li, X., Hao, G., Han, Q., ... Zhao, T. (2020). Raffinose synthase enhances drought tolerance through raffinose synthesis or galactinol hydrolysis in maize and Arabidopsis plants. *Journal of Biological Chemistry*, 295, 8064–8077. <https://doi.org/10.1074/jbc.RA120.013948>
- Li, Y., Li, W., Yang, X., Kang, Y., Zhang, H., Liu, Y., & Lei, B. (2021). Salvia miltiorrhiza-derived carbon dots as scavengers of reactive oxygen species for reducing oxidative damage of plants. *ACS Applied Nano Materials*, 4, 113–120. <https://doi.org/10.1021/acsnano.0c02419>
- Lu, N., Yan, L., Zheng, C., Yin, H., Guo, S., & Xie, X. (2017). Effects of salt stress on growth and agronomic traits of Yanfeng 47 and Yanjing 456. *Crops*, 180, 106–111. <https://doi.org/10.16035/j.issn.1001-7283.2017.05.018>
- Lv, J., Christie, P., & Zhang, S. (2019). Uptake, translocation, and transformation of metal-based nanoparticles in plants: Recent advances and methodological challenges. *Environmental Science: Nano*, 6, 41–59. <https://doi.org/10.1039/C8EN00645H>
- Mehrabanjoubani, P., Abdolzadeh, A., Sadeghipour, H. R., Aghdasi, M., Bagherieh Najjar, M. B., & Barzegargolchini, B. (2019). Silicon increases cell wall thickening and lignification in rice (*Oryza sativa*) root tip under excess Fe nutrition. *Plant Physiology and Biochemistry*, 144, 264–273. <https://doi.org/10.1016/j.plaphy.2019.09.047>
- Mekawy, A. M. M., Abdelaziz, M. N., & Ueda, A. (2018). Apigenin pretreatment enhances growth and salinity tolerance of rice seedlings. *Plant Physiology and Biochemistry*, 130, 94–104. <https://doi.org/10.1016/j.plaphy.2018.06.036>
- Rahman, A., Alam, M. U., Hossain, M. S., Mahmud, J. A., Nahar, K., Fujita, M., & Hasanuzzaman, M. (2023). Exogenous gallic acid confers salt tolerance in rice seedlings: Modulation of ion homeostasis, osmoregulation, antioxidant defense, and methylglyoxal detoxification systems. *Agronomy*, 13, 16. <https://doi.org/10.3390/agronomy13010016>
- Rahman, A., Nahar, K., Hasanuzzaman, M., & Fujita, M. (2016). Calcium supplementation improves Na<sup>+</sup>/K<sup>+</sup> ratio, antioxidant defense and glyoxalase systems in salt-stressed rice seedlings. *Frontiers in Plant Science*, 7, 609. <https://doi.org/10.3389/fpls.2016.00609>
- Richter, A., Powell, A. F., Mirzaei, M., Wang, L. J., Movahed, N., Miller, J. K., ... Jander, G. (2021). Indole-3-glycerolphosphate synthase, a branchpoint for the biosynthesis of tryptophan, indole, and benzoxazinoids in maize. *The Plant Journal*, 106, 245–257. <https://doi.org/10.1111/tpj.15163>
- Ruiz, V., Yate, L., García, I., Cabanero, G., & Grande, H. (2017). Tuning the antioxidant activity of graphene quantum dots: Protective nanomaterials against dye decoloration. *Carbon*, 116, 366–374. <https://doi.org/10.1016/j.carbon.2017.01.090>
- Villora, G., Moreno, D. A., Pulgar, G., & Romero, L. (2000). Yield improvement in zucchini under salt stress: determining micronutrient balance. *Scientia Horticulturae*, 86, 175–183. [https://doi.org/10.1016/S0304-4238\(00\)00149-7](https://doi.org/10.1016/S0304-4238(00)00149-7)
- Wang, C., Yang, H., Yue, L., Sun, W., Chen, F., Cao, X., ... Xing, B. (2022). Physiological and molecular level understanding of advanced carbon dots to enhance maize drought tolerance: Modulation of photosynthesis and signaling molecules. *Environmental Science: Nano*, 9, 3821–3832. <https://doi.org/10.1039/D2EN00176D>
- Wang, P., Lombi, E., Zhao, F., & Kopittke, P. M. (2016). Nanotechnology: A new opportunity in plant sciences. *Trends in Plant Science*, 21, 699–712. <https://doi.org/10.1016/j.tplants.2016.04.005>
- Wasternack, C. (2017). A plant's balance of growth and defense – Revisited. *New Phytologist*, 215, 1291–1294. <https://doi.org/10.1111/nph.14720>
- Xu, C., Wei, L., Huang, S., Yang, C., Wang, Y., Yuan, H., Xu, Q., Zhang, W., Wang, M., Zeng, X., & Luo, J. (2021). Drought resistance in Qingke involves a reprogramming of the phenylpropanoid pathway and UDP-glucosyltransferase regulation of abiotic stress tolerance targeting flavonoid biosynthesis. *Journal of Agricultural and Food Chemistry*, 69, 3992–4005. <https://doi.org/10.1021/acs.jafc.0c07810>
- Yadavalli, V., Neelam, S., Rao, A. S. V. C., Reddy, A. R., & Subramanyam, R. (2012). Differential degradation of photosystem I subunits under iron deficiency in rice. *Journal of Plant Physiology*, 169, 753–759. <https://doi.org/10.1016/j.jplph.2012.02.008>
- Yang, H., Li, P., Zhang, A., Wen, X., Zhang, L., & Lu, C. (2017). Tetratricopeptide repeat protein Pyg7 is essential for photosystem I assembly by interacting with Psac in Arabidopsis. *The Plant Journal*, 91, 950–961. <https://doi.org/10.1111/tpj.13618>
- Yao, L., Zhao, M., Luo, Q., Zhang, Y., Liu, T., Yang, Z., ... Zeng, C. (2022). Carbon quantum dots-based nanozyme from coffee induces cancer cell ferroptosis to activate antitumor immunity. *ACS Nano*, 16, 9228–9239. <https://doi.org/10.1021/acsnano.2c01619>
- Zhang, M., Wang, H., Liu, P., Song, Y., Huang, H., Shao, M., Liu, Y., Li, H., & Kang, Z. (2019). Biototoxicity of degradable carbon dots towards microalgae *Chlorella vulgaris*. *Environmental Science: Nano*, 6, 3316–3323. <https://doi.org/10.1039/C9EN00829B>



# Dual-mode photochromic luminescence of carbon dots induced by photoinduced electron transfer

Jueran Cao, Enlin Huang, Ziting Zhong, Tingjie Jiang, Haoran Zhang, Wei Li, Xuejie Zhang, Chaofan Hu\* and Bingfu Lei\*

**ABSTRACT** The integration of photochromism and photoluminescence in functional materials presents significant challenges, particularly in achieving broad-spectrum color modulation and rapid response. In this work, we have developed sodium-doped and sodium/boron co-doped CDs that exhibit dual-mode photochromic luminescent behavior through a novel radical-mediated mechanism. The Na-CDs demonstrated a 180 nm red-shift in emission, transitioning from 450 to 630 nm. The Na, B-CDs achieved blue-shifted, multicolor emission, progressing from orange to yellow and green under 30-s UV irradiation. Notably, the photochromic states spontaneously reverted to their initial configurations without external stimuli. These phenomena arise from photoinduced electron transfer between pristine CDs and light-generated anionic radicals. Leveraging these unique photochromic properties, we implemented reversible anti-counterfeiting systems and information encryption platforms. Furthermore, the photochromic CDs exhibit daylight-responsive UV detection capabilities and are functional in plant cell imaging, significantly expanding their potential applications in optoelectronic devices.

**Keywords:** carbon dots, photochromic, photoinduced electron transfer, reversible, fluorescence

## INTRODUCTION

The development of reversible, light-responsive materials has made significant strides in applications such as information storage, bioimaging, optical switches, and security devices [1–3]. Among these systems, photochromic materials are particularly promising for light-responsive applications [4–6]. Organic photochromic compounds exhibit reversible color transitions upon light irradiation, a phenomenon originating from molecular transformations where photoexcitation induces either electronic transitions or structural rearrangements, thereby altering optical properties. Representative systems include spiropyran, azobenzene, and diarylethene derivatives [7–9]. Zhu *et al.* [10] designed a sterically hindered ethene-bridged photochromic triad integrated with ferrocene and naphthalimide, achieving redox-gated photochromism and photoinduced electron transfer (PET)-modulated fluorescence switching through controlled electron transfer between ferrocene redox states and

the chromophore. Zhou *et al.* [11] successfully achieved reversible photochromism of viologen derivatives in multiple solvents by introducing triethylamine (TEA) as an electron donor to form charge-transfer complexes, which effectively facilitated the PET process. Wang *et al.* [12] developed a dual-emitting luminescent hybrid film UPTES-SPn-Tb-hfa based on photochromic spiropyran and terbium (Tb) complexes. By utilizing the ring-closing (SP)/ring-opening (MC) isomerization of SP to achieve fluorescence resonance energy transfer (FRET), the film exhibits reversible dynamic luminescence under alternating UV and visible light irradiation. However, photochromic materials still face challenges such as insufficient photostability, slow response rates, and limited reversibility.

Carbon dots (CDs), a type of 0D luminescent carbon nanomaterial, have attracted significant attention due to their diverse physicochemical properties, biocompatibility, unique optical characteristics, low cost, and eco-friendliness [13,14]. By tuning their chemical structures and dopants, CDs can be engineered into a variety of fluorescent behaviors [15–18]. However, there are currently limited reports on the photochromic properties of carbon dots, and the underlying mechanisms have not been thoroughly investigated. Liu *et al.* [19] reported the development of smart photochromic nanocomposites by integrating CDs with titanium dioxide (TiO<sub>2</sub>) porous films, which exhibit bidirectional photochromism (coloration or discoloration) under single-wavelength visible light irradiation. Fu *et al.* [20] synthesized photochromic CDs via a one-step solvent-free microwave-assisted method using naphthalene tetracarboxylic acid, urea, and boric acid; these CDs exhibit reversible fluorescence color switching under UV light in amine solvents, and highlight their potential applications in UV detection and dynamic anti-counterfeiting. Guo *et al.* [21] fabricated CDs-based materials with intrinsic photochromism, multi-stimulation-responsive afterglow (lifetime of 253 ms), and dynamic color regulation by embedding naphthalimide structures in CDs and using polyvinylpyrrolidone encapsulation. However, most reported photochromic CDs materials achieve only a single-color change with a relatively small emission range span, while their slow response and poor reversibility make them unsuitable for complex application scenarios.

Here, 1,4,5,8-Naphthalenetetracarboxylic dianhydride (NTCDA) was used as a precursor, employing conventional hydrothermal synthesis to prepare photochromic CDs through

Key Laboratory for Biobased Materials and Energy of Ministry of Education/Guangdong Provincial Engineering Technology Research Center for Optical Agriculture, College of Materials and Energy, South China Agricultural University, Guangzhou 510642, China

\* Corresponding author (email: [tleibf@scau.edu.cn](mailto:tleibf@scau.edu.cn); [thucf@scau.edu.cn](mailto:thucf@scau.edu.cn))

Na and B co-doping, enabling the CDs solution to exhibit multicolor photochromism (Fig. 1a). The resulting CDs achieved rapid emission changes: Na-CDs transitioned from blue to red, while Na, B-CDs progressed from blue to red and then to green under UV irradiation, establishing multicolor photochromic behavior (Fig. 1b). We propose that this luminescence mechanism occurs because UV irradiation causes excitons to reach the excited state, while partial energy transfer to new energy levels induces photochromic phenomena (Fig. 1c). Notably, these photochromic CDs maintain dynamic color transitions when incorporated into PVA hydrogels, offering a viable pathway for secure data encryption and UV detection by utilizing this unique fluorescent property.

## MATERIALS AND METHODS

### Materials and measurement

Reagents including boric acid (BA), sodium carbonate ( $\text{Na}_2\text{CO}_3$ ), 1,4,5,8-naphthalenetetracarboxylic dianhydride (NTCDA), polyvinyl alcohol (PVA, Type 1799), dimethyl sulfoxide (DMSO), polyethylene glycol (PEG), and *N,N*-dimethylformamide (DMF) were sourced from Aladdin and used without

further purification. Deionized (DI) water was employed throughout the study.

Transmission electron microscopy (TEM) images were obtained on a JEOL JEM-F200. High-resolution transmission electron microscopy (HR-TEM) characterization was implemented on a 200 kV TEM microscope. X-ray photoelectron spectroscopy (XPS) measurements were performed on a Thermo Scientific K-Alpha. Fourier transform infrared (FT-IR) spectra were obtained on a Thermo Fisher. UV-visible absorption spectra were scanned using UV-2600i (Shimadzu). Photoluminescence spectra (PL) were obtained on an Edinburgh FLS 1000 fluorescence spectrophotometer equipped with a xenon arc lamp (Xe900) and a microsecond flash-lamp ( $\mu\text{F900}$ ). Fluorescence lifetime curves of CDs in solution were determined using a steady-state fluorescence spectrometer (Edinburgh FLS1000, UK). Photographs were taken by an EOS 40D camera under ambient conditions. Electron spin resonance (ESR) signals were obtained on a Bruker EMXplus-6/1 spectrometer, and the samples were excited using a 365 nm UV lamp. A Nikon Ds-R2 Inverted Fluorescence Microscope takes photos of plant cells.

Density functional theory (DFT) calculations were carried out with the Gaussian 16 software. The B3LYP functional was

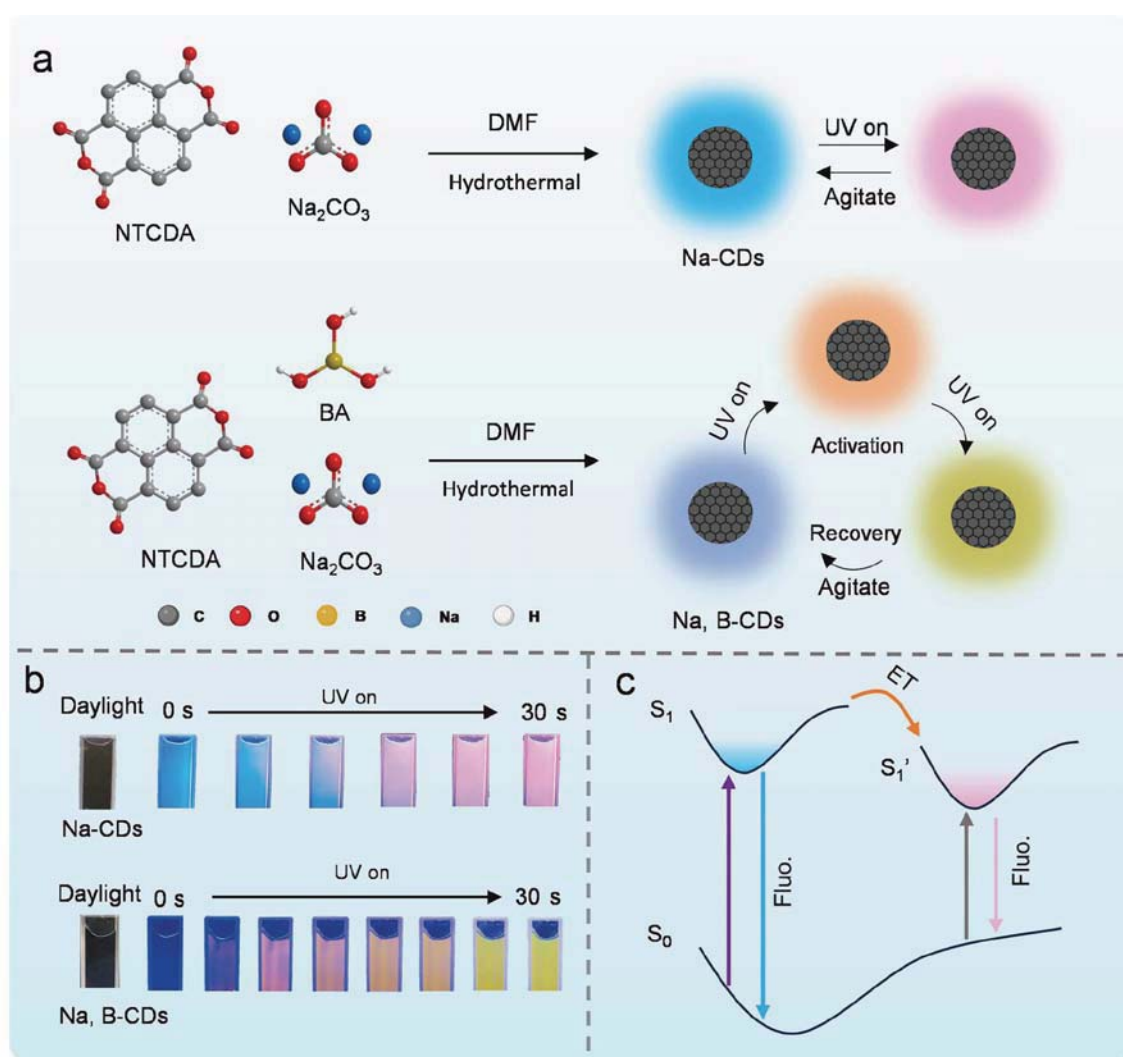


**Figure 1** Stimulating photochromism in CDs. (a) Preparation of the photochromic CDs. (b) UV light stimulation of CDs in response to photochromic pictures. (c) Proposed mechanism for photochromic CDs.



adopted for all calculations in combination with the D3BJ dispersion correction. For geometry optimization and frequency analysis, the 6-31+G (d, p) basis set was utilized for all atoms. Single-point calculations were carried out at the M062X-D3/6-311+G (d, p) level. The Solvation Model Based on Density (SMD) implicit solvation model was applied to account for solvation effects during optimization and frequency calculations, with DMF chosen as the solvent. Frontier orbital analysis was conducted using the Multiwfn and VMD software packages.

### Synthesis and preparation

#### *Synthesis of the Na-carbon dots (Na-CDs)*

First, 0.2 g of sodium carbonate and 0.2 g of NTCDA were added to the liner of a 100 mL autoclave. Then, 50 mL of DMF was introduced and stirred vigorously. Subsequently, the mixture was reacted at 200 °C for 6 h in an oven. After cooling, the resulting solution was filtered through a 0.22  $\mu\text{m}$  organic filter membrane and dialyzed using a 500 Da dialysis bag for 4 h to obtain the Na-CDs.

#### *Synthesis of the Na, B-CDs*

1 g of BA and 0.2 g of sodium carbonate were added into the liner of a 100 mL reaction kettle; 50 mL of DMF was added and stirred vigorously. Then, 0.2 g of NTCDA was added into the reaction kettle and homogenized. The mixture was heated at 200 °C for 5 h in an oven. After the reaction, the solution was filtered through a 0.22  $\mu\text{m}$  organic filter membrane, and the precipitate was collected. The precipitate was dissolved in 50 mL of deionized water, sonicated, and centrifuged at 10,000 r/min for 5 min to remove insoluble impurities, yielding Na, B-CDs.

#### *Preparation of the CDs-PVA film*

0.5 g PVA was mixed with 10 mL  $\text{H}_2\text{O}$  and 1 mL Na-CDs solution at 90 °C oil bath condensation reflux for 1 h, poured into the mold placed in a ventilated place air-drying static overnight, and then placed in an 80 °C oven drying.

#### *Preparation of the CDs-PVA hydrogel*

10 g PVA was dissolved in 90 g  $\text{H}_2\text{O}$  at 85 °C to form a PVA aqueous solution; separately, 10 g PVA was dissolved in 90 g DMSO at 85 °C to form a PVA-DMSO solution. Then, 3 g of PVA aqueous solution and 7 g of PVA-DMSO solution were mixed thoroughly, followed by the addition of 1 mL of Na-CDs and further mixing. The mixture was centrifuged at 4000 r/min for 2 min to remove bubbles. The resulting CDs-PVA hydrogels were poured into a mold and stored at 4 °C overnight.

#### *Preparation of the CDs ink*

2 g of PEG<sub>800</sub> was melted by heating and mixed with 1 mL of Na-CDs by ultrasonication, and left to stand overnight, and then added the appropriate amount into the stamp with a dropper and left to stand for 15 min; PEG<sub>200</sub> was mixed with Na, B-CDs by ultrasonication according to the ratio of 1:1.

#### *Na, B-CDs in plant cell imaging*

Mung bean seeds were soaked in deionized water overnight and subsequently transferred to a dark room for incubation for 5 days, and observed daily for growth. The mung bean sprout stems were placed in CDs solution for overnight incubation when they grew to about 10 cm. The cultured mung bean sprout

stems were taken, and thin cross-section samples were prepared by the freehand sectioning method.

## RESULTS AND DISCUSSION

### Preparation and characterization of the photochromic CDs

The morphologies of Na-CDs and Na, B-CDs were characterized using transmission electron microscopy (TEM). Both CDs exhibited good dispersion with quasi-spherical shapes and showed similar particle sizes, averaging 2.36 nm for Na-CDs and 2.40 nm for Na, B-CDs. The high-resolution TEM (HRTEM) images revealed well-resolved lattice fringes having a spacing of 0.21 nm, indicating a graphite-like core structure (Fig. 2a, b) [22]. Fourier transform infrared spectroscopy (FTIR), and X-ray photoelectron spectroscopy (XPS) were used to analyze the surface functional groups of Na-CDs and Na, B-CDs (Fig. 2c, d). Like the precursor, synthesized CDs (NTCDA) exhibited vibrational signals of about  $3450\text{ cm}^{-1}$ , indicating the presence of  $-\text{OH}$  groups, suggesting hydrophilicity of the CDs. Peaks at  $1630$  and  $1380\text{ cm}^{-1}$  this is due to stretching vibrations of  $\text{C}=\text{O}$  and  $\text{C}-\text{N}$  [23]. The characteristic absorption at  $1187$  and  $952\text{ cm}^{-1}$  is due to the bending vibration of  $\text{B}-\text{O}-\text{H}$  and the telescopic vibration of  $\text{B}-\text{C}$  [24,25]. The integrated XPS spectra (Fig. 2d) of the CDs showed the presence of C, N, O and Na, in addition to which, the B element was also present in the Na, B-CDs. The high-resolution XPS spectra of C 1s, N 1s, O 1s, and Na 1s for Na-CDs and Na, B-CDs were examined. In the Na-CDs C 1s XPS spectrum, distinct peaks were observed:  $\text{C}-\text{C}/\text{C}=\text{C}$  ( $284.8\text{ eV}$ ), with a peak area percentage of 89.73% after convolution fitting;  $\text{C}-\text{O}/\text{C}-\text{N}$  ( $286.2\text{ eV}$ ), with a peak area percentage of 3.07% after convolution fitting; and  $\text{C}=\text{O}$  ( $288.4\text{ eV}$ );  $\text{C}-\text{N}$  ( $399.3\text{ eV}$ ) and  $\text{N}-\text{H}$  ( $400.1\text{ eV}$ ) in N 1s XPS spectrum;  $\text{C}=\text{O}$  ( $531.2\text{ eV}$ ) and  $\text{C}-\text{O}/\text{O}-\text{H}$  ( $532.9\text{ eV}$ ) in the O 1s XPS spectra, and Na Auger ( $535.6\text{ eV}$ ); in the Na 1s XPS spectra, the binding energy of Na was  $1071.3\text{ eV}$  (Fig. 2e, f; Fig. S1). Significant peaks can be seen in Na, B-CDs XPS spectra:  $\text{C}-\text{C}/\text{C}=\text{C}$  ( $284.8\text{ eV}$ ) with a convolved fitted peak area percentage of 69.65%,  $\text{C}-\text{O}/\text{C}-\text{N}$  ( $286.4\text{ eV}$ ) with a convolved fitted peak area percentage of 11.50% and  $\text{C}=\text{O}$  ( $288.0\text{ eV}$ ); N 1s XPS spectra for  $\text{C}-\text{N}$  ( $399.0\text{ eV}$ ) and  $\text{N}-\text{H}$  ( $400.1\text{ eV}$ );  $\text{C}=\text{O}$  ( $531.3\text{ eV}$ ) and  $\text{C}-\text{O}/\text{O}-\text{H}$  ( $532.6\text{ eV}$ ) in the O 1s XPS spectra, and Na Auger ( $536.4\text{ eV}$ ); in the Na 1s XPS spectra, the binding energy of Na was  $1071.8\text{ eV}$ ; in the B 1s XPS spectra, the binding energy of  $\text{B}-\text{O}$  ( $192.3\text{ eV}$ ) and  $\text{B}-\text{C}$  ( $192.5\text{ eV}$ ) (Fig. 2g-i; Fig. S2) [24]. The area ratio of  $\text{C}-\text{C}/\text{C}=\text{O}$  convolution peaks in Na, B-CDs decreased compared to that of Na-CDs, while the percentage area of  $\text{C}-\text{O}/\text{C}-\text{N}$  convolution peaks increased, indicating that the doping with electron-deficient B elements results in a reduction of the structure of the  $\text{sp}^2$  conjugated domain of the CDs [26,27].

### Photophysical property investigations

The prepared Na-CDs and Na, B-CDs exhibit similar photophysical properties. To elucidate their photophysical processes, transient absorption spectroscopy and transient fluorescence spectroscopy were conducted on both CDs. Na-CDs in DMF solution and Na, B-CDs in aqueous solution at room temperature and without activation showed an absorption peak at 210 nm. This indicates the presence of aromatic  $\text{C}-\text{C}$  structure in the carbon nucleus and a strong  $\text{n}-\pi^*$  absorption band roughly at 340 nm. With the increase of UV irradiation time

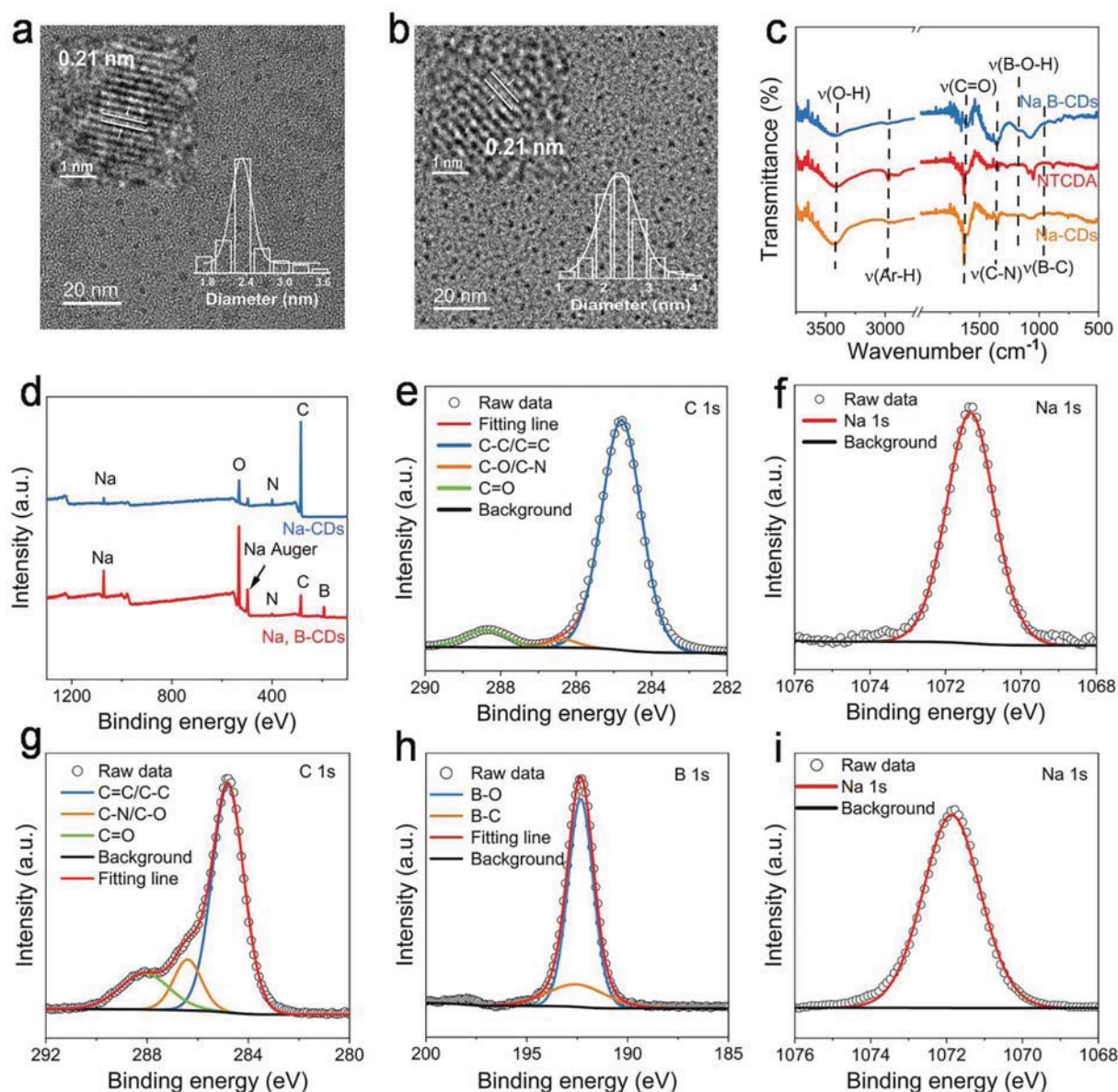


**Figure 2** Structure characterization of photochromic CDs. TEM image of the CDs with the size distribution diagram and HRTEM images of the (a) Na-CDs and (b) Na, B-CDs (inset). (c) FTIR spectra of the Na-CDs, NTCDA, and Na, B-CDs. (d) XPS of Na-CDs and Na, B-CDs. High-resolution XPS spectra of (e) C 1s and (f) Na 1s of the Na-CDs. High-resolution XPS spectra of (g) C 1s, (h) B 1s, and (i) Na 1s of the Na, B-CDs.

(within 30 s), it can be found that the absorption bands of the two kinds of CDs between 450–650 nm gradually enhanced. The appearance color of the Na-CDs solution gradually became darker, while the appearance color of Na, B-CDs solution did not change significantly (Fig. 3a, Figs S3–S5). The newly generated absorption bands indicate the production of new substances under the excitation of UV light, which is attributed to the PET behavior of the surface of the CDs due to the generation of anionic radicals from UV irradiation.

In addition, the photochromic behavior of Na-CDs and Na, B-CDs under UV irradiation was investigated. Na-CDs fluoresced at 450, 525 and 420 nm under 365 nm excitation. Under continuous irradiation at 365 nm, the fluorescence intensity of Na-CDs at 450 and 525 nm was gradually increased at the beginning, reflecting a photoactivation phenomenon [28,29]. Subsequently, the fluorescence intensity gradually decreased and the

fluorescence peak position shifted to 630 nm. With photochromism, the fluorescence color also changed from blue to red, and an obvious redshift occurred (Fig. 3b, Video S1). The main emission peak of Na, B-CDs was at 400 nm, and a peak at about 600 nm appeared within 2 s of UV irradiation, followed by a gradual blueshift of the peak to 520 nm. With photochromism, the fluorescence color changed from blue-violet to orange and then gradually to yellow, and finally blue-shifted to green, and the change was more rapid (Fig. 3c, Video S2). There is an overlap between the fluorescence spectrum after UV activation and the newly generated absorption peaks in the UV-visible absorption spectrum after photoactivation, which provides the feasibility for CDs to realize the PET process (Fig. 3d) [30,31]. It was interesting to note that in addition to the 365 nm excitation that produces the photochromic process, 395 nm excitation also produces a different color change for these two CDs. The Na-

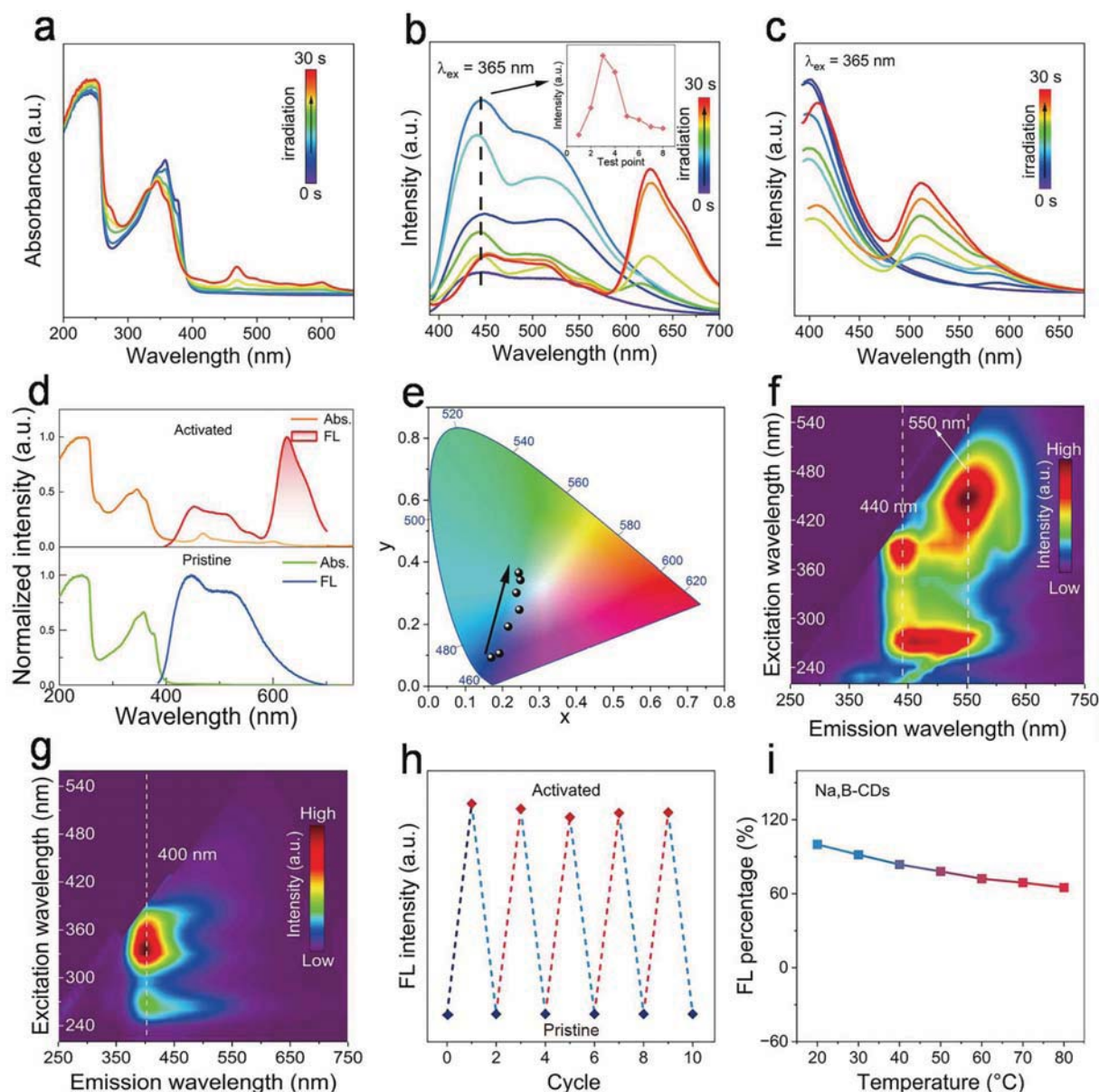


**Figure 3** Photophysical properties of the CDs before (pristine) and after (activated) the photoirradiation. *In situ* absorption spectra of (a) Na-CDs under 365 nm irradiation for different times. Under 365 nm activation, transient fluorescence spectra of (b) Na-CDs and (c) Na, B-CDs. (d) Photophysical properties of Na-CDs *in situ* and after activation, absorption (blue), fluorescence spectra (red). (e) CIE coordinates of Na, B-CDs after irradiation for different times. Excitation-emission mapping of the photoactivated (f) Na-CDs and (g) Na, B-CDs. (h) Reversibility of the activated and deactivated PL. (i) Temperature profiles of Na, B-CDs with respect to fluorescence correlation.

CDs changed from green to red under 395 nm excitation, and the Na, B-CDs changed from blue to orange (Fig. S6). Further analysis by means of the 1931 International Commission on Illumination (CIE) chromaticity diagram to examine the fluorescence changes of Na-CDs and Na, B-CDs before and after UV irradiation showed that the fluorescence color changes characterized by the CIE spectra agree with the visual observations (Fig. 3e, Fig. S7).

We found a meaningful phenomenon. To explore the effect of doping with other metal elements, we synthesized K-CDs, Rb-CDs, and Mg-CDs with similar structures to NTCDA. By studying the transient fluorescence spectra under UV light irradiation, it is interesting to note that the photochromic color changes vary after light excitation. However, all the CDs

exhibited three emission peaks at 430, 530 and 630 nm. This suggests that ionic doping mainly modifies the non-radiative recombination paths through surface modification, thus modulating the fluorescence intensity. It indicates that ion doping mainly modifies the non-radiative recombination paths of CDs through surface modifications (e.g., passivating defects, modulating charge transfer) to modulate the fluorescence intensity, whereas the surface state energy levels are not significantly altered, and thus the positions of the emission peaks remain stable (Fig. S8) [32–34]. Furthermore, excitation-emission mapping shows that Na-CDs could be excited in the 240–530 nm range, exhibiting excitation-dependent behavior due to abundant surface states (Fig. 3f) [35]. Na, B-CDs can be excited in the 240–390 nm range, with excitation wavelength-



independent PL emission peaking at 400 nm (Fig. 3g). It should also be noted that activated CDs can be inactivated by shaking or standing and then reactivated again by UV light with excellent reversibility (Fig. 3h, Fig. S9). To evaluate the thermal stability of Na, B-CDs, the fluorescence intensity of the CDs was measured by placing the CDs at different temperatures. Na, B-CDs could still retain 65% of their fluorescence intensity at a high temperature of 80 °C, and Na-CDs can also maintain around 55%, indicating that both CDs have good stability and can remain stable in extreme environments (Fig. 3i, Fig. S10).

### Mechanism investigations

To further investigate the luminescence mechanism of photochromic CDs, we performed electron paramagnetic resonance (EPR) tests. The EPR signals were significantly enhanced upon UV irradiation, and the strong resonance signal with a g-factor of 2.003 indicated the generation of associated free radicals,

which corresponds to the previous conclusions (Fig. 4a, d) [36,37]. Therefore, the original CDs can be activated by light and then transfer energy to the newly generated radicals through PET [38,39]. The fluorescence lifetime of Na-CDs decreased from 2.5 to 1.49 ns after UV irradiation ( $\lambda_{\text{em}} = 450$  nm), while the fluorescence lifetime at 630 nm only increased from 5.6 to 5.87 ns (Fig. 4b, c). Na, B-CDs showed similar properties: the fluorescence lifetime at 520 nm increased from 5.46 to 8.21 ns, while that at 400 nm decreased (Fig. 4e, f). This provides additional evidence for the dynamic nature of fluorescence changes. It has been reported that the reaction of 1,4,5,8-naphthalenetetracarboxylic acid dianhydride in DMF yields a naphthalene diimide structure [40]. Therefore, we hypothesized that CDs containing naphthalene diimines are generated during the reaction process. Subsequently, density-functional theory (DFT) studies were performed to verify our conjecture regarding the luminescence mechanism [22,41]. The DFT results indicate that

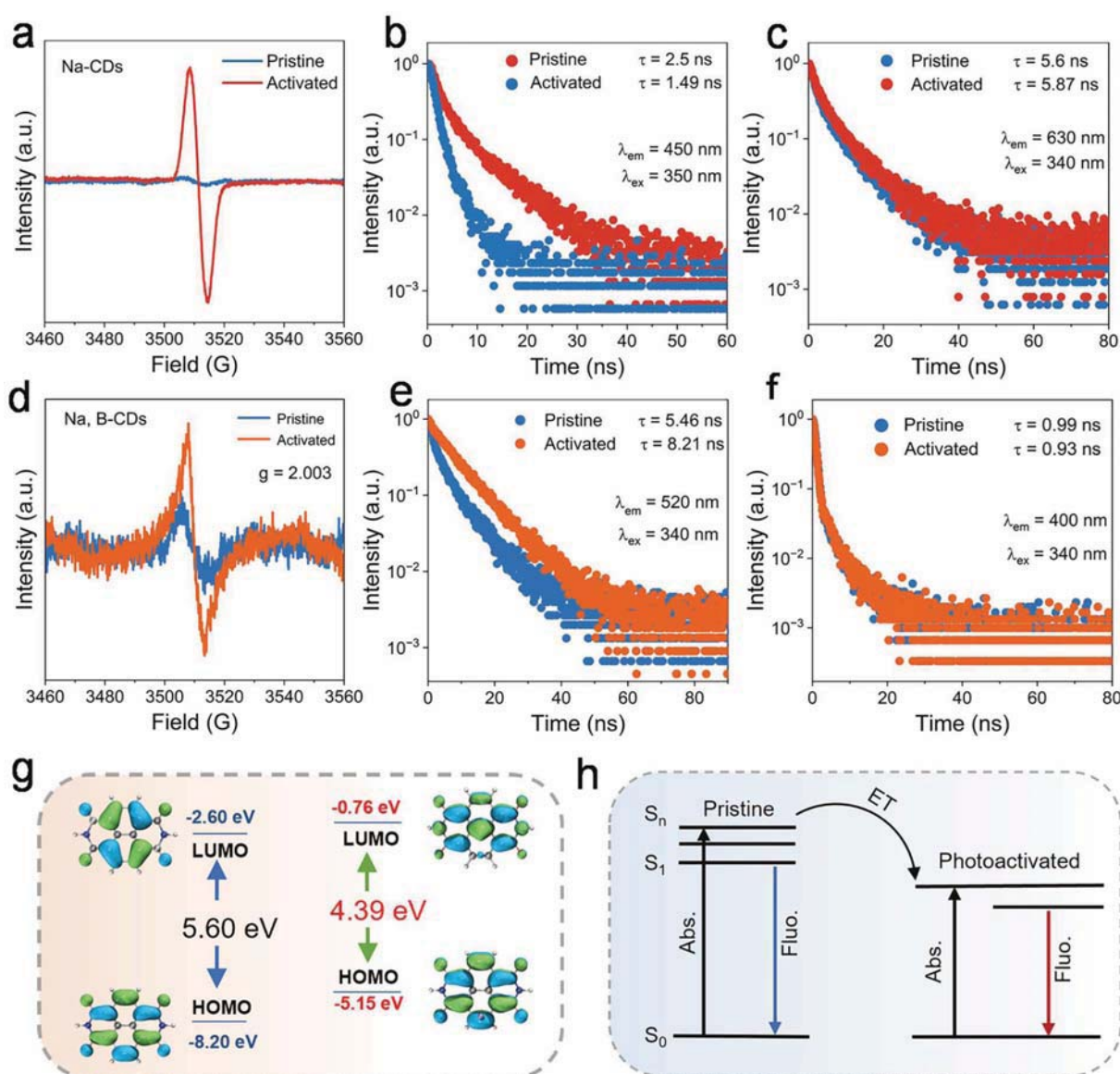


**Figure 4** Photochromic mechanisms. (a) EPR spectra of Na-CDs. Fluorescence at (b) 450 nm (c) 630 nm decay profiles of the pristine (blue line) and photoactivated (orange line) Na-CDs. (d) EPR spectra of Na, B-CDs. Fluorescence at (e) 520 nm (f) 400 nm decay profiles of the pristine (yellow line) and photoactivated (red line) Na, B-CDs. (g) DFT calculated the energy levels of HOMO-LUMO. (h) Proposed mechanism for the reversible photochromic behavior.

doping Na into CDs introduces additional electrons into the electronic system of CDs, thereby elevating the HOMO orbital energy. Consequently, the energy of LUMO orbitals is also elevated due to the redistribution of electron cloud density, ultimately reducing the HOMO-LUMO energy gap and causing a redshift in the color of CDs (Fig. 4g) [42,43].

Based on the above analysis, we propose a possible mechanism for photochromic CDs (Fig. 4h). Under UV light excitation, the original Na-CDs are excited to the  $S_1$  state via light absorption. The  $S_1$  exciton can decay back to the  $S_0$  state to produce fluorescence. Under continuous UV irradiation, photoactivation generates corresponding radicals, leading to photochromism. The transition of these radicals accelerates PET between differ-

ent energy levels of Na-CDs and causes a transition to a new emission level, resulting in the appearance of new absorption peaks and thus achieving a change in fluorescence color [44]. The photochromic mechanism of Na, B-CDs is similar to that of Na-CDs. UV irradiation induces radical formation on the surface, leading to the occurrence of PET and a change in fluorescence color.

#### Cryptographic anti-counterfeiting applications, UV detectors, and plant cell imaging

The unique photochromic properties of CDs were harnessed for multilevel information security, encryption/decryption, and UV detection in combination with polyethylene glycol (PEG) and

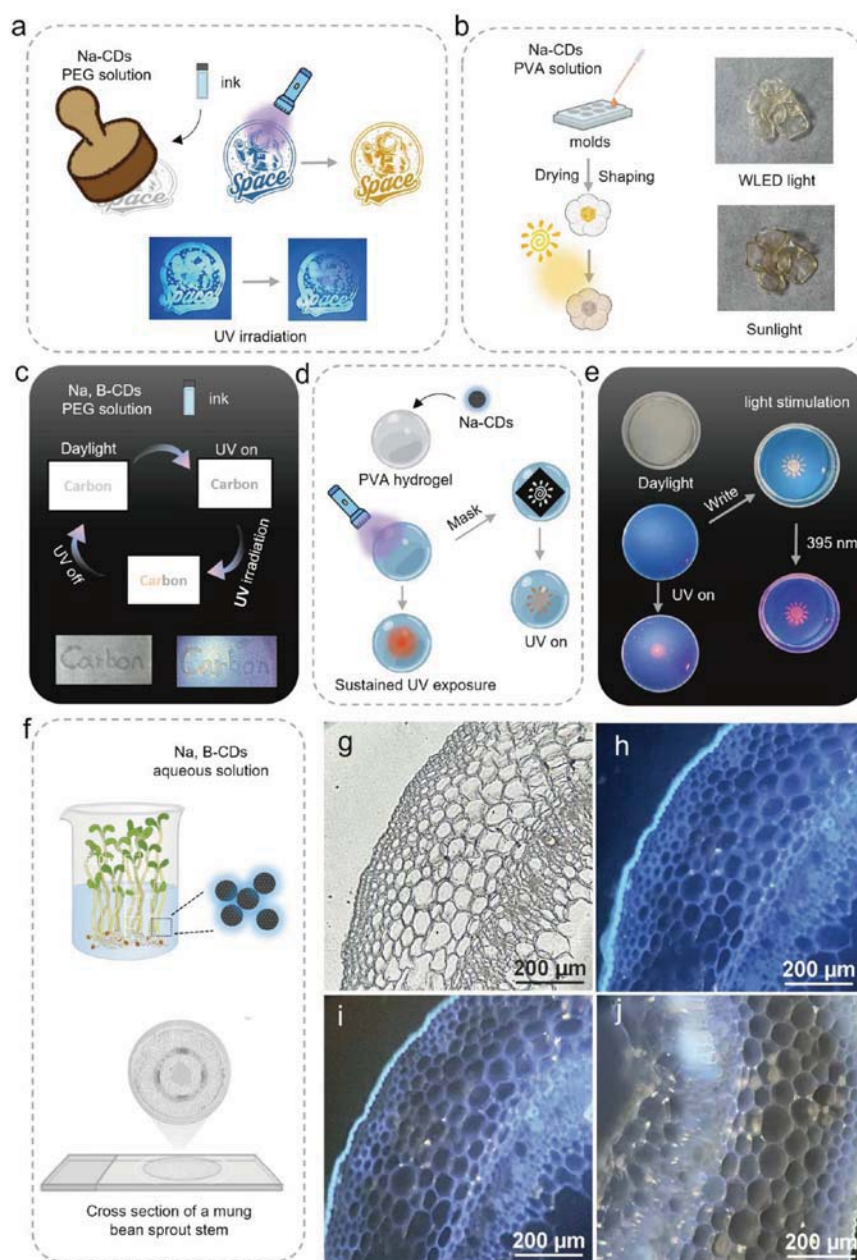


**Figure 5** Applications in data anti-counterfeiting, information encryption, and UV detection. Schematic diagram of the application process of (a) dynamic information security, (b) UV detection, (c) information encryption ink, and (d, e) data writing and erasure, (f) Cross-sectional imaging of mung bean sprout stems. (g) Photograph of plant cells under bright field. (h) Photograph of plant cells under dark field (UV on). (i) Photograph of plant cells irradiated with 365 nm for 10 s in a dark field. (j) Photograph of plant cells irradiated with 365 nm for 20 s in a dark field.

polyvinyl alcohol (PVA). Na-CDs were employed as ink for stamps, with patterns printed on non-fluorescent paper. Upon exposure to 365 nm UV light for 10 s, the patterns gradually shifted from blue to brown in the strongly irradiated areas, while the remaining regions retained their initial color (Fig. 5a). Since the Na-CDs-PVA membranes have a sensitive detection effect on UV light, and the Na-CDs-PVA membranes gradually changed from light yellow to dark brown under UV irradiation, we prepared UV detection patterns with UV response (Fig. 5b). When the film was placed under the sun, the film rapidly changed to dark brown, and after the sun went down, the Na-CDs-PVA film gradually returned to the initial state, and the change was reversible. Subsequently, the Na-CDs-PVA film was made into a flower, and the edges of the flower darkened when exposed to sunlight (UV index = 6) and returned to the original state after the sun went down, which demonstrated that our detection device is suitable for UV detection.

Additionally, the unique photochromic properties of CDs were exploited, employing an aqueous solution of Na, B-CDs as a cryptographic security ink for monochrome printing (Fig. 5c). By using Na, B-CDs ink and PEG<sub>200</sub> to write the “Carbon” message on paper, the “Carbon” message was displayed under UV light, and when the message is exposed to UV light for a long time, the CDs are activated by light, and their apparent color changes to orange, and finally the “Car” message was decrypted through the photochromic effect. Masked patterns on 25 cm<sup>2</sup> of Na-CDs PVA hydrogels were used as writing instruments, in which the designed patterns were printed by UV irradiation for 10 s. The photoactivated photochromic patterns are very stable to UV excitation, can be easily deactivated by standing, and are highly reversible for multiple cycles (Fig. 5d, e). By using an inverted fluorescence microscope to observe the cross-sections of mung bean sprouts, when the plant cells were irradiated with 365 nm fluorescence in the dark field, the cells showed blue fluorescence, and the outline of the cells could be clearly seen; the color of the cells gradually changed to orange as the irradiation time increased. These images show that Na, B-CDs can be fluorescently imaged in plants and are accompanied by color changes (Fig. 5f–j).

## CONCLUSIONS

In summary, we have successfully synthesized CDs exhibiting fluorescent photochromism, which can be photoactivated to generate corresponding free radicals under external UV light stimulation. Na-CDs can be transformed from blue to red under 365 nm excitation, while Na, B-CDs exhibit blue-orange-green color change. By further combining with PVA, PEG, and other polymers, these materials have been realized for applications in information security, data encryption/decryption, UV detection, and plant cell imaging. This work provides a new approach for developing light-responsive, color-changing CDs and offers a design strategy for exploring multicolor color-changing materials.

Received 9 June 2025; accepted 10 July 2025;  
published online 12 August 2025

- 1 Lin Z, Yang J, Zeng Q, *et al.* Deep blue photoluminescence and optical gain from sodium-doped carbon dots. *J Lumin*, 2022, 246: 118856
- 2 Zhang J, Zou Q, Tian H. Photochromic materials: more than meets the eye. *Adv Mater*, 2013, 25: 378–399

- 3 Julià-López A, Hernando J, Ruiz-Molina D, *et al.* Temperature-controlled switchable photochromism in solid materials. *Angew Chem Int Ed*, 2016, 55: 15044–15048
- 4 Xiao Y, Shen M, Li J, *et al.* Thermally activated photochromism: realizing temperature-gated triphenylethylene photochromic materials. *Adv Funct Mater*, 2024, 34: 2312930
- 5 Thaggard GC, Kankanamalage BKP, Park KC, *et al.* Switching from molecules to functional materials: breakthroughs in photochromism with MOFs. *Adv Mater*, 2024, 2410067
- 6 Wu NM, Ng M, Yam VW. Photochromic benzo[*b*]phosphole alkynylgold(I) complexes with mechanochromic property to serve as multistimuli-responsive materials. *Angew Chem Int Ed*, 2019, 58: 3027–3031
- 7 Sekar R, Basavegowda N, Jena S, *et al.* Recent developments in heteroatom/metal-doped carbon dot-based image-guided photodynamic therapy for cancer. *Pharmaceutics*, 2022, 14: 1869
- 8 Khandelwal H, Schenning APHJ, Debije MG. Infrared regulating smart window based on organic materials. *Adv Energy Mater*, 2017, 7: 1602209
- 9 Li XT, Li MJ, Tian YL, *et al.* A reversible photochromic covalent organic framework. *Nat Commun*, 2024, 15: 8484
- 10 Cai Y, Gao Y, Luo Q, *et al.* Ferrocene-grafted photochromic triads based on a sterically hindered ethene bridge: redox-switchable fluorescence and gated photochromism. *Adv Opt Mater*, 2016, 4: 1410–1416
- 11 Guo Z, Su Y, Zong H, *et al.* A universal strategy for reversible photochromism of viologen derivatives in solutions. *Adv Opt Mater*, 2024, 12: 2401791
- 12 Bai Z, Guo L, Zhao D, *et al.* Photochromic spiropyran-based dual-emitting luminescent hybrid films for dynamic information anticounterfeiting. *ACS Appl Mater Interfaces*, 2024, 16: 44018–44025
- 13 Miao S, Liang K, Zhu J, *et al.* Hetero-atom-doped carbon dots: doping strategies, properties and applications. *Nano Today*, 2020, 33: 100879
- 14 Liu H, Zhong X, Pan Q, *et al.* A review of carbon dots in synthesis strategy. *Coord Chem Rev*, 2024, 498: 215468
- 15 Zhang C, Zheng K, Ye X, *et al.* Effects of nonmetallic heteroatoms doping on the catalytic performance of carbon materials. *Chem Eng Sci*, 2025, 304: 120980
- 16 K. Algethami F, Abdelhamid HN. Heteroatoms-doped carbon dots as dual probes for heavy metal detection. *Talanta*, 2024, 273: 125893
- 17 Zhang X, Hou L, Samori P. Coupling carbon nanomaterials with photochromic molecules for the generation of optically responsive materials. *Nat Commun*, 2016, 7: 11118
- 18 Fu Q, Sun S, Lu K, *et al.* Boron-doped carbon dots: doping strategies, performance effects, and applications. *Chin Chem Lett*, 2024, 35: 109136
- 19 Wu J, Fu S, Zhang X, *et al.* Bidirectional photochromism via anchoring of carbon dots to TiO<sub>2</sub> porous films. *ACS Appl Mater Interfaces*, 2020, 12: 6262–6267
- 20 Zhang K, Fu Q, Sun S, *et al.* Photoluminescent multicolor carbon dots for UV detection and dynamic anticounterfeiting. *ACS Appl Mater Interfaces*, 2024, 16: 52833–52841
- 21 Guo Z, Brian Y, Zhang L, *et al.* Multi-stimuli-responsive carbon dots with intrinsic photochromism and *in situ* radical afterglow. *Adv Mater*, 2024, 36: 2409361
- 22 Sun J, Liu Y, Han Y, *et al.* Enabling controllable time-dependent phosphorescence in carbonized polymer dots based on chromophore excited triplet energy level modulation by ionic bonding. *Angew Chem Int Ed*, 2025, 64: e202415042
- 23 Ran Z, Jia H, Zhong Z, *et al.* Time-dependent room-temperature afterglow of carbon dots constructed by trap-induced multiemission centers. *Nano Lett*, 2025, 25: 6993–7002
- 24 Liu Y, Li W, Wu P, *et al.* Hydrothermal synthesis of nitrogen and boron co-doped carbon quantum dots for application in acetone and dopamine sensors and multicolor cellular imaging. *Sens Actuat B-Chem*, 2019, 281: 34–43
- 25 Hao H, Wang M, Cao Y, *et al.* Boron-doped engineering for carbon quantum dots-based memristors with controllable memristance stability. *Small Methods*, 2024, 8: 2301454
- 26 Tomskaya AE, Prosvirin IP, Egorova MN, *et al.* Structural and optical



- properties of N-doped and B-doped carbon dots. *J Struct Chem*, 2020, 61: 818–825
- 27 Liu L, Lu Y, Wang S, *et al.* B, N stabilization effect on multicavity carbon microspheres for boosting durable and fast potassium-ion storage. *J Colloid Interface Sci*, 2022, 620: 24–34
  - 28 Jiang L, Ding H, Lu S, *et al.* Photoactivated fluorescence enhancement in F, N-doped carbon dots with piezochromic behavior. *Angew Chem Int Ed*, 2020, 59: 9986–9991
  - 29 Liao L, Qi J, Gao J, *et al.* Nitrogen-doped carbon quantum dots with photoactivation properties for ultraviolet ray detection. *ACS Appl Mater Interfaces*, 2024, 16: 42632–42640
  - 30 Kudr J, Richtera L, Xhaxhiu K, *et al.* Carbon dots based FRET for the detection of DNA damage. *Biosens Bioelectron*, 2017, 92: 133–139
  - 31 Wang Y, Zhou S, Pan S, *et al.* Color-tunable carbon dots with aggregation-induced emission constructed by FRET between surface luminescence centers. *Adv Opt Mater*, 2024, 12: 2301486
  - 32 Yan Y, Zhang NN, Tauche LM, *et al.* Direct synthesis of a stable radical doped electrically conductive coordination polymer. *Inorg Chem Front*, 2022, 9: 5016–5023
  - 33 Li X, Fu Y, Zhao S, *et al.* Metal ions-doped carbon dots: synthesis, properties, and applications. *Chem Eng J*, 2022, 430: 133101
  - 34 Yu R, Ou M, Hou Q, *et al.* Metal and non-metal doped carbon dots: properties and applications. *gxjzz*, 2024, 5: 1
  - 35 Xu Y, Wu M, Feng X, *et al.* Reduced carbon dots versus oxidized carbon dots: photo- and electrochemiluminescence investigations for selected applications. *Chem Eur J*, 2013, 19: 6282–6288
  - 36 Li GP, Zhu H, Hao P, *et al.* The modulation effect of carboxylic acid ligands on the electron transfer photochromism of NDI-derived coordination polymers. *Dalton Trans*, 2021, 50: 15153–15161
  - 37 Liu JJ, Wang ZJ, Xia SB, *et al.* Photochromic and photocontrolled luminescence properties of two metal-organic frameworks constructed from a naphthalene diimide derivative. *Dyes Pigments*, 2020, 172: 107856
  - 38 Harvey CP, Tovar JD. Main-chain photochromic conducting polymers. *Polym Chem*, 2011, 2: 2699
  - 39 Li L, Zeng JG, Zhang NN, *et al.* Naphthalene diimide-based crystalline hybrid photochromic materials: structural types, photochromic mechanism, and applications. *Inorg Chem Front*, 2025, 12: 11–38
  - 40 Xiao P, Dumur F, Graff B, *et al.* Design of high performance photo-initiators at 385–405 nm: search around the naphthalene scaffold. *Macromolecules*, 2014, 47: 973–978
  - 41 Sun J, Liu Y, Han Y, *et al.* Enabling controllable time-dependent phosphorescence in carbonized polymer dots based on chromophore excited triplet energy level modulation by ionic bonding. *Angew Chem Int Ed*, 2025, 64: e202415042
  - 42 Xiong T, Cen W, Zhang Y, *et al.* Bridging the g-C<sub>3</sub>N<sub>4</sub> interlayers for enhanced photocatalysis. *ACS Catal*, 2016, 6: 2462–2472
  - 43 Jiang J, Cao S, Hu C, *et al.* A comparison study of alkali metal-doped g-C<sub>3</sub>N<sub>4</sub> for visible-light photocatalytic hydrogen evolution. *Chin J Catal*, 2017, 38: 1981–1989
  - 44 You MH, Li MH, Li HH, *et al.* The impact of metal cations on the photochemical properties of hybrid heterostructures with infinite alkaline-earth metal oxide clusters. *Dalton Trans*, 2019, 48: 17381–17387

**Acknowledgement** This work was supported by the National Natural Science Foundation of China (12274144 and 52472160) and the Natural Science Foundation of Guangdong Province (2023A1515012003 and 2025A1515010658).

**Author contributions** Cao J was responsible for synthesis and characterization and drafted the initial manuscript. Huang E, Zhong Z, and Jiang T characterized the properties of CDs. Li W, Zhang H, and Zhang X provided academic advice. Lei B and Hu C revised the initial manuscript, provided academic advice, and obtained funding. All authors participated in the overall discussion.

**Conflict of interest** The authors declare that they have no conflict of interest.

**Supplementary information** Supplementary materials are available in the online version of the paper.



**Jueran Cao** is a master's student at the School of Materials and Energy, South China Agricultural University, where her research focuses on the photochromic properties of fluorescent carbon dots.



**Chaofan Hu** is currently an associate professor at the School of Materials and Energy, South China Agricultural University. His research group focuses on the photoluminescence properties of carbon nanomaterials, including fluorescent carbon dots, graphene quantum dots, and polymer dots. They also explore the applications of these materials in bioimaging.



**Bingfu Lei** is currently a professor at the School of Materials and Energy, South China Agricultural University. His research group focuses on designing and synthesizing inorganic non-metallic materials and organic/inorganic hybrid materials. They also analyze the optical and electrical properties of rare-earth functional materials and conduct applied basic research.

## 光电子转移诱导的碳点双模式光致变色发光

曹珏然, 黄恩临, 钟紫婷, 江霆杰, 张浩然, 李唯, 张学杰, 胡超凡\*, 雷炳富\*

**摘要** 在功能材料中整合光致变色和光致发光面临着实现宽光谱颜色调制和快速响应的严峻挑战。在此, 我们开发了掺杂钠和钠/硼共掺杂碳点(CDs), 它们通过一种新的自由基介导机制表现出双模光致变色发光行为。钠掺杂的CDs在 450到 630 nm的波长范围内实现了180 nm的红移发射, 而钠/硼共掺杂的CDs则实现了蓝移多色发射, 在30 s紫外辐照下从橙色逐渐过渡到黄色和绿色。值得注意的是, 光致变色态在没有外部刺激的情况下会自发恢复到初始状态。这些现象源于原始CDs与光产生的阴离子自由基之间的光诱导电子转移。利用这些独特的光致变色特性, 我们实现了可逆防伪系统和信息加密平台。此外, 光致变色CDs还具有日光响应紫外检测能力和植物细胞成像能力, 这大大拓展了光致变色CDs的应用前景。

# Enhancement of Fluorescence Emission for Tricolor Quantum Dots Assembled in Polysiloxane toward Solar Spectrum-Simulated White Light-Emitting Devices

Guangqi Hu, Yuqiong Sun, Jianle Zhuang, Xuejie Zhang, Haoran Zhang, Mingtao Zheng, Yong Xiao, Yeru Liang, Hanwu Dong, Hang Hu, Bingfu Lei,\* Chaofan Hu,\* and Yingliang Liu\*

Commercial white light-emitting diodes (LEDs) have the undesirable characteristics of blue-rich emission and low color rendering index (CRI), while the constituent quantum dots (QDs) suffer from aggregation-induced fluorescence quenching and poor stability. Herein, a strategy is developed to assemble tricolor QDs into a polysiloxane matrix using a polymer-mediated hybrid approach whereby the hybrid composite exhibits a significant enhancement of aggregation-dispersed emission, outstanding photostability, high thermal stability, and outstanding fluorescence recovery. Using the as-prepared hybrid fluorescent materials, the fabricated LEDs exhibit solar spectrum-simulated emission with adjustable Commission Internationale de L'Eclairage coordinates, correlated color temperature, and a recorded CRI of 97. Furthermore, they present no ultraviolet emission and weak blue emission, thus indicating an ideal healthy and high-CRI white LED lighting source.

simple fabrication process, commercial white light-emitting diodes (LEDs) are commonly based on UV or blue-emissive LED chips,<sup>[12,13]</sup> which limits the color rendering index (CRI), making it difficult to exceed 90. This seriously inhibits the application of UV/blue LEDs in color-critical environments especially for medical and painting lighting.<sup>[14]</sup> Hence, a high-performance white LED with high CRI, solar spectrum-simulated emission, without UV light and weak-blue-light emission is becoming our desirable and ideal lighting source.

To achieve this ideal WLED, promising luminescent materials can be classified into three categories: rare-earth-based inorganic phosphors, organic phosphors, and quantum dots (QDs).<sup>[15–18]</sup> QDs with

## 1. Introduction

Since the GaN-based blue-emissive light-emitting diode (LED) chip was successfully introduced in 1993, it has been extensively commercialized, improved and widely used in the field of lighting.<sup>[1,2]</sup> However, research into the health aspects of blue-emissive LED chips has revealed blue-light-induced damage, such as yellow spots on eye ground, inhibition of melatonin secretion, myopia, precocious puberty,<sup>[3–5]</sup> and the hazards of dark complexion, erythema, and even skin cancer caused by ultraviolet (UV) LED radiation.<sup>[6–8]</sup> Regrettably, the white LED (WLED) based on luminous materials and UV/blue emissive LED chips inevitably lead to hazards induced by UV or blue-light irradiation.<sup>[9–11]</sup> Additionally, due to the low cost and

tunable spectrum and wide-band emission have been considered as the most promising materials.<sup>[19,20]</sup> By coating with green- and red-emissive CdSe–ZnSe QDs, the fabricated WLED based on the blue InGaN chip presents a CRI of 91; however, its high cost and toxicity restrict its use in the field of lighting.<sup>[21–23]</sup> Recently, highly luminescent and hydrophobic Ag/CuInS<sub>2</sub>@ZnS QDs have been successfully utilized in the WLEDs that exhibit similar solar spectrum-simulated emission, but high production costs limit their widespread application.<sup>[24–27]</sup> Although the water-soluble CuInS<sub>2</sub>@ZnS QDs present significantly lower cost than hydrophobic QDs, their photoluminescence quantum yields (PLQYs) are markedly less than those of hydrophobic QDs.<sup>[28]</sup> Therefore, it is necessary to develop non-semiconductor QDs, such as carbon/grapheme QDs to achieve high-CRI and healthy WLED lighting.<sup>[29–33]</sup> Unfortunately, these QDs generally have low PLQYs, suffer from aggregation-quenching, and show poor photo or thermal stability. Therefore, it will be of great significance for these low-cost and environmentally friendly non-semiconductor QDs if they are assembled into a suitable matrix. For instance, the carbon QDs assembled into BaSO<sub>4</sub> and SiQ<sub>2</sub> matrices increased their luminous efficiency in 27% and 40%,<sup>[34,35]</sup> respectively, but both of them faced severe light decay under photoirradiation, especially UV irradiation. The graphene QDs encapsulated in melamine–formaldehyde or agar composites effectively overcome the disadvantage of aggregation quenching of QDs,<sup>[36,37]</sup>

Dr. G. Hu, Y. Sun, Dr. J. Zhuang, Dr. X. Zhang, Dr. H. Zhang, Dr. M. Zheng, Prof. Y. Xiao, Prof. Y. Liang, Dr. H. Dong, Dr. H. Hu, Prof. B. Lei, Dr. C. Hu, Prof. Y. Liu  
Guangdong Provincial Engineering Technology Research Center for Optical Agriculture  
College of Materials and Energy  
South China Agricultural University  
Guangzhou 510642, China  
E-mail: tliebf@scau.edu.cn; thucf@scau.edu.cn; tliuyl@scau.edu.cn



The ORCID identification number(s) for the author(s) of this article can be found under <https://doi.org/10.1002/smll.201905266>.

DOI: 10.1002/smll.201905266

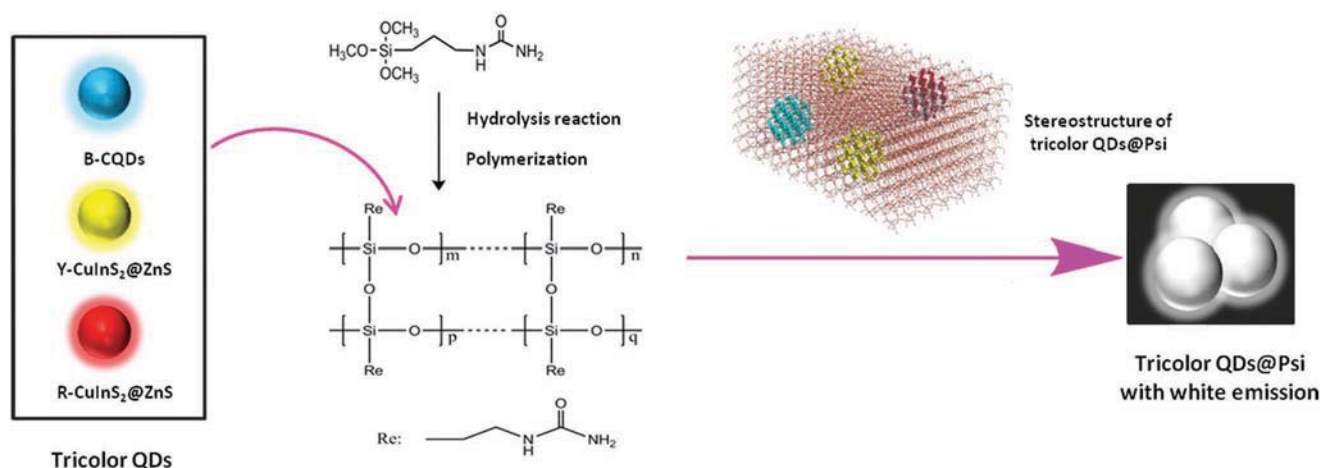


**Figure 1.** Preparation of QDs@Psi microspheres (B-CQDs, Y-CuInS<sub>2</sub>@ZnS, and R-CuInS<sub>2</sub>@ZnS) with spectrum-simulated white emission and high thermal stability.

however, poor thermal stability and low PLQYs are still present. Therefore, it is necessary to develop QD-based hybrid materials with enhanced fluorescence and adequate stability for the production of high-CRI and eye-protecting WLEDs.

## 2. Results and Discussion

In this work, in order to produce a healthy LED lighting source with high-CRI and high-efficiency based on water-soluble CQDs and CuInS<sub>2</sub>@ZnS QDs, we have for the first time developed a polymer-mediated tricolor quantum dots aggregation and encapsulation strategy using polysiloxane (Psi) microspheres as a polymer matrix. As shown in **Figure 1**, the synthesized tricolor QDs were added to an aqueous solution containing 1-[3-(trimethoxysilyl)propyl]urea, and through the reactions of hydrolysis and polymerization, they were assembled into the Psi. Psi consists of poly( $\text{Si-O-Si}$ ) with a stereo-structure, as shown in the inset of **Figure 1**. The obtained tricolor QDs@Psi exhibited white emission that is especially suitable for application in LED lighting.

In white-emissive tricolor QDs@Psi, as shown in **Figure S1** (Supporting Information), the blue-emissive CQDs (B-CQDs) were synthesized by a hydrothermal reaction using citric acid and glycine as raw materials according to our previous work.<sup>[34,38]</sup> The B-CQDs presented an average size of 2.8 nm with a lattice space of 0.21 nm (**Figure 2a**), which is wider than the one reported for silicon QDs.<sup>[39]</sup> They exhibited a blue light emission with centered wavelength at 445 nm, but also displayed significant fluorescence quenching when freeze-dried to a solid state, indicating their incompatibility for solid-state LED lighting. Moreover, to assemble CuInS<sub>2</sub>@ZnS QDs into the Psi matrix in an aqueous solution, we developed a two-step approach to synthesize water-soluble yellow and red emissive CuInS<sub>2</sub>@ZnS QDs (Y-CuInS<sub>2</sub>@ZnS and R-CuInS<sub>2</sub>@ZnS). First, the CuInS<sub>2</sub> core was synthesized through a hydrothermal reaction at 150 °C for 18 h. Then, by regulating the reaction temperature and time from (130 °C, 6 h) to (140 °C, 8 h), the Y-CuInS<sub>2</sub>@ZnS and R-CuInS<sub>2</sub>@ZnS were obtained with an average size of 3.8 and 4.3 nm, respectively (**Figure 2b,c**).

Based on the as-synthesized tricolor quantum dots, the prepared tricolor QDs@Psi were characterized by scanning electron microscopy and fluorescence microscopy. In **Figure 2d1**, we observe that the QDs exhibit the morphology of a smooth microsphere with an average size of 2.3  $\mu\text{m}$ . The corresponding size distribution is shown in **Figure 2d2**. However, since the tricolor QDs were assembled in the inner part of the microspheres, the tricolor QDs distribution in the Psi polymer matrix cannot be directly observed, even by using high-resolution transmission electron microscopy (HRTEM). Moreover, according to the luminescent intensity of the aqueous solution before and after assembly, more than 80% of the B-CQDs and nearly 100% of Y-CuInS<sub>2</sub>@ZnS and R-CuInS<sub>2</sub>@ZnS were encapsulated into the Psi matrix. This result is attributed to the electrostatic assembly between tricolor QDs with negative charges on the surfaces and 1-[3-(trimethoxysilyl)propyl]urea with positive charges (**Table S1**, Supporting Information). Thus, the resultant tricolor QDs@Psi were synthesized by a hybrid approach rather than simple physical assembly, indicating that QDs@Psi can be probably endowed with good stability. Additionally, fluorescence images of tricolor QDs@Psi obtained using different channels are highly consistent (**Figure 2e1**) and showed that the microspheres have strong emission in the blue, yellow, and red channels (**Figure 2e2–e4**). It proves that the tricolor QDs were successfully assembled into the Psi matrix and the single emission of the tricolor QDs@Psi is derived from the highly uniform distribution of each individual QDs. To further analyze the tricolor QDs assembled into the Psi matrix, we compared the changes of X-ray diffraction (XRD) and X-ray photoelectron spectroscopy (XPS) spectra between B-CQDs@Psi, (Y-CuInS<sub>2</sub>@ZnS)@Psi, (R-CuInS<sub>2</sub>@ZnS)@Psi, and pure Psi. As shown in **Figure S2a** (Supporting Information), the characteristic diffraction peaks of B-CQDs were not observed in the XRD pattern due to the similar element composition. On the other hand, in the XRD patterns of (Y-CuInS<sub>2</sub>@ZnS)@Psi and (R-CuInS<sub>2</sub>@ZnS)@Psi, characteristic diffraction peaks of Y-CuInS<sub>2</sub>@ZnS and R-CuInS<sub>2</sub>@ZnS were observed at 28.1°, 47.5°, and 55.7°, corresponding to the (112), (220), and (312) planes of the tetragonal structure (**Figure S2b,c**, Supporting Information).<sup>[40]</sup> Similarly, in the XPS spectra shown



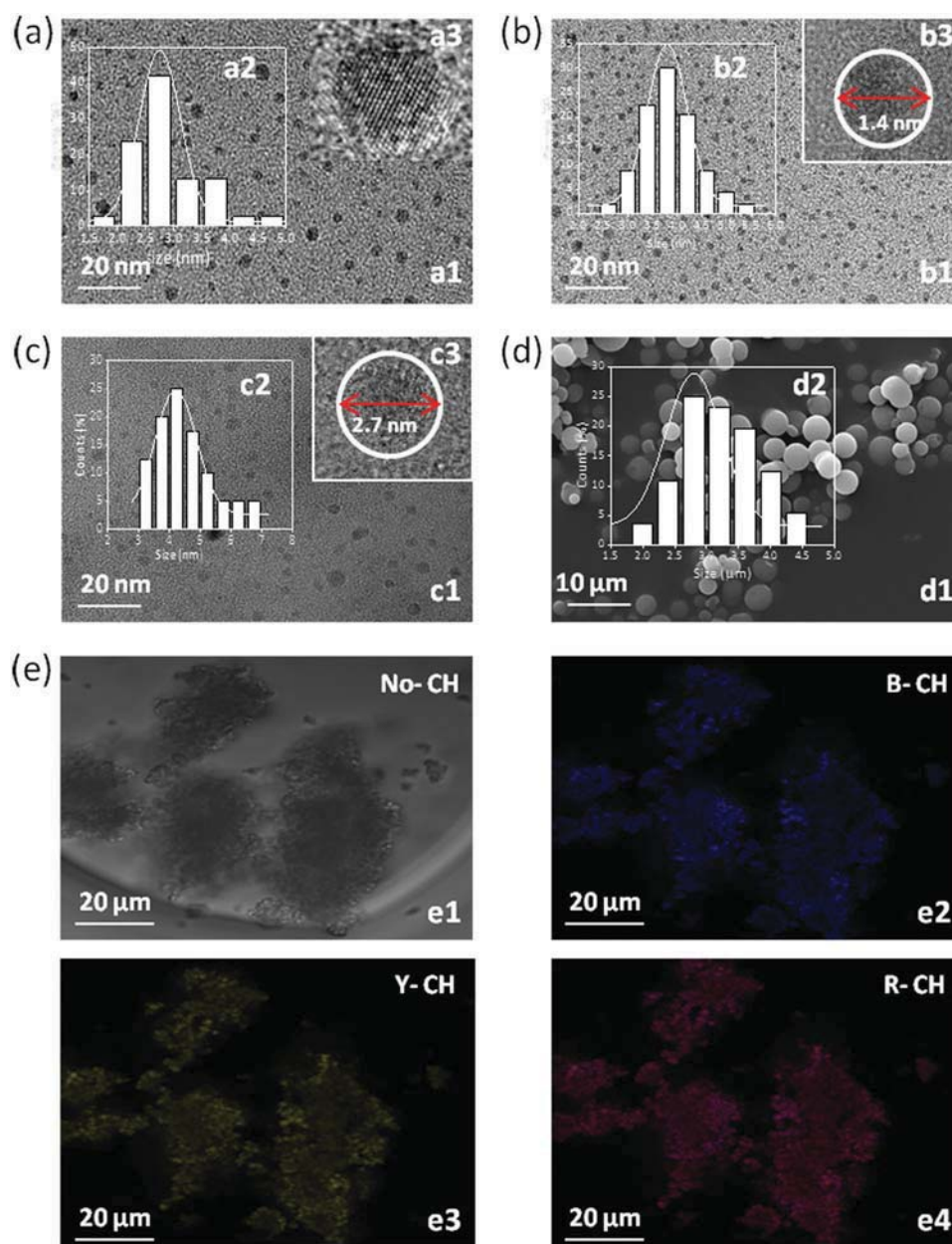


**Figure 2.** HRTEM images of B-CQDs a1,a2) and the related size distribution a3). HRTEM images of Y-CuInS<sub>2</sub>@ZnS b1,b2) and the related size distribution b3). HRTEM images of Y-CuInS<sub>2</sub>@ZnS c1,c2) and the related size distribution c3). SEM images of (B-CQDs, Y-CuInS<sub>2</sub>@ZnS, and R-CuInS<sub>2</sub>@ZnS)@Psi d1) and the related size distribution d2). e1–e4) Fluorescence microscopy images of tricolor QDs@Psi microspheres, with a UV excitation wavelength of 390 ± 10 nm and a blue (450 ± 30 nm), green (560 ± 20 nm), or red (610 ± 15 nm) emission filter.

in Figure S3a–c (Supporting Information), the weak peak positions of S 2p, In 3d, and Cu 2p, which are representative of CuInS<sub>2</sub>@ZnS, were observed.<sup>[38]</sup> These results give further confirmation that the tricolor QDs were indeed assembled into the PSi matrix and the fluorescence emission was generated by B-CQDs, Y-CuInS<sub>2</sub>@ZnS, and R-CuInS<sub>2</sub>@ZnS.

As shown in Figure 3a, under the excitation of 365 nm, B-CQDs@Psi, (Y-CuInS<sub>2</sub>@ZnS)@Psi, and (R-CuInS<sub>2</sub>@ZnS)@Psi powders present brighter blue, yellow, and red fluorescence emission, respectively, than the corresponding QDs aqueous solutions, which indicates the

enhancement of fluorescence after assembling of QDs into the Psi matrix. To further confirm the enhanced fluorescence, we tested the fluorescence spectra of B-CQDs@Psi, (Y-CuInS<sub>2</sub>@ZnS)@Psi, and (R-CuInS<sub>2</sub>@ZnS)@Psi powders and the QD solutions that correspond to the concentration with the strongest fluorescent intensity. In Figure 3b, it is possible to observe that the B-CQDs@Psi powder presents the same emission spectrum of the B-CQDs solution, with an emission peak at 441 nm and a full width at half-maximum (FWHM) of 76 nm. It significantly exhibits a remarkable enhancement of the fluorescence intensity (up to 74 times), which is

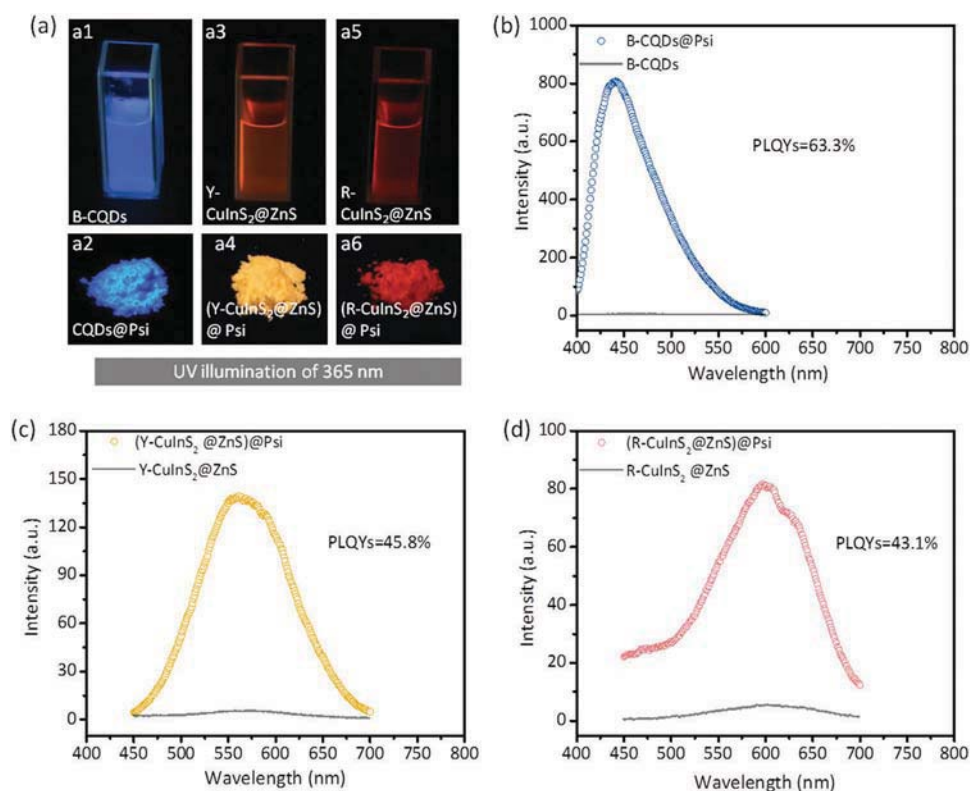


**Figure 3.** a) The photographs under UV illumination, and b–d) the fluorescence spectra of B-CQDs@Psi, (Y-CuInS<sub>2</sub>@ZnS)@Psi, and (R-CuInS<sub>2</sub>@ZnS)@Psi powders compared with the corresponding QD solutions, respectively.

the highest enhancement currently recorded. In addition, (Y-CuInS<sub>2</sub>@ZnS)@Psi and (R-CuInS<sub>2</sub>@ZnS)@Psi powders present optical properties with, emission peaks at 560 and 608 nm, FWHM of 110 and 125 nm, and fluorescence intensity enhancements of 26 and 15 times, respectively, compared with the corresponding QDs aqueous solutions. However, for the matrices of CaF<sub>2</sub>, PVA, and PMMA assembled into the three QDs, there was also an enhancement of fluorescence intensity, but with a maximum increase of two times or less. Besides, as shown in Table S2 (Supporting Information), B-CQDs@Psi, (Y-CuInS<sub>2</sub>@ZnS)@Psi, and (R-CuInS<sub>2</sub>@ZnS)@Psi show photoluminescence quantum yields (PLQYs) of 63.3%, 45.8%, and 43.1%, respectively, which are higher than those of the corresponding QD solutions (9.4%, 8.3%, and 7.1%), and are the highest values among all reported PLQY of QD-based solid luminophores.<sup>[41–43]</sup>

The enhanced PLQYs of QDs@Psi compared with QDs aqueous solution can be attributed to three reasons. First, Förster resonance energy transfer (FRET), generally reduces PLQYs through nonradiative energy transfer between nearby QDs. However, QDs@Psi achieve a uniform dispersion of QDs in a Psi cage that limits close proximity and hence reduces FRET among QDs to improve the PLQYs.<sup>[44]</sup> This can be further demonstrated by comparing PL decay curves.<sup>[34,45]</sup> According to Figure S4 (Supporting Information), the luminescence lifetimes of the hybrid B-CQDs@Psi, (Y-CuInS<sub>2</sub>@ZnS)@Psi, and (R-CuInS<sub>2</sub>@ZnS)@Psi composites are significantly longer than those of the corresponding QDs aqueous solution. The results indicate that the three kinds of QDs can

be separately well embedded and protected by the Psi matrix during the hybrid assembly process, which can effectively avoid energy loss induced by water molecules in order to increase PLQYs. Comparing with CDs@BaSO<sub>4</sub> (PLQYs of 27%) and CDs@PVA (PLQYs of 16%), the higher PLQYs of CQDs@Psi of 63.3% can be assigned to a lower energy loss of Psi than that of BaSO<sub>4</sub>. Furthermore, according to results of the fluorescence intensity analysis of the aqueous solution before and after assembly, we found that more than 80% of the B-CQDs and nearly 100% of Y-CuInS<sub>2</sub>@ZnS and R-CuInS<sub>2</sub>@ZnS were encapsulated into the Psi matrix. This result is attributed to the hybrid approach that leads to new chemical bonds between the tricolor QDs and Psi. For the B-CQDs@Psi composites, new chemical groups of –NH–OOCH– and –NH–O– on B-CQD surface and –NH–S–(CH<sub>2</sub>)<sub>2</sub>–COO– group on R/Y-CuInS<sub>2</sub>@ZnS surface are formed, which further passivate the three QDs compared with the corresponding QD solutions. Therefore, the PLQYs of QDs are enhanced due to the lead role of surface-state (molecule) in the luminescence of QDs.<sup>[46,47]</sup> Besides, as shown in Figure S5 (Supporting Information), as the concentration of B-CQDs in Psi increases, the fluorescence intensity gradually increases. However, when the doping concentration is excessive, there is a decrease in the fluorescence intensity which is associated with fractional fluorescence quenching when QDs are reunited.

To confirm whether QDs@Psi are applicable to LED technology, we have researched their photo and thermal stability. As shown in Figure 4a–c, the fluorescence intensity of all the three QD aqueous solutions show a significant decrease due to the

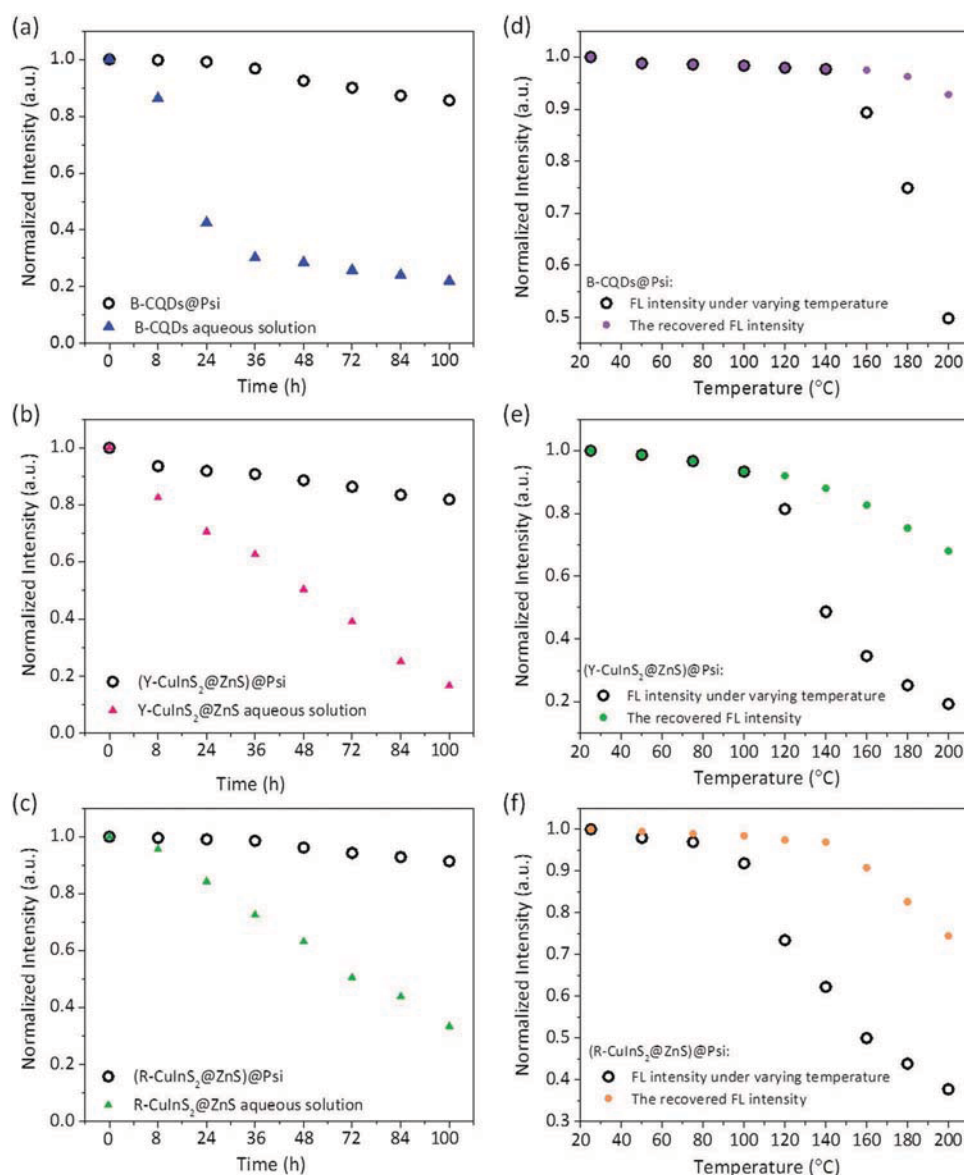


**Figure 4.** a–c) The normalized fluorescence intensity of B-CQDs@Psi, (Y-CuInS<sub>2</sub>@ZnS)@Psi and (R-CuInS<sub>2</sub>@ZnS)@Psi, and their corresponding QD solutions under UV-lamp ( $\lambda_{\text{max}}$ : 365 nm; power: 800 W) radiation, respectively. d–f) The variable temperature and the recovered normalized fluorescence intensity of B-CQDs@Psi, (Y-CuInS<sub>2</sub>@ZnS)@Psi and (R-CuInS<sub>2</sub>@ZnS)@Psi, and their corresponding QD solutions, respectively.

destruction of ligands on QDs surface induced by UV irradiation causing fluorescence quenching after about 100 h. However, although under the extreme UV irradiation, B-CQDs@Psi, (Y-CuInS<sub>2</sub>@ZnS)@Psi, and (R-CuInS<sub>2</sub>@ZnS)@Psi powders exhibited remarkable photostability. When the continuous irradiation time reaches 100 h, their fluorescent intensities still maintain over 85% of the initial values. Moreover, tricolor QDs@Psi have an outstanding heat-resisting property since they present bright fluorescence emission up to a treatment temperature of approximately 125 °C (Figure S6, Supporting Information). As shown in Figure 4d, the fluorescence intensity of B-CQDs@Psi powder keeps unchanged below 160 °C. Even with the increasing temperature, its luminous intensity decreases, but it can recover more than 90% of the initial fluorescence

intensity when the temperature drops to room temperature. Additionally, as shown in Figure 4e,f, (Y-CuInS<sub>2</sub>@ZnS)@Psi and (R-CuInS<sub>2</sub>@ZnS)@Psi also present the performance of thermal stability and fluorescence recovery. These effects are related to the  $-(\text{Si}-\text{O}-\text{Si})-$  structure of PSi matrix since it has a thermal conductivity lower than  $0.25 \text{ W m}^{-1} \text{ K}^{-1}$  and the bond energy of Si–O ( $460 \text{ kJ mol}^{-1}$ ) is higher than UV energy. Thus, the fluorescent B-CQDs, Y-CuInS<sub>2</sub>@ZnS, and R-CuInS<sub>2</sub>@ZnS are protected from UV light and thermal irradiation. An intuitive schematic diagram that describes the heat-resisting property of tricolor QDs@Psi was proposed and shown in Figure S7 (Supporting Information). All three QDs@Psi composites comply with the thermal stability requirement of normal working LED devices.



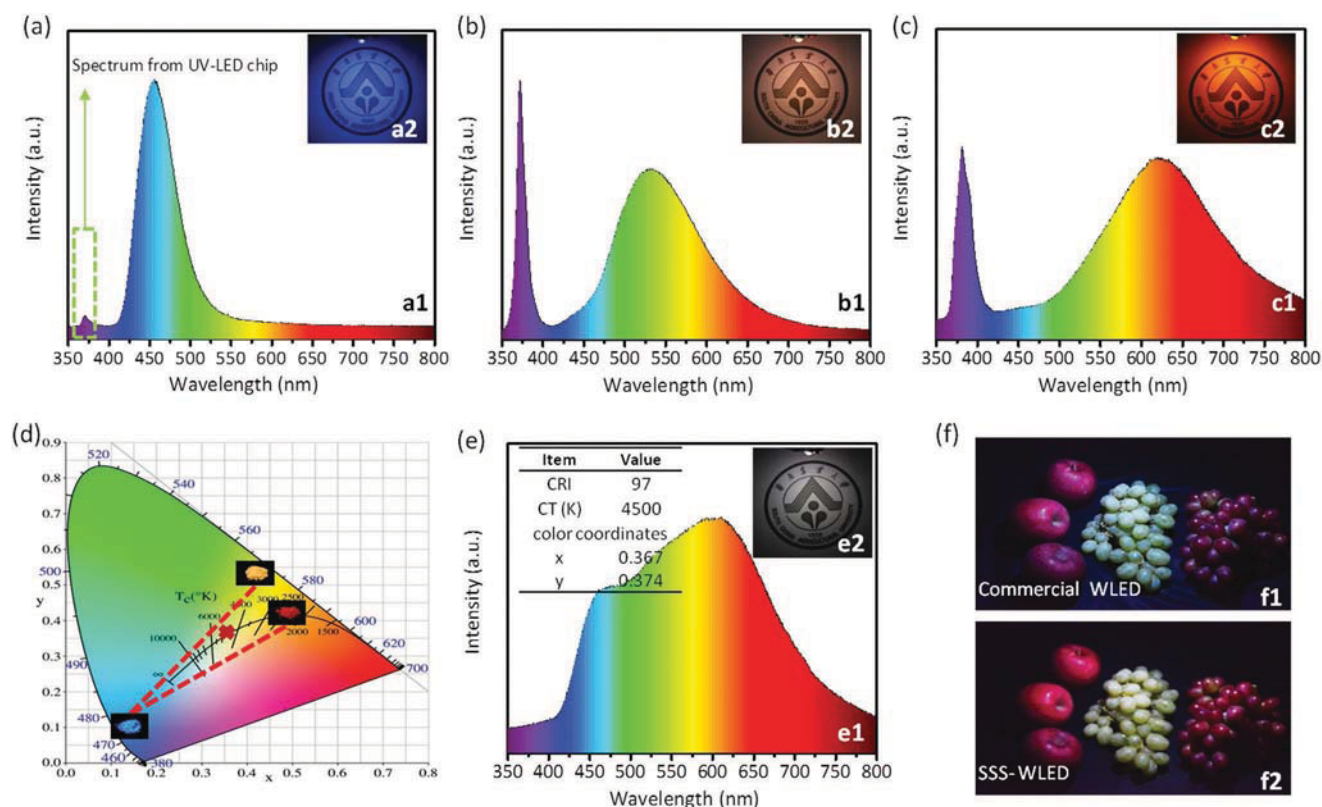


**Figure 5.** a–c) The photoluminescence spectrum of single emissive LED coating B-CQDs@Psi, (Y-CuInS<sub>2</sub>@ZnS)@Psi, (R-CuInS<sub>2</sub>@ZnS)@Psi powders, respectively, and their photographs inset of figures. d) CIE 1931 chromaticity coordinates diagram of B-CQDs@Psi, (Y-CuInS<sub>2</sub>@ZnS)@Psi, and (R-CuInS<sub>2</sub>@ZnS)@Psi powders. e) The photoluminescence spectrum of white LED coating tricolor QDs@Psi. f1) Fruit color under the commercial WLED and f2) the tricolor QDs@Psi-based WLED.

Based on broadband emission spectra covering the whole visible region, outstanding luminous property, and thermal stability, tricolor QDs@Psi have the potential to achieve solar spectrum-simulated emission. We fabricated LED lighting sources according to the traditional LED manufacturing process based on the chips with the peak emission wavelengths centered at 395 nm.

As shown in Figure 5a, the photoluminescence spectrum of blue-emissive LED (B-LED) presents the approximate emission with the coated B-CQD powder, which corresponds to the Commission Internationale de L'Eclairage (CIE) coordinates of (0.16, 0.12) and the illuminating photograph of the B-LED as shown in the inset of Figure 5a. However, the UV light marked in green color in Figure 5a emitted by the UV-emitting LED chip is completely absorbed, as shown in Figure S8 (Supporting Information). According to our previous work, we propose that this effect is assigned to  $n \rightarrow \pi^*$  and  $\pi \rightarrow \pi^*$  electronic transition induced by the conjugated structures inside of B-CQDs.<sup>[39]</sup> Infrared images demonstrated that the luminous energy was released as thermal radiation except for fluorescent emission, which laid the foundation for a healthy LED light source without UV emission. As shown in Figure 5b,c, the photoluminescence spectra and illuminating photographs are representative of the fabricated yellow and red emissive LED lighting sources with coated (Y-CuInS<sub>2</sub>@ZnS)@Psi and (R-CuInS<sub>2</sub>@ZnS)@Psi powders,

which correspond to the CIE color coordinates of (0.43, 0.52) and (0.46, 0.44), respectively.

From the CIE 1931 chromaticity diagram that marked the CIE coordinates of the three single-emissive QDs@Psi (Figure 3d), it is clearly observed that the correlated color temperature (CCT) is adjustable from 2700 to 10 000 K. Therefore, by using the three QDs@Psi, warm, positive, and cool, white LEDs can be achieved complying with the requirements of various environments. In Figure 5e, the fabricated LED using tricolor QDs@Psi powder presents the solar spectrum-simulated emission with CCT of 4500 K that is close to the so-called “warm” white light source.<sup>[48]</sup> The CIE color coordinates of (0.37, 0.37) were marked in red multiplication sign color in Figure 5d. Its luminous efficiency reaches up to 127.5 lm W<sup>-1</sup> which is much higher than pure UV LED and LEDs coated the three QD hybrid materials separately (Table S3, Supporting Information). Significantly, it is first reported that the solar spectrum-simulated LED (SSS-LED) lighting source presents no UV and weak blue-light emission that are assigned to the  $n \rightarrow \pi^*$  and  $\pi \rightarrow \pi^*$  electronic transitions induced by conjugated structures in B-CQD and the spectral overlap between the absorption cross-section of CuInS<sub>2</sub>@ZnS and the PL emission spectrum of B-CQDs, respectively, which effectively avoids the UV damage and blue-emission hazards of blue-emitting LED chip-based commercial white LEDs (Figure S9, left, Supporting Information). In addition, the SSS-LED features a recorded color

rendering index (CRI) of 97, much higher than that of the previously reported QD-based WLED and the highest record for a GaN chip-based WLED.<sup>[49–51]</sup> Furthermore, two photographs of fruits taken under two kinds of LED lighting sources are shown in Figure 5f, apparently, the SSS-LED is more capable of showing the true color of the fruits than the commercial white LED (CRI =  $\approx 82$ ) (Figure S9, right, Supporting Information).<sup>[39]</sup> In brief, all of which above indicate that it is a high-quality illuminating source for the SSS-LED that is expected to be widely used in the fields of healthy lighting based on its non-UV and weak blue-light emission, and medical and painting lighting based on its high CRI.

### 3. Conclusion

In summary, we have developed a polymer-mediated QD assembly strategy that produces tricolor QDs@Psi powders with a microsphere morphology and white emission, prepared by hybrid approach. The as-prepared B-CQDs@Psi, (Y-CuInS<sub>2</sub>@ZnS)@Psi, and (R-CuInS<sub>2</sub>@ZnS)@Psi, when compared to the corresponding tricolor QDs, exhibit remarkable enhancement of aggregation-dispersed emission up to 74, 26, 15 times, respectively, which is far superior to the previously reported QDs or QD-based composites. The tricolor QDs@Psi present outstanding photostability that are significantly superior to corresponding QD aqueous solutions and exhibit high thermal stability with outstanding fluorescent emission recovery, which decides the application potential in white LEDs. The fabricated LED exhibits solar spectrum-simulated emission with luminous efficiency up to 127.5 lm W<sup>-1</sup> and CIE coordinates of (0.37, 0.37) and CCT of 4500 K that are adjustable. Significantly, compared to commercial white LEDs, it shows that the UV light is wholly absorbed by conjugated structures in B-CQDs and weak blue-light emission owing to the spectral absorption of CuInS<sub>2</sub>@ZnS, which provides a healthy LED lighting source. Moreover, the fabricated LED based on QDs featured a recorded CRI of 97, which is expected to be used in specialist fields that require a high CRI.

### 4. Experimental Section

**Materials:** 1-[3-(Trimethoxysilyl)propyl]urea, citric acid, glycine, copper acetate, indium acetate, sodium sulfide, and 3-mercaptopropionic acid (NPA) were purchased from Aladdin Chemistry Co., Ltd. Silicone (OE6630, Dow Corning) was purchased from Shenzhen MAIJLE Science and Technology Co., Ltd. All materials were used without further purification. UV light chips (395 nm, IVL-4545-U16-L54-BW9) were purchased from Invenluxe Optoelectronics (China) Co., Ltd.

**Synthesis of Tricolor QDs:** Synthesis of blue-emissive CQDs: the CQDs were synthesized according to the previous work of the authors of this paper.<sup>[31]</sup> Synthesis of yellow-emissive CuInS<sub>2</sub>@ZnS QDs: indium acetate (0.06 g), copper acetate (0.05 g), 3-mercaptopropionic acid (0.30 g), and sodium hydroxide (0.05 g) were dissolved in deionized water (15 mL), stirred for 30 min and sodium sulfide (0.11 g) was added, and then the mixed solution was transferred into a polytetrafluoroethylene hydrothermal reactor (40 mL) and heated at 150 °C for 18 h, the reaction solution were cooled to room temperature naturally and centrifuged to obtain CuInS<sub>2</sub> quantum dot solution, after zinc acetate (0.05 g), 3-mercaptopropionic acid (0.30 g), and sodium

sulfide (0.02 g) were added in the obtained CuInS<sub>2</sub> quantum dot solution, the mixed solution was transferred into a polytetrafluoroethylene hydrothermal reactor (40 mL) and heated at 130 °C for 6 h, cooled to room temperature naturally, and then yellow-emissive CuInS<sub>2</sub>@ZnS QDs were obtained. Synthesis of red-emissive CuInS<sub>2</sub>@ZnS QDs: the synthesis procedure is the same as the yellow-emissive CuInS<sub>2</sub>@ZnS QDs above except for (130 °C, 6 h) updated to (140 °C, 8 h).

**Preparation of Tricolor QDs@Psi:** The as-synthesized B-CQDs (0.012 g), Y-CuInS<sub>2</sub>@ZnS (0.058 g), and R-CuInS<sub>2</sub>@ZnS (0.072 g) were successively added in an aqueous solution (30 mL) containing 1-[3-(trimethoxysilyl)propyl]urea (1.5 mL), after stirred for 30 min, the mixed solution was placed in water bath at 50 °C for 24 h, and then the tricolor QDs@Psi would be received when the obtained white precipitation was filtered, washed, and vacuum dried. Similarly, B-CQDs@Psi, (Y-CuInS<sub>2</sub>@ZnS)@Psi, and (R-CuInS<sub>2</sub>@ZnS)@Psi were obtained according to the above preparation procedure.

**Fabrication of LEDs:** UV-emitting chips with the peak emission wavelength centered at 395 nm were used to fabricate white LED. The mixture with a certain ratio of tricolor QDs@Psi and silicone was mixed uniformly and then coated on the chips to achieve the white-emitting LEDs. Similarly, the single emitting LEDs were obtained according to the above preparation procedure when B-CQDs@Psi, (Y-CuInS<sub>2</sub>@ZnS)@Psi, and (R-CuInS<sub>2</sub>@ZnS)@Psi replaced tricolor QDs@Psi, respectively.

**Characterization:** Fluorescence spectra curves were recorded with a fluorescence spectrofluorometer (F-7000, Hitachi). The infrared images were recorded by infrared imager (R500EXPro, AVIO, Japan). XRD pattern was collected using a persee XD-2X/M4600. HRTEM images were taken in a JEOL-2010 electron microscope. SEM images were carried out using an XL-30-ESEM (FEI). X-ray photoelectron spectroscopy (XPS) spectra were detected by employing an X-ray photoelectron spectroscope (AXIS ULTRA DLD, Kratos). The fluorescence decay curves were measured on an FLS980 fluorescence spectrophotometer. Photoluminescence quantum yield measurements were performed with a calibrated integrating sphere on an Edinburgh FL5980 spectrometer. The fluorescence microscopy images were taken in a confocal laser scanning microscope (LSM 7 DUO, Zeiss). The photoelectric properties of the fabricated LEDs were measured by an integrating sphere spectroradiometer system (ZPH1272, Zhongpu).

### Supporting Information

Supporting Information is available from the Wiley Online Library or from the author.

### Acknowledgements

This work was supported by the National Natural Science Foundations of China (Grant Nos. 21571067 and 21671070) and the Project supported by GDUPS (2018) for Prof. Bingfu LEI.

### Conflict of Interest

The authors declare no conflict of interest.

### Keywords

enhancement of fluorescence emission, healthy white light emitting, high color rendering index, hybrid microspheres, tricolor quantum dots

Received: September 16, 2019

Revised: November 8, 2019

Published online:

- [1] T. Hashimoto, F. Wu, J. S. Speck, S. Nakamura, *Nat. Mater.* **2007**, 6, 568.
- [2] S. Pimputkar, J. S. Speck, S. P. DenBaars, S. Nakamura, *Nat. Photonics* **2009**, 3, 180.
- [3] K. E. West, M. R. Jablonski, B. Warfield, K. S. Cecil, M. James, M. A. Ayers, J. Maida, C. Bowen, D. H. Sliney, M. D. Rollag, *J. Appl. Physiol.* **2011**, 110, 619.
- [4] J. H. Jou, H. H. Yu, F. C. Tung, C. H. Chiang, Z. K. He, M. K. Wei, *J. Mater. Chem. C* **2017**, 5, 176.
- [5] M. Hatori, C. Gronfier, G. R. N. Van, P. S. Bernstein, J. Carreras, S. Panda, F. Marks, D. Sliney, C. E. Hunt, T. Hirota, T. Furukawa, K. Tsubota, *npj Aging Mech. Dis.* **2019**, 3, 9.
- [6] A. Bércesa, A. Fekete, S. Gáspár, P. Gróf, P. Rettberg, G. H. GyRontó, *J. Photochem. Photobiol., B* **1999**, 53, 3.
- [7] H. Hacham, S. E. Freeman, R. W. Gange, D. J. Maytum, J. C. Sutherland, B. Sutherland, *Photochem. Photobiol.* **1991**, 53, 559.
- [8] P. Gróf, S. Gáspár, G. Y. Rontó, *Photochem. Photobiol.* **1996**, 64, 800.
- [9] Y. F. Wang, K. Wang, Z. X. Han, Z. M. Yin, C. J. Zhou, F. L. Du, S. Y. Zhou, P. Chen, Z. Xie, *J. Mater. Chem. C* **2017**, 5, 9629.
- [10] J. K. Sheu, S. J. Chang, C. H. Kuo, Y. K. Su, L. W. Wu, Y. C. Lin, W. C. Lai, J. M. Tsai, G. C. Chi, R. K. Wu, *IEEE Photonics Technol. Lett.* **2003**, 15, 18.
- [11] C. Sun, Y. Zhang, C. Ruan, C. Y. Yin, X. Y. Wang, Y. D. Wang, W. W. Yu, *Adv. Mater.* **2016**, 28, 10088.
- [12] B. S. Sun, L. Zhang, T. Y. Zhou, C. Shao, L. Zhang, Y. L. Ma, Q. Yao, Z. G. Jiang, F. A. Selim, H. Chen, *J. Mater. Chem. C* **2019**, 7, 4057.
- [13] H. R. Abd, Z. Hassan, N. M. Ahmed, F. H. Alsultany, A. F. Omar, *Opt. Eng.* **2019**, 58, 027110.
- [14] P. Pust, V. Weiler, C. Hecht, A. Tucks, A. S. Wochnik, A. K. Henss, D. Wiechert, C. Scheu, P. J. Schmidt, W. Schnick, *Nat. Mater.* **2014**, 13, 891.
- [15] H. M. Zhu, C. C. Lin, W. Q. Luo, S. T. Shu, Z. G. Liu, Y. S. Liu, J. T. Kong, E. Ma, Y. G. Gao, R. S. Liu, X. Y. Chen, *Nat. Commun.* **2014**, 5, 4312.
- [16] J. H. Oh, S. J. Yang, Y. R. Do, *Light: Sci. Appl.* **2014**, 3, e141.
- [17] M. Nyman, L. E. Shea-Rohwer, J. E. Martin, P. Provencio, *Chem. Mater.* **2009**, 21, 1536.
- [18] Y. Shirasaki, G. J. Supran, M. G. Bawendi, V. Bulovic, *Nat. Photonics* **2013**, 7, 13.
- [19] X. B. Wang, X. S. Yan, W. W. Li, K. Sun, *Adv. Mater.* **2012**, 24, 2742.
- [20] Y. J. Chang, X. D. Yao, L. F. Mi, G. P. Li, S. D. Wang, H. Wang, Z. P. Zhang, Y. A. Jiang, *Green Chem.* **2015**, 17, 4439.
- [21] K. W. Song, R. Costi, V. Bulovic, *Adv. Mater.* **2013**, 25, 1420.
- [22] W. L. Zhang, M. F. Prodanov, J. Schneider, S. K. Gupta, T. Dudka, V. V. Vashchenko, A. L. Rogach, A. K. Srivastava, *Adv. Funct. Mater.* **2019**, 29, 1805094.
- [23] H. S. Chen, C. K. Hsu, H. Y. Hong, *IEEE Photonics Technol. Lett.* **2006**, 1, 193.
- [24] W. S. Song, H. Yang, *Chem. Mater.* **2012**, 24, 19617.
- [25] W. S. Song, J. H. Kim, J. H. Lee, H. S. Lee, Y. R. Do, H. Yang, *J. Mater. Chem.* **2012**, 22, 21901.
- [26] S. H. Park, A. Hong, J. H. Kim, H. Yang, K. Lee, H. S. Jang, *ACS Appl. Mater. Interfaces* **2015**, 7, 6764.
- [27] A. Aboulaich, M. Michalska, R. Schneider, A. Potdevin, J. Deschamps, R. Deloncle, G. Chadeyron, R. Mahiou, *ACS Appl. Mater. Interfaces* **2014**, 6, 252.
- [28] X. J. Kang, Y. C. Yang, L. Wang, S. Wei, D. C. Pan, *ACS Appl. Mater. Interfaces* **2015**, 7, 27713.
- [29] F. L. Yuan, Z. B. Wang, X. H. Li, Y. C. Li, Z. A. Tan, L. Z. Fan, S. H. Yang, *Adv. Mater.* **2017**, 29, 1604436.
- [30] J. Y. Zhu, X. Bai, Y. Zhai, X. Chen, Y. S. Zhu, G. C. Pan, H. Z. Zhang, B. A. Dong, H. W. Song, *J. Mater. Chem. C* **2017**, 5, 11416.
- [31] F. Zhang, X. T. Feng, Y. Zhang, L. P. Yan, Y. Z. Yang, X. G. Liu, *Nanoscale* **2016**, 8, 8618.
- [32] Z. T. Kang, B. Arnold, C. J. Summers, B. K. Wagner, *Nanotechnology* **2006**, 17, 4477.
- [33] T. Ghosh, E. Prasad, *J. Phys. Chem. C* **2015**, 119, 2733.
- [34] D. Zhou, Y. C. Zhai, S. N. Qu, D. Li, P. T. Jing, W. Y. Ji, D. Z. Shen, A. L. Rogach, *Small* **2017**, 13, 1602055.
- [35] D. Zhou, L. Di, P. T. Jing, Y. C. Zhai, D. H. Shen, S. N. Qu, A. L. Rogach, *Chem. Mater.* **2017**, 29, 1779.
- [36] Y. S. Wu, H. Zhang, A. Z. Pan, Q. Wang, Y. F. Zhang, G. J. Zhou, L. He, *Adv. Sci.* **2019**, 6, 1801432.
- [37] C. M. Luk, L. B. Tang, W. F. Zhang, S. F. Yu, K. S. Teng, S. P. Lau, *J. Mater. Chem.* **2012**, 22, 22378.
- [38] G. Q. Hu, B. F. Lei, X. F. Jiao, S. S. Wu, X. J. Zhang, J. L. Zhuang, X. T. Liu, C. F. Hu, Y. L. Liu, *Opt. Express* **2019**, 27, 7629.
- [39] G. Q. Hu, Y. Q. Sun, Y. X. Xie, S. S. Wu, X. J. Zhang, J. L. Zhuang, C. F. Hu, B. F. Lei, Y. L. Liu, *ACS Appl. Mater. Interfaces* **2019**, 11, 6634.
- [40] P. H. Chuang, C. C. Lin, R. S. Liu, *ACS Appl. Mater. Interfaces* **2014**, 6, 15379.
- [41] Y. Wang, S. Kalytchuk, L. Y. Wang, O. Zhovtiuk, K. Cepe, R. Zboril, A. L. Rogach, *Chem. Commun.* **2015**, 51, 2950.
- [42] F. Wang, Z. Xie, H. Zhang, C. Y. Liu, Y. G. Zhang, *Adv. Funct. Mater.* **2011**, 21, 1027.
- [43] Z. Xie, F. Wang, C. Y. Liu, *Adv. Mater.* **2012**, 24, 1716.
- [44] S. J. Zhu, Q. N. Meng, L. Wang, J. H. Zhang, Y. B. Song, H. Jin, K. Zhang, H. C. Sun, H. Y. Wang, B. Yang, *Angew. Chem., Int. Ed.* **2013**, 52, 3953.
- [45] M. Y. Sun, S. N. Qu, Z. D. Hao, W. Y. Ji, P. T. Jing, H. Zhang, L. G. Zhang, J. L. Zhao, D. Z. Shen, *Nanoscale* **2014**, 6, 13076.
- [46] D. E. Nam, W. S. Song, H. Yang, *J. Mater. Chem.* **2011**, 21, 18220.
- [47] G. Y. Kim, S. Kim, J. Y. Choi, M. Kim, H. Lim, T. W. Nam, W. Choi, E. N. Cho, H. J. Han, C. H. Lee, J. C. Kim, H. Y. Jeong, S. Y. Choi, M. S. Jang, D. Y. Jeon, Y. S. Jung, *Nano Lett.* **2019**, 19, 6827.
- [48] X. Bai, G. Caputo, Z. D. Hao, V. T. Freitas, J. H. Zhang, R. L. Longo, O. L. Malta, R. A. S. Ferreira, N. Pinna, *Nat. Commun.* **2014**, 5, 5702.
- [49] Z. F. Wang, F. L. Yuan, X. H. Li, Y. C. Li, H. Z. Zhong, L. Z. Fan, S. H. Yang, *Adv. Mater.* **2017**, 29, 1702910.
- [50] Z. Tian, X. T. Zhang, D. Li, D. Zhou, P. T. Jing, D. Z. Shen, S. N. Qu, R. Zboril, A. L. Rogach, *Adv. Opt. Mater.* **2017**, 5, 1700416.
- [51] M. H. Fang, C. C. Ni, X. J. Zhang, Y. T. Tsai, S. Mahlik, A. Lazarowska, M. Grinberg, H. S. Sheu, J. F. Lee, B. M. Cheng, R. S. Liu, *ACS Appl. Mater. Interfaces* **2019**, 8, 30677.





# Anchoring Carbon Nanodots onto Nanosilica for Phosphorescence Enhancement and Delayed Fluorescence Nascence in Solid and Liquid States

Jiangling He, Yonghao Chen,\* Youling He, Xiaokai Xu, Bingfu Lei, Haoran Zhang, Jianle Zhuang, Chaofan Hu,\* and Yingliang Liu\*

Carbon nanodots (CDs) anchored onto inorganic supporter (amorphous nanosilica, SiO<sub>2</sub>) like a core-satellite structure have enhanced the room-temperature phosphorescence (RTP) intensity along with ultralong lifetime of 1.76 s. Special and quite stable structure should account for these superiorities, including hydrogen network, covalent bond, and trap-stabilized triplet-state excitons that are responsible for the generation of phosphorescence. These multiple effects have efficaciously protected CDs from being restrained by the external environment, providing such long-lived emission (LLE) that can subsist not only in powdery CDs–SiO<sub>2</sub> but also coexist in aqueous solution, pushing a big step forward in the application prospects of liquid-state phosphorescence. Through construction of CDs–SiO<sub>2</sub> compound, electron trap is reasoned between CDs and SiO<sub>2</sub> by analyzing thermoluminescent glow curve. Electron trap can capture, store, and gradually release the electrons just like an electron transporter to improve the intersystem crossing (ISC) and reserved ISC, having provided the more stabilized triplet excitons, stronger and longer phosphorescence, and also triggered the formation of thermally activated delayed fluorescence (TADF), offering a new mechanism for exploiting LLE among CD-based field. Moreover, it is more beneficial to the formation of TADF as temperature increases, thus the afterglow color can change with the temperature.

## 1. Introduction

Carbon nanodots (CDs), 0D luminescent nanomaterials, have caught increasing attention recently owing to their fascinating

photophysical properties that are potentially useful for different applications.<sup>[1–5]</sup> One of the many fascinating properties of CDs is its fluorescence. Many reports have shown that the fluorescence of CDs originates from the surface fluorophore and graphitizing core.<sup>[6–9]</sup> However, the transition between singlet and triplet states occurs with extremely low probability due to the spin-forbidden, hence the room temperature phosphorescence (RTP, T<sub>1</sub>→S<sub>0</sub>) and thermally activated delayed fluorescence (TADF, transitions T<sub>1</sub>→S<sub>1</sub>→S<sub>0</sub>) are difficult to be achieved under ambient conditions.<sup>[10–12]</sup> Other than that, afterglow from pure CDs is seldom observed and studied.<sup>[13–17]</sup> A self-quenching resistance CDs with RTP lifetime of 13.4 ms were induced by polyvinyl alcohol (PVA) chains from Liu's group.<sup>[13]</sup> Through seeded growth method, Andrey et al. prepared several phosphorescent CDs powders with average decay lifetime ranging from 52 to 419 ms.<sup>[14]</sup> Yang's group focused on suppressing the non-

radiative transitions having achieved the adjustable decays between 188 and 658 ms.<sup>[15]</sup> Feng and co-workers found that fluorine and nitrogen codoped CDs with RTP could realize the decay lifetime of 141 to 1210 ms by adjusting pH values.<sup>[16]</sup> It is noteworthy that long-lived emission (LLE) about 1.46 s of CDs powder was successfully achieved via microwave irradiation but with very poor ability to resist moisture that RTP totally disappeared in solution and also quite faint emission intensity only with quantum yield (QY) of 3.53% by Lin et al.<sup>[17]</sup> As for these pure CDs, phosphorescence that is responsible for the total afterglow without TADF component only lasts for a few seconds accompanied by a relatively low phosphorescent efficiency. Furthermore, these pure CDs have extremely poor stability, thus afterglow of them was completely quenched by oxygen or moisture, causing the RTP to be only captured in powdery CDs rather than solution.<sup>[13–17]</sup>

Nevertheless, a great deal of effort was devoted to improving the afterglow behavior. In some cases, the RTP can be ameliorated by introducing heavy atoms, such as halogens and metals which enhanced the intersystem crossing (ISC) process attributed to the strong spin–orbit coupling.<sup>[18,19]</sup> Alternatively, embedding CDs in solid matrices that serve

J. He,<sup>[†]</sup> Dr. Y. Chen,<sup>[††]</sup> Y. He, X. Xu, Prof. B. Lei, Prof. H. Zhang, Prof. J. Zhuang, Prof. C. Hu, Prof. Y. Liu  
Key Laboratory for Biobased Materials and Energy of Ministry of Education  
Guangdong Provincial Engineering Technology Research Center for Optical Agriculture  
College of Materials and Energy  
South China Agricultural University  
Guangzhou 510642, P. R. China  
E-mail: YCHEN053@e.ntu.edu.sg; thucf@scau.edu.cn; tliuyl@scau.edu.cn

The ORCID identification number(s) for the author(s) of this article can be found under <https://doi.org/10.1002/sml.202005228>.

<sup>[†]</sup>Present address: Department of Chemistry, National University of Singapore, 3 Science Drive 3, Singapore 117543, Singapore

<sup>[††]</sup>Present address: School of Chemical and Biomedical Engineering, Nanyang Technological University, 70 Nanyang Drive, Singapore 637457, Singapore

DOI: 10.1002/sml.202005228

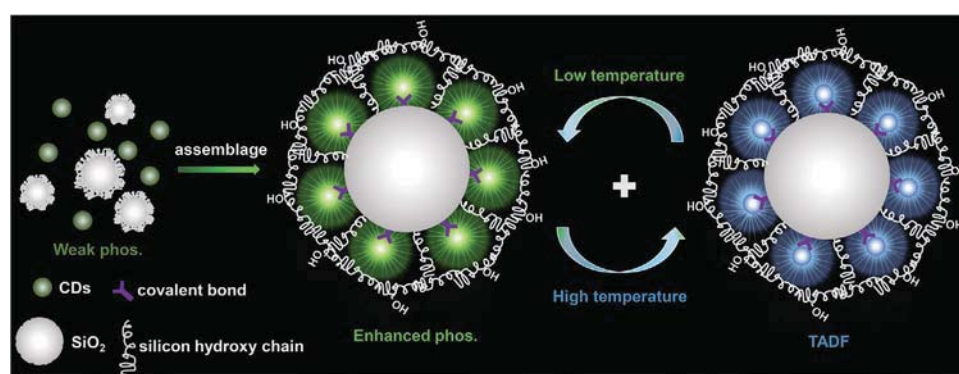
as rigidity-holder and oxygen-barrier can also enhance the afterglow behavior.<sup>[20–24]</sup> The latter method is more attractive because it can avoid cytotoxicity, high cost, and complex synthetic procedures without the introduction of any heavy atoms. To date, RTP was suggested as the single result of rigidization by vibration suppression, surface adsorption, defect stabilizing, hydrogen bonding, or covalent fixation between CDs and matrices such as PVA, cyanuric acid (CA), potash alum, silica gel, urea, biuret/urea, polyurethane (PU) and crystalline Mn-containing framework.<sup>[19,21,25–32]</sup> After the rigidization design by these matrices, solid-state phosphorescence of all these CDs was triggered and enhanced, but almost all of these CDs-based compounds failed to emit afterglow (phosphorescence or TADF) in aqueous solution because phosphorescence/TADF can be quite easily obliterated by dampness or dissolved oxygen molecules except the triumphant attempts by Zhou and co-workers<sup>[25]</sup> and Lin and co-workers<sup>[26]</sup>. The CDs-CA suspension succeeded to display phosphorescence with a lifetime of 687 ms via hydrogen-bonded networks.<sup>[25]</sup> Another CDs-based aqueous solution exhibiting afterglow (predominant component was TADF) was realized by covalent fixation action along with the lifetime of 703 ms.<sup>[26]</sup> Both of these two CDs-based aqueous dispersions could suffer from severe quenching in bulk water because it is difficult for a single protective effect of hydrogen bond or covalent fixation to maintain their stability in aqueous solution, and they also have relatively short lifetimes and low efficiencies, thus some potential applications will be prevented.

Inspired by mechanism of interaction between these dopants and matrices, inorganic nanosilica can be a great candidate to enhance the afterglow behavior of CDs. Surprisingly, inorganic nanosilica has the typical superiorities of low/non-toxicity and sufficient trap centers (defects) on its surface that can facilitate the storage of electrons and control the action of electrons.<sup>[33,34]</sup> Inorganic nanosilica nanoparticle is beneficial for motivating, enhancing, and prolonging the afterglow, because it can also prevent the oxygen diffusion and block the complex mobility, offering higher efficiency and enhanced stability.<sup>[35,36]</sup> Exploring the corresponding mechanism of nanosilica-induced afterglow enhancement with new concept is a quite valuable topic to meet with the growing requirements of emerging applications.

In this work, we realized RTP and TADF from CDs-decorated amorphous silica (CDs-SiO<sub>2</sub>) both in powdery and aqueous states through a one-pot sol-gel method without adding any heavy atom perturbors and removing dissolved oxygen. As-prepared CDs-SiO<sub>2</sub> exhibits strong afterglow and ultralong lifetime owing to general functions including hydrogen networks and covalent bonds besides trap-stabilized triplet-state excitons. On the basis of the first observation of thermoluminescent glow curve, it was reasoned that the electron trap localized like a transfer station that can capture, store and transport electrons between S<sub>1</sub> to T<sub>1</sub>, having greatly enhanced the rate of ISC and RISC (reversed ISC) and stabilized the triplet excited states so that the generation of LLE (**Scheme 1** and Figure 4). Owing to the ultralong lifetime, high efficiency, and opposite response to the temperature changes of TADF and phosphorescence, a simple and portable temperature sensor for naked eyes recognition is established. Furthermore, aqueous CDs-SiO<sub>2</sub> has also exhibited excellent prospects, especially in bioimaging.

## 2. Results and Discussions

The characterization of as-prepared CDs powder<sup>[37]</sup> is presented in Figure S1–S3 in the Supporting Information, and the detailed discussion for CDs is also presented in the Supporting Information. To confirm our concept of trap-mediated LLE, the structure of this CDs-SiO<sub>2</sub> nanoemitter has firstly been investigated. The aqueous CDs-SiO<sub>2</sub> is revealed as the mono-dispersed nanoparticles with size about 10–20 nm (**Figure 1b**), which is found as a core-satellites structure with CDs (1–2 nm) surrounding the quasi-spherical amorphous SiO<sub>2</sub> (**Figure 1c–e**). This small size enables the materials in biomedical applications. Another favorable condition for practical applications is that CDs-SiO<sub>2</sub> dispersion keeps stable in water for months without aggregation or gelation. But once the composite is dried to xerogel or powder (**Figure 1f,g**), it is difficult to be redispersed in water attributed to the crosslink of particles by dehydration causing abundant Si–O–Si groups at 1200–1000 cm<sup>–1</sup> region<sup>[38]</sup> (**Figure 3c**). Seen from **Figure S4** in the Supporting Information, phosphorescence intensity of CDs-SiO<sub>2</sub> is only with a reduction of about 10%, so the bulky CDs-SiO<sub>2</sub> could be used as the conventional inorganic phosphors. In other words,



**Scheme 1.** The schematic illustration of CDs anchored onto SiO<sub>2</sub> for phosphorescence enhancement and TADF nascence, and the conversion between them with the change of temperature.

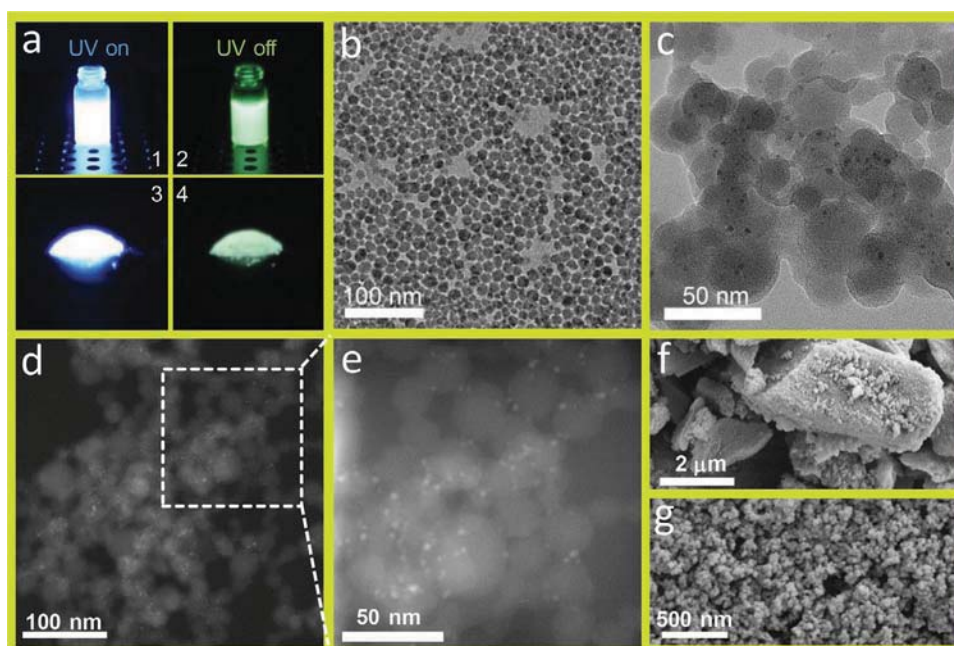


**Figure 1.** a) Digital photos of CDs-SiO<sub>2</sub> aqueous solution (1, 2) and powder (3, 4) with and without UV-light irradiation. b, c) TEM, and d, e) STEM of CDs-SiO<sub>2</sub>. f, g) SEM images of CDs-SiO<sub>2</sub> powder.

the storage form (removal of water or not) should be carefully considered prior to the use of this material for a specific aspect.

The blue fluorescent CDs-SiO<sub>2</sub> presents intense green afterglow after stopping the excitation. This phenomenon occurs not only in solid state but also in aqueous solution (Figure 1a; Video S1, Supporting Information), which makes it promising in biomedical as well as displaying applications. Both of the fluorescence stability and phosphorescence stability of the CDs-SiO<sub>2</sub> aqueous solution were measured shown in Figure S5 in the Supporting Information, in which the fluorescence and phosphorescence spectra can be well coupled together after irradiation for ten cycles. Furthermore, when CDs-SiO<sub>2</sub> solution were continuously being exposed under UV-inspired light for 9 h, the fluorescence intensity (monitored at 418 nm) and phosphorescence intensity (monitored at 516 nm) can still keep great strength without obvious photobleaching or quenching, illustrating that both of them can still keep excellent stability even up to 9 h illumination. The emissive moiety, CDs, however, do not individually exhibit any afterglow in a solvent when light source is cut off. Though faint afterglow can be observed in aggregated CDs,<sup>[13]</sup> the intensity, lifetime and stability cannot compare with that of CDs-SiO<sub>2</sub> at all. Hence it is easy to deduce that the introduction of silica makes such great difference in generating strong afterglow.

Undoubtedly, the structure of CDs-SiO<sub>2</sub> and the relationship between the two components must play a key role in this unique optical process. In order to clarify the intrinsic relevancy, the two other carbon dots such as EDA<sub>200</sub>, PVA<sub>200</sub> are substituted for CDs as shown in Figure S6a in the Supporting Information, CDs-SiO<sub>2</sub> stands out among all of them by comparing their phosphorescence spectra. If CDs are simply mixed with SiO<sub>2</sub> together, CDs/SiO<sub>2</sub> just exhibit quite faint phosphorescence,

almost unrecognizable to the naked eyes. Taking CDs-SiO<sub>2</sub>, EDA<sub>220</sub>-SiO<sub>2</sub>, PVA<sub>220</sub>-SiO<sub>2</sub> into consideration, the generation of phosphorescence is an integral connection with the amino group (-NH<sub>2</sub>). Meanwhile, the intensity of compounds is positively correlated to that of the original carbon sources (CDs, QY = 35%; EDA<sub>220</sub>, QY = 8%; PVA<sub>220</sub>, QY = 1%).<sup>[37]</sup> Preliminary conclusion can be made that the carbon sources rich in amino functional groups (-NH<sub>2</sub>) are propitious to the realization of intense afterglow, and the supporter of inorganic SiO<sub>2</sub> nanoparticles plays a vital role to enhance the afterglow through the chemical bond formation between -NH<sub>2</sub> and silica rather than by crude mixing both of them together. The importance of -NH<sub>2</sub> to ameliorate the afterglow strength was further confirmed by Figure S6b in the Supporting Information, in which the resulting afterglow is only related to the acidity/alkalinity of the solutions during the heating reaction, regardless of the hydrolysis form of TEOS molecules. It is obvious that the alkaline environment is conducive to the enhancement of afterglow, because more -NH<sub>2</sub> groups are in such situation, then have higher affinity with silica. These presented reactions may be an inspiration to design the similar materials with afterglow property.

The corresponding fluorescence and phosphorescence spectra excited by various light irradiations were summarized in Figure S7 in the Supporting Information, among which the optimum excitation wavelength of 340 nm is selected as the monitoring wavelength for afterglow spectra acquisition in this work. The afterglow of CDs-SiO<sub>2</sub> is composed of two components of LLE under ambient condition, i.e., phosphorescence and delayed fluorescence. A shoulder peak of the room temperature LLE at about 418 nm (Figure 2a), however, which cannot be observed at 80 K (Figure 2b), matches the fluorescence spectrum with a maximum of 414 nm,<sup>[37]</sup> implying the



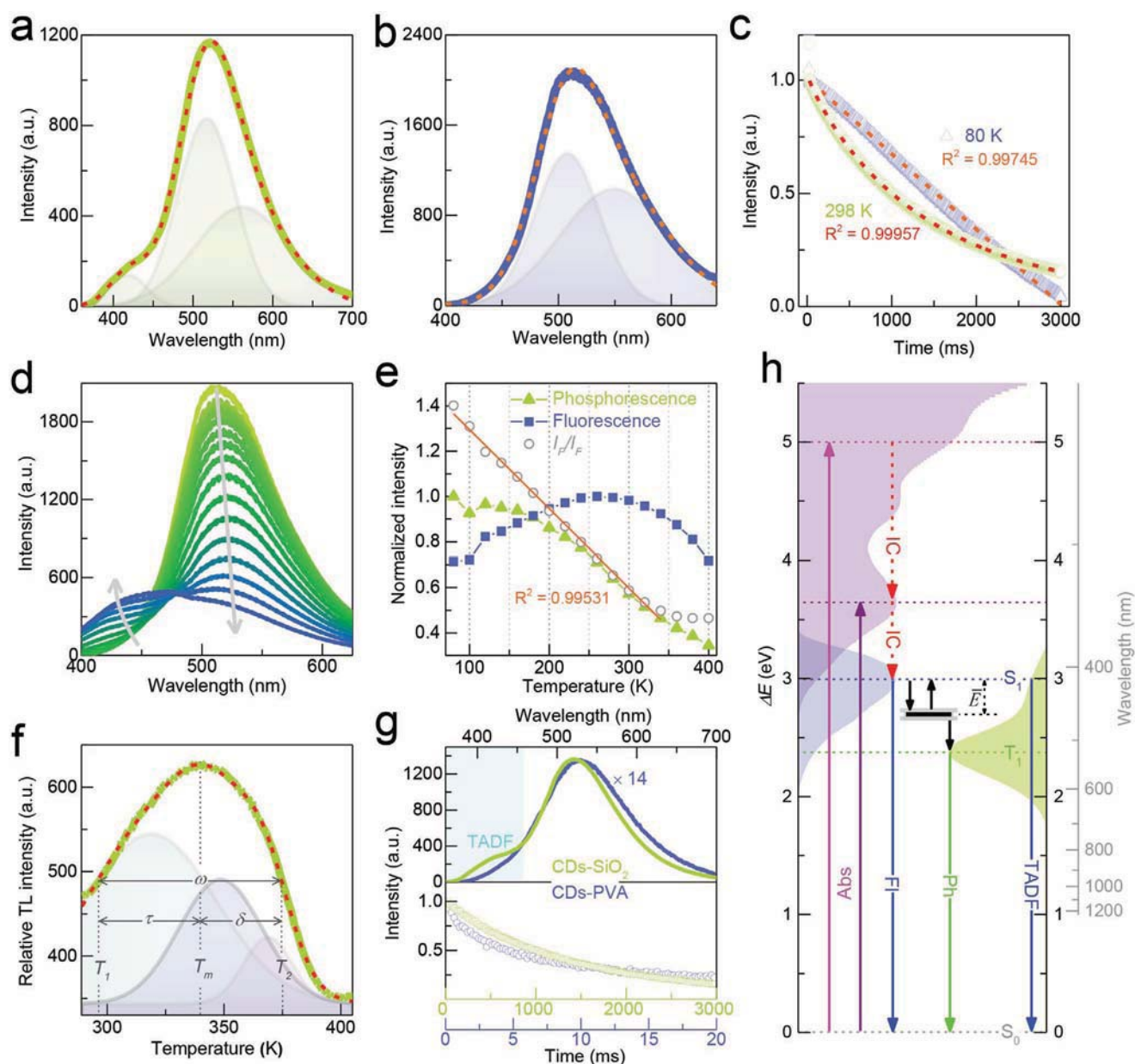


**Figure 2.** Phosphorescence spectra of CDs-SiO<sub>2</sub> powder at a) 298 K (room temperature) and b) 80 K, and c) the relevant LLE decay curves (solid lines: recorded data; colored areas: peak fitting; dashed lines: accumulated fitting). d) Temperature-dependent LLE spectra and e) the corresponding normalized integral intensity comparing with temperature dependence ( $I_P/I_F$ : ratio of phosphorescence to fluorescence intensity; solid line: fitting). f) Thermoluminescence spectra of CDs-SiO<sub>2</sub> powder (green solid line: recorded data; colored areas: peak fitting; red dashed line: accumulated fitting). g) Comparison of emission spectra (top) and LLE decay curves (bottom) between CDs-SiO<sub>2</sub> powder and CDs-PVA film. h) A scheme representing the absorption and photoluminescence.

probable occurrence of TADF. It is monitored that temperature-dependent transient PL decay curves of CDs-SiO<sub>2</sub> composite to prove the TADF at 418 nm. The PL of CDs-SiO<sub>2</sub> at 418 nm decays in a two scales comprised of a quite fast component, and a slow one as shown in Figure S8 in the Supporting Information. For this quite fast component, it belongs to prompt fluorescence, which is almost overlapped at various temperatures without showing temperature-dependence characteristic. Contrarily, an obvious temperature dependence is demonstrated

for this slow component comprised of a short lifetime (milli-second level) and a long lifetime (second level), corresponding to the TADF emission and phosphorescence emission, respectively. Because the average lifetime decreases when temperature increases, and the higher percentages of TADF emission was found with increasing temperature from 83.98 to 480.12 K as shown in inset of Figure S8 in the Supporting Information, and this is in good accordance with the facts that the molecular vibrations,  $k_{RISC}$ , and nonradiative loss would greatly increase

under higher temperatures, also the high temperature can promote RISC process.<sup>[26,39]</sup> The slow component with the short lifetime should be attributed to the TADF component occurring via the RISC process, which is similar to the temperature dependence for other typical TADF emitters.<sup>[26,40,41]</sup> Therefore, there is indeed a TADF component in emission of 418 nm. The attenuation behaviors of the LLE at 298 and 80 K are quite different that the former is in accordance with triexponential decay whereas the latter follows unusual linear decay (Figure 2c). The corresponding lifetimes are evaluated about 1.76 and 1.92 s, respectively, which are several orders of magnitude longer than those of most organic fluorophores so far. In view of the corresponding exponential decay type, the room temperature LLE consists of three emissive species with luminescence at 418, 517, and 562 nm respectively, which is further proved by the result of peak fitting. The emissions at 517 and 562 nm compose the phosphorescence involving triplet–singlet transition from two different triplet states (to simplify, herein they are just combined and regarded as  $T_1$ ).<sup>[13]</sup> In addition, the two fitting peaks (508 and 550 nm) indicate that low temperature LLE comprises two components, which are considered as the same origin as those two (517 and 562 nm) of room temperature LLE. The disappearance of delayed fluorescence may be the reason why the low temperature LLE decays linearly instead of exponentially. In other words, the temperature has evident effect on the LLE so that it may be an important key to explore the mechanism of LLE.

To investigate how temperature affects the LLE behavior, we measured the LLE spectra of CDs–SiO<sub>2</sub> powder at temperature from 80 to 400 K with an increment of 20 K (Figure 2d). As the temperature rose, the delayed fluorescence enhanced whereas the phosphorescence weakened substantially. It is known that the temperature-dependence of common luminescence (i.e., fluorescence and phosphorescence) is ascribed to the thermally activated nonradiative decay that competes with the radiative processes.<sup>[42]</sup> So the higher temperature, the fast nonradiative decay the excited states suffer and then the lower intensity the phosphorescence reaches. However, heating provides energy for re-exciting a proportion of electrons to the singlet state from triplet or trap states. Those electrons finally experience the same radiative process as the fluorescence but with a longer lifetime. Thus the delayed fluorescence is thermally activated and direct proportional to temperature. The integral intensity of the LLE, on the whole, decreases as the temperature increases (Figure 2e). This trend does not agree well with linearity, which makes it inappropriate to be using in temperature sensing, and the same to the fluorescence which ascends and then descends with the rise of temperature. But intriguingly, the ratio of the intensity of LLE and fluorescence ( $I_p/I_f$ ) declines linearly ( $R^2 = 0.995$ ) when temperature widely ranged from 80 to 340 K. Therefore, contrasting the LLE with fluorescence of CDs–SiO<sub>2</sub> may be a potential method for evaluating the surrounding temperature.

Thermoluminescence, the thermally stimulated luminescence, is one of the useful tools to be used in studying the trap-mediated LLE of inorganic phosphors. The glow curve that expresses the temperature dependence of the emission intensity is an excellent means to acquire the trap depth (i. e., the activation energy of traps).<sup>[43]</sup> However, glow curve is never employed to investigate the phosphorescence and TADF of CDs because of their different mechanism from that of afterglow of inorganic phosphors which is involved in trapping and releasing of excited electrons. And actually there is not evident signal of this measurement could be detected in organic-fluorophores-contained materials with phosphorescence and TADF simultaneously, e.g., CDs/PVA film and aerogel which were prepared in our previous work (Figure S9a, Supporting Information).<sup>[13,32]</sup> Herein, inspired by the trap-mediated long-lived emissive inorganic phosphors, we hypothesize that the LLE of CDs–SiO<sub>2</sub> benefits from the electron traps localized between SiO<sub>2</sub> and CDs, on the basis of the readout peak at 340 K of glow curve (Figure 2f). The average trap depth ( $\bar{E}$ ) of CDs–SiO<sub>2</sub> is calculated to be 0.297 eV with average lifetime of 143 s reaching agreement with the result of afterglow attenuation curve ( $\approx 134$  s, Figure S10c, Supporting Information) by the parameters indicated in the measured glow curve and the relevant equations (Table 1; Table S1, Supporting Information).<sup>[44–46]</sup> This trap depth is much smaller than the evaluated energy gap (0.568 eV, gained at 77 K for avoiding thermal relaxation in Figure S11 in the Supporting Information) between  $S_1$  and  $T_1$ . There may be two main species within the material according to the fitting glow curve, i.e., shallow trap (0.294 eV) and the deep trap (0.710 eV) indicated by fitting peak 1 and 2 (P1, P2). Comparing the above activation energy, it is suggested that the dominated segment is shallow trap, which is generally required for the persistent luminescence.<sup>[43]</sup> Benefiting from such appropriate activation energy of the shallow trap, CDs–SiO<sub>2</sub> can persistently radiate light after cut-off of excitation at room temperature, with lifetime nearly two orders of magnitude longer than that of phosphorescent CDs/PVA film (20.3 ms) which does not have TADF (Figure 2g). To depict how the trap gives rise to LLE, we established a spectra-Jablonski diagram according to the above results (Figure 2h). In this scenario, after excitation by absorbing light, the excited electrons immediately relax to  $S_1$  via internal conversion (IC) and some are then captured by traps due to the small energy gap (0.297 eV) between  $S_1$  and trap state. The untrapped electrons may return to  $S_0$  by irradiating fluorescence, whereas the trapped electrons may be re-excited to  $S_1$  and then back to  $S_0$  as TADF, or cross to  $T_1$  benefiting from the small energy gap (0.271 eV) and then return to  $S_0$  by irradiating phosphorescence. Therefore, the electron trap state between CDs and SiO<sub>2</sub> plays a very vital role in the emission processes of both hugely enhanced phosphorescence and new-born TADF.

The proposed emission mechanism was further confirmed by the temperature-dependent measurements on CDs–SiO<sub>2</sub>

**Table 1.** Parameters and calculation about thermoluminescence of CDs–SiO<sub>2</sub> powder.

$T_1$ [K]	$T_m$ [K]	$T_2$ [K]	$T$ [K]	$\delta$ [K]	$\omega$ [K]	$\mu'_g$	$E_t$ [eV]	$E_\delta$ [eV]	$E_\omega$ [eV]	$\bar{E}$ [eV]	$S$ [s <sup>-1</sup> ]	$\tau_t$ [s]
297	340	375	43.4	34.6	78.0	0.444	0.265	0.332	0.295	0.297 ± 0.034	734	143

(control) and CDs-SiO<sub>2</sub>\* samples, where SiO<sub>2</sub>\* means the SiO<sub>2</sub> powder was preannealed at selected temperature before recombination with CDs. These measurements can prove the effect of electron trap state on both phosphorescence enhancement and delayed fluorescence formation in more detail. As shown in Figure 3a, there is no significant changes in the luminosities of CDs-SiO<sub>2</sub>\* including fluorescence intensity and phosphorescence intensity when SiO<sub>2</sub>\* powder was beforehand calcined below 900 °C. In contrast, once the calcination temperature exceeded 950 °C, the luminosities drop suddenly and approach to zero upon up to 1000 °C. It is because the surface of the amorphous silica gradually melts and begins to crystallize. For the X-ray diffraction (XRD) patterns of these CDs-SiO<sub>2</sub>\* samples as given in Figure 3b, a diffusion peak at around 22° was noticed. Meanwhile, the diffused peak gently weakened at 22°, disclosing an incipient crystallization process evolved from amorphous form.<sup>[47,48]</sup> The process of gradual crystallization can be also approved by Fourier transform infrared (FTIR) spectra and X-ray photoelectron spectroscopy (XPS) curves. FTIR spectra of thermally treated CDs-SiO<sub>2</sub>\* were shown in Figure 3c, demonstrating the stretching vibration of O-H groups.<sup>[49]</sup> As the thermal treatment proceeding, it indicated the more severe hydroxyl condensation inside silica along with the gradual decrease of total intensity of oxyhydrogen vibration band with respect to the promotion of crystal framework transition.<sup>[49,50]</sup> By more insights into XPS (Figure 3d; Figure S9b, Supporting Information) survey for surface functional groups, there are abundant silicon, oxygen, carbon elements on

CDs-SiO<sub>2</sub>\* compounds. The Si<sub>2p</sub> curve comprises two peaks that are designated as Si-O (SiO<sub>2</sub>, 103.4 eV) and Si-O (SiO<sub>2</sub> gel, 103.8 eV). The C<sub>1s</sub> spectrum approves the existence of dominant C-C/C=C (184.9 eV) group. The O<sub>1s</sub> curve involves two peaks including Si-O (533.2 eV) and C-O (532.9 eV). In a whole, silanol peaks are intense at relatively low temperature environments, whereas failed to be recognized after much more enough thermal treatment. Besides the C<sub>1s</sub> spectrum experienced a rebound, bouncing to a quite strong carbonation peak and spacing became compact between Si-O groups. All of these further proving a compression that the loose amorphous structure is experiencing a transition into a crystalline one. The significance of physical properties of both CDs and inorganic SiO<sub>2</sub> for the LLE can be also confirmed by EPR probes as given in Figure 3e; Figure S12 in the Supporting Information. A sharp EPR signal from CDs (Figure S12, Supporting Information) was detected and its g-value was 2.0001, implicating the rich existence of single electron.<sup>[51,52]</sup> EPR probes were also touched on SiO<sub>2</sub> and CDs-SiO<sub>2</sub> in Figure 3e, which presents a quite broad valley signal in SiO<sub>2</sub> implying extensive paramagnetic defects on silica particles and external environments including temperatures and light sources take no effect on these trap centers (defects). It can be concluded that inorganic SiO<sub>2</sub> can play the role of paramagnetic defects well. Due to the advantageous defects from SiO<sub>2</sub>, EPR signals can be also detected after CDs attached onto amorphous SiO<sub>2</sub>. In detail, at 80 K, prominent EPR signals were caught under UV-light irradiation not because these are in full agreement with the signal

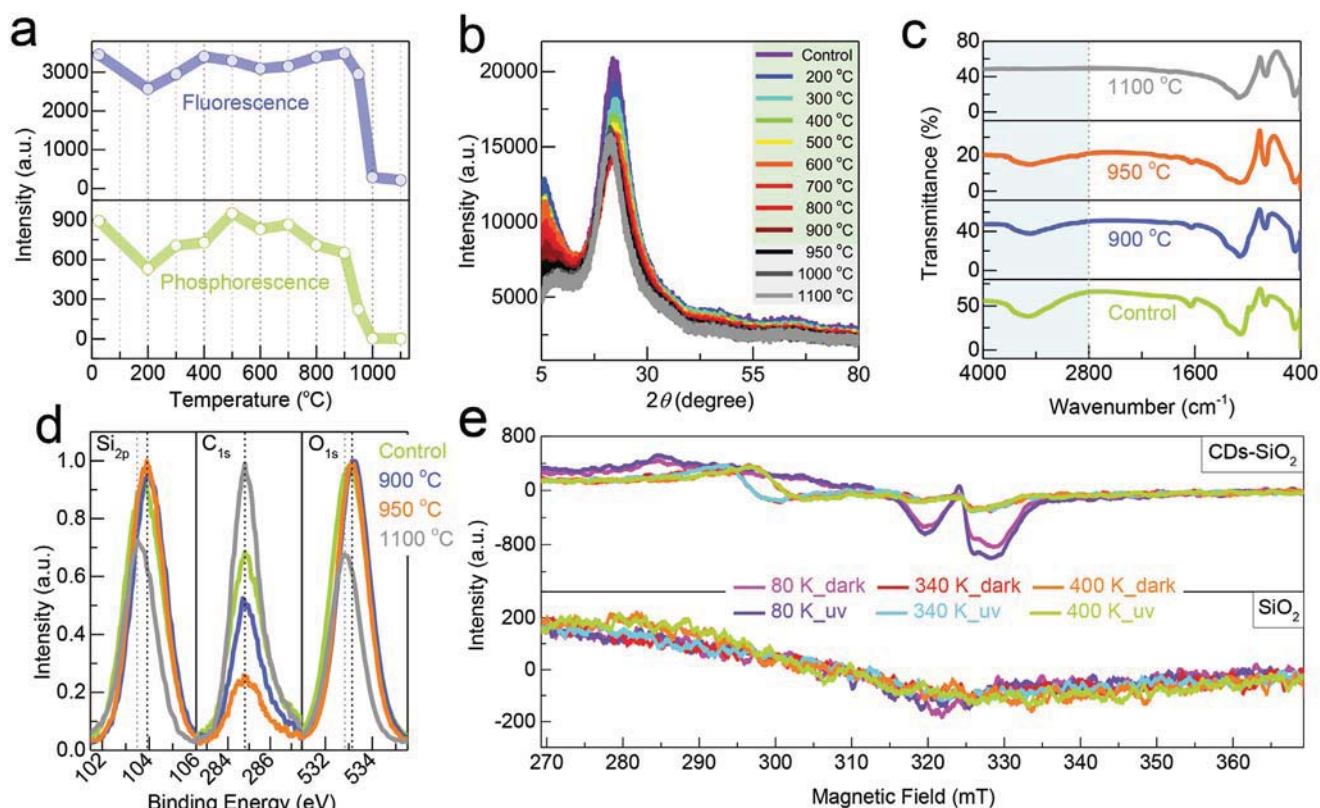


**Figure 3.** a) Fluorescence and phosphorescence intensity, b) XRD patterns, c) FTIR spectra and d) XPS spectra of CDs-SiO<sub>2</sub>\* (SiO<sub>2</sub>\* indicates the SiO<sub>2</sub> preannealed at selected temperature before reaction). e) EPR spectra of CDs-SiO<sub>2</sub> and SiO<sub>2</sub> with/without UV irradiation at 80, 340, and 400 K.



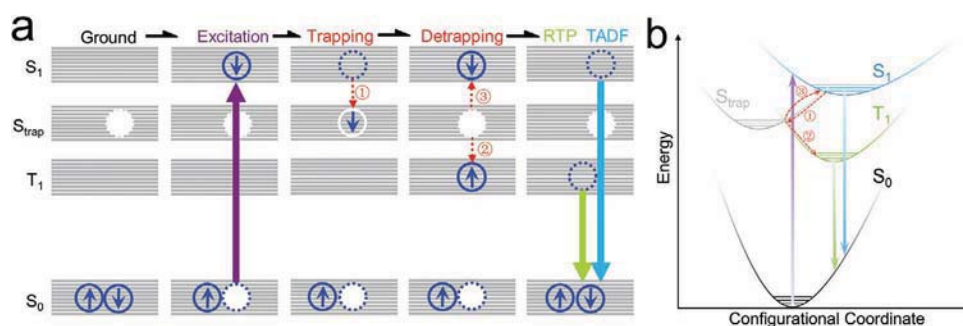


**Figure 4.** a) Mechanism of electron-trap-mediated LLE in terms of a) Jablonski diagram and b) configuration coordinate curves.

from CDs, but the weak EPR signals from CDs-SiO<sub>2</sub> could still be recognized at 340 or 400 K. The contrast between these two kinds of signals is consistent with the LLE intensities presented in Figure 2d. The lower-temperature atmosphere is beneficial to the storage of electrons in traps, hence the more obvious EPR signals from single electron on CDs-SiO<sub>2</sub> coexist with the stronger integrated luminosities. The appearance of inorganic SiO<sub>2</sub> acting as electron traps can effectively decelerate the electron transfer processes, therefore giving rise to the LLE.

On the basis of above results, the exquisite electron transfer processes responsible for the LLE can be reasoned in Figure 4a,b. The ground-state (S<sub>0</sub>) electrons of CDs-SiO<sub>2</sub> nanoemitter are excited to singlet excited states (S<sub>1</sub>) by photon stimulation. Partial excitons in S<sub>1</sub> can be captured and stored by trap center between S<sub>1</sub> and T<sub>1</sub> (triplet excited states). Some electrons in trap state will also strive to detrapping to T<sub>1</sub> or S<sub>1</sub>, then escaping to S<sub>0</sub> as the form of phosphorescence or delayed fluorescence, respectively. Throughout the whole processes, electron trap has played a very important role in capturing, storing, transporting electrons, and also stabilizing T<sub>1</sub>, therefore the generation of LLE.

### 3. Multifunctional Applications of CDs-SiO<sub>2</sub> Compounds

#### 3.1. Powdery CDs-SiO<sub>2</sub> for Temperature Sensing

As discussed in Figure 2e, it plots the intensity ratio of phosphorescence to fluorescence versus temperature (80–400 K). The distribution of  $I_P/I_F$  values fits a good linearity in the range of 80–340 K with correlation coefficient of 0.995, and the relationship can be described as below

$$I_P/I_F = 1.65 - 0.0035T \quad (1)$$

or

$$T = 471.43 - 285.71 I_P/I_F \quad (2)$$

where  $T$  is represents the temperature of powdery CDs-SiO<sub>2</sub> system (K). Regarding to the ratiometric luminescence-temperature sensor, the sensitivity is determined by this equation<sup>[32]</sup>

$$S = \frac{\partial(I_P/I_F)/\partial T}{I_P/I_F} \quad (3)$$

Therefore, the sensitivity of this thermometer obtained a maximal value of 0.7% at 340 K. A linear dependence achieved for this thermometer from ultralow temperature to the middle-high temperature, meaning CDs-SiO<sub>2</sub> powder is a reliable and useful luminescence thermometer.

#### 3.2. Aqueous CDs-SiO<sub>2</sub> Used for Ink/Pigment

Aqueous CDs-SiO<sub>2</sub> ink was applied to depict musical symbols in Figure 5a, in which these symbols can emit blue fluorescence with UV irradiation, and turn to green phosphorescence in an instant after stoppage of UV light. Fluorescence display is difficult to distinguish from the surrounding due to its blue illumination. However, phosphorescence display is much easily distinguishable showing high resolution without disturbance or interference. CDs-SiO<sub>2</sub> fully demonstrated the advantages of phosphorescence in display.

#### 3.3. Temperature Recognition with Naked Eyes through Using Powdery CDs-SiO<sub>2</sub>

Inspired by Figure 2d that described the gradual transition from phosphorescence (green) to TADF (blue) as temperature increased, a powdery CDs-SiO<sub>2</sub> temperature sensor from color discrimination was firstly established as shown in Figure 5b. A heating stage was used to control the temperatures including RT, 50, 100, 150, and 200 °C, the corresponding afterglow color was correspondingly changed from green to blue passing through cyan. These color changes can be easily perceived with the naked eyes, which is because of the enough time to identify with delay time as long as about 20 s, demonstrating the simplicity and convenience of this temperature sensor. This temperature sensor based on color change is proposed for the first time in CDs field, providing some application prospects for other research fields.

#### 3.4. Aqueous CDs-SiO<sub>2</sub> for Fluorescence/Phosphorescence Imaging in HeLa Cancer Cells

Since as-prepared CDs-SiO<sub>2</sub> aqueous solution has high PL quality and stability, this aqueous solution is proposed to cellular imaging field. Figure 5c presents the fluorescence and

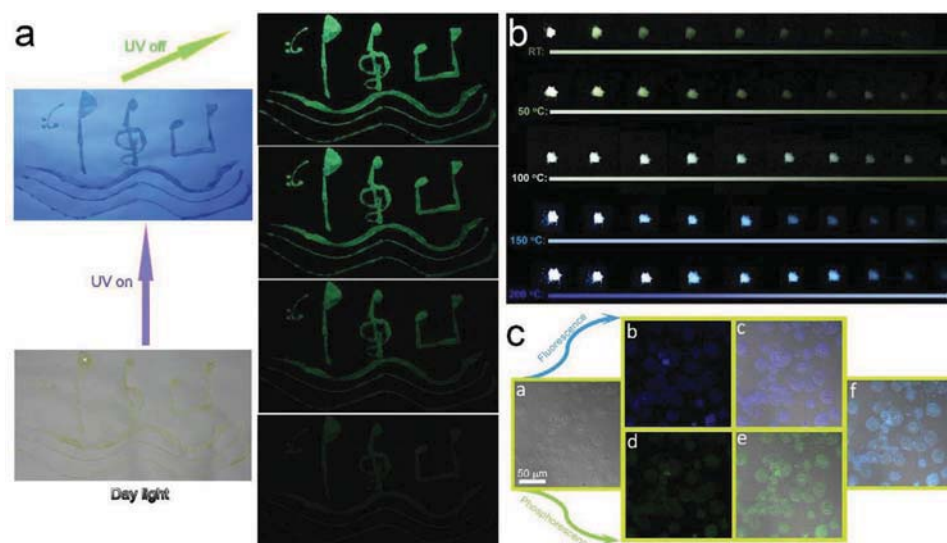


**Figure 5.** a) Musical notes presented on common A4-paper by CDs-SiO<sub>2</sub> ink/pigment irradiated by day light, UV light and removing UV light. b) The time-delayed afterglow color of powdery CDs-SiO<sub>2</sub> under various ambient temperatures. c) The confocal images of HeLa cells incubated with CDs-SiO<sub>2</sub> solution for 4 h. a) Bright field, b) fluorescence imaging and d) phosphorescence imaging in the range of 420–500 and 450–700 nm, respectively. c–f) Merged images for fluorescence overlay, phosphorescence overlay, and total overlay, respectively (e.g., 405 nm).

phosphorescence images of HeLa cancer cells under confocal laser of 405 nm. Bright blue-fluorescence and green-phosphorescence images were captured in cytoplasmic regions respectively, indicating CDs-SiO<sub>2</sub> has excellent translocation through cytomembrane and then enters the cancer cells. These cells were only stained for 20 min with CDs-SiO<sub>2</sub> solution. Such a feature further endows CDs-SiO<sub>2</sub> solution with great advantage and potential in biological imaging. As far as we have known, this is the first observation of phosphorescence imaging by applying CD-based materials in biological field.

To test the imaging specificity of CDs-SiO<sub>2</sub>, the co-localization experiment with the endoplasmic reticulum (ER) tracker red was conducted. After incubation of HeLa cells with both commercial ER-tracker red ( $1 \times 10^{-6}$  M, 1 mL) and 30 μL of as-prepared CDs-SiO<sub>2</sub> aqueous solution ( $1.5 \text{ mg mL}^{-1}$ ) at 37 °C for 20 min, the HeLa cells embedded with both of them were washed twice with PBS buffer solution before CLSM characterization. As shown in Figure S13 in the Supporting Information, the fluorescence images from ER-Tracker red and CDs-SiO<sub>2</sub> can be well overlapped together with coefficient of 0.80, meaning the CDs-SiO<sub>2</sub> stained in ER within cytoplasm. Therefore, these CDs-SiO<sub>2</sub> composites can be used for specific staining of the ER.

The stability of CDs-SiO<sub>2</sub> NPs and commercial dye (ER-Tracker red) in cellular imaging is also studied as shown in Figure S14–S16 in the Supporting Information. Figure S14 in the Supporting Information provides the CLSM images of HeLa cells incubated with CDs-SiO<sub>2</sub> NPs (Figure S14a–c, Supporting Information) and ER-Tracker red (Figure S14d–f, Supporting Information), where fluorescence signals from three experimental regions (red, green, and blue) and two control regions (yellow and cyan) were selected for comparison. The fluorescence intensity of these regions versus irradiation time was summarized in Figure S14g in the Supporting Information

which shows that fluorescence intensity of HeLa cells embedded with CDs-SiO<sub>2</sub> is almost no significant reduction after irradiation for 20 min. However, the fluorescence intensity from commercial dye (ER-Tracker Red) is totally quenched after 17 min of sustained irradiation. The detailed CLSM images for both of them are also presented in Figure S15 and Figure S16 in the Supporting Information, respectively. Fluorescence signal from CDs-SiO<sub>2</sub> NPs can be easily collected within 20 min seen in Figure S15 in the Supporting Information, while fluorescence signal from commercial dye is hardly recognized after irradiation for 17 min in Figure S16 in the Supporting Information. Therefore, these CDs-SiO<sub>2</sub> NPs can exhibit great stability comparing to the commercial dye, providing more potentials for practical applications.

### 3.5. Powdery CDs-SiO<sub>2</sub> for Oxygen Sensing

CDs-SiO<sub>2</sub> sample was subjected to an atmosphere with periodical transformation between pure oxygen and pure nitrogen as shown in Figure S4 in the Supporting Information, which presents the dynamic fluorescence response and phosphorescence response to the time delay. Fluorescence is more sensitive to the atmosphere change compared with phosphorescence, which just indicated about 10% divergence in the response of nitrogen and oxygen. Nevertheless, fluorescence signal of CDs-SiO<sub>2</sub> can react quickly to the oxygen with seducement of 62% that signifies CDs-SiO<sub>2</sub> is a great optical oxygen sensor.

## 4. Conclusion

On the whole, the LLE from CDs-SiO<sub>2</sub> can be stably present not only in solid state, but also in aqueous solution. This is

closely related to the adamantane structure of CDs-SiO<sub>2</sub> or multiple effects including hydrogen bond, covalent bond, and trap effect stabilized triplet state between CDs and inorganic SiO<sub>2</sub>. For the first time, the thermoluminescence spectrum of CD-based matrix was observed and studied. Inorganic defects from SiO<sub>2</sub> can act on the energy levels of CDs, thus affecting the behavior of phosphorescence and TADF. A new mechanism is proposed, especially the combination of inorganic defect mechanism and CDs triplet mechanism. After the introduction of inorganic SiO<sub>2</sub>, the phosphorescence of CDs showed huge enhancement and TADF was triggered to formation. As-prepared CDs-SiO<sub>2</sub> exhibited multifunctional applications, especially bioimaging field by using the advantageous LLE of aqueous phosphorescence with quite weak or non-autofluorescence interference. Among multifunctional applications, the CDs-SiO<sub>2</sub> solution can show specific imaging in ER of cancer cell and also exhibit excellent stability compared to commercial dye. The powdery CDs-SiO<sub>2</sub> can be utilized to recognize the temperature changes, which can regulate the conversion of phosphorescence (green) and TADF (blue), thus the color-based temperature sensor of CDs-related field was firstly established, in which the temperature change could be clearly sensed with the naked eyes providing a very simple method to estimate the temperature.

## 5. Experimental Section

Experimental methods and characterizations can be found in Supporting Information.

## Supporting Information

Supporting Information is available from the Wiley Online Library or from the author.

## Acknowledgements

This work was supported by National Natural Science Foundation of China (Grant No. 21571067, 21671070), and the National Natural Science Foundation of China Joint Fund with Guangdong under Key Project (Grant No. U1501242).

## Conflict of Interest

The authors declare no conflict of interest.

## Keywords

liquid phosphorescence, thermally activated delayed fluorescence, thermoluminescent glow curve, trap-stabilized triplet-state excitons, ultralong lifetime

Received: August 25, 2020

Revised: October 8, 2020

Published online:

- [1] A. A. Bakulin, A. Rao, V. G. Pavelyev, P. H. M. Loosdrecht, M. S. Pshenichnikov, D. Niedzialek, J. Cornil, D. Beljonne, R. H. Friend, *Science* **2012**, 335, 1340.
- [2] W. Shi, J. Yao, L. Bai, C. Lu, *Adv. Funct. Mater.* **2018**, 28, 1804961.
- [3] G. Xing, N. Mathews, S. Sun, S. S. Lim, Y. M. Lam, M. Grätzel, S. Mhaisalkar, T. C. Sum, *Science* **2013**, 342, 344.
- [4] J. Tang, B. Kong, H. Wu, M. Xu, Y. Wang, Y. Wang, D. Zhao, G. Zheng, *Adv. Mater.* **2013**, 25, 6569.
- [5] J. He, H. Zhang, J. Zou, Y. Liu, J. Zhuang, Y. Xiao, B. Lei, *Biosens. Bioelectron.* **2016**, 79, 531.
- [6] M. J. Krysmann, A. Kelarakis, P. Dallas, E. P. Giannelis, *J. Am. Chem. Soc.* **2012**, 134, 747.
- [7] S. Y. Lim, W. Shen, Z. Gao, *Chem. Soc. Rev.* **2015**, 44, 362.
- [8] S. Zhu, Y. Song, X. Zhao, J. Shao, J. Zhang, B. Yang, *Nano Res.* **2015**, 8, 355.
- [9] J. He, Y. He, Y. Chen, B. Lei, J. Zhuang, Y. Xiao, Y. Liang, M. Zheng, H. Zhang, Y. Liu, *Small* **2017**, 13, 1700075.
- [10] A. Segura-Carretero, C. Cruces-Blanco, B. Cañabate-Díaz, J. F. Fernández-Sánchez, A. Fernández-Gutiérrez, *Anal. Chim. Acta* **2000**, 417, 19.
- [11] C. C. Kenry, B. Liu, *Nat. Commun.* **2019**, 10, 2111.
- [12] J. Liu, N. Wang, Y. Yu, Y. Yan, H. Zhang, J. Li, J. Yu, *Sci. Adv.* **2017**, 3, e1603171.
- [13] Y. Chen, J. He, C. Hu, H. Zhang, B. Lei, Y. Liu, *J. Mater. Chem. C* **2017**, 5, 6243.
- [14] J. Zhu, X. Bai, X. Chen, H. Shao, Y. Zhai, G. Pan, H. Zhang, E. V. Ushakova, Y. Zhang, H. Song, A. L. Rogach, *Adv. Opt. Mater.* **2019**, 7, 1801599.
- [15] S. Tao, S. Lu, Y. Geng, S. Zhu, S. A. T. Redfern, Y. Song, T. Feng, W. Xu, B. Yang, *Angew. Chem., Int. Ed.* **2018**, 57, 2393.
- [16] P. Long, Y. Feng, C. Cao, Y. Li, J. Han, S. Li, C. Peng, Z. Li, W. Feng, *Adv. Funct. Mater.* **2018**, 28, 1800791.
- [17] K. Jiang, Y. Wang, X. Gao, C. Cai, H. Lin, *Angew. Chem., Int. Ed.* **2018**, 57, 6216.
- [18] L. Lin, X. Wang, S. Lin, L. Zhang, C. Lin, Z. Li, J. Liu, *Spectrochim. Acta, Part A* **2012**, 95, 555.
- [19] B. Wang, Y. Yu, H. Zhang, Y. Xuan, G. Chen, W. Ma, J. Li, J. Yu, *Angew. Chem., Int. Ed.* **2019**, 58, 18443.
- [20] M. S. Kwon, D. Lee, S. Seo, J. Jung, J. Kim, *Angew. Chem., Int. Ed.* **2014**, 53, 11177.
- [21] Y. Deng, D. Zhao, X. Chen, F. Wang, H. Song, D. Shen, *Chem. Commun.* **2013**, 49, 5751.
- [22] D. Lee, O. Bolton, B. C. Kim, J. H. Youk, S. Takayama, J. Kim, *J. Am. Chem. Soc.* **2013**, 135, 6325.
- [23] S. Hirata, K. Totani, J. Zhang, T. Yamashita, H. Kaji, S. R. Marder, T. Watanabe, C. Adachi, *Adv. Funct. Mater.* **2013**, 23, 3386.
- [24] R. A. Paynter, S. L. Wellons, J. D. Winefordner, *Anal. Chem.* **1974**, 46, 736.
- [25] Q. Li, M. Zhou, M. Yang, Q. Yang, Z. Zhang, J. Shi, *Nat. Commun.* **2018**, 9, 734.
- [26] K. Jiang, Y. Wang, C. Cai, H. Lin, *Chem. Mater.* **2017**, 29, 4866.
- [27] J. Joseph, A. A. Anappara, *Phys. Chem. Chem. Phys.* **2017**, 19, 15137.
- [28] C. Lin, Y. Zhuang, W. Li, T. L. Zhou, R. J. Xie, *Nanoscale* **2019**, 11, 6584.
- [29] X. Dong, L. Wei, Y. Su, Z. Li, H. Geng, C. Yang, Y. Zhang, *J. Mater. Chem. C* **2015**, 3, 2798.
- [30] Q. Li, M. Zhou, Q. Yang, Q. Wu, J. Shi, A. Gong, M. Yang, *Chem. Mater.* **2016**, 28, 8221.
- [31] J. Tan, R. Zou, J. Zhang, W. Li, L. Zhang, D. Yue, *Nanoscale* **2016**, 8, 4742.
- [32] J. He, Y. He, Y. Chen, X. Zhang, C. Hu, J. Zhuang, B. Lei, Y. Liu, *Chem. Eng. J.* **2018**, 347, 505.
- [33] T. E. Tsai, D. L. Griscom, E. J. Friebele, *Phys. Rev. Lett.* **1988**, 61, 444.



- [34] C. Nelson, R. Weeks, *J. Am. Ceram. Soc.* **1960**, 43, 396.
- [35] P. L. Suárez, M. García-Cortés, M. T. Fernández-Argüelles, J. R. Encinar, M. Valledor, F. J. Ferrero, J. C. Campo, J. M. Costa-Fernández, *Anal. Chim. Acta* **2019**, 1046, 16.
- [36] S. Titos-Padilla, E. Colacio, S. J. A. Pope, J. J. Delgado, M. Melgosa, J. M. Herrera, *J. Mater. Chem. C* **2013**, 1, 3808.
- [37] Y. Chen, M. Zheng, Y. Xiao, H. Dong, H. Zhang, J. Zhuang, H. Hu, B. Lei, Y. Liu, *Adv. Mater.* **2016**, 28, 312.
- [38] R. Al-Oweini, H. El-Rassy, *J. Mol. Struct.* **2009**, 919, 140.
- [39] J. Guo, X. Li, H. Nie, W. Luo, S. Gan, S. Hu, R. Hu, A. Qin, Z. Zhao, S. Su, B. Z. Tang, *Adv. Funct. Mater.* **2017**, 27, 1606458.
- [40] H. Uoyama, K. Goushi, K. Shizu, H. Nomura, C. Adachi, *Nature* **2012**, 492, 234.
- [41] J. Li, B. Wang, H. Zhang, J. Yu, *Small* **2019**, 15, 1805504.
- [42] G. Liebsch, I. Klimant, O. S. Wolfbeis, *Adv. Mater.* **1999**, 11, 1296.
- [43] S. Shionoya, W. M. Yen, H. Yamamoto, *Phosphor Handbook*, 2nd ed., CRC press, Boca Raton, FL **2006**.
- [44] S. Basu, *Crystalline Silicon-Properties and Uses*, InTech, Rijeka, Croatia **2011**, p. 139.
- [45] R. Chen, S. A. A. Winer, *J. Appl. Phys.* **1970**, 41, 5227.
- [46] X. Zhang, X. Xu, Q. He, J. Qiu, X. Yu, *ECS J. Solid State Sci. Technol.* **2013**, 2, R225.
- [47] V. P. Della, I. Kühn, D. Hotza, *Mater. Lett.* **2002**, 57, 818.
- [48] M. A. Hamad, I. A. Khattab, *Thermochim. Acta* **1981**, 48, 343.
- [49] S. P. Zhdanov, *Langmuir* **1987**, 3, 960.
- [50] R. Hofman, J. G. F. Westheim, I. Pouwel, T. Fransen, P. J. Gellings, *Surf. Interface Anal.* **1996**, 24, 1.
- [51] Q. Yang, C. Li, S. Yuan, J. Li, P. Ying, Q. Xin, W. Shi, *J. Catal.* **1999**, 183, 128.
- [52] Y. Tamai, S. Mori, *Z. Anorg. Allg. Chem.* **1981**, 476, 221.

REVIEW

View Article Online  
View Journal



Cite this: DOI: 10.1039/c9qm00614a

Received 5th October 2019,  
Accepted 28th November 2019

DOI: 10.1039/c9qm00614a

rsc.li/frontiers-materials

# A review on the effects of carbon dots in plant systems

Yadong Li, , Xiaokai Xu, Ying Wu, Jianle Zhuang, , Xuejie Zhang, ,  
Haoran Zhang, Bingfu Lei, \* Chaofan Hu\* and Yingliang Liu \*

Carbon dots (CDs), a novel member of the renowned carbon-based nanomaterials family, have gained tremendous attention in various fields. Their extraordinary properties, including facile synthesis procedure, photoluminescence, biocompatibility, tunable surface functionalities, water solubility and low toxicity, have introduced them extensively in biological applications, such as bioimaging, biosensing, photocatalysis and molecule delivery. Recently, CDs have attracted significant interest in agriculture to improve the growth and production of plants and great progress has been achieved in this area. Here, we will review the interactions of CDs with plant systems for the first time, including symptomatic plant growth, internal physiological processes and other external factors involved in plant growth. Furthermore, the current challenges and future perspective of CDs in the field of agriculture are discussed. Looking forward, it indicates that CDs might play an important role in the future of agriculture.

## 1. Introduction

Cultivation of plants for food is one of the most critical human endeavors that has taken place in the history of human civilization. Due to the advances in agricultural production technology, the number of undernourished people has roughly halved in the past 20 years.<sup>1</sup> However, there are almost a billion people still suffering from insufficient nutrition.<sup>1</sup> In order to

feed the continuously increasing population and supply industry, the amount of resources consumed by agriculture is staggering. It has been roughly calculated that over 3 billion metric tons of crops are produced annually in the world, requiring 187 million metric tons of fertilizer, nearly 4 million tons of pesticides, and 2.7 trillion cubic meters of water (about 70% of all global freshwater consumption).<sup>2</sup> Ubiquitous and inefficient use of pesticides and herbicides pose a severe threat to biodiversity and the ecosystem and have caused serious resistance to these substances.<sup>3,4</sup> Furthermore, climate change, such as extreme weather and epidemics involving pests and diseases, is bound to put increasing stress on food production and distribution.<sup>5</sup> In this context, the agricultural industry urgently requires the

Guangdong Provincial Engineering Technology Research Center for Optical Agriculture, College of Materials and Energy, South China Agricultural University, Guangzhou 510642, China. E-mail: tleibf@scau.edu.cn, thucf@scau.edu.cn, tliuyi@scau.edu.cn



Yadong Li

Yadong Li received his BS degree in 2015 and MS degree in 2018 from Shihezi University. From 2016 to 2018, he did combined training at the Shihezi University and the Guangdong Institute of Eco-environmental Science & Technology. Currently, he is pursuing a PhD degree in the group of Prof. Yingliang Liu at South China Agricultural University (SCAU). His research interests involve the synthesis and application of specifically functionalized carbon dots in agriculture.



Jianle Zhuang

Jianle Zhuang received his PhD degree in materials physics and chemistry from Sun Yat-Sen University in 2009. During 2011–2013, he was a postdoctoral fellow at The Hong Kong University of Science and Technology. Currently, he is an associate professor at South China Agricultural University. His research interests focus on the synthesis and application of luminescent materials, including lanthanide-doped nanomaterials, upconversion materials and carbon dots.

development of new environmentally-friendly technologies to face the challenge of increasing food production.

Nanomaterials are believed to play a key role in addressing these challenges faced by agriculture in the future. Over the past few decades, abundant nanomaterials have been developed and applied in agriculture to monitor crop health,<sup>6</sup> promote the growth of crops,<sup>7–9</sup> improve the efficiency of fertilizer and pesticides,<sup>10,11</sup> and manage diseases,<sup>12</sup> pests,<sup>13</sup> and environmental stresses.<sup>14</sup> Compared to other metal-based nanomaterials, carbon-based nanomaterials show much lower environmental toxicity and higher biocompatibility due to their non-toxic carbon backbone.<sup>15–17</sup> Thus, carbon-based nanomaterials have been widely applied in agriculture.<sup>18–20</sup> As a novel member of the carbon nanomaterial family, carbon dots (CDs) possess a size of less than 10 nm and have inherent photoluminescence (PL) properties. In recent years, CDs have been the focal point of interest for many researchers, since they have superior and universal properties, including excellent photostability, small size, biocompatibility, water solubility, highly tunable PL properties, easy functionalization with biomolecules and chemical

inertness.<sup>21,22</sup> Although it is not very long since the discovery of CDs in 2004, carbon quantum dots (CQDs) have been the subject of numerous optical research studies, for use in areas such as biomonitoring, sensing, photocatalysis, drug and gene delivery, solar energy conversion and LEDs.<sup>23</sup> What is more, CDs have been considered as alternatives to conventional semiconductor quantum dots in order to overcome their toxicity and environmental concerns.<sup>24</sup>

Since the biocompatibility of CDs with bean sprouts was revealed by Qu *et al.*,<sup>25</sup> the potential effects that CDs have on various crop plant growth have attracted more and more attention from researchers worldwide. Up to now, superior performance of CDs in several physiological processes of plants has been demonstrated, including growth, photosynthesis, and resistance to abiotic/biotic stress.<sup>26–28</sup> Additionally, CD treatments has also shown enhanced effects of the biological nitrogen fixation by azotobacter.<sup>29</sup> Furthermore, CDs play a role in the delivering of siRNA in a model plant and the *in situ* imaging of environmental pollutants.<sup>30,31</sup> Nevertheless, there is no review that focuses on the biological functions of CDs in the



**Xuejie Zhang**

include phosphors and luminescent glass-ceramic materials together with their applications in displays and lighting.

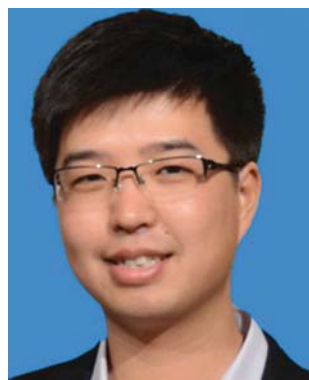
*Xuejie Zhang is currently an associate professor at the college of materials and energy in South China Agricultural University (SCAU). He obtained his BS degree from the Zhoukou Normal University in 2010 and was a graduate student at the Sun Yat-sen University, and received a PhD degree in 2015. After graduation, he worked as a postdoctoral researcher at Taiwan University for one year. His current research interests*



**Bingfu Lei**

silicon dots materials together with their applications in plant growth, lighting, biolabeling, and sensing. He has published more than 300 peer-reviewed journal articles in related fields.

*Bingfu Lei is a professor at the college of materials and energy at South China Agricultural University (SCAU). He received his BS and MS from the department of chemistry at Jinan University (JNU), and the PhD degree at Changchun Institute of Optics, Fine Mechanics and Physics, Chinese Academy Sciences. After graduation, he worked as a postdoctoral fellow (JSPS) at Osaka University for two years. His research interests include phosphors, carbon dots, and*



**Chaofan Hu**

*Chaofan Hu received his BS degree from Hebei Polytechnic University in 2007 and MS degree from South China Normal University in 2010 and obtained his PhD degree from Jinan University in 2013 and then joined Taiyuan University of Technology as a lecturer. Currently, he is an associate professor at South China Agricultural University. His research interests include the synthesis of luminescent nanomaterials and their bio-applications.*



**Yingliang Liu**

*Yingliang Liu received his master's degree from Changchun Institute of Applied Chemistry, Chinese Academy of Sciences in 1989 and his doctor's degree from Zhongshan University in 1994. He has engaged in research on carbon quantum dots and their agricultural applications.*



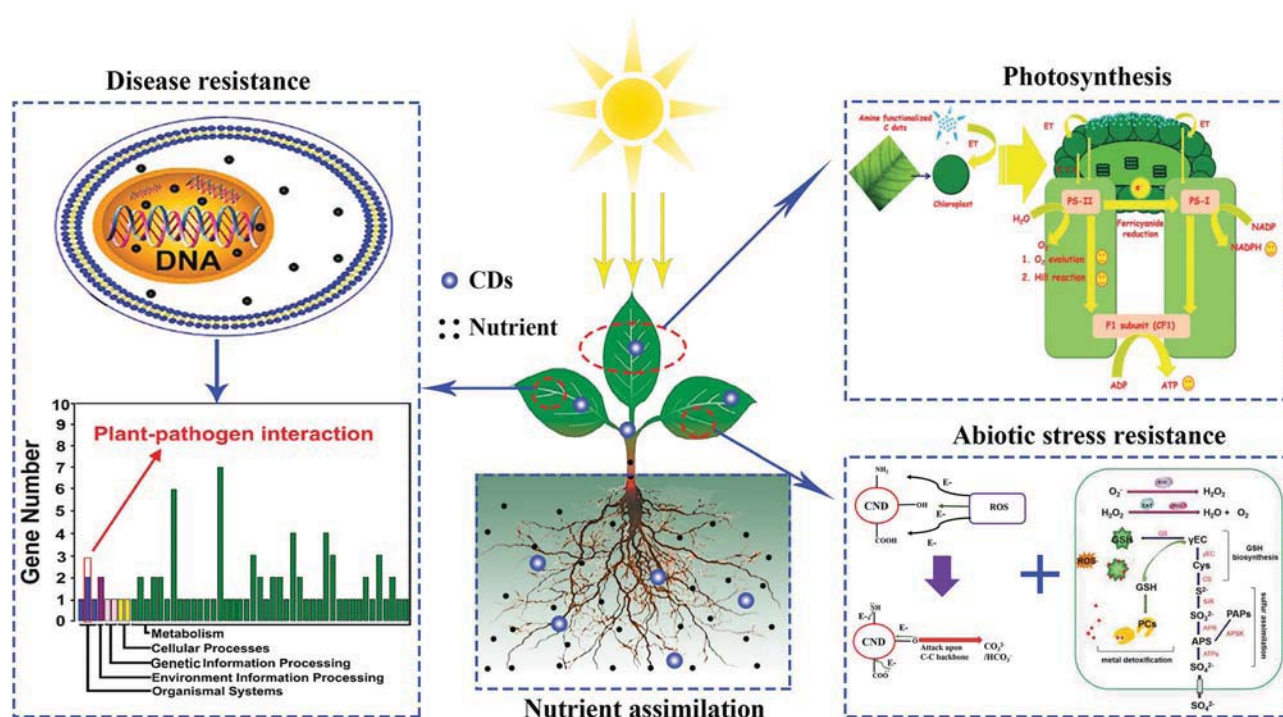


Fig. 1 Different applications of CDs in agriculture.<sup>28,60,69,74</sup> Reprinted with permission from the American Chemical Society, Copyright 2018 (ref. 28); the Royal Society of Chemistry, Copyright 2014 (ref. 60 and 69); Elsevier, Copyright 2019 (ref. 74).

growth and development of crops. In this review we will first focus on the effects that CDs have on the growth of plants in agriculture. Next, we will summarize the underlying mechanism of CDs in promoting or inhibiting plant growth. Following that, the functions of CDs in the resistance of plants against abiotic/biotic stresses will be surveyed (Fig. 1). Lastly, some perspectives regarding the challenges and opportunities for CD studies will be discussed. Generally, CDs mainly include graphene quantum dots (GQDs), carbon nanodots (CNDs) and polymer dots (PDs),<sup>32</sup> all of them are consistently referred to as CDs in this review.

## 2. Uptake, translocation and accumulation of CDs in plants

The stable and unique fluorescence signal of CDs provides a promising approach by which to trace them in plants. Several studies have revealed the uptake of CDs by plants through fluorescence imaging, transmission electron microscopy (TEM) observations or Raman spectroscopic measurements.<sup>26,28,33–36</sup> For example, Loukanov *et al.* used tobacco bright yellow-2 (BY-2) plant cells to investigate the real time monitoring and quantification of CD uptake by fluorescence and confocal microscopy.<sup>37</sup> In our previous study, the mung bean was adopted as a model plant to investigate the uptake, and translocation of CDs in plants.<sup>33</sup> Hydroponics guarantee that the CDs are readily available for adsorption and uptake by the roots of the mung bean plants. After 5 days of cultivation at 25 °C, the germination of the seeds and growth of the mung bean seedlings were promoted. The clear concentration-dependent reddish-orange fluorescence

under 365 nm UV light provided evidence for the increased absorption of CDs by the mung bean plant (Fig. 2A). A confocal laser scanning microscope was employed to image the root, stem, cotyledon and leaves to locate the CDs in the mung bean seedlings after 5 days of incubation. As can be seen from the cross and longitudinal sections of the mung bean sprouts in Fig. 2B and C, the fluorescence signals of the CDs were found to be mainly located in the vascular system in the parts of the root, stem and leaves. TEM images of the cross sections of mung bean seedlings from the control and CD treatments showed the presence of CDs that were agglomerated and formed relatively larger clusters in the intercellular space (Fig. 2D). It can be concluded that the CDs penetrate the seed coating *via* the intercellular space and accumulate in the cotyledons to accelerate seed germination. After the root emerged, the CDs were adsorbed on the root surface and penetrated into the root vascular bundles. Then, the CDs were transferred from the roots to the stems and leaves through the vascular system and were found to be finally located in the veins of the leaves rather than the mesophyll system (Fig. 2E). A similar upward transport of CDs from the root of mung beans to the stem and leaves was reported by Kang *et al.*<sup>26,36</sup> It should be noted that the distribution pattern of CDs in plants depends on their surface modification.<sup>38</sup>

## 3. Effects of CDs on plant growth and development

Crop plants play a key role in maintaining ecological balance and as food for human survival and feedstocks for industrial

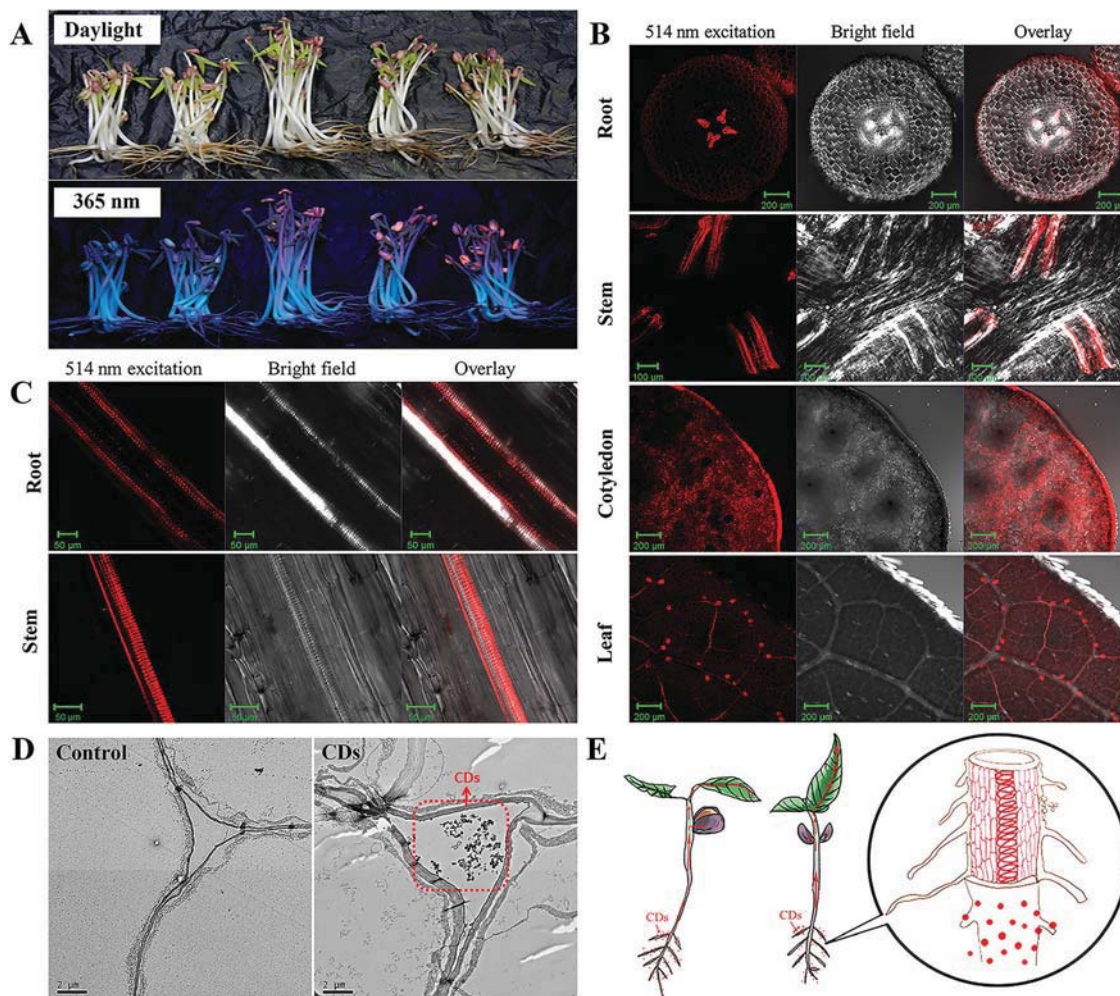


**Fig. 2** Uptake and translocation of CDs in mung bean plants. (A) Digital photos of mung bean sprouts under daylight and 365 nm UV light; LSM images of transverse sections from root, stem, cotyledon, leaf (B) and longitudinal sections from root, stem (C) of mung beans cultured with CDs ( $1.0 \text{ mg mL}^{-1}$ ) for 5 d; (D) TEM image of mung bean roots cultured with pure water and CDs ( $1.0 \text{ mg mL}^{-1}$ ) after 5 d; (E) schematic illustration of uptake, transport, and accumulation of CDs by a mung bean plant.<sup>33</sup> Adapted with permission from the American Chemical Society, Copyright 2016 (ref. 33).

production, which are facing the challenge of an increase in production in the wake of the increasing world population.<sup>5</sup> Qu *et al.* first reported the biocompatibility of CDs using the bean sprout as a model.<sup>25</sup> In their study, CDs prepared from citric acid and urea showed nontoxicity to the bean sprout plant, which were used as a new type of biocompatible fluorescent ink. Subsequently, Ma *et al.* conducted parallel comparative studies on the toxic effects of unmodified CdTe quantum dots, gold nanoparticles, and carbon nanodots on live cells as well as green gram sprouts.<sup>39</sup> The CDs were found to exert no obvious toxicity on both live cells and the growth of green gram sprouts, showing the best biocompatibility compared to CdTe quantum dots and gold nanoparticles. And then, the potential effect of CDs on the growth of various crop plants was sequentially reported.

### 3.1. Enhancement effect

Mung bean is the most commonly used plant model in studies due to its fast growing rate.<sup>18,26,33,36,40</sup> Among these studies, CDs played a role in the elongation of root and stem, biomass

accumulation, and enhanced the carbohydrates content and photosynthesis (mentioned below) of the mung bean sprouts. For example, Kang *et al.* exposed mung bean sprouts to CDs, in which CDs at  $0.02 \text{ mg mL}^{-1}$  were found to improve the root length, stem length, root vigor and single plant fresh weight by 29.9%, 18.3%, 36.1% and 14.9%, respectively (Fig. 3A).<sup>26</sup> Similar results were obtained with CDs prepared from *p*-phenylenediamine in our previous study, where the optimal concentration of CDs was  $0.4 \text{ mg mL}^{-1}$ .<sup>18</sup> Simultaneously, Kang's group further prepared a chiral CD sample *via* a one-pot hydrothermal method from chiral molecules of cysteine and citric acid. These chiral CDs were further used to investigate the systemic effects on the growth of the mung bean plant. The results indicated that the D-CDs showed better enhancement effect on the growth of the mung bean plant than L-CDs, especially in the root vigor and the activity of the Rubisco enzyme, and carbohydrate accumulation.<sup>36</sup> Furthermore, Li *et al.* prepared nitrogen-rich (20%) CDs using a solid-state method from citric acid and thiourea, which were applied as a nanofertilizer.<sup>40</sup> They found



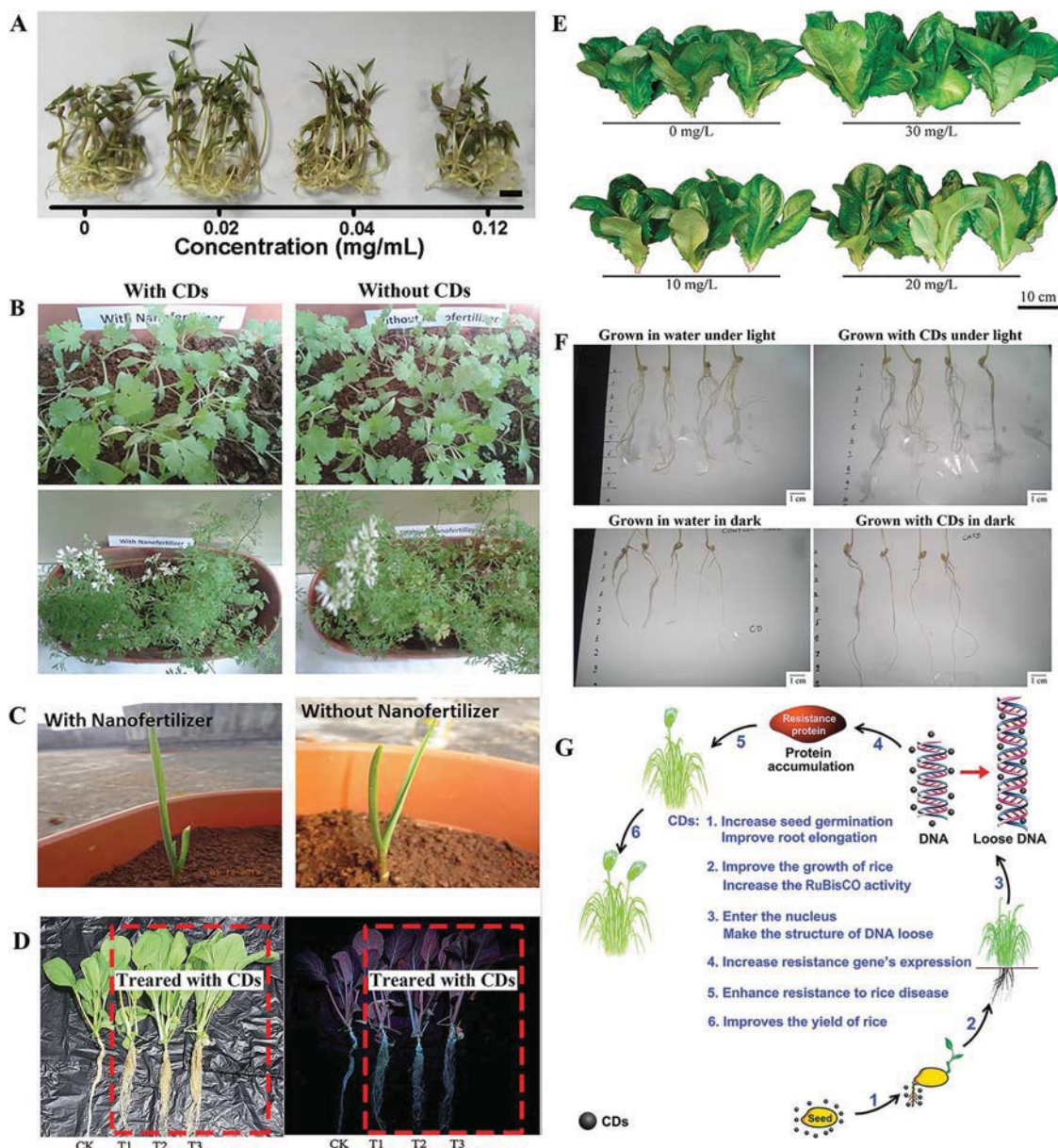


Fig. 3 Enhancement effect of CDs on the growth of (A) mung bean,<sup>26</sup> (B) coriander, (C) garlic,<sup>41</sup> (D) *Brassica parachinensis* L.,<sup>43</sup> (E) romaine lettuce,<sup>44</sup> (F) wheat<sup>35</sup> and (G) rice plants.<sup>28</sup> Reprinted with permission from Elsevier, Copyright 2018 (ref. 26); the Society of Chemical Industry, Copyright 2015; the Royal Society of Chemistry, Copyright 2017 (ref. 43 and 69); the American Chemical Society, Copyright 2017 (ref. 44 and 28); the Author (ref. 35).

that 17.45% more bean sprouts were yielded by the same amount of mung bean seeds when cultured in an aqueous solution ( $0.2 \text{ mg mL}^{-1}$ ) of the CDs than in the pure water control. The fertilizing effects of the CDs were much more efficient than those of urea, which has a much higher N content (46%). They determined that the fabricated N-CDs demonstrate great potential as a luminescent nanofertilizer.

Besides the mung bean, various other species of crop plants have been employed to investigate the potential effect of CDs on their growth. Late *et al.* fabricated graphene quantum dots (GQDs) from graphite powder as a plant growth regulator, which enhanced the growth rate of coriander and garlic plants, including leaves, roots, shoots, flowers and fruits (Fig. 3B and C).<sup>41</sup> Tripathi *et al.*

compared the influence of the morphology of carbon nanostructures on the stimulated growth of a gram plant. In their study, the CDs showed significant enhancement of the growth of the gram plant, although to a lesser extent than the performance of single-walled carbon nanotubes and carbon nanowhiskers.<sup>42</sup> In our previous studies, CDs that were prepared from pollen exhibited significant promoting effects on the growth of *Brassica parachinensis* L. and Romaine lettuce (*Lactuca sativa*) (Fig. 3D and E).<sup>43,44</sup> Furthermore, the enhancement effects of CDs on the two main grain crops of wheat and rice were reported.<sup>28,35</sup> In a seed germination experiment on wheat, CDs were found to enhance the growth of the roots more than the shoot both under light and dark conditions (Fig. 3F).<sup>25</sup> Kang's group conducted a



systematic investigation on how CDs affect the growth of rice plants over a whole growth season.<sup>26</sup> They found that CDs (0.56 mg mL<sup>-1</sup>) were capable of entering the cells of the plants, reaching the nuclei and then promoting plant growth, through the expression of disease-resistant genes, leading to a 14.8% enhancement in the total rice yield (mentioned in detail below) (Fig. 3G). Simultaneously, the same CDs significantly improved the yield of 8 different dicotyledons (soybean, tomato, eggplant, capsicum, watermelon, radish, celery and cabbage) by 20% in another of their studies.<sup>45</sup>

### 3.2. Inhibition effect

Despite the promoting functions of CDs on the growths of various crop plants mentioned above, inhibition of the growth of crops was also observed. After exposure to maize plants in a sand matrix for 4 weeks, CDs at 1000 and 2000 mg L<sup>-1</sup> significantly reduced the fresh weights of the roots (57% and 68%) and shoots (38% and 72%) of the plants (Fig. 4A).<sup>34</sup> Meanwhile, CDs at such high concentrations caused oxidative damage (higher H<sub>2</sub>O<sub>2</sub> content and lipid peroxidation) in the maize plants. In response, the antioxidant defense systems (catalase, ascorbate peroxidase, guaiacol peroxidase and superoxide dismutase) of the maize plants were enhanced to alleviate the CD-mediated oxidant damage. Similarly, Wang *et al.* integrated transcriptomic, physiological and metabolomic techniques to systematically investigate the fate and phytotoxicity of CDs using *Arabidopsis thaliana* (L.) as a plant model.<sup>46</sup> CDs at over 125 mg L<sup>-1</sup> significantly reduced the root elongation of *Arabidopsis thaliana* (L.) compared with that of the control groups, while 62.5 mg L<sup>-1</sup> of CDs had no influence (Fig. 4B). In further RNA-seq analyses of the treated *Arabidopsis thaliana* (L.) with CDs at 1000 mg L<sup>-1</sup>, 715 and 636 genes in roots and shoots were up-regulated, which were involved in stimulus response, UDP-glycosyltransferase activity and cellular response to phosphate starvation. Meanwhile, 552 and 707 down-regulated genes in roots and shoots, respectively, were mainly involved in chloroplast structure and function. Similarly, the physiological results indicated that the antioxidant response (activities of

glutathione reductase) of *Arabidopsis thaliana* (L.) was activated and the photosynthesis enzymes (Rubisco, FBP and FDA) were reduced.

Summarized from the studies mentioned above, the potential effects of CDs on the growth of crop plants were found to be concentration-dependent, *i.e.*, CDs at a relatively lower dose contribute to crop growth, while a higher dose inhibits it. Generally, several internal and external factors are responsible for the growth of the plant. These internal factors include photosynthesis, nutrient assimilation and plant resistance,<sup>47–50</sup> and the external factors involve biological nitrogen fixation,<sup>51</sup> pest infection, environmental stress injury, *etc.* Therefore, in the following section, we will focus on the interaction between CDs and these physiological processes in plants, as well as the external factors involved in plant growth.

## 4. Effects of CDs on photosynthesis in plants

Photosynthesis plays a key role in plant growth and biomass accumulation. As is well known, two energy conversion processes are involved in the photosynthesis of plants, including conversion from optical to electric energy and then to chemical energy. Chromophores such as chlorophylls and xanthophylls on the thylakoid membrane of the chloroplasts act as antennae to harvest light during photosynthesis.<sup>52</sup> Then, the energy absorbed by the chromophores is transported to photosystems I and II through a series of electron transfer chains, accompanied by the production of oxygen and adenosine triphosphate (ATP) as a result of water splitting and the reduction of nicotinamide adenine dinucleotide phosphate (NADP) to NADPH.<sup>53</sup> Finally, the ATP and NADPH are involved in CO<sub>2</sub> assimilation, in which CO<sub>2</sub> is fixed and transformed to carbohydrate, catalyzed by photosynthetic enzymes.<sup>53</sup> Therefore, the intermediate process of electron transfer and the immobilization of CO<sub>2</sub> play key roles in the rate of photosynthesis.

CDs, as a good electron donor as well as acceptor,<sup>54,55</sup> have been employed in light energy conversion applications.<sup>56,57</sup>

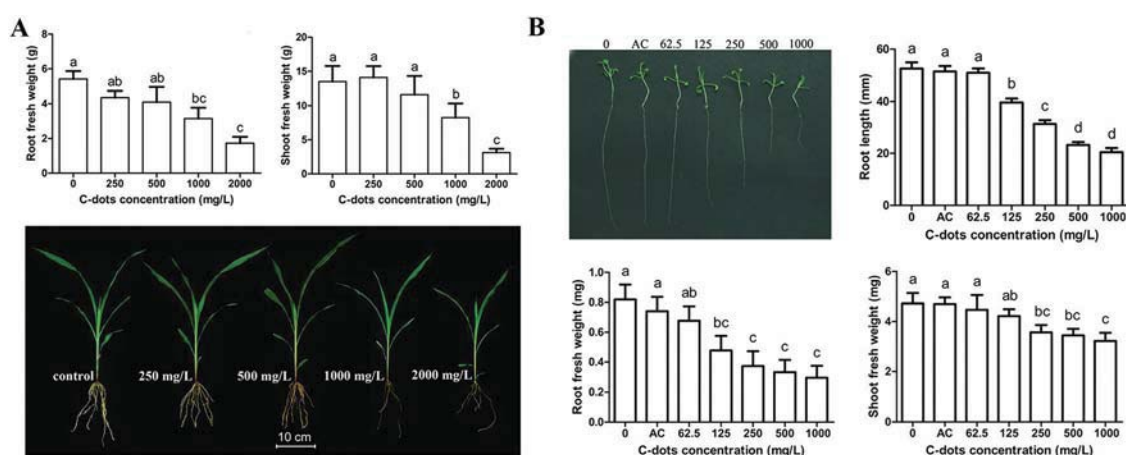


Fig. 4 Inhibition of CDs on the growth of (A) maize<sup>34</sup> and (B) *Arabidopsis thaliana* (L.).<sup>46</sup> Reprinted with permission from Taylor & Francis, Copyright 2016 (ref. 34); the Royal Society of Chemistry, Copyright 2018 (ref. 46).

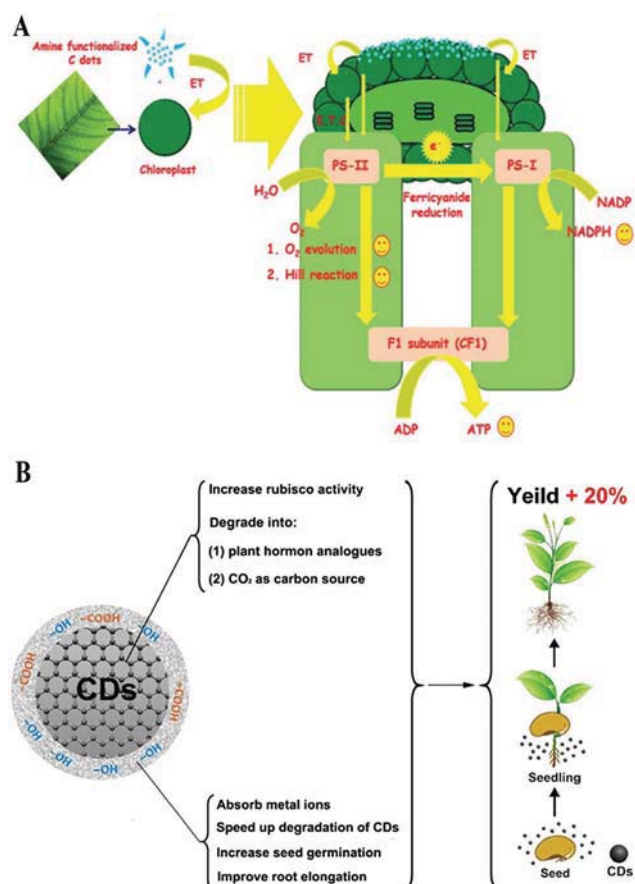


Fig. 5 Schematic representation illustrating the function of CDs in the (A) electron transfer PS II<sup>60</sup> and (B) nutrition assimilation.<sup>45</sup> Reprinted with permission from the Royal Society of Chemistry, Copyright 2014 (ref. 60); Tsinghua University Press and Springer-Verlag GmbH Germany, part of Springer Nature, Copyright 2019 (ref. 45).

The doping modification of CDs can increase the transfer of charges to form more electronic holes under light irradiation, which increases the photoelectric conversion efficiency.<sup>58,59</sup> Chandra *et al.* first proposed CD-based light stimulated electron transfer processes in photosynthetic system/light harvesting complexes (Fig. 5A).<sup>60</sup> In their study, the amine functionalized CDs were found to strongly conjugate over the surface of the chloroplast and transfer electrons towards the chloroplast via the assistance of absorbed light or photons, which directly accelerates the whole chain electron transfer pathway in the light reaction of photosynthesis. As a result, photosynthesis is promoted by CDs. Subsequently, this property of CDs of accelerating the transfer of electrons was further demonstrated in further studies.<sup>26,61</sup>

Besides the light reaction of photosynthesis, CO<sub>2</sub> assimilation is mainly responsible for the conversion of electrical energy to chemical energy in photosynthesis. Ribulose biphosphate carboxylase oxygenase (Rubisco) is a key enzyme in the Calvin cycle that fixes CO<sub>2</sub> in photosynthesis.<sup>53</sup> The activity of Rubisco directly affects the photosynthetic rate and the accumulation of carbohydrates. Kang *et al.* first determined the enhancing effect of CDs on Rubisco activity using mung bean as a model.<sup>26</sup>

They found that CD-treated mung bean seedlings showed 30.9% higher Rubisco activity than those in the control group. Subsequently, they reported a similar enhancing effect of CDs on the Rubisco activity of rice, *Trifolium repens* L. and *Arabidopsis thaliana* plants.<sup>28,45</sup> Additionally, the CDs were degraded by horseradish peroxidase (HRP) and H<sub>2</sub>O<sub>2</sub> in plants to form plant-hormone analogues and CO<sub>2</sub>. And then, the hormone analogues promoted plant growth, while the CO<sub>2</sub> was converted into carbohydrates through the Calvin cycle in photosynthesis (Fig. 5B). Finally, the CD-treated plants showed a 14.8–20% increase in yield.<sup>28,45</sup> This result was consistent with the degradation of graphene to CO<sub>2</sub> in rice plants reported by Huang *et al.* using <sup>14</sup>C-labeled graphene.<sup>62</sup> The same enhancing effect of CDs on photosynthesis was also demonstrated in *Chlorella vulgaris*.<sup>63</sup> Furthermore, the fluorescence of CDs means that they can serve as a UV-to-blue light conversion material in a plant to accelerate its rate of photosynthesis.<sup>64</sup>

## 5. Effects of CDs on nutrition assimilation by plants

Besides photosynthesis, nutrition assimilation is another key factor that affects plant growth. The hydrophilic groups (hydroxyl and carboxyl groups) on the surface of CDs provide abundant binding sites for water molecules, which enter the plant along with the CDs. Finally, adequate moisture in plant seeds can promote their germination and accelerate the growth of plant seedlings.<sup>28,45</sup> In a seed germination test, CD-treated mung bean seeds showed 34.9% higher moisture levels than those in the control group, indicating that CDs can promote the water uptake capacity of seeds.<sup>26</sup> Water uptake by plants is accompanied by the uptake of nutrition. The hydroxyl and carboxyl groups on their surface endows CDs with adsorbent capability for various metal ions (K<sup>+</sup>, Ca<sup>2+</sup>, Mg<sup>2+</sup>, Cu<sup>2+</sup>, Zn<sup>2+</sup>, Mn<sup>2+</sup> and Fe<sup>3+</sup>), which are important nutrients for plant growth. The higher metal nutrient content in CD-treated plants than in the controls indicates that CDs are able to deliver them into plants (Fig. 5B).<sup>45</sup>

## 6. Effects of CDs on the resistance of plants toward abiotic/biotic stress

### 6.1. Abiotic stress

According to a report by the Food and Agriculture Organization of the United Nations (FAO) in 2007, more than 96% of global rural land area is affected by various abiotic stresses (drought, cold, salt, strong solar radiation, abuse of pesticides, *etc.*) that annually lead to about half of the crop yield lost worldwide.<sup>65</sup> Elevation in the generation of reactive oxygen species (ROS) is the main pathway for abiotic stresses that affect plant growth. Accumulation of ROS in cells usually leads to oxidative damage to proteins, lipids, carbohydrates and DNA.<sup>66,67</sup> In recent years, CDs with radical scavenging properties due to the electron donor and acceptor carboxyl and amino groups on their surface have been reported.<sup>68,69</sup> Through a hydrogen atom transfer

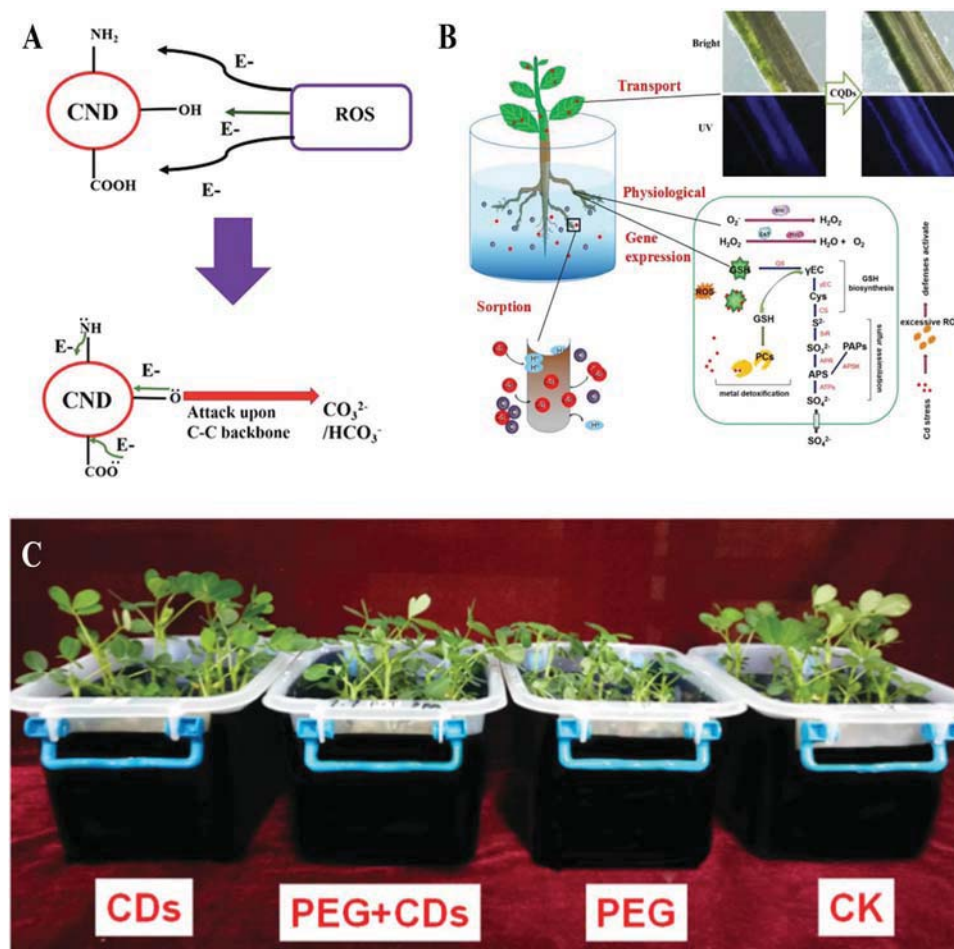


Fig. 6 (A) Mechanism for ROS scavenging<sup>69</sup> and (B) alleviating abiotic stress<sup>74</sup> of CDs; (C) anti-drought effect of CDs on peanut seedlings.<sup>27</sup> Reprinted with permission from the Royal Society of Chemistry, Copyright 2014 (ref. 69); Elsevier, Copyright 2019 (ref. 74); the American Chemical Society, Copyright 2018 (ref. 27).

mechanism, DPPH• radicals can be converted to stable DPPH-H by CDs (Fig. 6A). Additionally, Su *et al.* studied the effects of CDs on peanut growth under PEG simulated drought conditions.<sup>27</sup> It was found that drought severely inhibits the growth of peanuts, which was relieved by the CDs. The antioxidant enzyme activities in the CD-treated peanuts were further investigated and the results showed that CDs increased the activities of superoxide dismutase (SOD), peroxidase (POD) and catalase (CAT) in peanuts and reduced their malondialdehyde (MDA) content. Therefore, they concluded that CDs increased the stress resistance of peanuts, thereby alleviating the drought stress they experienced (Fig. 6C).<sup>27</sup> With the combination of radical scavenging properties and the promotion of antioxidant enzyme activities, CDs can protect plants from abiotic stress (Fig. 6B).<sup>38,70–72</sup> This function of CDs was further demonstrated using *Chlorella vulgaris*, in which CDs acting as an antioxidant can protect the plants against UV radiation damage and enhance their growth rate and biomass.<sup>63</sup> Furthermore, Li *et al.* treated wheat and citrus seedlings with CDs under their exposure to heavy metal Cd<sup>2+</sup> ions. It was found that CDs can bind with freely dissolved Cd<sup>2+</sup> ions and then inhibit their absorption into the plants. Meanwhile, CDs

prevented the Cd<sup>2+</sup>-mediated inhibition of plant growth by reinstating the anthocyanin content, promoting the activity of the antioxidant enzymes and alleviating cell membrane peroxidation damage (Fig. 6B).<sup>73,74</sup> Therefore, CDs can alleviate abiotic stress in plants, which lays the foundation for their application in environmental protection and agricultural production.

## 6.2. Biotic stress

Infection with phytopathogens is a typical biotic stress, which annually leads to severe reduction in crop production. In an *in vivo* inoculation of sheath blight, CD pre-cultured rice leaves showed high resistance to infection with the disease, since the length of the scabs on the leaves decreased by about 60% in comparison to that in the control, in seedlings aged 60 to 120 days (Fig. 7A).<sup>28</sup> A series of experimental results confirmed that CDs enter the nucleus and bond to DNA. Among the expressions of genes up-regulated by CDs, three genes were found to be related to plant–pathogen interactions, which may strongly account for the plant disease resistance though only one gene, Os06g32600 (predicted as the thionin gene), confirmed by real-time polymerase chain reaction (PCR) (Fig. 7B–D). All of



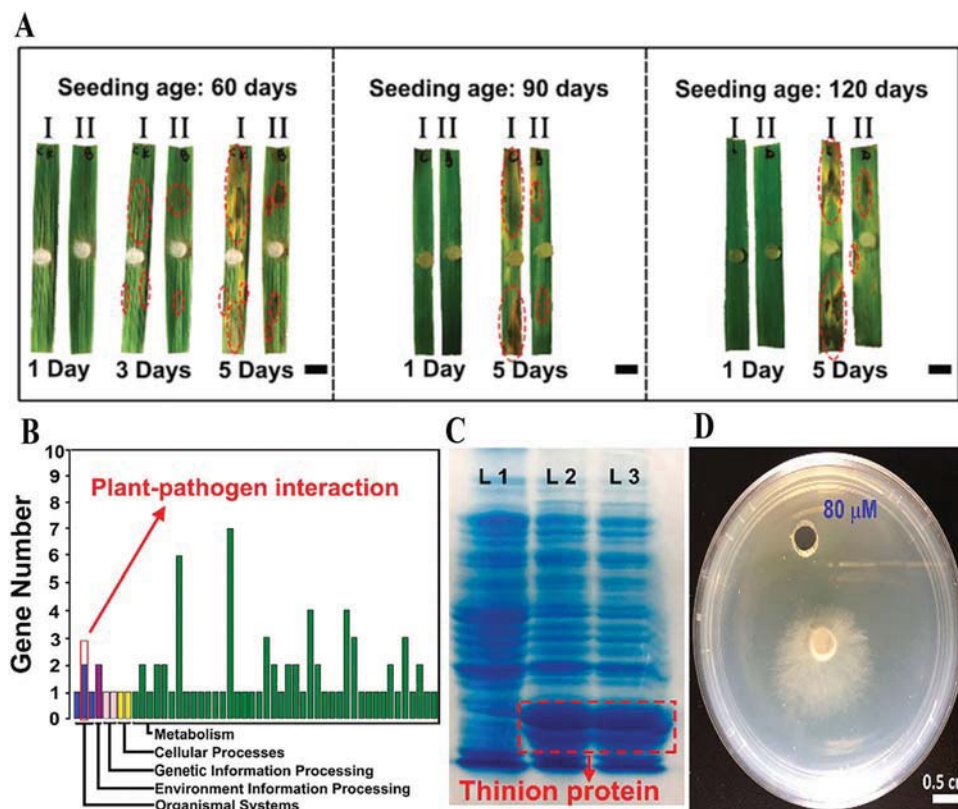


Fig. 7 (A) Digital photographs of sheath blight-infected rice leaves with and without CDs in different aged seedlings; (B) expression of plant-pathogen interaction genes of *Os06g32600*; (C) the image of nondenaturing gel electrophoresis (red traces: expression of GST-fused thionin protein). (D) The effect of *Rhizoctonia solani* growth on 80 μM pure thionin-like protein.<sup>28</sup> Reprinted with permission from the American Chemical Society, Copyright 2018 (ref. 28).

these results suggest that CD treatment may have an important function in enhancing the disease resistance of crops through inducing the over-expression of related genes.

## 7. Effects of CDs on nitrogen fixation by azotobacter chroococcum

Nitrogen is the most important nutrient for plant growth and the soil loses a lot of nitrogen every year.<sup>75</sup> The atmosphere contains an abundance of nitrogen gas ( $N_2$ ), which is not directly available to plants. Interestingly, specific nitrogen-fixing bacteria are able to convert  $N_2$  to ammonia ( $NH_3$ ) in the presence of nitrogenase, which is then available for the plant to absorb. Nitrogen fixation by nitrogen-fixing bacteria is a key stage in the nitrogen cycle.<sup>76,77</sup> Kang *et al.* conducted an investigation to study the impact of CDs on biological nitrogen fixation using azotobacter chroococcum as a model nitrogen-fixing bacterium.<sup>29</sup> In azotobacter chroococcum, they found that CDs can improve the activity of nitrogenase by affecting the secondary structure of nitrogenase and improving the electron transfer in the biocatalytic process (Fig. 8). Finally, the activity of azotobacter treated with 4 μg mL<sup>-1</sup> of CDs was increased by 158% compared to that of the control group. CDs provide an economical and environmentally friendly approach to

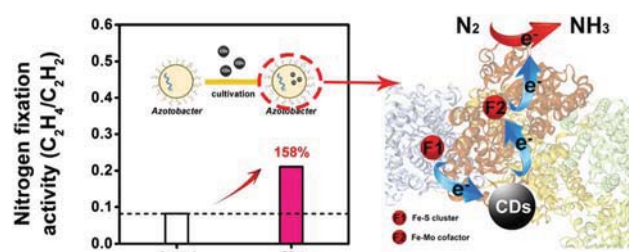


Fig. 8 Schematic representation illustrating the function of CDs in the nitrogen fixation of azotobacter chroococcum.<sup>29</sup> Adapted with permission from the American Chemical Society, Copyright 2018 (ref. 29).

improving biological nitrogen fixation by nitrogen-fixing bacteria when there is insufficient nitrogen fertilizer available in agriculture.

## 8. Antibacterial activity of CDs

In order to control the infection of phytopathogens into crops, bactericides/fungicides have been widely applied in agriculture. Ubiquitous and inefficient use of pesticides severely threatens biodiversity and ecosystem functions.<sup>3,4</sup> Up to now, various nano-materials have been applied in the control of plant disease.<sup>12,78</sup> Although there is no related application of CDs in agriculture for the control of crop diseases, the broad-spectrum antibacterial/antifungal

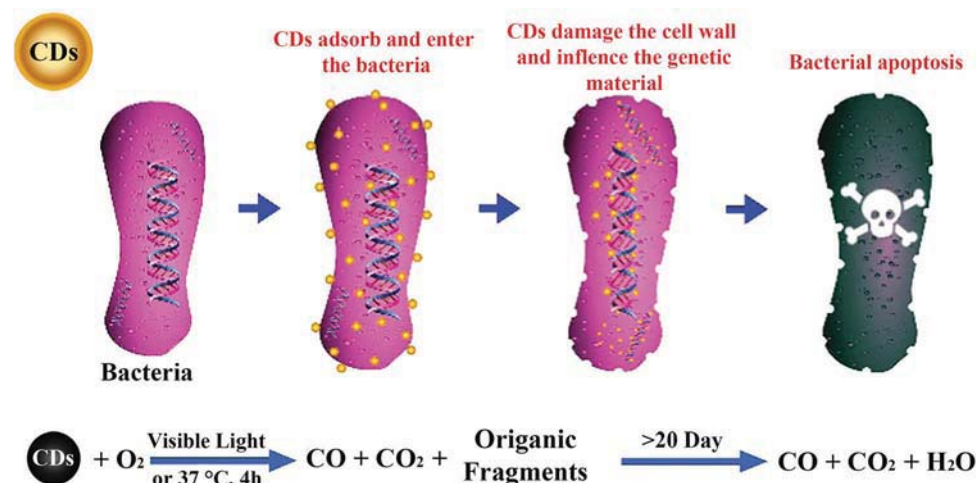


Fig. 9 Antibacterial mechanism of CDs.<sup>80</sup> Reprinted with permission from the American Chemical Society, Copyright 2018 (ref. 80).

activity of CDs has been reported, which lays the foundation for their application in the control and management of crop diseases. Yang *et al.* prepared CDs using metronidazole (a selective anaerobic microbicide), which exhibited selective antibacterial activity against obligate anaerobic microorganisms for the first time.<sup>79</sup> Subsequently, Kang's group fabricated low-toxic and degradable CDs from vitamin C and demonstrated their broad-spectrum antibacterial/antifungal activity against Gram-positive (*S. aureus* and *B. subtilis*) and Gram-negative (*Bacillus* sp. WL-6 and *E. coli*) bacteria, as well as a pathogenic fungus (*R. solani* and *P. grisea*).<sup>80</sup> Their antibacterial and antifungal mechanisms indicate that CDs can destroy bacterial walls and the secondary structures of DNA/RNA in bacteria and fungi, and finally kill them (Fig. 9). These CDs were then used as a secure and economical additive to prepare protective coatings with robust antibiofilm and anticorrosion properties.<sup>81</sup> Although these studies have laid the foundation for the applications in the control and management of crop diseases, further investigations are required on the feasibility of the antibacterial/antifungal activity of CDs prepared from different precursors as well as on phytopathogens.

## 9. Summary and outlook

Applications of CDs on crops have been an emerging theme in recent years. In this article, we reviewed the recent developments made towards the applications of CDs in agriculture, focusing on the interactions between crops and CDs in great detail. The CDs in most of the studies showed a positive effect on crop plants, including their growth and resistance against abiotic and biotic stresses, unless they were applied at higher concentrations. CDs at an optimal dose can promote the growth of crop plants through accelerating the photosynthesis and nutrition assimilation in plants as well as the nitrogen fixation of azotobacter. Due to their intrinsic free radical scavenging properties and influence on the antioxidant defense system and expression of disease-resistance genes, CDs can enhance the resistance of crops to

abiotic/biotic stresses. Besides this, CDs show broad-spectrum antibacterial activity against bacteria and fungi.

Although important progress has been achieved in this field with CDs, more efforts are still required for the applications of CDs in agriculture. (1) As demonstrated by an ever-increasing number of studies, abundant cheap and easily available starting materials and versatile easy synthesis methods have been developed for the preparation of CDs. However, their low yield is the main limitation for the application of CDs in agriculture. Besides this, due to the abundant hydrophilic groups on their surface, it is difficult to obtain CDs as a solid powder, limiting their storage and long-distance transportation prospects. Therefore, there is great demand for the preparation of solid-state CDs in a higher yield. (2) Most studies on the effects of CDs on plant focus on the growth or resistance of plants, while few efforts have been devoted to the quality of crops. In addition, studies on the systematic effect of CDs on different biological species (microorganisms, aquatic organisms, insects, *etc.*) and their fate in the environment would greatly improve our knowledge about the biological effects of CDs and their applications in agriculture. (3) The excellent photoluminescence of CDs, which is mainly employed to detect and degrade contaminants in the environment,<sup>82–84</sup> is rarely involved in their applications in plants, except for photosynthesis, whereas, it is unknown whether the function of CDs on plants depends on their photoluminescence, in terms of quantum yield, emission wavelength, *etc.* (4) The easy surface functionalization of CDs suggests that they can act as a promising deliverer of specific molecules into plants, such as pesticides, nutrients, plant growth regulators, *etc.*

## Conflicts of interest

There are no conflicts to declare.

## Acknowledgements

The present work was supported by the National Natural Science Foundation of China (Grant No. 21571067 and 21671070).

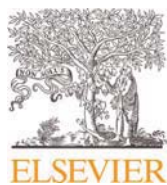
The plant pattern diagram in Scheme 1 was provided by <https://www.qianqianhua.com>.

## References

- 1 F. Pulizzi, *Nat. Nanotechnol.*, 2019, **14**, 507.
- 2 G. V. Lowry, A. Avellan and L. M. Gilbertson, *Nat. Nanotechnol.*, 2019, **14**, 517–522.
- 3 M. A. Beketov, B. J. Kefford, R. B. Schäfer and M. Liess, *Proc. Natl. Acad. Sci. U. S. A.*, 2013, **110**, 11039.
- 4 D. Goulson, *J. Appl. Ecol.*, 2013, **50**, 977–987.
- 5 C. Zhao, B. Liu, S. Piao, X. Wang, D. B. Lobell, Y. Huang, M. Huang, Y. Yao, S. Bassu, P. Ciais, J.-L. Durand, J. Elliott, F. Ewert, I. A. Janssens, T. Li, E. Lin, Q. Liu, P. Martre, C. Müller, S. Peng, J. Peñuelas, A. C. Ruane, D. Wallach, T. Wang, D. Wu, Z. Liu, Y. Zhu, Z. Zhu and S. Asseng, *Proc. Natl. Acad. Sci. U. S. A.*, 2017, **114**, 9326.
- 6 J. P. Giraldo, H. Wu, G. M. Newkirk and S. Kruss, *Nat. Nanotechnol.*, 2019, **14**, 541–553.
- 7 O. Zaytseva, G. J. C. Neumann and B. T. I. Agriculture, *Chem. Biol. Technol. Agric.*, 2016, **3**, 17.
- 8 Y. Li, Q. Jin, D. Yang and J. Cui, *J. Agric. Food Chem.*, 2018, **66**, 4013–4021.
- 9 R. Prasad, A. Bhattacharyya and Q. D. Nguyen, *Front. Microbiol.*, 2017, **8**, 1014.
- 10 P. Solanki, A. Bhargava, H. Chhipa, N. Jain and J. Panwar, in *Nanotechnologies in Food and Agriculture*, ed. M. Rai, C. Ribeiro, L. Mattoso and N. Duran, Springer International Publishing, Cham, 2015, pp. 81–101, DOI: 10.1007/978-3-319-14024-7\_4.
- 11 M. Nuruzzaman, M. M. Rahman, Y. Liu and R. Naidu, *J. Agric. Food Chem.*, 2016, **64**, 1447–1483.
- 12 Y. Li, D. Yang and J. Cui, *RSC Adv.*, 2017, **7**, 38853–38860.
- 13 C. G. Athanassiou, N. G. Kavallieratos, G. Benelli, D. Losic, P. Usha Rani and N. Desneux, *J. Pestic. Sci.*, 2018, **91**, 1–15.
- 14 H. Wu, N. Tito and J. P. Giraldo, *ACS Nano*, 2017, **11**, 11283–11297.
- 15 K. Bhattacharya, S. P. Mukherjee, A. Gallud, S. C. Burkert, S. Bistarelli, S. Bellucci, M. Bottini, A. Star and B. Fadeel, *Nanomedicine*, 2016, **12**, 333–351.
- 16 D. Chen, C. A. Dougherty, K. Zhu and H. Hong, *J. Controlled Release*, 2015, **210**, 230–245.
- 17 A. Mukherjee, S. Majumdar, A. D. Servin, L. Pagano, O. P. Dhankher and J. C. White, *Front. Plant Sci.*, 2016, **7**, 172.
- 18 T. R. Shojaei, M. A. M. Salleh, M. Tabatabaei, H. Mobli, M. Aghbashlo, S. A. Rashid and T. Tan, in *Synthesis, Technology and Applications of Carbon Nanomaterials*, ed. S. A. Rashid, R. N. I. Raja Othman and M. Z. Hussein, Elsevier, 2019, pp. 247–277, DOI: 10.1016/B978-0-12-815757-2.00011-5.
- 19 S. K. Verma, A. K. Das, S. Gantait, V. Kumar and E. Gurel, *Sci. Total Environ.*, 2019, **667**, 485–499.
- 20 A. Mukherjee, S. Majumdar, A. D. Servin, L. Pagano, O. P. Dhankher and J. C. White, *Front. Plant Sci.*, 2016, **7**, 172.
- 21 X. T. Zheng, A. Ananthanarayanan, K. Q. Luo and P. Chen, *Small*, 2015, **11**, 1620–1636.
- 22 Z. Peng, X. Han, S. Li, A. O. Al-Youbi, A. S. Bashammakh, M. S. El-Shahawi and R. M. Leblanc, *Coord. Chem. Rev.*, 2017, **343**, 256–277.
- 23 M. J. Molaei, *Talanta*, 2019, **196**, 456–478.
- 24 P. Zuo, X. Lu, Z. Sun, Y. Guo and H. He, *Microchim. Acta*, 2016, **183**, 519–542.
- 25 S. Qu, X. Wang, Q. Lu, X. Liu and L. Wang, *Angew. Chem., Int. Ed.*, 2012, **51**, 12215–12218.
- 26 H. Wang, M. Zhang, Y. Song, H. Li, H. Huang, M. Shao, Y. Liu and Z. Kang, *Carbon*, 2018, **136**, 94–102.
- 27 L.-X. Su, X.-L. Ma, K.-K. Zhao, C.-L. Shen, Q. Lou, D.-M. Yin and C.-X. Shan, *ACS Omega*, 2018, **3**, 17770–17777.
- 28 H. Li, J. Huang, F. Lu, Y. Liu, Y. Song, Y. Sun, J. Zhong, H. Huang, Y. Wang, S. Li, Y. Lifshitz, S.-T. Lee and Z. Kang, *ACS Appl. Bio Mater.*, 2018, **1**, 663–672.
- 29 H. Wang, H. Li, M. Zhang, Y. Song, J. Huang, H. Huang, M. Shao, Y. Liu and Z. Kang, *ACS Appl. Mater. Interfaces*, 2018, **10**, 16308–16314.
- 30 S. H. Schwartz, B. Hendrix, P. Hoffer, R. A. Sanders and W. Zheng, *bioRxiv, Biochem.*, 2019, 722595, DOI: 10.1101/722595.
- 31 Z. Yao, Z. Lai, C. Chen, S. Xiao and P. Yang, *Analyst*, 2019, **144**, 3685–3690.
- 32 S. Zhu, Y. Song, X. Zhao, J. Shao, J. Zhang and B. Yang, *Nano Res.*, 2015, **8**, 355–381.
- 33 W. Li, Y. Zheng, H. Zhang, Z. Liu, W. Su, S. Chen, Y. Liu, J. Zhuang and B. Lei, *ACS Appl. Mater. Interfaces*, 2016, **8**, 19939–19945.
- 34 J. Chen, R. Dou, Z. Yang, X. Wang, C. Mao, X. Gao and L. Wang, *Nanotoxicology*, 2016, **10**, 818–828.
- 35 S. Tripathi and S. Sarkar, *Appl. Nanosci.*, 2015, **5**, 609–616.
- 36 M. Zhang, L. Hu, H. Wang, Y. Song, Y. Liu, H. Li, M. Shao, H. Huang and Z. Kang, *Nanoscale*, 2018, **10**, 12734–12742.
- 37 A. Loukanov, P. Mladenova, S. Toshev, A. Karailiev, E. Ustinovich and S. Nakabayashi, *Microsc. Res. Tech.*, 2018, **81**, 1541–1547.
- 38 K. Qian, H. Guo, G. Chen, C. Ma and B. Xing, *Sci. Rep.*, 2018, **8**, 7991.
- 39 Y. Song, D. Feng, W. Shi, X. Li and H. Ma, *Talanta*, 2013, **116**, 237–244.
- 40 A. Wang, F. Kang, Z. Wang, Q. Shao, Z. Li, G. Zhu, J. Lu and Y. Y. Li, *Adv. Sustainable Syst.*, 2019, **3**, 1800132.
- 41 D. Chakravarty, M. B. Erande and D. J. Late, *J. Sci. Food Agric.*, 2015, **95**, 2772–2778.
- 42 S. Tripathi, S. Kapri, A. Datta and S. Bhattacharyya, *RSC Adv.*, 2016, **6**, 43864–43873.
- 43 Y. Zheng, H. Zhang, W. Li, Y. Liu, X. Zhang, H. Liu and B. Lei, *RSC Adv.*, 2017, **7**, 33459–33465.
- 44 Y. Zheng, G. Xie, X. Zhang, Z. Chen, Y. Cai, W. Yu, H. Liu, J. Shan, R. Li, Y. Liu and B. Lei, *ACS Omega*, 2017, **2**, 3958–3965.
- 45 H. Li, J. Huang, Y. Liu, F. Lu, J. Zhong, Y. Wang, S. Li, Y. Lifshitz, S.-T. Lee and Z. Kang, *Nano Res.*, 2019, **12**, 1585–1593.
- 46 J. Chen, B. Liu, Z. Yang, J. Qu, H. Xun, R. Dou, X. Gao and L. Wang, *Environ. Sci.: Nano*, 2018, **5**, 2672–2685.
- 47 D. R. Ort, S. S. Merchant, J. Alric, A. Barkan, R. E. Blankenship, R. Bock, R. Croce, M. R. Hanson, J. M. Hibberd,



- S. P. Long, T. A. Moore, J. Moroney, K. K. Niyogi, M. A. J. Parry, P. P. Peralta-Yahya, R. C. Prince, K. E. Redding, M. H. Spalding, K. J. van Wijk, W. F. J. Vermaas, S. von Caemmerer, A. P. M. Weber, T. O. Yeates, J. S. Yuan and X. G. Zhu, *Proc. Natl. Acad. Sci. U. S. A.*, 2015, **112**, 8529.
- 48 A. V. Barker and D. J. Pilbeam, *Handbook of plant nutrition*, CRC press, Boca Raton, 2nd edn, 2015.
- 49 L. Király, B. Barna and Z. Király, *J. Phytopathol.*, 2007, **155**, 385–396.
- 50 S. J. Roy, E. J. Tucker and M. Tester, *Curr. Opin. Plant Biol.*, 2011, **14**, 232–239.
- 51 A. R. Fox, G. Soto, C. Valverde, D. Russo, A. Lagares Jr, Á. Zorreguieta, K. Alleva, C. Pascuan, R. Frare, J. Mercado-Blanco, R. Dixon and N. D. Ayub, *Environ. Microbiol.*, 2016, **18**, 3522–3534.
- 52 A. Segalla, I. Szabò, P. Costantini and G. M. Giacometti, *J. Chem. Inf. Model.*, 2005, **45**, 1691–1700.
- 53 M. Paul, *Ann. Bot.*, 2012, **111**, ix.
- 54 L. Cao, S. Sahu, P. Anilkumar, C. E. Bunker, J. Xu, K. A. S. Fernando, P. Wang, E. A. Gulians, K. N. Tackett and Y.-P. Sun, *J. Am. Chem. Soc.*, 2011, **133**, 4754–4757.
- 55 S. Mitra, S. Chandra, P. Patra, P. Pramanik and A. Goswami, *J. Mater. Chem.*, 2011, **21**, 17638–17641.
- 56 S. N. Baker and G. A. Baker, *Angew. Chem., Int. Ed.*, 2010, **49**, 6726–6744.
- 57 H. Li, Z. Kang, Y. Liu and S.-T. Lee, *J. Mater. Chem.*, 2012, **22**, 24230–24253.
- 58 Y. Gong and J. Zhao, *J. Agric. Food Chem.*, 2018, **66**, 9159–9161.
- 59 Y. Wang and A. Hu, *J. Mater. Chem. C*, 2014, **2**, 6921–6939.
- 60 S. Chandra, S. Pradhan, S. Mitra, P. Patra, A. Bhattacharya, P. Pramanik and A. Goswami, *Nanoscale*, 2014, **6**, 3647–3655.
- 61 W. Li, S. Wu, H. Zhang, X. Zhang, J. Zhuang, C. Hu, Y. Liu, B. Lei, L. Ma and X. Wang, *Adv. Funct. Mater.*, 2018, **28**, 1804004.
- 62 C. Huang, T. Xia, J. Niu, Y. Yang, S. Lin, X. Wang, G. Yang, L. Mao and B. Xing, *Angew. Chem., Int. Ed.*, 2018, **57**, 9759–9763.
- 63 M. Zhang, H. Wang, Y. Song, H. Huang, M. Shao, Y. Liu, H. Li and Z. Kang, *ACS Appl. Bio Mater.*, 2018, **1**, 894–902.
- 64 L. Sai, S. Liu, X. Qian, Y. Yu and X. Xu, *Colloids Surf., B*, 2018, **169**, 422–428.
- 65 G. R. Cramer, K. Urano, S. Delrot, M. Pezzotti and K. Shinozaki, *BMC Plant Biol.*, 2011, **11**, 163.
- 66 F. K. Choudhury, R. M. Rivero, E. Blumwald and R. Mittler, *Plant J.*, 2017, **90**, 856–867.
- 67 S. S. Gill and N. Tuteja, *Plant Physiol. Biochem.*, 2010, **48**, 909–930.
- 68 S. Zhao, M. Lan, X. Zhu, H. Xue, T.-W. Ng, X. Meng, C.-S. Lee, P. Wang and W. Zhang, *ACS Appl. Mater. Interfaces*, 2015, **7**, 17054–17060.
- 69 B. Das, P. Dadhich, P. Pal, P. K. Srivas, K. Bankoti and S. Dhara, *J. Mater. Chem. B*, 2014, **2**, 6839–6847.
- 70 H. Wang, Y. Xie, X. Na, J. Bi, S. Liu, L. Zhang and M. Tan, *Food Chem.*, 2019, **286**, 405–412.
- 71 Y. Chong, C. Ge, G. Fang, X. Tian, X. Ma, T. Wen, W. G. Wamer, C. Chen, Z. Chai and J.-J. Yin, *ACS Nano*, 2016, **10**, 8690–8699.
- 72 F. Li, T. Li, C. Sun, J. Xia, Y. Jiao and H. Xu, *Angew. Chem., Int. Ed.*, 2017, **56**, 9910–9914.
- 73 L. Xiao, H. Guo, S. Wang, J. Li, Y. Wang and B. Xing, *Environ. Sci.: Nano*, 2019, **6**, 1493–1506.
- 74 J. Li, L. Xiao, Y. Cheng, Y. Cheng, Y. Wang, X. Wang and L. Ding, *Chemosphere*, 2019, **236**, 124385.
- 75 B. B. Bohlool, J. K. Ladha, D. P. Garrity and T. George, *Plant Soil*, 1992, **141**, 1–11.
- 76 B. M. Hoffman, D. Lukyanov, Z.-Y. Yang, D. R. Dean and L. C. Seefeldt, *Chem. Rev.*, 2014, **114**, 4041–4062.
- 77 J. Kim and D. C. Rees, *Biochemistry*, 1994, **33**, 389–397.
- 78 A. Servin, W. Elmer, A. Mukherjee, R. De la Torre-Roche, H. Hamdi, J. C. White, P. Bindraban and C. Dimkpa, *J. Nanopart. Res.*, 2015, **17**, 92.
- 79 J. Liu, S. Lu, Q. Tang, K. Zhang, W. Yu, H. Sun and B. Yang, *Nanoscale*, 2017, **9**, 7135–7142.
- 80 H. Li, J. Huang, Y. Song, M. Zhang, H. Wang, F. Lu, H. Huang, Y. Liu, X. Dai, Z. Gu, Z. Yang, R. Zhou and Z. Kang, *ACS Appl. Mater. Interfaces*, 2018, **10**, 26936–26946.
- 81 C. Zhu, H. Li, H. Wang, B. Yao, H. Huang, Y. Liu and Z. Kang, *Small*, 2019, **15**, 1900007.
- 82 A. Bhati, S. R. Anand, Gunture, A. K. Garg, P. Khare and S. K. Sonkar, *ACS Sustainable Chem. Eng.*, 2018, **6**, 9246–9256.
- 83 H. Wang, J. Zhuang, D. Velado, Z. Wei, H. Matsui and S. Zhou, *ACS Appl. Mater. Interfaces*, 2015, **7**, 27703–27712.
- 84 H. Safardoust-Hojaghan and M. Salavati-Niasari, *J. Cleaner Prod.*, 2017, **148**, 31–36.



## Communication

## Red, green and blue aggregation-induced emissive carbon dots

Xiaokai Xu<sup>a,b</sup>, Luoqi Mo<sup>a,b</sup>, Wei Li<sup>a,b</sup>, Yadong Li<sup>a,b</sup>, Bingfu Lei<sup>a,b</sup>, Xuejie Zhang<sup>a,b</sup>, Jianle Zhuang<sup>a,b,\*</sup>, Chaofan Hu<sup>a,b,\*</sup>, Yingliang Liu<sup>a,b,\*</sup>

<sup>a</sup>Key Laboratory for Biobased Materials and Energy of Ministry of Education/Guangdong Provincial Engineering Technology Research Center for Optical Agriculture, College of Materials and Energy, South China Agricultural University, Guangzhou 510642, China

<sup>b</sup>Guangdong Laboratory for Lingnan Modern Agriculture, Guangzhou 510642, China

## ARTICLE INFO

## Article history:

Received 3 March 2021

Revised 21 May 2021

Accepted 24 May 2021

Available online 8 June 2021

## Keywords:

Carbon dots

Solid-state fluorescence

Multicolor

LED

Fingerprint detection

## ABSTRACT

As one of the most promising fluorescent nanomaterials, carbon dots (CDs) have been extensively studied for their fluorescent properties in solution. However, research on the synthesis of multicolor solid-state fluorescence (SSF) CDs (from blue to red) is rarely reported. Herein, we used *o*-phenylenediamine, *m*-phenylenediamine and *p*-phenylenediamine with dithiosalicylic acid (DTSA) in the solvothermal reaction using acetic acid as a solvent to obtain aggregation-induced emissive (AIE) CDs of red (620 nm), green (520 nm), and blue (478 nm), respectively. XPS spectra and TEM image show that with the red-shift of luminescence, the particle size and content of C=O of the CDs gradually increases. Finally, based on the non-matrix solid-state multicolor luminescence characteristics of CDs, the application of white light LED devices is realized. Besides, based on the fat-soluble properties of CDs, fingerprint detection applications are realized.

© 2021 Published by Elsevier B.V. on behalf of Chinese Chemical Society and Institute of Materia Medica, Chinese Academy of Medical Sciences.

Carbon dots (CDs) are a kind of carbon-based luminescent nanomaterials that have emerged in recent years [1–4]. Easy preparation and purification, adjustable optical and surface properties, and superior biocompatibility make them as fascinating luminescent materials [5–7]. However, CDs in solid-state tend to aggregation-caused quenching (ACQ) like organic molecules due to excessive resonance energy transfer (RET) or direct  $\pi$ - $\pi$  interactions [8–10]. Therefore, most researchers embed CDs in solid substrates to realize the solid-state self-stable state of CDs-based composites [11–13]. However, these methods are complicated and the CDs loading rate is low. It is difficult to maintain the excellent fluorescence performance in the CDs aqueous solution, and the high loading fraction still leads to a serious decrease in the PLQYs of CDs [14,15].

Realizing the SSF of CDs still faces severe challenges [4]. Although there are various reports on CDs with high QY in solution [15–18], it seems difficult to avoid the strong quenching effect in SSF CDs. Some recent studies have shown that some CDs have been found to achieve effective SSF and resistance to self-quenching [19–21]. Possible solution is to introduce a certain steric hindrance between the CD particles. For example, the CD can be

kept at a proper interval by introducing a long chain structure on the outer surface to reduce the CD interaction and ensure the SSF of CDs [10,22,23]. However, to meet the strong demand for white light SSF materials for LEDs, it is still a key challenge for the synthesis of CDs with multicolor SSF. One of the main characteristics of quantum dots is that they tend to exhibit quantum confinement effects [24]. These effects occur when the CDs are smaller than their exciton Bohr radius. In general, the size, doping, and functionalization of CDs affect their luminescence performance [25–27]. According to molecular orbital theory, the smaller the particle, the bluer the shift in emission frequency (that is, it shifts to higher energy).

Based on the above situation, we found a method that can effectively maintain the CDs of SSF, rather than introducing CDs into the solid-state dispersion system. The solvothermal reaction of dithiosalicylic acid (DTSA) with *o*-phenylenediamine (*o*-PD), *m*-phenylenediamine (*m*-PD), and *p*-phenylenediamine (*p*-PD) in acetic acid solution generates red, green, and blue SSF CDs, respectively. First, 490.16 mg of DTSA was dissolved in 40 mL of acetic acid solution with stirring until dissolved completely. Then 137.02 mg of *o*-PD was added to the mixed solution and stirred for 1 h. Subsequently, the mixed solution was transferred into the 100 mL Teflon reactor and kept at 180 °C for 10 h. After cooling down to room temperature naturally, the reaction solution was poured into 1 L boiling water, then it was filtered and dried to get

\* Corresponding authors.

E-mail addresses: [zhuangjl@scau.edu.cn](mailto:zhuangjl@scau.edu.cn) (J. Zhuang), [thucf@scau.edu.cn](mailto:thucf@scau.edu.cn) (C. Hu), [ltiuyt@scau.edu.cn](mailto:ltiuyt@scau.edu.cn) (Y. Liu).

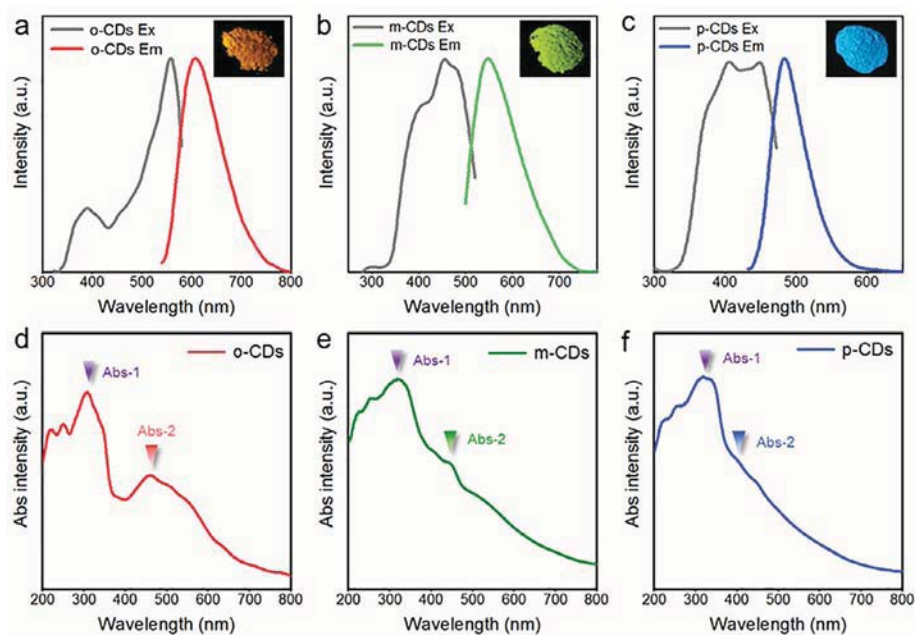


**Fig. 1.** PL excitation and emission spectra of o-CDs (a), m-CDs (b), and p-CDs (c). Inset image: photographs of m-CDs, o-CDs, and p-CDs. (d–f) UV-vis absorption spectra of o-CDs, m-CDs, and p-CDs, separately.

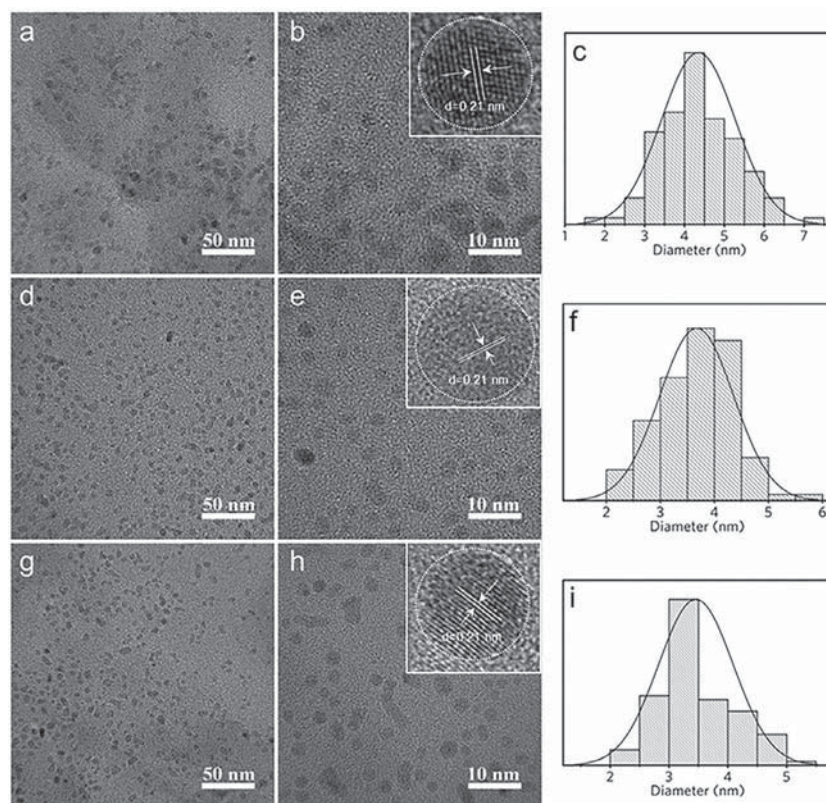


**Fig. 2.** TEM images of o-CD (a, b), m-CD (d, e), and p-CDs (g, h) and corresponding HRTEM images inserted. (c, f, i) Particles size distribution of o-CD, m-CD, and p-CDs measured by TEM images.

pure o-CDs. The preparation of m-CDs and p-CDs is in the similar way. The position of the amino group in the aniline in the reaction precursor is changed to adjust the emission color of the SSF CDs, and the quantum yield (QY) reaches 20.77%.

As described above, DTSA was chosen as the carbon source and sulfur source and phenylenediamines as the nitrogen source

attributed to its large conjugated structure, which can increase the conjugated  $\pi$ -domain and synthesize narrow bandgap CDs for long-wavelength emission. Surprisingly, the o-CDs, m-CDs, and p-CDs powders display red, green, and blue PL emission as shown in Figs. 1a–c. Optimum excitation of o-CDs, m-CDs, and p-CDs powders is 560 nm, 460 nm, 460 nm, and optimum emis-



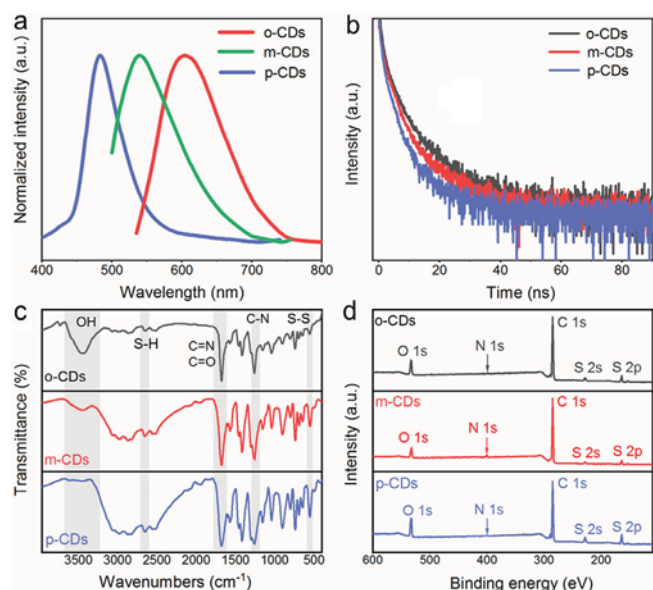


Fig. 3. (a) Normalized PL, (b) Lifetime, (c) FT-IR, and (d) XPS spectra of o-CDs, m-CDs, and p-CDs.

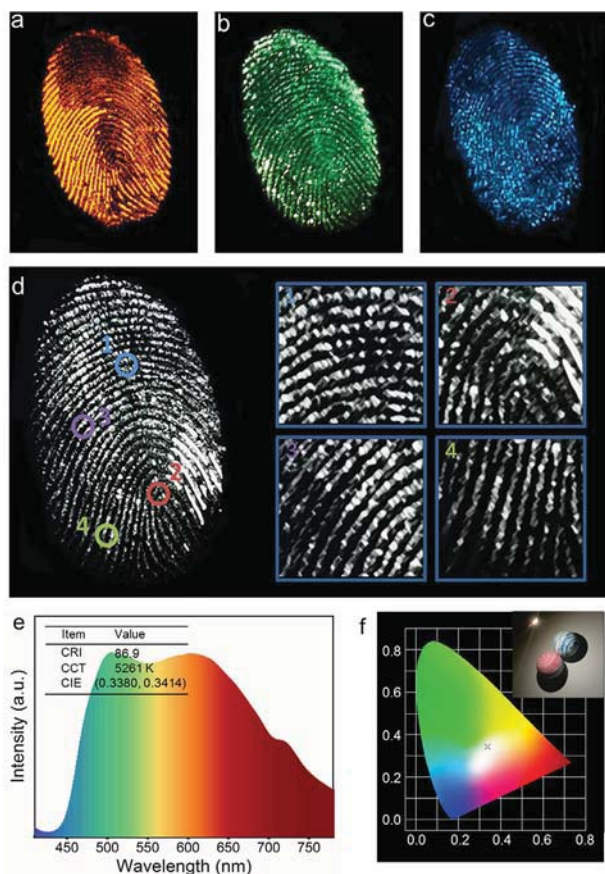


Fig. 4. (a-d) Photographs of the o-CD, m-CD, p-CD and tripartite mixed powder-stained latent fingerprints (LFPs) on glass substrates under UV light irradiation, respectively. (d1-d4) Photographs of the tripartite mixed powder magnified images showing four kinds of details in LFPs. (e) Emission spectrum of working WLED prepared by o-CD, m-CD, and p-CD mixed powder operated at 3.5 V. (f) CIE coordinates of o-CD, m-CD, and p-CD mixed powder under UV light (365 nm). Inset: the image of working WLED.

sion of o-CDs, m-CDs, and p-CDs powders is 620 nm, 560 nm, 478 nm, respectively. The spectra in Figs. 1d-f reveal that all of the Abs-1 wavelengths of o-CDs, m-CDs, and p-CDs are in the range of 250–350 nm, with corresponding Abs-2 wavelengths of about 450–550 nm, 450 nm, and 400 nm, respectively. Furthermore, Abs-2 matches the fluorescence optimum excitation center (Figs. 1a-c) well, indicating that emission centers of CDs contribute to Abs-2 bands, but the absorption peaks at 250–350 nm do not.

The three typical CDs are examined by transmission electron microscopy (TEM) to study their sizes. In Figs. 2a, d and g, the TEM images reveal that these CDs are homogeneous and well dispersed, with average particle sizes of about 4.5 nm, 4.0 nm and 3.5 nm for o-CDs, m-CDs, and p-CDs (Figs. 2c, f and i), respectively. Moreover, it can be seen that the central wavelength of the emission spectra shifts to a longer wavelength with the increase of the particle size. The high resolution TEM (HRTEM) images (Figs. 2b, e and h) show that all samples have similar well resolved lattice fringes with a spacing of 0.21 nm, attributed to the (100) lattice distance of the graphitic carbon. Normalized PL spectra of o-CDs, m-CDs, and p-CDs show that the fluorescence peak width gradually narrows with the blue shift of the luminescence (Fig. 3a). Time-resolved PL decay curves were measured for the different emissions of these samples under 450 nm excitation, the average lifetime of o-CDs, m-CDs, and p-CDs were measured to be 3.16, 2.85 and 2.11 ns, respectively (Fig. 3b and Table S1 in Supporting information).

The functional groups were characterized by Fourier transform infrared (FT-IR) and X-ray photoelectron spectroscopy (XPS). Fig. 3c shows the FT-IR absorption band at 3505  $\text{cm}^{-1}$  is assigned to the O–H stretching vibration. The absorption band at 2651  $\text{cm}^{-1}$  is ascribed to S–H stretching vibration and the absorption band at 1677  $\text{cm}^{-1}$  is ascribed to C=N/C=O stretching vibration. Besides, CDs obtained by solvothermal synthesis reserve the S–S bond at 554  $\text{cm}^{-1}$ . These functional groups could play roles in serving as sub-fluorophores for producing PL. In Fig. 3d and Table S2 (Supporting information), the full XPS spectra display five typical peaks at 164, 228, 285, 400 and 532 eV for S 2p, S 2s, C 1s, N 1s, and O 1s, respectively, indicating that all the CDs consisted of the same elements. In the high resolution XPS spectra (Fig. S1 and Table S3 in Supporting information), the S 2p spectra display three peaks at 162.7, 163.1 and 164.1 eV which can be attributed to S–C, S–H, and S–S, respectively. These three high-resolution spectra collectively indicate the successful insertion of S and N atoms into these CDs. However, the nitrogen content in o-CDs and p-CDs is low, the nitrogen in m-CDs contains two peaks at 398.9 and 399.6 eV, ascribing to graphite nitrogen and N–H (Fig. S1). The QY of o-CDs, m-CDs, and p-CDs is 4.05%, 20.77%, and 1.76%, which is attributed to the synergistic effect between carbon and nitrogen (Table S4 in Supporting information). The C 1s band can be deconvoluted into four binding energy peaks at 283.7, 284.3 and 288.1 eV, which could be assigned to C–C/C=C, C–N/C–O and C=N/C=O, respectively (Fig. S1 and Table S5 in Supporting information). The O 1s spectra contain two peaks at 531.1 and 533.3 eV for C=O and C–OH/C–O–C bands, respectively (Fig. S1 and Table S6 in Supporting information). The atomic ratio between carbon and oxygen decreases from 11.09% (o-CDs) to 5.47% (p-CDs), suggesting a decreasing degree of graphitization in these CDs (Table S2). Moreover, the C=O gradually decreases from 63.85% (o-CDs) to 42.58% (p-CDs), implying emission red-shift may be related to C=O on the surface of CDs. In brief, o-CDs, m-CDs, and p-CDs have abundant oxygen/nitrogen surface groups, and the CD's particle sizes decrease and their PL emission shift from red to blue. To further reveal the photoluminescence mechanism of CDs, we analyzed the PL spectra of CDs in solution as shown in Fig. S2 (Supporting information). When water is introduced, the hydrophobic effect causes the aggregation of CDs, so the CDs maintain their SSF characteristics in water. When dis-

solved in acetic acid, o-CDs, m-CDs, and p-CDs exhibit blue, green, and blue fluorescence, respectively. These phenomena reveal that o-CDs conform to the phenomenon of aggregation-induced emission (AIE) [21]. The surface groups of o-CDs may rotate around the intramolecular S-S bonds and consume the absorbed energy in the dissolved state, so o-CDs solution will not produce red fluorescence and exhibit similar PL characteristics as the reported blue emission CDs. However, in the solid-state, as a result of the intramolecular rotation being banned, the excitation energy can transfer dominantly into fluorescence [21]. When fully dispersed as a homogeneous solution, m-CDs and p-CDs do not conform to the AIE phenomenon and exhibit the same luminous color as solid.

Figs. 4a–c displays the images of latent fingermarks after being applied with o-CDs, m-CDs, p-CDs, and tripartite mixture excited by UV light source, where each image of fingermarks in a different color are bright and clear. A possible mechanism of good effect was that the extremely small size and lipophilic characteristics of the nanomaterial increased the adhesion of the nanoparticle to fingermark. In contrast, the glossy and sharpened fingermark white-light image with better contrast and more details can be attained through the treatment of tripartite mixture excited at 365 nm (Fig. 4d). Besides, the WLED may be achieved solely by those CDs phosphors with appropriate commercial UV chips. As shown in Figs. 4e and f, warm-white light LEDs with high color rendering index of 86.9 approaching the coordinate (0.3380, 0.3414) can be achieved by a mixture of o-CDs, m-CDs, and p-CDs. Under 400 nm excitation wavelength, variable temperature spectroscopy image (Fig. S3 in Supporting information) shows that fluorescence intensity of o-CDs, m-CDs, and p-CDs remained stable as the temperature increased from 303 K to 443 K. When the temperature reached 443 K, the PL intensity can still remain 75% of the PL intensity at 303 K. The results show that the PL intensities remain nearly unchanged, indicating high thermal stability of those CDs.

In short, the multicolor SSF of CDs were prepared by the one-pot solvothermal method. In the aggregate state, these CDs can resist self-quenching and maintain stable fluorescence emission. Through data analysis, there are abundant S-S, C=O, C=N, and other functional groups on the surface of the CDs. The degree of graphitization and the increase of C=O content of CDs are the main reasons for emission redshift. Besides, the particle size of the CDs shows a trend of o-CDs > m-CDs > p-CDs, that is, as the particle size of the CDs becomes larger, the emission redshifts. On this basis, white light LEDs were prepared using hybrid multi-color SSF-CDs. It can also be used for fingerprint recognition to meet different application.

## Declaration of competing interest

The authors declare that they have no known competing financial interests or personal relationships that could have appeared to influence the work reported in this paper.

## Acknowledgments

This work was supported by the National Natural Science Foundation of China (No. 51602108), the Guangdong Basic and Applied Basic Research Foundation (Nos. 2020A1515011210, 2017A030313256), and Guangzhou Science and Technology Project (Nos. 202007020005, 202102080288).

## Supplementary materials

Supplementary material associated with this article can be found, in the online version, at doi:10.1016/j.ccl.2021.05.056.

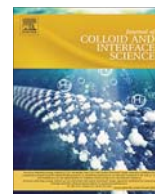
## References

- [1] D. Yoo, Y. Park, B. Cheon, M.H. Park, *Nanoscale Res. Lett.* 14 (2019) 272.
- [2] Y.J. Chung, J. Kim, C.B. Park, *ACS Nano* 14 (2020) 6470–6497.
- [3] S. Tao, S. Zhu, T. Feng, C. Zheng, B. Yang, *Angew. Chem. Int. Ed.* 59 (2020) 9826–9840.
- [4] A. Xu, G. Wang, Y. Li, et al., *Small* 16 (2020) 2004621.
- [5] K.K. Chan, S.H.K. Yap, K.T. Yong, *Nano-Micro Lett.* 10 (2018) 72.
- [6] D.L. Zhao, T.S. Chung, *Water Res.* 147 (2018) 43–49.
- [7] X.T. Tian, X.B. Yin, *Small* 15 (2019) 1901803.
- [8] C.L. Chiang, M.T. Wu, D.C. Dai, et al., *Adv. Funct. Mater.* 15 (2005) 231–238.
- [9] Y. Ooyama, S. Yoshikawa, S. Watanabe, K. Yoshida, *Org. Biomol. Chem.* 4 (2006) 3406–3409.
- [10] Y. Chen, M. Zheng, Y. Xiao, et al., *Adv. Mater.* 28 (2016) 312–318.
- [11] C.L. Shen, Q. Lou, C.F. Lv, et al., *Adv. Sci.* 6 (2019) 1802331.
- [12] Y. Wang, S. Kalytchuk, Y. Zhang, et al., *J. Phys. Chem. Lett.* 5 (2014) 1412–1420.
- [13] C.L. Chiang, M.F. Wu, D.C. Dai, et al., *Adv. Funct. Mater.* 15 (2005) 231–238.
- [14] F. Yan, Y. Jiang, X. Sun, et al., *Nano Res.* 13 (2020) 52–60.
- [15] S. Qu, D. Zhou, D. Li, et al., *Adv. Mater.* 28 (2016) 3516–3521.
- [16] K. Zheng, X. Li, M. Chen, et al., *Chem. Eng. J.* 380 (2020) 122503.
- [17] S.Y. Lu, R.D. Cong, S.J. Zhu, et al., *ACS Appl. Mater. Interfaces* 8 (2016) 4062–4068.
- [18] S. Lu, L. Sui, J. Liu, et al., *Adv. Mater.* 29 (2017) 1603443.
- [19] D. Zhou, P. Jing, Y. Wang, et al., *Nanoscale Horiz* 4 (2019) 388–395.
- [20] Y. Zhang, P. Zhuo, H. Yin, et al., *ACS Appl. Mater. Interfaces* 11 (2019) 24395–24403.
- [21] H. Yang, Y. Liu, Z. Guo, et al., *Nat. Commun.* 10 (2019) 1789.
- [22] B.P. Jiang, Y.X. Yu, X.L. Guo, et al., *Carbon* 128 (2018) 12–20.
- [23] S. Tao, S. Lu, Y. Geng, et al., *Angew. Chem. Int. Ed.* 57 (2018) 2393–2398.
- [24] M.A. Sk, A. Ananthanarayanan, L. Huang, K.H. Lim, P. Chen, *J. Mater. Chem. C* 2 (2014) 6954–6960.
- [25] Y.F. Shen, Y. Liang, Y.P. Wang, C.L. Liu, X.Y. Ren, *J. Nanopart. Res.* 20 (2018) 229.
- [26] T.H.T. Dang, V.T. Mai, Q.T. Le, N.H. Duong, X.D. Mai, *Chem. Phys.* 527 (2019) 110503.
- [27] S. Do, W. Kwon, Y.H. Kim, et al., *Adv. Opt. Mater.* 4 (2016) 276–284.



Contents lists available at ScienceDirect

## Journal of Colloid and Interface Science

journal homepage: [www.elsevier.com/locate/jcis](http://www.elsevier.com/locate/jcis)

## Regular Article

## Synthesis of dual-emissive carbon dots with a unique solvatochromism phenomenon

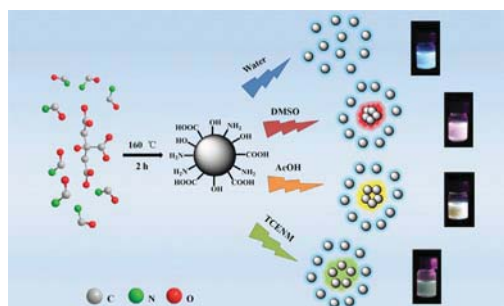


Shuangshuang Wu, Wei Li, Yuqiong Sun, Xuejie Zhang, Jianle Zhuang, Hang Hu, Bingfu Lei\*, Chaofan Hu\*, Yingliang Liu\*

Guangdong Provincial Engineering Technology Research Center for Optical Agriculture, College of Materials and Energy, South China Agricultural University, Guangzhou 510642, China

## GRAPHICAL ABSTRACT

In our work, a type of CDs is designed to realize continuously tunable multicolor emission by simply adjusting the solvents. Schematic illustration of the formation of DS-CDs and possible dispersion morphology of DS-CDs in diverse polar solvents.



## ARTICLE INFO

## Article history:

Received 28 April 2019

Revised 5 July 2019

Accepted 29 July 2019

Available online 29 July 2019

## Keywords:

Dual-emissive

Solvatochromism

Hydrogen bonding

Aggregation

Ratio fluorescent approach

## ABSTRACT

Carbon dots as an emerging photoluminescent material has attracted growing attention. Hence, there is a highly urgent to develop kinds of multicolor emission carbon dots materials. Here, we report a new kind of dual-emissive carbon dots which display two emission band located at 457 and 643 nm (blue and red) in alcohols solvent, respectively. In particular, the red emission band of carbon dots independent of the excitation wavelength can be manipulated by changing the polarity of the solvent, which is called solvatochromic phenomenon. It is incredibly rare for bare carbon dots to have both dual-emission and solvatochromic phenomenon at the same time. The temperature-dependent emission spectra of synthesized carbon dots have been measured to go insight into the hydrogen bond interaction, and the aggregation in microscale is observed by transmission electron microscopy. Results indicates that the special dual-emission and solvatochromic phenomenon stem from partially nanoparticle agglomerates which caused by intermolecular hydrogen bond (between solvents and carbon dots). Benefiting from the special optical characteristics, the applications of ratiometric detecting water in ethanol was carried out.

© 2019 Published by Elsevier Inc.

## 1. Introduction

For the past few years, much attention has been paid to carbon-base nanomaterial which consist of a widespread common and pollution free element—carbon. The carbon-based materials had

\* Corresponding authors.

E-mail addresses: [tlei@scau.edu.cn](mailto:tlei@scau.edu.cn) (B. Lei), [thucf@scau.edu.cn](mailto:thucf@scau.edu.cn) (C. Hu), [tiuyyl@scau.edu.cn](mailto:tiuyyl@scau.edu.cn) (Y. Liu).<https://doi.org/10.1016/j.jcis.2019.07.089>

0021-9797/© 2019 Published by Elsevier Inc.



been investigated wildly in the nanotechnology field [1–3]. Luminescent carbon dots (CDs) as an extremely small carbon material possesses various advantages for simple synthetic [4,5], tunable emission spectrum [6,7], low toxicity [1,8], and environment-friendliness, which have already played a potential role in imaging [9,10], sensing [11,12], photocatalysis [13,14] and photovoltaics [15,16]. However, some of the major shortcoming of CDs usually show short-wavelength from blue to green light emission and lack of multicolor emissive products. Hence, there is a highly urgent to develop kinds of multicolor emission CDs materials and to investigate the mechanisms of multicolor emission.

Dual-emissive phenomenon of CDs as a novel and important phenomenon of carbon dots was studied in the past few years. Although a few researchers have advanced the viewpoint of the fluorescence of CDs are ascribed to quantum confinement effect of the carbon core or the energy gap trap of surface-localized states, the origin of the dual-emissive CDs is until now still unclear [17–22]. However, among the previous research results (Table S1), those optical properties of CDs were only studied in water. And their emission originations were simply summarized as from carbon core emission and surface functional groups emission. Therefore, it is greatly need to develop a practical method to achieve CDs with multicolor emission, and its related mechanism of carbon dots emission should be further discussed in detail.

Solvatochromism as an important optical phenomenon was also observed when we disperse our CDs in diverse solvents. So far, some reports have described and explained tunable photoluminescence emission wavelength of CDs by varying the polarity of solvents. For example, Zhang et al. prepared solvent-dependent CDs by hydrothermal method using *o*-phenylenediamine as carbon source, which emission wavelength ranges from 512 to 565 nm [23]. Yu and coworkers found that when dispersed in different solvents, the CDs synthesized from *p*-phenylenediamine has a emission wavelength ranging from 511 to 615 nm [24]. Pan et al. selected 1,3,6-trinitropyrene as precursors to prepare CDs and achieved tunable fluorescence emission wavelength from 606 to 662 nm via changing the polarity of solvent [25]. Xie and coworkers synthesized one kind of CDs from (Z)-4-(2-cyano-2-(4'-(diphenylamino)-[1,1'-biphenyl]-4-yl)-vinyl)benzonitrile and PEG2k which showed various fluorescence emission wavelength from 606 to 662 nm through changing the polarity of solvents [26]. The above research results all ascribed solvatochromism phenomenon changes the density distribution of surface electron cloud. In other words, when changing the polarity of solvent, the surface electronic state was influenced by the hydrogen bond interaction. However, the action mechanism of hydrogen bond has not been clearly and intuitively explained. Therefore, it's a meaningful work to explore how exactly did solvatochromism phenomenon happen. Although aggregation-induced emission (AIE) has been found in CDs in recent years, no research connected solvatochromism with AIE yet [27–30]. Nevertheless, there is no research connect solvatochromism with AIE. In response to this issue, we develop a connection among solvatochromism, hydrogen bond and AIE.

In this paper, we prepared a new kind of dual-emissive solvatochromic carbon dots (DS-CDs) from citric acid and formamide by solvothermal method under the atmosphere of nitrogen. The synthetic CDs exhibit blue/red dual-emission in alcohols solvent (which display one emission band located at 457 nm and the other located at 643 nm), and the solvatochromism phenomenon of the DS-CDs was discussed in several diverse polar solvents. The key role of hydrogen bond for solvatochromism between CDs and solvents were inspected by temperature-dependent emission spectra. The aggregation in microscale was observed by transmission electron microscopy, and the cause of dual-emission stems from partially nanoparticle agglomerates was demonstrated. Through

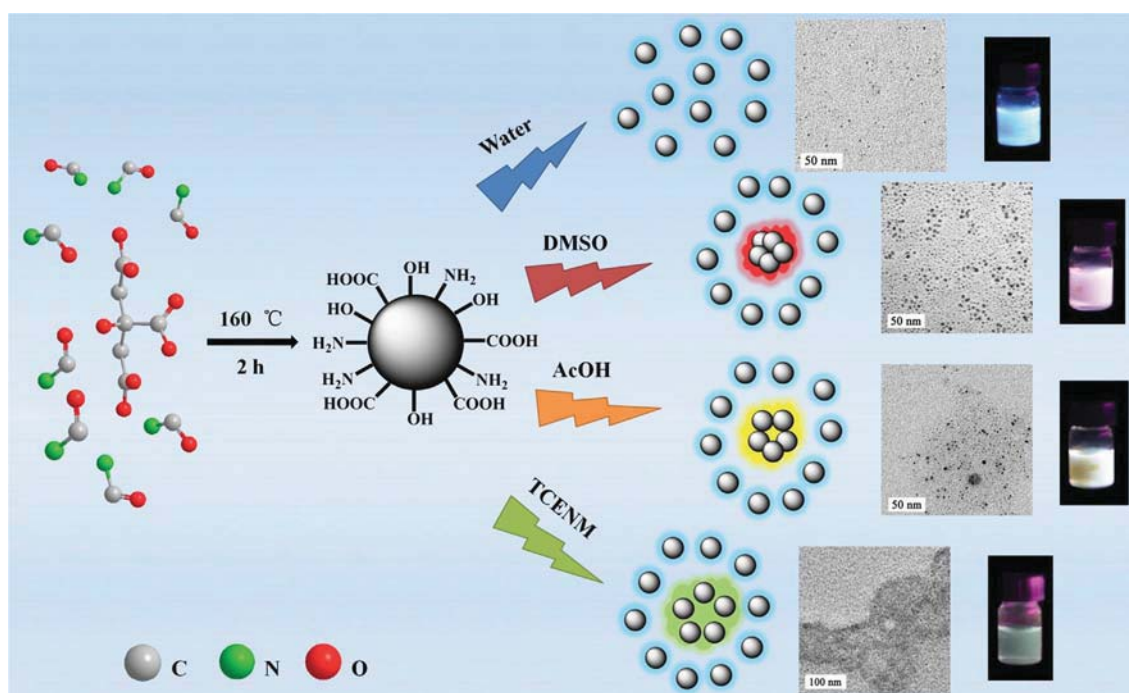
spectroscopy and microstructures measurement, the results show that the solvatochromism originates from specific hydrogen bond interactions between CDs and solvents (which caused partially nanoparticle agglomerates eventually). That is, the hydrogen bond interactions between CDs and solvents are going to cause partially nanoparticle agglomerates, and then, forming such a solvatochromism coexist with dual-emissive phenomenon of CDs in different solvents. As a result, a much simpler and more efficient radiometric detecting water content in ethanol was realized based on the as-synthesized DS-CDs.

## 2. Results and discussion

The details of how DS-CDs is synthesized are given in the Experimental Section (Scheme 1, S1). In order to know the microstructure of the synthetic DS-CDs, high resolution transmission electron microscopy (HR-TEM), X-ray diffraction (XRD), and Raman spectroscopy were performed. Fig. 1a shows the HRTEM image of the DS-CDs, which was visible particulate, exhibited a good agreement among the mean particle size around 3.51 nm (Fig. 1b), and discernible lattice structures reveal an crystalline interplanar spacing of 0.21 nm, which is corresponding to the (1 0 0) facet of graphite [31]. The XRD pattern of the DS-CDs (Fig. 1c) shows one broad diffraction peak at  $2\theta = 21^\circ$ , which is assigned to the interlayer spacing of 0.42 nm [32]. As shown in Fig. 1d, the Raman spectrum of DS-CDs exhibits two major bands for G-band at  $1590\text{ cm}^{-1}$  and D-band at  $1354\text{ cm}^{-1}$ , which are assigned to  $\text{sp}^2$  and  $\text{sp}^3$  hybridized orbital of carbon atom, respectively. These experimental results reveal that the DS-CDs has been successfully fabricated.

To verify the surface structure and composition of DS-CDs, the Fourier transform infrared (FT-IR) spectroscopy, and X-ray photoelectron spectroscopy (XPS) were measured. As shown in Fig. 1e, the peak at  $3430\text{ cm}^{-1}$  is due to stretching vibration of  $\text{—OH}$  and  $\text{N—H}$  bonds. The absorption peaks at 2921, 2846,  $1380\text{ cm}^{-1}$  are corresponding to  $\text{C—H}$  symmetric stretching,  $\text{C—H}$  asymmetric stretching, and symmetric bending vibration of the methyl or methylene group, respectively. The absorption peaks at  $1634\text{ cm}^{-1}$  was ascribed to stretching vibration of  $\text{C=N}$  and  $\text{C=O}$  groups. The absorption peaks at 1384 and  $1084\text{ cm}^{-1}$  stem from stretching vibration of  $\text{C=C/C=N}$  and  $\text{C—O}$ , respectively. The results markedly imply the surface of DS-CDs are rich in hydrophilic group, such as hydroxyl, carboxyl and amine groups, thus lead to its well dispersed in most of the polar solvents. The three pinnales lies within 284.84, 400.11 and  $532.14\text{ eV}$  in XPS should be put down to C 1s, N 1s, and O 1s (Fig. 1f), and the corresponding proportion of atom are  $\text{C:N:O} = 72.85:18.49:8.66$ . Based on Fig. 1g, h and i, the high resolution C 1s spectrum at 284.6, 285.3 and  $288.3\text{ eV}$  are assigned to  $\text{C=C}$ ,  $\text{C—N/C—O}$  and  $\text{C=N/C=O}$  [33–35], respectively, the high resolution N 1s spectrum at 399.9 and  $400.5\text{ eV}$  are assigned to  $\text{C=N}$  and  $\text{N—H}$ , while high resolution O 1s spectrum at  $532.14\text{ eV}$  is assigned to  $\text{C—O}$ . The presence of various functional groups is in accordance with the result of FT-IR spectrum and characteristic peaks have been mentioned in the previous report [36–38]. Both the information of FT-IR and XPS reveal the surface of DS-CDs are rich in hydrophilic groups and bring about their good solubility. The hydrophilic groups on the surface of DS-CDs may contribution to defect luminescence.

To thoroughly investigate the luminescent properties of the DS-CDs, a series of optical characterizations were performed. Fig. 2a shows the absorption, optimal excitation and emission spectra of as-synthesized DS-CDs (correspond to black, green and blue lines, respectively). The absorption shows two main characteristic peaks at around 345 nm and 450 nm. The first peak at 345 nm should be due to lone pair electrons of  $\text{C=N/C=O}$  transitions between the  $n$ -orbital to the  $\pi$ -orbital, and the band at



**Scheme 1.** Schematic illustration of the formation of DS-CDs and possible dispersion morphology of DS-CDs in diverse polar solvents.

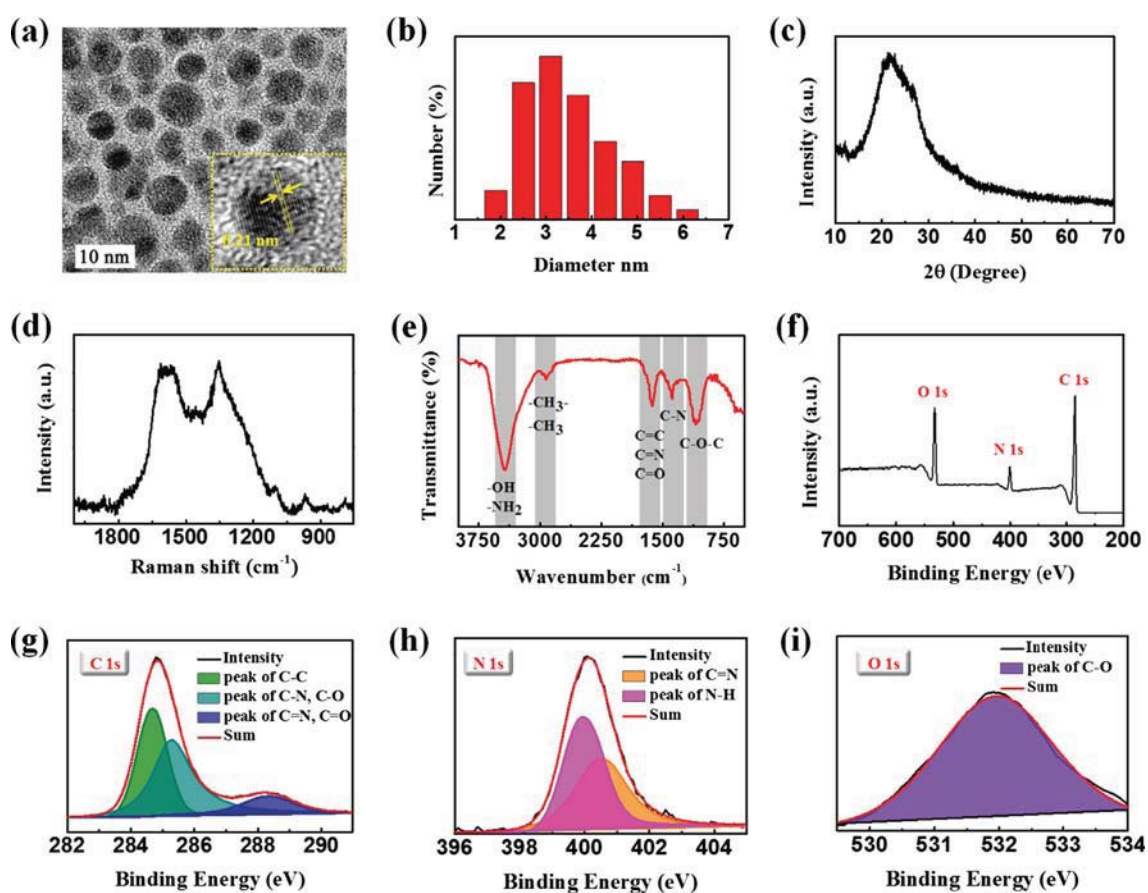


**Fig. 1.** (a) HR-TEM image, (b) Particle size distribution, (c) The XRD pattern, (d) Raman spectrum, (e) FT-IR spectrum, (f) XPS spectrum, (g) XPS C 1s spectrum, (h) XPS N 1s spectrum, and (i) XPS O 1s spectrum of DS-CDs.

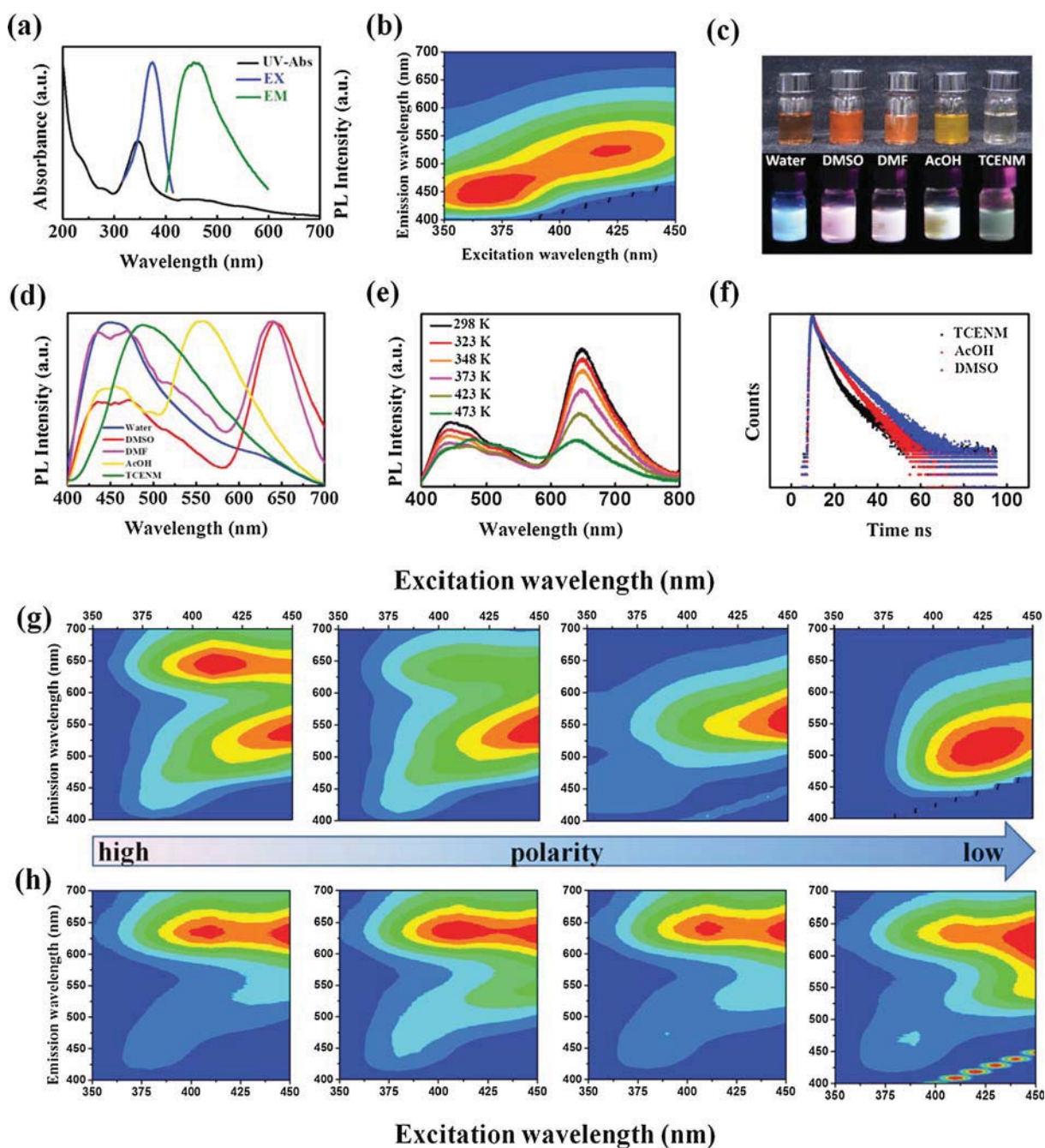


**Fig. 2.** (a) UV-Vis absorption and fluorescence spectra of DS-CDs, optimal excitation and emission spectra, (b) Excitation-emission two dimensional plots of DC-CDs in water, (c) Photographs taken under 365 nm UV light and (d) Fluorescence spectra under excitation wavelength at 380 nm of DS-CDs in diverse polar solvents. (e) Temperature-dependent emission spectra of CDs in DMSO, and (f) DL spectrum of DS-CDs in different solvents. Excitation-emission two dimensional plots of DS-CDs in (g) DMSO, DMF, AcOH and TCENM (from left to right), and (h) methanol, ethanol, glycol, and glycerol (from left to right).

450 nm is attributed to the  $n-\pi$  transition of the conjugated  $C=N$  bonds [10,39]. This exposed that DS-CDs has a certain amount of conjugated structure which result in blue-light emission (the optimal excitation in 375 nm, corresponding to the optimal emission around in 457 nm). The spectra also show overlap between absorption peak (450 nm) and emission peak, which can lead to a significant re-absorption and will be discussed further later. As shown in Fig. 2b, the as-synthesized DS-CDs shows the explicit excitation-dependent fluorescence behavior in water, that is, the observed emissions of as-synthesized DS-CDs can transform blue into green, while the excitation wavelengths changing from 350 nm to 450 nm. And some similarly results were extensively published in photoluminescence CDs [36,40]. Many researchers

considered that the excitation-dependent fluorescence behavior of CDs was derived from the energy gap trap of surface-localized states, that is, the photoluminescence behavior closely related to surface states [41–43]. The as-synthesized DS-CDs show a result of the oxygen-containing groups on the surface which bring about the different emission centers. To prove this theory, a number of environmental factors were implemented in DS-CDs. According to previous works [19,20], the charged ions violently influence the optical behavior of carbon dots due to complexation reaction between ions with the surface of carbon dots, which is also noticed in this our experiment. The Fig. S1 shows that the fluorescence peak of the as-synthesized is completely quenched by both  $Cu^{2+}$ ,  $Fe^{2+}$  and  $Fe^{3+}$  ions. The luminescent properties of DS-CDs in



different pH were compared in detail (Fig. S2). The result shows the DS-CDs was completely quenched by the strong acid, the alkalinity solution, but remained relatively steady in pH value ranging

among 4–7. The results show the same conclusions, that is, the oxygen-containing groups on the surface on DS-CDs caused excitation-dependent fluorescence behavior.

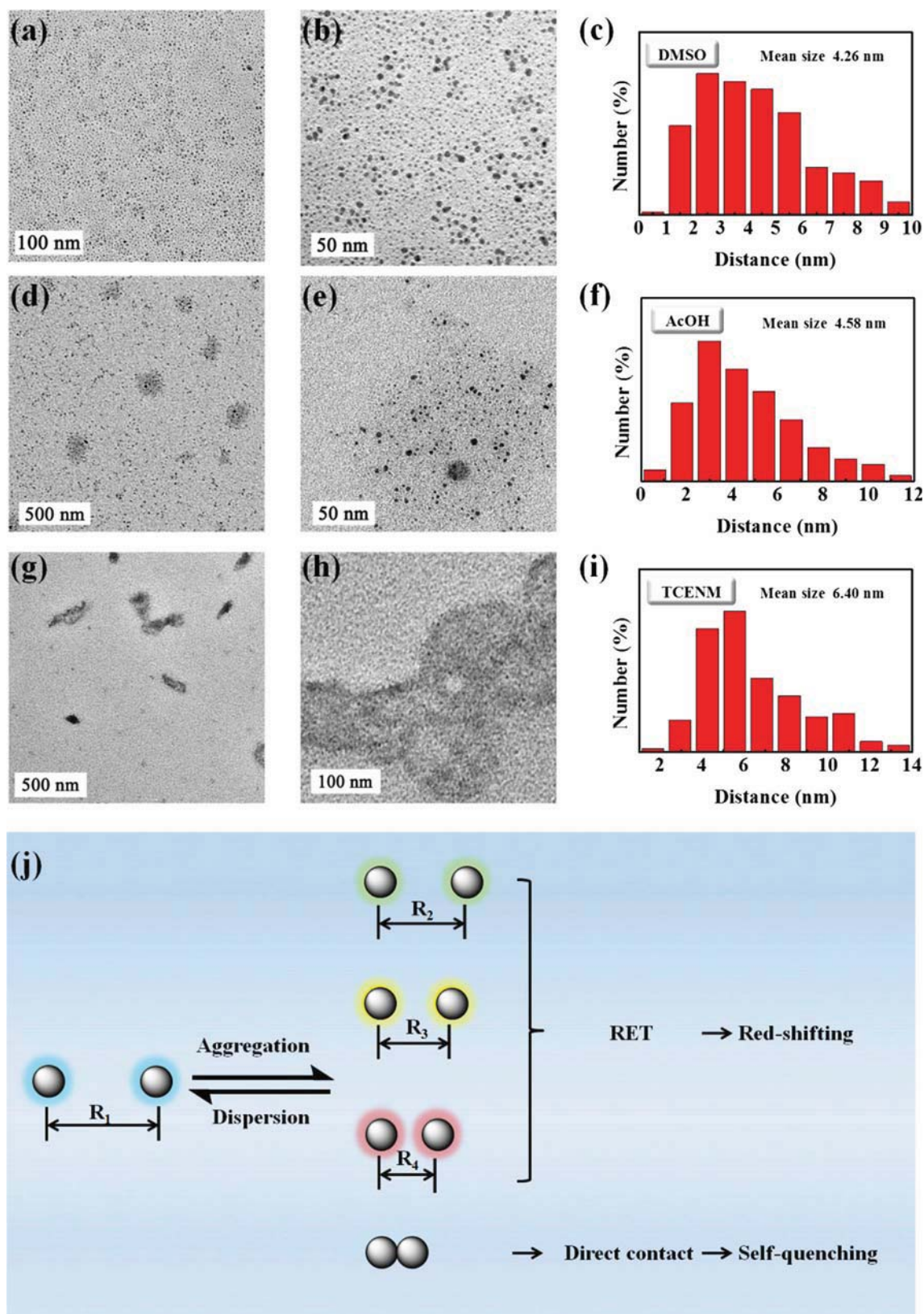


**Fig. 3.** TEM images of DS-CDs in (a, b) DMSO, (d, e) AcOH, (g, h) TCENM. The distance between DS-CDs in (c) DMSO, (f) AcOH, (i) TCENM. (j) Schematic of Förster resonance energy transfer (RET) of DS-CDs in different solvents.

Interestingly, beside the excitation-dependent fluorescence behavior, another attractive long-wavelength emission spectrum of DS-CDs was observed in non-aqueous solvent. As shown in Fig. 2c, these solutions emit bright red to green fluorescence colors with the decrease of the polarity of solvent besides blue luminescence in water under 365 nm ultraviolet radiation. In Fig. 2d, the photoluminescence spectra of DS-CDs were studied under 380 nm excitation wavelengths in diverse solvents. A obvious dual-emission phenomenon in most non-aqueous was found in as-synthesized DS-CDs. The shorter excitation-dependent fluorescence emission wavelength located at 450 nm, and the longer emission wavelength around at 643 nm could visibly blueshift as the polarity of the solvent decreases (Fig. 2g).

In order to speculate the dual-emissive solvatochromism behavior, the photoluminescence (PL) spectra, transmission electron microscopy (TEM), and photoluminescence decay (DL) spectrum were implemented in diverse polar solvents. In the PL spectra of DS-CDs in dimethyl sulfoxide (DMSO,  $\mu = 3.999$  D), N,N-dimethylformamide (DMF,  $\mu = 3.861$  D), and acetic acid (AcOH,  $\mu = 1.679$  D), the secondly emission peak were excitation-independent locating at 643, 637 and 555 nm, respectively. And the DS-CDs that dispersed in nitromethane (TCENM) only exhibited one excitation-dependent fluorescence peak from 450 to 500 nm, it might be caused by the closely overlapped double emission bands. This relative blueshift of PL spectra in several different polar solvents under the same excitation wavelength suggests the possibility of the hydrogen bond interactions between the various hydrophilic functional groups with hydroxyl of solvents. The nitrogen and oxygen in surface of DS-CDs can induce the charge transfer of electrons towards the edge, then transform of electron density distribution, and result in energy gap and extra electronic transition. Therefore, in protic solvent, with the increase in the polarity of solvents, the hydrophilic functional groups tend to form hydrogen bonding with solvent, result in a smaller band gap, then, lead to the redshift of the fluorescence emission wavelength [24,44]. In order to prove the key role of the hydrogen bonding in emission wavelength shift, the temperature-dependent emission spectra in DMSO was measured. From Fig. 2e, as temperatures rise, the longer

wavelength emission peak decreased sharply and shorter wavelength emission peak reduced little bit. This is due to when temperatures rise, the hydrogen-bond was broken firstly. In addition, the DL spectrum of DS-CDs in different polar solvents were measured to farther demonstrate the above assumption (Fig. 2f). The PL lifetimes of DS-CDs in solvents decreased with decreasing polarity. However, the DS-CDs in alcohols solvents had similar photoluminescence spectra were quite independence of polarity. Those results also certify that hydrogen bonding play a key role in solvatochromism behavior. Most importantly, the micro-morphology of DS-CDs in different solvents was explored to account for how does hydrogen bond work. From the TEM images (Fig. 3a, b, d, e, g, h), a kind of obvious aggregated distribution pattern was found out. There is an increase of the size of aggregate particles as the polarity of solvents decreased. In addition, the distance between DS-CDs particles was shorten (Fig. 3c, f, i). Thus, the aggregation should make a great contribution to solvatochromism behavior, which come of hydrogen bond interaction between CDs and solvents. Base on above experiment results, a possible dispersion morphology of DS-CDs in diverse polar solvents was shown in Scheme 1. According to the above spectral and aggregate phenomena, which is believed cause by Förster resonance energy transfer (FRET) and re-absorption. That is, when the distance between the nanoparticles was shorter than  $R_0$  (Förster distance), energy is transferred from a donor to an acceptor by an induced-dipole as a nonradiative process, and the emission light of donor can be used to excite the acceptor [45,46]. Then, the FRET phenomena will be occurred, and lead to a large redshift in DS-CDs solution (Fig. 3j). Thus, the longer wavelength emission was irrelevant to the concentration of solution, but related to aggregation phenomena between DS-CDs, which was also demonstrated by PL spectra and TEM images of solution with different concentrations (Fig. S3–5). That is, the hydrogen bond interactions between CDs and solvents are going to cause partially nanoparticle agglomerates, and then, forming such a solvatochromism coexist with dual-emissive phenomenon of CDs in different solvents.

Water not only as a kind of the key components which is needed to keep the ordinary life and function of human body,

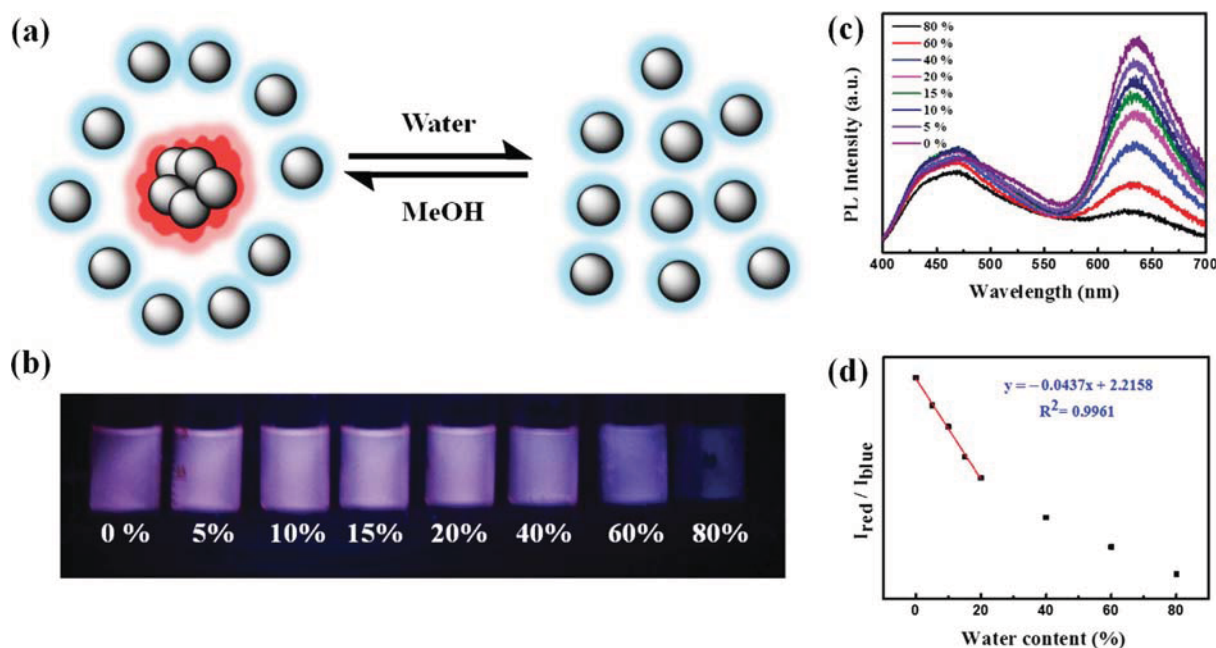


**Fig. 4.** (a) A possible process of detection water content in ethanol, (b) Photographs taken under 365 nm UV light of different water content in ethanol, (c) Fluorescence spectra of different water content in ethanol under excitation wavelength at 380 nm, (d) Plot of the  $I_{red}/I_{blue}$  versus the water content in ethanol under excitation wavelength at 380 nm.

but also the commonest kind of injurant component that can be harmful to the process of organic synthesis and industrial processes [47,48]. Hence, a more efficient detection methodology of water in ethanol is looking towards for the further development of industry. Various kinds of traditional methods have been used to work out, but there still many problems existing, such as the demand of specific instruments and trained professionals [49,50]. A convenient and efficient fluorescence ratio sensor has been developed for few years, but most of them refer to two kinds of fluorescent materials and two-step process [51,52]. Benefiting from the unique optical properties (dual-emissive and solvatochromism), sensing can be carried out to detect the water content in ethanol. Initially, the emission spectra present a lower intensity blue-wavelength band and a higher intensity red-wavelength band, when DS-CDs powders dissolved in different concentration ethanol solution under 380 nm excitation (Fig. 4a). Then, along with the increase of water content in ethanol, the fluorescence intensity of red-wavelength band is significantly reduced, while the blue-wavelength band is almost invariably (Fig. 4b, c). From the information shown in Fig. 4d, it could be seen that the fluorescence emission ratio of the  $I_{\text{red}} / I_{\text{blue}}$  is directly proportional to the water content in the range from 0% to 20%. In addition, the DS-CDs can also be applied to detect water content in other organics, such as DMSO and acetic acid, etc.

### 3. Conclusions

In conclusion, we prepared a new kind of carbon dots which both owning dual-emission and solvatochromism phenomenon simultaneously. A series of characterizations had been carried out to explain its special optical properties. The dual-emissive solvatochromic phenomenon stems from partially nanoparticle agglomerates which originates from specific hydrogen bond interactions between carbon dots and solvents. It is worth stressing that, the results of these optical phenomena are not simply generated from nanoparticle agglomerates or hydrogen bond interactions, but accomplished by the joint effect of them simultaneously. Our findings indicate that the hydrogen bond interactions between carbon dots and solvents are going to cause aggregation-induced emission, and lead to dual-emissive solvatochromic phenomenon eventually. Moreover, as opposed to the traditional solvatochromism phenomenon (analyzing only by their spectral results) of the past, the influence with hydrogen bond fracture and aggregation in microscale was visible for the first time. In consideration of the unique optical properties, a ratio fluorescent approach to detect the water in ethanol was realized. Not only does this method offer a fascinating optical phenomenon for the dual-emission and solvatochromic phenomenon at the same time, but also offering an excellent compass to explaining the luminescence mechanism of carbon dots for the related research.

## 4. Experimental section

### 4.1. Materials

All chemicals from commercial sources were of reagent grade and used without further purification. Citric acid, formamide, acetone, dimethyl sulfoxid (DMSO), N, N – dimethylformamide (DMF), acetic acid (AcOH), nitromethane (TCENM), methanol, ethanol, glycol, and glycerol. The hydrophobic membranes (nylon, 0.22  $\mu\text{m}$ , made in Jinlong). Deionized water was produced through a Millipore water purification system ( $\geq 18 \text{ M}\Omega$ , Milli-Q, Millipore) and used throughout the whole experiments.

### 4.2. Instruments and measurements

UV–Vis absorption spectra of the sample were performed using a Shimadzu UV-2550 ultraviolet–visible spectrophotometer wavelength scanning from 800 nm to 200 nm is carried out. PL spectra measurements were recorded using a Hitachi FL7000 fluorescence spectrophotometer instrument apparatus, equipped with the 150 W Xenon lamp as the excitation source. The XRD pattern was collected using a XD-2X/M4600, and operating at 36 kV and 30 mA with a scanning step of  $0.02^\circ(2\theta)$  and a scanning speed of  $8^\circ \text{ min}^{-1}$ . Transmission electron microscopy (TEM) images were taken in a FEI Tecnai12 transmission electron microscope operating at 200 kV. The HRTEM images were recorded using a JEOL-2010 electron microscope operating at 200 kV. FT-IR spectra were taken on a Nicolet Avatar 360 FT-IR spectrophotometer. Raman spectra were registered by a JobinYvon HR 800 microRaman spectrophotometer. X-ray photoelectron spectroscopy (XPS) experiments were performed using a Kratos AXIS Ultra DLD X-ray photoelectron spectrometer with a monochromatic Al K $\alpha$  X-ray source. Fluorescence lifetimes were measured using a Horiba FM-4P time corrected singlephoton-counting (TCSPC) system. The quantum efficiency was measured on a FLS980 fluorescence spectrophotometer.

### 4.3. Synthesis route of DS-CDs

A typical synthetic method was shown in Scheme S1. 5.60 g of citric acid were added in 100 ml formamide by ultrasound for several minutes until dissolved. Then, the solution was transferred into a 250 ml three-necked flask, which protected by a continuous nitrogen flow and stirred at  $160^\circ \text{C}$  for 2 h to get a crimson solution. After cooled to room temperature, the product was settled by added 500 ml of acetone. Then, store it into refrigerator under  $-20^\circ \text{C}$  by two days. The black suspension was separated by vacuum filtered and washed with the acetone/methanol mixture. The sediments were dissolved in methanol and vacuum filtered by  $0.22 \mu\text{m}$  hydrophobic membranes to obtain burgundy solution. After removal of solvent by a decompression distillation plant, the DS-CDs were finally obtained as a black powder by freeze-dried ( $-40^\circ \text{C}$ ) after added a little water. The CDs were synthesized in air (recorded as CDs-A) as a comparison group, the fluorescence spectra as shown in Fig. S6.

### 4.4. A ratio fluorescent approach to detect the water in ethanol

Black powder samples of DS-CDs used to detect a suite of concentration gradients ethanol solvents with different concentrations of water (0–80%) at normal temperature and pressure. DS-CDs powders (0.3 mg) were added into as-prescribed ethanol-water solvents (10 ml) directly. After that, the mixtures were shocked until it completely dissolves. Then photoluminescence spectra measurements were taken under excitation wavelength at 380 nm.

## Acknowledgements

The present work was supported by the National Natural Science Foundation of China (grant numbers 21571067, 51402207, 21671070, 51602108, 51802101); the Teamwork Projects Funded by the Guangdong Natural Science Foundation (grant number S2013030012842).

## Appendix A. Supplementary material

Supplementary data to this article can be found online at <https://doi.org/10.1016/j.jcis.2019.07.089>.



## References

- [1] M. Zhang, W. Wang, N. Zhou, P. Yuan, Y. Su, M. Shao, C. Chi, F. Pan, Near-infrared light triggered photo-therapy, in combination with chemotherapy using magnetofluorescent carbon quantum dots for effective cancer treating, *Carbon* 118 (2017) 752–764.
- [2] H. Wang, Y. Sun, J. Yi, J. Fu, J. Di, Alejandra Alonso, S. Zhou, Fluorescent porous carbon nanocapsules for two-photon imaging, NIR/pH dual-responsive drug carrier, and photothermal therapy, *Biomaterials* 53 (2015) 117–126.
- [3] F. Wu, M. Zhang, H. Lu, D. Liang, Y. Huang, Y. Xia, Y. Hu, S. Hu, J. Wang, X. Yi, J. Zhang, Triple stimuli-responsive magnetic hollow porous carbon-based nanodrug delivery system for magnetic resonance imaging-guided synergistic photothermal / chemotherapy of cancer, *ACS Appl. Mater. Interfaces* 10 (2018) 21939–21949.
- [4] H. Peng, J. Trivas-Sejdic, Simple aqueous solution route to luminescent carbogenic dots from carbohydrates, *Chem. Mater.* 21 (2009) 5563–5565.
- [5] S. Sahu, B. Behera, T.K. Maiti, S. Mohapatra, Simple one-step synthesis of highly luminescent carbon dots from orange juice: application as excellent bio-imaging agents, *Chem. Commun.* 48 (2012) 8835–8837.
- [6] K. Holá, M. Sudolská, S. Kalytchuk, D. Nachtigallová, A.L. Rogach, M. Otyepka, R. Zbořil, Graphitic nitrogen triggers red fluorescence in carbon dots, *ACS Nano* 11 (2016) 12402–12410.
- [7] J. Shao, S. Zhu, H. Liu, Y. Song, S. Tao, B. Yang, Full-color emission polymer carbon dots with quench-resistant solid-state fluorescence, *Adv. Sci.* 4 (2017) 1700395.
- [8] P. Gong, L. Sun, F. Wang, X. Liu, Z. Yan, M. Wang, L. Zhang, Z. Tian, Z. Liu, J. You, Highly fluorescent N-doped carbon dots with two-photon emission for ultrasensitive detection of tumor marker and visual monitor anticancer drug loading and delivery, *Chem. Eng. J.* 356 (2019) 994–1002.
- [9] G. Zuo, A. Xie, J. Li, T. Su, X. Pan, W. Dong, Large emission red-shift of carbon dots by fluorine doping and their applications for red cell imaging and sensitive intracellular Ag<sup>+</sup> detection, *J. Phys. Chem. C* 121 (2017) 26558–26565.
- [10] H. Kim, Y. Park, S. Beack, S. Han, D. Jung, H.J. Cha, W. Kwon, S.K. Hahn, Dual-color-emitting carbon nanodots for multicolor bioimaging and optogenetic control of ion channels, *Adv. Sci.* 4 (2017) 1700325.
- [11] M. Zhang, W. Wang, P. Yuan, C. Chi, J. Zhang, N. Zhou, Synthesis of lanthanum doped carbon dots for detection of mercury ion, multi-color imaging of cells and tissue, and bacteriostasis, *Chem. Eng. J.* 330 (2017) 1137–1147.
- [12] S. Takalkar, K. Baryeh, G. Liu, Fluorescent carbon nanoparticle-based lateral flow biosensor for ultrasensitive detection of DNA, *Biosens. Bioelectron.* 98 (2017) 147–154.
- [13] L. Xu, X. Bai, L. Guo, S. Yang, P. Jin, L. Yang, Facial fabrication of carbon quantum dots (CDs)-modified N-TiO<sub>2</sub>-x nanocomposite for the efficient photoreduction of Cr(VI) under visible light, *Chem. Eng. J.* 257 (2019) 473–486.
- [14] Y. Deng, L. Tang, C. Feng, G. Zeng, J. Wang, Y. Lu, Y. Liu, J. Yu, S. Chen, Y. Zhou, Construction of plasmonic Ag and nitrogen-doped graphene quantum dots decorated ultrathin graphitic carbon nitride nanosheet composites with enhanced photocatalytic activity: full-spectrum response ability and mechanism insight, *ACS Appl. Mater. Inter.* 9 (2017) 42816–42828.
- [15] F. Wang, D. Chen, Z. Hu, L. Qin, X. Sun, Y. Huang, In situ decoration of CuSCN nanorod arrays with carbon quantum dots for highly efficient photoelectrochemical performance, *Carbon* 125 (2017) 344–351.
- [16] X. Xu, W. Tang, Y. Zhou, Z. Bao, Y. Su, J. Hu, H. Zeng, Steering photoelectrons excited in carbon dots into platinum cluster catalyst for solar-driven hydrogen production, *Adv. Sci.* 4 (2017) 1700273.
- [17] W. Zhou, J. Zhuang, W. Li, C. Hu, B. Lei, Y. Liu, Toward efficient dual-emissive carbon dots through sulfur and nitrogen co-doped, *J. Mater. Chem. C* 5 (2017) 8014–8021.
- [18] L. Yu, G. Ren, M. Tang, B. Zhu, F. Chai, G. Li, D. Xu, Effective determination of Zn<sup>2+</sup>, Mn<sup>2+</sup>, and Cu<sup>2+</sup> simultaneously by using dual-emissive carbon dots as colorimetric fluorescent probe, *Eur. J. Inorg. Chem.* 29 (2018) 3418–3426.
- [19] J. Liu, Y. Dong, Y. Ma, Y. Han, S. Ma, H. Chen, X. Chen, One-step synthesis of red / green dual-emissive carbon dots for ratiometric sensitive ONOO<sup>-</sup> probing and cell imaging, *Nanoscale* 10 (2018) 13589–13598.
- [20] W. Song, W. Duan, Y. Liu, Z. Ye, Y. Chen, H. Chen, S. Qi, J. Wu, D. Liu, L. Xiao, C. Ren, X. Chen, Ratiometric detection of intracellular lysine and pH with one-pot synthesized dual emissive carbon dots, *Anal. Chem.* 89 (2017) 13626–13633.
- [21] Y. Ma, Y. Chen, J. Liu, Y. Han, S. Ma, X. Chen, Ratiometric fluorescent detection of chromium(VI) in real samples based on dual emissive carbon dots, *Talanta* 185 (2018) 249–257.
- [22] P. Zhu, Z. Cheng, L. Du, Q. Chen, K. Tan, Synthesis of the Cu-doped dual-emission fluorescent carbon dots and its analytical application, *Langmuir* 34 (2018) 9982–9989.
- [23] D. Chao, W. Lyu, Y. Liu, L. Zhou, Q. Zhang, R. Deng, H. Zhang, Solvent-dependent carbon dots and their application in detection of water in organic solvents, *J. Mater. Chem. C* 6 (2018) 7527–7532.
- [24] H. Wang, C. Sun, X. Chen, Y. Zhang, V.L. Colvin, Q. Rice, J. Seo, S. Feng, S. Wang, W.W. Yu, Excitation wavelength independent visible color emission of carbon dots, *Nanoscale* 9 (2017) 1909–1915.
- [25] M. Wu, J. Zhan, B. Geng, P. He, K. Wu, L. Wang, G. Xu, Z. Li, L. Yin, D. Pan, Scalable synthesis of organic-soluble carbon quantum dots: superior optical properties in solvents, solids and LEDs, *Nanoscale* 9 (2017) 13195–13202.
- [26] M. Zheng, Y. Li, Y. Zhang, Z. Xie, Solvatochromic fluorescent carbon dots as optic noses for sensing volatile organic compounds, *RSC Adv.* 6 (2016) 83501–83504.
- [27] D. Li, D. Han, S.N. Qu, L. Liu, P.T. Jing, D. Zhou, W.Y. Ji, X.Y. Wang, T.F. Zhang, D.Z. Shen, Supra-(carbon nanodots) with a strong visible to near-infrared absorption band and efficient photothermal conversion, *Light-Sci. Appl.* 5 (2016) e16120.
- [28] M.X. Gao, C.F. Liu, Z.L. Wu, Q.L. Zeng, X.X. Yang, W.B. Wu, Y.F. Lia, C.Z. Huang, A surfactant-assisted redox hydrothermal route to prepare highly photoluminescent carbon quantum dots with aggregation-induced emission enhancement properties, *Chem. Commun.* 49 (2013) 8015–8017.
- [29] Y. Li, H. Lin, C. Luo, Y. Wang, C. Jiang, R. Qi, R. Huang, T. Jadranka, H. Peng, Aggregation induced red shift emission of phosphorus doped carbon dots, *RSC Adv.* 7 (2017) 32225–32228.
- [30] S. Chen, J.W. Liu, M.L. Chen, X.W. Chen, J.H. Wang, Unusual emission transformation of graphene quantum dots induced by self-assembled aggregation, *Chem. Commun.* 48 (2012) 7637–7639.
- [31] H. Nie, M. Li, Q. Li, S. Liang, Y. Tan, L. Sheng, W. Shi, S.X. Zhang, Carbon dots with continuously tunable full-color emission and their application in ratiometric pH sensing, *Chem. Mater.* 26 (2014) 3104–3112.
- [32] B. De, N. Karak, A green and facile approach for the synthesis of water soluble fluorescent carbon dots from banana juice, *RSC Adv.* 3 (2013) 8286.
- [33] F. Wang, P. Chen, Y. Feng, Z. Xie, Y. Liu, Y. Su, Q. Zhang, Y. Wang, K. Yao, W. Lv, G. Liu, Facile synthesis of N-doped carbon dots/g-C<sub>3</sub>N<sub>4</sub> photocatalyst with enhanced visible-light photocatalytic activity for the degradation of indomethacin, *Applied Catalysis B: Environmental* 207 (2017) 103–113.
- [34] Y. Hu, L. Zhang, X. Li, R. Liu, L. Lin, S. Zhao, Green preparation of S and N co-doped carbon dots from water chestnut and onion as well as their use as an off-on fluorescent probe for the quantification and imaging of coenzyme A, *ACS Sustainable Chem. Eng.* 5 (2017) 4992–5000.
- [35] H. Zhang, S. Kang, G. Wang, Y. Zhang, H. Zhao, Fluorescence determination of nitrite in water using prawn-shell derived nitrogen-doped carbon nanodots as fluorophores, *ACS Sens.* 1 (2016) 875–881.
- [36] S. Bhattacharyya, F. Ehrat, P. Urban, R. Teves, R. Wyrwich, M. Döblinger, J. Feldmann, A.S. Urban, J.K. Stolarczyk, Effect of nitrogen atom positioning on the trade-off between emissive and photocatalytic properties of carbon dots, *Nat. Commun.* 8 (2017) 1401.
- [37] P. Das, M. Bose, S. Ganguly, S. Mondal, A.K. Das, S. Banerjee, N.C. Das, Green approach to photoluminescent carbon dots for imaging of gram-negative bacteria *escherichia coli*, *Nanotechnology* 28 (2017) 195501.
- [38] S. Dutta Choudhury, J.M. Chethodil, P.M. Gharat, P.P.K.H. Pal, PH-elicited luminescence functionalities of carbon dots: mechanistic insights, *J. Phys. Chem. Lett.* 8 (2017) 1389–1395.
- [39] X. Miao, X. Yan, D. Qu, D. Li, F.F. Tao, Z. Sun, Red emissive sulfur, nitrogen codoped carbon dots and their application in ion detection and theranostics, *ACS Appl. Mater. Inter.* 9 (2017) 18549–18556.
- [40] L. Pan, S. Sun, A. Zhang, K. Jiang, L. Zhang, C. Dong, Q. Huang, A. Wu, H. Lin, Truly fluorescent excitation-dependent carbon dots and their applications in multicolor cellular imaging and multidimensional sensing, *Adv. Mater.* 27 (2015) 7782–7787.
- [41] D. Pan, J. Zhang, Z. Li, C. Wu, X. Yan, M. Wu, Observation of pH-, solvent-, spin-, and excitation-dependent blue photoluminescence from carbon nanoparticles, *Chem. Commun.* 46 (2010) 3681.
- [42] A. Pramanik, S. Biswas, P. Kumbhakar, Solvatochromism in highly luminescent environmental friendly carbon quantum dots for sensing applications: conversion of bio-waste into bio-asset, *Spectrochim. Acta Part A Mol. Biomol. Spectrosc.* 191 (2017) 498–512.
- [43] J. Liu, N. Wang, Y. Yu, Y. Yan, H. Zhang, J. Li, J. Yu, Carbon dots in zeolites: a new class of thermally activated delayed fluorescence materials with ultralong lifetimes, *Sci. Adv.* 3 (2017) e1603171.
- [44] S. Mukherjee, E. Prasad, Chadha, H-bonding controls the emission properties of functionalized carbon nano-dots, *Phys. Chem. Chem. Phys.* 19 (2017) 7288–7296.
- [45] T. Ha, T. Enderle, D. Ogletree, D. Chemla, P. Selvin, S. Weiss, Probing the interaction between two single molecules: fluorescence resonance energy transfer between a single donor and a single acceptor, *Proc. Natl. Acad. Sci.* 93 (1996) 6264–6268.
- [46] K. Sapsford, L. Berti, I. Medintz, Materials for fluorescence resonance energy transfer analysis: beyond traditional donor-acceptor combinations, *Angew. Chem. Int. Ed.* 45 (2016) 4562–4588.
- [47] A. Peyvandi, P. Soroushian, N. Abdol, A.M. Balachandra, Surface-modified graphite nanomaterials for improved reinforcement efficiency in cementitious paste, *Carbon* 63 (2013) 175–186.
- [48] A. Douvali, A.C. Tsipis, S.V. Eliseeva, S. Petoud, G.S. Papaefstathiou, C.D. Malliakas, I. Papadas, G.S. Armatas, I. Margiolaki, M.G. Kanatzidis, T. Lazarides, M.J. Manos, Turn-on luminescence sensing and real-time detection of traces of water in organic solvents by a flexible metal-organic framework, *Angew. Chem. Int. Ed.* 54 (2015) 1651–1656.
- [49] Y.Y. Liang, Automation of karl fischer water titration by flow injection sampling, *Anal. Chem.* 62 (1990) 2504–2506.
- [50] Y. Sakai, M. Matsuguchi, T. Hurokawa, Humidity sensor using cross-linked poly (chloromethyl styrene), *Sens. Actuators, B* 66 (2000) 135–138.
- [51] Y. Dong, J. Cai, Q. Fang, X. You, Y. Chi, Dual-emission of lanthanide metal-organic frameworks encapsulating carbon-based dots for ratiometric detection of water in organic solvents, *Anal. Chem.* 88 (2016) 1748–1752.
- [52] G. Ji, J. Wang, X. Gao, J. Liu, W. Guan, H. Liu, Z. Liu, Hypersensitive self-referencing detection traces of water in ethyl alcohol by dual-emission lanthanide metal-organic frameworks, *J. Subst. Abuse Treat.* 13 (1996) 287–288.



Contents lists available at ScienceDirect

Chemical Engineering Journal

journal homepage: [www.elsevier.com/locate/cej](http://www.elsevier.com/locate/cej)

# Magnesium-nitrogen co-doped carbon dots enhance plant growth through multifunctional regulation in photosynthesis

Yadong Li<sup>a,b</sup>, Xiaokai Xu<sup>a,b</sup>, Bingfu Lei<sup>a,b</sup>, Jianle Zhuang<sup>a,b</sup>, Xuejie Zhang<sup>a,b</sup>, Chaofan Hu<sup>a,b,\*</sup>, Jianghu Cui<sup>c,d,\*</sup>, Yingliang Liu<sup>a,b,\*</sup>

<sup>a</sup> Key Laboratory for Biobased Materials and Energy of Ministry of Education/Guangdong Provincial Engineering Technology Research Center for Optical Agriculture, College of Materials and Energy, South China Agricultural University, Guangzhou 510642, China

<sup>b</sup> Guangdong Laboratory of Lingnan Modern Agriculture, Guangzhou 510642, China

<sup>c</sup> Guangdong Key Laboratory of Integrated Agro-environmental Pollution Control and Management, Guangdong Institute of Eco-environmental Science & Technology, Guangzhou 510650, China

<sup>d</sup> National-Regional Joint Engineering Research Center for Soil Pollution Control and Remediation in South China, Guangzhou 510650, China

## ARTICLE INFO

### Keywords:

Magnesium  
Carbon dots  
Photosynthesis  
Chlorophyll metabolism  
Plant growth

## ABSTRACT

Herein, we designed and prepared a magnesium and nitrogen co-doped carbon dots (Mg,N-CDs) for plant photosynthesis, in which Mg and N were in carbonate-like and graphite N forms with 5.38% and 3.83% contents, respectively. During a 1-h incubation with chloroplast suspension, Mg,N-CDs entered chloroplasts and transferred energy to them under a xenon lamp, which increased their photosynthetic activity to reduce DCPIP and ferricyanide by up to 52.48% and 41.86%, respectively. After 16 days of foliar spraying, Mg,N-CDs at 300  $\mu\text{g}\cdot\text{mL}^{-1}$  up-regulated the gene expressions of enzymes (15.26–115.02%) related to chlorophyll synthesis and metabolism in rice plants, increasing chlorophyll *a* and chlorophyll *b* contents by 14.39% and 26.54%, respectively. The rice seedlings treated with Mg,N-CDs at 300  $\mu\text{g}\cdot\text{mL}^{-1}$  exhibited 109.54%, 104.48%, and 127.16% higher photosynthetic activity, electron transport rate, and photosynthetic efficiency relative to the control, respectively. Moreover, Mg,N-CDs also increased the RuBisCO activity of rice plants by 46.62%. With the energy transformation and physiological regulation, Mg,N-CDs (300  $\mu\text{g}\cdot\text{mL}^{-1}$ ) increased the height and fresh biomass of rice plants by 22.34% and 70.60%, respectively, through the overall improvement of photosynthesis. This study suggests the great potential of Mg,N-CDs in increasing global agricultural production in the future.

## 1. Introduction

Food security is still one of the major challenges facing the world today. According to FAOSTAT data (<http://www.fao.org/3/ca9692en/online/ca9692en.html#chapter-1.1>), about 8.9%, *i.e.*, 687.8 million, people in the world experienced a lack of food in 2019. Even worse, global agriculture is threatened by various biotic and abiotic challenges, such as crop pests, climate change events, low nutrient use efficiency, and losses of farmland [1,2]. Currently, food production is mainly dependent upon the heavy input of pesticides and fertilizers, which have seen a plateau in increasing crop yield and led to substantial destruction to the environment, ecological balance, and biodiversity [3]. An environmentally friendly strategy to enhance crop productivity is the primary challenge facing agricultural science.

Crop productivity largely depends on photosynthesis, which captures

and converts solar radiation into chemical energy to drive  $\text{CO}_2$  fixation into carbohydrates [4]. It is estimated that more than 90% of crop biomass is produced by photosynthesis. However, the photosynthetic efficiency of crops usually underperforms the theoretical maximum due to the limited utilization efficiency of solar energy. Weak capacity and narrow coverage (400–500 nm and 640–660 nm) of photosynthetic pigments to absorb light and the photoinhibition under high light are the main factors restricting the enhancement of photosynthesis [5,6]. As the light antenna, photosynthetic pigments are involved in all aspects of photosynthesis, including light-harvesting, energy transfer, and light energy conversion [7]. Magnesium (Mg) and nitrogen (N) are both two key components of chlorophyll molecules, photosynthetic proteins, and enzymes. The leaf chlorophyll, Mg, and N contents are often cited as the primary mechanism controlling the photosynthetic rate of plants [8–11].

A nanomaterial-led revolution in agriculture is emerging, intending

\* Corresponding Authors.

E-mail addresses: [thucf@scau.edu.cn](mailto:thucf@scau.edu.cn) (C. Hu), [lantian9426@163.com](mailto:lantian9426@163.com) (J. Cui), [tliuy1@scau.edu.cn](mailto:tliuy1@scau.edu.cn) (Y. Liu).

<https://doi.org/10.1016/j.cej.2021.130114>

Received 10 February 2021; Received in revised form 16 April 2021; Accepted 25 April 2021

Available online 29 April 2021

1385-8947/© 2021 Elsevier B.V. All rights reserved.

to make agriculture more efficient, resilient and sustainable [12]. With small sizes (<100 nm), nanomaterials show excellent physicochemical properties, and they can easily diffuse into the plant vasculature across biological barriers, and then play their roles in plant physiology and biochemistry. Fluorescent carbon dots (CDs) have been widely studied due to their excellent ultraviolet absorption, coordinated fluorescence, high photostability, biocompatibility, and low cost [13–15]. Coupled with easy functionalization, CDs have become one of the best precursors for functionalization or doping for specific applications [16–18]. Recently, CDs have been reported to increase plant growth, resistance, and photosynthesis [19–22]. Especially in photosynthesis, the excellent photoluminescence of CDs can convert light or transfer energy to chloroplasts, thereby improving their photosynthetic activity [20,23]. Furthermore, CDs can also contribute to the chlorophyll synthesis and CO<sub>2</sub> assimilation of plants [20,24].

Considering the key role of chlorophyll in all aspects of photosynthesis, we designed and prepared Mg and N co-doped CDs (Mg,N-CDs) for improving photosynthesis by promoting chlorophyll synthesis. The formation mechanisms, structure, and composition of Mg,N-CDs were fully studied. Subsequently, Mg,N-CDs were applied to systematically investigate their effect on plant growth and photosynthesis using rice seedlings and isolated chloroplasts as models. This study provides an ideal platform to drive the functionalization of CDs in agriculture, helping the green and sustainable development of agriculture.

## 2. Experimental section

### 2.1. Preparation of Mg,N-CDs

The Mg,N-CDs were prepared by a one-pot hydrothermal method using citric acid (CA), ethanalamine (EA), and magnesium hydrate [Mg(OH)<sub>2</sub>]. Briefly, CA (2.1 g), EA (241 μL), and Mg(OH)<sub>2</sub> (0.2 g) were dissolved into ultrapure water (20 mL) by sonication (300 W) for 30 min. Then, the transparent solution was transferred into a 50 mL Teflon-lined stainless steel autoclave and heated at 200 °C in an oven for 6 h. After naturally cooling down to room temperature, the obtained brown solution was filtered through a 0.22-μm filter membrane and dialyzed (MW 100–500) against ultrapure water for 12 h (refreshing the water every two hours). Finally, the Mg,N-CDs were obtained after vacuum freeze-drying. The N doped CDs (N-CDs) were synchronously prepared by the same method using CA and EA. The relative quantum yield (QY) of Mg,N-CDs was determined using quinine sulfate (0.1 M H<sub>2</sub>SO<sub>4</sub> as the solvent, QY = 54%) as a reference according to a method in the literature [25].

### 2.2. Characterization of Mg,N-CDs

The morphology of Mg,N-CDs was observed using a JEM-2100F field emission transmission electron microscope (TEM) and SPA-400 atomic force microscope (AFM). The components of Mg,N-CDs were determined using a Thermo Scientific Nicolet 6700 FTIR spectrophotometer and Thermo Scientific K-alpha X-ray photoelectron spectroscopy (XPS). Fluorescence (FL) spectra and the FL lifetime decay profile were measured using F-7000 Hitachi and FLS 1000-STM fluorescence spectrophotometer, respectively. The UV–Vis absorption spectrum was measured using a Perkin Elmer UV–Vis spectrophotometer (Lambda 750). Thermogravimetric analysis was performed on a TGA-DSC system (LabSys STA) equipped with mass spectrometry (LC-DZOOM Pro) (TG-MS) from room temperature to 800 °C at a rate of 10 °C/min in air atmosphere. X-ray diffraction profiles (XRD) were recorded at different temperatures by an Xpert Pro MPD X-ray diffractometer (XRD) employing a Cu target in the 2θ range from 5° to 80°.

### 2.3. Exposure of isolated chloroplast to Mg,N-CDs and the photosynthetic activity

With similar structure and function among different plant species, the chloroplast was isolated from lettuce (*Lactuca sativa* L.) as a model to study the light conversion of Mg,N-CDs for photosynthesis according to a literature method (SI-1) [26]. A chloroplast suspension containing 10 μg·mL<sup>-1</sup> chlorophyll was incubated with Mg,N-CDs at 10, 50, and 100 μg·mL<sup>-1</sup> in the dark. After 1 h, the composites of chloroplast and Mg,N-CDs (Mg,N-CDs@Chl) were obtained by centrifugation at 3000 rpm for 3 min at 4 °C. Then, an FEI Verios 460 scanning electron microscope (SEM) and an inverted fluorescence microscope (Nikon, ECLIPSE Ti2-U) equipped with a Nikon DS-Ri2 microscope camera were used to observe the distribution of Mg,N-CDs in chloroplasts according to a standard protocol (SI-2) [23]. Furthermore, the UV–Vis spectra, fluorescence emission spectra, and fluorescence lifetime of chloroplast and Mg,N-CDs@Chl suspensions were recorded.

Subsequently, Hill reaction was conducted to study the effect of Mg,N-CDs on the photosynthetic activity of chloroplasts in terms of the reduction rate of DCPIP and potassium ferricyanide [26]. Briefly, DCPIP (final concentration of 60 μM) was added into the suspensions of Mg,N-CDs@Chl, or chloroplast. The mixture was immediately radiated under 1000 LUX or 9000 LUX (higher than the light saturation point of the chloroplast, Figure S1) light at room temperature. The reduction of DCPIP was recorded by a decrease in the absorbance at 600 nm against chloroplast suspension at a 2-minute interval. Then, the reduction of potassium ferricyanide by Mg,N-CDs@Chl and chloroplast was measured to further confirm the results of DCPIP. The method was similar to that of DCPIP reduction, but the irradiation intensity was 3000 LUX and the decrease in the absorbance at 420 nm was recorded. The pure chloroplast suspension was used as the control to zero the UV–Vis spectrophotometer and three replications were measured for each treatment, with an acceptable standard deviation of <10%. The reductions of DCPIP and potassium ferricyanide were calculated using the following formula:

$$\text{DCPIP or potassium ferricyanide reduction (\%)} = (A_0 - A_t) / A_0 \times 100\% \quad (1)$$

where  $A_0$  and  $A_t$  represented the absorbance of the suspension at 0 min and  $t$  min, respectively. From a preliminary experiment, Mg,N-CDs alone exhibited an insignificant reduction of DCPIP and potassium ferricyanide (no data was presented).

### 2.4. Rice plant cultivation and exposure to Mg,N-CDs

Rice seedlings ('Huahang 31') were cultured by hydroponics as described previously [27]. Rice seeds were sterilized with 75% ethanol and germinated using half-strength of nutrient solution (Table S1) on a germination tray at 30 °C in the dark. After 3 days, the germination tray was transferred to a greenhouse (22–30 °C, 70% relative humidity, 400 μmol m<sup>-2</sup>·s<sup>-1</sup> light intensity with a 16 h light/8h dark regime). Then, homogeneous 7-day-old rice seedlings were transplanted to pots containing nutrient solution with a density of 12 seedlings per pot. The nutrient solution was refreshed once a week. Mg,N-CDs solutions at 50, 100, and 300 μg·mL<sup>-1</sup> were sprayed on rice seedlings with a dosage of 5 mL·pot<sup>-1</sup> on the second day after transplantation, ensuring that all leaves were covered with droplets without any runoff. Each treatment was replicated three times, and ultrapure water was sprayed as the control. The foliar spray was conducted every two days for 16 days. Then, the height and fresh weight of more than 10 rice seedlings from each treatment were measured. The top two leaves of 5 rice seedlings from each treatment were collected for the measurement of chlorophyll content according to a reported method (SI-3) [28]. The distribution of Mg,N-CDs in rice seedlings was visualized by TEM according to a standard protocol (SI-4) [29].



## 2.5. Chlorophyll fluorescence measurements

Before the measurement, the treated rice seedlings for 16 days were adapted in the dark overnight for the equilibration of photosystem II (PS II) redox states. Then, the second top leaf of each seedling was collected to measure the chlorophyll fluorescence parameters (Table 1) on a pulse-amplitude modulated (PAM) chlorophyll fluorescence imaging system (Phyto-PAM ED, Walz, Germany) under gradient-elevated photosynthetic active radiations (PAR) (0, 36, 81, 146, 231, 396, 461, 611, 801, 1076, and 1251  $\mu\text{mol}\cdot\text{m}^{-2}\cdot\text{s}^{-1}$ ). Six rice seedlings from each treatment and ten points of each leaf were measured for accuracy. The rice seedlings sprayed with deionized water were measured as the control.

## 2.6. RuBisCO carboxylase activity

The leaf samples of 12 rice seedlings from each treatment were divided into 3 groups and ground into powder using liquid nitrogen, and the rice seedlings sprayed with ultrapure water were used as control. Then, about 0.1 g powder samples from each group were homogenized into 1 mL of 0.04 mol·L<sup>-1</sup> Tris-HCl buffer (pH 7.6) that contained 10 mmol·L<sup>-1</sup> of MgCl<sub>2</sub>, 0.25 mmol·L<sup>-1</sup> of EDTA, and 5 mmol·L<sup>-1</sup> of glutathione by sonication for 15 min in an ice bath. After centrifugation at 10000 × g and 4 °C for 10 min, 6  $\mu\text{L}$  of the supernatants were mixed with 7  $\mu\text{L}$  of glyceraldehyde-3-phosphate dehydrogenase, 7  $\mu\text{L}$  of phosphoglycerate kinase, and 180  $\mu\text{L}$  of working solution (1 mM ATP, 4 mM NADH, 10 mmol·L<sup>-1</sup> RuBP, 100 mmol·L<sup>-1</sup> phosphocreatine). After thoroughly mixing, the oxidation of NADH was recorded as the decrease in absorbance at 340 nm within 2 min. One unit of carboxylase activity by RuBisCO was initially defined based on the nanomolars of NADH oxidized within 1 min by 1 g of fresh rice leaves.

## 2.7. Quantitative real-time (qRT)-PCR analysis

The genes expression levels of two subunits (ChlD and ChlI, LOC4334537 and LOC4333259) of Mg-dechelate, chlorophyll synthetase (ChlG, LOC4338498), and chlorophyllase-2 (LOC4348648) were measured by quantitative real-time (qRT)-PCR analysis using 18S rRNA (LOC4331056) as an internal reference. The genes sequences were retrieved from National Center for Biotechnology Information (NCBI) to design primers (Table S2) using Primer Premier software, version 5. Twelve rice leaves from each treatments were collected into three groups and immediately frozen in liquid nitrogen, and the rice seedlings sprayed with ultrapure water were used as control. The total RNA in these rice leaves was extracted and reverse-transcribed to cDNA using a Plant Total RNA Isolation Kit (BioBase, Chengdu, China) and TRUEScript 1st Strand cDNA SYNTHESIS Kit (Aidlab, Beijing, China) following the manufacturer's instructions, respectively. Then, the qRT-PCR analysis was performed on the QTOWER2.2 Real-Time PCR System (ANALYTIKJENA, Germany) with standard protocol and a 10  $\mu\text{L}$  reaction system (5  $\mu\text{L}$  of 2 × SYBR® Green Supermix, 0.5  $\mu\text{L}$  forward and 1  $\mu\text{L}$  reverse primer, 1  $\mu\text{L}$  cDNA sample, and 3  $\mu\text{L}$  RNase free H<sub>2</sub>O). Finally, the relative gene

expression level was calculated using the 2<sup>- $\Delta\Delta C_T$</sup>  method [30].

## 2.8. Statistical analysis

Values presented in this paper were expressed as means ± standard deviation (SD). Statistical significance of all data was determined using a one-way analysis of variance (ANOVA) and compared using Duncan's test at  $p < 0.05$  levels by SPSS 24.

## 3. Results and discussion

### 3.1. Optical characterization of Mg,N-CDs

Mg,N-CDs were prepared via a one-pot hydrothermal treatment of CA, EA, and Mg(OH)<sub>2</sub>. Under UV irradiation (365 nm, 16 W), the Mg,N-CDs solution visually emits blue fluorescence (FL) (Fig. 1A). The UV-Vis absorption spectra of Mg,N-CDs (Fig. 1B, red line) display two electronic transitions at 320 nm and 370 nm, corresponding to  $n\rightarrow\pi^*$  transitions of p- $\pi$  orbit between the surface organic moieties and the conjugate structure [31,32]. The FL spectra of Mg,N-CDs presents the maximum FL excitation spectra (green line) and emission spectra (blue line) at 374 nm and 485 nm (Fig. 1B), respectively. The FL excitation and emission peaks are divided into two peaks at 343 nm and 378 nm, and 483 nm and 519 nm, respectively. Under elevating excitation wavelength, Mg,N-CDs exhibit excitation-dependent FL emissions from 400 nm to 550 nm (Figure S2). Furthermore, two FL lifetimes, 2.41 ns (96.50%) and 20.49 ns (3.50%), were detected in Mg,N-CDs, with an average value of 3.04 ns (Fig. 1C).

In comparison, the N-doping CDs (N-CDs) display a weak and broad absorption peak around 320 nm. Similarly, two peaks are divided from both FL excitation (347 nm) and FL emission (425 nm) peaks at 328 nm and 358 nm, and 422 nm and 455 nm, respectively. (Figure S3A). Moreover, the FL lifetimes of N-CDs is measured as 7.79 ns (27.08%) and 12.85 ns (72.92%) with an average value of 11.48 ns (Figure S3B). The redshift of FL emission and the decrease of FL lifetime of Mg,N-CDs can result from the low energy levels caused by Mg doping.

### 3.2. Morphology of Mg,N-CDs

Fig. 1D shows the torispherical morphology and uniform distribution of Mg,N-CDs, with an average particle size of 2.53 nm. High-resolution TEM (H-R TEM) images (Fig. 1E and F) display two lattice spacing of 0.21 nm and 0.24 nm, which are assigned to the (100) and (1120) crystal phases of graphite, respectively [33,34]. The XRD profile of Mg,N-CDs exhibits two broad diffraction peaks around  $2\theta$  of 18.8° and 34.5° (Fig. 1G), suggesting disordered carbon species. The AFM image (Fig. 1H) shows the height of Mg,N-CDs as about 2 nm (Fig. 1I), suggesting their torispherically spatial structure. The  $\zeta$ -potential characterization (Zetasizer Nano ZSE, Malvern) confirms the negatively charged surface ( $-5.8 \pm 0.66$  mV) of Mg,N-CDs (Fig. 1J), which contribute to their ability to enter plant cells in the following study of plant photosynthesis [35].

### 3.3. Chemical composition of Mg,N-CDs

The chemical composition of Mg,N-CDs was studied by FTIR and XPS spectra. Fig. 2A shows the FTIR spectrum of Mg,N-CDs. Strong stretching vibration of hydroxyl groups or N-H bond is observed around 3390 cm<sup>-1</sup>. The peak at 1585 cm<sup>-1</sup> suggests the presence of alkyl primary amides on the surface of Mg,N-CDs. The peak at 1417 cm<sup>-1</sup> is ascribed to the in-plane bending vibrations of hydroxyl groups or the stretching vibrations of C-N in primary amides. The peaks at 1278 cm<sup>-1</sup> and 1076 cm<sup>-1</sup> are assigned to C-O and C-N stretching vibrations, respectively. These infrared transmittance features confirm the hydrophilic surface of Mg,N-CDs, which are conducive to biological applications. Compared to the FTIR of N-CDs (Figure S4), the characteristic peak of -COOH at 1695

**Table 1**  
Definition of chlorophyll fluorescence parameters.

Parameters	Definition
NPQ	Non-photochemical fluorescence quenching parameter describing regulated dissipation of excess energy, reflecting the light protection ability of plant
qP	Photochemical fluorescence quenching parameter estimating the fraction of open PS II centers based on a lake model, reflecting the photosynthetic activity
Y(NPQ)	Quantum yield of regulated non-photochemical energy loss in PS II
Y(NO)	Quantum yield of non-regulated non-photochemical energy loss in PS II
Y(II)	Quantum yield of photochemical energy conversion in PS II
ETR	Electron transport rate in PS II

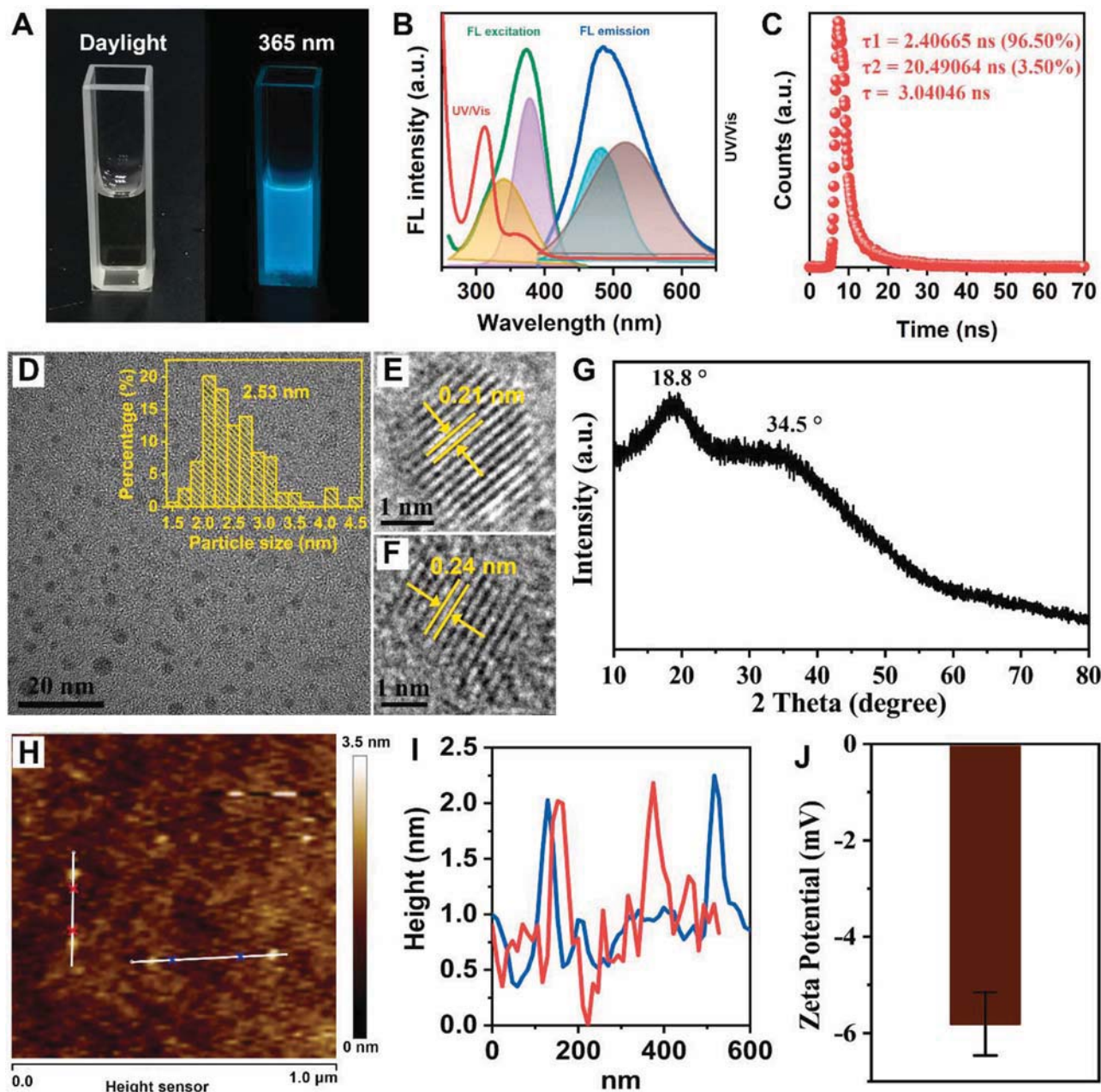


**Fig. 1.** Photographs of Mg,N-CDs under daylight and 365 nm (A), UV–Vis, maximum FL excitation and emission spectra of Mg,N-CDs (B), and FL decay lifetime of Mg,N-CDs (C); TEM images (D), inset: the size distribution histograms, HRTEM images (E and F), XRD pattern (G), AFM image (H), line-scan height profile of the marked particles (the white line) in AFM image (I) and the Zeta potential (J) of Mg,N-CDs.

$\text{cm}^{-1}$  disappears in Mg,N-CDs. Therefore, we infer that  $\text{Mg}^{2+}$  firstly chelates with the  $-\text{COOH}$  groups in CA, and then is doped into Mg,N-CDs after carbonization. This result is further demonstrated by the higher pH value of Mg,N-CDs ( $\text{pH}5.52 \pm 0.03$ ) than N-CDs ( $\text{pH}3.5 \pm 0.05$ ) at the same concentration (Figure S5).

X-ray photoelectron spectroscopy (XPS) was carried out to further characterize the chemical composition of Mg,N-CDs. Fig. 2B shows the full-band XPS spectrum of Mg,N-CDs with  $\text{C}_{1s}$  (284.4 eV),  $\text{N}_{1s}$  (400.6 eV),  $\text{O}_{1s}$  (531.86 eV),  $\text{Mg}_{1s}$  (1304.25 eV),  $\text{Mg}_{2s}$  (89.52 eV),  $\text{Mg}_{2p}$  (50.79 eV), and Mg Auger peaks ( $\text{Mg}_{KLL}$ , 306.2 eV) signals. The high-resolution spectrum of  $\text{C}_{1s}$  (Fig. 2C) reveals three C forms in C–C, C–O–C, and O–C = O at 284.8 eV, 286.3 eV, and 288.7 eV, respectively. The high-resolution spectrum of  $\text{O}_{1s}$  band (Fig. 2D) is deconvoluted into metal carbonates at 531.8 eV and a C = O bond at 533.3 eV, suggesting the carbonate-like mode of Mg in Mg,N-CDs. Only graphitic N signal at

400.24 eV is observed in the high-resolution spectrum of  $\text{N}_{1s}$  (Fig. 2E). The  $\text{Mg}_{1s}$  peak is assigned to the Mg native oxide and the  $\text{Mg}_{2p}$  peak was assigned to  $\text{Mg-CO}_3$  (Fig. 2F–H) [36–38]. Besides, the  $\text{Mg}_{KLL}$  accompanying  $\text{Mg}_{1s}$  indicates the Mg buried in carbon nuclear. About 6.39% and 3.83% of Mg and N contents in Mg,N-CDs were detected by XPS analysis.

To further determine the amount and existing form of Mg in Mg,N-CDs, TG-MS and high-temperature XRD analyses were carried out. Three stepwise weight-loss processes are observed in the TG curve of Mg,N-CDs at 25–220 °C (endothermic reaction), 220–500 °C, and 500–545 °C (exothermic reaction), with weight losses of 27.92%, 38.26%, and 24.75%, respectively (Figure S6A–C). Figure S6D shows that the weight losses during 25–220 °C and 220–500 °C are ascribable to the evaporation of water molecules and the escape of  $\text{NH}_3$ ,  $\text{CO}_2$ , and  $\text{NO}_2$  due to the decomposition of amide bond in Mg,N-CDs [39]. At 500–545 °C, the majority of weight loss results from the breakdown of



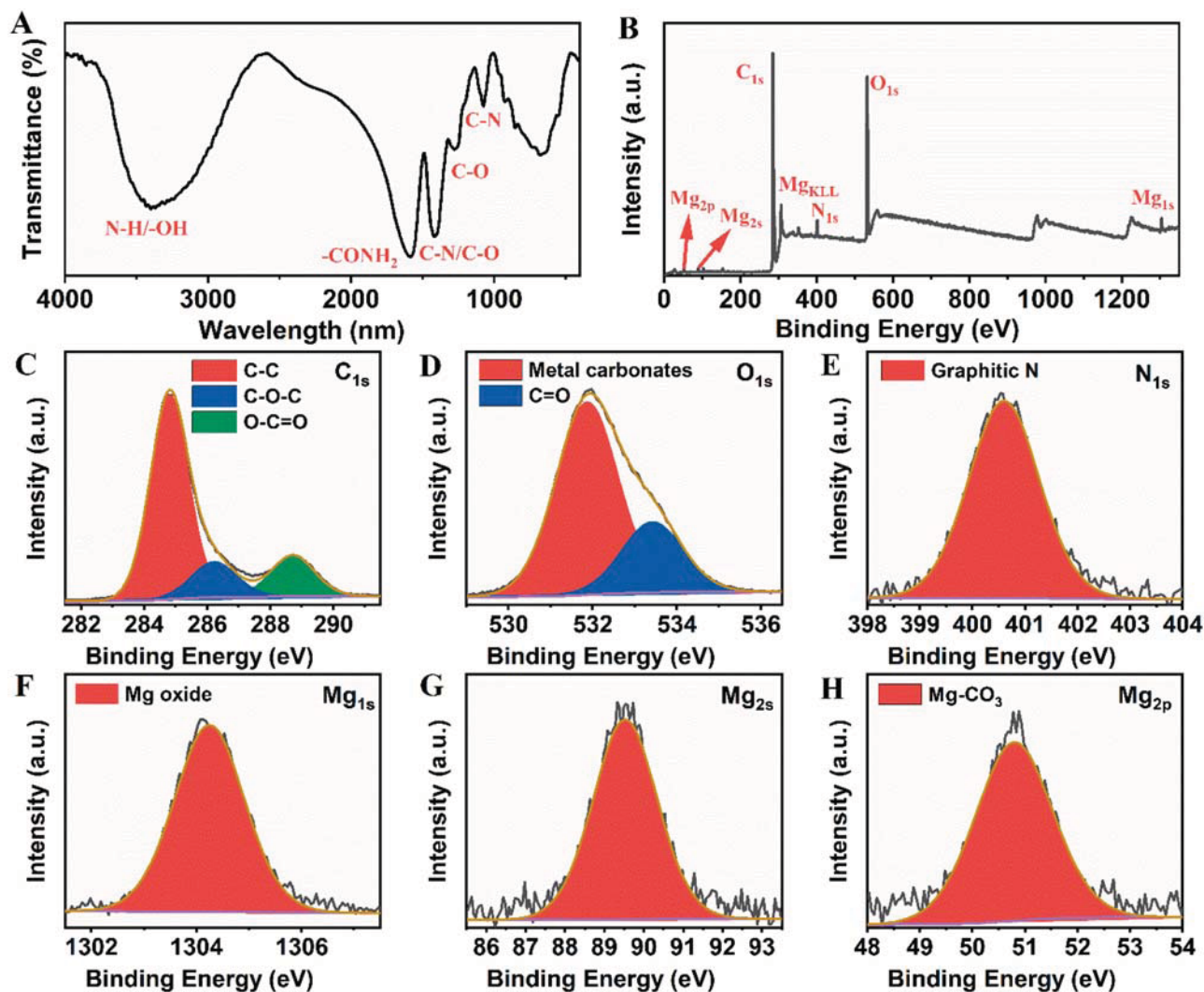


Fig. 2. FTIR spectra (A), full XPS patterns (B) and high-resolution XPS spectra of C<sub>1s</sub> (C), O<sub>1s</sub> (D), N<sub>1s</sub> (E), Mg<sub>1s</sub> (F), Mg<sub>2s</sub> (G), Mg<sub>2p</sub> (H) peaks of Mg,N-CDs.

carbon skeleton and doped graphite N, releasing NH<sub>3</sub>, H<sub>2</sub>O, CO<sub>2</sub>, NO<sub>2</sub>, and small amounts of NO [40–42]. These results correspond to the chemical composition analyzed by FTIR and XPS. After complete decomposition at 800 °C, the remaining sample of Mg,N-CDs is ascribed to MgO from the XRD profile (Figure S6E). The characteristic peaks of MgO are initially detected at 550 °C, which corresponds to the thermal decomposition temperature of MgCO<sub>3</sub> [43]. This result further suggests that the doped Mg in Mg,N-CDs is in carbonate-like mode. The Mg content in Mg,N-CDs is calculated as 5.38% according to approximately 8.96% of the residual MgO at 800 °C in the TG curve, which is consistent with the 6.39% in the XPS result.

Based on the above results, we analyze the formation mechanism of Mg,N-CDs, and the effect of doped Mg on the FL emission. As shown in Figure S7A, EA and Mg(OH)<sub>2</sub> firstly react with CA via amidation and chelation, and then polymer-like macromolecules are formed through further intermolecular/intramolecular dehydration during the hydrothermal treatment. Finally, the Mg,N-CDs are obtained after carbonization. Moderate graphite N doping can significantly increase the QY of CDs [20,31,32]. In this study, the N-CDs display a relative QY as high as 57.37%, which decreased to 19.58% in Mg,N-CDs (Figure S8). We conclude that the doped Mg reacts with the oxygen-containing moieties in Mg,N-CDs, decreasing the energy levels and increasing the vibration relaxation of the energy levels (Figure S7B) [44]. Therefore, compared to N-CDs, Mg,N-CDs exhibit decreased QY and FL lifetime and red-shifted FL emission, even though light absorption increased.

#### 3.4. Light conversion of the Mg,N-CDs in photosynthesis

Photoluminescence makes CDs good electron donors and acceptors in energy conversion and electron transfer during photosynthesis [26,45]. The chloroplast is isolated from lettuce as a model to investigate the effect of Mg,N-CDs on photosynthesis. After 1-h incubation in the dark, Mg,N-CDs induce no obvious changes in the morphology of chloroplast compared to the control (Fig. 3A and B). Under the excitation of 361–389 nm by an inverted fluorescence microscope, the Mg,N-CDs@Chl emit a blue FL signal (Fig. 3D), indicating the internalization of Mg,N-CDs by chloroplasts. Under the excitation of 515–565, the red FL signal is emitted from the chlorophyll molecule on the thylakoid membrane (Fig. 3E). The blue completely overlaps with the red FL signals in Fig. 3F, suggesting the same distribution of Mg,N-CDs and chlorophyll molecules in the chloroplast. There is an overlap between the FL emission spectrum of Mg,N-CDs and the absorption spectrum of chloroplast (Figure S9A). In addition, Mg,N-CDs@Chls exhibit weaker FL intensity in the blue light region than Mg,N-CDs (Figure S9B), and higher light absorption from 300 to 340 nm than chloroplasts alone (Figure S9C). From Fig. 3G, the FL lifetime of Mg,N-CDs decreases from 3.04 ns to 2.00 ns in chloroplasts. These results confirm that the energy of Mg,N-CDs excited by UV light can be harvested and reabsorbed by chloroplasts [23]. Subsequently, the photosynthetic activity of the Mg,N-CDs@Chl was measured by Hill reaction using DCPIP and ferricyanide, with the comparison of chloroplasts. From Fig. 3H and I, Mg,N-CDs cause a concentration-dependent



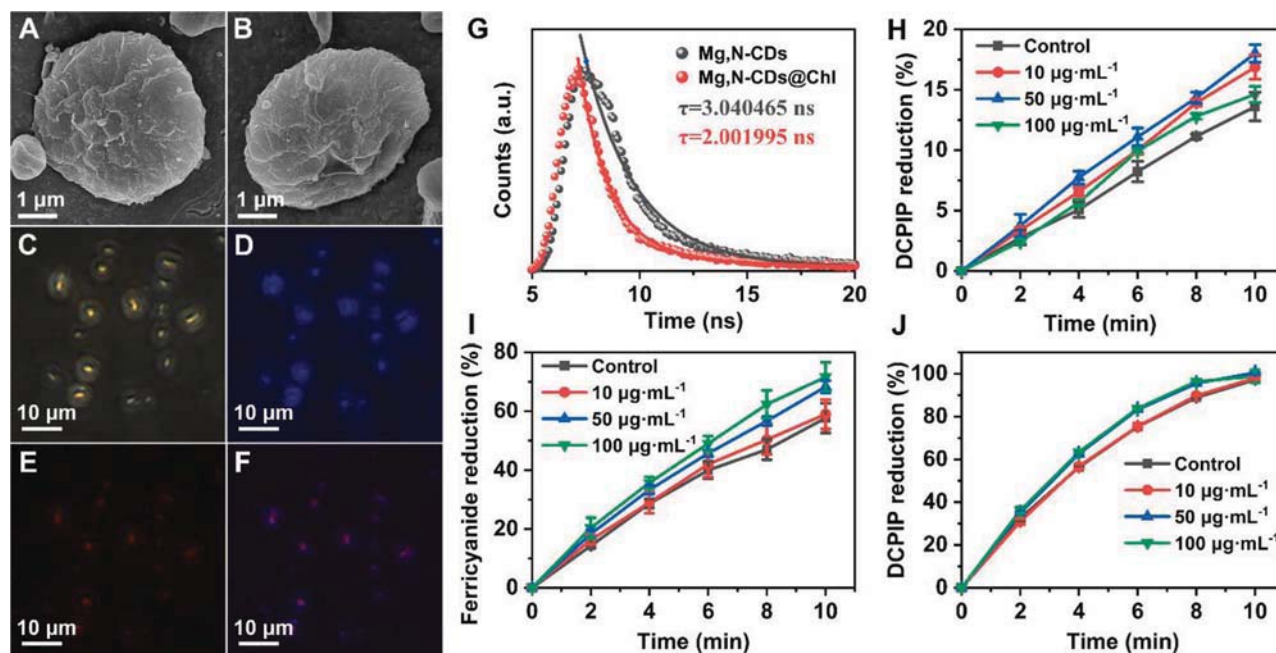


Fig. 3. SEM images of the extracted chloroplast in control (A) and Mg,N-CDs at 300  $\mu\text{g}\cdot\text{mL}^{-1}$  treatment (B); Fluorescent images of Mg,N-CDs at 300  $\mu\text{g}\cdot\text{mL}^{-1}$  treated chloroplast: bright field (C), 361–389 excitation (D), 515–565 excitation (E) and overlaid image of D and E (F); FL lifetimes of Mg,N-CDs before and after binding with chloroplasts (Mg,N-CDs@chl) (G); DCPIP (H) and ferricyanide (I) reductions of the chloroplast conjugated with Mg,N-CDs at different concentrations under 1000 LUX and 3000 LUX irradiation, respectively; DCPIP reduction of the chloroplast conjugated with Mg,N-CDs at different concentrations under saturated irradiation (9000 LUX) (J). Error bars correspond to standard deviation ( $n = 3$  and  $p < 0.05$ ).

increase ( $p < 0.05$ ) in DCPIP and ferricyanide reduction, with maximum enhancements of 52.48% and 41.86% at 50 and 100  $\mu\text{g}\cdot\text{mL}^{-1}$ , respectively. Interestingly, even under saturated light (9000 LUX), Mg,N-CDs at 50 and 100  $\mu\text{g}\cdot\text{mL}^{-1}$  also significantly increase ( $p < 0.05$ ) the DCPIP reduction of chloroplasts (Fig. 3J). These results prove that Mg,N-CDs can promote the photosynthetic activity of chloroplasts by transferring excited energy to the latter.

### 3.5. Effect of Mg,N-CDs on the growth of rice

The rice plants were sprayed with Mg,N-CDs at 50, 100, and 300  $\mu\text{g}\cdot\text{mL}^{-1}$  every two days for 16 days. Figure S10 shows that the growth of Mg,N-CDs-treated rice seedlings are remarkably more promoted than the control. In detail, Mg,N-CDs at 50, 100, and 300  $\mu\text{g}\cdot\text{mL}^{-1}$  significantly increases ( $p < 0.05$ ) the height of rice seedlings by 19.87%, 22.55%, and 22.34% (Fig. 4A), and the fresh biomass by 33.90%, 55.25%, and 70.60% (Fig. 4B) compared to the control, respectively. Furthermore, the rice seedlings treated with Mg,N-CDs at 50, 100 and 300  $\mu\text{g}\cdot\text{mL}^{-1}$  also exhibit significant increases ( $p < 0.05$ ) in both chlorophyll *a* (11.52%, 12.06% and 14.39%) and chlorophyll *b* (15.57%, 20.31% and 26.54%) contents (Fig. 4C). Moreover, the ratio of chlorophyll *a* and *b* significantly decreases ( $p < 0.05$ ) from 4.39 in control to 3.95 in Mg,N-CDs at 300  $\mu\text{g}\cdot\text{mL}^{-1}$  in a dose-dependent manner. However, Mg,N-CDs at 50, 100, and 300  $\mu\text{g}\cdot\text{mL}^{-1}$  induce a concentration-dependent decrease ( $p < 0.05$ ) in the carbohydrate contents in rice seedlings by 6.50%, 21.37%, and 34.12% (Fig. 4D), respectively. The enhanced chlorophyll content in Mg,N-CDs-treated rice plants was consistent with the expected purpose of designing Mg,N-CDs.

### 3.6. Gene expression of enzymes related to chlorophyll metabolism

To determine the mechanism of Mg,N-CDs increasing the chlorophyll contents, the gene expression of chlorophyll metabolism-related enzymes in rice seedlings were measured, including Mg-dechelatase subunit (*ChlI* and *ChlD*), chlorophyll synthase (*ChlG*), and *chlorophyllase-2*. As shown in Fig. 4E–H, Mg,N-CDs at 300  $\mu\text{g}\cdot\text{mL}^{-1}$  significantly increase

( $p < 0.05$ ) the expressions of *ChlI*, *ChlD*, *ChlG*, and *chlorophyllase-2* genes of rice seedlings by 93.55%, 15.26%, 115.02%, and 29.75%, respectively. However, Mg,N-CDs at 50 and 100  $\mu\text{g}\cdot\text{mL}^{-1}$  induce insignificant effects on the expressions of *ChlI* gene, and significant decreases in *ChlD* (33.86% and 34.42%) and *chlorophyllase-2* (33.33% and 33.10%) expression. For the expression of the *ChlG* gene, 50  $\mu\text{g}\cdot\text{mL}^{-1}$  of Mg,N-CDs leads to a significant decrease of 31.58%, while no significant effect is observed in the 100  $\mu\text{g}\cdot\text{mL}^{-1}$  treatment. Based on these results, we conclude that Mg,N-CDs accelerate the biosynthesis and metabolism of chlorophyll in rice plants through regulating the expression of related genes, thereby improving the content and activity of chlorophyll in rice plants.

### 3.7. Effect of Mg,N-CDs on the photosynthesis of rice

Before the measurement of photosynthesis, the distribution of Mg,N-CDs in rice leaves was observed using TEM. Compared to the control (Fig. 5A), a large number of black particles are observed in the cytoplasm and chloroplasts of rice leaves treated with Mg,N-CDs (300  $\mu\text{g}\cdot\text{mL}^{-1}$ ) (Fig. 5B), suggesting the uniform distribution of Mg,N-CDs. Then, PAM chlorophyll fluorescence imaging (Imaging-PAM) was used to study the photosynthesis of rice seedlings. The Mg,N-CDs show PAR- and concentration-dependent effects ( $p < 0.05$ ) on the chlorophyll fluorescence parameters (Fig. 5C–H). Under weaker PAR than 81  $\mu\text{mol}\cdot\text{m}^{-2}\cdot\text{s}^{-1}$ , Mg,N-CDs at all concentrations significantly decrease the NPQ, qP, ETR, Y(NPQ), Y(II), and increase the Y(NO) of rice seedlings. The Mg,N-CDs at 50  $\mu\text{g}\cdot\text{mL}^{-1}$  significantly increase the NPQ of rice seedling under PAR of 146  $\mu\text{mol}\cdot\text{m}^{-2}\cdot\text{s}^{-1}$  or higher and induce no significant decrease in qP and ETR until PAR up to 611 and 461  $\mu\text{mol}\cdot\text{m}^{-2}\cdot\text{s}^{-1}$ , respectively. Subsequently, Mg,N-CDs at 50  $\mu\text{g}\cdot\text{mL}^{-1}$  induce a significant increase in Y(NPQ), a decrease in Y(NO), and no significant effect in Y(II) of the rice seedlings under PAR from 231 to 611  $\mu\text{mol}\cdot\text{m}^{-2}\cdot\text{s}^{-1}$ . However, under PAR higher than 146  $\mu\text{mol}\cdot\text{m}^{-2}\cdot\text{s}^{-1}$ , Mg,N-CDs at 100 and 300  $\mu\text{g}\cdot\text{mL}^{-1}$  significantly increase the qP and ETR of the rice seedlings, thereby leading to significant decreases in Y(NPQ) and Y(NO) and an increase in Y(II). For the NPQ of rice seedlings, a

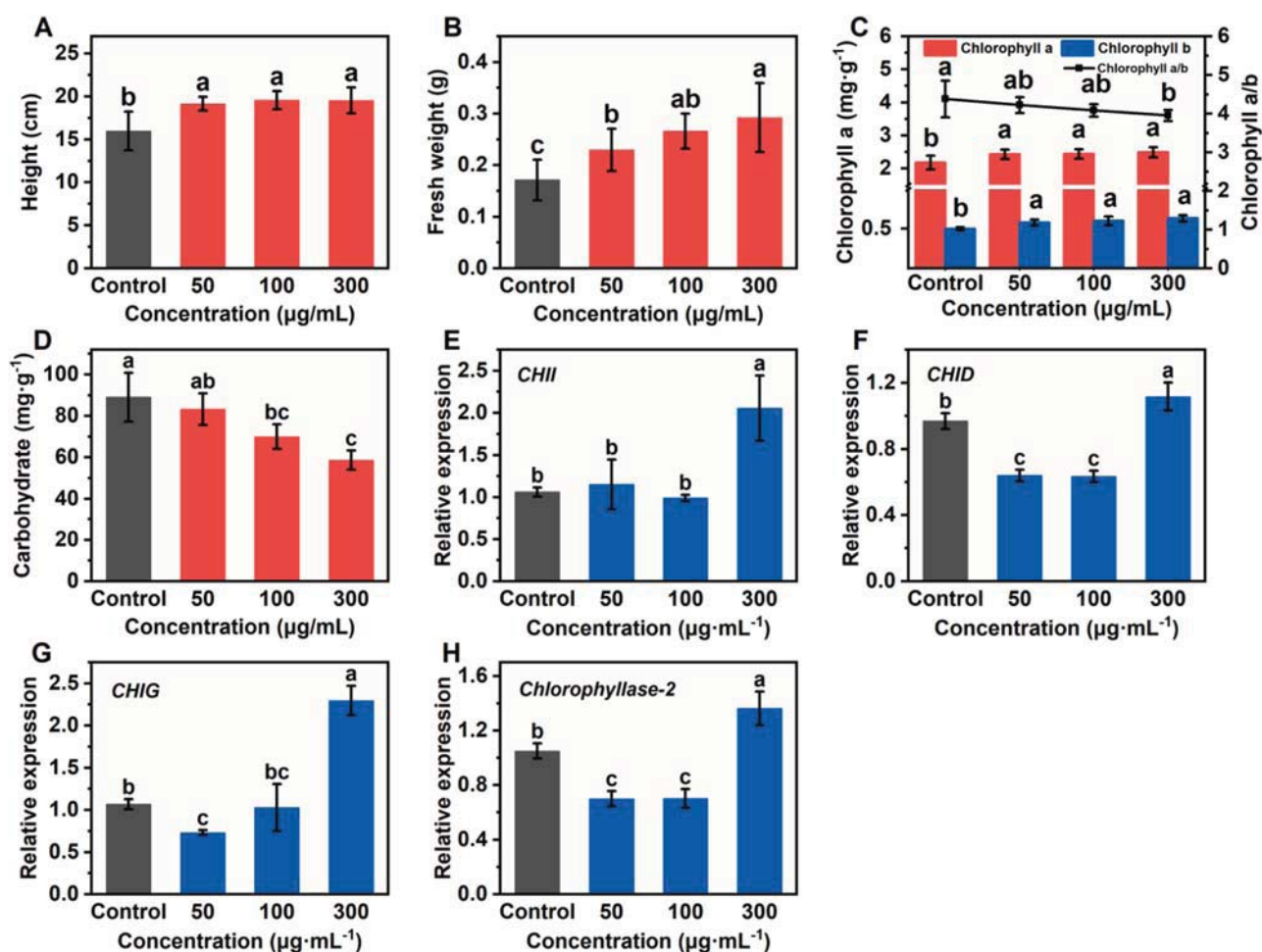


Fig. 4. The height (B), fresh weight (C), chlorophyll content (D), carbohydrate content (E), and relative gene expression levels of *ChlI* (E), *ChlD* (F), *chlorophyll synthase* (*ChlG*) (G), *chlorophyllase-2* (H) of rice seedlings in control and Mg,N-CDs (50, 100 and 300 µg·mL<sup>-1</sup>) treatments. Error bars correspond to standard deviation (n ≥ 5). Marked with different letters indicate a significant difference (p < 0.05).

significant increase is induced by Mg,N-CDs at 100 µg·mL<sup>-1</sup> from PAR of 231 to 611 µmol·m<sup>-2</sup>·s<sup>-1</sup>, and by Mg,N-CDs at 300 µg·mL<sup>-1</sup> from 461 to 611 µmol·m<sup>-2</sup>·s<sup>-1</sup>. Generally, Mg,N-CDs at 300 µg·mL<sup>-1</sup> lead to the best effect on the photosynthesis of rice seedlings under PAR of 461 µmol·m<sup>-2</sup>·s<sup>-1</sup> (Fig. 6A), significantly increasing NPQ, qP, ETR, and Y(II) of rice seedlings by 6.01%, 109.54%, 104.48%, and 127.16%, respectively. In addition, the maximum increase (15.06%) in NPQ is achieved by Mg,N-CDs at 100 µg·mL<sup>-1</sup> under 611 µmol·m<sup>-2</sup>·s<sup>-1</sup>. The PAR received by plants on the Earth is always higher than 146 µmol·m<sup>-2</sup>·s<sup>-1</sup> [46]. Therefore, Mg,N-CDs contribute to the photosynthetic activity (qP), light protection ability (NPQ), and electron transport rate (ETR) of the plants, reduce the non-photochemical energy loss [Y(NPQ) and Y(NO)] and enhance the photochemical energy conversion [Y(II)] in the light reaction of photosynthesis. The enhanced photosynthetic activity of rice plants could be closely related to the activated biosynthesis and metabolism of chlorophyll by Mg,N-CDs.

Following the light reaction, the Calvin cycle in photosynthesis can convert CO<sub>2</sub> to carbohydrate, powered by the ATP and NADPH produced in light reaction, which directly determines the accumulation of plant biomass [47]. RuBisCO is a key enzyme in carbon assimilation, and its activity largely influences the photosynthetic rate [21,24]. As shown in Fig. 6B, Mg,N-CDs lead to a concentration-dependent increase in the carboxylase activity of RuBisCO, with a maximum enhancement of 46.62% at 300 µg·mL<sup>-1</sup>. Summarized from the above results, Mg,N-CDs treatments can improve both light reaction and CO<sub>2</sub> assimilation in photosynthesis, which finally promote the growth of rice plants.

From the above results, we conclude that Mg,N-CDs promote the

photosynthesis of plants through adjusting (1) the biosynthesis and metabolism of chlorophyll, (2) light absorption, (3) photosynthetic electron transport, and (4) CO<sub>2</sub> assimilation (Scheme 1). Chlorophyll is closely associated with all aspects of the primary events, including light harvest, energy transfer, and light energy conversion [7]. The chelation of Mg<sup>2+</sup> into protoporphyrin IX catalyzed by Mg-chelatase (Mg-protoporphyrin IX chelatase) and the esterification of chlorophyllide a and b with phytol or geranyl-geranyl pyrophosphate catalyzed by chlorophyll synthase (ChlG) are two key intermediates in the chlorophyll biosynthetic pathway [48,49]. The chlorophyllase determines the degradation of chlorophyll [50]. In this study, the gene expressions of the chlorophyll synthetase (ChlG), two subunits (ChlI and ChlD) of Mg-chelatase, and chlorophyllase-2 in rice seedlings are synchronously improved by Mg,N-CDs at 300 µg·mL<sup>-1</sup>. Therefore, the synthesis and metabolism of chlorophyll in rice seedlings are accelerated by Mg,N-CDs, which maintains high contents and activity of chlorophyll for light harvest, energy transfer, and conversion. In previous reports, CDs synthesized by electrochemical etching graphite rod with less surface groups lead to insignificant effects on chlorophyll content in plants [15,24]. However, the chlorophyll content was significantly increased by the CDs after being treated with ammonium hydroxide [21]. Besides, CDs prepared using citric acid and ethanolamine also can promote the chlorophyll synthesis of rice plants [20]. Therefore, we speculate that the regulation of Mg,N-CDs to chlorophyll synthesis is closely related to the surface groups, especially those containing N. Li et al. revealed that CDs in plants could be degraded by horseradish peroxidase and H<sub>2</sub>O<sub>2</sub> [15]. Furthermore, after being degraded, Mg,N-CDs can provide precursors for the



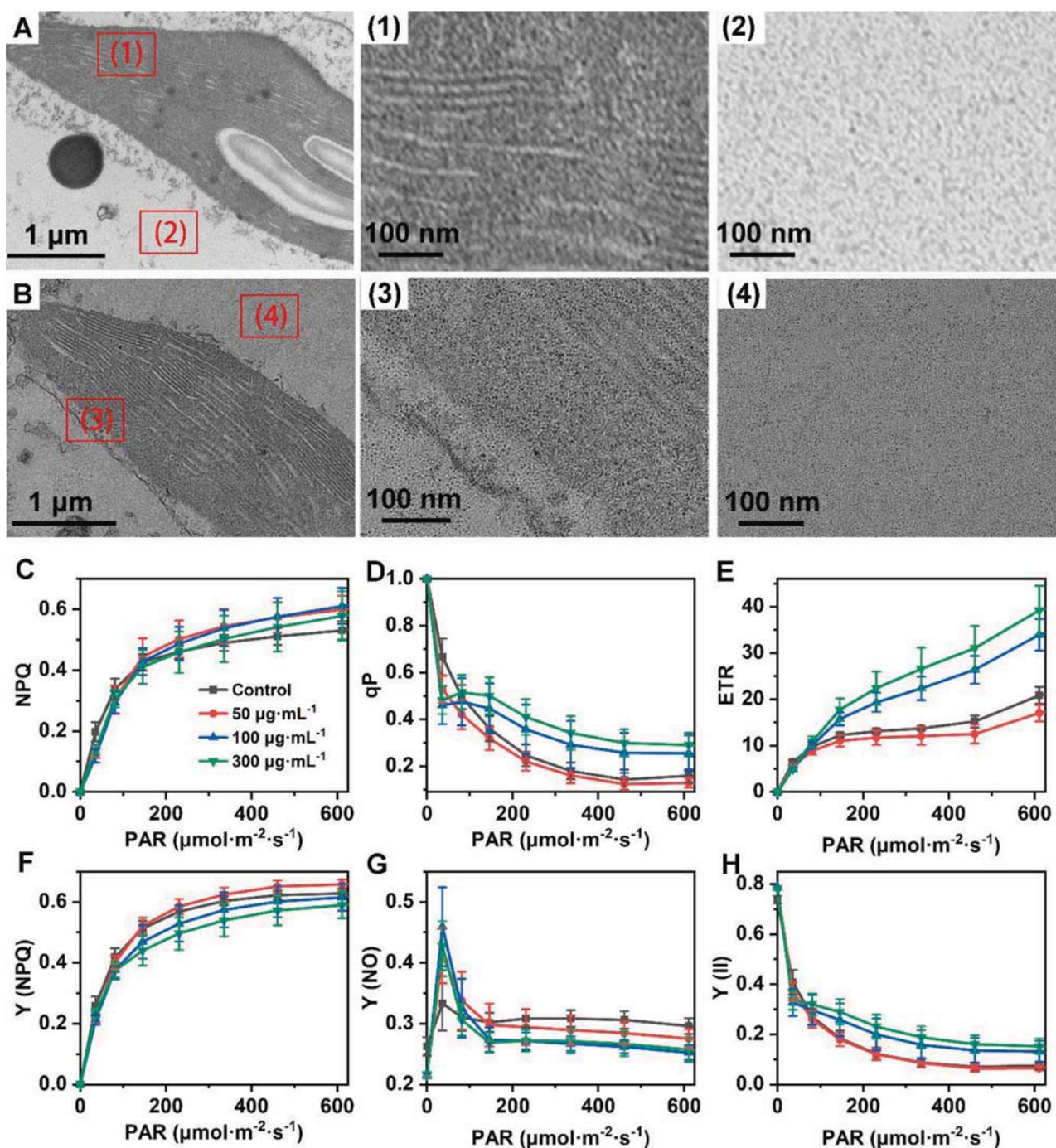


**Fig. 5.** TEM images of rice leaves in control (A) and Mg,N-CDs at 300 µg·mL<sup>-1</sup> (B) treatments; NPQ (C), qP (D), ETR (E), Y(NPQ) (F), Y(NO) (G), and Y(II) (H) of rice leaves in control and Mg,N-CDs at different concentrations. Error bars in (C–H) correspond to standard deviation ( $n \geq 5$  and  $p < 0.05$ ).

synthesis of chlorophyll molecules, photosynthetic proteins, and enzymes, because both magnesium (Mg) and nitrogen (N) element are key components of these biomolecules [8–10]. Apart from the chlorophyll, Mg,N-CDs in chloroplasts can absorb UV light and emit blue FL. The excited energy of Mg,N-CDs can be reabsorbed by chloroplasts for photosynthesis, thereby protecting the chloroplast from UV light and increasing the photosynthesis. The decreased chlorophyll *a/b* ratio in rice seedlings by Mg,N-CDs contributes to the absorption of blue FL of Mg,N-CDs [51]. The Calvin cycle is one of the key steps of photosynthesis that transforms CO<sub>2</sub> into carbohydrates using ATP and NADPH produced in light reactions [47], and RuBisCO is an important enzyme in Calvin cycle that determines the carbon assimilation rate [52]. Mg,N-

CDs can increase the carboxylase activity of RuBisCO in rice, thereby promoting the CO<sub>2</sub> assimilation. Therefore, Mg,N-CDs integrally improve the photosynthesis of rice plants, and increase their growth.

Additionally, the total carbohydrate content in rice seedlings decreases with the increase of Mg,N-CDs concentration. This result implies that Mg,N-CDs may contribute to the subsequent conversion of carbohydrates into other organic substances in plants, which needs further investigation in the future. Additionally, Mg,N-CDs at 50 and 100 µg·mL<sup>-1</sup> induce no significant effect or decrease to the gene expressions of *ChlG*, *ChlI*, *ChlD*, and *chlorophyllase-2* in rice seedlings, in particular, 50 µg·mL<sup>-1</sup> of Mg,N-CDs results in an insignificant effect on Y(II) and decrease in ETR of PS II in rice seedlings. Previous studies reported that



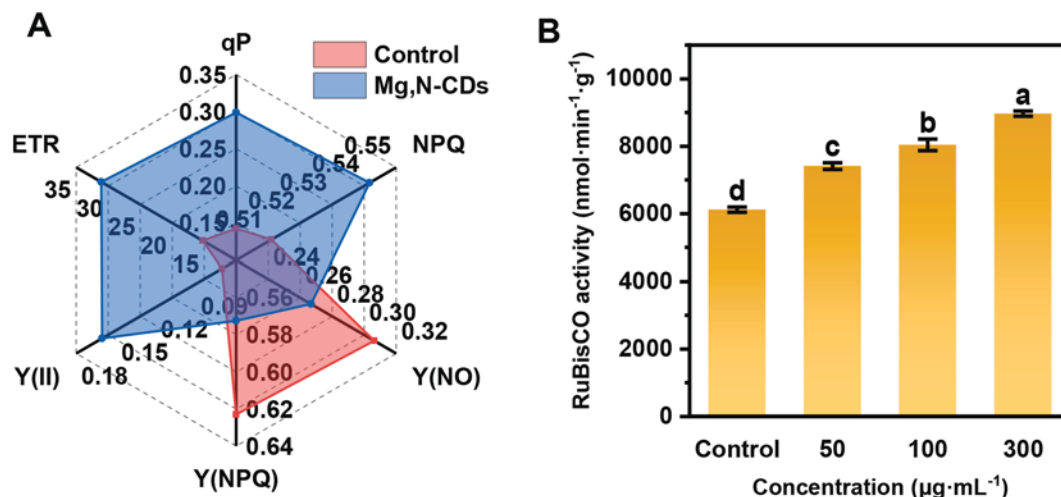
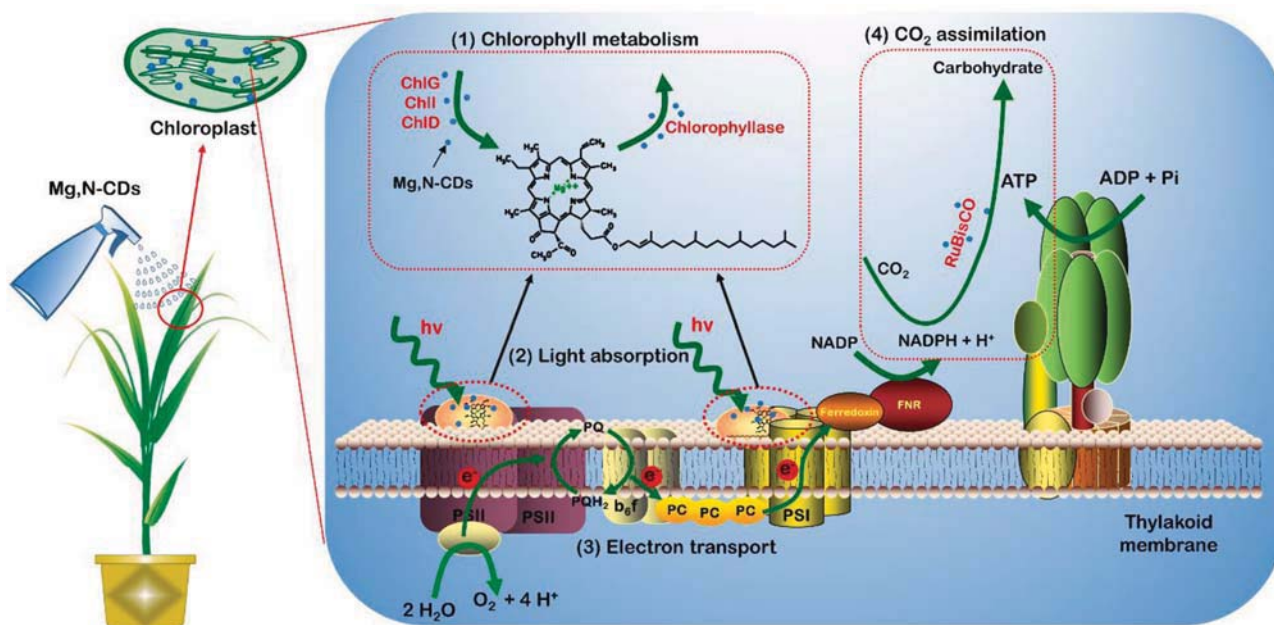


**Fig. 6.** (A) NPQ, qP, Y(NPQ), Y(NO), Y(II), and ETR of the rice leaves in control and Mg,N-CDs at 300 µg·mL<sup>-1</sup> under 461 µmol·m<sup>-2</sup>·s<sup>-1</sup>; (B) RuBisCO activity of rice seedlings in control and Mg,N-CDs (50, 100 and 300 µg·mL<sup>-1</sup>) treatments. Error bars correspond to standard deviation ( $n \geq 5$ ). Marked with different letters indicate a significant difference ( $p < 0.05$ ).



**Scheme 1.** Schematic representation of the mechanism for Mg,N-CDs enhancing the plant growth through multifunctional regulation in photosynthesis.

CDs in plants could be degraded into plant hormone analogs and CO<sub>2</sub>, which regulate plant growth and participate in the Calvin cycle, respectively [15,24]. Therefore, the enhancement by Mg,N-CDs at 50 and 100 µg·mL<sup>-1</sup> of chlorophyll content and growth of rice seedlings could be induced mainly by providing precursors for the chlorophyll molecules, photosynthetic proteins, enzymes, and CO<sub>2</sub> assimilation.

#### 4. Conclusion

In this study, we designed and prepared Mg,N-CDs for the chlorophyll synthesis of plant photosynthesis. The Mg<sup>2+</sup> and N were doped into Mg,N-CDs in carbonate-like and graphite N forms, respectively. The Mg doping changes the electron transition modes and redshifts the FL of CDs by decreasing the energy levels. Under white light, the excited energy of Mg,N-CDs in chloroplasts by UV part can be reabsorbed by the latter, thereby enhancing their photosynthetic activity. After rice seedlings were exposed, the Mg,N-CDs entered the rice leaves with uniform

distribution. Furthermore, Mg,N-CDs at 300 µg·mL<sup>-1</sup> can accelerate the regeneration and metabolism of chlorophyll in rice plants by up-regulating the gene expressions of chlorophyll metabolism-related enzymes and increase the RuBisCO activity for CO<sub>2</sub> assimilation. Through the synergistic effect between these functions of Mg,N-CDs in photosynthesis, the growth of rice seedlings is significantly improved.

#### Declaration of Competing Interest

The authors declare that they have no known competing financial interests or personal relationships that could have appeared to influence the work reported in this paper.

#### Acknowledgments

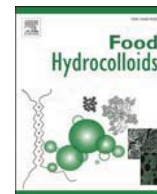
This work was supported by the National Natural Science Foundation of China (Grant No. 21571067, 21671070).

## Appendix A. Supplementary data

Supplementary data to this article can be found online at <https://doi.org/10.1016/j.cej.2021.130114>.

## References

- [1] T. Dresselhaus, R. Hückelhoven, Biotic and Abiotic Stress Responses in Crop Plants, *Agronomy* 8 (2018).
- [2] A.K. Dangi, B. Sharma, I. Khangwal, P. Shukla, Combinatorial Interactions of Biotic and Abiotic Stresses in Plants and Their Molecular Mechanisms: Systems Biology Approach, *Mol. Biotechnol.* 60 (2018) 636–650.
- [3] L. Zhang, C. Yan, Q. Guo, J. Zhang, J. Ruiz-Menjivar, The impact of agricultural chemical inputs on environment: global evidence from informetrics analysis and visualization, *International Journal of Low-Carbon Technologies* 13 (2018) 338–352.
- [4] T. Cardona, S. Shao, Peter J. Nixon, Enhancing photosynthesis in plants: the light reactions, *Essays in Biochemistry* 62 (2018) 85–94.
- [5] C. Jansson, J. Vogel, S. Hazen, T. Brutnell, T. Mockler, Climate-smart crops with enhanced photosynthesis, *J. Exp. Bot.* 69 (2018) 3801–3809.
- [6] W. Huang, M. Tikkanen, S.-B. Zhang, Photoinhibition of photosystem I in *Nephrolepis falciformis* depends on reactive oxygen species generated in the chloroplast stroma, *Photosynth. Res.* 137 (1) (2018) 129–140.
- [7] S. Park, C.J. Steen, D. Lyska, A.L. Fischer, B. Endelman, M. Iwai, K.K. Niyogi, G. R. Fleming, Chlorophyll-carotenoid excitation energy transfer and charge transfer in *Nannochloropsis oceanica* for the regulation of photosynthesis, *Proc. Natl. Acad. Sci.* 116 (2019) 3385.
- [8] Y.Y. Peng, L.L. Liao, S. Liu, M.M. Nie, J. Li, L.D. Zhang, J.F. Ma, Z.C. Chen, Magnesium Deficiency Triggers SGR-Mediated Chlorophyll Degradation for Magnesium Remobilization, *Plant Physiol.* 181 (2019) 262.
- [9] S. Wang, K. Guan, Z. Wang, E.A. Ainsworth, T. Zheng, P.A. Townsend, K. Li, C. Moller, G. Wu, C. Jiang, Unique contributions of chlorophyll and nitrogen to predict crop photosynthetic capacity from leaf spectroscopy, *J. Exp. Bot.* (2020).
- [10] H. Croft, J.M. Chen, X. Luo, P. Bartlett, B. Chen, R.M. Staebler, Leaf chlorophyll content as a proxy for leaf photosynthetic capacity, *Glob. Change Biol.* 23 (9) (2017) 3513–3524.
- [11] S. Chou, B. Chen, J. Chen, M. Wang, S. Wang, H. Croft, Q. Shi, Estimation of leaf photosynthetic capacity from the photochemical reflectance index and leaf pigments, *Ecol. Ind.* 110 (2020), 105867.
- [12] G.V. Lowry, A. Avellan, L.M. Gilbertson, Opportunities and challenges for nanotechnology in the agri-tech revolution, *Nat. Nanotechnol.* 14 (6) (2019) 517–522.
- [13] M. Han, S. Zhu, S. Lu, Y. Song, T. Feng, S. Tao, J. Liu, B. Yang, Recent progress on the photocatalysis of carbon dots: Classification, mechanism and applications, *Nano Today* 19 (2018) 201–218.
- [14] L. Xiao, H. Guo, S. Wang, J. Li, Y. Wang, B. Xing, Carbon Dots Alleviate the Toxicity of Cadmium Ions ( $Cd^{2+}$ ) toward Wheat Seedlings, *Environ. Sci. Nano* 6 (2019) 1493–1506.
- [15] H. Li, J. Huang, F. Lu, Y. Liu, Y. Song, Y. Sun, J. Zhong, H. Huang, Y. Wang, S. Li, Y. Lifshitz, S.-T. Lee, Z. Kang, Impacts of Carbon Dots on Rice Plants: Boosting the Growth and Improving the Disease Resistance, *ACS Appl. Bio Mater.* 1 (3) (2018) 663–672.
- [16] J. Li, S. Yang, Y. Deng, P. Chai, Y. Yang, X. He, X. Xie, Z. Kang, G. Ding, H. Zhou, X. Fan, Emancipating Target-Functionalized Carbon Dots from Autophagy Vesicles for a Novel Visualized Tumor Therapy, *Adv. Funct. Mater.* 28 (2018) 1800881.
- [17] S. Pandit, P. Behera, J. Sahoo, M. De, In Situ Synthesis of Amino Acid Functionalized Carbon Dots with Tunable Properties and Their Biological Applications, *ACS Appl. Bio Mater.* 2 (8) (2019) 3393–3403.
- [18] F. Li, T. Li, C. Sun, J. Xia, Y. Jiao, H. Xu, Selenium-Doped Carbon Quantum Dots for Free-Radical Scavenging, *Angew. Chem. Int. Ed.* 56 (33) (2017) 9910–9914.
- [19] Y. Li, X. Xu, Y. Wu, J. Zhuang, X. Zhang, H. Zhang, B. Lei, C. Hu, Y. Liu, A review on the effects of carbon dots in plant systems, *Mater. Chem. Front.* 4 (2) (2020) 437–448.
- [20] Y. Li, X. Pan, X. Xu, Y. Wu, J. Zhuang, X. Zhang, H. Zhang, B. Lei, C. Hu, Y. Liu, Carbon dots as light converter for plant photosynthesis: Augmenting light coverage and quantum yield effect, *J. Hazard. Mater.* 410 (2021) 124534.
- [21] H. Wang, M. Zhang, Y. Song, H. Li, H. Huang, M. Shao, Y. Liu, Z. Kang, Carbon dots promote the growth and photosynthesis of mung bean sprouts, *Carbon* 136 (2018) 94–102.
- [22] L.-X. Su, X.-L. Ma, K.-K. Zhao, C.-L. Shen, Q. Lou, D.-M. Yin, C.-X. Shan, Carbon Nanodots for Enhancing the Stress Resistance of Peanut Plants, *ACS Omega* 3 (12) (2018) 17770–17777.
- [23] S. Chandra, S. Pradhan, S. Mitra, P. Patra, A. Bhattacharya, P. Pramanik, A. Goswami, High throughput electron transfer from carbon dots to chloroplast: a rationale of enhanced photosynthesis, *Nanoscale* 6 (2014) 3647–3655.
- [24] H. Li, J. Huang, Y. Liu, F. Lu, J. Zhong, Y. Wang, S. Li, Y. Lifshitz, S.-T. Lee, Z. Kang, Enhanced RuBisCO activity and promoted dicotyledons growth with degradable carbon dots, *Nano Res.* 12 (7) (2019) 1585–1593.
- [25] P. Wu, W. Li, Q. Wu, Y. Liu, S. Liu, Hydrothermal Synthesis of Nitrogen-Doped Carbon Quantum Dots from Microcrystalline Cellulose for the Detection of  $Fe^{3+}$  Ions in an Acidic Environment, *RSC Adv.* 7 (2017) 44144–44153.
- [26] W. Li, S. Wu, H. Zhang, X. Zhang, J. Zhuang, C. Hu, Y. Liu, B. Lei, L. Ma, X. Wang, Enhanced Biological Photosynthetic Efficiency Using Light-Harvesting Engineering with Dual-Emissive Carbon Dots, *Adv. Funct. Mater.* 28 (2018) 1804004.
- [27] Y. Li, Q. Jin, D. Yang, J. Cui, Molybdenum sulfide induce growth enhancement effect of rice (*Oryza sativa* L.) through regulating the synthesis of chlorophyll and the expression of aquaporin gene, *J. Agric. Food Chem.* 66 (2018) 4013–4021.
- [28] Y. Li, Y. Liu, D. Yang, Q. Jin, C. Wu, J. Cui, Multifunctional molybdenum disulfide-copper nanocomposite that enhances the antibacterial activity, promotes rice growth and induces rice resistance, *J. Hazard. Mater.* 394 (2020), 122551.
- [29] Y. Li, D. Yang, J. Cui, Graphene oxide loaded with copper oxide nanoparticles as an antibacterial agent against *Pseudomonas syringae* pv. tomato, *RSC Adv.* 7 (62) (2017) 38853–38860.
- [30] K.J. Livak, T.D. Schmittgen, Analysis of Relative Gene Expression Data Using Real-Time Quantitative PCR and the  $2^{-\Delta\Delta CT}$  Method, *Methods* 25 (4) (2001) 402–408.
- [31] Y. Zhang, X. Liu, Y. Fan, X. Guo, L. Zhou, Y. Lv, J. Lin, One-step microwave synthesis of N-doped hydroxyl-functionalized carbon dots with ultra-high fluorescence quantum yields, *Nanoscale* 8 (33) (2016) 15281–15287.
- [32] J. Sun, S. Yang, Z. Wang, H. Shen, T. Xu, L. Sun, H. Li, W. Chen, X. Jiang, G. Ding, Z. Kang, X. Xie, M. Jiang, Ultra-High Quantum Yield of Graphene Quantum Dots: Aromatic-Nitrogen Doping and Photoluminescence Mechanism, *Part. Part. Syst. Char.* 32 (4) (2015) 434–440.
- [33] Y. Dong, H. Pang, H.B. Yang, C. Guo, J. Shao, Y. Chi, C.M. Li, T. Yu, Carbon-Based Dots Co-doped with Nitrogen and Sulfur for High Quantum Yield and Excitation-Independent Emission, *Angew. Chem. Int. Ed.* 52 (30) (2013) 7800–7804.
- [34] J. Peng, W. Gao, B.K. Gupta, Z. Liu, R. Romero-Aburto, L. Ge, L. Song, L. B. Alemamy, X. Zhan, G. Gao, S.A. Vithayathil, B.A. Kaiparettu, A.A. Marti, T. Hayashi, J.-J. Zhu, P.M. Ajayan, Graphene Quantum Dots Derived from Carbon Fibers, *Nano Lett.* 12 (2) (2012) 844–849.
- [35] S.-Y. Kwak, T.T.S. Lew, C.J. Sweeney, V.B. Koman, M.H. Wong, K. Bohmert-Tatarev, K.D. Snell, J.S. Seo, N.-H. Chua, M.S. Strano, Chloroplast-selective gene delivery and expression in planta using chitosan-complexed single-walled carbon nanotube carriers, *Nat. Nanotechnol.* 14 (5) (2019) 447–455.
- [36] Y. Inoue, I. Yasumori, Catalysis by Alkaline Earth Metal Oxides. III. X-Ray Photoelectron Spectroscopic Study of Catalytically Active MgO, CaO, and BaO Surfaces, *BCSJ* 54 (5) (1981) 1505–1510.
- [37] S. Mandal, J. Pal, R. Subramanian, P. Das, Amplified fluorescence of  $Mg^{2+}$  selective red-light emitting carbon dot in water and direct evaluation of creatine kinase activity, *Nano Res.* 13 (10) (2020) 2770–2776.
- [38] F. Li, C. Liu, J. Yang, Z. Wang, W. Liu, F. Tian, Mg/N double doping strategy to fabricate extremely high luminescent carbon dots for bioimaging, *RSC Adv.* 4 (7) (2014) 3201–3205.
- [39] J.D. Van Dyke, K.L. Kasperski, Thermogravimetric study of polyacrylamide with evolved gas analysis, *Journal of Polymer Science Part A: Polymer Chemistry* 31 (1993) 1807–1823.
- [40] B.P. Ramesh, W.J. Blau, P.K. Tyagi, D.S. Misra, N. Ali, J. Gracio, G. Cabral, E. Titus, Thermogravimetric analysis of cobalt-filled carbon nanotubes deposited by chemical vapour deposition, *Thin Solid Films* 494 (1–2) (2006) 128–132.
- [41] V. Datsyuk, M. Kalyva, K. Papagelis, J. Parthenios, D. Tasis, A. Siokou, I. Kallitsis, C. Galiotis, Chemical oxidation of multiwalled carbon nanotubes, *Carbon* 46 (6) (2008) 833–840.
- [42] E. Botines, L. Franco, J. Puiggalí, Thermal stability and degradation studies of alternating poly(ester amide)s derived from glycolic acid and  $\omega$ -amino acids, *J. Appl. Polym. Sci.* 102 (6) (2006) 5545–5558.
- [43] S. Devasahayam, V. Strezov, Thermal decomposition of magnesium carbonate with biomass and plastic wastes for simultaneous production of hydrogen and carbon avoidance, *J. Cleaner Prod.* 174 (2018) 1089–1095.
- [44] F. Qian, X. Li, L. Tang, S.K. Lai, C. Lu, S.P. Lau, Potassium doping: Tuning the optical properties of graphene quantum dots, *AIP Adv.* 6 (2016), 075116.
- [45] D. Li, W. Li, H. Zhang, X. Zhang, J. Zhuang, Y. Liu, C. Hu, B. Lei, Far-Red Carbon Dots as Efficient Light-Harvesting Agents for Enhanced Photosynthesis, *ACS Appl. Mater. Interfaces* 12 (18) (2020) 21009–21019.
- [46] Y. Ryu, C. Jiang, H. Kobayashi, M. Detto, MODIS-derived global land products of shortwave radiation and diffuse and total photosynthetically active radiation at 5 km resolution from 2000, *Remote Sens. Environ.* 204 (2018) 812–825.
- [47] C.A. Raines, The Calvin cycle revisited, *Photosynth. Res.* 75 (2003) 1–10.
- [48] H. Zhang, J. Li, J.-H. Yoo, S.-C. Yoo, S.-H. Cho, H.-J. Koh, H.S. Seo, N.-C. Paek, Rice *Chlorina-1* and *Chlorina-9* encode ChlD and ChlI subunits of Mg-chelatase, a key enzyme for chlorophyll synthesis and chloroplast development, *Plant Mol. Biol.* 62 (3) (2006) 325–337.
- [49] N. Shalgyo, O. Czarnecki, E. Peter, B. Grimm, Expression of chlorophyll synthase is also involved in feedback-control of chlorophyll biosynthesis, *Plant Mol. Biol.* 71 (2009) 425.
- [50] C.E. Benedetti, P. Arruda, Altering the Expression of the Chlorophyllase Gene *ATHCOR1* in Transgenic Arabidopsis Causes Changes in the Chlorophyll-to-Chlorophyllide Ratio, *Plant Physiol.* 128 (2002) 1255.
- [51] W. Kowalik, R. Schürmann, Chlorophyll a/Chlorophyll b Ratios of *Chlorella vulgaris* in Blue or Red Light, in: H. Senger (Ed.), *Blue Light Effects in Biological Systems*, Springer, Berlin Heidelberg, Berlin, Heidelberg, 1984, pp. 352–358.
- [52] M.T. Lin, A. Occhialini, P.J. Andralojc, M.A.J. Parry, M.R. Hanson, A faster Rubisco with potential to increase photosynthesis in crops, *Nature* 513 (7519) (2014) 547–550.



# Multifunctional carbon dots reinforced gelatin-based coating film for strawberry preservation

Baoyan Guo<sup>a</sup>, Guo Liu<sup>b</sup>, Weihao Ye<sup>a</sup>, Zhiqiang Xu<sup>a</sup>, Wei Li<sup>a</sup>, Jianle Zhuang<sup>a</sup>, Xuejie Zhang<sup>a</sup>, Lashuang Wang<sup>c</sup>, Bingfu Lei<sup>a</sup>, Chaofan Hu<sup>a,\*\*\*</sup>, Yingliang Liu<sup>a,\*</sup>, Hanwu Dong<sup>a,\*\*</sup>

<sup>a</sup> Key Laboratory for Biobased Materials and Energy of Ministry of Education/Guangdong Provincial Engineering Technology Research Center for Optical Agriculture, College of Materials and Energy, South China Agricultural University, Guangzhou, 510642, China

<sup>b</sup> College of Horticulture, South China Agricultural University, Guangzhou, 510642, China

<sup>c</sup> Guangdong Tianzi Natural Inc, Guangzhou, 510642, China

## ARTICLE INFO

### Keywords:

Carbon dots  
Broadband UV absorption  
Antioxidant  
Coating  
Bacterial community  
Preservation

## ABSTRACT

The development of safe, non-toxic, multifunctional nano preserved materials with excellent performance has become a hot research topic. Multifunctional *Sophora Japonica* extract (95% rutin)-derived carbon dots (R-CDs) were prepared by hydrothermal method. The  $\pi$ - $\pi$  conjugation structure of R-CDs enabled them UV broadband absorption properties. The excellent antioxidant properties of R-CDs were attributed to the presence of the  $sp^2$  carbon in core and a large number of hydroxyl groups at the edges, and their degradation rate of potassium permanganate and scavenging activity of superoxide anion radical were better than that of ascorbic acid. The presence of C=O bond may be the site for the generation of reactive oxygen species (ROS) and thus they could kill *Staphylococcus aureus* (*S. aureus*), *Bacillus subtilis* (*B. subtilis*) and *Listeria monocytogenes* (*L. monocytogenes*) at a concentration of 2 mg/mL and inhibited the growth of fungi (*Botrytis cinerea*). Then R-CDs were uniformly dispersed in gelatin-based solution, and the as-prepared films had smooth surface, good hydrophilicity, strong mechanical properties and good biocompatibility. With the increase of R-CDs addition, the tensile strength increased and then decreased, and the elongation at break rose to 358%. The film inherited the broadband UV absorption, antioxidant and antibacterial properties of R-CDs. The storage period of strawberries was prolonged after coating. The variety and abundance of microorganisms on the surface of strawberries was reduced and the growth of harmful bacteria was inhibited. This work provides more possibilities for the application of nano-materials in fruit preservation.

## 1. Introduction

Fruits are susceptible to microbial infection and intolerant to storage because of their high moisture content and constant biological processes afterharvest (Ezati, Rhim, Molaei, Priyadarshi, & Han, 2022). The economic value of strawberry is considerable, but the fruit is delicate and easily spoiled (Muhammad, Shaghef, Rana, Mumtaz, & Rashad, 2019). Currently, strawberry preservation mainly includes temperature control, gas regulation, irradiation, ultra-high pressure and other physical means (Gol, Patel, & Rao, 2013), as well as the addition of preservatives, oxidants and other chemical methods (Freche, Gieng, Pignotti, Ibrahim, & Feng, 2022). However, physical means have the problems of

complicated equipment, high operation requirements and large investments, while chemical means have unsafe problems such as pesticide safety, teratogenicity and chronic food poisoning. The coating preservation of natural products as a safe and effective method has attracted a lot of attention in recent years (Bose, Howlader, Jia, Wang, & Yin, 2019; Maringgal, Hashim, Mohamed Amin Tawakkal, & Muda Mohamed, 2020).

Gelatin is an animal protein with good film forming, safety, moisture resistance and other properties (Guo, Ge, Li, Mu, & Li, 2014). However, compared to conventional packaging, gelatin has the disadvantages of low heat resistance, low water vapor permeability, weak hydrophobicity, and poor mechanical properties (Kumar, Shukla, Baul, Mitra, &

\* Corresponding author.

\*\* Corresponding author.

\*\*\* Corresponding author.

E-mail addresses: [thucf@scau.edu.cn](mailto:thucf@scau.edu.cn) (C. Hu), [tliuyl@scau.edu.cn](mailto:tliuyl@scau.edu.cn) (Y. Liu), [hanwu@scau.edu.cn](mailto:hanwu@scau.edu.cn) (H. Dong).

<https://doi.org/10.1016/j.foodhyd.2023.109327>

Received 25 June 2023; Received in revised form 16 August 2023; Accepted 22 September 2023

Available online 30 September 2023

0268-005X/© 2023 Elsevier Ltd. All rights reserved.



Halder, 2018). Typically, gelatin was combined with other active substances to improve the performance of coating solutions or packaging films, such as essential oil (Aitboulahsen, et al., 2018), chitosan (Choi, Choi, Lee, & Chang, 2022), probiotic powder (TemizÖzdemir, 2021) and nano-antibacterial materials (Li, Shan, Yu, Li, & Peng, 2023) etc.

Carbon dots (CDs) is a class of spherical 0 - dimensional nanometer materials with diameter less than 10 nm (Yao, Huang, Liu, & Kang, 2019). Since its discovery in 2004, it has received extensive attention and research due to its excellent luminescence wavelength adjustable, easy surface functionalization modification and good biocompatibility (Guo, Liu, & Li et al., 2022). The large number of  $\pi$ - $\pi$  conjugated groups in the core of CDs give it good UV absorption performance (Chen, et al., 2022). Its excellent electron donor and electron acceptor functions confer its antioxidant properties (Liu, Li, & Yang, 2020). Its antibacterial properties are attributed to the production of ROS and photoelectric and photothermal effects (Wang, et al., 2021). Most CDs have UV absorption properties, but usually only absorb in a narrow band around 365 nm. Broadband UV (200–400 nm) absorption is rare, and such CDs are usually synthesized from multiple precursors (Qiu, et al., 2022). Based on the excellent properties of CDs, some researchers reported that they could be added to coating solution or composite film for the preservation of fruits, vegetables and meat. For example, CDs with antioxidant and antibacterial properties was synthesized from potato skins by hydrothermal method and the CDs had low cytotoxicity (Min, Ezati, & Rhim, 2022). However, the UV absorption spectra of the prepared potato skins-derived CDs showed only a sharp peak at 315 nm. Spent coffee ground – derived CDs were made by hydrothermal method (Min, Ezati, Yoon, & Rhim, 2023). Multifunctional packaging films were prepared by adding CDs to gelatin/polyvinyl alcohol (Gel/PVA) films and grapefruit seed extract (GSE). The composite film has the properties of UV protection, antioxidant and antibacterial, however, the antioxidant and antibacterial properties of the film were realized by the addition of grape seed extract. Grape leaves derived CDs had antioxidant and antibacterial properties but had a narrow UV absorption wavelength (230–300 nm). In addition, oxidized dialdehyde persian gum (PG) was needed to improve the mechanical properties of the composite film (Khoshkhalampour, Ghorbani, & Ghasempour, 2023). To the best of our knowledge, the CDs prepared by single component precursor with broadband UV absorption, strong antioxidant and antibacterial properties has not been reported. A comparison of this paper with other published articles was presented in Table S1.

In this work, a multifunctional R-CDs with UV broadband absorption, strong antioxidant and antibacterial properties was prepared by hydrothermal method with the biomass *Sophora Japonica* extract (95% rutin) as a single precursor. Rutin, as the main extract component of the Chinese herb *Sophora Japonica*, has a wide range of biological activities such as anti-inflammatory, antioxidant, and anti-tumor (He, et al., 2016; Krishna, KNV, S, & Banji, 2012). The raw material is readily available and inexpensive, and the prepared CDs may be more biocompatible than small molecule precursors (Wareing, Gentile, & Phan, 2021). R-CDs were added to a gelatin-based coating solution that also inherited the multifunctional properties of R-CDs and had good biocompatibility. The surface of the film formed by the coating solution was flat and smooth. Compared with gelatin, the hydrophilicity and mechanical properties of the film were improved. The shelf life of strawberries coated with the nano-coating solution was extended at room temperature. The rotting rate and weight loss rate of strawberry during storage were reduced and the hardness was increased. Strawberry ripening and senescence were inhibited. The composition and abundance of microbial community on strawberry surface after storage was investigated. It was revealed that the R-CDs inhibited the growth of harmful microorganisms on strawberry surface and promoted the growth of beneficial bacteria. The coating solution provides a new possibility for the preservation application of postharvest fruits.

## 2. Material and methods

### 2.1. Materials

The *sophora japonica* extract (95% rutin) was provided by Guangdong Tianzi Natural Inc. Anhydrous ethanol was purchased from Aladdin Industries, Inc. Gelatin was purchased from Rousselot Co., Ltd. (China). Fresh strawberries of uniform size and ripeness, without mechanical damage were purchased from local market.

### 2.2. Preparation and characterization of R-CDs

#### 2.2.1. Preparation of R-CDs

The R-CDs was prepared according to the reported method with some modifications (Xu, et al., 2023). Briefly, 0.9 g of *sophora japonica* extract was dissolved in 60 mL anhydrous ethanol, stirred evenly, and fully dissolved by ultrasound for 30 min. The mixture was placed in a Teflon lined stainless steel reactor (100 mL) and heated in an oven to 180 °C for 6 h. After cooling, the supernatant was filtered through a 0.22  $\mu$ m Whatman membrane to remove impurities. The filtrate was then placed in an 80 °C oven for 72 h to obtain the powder, which was stored in a dryer prior to further testing.

#### 2.2.2. Characterization of R-CDs

The structural characteristics of R-CDs were analyzed by FEI Tecnai 12 transmission electron microscope (TEM), Nicolet Avatar 360 FTIR spectrophotometer and Xpert Pro MPD X-ray diffractometer (XRD). The UV-visible absorption spectra of CDs were determined by a Perkins Elmer UV-Vis spectrophotometer (Lambda 750).

The antioxidant properties of R-CDs were evaluated by KMnO<sub>4</sub> reduction rate, 1,1-Diphenyl-2-picrylhydrazyl (DPPH) scavenging activity and O<sub>2</sub><sup>•</sup> scavenging activity. After mixing 100  $\mu$ L R-CDs solution with the same volume of 1 mM KMnO<sub>4</sub> and 100  $\mu$ g/mL DPPH, the absorbance of the mixture at 515 nm and 517 nm was determined for 30 min in the dark. The solution without R-CDs was used as the control. KMnO<sub>4</sub> reduction rate and DPPH scavenging activity were calculated according to the following formula:

$$(A1-A2)/A1 \times 100\% \quad (1)$$

where A1 and A2 represent the absorbance values at 515nm/517 nm of the mixture of control group and R-CDs treatment group with different concentrations, respectively. The O<sub>2</sub><sup>•</sup> scavenging activity of R-CDs was determined by nitroterazolium blue chloride (NBT). First, all reagents were prepared with a 0.05 M phosphate buffer (pH = 7.8). Then, 30 mL buffer solution, 6 mL 130 mM methionine solution, 6 mL 750  $\mu$ M NBT, 6 mL 100  $\mu$ M EDTA-Na<sub>2</sub>, 6 mL 20  $\mu$ M riboflavin, and 5 mL distilled water were mixed as mother liquor (ready for use). R-CDs solution of different concentrations was mixed with mother liquor in the same volume, and the mixture without R-CDs was used as the control. The mixture was treated under 4000 Lux for 30 min, and the absorption value was measured at 560 nm. The O<sub>2</sub><sup>•</sup> scavenging activity was calculated by referring to equation (1).

The antimicrobial activity of R-CDs was determined according to the reported method with some modification (Li, et al., 2018). *S. aureus* (CMCC (B) 26003) and *B. subtilis* (CMCC (B) 63501) were activated by overnight incubation in Luria-Bertani (LB) liquid medium at 37 °C, and *Listeria monocytogenes* (ATCC 19114) was activated by trypticase soy broth (TSB) medium. The optical density (OD) of the bacteria at 600 nm wavelength indicates the concentration of the bacteria. The OD<sub>600</sub> value of the bacterial solution was diluted to 0.1 with liquid medium, followed by a 100-fold dilution of the above bacterial solution, and 100  $\mu$ L of the bacterial solution was placed in a 96-well plate. Before this, the concentration of the R-CDs solution was diluted into a series of concentrations by a double dilution method, and the final volume of the R-CDs solution was 100  $\mu$ L. Then 100  $\mu$ L R-CDs solution with different

concentrations and 100  $\mu\text{L}$  bacterial solution were co-cultured at 37 °C for 24 h. The optical density of the mixture was measured at regular intervals to obtain the antibacterial curve of the R-CDs. Then the mixture of 20  $\mu\text{L}$  R-CDs and bacterial solution was coated on agar plate and cultured at 37 °C for 24 h. Bacterial viability was calculated according to formula (2).

$$\text{OD}_{600-1} / \text{OD}_{600-2} \times 100\% \quad (2)$$

where  $\text{OD}_{600-1}$  was  $\text{OD}_{600}$  value of different concentrations of R-CDs cocultured with bacteria for 24 h.  $\text{OD}_{600-2}$  was the  $\text{OD}_{600}$  value of bacterial solution without R-CDs cultured for 24 h.

To further investigate the effect of R-CDs on bacterial cells, the morphological changes of bacteria treated with R-CDs were observed by scanning electron microscopy (SEM) (Verios 460, FEI, Thermo Fisher, USA). Bacteria treated with R-CDs were centrifuged to collect the precipitate. The bacteria were washed three times with sterile water, then soaked in 2.5% glutaraldehyde and placed at 4 °C for 6 h. After centrifugation to remove glutaraldehyde, the bacteria were dehydrated with ethanol at a concentration gradient (50, 70, 90, 95 and 100%). Finally, freeze-dried bacterial samples were obtained for SEM observation.

Methods of antifungal activity of R-CDs demonstrated in support materials.

### 2.3. Preparation of R-CDs reinforced gelatin coatings and films

The coating solution (TemizÖzdemir, 2021) and the films (Yang, et al., 2023) were prepared according to reported methods. Firstly, 10 g of gelatin was dissolved in 200 mL distilled water and continuously stirred at 50 °C to obtain a 5% (m/V) clear gelatin solution. Then 0.5%, 1% and 1.5% (m/V) R-CDs was added to the gelatin solution, respectively, and stirred continuously for 30 min. Then 0.5% (m/v) glycerin was added as a plasticizer. The above were coating solutions for subsequent immersion experiments. To make films, pour 10 mL of coating solution into a sterile Petri dish with a diameter of 9 cm and dried it at 45 °C for 8 h. The film was carefully removed and placed in a 27 °C, 45% RH dryer for further testing.

### 2.4. Characterization of CDs reinforced gelatin films

#### 2.4.1. Morphology property and Fourier Transform infrared spectrophotometer (FTIR)

The surface morphology of the film samples was analyzed by a field emission scanning electron microscope (SEM) (Verios 460, FEI, Thermo Fisher, USA). The chemical structure of the film samples was determined by a Nicolet Avatar 360 Fourier Transform infrared spectrophotometer.

#### 2.4.2. Mechanical properties

The mechanical properties of the films (30 mm  $\times$  10 mm), including tensile strength and elongation at break were measured by electronic universal testing machine instrument (UTM-4204, Shenzhen sansi-zongheng technology co., Ltd., Shenzhen, China) at the speed of 25 mm/min. Each treatment was measured in six replicates.

#### 2.4.3. Water contact angle (WCA)

The WCA of the films was measured using a contact angle meter (SDC-100, Dongguan Shengding Precision Instruments Co., Ltd., Dongguan, China). The film samples (20 mm  $\times$  30 mm) were fixed on a slide and then placed on the contact angle meter. Use a micro syringe to drop 10  $\mu\text{L}$  of distilled water onto the surface of the films. Take a picture of the moment the water fell on the surface of the film and read the WCA immediately.

#### 2.4.4. UV-visible

The UV-visible absorption spectra of films were determined by a Perkins Elmer UV-Vis spectrophotometer (Lambda 750).

#### 2.4.5. Antioxidant property (DPPH scavenging activity)

The antioxidant property of composite films was determined according to the reported method (Min, et al., 2023). A film sample of 50 mg was added to 10 ml of 0.06 mM DPPH ethanol solution and the reaction was carried out in the dark at room temperature for 30 min, and then the absorbance was measured at 517 nm. The DPPH scavenging activity can be calculated as follows:

$$(\text{A1}-\text{A2}) / \text{A1} \times 100\% \quad (3)$$

where A1 and A2 were the absorbance of DPPH solution of the control and the test solutions.

The migration of R-CDs was shown in the supporting information.

#### 2.4.6. Antimicrobial property

The antibacterial property of the films was evaluated by assessing the number of colony units reduced by bacteria in direct contact with the films (Chang, Xu, Yang, Liu, & Qiu, 2023). Simply, *S. aureus*, *B. subtilis* and *L. monocytogenes* were activated by overnight incubation in liquid medium at 37 °C. The optical density of the bacterial suspension was adjusted to 0.1 at 600 nm and diluted 100 times. A 6-well plate with films was added with 1 ml of bacterial solution and co-cultured at 37 °C for 1 h. 20  $\mu\text{L}$  bacterial suspensions were plated on corresponding solid agar plates. After incubation at 37 °C for 24 h, colonies were photographed and counted online with Image J (<https://ij.imjoy.io>). Each sample was tested in triplicate. The antibacterial rate (%) was calculated according to equation (4).

$$\text{Antibacterial rate (\%)} = (1 - \text{C}_1/\text{C}_2) \times 100\% \quad (4)$$

where  $\text{C}_1$  is the number of colonies in the films contact treatment group,  $\text{C}_2$  is the number of colonies in the control group.

#### 2.4.7. Cytotoxicity

The biosafety of the different films was assessed by MTT assay on mouse fibroblast L929 cells according to the reported method with some modifications (Du, et al., 2022). Briefly, all films were first sterilized by UV irradiation for 30 min. After that, 20 mg of the film was weighted and soaked in 2 ml of medium solution for 24 h. The filtrate was filtered through a 0.22  $\mu\text{m}$  filter membrane and taken for testing. L929 cells were cultured in complete medium (containing 10% fetal bovine serum) for 24 h in a 37 °C/5%  $\text{CO}_2$  thermostatic incubator. Approximately 8000 cells were inoculated into 96-well plates and cultured for 24 h. Afterwards, 100  $\mu\text{L}$  of fresh medium was added to the control group and 100  $\mu\text{L}$  of sample extract was added to the experimental group and treated for 24 h. After that, the medium was removed, each well was washed three times with PBS, and 100  $\mu\text{L}$  of medium containing 0.5 mg/mL MTT was added to each well and incubated for another 4 h. The supernatant was discarded and 100  $\mu\text{L}$  of DMSO was added to each well. The absorbance at 570 nm was measured after gentle shaking for 10 min. Cell viability was calculated according to the formula:

$$\text{Cell viability (\%)} = (\text{A}_s - \text{A}_b) / (\text{A}_c - \text{A}_b) \times 100 \quad (5)$$

where  $\text{A}_s$  is the absorbance value of the sample,  $\text{A}_c$  is the absorbance value of the control, and  $\text{A}_b$  is the absorbance value of background.

### 2.5. Coating application on strawberries

The fresh, uniform in size, shape and color, and free of surface damage strawberries were purchased from local markets, rinsed in distilled water and left to dry. Preparation of coating solution was as described in 2.3. Different coating solutions were prepared by adding R-CDs with different concentrations to a 5% (m/V) gelatin base solution. There were five groups of coating solutions: (1) Control (distilled water), (2) Gelatin, (3) Gelatin +0.5% R-CDs, (4) Gelatin +1% R-CDs, (5) Gelatin +1.5% R-CDs. Strawberries were soaked in the coating solution for 1 min and left to dry at room temperature. The treated strawberries

were then placed on trays at room temperature for eight days. A digital camera was used to record visible changes in the strawberries. They were sampled every other day for analysis.

#### 2.5.1. Rotting rate

According to reported method (Yuan, et al., 2023), the rotting rate of strawberry was expressed as the ratio of the number of decayed strawberries to the total number of initial strawberries.

#### 2.5.2. Weight loss

The weight loss rate of strawberries was the weight loss at the time of sampling divided by the initial weight. Each treatment was measured in six replicates.

#### 2.5.3. Firmness

The texture analyzer (TA-XT, Stable Micro Systems, Godalming, England) was used to measure the firmness of strawberries. The test speed was 2 mm/s. The trigger force was 5 g. The strain was 30%. Each treatment was measured in six replicates.

Nutritional indicators titratable acidity and total phenolic content of strawberries were shown in the supporting information.

#### 2.5.4. Analysis of bacterial composition and diversity on strawberry surface

The bacteria on strawberry surface after 8 days of storage were collected according to the reported method (Cai, et al., 2022). In each group, 10 strawberries (about 130 g) were continuously stirred in 40 mL sterile normal saline for 30 s. The solution was centrifuged to collect the precipitation, and the precipitation was placed at  $-80^{\circ}\text{C}$  until analysis. Total DNA was extracted by using CTAB extraction. DNA concentration and purity was monitored on 1% agarose gels. The V3–V4 variable regions of 16S rRNA genes were amplified using the specific primer 341F (CCTAYGGGRBGCASCAG) and 806R (GGACTACNNGGGTATCTAAT) along with barcode. Then, amplification was performed with a Bio-rad T100 gradient PCR instrument. The mixed PCR products were purified using the GeneJET Gel Extraction Kit (Thermo Scientific). Library construction was performed using Illumina TruSeq DNA PCR-Free Library Preparation Kit (Illumina, USA), and after passing the quantification and

library detection by Qubit@ 2.0 fluorometer (Thermo Scientific), the library was tested using NovaSeq 6000 for up-sequencing. Sequences were analyzed using the Quantitative Insights Into Microbial Ecology (QIIME) software package. Reads were filtered through the QIIME quality filter. Sequences with  $\geq 97\%$  similarity were assigned to the same operational taxonomic unit (OTU). Multiple sequence comparisons of OTUs were performed to obtain differences in colony results for different groupings. Statistical analysis methods such as T-test, MetaStat, LefSe, Anosim and MRPP were selected to analyze the results for significance. Six replicates were performed for each group.

#### 2.6. Statistical analysis

All experiments in this paper were conducted at least in triplicate. And the results were reported as mean  $\pm$  standard deviation. The data were analyzed by ANOVA and LSD ( $P < 0.05$ ) using SPSS statistical software.

### 3. Results and discussion

#### 3.1. Characterization of R-CDs

Well-dispersed, non-aggregated and stable R-CDs were prepared by a one-step hydrothermal method using *Sophora japonica* extract (95% rutin) as a single precursor with a yield of 90%. As shown in Fig. 1a, R-CDs were nearly spherical with an average size of 5.60 nm and a lattice spacing of 0.21 nm. Compared to the complex FTIR spectral peaks of raw material (Fig. 1b), the R-CDs had only two characteristic peaks, which were caused by stretching vibrations of  $-\text{OH}$  at  $3452\text{ cm}^{-1}$  and stretching bending vibrations of  $\text{C}=\text{C}$  at  $1633\text{ cm}^{-1}$  (Khoshkalampour, et al., 2023). This indicated that the structure of R-CDs was relatively pure and the polyhydroxyl group of raw material was retained. Fig. 1c showed the XRD pattern of the R-CDs with the peak at  $24.5^{\circ}$  corresponding to the (002) crystal planes of graphite (Ezati et al., 2022). The XPS results (Fig. 1d) showed that R-CDs were mainly composed of C (64.8%) and O (35.2%) elements. The C 1s spectrum confirmed the presence of  $\text{sp}^2$  carbon in R-CDs. The presence of  $\text{C}-\text{O}$  and  $\text{C}=\text{O}$  in the

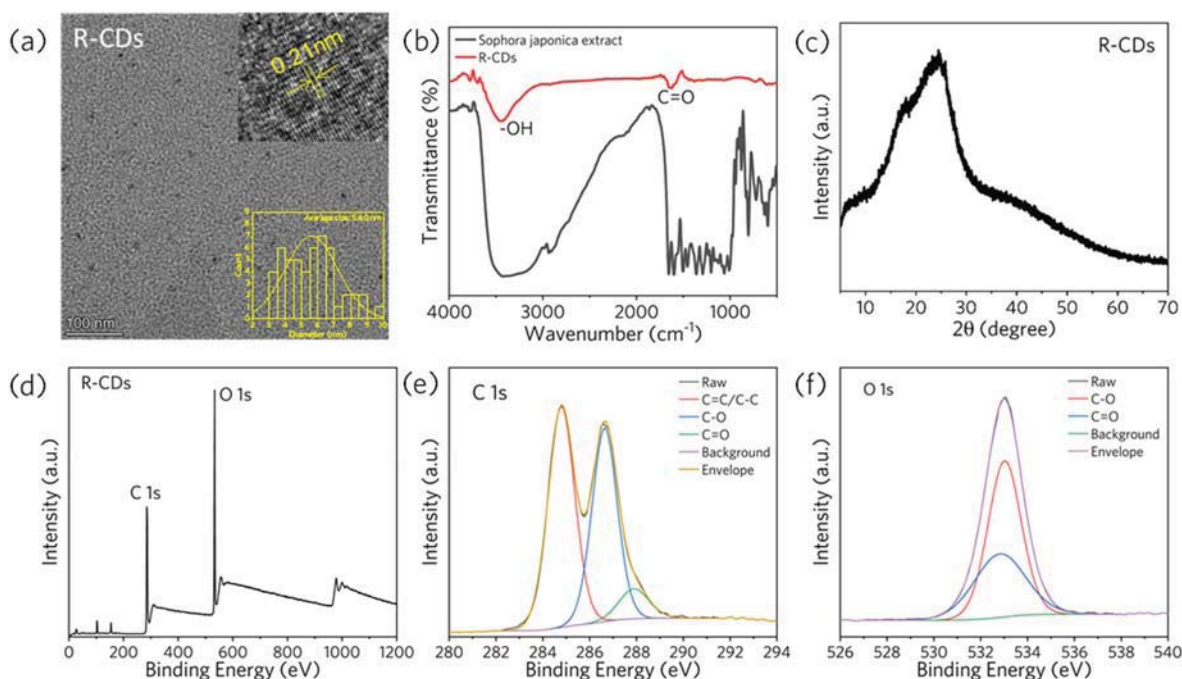


**Fig. 1.** (a) TEM image and particle size distribution of R-CDs. (b) FTIR spectra and (c) XRD of R-CDs. The XPS spectra (d) and high-resolution C 1s (e) and O 1s spectra (f) of R-CDs.



spectra (Fig. 1e and f) indicated that the existence of carboxyl groups on the surface of CDs. Higher peak intensities of C–O than C=O were observed in both C 1s and O 1s spectra, indicating that the C=O structure of the raw material was oxidized by hydrothermal treatment to generate C–O, and thus the surface of R-CDs was enriched with more hydroxyl groups, which was consistent with the FTIR results. It has been reported that the high content of  $sp^2$  carbon in the core of CDs and –OH as a proton donor at the edge were the key structures for the antioxidant activity of CDs (InnocenziStagi, 2023). In addition, this report also indicated that the abundant oxygen functional groups on the surface of CDs, especially the ketonic carbonyl group, can promote the production of ROS and thus have antibacterial effects (InnocenziStagi, 2023).

### 3.2. The UV–vis spectrum and antioxidant properties of R-CDs

Fig. 2a showed the UV–Vis absorption spectrum of R-CDs. Two absorption peaks were observed at 255 nm and 354 nm. The absorption peak at 255 nm was caused by the  $\pi$ – $\pi^*$  transition of the benzene ring C=C bond on the surface of the carbon core (Niu, Song, & Xiong, 2021). The absorption peak at 354 nm was due to the  $n$ – $\pi^*$  transition of the C=O bond (Fang, et al., 2017). With the increase concentration of R-CDs, the absorption intensity increased. However, even at very low concentrations (0.05 mg/mL), R-CDs still had the characteristics of broadband UV absorption (200–400 nm), which was relatively rare in the CDs prepared from a single raw material (Xu, et al., 2023). The transmittance spectra (Fig. 2b) of R-CDs also confirmed its excellent UV shielding properties.

Fig. 2c, d, e showed the antioxidant activities of R-CDs. R-CDs showed enhanced effects on  $KMnO_4$  reduction rate, DPPH scavenging activity and  $O_2^{\cdot-}$  scavenging activity with the increase of concentration. The  $KMnO_4$  reduction rate and the  $O_2^{\cdot-}$  scavenging activity were even stronger than the positive control ascorbic acid (VC). The original  $sp^2$  domain can be used as a radical scavenging site, which can destroy the free radicals through adduction and delocalization with the spin on the conjugated graphene main chain (Ruiz, Yate, García, Cabanero, & Grande, 2017). In addition, the abundant hydroxyl group on the surface of the R-CDs can be used as proton donor to transfer the unpaired electrons of the radical to the carbon core containing the C–C backbone structure (Das, et al., 2014). DPPH is a stable free radical at the center of nitrogen. Its stability comes from  $\pi$ – $\pi$  conjugated interaction of three

benzene rings and spatial barriers that prevent unpaired electrons from interacting with nitrogen atoms (Guo, et al., 1999). Compared with VC, the abundant functional groups on the surface of R-CDs enhanced the steric hindrance between carbon and DPPH and reduced the scavenging activity.

### 3.3. Antimicrobial activity of R-CDs

Fig. 3a, b and c showed the growth of *S. aureus*, *B. subtilis* and *L. monocytogenes* cocultured with different concentrations of R-CDs for 24 h. With the extension of time, the growth of bacteria was inhibited by the high concentration of R-CDs. Compared to the control group, where *S. aureus* began to proliferate after 4 h of incubation, the growth of *S. aureus* was inhibited in the R-CDs-treated group as its concentration increased, and at 2 mg/mL, no bacterial proliferation was observed until 24 h. Interestingly, *B. subtilis* did not proliferate after 24 h when the concentration of R-CDs was 1 mg/mL. However, even low concentrations of R-CDs still inhibited *L. monocytogenes* growth in the first 12 h. Only high concentrations of R-CDs could effectively inhibit *L. monocytogenes* growth for 24 h. In addition, the standard plate counting method was used to test the bacterial survival rate after 24 h R-CDs treatment, as shown in Fig. 3e, with the increase of R-CDs concentration, the number of colonies decreased. Several bacteria colony still grew at the concentration of 1 mg/mL, while no colony can be observed when the concentration increased to 2 mg/mL, indicating that 2 mg/mL was the bactericidal concentration of R-CDs. At the same time, we also tested the bacterial viability (Fig. 3d) after R-CDs treatment for 24 h. The results showed that the bacterial viability decreased from 100% to approximately 6% as the concentration of R-CDs increased. In fact, at the concentration of 2 mg/mL, the colony coating proved that there was no colony growth, because the R-CDs itself was colored, resulting in a certain OD<sub>600</sub> reading even if no colonies grew at 24 h of co-culture. After co-culturing the R-CDs with the bacteria, a significant change in the morphology of the bacteria was observed by SEM, as shown in Fig. 3f. The control group of *B. aureus* was round and full, and after R-CDs treatment, *B. aureus* was broken and deformed, flattened in shape and aggregated and adhered (as shown in the red dashed box). In the control group, *B. subtilis* was in the shape of a full and straight rod, and after R-CDs treatment, the rod was deformed and bent, and the broken contents leaked out (as shown in the red dashed box). Similar

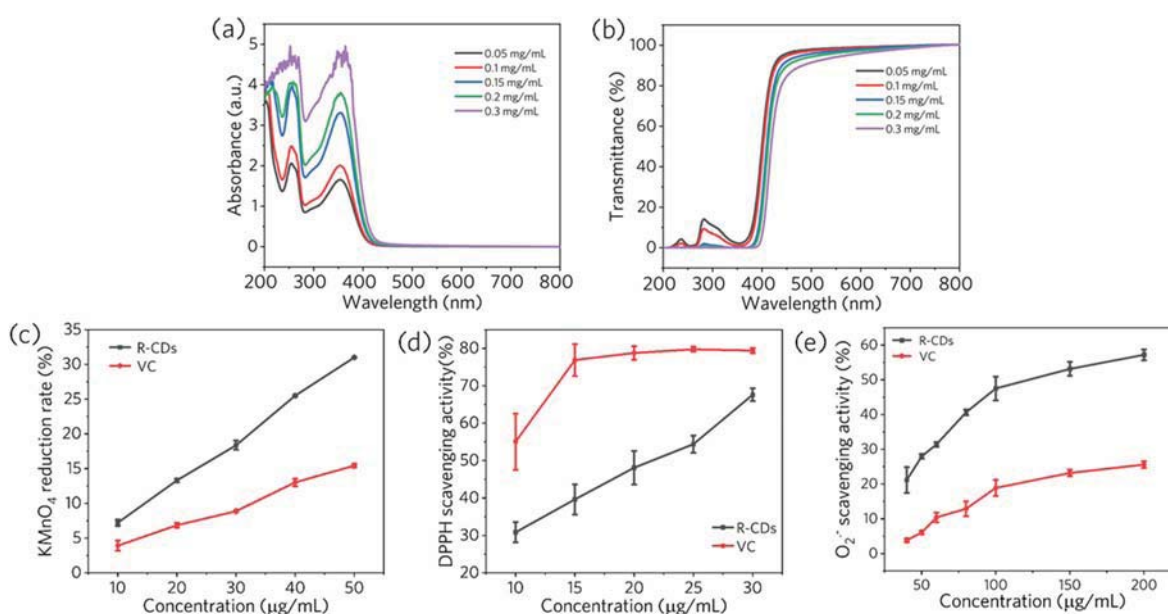
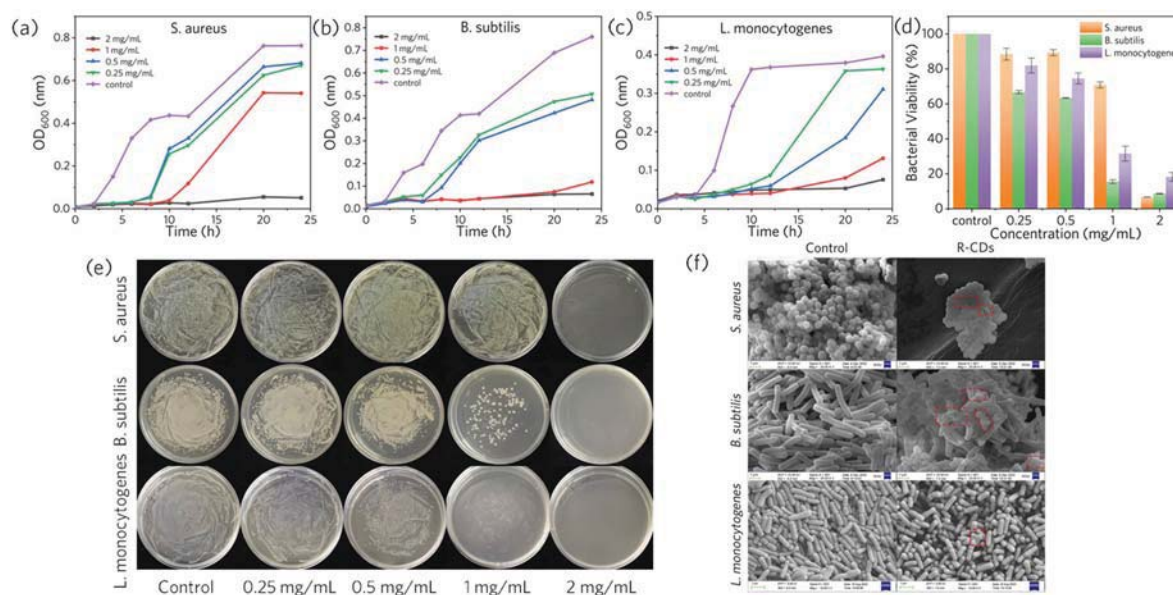


Fig. 2. The (a) UV–Vis and (b) transmittance spectra of R-CDs. The antioxidant properties of R-CDs, including (c)  $KMnO_4$  reduction rate, (d) DPPH scavenging activity, (e)  $O_2^{\cdot-}$  scavenging activity.



**Fig. 3.** The growth curve of different concentrations of R-CDs cocultured with *S. aureus* (a), *B. subtilis* (b) and *L. monocytogenes* (c) for 24 h. (d) Evaluation of bacterial viability at different concentration of R-CDs. (e) The colony growth of bacteria treated with different concentrations of R-CDs for 24 h. (f) Morphological changes of bacteria before and after R-CDs treatment.

morphological disruption of *L. monocytogenes* by R-CDs has also been observed. *B. cinerea* is the main causal fungus of postharvest spoilage in strawberries (Sun, et al., 2021). As shown in Fig. S1, the R-CDs had an inhibitory effect on the mycelium growth of *B. cinerea*, and the inhibitory effect became more pronounced as the concentration increased, inhibiting 50% mycelium growth of *S. cinerea* at a concentration of 2 mg/mL. The XPS results confirmed the presence of a large amount of C=O in the R-CDs, and it has been reported in the literature that C=O may be the site of ROS production (InnocenziStagi, 2023), and it is speculated that the ROS produced by the C=O site of R-CDs may have damaged the cell wall of the bacteria, leading to the leakage of the contents and causing bacterial death.

Although there were some reports of antimicrobial activities of CDs at low concentration (Li, et al., 2018; Wang et al., 2019; Zhu et al., 2019), the source of CDs, the preparation method, the concentration of bacteria used in antibacterial experiments, and the amounts of bacteria were all different. The concentration of CDs used in this investigation is similar to that used by other researchers. For example, CDs synthesized from red onion can resist *pseudomonas* (Lin, Cheng, & Tan, 2022). The minimum antibacterial concentration of CDs was 2 mg/mL, and the minimum bactericidal concentration was 4 mg/mL. The CDs was synthesized from the supernatant of lactic acid bacteria, and the antibacterial concentration was 500 mg/mL (Kousheh, Moradi, Tajik, & Molaei, 2020). When the antibacterial nanocellulose paper was prepared, the loading capacity of CDs was 71.8 mg/cm<sup>2</sup>.

R-CDs exhibited specific antibacterial effects against gram-positive bacteria (*S. aureus*, *B. subtilis* and *L. monocytogenes*), as demonstrated by others (Yu, et al., 2022). They synthesized FA-CDs using folic acid as raw material to kill *S. aureus* under acidic conditions. FA-CDs showed significant therapeutic effect on the back wound model of mouse infected with *S. aureus*. The authors speculated that FA-CDs was more likely to aggregate on the surface of *S. aureus* due to the difference in cell membrane structure between *S. aureus* and *Escherichia coli* (*E. coli*), leading to the destruction of cell membrane structure. Similar results have been reported (Ezati, et al., 2022). The antibacterial activity of GCDs synthesized by them against Gram-positive bacteria was stronger than that of Gram-negative bacteria, which was due to the differences in cell wall structure and affinity of bacteria for interaction with GCDs. Gram-positive bacteria had a relatively simple cell wall structure and lacked an outer membrane, making them more susceptible to the

harmful effects of reactive oxygen species. Gram-negative bacteria had complex cell walls. Due to the hydrophobicity of the latter, GCDs were unable to successfully penetrate the outer cell membrane, which resulted in an osmotic barrier to foreign compounds, resulting in relatively weak interactions that prevented GCDs from entering the bacterial cell and therefore had a weak antibacterial effect.

### 3.4. Characteristics of the films

Based on the excellent UV broadband absorption, antioxidant and antimicrobial properties of R-CDs, they were incorporated into gelatin-based coating solutions and the films were prepared, then the physico-chemical properties of the films were explored.

#### 3.4.1. The microscopic morphology, mechanical property, water contact angle and FTIR of films

The microscopic morphology of different films was observed by SEM and shown in Fig. 4a. The films were basically smooth and no cracks can be observed. However, due to the addition of R-CDs, some small particles appeared on the upper surface. A similar phenomenon has emerged in other reports (Alizadeh-Sani, Khezerlou, & Ehsani, 2018; Yuan et al., 2023). It may be because the upper surface of the film was in direct contact with the air. When the film was dried, the water was lost faster than that on the lower surface, resulting in the change of molecular forces between different components (Da Silva Scudeler, de Lima Costa, Cortez-Vega, Prentice, & Fonseca, 2020). And the loss of water, tended to lead to the aggregation of R-CDs. However, the upper surface of the film with 1.5% R-CDs was smoother, indicating that R-CDs was more evenly dispersed in the gelatin matrix at this concentration, and the solution formed a more stable and uniform network structure. This may be related to the solubility of R-CDs and the force between R-CDs and gelatin, possibly at 1.5% concentration, the two form a stable structure unaffected by water loss, the exact reason for this needs to be proved by further experiments.

Packaging film must be of sufficient mechanical strength and integrity to prevent breakage or leakage, thereby protecting food during storage and transportation (Yang, et al., 2023). As can be seen from Fig. 4b, the addition of R-CDs can improve the tensile strength of gelatin film. With the increase of R-CDs concentration, the tensile strength increased, reaching the highest value at 1% R-CDs concentration, and

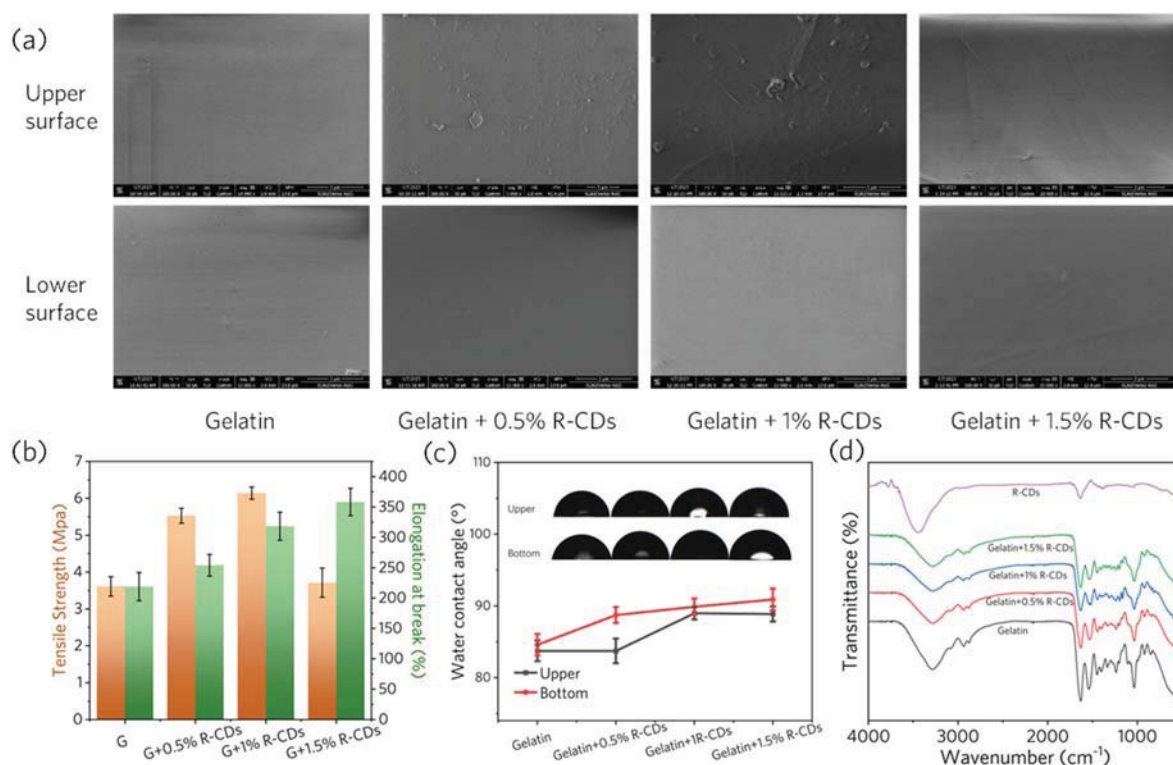


Fig. 4. (a) The microscopic morphology of different films. The upper surface was the side in contact with dry air, and the lower surface was the side in contact with the sterile petri dishes. (b) The mechanical property, (c) water contact angle and (d) FTIR of films.

then decreased. This indicates that the interfacial interaction and hydrogen bond between gelatin and CDs increased at low concentration, and the rigidity of the film can be improved with the appropriate concentration of R-CDs. When a high concentration of R-CDs was added, R-CDs aggregated, obstructed or destroyed the network structure of gelatin, and reduced the tensile strength of the film. Different from the tensile strength, the elongation at break of the film increased with the increase of R-CDs concentration, and the highest amount of R-CDs addition was reached at 1.5%, indicating that the addition of R-CDs can improve the flexibility of the film. Similar results were reported (Khoshkalampour, et al., 2023). The film with 5% CDs added had an increase in TS compared with the control, and a significant decrease in TS for films with more than 5% CDs added, possibly due to the aggregation of CDs (Ezati et al., 2022). It was reported that the TS of chitosan film increased only when the addition amounts of CDs was up to 3%, and the TS decreased when it exceeded 3% (L. Wang, Liu, et al., 2022).

Water contact Angle (WCA) represents the water resistance of the film, which is mainly affected by surface hydrophobicity and surface morphology (roughness, porosity and pore size). The wettability between the film and the fruit peel will also affect the formation and adhesion of the film in situ, thus affecting the preservation performance. The surface wettability of the film was evaluated by WCA. When WCA value exceeded  $90^\circ$ , the surface of the film was hydrophobic (J. Wang, Liu, et al., 2022). When WCA value was less than  $65^\circ$ , the film surface was considered to be hydrophilic (Kim, Kim, Yoon, & Rhim, 2023; Vogler, 1998). The Upper was the rough surface of the film, and the bottom was the smooth surface of the film. As can be seen from Fig. 4c, pure gelatin film was hydrophilic, and the WCA value of the film increased with the increase of R-CDs concentration. The addition of R-CDs increased the interaction with the film matrix and reduced the effective hydrophilic groups on the film surface. The WCA of a rough surface was smaller than that of a smooth surface. It may be that when the film's structure was uniform and dense, it prevented water from penetrating into the membrane, resulting in an increase in hydrophobic

surfaces (Hosseini, Ghaderi, & Gómez-Guillén, 2021).

The chemical interaction between gelatin and R-CDs was evaluated by FTIR spectra (Fig. 4d). In pure gelatin films, the O–H, C–H and amido-I vibrations of COO- related C–O groups in the structure were observed at  $3278\text{ cm}^{-1}$ ,  $2937\text{ cm}^{-1}$  and  $1627\text{ cm}^{-1}$ , respectively (RoyRhim, 2021). Bands around  $1629\text{ cm}^{-1}$  and  $1542\text{ cm}^{-1}$  represented amido-I band vibrations due to C=O stretching and amido-II vibrations caused by N–H bending (Riahi, Priyadarshi, Rhim, & Bagheri, 2021). The absorption bands at  $1453\text{ cm}^{-1}$  and  $1403\text{ cm}^{-1}$  were attributed to C–N and N–H tensile vibrations. The peak at  $1240\text{ cm}^{-1}$  belonged to the amido-III vibration band and represented the vibration in the plane of the C–N and N–H groups binding the amide (Papaioannou, et al., 2018). In addition, an absorption band of C–O tensile vibration was observed at  $1030\text{ cm}^{-1}$  (Roy, Van Hai, Kim, Zhai, & Kim, 2020). In agreement with our results, other researchers have also reported that all CDs-added gelatin films showed nearly identical FTIR spectra in gelatin films (Ezati, et al., 2022; Min et al., 2023). FTIR spectra showed that the peak intensity of R-CDs doped films decreased, but did not change the frequency region of the spectrum, indicating that R-CDs and gelatin polymer matrix were completely mixed to form a compatible film (Agarwal, Hoque, Bandara, Pal, & Sarkar, 2020). The results and discussion on the migration of R-CDs were shown in the supporting document.

#### 3.4.2. The UV transmittance, antioxidant and antimicrobial properties of films

Fig. 5 showed the UV absorption, antioxidant, and antibacterial properties of films made from a gelatin-based coating solution. As can be seen from Fig. 5a, pure gelatin film had no blocking ability to UV at 200–400 nm, while the gelatin film added with R-CDs can achieve UV broadband absorption even at a very low concentration (0.5%). The addition of low concentration of R-CDs can greatly improve the DPPH scavenging activity of pure gelatin film (Fig. 5b). The scavenging activity was significantly improved with the increase concentration of R-CDs. In addition to UV absorption and antioxidant properties, the films



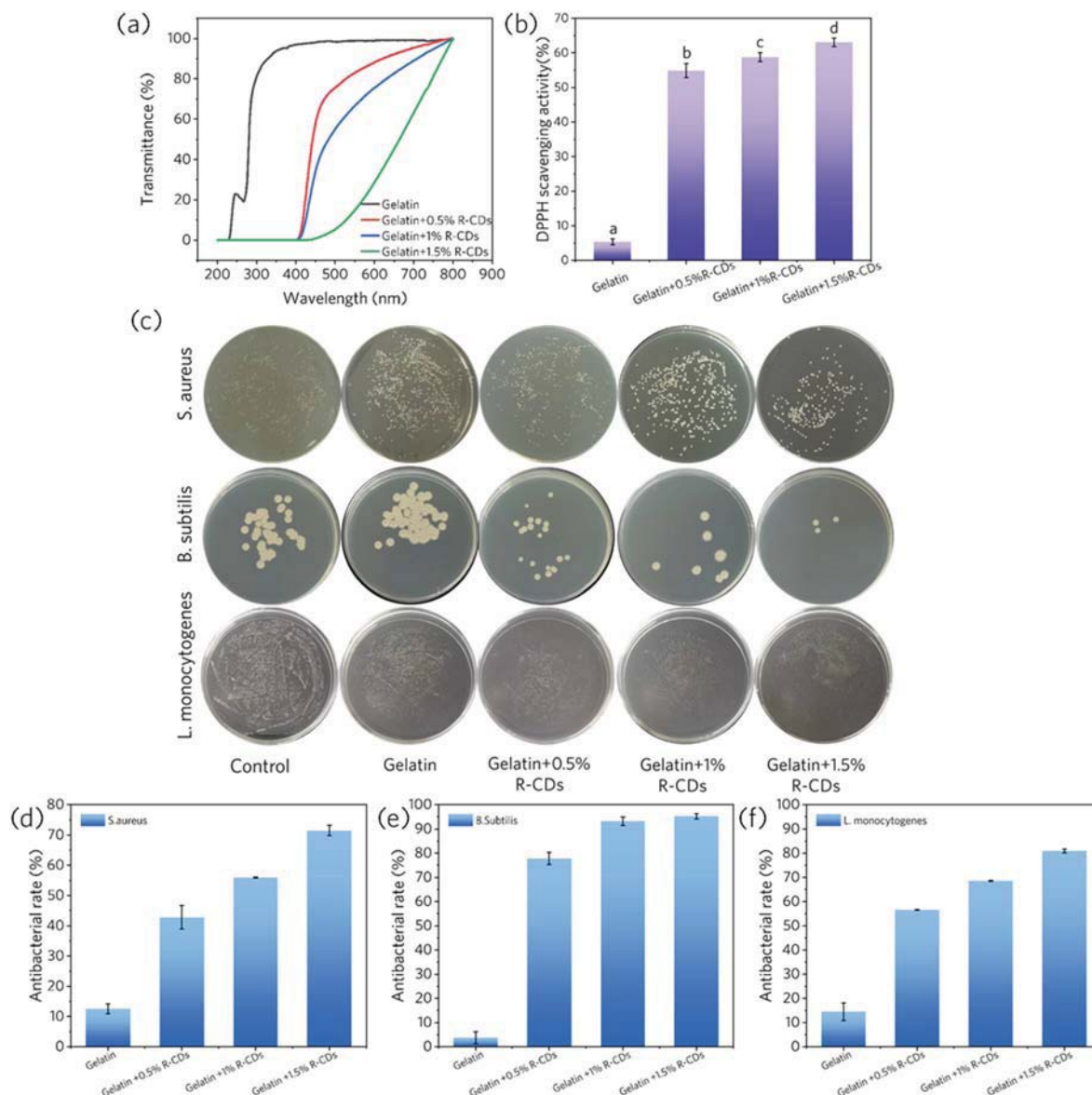


**Fig. 5.** The UV-Vis transmission spectrum (a) and DPPH scavenging activity (b) of different films. (c) Photographs of *S. aureus*, *B. subtilis* and *L. monocytogenes* colonies on agar plates after incubation with coating solution fortified with R-CDs of different concentrations and uncoated (control) substrates. The antibacterial rate of films against *S. aureus* (d), *B. subtilis* (e) and *L. monocytogenes* (f).

also inherited the antibacterial effect of R-CDs against *S. aureus*, *B. subtilis* and *L. monocytogenes*. As shown in Fig. 5c, d, e and f, the antibacterial ability of the film against three kinds of Gram-positive bacteria was enhanced with the increase of R-CDs concentration in the film. Compared with the gelatin group, the antibacterial rate of the film with 1.5% R-CDs addition was increased by 58.96% against *S. aureus*, 91.45% against *B. subtilis*, 66.44% against *L. monocytogenes*. Table S1 demonstrated the inhibition zone of films against *B. cinerea* growth, with normal mycelial growth in the control group and no inhibitory effect of gelatin on the fungus. Films with added R-CDs inhibited mycelial growth, but there was no significant difference between the different additions. It indicated that the films inherited the property of R-CDs to inhibit fungal growth. The fungal growth inhibition property of the films is favorable for its application in fruit preservation.

UV radiation triggers the oxidation of food ingredients, destroying nutrients and active ingredients, leading to food oxidation rancidity, odor, discoloration and the production of toxic chemicals (EzatiRhim, 2021). Oxidative degradation of food is one of the main reasons for food quality degradation, so antioxidant activity is also one of the needs of

food packaging (Liu, et al., 2019). Other studies reported that gelatin-based coating or film added with CDs or active substances has UV-blocking, antioxidant (TammimaRhim, 2023) and antibacterial properties (Ezati, et al., 2022; Yang et al., 2023). However, generally, the reported films can only block partial wavelengths of UV radiation (Wan, et al., 2023), while the multifunctional role of antioxidant and antibacterial requires the addition of multiple functional components to achieve (Du, et al., 2022; Min et al., 2023). To the best of our knowledge, it is the first report that the as-prepared R-CDs reinforced adhesive film can achieve broadband UV-blocking, excellent antioxidant and antibacterial multifunctionality.

#### 3.4.3. The biocompatibility study of films

In order to confirm the biocompatibility of the films, the cytotoxicity of the films against L929 mouse fibroblasts was tested in vitro by MTT assay. The results indicated that the cytotoxicity of the films was negligible, that was, the cell viability of the films was higher than that of the control, and the addition of CDs increased the cell viability (Fig. 6). This was in agreement with other reports (Khoshkalampour, et al.,

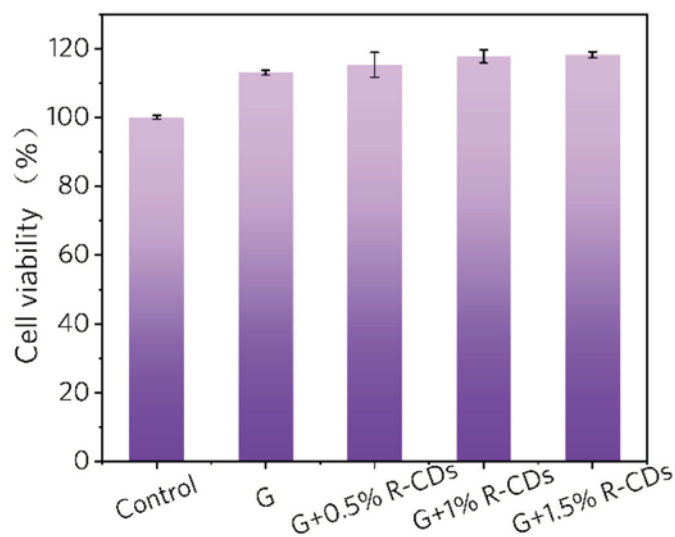


Fig. 6. Cell viability of mouse fibroblast L929 cells after co-culture with different film extracts for 24h.

2023), which also showed a proliferative effect on NIH3T3 cells when grape-leaf-derived CDs was added to gelatin-prepared nanocomposite films. In general, CDs prepared from biomass as precursor systems were almost non-toxic (Guo, Liu, & Wei, et al., 2022; Qu, Wei, & Sun, 2018). Other reports have also shown that plastic wrap mixed with CDs has no

toxicity or low toxicity (Ezati, et al., 2022; Ezati et al., 2022; Khoshkalampour et al., 2023; Lin, Huang, et al., 2022).

### 3.5. Strawberries coating with R-CDs reinforced gelatin solution

#### 3.5.1. The appearance, rotting rate, weight loss, firmness and nutrient of strawberries during storage

As shown in Fig. 7a, there was no significant difference in the appearance of strawberries among all groups on day 0. On the second day of storage, the ripeness and color of strawberries in each group increased significantly. The gelatin+0.5% R-CDs treatment group had one strawberry with mold. There was no mildew in the control, possibly due to individual differences in each strawberry. On the sixth day of storage, three strawberries in the control group had mildew, and one of them had mildew area exceeding 75%, while two strawberries in the gelatin coating group had spoilage. Strawberries in the gelatin +0.5% R-CDs group that decayed on the second day had approximately 30% decay area after six days. Surprisingly, strawberries in the gelatin+1.5% R-CDs group were full and intact after six days of storage at room temperature. By the end of the eighth day of storage, the rotting rate of strawberries in the control group was about 75% (Fig. 7b), and most strawberries were shriveled or infested with bacteria. In contrast, the strawberries treated with Gelatin+1.5%R-CDs were mostly full and rosy, and the rotting rate was about 4.17% (Fig. 7b). In the first 4 days, the rotting rate was lower in the 1% and 1.5% R-CDs treatment groups, and no decay was even observed at 1.5% R-CDs treatment group, indicating that the addition of R-CDs can effectively inhibit strawberry decay. In the control group, the rotting rate increased significantly with the

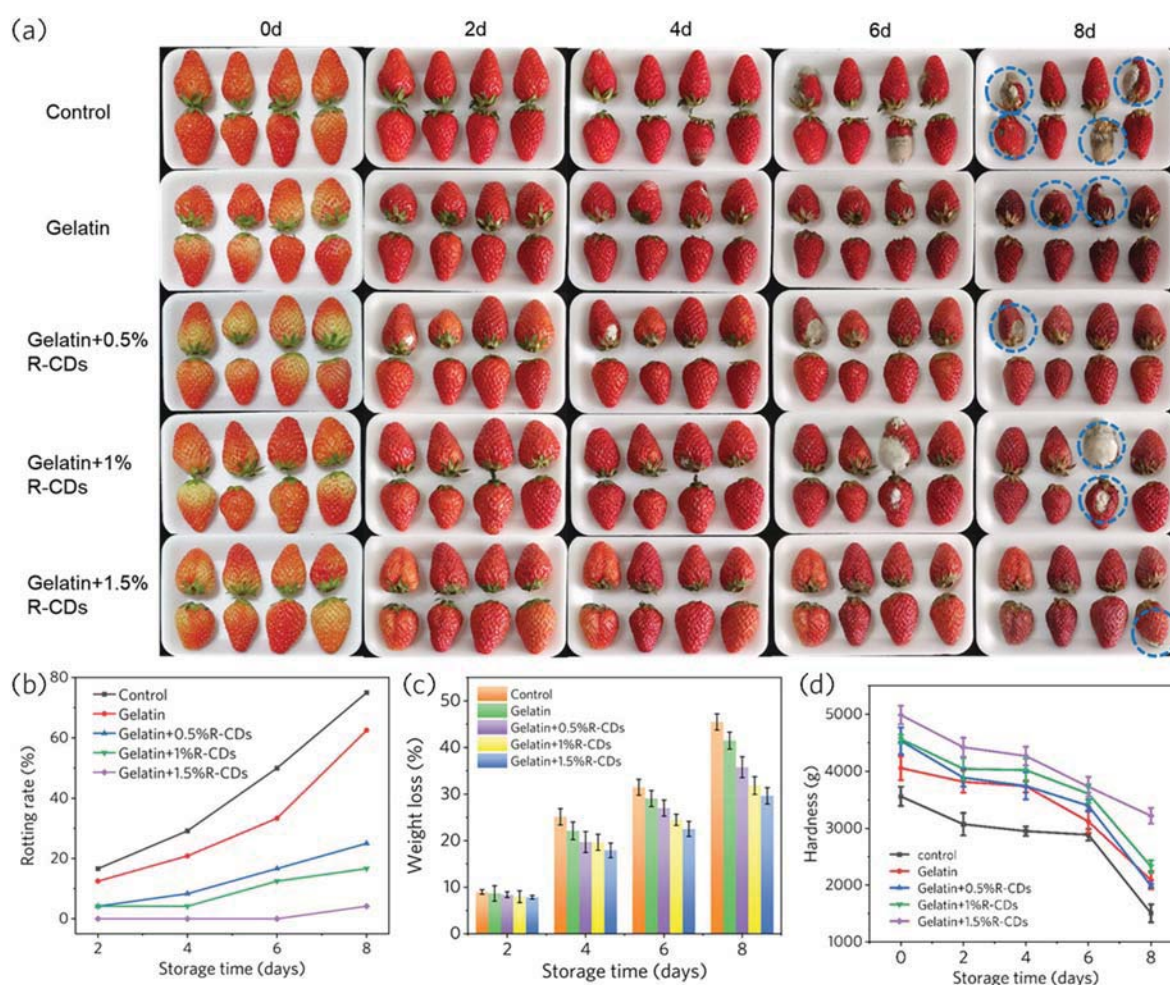


Fig. 7. The appearance (a), rotting rate (b), weight loss (c) and hardness (d) of strawberries during storage.

extension of time.

Weightlessness is a natural feature of fruit during storage. It is mainly caused by carbon loss during the formation of carbon dioxide during respiration and water loss caused by water evaporation, which leads to fruit shrinkage and dehydration, promotes fruit aging, and affects fruit appearance. The five groups lost more weight on the second day of storage because of the strawberry respiration (Fig. 7c). With the extension of time, the weight loss of the control group was the highest on the fourth day, while the weight loss of the coating group containing 1.5%R-CDs was relatively light. The possible reason is that the addition of R-CDs results in the formation of denser gel network, which reducing water evaporation, or inhibiting the strawberry's respiration. This trend remained until the end day of storage, when the weight loss rate of the control group was 45.47% and that of the 1.5% R-CDs group was 29.63%.

Pectin and other cell wall components were solubilized by pectinase during storage and the subsequent changes in hardness were mainly related to its weight loss and deterioration. During ripening, strawberries soften significantly due to the softness of the middle lamella of the cell wall. Cortical parenchyma cells, cell wall strength, intercellular contact, and cell turgor pressure also affect hardness. The hardness results on day 0 (Fig. 7d) showed that strawberries coated with gelatin or a mixture of gelatin and R-CDs solution could significantly increase hardness compared to the control group, attributed to the strong mechanical properties of the film formed by the solution covering the surface of the strawberries. (Fig. 4b). Gelatin treatment and gelatin combined with R-CDs treatment can reduce water loss, avoid strawberry oxidation, reduce respiration and reduce microbial infection to a certain extent. The addition of R-CDs may delay the decomposition of pectinase in strawberry fruit, thus reducing the hardness of strawberry. Results and discussion of titratable acidity and total phenolic content of strawberries during storage were shown in the supporting document.

### 3.5.2. Effects of different coating solutions on bacterial communities on strawberry surface

The microbial communities on the surface of strawberry after storage were sequenced to further reveal the preservation mechanism of R-CDs.

As shown in Fig. 8, the diversity and richness of bacterial communities on the surface of strawberry were shown by chao1 index and shannon's diversity index. Chao1 is used to estimate the total number of species contained in a community sample. The more low-abundance species in a community, the larger chao1 index will be (Cruz, Barka, Sylla, & Reinke, 2018). The total number of species on strawberry surface decreased treated with the Gelatin +1.5%R-CDs coating solution compared with the control group (Fig. 8a), indicating that R-CDs inhibited the growth of some microorganisms on strawberry surface. Shannon's diversity index refers to the total number and proportion of the samples. The higher the community diversity, the more uniform the species distribution, and the larger the shannon's diversity index (Artimová, et al., 2023). The results of shannon's diversity index in Fig. 8b were consistent with those of chao1, and the diversity of microbial colonies on the surface of strawberry samples treated with R-CDs decreased. However, there was no significant difference compared with the control group, which was consistent with the reported results (Cai, et al., 2022).

Based on the annotation results of species at different classification levels, the top 10 species with maximum abundance in each sample were selected for each phylum and genus level, and the columnar accumulation diagram of relative abundance was generated to visually view the species with high relative abundance and their proportion in each sample at different classification levels. As shown in Fig. 8c, at the phylum level, the main dominant bacteria in the control group were Proteobacteria (89.1%), Firmicutes (6.4%), followed by Cyanobacteria (0.9%), Bacteroidota (0.9%) and Actinobacteriota (0.7%). The dominant bacteria in R-CDs treatment group were Proteobacteria (96.0%), followed by Firmicutes (0.5%), Cyanobacteria (0.6%), Bacteroidota (0.4%) and Actinobacteriota (0.7%). The results showed that the growth of other bacteria except Proteobacteria was inhibited after R-CDs treatment, making Proteobacteria become the dominant bacteria group, which may also be the main reason for the decrease of Firmicutes with more beneficial bacteria. Proteobacteria is also the dominant bacterial community of vegetables such as spinach, lettuce and tomato (LeffFierer, 2013). A similar distribution of relative abundance was also found in the phyllosphere microbial community in strawberry (Sun, et al., 2022).

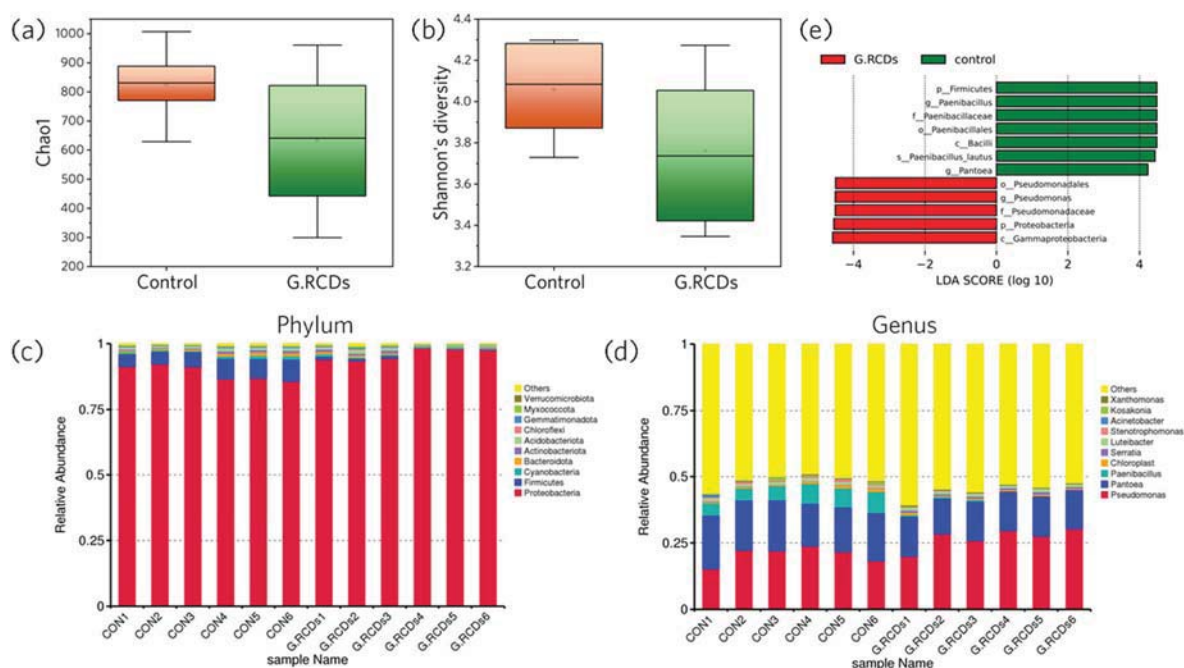


Fig. 8. Alpha diversity index (a) chao1 (b) Shannon's diversity, relative abundance of colonies at phylum level (c) and genus level (d), histogram of LDA score distribution analyzed by LEfSe analysis (e), LDA score threshold >4.0 was seen as significantly different among groups at phylum, class, order, family, genus, and species levels.



At the genus level (Fig. 8d), the dominant bacteria in the control group were *Pseudomonas* (20.5%), *Pantoea* (18.3%) and *Paenibacillus* (6.2%), followed by *Chloroplast* (0.8%) and *Serratia* (0.3%). After R-CDs treatment, the relative abundance of *Pseudomonas* increased to 26.9%, which was significantly higher than that of the control group (Fig. 8e), while the relative abundance of other genus decreased. The results showed that R-CDs inhibited the growth of other genera. Some bacteria of the genus *Pseudomonas*, such as *P. fluorescens*, can symbiotically fight plant diseases. They can be used as important potassium-dissolving and scaling bacteria in soil to improve the utilization rate of soil nutrients (Bai, Hu, Zhang, Feng, & Xu, 2014). These bacteria are also effective in reducing the incidence of gray mold and acid rot in post-harvest preservation of strawberries, apples and grapes (IlhanKarabulut, 2013). In addition, *pseudomonas* and *rhizobia* were found to inhibit the growth of *Xanthomonas fragariae*, the pathogen of strawberry bacterial hornspot (Henry, Gebben, Tech, Yip, & Leveau, 2016). In summary, the addition of R-CDs effectively inhibited the growth of harmful bacteria on the surface of strawberry, and improved the relative abundance of beneficial bacteria, so that R-CDs showed excellent ability in strawberry preservation application.

#### 4. Conclusion

In this work, R-CDs with UV broadband absorption, excellent antioxidant and antimicrobial properties were successfully prepared. Subsequently, R-CDs were homogeneously dispersed in the gelatin matrix and a composite coating solution was prepared, which was non-cytotoxic and had excellent hydrophilic and mechanical properties. The addition of R-CDs imparted strong antioxidant and antimicrobial properties to the gelatin film, and the UV broadband shielding effect of the film was achieved only by the addition of R-CDs prepared from a single inexpensive and safe raw material. Freshness of strawberries coated with the R-CDs reinforced solution were maintained and shelf life was extended successfully. The harmful bacteria on the surface of strawberry were suppressed and the helpful bacteria proliferated after coating. The multifunctional R-CDs, as a functional enhancer, could be added to the edible coating solution substrate to produce a low-cost and high-efficiency active packaging material for the preservation of post-harvest fruits. Next, the antimicrobial mechanism of R-CDs and the generality of the preservation effect on different fruits will be further investigated.

#### Author statement

Baoyan Guo: Conceptualization, Methodology, Validation, Date curation, Investigation, Formal Analysis, Writing - Original Draft. Guo Liu: Methodology, Visualization, Investigation. Weihao Ye: Formal Analysis. Zhiqiang Xu: Resources, Investigation. Wei Li: Methodology, Supervision. Jianle Zhuang: Validation. Xuejie Zhang: Visualization. Lashuang Wang: Resources. Bingfu Lei: Visualization, Writing - Review & Editing. Chaofan Hua: Writing - Review & Editing. Yingliang Liu: Conceptualization, Funding Acquisition, Resources, Supervision, Writing - Review & Editing. Hanwu Dong: Conceptualization, Funding Acquisition, Resources, Supervision, Writing - Review & Editing.

#### Declaration of competing interest

Authors declare that they have no known competing financial interests or personal relationships that could have appeared to influence the work reported in this paper.

#### Data availability

Data will be made available on request.

#### Acknowledgements

This work was financially supported by the National Natural Science Foundation of China (Grant No. 12174119 and 52172142), Science and Technology Program of Guangzhou, China (Grant No. 202103000059).

#### Appendix A. Supplementary data

Supplementary data to this article can be found online at <https://doi.org/10.1016/j.foodhyd.2023.109327>.

#### References

- Agarwal, S., Hoque, M., Bandara, N., Pal, K., & Sarkar, P. (2020). Synthesis and characterization of tamarind kernel powder-based antimicrobial edible films loaded with geraniol. *Food Packaging and Shelf Life*, 26. <https://doi.org/10.1016/j.fpsl.2020.100562>. Article 100562.
- Aitboulahsen, M., Zantar, S., Laglaoui, A., Chair, H., Arakrak, A., Bakkali, M., et al. (2018). Gelatin-based edible coating combined with *mentha pulegium* essential oil as bioactive packaging for strawberries, 2018 *Journal of Food Quality*. <https://doi.org/10.1155/2018/8408915>. Article 8408915.
- Alizadeh-Sani, M., Khezerlou, A., & Ehsani, A. (2018). Fabrication and characterization of the bionanocomposite film based on whey protein biopolymer loaded with TiO2 nanoparticles, cellulose nanofibers and rosemary essential oil. *Industrial Crops and Products*, 124, 300–315. <https://doi.org/10.1016/j.indcrop.2018.08.001>
- Artimová, R., Játiová, M., Baumgartnerová, J., Lipková, N., Petrová, J., Maková, J., et al. (2023). Microbial communities on samples of commercially available fresh-consumed leafy vegetables and small berries. *Horticulturae*, 9(2), 150. <https://doi.org/10.3390/horticulturae9020150>
- Bai, W., Hu, R., Zhang, J., Feng, L., & Xu, H. (2014). Effects of phosphate-solubilizing bacteria on growth and phosphorus uptake of corn seedling. in *Chinese Ecological Science*, 33(3), 401–407.
- Bose, S. K., Howlader, P., Jia, X., Wang, W., & Yin, H. (2019). Alginate oligosaccharide postharvest treatment preserve fruit quality and increase storage life via Abscissic acid signaling in strawberry. *Food Chemistry*, 283, 665–674. <https://doi.org/10.1016/j.foodchem.2019.01.060>
- Cai, J., Lu, W., Kan, Q., Chen, X., Cao, Y., & Xiao, J. (2022). Volatile composition changes of fruits in a biopolymer-coated polyethylene active packaging: Effects of modified atmosphere and packaging-shaped bacterial community. *Food Research International*, 152. <https://doi.org/10.1016/j.foodres.2021.110843>. Article 110843.
- Chang, L., Xu, L., Yang, Z., Liu, L., & Qiu, D. (2023). Antibacterial and antioxidative biogenic films for room-temperature strawberry preservation. *Food Chemistry*, 405. <https://doi.org/10.1016/j.foodchem.2022.134893>. Article 134893.
- Chen, C., Xu, Z., Qiu, J., Ye, W., Xu, X., Wang, R., et al. (2022). Synthesis of carbon dots with carbogenic  $\pi$ -conjugated domains for full-band UV shielding. *ACS Applied Nano Materials*, 5(7), 9140–9149. <https://doi.org/10.1021/acsanm.2c01444>
- Choi, H., Choi, S., Lee, N., & Chang, H. (2022). Antimicrobial activity of chitosan/gelatin/poly(vinyl alcohol) ternary blend film incorporated with duchesnea indica extract in strawberry applications. *Foods*, 11(24), 3963. <https://doi.org/10.3390/foods11243963>
- Cruz, A. F., Barka, G. D., Sylla, J., & Reineke, A. (2018). Biocontrol of strawberry fruit infected by *Botrytis cinerea*: Effects on the microbial communities on fruit assessed by next-generation sequencing. *Journal of Phytopathology*, 166(6), 403–411. <https://doi.org/10.1111/jph.12700>
- Da Silva Scudeler, C. G., de Lima Costa, T., Cortez-Vega, W. R., Prentice, C., & Fonseca, G. G. (2020). Development and characterization of Nile tilapia (*Oreochromis niloticus*) protein isolate-based biopolymer films incorporated with essential oils and nanoclay. *Food Packaging and Shelf Life*, 25. <https://doi.org/10.1016/j.fpsl.2020.100542>. Article 100542.
- Das, B., Dadhich, P., Pal, P., Srivas, P. K., Bankoti, K., & Dhara, S. (2014). Carbon nanodots from date molasses: New nanolights for the in vitro scavenging of reactive oxygen species. *Journal of Materials Chemistry B*, 2(39), 6839–6847. <https://doi.org/10.1039/C4TB01020E>
- Du, H., Min, T., Sun, X., Bian, X., Zhu, Z., & Wen, Y. (2022). Multifunctional film based on gelatin with titanium dioxide and thymol/ $\beta$ -cyclodextrins for fresh-keeping packaging. *Food Bioscience*, 50. <https://doi.org/10.1016/j.fbio.2022.102168>. Article 102168.
- Ezati, P., & Rhim, J. (2021). Fabrication of quercetin-loaded biopolymer films as functional packaging materials. *ACS Applied Polymer Materials*, 3(4), 2131–2137. <https://doi.org/10.1021/acsapm.1c00177>
- Ezati, P., Rhim, J., Molaei, R., Priyadarshi, R., & Han, S. (2022). Cellulose nanofiber-based coating film integrated with nitrogen-functionalized carbon dots for active packaging applications of fresh fruit. *Postharvest Biology and Technology*, 186. <https://doi.org/10.1016/j.postharvbio.2022.111845>. Article 111845.
- Ezati, P., Rhim, J., Molaei, R., Priyadarshi, R., Roy, S., Min, S., et al. (2022). Preparation and characterization of B, S, and N-doped glucose carbon dots: Antibacterial, antifungal, and antioxidant activity. *Sustainable Materials and Technologies*, 32, e397. <https://doi.org/10.1016/j.susmat.2022.e00397>
- Ezati, P., Rhim, J., Molaei, R., & Rezaei, Z. (2022). Carbon quantum dots-based antifungal coating film for active packaging application of avocado. *Food Packaging and Shelf Life*, 33. <https://doi.org/10.1016/j.fpsl.2022.100878>. Article 100878.

- Ezati, P., Roy, S., & Rhim, J. (2022). Pectin/gelatin-based bioactive composite films reinforced with sulfur functionalized carbon dots. *Colloids and Surfaces A: Physicochemical and Engineering Aspects*, 636. <https://doi.org/10.1016/j.colsurfa.2021.128123>. Article 128123.
- Fang, Q., Dong, Y., Chen, Y., Lu, C., Chi, Y., Yang, H., et al. (2017). Luminescence origin of carbon based dots obtained from citric acid and amino group-containing molecules. *Carbon*, 118, 319–326. <https://doi.org/10.1016/j.carbon.2017.03.061>
- Freche, E., Gieng, J., Pignotti, G., Ibrahim, S. A., & Feng, X. (2022). Applications of lemon or cinnamon essential oils in strawberry fruit preservation: A review. *Journal of Food Processing and Preservation*, 46(9), Article e16526. <https://doi.org/10.1111/jfpp.16526>
- Gol, N. B., Patel, P. R., & Rao, T. V. R. (2013). Improvement of quality and shelf-life of strawberries with edible coatings enriched with chitosan. *Postharvest Biology and Technology*, 85, 185–195. <https://doi.org/10.1016/j.postharvbio.2013.06.008>
- Guo, J., Ge, L., Li, X., Mu, C., & Li, D. (2014). Periodate oxidation of xanthan gum and its crosslinking effects on gelatin-based edible films. *Food Hydrocolloids*, 39, 243–250. <https://doi.org/10.1016/j.foodhyd.2014.01.026>
- Guo, B., Liu, G., Li, W., Hu, C., Lei, B., Zhuang, J., et al. (2022). The role of carbon dots in the life cycle of crops. *Industrial Crops and Products*, 187. <https://doi.org/10.1016/j.indcrop.2022.115427>. Article 115427.
- Guo, B., Liu, G., Wei, H., Qiu, J., Zhuang, J., Zhang, X., et al. (2022). The role of functionalized carbon dots in crops: Mechanism and applications. *SmartMat*, 3(2), 208–225. <https://doi.org/10.1002/smm2.1111>
- Guo, Q., Zhao, B., Shen, S., Hou, J., Hu, J., & Xin, W. (1999). ESR study on the structure-antioxidant activity relationship of tea catechins and their epimers. *Biochimica et Biophysica Acta (BBA) - General Subjects*, 1427(1), 13–23. [https://doi.org/10.1016/S0304-4165\(98\)00168-8](https://doi.org/10.1016/S0304-4165(98)00168-8)
- He, X., Bai, Y., Zhao, Z., Wang, X., Fang, J., Huang, L., et al. (2016). Local and traditional uses, phytochemistry, and pharmacology of *Sophora japonica* L.: A review. *Journal of Ethnopharmacology*, 187, 160–182. <https://doi.org/10.1016/j.jep.2016.04.014>
- Henry, P. M., Gebben, S. J., Tech, J. J., Yip, J. L., & Leveau, J. H. J. (2016). Inhibition of *xanthomonas fragariae*, causative agent of angular leaf spot of strawberry, through iron deprivation. *Frontiers in Microbiology*, 7. <https://doi.org/10.3389/fmicb.2016.01589>. Article 1589.
- Hosseini, S. F., Ghaderi, J., & Gómez-Guillén, M. C. (2021). *trans*-Cinnamaldehyde-doped quadripartite biopolymeric films: Rheological behavior of film-forming solutions and biofunctional performance of films. *Food Hydrocolloids*, 112. <https://doi.org/10.1016/j.foodhyd.2020.106339>. Article 106339.
- Ilhan, K., & Karabulut, O. A. (2013). Efficacy and population monitoring of bacterial antagonists for gray mold (*Botrytis cinerea* Pers. ex. Fr.) infecting strawberries. *Biocontrol*, 58(4), 457–470. <https://doi.org/10.1007/s10526-012-9503-x>
- Innocenzi, P., & Stagi, L. (2023). Carbon dots as oxidant-antioxidant nanomaterials, understanding the structure-properties relationship. A critical review. *Nano Today*, 50. <https://doi.org/10.1016/j.nantod.2023.101837>. Article 101837.
- Khoshkalampour, A., Ghorbani, M., & Ghasempour, Z. (2023). Cross-linked gelatin film enriched with green carbon quantum dots for bioactive food packaging. *Food Chemistry*, 404. <https://doi.org/10.1016/j.foodchem.2022.134742>. Article 134742.
- Kim, Y. H., Kim, H., Yoon, K. S., & Rhim, J. (2023). Cellulose nanofiber/deacetylated quaternary chitosan composite packaging film for growth inhibition of *Listeria monocytogenes* in raw salmon. *Food Packaging and Shelf Life*, 35. <https://doi.org/10.1016/j.foodpsl.2023.101040>. Article 101040.
- Kousheh, S. A., Moradi, M., Tajik, H., & Molaei, R. (2020). Preparation of antimicrobial/ultraviolet protective bacterial nanocellulose film with carbon dots synthesized from lactic acid bacteria. *International Journal of Biological Macromolecules*, 155, 216–225. <https://doi.org/10.1016/j.ijbiomac.2020.03.230>
- Krishna, P. M., Kmv, R., S., & Banji, D. (2012). A review on phytochemical, ethnomedical and pharmacological studies on genus *Sophora*, Fabaceae. *Revista Brasileira de Farmacognosia*, 22, 1145–1154. <https://doi.org/10.1590/S0102-695X2012005000043>
- Kumar, S., Shukla, A., Baul, P. P., Mitra, A., & Halder, D. (2018). Biodegradable hybrid nanocomposites of chitosan/gelatin and silver nanoparticles for active food packaging applications. *Food Packaging and Shelf Life*, 16, 178–184. <https://doi.org/10.1016/j.foodpsl.2018.03.008>
- Leff, J. W., & Fierer, N. (2013). Bacterial communities associated with the surfaces of fresh fruits and vegetables. *PLoS One*, 8(3), Article e59310. <https://doi.org/10.1371/journal.pone.0059310>
- Li, H., Huang, J., Song, Y., Zhang, M., Wang, H., Lu, F., et al. (2018). Degradable carbon dots with broad-spectrum antibacterial activity. *ACS Applied Materials & Interfaces*, 10(32), 26936–26946. <https://doi.org/10.1021/acsami.8b08832>
- Lin, R., Cheng, S., & Tan, M. (2022). Green synthesis of fluorescent carbon dots with antibacterial activity and their application in Atlantic mackerel (*Scomber scombrus*) storage. *Food & Function*, 13(4), 2098–2108. <https://doi.org/10.1039/D1FO03426J>
- Lin, W., Huang, G., Yang, W., Zeng, S., Luo, X., Huang, J., et al. (2022). A dual-function chitosan packaging film for simultaneously monitoring and maintaining pork freshness. *Food Chemistry*, 392. <https://doi.org/10.1016/j.foodchem.2022.133242>. Article 133242.
- Li, Y., Shan, P., Yu, F., Li, H., & Peng, L. (2023). Fabrication and characterization of waste fish scale-derived gelatin/sodium alginate/carvacrol loaded ZIF-8 nanoparticles composite films with sustained antibacterial activity for active food packaging. *International Journal of Biological Macromolecules*, 230. <https://doi.org/10.1016/j.ijbiomac.2023.123192>. Article 123192.
- Liu, J., Li, R., & Yang, B. (2020). Carbon dots: A new type of carbon-based nanomaterial with wide applications. *ACS Central Science*, 6(12), 2179–2195. <https://doi.org/10.1021/acscentsci.0c01306>
- Liu, Y., Qin, Y., Bai, R., Zhang, X., Yuan, L., & Liu, J. (2019). Preparation of pH-sensitive and antioxidant packaging films based on κ-carrageenan and mulberry polyphenolic extract. *International Journal of Biological Macromolecules*, 134, 993–1001. <https://doi.org/10.1016/j.ijbiomac.2019.05.175>
- Maringgal, B., Hashim, N., Mohamed Amin Tawakkal, I. S., & Muda Mohamed, M. T. (2020). Recent advance in edible coating and its effect on fresh/fresh-cut fruits quality. *Trends in Food Science & Technology*, 96, 253–267. <https://doi.org/10.1016/j.tifs.2019.12.024>
- Min, S., Ezati, P., & Rhim, J. (2022). Gelatin-based packaging material incorporated with potato skins carbon dots as functional filler. *Industrial Crops and Products*, 181. <https://doi.org/10.1016/j.indcrop.2022.114820>. Article 114820.
- Min, S., Ezati, P., Yoon, K. S., & Rhim, J. (2023). Gelatin/poly(vinyl alcohol)-based functional films integrated with spent coffee ground-derived carbon dots and grapefruit seed extract for active packaging application. *International Journal of Biological Macromolecules*, 231. <https://doi.org/10.1016/j.ijbiomac.2023.123493>. Article 123493.
- Muhammad, A., Shaghef, E., Rana, N. U. R., Mumtaz, K., & Rashad, Q. (2019). In A. T. Strawberry, & M. A. (Eds.), *Postharvest quality management of strawberries* (Vol. 4). Rijeka: IntechOpen.
- Niu, X., Song, T., & Xiong, H. (2021). Large scale synthesis of red emissive carbon dots powder by solid state reaction for fingerprint identification. *Chinese Chemical Letters*, 32(6), 1953–1956. <https://doi.org/10.1016/j.cclet.2021.01.006>
- Papaioannou, N., Marinovic, A., Yoshizawa, N., Goode, A. E., Fay, M., Khloubystov, A., et al. (2018). Structure and solvents effects on the optical properties of sugar-derived carbon nanodots. *Scientific Reports*, 8(1). <https://doi.org/10.1038/s41598-018-25012-8>. Article 6559.
- Qiu, J., Ye, W., Xu, X., Congcong, C., Xu, Z., Lei, B., et al. (2022). One-step hydrothermal synthesis of nitrogen-doped carbonized polymer dots with full-band absorption for skin protection. *ACS Sustainable Chemistry & Engineering*, 10(36), 11958–11968. <https://doi.org/10.1021/acscuschemeng.2c03324>
- Qu, J., Wei, Q., & Sun, D. (2018). Carbon dots: Principles and their applications in food quality and safety detection. *Critical Reviews in Food Science and Nutrition*, 58(14), 2466–2475. <https://doi.org/10.1080/10408398.2018.1437712>
- Riahi, Z., Priyadarshi, R., Rhim, J., & Bagheri, R. (2021). Gelatin-based functional films integrated with grapefruit seed extract and TiO<sub>2</sub> for active food packaging applications. *Food Hydrocolloids*, 112. <https://doi.org/10.1016/j.foodhyd.2020.106314>. Article 106314.
- Roy, S., & Rhim, J. (2021). Fabrication of bioactive binary composite film based on gelatin/chitosan incorporated with cinnamon essential oil and rutin. *Colloids and Surfaces B: Biointerfaces*, 204. <https://doi.org/10.1016/j.colsurfb.2021.111830>. Article 111830.
- Roy, S., Van Hai, L., Kim, H. C., Zhai, L., & Kim, J. (2020). Preparation and characterization of synthetic melanin-like nanoparticles reinforced chitosan nanocomposite films. *Carbohydrate Polymers*, 231. <https://doi.org/10.1016/j.carbpol.2019.115729>. Article 115729.
- Ruiz, V., Yate, L., García, I., Cabanero, G., & Grande, H. (2017). Tuning the antioxidant activity of graphene quantum dots: Protective nanomaterials against dye decoloration. *Carbon*, 116, 366–374. <https://doi.org/10.1016/j.carbon.2017.01.090>
- Sun, Y., Wang, Y., Xu, Y., Chen, T., Li, B., Zhang, Z., et al. (2021). Application and mechanism of benzyl-isothiocyanate, a natural antimicrobial agent from cruciferous vegetables, in controlling postharvest decay of strawberry. *Postharvest Biology and Technology*, 180. <https://doi.org/10.1016/j.postharvbio.2021.111604>. Article 111604.
- Sun, P., Wu, J., Lin, X., Wang, Y., Zhu, J., Chen, C., et al. (2022). Effect of ozonated water, mancozeb, and thiophanate-methyl on the phyllosphere microbial diversity of strawberry. *Frontiers in Plant Science*, 13. <https://doi.org/10.3389/fpls.2022.967797>. Article 967797.
- Tammina, S. K., & Rhim, J. (2023). Carboxymethylcellulose/agar-based functional film incorporated with nitrogen-doped polyethylene glycol-derived carbon dots for active packaging applications. *Chemosphere*, 313. <https://doi.org/10.1016/j.chemosphere.2022.137627>. Article 137627.
- Temiz, N. N., & Özdemir, K. S. (2021). Microbiological and physicochemical quality of strawberries (*Fragaria × ananassa*) coated with *Lactobacillus rhamnosus* and inulin enriched gelatin films. *Postharvest Biology and Technology*, 173. <https://doi.org/10.1016/j.postharvbio.2020.111433>. Article 111433.
- Vogler, E. A. (1998). Structure and reactivity of water at biomaterial surfaces. *Advances in Colloid and Interface Science*, 74(1), 69–117. [https://doi.org/10.1016/S0001-8686\(97\)00040-7](https://doi.org/10.1016/S0001-8686(97)00040-7)
- Wang, L., Liu, X., Qi, P., Sun, J., Jiang, S., Li, H., et al. (2022). Enhancing the thermostability, UV shielding and antimicrobial activity of transparent chitosan film by carbon quantum dots containing N/P. *Carbohydrate Polymers*, 278. <https://doi.org/10.1016/j.carbpol.2021.118957>. Article 118957.
- Wang, L., Li, Y., Wang, Y., Kong, W., Lu, Q., Liu, X., et al. (2019). Chlorine-doped graphene quantum dots with enhanced anti- and pro-oxidant properties. *ACS Applied Materials & Interfaces*, 11(24), 21822–21829. <https://doi.org/10.1021/acsami.9b03194>
- Wang, B., Song, H., Qu, X., Chang, J., Yang, B., & Lu, S. (2021). Carbon dots as a new class of nanomedicines: Opportunities and challenges. *Coordination Chemistry Reviews*, 442. <https://doi.org/10.1016/j.ccr.2021.214010>. Article 214010.
- Wang, J., Sun, X., Zhang, H., Dong, M., Li, L., Zhangsun, H., et al. (2022). Dual-functional intelligent gelatin based packaging film for maintaining and monitoring the shrimp freshness. *Food Hydrocolloids*, 124. <https://doi.org/10.1016/j.foodhyd.2021.107258>. Article 107258.
- Wan, S., Liu, Q., Yang, D., Guo, P., Gao, Y., Mo, R., et al. (2023). Characterization of high amylose corn starch-cinnamaldehyde inclusion films for food packaging. *Food Chemistry*, 403. <https://doi.org/10.1016/j.foodchem.2022.134219>. Article 134219.

- Wareing, T. C., Gentile, P., & Phan, A. N. (2021). Biomass-based carbon dots: Current development and future perspectives. *ACS Nano*, 15(10), 15471–15501. <https://doi.org/10.1021/acsnano.1c03886>
- Xu, Y., Xu, Z., Chen, C., Ye, W., Guo, B., Qiu, J., et al. (2023). Synthesis of efficient broad-spectrum UV-absorbing carbon dots as UV absorbers using natural rutin as raw material and their multifunctional applications under acid-base amphoteric conditions. *Surfaces and Interfaces*, 38. <https://doi.org/10.1016/j.surfin.2023.102810>. Article 102810.
- Yang, D., Liu, Q., Gao, Y., Wan, S., Meng, F., Weng, W., et al. (2023). Characterization of silver nanoparticles loaded chitosan/polyvinyl alcohol antibacterial films for food packaging. *Food Hydrocolloids*, 136. <https://doi.org/10.1016/j.foodhyd.2022.108305>. Article 108305.
- Yao, B., Huang, H., Liu, Y., & Kang, Z. (2019). Carbon dots: A small conundrum. *Trends in Chemistry*, 1(2), 235–246. <https://doi.org/10.1016/j.trechm.2019.02.003>
- Yuan, S., Xue, Z., Zhang, S., Wu, C., Feng, Y., & Kou, X. (2023). The characterization of antimicrobial nanocomposites based on chitosan, cinnamon essential oil, and TiO<sub>2</sub> for fruits preservation. *Food Chemistry*, 413. <https://doi.org/10.1016/j.foodchem.2023.135446>. Article 135446.
- Yu, M., Guo, X., Lu, H., Li, P., Huang, R., Xu, C., et al. (2022). Carbon dots derived from folic acid as an ultra-succinct smart antimicrobial nanosystem for selective killing of *S. aureus* and biofilm eradication. *Carbon*, 199, 395–406. <https://doi.org/10.1016/j.carbon.2022.07.065>
- Zhu, C., Li, H., Wang, H., Yao, B., Huang, H., Liu, Y., et al. (2019). Negatively charged carbon nanodots with bacteria resistance ability for high-performance antibiofilm formation and anticorrosion coating design. *Small*, 15(23), Article 1900007. <https://doi.org/10.1002/sml.201900007>



# Synthesis of Silicon Quantum Dots with Highly Efficient Full-Band UV Absorption and Their Applications in Antiyellowing and Resistance of Photodegradation

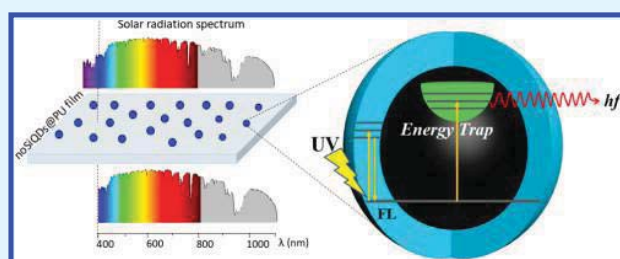
Guangqi Hu, Yuqiong Sun, Yixuan Xie, Shuangshuang Wu, Xuejie Zhang,<sup>✉</sup> Jianle Zhuang,<sup>✉</sup> Chaofan Hu,<sup>✉</sup> Bingfu Lei,<sup>✉</sup> and Yingliang Liu<sup>✉</sup>

Guangdong Provincial Engineering Technology Research Center for Optical Agriculture, College of Materials and Energy, South China Agricultural University, Guangzhou 510642, China

## S Supporting Information

**ABSTRACT:** UV absorbers are very effective in the fields of antiyellowing, resistance of photocatalytic degradation, and sunscreen cosmetics. However, commercialized UV absorbers have the drawbacks of toxicity, low absorption efficiency, transparency, etc. Here, we report for the first time silicon quantum dots as full-band UV absorbers. The NH-refunctionalized silicon quantum dots with high-performance UV absorption were successfully synthesized under the synergistic effect of sodium citrate and ethanediamine, and the (NH, OH)-functionalized silicon quantum dots (SiQDs) with full-band UV absorption can be achieved by reregulating  $-\text{NH}_2$  and  $-\text{OH}$  groups on the surface. The as-prepared (NH, OH)-functionalized SiQDs exhibited good stability and underwent treatment of varying pH and temperature. Furthermore, experimental results demonstrated that compared to commercial water-soluble organic UV absorbers, the (NH, OH)-functionalized SiQDs showed better antiyellowing performance for polyurethane and resistance of photocatalytic degradation for rhodamine B, and presented huge application potential in sunscreen cosmetics. Finally, the UV absorption mechanism of SiQDs was explained to be mainly related to  $\Gamma \rightarrow \Gamma$  direct band gap transition, which absorb UV light and release it as thermal radiation.

**KEYWORDS:** silicon quantum dots, ultraviolet absorption, antiyellowing, resistance of photodegradation, sunscreen



## INTRODUCTION

UV absorbers have long been used to effectively inhibit UV radiation aimed at protecting polymers from photodegradation, discoloration, and surface cracking and humans from complexion, erythema, and even skin cancer during long-term exposure to solar light.<sup>1–3</sup>

Inorganic UV absorbers mainly include nano- $\text{TiO}_2$  and ZnO without toxicity that have been commercialized and widely used as UV blocking agents.<sup>4–8</sup> A lot of in-depth research have been carried out to optimize the UV absorption efficiency for wider application, and higher UV absorption efficiency and higher polymer transparency were achieved by structural and particle size regulations of nano- $\text{TiO}_2$  and ZnO compared to early commercial materials.<sup>9</sup> However, in any case, inorganic UV absorbers are inferior in haze, transparency, and visible transmittance, cause degradation of the mechanical and physical properties of polymers, and are even phototoxic to human skin when added to sunscreen cosmetic.<sup>10–12</sup> To overcome the disadvantages of inorganic UV absorbers, quantum dots (QDs) as UV absorbers have recently attracted considerable interest. Initially, ZnO QDs with significant UV absorption performance by incorporating into PMMA matrix was reported,<sup>13,14</sup> then the UV absorption performances of other QDs, including Sn- and

Ag-modified ZnO, CdSe,  $\text{SnO}_2$ , and  $\text{SnS}_2$  QDs compositing with various polymers, were studied.<sup>15–18</sup> Despite the obvious improvement in the physical properties of polymers, these QDs are still unable to meet practical requirements due to the defects of narrow-band UV absorption, weak stability, and even toxicity for semiconductor quantum dots. Recently, graphene QDs and carbon QDs with wide UV absorption band, outstanding efficiency, and good biocompatibility have been reported,<sup>19–21</sup> which present excellent function of antiphotodegradation and are promising candidates for high-performance UV absorbers. However, the discoloration of polymers induced by groups on the surface of graphene and carbon QDs that lead to the significant decrease of UV absorption efficiency, and the high cost, especially, of graphene QDs if applied in mass products such as sunscreen cosmetic have become a huge obstacle to applications. Actually, organic UV absorbers (mainly benzophenone and benzotriazole) are the most successful commercial products and widely used in many fields especially polymers and sunscreen cosmetics.<sup>22–24</sup> But the drawbacks such

**Received:** November 15, 2018

**Accepted:** January 17, 2019

**Published:** January 17, 2019

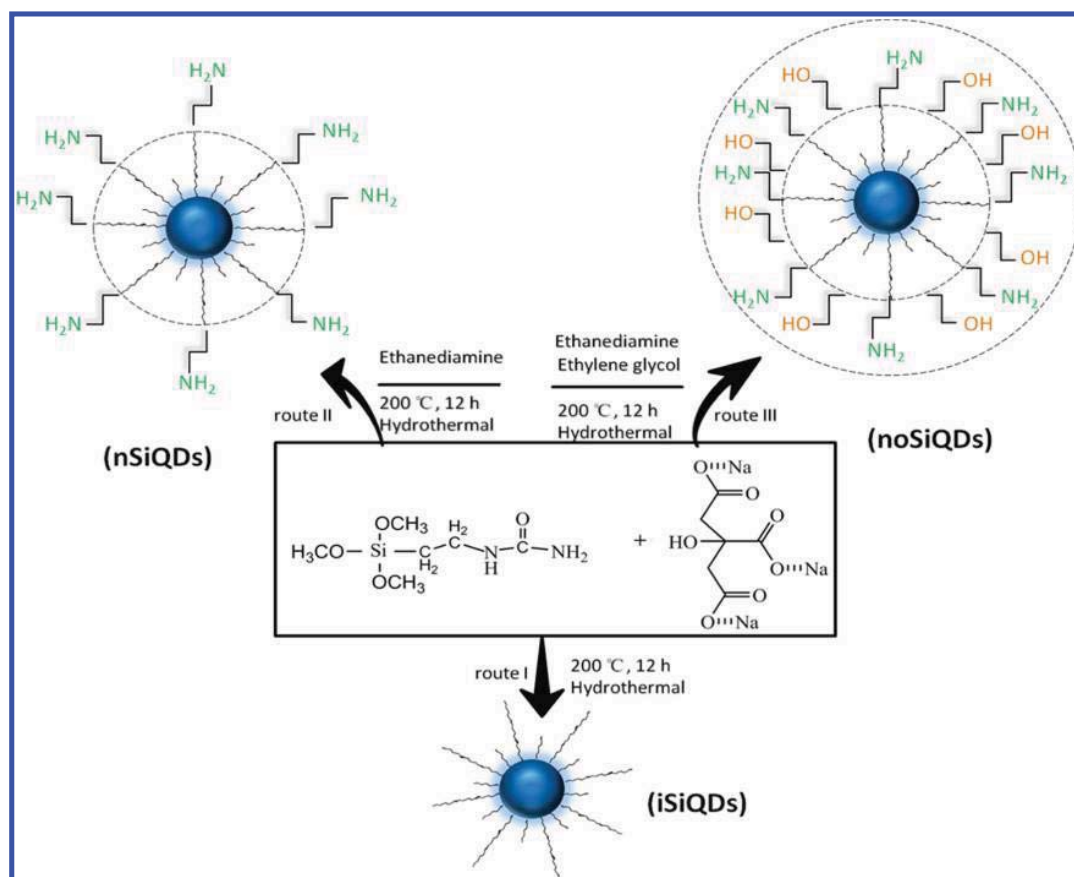


**Figure 1.** Synthetic scheme of the functionalized silicon quantum dots (SiQDs). iSiQDs were polymerized with 1-[3-(trimethoxysilyl) propyl]urea and CA-Na, nSiQDs were polymerized with 1-[3-(trimethoxysilyl) propyl]urea and the synergistic effect between CA-Na and EDA, and noSiQDs were polymerized under modification of EG based on nSiQDs.

as easy migration into the environment due to their low molecular weight and incompatibility with polymers, especially toxicity, cause a potential huge threat to humans or animals by natural circulation.<sup>25,26</sup> To solve the toxicity problem of organic polymer UV absorbers, the construction of nontoxic poly(vinyl chloride) (PVC)-UV absorber has been achieved successfully, and it shows outstanding resistance to UV photoaging for PVC, but this technical route is difficult to promote due to the complexity of the process and the high cost.<sup>27</sup> Very regrettably, there are few water-soluble UV absorbers, even though there exists great market demand in waterborne coatings and sunscreen cosmetics. At present, only 2-hydroxy-4-methoxybenzophenone-5-sulfonic acid (BP-4) and 2-phenylbenzimidazole-5-sulfonic acid (UV-T) have been successfully commercialized, but they have the limitations of very high cost and relatively narrow-band UV absorption.

Fortunately, due to the several silicon sources and rich groups on the surface, silicon quantum dots (SiQDs) present colorful luminescent and absorbent properties by adjusting the groups on SiQDs surface so that they can emit light from blue to red.<sup>28–31</sup> Based on their luminescent properties, many applications are possible, such as photostable biological probes,<sup>28</sup> light-emitting diode,<sup>32</sup> alkaline phosphatase detection,<sup>33</sup> etc. But there are no studies on the detailed absorption properties of water-soluble SiQDs with low cost, especially UV absorption and related applications, and their UV absorption mechanism has not been reported to date.

In this work, we synthesized full-band UV absorbent water-soluble (NH, OH)-functionalized silicon quantum dots (noSiQDs) and investigated their stability under treatment of varying pH value and temperature and dispersion in different solvents. Meanwhile, we studied the effects of UV absorption of noSiQDs on the performances of antiyellowing for polyurethane (PU), compared to water-soluble and commercial BP-4 UV absorber, photodegradation for rhodamine B (RhB), and theoretically calculated the sun protection factor (SPF) according to computational formula 3 shown in the [Materials and Methods](#) section and industry standard curve between SPF value and UVB absorption rate (Figure S1). Finally, we proposed the UV absorption mechanism of noSiQDs, which was explained to be mainly related to  $\Gamma \rightarrow \Gamma$  direct band gap transition and confirmed by infrared imaging and fluorescence quenching.

## RESULTS AND DISCUSSION

**Schematic Spectrograms of UV Absorption.** Three typical silicon quantum dots (iSiQDs: without NH-functionalized silicon quantum dots; nSiQDs: NH-functionalized silicon quantum dots; and noSiQDs: (NH, OH)-functionalized silicon quantum dots) were synthesized by regulating the reaction solvent and passivating agent via the bottom-up approach, as shown in Figure 1. The reaction route I is a conventional synthesis method of iSiQDs, which has been largely reported,<sup>28,29,34</sup> that is, 1-[3-(trimethoxysilyl) propyl]urea is

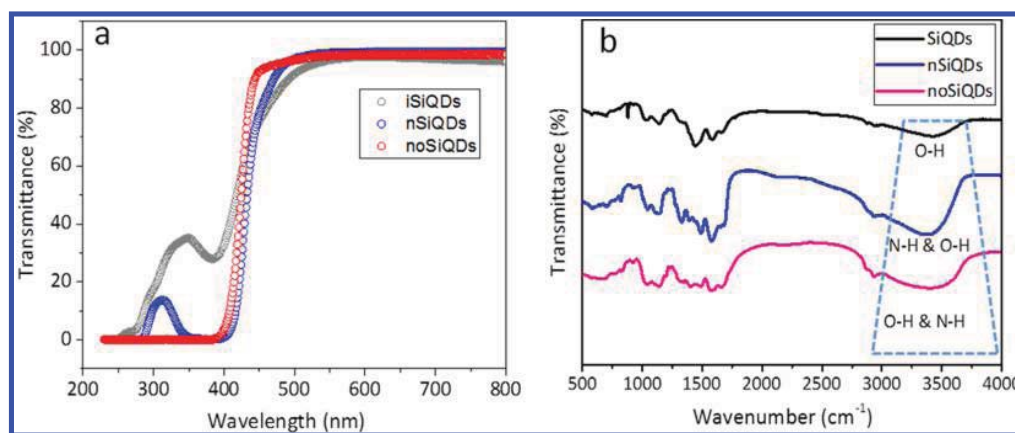


**Figure 2.** Ultraviolet–visible (UV–vis) transmittance spectra of (a) iSiQDs, nSiQDs, and noSiQDs and (b) their corresponding Fourier transform infrared spectroscopy (FT-IR) spectra.

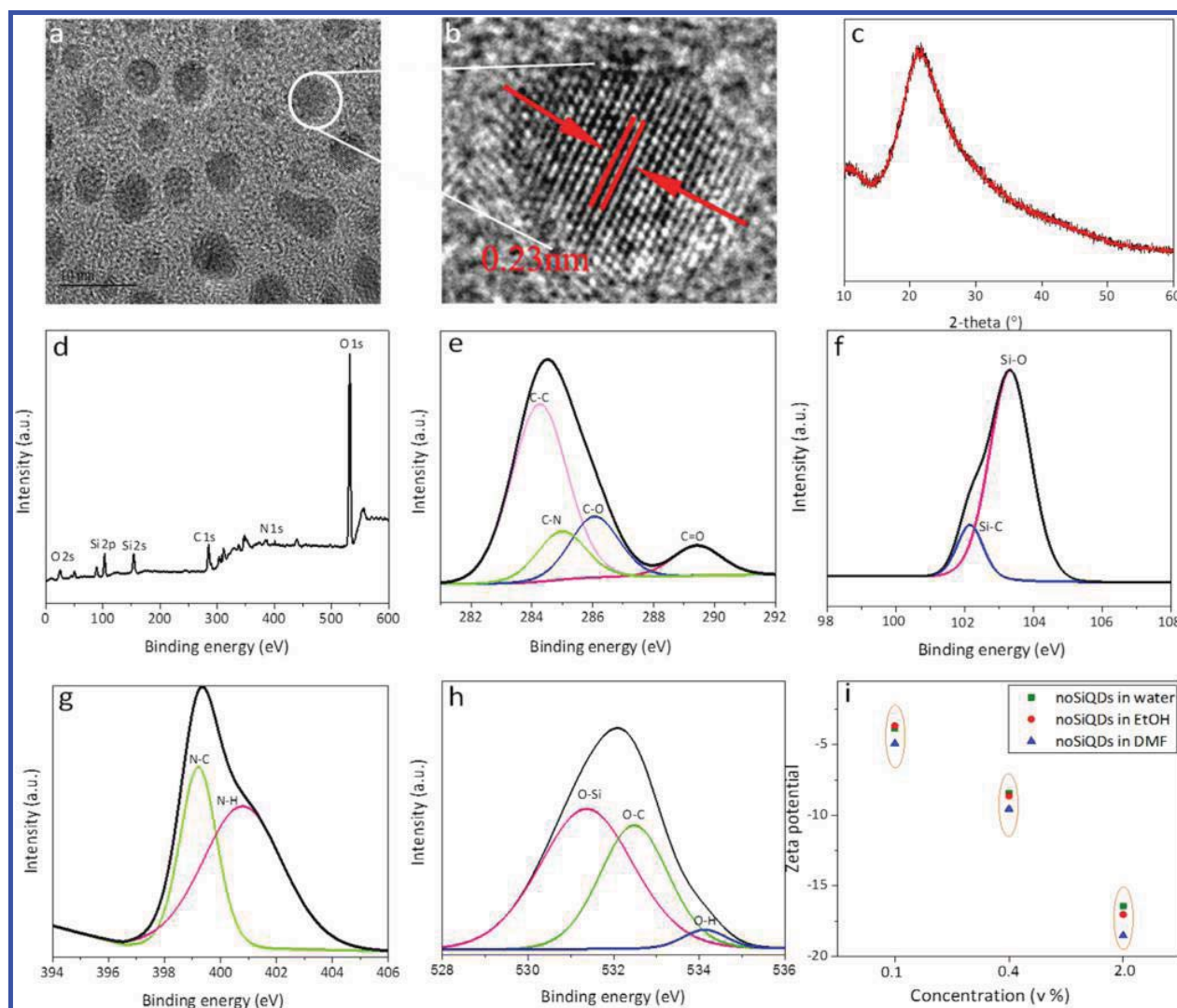


**Figure 3.** HRTEM image (a), lattice fringe image (b), XRD pattern (c), survey spectrum of X-ray photoelectron spectroscopy (XPS) images (d), and high-resolution XPS images of C 1s (e), Si 2p (f), O 1s (g), and N 1s (h) of full-band UV-absorbing noSiQDs and their  $\zeta$ -potentials (i) in water, EtOH, and dimethylformamide (DMF).



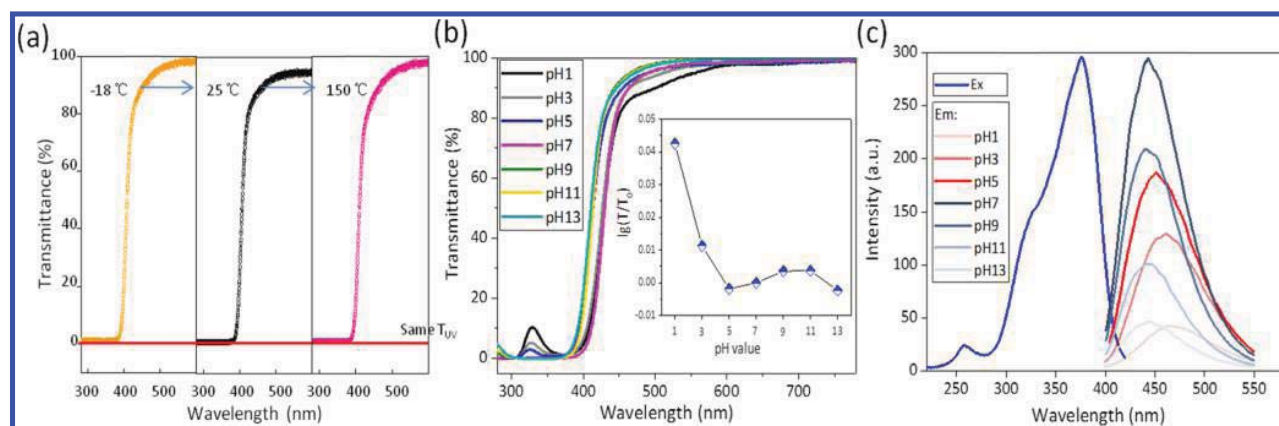


**Figure 4.** (a) Transmittance spectra of noSiQDs@PU under treatment of different temperatures. UV-vis transmittance spectra (b) and the corresponding fluorescence spectra (c) of noSiQDs aqueous solution under varying pH values.

polymerized under high temperature and high pressure by sodium citrate (CA-Na) as chelating agent and catalyst into iSiQDs, and the functionalized iSiQDs, which lead to  $n-\pi^*$  transition and induce the UV absorption band with a band gap of 3.44–4.13 eV (Figure S2, green lines) together with silicon cores that induce  $\pi-\pi^*$  transition, which presents weak UVA absorption band, as shown in Figure 2a, marked by the black line. For reaction route II, when deamination reaction occurs between  $-\text{NH}_2$  from 1-[3-(trimethoxysilyl) propyl]urea and ethanediamine (EDA), the absorbent spectrum band that nSiQDs correspond to occurs blue shift wholly so as to UVB absorption band is formed as presented in Figure 2a marked in blue line. However, there are no fluorescence for SiQDs by silane and EDA reaction, indicating that EDA and CA-Na have a synergistic effect on the formation of nSiQDs with bright blue emission and strong UV absorption, whereas for reaction route III, the absorption band gap of the noSiQDs further amplifies when carboxyamidine reaction occurs between  $-\text{NH}_2$  and  $-\text{OH}$  from ethylene glycol (EG), thereby forming a full UV absorption band of 3.10–4.43 eV (Figure S2, red lines) containing both UVA and UVB presented in Figure 2a marked by the pink line. This shows that  $-\text{OH}$  groups modified on SiQDs surface are beneficial to enhance the absorption in the wavelength range of 290–310 nm.

To check the changes of UV absorption performance induced by the chemical groups on SiQDs surface, the measurement of Fourier transform infrared spectroscopy (FT-IR) spectra shown in Figure 2b was carried out. Obviously, due to the same silane raw material for iSiQDs, nSiQDs, and noSiQDs, there contain Si–O ( $1044\text{ cm}^{-1}$ ), Si–C ( $1411\text{ cm}^{-1}$ ), C–N ( $1584\text{ cm}^{-1}$ ), and C=O ( $1680\text{ cm}^{-1}$ ) characteristic groups, which correspond to the groups of  $-\text{OCH}_3$  and  $-\text{CH}_2-\text{CH}_2-\text{NH}-\text{CO}-\text{NH}_2$ . However, for three typical SiQDs in the range of  $3300\text{--}3700\text{ cm}^{-1}$ , the absorption peak presents gradual widening and enhancement, which is attributed to  $-\text{NH}$  and  $-\text{OH}$  formed during the deamination and carboxyamidine reactions due to the introduction of EDA and EG that induce the variation of functional groups. In addition, noSiQDs@PU films with different noSiQD doping concentrations were prepared and their transmittance spectra were tested (Figure S3), where the  $T_{\text{UV}}$  value of noSiQDs@PU film (thickness, 0.035 mm) decreases to almost 0% for the transmittance of UVB (280–320 nm) and less than 2% for the transmittance of UVA (320–

400 nm) at a dosage of 0.8 vol %, which is much lower than the advising dosage of 3–5% for commercial UV absorber.

In short, the organic groups on SiQDs surface and silicon cores induce subsequent changes in the transition energy levels of  $n-\pi^*$  and  $\pi-\pi^*$  and show that the synergistic effect of CA-Na and EDA causes widening of UV absorption band and improvement of the absorption efficiency. The presence of  $-\text{OH}$  groups on SiQDs surface is advantageous for enhancing the absorption of UVB so that they achieve full-band UV absorption, which indicates the huge application potential of noSiQDs in anti-UV products.

**Qualitative Analysis of noSiQDs with Full-Band UV Absorption.** The high-resolution transmission electron microscopy (HRTEM) image in Figure 3a shows that the average particle size of regular sphere noSiQDs is appropriately 4–6 nm (Figure S4), which shows that it will be suitable for high transparency, low haze, and high clarity values of products blended with noSiQDs, and the lattice stripe radius shown in Figure 3b is 0.23 nm, which will be the identification between SiQDs and CDs compared to that of 0.21 nm for CDs.<sup>35</sup> Furthermore, the absorption spectra of silicon and carbon quantum dots after adding NaOH aqueous solution (Figure S5) confirm that the as-prepared noSiQDs should be silica quantum dots because of which NaOH is incapable of dissolving CDs. The X-ray diffraction (XRD) pattern shown in Figure 3c illustrates that noSiQDs compared to that of the (100) plane presents the same crystalline structure as majorly reported for various types of CDs and SiQDs.<sup>36,37</sup>

Then, to further confirm whether the measured signal for UV absorption originates from functional groups on noSiQDs surface, the X-ray photoelectron spectroscopy (XPS) measurement of noSiQDs underwent dialysis and freeze drying was performed. As shown in Figure 3d, the XPS survey spectrum of noSiQDs sample demonstrates five main peaks and a weak peak, which correspond to Si 2s, Si 2p, C 1s, O 1s, O 2s, and N 1s elements, indicating that the noSiQDs are mainly composed of Si, C, O, and N elements, and the corresponding atom weight percentages are 28.7, 46.9, 20.9, and 13.5% from energy-dispersive X-ray spectroscopy (EDS) (Figure S6). It can be seen that the high-resolution XPS images of C 1s shown in Figure 3e confirm C–C (284.0 eV), C–N (285.5 eV), C–O (286.0 eV), and C=O (288.5 eV) bonds,<sup>38,39</sup> and XPS images of Si 2p shown in Figure 3f present that the chemical bond composition only includes the two bonds of Si–C (102.3 eV) and Si–O

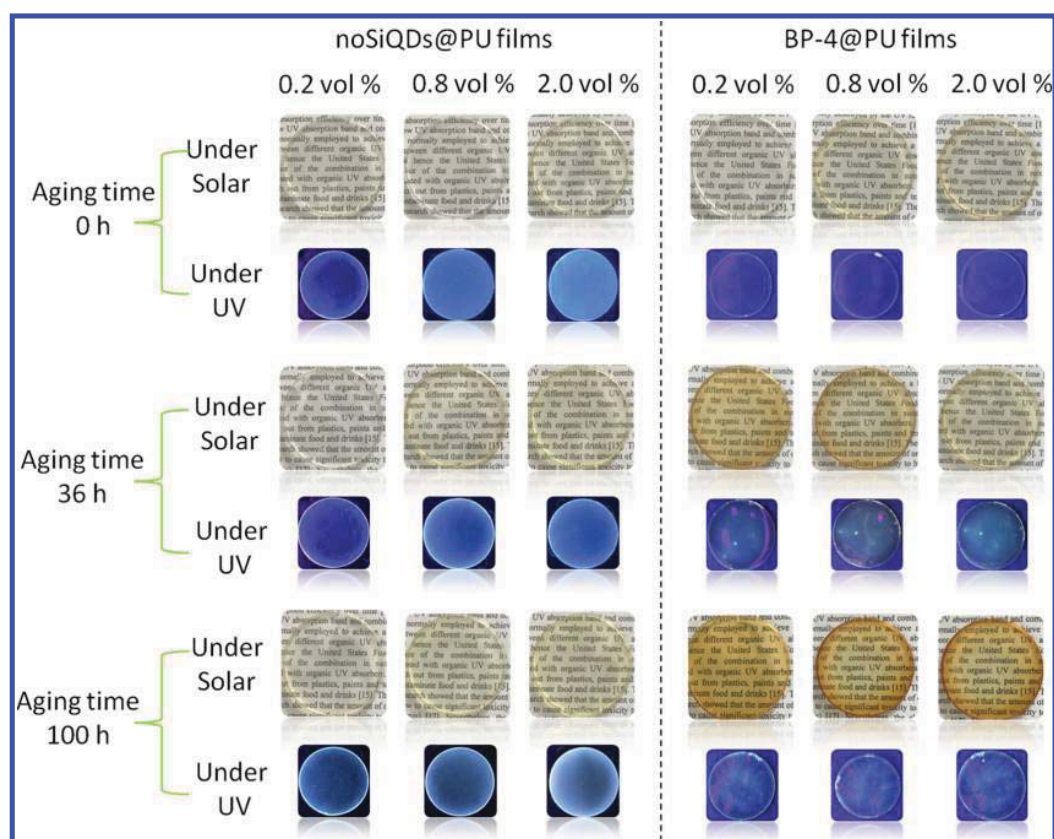


**Figure 5.** Yellowing and corresponding fluorescence overview of noSiQDs@PU films with three concentrations of noSiQDs under radiation of xenon lamp with power of 6000 W for 0, 36, and 100 h. In contrast, the same treatments and measurements of BP-4@PU films with the same concentration of BP-4 were carried out.

(103.0 eV),<sup>38,40</sup> which are all from the raw material (silane), indicating that on the noSiQDs surface, there are no chemical bonds between Si and other elements such as N formed during reaction. The N 1s spectra in Figure 3h confirm the existence of abundant nitrogen heterocyclic, including amino N (399.1 eV) and pyrrolic N (401.6 eV).<sup>29</sup> The O 1s high-resolution spectra shown in Figure 3g can be divided into O–Si (531.4 eV), O–C (532.7 eV), and O–H (534.3 eV) bond species.<sup>30</sup> All of the above XPS image analyses indicate that there are rich functional groups on SiQDs surface, which decide the performance of UV absorption together with SiQDs core and are well correlated to FT-IR data.

Due to the characteristic of easy agglomeration for most of quantum dots, which causes a decrease in UV absorption efficiency and yellowing, for practical application, we studied the  $\zeta$ -potentials of noSiQDs with different concentrations in water, ethanol, and DMF. The results in Figure 3i show that the absolute values of the  $\zeta$ -potentials show a gradual increasing trend with the enhancement of noSiQDs doping concentration in varying solvents, making sure the potential applications such as sunscreen as UV absorbers.

**Stability of UV Absorption.** To simulate the actual application environmental conditions, we investigated the stability of UV absorption property of noSiQDs under varying temperature and pH and their corresponding change law of fluorescence. Figure 4a presents the variation of UV transmittance spectra of 2.0 vol % noSiQDs@PU films under solar radiation with increase of temperature from  $-18$  to  $150$  °C. Obviously, when the processing temperature is  $-18$  °C, the UV

transmittance (280–400 nm) decreases to approximately 0% the same efficiency as 25 and  $150$  °C while keeping excellent visible transmittance. Subject to the embrittlement and yellowing temperature of PU films, if better temperature-resistant polymer was used as matrix, the as-prepared noSiQDs will still keep stable UV absorption efficiency under higher temperature because of the synthesis temperature at  $200$  °C. Usually, chemical-added UV absorbers to prevent decomposition are used in outdoor environment, which requires exceedingly good acid and alkali resistance for UV absorbers. On the basis of the background, we have studied the UV absorption property of noSiQDs aqueous solution under varying pH values shown in Figure 4b. When the pH value increases to 13 from 7, the UV absorption spectra show blue shift wholly at an amplitude of  $\sim 12$  nm compared to pH < 7, and there is a distinct decrease of transmitted spectral intensity in the range of 300–350 nm. From the inset graph in Figure 4b, it can be seen that under strong acidic condition, the UV absorption efficiency slightly decreases in contrast to pH > 5, but still keeps high UV absorption efficiency.

To verify the correlation between UV absorption and fluorescence performance, we further characterized the fluorescence spectra under varying pH as shown in Figure 4c. Interestingly, there presents the strongest luminescent intensity under neutral condition, which gradually decreases with increasing or decreasing pH value, indicating that strong acid and alkali can quench the fluorescence of noSiQDs, but have nearly no effect on UV absorption efficiency. Thus, noSiQDs have outstanding stability under high temperature and strong

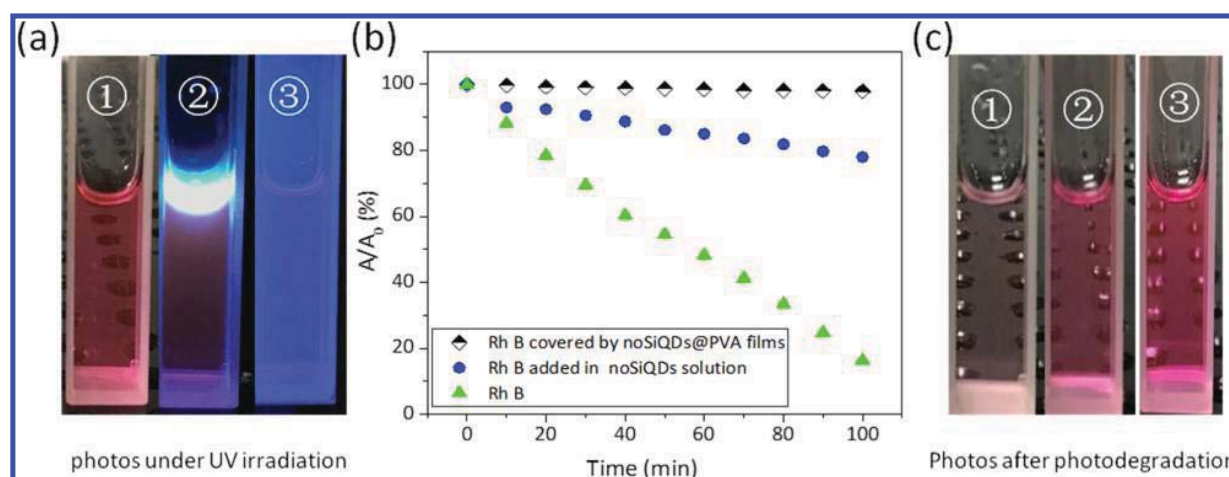


**Figure 6.** Photographs under UV irradiation (a), variations of absorption intensity at 550 nm (b), and the corresponding photographs after photodegradation (c) of pure RhB, adding 0.8 vol % noSiQDs in pure RhB and coating 0.8 vol % noSiQDs@PVA emulsion on pure RhB.

**Table 1.** Analysis of the UV Blocking Rate, Corresponding SPF, and Visible Transmittance of noSiQDs@PU Films

sample	blocking rate (%)			SPF	transmittance (%) 400–780 nm
	UV	UVB	UVA		
pure PU	0	0	0	0	100.00
noSiQDs: 0.1 vol %	50.59	62.45	44.66	3.50	98.12
noSiQDs: 0.2 vol %	75.09	82.79	71.24	6.25	97.93
noSiQDs: 0.4 vol %	80.92	95.20	73.79	22.50	97.85
noSiQDs: 0.8 vol %	89.92	99.55	85.10	>50.00	97.41
noSiQDs: 1.6 vol %	94.47	99.97	91.72	>50.00	96.67
noSiQDs: 2.0 vol %	98.83	100.00	98.25	>50.00	94.22

acid and alkali, which indicates that noSiQDs are suitable for most of practical applications.

**Comparison of Antiyellowing Performance.** Yellowing is caused by photooxidation or photodegradation of polymers upon UV irradiation, which is a common phenomenon especially for those polymers with aromatic structure,<sup>41</sup> and it annually brings huge economic losses. Generally, organic absorbers, such as UV-531, UV-327, Tinuvin series, etc., are most commonly used to prevent the yellowing of polymers by absorbing UV radiation energy.<sup>42,43</sup> To mitigate yellowing of polymers, 1H,1H,2H,2H-perfluorooctanol and nanocrystalline cellulose with well-deserved environmental compatibility and biodegradability were found to be introduced into PU to improve their yellowing resistance,<sup>44,45</sup> but it has very little effect and faces higher cost.

Here, to assess the performance of antiyellowing of noSiQDs and dissimilarity with BP-4, we chose PU as matrix to prepare noSiQDs@PU and BP-4@PU films with the same concentrations of 0.2, 0.8, and 1.6 vol % and carried out the accelerated aging test under radiation of a xenon lamp with power of 6000 W for 0, 36, and 100 h, respectively. As shown in Figure 5, for noSiQDs@PU or BP-4@PU films, there is almost no difference in the initial transparency or light transmittance under natural light, and the difference between them is that the brightness of noSiQDs@PU films under UV irradiation exhibits regular enhancement as the doping concentration increases. However, with extension of the aging time, the yellowing appears to gradually deepen and is especially obvious for 0.2 vol % BP-4@PU films. There is almost no yellowing for noSiQDs@PU films, and there is a slight decrease of fluorescence intensity and visible transmittance, whereas no fluorescence is observed for BP-4@

PU films. The distinction between noSiQDs@PU and BP-4@PU is mainly responsible for the fact that noSiQDs have a wider UV absorption band, including UVA and UVB, than BP-4 (Figure S7) and they can absorb nearly 100% UV radiation from xenon lamp at the same doping concentration with BP-4 in PU. In short, the noSiQDs exhibit better antiyellowing performance than BP-4 due to their excellent UV absorption efficiency and full-band UV absorption, but because of that, the synthesis of noSiQDs on a large scale is relatively expensive compared to zinc oxide or titanium dioxide nanoparticles, which indicates that the commercial potential of noSiQDs as a novel UV absorber only appears in the fields of high-end products such as sunscreen cosmetics.

**Resistance of Photocatalytic Activity.** The photocatalytic activities of noSiQDs were determined by the photocatalytic degradation of RhB under lateral UV radiation with a power of 450 W. Figure 6a shows the photographs of three samples under UV radiation at the initial time; obviously, there present three kinds of fluorescent states corresponding to the existing forms (locations ①, ②, ③) of noSiQDs. With the extension of UV radiation time, the decay curves of the absorption peak of RhB aqueous solutions present marked difference, as shown in Figure 6b. Pure RhB aqueous solution almost completely degraded after 100 min of UV irradiation; nevertheless, for RhB aqueous solution added 0.8 vol % noSiQDs, only approximately 20% of degradation rate was obtained, which is assigned to the fact that noSiQDs in RhB aqueous solution just form an obstacle-like “fishing net” to prevent UV radiation, but it is unable to provide 100% protection. Interestingly, when noSiQDs coated the RhB aqueous solution by the matrix of poly(vinyl alcohol) (PVA), a layer-like “cloth” was obtained, which is extremely beneficial to



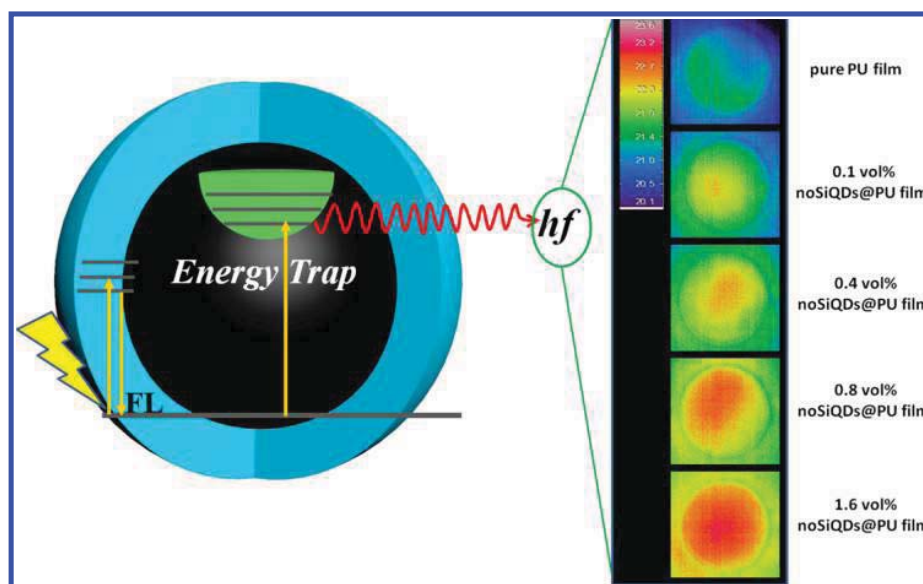


**Figure 7.** Mechanism illustration of noSiQDs as UV absorber (left), and infrared images of PU films with different doping concentrations of fluorescence-quenched noSiQDs (right).

prevent UV radiation so that there is only slight photo-degradation, which is far better than ZnO QD@SiO<sub>2</sub> nanoparticles in resistance of photocatalytic activity of RhB.<sup>46</sup> Under solar light, the corresponding graphical results of photo-degradation after 100 min of UV irradiation are clearly shown in Figure 6c.

**Potential Application in Sunscreen.** Actually, various organic chemical UV absorbers, nano-TiO<sub>2</sub>, and ZnO are widely used in sunscreen cosmetics.<sup>11,47,48</sup> However, there exist drawbacks of narrow absorption range and more or less toxicity on skin for most of chemical absorbers.<sup>49,50</sup> Here, to evaluate whether the noSiQDs have sun protection function (SPF), we theoretically calculated the sun protection parameters according to eqs 1–4.

As shown in Table 1, as the doping concentration increases, the blocking rate including UVA, UVB, and the full UV region gradually increases, and when the dosage is 0.8 vol %, according to the curve between SPF and UVB blocking rate, the corresponding SPF reaches above 50, which is far higher than many commercial sunscreen cosmetics. The UVA sun protection index theoretically calculated can reach PA+++, which means that an effective protection from black skin is induced by UVA. Importantly, visible light (400–780 nm) transmittance has been maintained above 90% even if the dosage is 2.0 vol %, which shows that it is particularly suitable for people of various skin colors and not like TiO<sub>2</sub> and ZnO that will whiten the human skin. Consequently, the performance of full-band UV absorption and outstanding absorption efficiency for noSiQDs manifests that it is a potential revolutionary of UV absorbers used in sunscreen cosmetics. Of course, due to the possible existence of polyaromatic carbons with carcinogens during the synthesis and the quantum size of noSiQDs that possibly penetrate into the skin inducing potential risk, further studies need to be conducted on application in sunscreen cosmetics.

**Mechanism of UV Absorption.** On the basis of the relationship between the UV transmittance spectra, functional groups, and fluorescence properties of silicon quantum dots described above, we propose the mechanism model of UV absorption of noSiQDs as shown in Figure 7 (left). We think

that the full-band UV absorption should originate from  $n \rightarrow \pi^*$  transition and  $\Gamma \rightarrow \Gamma$  direct band gap transition, which correspond to the transitions of fluorophores on noSiQDs surface and noSiQDs core, respectively, and there are mainly three pathways to absorb or block UV radiation, which are detailed as follows.

The first pathway is that huge numbers of noSiQDs particles can effectively scatter part of UV light, because of which, based on the particle size of 4–6 nm of noSiQDs, the dimensionless scale number of  $a$  is far much less than 0.1 of the requirement of Rayleigh scattering, and when the distance between noSiQDs particles is less than  $R_0$  (Figure S8), the wave function overlaps so that their excited-state energy transfers into energy traps in a nonradiation manner. The pathway II is the UV absorption of electronic transition from ground state to excited state along with strong fluorescence emission. To check whether it is the primary reason of UV absorption, we quenched the fluorescence by adjusting the pH value to high alkalinity or acidity and tested the corresponding UV absorption spectra as shown in Figure S9; the results exhibited that the maximum UV transmittance only decreases by about 2%, whereas fluorescence intensity decays by 99%. Apparently, fluorescent absorption is not the fundamental cause of UV absorption.

For further confirmation, we carried out the measurement of infrared imaging of fluorescence-quenched noSiQDs@PU films as shown in Figure 7 (right) and found that there was a distinct heat effect for noSiQDs@PU film compared to pure film. We presented that higher the concentration, stronger the thermal effect. Thus, we think that the origin of UV absorption should be attributed to  $\Gamma \rightarrow \Gamma$  direct band gap transition, which has an extremely high capacity to absorb UV light<sup>51,52</sup> and release it as thermal radiation.

## CONCLUSIONS

In summary, we have developed a one-pot bottom-up strategy for the synthesis of (N, OH)-functionalized SiQDs. Significantly, the as-prepared noSiQDs exhibit full-band UV absorption by introduction of  $-\text{NH}_2$  and  $-\text{OH}$  groups and outstanding UV absorption efficiency and present good thermal

stability and stable UV absorption efficiency even under strong acid and alkali conditions. Experiments reveal that noSiQDs are very effective in preventing yellowing of PU, which is better than BP-4, inhibiting photocatalytic degradation of RhB, and protecting the human skin from UV radiation based on outstanding sun protection parameters. Furthermore, we propose the UV absorption mechanism of noSiQDs and confirm that the thermal radiation transition's absorption plays a fundamental role that is responsible for the  $\Gamma \rightarrow \Gamma$  direct band gap transition originating from the noSiQDs core. Consequently, the present full-band UV absorbent noSiQDs facilitate potential applications in many fields as UV absorber and will be revolutionary of water-soluble UV absorbers.

## MATERIALS AND METHODS

**Chemicals.** Sodium citrate (AR), rhodamine B, 1-[3-(trimethoxysilyl) propyl]urea (97%), ethylene glycol (99%), ethanediamine (99%), poly(vinyl alcohol) (AR, molecular weight: 72 600–81 400), and BP-4 (98%) were purchased from Aladdin Industrial Corporation. Polyurethane was purchased from Rouse Industries, Inc. All reagents were used without further purification.

**Preparation of iSiQDs.** CA-Na (0.8 g) was dissolved in deionized water (28 mL), then 1-[3-(trimethoxysilyl) propyl]urea (1.5 mL) was added to form a mixed solution, and finally, the mixed solution was transferred into a poly(tetrafluoroethylene) hydrothermal reactor (40 mL) and heated at 200 °C for 12 h.

**Preparation of nSiQDs.** The procedure is the same as the iSiQDs synthesis except for the addition of EDA (1.0 mL).

**Preparation of noSiQDs.** On the basis of the preparation of nSiQDs, the solvent was changed to be a mixed solvent with 40 vol % water and 60 vol % EG. The whole reaction solution was cooled to room temperature naturally, filtered (using a water-phase needle filter with a hole diameter of 0.22  $\mu\text{m}$ ), dialyzed for 24 h (using a dialysis bag with a molecular weight of 1000), and suspension-steamed at 70 °C under vacuum.

**Preparation of noSiQDs@PU Composite Films.** Water-soluble PU was blended with 0, 2, 4, 8, 16, 32, and 40  $\mu\text{L}$  of noSiQDs. Pure PU and noQD@PU emulsion were obtained, then transferred into a glass dish (coating amount: 0.05 g/cm<sup>2</sup>) and dried at 80 °C for 2 h. Finally, the films with concentrations of 0, 0.1, 0.2, 0.4, 0.8, 1.6, and 2.0 vol % noSiQDs were obtained.

**Preparation of BP-4@PU Composite Films.** The procedure is the same as the preparation of noSiQDs@PU composite films except for the replacement of noSiQD by BP-4.

**UV Blocking Rate Calculation.** UV transmittance spectra of noSiQDs@PU composite films were recorded by a UV–vis spectrofluorometer using PU blank film as the reference. Then, the UV blocking rates of UV ( $B_{\text{UV}}$ ), UVA ( $B_{\text{UVA}}$ ), and UVB ( $B_{\text{UVB}}$ ) and the visible (400–780 nm) transmittance ( $T_{\text{vis}}$ ) were calculated according to eqs 1–4 as follows

$$B_{\text{UV}} = \frac{S_0 - S_1}{S_0} = \frac{\int_{280}^{400} Q(\lambda) d\lambda}{\int_{280}^{400} Q_0(\lambda) d\lambda} \times 100\% \quad (1)$$

$$B_{\text{UVA}} = \frac{A_0 - A_1}{A_0} = \frac{\int_{320}^{400} Q(\lambda) d\lambda}{\int_{320}^{400} Q_0(\lambda) d\lambda} \times 100\% \quad (2)$$

$$B_{\text{UVB}} = \frac{M_0 - M_1}{M_0} = \frac{\int_{280}^{320} Q(\lambda) d\lambda}{\int_{280}^{320} Q_0(\lambda) d\lambda} \times 100\% \quad (3)$$

$$T_{\text{vis}} = \frac{R_1}{R_0} = \frac{\int_{400}^{780} Q(\lambda) d\lambda}{\int_{400}^{780} Q_0(\lambda) d\lambda} \times 100\% \quad (4)$$

where  $Q(\lambda)$  and  $Q_0(\lambda)$  represent the transmittance spectra of noSiQD@PU composite and pure PU films, respectively, and  $S_0$ ,  $S_1$ ,  $A_0$ ,  $A_1$ ,  $M_0$ ,  $M_1$ ,  $R_0$ , and  $R_1$  represent spectral integral areas of  $Q_0(\lambda)$  and  $Q(\lambda)$  in different wavelength intervals.

**Characterization.** The transmittance spectra were recorded by a UV–vis spectrofluorometer (UV-2550, Shimadzu). The thicknesses of the films were measured by a vernier caliper, and infrared imaging of PU and noSiQDs@PU films was performed by an infrared imager (RS00EXPro, AVIO, Japan). The FT-IR spectra of noSiQDs were recorded on a Nicolet Avatar 360 FT-IR spectrophotometer. The XRD pattern was collected using a persee XD-2X/M4600. XPS images were detected by employing an X-ray photoelectron spectrometer (AXIS ULTRA DLD, Kratos). The HRTEM images were obtained by a JEOL-2010 electron microscope. The absorbance intensity was determined with a UV–vis spectrophotometer. Fluorescence spectra curves were recorded with a fluorescence spectrofluorometer (F-7000, Hitachi). Percentage of elements was recorded by energy-dispersive X-ray spectroscopy (EDS) (EDX-GP, Shimadzu, Japan).

## ASSOCIATED CONTENT

### Supporting Information

The Supporting Information is available free of charge on the ACS Publications website at DOI: 10.1021/acsami.8b20138.

Curve of SPF versus the blocking rate of UVB; transition energy level diagram; size distribution; EDS analysis; transmittance, absorption, fluorescence, and XPS images; schematic of energy transmission; and infrared images (PDF)

## AUTHOR INFORMATION

### Corresponding Authors

\*E-mail: [thucf@scau.edu.cn](mailto:thucf@scau.edu.cn). Tel: +86-20-85283133. Fax: +86-20-85282603 (C.H.)

\*E-mail: [tleibf@scau.edu.cn](mailto:tleibf@scau.edu.cn). Tel: +86-20-85283133. Fax: +86-20-85282603 (B.L.)

\*E-mail: [tluiyl@scau.edu.cn](mailto:tluiyl@scau.edu.cn). Tel/Fax +86-20-85283133.

### ORCID

Xuejie Zhang: 0000-0002-4029-7000

Jianle Zhuang: 0000-0002-4649-1939

Chaofan Hu: 0000-0003-2311-8733

Bingfu Lei: 0000-0002-6634-0388

Yingliang Liu: 0000-0002-5378-3577

### Notes

The authors declare no competing financial interest.

## ACKNOWLEDGMENTS

The present work was supported by the National Natural Science Foundations of China (Grant nos 21571067, 21671070, and 51402207), the Project for Construction of High-level University in Guangdong Province of China, the Key Foundation for Basic and Application Research in Higher Education of Guangdong, China (No. 2017KZDXM005), and the Guangzhou Science & Technology Project, China (No. 201707010033).

## REFERENCES

- (1) Cohen, S.; Haham, H.; Pellach, M.; Margel, S. Design of UV-Absorbing Polypropy Films with Polymeric Benzotriazole based Nano- and Microparticle Coatings. *ACS Appl. Mater. Interfaces* **2017**, *9*, 868–875.
- (2) McKenzie, R.; Connor, B.; Bodeker, G. Increased Summertime UV Radiation in New Zealand in Response to Ozone Loss. *Science* **1999**, *285*, 1709–1711.

- (3) Capocci, G.; Hubbard, M. A radically new UV stabilizer for Flexible PVC Roofing Membranes. *J. Vinyl Addit. Technol.* **2005**, *11*, 91–94.
- (4) Sendra, M.; Sánchez-Quiles, D.; Blasco, J.; Moreno-Garrido, I.; Lubián, L. M.; Pérez-García, S.; Tovar-Sánchez, A. Effects of TiO<sub>2</sub> Nanoparticles and Sunscreens on Coastal Marine Microalgae: Ultra-violet Radiation is Key Variable for Toxicity Assessment. *Environ. Int.* **2017**, *98*, 62–68.
- (5) Lewicka, Z. A.; Yu, W. W.; Oliva, B. L.; Contreras, E. Q.; Colvin, V. L. Photochemical Behavior of Nanoscale TiO<sub>2</sub> and ZnO Sunscreen Ingredients. *J. Photochem. Photobiol., A* **2013**, *263*, 24–33.
- (6) Parisi, O. I.; Aiello, D.; Casula, M. F.; Puoci, F.; Malivindi, R.; Scrivano, L.; Testa, F. Mesoporous nanocrystalline TiO<sub>2</sub> Loaded with Ferulic acid for Sunscreen and Photo-protection: Safety and Efficacy Assessment. *RSC Adv.* **2016**, *6*, 83767–83775.
- (7) Li, M.; Li, G.; Jiang, J.; Zhang, Z. S.; Dai, X.; Mai, K. C. Ultraviolet Resistance and Antimicrobial Properties of ZnO in the Polypropylene Materials: A Review. *J. Mater. Sci. Technol.* **2015**, *31*, 331–339.
- (8) Wang, C.; Zuo, S. X.; Liu, W. J.; Yao, C.; Li, X. Z.; Li, Z. Y. Preparation of Rutile TiO<sub>2</sub>@Avobenzon Composites for Further Enhancement of Sunscreen Performance. *RSC Adv.* **2016**, *6*, 111865–111871.
- (9) Tuzuki, T.; Innes, B.; Dawkins, H.; Dunlop, J.; Trotter, G.; Nearn, M. R.; McCormick, P. G. Nanotechnology and the Cosmetic Chemist. *Cosmet. Aerosol. Toilet. Aus.* **2003**, *15*, 44–53.
- (10) Koziej, D.; Fischer, F.; Kranzlin, N.; Caseri, W. R.; Niederberger, M. Nonaqueous TiO<sub>2</sub> Nanoparticle Synthesis: A UV-Absorbing Composite Films. *ACS Appl. Mater. Interfaces* **2009**, *1*, 1097–1104.
- (11) Zayat, M.; Garcia-parejo, P.; Levy, D. Preventing UV-Light Damage of Light Sensitive Materials Using a Highly Protective UV-Absorbing Coating. *Chem. Soc. Rev.* **2007**, *36*, 1270–1281.
- (12) Pierzchała, K.; Lekka, M.; Magrez, A.; Kulik, A. J.; Forro, L.; Sienkiewicz, A. Photocatalytic and Phototoxic Properties of TiO<sub>2</sub>-Based Nanofilaments: ESR and AFM Assays. *Nanotoxicology* **2012**, *6*, 813–824.
- (13) Li, S. H.; Toprak, M. S.; Jo, Y. S.; Dobson, J.; Kim, D. K.; Muhammed, M. Bulk Synthesis of Transparent and Homogeneous Polymeric Hybrid Materials with ZnO Quantum Dots and PMMA. *Adv. Mater.* **2007**, *19*, 4347–4352.
- (14) Eita, M.; Wagberg, L.; Muhammed, M. Spin-Assisted Multilayers of Poly (methyl methacrylate) and Zinc Oxide Quantum Dots for Ultraviolet-Blocking Applications. *ACS Appl. Mater. Interfaces* **2012**, *4*, 2920–2925.
- (15) Soumya, S.; Sheemol, V. N.; Amba, P.; Mohamed, A. P.; Ananthakumar, S. Sn and Ag Doped ZnO Quantum Dots with PMMA by in Situ Polymerization for UV/IR Protective, Photochromic Multifunctional Hybrid Coatings. *Sol. Energy Mater. Sol. Cells* **2018**, *174*, 554–565.
- (16) Han, H.; Cai, Y. W.; Liang, J. G.; Sheng, Z. H. Interactions Between Water-Soluble CdSe Quantum Dots and Gold Nanoparticles Studied by UV-Visible Absorption Spectroscopy. *Anal. Sci.* **2007**, *23*, 651–654.
- (17) Zhuang, S. D.; Xu, X. Y.; Yu, J. Y.; Feng, B.; Xu, W.; Hu, J. G. Transparent SnO<sub>2</sub> QDs-Based Multifunctional Glass for Ultraviolet-Blocking and Enhanced Hydrophobicity. *Mater. Lett.* **2014**, *128*, 291–294.
- (18) Fu, X.; Ilanchezhian, P.; Kumar, G. M.; Cho, H. D.; Zhang, L.; Chan, A. S.; Lee, D. J.; Panin, G. N.; Kang, T. W. Tunable UV-Visible Absorption of SnS<sub>2</sub> Layered Quantum Dots Produced by Liquid Phase Exfoliation. *Nanoscale* **2017**, *9*, 1820–1826.
- (19) Xie, Z.; Du, Q. Q.; Wu, Y. Z.; Hao, X. P.; Liu, C. Y. Full-Band UV Shielding and Highly Daylight Luminescent Silane-Functionalized Graphene Quantum Dot Nanofluids and Their Arbitrary Polymerized Hybrid Gel Glasses. *J. Mater. Chem. C* **2016**, *4*, 9879–9886.
- (20) Hess, S. C.; Permatasari, F. A.; Fukazawa, H.; Schneider, E. M.; Balgis, R.; Ogi, T.; Okuyama, K.; Stark, W. J. Direct Synthesis of Carbon Quantum Dots in Aqueous Polymer Solution: One-Pot Reaction and Preparation of Transparent UV-Blocking Films. *J. Mater. Chem. A* **2017**, *5*, 5187–5194.
- (21) Feng, X.; Zhao, Y. F.; Jiang, Y. Q.; Miao, M.; Cao, S. M.; Fang, J. H. Use of carbon dots to enhance UV-blocking of transparent nanocellulose films. *Carbohydr. Polym.* **2017**, *161*, 253–260.
- (22) Catalan, J.; Fabero, F.; Guijarro, M. S.; Claramunt, R. M.; Maria, M. D.; Concepcion Foces-foces, M. D.; Cano, F. H.; Elguero, J.; Sastre, R. Photoinduced Intramolecular Proton Transfer as The Mechanism of Ultraviolet Stabilizers: A Reappraisal. *J. Am. Chem. Soc.* **1990**, *112*, 747–759.
- (23) Nakata, H.; Murata, S.; Filatreau, J. Occurrence and Concentrations of Benzotriazole UV Stabilizers in Marine Organisms and Sediments from the Ariake Sea, Japan. *Environ. Sci. Technol.* **2009**, *43*, 6920–6926.
- (24) Paerson, M. J.; Robb, M. A.; et al. Theoretical Study of Benzotriazole UV Photostability: Ultrafast Deactivation through Coupled Proton and Electron Transfer Triggered By a Charge-Transfer State. *J. Am. Chem. Soc.* **2004**, *126*, 2912–2922.
- (25) Pospíšil, J. Functionalized Oligomers and Polymers as Stabilizers for Conventional Polymers. *Adv. Polym. Sci.* **1991**, *101*, 65–167.
- (26) Nakagawa, Y.; Suzuki, T.; Tayama, S. Metabolism and Toxicity of Benzophenone in Isolated Rat Hepatocytes and Estrogenic Activity of its Metabolites in MCF-7 Cells. *Toxicology* **2000**, *156*, 27–36.
- (27) Huang, Z.; Ding, A. S.; Guo, H.; Lu, G. L.; Huang, X. Y. Construction of Nontoxic Polymeric UV-Absorber with Great Resistance to UV-Photoaging. *Sci. Rep.* **2016**, *6*, No. 25508.
- (28) Zhong, Y. L.; Peng, F.; Bao, F.; Wang, S. Y.; Ji, X. Y.; Yang, L.; Su, Y. Y.; Lee, S. T.; He, Y. Large-Scale Aqueous Synthesis of Fluorescent and Biocompatible Silicon Nanoparticles and Their Use as Highly Photostable Biological Probes. *J. Am. Chem. Soc.* **2013**, *135*, 8350–8356.
- (29) Wu, F. G.; Zhang, X. D.; Kai, S. Q.; Zhang, M. Y.; Wang, H. Y.; Myers, J. N.; Weng, Y. X.; Liu, P. D.; Gu, N.; Chen, Z. One-Step Synthesis of Superbright Water-Soluble Silicon Nanoparticles with Photoluminescence Quantum Yield Exceeding 80%. *Adv. Mater. Interfaces* **2015**, *2*, No. 1500360.
- (30) Anderson, R. T.; Zang, X. N.; Fernando, R.; Dzara, M. J.; Ngo, C. L.; Sharps, M.; Pinals, R.; Pylypenko, S.; Lusk, M. T.; Sellinger, A. Direct Conversion of Hydride-to Siloxane-Terminated Silicon Quantum Dots. *J. Phys. Chem. C* **2016**, *120*, 25822–25831.
- (31) Fujii, M.; Sugimoto, H.; Kano, S. Silicon Quantum Dots with Heavily Boron and Phosphorus Codoped Shell. *Chem. Commun.* **2018**, *54*, 4375–4389.
- (32) Gu, W.; Liu, X. K.; Pi, X. D.; Dai, X. L.; Yao, L.; Yao, L.; Li, D. S.; Jin, Y. Z.; Xu, M. S.; Yang, D. R.; Qin, G. G. Silicon-Quantum-Dot Light-Emitting Diodes with Interlayer-Enhanced Hole Transport. *IEEE Photonics J.* **2017**, *9*, 1–11.
- (33) Li, Z.; Ren, X. L.; Hao, C. X.; Meng, X. W.; Li, Z. H. Silicon Quantum Dots with Tunable Emission Synthesized via One-Step Hydrothermal Method and Their Application in Alkaline Phosphatase Detection. *Sens. Actuators, B* **2018**, *260*, 426–431.
- (34) Guo, Y. M.; Zhang, L. F.; Cao, F. P.; Mang, L. H.; Lei, X. L.; Cheng, S. J.; Song, J. T. Hydrothermal Synthesis of Blue-Emitting Silicon Quantum Dots for Fluorescent Detection of Hypochlorite in Tap Water. *Anal. Methods* **2016**, *8*, 2723–2728.
- (35) Zhang, T.; Zhu, J. Y.; Zhai, Y.; Wang, H.; Bai, X.; Dong, B.; Wang, H. Y.; Song, H. W. A Novel Mechanism for Red Emission Carbon Dots: Hydrogen Bond Dominated Molecular States Emission. *Nanoscale* **2017**, *9*, 13042–13051.
- (36) Cui, M. J.; Ren, S. M.; Xue, Q. J.; Zhao, H. C.; Wang, L. P. Carbon Dots as New Eco-Friendly and Effective Corrosion Inhibitor. *J. Alloys Compd.* **2017**, *726*, 680–692.
- (37) Lopez, T.; Mangolini, L. Low Activation Energy for the Crystallization of Amorphous Silicon Nanoparticles. *Nanoscale* **2014**, *6*, 1286–1294.
- (38) Zhou, T.; Anderson, R. T.; Li, H. S.; Bell, J.; Yang, Y. A.; Gorman, B. P.; Pylypenko, S.; Lusk, M. T.; Sellinger, A. Bandgap Tuning of Silicon Quantum Dots by Surface Functionalization with Conjugated Organic Groups. *Nano Lett.* **2015**, *15*, 3657–3663.
- (39) Anderson, R. T.; Zang, X. N.; Fernando, R.; Dzara, M. J.; Ngo, C.; Sharps, M.; Pinals, R.; Pylypenko, S.; Lusk, M. T.; Sellinger, A. Direct



Conversion of Hydride- to Siloxane-Terminated Silicon Quantum Dots. *J. Phys. Chem. C* **2016**, *120*, 25822–25831.

(40) Han, Y. X.; Chen, Y. L.; Liu, J. J.; Niu, X. Y.; Ma, Y. X.; Ma, S. D.; Chen, X. G. Room-Temperature Synthesis of Yellow-Emitting Fluorescent Silicon Nanoparticles for Sensitive and Selective Determination of Crystal Violet in Fish Tissues. *Sens. Actuators, B* **2018**, *263*, 508–516.

(41) Rosu, D.; Rosu, L.; Cascaval, C. N. IR-Change and Yellowing of Polyurethane as A Result of UV Irradiation. *Polym. Degrad. Stab.* **2009**, *94*, 591–596.

(42) Chu, C. C.; Fischer, T. E. Evaluation of Sunlight Stability of Polyurethane Elastomers for Maxillofacial Use. *J. Biomed. Mater. Res.* **1978**, *12*, 347–359.

(43) Jana, R. N.; Bhunia, H. Accelerated Hydrothermal and UV aging of Thermoplastic Polyurethanes. *High Perform. Polym.* **2010**, *22*, 3–15.

(44) Ping, T.; Zhou, Y.; He, Y.; Tang, Y. H.; Yang, J. L.; Akram, M. Y.; Nie, J. Preparation and Characterization of Yellowing Resistance and Low Volume Shrinkage of Fluorinated Polysiloxane Urethane Acrylate. *Prog. Org. Coat.* **2016**, *97*, 74–81.

(45) Zhang, H.; Chen, H. Y.; She, Y.; Zheng, X.; Pu, J. W. Anti-Yellowing Property of Polyurethane Improved by the Use of Surface-Modified Nanocrystalline Cellulose. *BioResources* **2014**, *9*, 673–684.

(46) Wang, X. L.; Zhou, S. X.; Wu, L. M. Facile Encapsulation of SiO<sub>2</sub> on ZnO Quantum Dots and Its Application in Waterborne UV-Shielding Polymer Coatings. *J. Mater. Chem. C* **2013**, *1*, 7547–7553.

(47) Tyner, K. M.; Wokovich, A. M.; Godar, D. E.; Doub, W. H.; Sadrieh, N. The State of Nano-Sized Titanium Dioxide (TiO<sub>2</sub>) May Affect Sunscreen Performance. *Int. J. Cosmet. Sci.* **2011**, *33*, 234–244.

(48) Hüglin, D. Advanced UV Absorbers for the Protection of Human Skin. *Chimia* **2016**, *70*, 496–501.

(49) Dobashi, Y.; Ohkatsu, Y. Dependence of Ultraviolet Absorber's Performance on Ultraviolet Wavelength. *Polym. Degrad. Stab.* **2008**, *93*, 436–447.

(50) Morabito, K.; Shapley, N. C.; Steeley, K. G.; Tripathi, A. Review of Sunscreen and the Emergence of Non-Conventional Absorbers and Their Applications in ultraviolet protection. *Int. J. Cosmet. Sci.* **2011**, *33*, 385–390.

(51) Holmes, J. D.; Ziegler, K. J.; Doty, R. C.; Pell, L. E.; Johnston, K. P.; Korgel, B. A. Highly luminescent Silicon Nanocrystals with Discrete Optical Transitions. *J. Am. Chem. Soc.* **2001**, *123*, 3743–3748.

(52) Warner, J. H.; Hoshino, A.; Yamamoto, K.; Tilley, R. D. Water-Soluble Photoluminescent Silicon Quantum Dot. *Angew. Chem., Int. Ed.* **2005**, *44*, 4550–4554.



# 广东省自然科学奖 证书

为表彰 2021 年度广东省自然科学奖获得者，特颁发此证书。

项目名称: 新型碳材料微纳结构调控和性能研究

奖励等级: 二等奖

获奖者: 胡超凡 (华南农业大学)

粤府证【2022】0048 号

项目编号: Z07-2-01-R04





证书号第 4740874 号



# 发 明 专 利 证 书

发 明 名 称：一种溶剂敏感的多模荧光碳量子点墨水及其制备方法和应用

发 明 人：胡超凡;杨海遥;刘应亮;雷炳富;庄健乐;张学杰

专 利 号：ZL 2019 1 0092285.9

专 利 申 请 日：2019 年 01 月 30 日

专 利 权 人：华南农业大学

地 址：510642 广东省广州市天河区五山路 483 号

授 权 公 告 日：2021 年 10 月 19 日

授 权 公 告 号：CN 109943148 B

国家知识产权局依照中华人民共和国专利法进行审查，决定授予专利权，颁发发明专利证书并在专利登记簿上予以登记。专利权自授权公告之日起生效。专利权期限为二十年，自申请日起算。

专利证书记载专利权登记时的法律状况。专利权的转移、质押、无效、终止、恢复和专利权人的姓名或名称、国籍、地址变更等事项记载在专利登记簿上。



局长  
申长雨

申长雨



第 1 页 (共 2 页)

其他事项参见续页  
328



证书号第 4739252 号



# 发明专利证书

发明名称：一种红色固态荧光碳点及其制备方法和应用

发明人：胡超凡;杨海遥;刘应亮;雷炳富;张学杰;庄健乐

专利号：ZL 2019 1 0091560.5

专利申请日：2019 年 01 月 30 日

专利权人：华南农业大学

地址：510642 广东省广州市天河区五山路 483 号

授权公告日：2021 年 10 月 19 日

授权公告号：CN 109825288 B

国家知识产权局依照中华人民共和国专利法进行审查，决定授予专利权，颁发发明专利证书并在专利登记簿上予以登记。专利权自授权公告之日起生效。专利权期限为二十年，自申请日起算。

专利证书记载专利权登记时的法律状况。专利权的转移、质押、无效、终止、恢复和专利权人的姓名或名称、国籍、地址变更等事项记载在专利登记簿上。



局长  
申长雨

申长雨



第 1 页 (共 2 页)

其他事项参见续页

证书号第3413703号



# 发明专利证书

发明名称：一种溶剂热法制备荧光氧化钨量子点的方法及其制备而成的荧光氧化钨量子点和应用

发明人：胡超凡;刘应亮;战岩;雷炳富;庄健乐;张浩然

专利号：ZL 2017 1 0501762.3

专利申请日：2017年06月27日

专利权人：华南农业大学

地址：510642 广东省广州市天河区五山路483号

授权公告日：2019年06月14日

授权公告号：CN 107416906 B

国家知识产权局依照中华人民共和国专利法进行审查，决定授予专利权，颁发发明专利证书并在专利登记簿上予以登记。专利权自授权公告之日起生效。专利权期限为二十年，自申请日起算。

专利证书记载专利权登记时的法律状况。专利权的转移、质押、无效、终止、恢复和专利权人的姓名或名称、国籍、地址变更等事项记载在专利登记簿上。



局长  
申长雨

申长雨



第1页(共2页)





# 荣誉证书

刘金坤、陈春锦、陈易升、万芷君、林晓敏同学：

在第十二届“华港杯”广东大学生材料创新大赛分赛区决赛中，荣获

三等奖

特发此证，以资鼓励。

作品名称：氧化物缺陷对碳点室温长余辉发光的影晌机制研究

指导教师：胡超凡



二〇二三年三月



# 荣誉证书

钟紫婷、李钰祺、贾宏洁、冉准 同学：

在第十三届“华港杯”广东大学生材料创新大赛分赛区决赛中，荣获

## 三等奖

特发此证，以资鼓励。

作品名称：缺陷诱导的时间依赖型变色长余辉材料

指导教师：胡超凡

承办单位：

中山大学材料科学与工程学院

主办单位：

广东省材料研究学会

二零二四年十月



# 获奖证书

钟紫婷、黄光攀、黄学智、石昆衡 同学

在第十四届“华港杯”广东大学生材料创新大赛中，荣获



特发此证，以资鼓励。

作品名称：《具有紫外、红光双模余辉发射的碳点/铝酸镁复合材料》

指导教师：胡超凡



承办单位：

华南农业大学材料学院



主办单位：  
广东省材料研究学会

二〇二五年十一月





# 获奖证书

曹珏然、李钰祺、徐文跃、吴博、刘静怡 同学

在第十四届“华港杯”广东大学生材料创新大赛中，荣获

## 三等奖

特发此证，以资鼓励。

作品名称：《新型碳点基双介质光致变色材料的合成和多功能应用研究》

指导教师：胡超凡

承办单位：

华南农业大学材料与能源学院



主办单位：

广东省材料研究学会



二〇二五年十一月